Saint Petersburg OPEN 2023

10th International School
and Conference
May 23-26, 2023

10PEN CONFERENCE

# BOOK of ABSTRACTS

## 10th International School and Conference on Optoelectronics, Photonics, Engineering and Nanostructures

May, 23-26, 2023

Saint-Petersburg, Russia

Copyright © by 2023 National Research University Higher School of Economics - St. Petersburg and individual contributors. All rights reserved. No parts of this electronic publication may be multiple copied, stored in a retrieval system or
transmitted in any form or by any means, electronic, mechanical, photocopying, recording or otherwise, without the written permission of the publisher. Single photocopies of single articles may be made for private study or research.

10 th International School and Conference “Saint Petersburg OPEN 2023” on

Optoelectronics, Photonics, Engineering and Nanostructures carries on the tradition of annual conferences and schools organized at St Petersburg Academic University for students, PhD students and young scientists. More detailed information on the School and Conference is presented on https://spb.hse.ru/spbopen/ The Book of Abstracts includes abstracts of contributed works accepted for presentation at the Conference. The volume was composed by HSE University - St. Petersburg from electronic files submitted by the authors. Only minor technical corrections were made by the composers.

Chief Editor: A. E. Zhukov Published by HSE University - St. Petersburg, Soyuza Pechatnikov 16, 190121, St Petersburg, Printed in Russian Federation

**Head of Program Committee**

Alexey E. Zhukov corr. member of the RAS, HSE University, Russia

**Program Committee**

Andrey A. Lipovskii (Peter the Great St.Petersburg Polytechnic University, Russia) George E. Cirlin (Alferov University, Russia)

Valentina V. Zhurikhina (Peter the Great St.Petersburg Polytechnic University, Russia) Natalia V. Kryzhanovskaya (HSE University- St.Petersburg)

**Head of Organizing Committee**

**Alexey E. Zhukov (HSE University- St.Petersburg)**

**Organizing Committee**

Mikhail V. Maximov (Ioffe Institute, Alferov University, Russia)

Andrey A. Lipovskii (Peter the Great St.Petersburg Polytechnic University, Russia)

Valentina V. Zhurikhina (Peter the Great St.Petersburg Polytechnic University, Russia)

Vladimir V. Korenev (Alferov University, Russia)

Eduard I. Moiseev (HSE University- St.Petersburg)

Anastasia Baryshnikova (HSE University- St.Petersburg)

# Conference Schedule

## May 23, 2023 (Tuesday)

15:00–16:00 **Pre-registration, welcome party**
**(Higher School of Economics – St. Petersburg, site on Kantemirovskaya 3)**

## May 24, 2023 (Wednesday)

09:00–10:00 **On-site registration (Higher School of Economics – St. Petersburg, site on Kantemirovskaya 3)**

10:00–10:10 **Opening ceremony**
**Alexey Zhukov** *(Higher School of Economics – St. Petersburg, Russia)*

10:10–10:40 **High-power mid-infrared quantum-cascade lasers and detectors** **Grigorii Sokolovskii** *(Ioffe Institute, Russia)*

10:40–11:10 **Hybrid structures "quantum well-dots": synthesis, properties, applications**
**Alexei Nadtochy** *(Higher School of Economics – St. Petersburg, Russia)*

11:10–11:40 **Observation of stimulated emission at a frequency of 9.5 THz due to suppression of Auger recombination of Dirac fermions in HgCdTe quantum wells**
**Alexander Dubinov** *(IPM RAS, Russia)*

11:40–12:00 **Coffee Break**

12:00–12:30 **Ferrite-garnet films: physical properties and applications - *online*** **Sergey Polulyakh** *(Crimean Federal University, Russia)*

12:30–12:50 **Quantum dot lasers for optical interconnect (preliminary) - *online*** **Vladimir Mikhrin** *(Innolume, Germany)*

12:50–13:20 **Presentations by sponsors**
**Nano-positioners in quantum sensing applications**
**Zivkovic Alina** *(Special Systems. Photonics, Russia)*

13:20–14:00 **Elevator speech session I**

Young scientists explain key idea of their posters in 1 minute presentation using 1-2 slides:

Сомов Артем Игоревич
Баева Мария Григорьевна
Бурмистров Олег Ильич
Чернев Игорь Михайлович
Кузнецов Юрий Михайлович
Song Qinghao

14:00–15:00 **Lunch**

15:00–16:30 **Poster Session I**

1. Lasers, solar cells and other optoelectronic devices
2. Electric, Magnetic and Microwave Devices
3. Crystal growth and structural properties of semiconductor materials and nanostructures

16:30–17:00 **Coffee Break**

17:00–18:00 **Poster Session I**

1. Lasers, solar cells and other optoelectronic devices
2. Electric, Magnetic and Microwave Devices
3. Crystal growth and structural properties of semiconductor materials and nanostructures

## May 25, 2023 (Thursday)

09:00–10:00 **On-site registration**

10:00–10:30 **MBE growth and properties of III-V hybrid nanostructures on the silicon surface** **Rodion Reznik** *(St. Petersburg State University, Russia)*

10:30–11:00 **Surface generation of second optical harmonic in micro- and nanostructures** **Sergey Scherbak** *(Peter the Great St. Petersburg Polytechnic University, Russia)*

11:00–11:30 **Vertical cavity surface emitting lasers for compact atomic sensors** **Sergey Blokhin** *(Ioffe Institute, St. Petersburg, Russia)*

11:30–12:00 **Coffee Break**

12:00–12:30 **Micro-LEDs and key factors determining their efficiency** **Sergey Karpov** *(Soft Impact, Russia)*

12:30–13:00 **III-V semiconductor lasers epitaxially grown on Si for monolithically-integrated Silicon photonics - *online***
**Wang Qi** *(BUPT, China)*

13.00–13.30 **Presentations by sponsors: Scanning probe microscopy integrated with time-resolved photoluminescence imaging**
**Vladislav I. Shcheslavskiy** *(Privolzhsky Research Medical University Becker&Hickl GmbH, PhD NTMDT)*

13:30–14:00 **Elevator speech session II** young scientists explain key idea of their posters in 1 minute presentation using 1-2 slides:

Жуков Михаил Валерьевич
Романова Вероника Вячеславовна
Селиверстов Сергей Валерьевич
Аникина Мария Александровна
Чуманов Иван Викторович
Кашапов Артем Ильясович
Михайловский Михаил Сергеевич
Николаева Александра Владиславовна
Рудаков Артур Олегович
Васильева Ольга Васильевна
Заневская Мария Юрьевна

14:00–15:00 **Lunch**

15:00–16.30 **Poster Session II**

4. Nanophotonics, Spectroscopy, Microcavities, Optics, Plasmonics, Spintronics, Electro- and Magnetooptics
5. Nanobiotechnology, Biophysics and Biophotonics
6. Other Aspects of Nanotechnology

16:30–17:00 **Coffee Break**

17:00–18:00 **Poster Session II**

4. Nanophotonics, Spectroscopy, Microcavities, Optics, Plasmonics, Spintronics, Electro- and Magnetooptics
5. Nanobiotechnology, Biophysics and Biophotonics
6. Other Aspects of Nanotechnology

18:00–18:30 **Closing remarks and award ceremony**
**Alexey Zhukov** *(Higher School of Economics – St. Petersburg, Russia)*

## May 26, 2023 (Friday)

The whole day **Departure, free time**

**Optional: Guided tour at the Int. Lab. of Quantum Optoelectronics, HSE – St Petersburg (11.00-12.00)**

# 1. Lasers, solar cells and other optoelectronic devices

## May 24, 2023

## 15:30 - 18:00 Poster Session I

| | | | | | |
|---|---|---|---|---|---|
| 1-1 | Адам | Юрий | Александрович | Университет ИТМО | Practical realization of free-space continuous-variable quantum key distribution |
| 1-2 | Андрюшкин | Владислав | Васильевич | Университет ИТМО | Effect of sulfide–polyamide passivation on dark currents of the InAlAs/InGaAs/InP avalanche photodiodes |
| 1-3 | Аринушкина | Ксения | Геннадьевна | Санкт-Петербургский государственный университет телекоммуникаций им. проф. М.А. БончБруевича | Features of the operation of a laser profilometer in an automated rolling stock control system |
| 1-5 | Баева | Мария | Григорьевна | СПбАУ РАН им. Ж.И. Алферова | Hybrid perovskite/GaP nanowires solar cells with enhanced photovoltaic performance |
| 1-6 | Баева | Мария | Григорьевна | СПбАУ РАН им. Ж.И. Алферова | Light-Emitting and Light-Detecting Perovskite Electrochemical Cell on Silicon |
| 1-7 | Бекман | Артем | Александрович | ФТИ им. А.Ф. Иоффе | Features of two-state generation in InGaAs/GaAs quantum well-dot lasers |
| 1-8 | Буджемила | Линда | | Санкт-Петербургский политехнический университет Петра Великого | Impedance spectroscopy of the dynamics of charge carriers of CsPbI3 and CsPbBr3 nanoparticles deposited on a tandem solar cells |
| 1-9 | Вильченко | Сеергей | Андреевич | ННГУ им. Лобачевского | KDP crystals as an optical element in highpower laser system |
| 1-10 | Вторыгин | Георгий | Эдуардович | СПбАУ РАН им. Ж.И. Алфёрова | Investigation of electrophysical properties of BP layers grown by PECVD mode |
| 1-11 | Вячеславова | Екатерина | Александровна | СПбАУ РАН им. Ж.И. Алфёров | Heterojunction solar cells based on nanostructured black silicon |
| 1-12 | Герасин | Илья | Сергеевич | МФТИ | ANALYSIS OF NON-IDEALITIES OF QUANTUM STATES FOR TIME-BIN ENCODING |
| 1-13 | Горанская | Светлана | Андреевна | Санкт-Петербургский государственный университет телекоммуникаций им. проф. М.А.Бонч-Бруевича | Новая методика расчета спектральных дифракционных линз для фокусировки лазерного излучения различных длин волн |
| 1-14 | Грязнова | Екатерина | Михайловна | Санкт-Петербургский государственный университет телекоммуникаций им. проф. М.А.Бонч-Бруевича | Two-channel fiber-optic communication line for measuring the parameters of active phased antenna arrays in the far zone a landfill conditions |
| 1-15 | Двуреченский | Александр | Александрович | МФТИ/МИСиС | Influence of detector dead time on the key generation rate in Measurement-DeviceIndependent QKD |
| 1-16 | Джабр | Яра | Джамал | Saint Petersburg Electrotechnical University “LETI” | A Method for Studying of color characteristics of pigments by spectrophotometry |

| | | | | | |
|---|---|---|---|---|---|
| 1-17 | Дмитриева | Диана | Сергеевна | Санкт-Петербургский государственный университет телекоммуникаций им. проф. М.А. БончБруевича | The methods of recovery the optical properties in FOCL during analog signal transmission under γ-radiation influence |
| 1-18 | Дэн | Юаньбяо | | Санкт-Петербургский политехнический университет Петра Великого | Features of photovoltaic cell degradation of solar power plants in Hong Kong and Saint Petersburg |
| 1-19 | Елисов | Максим | Вячеславович | Самарский университет | Modeling the photo- beta-converter with distributed resistance |
| 1-20 о | Заводиленк | Владимир | Владимирович | Национальный исследовательский университет «Высшая школа экономики» / ООО «КуРэйт» | Investigation on the effects of the multiplication area shape on the dark count rate in InGaAs/InAlAs single-photon avalanche photodiodes |
| 1-21 | Иванов | Федор | Леонтьевич | Московский государственный университет имени М.В.Ломоносова | Neuromorphic computing system based on semiconducting metal oxides |
| 1-22 | Ивченко | Егор | | МФТИ | Detection-efficiency mismatch in a satelliteto-ground quantum communication |
| 1-23 | Игнатьев | Андрей | Николаевич | FSUE “FRNC-VNIITF named after Academ. E. I. Zababakhin” | Laser diode module over 350 W power output with 200 µm / NA 0.22 fiber |
| 1-24 | Кадигроб | Екатерина | Владимировна | Всероссийский научно-исследовательский институт технической физики имени академика Е.И. Забабахина | Design and simulation of an optical system of high-power fiber-coupled laser module |
| 1-25 | Климов | Александр | Алексеевич | ФТИ им. Иоффе | HOT mid infrared LEDs based on P-InAsSbP/nInAs(Sb)/N-InAsSbP heterostructure |
| 1-26 | Ковач | Яков | Николаевич | Университет ИТМО/ ФТИ им. Иоффе | Emission linewidth and α-factor of 1.3 µmrange vertical cavity surface emitting laser based on InGaAs/InGaAlAs superlattice |
| 1-27 | Корнышов | Григорий | Олегович | СПбАУ РАН им. Ж.И. Алферова | Broadband emitting from multilayer structures with quantum well-dots active region |
| 1-28 | Костромин | Никита | Андреевич | Санкт-Петербургский политехнический университет Петра Великого | Calculation the mode loss spectra in MIR and THz with double metal waveguides |
| 1-29 | Кунков | Роман | Эдуардович | Физико-технический институт им. А. Ф. Иоффе РАН | Длинноволновые ИК фотоприемники (λ0.5 ≥ 12 µм) на основе твердых растворов InAsSbx (x ≥ 0.4) |

| | | | | | |
|---|---|---|---|---|---|
| 1-30 | Куприянов | Павел | Андреевич | Московский физикотехнический институт/ НИТУ МИСИС (работа) | Влияние неидеальностей квантовых состояний на уровень ошибок в детектор-независимом КРК |
| 1-31 | Лосев | Антон | Вадимович | ООО «КуРэйт» | Investigation of the avalanche delay effect in sine-gated single-photon detector |
| 1-32 | Ляпина | Дарья | Александровна | Самарский университет им. Королева | Tandem solar cells based on porous silicon and perovskites. |
| 1-33 | Малышева | Наталья | Сергеевна | Самарский национальный университет имени академика С.П. Королева | Параметры солнечных элементов на основе исследовательского пористого кремния |
| 1-34 | Маргарян | Игорь | Владимирович | Университет ИТМО | Optimization of SnO2/FAPbI3 interface by carbon dots interlayer |
| 1-35 | Махлуф | Мазен | Мамдух | МИЭМ НИУ ВШЭ | A High precision Two Channel TDC Based on FPGA for ToF Measurement |
| 1-36 | Можайко | Анна | Анатольевна | Санкт-Петербургский политехнический университет Петра Великого | Theoretical and experimental study of laser treatment of nickel using a diode laser |
| 1-37 | Назарова | Ксения | Сергеевна | СПбПУ Петра Великого | Creation of an automated system for adjusting the position of the laser radiation axis for the air communication channel |
| 1-38 | Наумова | Виктория | Викторовна | Санкт-Петербургский Политехнический университет Петра Великого/ФГУП Всероссийский научно-исследовательский институт метрологии им. Д. И. Менделеева | Compact solid-state laser with diode optical pumping and high frequency stability |
| 1-39 | Неелова | Ангелина | Дмитриевна | СПбГЭТУ "ЛЭТИ" | A Study of Chemical and Mechanical Properties of Paper Under Its Laser Cleaning |
| 1-40 | Немыгина | Елизавета | Максимовна | Факультет наук о материалах, Московский Государственный Университет имени М.В.Ломоносова | 2-mercaptoethylammonium chloride as a promising passivator for perovskite solar cells with increased stability |

| | | | | | |
|---|---|---|---|---|---|
| 1-41 | Оасереле | Денис | Владимирович | федеральное государственное бюджетное образовательное учреждение высшего образования «Санкт-Петербургский государственный университет телекоммуникаций им. проф. М.А. БончБруевича» | Development of a photodetector for an analog extended fiber-optic communication line |
| 1-42 | Овезов | Максат | Кемалович | ФТИ им. Иоффе | Investigation of the current-voltage characteristics of MAPbI3 perovskite films formed by a single-stage spin-coat method |
| 1-43 | Парфенов | Михаил | Владимирович | ФТИ им. А. Ф. Иоффе РАН | Efficient thin-film lithium niobate integrated optical modulator with wide waveguides fabricated by contact photolithography |
| 1-44 | Поставной | Николай | Юрьевич | СНИУ имени С.П. Королева | Development of a Device for Measuring Temperature Dependence of Current in a Porous Silicon Solar Cell |
| 1-45 | Резников | Богдан | Константинович | Санкт-Петербургский государственный университет телекоммуникаций им. проф. М.А. БончБруевича | Peculiarities of telemetry information transmission using analog fiber-optic communication line over long distances in a complex electromagnetic environment |
| 1-46 | Резников | Богдан | Константинович | Санкт-Петербургский государственный университет телекоммуникаций им. проф. М.А. БончБруевича | Development of a simulator for testing methods for generating analog signals in the form of a sequence of command codes in an optical communication channel |
| 1-47 | Рудавин | Никита | Владимирович | НИУ ВШЭ | REAL-TIME CALIBRATION METHODS FOR A COMMERCIAL MDI-QKD SYSTEM |
| 1-48 | Саенко | Александр | Викторович | Южный федеральный университет | Investigation of the photoelectric parameters of an oxide solar cell based on a ZnO/Cu2O heterojunction |
| 1-49 | Синицкая | Олеся | Алексеевна | Санкт-Петербургский национальный исследовательский Академический университет имени Ж. И. Алфёрова Российской академии наук | The effect of the dielectric SiO2 layer on the characteristics of visible-blind ultraviolet photodetectors based on ultrathin GaN epitaxial layers grown on c-Al2O3 substrates |
| 1-50 | Ткач | Маргарита | Андреевна | Самарский национальный исследовательский университет имени академика С.П. Королева | Электрические характеристики солнечных элементов с наноструктурами кремния |
| 1-51 | Тойкка | Андрей | Сергеевич | СПбГЭТУ "ЛЭТИ" | FORMATION OF ITO-BASED ANISOTROPY ORIENTING LAYERS FOR LIQUID CRYSTAL DEVICES |

| | | | | | |
|---|---|---|---|---|---|
| 1-52 | Филяев | Александр | Александрович | Национальный исследовательский университет «Высшая школа экономики» / Национальный исследовательский технологический университет МИСИС | Evaluation of quantum efficiency of InGaAs/InP single-photon detectors in quantum key distribution systems |
| 1-53 | Фролов | Илья | Владимирович | Ульяновский филиал Института радиотехники и электроники им.В.А.Котельникова Российской академии наук | Measurement of threshold current in local areas of the LED chip |
| 1-54 | Хомякова | Кристина | Игоревна | Национальный исследовательский томский государственный университет | Modeling of avalanche photodiodes based on Ge/Si |
| 1-55 | Шишкин | Владислав | Александрович | Самарский национальный исследовательский университет имени академика С.П. Королева | Development of a device for measuring voltampere and volt-watt characteristics of experimental solar cells |
| 1-56 | Иванов | Антон | | НТЦ микроэлектроники РАН | Comparative study of energy characteristics of high-power flip-chip AlInGaN LEDs (λ = 440–510 nm) for laser pumping |
| 1-57 | | Александр Куркова | Дмитриевна | Санкт-Петербургский Lasers of metrological appropriation a политехнический университет Петра Великого/ФГУП Вниим им Д. И. Менделеева | |

## 2. Electric, Magnetic and Microwave Devices

## May 24, 2023

## 15:30 - 18:00 Poster Session I

| | | | | | |
|---|---|---|---|---|---|
| 2-1 | Аринушкина | Ксения | Геннадьевна | Санкт-Петербургский государственный университет телекоммуникаций им. проф. М.А. Бонч-Бруевича | Modernization of quantum frequency standard with optical pumping |
| 2-2 | Бурмистров | Олег | Ильич | Университет ИТМО | Электрические, магнитные и СВЧ характеристики и устройства |
| 2-3 | Валов | Антон | Петрович | СПбГУТ им. проф. М.А. Бонч-Бруевича | Investigation of a method for improving phase noise in the frequency standard generator block |
| 2-4 | Ван | Дин | - | СПбПУ | |
| 2-5 | Василькова | Елена | Игоревна | СПбАУ РАН им. Ж.И. Алферова | Long-term stability of GaAs-based pseudomorphic transistor heterostructures with InGaAs channel |
| 2-6 | Ведь | Михаил | Владиславович | ННГУ им. Н.И. Лобачесвского | Magnetic field detector based on a magnetically controlled spin LED |

| | | | | | |
|---|---|---|---|---|---|
| | | | | Санкт-Петербургский политехнический университет Петра Великого | Modernization of a quantum frequency |
| 2-8 | Козловская | Екатерина | Андреевна | «Национальный исследовательский университет «Московский институт электронной техники» | |
| 2-7 | Исупова | Екатерина | Васильевна | | Модель вольт-амперных характеристик резонансно-туннельных структур в задачах standard temperature controller with a rubidium gas cell |
| 2-9 | Куимов | Евгений | Владимирович | МГТУ им. Баумана | исследования целевых функций методик оптимизации резонансно-туннельных диодов |
| 2-10 | Львов | Андрей | Валерьевич | Московский педагогический государственный университет | Reconfigurable Reflectarrays for 5/6G Wireless Systems with Linear Polarization |
| 2-11 | Макаров | Павел | Андреевич | ФМИ ФИЦ Коми НЦ УрО РАН | Simulation of electromagnetic signals propagation in dynamic gratings |
| 2-12 | Михеев | Илья | Игоревич | Московский физикотехнический институт | Using Mobile Phone as a Ripeness Sensor |
| 2-13 | Морозов | Матвей | Олегович | ЯРГУ им. П.Г. Демидова/ЯФ ФТИАН им. К.А. Валиева РАН | Modeling of a capacitive MEMS-switch with «floating» electrode |
| 2-14 | Нигаматдьянов | Марат | Газимьянович | Университет ИТМО | Разработка оптического датчика искрового пробоя для распределительных щитов электросетей |
| 2-15 | Орлов | Виктор | Олегович | НИИМЭ | "Разработка и применение электромеханических систем" |
| 2-16 | Патарашвили | Антон | Николаевич | МФТИ | Development and research of charger operation modes type "needle - plate" for nanoparticle charging |
| 2-18 | Селиванова | Дарья | Игоревна | ЮФУ ИНЭП | Modeling the output voltage of a nanogenerator based on vertically aligned carbon nanotubes |
| 2-19 | Сомов | Артём | Игоревич | Самарский национальный исследовательский университет имени академика С.П. Королева | Initialization of synthesis in quadrupole magnetic traps using controlled plasma instabilities and spherical cumulation of shock magnetic waves. |
| 2-20 | Фадеенко | Варвара | Борисовна | Санкт-Петербургский политехнический университет Петра Великого | Разработка волоконно-оптической системы для задания выходной частоты генератора управляемых напряжений на антенном комплексе радиолокационной станции |

| | | | | | |
|---|---|---|---|---|---|
| 2-21 | Чижиков | Сергей | Владимирович | МГТУ им. Н.Э. Баумана | NUMERICAL SIMULATION OF THE PARAMETERS OF A LOW-NOISE TRANSISTOR WITH LOW POWER CONSUMPTION FOR USE AS PART OF MONOLITHIC INTEGRATED CIRCUITS OF AN ENERGY-EFFICIENT LOW-NOISE AMPLIFIER FOR USE IN THE AMPLIFICATION PATH OF A MINIATURE RADIOTHERMOGRAPH |
| 2-22 | Чистяков | Василий | Владимирович | Институт физики металлов имени М.Н. Михеева Уральского отделения РАН | Galvanomagnetic properties in “size” topological insulators Bi2Se3 |
| 2-23 | Шавшин | Артём | Владимирович | Санкт-Петербургский Политехнический Университет Петра Великого | Improving microwave output in rubidium-87 atomic frequency standard with new automatic gain control |
| 2-24 | Шаншо | Ахмад | | Национальный исследовательский Томский государственный университет, Томск, Россия | Developing a high precision measurement system in the millimeter wave V-band |
| 2-25 | Шлепаков | Павел | Сергеевич | ЯФ ФТИАН им. К. А. Валиева РАН | Testing the fast electrochemical micropump with PDMS membrane |
| 2-26 | Шугуров | Константин | Юрьевич | СПбАУ им. Ж.И. Алферова | Extremely high frequency Schottky diodes based on single GaN nanowires |
| 2-27 | Ярополов | Терентий | Андреевич | Московский педагогический государственный университет | Hardware- and User-Induced Micromobility Effects in In-Door Radio Access at 140 GHz |
| 2-28 | Burtsev | Vladimir | Denisovich | Center for Photonics and 2D Materials, MIPT | Magneto-Electric Dipole Antenna as an Transceive Element in a Phased Array |
| 2-29 | Белозеров | Игорь | Александрович | ЯрГУ им. П.Г. Демидова | A cantilever type MEMS switch with enhanced contact force: the first results |

## 3.Crystal growth and structural properties of semiconductor materials and nanostructures

## May 24, 2023

## 15:30 - 18:00 Poster Session I

| | | | | | |
|---|---|---|---|---|---|
| 3-1 | Абраменко | Никита | Дмитриевич | Университет ИТМО | Simulation of elastic characteristics of pseudo-graphenes |
| 3-2 | Андрюшкин | Владислав | Васильевич | Университет ИТМО | Matrix composition effect on InGaP(As) quantum dots photoluminescence |

| | | | | | |
|---|---|---|---|---|---|
| 3-3 | Балакирев | Сергей | Вячеславович | Институт нанотехнологий, электроники и приборостроения, Южный федеральный университет | Droplet epitaxy of site-controlled In/GaAs(001) nanostructures with a variable distance: experiments and simulations |
| 3-4 | Быков | Дмитрий | Сергеевич | СПбПУ Петра Великого | Terahertz difference frequency generation in photonic crystals |
| 3-5 | Воронцова | Юлия | Александровна | НИУ ВШЭ, ИОФ РАН | First-principle study of phosphorus incorporation into silicon by PBr3 adsorption on Si(100) |
| 3-6 | Гайнуллин | Радис | Рушанович | Институт органической и физической химии им. А.Е. Арбузова | Interdigital gold electrodes for a conductometric gas sensor on the glass surface |
| 3-7 | Гращенко | Александр | Сергеевич | Институт проблем машиноведения РАН | Структурные характеристики поверхности пленок нитрида алюминия-галлия на нанослоях карбида кремния на кремнии |
| 3-8 | Гридчин | Владислав | Олегович | СПбАУ РАН им. Ж.И. Алфёрова | Selective Area Growth of GaN/InGaN Nanowires on Si Substrates |
| 3-9 | Дарханов | Евгений | Владленович | МИЭМ ВШЭ/АО "НИИграфит" | Carboxymethylcellulose as effective agent to regulate properties of silver nanoparticle-based conductive inks |
| 3-10 | Дерибина | Екатерина | Игоревна | Санкт-Петербургский государственный Университет | Капельная эпитаксия квантовых точек GaAs/AlGaAs различной плотности и их оптические свойства |
| 3-11 | Духан | Денис | Дмитриевич | Южный Федеральный Университет/ Лаборатория эпитаксиальных технологий | Ab initio modelling of In wetting layer formation on As-stabilized GaAs during first stages of droplet epitaxy. |
| 3-12 | Ерёменко | Михаил | Михайлович | Институт нанотехнологий, электроники и приборостроения ЮФУ | Effect of plasma-chemical treatment of Si(001) substrates on the subsequent epitaxial growth of GaAs |
| 3-13 | Еуров | Даниил | Александрович | ФТИ им. А.Ф. Иоффе | Hard-template synthesis of microporous SiO2 particles |
| 3-14 | Жигаев | Данила | Алексеевич | Самарский национальный исследовательский университет имени академика С.П. Королева | Analysis of parameters of photosensitive structures based on silicon carbide heterostructures on silicon |
| 3-15 | Золотухин | Дмитрий | Сергеевич | ФГБОУ ВГУ | Study of morphology and composition of nanoscale GaN and AlGaN heterostructures obtained by PA MBE technique on the silicon substrates with the use of porous silicon as the buffer layer |
| 3-16 | Иванищева | Александра | Павловна | Институт нанотехнологий, электроники и приборостроения, Южный федеральный университет | Study of the temperature dependence of the conductivity of ZnO/Au nanorod arrays exposed to ultraviolet irradiation |
| 3-17 | Илькив | Игорь | Владимирович | Санкт-Петербургский академический университет | FORMATION OF GE-BASED NANOSTRUCRUTRES ON WURTZITE A3B5 NANOWIRES |

| | | | | | |
|---|---|---|---|---|---|
| 3-18 | Кадинская | Светлана | Алексеевна | Санкт-Петербургский академический университет - научно-образовательный центр нанотехнологий РАН | Deep-level emission tailoring in ZnO nanostructures grown via hydrothermal synthesis |
| 3-19 | Казаков | Валерий | Алексеевич | ФГБОУ ВО Чувашский государственный университет им. И.Н. Ульянова | Investigation of the optical properties of carbon films in the sp2, sp3- hybridized state during thermal annealing |
| 3-20 | Ирина | Леонидовна | | ННГУ им. Н.И. Лобачевского | Creation of a GaMnAs ferromagnetic Калентьева semiconductor by a combined laser method |
| 3-21 | Калякин | Тимофей | Сергеевич | РХТУ им. Д.И. Менделеева / АО «НИИграфит» | Determination of graphene concentration in dispersions using integral methods. |
| 3-22 | Каменева | Екатерина | Игоревна | Московский физикотехнический институт (национальный исследовательский университет) | Technology of manufacturing thin-film aluminum nanostructures by dry aerosol printing |
| 3-23 | Кенесбай | Рамазан | - | Санкт-Петербургский национальный исследовательский Академический университет Российской академии наук | Influence of double layer PMHS/PDMS encapsulation on CsPbBr3 PeLEC properties in high humidity conditions |
| 3-24 | Ким | Ксения | Борисовна | ФГБОУ ВО "ВГУИТ" | The features of formation of oxide porous structures based on SiO2 – SnO2 |
| 3-25 | Кириченко | Данил | Владимирович | ФГАОУ ВО "ЮФУ", Институт нанотехнологий, электроники и приборостроения | Study of arsenic flux effect on thermal desorption of GaAs native oxide and surface morphology |
| 3-26 | Кирьянов | Филипп | Дмитриевич | Московский государственный университет имени М. В. Ломоносова | Approximation capabilities of neural networks for designing semiconductor tunable metasurfaces. |
| 3-27 | Кожевников | Василий | Юрьевич | ФГБУН Институт сильноточной highэлектроники СО РАН | Novel methods for synthesizing high-quality thin films through short and ultrashort power pulsed magnetron sputtering |
| 3-28 | Комаров | Иван | Александрович | АО "НИИграфит" | On the wetting of PET substrates with Multicomponent Graphene Oxide Dispersions |
| 3-29 | Конюх | Дмитрий | Александрович | ФТИ Иоффе | Local elastic heterogeneity significantly affects the stiffness of composite systems |
| 3-30 | Костин | Алексей | Александрович | САФУ | СПЕКТРОСКОПИЯ АЛМАЗНЫХ ПЛАСТИН ЛЕГИРОВАННЫХ БОРОМ И НИКЕЛЕМ |
| 3-31 | Кузнецов | Юрий | Михайлович | Нижегородский государственный университет им. Н.И. Лобачевского | Doping and thermoelectric characteristics of Ge0.3Si0.7:Pδ synthesized by powder sintering |
| | | | | Национальный | |

| | | | | | |
|---|---|---|---|---|---|
| 3-32 | Кукенов | Олжас | Игоревич | исследовательский Томский государственный университет | Analysis of homoepitaxial growth of Si on Si(100) in a wide temperature range by reflection high-energy electron diffraction |
| 3-33 | Куртина | Дарья | Андреевна | Московский Государственный Университет им. М.В. Ломоносова | Chirality induction in atomically thin colloidal CdSe nanostructures |
| 34 | Лахина | 3- Екатерина | Александровна | Южный федеральный университет | Formation of symmetrical nanoholes by local droplet etching for site-controlled growth of single quantum dots |
| 35 | Лебедева | 3- Эльгина | Маратовна | Институт органической и физической химии им. А.Е. Арбузова | Optical and electrochemical properties of a composite material based on PEDOT-PSS and oriented nickel fibers |
| 36 | Лосин | 3- Артур | Леонидович | Университет ИТМО | Effect of femtosecond irradiation on the luminescence of CsPbI3 perovskite crystals in borogermanate glass |
| 3-37 | Максимова | Алина | Андреевна | СПбГЭТУ "ЛЭТИ" | Boron phosphide grown by PECVD and its optical properties |
| 3-38 | Масталиева | Виктория | Анатольевна | СПбАУ РАН им. Ж.И. Алфёрова | Flexible Green Perovskite CsPbBr3 LED Integrated with SiNW Array |
| 3-39 | Морозова | Юлия | Викторовна | Южный Федеральный Университет | Formation of metal oxide nanostructures by magnetron sputtering, for photonics and optoelectronics devices |
| 3-40 | Мумляков | Александр | Михайлович | ИНМЭ РАН | Study of n-diamond and carbon nanowalls structure synthsized by the RF-PECVD |
| 3-41 | Мурашко | Денис | Тарасович | НИУ МИЭТ | Two-photon lithography of composite nanostructures for bioelectronic applications |
| 42 | Насиров | 3- Павел | Денисович | ФГБОУ ВО "Университет Дубна" | Microwave synthesis and modification of carbon dots for application as labels in immunoassay |
| 43 | Новикова | 3-Кристина | Николаевна | СПбАУ РАН им. Ж.И. Алферова/ ФГАОУ ВО СПбПУ | Investigation of gallium phosphide nanowires conductivity with a doped shell |
| 3-44 | Пепеляев | Дмитрий | Валерьевич | НИУ МИЭТ | Investigations of the mobility and concentration of charge carriers in nanostructured thermoelectric materials PbTe and GeTe obtained by spark plasma sintering |
| 45 | Пешков | 3- Ярослав | Анатольевич | Воронежский государственный университет | A change in the morphology of multilayer porous silicon with a stepwise decrease in the etching current density |
| 46 | Самарцев | 3- Илья | Владимирович | ННГУ им. Н.И. Лобачевского | Metamorphic epitaxial structures for lowbarrier mixing microwave diodes |
| 3-47 | Смирнова | Мария | Александровна | ЯрГУ им. П.Г. Демидова | Development of the surface morphology of germanium upon irradiation with gallium ions |
| | | | | Санкт-Петербургский | |

| | | | | | |
|---|---|---|---|---|---|
| 3-48 | Соколова | Анастасия | Андреевна | Политехнический Университет Петра Великого | Quality Control Methods of Silicon Wafer Diode Array for TV Tubes |
| 3-49 | Стинская | Ксения | Брониславовна | Московский педагогический государственный университет | Electrochemical synthesis of CdTe nanostructures |
| 3-50 | Строкин | Павел | Дмитриевич | Саратовский национальный исследовательский государственный университет имени Н.Г. Чернышевского | Модификация коллоидных квантовых точек состава CdZnSeS/ZnS тиолами для дальнейшего применения в аналитических системах |
| 3-51 | Студзинский | Виталий | Михайлович | Санкт-Петербургский Политехнический Университет Петра Великого | Photocatalytic properties of NiO – gold plasmonic nanocomposite |
| 3-52 | Татаринов | Дмитрий | Андреевич | Университет ИТМО | Optimization triple-cation perovskite thin films by PEAI additive |
| 3-53 | Трошкина | Наталья | Николаевна | Государственный университет Дубна | The effect of surface ligands on the physicochemical properties of chalcogenide CdTe/CdS/ZnS quantum dots |
| 3-54 | Чернев | Игорь | Михайлович | Институт автоматики и процессов управления Дальневосточного отделения Российской академии наук | Ultrathin Cr and Fe monosilicides on Si(111) substrate: formation, optical and thermoelectrical properties |
| 3-55 | Чернев | Игорь | Михайлович | Институт автоматики и процессов управления Дальневосточного отделения Российской академии наук | Mg2Si film on Si: Pulsed RDE Growth, Structure, Electrophysical, Thermoelectrical and Photoelectrical Properties |
| 3-56 | Черненко | Наталия | Евгеньевна | ИНЭП ЮФУ | Study of InAs/GaAs quantum dots formation in subcritical growth modes on patterned substrates |
| 3-57 | Шандыба | Никита | Андреевич | Институт нанотехнологий, электроники и приборостроения Южного федерального университета | Effect of ion dose and accelerating voltage during Si(111) surface FIB treatment on GaAs nanowires growth |
| 3-58 | Шепелева | Анастасия | Эдуардовна | АО "Научноисследовательский институт электронно-механических приборов" | Газовые сенсоры на основе наностержней оксида цинка с коллоидными квантовыми точками. |
| 3-59 | Шуклов | Иван | Алексеевич | МФТИ | PHOSPHINE-FREE SYNTHESIS OF SELENIDE COLLOIDAL QUANTUM DOTS |
| 3-60 | Смирнов | Александр | Вячеславович | Чувашский государственный университет имени И.Н. Ульянова | Application of linear chain carbon films for sensitive elements of humidity sensors |

| | | | | | |
|---|---|---|---|---|---|
| 61 | Goltaev 3- | Aleksandr | Sergeevich | Алфёровский университет | Investigation of Photoconverter in IR Range Based on an Array of InAs Nanowires Synthesized by the MBE Method |
| 62 | Song 3- | Qinghao | . | Microfluidics and Perovskite nanoparticles | Synthesis of Perovskite Nanoparticles in Suspension using Microfluidic Approach |
| 63 | Андрюшкин 3- | Владислав | Васильевич | Университет ИТМО | Epitaxial growth of highly stressed InGaAs/InAlAs layers on InP substrates by molecular-beam epitaxy |

## 4. Nanophotonics, Spectroscopy, Microcavities, Optics, Plasmonics, Spintronics, Electro- and Magnetooptics

## May 25, 2023

## 15:30 - 18:00 Poster Session II

| | | | | | |
|---|---|---|---|---|---|
| 4-1 | Абрамов | Артем | Николаевич | Университет ИТМО | Localization microscopy of single photon emitters in locally strained monolayer semiconductor |
| 4-2 | Аникина | Мария | Александровна | СПбАУ РАН им. Ж.И. Алферова | Photoluminescence anisotropy in hybrid nanostructures based on gallium phosphide nanowire and 2D transition metal dichalcogenides |
| 4-3 | Бабич | Екатерина | Сергеевна | Академический университет им. Ж. И. Алфёрова | The growth dynamic of Au/Ag alloy nanoparticles in glass |
| 4-4 | Бабичев | Андрей | Владимирович | ФТИ им. А.Ф. Иоффе | Photoluminescence study of InGaAs/GaAs quantum dots with bimodal inhomogeneous broadening |
| 4-5 | Бабичек | Илья | Викторович | МФТИ | Enhancing the Analytical Arrayed Waveguide Multiplexer Model with Spectrum Analysis |
| 4-6 | Бабухин | Данила | Валерьевич | QRate LLC | Excess leakage of information in QKD with passive side channels |
| 4-7 | Бажанова | Вероника | Александровна | СПбПУ Петра Великого | Features of monitoring the state of viscous media by refraction |
| 4-8 | Бастракова | Марина | Валерьевна | Нижегородский государственный университет им. Н.И. Лобачевского | Effect of a bifurcation meter on microwave transmission through a one-dimensional chain of qubits |
| 4-9 | Башегурова | Елена | Александровна | Санкт-Петербургский государственный университет | Optical spectroscopy of GaAs/AlGaAs quantum dots |
| 4-10 | Бондарева | Полина | Игоревна | Московский Педагогический Государственный Университет | Terahertz radiation detection using graphene noise thermometry method |
| 4-11 | Бородина | Любовь | Николаевна | Университет ИТМО | Luminescent nanoparticles' double-diffusion observed by fluorescence recovery technique using laser scanning microscopy |

| | | | | | |
|---|---|---|---|---|---|
| 4-12 | Василевский | Павел | Николаевич | Национальный исследователький университет "МИЭТ" | Spatial self-phase modulation of light in liquid dispersions based on conjugates of phthalocyanines and carbon nanotubes |
| 4-13 | Вершинина | Олеся | Валерьевна | Московский физикотехнический институт (национальный исследовательский университет) | The effect of laser radiation on properties of platinum nanoparticles produced in a gas discharge |
| 4-14 | Вовк | Николай | Александрович | НИУ ВШЭ/ ИНМЭ РАН | Modelling the influence of planar waveguide cladding thickness on the absorption efficiency of a superconducting NbN strip. |
| 4-15 | Глебов | Никита | Вячеславович | Университет ИТМО | Linear transmission of waveguides based on perovskite MAPbBr3 |
| 4-16 | Гольдберг | Артемий | Александрович | «Санкт-Петербургский политехнический университет Петра Великого» | Features of measuring the time of longitudinal relaxation T1 in condensed media by nuclear magnetic resonance using the modulation method in weak magnetic fields |
| 4-17 | Гольдберг | Артемий | Александрович | Санкт-Петербургский политехнический университет Петра Великого | Features of the research of liquid media by the optical differential method during express control |
| 4-18 | Горелов | Илья | Кириллович | Московский Государственный Университет им. М.В. Ломоносова | Narrowing of the linewidth of lasers self-injection locked to a high-Q microresonator with whispering gallery modes |
| 4-19 | Петров | Никита | Сергеевич | Университет ИТМО | Numerical simulation of endocytosis of metallic nanoparticles with various geometry |
| 4-20 | Дрязгов | Михаил | Александрович | Национальный исследовательский университет «Высшая школа экономики» (НИУ ВШЭ) | Pockels cell performance in N-photon demultiplexer |
| 4-21 | Ересько | Родион | Павлович | СПбАУ РАН им. Ж.И. Алферова/Лаборатория оптики гетерогенных структур и оптических материалов | Numerical simulation of the optical properties of a hybrid system based on gallium phosphide nanowires and 2D transition metal dichalcogenides |
| 4-22 | Жаркова | Алина | Александровна | НИТУ МИСиС | Luminescence kinetic of nanosized CsPbBr3 QDs |
| 4-23 | Завьялова | Есения | Сергеевна | СПБАУ РАН им. Ж. И. АЛФЕРОВА | Towards versatile photonics based on GaP nanowires decorated with carbon dots |
| 4-24 | Заневская | Мария | Юрьевна | Санкт-Петербургский государственный университет аэрокосмического приборостроения | Application of optical methods for quality control of dairy products using data mining |

| | | | | | |
|---|---|---|---|---|---|
| 4-25 | Калашников | Виктор | Андреевич | Санкт-Петербургский политехнический университет Петра Великого | Features of spectroscopy of hydrocarbon media by optical method using X-ray radiation |
| 4-26 | Камалов | Алмаз | Маратович | Санкт-Петербургский политехнический университет Петра Великого | CHARGE RELAXATION AFTER EXPOSURE TO BARRIER AND CORONA DISCHARGE OF POLYLACTIDE FILMS |
| 4-27 | Кан | Геннадий | | Алферовский университет | Glass poling: surface environment effect |
| 4-28 | Караборчев | Алексей | Александрович | Санкт-Петербургский кампус Национального исследовательского университета «Высшая школа экономики» (НИУ ВШЭ — Санкт-Петербург) | INVESTIGATION OF TWO STATE LASING IN MICRODISKS WITH InAs/GaAs QUATUM DOTS AT DIFFERENT TEMPERATURES |
| 4-29 | Кашапов | Артем | Ильясович | Самарский университет/ИСОИ РАН | Generation of spatiotemporal optical vortices using Kretschmann setup for transverse magnetic and transverse electric polarizations |
| 4-30 | Кондратьева | Анастасия | Сергеевна | СПбАУ им.Ж.И.Алферова | Surface modification influence on silica based pillars properties |
| 4-31 | Корнюшин | Денис | Владимирович | МФТИ | Effect of the thickness of plasmonic gold nanostructures on the Surface Enhanced Raman Scattering enhancement factor |
| 4-32 | Кузнецов | Алексей | Сергеевич | СПбАУ РАН им. Ж.И. Алферова | Self-assembled photonic nanoantenna based on GaP single nanowire |
| 4-33 | Курасова | Камилла | Константиновна | Университет ИТМО | Analysis of optical properties of quantum dots doped microspheres |
| 4-34 | Максимов | Матвей | Андреевич | Санкт-Петербургский Государственный Университет | Reflection spectroscopy of excitons in wide quantum well of InGaAs/GaAs |
| 4-35 | Мало | Дана | . | Московский Физико-Технический Институт (МФТИ) | Ultraviolet photoluminescence enhancement of zinc oxide nanocrystals in colloidal mixtures with spark discharge aluminum nanoparticles |
| 4-36 | Мельниченко | Иван | Алексеевич | Академический университет им. Ж.И. Алферова / НИУ ВШЭ | Optical studies of InGaAs/GaAs quantum well mesa structures treated with hydrogen plasma and passivated via AlOx layer |
| 4-37 | Мерещенко | Андрей | Сергеевич | Санкт-Петербургский государственный университет | Эффект со-легирования лантаноидами на структуру и люминесцентные свойства неорганических фторидных наноматериалов |
| 4-38 а | Митрофанов | Анастасия | Евгеньевна | АО «Научноисследовательский институт молекулярной электроники» | Investigation of phase shift in waveguides with chalcogenide glasses |
| 4-39 | Михайловский | Михаил | Сергеевич | Университет ИТМО | High-Q band-edge resonances in onedimensional arrays of dipolar scatterers |
| 4-40 | Мурзагалина | Софья | Маратовна | АО «Научноисследовательский институт молекулярной | The research of nonlinear optical phenomena in silicon slot waveguide |

| | | | | | |
|---|---|---|---|---|---|
| | | | | электроники», МФТИ(НИУ) | structures |
| 4-41 | Надоян | Ирина | Валерьевна | Санкт-Петербургский национальный исследовательский Академический университет имени Ж. И. Алфёрова Российской академии наук | Nanooscillators based on carbon whiskers for detectors of optomechanical effects |
| 4-43 | Никитин | Игорь | Юрьевич | Университет ИТМО, Центр "Информационные оптические технологии", Лаборатория "Фотофизика поверхности" | OPTICAL PROPERTIES A HYBRID STRUCTURE OF NANOPOROUS ALUMINA MATRIX ON SILVER NANOPRTICLE ARRAY SUBSTRATE |
| 4-44 | Ондар | Сайхо | Омаковна | Санкт-Петербургский государственный технологический институт (ТУ) Пермский | Manganese-doped red-emissive carbon dots as dual-modal nanoprobe for bioimaging |
| 4-42 | Некрасов | Никита | Петрович | Национальный исследовательский университет «Московский институт электронной техники» | Измерение фокусного расстояния и Mechanisms of Residual Polymer Removal in Solvent Mixtures after the Graphene Transfer and Effects on Channel Conductivity Gate Control |
| 4-45 | Паньков | Анатолий | Сергеевич | государственный национальный исследовательский университет | диаметра поля моды линзованного волокна, изготовленного методом химического травления и оплавления |
| 4-46 | Перетокин | Артем | Викторович | ННГУ им. Н.И. Лобачевского / ИФМ РАН | Tuning the luminescence response of a photonic crestal with Ge(Si) nanoislands by changing the etching depth of holes |
| 4-47 | Песняко | Владислав | Викторович | Университет ИТМО | Optical properties of photo-thermorefractive glasses doped with terbium |
| 4-48 | Поздняков | Артем | Андреевич | СПбГУТ | Experimental study of data transmission in a long-haul passive span fiber-optic line with high information capacity |
| 4-49 | Проскурин | Алексей | Алексеевич | Университет ИТМО | Analytical description of SPP generation with structured substrates |
| 4-50 | Рудаков | Артур | Олегович | Институт физики микроструктур РАН | Optimization of the multiple quantum well HgTe/CdHgTe heterostructures parameters for the 2D plasmon-phonon generation |
| 4-51 | Савельев | Дмитрий | Андреевич | Самарский национальный исследовательский университет им. академика С.П. Королева | The subwavelength optical elements optimization for the formation of specified diffraction patterns using high-performance computer systems |

| | | | | | |
|---|---|---|---|---|---|
| 4-52 | Селиверстов | Сергей | Валерьевич | Московский педагогический государственный университет | Optimization of a prism coupler for a THz photonic integrated metamaterial Si waveguide: simulation and experiment |
| 4-53 | Смолина | Екатерина | Олеговна | ИПФ РАН | Classifying Topology in Waveguide Lattices using Deep Learning |
| 4-54 | Согрин | Матвей | Александрович | Университет ИТМО | Influence of structural disorder on the metamaterial regime |
| 4-55 | Содномай | Амгалан | Булатович | Национальный исследовательский университет "Высшая школа экономики" | Passive optical scheme for BB84 protocol with polarization encoding on a silicon nitride platform |
| 4-56 | Степаненков | Григорий | Викторович | Санкт-Петербургский государственный университет телекоммуникаций им. проф. М. А. Бонч-Бруевича | Features of express control of volatile hydrocarbon media and their mixtures in visible light |
| 4-57 | Тебенева | Татьяна | Сергеевна | Российский квантовый центр | Fabrication of amorphous ZBLAN high-Q WGM microspheres |
| 4-58 | Фандеев | Александр | Андреевич | Университет ИТМО | Plasmonics of diffused silver nanoparticles in polymer thin film |
| 4-59 | Фоминых | Никита | Андреевич | Алферовский университет | Investigation of microdisk lasers with optically coupled waveguide |
| 4-60 | Хахулин | Семен | Андреевич | Санкт-Петербургский государственный электротехнический университет "ЛЭТИ" | Исследование анизотропии оптических свойств чёрного фосфора методами ИК фурье-спектроскопии |
| 4-61 | Чуманов | Иван | Викторович | Санкт-Петербургский государственный электротехнический университет «ЛЭТИ» им. В.И. Ульянова (Ленина) | Исследование температурной зависимости энергетического спектра метаморфных гетероструктур In(Ga,Al)As/GaAs с помощью метода инфракрасной фурье-спектроскопии фотоотражения |
| 4-62 | Шевченко | Даниил | Васильевич | СПбПУ Петра Великого | Development of a compact high-resolution digital microscope for the research of micro- and nanostructures |
| 4-63 | Шугабаев | Талгат | Маратович | Академический университет им. Ж.И. Алферова РАН | Optical properties of hybrid structures based on InGaN nanowires and colloidal quantum dots |
| 4-64 | Щербак | Сергей | Александрович | Санкт-Петербургский Политехнический университет Петра Великого | Surface generation of second optical harmonic in micro- and nanostructures |
| 4-65 | Якубенко | Богдан | Максимович | Физико-технический институт ФГАОУ ВО "Крымский федеральный университет им. В.И. Вернадского" | Logic gates “NOT” and “OR” Based on Carbon Nanotubes |
| 4-66 | Glukyenkaya | Viktoria | Borisovna | НИУ "МИЭТ" | Reversible multiple optical switching of Ge2Sb2Te5 thin films for reflective display applications. |

| | | | | | |
|---|---|---|---|---|---|
| 4-67 | Solomonov | Nikita | Aleksandrovich | СПбАУ РАН им. Ж.И. Алферова | Investigation of photon emission via inelastic tunneling of electrons from laser-printed gold nanobumps using scanning tunneling microscopy |
| 4-68 | Цыкарева | Юлиана | Витальевна | Северный Арктический Федеральный университет им. М.В. Ломоносова | HOM interference of coupled photons in a waveguide beam splitter |

## 5. Nanobiotechnology, Biophysics and BiophotonicsNanobiotechnology, Biophysics and Biophotonics

## May 25, 2023

## 15:30 - 18:00 Poster Session II

| | | | | | |
|---|---|---|---|---|---|
| 5-1 | Абелит | Анна | Андреевна | СПбАУ РАН им. Ж.И. Алферова | Insulinoma Living Cells Clusters Demonstrate Solids-Like Vibrations |
| 5-2 | Антипенко | Владимир | Викторович | ФГБОУ ВО "Пензенский государственный университет" | Development of an automated system for measuring bioimpedance for the study of body composition |
| 5-3 | Белоусова | Дарья | Алексеевна | СПбАУ РАН им. Ж.И. Алфёрова | Microfluidic Device for the Synthesis of Cellular Microspheroids in Double Emulsion Droplets for 3D Bioprinting |
| 5-4 | Винник | Виктор | Алексеевич | Санкт-Петербургский политехнический университет Петра Великого | Single-molecule characterization of nucleosome stability using ‘603’ nucleosome position sequence |
| 5-5 | Винокуров | Егор | Константинович | «Санкт-Петербургский политехнический университет Петра Великого», Лаборатория молекулярной нейродегенерации | Combining single-photon miniature fluorescence microscopy and electrophysiological recording to study the activity of mouse hippocampal neurons in vivo |

| | | | | | |
|---|---|---|---|---|---|
| 5-6 | Водяшкин | Андрей | Алексеевич | Российский университет дружбы народов | Development of a new synthesis pathway and pH-sensitivities' assessment of Sr-BDC Metal-Organic Frameworks (MOFs) |
| 5-7 | Волков | Денис | Андреевич | Санкт-Петербургский Политехнический университет/Физико-Технический институт им Иоффе | Molecular dynamics calculation of NADH rotational diffusion times in aqueous – methanol solutions |
| 5-8 | Давыдов | Роман | Вадимович | Санкт-Петербургский политехнический университет Петра Великого | New opportunities for studying the oxygen saturation of blood hemoglobin in capillaries and tissues |
| 5-9 | Денисова | Елена | Артемовна | Санкт-Петербургский политехнический университет Петра Великого (СПбПУ)/Институт аналитического приборостроения Российской академии наук | Application of a Pre-processing Algorithm for Ultra-high resolution Electrocardiosignals |
| 5-10 | Дубина | Филипп | Михайлович | СПбАУ РАН им. Ж.И. Алфёрова | Converting Bio-microscope into BioLithographer: Proof-of-Concept. |
| 5-11 | Евстратова | Ирина | Игоревна | Московский государственный педагогический университет МПГУ | Obtaining a phototoxic complex based on silver nanoparticles and riboflavin generating reactive oxygen species |
| 5-12 | Жуков | Михаил | Валерьевич | Institute for Analytical Instrumentation RAS | Effect of increasing in ion current flowing through a nanocapillary approaching the charged surface in liquid |
| 5-13 | Сидоров | Евгений | Александрович | Университет Дубна | Coating of hydrophilic chalcogenide quantum dots with carboxymethyl chitosan for lateral flow immunoassay applications |
| 5-14 | Кудрявцева | Анастасия | Сергеевна | Национальный исследовательский университет «Московский институт электронной техники | Study of Field-Effect Transistor Channel Based on Bioconjugate of Far-Red Fluorescent Proteins and Carbon Nanotube |
| 5-15 | Кузяева | Валерия | Ивановна | РХТУ им. Д.И. Менделеева | Fabrication of porous hydrogels containing hyaluronic acid by photoinduced crosslinking |
| 5-16 | Куксин | Артем | Викторович | Московский институт электронной техники МИЭТ | |
| 5-17 | Левин | Алексей | Игоревич | ФГБОУ ВО "Пензенский государственный университет" | Implementation of electrical impedance tomography |
| 5-18 | Мартиросян | Давид | Юрьевич | ФИЦ ХФ им. Н.Н. Семёнова РАН | Femtosecond laser oocyte enucleation without fluorescent dye. |
| 5-19 | Михайлова | Олеся | Александровна | Санкт-Петербургский государственный политехнический университет им.Петра Великого | Development of an experimental stand for studying the characteristics of ion currents |
| 5-20 | Мусаев | Андрей | Геннадьевич | Московский | |
| 5-21 | Наумов | Евгений | Игоревич | СПбАУ РАН им. Ж.И. Алферова | |

| | | | | | |
|---|---|---|---|---|---|
| 5-22 | Николаева | Мария | Евгеньевна | Московский педагогический университет | |
| 5-23 | Порфирьева | Елена | Витальевна | Санкт-Петербургский Политехнический университет Петра Великого | Features of using the esCCO method to determine a person's condition |
| 5-24 | Романова | Вероника | Вячеславовна | Санкт-Петербургский Государственный Технологический институт/Институт аналитического приборостроения РАН | Miniature potentiometric system for determination of H+, K+, Na+, Cl–, NO3– - and Ca2+ ions in liquid biological environment |
| 5-25 | Рудных | Сергей | | Федеральное государственное бюджетное образовательное учреждение высшего образования «Университет «Дубна» | Determination of the isoelectric point of the Константинови ч antibody to Sars-Cov-2 by molecular modeling for conjugation with quantum dots |
| 5-26 | Рябкин | Дмитрий | Игоревич | НИУ МИЭТ | Modelling of laser welding of biological tissues using focused radiation |
| 5-27 | Святкина | Виталия | Игоревна | Институт аналитического приборостроения РАН | Investigation of the interaction of narrow-band radiation with skin pathologies using a multispectral light source |
| 5-28 | Скрябин | Дмитрий | Семенович | Санкт-Петербургский политехнический университет Петра Великого | Development of a fiber optical system for assessing the state of peripheral circulation |
| 5-29 | Степанов | Максим | Евгеньевич | Московский Государственный Педагогический Университет | Albumin nanoparticles for Near Infrared Bioimaging |
| 5-30 | Сучкова | Виктория | Викторовна | Национальный исследовательский университет «Московский институт электронной техники» | Development of an Algorithm for Predicting the Strength of Laser Reconstruction of Biological Tissue |
| 5-31 | Сырчина | Мария | Сергеевна | ФГБУН ФИЦ ХФ РАН им. Н.Н. Семенова | Analysis of size-dependent optical properties of lysine carbon dots produced by femtosecond laser synthesis |
| 5-32 | Харламова | Анастасия | Александровна | Северный арктический федеральный университет | Mathematical modeling of determination of "Premeltons" sites in DNA by ultra short laser pulses |

| | | | | | |
|---|---|---|---|---|---|
| 5-33 | Шатов | Александр | Андреевич | Федеральный исследовательский центр химической физики им. Н.Н. Семенова Российской Академии наук (ФИЦ ХФ РАН) | Effect of laser pulse duration on ultrafast laser synthesis of carbon dots from toluene |
| 5-35 | Шиповская | Анна | Борисовна | Саратовский национальный исследовательский государственный университет имени Н.Г. Чернышевского | Optical activity anisotropy in thin films of chitosan L- and D-ascorbate |
| 5-36 | Ямановская | Анастасия | Юрьевна | Санкт-Петербургский Политехнический Университет Петра Великого | Development of a sample preparation unit |
| 5-37 | Яшков | Дмитрий | Владимирович | Санкт-Петербургский политехнический университет Петра Великого | |

## 6. Other Aspects of Nanotechnology

## May 25, 2023

## 15:30 - 18:00 Poster Session II

Санкт-

| | | | | | |
|---|---|---|---|---|---|
| 6-1 | Аксенова | Валерия | Владимировна | Петербургский политехнический университет Петра Великого | Scattering antireflective nanostructured ITO coatings |
| 6-2 | Багров | Александр | Романович | Самарский университет имени академика С.П. Королева, физический факультет, 4 курс | Thermal entanglement in three-qubit Tavis-Cummings model with detuning and Kerr nonlinearity |
| 6-3 | Бородин | Богдан | Романович | ФТИ им. А. Ф. Иоффе | Transition from indirect to direct bandgap in thin β-InSe layers |
| 6-4 | Василевская | Юлия | Олеговна | Национальный исследовательский университет "МИЭТ" / НПК "Технологический центр" | Fractional leaky integrate-and-fire node based on single-walled carbon nanotubes networks |
| 6-5 | Васильева | Ольга | Васильевна | Чувашский государственный университет им. И.Н. Ульянова | Filamentous crystals of potassium carbonate in a pyrotechnic flame |
| 6-6 | Воробьев | Александр | Андреевич | СПб АУ РАН им. Ж. И. Алфёрова | |
| 6-7 | Голубков | Павел | Евгеньевич | ФГБОУ ВО "Пензенский государственный университет" | Influence of process parameters on the properties of microarc oxide coatings |
| 6-8 | Грушевский | Егор | Алексеевич | ЯрГУ | Polishing methods for formation nanoporous anodized alumina |
| 6-9 | Гурин | Сергей | Александрович | ФГБОУ ВО "Пензенский государственный университет" | Synthesis of thin- film structures of vanadium oxide by spray- pyrolysis |
| 6-10 | Емельянов | Никита | Сергеевич | ФГБОУ ВО "Пензенский государственный университет" | Study of the Effect of Temperature on the Electrophysical Parameters of Ferroelectrics |
| 6-11 | Журина | Ангелина | Евгеньевна | ФГБОУ ВО "Пензенский государственный университет" | Determination of the electrophysical parameters of piezoelectrics using complex conductivity |
| 6-12 | Захаров | Родион | Константинович | Самарский национальный исследовательский университет имени академика С.П. Королева | Coherence-enhanced entanglement between isolated atom and Jaynes-Cummings atom in a cavity with Kerr media |
| 6-13 | Зинченко | Тимур | Олегович | ФГБОУ ВО "Пензенский государственный университет" | Synthesis of thin-film structures of tungsten oxide by the spray-pyrolysis method |

| | | | | | |
|---|---|---|---|---|---|
| 6-14 | Исокжанов | Шахбоз | Шокиржон угли | Национальный исследовательский университет "МИЭТ" | Study of composite electrode material formation features based on Super C45/RuO2 and Super C45/MnO2 for asymmetric planar supercapacitors |
| 6-15 | Капустин | Сергей | Николаевич | САФУ им. М. В. Ломоносова, кафедра фундаментальной и прикладной физики | Ice detector and chemical sensor based on superhydrophobic coating of carbon nanoparticles |
| 6-16 | Каратышова | Татьяна | Яковлевна | Саратовский национальный исследовательский государственный университет имени Н.Г.Чернышевского | Obtaining conductive ultrathin films on based on a mixture of "carbon nanotubes - arachidic acid" by the Langmuir-Blodgett method |
| 6-17 | Каратышова | Татьяна | Яковлевна | Саратовский государственный университет имени Н. Г. Чернышевского | Properties of Langmuir floating layers and Langmuir-Schaeffer films based on polyaniline and arachidic acid mixture |
| 6-18 | Каратышова | Татьяна | Яковлевна | СГУ им. Н. Г. Чернышевского | Investigation of the Transfer of Floating Layers of Porphin Derivatives to Solid Substrates |
| 6-19 | Козловский | Александр | Валерьевич | ФГБОУ ВО "СГУ имени Н.Г. Чернышевского" | Photo-assisted adsorption of enzyme molecules onto a surface-modified silicon substrate |
| 6-20 | Кондратьев | Валерий | Михайлович | Алфёровский университет | Novel impedance spectroscopy approach for nanowires based adsorption sensors |
| 6-21 | Крафт | Вадим | Евгеньевич | СПбПУ Петра Великого | Получение нетканого полотна и изучение его диэлектрических характеристик |
| 6-22 | Литовченко | Наталья | Александровна | Национальный исследовательский университет «Московский институт электронной техники» | The method of formation of planar lithiumion batteries with composite electrode materials |
| 6-23 | Ломакин | Андрей | Игоревич | МИЭМ НИУ ВШЭ/Лаборатория квантовых детекторов | SIGNATURES OF DEPHASING BY SURFACE MAGNETIC DISORDER IN MAGNETORESISTANCE IN EPITAXIAL TIN FILMS |
| 6-24 | Бондарева | Полина | Игоревна | МИЭМ НИУ ВШЭ/ МПГУ | REACTIVE ION ETCHING OF THIN NBSE2 FILMS FOR HIGH-PERFORMANCE SUPERCONDUCTING DEVICE DEVELOPMENT |
| 6-25 | Мельников | Олег | Андреевич | ФГБОУ ВО "Пензенский государственный университет" | Modeling of the dynamic current-voltage characteristic of micro-arc oxidation |
| 6-26 | Молодцова | Анастасия | Анатольевна | Университет ИТМО | Jamming transition and micellization in robotic swarms |
| 6-27 | Николаева | Александра | Владиславовна | СПбАУ РАН им. Ж. И. Алфёрова | ZnO-PDMS based pressure sensors |

| | | | | | |
|---|---|---|---|---|---|
| 6-28 | Новичков | Максим | Дмитриевич | АО "НИИЭМП" | Study of heterogeneous structures deposition on ion-exchange membranes |
| 6-30 | Пилипова | Валерия | Михайловна | Санкт-Петербургский государственный университет телекоммуникаций им. проф. М. А. Бонч-Бруевича | Investigation of the modal composition in microstructured fibers with six cores |
| 6-31 | Поздеев | Вячеслав | Алексеевич | СПбАУ РАН им. Ж.И. Алфёрова | Исследование влияния растворителей и поверхностно-активных веществ на электрические свойства плёнок поли(3,4-этилендиокситиофен) полистиролсульфоната |
| 6-32 | Поповский | Никита | Игоревич | Санкт-Петербургский государственный университет телекоммуникаций им. проф. М.А. Бонч-Бруевича | Features of the construction photonic tensor cores for neural networks |
| 6-33 | Стовпяга | Екатерина | Юрьевна | ФТИ им. А.Ф. Иоффе | A facile low-temperature approach for organics removal from SiO2-CTAB mesoporous particles |
| 6-34 | Тимкаева | Диана | Абдулхаковна | ФГБОУ ВО Ульяновский государственный университет/ НПК "Технологический центр" | Effect of Deformation on the Electronic and Optical Properties of Nanotubes Based on 2D Janus Materials SMoSiN2 |
| 6-35 | Чистиков | Илья | Евгеньевич | СПбАУ РАН им. Ж.И. Алферова | Mechanisms of formation of SiC by the method of substitution of atoms on Si of various phases |
| 6-36 | Шибалов | Максим | Викторович | ИНМЭ РАН | Properties of ultrathin epitaxial NbNx film on c-cut sapphire |
| 6-37 | Ширяев | Максим | Евгеньевич | МИЭТ | Effect of Al-CuO multilayer thermite structures thickness on combustion behavior |
| 6-38 | Golubchikov | Daniil | Olegovich | Lomonosov Moscow State University | Composite biomaterials of complex shape based on polycaprolactone/polylactide matrix for bone tissue engineering |
| 6-39 | Gurin | Sergey | Alexandrovich | ФГБОУ ВО "Пензенский государственный университет" | Synthesis of thin- film structures of vanadium oxide by spraypyrolysis |

# Practical realization of free-space continuous-variable quantum key distribution

**I. A. Adam** [1✉], **D. A. Kargina** [1], **A. S. Kolesnik** [1], **B. A. Nasedkin** [1]
[1] ITMO University, Saint-Petersburg, Russian Federation
✉iaadam@itmo.ru

**Abstract.** Secure information exchange between two parties is a main goal of quantum communication systems. Nowadays there are several commercial products of quantum key distribution systems realized in a fiber optic environment. Nevertheless, for subsequent development of quantum networks systems with a free-space channel must be investigated as a solvation to the "last-mile problem". In this aspect continuous variable quantum key distribution protocols are promising candidates of implementation in free-space communication scenario due to compact sizes, high key rates and low cost. As well these systems can be easily implemented in mobile devices, including self-driving cars and drones. In this work system architecture in the presence of free-space channel is discussed, influence of polarization and phase fluctuations on system performance in turbulent atmosphere and methods of their compensation are investigated. As well a secret key rate on small distances up to tens of meters is calculated. Obtained results shows promising employment of continuous variables protocols in free-space quantum communication systems.

**Keywords:** quantum communication, quantum key distribution, continuous-variables, Gaussian modulation, free-space channel, turbulent atmosphere.

**Funding:** The study is funded by RPMA grant of School of Physics and Engineering of ITMO University.

## Introduction

Quantum key distribution (QKD) is a new communication technique between two parties, theoretical security of which is guaranteed by the laws of quantum physics. Mainly QKD protocols may be divided into discrete-variables (DV) and continuous-variables (CV) [1]. The former uses single photon states (polarization, phase, time) to encode information about generated raw key whereas the latter uses quadrature components of electro-magnetic waves. Thus, CV protocols are able to use coherent detection methods as homodyne or heterodyne detection instead of single photon counters which leads to decline of size and cost of final product.

Nowadays there are number of QKD systems with free-space channels [2], which have high potential of implementation in quantum networks. However, current free-space systems, which as well must solve the "last-mile problem" [3] of distribution quantum keys to final users, are still far from compact and low-cost commercial products. The usage of CV protocols may become a solvation to current problems as it is involves only the use of balanced photodetector and optical hybrid (considering heterodyne detection and obligatory components) on the receiver side. Thus, the study of practical realization of CV-QKD systems should be explored.

## Materials and Methods

The experimental layout is based on the fiber CV-QKD systems, which are developed at ITMO University. The main parameters of the layout architecture are listed in Table 1. They were chosen for the reason of security, technical simplicity and high key rate [4].

Secure key rate calculation of the considered layout with free-space channel is done by Eq. (1) [5]:

$$K = f_{sym}\left(1-FER\right)\left(1-\nu\right)\left(\beta I_{AB}-\chi_{EB}\right), \quad (1)$$

where $f_{sym}$ – symbol rate, $FER$ – frame error rate, ν – key fraction disclosed for parameter estimation, β – post processing efficiency, $I_{AB}$ – mutual information between the transmitter (Alice) and receiver (Bob), $\chi_{EB}$ – Holevo bound.

Table 1

**Free-space CV-QKD layout parameters**

| Parameter | Value |
|---|---|
| Protocol | Continuous-variable |
| Wavelength, nm | 1550 |
| Modulation type | Gaussian |
| Detection type | Heterodyne (double homodyne) |
| Reconciliation type | Reverse |
| Local oscillator type | Transmitted (on the transmitter side) |
| Organization of free-space channel | Collimators, Telescope systems (self-made) |

For polarization multiplexing of the local oscillator and signal pulses it's fluctuation in the turbulent atmosphere should be investigated as well as the phase fluctuation compensation algorithm [6]. For this purpose, simplified optical scheme of considered CV-QKD layout was build and numerical experiments were taken.

## Results and Discussion

Obtained results shows that polarization state doesn't experience large fluctuations and could be compensated by passive polarization controller (for example, half-wave plate). Applied compensation algorithm has proven his efficiency on the small distances. The value of secret key rate on the distance of several meters (3.5 m) was in order of Kbit/s which makes the usage of CV protocols in free-space quantum communication quite promising.

## Conclusion

In conclusion, the obtained results confirm the possibility of implementing CV-QKD systems in free-space communication channel and the necessity for their further research and development.

## REFERENCES


1. **Pirandola S. et al.** Advances in quantum cryptography //Advances in optics and photonics. – 2020. – Т. 12. – №. 4. – С. 1012-1236.

2. **Xue, Y., Chen, W., Wang, S., Yin, Z., Shi, L., & Han, Z**., Airborne quantum key distribution: a review, Chinese Optics Letters, 19(12), 122702, 2021.

3. **Cao, Y., Zhao, Y., Wang, Q., Zhang, J., Ng, S. X., & Hanzo, L.**, The evolution of quantum key distribution networks: On the road to the qinternet, IEEE Communications Surveys & Tutorials, 24(2), 839-894, 2022.

4. **Goncharov R., Vorontsova I., Kirichenko D., Filipov I., Adam I., Chistiakov V., Smirnov S., Nasedkin B., Pervushin B., Kargina D., Samsonov E., Egorov V.**, The Rationale for the Optimal Continuous-Variable Quantum Key Distribution Protocol, Optics, Vol. 3 (4), 338-351, 2022.

5. **Laudenbach, F., Pacher, C., Fung, C. H. F., Poppe, A., Peev, M., Schrenk, B., ... & Hübel, H.**, Continuous-variable quantum key distribution with Gaussian modulation—the theory of practical implementations, Advanced Quantum Technologies, 1(1), 1800011, 2018.

6. **Soh, D. B., Brif, C., Coles, P. J., Lütkenhaus, N., Camacho, R. M., Urayama, J., & Sarovar, M.**, Self-referenced continuous-variable quantum key distribution protocol, Physical Review X, 5(4), 041010, 2015.

Conference materials
UDC 621.383.52
DOI: https://doi.org/10.18721/JPM.

# Effect of sulfide–polyamide passivation on dark currents of the InAlAs/InGaAs/InP avalanche photodiodes

**V. V. Andryushkin** [1✉], **N. A. Maleev** [2], **A. G. Kuzmenkov** [2], **M. M. Kulagina** [2], **Yu. A. Guseva** [2], **A. P. Vasil'ev** [3], **S. A. Blokhin** [2], **M. A. Bobrov** [2], **S. I. Troshkov** [2], **E. S. Kolodeznyi** [1], **V. M. Ustinov** [3]
[1] ITMO University, St. Petersburg 197101, Russia;
[2] Ioffe Institute, St. Petersburg 194021, Russia;
[3] SHM R&E Center, RAS, St. Petersburg 194021, Russia
✉vvandriushkin@itmo.ru

**Abstract.** The paper presents a study of the effect of passivation of the surface on performance of the InAlAs/InGaAs/InP avalanche photodiode with mesa structure using treatment in an aqueous solution of ammonium sulfide and subsequent protection by a layer of polyamide (sulfide-polyamide passivation). It is shown that avalanche photodiodes with a photosensitive area of 32 microns reproducibly demonstrate dark current below 10-20 nA at the level of 0.9 of the breakdown voltage. A homogeneous distribution of the breakdown voltage value over the sample area at -85V, as well as long-term stability of avalanche photodiode characteristics were observed.

**Keywords:** sulfide-polyamide passivation, avalanche photodiode, mesa structure.

**Funding:** This work was supported by the Ministry of Science and Higher Education of the Russian Federation, research project no. 2019-1442.

**Citation:** Maleev N. A., Kuzmenkov A. G., Kulagina M. M., Guseva Y. A., Vasil'ev A. P., Blokhin S. A., Bobrov M. A., Troshkov S. I., Kolodeznyi E. S., Ustinov V. M., Sulfide–polyamide passivation of the InAlAs/InGaAs avalanche photodiodes based on mesa structure, St. Petersburg State Polytechnical University Journal. Physics and Mathematics. 16 ( ) (2023) …–…. DOI: https://doi.org/10.18721/JPM.

This is an open access article under the CC BY-NC 4.0 license (https://creativecommons.org/licenses/by-nc/4.0/)

© Maleev N. A., Kuzmenkov A. G., Kulagina M. M., Guseva Y. A., Vasil'ev A. P., Blokhin S. A., Bobrov M. A., Troshkov S. I., Kolodeznyi E. S., Ustinov V. M., 2023. Published by Peter the Great St. Petersburg Polytechnic University.

Материалы конференции
УДК 621.383.52
DOI: https://doi.org/10.18721/JPM.

## Introduction

The development of modern light detection and ranging systems for pilotless vehicles requires the creation of compact, efficient, and highly sensitive detectors of laser emission in the eyes safe spectral range of 1300-1550 nm. One of the approaches to creation of such detectors is the use of arrays of avalanche photodiodes (APD) operating in Geiger mode [1]. APDs based on InAlAs/InGaAs/InP heterostructures have certain advantages over widely used InP/InGaAs APDs due to the large ratio of the ionization coefficients of charge carriers and their temperature stability, which reduces the noise of avalanche multiplication and improves the thermal stability of the breakdown voltage. The mesa structure is widely used to isolate the active area of the InAlAs/InGaAs APD in the lateral direction. A serious problem of APD designs with a mesa structure are surface leakage currents, which make the main contribution to the dark current. Methods of mesa structure etching and the passivation with dielectric films has a significant effect

on the surface leakage current value. For PIN photodiodes, an effective method of mesa structure passivation in an aqueous solution of ammonium sulfide ($(NH_4)_2S_x$), so-called sulfide passivation, was demonstrated, while an important point for obtaining a time-stable reduction of surface leakage currents is additional protection of the surface with the oxygen–free dielectric coating [2].

## Materials and Methods

APD heterostructures were grown by molecular beam epitaxy on semi-insulating InP(100) substrates. The structures comprised a highly doped n-type InGaAs contact layer, a highly doped n-type InAlAs layer, an undoped InAlAs multiplication layer with a thickness of 850 nm, a p-type InAlAs charge layer, an undoped InAlGaAs gradient layer, an undoped InGaAs absorbing layer with a thickness of 1700 nm, an undoped InAlGaAs gradient layer, a highly doped p-type InAlAs layer, and a thin highly doped p-type InGaAs contact layer. After the formation of a top ring Ti-Pt-Au contact, the mesa was etched in an $H_3PO_4$ : HBr : $K_2Cr_2O_7$ solution with penetration to highly doped n-type layers located between the multiplication layer and the substrate. Processing of the surface in an aqueous solution of ammonium sulfide followed by a protective layer of AD-9103-30 polyamide (sulfide–polyamide passivation) was investigated as an alternative option for the passivation of a sidewall of the mesa structure.

## Results and Discussion

The dependences of dark current and photocurrent on the applied voltage for a fabricated InAlAs/InGaAs APD with sulfide–polyamide passivation of the mesa structure with a diameter of 32μm at room temperature together with the corresponding dependence of the avalanche multiplication factor were measured. Characteristic values of the dark current under U = 0.9Ubr of the fabricated APDs were in the range of 10–11 nA, which confirms the effectiveness of the proposed passivation method. An important requirement on the passivation technology is to ensure the reproducibility and long-term stability of the parameters. The fabricated devices demonstrate high uniformity of the breakdown voltage whose value is 85 V. The spectral sensitivity (photoresponse) values in the 1550 nm region are 0.85–0.88 A/W, and their corresponding capacitance values are 0.11–0.12 pF. The dark current of the investigated diodes does not exceed 20 nA.

## Conclusion

The surface passivation of the mesa structure of InAlAs/InGaAs APDs using processing in an aqueous solution of ammonium sulfide followed by a protective layer of polyamide of the diodes with an active area diameter of 32 μm enabled reproducible achievement of dark current levels of 10–20 nA under an applied voltage of 0.9 of the breakdown voltage, uniform distribution of the breakdown voltage across the sample area at the level of −85 V, and long-term parameter stability.

## Acknowledgments

This work was supported by the Ministry of Science and Higher Education of the Russian Federation, research project no. 2019-1442).

## REFERENCES

1. **Baba T., Suzuki Y., Makino K., Fujita T., Hashi T., Adachi S., Nakamura S., Yamamoto K.**, Development of an InGaAs SPAD 2D array for flash LIDAR, Proceedings of SPIE. 10540 (2018) 105400L.

2. **Ravi M.R., DasGupta A., DasGupta N.**, Silicon nitride and polyimide capping layers on InGaAs/InP PIN photodetector after sulfur treatment, Journal of Crystal Growth. 268(3–4) (2004) 359–363.

## THE AUTHORS

**ANDRYUSHKIN Vladislav V.**
vvandriushkin@itmo.ru
ORCID: 0000-0002-7471-8627

**MALEEV Nicolai A.**
maleev.beam@mail.ioffe.ru
ORCID: 0000-0003-2500-1715

**KUZMENKOV Aleksandr G.**
kuzmenkov@mail.ioffe.ru
ORCID: 0000-0002-7221-0117

**KULAGINA Marina M.**
Marina.Kulagina@mail.ioffe.ru
ORCID: 0000-0002-8721-185X

**GUSEVA Julia A.**
Guseva.Julia@mail.ioffe.ru
ORCID: 0000-0002-7035-482X

**VASIL'EV Alexey P.**
Vasiljev@mail.ioffe.ru
ORCID: 0000-0002-2181-5300

**BLOKHIN Sergei A.**
blokh@mail.ioffe.ru
ORCID: 0000-0002-5962-5529

**BOBROV Mikhail A.**
bobrov.mikh@gmail.com
ORCID: 0000-0001-7271-5644

**TROSHKOV Sergey I.**
S.Troshkov@mail.ioffe.ru
ORCID: 0000-0002-3307-6226

**KOLODEZNYI Evgenii S.**
evgenii_kolodeznyi@itmo.ru
ORCID: 0000-0002-3056-8663

**USTINOV Victor M.**
vmust@beam.ioffe.ru
ORCID: 0000-0002-6401-5522

# Features of the operation of a laser profilometer in an automated rolling stock control system

**K. G. Arinushkina** [1,2✉], **A. S. Adadurov** [2], **I. Yu. Savelev** [2], **V. V. Davydov** [1]
[1] The Bonch-Bruevich Saint Petersburg State University of Telecommunications, Saint Petersburg, Russia;
[2] VNIIZhT-ENGINEERING LLC, Saint Petersburg, Russia
✉k-arinushkina@mail.ru

**Abstract.** Faulty wheelset treads were identified as one of the major problems in the early stages of car repairs. To reduce the stopping time of passing trains, laser profilometers were introduced on the railway tracks. In the course of the work, data obtained from measurements of various profiles of the surfaces of freight cars, including wheelsets, were analyzed in comparison with reference profiles. An increase in measurement accuracy has been established by minimizing the human factor, global digitalization of technological processes and automation of rolling stock control along the route.

**Keywords:** laser profilometer, geometrical parameters, railway transport, wheelset.

## Introduction

The traffic safety of railway transport largely depends on the quality of wheelset materials, design, manufacturing technology, their inspection and repair. Due to large static and dynamic loads, as well as violations of the rules for the technical operation of rolling stock, various defects occur in the wheelset. The requirements of the parameters of wheel sets in the automated control system for the operation of the rolling stock are met by laser profilometers, which are designed to measure: the height of the flange, rolled products, the thickness of the flange, the steepness of the flange, the thickness of the tire, the removal and analysis of the complete profile of the wheel tread, the support of the electronic wear database wheelsets, carrying out tolerance control and sorting during technical inspection, certification, repair and formation of railway wheelsets of rolling stock [1,2].

## Methods

The laser profilometer for determining the geometrical parameters of the surface profile contains a laser radiation source with a laser beam-to-line converter, an optical matrix receiver of reflected radiation, and an information processing device. The source of laser radiation is made in the form of a semiconductor laser operating in a pulsed mode. At least one narrow-band interference light filter is introduced along the reflected beam in front of the optical matrix receiver. In addition, a semiconductor laser operating in the visible red wavelength range was used. In addition, a semiconductor laser operating in the visible red wavelength range was used, the temperature stabilization system was made on the basis of Peltier elements with a control controller and a temperature sensor [3]. The information processing device is made in the form of a programmable logic controller with real-time signal processing and calculation of the surface profile. The block diagram of the laser profilometer is shown in Figure 1.

In contrast to the previously used templates for controlling the parameters of the wheel tread, which were applied by employees of the railway transport structure, the laser profilometer in the automated rolling stock control system fully automates this process. The laser signal leaves a wide line on the photomatrix covering several points at once. Based on the point cloud obtained on the basis of the image from the photodetector, the wheel profile is analyzed and control values are calculated. Based on the point cloud obtained on the basis of the image from the photodetector, the wheel profile is analyzed and control values are calculated. Since the wheel geometry changes during operation, it becomes impossible to describe the new profile shape with sufficient accuracy by the classes of initial functions.

To solve this problem, a polynomial model was developed. This model takes into account the features in the distortion of the reflected laser radiation from the changed profiles of the wheel

during its movement. Accounting for these features makes it possible to realize the restoration of the shape of the wheel pair profile more clearly in comparison with previously used methods.

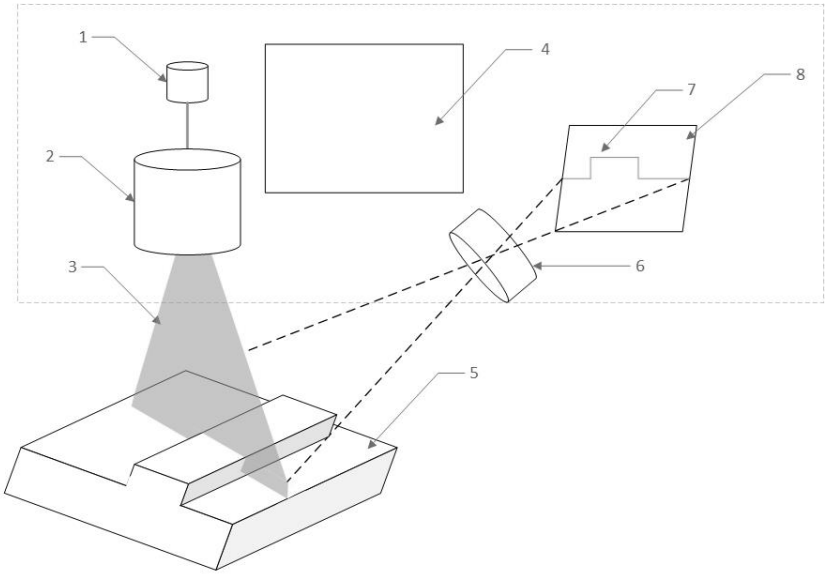


Fig. 1. Laser profilometer. 1 – laser module; 2 – line generator; 3 – plane of laser radiation; 4 – controller based on digital signal processor; 5 - controlled object; 6 - optical system of the photodetector; 7 - image of the probing laser radiation line on the photodetector; 8 - matrix photodetector

## Results and Discussion

The use of a new model made it possible, using a laser profilometer, to create an automated system that can more accurately control the geometric parameters of the surface profile, the contour dimensions of the object, the relative position of parts, and the deviation from flatness. The automated profilometer system allows not only taking pictures, analyzing the data obtained based on their comparison with the basic standard, but also transmitting information. This helps to estimate the number of errors in the received measurements and allows them to be converted into digital data. This made it possible to integrate it into the universal digital hardware and software platform of the automatic system for the operation of the rolling stock.

## Conclusion

Just as a template is applied to a real wheel for measurements during the technical inspection of a rolling stock car, so in the proposed method, measurements are made at points according to the template. The technical result is an increase in measurement accuracy by minimizing the human factor, global digitalization of technological processes and automation of rolling stock control along the route.

## REFERENCES

1. **Adadurov A.S., Usmendeyeva A.D.** Sistema monitoringa sostoyaniya podvizhnogo sostava dlya formirovaniya optimizirovannykh i sbalansirovannykh planov remonta i ekspluatatsii (chast' 1) / A.S. Adadurov, A.D. Usmendeyeva // Tekhnika zheleznykhdorog. –2018. 3 (43). 66−73.

2. **Chunsheng Li, Shihui Luo, Colin Cole, et al.** An overview: modern techniques for railway vehicle on-board health monitoring systems. Vehicle System Dynamics. 2017, Vol.55, No.7, p.1045.

3. **Romero**, Development and implementation of an optical profilometer by laser triangulation, 2020 9th International Congress of Mechatronics Engineering and Automation, CIIMA 2020 - Conference Proceedings 2020, Quintero, F.J. and Mendoza, K. and Romero, L.A. and Marrugo, A.G.

Conference materials
UDC
DOI:

# Hybrid perovskite/GaP nanowires solar cells with enhanced photovoltaic performance

**M. Baeva [1]✉, A. Furasova [1], Alexey Mozharov, [1] Pavel Tonkaev[2]**
[1] Alferov University, Khlopina 8/3, 194021, St. Petersburg, Russia
[2] Department of Physics and Engineering, ITMO University, Lomonosova 9, 197101, St. Petersburg, Russia
✉maria.baeva111@gmail.com

**Abstract.** In this work we report an improved photovoltaic performance of hybrid halide perovskite solar cell with integrated into a active layer GaP nanowires. The incorporation of GaP nanowires improves charge extraction from a perovskite layer. As a consequence, we boost the MAPbI3 perovskite solar cell efficiency up to 18.8% by VOC and JSC enhancement. The provided multi-physical theoretical simulations of the solar cells with the incorporated GaP nanowires describe the mechanism of charge extraction and optical absorption improvement.

**Keywords:** perovskite solar cells, GaP nanowires, electric field management, photon management.

**Funding:** This work was supported by State assignment of the Russian Science Foundation grant No. 22-79-10286.

**Citation:** M. Baeva, A. Furasova, *et. al.*, Hybrid perovskite/GaP nanowires solar cells with enhanced photovoltaic performance, St. Petersburg State Polytechnical University Journal. Physics and Mathematics. 16 ( ) (2023) …–…. DOI: ...

This is an open access article under the CC BY-NC 4.0 license (https://creativecommons.org/licenses/by-nc/4.0/)

© M. Baeva M., A. Furasova A., *et. al.*, 2023. Published by Peter the Great St. Petersburg Polytechnic University.

Материалы конференции
УДК
DOI:

## Introduction

Since the very first report on lead halide organo-inorganic perovskite solar cells (PeSCs) was published in 2009 [1] this research area saw an expeditious development due to the perovskites' unique electronic and optical properties, such as tunable direct bandgap, high absorption coefficient, low nonradiative recombination rate, high defects tolerance, and high charge carriers' mobility [2]. Integration of low dimension structures into the perovskite active material aid the PeSCs performance enhancement beyond physical limitations (i.e. optical losses in substrates and charge transport materials, the lower light absorption of perovskite in the red spectral range and charge recombination at interfaces between the perovskite and transport layers as well as between perovskite grains). GaP nanowires are promising nanostructure to incorporate in PeSCs due to high refractive index (n >3) allowing for strong light confinement, high transparency in the visible wavelengths range [3], optimal thermal conductivity for optoelectronic applications in addition to the band gap tunability via doping [4]. Here, we incorporate GaP (i-type) and GaP:Be (p-type doping) NWs to be placed between a mesoporous TiO2 hole-transport layer (HTL) and MAPbI3 perovskite photoactive layer of n-i-p PSC to enchance light-harvesting and improve electrical charge extraction inside of the perovskite layer. We report PCE 5.45% increment value for PSC

with integrated i-GaP NWs and 8.48% PCE increment for GaP:Be NWs with the best device possessing PCE 18.8%.

## Materials and Methods

The numerical modeling of SC optical properties was performed with COMSOL Multiphysics software. Self-catalyzed GaP NWs grown on Si(111) substrates by solid-source MBE using Ga as a catalyst were used in this study. The PeSCs were fabricated in n-i-p architecture with Glass/FTO/c-$TiO_2$/m-$TiO_2$/GaP NWs/$MAPbI_3$/SPIRO-MeOTAD/Gold structure. Our PeSCs underwent optical (i.e. photoluminescence (PL) intensity spectra, time-resolved photoluminescence (TPL) decay spectra) and functional (i.e. *J-V* curves characteristics, external quantum efficiency (EQE) and photocurrent) characterization

## Results and Discussion

According to our simulation results introduction of GaP NWs leads to the bending of bands near the NW edge, resulting in the emergence of a conductive channel inside of the perovskite layer around the surface of the nanowire for holes, in case of the p-doped GaP NWs, and holes and electrons in case of i-doped GaP NWs, respectively. Both effects improve PeSCs EQE, and, consequently enhanced when compared to the reference cell photocurrent at the wavelength range from 550 nm to 780 nm. After GaP NWs introduction perovskite film PL signal is improved by 12% and by 15% for the case of i-GaP and p-GaP NWs, respectively. PeSC reference best performance: PCE = 17.5%, $V_{OC}$ 1.00 V, $J_{SC}$ = 21.9 mA/cm$^2$ and FF of 80.2%. The cell with the highest PCE (18.8%) contained p-GaP NWs and demonstrated a $V_{OC}$ of 1.04 V, $J_{SC}$ of 23.6 mA/cm$^2$ and FF of 76.3%. The best cell with i-GaP NWs was achieved a PCE of 18.5% with $V_{OC}$ of 1.03 V, $J_{SC}$ of 22.4 mA/cm$^2$ and FF of 80.4%.

## Conclusion

We proposed a novel approach to PeSCs performance advancement via GaP NWs incorporation. The GaP NWs introduction improves electrical charge extraction and enchances light-harvesting inside of the perovskite layer We report PCE 5.45% increment value for PSC with integrated i-GaP NWs and 8.48% PCE increment for GaP:Be NWs with the best device possessing PCE 18.8%.

## Acknowledgments

This work was supported by State assignment of the Russian Science Foundation grant No. 22-79-10286.

## REFERENCES

1. **Kojima A., Teshima K., Shirai Y., Miyasaka T.** Organometal halide perovskites as visible-light sensitizers for photovoltaic cells. *Journal of the american chemical society* 2009, *131*, 6050–6051.

2. **Correa-Baena J.-P., Saliba M., Buonassisi T., Grätzel M., Abate A., Tress W., Hagfeldt A.** Promises and challenges of perovskite solar cells. *Science* **2017**, *358*, 739–744.

3. **Khmelevskaia D., Markina D., Fedorov V., Ermolaev G., Arsenin A., Volkov V., Goltaev A., Zadiranov Y., Tzibizov I., Pushkarev A., Samusev A., Shcherbakov A., Belov P., Mukhin I., Makarov S.,** Directly grown crystalline gallium phosphide on sapphire for nonlinear all-dielectric nanophotonics. *Applied Physics Letters* **2021**, *118*, 201101.

4. **Duan X., Wang J., Lieber C. M.,** Synthesis and optical properties of gallium arsenide nanowires. *Applied Physics Letters* **2000**, *76*, 1116–1118.

## THE AUTHORS

**BAEVA MARIA**
maria.baeva111@gmail.com
ORCID: 0000-0002-0331-5433

**FURASOVA ALEKSANDRA**
aleksandra.furasova@metalab.ifmo.ru
ORCID: 0000-0002-7277-5767

**MOZHAROV ALEXEY**
alex000090@gmail.com
ORCID: 0000-0002-8661-4083

**TONKAEV PAVEL**
pavel.tonkaev@anu.edu.au
ORCID: 0000-0003-1849-0654

Conference materials
UDC
DOI: https://doi.org/10.18721/JPM.

# Light-Emitting and Light-Detecting Perovskite Electrochemical Cell on Silicon

**Baeva M.,[1,2]✉ Gets D.,[2] Polushkin A.,[2] Vorobyov A.[1]**
[1] Alferov University, Khlopina 8/3, 194021, St. Petersburg, Russia
[2] Department of Physics and Engineering, ITMO University, Lomonosova 9, 197101, St. Petersburg, Russia
✉maria.baeva111@gmail.com

**Abstract.** Here we report on a novel architecture of inorganic perovskite light-emitting and light-detecting electrochemical cell formed on silicon substrate. The cell's active material layer consists of a composite material made: halide perovskite ($CsPbBr_3$) microcrystals, polymer support matrix (poly(ethylene oxide)) , and added mobile ions ($Li^+$). The proposed device emits light of 7000 cd/m$^2$ and electroluminescence efficiency of $1.3\cdot10^5$ lm/W at 523 nm. The light-detecting property of the device is characterized by sensitivity up to 0.75 A/W, specific detectivity of $8.56\cdot10^{11}$ Jones, and linear dynamic range of 48 dB. Moreover, since the device fabricated is fabricated on a silicon substrate it exhibits 40% lower Joule heating compared to the perovskite optoelectronic devices fabricated on conventional ITO/glass substrates.

**Keywords:** composite inorganic halide perovskite, silicon, light-emitting electrochemical cell, photodetector.

**Funding:** This work was supported by State assignment of the Russian Science Foundation grant No. 22-79-10286.

**Citation:** Baeva M., Gets D., *et. al*. "Light-Emitting and Light-Detecting Perovskite Electrochemical Cell on Silicon", St. Petersburg State Polytechnical University Journal. Physics and Mathematics. 16 ( ) (2023) …–…. DOI:….

This is an open access article under the CC BY-NC 4.0 license (https://creativecommons.org/licenses/by-nc/4.0/)

© Baeva M., Gets D., *et. al.*, 2023. Published by Peter the Great St. Petersburg Polytechnic University.

Материалы конференции
УДК
DOI:

## Introduction.

Halide perovskites are a type of semiconductor material that has many unique photoactive, optoelectronic and photonic properties. They have a general stoichiometry of ABX3, where A is usually either Cs, methylammonium (MA), or formamidinium (FA), and B is usually either Cl, Br, or I. The conventional perovskite light-emitting device is a perovskite LED (PeLED), which typically consists of number of different material layers that must be carefully selected and fabricated in a substantial number of technological steps [1-5]. On the other hand perovskite light-emitting electrochemical cells (PeLECs) are feasible alternative to PeLEDs. PeLEC consists of a single multifunctional layer [6] – composite perovskite material, i.e., the mixture of inorganic halide perovskite (e.g. $CsPbBr_3$) nanocrystals acting as an electroluminescent component embedded into polymer matrix (poly(ethylene oxide) (PEO) which aids ion transport and passivates crystal grains, and mobile ions ($Li^+$ from LiTFSI). In such a device, the dynamically formed intrinsic p-i-n structure is responsible for charge injection, facilitation of ion transport, enhanced photoluminescence quantum yield (PLQY) and efficient electroluminescence [7]. One of the significant issues in PeLEDs and PeLECs application for display design is Joule heating

poor endurance of conventional substrates (soda-lime glass, polyethylene terephthalate (PET), etc.) [8-10]. Finally, expanding the functionalities of halogen perovskite devices [11-16] by e.g. combining light-detection (or photovoltaic) regime of operation with light-emitting regime is still an ambitious challenge.

Here we demonstrate PeLEC device consisting of a single layer of composite inorganic perovskite material, i.e. $CsPbBr_3$:PEO:LiTFSI mixture. Owing to the fact that silicon thermal conductivity is substantially higher than that for the ITO/glass structure, our device sustains a much higher level of Joule heating during operation. Our device emits light at bias applied in forward direction and detects light when reversed bias is applied.

## Materials and Methods

*$Si^{++}$(111) substrate patterning*

The phosphorous-doped single-crystal silicon substrate <100> ($n^{++}$-Si(100)) was used for device fabrication. A thermally oxidated 200 nm thick $SiO_2$ layer was covered in a positive photoresist. Next, the photoresist was patterned, developed and washed away. After that the $SiO_2$ uncovered 2x2 $mm^2$ square areas were etched away with hydrofluoric acid (HF). The residual photoresist photoresist was removed using the organic solvent dimethyl sulfoxide (DMSO) and the substrate was then washed in deionized water. Finally, bottom aluminum (Al, thickness ~ 200 nm) contact was deposited on the back side of $n^{++}$-Si(100) substrate by vacuum thermal evaporation.

*Perovskite Solution Preparation.*

The $CsPbBr_3$ solution of 0.2 mmol/ml concentration was prepared by adding CsBr and $PbBr_2$ salts in a 1:1 molar ratio to anhydrous DMSO solvent and stirring the mixture overnight at 60 °C at 300 rpm. To mix a composite perovskite solution the prepared CsPbBr3 DMSO solution, poly(ethylene oxide) (PEO, $M_W = 10^6$ g/mol, concentration 20 $mg \cdot mL^{-1}$) DMSO solution, and lithium bis(trifluoromethanesulfonyl)imide (LiTFSI) DMSO solution (concentration 10 $mg \cdot mL^{-1}$) were mixed in 1:0.1:0.01 dry components wt. ratio, respectively, with subsequent overnight stirring at 60 °C and 300 rpm.

*Device fabrication.*

First, the patterned $n^{++}$-Si(100) substrates surface was activated in $O_2$ plasma (P = 10 W) for 2 mins. Then, the perovskite active region (thickness ~100 nm) was fabricated through spin-coating process in dry $N_2$ filled glovebox. After that, a ~40 nm thick layer of entangled SWCNt network was placed on top of the patterned structure and densified with anhydrous diisopropyl ether (DIPE).

*Device Characterization*

The device cross-section Sem imaging was performed using Zeiss Supra 25 SEM. The device's *J-V* curves and *J* tracking curves were acquired with a Keithley 2401 source meter. The device luminance measurements were carried out using Telescopic Optical Probe 150 of CAS 120 Instrument Systems spectroradiometer. For photodetector behavior measurements, a continuous-wave (CW) laser diode of 450 nm wavelength with the maximum output optical power density of 405.85 $mW/cm^2$ was used as an excitation source. Photodetector external quantum efficiency (EQE) spectra were obtained using a 200 W halide lamp, monochromator Solar Laser Systems M266, and calibrated reference Si solar cell. Heat distribution imaging was acquired with a commercially available IR-imaging camera "Seek Thermal".

## Results and Discussion

According to cross-section (CS) SEM measurements the perovskite film thickness constitutes ~140 nm with average grain size of ~ 150..200 nm. Our light emitting device is a light-emitting electrochemical cell, which provides light electroluminescence efficiency $1.3 \cdot 10^5$ lm/W and luminance more than 7000 $cd/m^2$. In the light-detecting regime of operation, sensitivity of our device reaches 0.75 A/W with specific detectivity $8.56 \cdot 10^{11}$ Jones and LDR 48 dB. We have

successfully shown that PeLEC devices withstand 40% lower thermal heating, when 32.7% higher electrical power is applied.

## Conclusion

We have demonstrated dual-function PeLEC (light-emitting ang light-detecting device) consisting of a single layer of composite inorganic perovskite material with improved Joule heating robustness.


## Acknowledgments

This work was supported by State assignment of the Russian Science Foundation grant No. 22-79-10286.


## REFERENCES


1. **Veldhuis, S.A., Boix, P.P., Yantara, N., Li, M., Sum, T.C., Mathews, N. and Mhaisalkar, S.G.**, "Perovskite Materials for Light-Emitting Diodes and Lasers," *Adv. Mater.*, vol. 28, no. 32, pp. 6804–6834, Aug. 2016.
2. **Shan, Q., Song, J., Zou, Y., Li, J., Xu, L., Xue, J., Dong, Y., Han, B., Chen, J., Zeng, H.**, "High Performance Metal Halide Perovskite Light-Emitting Diode: From Material Design to Device Optimization," *Small*, vol. 13, no. 45, p. 1701770, Dec. 2017.
3. **Jia, P., Lu, M., Sun, S., Gao, Y., Wang, R., Zhao, X., Sun, G., Colvin, V. L., Yu**, "Recent Advances in Flexible Perovskite Light-Emitting Diodes," *Adv. Mater. Interfaces*, vol. 8, no. 17, p. 2100441, Sep. 2021.
4. **Liu X.-K., Xu W., Bai S., Jin Y., Wang J., Friend R.H., Gao F.**, "Metal halide perovskites for light-emitting diodes," *Nat. Mater.*, vol. 20, no. 1, pp. 10–21, Jan. 2021.
5. **Lu M, Zhang Y., Wang S., Guo J., Yu W. W., and Rogach A. L.**, "Metal Halide Perovskite Light-Emitting Devices: Promising Technology for Next-Generation Displays," *Adv. Funct. Mater.*, vol. 29, no. 30, p. 1902008, Jul. 2019.
6. **Youssef K., Li Y., O'Keeffe S., Li L., and Pei Q**., "Fundamentals of Materials Selection for Light-Emitting Electrochemical Cells," *Adv. Funct. Mater.*, vol. 30, no. 33, p. 1909102, Aug. 2020.
7. **Gets, D., Alahbakhshi, M., Mishra, A., Haroldson, R., Papadimitratos, A., Ishteev, A., Saranin, D., Anoshkin, S., Pushkarev, A., Danilovskiy, E., Makarov, S., Slinker, J. D., Zakhidov, A. A.**, "Reconfigurable Perovskite LEC: Effects of Ionic Additives and Dual Function Devices," *Adv. Opt. Mater.*, vol. 9, no. 3, p. 2001715, Feb. 2021.
8. **Tien C.-H., Yeh N.-P., Lee K.-L., and Chen L.-C.,** "Achieving Matrix Quantum Dot Light-Emitting Display Based on All-Inorganic $CsPbBr_3$ Perovskite Nanocrystal Composites," *IEEE Access*, vol. 9, pp. 128919–128924, 2021.
9. **Teng P., Reichert S., Xu W., Yang S.-C., Fu F., Zou Y., Yin C., Bao C., Karlsson M., Liu X., Qin J., Yu T., Tress W., Yang Y., Sun B., Daibel C., Gao F.,** "Degradation and self-repairing in perovskite light-emitting diodes," *Matter*, vol. 4, no. 11, pp. 3710–3724, Nov. 2021.
10. **Bowring A. R., Bertoluzzi L., O'Regan B. C., and McGehee M. D**., "Reverse Bias Behavior of Halide Perovskite Solar Cells," *Adv. Energy Mater.*, vol. 8, no. 8, p. 1702365, Mar. 2018.
11. **Xie, J., Hang, P., Wang, H., Zhao, S., Li, G., Fang, Y., Liu, F., Guo, X., Zhu, H., Lu, X., Yu, X., Chan, C. C. S., Wong, K. S., Yang, D., Xu, J., Yan, K.,** "Perovskite Bifunctional Device with Improved Electroluminescent and Photovoltaic Performance through Interfacial Energy-Band Engineering," *Adv. Mater.*, vol. 31, no. 33, p. 1902543, Aug. 2019.
12. **Shan Q., Wei C., Jiang Y., Song J., Zou Y., Xu L., Fang T., Wang T., Dong Y., Liu J., Han B., Zhang F., Chen J., Wang Y., Zeng H**., "Perovskite light-emitting/detecting bifunctional fibres for wearable LiFi communication," *Light Sci. Appl.*, vol. 9, no. 1, p. 163, Dec. 2020.
13. **Shin D. H., Shin S. H., and Choi S.-H.,** "Self-powered and flexible perovskite photodiode/solar cell bifunctional devices with MoS2 hole transport layer," *Appl. Surf. Sci.*, vol. 514, p. 145880, Jun. 2020.

14. **Liu Z., Duan C., Liu F., Chan C.C.S., Zhu H., Yuan L., Li J., Li M., Zhou B., Wong K.S., Yan K.**, "Perovskite Bifunctional Diode with High Photovoltaic and Electroluminescent Performance by Holistic Defect Passivation," *Small*, vol. 18, no. 7, p. 2105196, Feb. 2022.
15. **Yang, S., Guo, Z., Gao, L., Yu, F., Zhang, C., Fan, M., Wei, G. and Ma, T.,** "Bifunctional Dye Molecule in All-Inorganic $CsPbIBr_2$ Perovskite Solar Cells with Efficiency Exceeding 10%," *Sol. RRL*, vol. 3, no. 9, p. 1900212, Sep. 2019.
16. **Yang, F., Wang, A., Yue, S. *et al.*,** "Lead-Free Perovskite-Based Bifunctional Device for Both Photoelectric Conversion and Energy Storage," *ACS Appl. Energy Mater.*, vol. 4, no. 8, pp. 7952–7958, Aug. 2021.

## THE AUTHORS

**BAEVA MARIA**
maria.baeva111@gmail.com
ORCID: 0000-0002-0331-5433

**GETS DMITRY**
dmitry.gets@metalab.ifmo.ru
ORCID: 0000-0001-6288-2123

**POLUSHKIN ARTEM**
artem.polushkin@metalab.ifmo.ru
ORCID: 0000-0001-6398-4092

**VOROBYOV ALEKSANDR**
alex.spbau@mail.ru
ORCID: 0000-0003-2077-1243

# Impedance spectroscopy of the dynamics of charge carriers of $CsPbI_3$ and $CsPbBr_3$ nanoparticles deposited on a tandem solar cells

**L. Boudjemila [1,4]✉, V. V. Davydov[1, 3] G.V. Nenashev [2], V.G. Malyshkin [2], E.I. Terukov [2], A.N. Aleshin [2]**

[1] Peter the Great Saint-Petersburg Polytechnic University, 29, Polytechnicheskaya, St. Petersburg 195251, Russia;

[2] Ioffe Institute, 26 Politekhnicheskaya, St Petersburg 194021, Russian Federation

[3]The Bonch-Bruevich Saint Petersburg State University of Telecommunications, Saint Petersburg, Russia;

[4] University of Science and Technology – Houari Boumediene, Algeria.

✉ lariessai21@gmail.com

## Introduction

As is known, Lead Halid Perovskite materials are making headlines in the scientific journals, for their promising optoelectronic properties in different fields and principally in the field of photovoltaics [1]. However, the Lead side in Perovskites materials poses a serious ecological problem. For this reason, came the choice of nanoparticles (NPS) $CsPbI_3$ and $CsPbBr_3$. The latter were deposited as active layer on a tandem cell prepared beforehand by the PECVD process. In this work we are more interested in the mobility of charge carriers within active layers and Bulk *c*-Si. This type of material is characterized by the presence of an extended phonon disorder, this phonon disorder gives rise to a unique electron-phonon coupling and dielectric responses. And to better understand this, a measurement of the Impedance spectroscopy IS was carried out.

## Methods and results

The measurement was made under identical conditions and the Bulk *c*-Si is taken as a reference substrate. The Cole-Cole plots presented in Fig.1 for the two *c*-Si/$CsPbI_3$ and *c*-Si/$CsPbBr_3$ structures with top ITO contact coincide with the equivalent circuit model and respectively represent the series resistance, the recombination resistance and the geometric capacity, which occur due to the accumulation of charge, the charge transfer resistance and/ or additional interfacial electronic states.

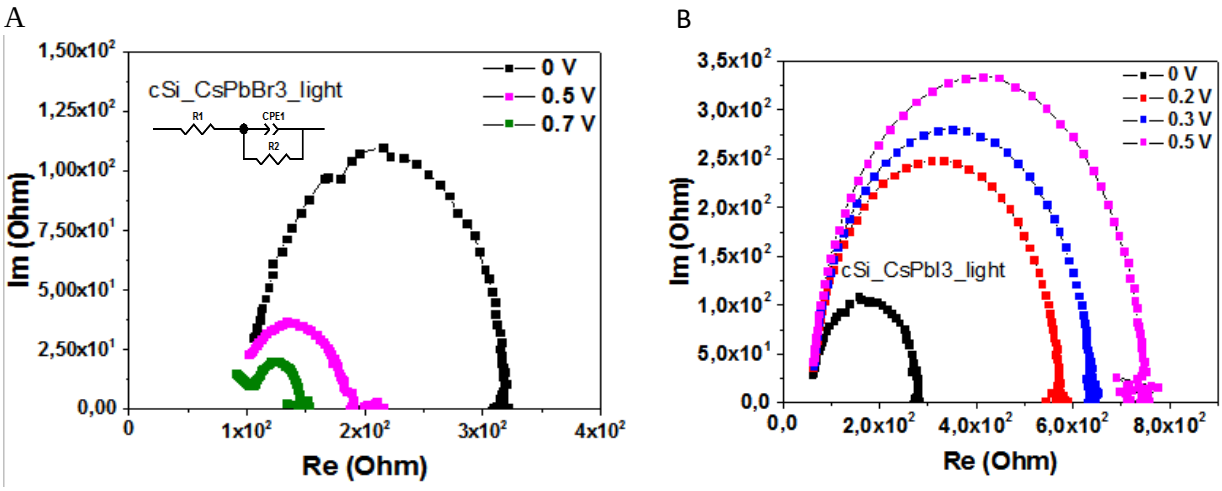


**Fig.1.** Representative impedance response for A – c-Si/CsPbBr3 under illumination at different biases, B – c-Si/CsPbI3 under illumination.

When applying the polarization, the ohmic resistance of the contacts manifests itself by a zero shift to the intersection of the semicircle with the axis of the high frequencies. This is in all substrates including the reference sample. The series resistance represented R1 in the equivalent circuit is quite important in the *c*-Si/$CsPbI_3$ substrates while for *c*-Si/$CsPbBr_3$ and *c*-Si is more and less similar. This is due to the interfacial interaction of charge carriers with ITO contact. A

smaller interception means a lower series resistance. Under polarization applied for *c-Si*/$CsPbBr_3$ and *c*-Si (reference substrate). Similar behavior is noticed, the interception is very small by comparing it to the interception without applied tension. It is also interpreted by the recombination resistance (R2) which is linked to the arc. A larger arc radius indicates a higher recombination resistance. The evolution of the diameter of the semicircles depends on the increase in the applied tension which is linked to the recombination process. [2] This can be explained by the fact that, as polarization through the N + -P junction, the Nyquist Plot radius increases due to an increase in the conductivity of the diode. R2 gradually increases with the increase in tension. On the other hand, a decrease in volume resistance is considered to be an answer to the introduction of load carriers. On the other hand, a decrease in volume resistance is considered to be an answer to the introduction of charge carriers.

In the Nyquist plot, a high frequency signature is observed with a line which is linked to the L1 element. It represents the parasitic tail in the Cole-Cole routes to high frequencies is attributed to the parasitic inductance coming cables and electrodes. The relative contribution of this component becomes significant under high polarization because the resistance of the cell decreases with the increase in polarization. The CPE1 element is a non -ideal capacitor associated with the P + -N junction in the layer of *c*-Si and the non -uniform distribution of the dielectric relaxation time presented by inhomogeneity in the perovskite layer. When the biases are applied, a significant decrease in the diameter of the semicircle arc is observed.

Fig. 2. clustered the two types of samples Studied in addition of the reference sample *c*-Si without applied bias and under illumination. The latter has a behavior that differs from the Substrates Coated on $CsPbBr_3$ and $CsPbI_3$ NPS. A presence of the recombination resistance is more imposing for *c*-Si while the series resistance is smaller in coated substrates with the Perovskite NPS.

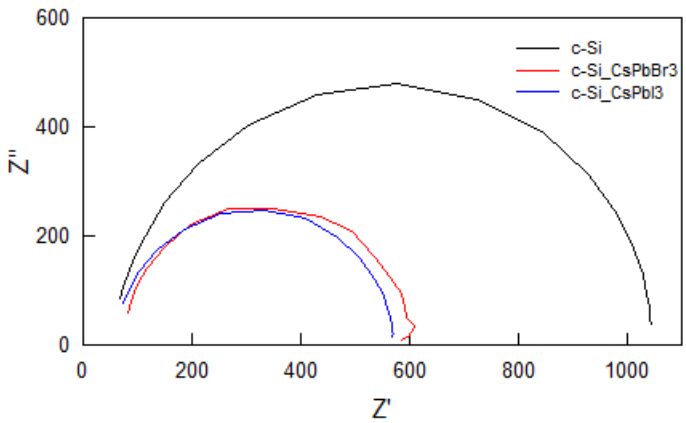


Figure2. Nyquist plot of heterostructures c-Si, c-Si_CsPbBr3, c-Si_CsPbBr3.

It turns out that the addition of the $CsPbI_3$ layer improves the photo-response under polarization, but such a photo-response leads to a decrease in direct current conductivity. On the contrary, the addition of the $CsPbBr_3$ layer blocks the photo response under the bias but slightly improves the photo response for zero bias. The results obtained make it possible to improve the performance of the next generation of SC *c*-Si in tandem with higher layers of NC in perovskite.

## REFERENCES

[1]. **L. Boudjemila, A.N. Aleshin, V.G. Malyshkin, P.A. Aleshin, I.P. Shcherbakov, V.N. Petrov, E.I. Terukov,** Electrical and Optical Characteristics of CsPbI3 and CsPbBr3 Lead Halide Perovskite Nanocrystal Films Deposited on c-Si Solar Cells for Photovoltaic Applications, Physics of the Solid State, 64 (2022) 1670

[2] **Li, J.; Gao, R.; Gao, F.; Lei, J.; Wang, H.; Wu, X.; Li, J.; Liu, H.; Hua, X.; Liu, S.** Fabrication of Efficient CsPbBr3 Perovskite Solar Cells by Single-Source Thermal Evaporation. J. Alloys Compd. 2020, 818, 152903.

# KDP crystals as an optical element in high-power laser system

**S.A. Vilchenko**[1✉], **V.V. Gribko**[2]

[1]Lobachevsky State University of Nizhniy Novgorod (UNN), faculty of physics, department of crystallography and experimental physics, Nizhny Novgorod, Russia;

[2]Institute of Applied physics of the Russian academy of science, Nizhny Novgorod, Russia.

✉sergey.vilchenko@yandex.ru

**Annotation.** This research presents a study of the dependence of the addition of ethylenediaminetetraacetic acid to the KDP crystal on the crystal growth kinetics and its physical-optical properties.

**Keywords: KDP crystal, potassium dihydrophosphate, EDTA, high-power lasers**

## Introduction

Studies of emissions from high-power lasers have shown that these lasers can be used as drivers for a fusion reactor. Such systems are being developed either in the United States (National Ignition Facility project), France (Megajoule project), and other. In Russia, these installations are based on iodine lasers - Iskra-4 and Iskra-5. A new laser system based on neodymium glass, the Iskra-6, is currently being designed. These lasers generate radiation in the near-infrared range. But for controlled thermonuclear fusion applications, lasers with visible and near-UV emission are required. To convert the infrared radiation to visible and near-UV radiation, frequency converters are made of potassium dihydrophosphate crystals (KDP). Also, optical elements made of KDP crystals perform the role of laser pulse shaping.

The main advantages of optical elements based on KDP crystals are their transparency in a wide frequency range, high threshold laser-induced damage and non-linearity coefficients. Another important factor is the nature of KDP crystals. They are grown from aqueous solutions based on the $KH_2PO_4$ salt at temperatures near to room temperature. The peculiarities of KDP growth made it possible to develop methods of growing large crystals, up to 1 m in cross-section [1].

Rapid growth techniques are used for growing crystals up to 1 m in cross-section [1, 2].Studies have shown that rapid growth techniques are more sensitive to the presence of trivalent metal impurities (e.g., $Al^{3+}$, $Fe^{3+}$) in the growth solutions. It is known that the addition of chelating agents to the growth solution leads to reduce the influence of such impurities on the growth process. One of such chemical compounds are ethylenediaminetetetraacetic acid (EDTA).Also experiments show that addition of EDTA to the solution leads to leads to higher growth rate of the boundary prism face, that is why there is interest in detailed study of EDTA influence on morphology and properties of crystals [3].

The aim of this work is to study the effect of ethylenediaminetetraacetic acid on the growth kinetics of faces and the optical properties of the KDP crystal.

## Results and Discussion

The following concentrations of impurity in the solution were chosen for the study: 0, 0.001, 0.005, 0.015, 0.02 mol %, the low concentration of EDTA is a consequence of the poor degree of solubility in water. In the work the kinetics of crystal growth was analyzed by adding EDTA to the growth solution. The dependences of crystal growth rate on the value of solution supersaturation were determined. It follows from the data obtained that the addition of EDTA to a decrease in the dead zone and an increase in the growth rate of the prism faces depending on supersaturation. The dead zone is the inert interval of the face growth rate at which the relative supersaturation of the solution grows, but there is no crystal face growth [4]. At low supersaturations (up to 0.3 ºC) all investigated samples show the increase of prism face growth rate. At increasing supersaturations, the greatest increase in the growth rate of the prism face shows solutions with concentrations of 0.001, 0.005, and 0.015 mol %.Such supersaturation is corresponds to the supersaturation region used in the rapid methods of growth. The

characteristics of the studied solutions are shown in Table 1 ($t_n$–is the saturation temperature, $T_d$–is the width of the dead zone, C–concentrations).

Table1

**Characteristics of the studied solutions**

| № | 0 | 1 | 2 | 3 | 4 | 5 |
|---|---|---|---|---|---|---|
| $t_n$, ºC | 49.1 | 48.99 | 48.8 | 49.25 | 48.98 | 48.41 |
| $T_d$, ºC | 0.3 | 0.3 | 0.22 | 0.23 | 0.24 | 0.22 |
| C, mol % | 0 | 0.001 | 0.005 | 0.01 | 0.015 | 0.02 |
| pH | 4.04 | 4.02 | 3.98 | 3.91 | 3.84 | 3.78 |

In the course of the work, crystals grown by the high-speed method [2] with concentrations of 0 and 0.005 mol % were obtained. Their transmission specter and the value of the laser-induced damage threshold were obtained.

The results obtained show the potential of investigating large concentrations of EDTA in solution, but there are limitations on its solubility.

## REFERENCES


1. **N. Zaitseva, L .Carman**. Rapid Growth of KDP-type Crystals
2. **V. I. Bespalov, V. I. Bredikhin, V. P. Ershov, V. I. Katsman, N. V. Kiseleva, and S. P. Kuznetsov** Optical properties of KDP and DKDP crystals grown with high speed. QuantumElectronics, Vol. 9, No. 11 (1982).
3. **Vinh Trung Phan , Khanh Duy Nguyen, Hung Vu Tuan Le**. Effect of some hydroxyl additives on the growth and optical properties of KDP crystals, Journal of Crystal Growth, Vol. 587 (2022) 126643
4. **V. N. Portnov**. Effect of impurities on the growth rate of crystal faces, Nizhny Novgorod State University Press. 2013

# Investigation of electrophysical properties of BP layers grown by PECVD mode.

**G. E. Vtorygin** [1], **A. I. Baranov** [1✉], **A. V. Uvarov** [1], **A. A. Maksimova** [1], **E.A. Vyacheslavova**[1], **A. S. Gudovskikh**[1]

[1] Alferov University, Saint-Petersburg, Russia

✉baranov_art@spbau.ru

**Abstract.** Boron phosphide is perspective material for solar cells based on BP/n-Si heterojunction. Here, we investigate influence of parameters of growth conditions on electrophysical properties of BP grown by PECVD. It was shown increase of conductivity with increasing of plasma power and additional flow of hydrogen, and formation of defects in BP layers and silicon wafers was detected by capacitance methods of admittance spectroscopy and DLTS.

**Keywords:** heterojunction, boron phosphide, capacitance-voltage profiling.

**Funding:** The reported study was supported by the Russian Science Foundation under the grant number 21-79-10413.

## Introduction

Silicon technology is the most advanced today, so the use of silicon substrates will remain an important condition for the implementation of a highly efficient solar cell for mass production. However, the developed methods for the formation of selective contact using amorphous silicon and oxides have significant drawbacks - parasitic absorption and insufficient thermal stability, respectively. Therefore, the perspective possibility is to use selective contacts based on phosphides - wide-gap materials that have good thermal stability and resistance to degradation when used in space, are more transparent in the ultraviolet region of solar radiation, and also have a band structure that allows creating potential barriers at a heterojunction with silicon. For example, it was theoretically shown in [1] that boron phosphide is one of the most promising binary compounds for the creation of p-type TCM (transparent conducting material) to n-Si substrates, since it is indirect-gap, has a large difference between the energy indirect (2 eV) and direct transition (4 eV), which leads to a large break of the conduction band at the p-BP/n-Si heterojunction, creating a selective contact for holes. In our previous work [2], BP layers were grown by plasma-enhanced chemical vapour deposition (PECVD) in continuous mode from gas mixtures of trimethylboron (TMB) and phosphine (PH3) used as precursors. However, high content of carbon was detected, and capacitance measurements revealed the presence of electron accumulation at the BP/Si interface, which can be explained by lowly doped or undoped BP and Fermi level pinning at the BP/Si interface due to the presence of interface defect states. In this study, we used diborane instead TMB to exclude carbon incorporation in BP layers, so here we investigate electrophysical properties of BP layers grown by PECVD under different conditions.

## Materials and Methods

Boron phosphide layers were grown in a standard Oxford PlasmaLab 100 PECVD (13.56 MHz) plasma chemical deposition in continuous PECVD mode. BP layers were deposited on n-type double-sided polished c-Si substrates with a doping level of $N_d = 1 \times 10^{15}$ $cm^{-3}$ at 350 °C, with a different plasma power (20-200 W) and pressure of 1000 mTorr. Furthermore, additional dilution by flow of hydrogen and argon also was used in samples. Flow ratio of precursors $PH_3$ and $B_2H_6$ was equal to 2. Then, ohmic contact was fabricated to rear side of silicon wafers, and gold was evaporated on BP to formation of Schottky barrier.

## Results and Discussion

Current-voltage characteristics were measured at room temperature using a Keithley 2400 source-meter (Figure 1). Obviously, conductivity of layers with increasing of plasma power and with additional flow of hydrogen in chamber. Furthermore, clear rectifying behavior is observed for sample grown with 200 W plasma power and 100 sccm of hydrogen flow. It means existence

of space charge region due to potential barrier at interface Au/BP that suggests donor doped BP layer. In this case, capacitance-voltage profiling was applied to this this sample at high frequency of 100 kHz to probe heterojunction BP/Si, and deep-level transient spectroscopy revealed defects with activation energy of 0.24 eV below conduction band. More detailed results of capacitance characterization (capacitance voltage profiling, admittance spectroscopy, DLTS) of different boron phosphide layers will be presented on the conference.

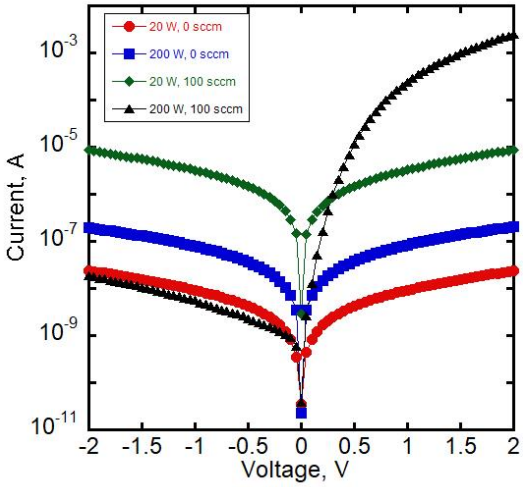


Fig. 1. Current-voltage characteristics for structures Au/BP/n-Si grown under different conditions.

## REFERENCES


1. **Varley J.B., Miglio A., Ha V., van Setten M.J., Rignanese G., Hautier G.**, High-Throughput Design of Non-oxide p-Type Transparent Conducting Materials: Data Mining, Search Strategy, and Identification of Boron Phosphide, Chem. Mater. 29 (6) (2017) 2568–2573.

2. **Maksimova A.A., Uvarov A.V., Baranov A.I., Gudovskikh A.S., Kudryashov D.A., Vyacheslavova E.A., Morozov I.A., LeGall S.S., Kleider J.P.**, Investigation of Plasma Deposited Boron Phosphide and Its Contact to Silicon, ACS Appl. Energy Mater. 5(5) (2022) 5367-5373.

# Heterojunction solar cells based on nanostructured black silicon

**E. A. Vyacheslavova** ✉, **A. V. Uvarov**, **A. A. Maksimova**, **A. I. Baranov**, **A. S. Gudovskikh**
Alferov University, St. Petersburg, Russia, 194021
✉cate.viacheslavova@yandex.ru

**Abstract.** The influence of the black silicon (*b*-Si) morphology on the photovoltaic properties of heterojunction *a*-Si:H/c-Si solar cell (SC) is investigated. We used cryogenic etching (-150 °C) in a $SF_6/O_2$ gas mixture to obtain *b*-Si structures and a total reflectance in the range of 1-3%. The height of the obtained *b*-Si structures varies from 200 to 760 nm, the shape from nanowires to cone-shaped. The heterojunction was fabricated via plasma-enhanced chemical vapor deposition (PECVD) at a temperature of 250 °C. The best heterojunction solar cell based on a 200 nm height cone-shaped *b*-Si demonstrates a promising passivation properties reaching open circuit voltage ($V_{OC}$) of 648 mV. With a short-circuit current density ($J_{SC}$) of 29.7 mA/cm$^2$ and fill factor (*FF*) of 67% an efficiency of 12.8% was achieved. The solar cells based on cone-shaped *b*-Si gain also in external quantum efficiency (*EQE*) compared to *b*-Si in the form of nanowires.

**Keywords:** black silicon, amorphous silicon, heterojunction solar cell.

**Funding:** The research was supported by the Russian Science Foundation Grant No. 23-29-00735.

## Introduction

The technology of solar cell production based on the *a*-Si:H/c-Si heterojunction (HJT) is one of the most promising concepts for a highly efficient silicon solar cell [1]. To reduce optical losses and increase the efficiency of industrial heterojunction solar cells, pyramidal texturing is used, obtained by the alkaline anisotropic etching [2, 3]. However, this approach works effectively in a narrow range of wavelengths and angles of incidence [4]. In turn, black silicon (b-Si) has excellent optical properties in both a wide wavelengths range and incidence angles [5]. Due to this property, *b*-Si is an extremely promising solution for photovoltaic applications. However, formation of *a*-Si:H/c-Si heterojunction based on *b*-Si faces a problem of Si surface passivation being an important issue for HJT SC.

In this article, the influence of the black silicon morphology on the photovoltaic properties of a solar cell based on *b*-Si is considered.

## Experimental section

The *n*-type conductivity silicon wafers (100) with a resistivity of 2-3 Ω•cm were used. The *b*-Si structures were obtained by cryogenic etching in $SF_6/O_2$ inductively coupled plasma without using a template. The substrates were cleaned using the Shiraki technology [6] after the cryogenic etching. The combination of *i*- and *p*-type *a*-Si:H layers were deposited on *b*-Si structures via PECVD from a gas mixture of silane ($SiH_4$) and hydrogen ($H_2$) at 250 °C. A *p*-type boron doping of *a*-Si:H layer was obtained by adding trimethylboron (TMB).

The *I–V* characteristics under AM1.5G illumination (Abet Technology SunLite) were measured using Keithley 2400 source-meter. The *EQE* spectra were carried out using a reference solar cell based on *c*-Si, a halogen lamp and an SLS M266 monochromator. The total reflection spectra were measured using an integrating sphere in the range of 250-1100 nm.

## Results and Discussion

According to SEM images, the *b*-Si height varies from 200 to 760 nm, the shape from nanowires to cone-shaped. Black silicon achieves a total reflectance below 3% in a wide spectral range. Photovoltaic parameters such as $V_{OC}$, $J_{SC}$, *FF* and efficiency were calculated from illuminated *I–V* characteristics. The $V_{OC}$ varies from 440 mV to 648 mV depending on the *b*-Si

geometry. $V_{OC}$ is higher for cone-shaped *b*-Si of lower height. In the case of *EQE*, the SC based on *b*-Si in the form of nanowires has lower values compared to that based on cone-shaped *b*-Si. For the cone-shaped *b*-Si *EQE* gradual decreases below 860 nm with increasing height *b*-Si.

## Conclusion

Amorphous/crystalline silicon heterojunction solar cells based on black silicon with different morphology have been fabricated. All structures of *b*-Si achieve a total reflectance below 3% in a wide spectral range. The best heterojunction solar cell based on a 200 nm height cone-shaped *b*-Si demonstrated an efficiency of 12.8%. However, the achieved value of $V_{OC}$ (648 mV) demonstrates that a good passivation of Si surface is obtained being a promising result for fabrication *a*-Si:H/c-Si heterojunction based on *b*-Si.


## Acknowledgments

The research was supported by the Russian Science Foundation Grant No. 23-29-00735.


## REFERENCES


1. **Taguchi M., Yano A., Tohoda S., Matsuyama K., Nakamura Yu., Nishiwaki T., Kazunori F., Maruyama E.**, 24.7 % Record efficiency HIT solar cell on thin silicon wafer, IEEE J. of Photovoltaics. 4 (1) (2014) 96–99.
2. **Chuchvaga N. A., Kislyakova N. M., Tokmoldin N. S. Rakymetov B. A., Serikkanov A. S.**, Problems arising from using KOH-IPA etchant to texture silicon wafers, Technical Physics. 65 (10) (2020) 1685–1689.
3. **Atobaev O. K., Terukov E. I., Shelopin G. G., Kabulov R. R.**, Wet Chemical Treatment of Monocrytalline Silicon Wafer Surfaces, Applied Solar Energy. 57 (2021) 363–369.
4. **Shpeyzman V. V., Nikolaev V. I., Pozdnyakov A. O., Bobyl' A. V., Timashov R. B., Averkin A. I., Nikitin S. E., Kon'kov O. I., Shelopin G., Terukov E. I., Nashchekin A. V.**, The effect of texturing of silicon wafer surfaces for solar photoelectric transducers on their strength properties, Technical Physics. 65 (7) (2020) 1123–1129.
5. **Liu X., Coxon P. R., Peters M., Hoex B., Cole J. M., Fray D. J.**, Black silicon: fabrication methods, properties and solar energy applications, Energy & Environmental Science. 7 (10) **(**2014) 3223–3263.
6. **Ishizaka A., Shiraki Y.**, Low Temperature Surface Cleaning of Silicon and Its Application to Silicon MBE, J. of the Electrochemical Society. 133 (1986) 666.

Conference materials
UDC 535.8
DOI: https://doi.org/10.18721/JPM.

# ANALYSIS OF NON-IDEALITIES OF QUANTUM STATES FOR TIME-BIN ENCODING

**I S Gerasin[1,2,3,4] ✉, N V Rudavin[1,3,4,5], P A Kupriyanov[1,2,3,4], A A Dvurechenskiy[1,2,3,4], R A Shakhovoy[1,2,3,4]**

[1]QRate, Novaya av. 100, Moscow, Russia
[2]Moscow Institute of Physics and Technology, 9 Institutskiy per., Dolgoprudny, Moscow Region, 141701, Russian Federation
[3]NTI Center for Quantum Communications, National University of Science and Technology MISiS, Leninsky prospekt 4, Moscow 119049, Russia
[4]Russian Quantum Center, Bolshoy Boulevard 30, bld. 1, Skolkovo, Moscow 121205, Russia
[5]HSE University, 20 Myasnitskaya ulitsa, Moscow 101000, Russia
✉i.gerasin@goqrate.com

**Abstract**. Quantum key distribution (QKD) is a technology that allows reaching unconditional security. However, QKD devices as well as a quantum channel connecting users inevitably have imperfections. In this wok, we analyse non-idealities of quantum states for time-bin encoding and introduce simple criteria, which allow to define measurable parameters for numerical evaluation of such imperfections. We implement the proposed method for the QKD system, where the time-bin encoding is performed with intensity and phase modulators.

**Keywords:** quantum key distribution, state preparation, weak coherent pulses with randomized phase.

**Funding:** The study was commissioned by JSCo «RZD».

**Citation:** Gerasin I. S., Rudavin N. V., Kupriyanov P. A., Dvurechensky A. A., Shakhovoy R. A., Analysis of non-idealities of quantum states for time-bin encoding, St. Petersburg State Polytechnical University Journal. Physics and Mathematics. 16 ( ) (2023) …–…. DOI: https://doi.org/10.18721/JPM.

This is an open access article under the CC BY-NC 4.0 license (https://creativecommons.org/licenses/by-nc/4.0/)

© Gerasin I. S., Rudavin N. V., Kupriyanov P. A., Dvurechenskiy A. A., Shakhovoy R. A., 2023. Published by Peter the Great St. Petersburg Polytechnic University.

Материалы конференции
УДК 535.8
DOI: https://doi.org/10.18721/JPM.

# АНАЛИЗ НЕИДЕАЛЬНОСТЕЙ КВАНТОВЫХ СОСТОЯНИЙ ДЛЯ ФАЗОВО-ВРЕМЕННОГО КОДИРОВАНИЯ

**И С Герасин[1,2,3,4], Н В Рудавин[1,3,4,5], П А Куприянов[1,2,3,4], А А Двуреченский[1,2,3,4], Р А Шаховой[1,2,3,4]**

[1]QRate, Новый проспект, 100, Москва, Россия
[2]Московский физико-технический институт, 141701, Московская область, г. Долгопрудный, Институтский пер., д. 9
[3]НТИ Центр квантовых коммуникаций, Национальный исследовательский технологический университет "МИСиС", 119049, Москва, Ленинский проспект, д. 4
[4]Российский Квантовый центр, Большой бульвар 30, стр. 1, Сколково, Москва 121205, Россия
[5]Национальный исследовательский университет «Высшая школа экономики», Мяснитская ул., 20, Москва 101000, Россия

✉i.gerasin@goqrate.com

**Аннотация.** Теоретически квантовое распределение ключей (КРК) позволяет достичь безусловной секретности, однако, устройства КРК, а также квантовый канал, соединяющий пользователей, неизбежно имеют различные несовершенства. В данной работе мы анализируем неидеальности квантовых состояний при фазово-временном кодировании и вводим простые критерии, позволяющие определить экспериментально измеримые параметры для численной оценки таких несовершенств. Мы реализуем предложенный метод для системы КРК, в которой фазово-временное кодирование осуществляется с помощью амплитудных и фазовых модуляторов.

**Ключевые слова:** квантовое распределение ключей, приготовление состояний, слабые когерентные импульсы с рандомизированной фазой (СКИРФ).

**Финансирование:** Исследовательская работа выполнена по заказу ОАО «РЖД».

**Ссылка при цитировании:** Герасин И. С., Рудавин Н. В., Куприянов П. А., Двуреченский А. А., Шаховой Р. А., Анализ неидеальностей квантовых состояний для фазово-временного кодирования // Научно-технические ведомости СПбГПУ. Физико-математические науки. 2023. Т. 16. № . С. …–… . DOI: https://doi.org/10.18721/ JPM.

Статья открытого доступа, распространяемая по лицензии CC BY-NC 4.0 (https://creativecommons.org/licenses/by-nc/4.0/)

© Герасин И. С., Рудавин Н. В., Куприянов П. А., Двуреченский А. А., Шаховой Р. А., 2023. Издатель: Санкт-Петербургский политехнический университет Петра Великого.

## Introduction

Quantum key distribution (QKD) is a promising technology that takes a step towards unconditional security. QKD protocols generally involve two sides: a transmitter and a receiver. The transmitter prepares quantum signals and send them to the receiver via a quantum channel, whereas the receiver performs quantum measurements in some basis. There are two widespread methods to encode quantum states in QKD: polarization and time-bin encoding [1]. Polarization encoding is common in free-space QKD, whereas the time-bin encoding is widely used in fiber systems since quantum states encoded in the phase between pulses or in the time of their arrival at the detector can be made immune to polarization distortions.

One often uses the quantum bit error rate (QBER) as a universal measure of the quantum states quality. However, QBER depends on various factors [2] and it is quite difficult to separate them and isolate the effects associated with non-idealities of quantum states. From an experimental point of view, such separation could be helpful during the system setup. In this work, we introduce simple criteria, which allow to define measurable parameters for numerical evaluation of such imperfections.

## Materials and Methods

The quantum state prepared for time-bin encoding can be represented by a tensor product of consecutive weak coherent pulses: $|\psi\rangle = |\alpha\rangle \otimes |\beta\rangle \equiv |\alpha, \beta\rangle$, where $\alpha$, $\beta$ are (complex) amplitudes of coherent states in neighboring bins (time slots). To characterize the quality of $|\psi\rangle$, we may use *fidelity* $F$, which is a measure of similarity of quantum states. For pure states $|\psi\rangle$ and $|\phi\rangle$, it is defined via the scalar product as $F = |\langle\psi|\phi\rangle|^2$. For the states in the $Z$-basis, we define fidelity as:

$$F_Z = \left|\left\langle vac, \sqrt{s} \middle| \sqrt{\zeta}, \sqrt{s} \right\rangle\right|^2 = e^{-\zeta}, \tag{0.1}$$

where $|vac\rangle$ is the signal in the absence of pulse (vacuum), $s$ is a mean photon number in the "non-empty" bin, and $\zeta$ is the intensity of the signal, which is prepared instead of a vacuum state due to modulator imperfections. Experimentally it is possible to measure mean photon number per quantum state $S_Z = s + \zeta$. Define the ratio of intensities in early and late time bins: $r_Z = s/\zeta$. Using the introduced relations, we will obtain:

$$\zeta = \frac{S_Z}{r_Z + 1} \tag{0.2}$$

For the states in the $X$-basis, we assume that intensity of laser pulses in the early and late time bins may differ by the value $\delta\gamma$, whereas the phase difference can be prepared with an error $\delta\theta$. In this case, fidelity is written as follows:

$$F_X = \left|\left\langle \sqrt{\gamma}, \sqrt{\gamma} \middle| \sqrt{\gamma}, e^{\delta\theta}\sqrt{\gamma+\delta\gamma}\right\rangle\right|^2 = e^{-2\zeta-\delta\gamma+2\sqrt{\gamma(\gamma+\delta\gamma)}\cos(\delta\theta)} = e^{-\gamma(1+r_X-2\sqrt{r_X}\cos(\delta\theta))} \tag{0.3}$$

where $r_X = (\gamma+\delta\gamma)/\gamma$. Such a fidelity depends on two parameters, $\delta\gamma$ and $\delta\theta$; therefore, it is convenient to define additional fidelities:

$$F_Z^\theta = F_X\,|_{\delta\gamma=0} = e^{-2\gamma(1-\cos(\delta\theta))} \tag{0.4}$$

$$F_X^r = F_X\,|_{\delta\theta=0} = e^{-\gamma(1+r_X-2\sqrt{r_X})} \tag{0.5}$$

Involving these parameters seems to be reasonable since $r_X$ и $\delta\theta$ can be easily measured separately. Using numerical calculations, it is easy to show that $F_X^\theta > 0.99$ if $\delta\theta < 10°$ and $F_X^r > 0.99$ if $r_X < 1.4$.

## Results and Discussion

Using photodetector and oscilloscope, we acquired the shape of pulses in different bases and calculated parameters $r_Z$, $r_X$, and $\delta\theta$. Calculated values and bounding criteria are presented in Table 1. One can see that experimental values of generated quantum states satisfy boundary values.

Table 1 – Experimental and bound values of introduced criteria.

| Parameter | $r_Z$ | $r_X$ | $\delta\theta$ |
|---|---|---|---|
| Bound | > 20 dB | <1.4 | <10° |
| Experimental value | 85±45 dB | 1.03±0.01 | 5±1° |

## Conclusion

In this work, we have introduced a method to estimate quality of quantum states. Proposed parameters can be easily measured experimentally. To verify our method, we generated quantum states within time-bin encoding scheme and evaluated these parameters. Obtained values demonstrate that fidelity of prepared quantum states was greater than 0.99.

## REFERENCES


1. **Gisin, Nicolas, et al.** Quantum cryptography. Reviews of modern physics 74.1 (2002): 145.
2. **Hiskett, Philip A., et al.** Long-distance quantum key distribution in optical fiber. New Journal of Physics 8.9 (2006): 193.

# A new methodology for calculating spectral diffraction lenses for focusing laser radiation of different wavelengths

**S. A. Goranskaia** [1]✉
[1]The Bonch-Bruevich Saint Petersburg State University of Telecommunications, Saint Petersburg, Russia.
✉svetlancho.zueva@yandex.ru

**Abstract.** A method for calculating spectral diffraction lenses for focusing radiation of different wavelengths at specified focal points has been developed, a method for calculating cascade metal-dielectric layered structures for optical filtering has been developed, and a method for obtaining neural network descriptors applicable to the analysis of hyperspectral data has been developed.

**Keywords:** spectral diffraction lenses, efficiency assessment, microrelief of spectral diffraction lenses.

## Introduction

The best-known diffractive lenses operating at multiple wavelengths are the so-called harmonic diffractive lenses (HDLs) [1-3]. Compared to diffractive lenses (DLs), HDLs have M times higher diffraction micro-relief and allow several different wavelengths to be focused into the same focus using different orders of diffraction. At the same time, the operating wavelengths of the GDLs must satisfy a certain analytical relation, which depends on M and the "main" operating wavelength.

## Materials and method

Previously [4] proposed a much simpler approach to calculating spectral diffraction lenses (SDLs) that does not require iterative calculations. This approach is based on minimizing the target function characterizing the deviation of the total transmittance functions of the SLLs at given wavelengths from the total transmittance functions of diffracted lenses calculated separately for each of these wavelengths. The results of comparing the TLSs calculated by the proposed method with the known TLSs calculated by the binary search method show that the proposed approach to the calculation of lenses provides a significantly higher efficiency.

To evaluate the effectiveness of the proposed method, an SDL focusing two wavelengths $\lambda_1$= 455 nm and $\lambda_2$ = 750 nm to two points in the plane $z = f$ = 70 mm with coordinates $x_1 = (-x_1, 0)$ and $x_2 = (x_2, 0)$, respectively, where $x_1$= 0.26 mm, was calculated. The selected wavelengths are used to calculate a modified infrared slope index used in "smart" agriculture to monitor forests and determine anomalies in the state of the vegetation cover [5]. The SDL is located in plane $z$=0 and has the following parameters: aperture radius R=2mm, maximum height of microrelief $h_{max}$ = μm, number of quantization levels Q=256. These parameters correspond to possibilities of the technological equipment used for SLD manufacturing. The values corresponding to the positive photoresist FP-3535, which is described by the following Cauchy model, were used as indices of refraction of the SDL material at the calculated wavelengths:

$$n(\lambda)=A+B/\lambda^2+C/\lambda^4 \quad (1)$$

whose parameters $A$=1.631, $B$=0.01267 μm$^2$ and $C$=0.00118 μm$^4$ were determined on the basis of ellipsometric measurements.

The topography of the SDL for these parameters is shown in Figure 1. When calculating the values of microrelief height $h_j$ were determined in nodes $u_j=(u_j,v_j)$ of a square grid with step Δ=2 μm.

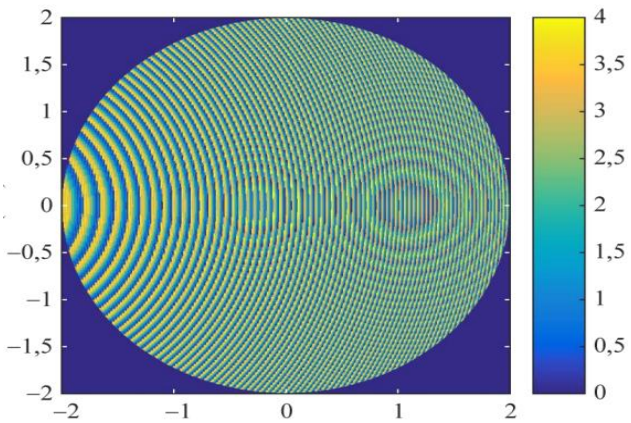


Fig.1. Microrelief of the SDL focusing wavelengths $\lambda_1$= 455 nm and $\lambda_2$ = 750 nm at two points.

To assess the efficiency of the SDL, the intensity distributions formed by the lens were calculated using the two-dimensional Fresnel-Kirchhoff integral. Based on these calculations, cross sections of the two-dimensional distributions along the x-axis were plotted and presented in Fig. 2.

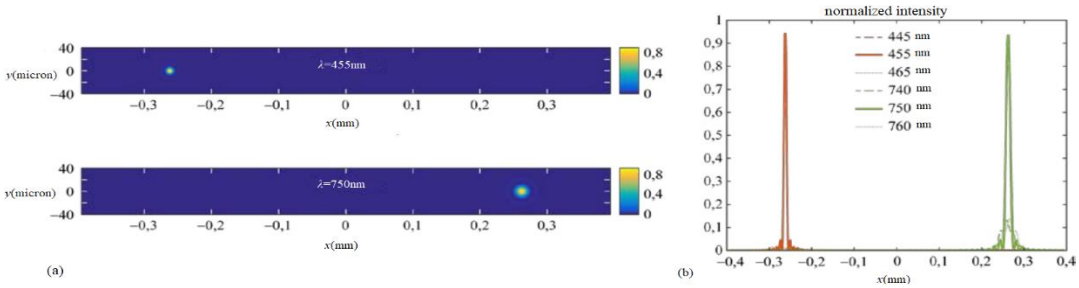


Fig.2. (a) Normalized two-dimensional intensity distributions formed by the calculated SDL at the operating wavelengths $\lambda_1$ = 455 nm (top) and $\lambda_2$ = 750 nm (bottom); (b) Sections of normalized intensity distributions along the x-axis for wavelengths $\lambda_1$, $\lambda_1$ ±10 nm and $\lambda_2$, $\lambda_2$ ±10 nm

## Conclusion

An analysis of obtained data shows that the calculated spectral lenses really focus the radiation of operating wavelengths to the given points, and the widths of the focal peaks coincide with a high accuracy with the diameters of diffraction spots to "ideal" diffractive lenses. This confirms the high efficiency of developed calculation method.

## REFERENCES

1. **Sweeney, D. W., Sommargren G. E.** Harmonic diffractive lenses. Applied Optics. 34(14) (1995) 2469-2475.

2. **Rossi, M., Kunz R. E., Herzig H. P.** Refractive and diffractive properties of planar micro-optical elements. Vol. 34, Applied Optics. 34(26) (1995) 5996-6007.

3. **Faklis, D., Morris G.M.** Spectral properties of multiorder diffractive lenses. Applied Optics. 34(14) (1995) 2462-2468.

4. **Doskolovich, L. L., Skidanov R.V., Bezus E.A., Ganchevskaya S.V., Bykov D.A., Kazanskiy N.L.** Design of diffractive lenses operating at several wavelengths. Vol.28, Optics Express, 28(8) (2020) 11705-11720.

5. **Bannari, A., Morin D., Bonn F., Huete A.R.** A review of vegetation indices. Vol. 13, Remote Sensing Reviews. 13 (1995) 95-120.

# Two-channel fiber-optic communication line for measuring the parameters of active phased antenna arrays in the far zone a landfill conditions

**E. M. Gryaznova[1]✉, E. D. Semicheva[2] and V. V. Davydov[1, 2]**
[1] The Bonch-Bruevich Saint Petersburg State University of Telecommunications, Saint Petersburg, Russia;
[2] Peter the Great Saint-Petersburg Polytechnic University, Saint Petersburg, Russia.
✉ katya.gryaznova@mail.ru

**Abstract.** The necessity of using fiber-optic communication lines (FOCL) for testing active phased antenna arrays (APAA) in landfill conditions in a complex electromagnetic environment is substantiated. The advantages of FOCL application for working with microwave signals during testing of various antennas especially in the far zone are noted. The developed two-channel FOCL for measuring APAA parameters in the far zone is presented. The choice of the components of the optical system for transmitting microwave signals is justified. The results of the study of the characteristics of the fiber optic and directional patterns of antenna arrays are presented.

**Keywords:** Fiber-optic communication line, laser radiation, active phased array antenna, microwave signal, far range, dynamic range, radiation pattern

## Introduction

One of the difficult tasks that developers of antenna arrays solve is related to their testing and configuration [1]. Especially the greatest difficulties arise with APAA due to the fact that it is necessary to suppress the side lobes in the APAA directional pattern, and this requires tests in the far zone [2, 3]. To ensure the conditions of the far zone it is necessary to spread the transmitting module and the reflecting element over at least 1000 m and place the receiving horn at the same distance or more. This will clearly determine the side lobes of the radiation pattern and the nature of their changes from various parameters as well as other characteristics of the antenna. This is only possible in landfill conditions. In this case it is necessary to solve the problem of transmitting information without distortion in the area of high-power electromagnetic interference. The most appropriate solution for the transmission of information in such conditions is the use of FOCL. The development of a FOCL design for APAA tests in the far zone in landfill conditions is the goal of this work.

## Design of Fiber-Optic System and Principle of Its Operation

To measure the APAA parameters in the far zone in the landfill conditions we have developed the following system the block diagram of which is shown in Fig. 1.

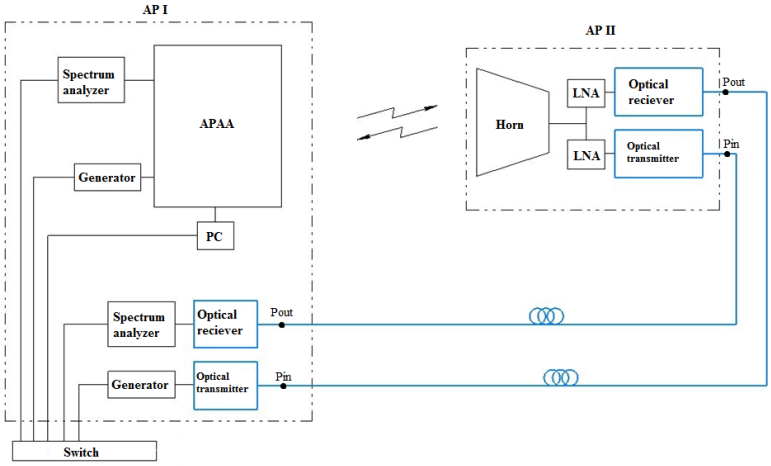


Fig. 1. Developed measuring system for testing APAA with FOCL.

The system consists of two antenna posts, the distance between which is 1 km. Antenna post 1 (AP1) includes the investigated APAA, microwave signal generators, spectrum analyzers, as well as PC placed in the operator's post to analyze the results. Antenna post 2 (AP2) contains an auxiliary horn. The signal between the antenna posts is transmitted via a fiber-optic communication line.

This system allows measuring APAA parameters in two modes: transmission mode and reception mode. The system also allows to work in two bands: 1-2 GHz and 8-12 GHz.

In the transmission mode the APAA unit connected to a generator and PC which control the APAA with computer simulator installed in it, emits a signal in one of two frequency ranges, which is received by the receiving horn. The signal from the horn goes to a low–noise amplifier (LNA), and then to an optical transmitter. The optical signal is sent via fiber to the receiver in AP1. Then the signal is sent via the switch to the PC at the operator's post. A signal is transmitted from the spectrum analyzer through the switch to the PC, which is emitted by the APAA.

During tests of the APAA in reception mode the signal of one of the ranges from the generator located in AP1 goes to the receiver through second channel of the FOCL, then to the LNA and the horn, which acts as an element of the microwave signal emission. The received APAA signal is sent to the spectrum analyzer, the information from which is displayed on the PC.

## Results and Discussion

Amplitude characteristic of the developed FOCL for various frequencies of microwave signal emission is presented. Analysis of the data obtained allows to establish that the dynamic range of the microwave signal transmission is 60 dBm. This value is sufficient for stable transmission of the microwave signal during APAA tests in various modes.

The frequency response of the FOCL was also measured at various temperatures. Results show that the frequency response of the developed FOCL practically does not change in the operating frequency range of APAA. This conclusion made it possible to conduct studies of changes in the APAA radiation pattern in the landfill conditions with high accuracy and determine the APAA parameters at which the suppression of the side lobes of the directional pattern is the lowest. An example of the APAA radiation patterns in landfill conditions using a coaxial cable and a fiber optic cable was obtained.

## Conclusion

Analysis of the data obtained shows that the developed design can be used to configure and test APAA in a landfill conditions in the frequency range from 1 to 12 GHz.

The results show that the developed design of the fiber optic cable is resistant to temperature fluctuations in a wide range of its changes. It was also established that the gradient in the refractive index that occurs in FOCL does not significantly affect the shape and structure of the transmitted microwave signal.

## REFERENCES

1. **Fadeenko V.B., Fadeenko I.V., Vasiliev I.V.,** Investigation of radiation formation (plasmoid) in the air environment by radar method," Journal of Physics: Conference Series 1697(1) (2020) 012057.

2. **Moroz A.V., Malanin K.Yu.,** Features of signal transmission through a fiber-optic system for an interference compensation module for an active phased array antenna, Journal of Physics: Conference Series.1695(1) (2020) 012159.

3. **Filatov D.I., Galichina A.A., Vysoczky M.G., Yalunina T.R., Rud' V.Yu.,** Features of transmission at analog intermediate frequency signals on fiber – optical communication lines in radar station," Journal of Physics: Conference Series. 917(8 (2017) 082005.

# Influence of detector dead time on the key generation rate in measurement-device-independent QKD

**A. A. Dvurechenskiy[1,2,3,4] ✉, P. A. Kupriyanov[1,2,3,4], D. D. Menskoy[1,2,3], I. V. Petrov[1,2,3], N. V. Rudavin[1,3,4,5], I. S. Gerasin[1,2,3,4], R. A. Shakhovoy[1,2,3,4]**

[1]QRate, Novaya av. 100, Moscow, Russia;

[2]Moscow Institute of Physics and Technology, 9 Institutskiy per., Dolgoprudny, Moscow Region, 141701, Russian Federation;

[3]NTI Center for Quantum Communications, National University of Science and Technology MISiS, Leninsky prospekt 4, Moscow 119049, Russia;

[4]Russian Quantum Center, Bolshoy Boulevard 30, bld. 1, Skolkovo, Moscow 121205, Russia;

[5]HSE University, 20 Myasnitskaya ulitsa, Moscow 101000, Russia

✉a.dvurechenskiy@goqrate.com

**Abstract**. Single photon detectors are required for registration of qubits in quantum key distribution. Real detectors have non-zero dead time, which leads to a reduction in the key generation rate. In our work, we evaluate the influence of detector dead time on the key generation rate in measurement-device-independent quantum key distribution scheme with 4 detectors. We compare the analytical estimate of the key generation rate with synchronous dead time and numerical modelling assuming asynchronous dead time.

**Keywords:** quantum cryptography, quantum key distribution, measurement-device-independent quantum key distribution, MDI QKD, single-photon detector, dead time.

**Funding:** The study was commissioned by JSCo «RZD».

## Introduction

Measurement device independent quantum key distribution (MDI QKD) is a protocol with great potential for development due to its unique features. It is easily scalable to create a network of quantum encryption devices. However, in practical implementation, there are many limitations that arise from imperfections in internal components that affect the key generation rate. The recovery time of the detectors does not affect the generation rate if the generation frequency is less than $1/\tau$, where $\tau$ is the detector dead time. However, modern frequencies at which generation occurs have an order of $10^8$ Hz, while the dead time of commonly used single-photon avalanche detectors (SPAD) is 0.1-10 $\mu s$ [1], i.e., $1/\tau$ is of the order of $10^6$ Hz. This fact clearly shows that we cannot neglect the consideration of dead time of detectors in calculations. In this work, we examine in detail the impact of detector dead time on the key generation rate in the MDI QKD protocol with four detectors proposed in [2].

## Materials and Methods

In general, the search an analytical solution when analyzing the influence of dead time of the SPAD on the speed of generating a secret key in a scheme with four detectors and time-bin encoding is a very difficult task. One of the advantages of this scheme compared to the classic scheme with two detectors [3] is the ability to register successful events even with one triggered detector, which increases the key generation speed. However, due to this fact, the analytical solution probably has a very complex form. It can be significantly simplified by performing calculations assuming synchronous dead time, i.e. excluding successful events if at least one of the detectors is in recovery mode. This estimation was made in [2]. It has the form

$$Q_{\gamma_a\gamma_b}^{B,\tau\neq 0} = \frac{Q_{\gamma_a\gamma_b}^{B,\tau=0}}{1+\tau R_{tot}}, \tag{1.1}$$

where $B \in \{Z, X\}$; $\gamma = s$, if $B = Z$; $\gamma \in \{\mu, \nu, \omega\}$, if $B = X$; $R_{tot}$ – the number of events where at least one SPAD triggers. The quantity $R_{tot}$ can be estimated as

$$R_{tot} = f \sum_{\psi_{ab}} \Pr(n_{click} \geq 1 | \psi_{ab}) p(\psi_{ab}), \tag{1.2}$$

where $\Pr(n_{click} \geq 1 | \psi_{ab})$ – is the probability that at least one SPAD will "click" given that $|\psi_{ab}\rangle = |\psi_a\rangle |\psi_b\rangle$ state has arrived at the QKD system; $p(\psi_{ab})$ – is the probability that Alice sent state $|\psi_a\rangle$, while Bob sent state $|\psi_b\rangle$; $f$ – is the frequency of laser pulse preparation.

For a more accurate estimation of the key generation rate, numerical simulation can be used. For example, one can use the Monte-Carlo method. A 'naïve' implementation cannot achieve good data processing speed. Therefore, we proposed a method of parallelization on graphics cards, where all events with a random nature were simulated. After that, keys for different distances and dead times of the detectors were obtained from the resulting data and it's post-processing.

## Results and Discussion

Using the parallelization method, the process of quantum key distribution was modeled for various distances and dead times of the detectors. The obtained results show that the generation speed is indeed slightly higher in asynchronous dead time mode. This fact is also an advantage of using a scheme with phase-time encoding and four detectors.

## Conclusion

In this work we provided the results of numerical modeling of the quantum key distribution process in a protocol with an untrusted central node. The modeling process used parallelization methods on graphics processing units to speed up data processing. The obtained results confirm the assumptions made in [2].

## REFERENCES


1. **Hadfield R. H.,** Single-photon detectors for optical quantum information applications. Nature Photonics, 3 (12) (2009) 696–705.
2. **Petrov I. V., Menskoy D. D., Tayduganov A. S.,** Phase-time-encoding MDI QKD tolerant to detector imperfections. St. Petersburg State Polytechnical University Journal. Physics and Mathematics, 15 (3.3) (2022) 365–370.
3. **Ma X., Razavi M.,** Alternative schemes for measurement-device-independent quantum key distribution. Phys. Rev. A, 86 (2012).

# The methods of recovery the optical properties in FOCL during analog signal transmission under γ-radiation influence

**D. S. Dmitrieva[1]✉, D. V. Dmitrieva[1] and V. V. Davydov[1, 2]**
[1] The Bonch-Bruevich Saint Petersburg State University of Telecommunications, Saint Petersburg, Russia.
[2] Peter the Great Saint-Petersburg Polytechnic University, Saint Petersburg, Russia;
✉ dmitrievadiana1405@gmail.com

**Abstract.** The necessity of using fiber-optic communication lines for the transmission of information is substantiated. The physical phenomena leading to an increase in the losses level in an optical fiber exposed to γ-radiation are considered. An experimental setup to measure the dependence of radiation-induced losses on changes in the exposure dose of radiation has been developed. A method for increasing the radiation resistance of an optical fiber under long-term γ-radiation influence for the case of analog optical signals transmission via fiber-optic communication lines is proposed. Experimental results are presented.

**Keywords:** Analog optical signal, fiber optic communication line, γ-radiation, exposure dose of radiation, radiation-induced losses, Rayleigh scattering.

## Introduction

Nowadays most of the ranges and stations need to organize high-quality communication systems that are resistant to negative impacts. The number of cases of signal and information transmission in a difficult environment has sharply increased. Communication systems should not only ensure high quality of transmitting signal, but also have a long lifetime, because the prompt replacement of failed components is not possible, as, for example, on mobile objects with a nuclear power plant. So, this is the reason, why preference is given to the use of a fiber-optic communication line (FOCL).

However, the use of FOCL on special objects is quite often difficult due to the sensitivity of the optical fiber to the effects of γ-radiation. Radiation accumulates in the fiber during its operation, the power losses in the transmitted signals increase. Moreover, fiber recovery in FOCL takes a long time period, during which the use of the communication line becomes impossible.

Previous researches [1, 2] confirmed the possibility of compensation of radiation-induced losses in an optical fiber using additional laser radiation. However, long-term experiments have established the following, that in an optical fiber with continuous using of this method, radiation losses gradually accumulate, because of the power of radiation, the temperature and the wavelengths of laser radiation, which is used for rapid relaxation. The application of the presented method for analog signal transmission does not solve this problem, so there is a necessity to provide additional research.

## Experimental setup for research the possibility of analog signal transmission via FOCL under γ-radiation influence

To provide the researches of the changes in radiation-induced losses, signal shapes and laser radiation spectrum from various factors, a previously developed experimental setup was modernized [2].

In the experimental setup, a white light source and a spectrum analyzer are used to measure the loss spectra. Tunable semiconductor laser (company Santec) 10. Three models of a tunable laser, in which the radiation power is adjustable in the range from 60 to 120 dB, were used in the setup. The wavelength ranges are: 380-760 nm, 740-1260 nm and 1240-1680 nm, respectively. And also, UV solid-state laser Wedge-HF-218 (Bright Solutions, Italy) with $\lambda$ = 218 nm, power P = 1-36 mW. Analog signals are transmitted via FOCL at two main wavelengths $\lambda_1$ = 0.85 μm and $\lambda_2$ = 1.3 μm.

## Results and Discussion

For the experiments were used various wavelengths of analog signal transmission via FOCL and additional laser radiation with λ=1310 nm and λ=1550 nm with a power of 80 mW. The exposure of additional laser radiation was performed several times to completely "clean" the fiber. The experimental results are presented at the Fig.1 and 2.

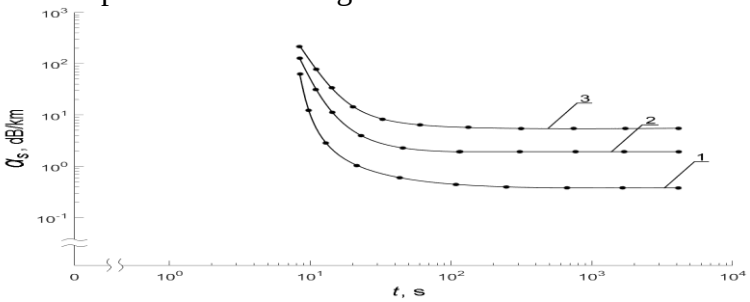


Fig. 1. The changes in the dependence of optical losses αs using additional laser irradiation with λ = 218 nm on time t in a single-mode fiber with $SiO_2$ – $GeO_2$ core (doping percentage 10%) at T = 294.3 K Graphs 1, 2 and 3 correspond to the different wavelengths λ at which the analog optical signal is transmitted in nm: 1310, 890, 680.

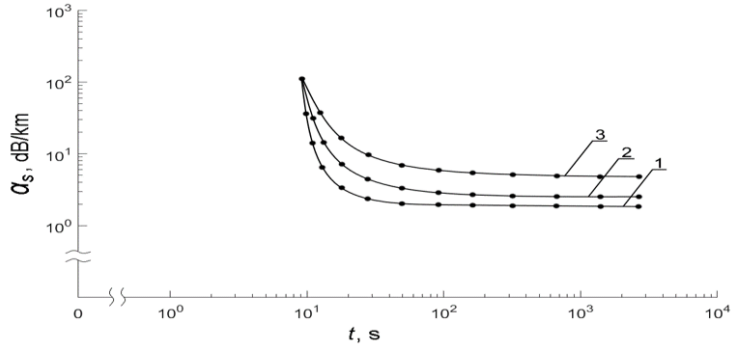


Fig. 2. The changes in the dependence of optical losses αs in laser radiation with λ = 890 nm on time t in a single-mode fiber with $SiO_2$ – $GeO_2$ core (doping percentage 10 %) at T = 294.3 K. Graphs 1, 2 and 3 correspond to different number of γ-radiation influence N on optical fiber in races; 30, 50, 100.

Experimental results allowed to establish the dependence of the change of optical losses for the fiber (after irradiation) on the wavelength of laser radiation. At the same laser radiation power, the cleaning efficiency shifts towards a decrease in λ.

The obtained results show almost complete restoration of optical properties of the fiber in the FOCL after significant γ-radiation influence (total exposure during the entire research cycle amounted to 3 kGy).

## Conclusion

Analysis of experimental results showed, that the presented method of “cleaning” optical fibers for analog signal transmission is appropriate for using on mobile objects with nuclear power plants and on special ranges, where there is a high γ-radiation level.

## REFERENCES


1. **Tomashuk A.L., Zabezhailov M.O.,** Formation mechanisms of precursors of radiation-induced color centers during fabrication of silica optical fiber perform. Journal of Applied Physics. 109 (2011) 083103.

2. **Dmitrieva, D.S., Pilipova, V.M., Davydov, R.V., Rud, V.Y**., Fiber-optical communication line with a system for compensation of radiation-induced losses during the transmission of information. Lecture Notes in Computer Science (including subseries Lecture Notes in Artificial Intelligence and Lecture Notes in Bioinformatics). 12526 LNCS (2022) 348–356.

Conference materials
UDC 53.089.52
DOI: https://doi.org/10.18721/JPM.

# Influence of detector dead time on the key generation rate in Measurement-device-independent QKD

**A. A. Dvurechenskiy[1,2,3,4] ✉, P. A. Kupriyanov[1,2,3,4], D. D. Menskoy[1,2,3], I. V. Petrov[1,2,3], R. A. Shakhovoy[1,2,3,4]**

[1]QRate, Novaya av. 100, Moscow, Russia
[2]Moscow Institute of Physics and Technology, 9 Institutskiy per., Dolgoprudny, Moscow Region, 141701, Russian Federation
[3]NTI Center for Quantum Communications, National University of Science and Technology MISiS, Leninsky prospekt 4, Moscow 119049, Russia
[4]Russian Quantum Center, Bolshoy Boulevard 30, bld. 1, Skolkovo, Moscow 121205, Russia
✉a.dvurechenskiy@goqrate.com

**Abstract**. Single photon detectors are required for registration of qubits in quantum key distribution. Real detectors have non-zero dead time, which leads to a reduction in the key generation rate. In our work, we evaluate the influence of detector dead time on the key generation rate in measurement-device-independent quantum key distribution scheme with 4 detectors. We compare the analytical estimate of the key generation rate with synchronous dead time and numerical modelling assuming asynchronous dead time.

**Keywords:** quantum cryptography, quantum key distribution, measurement-device-independent quantum key distribution, MDI QKD, single-photon detector, dead time.

**Funding:** The study was commissioned by JSCo «RZD».

**Citation:** Dvurechenskiy A. A., Kuprianov P. A., Menskoy D. D., Petrov I. V., Shakhovoy R. A., Influence of detector dead time on the key generation rate in measurement-device-independent QKD, St. Petersburg State Polytechnical University Journal. Physics and Mathematics. 16 ( ) (2023) …–…. DOI: https://doi.org/10.18721/JPM.

This is an open access article under the CC BY-NC 4.0 license (https://creativecommons.org/licenses/by-nc/4.0/)

© Dvurechenskiy A. A., Kuprianov P. A., Menskoy D. D., Petrov I. V., Shakhovoy R. A., 2023. Published by Peter the Great St. Petersburg Polytechnic University.

Материалы конференции
УДК 53.089.52
DOI: https://doi.org/10.18721/JPM.

# Влияние мертвого времени детекторов на скорость генерации ключа в КРК с недоверенным центральным узлом

**А. А. Двуреченский[1,2,3,4], П. А. Куприянов[1,2,3,4], Д. Д. Менской[1,2,3], И. В. Петров[1,2,3], Р. А. Шаховой[1,3,4]**

[1]QRate, Новый проспект, 100, Москва, Россия
[2]Московский физико - технический институт, 141701, Московская область, г. Долгопрудный, Институтский пер., д. 9
[3]НТИ Центр квантовых коммуникаций, Национальный исследовательский технологический университет "МИСиС", 119049, Москва, Ленинский проспект, д. 4
[4]Российский Квантовый центр, Большой бульвар 30, стр. 1, Сколково, Москва 121205, Россия
✉a.dvurechenskiy@goqrate.com

**Аннотация.** Детекторы одиночных фотонов необходимы для регистрации кубитов при распределении квантовых ключей. Реальные детекторы имеют ненулевое мертвое время, что приводит к снижению скорости генерации ключей. В нашей работе мы оцениваем влияние мертвого времени детектора на скорость генерации в схеме распределения квантовых ключей с недоверенным центральным узлом, содержащей 4 детектора. В работе проводится аналитическая оценка скорости генерации ключей с синхронным мертвым временем и численное моделирование в предположении асинхронного мертвого времени.

**Ключевые слова:** квантовая криптография, квантовое распределение ключей, детектор-независимое квантовое распределение ключей, КРК с НЦУ, детектор одиночных фотонов, мертвое время.

**Финансирование:** Исследовательская работа выполнена по заказу ОАО «РЖД».

**Ссылка при цитировании:** Двуреченский А. А., Куприянов П. А., Менской Д. Д., Петров И. В., Шаховой Р. А., Влияние мертвого времени на скорость генерации ключа в КРК с недоверенным центральным узлом // Научно-технические ведомости СПбГПУ. Физико-математические науки. 2023. Т. 16. № . С. …–… . DOI: https://doi.org/10.18721/ JPM.

Статья открытого доступа, распространяемая по лицензии CC BY-NC 4.0 (https://creativecommons.org/licenses/by-nc/4.0/)

© Двуреченский А., Куприянов П. А., Менской Д. Д., Петров И. В., Шаховой Р. А., 2023. Издатель: Санкт-Петербургский политехнический университет Петра Великого.

## Introduction

Measurement device independent quantum key distribution (MDI QKD) is a protocol with great potential for development due to its unique features. It is easily scalable to create a network of quantum encryption devices. However, in practical implementation, there are many limitations that arise from imperfections in internal components that affect the key generation rate. The recovery time of the detectors does not affect the generation rate if the generation frequency is less than $1/\tau$, where $\tau$ is the detector dead time. However, modern frequencies at which generation occurs have an order of $10^8$ Hz, while the dead time of commonly used single-photon avalanche detectors (SPAD) is 0.1-10 $\mu s$ [1], i.e., $1/\tau$ is of the order of $10^6$ Hz. This fact clearly shows that we cannot neglect the consideration of dead time of detectors in calculations. In this work, we examine in detail the impact of detector dead time on the key generation rate in the MDI QKD protocol with four detectors proposed in [2].

## Materials and Methods

In general, the search an analytical solution when analyzing the influence of dead time of the SPAD on the speed of generating a secret key in a scheme with four detectors and time-bin encoding is a very difficult task. One of the advantages of this scheme compared to the classic scheme with two detectors [3] is the ability to register successful events even with one triggered detector, which increases the key generation speed. However, due to this fact, the analytical solution probably has a very complex form. It can be significantly simplified by performing calculations assuming synchronous dead time, i.e. excluding successful events if at least one of the detectors is in recovery mode. This estimation was made in [2]. It has the form

$$Q_{\gamma_a\gamma_b}^{B,\tau\neq 0} = \frac{Q_{\gamma_a\gamma_b}^{B,\tau=0}}{1+\tau R_{tot}}, \tag{1.1}$$

where $B \in \{Z, X\}$; $\gamma = s$, if $B = Z$; $\gamma \in \{\mu, \nu, \omega\}$, if $B = X$; $R_{tot}$ – the number of events where at least one SPAD triggers. The quantity $R_{tot}$ can be estimated as

$$R_{tot} = f \sum_{\psi_{ab}} \Pr(n_{click} \geq 1 | \psi_{ab}) p(\psi_{ab}), \quad (1.2)$$

where $\Pr(n_{click} \geq 1 | \psi_{ab})$ – is the probability that at least one SPAD will "click" given that $|\psi_{ab}\rangle = |\psi_a\rangle |\psi_b\rangle$ state has arrived at the QKD system; $p(\psi_{ab})$ – is the probability that Alice sent state $|\psi_a\rangle$, while Bob sent state $|\psi_b\rangle$; $f$ – is the frequency of laser pulse preparation.

For a more accurate estimation of the key generation rate, numerical simulation can be used. For example, one can use the Monte-Carlo method. A 'naïve' implementation cannot achieve good data processing speed. Therefore, we proposed a method of parallelization on graphics cards, where all events with a random nature were simulated. After that, keys for different distances and dead times of the detectors were obtained from the resulting data and it's post-processing.

## Results and Discussion

Using the parallelization method, the process of quantum key distribution was modeled for various distances and dead times of the detectors. The obtained results show that the generation speed is indeed slightly higher in asynchronous dead time mode. This fact is also an advantage of using a scheme with phase-time encoding and four detectors.

## Conclusion

In this work we provided the results of numerical modeling of the quantum key distribution process in a protocol with an untrusted central node. The modeling process used parallelization methods on graphics processing units to speed up data processing. The obtained results confirm the assumptions made in [2].

## REFERENCES


1. **Hadfield R. H.,** Single-photon detectors for optical quantum information applications. Nature Photonics, 3 (12) (2009) 696–705.
2. **Petrov I. V., Menskoy D. D., Tayduganov A. S.,** Phase-time-encoding MDI QKD tolerant to detector imperfections. St. Petersburg State Polytechnical University Journal. Physics and Mathematics, 15 (3.3) (2022) 365–370.
3. **Ma X., Razavi M.,** Alternative schemes for measurement-device-independent quantum key distribution. Phys. Rev. A, 86 (2012).

# Features of photovoltaic cell degradation of solar power plants in Hong Kong and Saint Petersburg

**Deng Yuanbiao[1, 2]✉, and V. V. Davydov[1, 3]**
[1] Peter the Great Saint-Petersburg Polytechnic University, Saint Petersburg, Russia;
[2] Jiangsu Normal University,Xuzhou,China;
[3] The Bonch-Bruevich Saint Petersburg State University of Telecommunications, Saint Petersburg, Russia.
✉ dyuanbiao@gmail.com

**Abstract.** This thesis investigates the degradation characteristics of PV modules in two different climates, Hong Kong and St. Petersburg, in order to better understand the coupling effects of temperature, thermal cycling, UV exposure, relative humidity and other environmental factors on the performance of PV systems. Different optimization recommendations are given based on the different climates of Hong Kong and St. Petersburg.

**Keywords:** Photovoltaic Models, Solar Panels， degradation， damp-heat climate,humid continental climate,electroluminescence.

## Introduction

In the 21st century, the three major problems of energy shortage, environmental pollution and the greenhouse effect have spurred the development of renewable and clean energy sources. Solar energy, as a representative of clean energy, is being utilized in an ever-expanding range. Photovoltaic power plants are emblematic of the use of solar energy. Photovoltaic modules are the core components of photovoltaic power plants, and with the increase in use time, the performance decline is significant.

The performance deterioration of PV modules is divided into two main categories, one is internal factors, such as defects in the material itself or inadequate manufacturing processes. The other category is external environmental factors, which are greatly influenced by climate. Currently, there is a lack of research into the coupled effects of temperature, thermal cycling, UV exposure, relative humidity and other factors on PV systems [1]. There is therefore a need for a global database to determine the factors and characteristics of PV module degradation under different climatic conditions. This thesis compares the degradation characteristics of PV modules in Hong Kong and St. Petersburg.

## Materials and optimization methods for degradation of PV modules in Hong Kong and St. Petersburg

Hong Kong is located in southern China and has a humid subtropical climate, with average maximum temperatures above 30°C from June to September, rainfall greater than 300 mm and an average annual relative humidity of 78%, so the main problem facing PV modules in Hong Kong is the damp-heat climate.

Huili Han [2] carried out an analytical study of a PV module in a hot and humid region and Figure 1 shows an el image of this PV module. Three of the more obvious disadvantages can be observed in Figure 1. Defect A there is a distinct dark area between the busbars in the middle of the cell. defect B, there is a BRIGHT spot in the busbars of the cell. defect C, there is a black border in the cell. By comparing Figure 1(a, b) and Figure 1(c) it can be seen that the defects in the PV modules were caused by prolonged exposure to the field. Cracking of the solder interconnects (defect B) and corrosion of the silver metallization (defects A and C) have been caused by the hot and humid climate. Ways to reduce this hygrothermal degradation can be considered by using solders that do not contain tin or lead or by replacing EVA with new encapsulation materials.

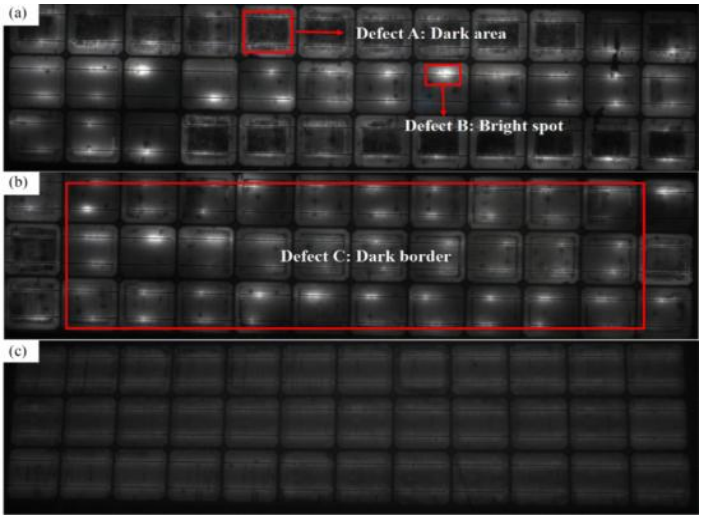


Fig. 1. The EL (electroluminescence) - photovoltaic module picture. Pictures: (a) is PV module exposed in the field; (b) is PV module exposed in the field; (c) is PV module stored indoors.

St. Petersburg is located at around 60 degrees north latitude and has a humid continental climate. During the summer months, the average daily incident shortwave solar energy is higher in St. Petersburg than in Hong Kong, as shown in Figure 2. This may be due to St. Petersburg's higher latitude, and therefore shorter daylight hours in winter and longer daylight hours in summer.

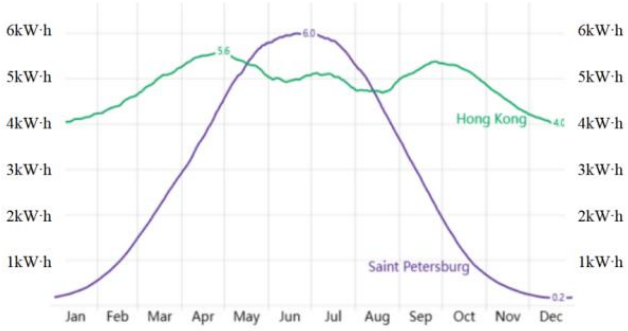


Figure 2. Average Daily Incident Shortwave Solar Energy

## Results and Discussion

The degradation of PV modules in Hong Kong should take into account its damp-heat climate and the degradation rate can be reduced by using solder without tin or lead or by using new encapsulation materials instead of EVA. The degradation of PV modules in St. Petersburg should take into account the frequent snowfall and can be reduced by considering improving the durability of module edge sealing and frame construction.

## Conclusion

We have analyzed the effects of two climates on PV modules in the Hong Kong region and the St. Petersburg region by examining PV modules from different regions. Different methods should be used to optimise degradation rates depending on the climate of different regions.

## REFERENCES

1. **Ndiaye A., Charki A., Kobi A., Cheikh M.F.K., Ndiaye, P.A., Sambou V.,** Degradations of silicon photovoltaic modules: A literature review,Solar Energy 96 (10)(2013)140-151.

2. **Huili H., Xian D., Bingzhi L., Huan Y., Pierre J. V., Jiangfeng L., Jiapei H., Zongcun L., Hui S.,** Degradation analysis of crystalline silicon photovoltaic modules exposed over 30 years in hot-humid climate in China,Solar Energy,170(8)(2018)510-519.

Conference materials
UDC 628.9.038
DOI: https://doi.org/10.18721/JPM.

# Comparative study of energy characteristics of high-power flip-chip AlInGaN LEDs ($\lambda$ = 440–510 nm) for laser pumping

**A. E. Ivanov** [1,2] ✉, **A. E. Chernyakov**[1], **N. A. Talnishnikh**[1], **A. L. Zakgeim**[1]
[1] SHM R&E Center, RAS, St. Petersburg, Russia;
[2] Ioffe Institute, St. Petersburg, Russia
✉a-e-ivano-v@yandex.ru

**Abstract.** The goal of work is to study the energy characteristics of high-power AlInGaN LEDs of the same design, but with different emission spectra in order to identify the physical reasons that limit the optical power and wall-plug-efficiency. During the work, the voltage-current, light-current and spectral characteristics of the flip-chip LEDs with three peak wavelengths $\lambda_{peak}$ = 440, 470, 510 nm were experimentally studied in a wide range of operating current density 0.01–2.5 kA/cm$^2$.

It was found that the external quantum efficiency for the studied LEDs is similar at low operating currents, but the effect «efficiency droop» is more for longer wavelength LEDs.

**Keywords:** AlInGaN, LEDs, quantum efficiency, light-current characteristic.

This is an open access article under the CC BY-NC 4.0 license (https://creativecommons.org/licenses/by-nc/4.0/)

## Introduction

LEDs operating under high pulsed current are of great interest for different applications, in particular, for VLC (LiFi) systems and laser pumping. The goal of this study is the examination of impact of the emission wavelength and relevant materials properties on electrical, optical, and thermal characteristics of LEDs operating at high currents required for pumping of solid-state laser (e.g. Ti:Sapphire) [1]. For this purpose, we have selected LEDs having a similar chip design, i.e. dimensions and contact geometry, but emitting light at different emission wavelengths: from 440 nm to 510 nm. The results obtained are discussed in terms of ABC-model and materials properties determining the coefficients of radiative and nonradiative recombination.

## Experiment

Commercial Luxeon Rubix Royal blue – $\lambda_{peak}$ = 440 nm, Blue – $\lambda_{peak}$ = 470 nm and Cyan – $\lambda_{peak}$ = 510 nm LEDs have the emission area of 1100×1100 μm$^2$ and similar flip-chip design have been investigated. The LEDs were mounted on AlN ceramic plate used as a thermal interface and then attached to the massive heat sink. Light-current characteristics (LCC) of the LEDs were obtained using the automated OL 770-LED High-speed LED Test and Measurement System by Optronic Laboratories Inc. The thermal resistance was measured by the forward-voltage relaxation method with the Thermal Transient Tester “T3Ster” by MicRed Ltd. As a power source at direct current was used Keithley 2410, at impulse mode (high current) - Agillent 8114A pulse generator with a PicoLAS LDP-V 80–100 V3.3 amplifier.

To analyze the dependence of output optical power on current density was used ABC-model [2]. In the ABC model, internal quantum efficiency is determined by the competition of three recombination mechanisms in the active area: nonradiative Shockley-Reed-Hall and Auger recombination and radiative bimolecular recombination [3].

## Results and Discussion

Fig. 1 compares the LCC of the three types of studied LEDs. One can see from their comparison that the optical power $P_{opt}$ and external quantum efficiency (EQE) of the Royal blue

LED (440 nm) are higher than of the Blue (470 nm) and noticeably higher than of the Cyan (510 nm) at high current density. This originates from differences in the values of A, B, C coefficients in the $In_xGa_{1-x}N$ quantum-wells even with a slight, at first glance, difference in the content of In(x).

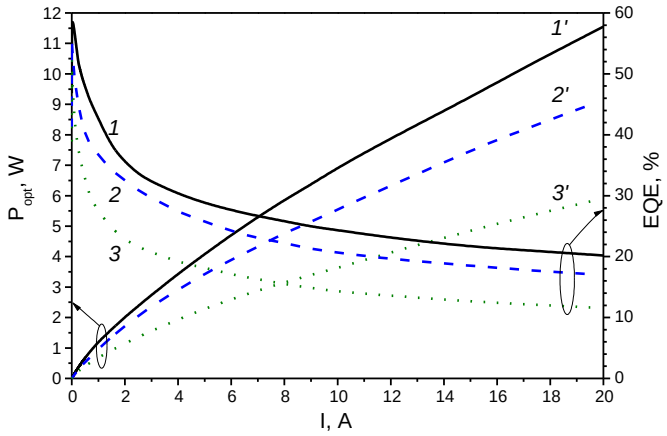


Fig. 1. Optical output power $P_{opt}$ (1',2',3') and EQE (1,2,3) of the LEDs dependences on current. 1 – 440 nm, 2 – 470 nm, 3 – 510 nm LEDs.

## Conclusion

In this work, the features of the current dependences of the LED energy characteristics: optical power and wall-plug-efficiency when emitting in the blue-cyan range (440-510 nm) are studied, as applied to the problems of pumping of solid-state lasers. It has been established that cyan (510nm) LEDs have some advantage in matching the emission and absorption spectra of Ti:Sapphire laser, but at the same time they lose in terms of emitting power and efficiency of the royal blue (440 nm) LED pump source.


## Acknowledgments

This work was carried out at the Center of Multi-User Facilities "Element Base of Microwave Photonics and Nanoelectronics: Technology, Diagnostics, and Metrology".


## REFERENCES


1. **Aladov A. V., Zakgeim A. L., Ivanov A. E., Chernyakov A. E.,** Spectral Efficiency of Ti:Sapphire Active Medium Pumping by AlInGaN LED Emission, Journal of Applied Spectroscopy 89 (1) (2022) 439-442.
2. **Zakgeim A. L., Aladov A. V., Ivanov A. E., Talnishnikh N. A., Chernyakov A. E.,** Limiting Energy Capabilities of Powerful AlInGaN LEDs, Technical Physics Letters. 48 (4) (2022) 192-195.
3. **Karpov, S. Yu.**, ABC-model for interpretation of internal quantum efficiency and its droop in III-nitride LEDs: a review, Opt. and Quantum Electron., 47 (6) (2015) 1293-1303.


## THE AUTHORS


**IVANOV Anton E.**
*SHM R&E Center, RAS*
26, Politekhnicheskaya street, Saint-Petersburg, 194021, Russian Federation
a-e-ivanov@yandex.ru
ORCID: 0000-0003-2819-1534

**TALNISHNIKH Nadezhda A.**
*SHM R&E Center, RAS*
26, Politekhnicheskaya street, Saint-Petersburg, 194021, Russian Federation
nadya.fel@mail.ru
ORCID: 0000-0003-1127-0973

**CHERNYAKOV Anton E.**
*SHM R&E Center, RAS*
26, Politekhnicheskaya street, Saint-Petersburg, 194021, Russian Federation
chernyakov.anton@yandex.ru
ORCID: 0000-0002-8153-9512

**ZAKGEIM Alexander L.**
*SHM R&E Center, RAS*
26, Politekhnicheskaya street, Saint-Petersburg, 194021, Russian Federation
zakgeim@mail.ioffe.ru
ORCID: 0000-0002-1887-2064

# Neuromorphic computing system based on semiconducting metal oxides

**Ivanov Fedor[1], Chezhegov Aleksandr[1], Krasnikov Victor[1], Balashov Igor[1] Artem[2], Grunin Andrey[1], Fedyanin Andrey[1]**

1.Faculty of Physics, Lomonosov Moscow State University, Moscow 119991, Russia

2.Faculty of Chemistry, Lomonosov Moscow State University, Moscow 119991, Russia
ivanov.fed@list.ru

**Abstract:** Modern architectures of computing systems have disadvantages that hinde their further development, this leads to the need to create devices based on new architectures. In our work we have created, modeled and trained a non-volatile computing device based on the principles of the brain. This work shows the possibility of creating fundamentally new devices based on semiconductor metal oxides.

**Keywords:** Photonics, data mining, neuromorphic photonics, artificial intelligence.

**Funding:** This study was funded by A. Grunin, grant number: 02/01-2022/ФФ-ЛАБ

## Introduction

Von Neumann architecture has peculiarities that leads to problems that cause speed and power efficiency limitations, which eventually lead to a violation of Moore's law[1]. Neuromorphic computing devices were inspired by the energy efficiency and speed of the human brain. Therefore, neuromorphic devices bypass the problems of the von Neumann architecture.

## Experimental unit

An artificial electro-optical synapse(Fig.1) based on semiconductor metal oxides was developed to create a neuromorphic device. To demonstrate and implement the training of spiking neural networks based on semiconductor metal nanocrystallites, a neuromorphic computing block scheme was created.

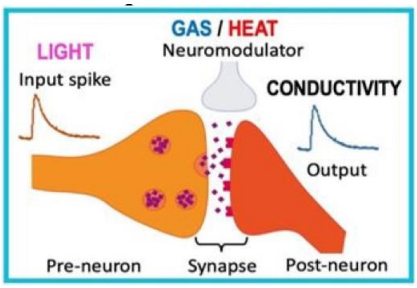


Figure 1: artificial synapse diagram

## Simulation

To demonstrate visual perception and learning of structures placed on a computational board, which contains 64 synaptic connections, we created a fully coupled spike neural network(Fig.2).

We used frequency coding and a simplified Integrate and fire model to describe the neuron. We trained the neural network using the STDP method. After 200 iterations of training, we recovered the image patterns shown in the figure 2.

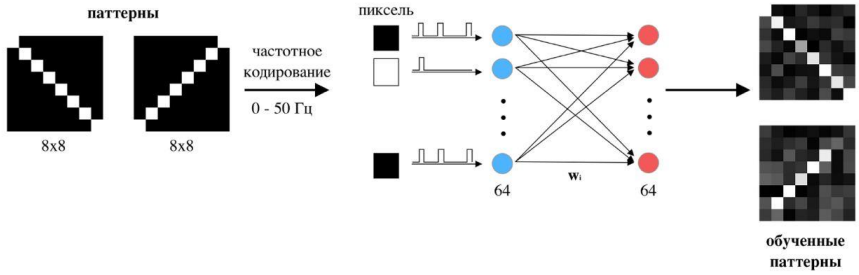


Figure 2: simulation schematic diagram

## Experiment

As a result of the simulation, an experiment was conducted in which an energy independent neuromorphic computing device based on artificial synapses was able to learn with high accuracy.

## Conclusion

As a result of this work, a neuromorphic computing device based on semiconducting metal oxides has been demonstrated.

This device is successfully trained and shows great potential for optoelectronic neuromorphic devices. It showed energy independence, high accuracy, as well as great potential in the development of neuromorphic technologies

## References

[1] J. R. Powell, "The Quantum Limit to Moore's Law," in Proceedings of the IEEE, vol. 96, no. 8, pp. 1247-1248, Aug. 2008, doi: 10.1109/JPROC.2008.925411.

[2] Bhavin J. Shastri, Alexander N. Tait, Thomas Ferreira de Lima, Mitchell A. Nahmias, Hsuan-Tung Peng and Paul R. Prucnal.Principles of Neuromorphic Photonics.//Department of Electrical Engineering, Princeton University, Princeton, NJ, USA - 2017

[3] Schuman C. D. et al. Opportunities for neuromorphic computing algorithms and applications //Nature Computational Science. – 2022. – . 2. – №. 1. – . 10-19.

# Detection-efficiency mismatch in a satellite-to-ground quantum communication

**E I Ivchenko[1,2,3,4*], A V Khmelev[1,2,3], and V L Kurochkin[1,2,3,4]**

[1] *Russian Quantum Center, Bolshoy Boulevard 30, bld. 1, Skolkovo, Moscow, Russia*
[2] *Moscow Institute of Physics and Technology, 9 Institutskiy per., Dolgoprudny, Russia*
[3] *QSpace Technologies, Lugovaya st. 4, Moscow, Russia*
[4] *NUST MISIS, Leninsky prospekt 4, Moscow, Russia*

*E-mail: `ivchenko.ei@phystech.edu`

**Abstract.** Practical schemes of the quantum key distribution system have drawbacks. Detection efficiency mismatch is one of them and is considered in this paper. We simulate the satellite-to-ground quantum key distribution using four unbalanced channels and calculate bounds for the secret key length. Based on measured characteristics of our ground station, when the detection-efficiency mismatching was at 1:2, the generation of the secure final key decreased by 20%.

## 1. Introduction

Satellite-based quantum key distribution (QKD) over long distances has made significant progress [1, 2], but its practical schemes have drawbacks. One of the practical challenges in satellite-to-ground QKD is the detection-efficiency mismatching of polarization photon states received by the ground station. This discrepancy includes the unequal optical efficiency of the polarization channels and the imbalance of the detectors. For fiber-optic systems with two detectors, the effect of efficiency mismatch on the secret key rate was studied [3, 4, 5]. Using satellite-to-ground QKD model, we investigate the influence of this mismatching on the final key rate for the system with four detectors.

## 2. Methods

In order to estimate the security of a practical implementation of the discrete variable QKD protocol with four detectors, we use the following assumptions:
1) The imbalance $\eta$ between accepting 0 and 1 in various bases equals.
2) The mismatch $t_{xz}$ between two bases is also considered.

Therefore, a positive operator-valued measure (POVM) with measurement probabilities for the X and Z bases, respectively, $p_x$ and $p_z$ for Bob can be described in the following form:

$$\begin{aligned} &P^B_{z,0} = p_z|0\rangle\langle 0|, \quad P^B_{z,1} = p_z\eta|1\rangle\langle 1|, \\ &P^B_{x,0} = p_x t_{xz}|+\rangle\langle +|, \quad P^B_{x,1} = p_x t_{xz}\eta|-\rangle\langle -|, \\ &P^B_{\emptyset} = I_3 - P^B_{z,0} - P^B_{z,1} - P^B_{x,0} - P^B_{x,1}. \end{aligned} \tag{1}$$

The conditions for the density matrix can be found from measurements of the observables:

$$\begin{aligned} \mathrm{Tr}\,\Gamma_1\rho_{AB} &= \mathrm{t}\eta\left(p_z + p_x t_{xz}\right), \\ \mathrm{Tr}\,\Gamma_2\rho_{AB} &= \mathrm{t}\eta\left(p_z + p_x t_{xz}\right)Q, \\ \mathrm{Tr}\,\Gamma_3\rho_{AB} &= p_{pass}. \end{aligned} \tag{2}$$

The final formulation of the secure key rate remains the same as in the article [4], with the values of $t$, $p_{pass}$ and $\gamma_2$ changed in accordance with Eqs. (2), as follows:

$$K\left(Q_z, Q_x, \eta, t, p_{\text{pass}}\right) = p_{\text{pass}}\left[h\left(\frac{1+\delta}{2p_{\text{pass}}}\right) - h\left(\lambda\left(Q_x, \eta, t, p_{\text{pass}}\right)\right) - h\left(Q_z\right)\right]. \quad (3)$$

## 3. Results

We chose the real parameters of our ground station with telescope aperture of 600mm [6] that gives as $\eta = 0.5$, $t_{xy} = 0.75$ and considered that $p_x, p_z = 0.5$. Figure 1 shows the dependence of the secret key rate on transmission efficiency. We are in the transmission range of 0.001 to 0.003 during the satellite's passage, which corresponds to deviation of the key rate of about 20%.

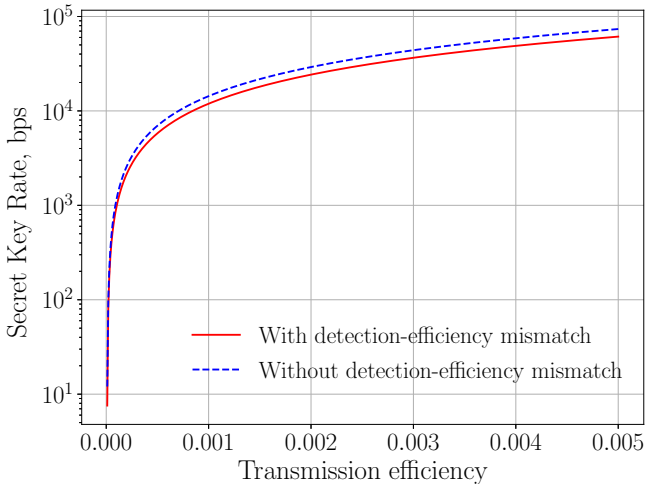


Figure 1: The secret key rate for the BB84 decoy-state protocol vs. the transmission efficiency. Solid line indicates a detector efficiency mismatch of 1:2; dashed line indicates no detector efficiency mismatch. The transmission bounds are taken from the real measurements of the ground station.

To sum up, we have estimated the effect of the detection efficiency mismatch on the final key rate in the satellite-based QKD system and calculated the bounds for the secret key. The analysis shows that the unbalance of the polarization channels in each measurement basis of around 1:2 is leading to a decrease in the key rate of just less than 20%.


### Acknowledgments

This work was supported by the Ministry of Education and Science of the Russian Federation in the framework of the Program of Strategic Academic Leadership "Priority 2030" (Strategic Project "Quantum Internet").


# References


[1] *Lu C. Y. et al.* Micius quantum experiments in space. Reviews of Modern Physics. **94**, 3 (2022).

[2] *Liao S. K. et al.* Satellite-to-ground quantum key distribution. Nature. **549**, 7670 (2017).

[3] *Lo H. K., Ma X., Chen K.* Decoy state quantum key distribution. Physical review letters. **94**, 23 (2005).

[4] *Bochkov M. K., Trushechkin A. S.* Security of quantum key distribution with detection-efficiency mismatch in the single-photon case: Tight bounds. Physical Review A. **99**, 3 (2019).

[5] *Trushechkin A.* Security of quantum key distribution with detection-efficiency mismatch in the multiphoton case. Quantum. **6**, 771 (2022).

[6] *Khmelev A. V. et al.*, Recording of a single-photon signal from low-flying satellites for satellite quantum key distribution. Technical Physics Letters. **47**, 858-861 (2021).

# Laser diode module over 350 W power output with 200 µm / NA 0.22 fiber

**A. V. Fomin, S. R. Usmanov, A. N. Ignatev✉, E. V. Kadigrob**
FSUE "FRNC-VNIITF named after Academ. E. I. Zababakhin", Snezhinsk, 456770, Russia
✉dep5@vniitf.ru

**Abstract.** The paper reports the development of a 915 nm laser module based on high-power single-emitter laser diodes. The optical system was designed for polarization combining of beams from two arrays of single-emitter laser diodes with the subsequent coupling into a silica-silica fiber with a core of 200 µm in diameter and a numerical aperture of 0.22. The CW output power of 368 W was reached at a rated current of 22 A and thermal stabilization temperature of 20 °C, the total efficiency of the laser module being of 47%.

**Keywords:** laser module**,** polarization beam combining, high power laser diodes.

## Introduction

Recently, the products based on high-power laser diodes (LD) have been widely used in medicine and processing applications due to such key advantages of laser diodes as high power, high reliability, and small size as compared to other laser radiation sources [1]. These products include fiber-coupled laser modules (LM) in which various designs for combining beams from several LDs are implemented to improve the output power: spatial, polarization, and spectral beam combining [2]. An LM with spatial combining of beams from 7 LDs is described in [3] with the LM power of 65 W reached at a rated current of 12 A. Since the LDs have a good polarization purity (>90%), polarization beam combining is an efficient and cost-effective technique which is relatively easy in implementation to further increase LM output power [4]. The objective of the present work is to develop and manufacture an LM of a power not less than 350 W with 200 µm / NA 0.22 fiber.

## Experimental design

A design involving spatial and polarization LD beam combining was suggested to obtain required LM parameters. The parameters of the LDs used in the work are listed in Table 1. Aspheric D-micro lenses and cylindrical lenses were used to collimate LD beams along the fast and slow axes, respectively. The total parallel beam was formed by reflecting collimated radiation from rotating mirrors mounted at different heights. The polarization plane of an array of single-emitter LDs was rotated by the passage of the laser beam through a half-wave plate. The beams from two arrays of single-emitter LDs were combined at the beam passage (TE polarization) and reflection (TM polarization) from the active surfaces of a polarized beam splitter. The total beam was focused onto the end of the receiving fiber using two cylindrical lenses.

Table 1

**LD Parameters**

| Parameter | Value |
|---|---|
| Maximum operating current, A | 22 |
| Output power, W (I=22A) | 21 |
| Efficiency, % | 60 |
| Polarization (TE), % | 98 |
| Center wavelength, nm | 915±10 |
| Emitter width, µm | 190 |
| Beam divergence(FWHM) along the fast axis, ° | 29 |
| Beam divergence (FWHM)along the slow axis, ° | 9 |

## Results

During implementation of the experimental LM design the laser light emitted by twenty one LDs was efficiently coupled into the optical fiber. The LM optical power and electro-optical efficiency versus drive current are shown in Figure 1. The maximum reached CW output power was 368 W at a nominal current of 22 A and thermal stabilization temperature of 20 °C, the total LM efficiency being of 47%.

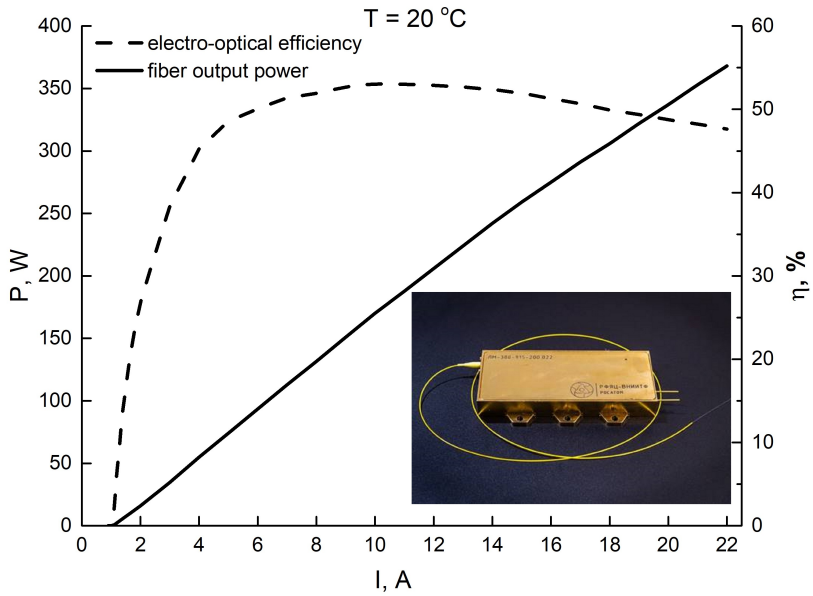


Fig. 1.The LM optical power and electro-optical efficiency versus drive current

## REFERENCES


[1] **Yan Y., Zheng Y., Sun H., Duan J.**, Review of Issues and Solutions in High-Power Semiconductor Laser Packaging Technology, Frontiers in Physics, Vol. 9, 2021.

[2] **Yu H., Liu Y., Braglia A., Rossi G., Perrone G.**, Investigation of collimating and focusing lenses' impact on laser diode stack beam parameter product, Applied Optics, 34 (54) (2015) 10240-10248.

[3] **Fomin A. V., Usmanov S. R., Ignatev A. N., Kadigrob E. V.,** Fiber coupled laser module with brightness exceeding 10 MW/cm$^2$·sr, Technical Physics, 4 (92) (2022) 616-619.

[4] **Kruschke B., Fritsche H., Kern H., Hagen T., Pahl U., Koch R., Grohe A., Gries W.,** Beam Combining Techniques for High-Power High-Brightness Diode Lasers, In:Proc. of SPIE, Vol. 9346, (2015).

**Design and simulation of an optical system of high-power fiber-coupled laser module**

**E. V. Kadigrob, A. V. Fomin, S. R. Usmanov**
FSUE "FRNC-VNIITF named after Academ. E.I. Zababakhin", Snezhinsk, 456770, Russia
E-mail: dep5@vniitf.ru

**Abstract.** The paper presents the simulation results for an optical system based on a high-power and high-brightness laser module. The module design implies spatial and polarization combining of beams from 24 single-emitter laser diodes. The core diameter of output fiber is set as 200μm with a numerical aperture (NA) of 0.22. The simulated result indicates that the module will have the coupling efficiency of 89 % which correlates with the results of experiments with the laboratory module prototype.

**Keywords:** laser module, optical system, laser diodes, spatial combining of beams, polarization beam combining.

## Introduction

Fiber-coupled laser modules are mostly used as highly efficient sources for high-power fiber laser pumping and also can be applied in material processing, medical equipment, and scientific studies. The onrush of laser technologies imposes the need in continuous power growth of fiber-coupled laser pumping modules. The choice and design of optical systems which allow multiplexing radiation from several laser sources and providing high coupling efficiency are a key challenge in the development of high-power modules. Single-emitter laser diodes (LDs) are the most preferred radiation sources due to their high efficiency, small size, and low cost.

## Optical design

A design providing spatial combining of beams from single LDs positioned with a vertical and horizontal step relative to each other was selected as the laser module structure design [1, 2]. Polarization beam combining is also used to increase the output power. The basic optical design of the module is given in Figure 1.

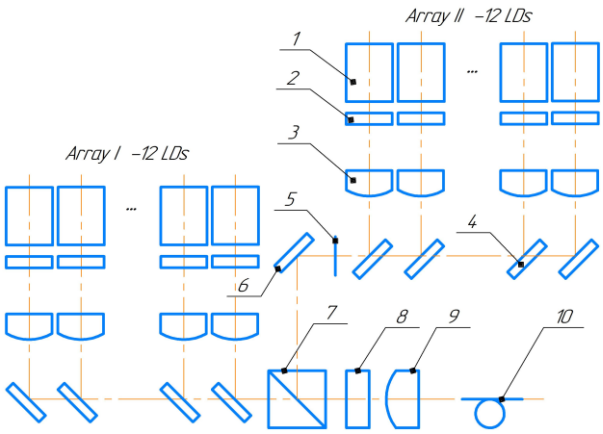


Fig. 1. The basic optical design of the laser module: 1 – LD, 2 – aspheric micro lenses, 3 – cylindrical lenses, 4 – rotating mirrors, 5 – half-wave plate, 6 – rotating mirror, 7 – polarized beam splitter (PBS), 8, 9 – focusing lenses, and 10 – optical fiber

The optical system was designed for 915 nm laser diodes with an emitter width of 190 μm. The LD beam divergence at the level of $1/e^2$ was 27° along the fast axis and 5.5° along the slow axis.

A high-quality beam requires collimating the LD radiation which is performed in series for fast and slow axes between two orthogonally placed lenses since the LD radiation is highly astigmatic. The laser radiation is collimated along the fast axis using an aspheric cylindrical lens (Figure 1, item 2) with an effective focal length of 0.3 mm. A cylindrical lens with and effective focal length of 13 mm is used for beam pattern narrowing.

The beam subject to spatial and polarization combining is focused using cylindrical lenses with effective focal lengths of 20 mm and 9.3 mm for the fast and slow axes, respectively. The beam parameters in each node of the optical system were analytically calculated according to the basic relationships used in designing laser optical systems [3]. The system analysis and optimization were performed using Zemax optical design software (Figure 2). The sizes of focusing spot at the fiber input end are 104 μm and 130 μm along the fast and slow axes, respectively. The far-field divergence angles of focusing spot are 8.6° and 8.1° along the fast and slow axes, correspondingly.

*a*) *b*)

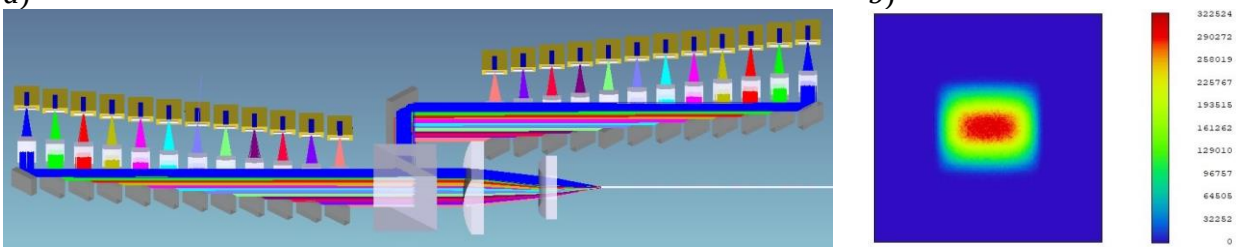


Fig. 2. The 3D model of the optical system with ray tracing (*a*) and beam cross-section in plane of the receiving fiber end (*b*)

## Results

The computer simulation results show that the beam fully correlates with the fiber in terms of the size and divergence. The coupling efficiency is 89 % considering the Fresnel loss, and the losses on the mirrors and the polarized beam splitter. The given optical system was designed as a laser module prototype with the fiber 200/225 μm with a numerical aperture (NA) of 0.22, the coupling efficiency being of 83 %. The CW output power of the module reached 368 W.

## REFERENCES

1. **Kadigrob E. V., Usmanov S. R., Fomin A. V.** Laser module and manufacturing method. RF Patent 2688888, IPC H01S 5/022, G02B 6/42, G02B 27/16 (2006.01), State Corporation Rosatom, FSUE “RFNC-VNIITF named after Academ. E. I. Zababakhin” Bulletin, 2019, No. 15 (in Russian).
2. **Ignatev A. N., Kadigrob E. V., Usmanov S. R., Fomin A. V.** Fiber coupled laser module with brightness exceeding 10 MW/cm$^2$·sr. *Technical Physics*, 4 (92), 2022, pp. 616-619.
3. **Pakhomov I. I., Tsybulya A. B.** *Design of optical systems for laser devices*, Moscow: Radio i svyaz [Radio and Communication], 1986, 152 p. (in Russian).

Conference materials
UDC 628.9.038
DOI: https://doi.org/10.18721/JPM.

# HOT mid infrared LEDs based on *P-InAsSbP/n-InAs(Sb)/N-InAsSbP* heterostructure

**A. A. Klimov[1]✉, R. E. Kunkov[1], S. A. Karandashev[1], A. A. Lavrov[1], T. S. Lukhmyrina[1], B. A. Matveev[1], M.A. Remennyi[1], A. A. Usikova[1].**
[1]IR Optoelectronics Laboratory, Ioffe Institute RAS, St. Petersburg 194021, Russia
✉ a.klimov@mail.ioffe.ru

**Abstract.** Currently, thermal sources of (infrared) IR radiation are successfully used in instrumentation and spectroscopy. However, the speed of thermal sources is modest, the frequency of their operation is significantly inferior to light-emitting diodes (LEDs). Operation in high-frequency mode gives the possibility to increase the signal-to-noise ratio, by cutting off low-frequency noise. Also high power consumption of thermal sources, due to the wide spectrum of radiation, complicates their use in compact portable systems.

LEDs are often cooled in order to increase the output optical power of radiation, which is small due to radiation-free recombination. Significant efforts are being made to reduce the cost, size, weight and power consumption of the system to increase the operating temperature in so-called high temperature (HOT) LEDs. Efforts were focused on the design of chips, in which, due to the shape of the mesa, the quantum efficiency of radiation output was increased. Recently, the dependence of nonradiative Auger recombination on the pump current density has been studied, which makes it possible to optimize not only the shape, but also the dimensions of the mesa.

This article presents a number of concepts for improving the characteristics of LEDs with an electroluminescence spectrum maximum from 3 to 5 μm ($\lambda_{max}$ = 3.3 to 4.2 μm) based on N-InAsSbP/InAs($Sb_x$)/P-InAsSbP heterostructures operating in the temperature range up to 500 K.

**Keywords:** HOT infrared LEDs, *InAs* LEDs, $A^3B^5$ LEDs, InAsSbP LEDs, HOT mid IR LEDs, LEDs IR 500 K, Light-emitting diodes InAsSbP 500 K.

## Introduction

LEDs based on InAs heterostructures and InAsSb, InAsSbP solid solutions operating in the mid-infrared region are used in gas analysis devices [1], for example, for carbon dioxide detection (λ=4.2 μm) in portable capnographs or for natural gas and alcohol vapor detection (λ=3.3 μm). In addition to known applications, there are applications for these components at elevated temperatures, such as in the oil and gas industry, where ambient temperatures can be as high as 200 C. However, the characteristics of LEDs, such as the emission spectrum and output power, undergo changes as the temperature rises. With increasing temperature there is a broadening and shift of the spectrum to the longwave region. As well as a drop in the radiation power due to an increase in the fraction of nonradiation recombination [2]. In this regard, the creation and research of LEDs operating at elevated temperatures is an urgent and very important task.

## Results and Discussion

The epitaxial heterostructure was obtained by liquid-phase epitaxy on InAs (100) substrates, with an InAs photosensitive layer. Samples of flip chip design with a contact-free substrate surface and a mesa of about 120 μm diameter were obtained. They were produced using multistage photolithography with sputtering of the multilayer contact on the mesa surface. The inclined shape of the mesa walls, as well as the reflecting contact surface, led to an increase in the quantum efficiency of the radiation output.

Figure 1 a shows the electroluminescence spectra (a), the current-voltage characteristics (b), and the current-power characteristic (c) over a wide temperature range. As can be seen, our emitters retain their diode character of the current-voltage characteristic up to a temperature of 500

K. At the same time, the achieved power values make it possible to use such sources in gas analysis devices at elevated temperatures without cooling.

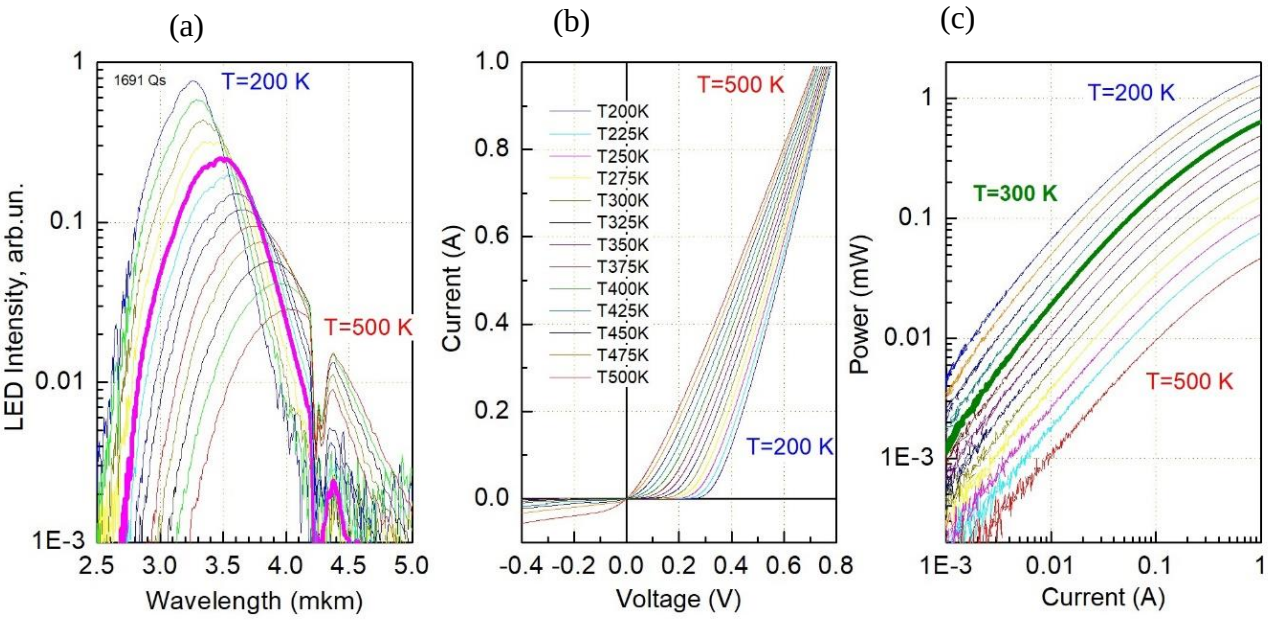


Fig. 1. Spectral electroluminescence (a), the current-voltage characteristics (b), and the current-power characteristic (c) in the temperature range 200 - 500 K.

## Conclusion

This paper demonstrates the possibility of producing LEDs based on P-InAsSbP/n-InAs(Sb)/N-InAsSbP heterostructures operating at elevated temperatures up to 500 K. These diodes were demonstrated to have optical output power over 1.5 mW at 200 K and over 45 μW at 500 K in a wide temperature range.

## REFERENCES


1. **A. Lambrecht, K. Schmitt**, in Mid-infrared Optoelectronics. Materials, Devices, and Application (Eds.: E. Tournié, L. Ceruttib), Woodhead Publishing Series in Electronic and Optical Materials, Woodhead Publishing, Duxford 2020.
2. **A. Krier, E. Repiso, F. Al-Saymari, P.J. Carrington, A.R.J. Marshall, L. Qi, S.E. Krier, K.J. Lulla, M. Steer, C. MacGregor, C.A. Broderick, R. Arkani, E. O'Reilly, M. Sorel, S.I. Molina, M. De La Mata**. Mid-infrared lightemitting diodes. In: Mid infrared Optoelectronics. Materials, Devices, and Application (Woodhead Publishing Series in Electronic and Optical Mater., 2020) p. 59.


## THE AUTHORS


**KLIMOV Aleksandr A.**
a.klimov@ioffe.mail.ru
ORCID: 0000-0001-5642-0483

**KARANDASHEV Sergey A.**
ORCID: 0000-0002-0255-7123

**KUNKOV Roman E.**
romunkov@yandex.ru
ORCID: 0000-0002-2377-2287

**LUKHMYRINA Tatyana S.**

h7k9g00@gmail.com
ORCID: 0000-0002-3989-6487

**LAVROV ALBERT A.**
lavrov_albert@list.ru
ORCID: 0000-0001-8961-2713

**MATVEEV Boris A.**
bmat@iropt3.ioffe.ru
ORCID: 0000-0002-7059-5690

**REMENNYÎ Maxim A.**
Mremennyy@mail.ioffe.ru
ORCID: 0000-0002-4735-9681

**USIKOVA Anna A.**
usikova@mail.ioffe.ru
ORCID 0000-0003-2235-2229

# Emission linewidth and α-factor of 1.3 μm-range vertical cavity surface emitting laser based on InGaAs/InGaAlAs superlattice

**Ya. N. Kovach[1,2✉], S. A. Blokhin[1], M. A. Bobrov[1], A. A. Blokhin[1], N.A. Maleev[1], A. G. Kuzmenkov[1], A. G. Gladyshev[2], I. I. Novikov[2], L. Ya. Karachinsky[2], K. O. Voropaev[3], A. Yu. Egorov[4], V. M. Ustinov[1]**

[1] Ioffe Institute, Saint Petersburg, Russia

[2] ITMO University, Saint Petersburg, Russia

[3] Yaroslav-the-Wise Novgorod State University, Veliky Novgorod, Russia

[4] Alferov University, Saint Petersburg, Russia

✉j-n-kovach@gmail.com

**Abstract.** Static, spectral and linewidth measurements of 1.3 μm-range vertical-cavity surface-emitting lasers based on InGaAs/InAlGaAs superlattice are presented. Minimum linewidth about 40-45 MHz was obtained at output power of 3.3 mW using the Fabry-Perot interferometer method. The linewidth enhancement factor (α-factor) of InGaAs/InAlGaAs superlattice is estimated about 7.7–9 depending on spontaneous emission factor.

**Keywords:** vertical-cavity surface-emitting laser, superlattice, wafer fusion, linewidth, α-factor

**Funding:** The authors from ITMO University acknowledge support in part by the Ministry of Science and Higher Education of the Russian Federation, research project no. 2019-1442 (project reference number FSER-2020-0013) for the static characteristic measurements.

## Introduction

Today vertical-cavity surface-emitting lasers (VCSELs) and VCSEL-based matrixes are used in optical data communication systems, industrial heating, 3D sensing for consumer electronics, and LIDAR object recognition [1]. Recently, much attention has been paid to the possible implementation of single-mode VCSELs for optical spectroscopy, including the creation of gas sensors. However, the development of long-wavelength VCSELs for real-time analysis of industrial gases is associated with a number of fundamental problems of the material systems InAlGaAs-GaAs and InAlGaAsP-InP [2].The most promising approach to the creation of long-wavelength VCSELs is the hybrid integration of the active region based on the InAlGaAsP-InP material system with high-contrast dielectric mirrors or with semiconductor distributed Bragg reflectors (DBR) GaAs/AlGaAs using the wafer fusion technology (WF-VCSEL). Recently, we successfully tested the use of an InGaAs/InAlGaAs superlattice (SL) as an active region of a VCSEL [3].

In this paper, the results of studying the linewidth of 1.3 μm-range single-mode WF-VCSEL based on InGaAs SL are presented and estimation of the α-factor is carried out.

## Materials and Methods

WF-VCSEL designed in the geometry of a vertical microcavity with carrier injection through n-InP intracavity contacts and a composite tunnel junction (TJ) $n^+$-InGaAs/$p^+$-InGaAs/$p^+$-InAlGaAs. For optical and current confinement, the concept of a buried tunnel junction was used, where mesas with 4 μm diameter were formed in the InGaAs layers of TJ. The active region was a superlattice consisting of 24 pairs of $In_{0.57}Ga_{0.43}As/In_{0.53}Ga_{0.20}Al_{0.27}As$ layers with thicknesses of 0.8 and 2 nm accordingly [4]. A detailed description of the WF-VCSEL heterostructure and the fabrication issue of the WF-VCSEL chips are presented in [3].

## Results and Discussion

The investigation of WF-VCSELs demonstrated lasing with a threshold current of ~3 mA and a differential efficiency of ~0.68 W/A. Due to the laser self-heating effect, output optical power reached saturation at currents above 10 mA. According to analysis of the emission spectra of the WF-VCSEL, that devices demonstrate lasing through the fundamental mode with a side-mode suppression ratio of more than 30 dB in the entire current range. In addition, the polarization

degeneracy of the fundamental mode was observed, which can be explained by to the asymmetry and/or the elasto-optical effect. Polarization study revealed the predominance of fixed direction for polarization with an orthogonal polarization suppression ratio (OPSR) of more than 20 dB in the entire operating range of currents without the presence of polarization switching (Fig. 1., *a*).

To measure WF-VCSEL linewidth a SA30-144 scanning Fabry-Perot interferometer was used; a chemical current source was used to minimize noise, and an optical isolator was used to suppress optical feedback. According to Fig. 1., *b*, with the output optical power of the WF-VCSEL increasement, the laser emission linewidth decreased inversely to 40–45 MHz (at 3.3 mW), and then begun to increase due to gain saturation during laser self-heating (i.e., when thermal bend in the watt-ampere characteristic is significant). The approximation of the linear section of the dependence gives the value of the residual linewidth $\Delta\nu_0$ about 6.5 MHz, which was associated with flicker noise and/or mode competition.

For the measured laser emission linewidth the α-factor was calculated using the Schawlow-Townes-Henry formula, which considers the behavior of the refractive index in semiconductor injection lasers [5]. Internal optical losses and internal quantum efficiency were found using the approach described in [4]. Since the spontaneous emission factor $n_{sp}$ is difficult to determine separately from the α-factor, the value of the latter was estimated at the level of 7.7–9 for $n_{sp}$ in range 2–1.5, respectively.

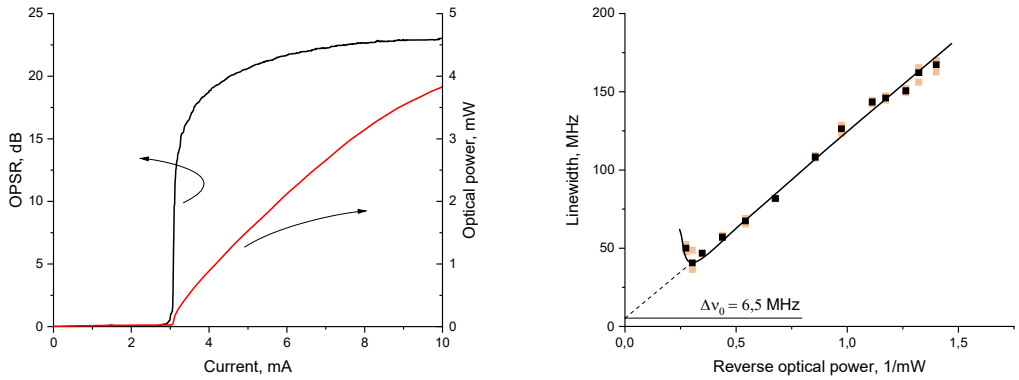


Fig. 1. OPSR and output optical power as function of current (a) and linewidth against inverse optical power (b) for WF-VCSEL with 4 µm BTJ mesa diameter measured at 20°C.

## Conclusion

In this work, we analyzed the emission 1.3 µm-range InGaAs/InAlGaAs SL-based WF-VCSEL. For 20°C, the linewidth drops to 40-45 MHz at 3.3 mW. The linewidth enhancement factor of 7.7–9 was estimated assuming spontaneous emission factor in the range of 2-1.5.

## REFERENCES

1. Padullaparthi B.D., Tatum J.A., Iga K. VCSEL industry : communication and sensing.
2. Kanakis et al. High-Speed VCSEL-Based Transceiver for 200 GbE Short-Reach Intra-Datacenter Optical Interconnects // Appl. Sci. 2019. Vol. 9, № 12. P. 2488. 10.3390/app9122488.
3. Blokhin S. et al. Wafer-fused 1300 nm VCSELs with an active region based on superlattice // Electron. Lett. 2021. Vol. 57, № 18. P. 697–698. 10.1049/ell2.12232.
4. Blokhin S.A. et al. High Power Single Mode 1300-nm Superlattice Based VCSEL: Impact of the Buried Tunnel Junction Diameter on Performance // IEEE J. Quantum Electron. 2022. Vol. 58, № 2. P. 1–15. 10.1109/JQE.2022.3141418.
5. Blokhin S.A. et al. Emission-Line Width and α-Factor of 850-nm Single-Mode Vertical-Cavity Surface-Emitting Lasers Based on InGaAs/AlGaAs Quantum Wells // Semiconductors. 2018. Vol. 52, № 1. P. 93–99. 10.1134/S1063782618010062.

# Broadband emitting from multilayer structures with quantum well-dots active region

**G.O. Kornyshov[1]✉, M.V. Maximov[1], N.Yu. Gordeev[2], Yu.M. Shernyakov[2], A.A. Beckman[2], A.S. Payusov[2], S.A. Mintairov[2], N.A. Kalyuzhnyy[2], M.M. Kulagina[2], Yu.A. Guseva[2], A.E. Zhukov[3]**

[1]Alferov University, 194021 Saint-Petersburg, Russia;
[2]Ioffe Institute, 194021 Saint-Petersburg, Russia;
[3] HSE University, 190008 St. Petersburg, Russia
✉supergrigoir@gmail.com

**Abstract.** Superluminescent diodes of a simplified design with active regions based on 5 and 7 layers of quantum well-dots have been studied. The individual quantum well-dot layers were grown to have spectral offsets of 15–20 nm in order to obtain broadened emission line without significant spectral dips with a central wavelength of about 1μm. For superluminescent diodes with active regions based on 7 and 5 QWD layers, the maximum emission linewidth at half maximum was 103 nm and 92 nm, respectively.

**Keywords:** superluminescent diode, quantum well dots, spectroscopy.

**Funding:** The study was supported by the Russian Science Foundation (grant No. 23-72-00038, https://rscf.ru/project/23-72-00038/).

## Introduction

Semiconductor electronics has found its application in many industries including medical technology. In particular, a key element of optical coherence tomography is superluminescent diodes (SLDs), which are characterized by wide emission spectra without significant spectral dips. This is achieved by suppressing positive feedback in the laser-like diodes, due to which the devices operates in the spontaneous emission regime even at high current densities. To achieve broad emission spectra at wavelengths about 1 μm chirped multiple InAs quantum dots [1,2] (layers of quantum dots with wide size dispersion) or “dot-in-a-well” [3,4]. In this work, we use quantum well-dots (QWD), heterostructures of transitional dimensionality (0D/2D), as the SLD active region. It was shown that due to the fluctuation of In concentration in the QWD layer, the gain spectrum as broad as 90 nm can be obtained [5].

## Materials and Methods

For our experiments, two wafers with 5 and 7 chirped InGaAs QWD layers were grown on GaAs substrates by metalorganic vapor-phase epitaxy. The active regions are inserted in GaAs waveguides sandwiched between n- and p-type $Al_{0.4}Ga_{0.6}As$ claddings. In the p-claddings, InGaP stop-layer was inserted to control the etching depth of the ridges. The ridges were formed at an angle of 5-7 deg. to the cavity facets. Lengths of SLDs were 0.25-0.3 mm and no reflective or antireflective coatings were applied. The measurements were carried out in a pulsed mode with pulses of 300 ns duration and a frequency of 2 kHz.

## Results and Discussion

Figure 1(a) shows the electroluminescence spectra of 7-layer QWD SLDs depending of the pump current. At low pump currents, the spectra contain only a long-wavelength peak (1070–1075 nm) originated from the QWD layer with the highest carrier localization energy. As the injection current increases, a contribution of the shorter-wavelength peaks from QWD layers with a lower carrier localization energy gradually increases, and the total width of the electroluminescence spectra increases. For the 5-layer QWD SLDs, the maximum full width at half maximum (FWHM) of the spectrum achieves 92 nm at the injection current of 150 mA (figure 1(b)). Increasing the number of QWD layers from 5 to 7 makes it possible to achieve half-width of the emission spectrum as broad as 103 nm.

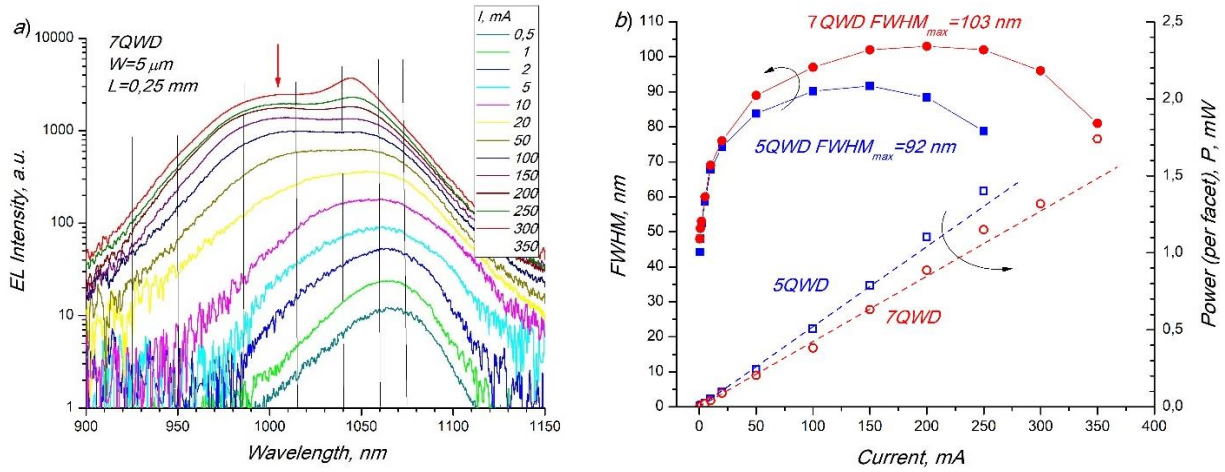


Figure 1. (a)Electroluminescence spectra of the 7-layer QWD SLD (cavity length 0.25 mm) at various pump currents. The vertical lines mark the positions of the PL maxima of the QWD layers, the arrows show the wavelengths of the laser with the cavity length of 0.25 mm processed from the same wafers. (b) Dependence of the FWHM of the spectrum and optical power from one facet on the current

The spectral positions of laser line in the samples with straight ridges are marked in Fig. 1(a) by an arrow. They correspond to the energy range with a high density of states in a multilayer active region, which emerges due to the superposition of the excited and ground states of several QWD layers. The absence of lasing in SLDs means that the use of the inclined ridge geometry allows effectively suppressing feedback in short cavity devices.

## Conclusion

Using chirped multiple QWDs as an active media of SLDs emitting at wavelength of 1μm allows achieving spectra of electroluminescence as broad as 100 nm. Despite the fact that the optical power reaches only a few milliwatts, we believe that further design optimization would allow suppressing stimulated emission in longer cavities and obtaining more optical power while keeping broad emission spectra.

## REFERENCES

1. **Kovsh A., Krestnikov I., Livshits D., Mikhrin S., Zhukov A. and Weimert J.**, Quantum dot laser with 75 nm broad spectrum of emission, Optics Letters, Vol. 32, No. 7 (2007) p. 793.

2. **Ozaki N., Yamauchi S., Hayashi Y., Watanabe E., Ohsato H., Ikeda N., Sugimoto Y., Furuki K., Oikawa Y., Miyaji K., Childs D. T. D. and Hogg R. A.**, Development of a broadband superluminescent diode based on selfassembled InAs quantum dots and demonstration of high-axial-resolution optical coherence tomography imaging, J. Phys. D: Appl. Phys. 52, (2019)225105.

3. **Maximov M. V., Tsatsul'nikov A. F., Volovik B. V., Sizov D. S., Shernyakov Y. M., Kaiander I. N., Zhukov A. E., Kovsh A. R., Mikhrin S. S., Ustinov V. M., Alferov Z. I., Heitz R., Shchukin V. A., Ledentsov N. N., Bimberg D., Musikhin Y. G. and Neumann W.**, Tuning quantum dot properties by activated phase separation of an InGa(Al)As alloy grown on InAs stressors, Phys. Rev. B 62 (2000) 16671–80.

4. **Chen S., Li W., Zhang Z., Childs D., Zhou K., Orchard J., Kennedy K., Hugues M., Clarke E., Ross I., Wada O. and Hogg R.**, GaAs-Based Superluminescent Light-Emitting Diodes with 290-nm Emission Bandwidth by Using Hybrid Quantum Well/Quantum Dot Structures, Nanoscale Research Letters, 10:340, (2015).

5. **Kornyshov G. O., Gordeev N. Yu., Payusov A. S., Serin A. A., Shernyakov Yu. M., Mintairov S. A., Kalyuzhnyy N. A., Maximov M. V. and Zhukov A. E.**,Gain spectra of lasers based on transitional dimension active region, Journal of Physics: Conference series Volume 1697, (2020)012177.

# Calculation the mode loss spectra in MIR and THz with double metal waveguides

**N.A. Kostromin[1,2,3], A.S. Dashkov[2,3], Barykin D. A.[1]**

[1]Peter the Great St.Petersburg Polytechnic University, Polytechnicheskaya str. 29, St.Petersburg, 195251, Russian Federation
[2]Alferov University, Khlopin str. 8/3, let. 'A', St.Petersburg, 194021, Russian Federation
[3]Saint Petersburg Electrotechnical University, Professor Popov str. 5, St. Petersburg, 197022, Russian Federation
e-mail: Kostromin.na@edu.spbstu.ru

**Abstract:** The aim of this work is to theoretically calculate the parameters of a double metal waveguide to minimize peak absorption losses in the metal and maintain a high value of the optical confinement factor. The Drude-Lorentz model is used to model the permittivity of metal and QCL layers. The optimization was carried out by minimizing the objective function using the methods of gradient descent and the Nelder-Mead method. The parameters of the waveguide, namely, the metal thickness, at which the minimum spectral mode loss in QCLs is achieved due to absorption in the metal, are determined. Was shown that the Drude-Lorentz model is a useful theory for modeling the permittivity of metal and QCL layers, and the optimization methods used in this study can be applied to other areas of research as well.

## Introduction

The principle of quantum cascade lasers (QCLs) operation was proposed as early as 1971. However, before the work of the group led by Capasso, published in 1994, no one had been able to implement emitters of sufficient power and efficiency [1, 2]**.** There is still high interest in creating new structures based on these constructions. Subsequently, with the help of QCLs, structures that emit light due to intersubband electronic transitions, the scientific community managed to create radiation sources for the mid-infrared (MIR) and terahertz (THz) frequency ranges. To date, in the MIR, and THz ranges, the QCL has become the only compact and powerful radiation source operating at temperatures close to room temperature.

The resonator is necessary to contain the radiation and provide optical feedback in such a way as to introduce minimal absorption losses. Currently, one of the most promising sources of radiation in the terahertz range of electromagnetic waves is quantum cascade lasers with a double metal waveguide [4]. Creating such lasers is a complex task that requires preliminary numerical experiments to analyze the mode loss spectrum of QCLs with a double metal waveguide (DDW). Maintaining a high optical confinement factor, $\Gamma$ (close to 1), is a necessary condition to improve laser performance. THz and MIR lasers with a DMW based on silver are especially interesting, because this metal has higher electric and thermal conductivities than gold and copper, which should lead to lower losses in Ag-based waveguides [4].

In this case, the task of optimizing a QCL with DDW was formulated as follows: select the parameters of the waveguide (the dielectric permeability) in such a way as to minimize absorption losses in the metal, with the value of the optical confinement factor, $\Gamma \sim 1$. Therefore, the aim of this work can be formulated as follows: theoretically calculate the parameters of a double metal waveguide in such a way as to reduce the peak absorption losses in the metal to a minimum, while maintaining a high value of $\Gamma \sim 1$.

## Numerical experiments methods

In the terahertz range of electromagnetic frequencies, the Drude-Lorentz model is used to theoretically describe the complex dielectric permittivity. To calculate the spectra, the refractive index and extinction coefficient (absorption index) are calculated by solving the Fresnel

equation. To obtain the transmission and reflection spectra of the entire structure, the transfer matrix method through the entire QCL structure is used. To optimize the structure of the waveguide, an objective function is introduced, which is minimized by various methods such as the gradient descent method and the Nelder-Mead method (simplex method).

In this paper, on optimizing the structure of a double metal waveguide, namely, to find the minimum absorption loss in the metal of the resonators based on metals such as silver, gold, copper and others. It is also proposed to estimate the numerical values of the reflection spectra of the metal/semiconductor interfaces of QCL structures for various metal thicknesses numerically determined in solving the optimization problem. Numerical results show, that it is expected that the silver-based dual metal waveguide will perform better than the copper-gold based one due to its greater electrical and thermal conductivity.

**Conclusion**

This paper aims to discuss the principles of quantum cascade lasers (QCLs) and their use as radiation sources for the mid-infrared and terahertz frequency ranges. It focuses on optimizing QCLs with double metal waveguides to minimize absorption losses while maintaining a high optical confinement factor. The paper describes the numerical methods used to calculate the spectra and optimize the waveguide structure.

The Drude-Lorentz model is a useful tool for modeling the permittivity of metal and QCL layers, and the optimization methods used in this study can be applied to other areas of research as well.

**Acknowledgements**

This work was supported by Russian Scientific Foundation (project No 23-29- 00216).

**References**

[1] Kazarinov R. F., Suris R. A. On the possibility of amplifying electromagnetic waves in a semiconductor with superlattices, Physics and Technology of Semiconductors. - 5 (4) (1971), 797–801.

[2] Faist J., Capasso F., Sivco D.L., Sirtori C., Hutchinson A. L., Cho A. Y., Quantum Cascade Laser, Physical Review B, 50 (12) (1994), 8663–8667.

[3] Williams B. S., Terahertz quantum cascade lasers: in partial fulfillment of the requirements for the degree of Doctor of Philosophy, 117–137.

[4] D.V. Ushakov, A.A. Afonenko, A.A. Dubinov, V.I. Gavrilenko, I.S. Vasil'evskii, N.V. Shchavruk, D.S. Ponomarev, R.A. Khabibullin Mode loss spectra in THz quantum-cascade lasers with gold- and silver-based double metal waveguides, TERAHERTZ RADIATION, 48 (11) (2018), 1005–1008

# Long Wave Infrared ($\lambda_{0.5} \geq 12$ μm) photodetectors based on $InAsSb_x$ ($x \geq 0.4$) solid solution.

***Kunkov R. E.[1], Karandashev, S.A.[1], Klimov A.A.[1], Lebedeva N. M.[1], Lukhmyrina T. S.[1], Matveev B. A.[1], Remennyy, M.A.[1], Usikova A. A.[1]***

[1] Ioffe Institute RAS, Saint Petersburg 194021, Russia;

✉romunkov@yandex.ru

**Abstract.** The results of a study of multilayer p-n heterostructures based on $InAsSb_x$ solid solution ($x \geq 0.4$), with a long-wavelength photosensitivity boundary of $\lambda_{0.5} \approx 12$ μm at room temperature are presented. The volt-ampere and spectral characteristics of photosensitivity were analyzed in the temperature range 175 – 325 K. In order to improve the performance of the photodetector, a number of design solutions have been used, aimed at increasing the zero bias resistance while maintaining the optically active area of the chip. It is shown that the photoelectric properties are determined by the diffusion mechanism of current flow, and experimental samples of photodetectors based on them are characterized by a quantum efficiency of $S_i \approx 1$ A / W.

**Keywords:** InAsSb solid solution, LWIR photodetector, long-wavelength photodiodes, InAsSb heterostructures.

## Introduction

Photodetectors operating in the long-wave infrared spectrum (8 – 14 microns) are key components of such systems as: thermal imaging, thermal sensing, gas analysis of both hazardous gases (sarin, soman, tabun) in life safety systems, and halogen-containing anesthetics in medical equipment. [1]. One of the promising materials for long-wave infra-red (LWIR) photodetectors is $InAsSb_x$-based semiconductor diode heterostructures, which, depending on active region composition, can be photosensitive to both mid-wave (3 – 5 μm) [2] and long-wave IR radiation [3]. Though the theory asserts the possibility of obtaining photodetectors with a long-wave limit of photosensitivity $\lambda_{0.5}$ up to 14 μm, the information about obtaining such photodetectors is extremely scarce.

As the compositions 'move' into the long-wave region of the spectrum, the densities of dark currents increase proportionally $e^{-\frac{h\nu_{0.1}}{kT}}$ [4]. This leads to a desire by researchers to design long wavelength IR photodetector chips with as small an active area as possible. However, this can lead to a serious reduction in the luminosity of the photodetector, so against the desire of researchers to reduce the p-n junction area, there is a need to ensure sufficient optically active photodetector area or sufficient viewing angle of an immersion photodetector with a lens.

## Experimental results

Epitaxial heterostructures were obtained on InAs (100) substrates, and contained: N-InAsSb buffer layers with a total thickness of 4-6 μm, a photosensitive $InAsSb_x$ layer ($x \approx 0.45$) 2-3 μm thick, a P-InAsSb (P) contact layer, 2 microns thick. To obtain the mesa structure, multistage photolithographic techniques using plasma-chemical etching were used. The result was a "flip chip" sample design with a common anode and a circular mesa, about 140 μm in diameter, split into 4 equal quadrant cathodes. The width of the separation groove did not exceed 5 μm. Subsequently, immersion docking of the obtained samples with a Ge lens of 3.5 mm diameter was performed. The spectral dependences of photosensitivity and volt-ampere characteristics were investigated with the help of evacuated cryostat in the temperature range of 200 – 325 K. Photographs of experimental samples obtained and spectral dependences of photoresponse are shown in Fig. 1.

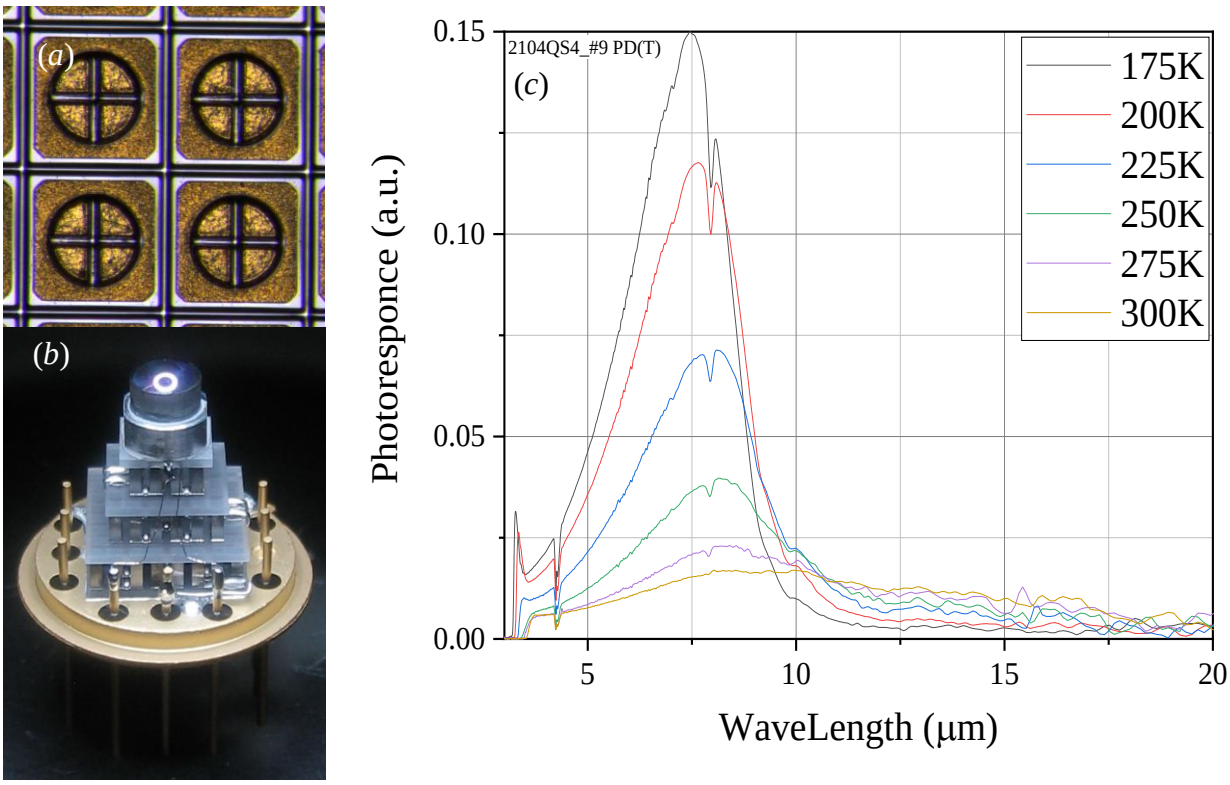


Fig. 1. Photographs of the obtained chips (*a*), experimental sample photodetector (*b*) and spectral dependences of photoresponse in the temperature range 175 - 300 K (*c*).

## Conclusion

This paper demonstrates the possibility of obtaining long-wavelength photodetectors with a red cut-off $\lambda_{0.5} \approx 12$ μm at room temperature, capable of operating under thermoelectric cooling. The design of photodetector, which is a quadrant immersion photodiode, has been proposed, which allows obtaining lower values of dark currents while maintaining the optically active area. The experimental samples obtained show total current sensitivity $S_i \approx 1$ A/W.

## REFERENCES

1. **A. Rogalski,** Recent progress in HgCdTe infrared detector technologies, Infrared Physics & Technology, 2011, Vol. 54, No. 3, P. 136–154.

2. **N.D. Il'inskaya, S.A. Karandashev, A.A. Lavrov, B.A. Matveev, M.A. Remennyi, N.M. Stus', and A.A. Usikova,** P-InAsSbP/p-$InAs_{0.88}Sb_{0.12}$/n-$InAs_{0.88}Sb_{0.12}$/$n^+$-InAs PDs with a smooth p-n junction, Infrared Physics & Technology 88 (2018) 223–227

3. **D. H. Wu, A. Dehzangi, Y. Y. Zhang, M. Razeghi,** Demonstration of long wavelength infrared type-II InAs/$InAs_{1-x}Sb_x$ superlattices photodiodes on GaSb substrate grown by metalorganic chemical vapor deposition, Appl. Phys. Lett., 2018, Vol. 112, No. 24, Article No: 241103, 4 p.

4. **A.A. Klimov, R.E. Kunkov, A.A. Lavrov, N.M. Lebedeva, T.C. Lukhmyrina, B.A. Matveev, M.A. Remennyi**, Long-wave infrared $InAs_{0.6}Sb_{0.4}$ photodiodes grown onto n-InAs substrates, Journal of Physics: Conference Series, 2020, 1695(1), 012077.

# Influence of quantum states imperfections on the error rate in measurement-device-independent QKD

**P. A. Kupriyanov[1,2,3,4] ✉, N. V. Rudavin[1,3,4,5], I. S. Gerasin[1,2,3,4], A. P. Dvurechenskiy[1,2,3,4], I. V. Petrov[1,3], D. D. Menskoy[1,3], R. A. Shakhovoy[1,3,4]**

[1]QRate, Novaya av. 100, Moscow, Russia;

[2]Moscow Institute of Physics and Technology, 9 Institutskiy per., Dolgoprudny, Moscow Region, 141701, Russian Federation;

[3]NTI Center for Quantum Communications, National University of Science and Technology MISiS, Leninsky prospekt 4, Moscow 119049, Russia;

[4]Russian Quantum Center, Bolshoy Boulevard 30, bld. 1, Skolkovo, Moscow 121205, Russia;

[5]HSE University, 20 Myasnitskaya ulitsa, Moscow 101000, Russia

✉kupriianov.pa@phystech.edu

**Abstract**. Quantum key distribution (QKD) is a modern technology that allows two legitimate users obtaining a shared cryptographic key completely secure. Unfortunately, real implementations of QKD systems contain vulnerabilities, such that an eavesdropper can still get information about the key. Therefore, QKD protocols generally use privacy amplification procedures that reduce the size of the key depending on the level of errors that are generally assumed to be caused by a non-legitimate user. So, the quantum bit error rate (QBER) becomes an important parameter significantly affecting the rate of key distribution. In this work, we investigate the influence of quantum states imperfections on the QBER in the measurement-device-independent QKD protocol with time-bin encoding.

**Keywords:** measurement-device-independent quantum key distribution, imperfect states, time-bin phase-encoding.

**Funding:** The study was commissioned by JSCo «RZD».

## Introduction

Legitimate users participating in quantum key distribution (QKD) need to prepare quantum states with a high degree of accuracy. Our experimental setup uses time-bin encoding [1], for which the intensity modulator cuts out short pulses from the continuous laser. If Alice prepares "0" in the *X*-basis, then equal pulses are created in both time slots (we refer them to *E*- and *L*-pulses – early and late). In the case of sending "1", it is necessary to additionally apply the phase $\pi$ between the pulses. Preparing states in the *Z*-basis, intensity modulator creates a pulse in only one of the two time slots. Here, non-ideality is related to the fact that "empty" time slot still contains some non-zero intensity. For the *X*-basis, there is always a slight intensity difference between the pulses in different time slots as well as deviation of the phase difference from 0 or $\pi$. These imperfections lead to false clicks of detectors and to an increase in QBER.

## Materials and Methods

We first considered the problem of the interference of weak coherent pulses on a beam splitter. Alice and Bob send *L*-pulses with intensities $s_a$ and $s_b$, respectively, while the time slot corresponding to the *E*-pulse gets noise intensities $\zeta_a$ and $\zeta_b$, caused by imperfect operation of the amplitude modulator. The mutual state of Alice and Bob can be thus written as

$$\left|Z_1 Z_1\right\rangle_{ab} = \left|\sqrt{\zeta_a} e^{i\varphi_a}\right\rangle_{a_E} \left|\sqrt{s_a} e^{i\varphi_a}\right\rangle_{a_L} \left|\sqrt{\zeta_b} e^{i\varphi_b}\right\rangle_{b_E} \left|\sqrt{s_b} e^{i\varphi_b}\right\rangle_{b_L} \quad (1)$$

As is known, complex numbers representing coherent pulses at the input of the beam splitter are added and subtracted at the output ports [2]. Thus, we can calculate the states after passing through quantum channels with losses $t_a$ and $t_b$ respectively and after interference on the beam splitter.

We calculated the gain corresponding to the clicking of detectors in orthogonal time modes. Such events when sending the same bits in the $Z$-basis will lead to errors:

$$Q_{s_a s_b}^{Z,err} = y_{s_a,s_b} y_{\zeta_a,\zeta_b} (2y_{s_a,s_b} y_{\zeta_a,\zeta_b} - 2y_{\zeta_a,\zeta_b} I_0(x_{s_a,s_b}) + I_0(x_{s_a,s_b} - x_{\zeta_a,\zeta_b}) \\ -2y_{s_a,s_b} I_0(x_{\zeta_a,\zeta_b}) + I_0(x_{s_a,s_b} + x_{\zeta_a,\zeta_b})), \quad (2)$$

where $y_{\nu,\mu} = (1-p_{dc})e^{\eta(t_a\nu + t_b\mu)/4}$, $x_{\nu,\mu} = \frac{\eta}{2}\sqrt{t_a t_b \nu\mu}$, and $I_0(x)$ is a modified Bessel function of the first kind. In our model, we assume that probability of dark counts $p_{dc}$ and efficiency $\eta$ are the same for all detectors.

Similarly, considering the sending of different bits in the $Z$-basis, we calculated the gain for correct events $Q_{s_a s_b}^{Z,corr}$. QBER in $Z$-basis can be calculated with the formula:

$$E_{s_a,s_b}^{Z} = \frac{e_d Q_{s_a,s_b}^{Z,corr} + (1-e_d) Q_{s_a,s_b}^{Z,err}}{Q_{s_a,s_b}^{Z,corr} + Q_{s_a,s_b}^{Z,err}} \quad (3)$$

where $e_d$ denotes the probability of error in the detection system, which can be caused by distortions in the quantum channel that were not considered in our model.

In the case of sending X-basis, the imperfect phase between the $E$- and $L$-pulses leads to additional errors. If we do not accurately select the voltage supplied to the phase modulator, an erroneous phase difference $\delta\Theta_{ab}$ appears. In a similar way, we calculated QBER for X-basis (not shown here due to the lack of space).

## Results and Discussion

Considering the interference of weak coherent pulses, we obtained dependences of the error rates on the imperfections of the preparation of states. The plot of this dependence for the $Z$-basis is presented in the Fig. 1.

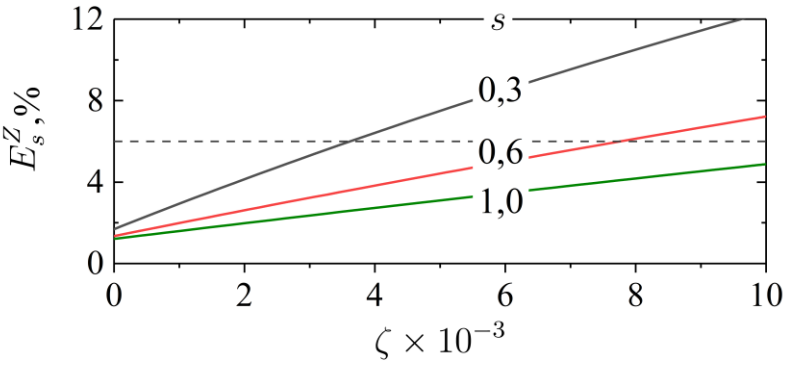


Fig. 1. Dependence of $E_{s_a s_b}^{Z}$ on the imperfect noise intensity $\zeta$=$\zeta_a$=$\zeta_b$.

## Conclusion

In this work, we derived formulas that allow estimating the error rate in the MDI-QKD protocol. We can also use them to solve the inverse problem: to find the characteristics of experimental equipment that allow us not to exceed a certain QBER value.

## REFERENCES


1. **Tang, G. Z., Sun, S. H., Chen, H., Li, C. Y., & Liang, L. M.**, Time-bin phase-encoding measurement-device-independent quantum key distribution with four single-photon detectors. Chinese Physics Letters 33.12 (2016): 120301.

2. **Chen, H., An, X. B., Wu, J., Yin, Z. Q., Wang, S., Chen, W., & Han, Z. F.**, Hong–Ou–Mandel interference with two independent weak coherent states. Chinese Physics B 25.2 (2016): 020305.

# Lasers of metrological appropriation

**Y.G. Zacharenko[1], N.A. Kononova[1], A.D. Kurkova[2]✉, E.I. Logvinuk[1], Z.V. Fomkina[1]**
[1] D.I. Mendeleyev Institute for Metrology (VNIIM), Saint Petersburg, Russia,
[2] Peter the Great Saint-Petersburg Polytechnic University, Saint Petersburg, Russia.
✉ kurkova.ad@edu.spbstu.ru

**Abstract.** Today laser measuring systems and sets, interferometers and other measuring units, which principle of operation is based on the use of stabilized laser radiation sources, are actively used to solve urgent problems in metrological laboratories of advanced enterprises of various industries and in leading scientific institutes. This article is about the use of lasers in metrology.

**Keywords:** laser, measuring instrument, State Primary Standard of the unit of length, working standard

## Introduction

With the advent of the first laser in the middle of the XX century, the rapid development of laser technology immediately began, which continues to this day. The laser does not cease to conquer new areas of applications due to its properties and characteristics, it becomes a reliable assistant to doctors, builders, archaeologists, criminologists, etc.

Now lasers are successfully used in modern industry, helping to solve a wide variety of tasks. Lasers are also widely used in metrology. As working measuring instruments, the metrological services of most manufacturing enterprises use laser-based measuring instruments, such as linear displacement sensors, distance measuring equipment, laser systems for shaft alignment, and others, to control their products. The assortment of laser-based measuring instruments are constantly expanding, newly developed measuring equipment are appearing, already available on the market measuring instruments are improving, their accuracy is increasing. Along with unstabilized laser radiation sources, in modern high-precision measuring equipment stabilized lasers are used. The principle of operation of such modern high-precision measuring systems as interferometers, lasers trackers, scanners, total stations, etc. is based on the use of stabilized laser radiation sources. Being the most accurate and capable of solving many technical problems, measuring instruments based on stabilized lasers occupy an important place in the technical control services of products and services and successfully replace the traditional measuring instrument [1].

Stabilized laser radiation sources are successfully used to realize, store and transfer of the unit of length all over the world. Stabilized lasers and systems based on them are successfully used for transfer the unit of length both as independent measuring instruments and as a part of various measuring equipment and systems. This article is about the use of stabilized laser radiation sources in the field of linear measurements.

## Stabilized laser radiation sources in metrology

In accordance with the Recommendation of the BIPM, leading scientific metrological institutes of the world use in national standards stabilized laser radiation sources. In the Russia the realization of the unit of length is by two He-Ne/$I_2$ and one Nd:YAG lasers from the State Primary Standard of the Unit of Length – metre GET 2-2021. GET 2-2021 provides realization of the unit of length at the wavelength of 0,633 μm with the standard deviation – $1{,}6\cdot10^{-12}$, and $1{,}3\cdot10^{-12}$ at 0,532 μm. GET 2-2021 also includes the set for measuring the frequency difference of laser radiation sources, the complex of equipment for measuring a frequency of lasers in the wavelength range from 500 to 1050 nm (optical frequency comb) with the hydrogen standard of frequency and four linear laser interferometers in the range from $1\cdot10^{-9}$ to 30 m, the basis of the measuring system of which are also frequency stabilized lasers [2, 3].

Stabilized laser radiation sources used for realization of the unit of length are developed directly by national metrological institutes or other scientific organizations. Today a serial production of frequency-stabilized lasers of such precision is carried out only by «Winters Electro-Optics, Inc.» (USA). In accordance with the Recommendation of the BIPM, the absolute frequency accuracy of such lasers is less than $2{,}5\cdot10^{-11}$ [4].

The metre as one of the seven basic units of the International System of Units SI is included in a number of derived units, so the realization of many derived units is impossible without the use of equipment of storing and transferring of the unit of length. In the Russia, stabilized laser radiation sources are a part of a number of such State Primary standards as the State Primary Standard of the Flat Angle Unit GET 22-2014, the State Primary Standard of the Unit of the Temperature Coefficient of Linear Expansion of Solids GET 24-2018, the State Primary Standard of the Unit of Pressure GET 101-2011, etc.

To store and transfer of the unit of length to frequency-stabilized lasers, wavelength meters, etc., stabilized laser radiation sources in the range from 0,4 to 11 microns are used as secondary standards. Stabilized laser radiation sources are also as a part of sets for calibration of linescales and gauge blocks are used as secondary standards, and as a part of laser displacement meters in the range from $10^{-9}$ to $10^{-2}$ m for transferring the unit of length to laser interferometers and laser displacement meters. The main manufacturers of such lasers today are JSC «Plasma» (Russia), «Meßtechnik GmbH» (Germany), «Thorlabs Inc.» (USA). The absolute frequency accuracy of such lasers is near $2\cdot10^{-8}$.

Stabilized lasers are a part of modern high-precision measuring equipment, such as laser measuring systems, mobile coordinate measuring machines (trackers), laser interferometers and others. The operating principle of such measuring equipment is based on the method of laser interferometry, which is one of the most highly accurate method of transferring of the unit of length. Laser measuring systems are widely used to solve a variety of scientific and technical problems in the most important sectors of the national industry. Laser measuring systems of the following manufacturers are mostly used: «Renishaw plc.» (Great Britain), «Automated Precision Inc.» (USA), «Chotest Technology Inc.» (China) [5].

## Experimental researching

Experimental researching of widely used stabilized lasers carried out by GET2 at the following conditions:

- ambient temperature, °C 20±3;
- max. temperature's transformation during an hour, °C 0,2;
- relative humidity of the air, %, no more 80;
- atmospheric pressure, kPa 100±6.

The following results were obtained, which are presented in table 1.

Table 1

**Results**

| Model | The wavelength, nm | The expanded uncertainty in relative units |
|---|---|---|
| Iodine-stabilized He-Ne laser, model 100, by "Winters Electro-Optics, Inc." | 632,99121257 | $1{,}5\cdot10^{-11}$ |
| Stabilized He-Ne laser LGN-302 | 632,99097 | $1\cdot10^{-8}$ |
| Stabilized He-Ne laser SIOS SL 02/1 | 632,99099 | $2\cdot10^{-8}$ |
| Differential laser interferometer SIOS SP 2000 | 632,99083 | $2\cdot10^{-8}$ |
| Laser measuring system Renishaw XL-80 | 632,99058 | $2\cdot10^{-8}$ |

| | | |
|---|---|---|
| Stabilized He-Ne laser Thorlabs HRS015 | 632,99152 | $3 \cdot 10^{-8}$ |

## Conclusion

The role and importance of stabilized lasers and laser measuring systems based on them cannot be overestimated. The list of applications of measuring instruments based on laser sources is constantly growing due to their high accuracy characteristics. The dynamics of the global market of metrological services is defined by constantly growing needs for changes in new areas of activity and increasing requirements for their accuracy. The development of new technologies requires constant improvement of the state standards base, the development of new measuring technologies and equipment for the traceability of measurements. Stabilized laser radiation sources are the reliable basis for these goals.

## REFERENCES


1. Zackharenko Yu. G., Kononova N.A., Kosmina M. A., Fomkina Z.V., Chekirda K.V. The current state of the reference base of the Russian Federation in the field of measurements of length and angle measurements. Measurement Techniques, 2022, no. 7, pp. 18-23. DOI: 10.32446/0368-1025it.2022-7-18-23.
2. Akimova T. P., Zackharenko Y. G., Kononova N. A., Fedorin V. L., Fomkina Z. V., Chekirda K. V. The State primary standard of the unit of length – metre GET 2-2021. Measurement Techniques, 2021, no. 10, pp. 3-7. DOI: 10.32446/0368-1025it.2021-10-3-7.
3. Kononova N.A., Zackharenko Yu. G., Fomkina Z.V. The State Primary Standard of the Unit of Length - the meter GET 2. International Conference Laser Optics (ICLO). Saint Petersburg, 2022.
4. Kononova N. A., Zackharenko Yu. G., Fedorin V. L., Fomkina Z. V. Investigations of metrological characteristics of the “Winters Electro-Optics, Inc.” iodine-stabilized He-Ne laser by The State Primary Standard of the Unit of Length – GET 2-2010. 18th International Conference on Laser Optics (ICLO). Saint Petersburg, 2018.
5. Chekirda K.V., Zakharenko Yu.G., Kononova N.A., Fomkina Z.V. Current state and prospects for the developments of a reference base in the field of length measurements. IX International symposium «Metrology of time abd space» (September, 12-14). 2018, no. 4, pp. 190-194.

# Tandem solar cells based on porous silicon and perovskites.

D.A. Lyapina, D.A. Shishkina, N.A. Poluektova
Samara National Research University, Samara, Russia
✉dashalyapina66@gmail.com

**Abstract.** Porous silicon-based and perovskite-based solar cells are promising in the field of solar energy. Silicon is used as a substrate for perovskite layers to create porous structures.

**Keywords:** Porous silicon, perovskites, solar cells, porous structures, solar energy.

## Introduction

Tandem solar cells based on porous silicon and perovskites represent a promising technology in the field of solar energy. This technology allows for higher efficiency in converting solar energy to electricity than traditional solar cells. In addition, it has low production costs and can be used to create more efficient and cost-effective solar panels. Therefore, research in the field of tandem solar cells based on porous silicon and perovskites is relevant and has great potential for application in solar energy.

## Materials and Methods

Using porous silicon as a substrate for perovskite layers allows for improved quality of the perovskite film and increased efficiency of the solar cell. To create tandem solar cells based on porous silicon and perovskites, a sequential deposition method is used, which allows for layered structures with high control over layer thickness and composition.

One of the main advantages of tandem solar cells based on porous silicon and perovskites is the ability to combine two materials with different optical properties, which allows for a wider range of light absorption and increased energy conversion efficiency.

An important aspect of research in solar cells based on porous silicon and perovskites is the optimization of processes for forming and modifying the surface of porous silicon to provide optimal conditions for perovskite layer growth and improve the efficiency of the solar cell.

One of the challenges in developing solar cells based on porous silicon and perovskites is increasing their stability against degradation caused by moisture and temperature. To address this issue, additional research is needed in the field of stabilizing perovskite layers and protecting them from external factors.

## Results

Introducing perovskite materials into porous structures improves the electrical properties of the materials.

The method of obtaining tandem solar cells with a perovskite film in a porous silicon structure allows achieving a solar energy conversion efficiency of more than 20%.

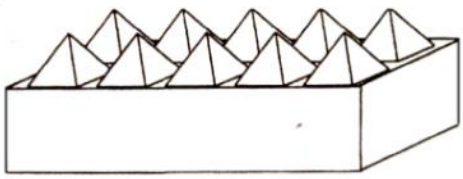

Figure 1 - Schematic representation of an idealized textured surface of silicon.

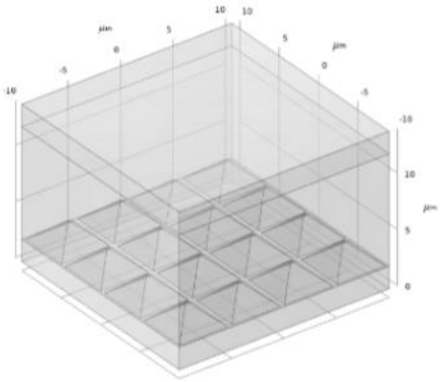

Figure 2 - External view of the silicon wafer model.

Optimization of the thickness of porous silicon and pore size can increase energy conversion efficiency by 5-10%.

The incorporation of perovskites into porous materials can improve their stability against degradation under the influence of moisture and temperature.

The integration of perovskites into porous structures has great potential for use in solar energy conversion and other electrochemical devices.

Further research and optimization of the parameters of porous structures are necessary to achieve optimal results.

## Conclusion

The technology of tandem solar cells based on porous silicon and perovskites has great potential in solar energy due to high efficiency and low production costs. The use of porous silicon and the method of sequential deposition of layers allow improving the quality and control over the thickness and composition of the layers. Optimization of porous silicon and pore sizes can increase energy conversion efficiency by 5-10%. However, a challenge is the stability against degradation under the influence of moisture and temperature, requiring further research.

## ЛИТЕРАТУРА


1. **P. Reinhard, S. Buecheler, A. N. Tiwari** Technological status of Cu(In,Ga)(Se,S)2-based photovoltaics Sol. Energy Mater. Sol. Cells. – 2013. – С. 287-290.

2. **T. Baikie, Y. Fang, J. M. Kadro, M. K Schreyer, F. Wei, S. G. Mhaisalkar, M. Graetzel, T. J. White, T** Synthesis and crystal chemistry of the hybrid perovskite (CH3NH3) PbI3 for solid-state sensitised solar cell applications Journal of Materials Chemistry A. –2013. –С.3-10.

3. **Q. Liu, Z. Tang, M. Wu, Z. Zhou** Design, preparation, and application of conjugated microporous polymers Polymer International, 2014. – С. 381-392.

4. **Jeon N. J.,** Compositional engineering of perovskite materials for 43 high-performance solar cells – 2015. – С. 476-480.

# Optimization of $SnO_2/FAPbI_3$ interface by carbon dots interlayer

**I.V. Margaryan [1✉], A.A. Vedernikova[1], E.V. Ushakova[1], A.P. Litvin[2]**
[1] ITMO University, 14, Birzhevaya line, St.Petersburg, 199034 Russia;
[2] Jilin University, Changchun, 130012, China
✉ igormargaryan@niuitmo.ru

**Abstract.** Solar cells based on organic-inorganic (hybrid) perovskites attracted much attention due to rapid growth of their power conversion efficiency (PCE). However, defects at grain boundaries and at interfaces limit further increase of PCE and lead to degradation of the device. Carbon dots with appropriate surface groups can improve the charge extraction from perovskite to electron transport layer (ETL), affect the morphology of perovskite layer and reduce the recombination rate at interfaces. Current study demonstrates that carbon dots as an interlayer between $SnO_2$ ETL and $FAPbI_3$ enhance the morphology and optical properties of perovskite layer. This improvement results in increase of short circuit current ($J_{SC}$), fill factor (FF) and PCE of carbon dots-based perovskite solar cell.

**Keywords:** perovskites, carbon dots, luminescence, atomic force microscopy.
**Funding:** This work was supported by the Russian Science Foundation (19-13-00332П).

## Introduction

Metal-halide hybrid perovskites have recently emerged as a promising material in a field of optoelectronics. Hybrid perovskite solar cells (PSCs) draw tremendous attention as their PCE has increased from 3.8% to 25.6% since 2009. This incredible progress became possible due to outstanding properties of perovskites such as high charge carriers mobility, large diffusion length, and high absorption coefficient [1]. However, Pb and I dangling bonds at perovskite grain boundaries and defects at the interface between ETL and perovskite active layer create trap states acting as recombination centres, hindering charge extraction, and lowering PCE. Carbon dots (CDs) as emerging carbon nanoparticles with unique optical parameters have been studied as a perspective candidate for defect passivation in PSCs [2].

## Materials and Methods

$SnO_2$ precursor was spun on ITO substrate at 2000 rpm for 5 s and at 4000 rpm for 30 s followed by annealing at 180 °C for an hour to form ETL. Prior to deposition of the next layer annealed $SnO_2$ substrates were treated with ultraviolet ozone for 20 min. To form $SnO_2/CD_E$ and $SnO_2/CD_{EO}$ layers 50 µL of $CD_E$ and $CD_{EO}$ solutions were spun on the $SnO_2$ layer at 4000 rpm for 40 s, followed by annealing at 130 °C for 15 minutes. 36 µL of $Cs_{0.1}FA_{0.9}PbI_3$ perovskite precursor was spun at 1000 rpm for 10 s and 5000 rpm for 30 s. 100 µL of chlorobenzene was dripped onto the spinning substrate at the 25th second from the beginning. Thereafter, the perovskite films were annealed at 150 °C for 10 min. Once the samples cooled to room temperature 25 µL of Spiro-OMeTAD precursor was spin-coated at 5000 rpm for 30 s to form a hole-transporting layer. Finally, 80 nm thick Ag electrodes were deposited by thermal evaporation.

## Results and Discussion

Two types of CD were used in the work: the first type was synthesized from ethylenediamine ($CD_E$), and the second, from ethylenediamine and o-phenylenediamine ($CD_{EO}$). The CD layer deposited on $SnO_2$ reduced the surface roughness from 0.86 nm for $SnO_2$ to 0.43 nm and 0.23 nm for $CD_E$ and $CD_{EO}$. The smoother surface reduced the number of small grains (depicted in yellow circles) and increased their average size from 288 nm when deposited on $SnO_2$ to 391 nm and 401 nm when deposited on $CD_E$ and $CD_{EO}$, respectively, which implies a decrease in trapping states and recombination at grain boundaries defects (Figure 1).

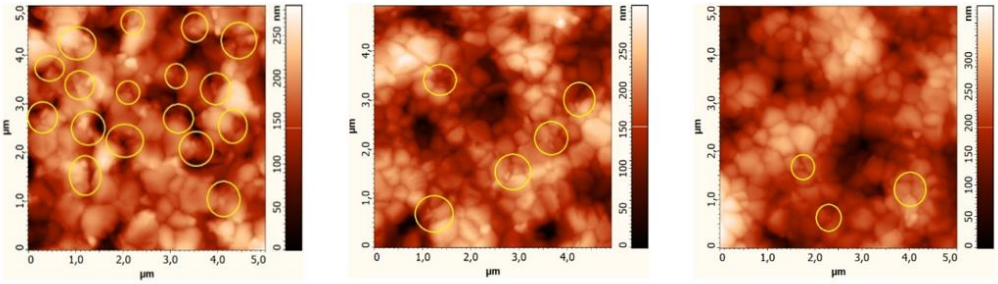

$SnO_2$ $SnO_2/CD_E$ $SnO_2/CD_{EO}$

Fig. 1. AFM images (b) and grain size distributions (c) for $Cs_{0.1}FA_{0.9}PbI_3$ perovskite films formed on ITO/$SnO_2$, ITO/$SnO_2$/$CD_E$, and ITO/$SnO_2$/$CD_{EO}$

A study of photoluminescence (PL) showed a decrease in the intensity and average decay times of PL when the perovskite layer was deposited on $CD_E$ and $CD_{EO}$, respectively, which indicates a more efficient extraction of charge carriers into the ETL (Figure 2a,b). More efficient charge transfer and larger grain sizes resulted in an increase in the short circuit current density (Jsc) from 6.8 mA/cm$^2$ to 8.5 mA/cm$^2$ and 11.8 mA/cm$^2$ and the fill factor (FF) from 57% to 71% and 76% for $SnO_2$, $CD_E$ and $CD_{EO}$, respectively. As a result, PCE increased from 2.9% in the absence of the CD layer to 4.8% and 6.9% with $CD_E$ and $CD_{EO}$, respectively (Figure 2c).

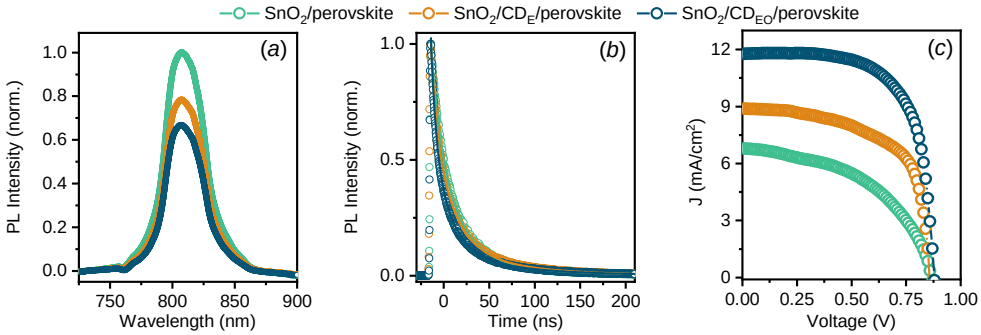


Fig. 2. (a) Steady-state PL spectra, (b) PL decay curves, and (c) J-V curves of ITO/$SnO_2$/Perovskite, ITO/$SnO_2$/$CD_E$/Perovskite, and ITO/SnO2/$CD_{EO}$/Perovskite photovoltaic devices.

## Conclusion

Passivation of the ETL/perovskite interface with carbon dots synthesized from ethylenediamine and O-phenylenediamine provides a better perovskite layer morphology with a larger average grain size and a reduction in small grains. The study of PL has shown that the auxiliary layers of CD contribute to a better extraction of photoexcited charge carriers. As a result, we showed that perovskite-based photovoltaic devices with CD auxiliary layers demonstrate an improvement in photovoltaic performance mainly due to an increase in Jsc and FF.


## Acknowledgments

The authors express their gratitude to the ITMO University Core Facility Center “Nanotechnologies”.


## REFERENCES


1. **Zhang, X., Zeng, Q., Xiong, Y., Ji, T., Wang, C., Shen, X., Zheng, W.** Energy level modification with carbon dot interlayers enables efficient perovskite solar cells and quantum dot based light-emitting diodes. Advanced Functional Materials, 30(11), 1910530. (2020).
2. **Mahapatra, A., Kumar, S., Kumar, P., Pradhan, B.**. Recent progress in perovskite solar cells: challenges from efficiency to stability. Materials Today Chemistry, 23, 100686. (2022).

# Theoretical and experimental study of laser treatment of nickel using a diode laser

**A A Mozhayko[1,2]✉, D A Gerashchenkov[2] and V. V. Davydov[1]**
[1] Peter the Great Saint-Petersburg Polytechnic University, Saint Petersburg, Russia;
[2] NRC "Kurchatov Institute" - CRISM "Prometey", St. Petersburg, Russia
✉ annaanna-1996@mail.com

**Abstract.** In recent years, laser surface treatment (LST) has widely used to improve the properties of nickel coatings. LST has many advantages, however, different coating thicknesses require different modes, which can be selected using simulation. In this study, the modeling process is considered and an experiment is conducted to study the effect of LST process parameters on melt pool sizes. The aim of this research was therefore to reveal the dependence of the melt pool depth, namely the thickness of the layer in which the mixing process of components takes place, on the scan speed using a diode laser. Experimental results have shown that the use of a diode laser for the processing of a precursor coating makes it possible to ensure a uniform distribution of the alloying component in the processing area.

**Keywords:** laser surface treatment; thermal modeling; finite element method; nickel; melt pool; cold spraying

## Introduction

Among various surface modification techniques, laser surface treatment (LST) has attracted significant interests. The main feature of this process is localized laser-assisted melting and solidification within a short time and shallow depth, resulting in changes in the microstructure and the material properties [1].

LST improves the mechanical and chemical properties of the material, such as adhesion, microhardness and corrosion resistance due to microstructural changes in the laser impact zone.

Diode modular lasers are used for processing large surfaces. They make it possible to achieve a uniform coating thickness and accelerate the laser processing process.

The microstructure and thickness of coating obtained by the LST depends on many technological parameters, for example, the scanning speed. This paper studies the process of modeling and conducts the experiment to analyze the effect of LST process parameters on the melt pool sizes.

## Method of constructing and modeling the operation of the thermostat

The Comsol Multiphysics package and 3D finite element method are used to model thermal effects. A three-dimensional numerical model was built with dimensions of 10 mm x 8 mm x 4 mm. Nickel was chosen as the coating material, and St3 steel as the substrate material. Steel St3 was chosen for modeling, since its physical properties are known from open sources, and it is similar to steel 09G2S. The studies were carried out for speeds of 7.5 mm/s - 15 mm/s and for the thickness of the nickel coating 70 μm and 140 μm.

The main mechanisms of heat transfer in the LST process in the thermal model are the thermal conductivity of the sample, laser heating of the precursor coating, and thermal convection between the boundaries of the coating and the ambient (Figure 1) [2].

To LST, a PLD-6 diode laser was used, consisting of 12 point sources arranged in two rows of 6 pcs. In each case, when processing the surface of the precursor coating, the total laser power was 1680 W. Nickel powder with the addition of corundum was used as the initial powder material. Sheets of steel grade 09G2S were used as a substrate. Several processing modes were performed with different speeds of the laser beam movement.

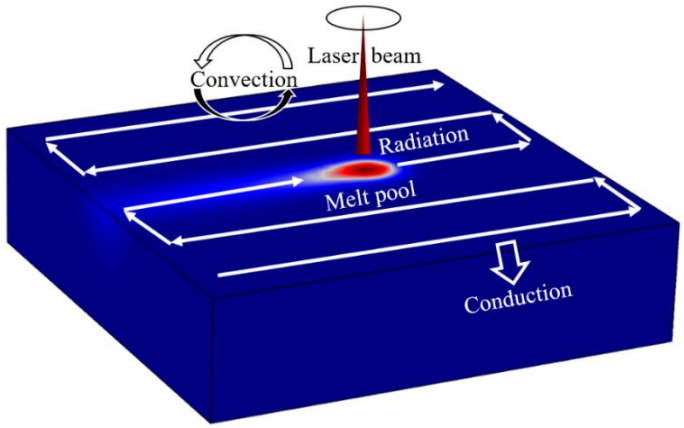


Fig. 1. Schematic illustration of the LST process.

The experiment consists of two stages. At the first stage, the cold spraying method [3] forms an aluminum coating with a thickness of 70 and 140 μm. For applying coatings by cold spraying, a Dimet-403 installation was used. The 09G2S steel substrate was coated with different thicknesses: 70 and 140 μm.

The second stage includes laser surface treatment to form a coating with improved characteristics. Laser surface treatment is performed at PLD-6 using an diode laser in a protective argon atmosphere.

## Results and Discussion

The simulation results showed that the melt pool has an elongated shape, which makes it possible to process a 7 mm wide surface in one pass of the laser beam. With an increase in speed from 7.5 to 15 mm/s, an almost linear decrease in the depth of the melt pool was observed. At speeds above 15 mm/s, the melt pool depth was less than the coating thickness.

Measurements of the coating thickness of the manufactured samples also showed that at speeds above 15 mm/s there is no mutual mixing of the coating components and the substrate.

## Conclusion

With an increase in scan speed from 7.5 mm/s to 15 mm/s, the melting depth decreases and, consequently, the content of alloying nickel increases. With a further increase in the speed, the melt pool depth does not reach the substrate and there is no mutual mixing of the components of the coating and the substrate, no alloying occurs.

## REFERENCES

1. **Samant, A. N.; Du, B.; Paital, S. R.; Kumar, S.; Dahotre, N. B**. Pulsed laser surface treatment of magnesium alloy: Correla-tion between thermal model and experimental observations. Journal of Materials Processing Technology 2009, 209, 5060–5067.

2. **Kuznetsov, P.; Shakirov, I.; Mozhayko, A.; Zhukov, A.; Bobyr, V.** Comparison of sequential and circular scanning thermal fields and their influence on microstructure of Alnico alloy produced by laser powder bed fusion. J. Phys.: Conf. Ser. 2021, 1967, 012064

3. **Geraschenkova, E.Y.; Markov, M.A.; Gerashenkov, D.A.; Farmakovsky, B.V.; Kravchenko, I.N.; Bystrov, R.Y., Bykova, A.D.** Obtaining electrically conductive wear-resistant coatings using cold gas-dynamic spraying method. J. Phys. Conf. Ser. 2021, 1990(1), 012066.

# Creation of an automated system for adjusting the position of the laser radiation axis for the air communication channel

**K. S. Nazarova**[1✉], **V. V. Davydov**[1, 2]
[1] Peter the Great Saint-Petersburg Polytechnic University, Saint Petersburg, Russia;
[2] The Bonch-Bruevich Saint Petersburg State University of Telecommunications, Saint Petersburg, Russia.
✉ knazarova0@ya.ru

**Abstract.** A model of an optical system for adjusting the axis of laser radiation on a photodetector module in a plane perpendicular to laser radiation has been developed. The operation of the optical system for controlling the position of the laser radiation axis on the photosensitive layer of the photodetector is simulated. Experimental studies are presented on correcting the position of the plates relative to the direction of the laser radiation axis and the value of stresses to change their refractive indices. The technique for determining the optimal parameters of the plates in the developed optical system for various tasks has been confirmed.

**Keywords:** Optical system, semiconductor laser, laser radiation axis, quartz plates, refractive index, linear and quadratic approximations.

## Introduction

At present, many designs have been developed for adjusting the position of the laser radiation axis based on measuring the maximum power recorded using a photodetector module [1, 2]. In these designs, the adjustment principle is based on moving the laser or photodetector, or mirrors, or lenses. This in some cases creates difficulties in the automatic adjustment of the system, especially in severe frost. Therefore, we have developed a fundamentally new design in which this drawback is eliminated.

## The design of the aerial optical communication channel and the system of automatic adjustment of the axis of laser radiation.

On fig. 1 shows the design of an airborne optical communication channel developed by us with a new auto-tuning module. On fig. 2 shows the design developed by us, one of the parts of the automatic system for adjusting the position of the laser radiation axis 3 for the proposed airborne optical communication channel.

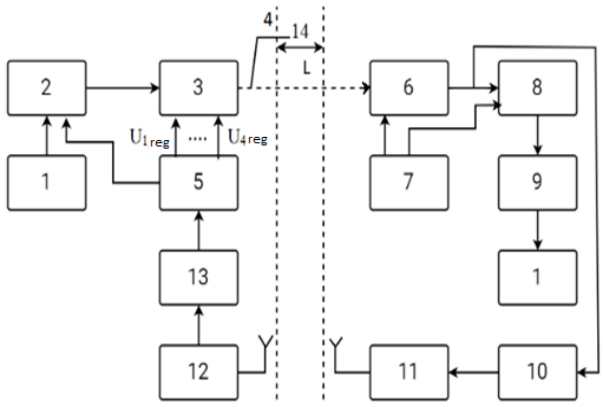


Fig. 1. Block diagram of an aerial optical communication channel: 1 – server, 2 – laser transmitting module with electro–optical modulator, 3 – automatic system for adjusting the position of the laser radiation axis, 4 – laser radiation, 5 – multifunctional power supply, 6 – photodetector module, 7 – photodetector power supply, 8 - ADC, 9 – processing device 10 – current meter, 11 – data processing and transmission device, 12 –radio receiving device, 13 - information processing and control device, 14 – airspace.

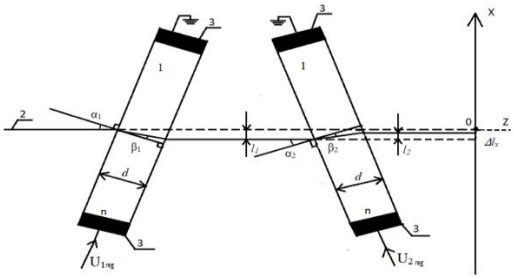

Fig. 2. Block diagram of a part of an automatic system for adjusting the position of the laser radiation axis along the X coordinate in a plane perpendicular to oZ: 1 – quartz plate, 2 – laser radiation, 3 – copper plate.

To change the position of the laser radiation axis in the oY plane, the plates will be oriented to the plane of incidence of laser radiation along the oZ axis at a different angle, but the design of the optical system will be similar. Based on the presented design of the optical system (Fig. 2), a calculation was performed to determine the displacement of the radiation axis in the oX plane.

$$\Delta l_x = d\ \left(\sin(a_1) - \frac{\frac{\sin(a_1)*n}{n_0}*\cos(a_1)}{\sqrt{1-\left(\frac{\sin(a_1)*n}{n_0}\right)^2}}\right) - d\left(\sin(a_2) - \frac{\frac{\sin(a_2)*n}{n_0}*\cos(a_2)}{\sqrt{1-\left(\frac{\sin(a_2)*n}{n_0}\right)^2}}\right) \quad (1)$$

## Results and Discussion

As an example, in fig. Figures 3 and 4 present the results of a study of the operation of the developed optical system.

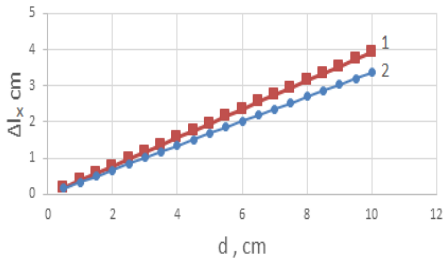


Fig. 3. Comparison of the dependencies of *Δlx* on *d* (1 – $n_{lin}$, 2 – $n_{sq}$)

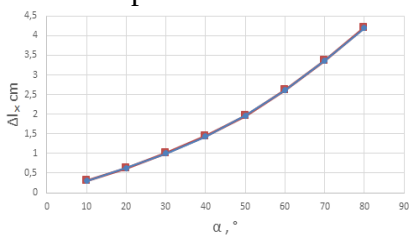


Fig. 4. Calculation of the change in the displacement of the laser radiation axis from the angle of inclination of the plates for various refractive indices of quartz

## Conclusion

The results showed that our automatic system can be used on a photodetector in the range of ±12 mm in an air optical communication channel, surpassing analogues by 4 mm [1, 2]. Dependences for Δl make it possible to choose the parameters of optical components, the position of their placement, and the range of controlled voltages in accordance with the weight and size characteristics of the AOCC.

## REFERENCES


1. **Aviev, A.A.** Two-coordinate optical-electronic system for determining the position of a ring laser, Radio optics. 2(2016) 11–25.

2. **Kozlova, T.I.,** Konovaltsev, M.I., Lebedev, R.S., Techko, O.L. Method for correcting the position of the laser beam, Photon - Express. 6(2021) 201-205.

3. **Popovskiy, N.I.,** Davydov, V.V., Gureeva, I.M. Development to high-rate fiber optic communication line with code division multiplexing, ACM International: Conference Proceeding Series. (2021) 527–531.

# Compact solid-state laser with diode optical pumping and high frequency stability

[1,2] **V.V. Naumova** ✉, [2] **O.A. Orlov**
[1] Peter the Great Saint-Petersburg Polytechnic University, Saint Petersburg, Russia
[2] D.I. Mendeleyev Institute for Metrology (VNIIM), Saint Petersburg, Russia
✉ naumova.vv@edu.spbstu.ru

**Abstract.** Continuous single-frequency solid-state lasers with intracavity frequency doubling $Nd^{+3}$/YVO/KTP, whose frequency is stabilized along the absorption lines of molecular iodine, are currently widely used in laser interferometers. The paper describes a small-sized laser with frequency instability at the level of $10^{-12}$ with an averaging time of 1 second. It has been shown that this level of stability is limited by the amplitude noise of the laser, which in turn are determined by fluctuations in the laser pumping. Reducing the amplitude noise and increasing the signal-to-noise ratio in the stabilization system made it possible to further increase the frequency stability of laser radiation..

**Keywords:** solid-state laser, laser diode, amplitude noise, bragg grating.

## Introduction

An iodine-stabilized diode-pumped solid-state laser (DPSS laser) with a wavelength of 532 nm is not only a good secondary frequency standard but is also a good laser source with a wavelength (frequency) for implementing a meter using laser interferometry.

Many of the lasers usually described in all references are quite large [1-3]. The compactness and low weight of the laser can be critical parameters for use in laser displacement interferometry, for example, in industrial laser interferometers and in absolute ballistic gravimeters.

The paper describes a small-sized laser with frequency instability at the level of $10^{-12}$ with an averaging time of 1 second. It has been shown that this level of stability is limited by the amplitude noise of the laser, which in turn are determined by fluctuations in the laser pumping. Reducing the amplitude noise and increasing the signal-to-noise ratio in the stabilization system made it possible to further increase the frequency stability of laser radiation.

## Materials and methods

Figure 1 shows the optical scheme of the developed laser resonator.

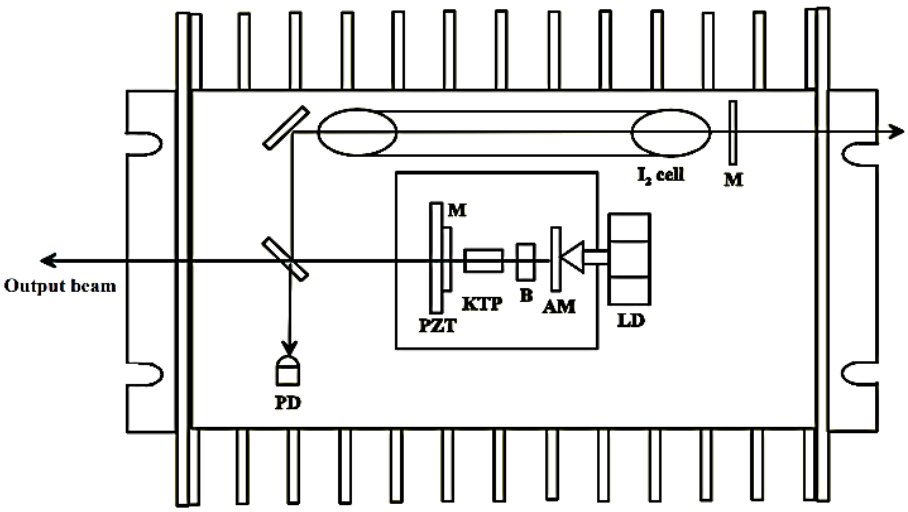


Fig. 1. Optical scheme of a $Nd^{+3}$/YVO/KTP/$I_2$ iodine stabilized laser resonator with a wavelength of 532 nm.

This linear resonator consists of a laser diode LD with a wavelength of 808 nm, a plate of the active medium Nd: $YVO_4$ AM, a Brewster plate B, a nonlinear crystal KTP with frequency

doubling and a mirror of the output coupler M mounted on a piezoelectric disk PZT (lead zirconate titanate). The active medium Nd:$YVO_4$, illuminated by a laser diode, generates radiation with a wavelength of 1064 nm. The power of the laser diode is about 0.5 watts. The intracavitary KTP crystal doubles the frequency of this radiation. PD is a photodetector.

The third harmonic method [4, 5] with a modulation frequency of 3.3 kHz is used to stabilize the frequency.

The frequency stability of the compact laser was measured using a stationary Nd:YAG/MgO:$LiNbO_3$/$I_2$ BIPM laser at 532 nm.

A relatively good frequency stability of $10^{-12}$ was achieved during averaging of 1 s, but it is still far from a stationary laser. It was found out that this level of stability is limited by the amplitude noise of the laser, which in turn are determined by fluctuations in the laser pumping. It was decided to replace the multimode laser diode with a single-frequency laser diode with a volumetric Bragg lattice. The use of Bragg gratings makes it possible to narrow the radiation band of multimode laser diodes and laser lines, fine-tune the operating wavelength and significantly reduce the dependence on temperature exposure. Reducing the amplitude noise and increasing the signal-to-noise ratio in the stabilization system made it possible to further increase the frequency stability of laser radiation.

## Conclusion

A compact solid-state Nd: $YVO_4$/KTP/$I_2$ diode-pumped, iodine-stabilized laser at a wavelength of 532 nm was developed and investigated. Metrological (frequency stability and reproducibility) and technical (laser power, size and weight of laser blocks) characteristics suggest that such lasers will find wide application in laser displacement interferometry, including laser interferometers for absolute ballistic gravimeters, as well as portable secondary frequency standards in the visible optical frequency range.

## REFERENCES

1. **Feng-Lei Hong** Portable I2-stabilized Nd:YAG laser for wavelength standards at 532 nm and 1064 nm/ Feng-Lei Hong, Jun Ishikawa, Tai Hyin Yoon, Long-Sheng Ma, Jun Ye, Hall J. L.// Recent Developments in Optical Gauge Block Metrology – 1998. – P. 2–10.

2. **Feng-Lei Hong** Portable I2-stabilized Nd:YAG laser for wavelength standards at 532 nm and 1064 nm/ Feng-Lei Hong, Jun Ishikawa, Jun Yoda, Jun Ye, Long-Sheng Ma, John L.// IEEE TRANSACTIONS ON INSTRUMENTATION AND MEASUREMENT – 1999. – Vol 48(2). – P. 532–536.

3. **Gianluca Gaizerano** Frequency stabilization of frequency-doubled Nd:YAG lasers at 532 nm by frequency modulation spectroscopy technique/ Gianluca Gaizerano, Elio Bava, Marco Bisi, Fabrizio Bertinetto, Cesare Svelto// IEEE TRANSACTIONS ON INSTRUMENTATION AND MEASUREMENT– 1999. – Vol. 48(2). – P. 540–543.

4. **Okhapkin M.V.** Tunable single-frequency diode-pumped Nd:YAG ring laser at 1064/532 nm for optical frequency standard applications, / Okhapkin M.V., Skvortsov M.N., Belkin A.M., Kvashnin N.L., Bagaev S.N.// Optics communications –2002. – Vol. 203. –P. 359–362.

5. **Youichi Bitou** Compact I2-stabilized frequency doubled Nd:YAG laser for long gauge block interferometer/ Youichi Bitou, Kaoru Sasaki, Shigeo Iwasaki, Feng-Lei Hong// Japanese Journal of Applied Physics – 2003. – Vol. 42(2). – P. 2867–2871.

# Optimization of $SnO_2/FAPbI_3$ interface by carbon dots interlayer

**I.V. Margaryan [1✉], A.A. Vedernikova[1], E.V. Ushakova[1], A.P. Litvin[2]**

[1] ITMO University, 14, Birzhevaya line, St.Petersburg, 199034 Russia
[2] Jilin University, Changchun, 130012, China
✉igormargaryan@niuitmo.ru

**Abstract**. Solar cells based on organic-inorganic (hybrid) perovskites attracted much attention due to rapid growth of their power conversion efficiency (PCE). However, defects at grain boundaries and at interfaces limit further increase of PCE and lead to degradation of the device. Carbon dots with appropriate surface groups can improve the charge extraction from perovskite to electron transport layer (ETL), affect the morphology of perovskite layer and reduce the recombination rate at interfaces. Current study demonstrates that carbon dots as an interlayer between $SnO_2$ ETL and $FAPbI_3$ enhance the morphology and optical properties of perovskite layer. This improvement results in increase of short circuit current ($J_{SC}$), fill factor (FF) and PCE of carbon dots-based perovskite solar cell.

## 1. Introduction

Metal-halide hybrid perovskites have recently emerged as a promising material in a field of optoelectronics. Hybrid perovskite solar cells (PSCs) draw tremendous attention as their PCE has increased from 3.8% to 25.6% since 2009. This incredible progress became possible due to outstanding properties of perovskites such as high charge carriers mobility, large diffusion length, and high absorption coefficient [1]. However, Pb and I dangling bonds at perovskite grain boundaries and defects at the interface between ETL and perovskite active layer create trap states acting as recombination centres, hindering charge extraction, and lowering PCE. Carbon dots (CDs) as emerging carbon nanoparticles with unique optical parameters have been studied as a perspective candidate for defect passivation in PSCs [2].

## 2. Materials and methods

$SnO_2$ precursor was spun on ITO substrate at 2000 rpm for 5 s and at 4000 rpm for 30 s followed by annealing at 180 °C for an hour to form ETL. Prior to deposition of the next layer annealed $SnO_2$ substrates were treated with ultraviolet ozone for 20 min. To form $SnO_2/CD_E$ and $SnO_2/CD_{EO}$ layers 50 µL of $CD_E$ and $CD_{EO}$ solutions were spun on the $SnO_2$ layer at 4000 rpm for 40 s, followed by annealing at 130 °C for 15 minutes. 36 µL of $Cs_{0.1}FA_{0.9}PbI_3$ perovskite precursor was spun at 1000 rpm for 10 s and 5000 rpm for 30 s. 100 µL of chlorobenzene was dripped onto the spinning substrate at the 25th second from the beginning. Thereafter, the perovskite films were annealed at 150 °C for 10 min. Once the samples cooled to room temperature 25 µL of Spiro-OMeTAD precursor was spin-coated at 5000 rpm for 30 s to form a hole-transporting layer. Finally, 80 nm thick Ag electrodes were deposited by thermal evaporation.

## 3. Results

Two types of CD were used in the work: the first type was synthesized from ethylenediamine ($CD_E$), and the second, from ethylenediamine and o-phenylenediamine ($CD_{EO}$). By the means of atomic force microscopy, their average sizes were determined, which are 6.2±2.4 nm and 2.4±0.9 nm, respectively. The CD layer deposited on $SnO_2$ reduced the surface roughness from 0.86 nm for $SnO_2$ to 0.43 nm and 0.23 nm for $CD_E$ and $CD_{EO}$. The smoother surface reduced the number of small grains (depicted in

yellow circles) and increased their average size from 288 nm when deposited on $SnO_2$ to 391 nm and 401 nm when deposited on $CD_E$ and $CD_{EO}$, respectively, which implies a decrease in trapping states and recombination at grain boundaries defects (Figure 1).

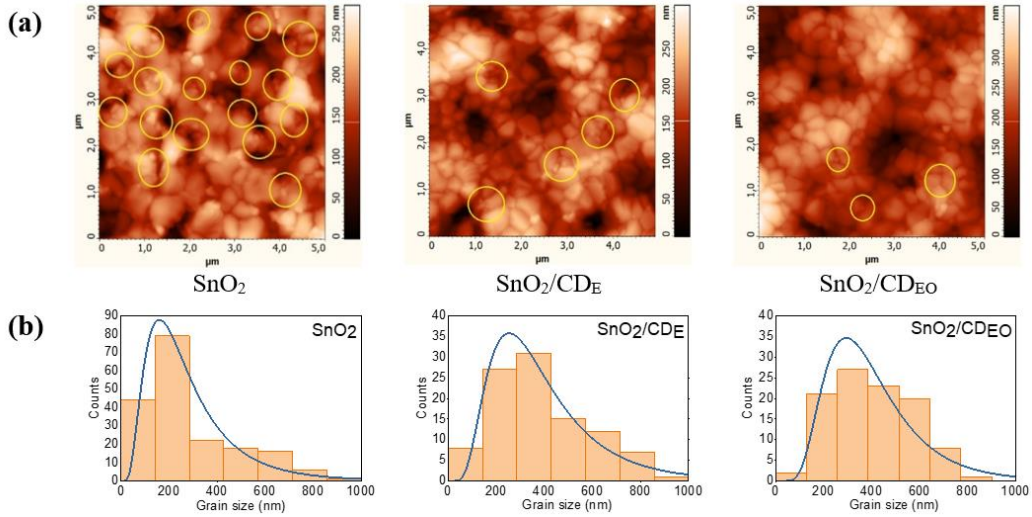


**Figure 1**. AFM images (b) and grain size distributions (c) for $Cs_{0.1}FA_{0.9}PbI_3$ perovskite films formed on ITO/$SnO_2$, ITO/$SnO_2$/$CD_E$, and ITO/$SnO_2$/$CD_{EO}$

A study of photoluminescence (PL) showed a decrease in the intensity and average decay times of PL from 26.5 ns to 21.9 ns and 20.8 ns when the perovskite layer was deposited on $CD_E$ and $CD_{EO}$, respectively, which indicates a more efficient extraction of charge carriers into the ETL (Figure 2a,b). More efficient charge transfer and larger grain sizes resulted in an increase in the short circuit current density (Jsc) from 6.8 mA/cm$^2$ to 8.5 mA/cm$^2$ and 11.8 mA/cm$^2$ and the fill factor (FF) from 57% to 71% and 76% for $SnO_2$, $CD_E$ and $CD_{EO}$, respectively. As a result, PCE increased from 2.9% in the absence of the CD layer to 4.8% and 6.9% with $CD_E$ and $CD_{EO}$, respectively (Figure 2c).

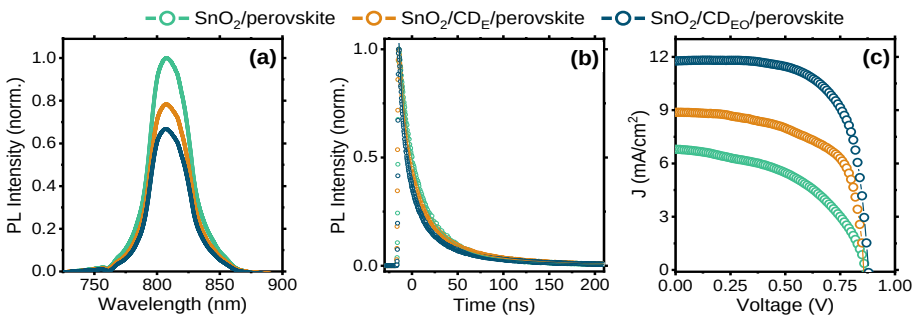


**Figure 2**. (a) Steady-state PL spectra, (b) PL decay curves, and (c) J-V curves of ITO/$SnO_2$/Perovskite, ITO/$SnO_2$/$CD_E$/Perovskite, and ITO/SnO2/$CD_{EO}$/Perovskite photovoltaic devices.

## 4. Conclusion

Passivation of the ETL/perovskite interface with carbon dots synthesized from ethylenediamine and O-phenylenediamine provides a better perovskite layer morphology with a larger average grain size and a reduction in small grains. The study of PL has shown that the auxiliary layers of CD contribute to a better extraction of photoexcited charge carriers. As a result, we showed that perovskite-based

photovoltaic devices with CD auxiliary layers demonstrate an improvement in photovoltaic performance mainly due to an increase in Jsc and FF.

**Acknowledgments**
This work was supported by the Russian Science Foundation (19-13-00332П). A.V., S.C., and E.U. thank the Priority 2030 Federal Academic Leadership Program.

## References

[1] Mahapatra, A; S., Kumar, P.; Kumar, P.; B, Pradhan. 2022. Materials Today Chemistry. **23**, 100686.
[2] Zhang, X., Zeng, Q., Xiong, Y., Ji, T., Wang, C., Shen, X., Zheng, W. 2020. Advanced Functional Materials, **30**, 1910530.

Conference materials
UDC
DOI: https://doi.org/10.18721/JPM.

# A study of chemical and mechanical properties of paper under its laser cleaning

**A. D. Neelova** [1✉], **E. M. Shepilova** [2]
**E.I. Nosova** [2] , **S.L. Rongonen** [3], **V.A. Parfenov** [1]
[1] Saint-Petersburg State Electrotechnical University «LETI», Saint-Petersburg, Russia;
[2] Saint-Petersburg Institute of History of the RAS, Saint-Petersburg, Russia;
[3] Saint-Petersburg Branch of Archive of the RAS, Saint-Petersburg, Russia
✉angelina.neelova@gmail.com

**Abstract.** This paper is devoted to investigation of chemical and mechanical paper properties after laser cleaning. In recent years, laser technologies have been widely used in the preservation of Cultural Heritage (CH). One of the main fields of laser application in this area is the cleaning of surfaces of CH objects from natural and anthropogenic contaminations. Comparison of paper properties before and after laser cleaning may prove the safety of laser cleaning. One of the most important parameters that characterise paper strength and durability are hydrogen ion concentration (pH) and absorptivity. We will present experimental results on pH value measurements of paper as well as results on paper absorptivity performed on model samples and real historical artefacts such as books and fragments of newspapers.

## Introduction

For the last decade studies have shown that laser cleaning has a significant potential for removal of surface contaminations from paper [1-3]. However, there are debates regarding the safety of laser cleaning of books and documents. Thus, proving the inalterability of chemical and mechanical properties of paper before and after laser cleaning might be considered as confirmation of its safety. Most significant parameters of paper in conservation practice are hydrogen ion concentration and absorptivity. pH value of paper characterises strength and durability of paper. Increased acidity is one of the main factors that causes accelerated ageing. The ability of paper to absorb moisture from the air is determined by its absorptivity. Excessive dryness leads to fragility of paper and its early destruction for dry paper loses its mechanical durability. Earlier the authors of this work reported about laser cleaning of different kinds of paper using Ytterbium fibre laser [4-5]. It was shown that use of laser with following parameters: wavelength of 1064 nm, pulse duration of 100 ns, peak power density varies from $1.6 \cdot 10^5$ W/cm$^2$ to $3.2 \cdot 10^5$ W/cm$^2$, the pulse repetition frequency of 20 kHz makes possible effective removal of contaminants.

## Experiment

Three types of old paper samples were cleaned during the experiments and further their chemical and mechanical properties were studied. To simulate surface contamination of paper graphite or charcoal dust were rubbed onto the surface of samples. Real artefacts such as books from the late third of the XVIIIth century to the beginning of the XXth century were cleaned as well. Contaminations that occur in studied artefacts are worn-in dust, traces of grease and of unknown origin.

## Results and Discussion

The pH test was performed by the method of aqueous extract in concordance with “Direction of pH value measuring using the contact method” with electronic pH-metre. The measurement was performed in two points on the page of a given sample or artefact: one in the area that was treated by the laser and another in the untreated area. Results of pH value measuring are shown in Table 1.

Table 1

**Summary table of measured pH values of paper samples**

| Sample | Without cleaning | After cleaning | Sample | Without cleaning | After cleaning |
|---|---|---|---|---|---|
| Model samples | | | 3 | 6.56 | 6.23 |
| Copy paper | 9.15 | 8.89 | 4 | 5.57 | 5.66 |
| № | Soviet paper samples | | 5 | 5.83 | 6.05 |
| 1 | 4.75 | 5.32 | 6 | 4.20 | 4.40 |
| 2 | 4.75 | 5.32 | 7 | 4.40 | 4.60 |
| 3 | 4.91 | 4.90 | 8 | 4.00 | 4.40 |
| Artefacts | | | 9 | 5.55 | 5.55 |
| 1 | 5.55 | 5.88 | 8 | 4.00 | 4.40 |
| 2 | 4.29 | 4.55 | 9 | 5.55 | 5.55 |

While performing pH value measuring it was noted that laser treated areas absorb water differently than non-treated areas. It was suggested that the absorptivity of paper declines due to processes that happen under laser irradiation. The experiment was carried out in accordance with the Soviet Union State Standard 12605-97 “Paper and board. Method for determination of surface water absorptiveness at one-sided wetting (Cobb method)”. Regarding the obtained results it could not be unambiguously said that paper loses its absorptivity after laser cleaning.

## Conclusion

pH measurement of paper samples and artefacts showed overall the tendency for neutralising of paper after laser irradiation. The investigation of the absorptivity of paper gave no unequivocal result, it could be speculated that some paper really loses its absorptivity after laser impact as it was suggested happened with the newspaper fragment, which is a negative fact for it leads to fragility of paper, though some paper does not lose it. Nevertheless further investigations of the laser irradiation influence on paper and its chemical and mechanical as well as other properties are needed.

## REFERENCES


1. Zekou E., Tsilikas I., Chatzitheodoridis E., Serafetinides A. // Proceedings of 19th International Conference and School on Quantum Electronics: Laser Physics and Applications, 2017, V. 10226, 1022605
2. Mokrushin Yu. M., Parfenov V. A. // Journal of Optical Technology, 2008, V. 75, P. 476-477.
3. Parfenov V. A., Titov S. V. // Proceedings of the IEEE Conference of Russian Young Researchers in Electrical and Electronic Engineering (EIConRus). 2019, P. 903-906.
4. Neelova A. D., Vasilieva A. V., Rongonen S. L., Vasiliev O. S., Safronov D.V., Parfenov V. A. // Proceedings of the IEEE Conference of Russian Young Researchers in Electrical and Electronic Engineering (EIConRus). 2022, P. 1134-1137.
5. Parfenov V., Galushkin A., Tkachenko T., Aseev V. // Quantum Beam Science, 2022, V. 6, No. 3, P. 23.

# Optimization of $SnO_2/FAPbI_3$ interface by carbon dots interlayer

**I.V. Margaryan [1✉], A.A. Vedernikova[1], E.V. Ushakova[1], A.P. Litvin[2]**

[1] ITMO University, 14, Birzhevaya line, St.Petersburg, 199034 Russia
[2] Jilin University, Changchun, 130012, China
✉igormargaryan@niuitmo.ru

**Abstract**. Solar cells based on organic-inorganic (hybrid) perovskites attracted much attention due to rapid growth of their power conversion efficiency (PCE). However, defects at grain boundaries and at interfaces limit further increase of PCE and lead to degradation of the device. Carbon dots with appropriate surface groups can improve the charge extraction from perovskite to electron transport layer (ETL), affect the morphology of perovskite layer and reduce the recombination rate at interfaces. Current study demonstrates that carbon dots as an interlayer between $SnO_2$ ETL and $FAPbI_3$ enhance the morphology and optical properties of perovskite layer. This improvement results in increase of short circuit current ($J_{SC}$), fill factor (FF) and PCE of carbon dots-based perovskite solar cell.

## 1. Introduction

Metal-halide hybrid perovskites have recently emerged as a promising material in a field of optoelectronics. Hybrid perovskite solar cells (PSCs) draw tremendous attention as their PCE has increased from 3.8% to 25.6% since 2009. This incredible progress became possible due to outstanding properties of perovskites such as high charge carriers mobility, large diffusion length, and high absorption coefficient [1]. However, Pb and I dangling bonds at perovskite grain boundaries and defects at the interface between ETL and perovskite active layer create trap states acting as recombination centres, hindering charge extraction, and lowering PCE. Carbon dots (CDs) as emerging carbon nanoparticles with unique optical parameters have been studied as a perspective candidate for defect passivation in PSCs [2].

## 2. Materials and methods

$SnO_2$ precursor was spun on ITO substrate at 2000 rpm for 5 s and at 4000 rpm for 30 s followed by annealing at 180 °C for an hour to form ETL. Prior to deposition of the next layer annealed $SnO_2$ substrates were treated with ultraviolet ozone for 20 min. To form $SnO_2/CD_E$ and $SnO_2/CD_{EO}$ layers 50 µL of $CD_E$ and $CD_{EO}$ solutions were spun on the $SnO_2$ layer at 4000 rpm for 40 s, followed by annealing at 130 °C for 15 minutes. 36 µL of $Cs_{0.1}FA_{0.9}PbI_3$ perovskite precursor was spun at 1000 rpm for 10 s and 5000 rpm for 30 s. 100 µL of chlorobenzene was dripped onto the spinning substrate at the 25th second from the beginning. Thereafter, the perovskite films were annealed at 150 °C for 10 min. Once the samples cooled to room temperature 25 µL of Spiro-OMeTAD precursor was spin-coated at 5000 rpm for 30 s to form a hole-transporting layer. Finally, 80 nm thick Ag electrodes were deposited by thermal evaporation.

## 3. Results

Two types of CD were used in the work: the first type was synthesized from ethylenediamine ($CD_E$), and the second, from ethylenediamine and o-phenylenediamine ($CD_{EO}$). By the means of atomic force microscopy, their average sizes were determined, which are 6.2±2.4 nm and 2.4±0.9 nm, respectively. The CD layer deposited on $SnO_2$ reduced the surface roughness from 0.86 nm for $SnO_2$ to 0.43 nm and 0.23 nm for $CD_E$ and $CD_{EO}$. The smoother surface reduced the number of small grains (depicted in

yellow circles) and increased their average size from 288 nm when deposited on $SnO_2$ to 391 nm and 401 nm when deposited on $CD_E$ and $CD_{EO}$, respectively, which implies a decrease in trapping states and recombination at grain boundaries defects (Figure 1).

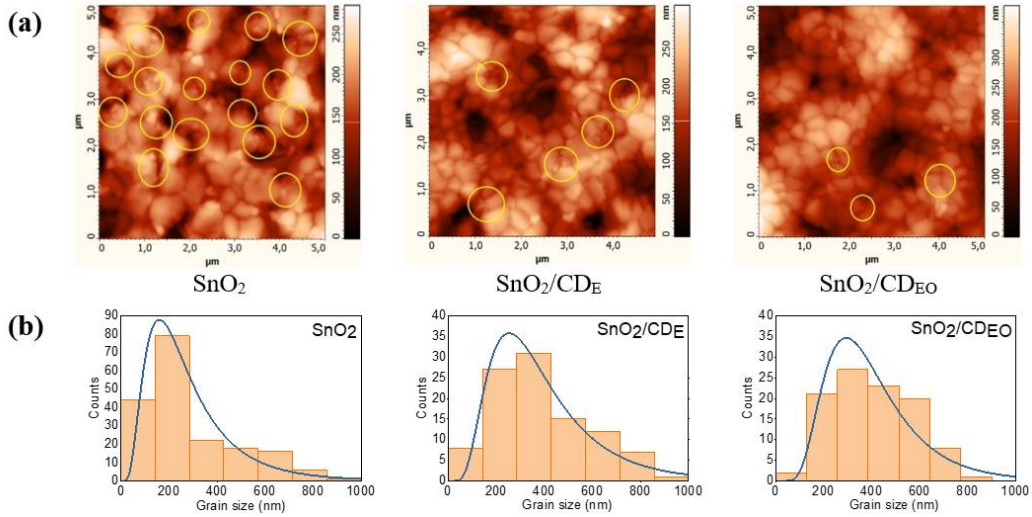


**Figure 1**. AFM images (b) and grain size distributions (c) for $Cs_{0.1}FA_{0.9}PbI_3$ perovskite films formed on ITO/$SnO_2$, ITO/$SnO_2$/$CD_E$, and ITO/$SnO_2$/$CD_{EO}$

A study of photoluminescence (PL) showed a decrease in the intensity and average decay times of PL from 26.5 ns to 21.9 ns and 20.8 ns when the perovskite layer was deposited on $CD_E$ and $CD_{EO}$, respectively, which indicates a more efficient extraction of charge carriers into the ETL (Figure 2a,b). More efficient charge transfer and larger grain sizes resulted in an increase in the short circuit current density (Jsc) from 6.8 mA/cm$^2$ to 8.5 mA/cm$^2$ and 11.8 mA/cm$^2$ and the fill factor (FF) from 57% to 71% and 76% for $SnO_2$, $CD_E$ and $CD_{EO}$, respectively. As a result, PCE increased from 2.9% in the absence of the CD layer to 4.8% and 6.9% with $CD_E$ and $CD_{EO}$, respectively (Figure 2c).

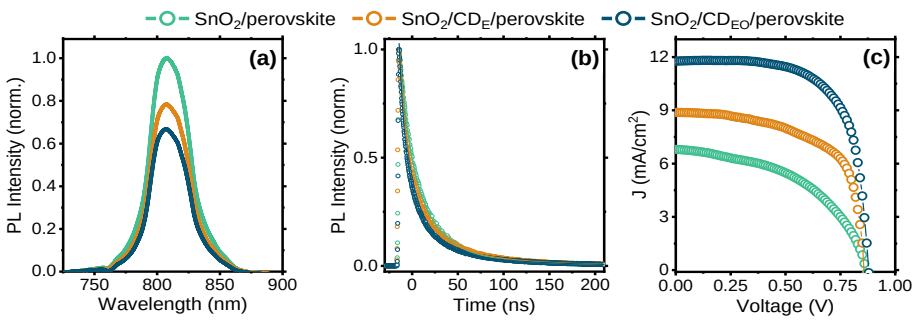


**Figure 2**. (a) Steady-state PL spectra, (b) PL decay curves, and (c) J-V curves of ITO/$SnO_2$/Perovskite, ITO/$SnO_2$/$CD_E$/Perovskite, and ITO/SnO2/$CD_{EO}$/Perovskite photovoltaic devices.

## 4. Conclusion

Passivation of the ETL/perovskite interface with carbon dots synthesized from ethylenediamine and O-phenylenediamine provides a better perovskite layer morphology with a larger average grain size and a reduction in small grains. The study of PL has shown that the auxiliary layers of CD contribute to a better extraction of photoexcited charge carriers. As a result, we showed that perovskite-based

photovoltaic devices with CD auxiliary layers demonstrate an improvement in photovoltaic performance mainly due to an increase in Jsc and FF.

**Acknowledgments**
This work was supported by the Russian Science Foundation (19-13-00332П). A.V., S.C., and E.U. thank the Priority 2030 Federal Academic Leadership Program.

## References

[1] Mahapatra, A; S., Kumar, P.; Kumar, P.; B, Pradhan. 2022. Materials Today Chemistry. **23**, 100686.
[2] Zhang, X., Zeng, Q., Xiong, Y., Ji, T., Wang, C., Shen, X., Zheng, W. 2020. Advanced Functional Materials, **30**, 1910530.

# Development of a photodetector for an analog extended fiber-optic communication line

**D. V. Oaserele[1]✉, V. V. Davydov[1, 2], A. F. Gordeeva[1], B. K. Reznikov[1]**
[1] The Bonch-Bruevich Saint Petersburg State University of Telecommunications, Saint Petersburg, Russia.
[2] Peter the Great Saint-Petersburg Polytechnic University, Saint Petersburg, Russia;
✉ oasereledenis@gmail.com

**Abstract:** Different designs of analog fiber-optic lines (FOCLs) for transmitting information at different distances in different frequency ranges are considered. The peculiarities of optical

Analog signals transmission, which will affect its registration in the FOCL photodetector module, are noted. The format of analog signals, which should be transmitted along the FOCL for distances over 500 km without the use of optical amplifiers, was determined. Based on the calculation of various parameters of the FOCL and its energy balance, the requirements to the design and characteristics of the photodetector module were determined. A laboratory mockup of the photodetector module was assembled. The results of its operation as a part of the analog FOCL with different distances of information transmission are presented.

**Keywords:** Analog optical signal, photodetector, laser radiation, wavelength, linewidth, dynamic range, detection bandwidth, signal-to-noise ratio.

## Introduction

Currently, a large number of different photodetectors for analog and digital fiber-optic communication lines of near-infrared radiation spectrum has been developed [1]. To calculate the parameters of digital and analog communication lines, methods that take into account the typical conditions of information transmission have been proposed. Taking into account these conditions, as well as the need for adaptation of fiber-optic construction to the required wavelength of laser radiation, a photodetector is selected and a photodetector module is developed [2].

Peculiarities of using the photodetector are related to the operating conditions of the module, the frequency of transmission and form of optical signals, as well as the signal to noise ratio. One of the tasks of developing or upgrading the module design is to transmit telemetric information about the state of the environment over a fiber-optic network in the area of the power line for distances greater than 500 km. Use of optical amplifiers is excluded, because powerful spark discharges on power lines change polarization of laser radiation. This leads to distortion of information in the transmitted optical signal. In the fiber-optic system it is necessary to use a powerful laser, which has a number of features in terms of the width of the spectrum and the formation of the optical signal.

Consequently, it is necessary to develop a photodetector module for a new design of fiber-optic system, which is used in the power transmission system, when transmitted signals with information $\lambda = 1550$ nm at long distances.

## Selection of the photodetector, determination of its parameters, connection diagram and operating principle

The main requirement to the material of the photodetector is the width of the band gap, the maximum absorption should be about 1.55 μm. In the photodetector it is more reasonable to use In0.53Ga0.47As based structure. This composition has a large absorption coefficient at a wavelength of 1.55 μm and a relatively low intrinsic concentration of charge carriers.

Analysis of various data allowed us to select photodetectors for the development of the PDA P-I-N photodetector module. In the heterostructure of these photodetectors with partially depleted absorption layer the effect of the spatial charge is reduced. For this purpose, additional InGaAs p-type and n-type absorption layers are included in the heterostructure. The advantage of PDA p-i-n-

PD is that high quantum efficiency, high photocurrent, operating speed, and low thermal resistance are achieved at low reverse voltages by minimizing the bulk charge accumulation effect. Figure 2 shows the design of the developed photodetector module for an analog long-range fiber optic system.

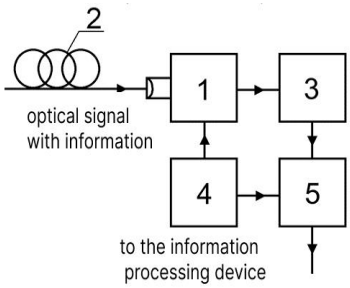


Fig. 2. Structural diagram of the photodetector module: 1 – photodetector, 2 – optical fiber, 3 – resonant LC-filter, 4 – multifunctional power supply, 5 – ADC

Optical signal at a frequency of 200 MHz is fed through fiber 2 to the photodetector. The load of the photodetector is a resonant LC-filter. Figure 2 shows optical signals in the form of rectangular pulses, which are used to transmit information in the form of a sequence of command codes in the analog FOCL.

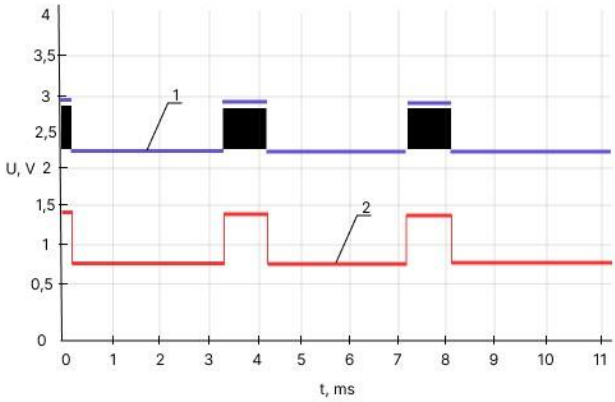


Fig. 3. Rectangular pulses for transmitting digits in numbers as a sequence of command codes. Graph 1 corresponds to the signal at the input to 2. Graph 2 corresponds to the signal at the output 3

After filtering, the subcarrier signal is extracted from the pulse, and the clean pulse is fed to the ADC. Then, after the ADC, the signal goes to the processing device to decode the transmitted information. With such a scheme of recording an optical signal it can be recorded with a signal to noise ratio of about 4 times, when it is necessary to ensure at least 20 dB in the digital fiber optic

## Conclusion

Analysis of the studies showed the stable operation of the developed photodetector with the following characteristics: bandwidth $\Delta F_f$ = 1 GHz, NEP = $10^{-14}$ W·Hz$^{1/2}$. Placement of resonant LC-filter and ADC in the design of the developed photodetector module is one of the features of its operation in power transmission lines. Such a design of the photodetector module allows to register signals with chirp, which are used as subcarriers. This increases the signal base by several orders of magnitude and allows the information to be recognized when the optical signal is registered below the noise level.

## References

[1] **Burlakov, I. D.** Shortwave IR detectors based on InGaAs (review) Advances in Applied Physics. - (2014) (2) 131-162.

# Development of a Device for Measuring Temperature Dependence of Current in a Porous Silicon Solar Cell

**N.Y. Postavnoy, D.A. Shishkina✉, I.A. Shishkin**
Samara National Research University, Samara, Russia
✉ shishkina.da@ssau.ru

**Abstract.** The demand for energy in the world has significantly increased due to sources of energy, especially green energy, obtained from solar energy using photovoltaic modules (PV). The advantages of this photovoltaic system are its simplicity, practicality, and fairly high efficiency, especially for tropical regions. The performance of a photovoltaic module can be directly linked to the volt-ampere characteristic (I-V curve) of output factors, such as short-circuit current (Isc), open-circuit voltage (Voc), and maximum power (Pmax) [1,2]. Accurate measurements of this data must be taken at short intervals of less than 1 minute due to the unstable solar intensity, which affects the maximum output power of the photovoltaic module at low intensity [3]. Therefore, a decision was made to create a device that would measure the current of the solar element. The basis for this was a solar element based on porous silicon. Measurements were taken in a special chamber with a very powerful light source. As a result, volt-ampere characteristics were obtained, and conclusions were drawn.

**Keywords:** solar element, porous silicon, volt-ampere characteristic.

## Introduction

The consumption of electricity is constantly increasing, but the reserves of traditional energy sources such as oil, coal, and gas are limited. Therefore, alternative sources of energy need to be found. According to experts' forecasts, at the current level of resource consumption, the reserves of oil and gas will be exhausted in half a century, while coal can only be used for the next 12 years. Among the numerous alternative sources of energy, the conversion of solar radiation into electricity appears to be the most promising in the context of future energy technologies. The amount of energy that reaches the Earth in a week exceeds the total energy of all the world's oil, coal, and gas reserves. The Russian Federation has enormous potential for solar energy, exceeding 200 billion tons of carbon equivalent, since the use of solar energy is one of the most promising areas of renewable energy. In connection with the resource crisis, solar energy becomes more relevant, and improving methods for measuring the parameters of photovoltaic modules becomes a key factor in research and production of solar cells.

## Materials and methods

The IV measurements were obtained using a Keithley 2450 source-measure unit. However, a practical solar cell would behave differently in a different environment. Repeat measurements are necessary to obtain characteristics of any available solar cell before their use, as this would help other calculations be more reliable with respect to different environmental conditions. Therefore, in this study, we propose a simple method for determining characteristics using a 90 W incandescent bulb. The measurement test results using the bulb will be compared to the standardized measurement condition.

## Results

During the research, a device was developed to measure the temperature-voltage-current characteristics of a solar cell. The housing was designed in KOMPAS-3D. As a result of the experiments, graphs of the voltage-current dependency were obtained.

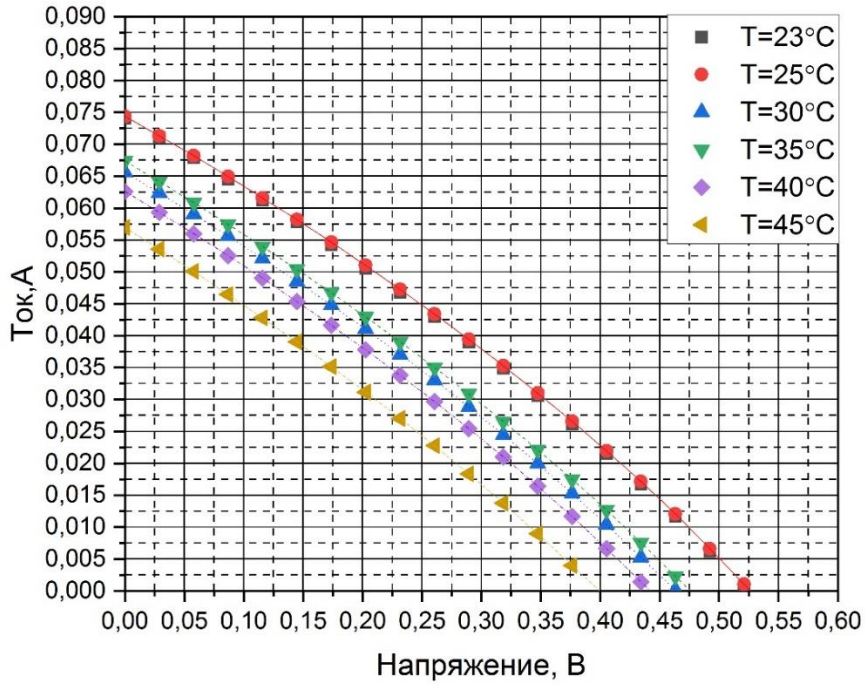


Drawing 1 – Total current-voltage characteristic of a solar cell

As a result of the device development, it was found that regular plastic used for printing the device cannot withstand the testing and begins to melt at a temperature of approximately ±40℃ . A heat-resistant plastic is required for measurement stability. In addition, voltage-current characteristics were obtained. The graphs show that as the temperature increases, the current and voltage values decrease.

## LITERATURE


1. **Farihah S., Nasrudin A.R., Hew W. P.,** “Zigbee-based data acquisition system for online monitoring of grid-connected photovoltaic system”, Expert Systems with Applications, Vol. 42, pp: 1730–1742, 2015.
2. **Moreno-Garcia, I.M.; Palacios-Garcia, E.J.; Pallares-Lopez, V.; Santiago, I.; Redondo, M.J.G.; Varo-Martinez, M.; Calvo, R.J.R**. Real-Time Monitoring System for a Utility-Scale Photovoltaic Power Plant. Sensors 2016, 16, 770. [CrossRef].
3. **W. Keogh and Blakers, A. W.,** “Natural Sunlight Calibration of Silicon Solar Cells.”, 17th European Photovoltaic Solar Energy Conference. Munich, Germany, (2001).

# Peculiarities of telemetry information transmission using analog fiber-optic communication line over long distances in a complex electromagnetic environment

**B. K. Reznikov[1]✉, S. A. Rodin[1], D. I. Isaenko[1] and V. V. Davydov[1, 2]**
[1] The Bonch-Bruevich Saint Petersburg State University of Telecommunications, Saint Petersburg, Russia.
[2] Peter the Great Saint-Petersburg Polytechnic University, Saint Petersburg, Russia;
✉rznkff@gmail.com

**Abstract.** The necessity of placing sensors for various purposes on power lines is considered. Particular attention is paid to solving the problems of environmental control with the help of multifunctional complexes using various sensors. The use of fiber-optic lines for transmitting this information using analog signals was justified. The design of an analog fiber-optic communication line for transmitting signals over 500 km without amplification was developed. The calculation of the developed communication line was performed. Preliminary experimental studies of the parameters of the developed fiber-optic communication line were carried out. The advantages and disadvantages of this method of telemetric information transmission are determined.

**Keywords:** telemetry information, laser radiation, optical fiber, loss, power, analog optical signal, signal-to-noise ratio, error probability

## Introduction

Currently, with the development of scientific and technological progress, the number of tasks associated with the transfer of information in a complex electromagnetic environment is constantly increasing [1-3]. The best solution in this situation is the use of fiber-optic communication lines (FOCL) [1-3]. Modern designs of FOCL allow information to be transmitted without amplification in conditions of high levels of electromagnetic interference, which is always present in the zone of power lines. distances up to 300 km. Digital signals are used to transmit such information. Equipment for the transmission of digital signals is expensive and the use of optical amplifiers for FOCL in the transmission line area is difficult [3]. This limits the distance for transmitting information in a digital code.

Therefore, in this situation, the actual solution is to develop an analog FOCL to transmit telemetry information of analog signals. For this purpose a fundamentally new way of transmitting information is proposed. Information about the number is set using rectangular pulses of different amplitudes. A certain value of pulse amplitude in relative units (0.95, 0.955, 0.96 .... 0.995) corresponds to numbers: 0, 1, 2, ..., 9. The amplitude value of 0.94 corresponds to a comma. Figure 1, for example, shows the coding of the temperature value $T$ = 294.5 K using the proposed sequence of command codes.

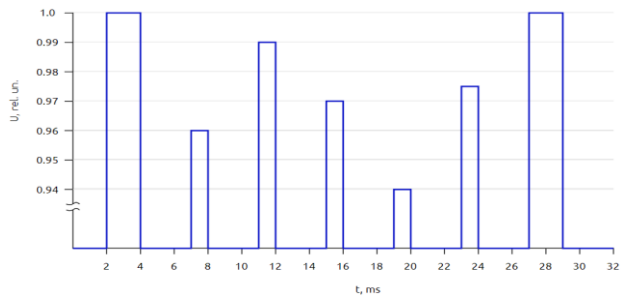


Fig.1. Sequence of command codes in the form of rectangular signals to transmit the temperature value $T$ = 294.3 K for transmission over analog FOCL

## Calculation of fiber-optic communication line

Information is transmitted at a wavelength of λ = 1550 nm. Optical power $P_l$ of the transmitting laser module (Emcore company) is 150 mW (21.8 dBm), modulation depth is 70 %,

line width $\Delta\lambda$ = 0.112 nm at this $P_l$, laser bandwidth $\Delta F_1$= 600 MHz, subcarrier frequency $F_s$ = 100 MHz. G.653 standard single-mode optical fiber with shifted zero dispersion (triangular profile) $M$ = 0.3 ps/(nm·km) with attenuation coefficient 0.195 dB/km is used for information transmission. Optical signal reception is carried out by a photodetector module, which has the following characteristics: bandwidth $\Delta F_2$ = 1 GHz, $NEP = 10^{-13}$ W/Hz$^{1/2}$.

The energy balance is calculated as follows formula (1):

$$a_\Sigma = a_1 - (a_2 + N\cdot\alpha_3 + a_4 + a_5) \quad (1)$$

$a_1 = p_{Tx} - p_{Rx}$ = 104.8 dB – optical loss budget; $p_{Tx} = p_{in}$ – 2 dB= 19.8 dBm – level of power injected into the optical fiber; $p_{in}$ = 21.8 dBm - transmitter power; $p_{Rx}$ = –87 dBm – sensitivity level of photodetector. Calculated for $SNR$ (dB) = 10, with bandwidth $\Delta F_t$ = 1 MHz by the formula (2):

$$p_{Rx} = 10\cdot\log(NEP/10^{-3}) + 5\cdot\log(\Delta F_t) + 0{,}5\cdot SNR \text{ (dB)} \quad (2)$$

$a_2$ – losses in the FOCL; $\alpha_{1550}$ = 0.195 dB/km – attenuation coefficient at a wavelength of 1550 nm; $L$ = 500 km – the length of the FOCL;

$$a_2 = 0.195\cdot 500 = 107.25 \text{ dB} \quad (3)$$

$a_3$ = 0.05 dB – losses at welded joints; $N$ = 50 – number of connections; $a_4$ = 1.5 dB – losses at 70 % signal modulation depth on the transmitting side; $a_5$ = 3 dB – operational margin.

$$a_\Sigma = 106.8 - (97.5 + 50\cdot 0.05 + 1.5 + 3) = 2.3 \text{ dB} \quad (4)$$

The obtained data show that the conditions, which confirm the stable transmission of information over fiber-optic cables at distances $L$ = 500 km will be satisfied.

## Experimental results and discussion

Based on T8 equipment and our developments an experimental analog FOCL with $L$ = 500 km and adjustable power of laser radiation Pin up to 23.6 dBm was assembled.

The experimental results fully confirmed the calculations for determining the value of $L$ and the energy balance of the line. It was found that the dynamic range of the developed FOCL for $L$ = 500 km is 8.7 dB, which allows its operation to conduct (if necessary) repair work without reducing the distance $L$.

## Conclusion

The analysis of the experimental and computational data obtained confirms the adequacy of the proposed developments for the implementation of FOCL design for the transmission of information from multifunctional complexes placed on power lines, for distances from 4 to 500 km and more (with various configurations, including the Russian equipment of Dilaz company).

## REFERENCES


1. **Davydov, R.** Parameter Control System for a Nuclear Power Plant Based on Fiber-Optic Sensors and Communication Lines / R. Davydov, V. Antonov, A. Moroz. // 2019 IEEE International Conference on Electrical Engineering and Photonics (EExPolytech). — 2019. — P. 42—45. — DOI: 10.1109 / EExPolytech.2019.8906791.
2. **Petrov, A.** Dynamic Range Improvement of Broad-Band Analog Fiber Optic Links with Special Lithium Niobate Integrated Optical Modulators / A. Petrov, M. Parfenov, V. Lebedev, I. Ilichev, P. Agruzov, A. Tronev, A. Shamray //. Internet of Things, Smart Spaces, and Next Generation Networks and Systems — 2020. — P. 357—363. — DOI: 10.1007/978-3-030-65729-1_31.
3. **Petrov, A.** Influence of external electrooptical modulator biasing on gain and nonlinear distortions in analog fiber-optic links / A. Petrov, I. Ilichev, P. Agruzov, V. Lebedev, E. Velichko, A. Shamray // Journal of Physics: Conference Series. — 2014. — Vol. 541, No 1. — P. 012047. — DOI: 10.1088/1742-6596/541/1/01204.

# Development of a simulator for testing methods for generating analog signals in the form of a sequence of command codes in an optical communication channel

**D.N. Titov[1]✉, B.K. Reznikov[2] and V. V. Davydov[1, 2]**
[1] Peter the Great Saint-Petersburg Polytechnic University, Saint Petersburg, Russia;
[2] The Bonch-Bruevich Saint Petersburg State University of Telecommunications, Saint Petersburg, Russia.
✉rznkff@gmail.com

***Abstract*:** The necessity of developing a simulator to test the operation of blocks forming a sequence of command codes based on the measured environmental parameters and their processing after transmission via an optical channel is substantiated. The design of the simulator using an aerial optical communication channel for transmitting information in the form of a sequence of command codes is presented. The features of using a sequence of command codes when transmitting analog signals in an optical communication channel are established. Confirmation of the validity of the use of the proposed technique for the formation of analog optical signals has been obtained.

**Keywords:** analog optical signal, command code, simulator, optical communication channel, subcarrier frequency signal, laser radiation

## Introduction

To transmit information from multifunctional environmental monitoring complexes that are placed on high-voltage power transmission lines (power lines), certain difficulties arise that digital fiber optic cables cannot adapt to, therefore, the purpose of the work is to develop a universal simulator design that allows you to test the principle of operation of an analog fiber optic cable both with fiber and when transmitting a signal in the air (free) space

Figure 1 shows a block diagram of a newly developed optical communication channel for transmitting information from sensors to a central computer.

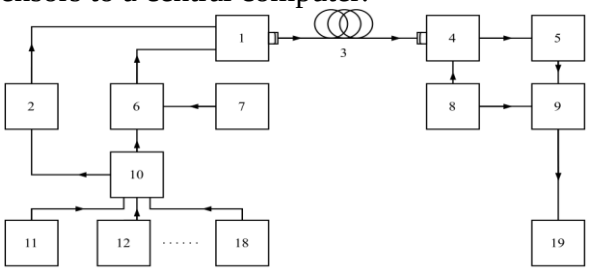


Fig.1. Block diagram of the information transmission system from an analog fiber optic cable: 1 – semiconductor laser with λ = 1550 nm, 2 – laser power supply, 3 – optical fiber, 4 – photodetector, 5 – tunable LC filter, 6 – electronic key, 7 – highly stable quartz oscillator, 8 – multifunctional power supply, 9 – information processing device, 10 – control device, 11 – 18 sensors, 19 – central computer.

In the developed design of the optical channel, it is necessary to: check the formation of information about environmental parameters in the form of a sequence of command codes; implement a function to control changes in the values of these parameters; check the operation of key elements for supplying a subcarrier signal to the laser power supply (pulses in the sequence of command codes are envelopes for the subcarrier signal); check the operation of the transmitted information processing device 9 (fig. 1).

A simulator was developed to solve these problems. Its block diagram is shown in Fig. 2.

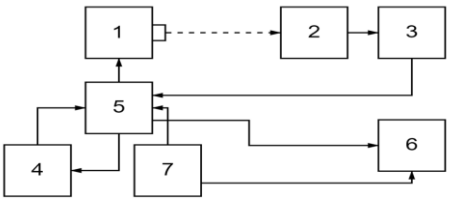


Fig. 2. Block diagram of the simulator: 1 – semiconductor laser, 2 – photodetector, 3 – processing device, 4 – personal computer, 5 – microcontroller, 6 – display device, 7 – power supply.

To transmit information, a laser diode is used, which transmits rectangular pulses from the microcontroller to the receiver. From the receiver, the pulses are then transmitted to the microcontroller, which processes them and outputs them to a personal computer, as well as to an indication device.

Figure 3 shows the generated sequence in the form of command codes (rectangular pulses), in which temperature data is encrypted.

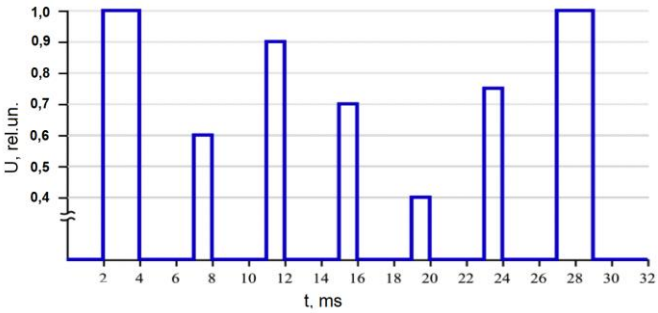


Fig. 3. Impulse sequence

In Figure 4 shows the test result of the analog FOCL – the data received and decrypted from the transmitter, displayed on the display

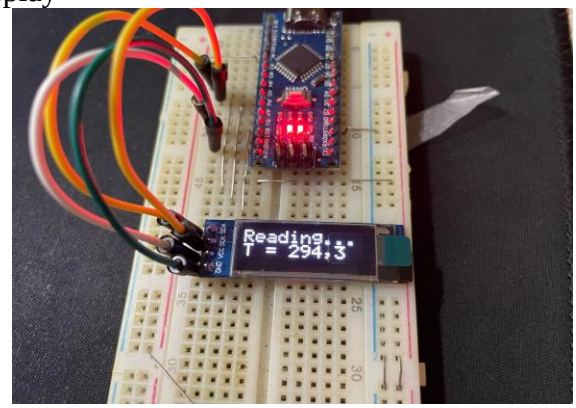


Fig. 4. Tests result

The obtained test results confirm the validity of the application of the information transmission technique developed by us (the decoded value of T from the receiving optical signal corresponds to a temperature of 294.3 K).

Our research has shown that for the first time in the Russian Federation we were able to propose the principle of constructing an analog fiber optic simulator, which can operate in two modes of optical signal transmission both by fiber and by air. This makes it possible not only to test the concept of building an analog HAIR, but also to identify features in the work of the considered design of the fiber optic cable during the formation and transmission of information.

## REFERENCES

1. **Davydov, R., V. Antonov, V. Moroz, A.** Parameter Control System for a Nuclear Power Plant Based on Fiber-Optic Sensors and Communication Lines. IEEE International Conference on Electrical Engineering and Photonics (EExPolytech-2019). 8906791 (2019) 295-297.
2. **Gelgor, A., Pavlenko, L., Fokin, G., Popov, E., Lavrukhin, Y.** LTE base stations localization. Lecture Notes in Computer Science (including subseries Lecture Notes in Artificial Intelligence and Lecture Notes in Bioinformatics). 8638 LNCS (2014) 191–204.
3. **Isaenko, D., Reznikov, B., Rodin, S.** Multifunctional ecological monitoring complex with optical communication channel. Proceeding 8th International Conference on Information Technology and Nanotechnology, ITNT 2022, 2022. 43-49.

# Real-time calibration methods for a commercial MDI-QKD system

**N. V. Rudavin[3,5]✉, I. S. Gerasin[1,2,3,4], P. A. Kupriyanov[1,2,3,4], A. P. Dvurechenskiy[1,2,3,4], R. A. Shakhovoy[1,2,3,4]**

[1]QRate, Novaya av. 100, Moscow, Russia

[2]Moscow Institute of Physics and Technology, 9 Institutskiy per., Dolgoprudny, Moscow Region, 141701, Russian Federation

[3]NTI Center for Quantum Communications, National University of Science and Technology MISiS, Leninsky prospekt 4, Moscow 119049, Russia

[4]Russian Quantum Center, Bolshoy Boulevard 30, bld. 1, Skolkovo, Moscow 121205, Russia

[5]HSE University, 20 Myasnitskaya ulitsa, Moscow 101000, Russia

✉n.rudavin@goqrate.com

**Abstract**. Nowadays, huge amount of information passing through the Internet requires protection. Quantum cryptography or rather quantum key distribution (QKD) is a significant step towards information-theoretically secure encryption. QKD is a well-studied field of science and is becoming a common technology. Commercial systems become more and more available. Such systems require high level of automatization. So, the set of real-time and prior calibrations is required for commercial QKD systems. In this work, we propose calibration algorithms that pre-tune the amplitude of pulses and the laser wavelength and also maintain phase and polarization of weak coherent pulses during generation. Described algorithms were implemented on a prototype commercial QKD system and demonstrated high results.

**Keywords:** quantum key distribution, Hong-Ou-Mandel effect, phase fluctuation, polarization distortion

**Funding:** The study was commissioned by JSCo «RZD».

## Introduction

At present, the amount of information transmitted via the Internet is rapidly increasing and this information needs to be protected. In contrast to quantum cryptography, classical cryptography has vulnerabilities that allow the eavesdropper (at least, in principle) to gain unauthorized access to sensitive data [1]. When this became clear, it became necessary to develop commercial QKD systems. For these systems, it is important to maintain the key generation procedure, so, the set of real-time calibrations is required for them. In our work, we propose the set of calibrations that are crucial for fiber-optic-based measurement device independent QKD (MDI QKD) systems.

## Materials and Methods

The MDI QKD is based on the Hong-Ou-Mandel effect, which consists in the bunching of single photons after their interference at the beam splitter. To observe this effect, photons must be fully indistinguishable. Therefore, it is necessary to align optical pulses in all their degrees of freedom: frequency, spatial, polarization, and intensity.

If we use lasers with high stability, their frequencies can be aligned at the initial setting, which in our case is based on measuring the beats observed in the interference of laser beams. As for the intensity calibration, we introduced the procedure that chooses one of the senders as a master and the second one as a slave and changes the attenuation on the slave to match master's power. These two calibrations are required only at the first setup; the two remaining degrees of freedom require the continuous control during the generation procedure.

Due to natural birefringence in optical fiber, it is necessary to compensate for polarization distortions occurring in the quantum channel. To compensate these distortions, we employ an active polarization control system that uses gradient-descend like algorithm to regularly recover the state of polarization at the receiver end back to the original one at the sender end [2]. Moreover, temperature variations in the fiber and physical influences on it change the time of arrival (the phase) of laser pulses sent by the transmitter, so, the phase (spatial) alignment is required. To

perform the phase alignment, we use an electrical delay (coarse tuning with the step of 400 ps) combined with an optical delay line (fine tuning with the step of few picoseconds). The number of detector clicks is used as a feedback control parameter.

## Results and Discussion

With the described methods, we run the key generation procedure on the prototype of a commercial system and measured the second order correlation function and the quantum bit error rate. Since we used weak coherent states with random phase, the minimum achievable value of second order correlation function was 50%. We obtained 52%. Obtained quantum bit error rate was 6%. The obtained values are appropriate for key generation.

## Conclusion

In this work, we describe a general calibration method for the MDI QKD system. The method includes pre-calibration procedures (performed during the setup of the device) and the on-the-fly procedures needed to successfully generate a quantum key. Described methods allow achieving high visibility of interference and low quantum bit error rate.

## REFERENCES

1. **Gisin, Nicolas, et al.** Quantum cryptography. Reviews of modern physics 74.1 (2002): 145.
2. **Mekhtiev, E. E., et al.** Polarization control algorithm for QKD systems. Journal of Physics: Conference Series. Vol. 2086. No. 1. IOP Publishing, 2021. 1

# Investigation of the photoelectric parameters of an oxide solar cell based on a $ZnO/Cu_2O$ heterojunction

**A. V. Saenko**✉, **G. E. Bilyk**, **S. P. Malyukov**
Institute of Nanotechnologies, Electronics, and Equipment Engineering,
Southern Federal University, Taganrog, Russia
✉avsaenko@sfedu.ru

**Abstract.** Numerical modeling of an oxide solar cell based on a $ZnO/Cu_2O$ heterojunction has been carried out to optimize its structure and increase the efficiency of energy conversion. The effect of the thickness and concentration of defects in $Cu_2O$ and ZnO layers on the efficiency of a solar cell is studied. It was found that the optimal thickness of $Cu_2O$ and ZnO layers is 5 μm and 20 nm, respectively. It is shown that to obtain a high efficiency of a solar cell, the concentration of defects (copper vacancies) in the $Cu_2O$ layer should be $10^{15}$ $cm^{-3}$, and the concentration of defects (oxygen vacancies) in the ZnO layer should be $10^{19}$ $cm^{-3}$. The maximum efficiency of a solar cell based on $ZnO/Cu_2O$ is 6 %.

**Keywords:** solar cell, numerical simulation, oxide semiconductors, layer thickness, defect concentration.

**Funding:** The study was supported by the grant of Russian Science Foundation № 23-29-00827, https://rscf.ru/project/23-29-00827/ at the Southern Federal University.

## Introduction

At present, interest in the development of oxide solar cells has increased significantly, since oxide semiconductors have the potential to reduce manufacturing costs, as well as being chemically stable and environmentally friendly materials. As a p-type photoactive oxide semiconductor, $Cu_2O$ with a band gap of 2.1 eV, which has a high absorption coefficient (~$10^5$ $cm^{-1}$), high mobility (100 $cm^2/V\cdot s$), and a large diffusion length of charge carriers (2-12 μm), as well as low electron affinity (3.2 eV) [1]. This makes $Cu_2O$ a promising material for use in solar cell structures as an absorber of solar radiation. A promising n-type oxide semiconductor for solar cell structures is ZnO, which is commonly used as a window (buffer) layer due to its large band gap (3.2 eV) and high carrier mobility (120 $cm^2/V\cdot s$).

## Materials and Methods

We considered the structure of a solar cell consisting of an oxide heterojunction and two contacts: a front contact (AZO), an n-type transparent window layer (ZnO), a p-type photoactive layer ($Cu_2O$), and a rear contact (Au). The nature of defects in oxide semiconductors differs significantly from conventional semiconductors (Si), since even without external introduction of impurities, oxide semiconductors exhibit a noticeable n- or p-type conductivity, which is determined by the low energies of formation of internal non-stoichiometry defects - anionic (oxygen) or cationic (metals) vacancies [2]. In modeling, it was assumed that the main defects in the ZnO layer are oxygen vacancies, which are also donors, and the main defects in the $Cu_2O$ layer are copper vacancies, which are acceptors. The absorption coefficients of $Cu_2O$ and ZnO layers were set equal to $5\cdot10^4$ $cm^{-1}$ and $10^5$ $cm^{-1}$, respectively. The mechanism of charge carrier recombination was described according to the Shockley-Reed-Hall theory [3]. The work function of the front contact (AZO) was 4.2 eV, and the work function of the back contact (Au) was 5.1 eV. The value of the series resistance in the solar cell was 3.3 $\Omega\cdot cm^2$ and the shunt resistance was 2500 $\Omega\cdot cm^2$. To simulate the current-voltage characteristics and calculate the efficiency of oxide solar cells, the SCAPS one-dimensional numerical simulation program was used.

## Results and Discussion

The main factor affecting the photoelectric parameters of a solar cell is the thickness of the photoactive layer, in this case $Cu_2O$, since it absorbs solar radiation and generates electron-hole pairs. Figure 1 (a) shows that the efficiency of the solar cell increases sharply (from 1.07 % to

5.29 %) with an increase in the thickness of the $Cu_2O$ layer to 3 μm, and then the increase becomes less pronounced (efficiency 5.69 % with a layer thickness of $Cu_2O$ 6 μm) after the short circuit current density becomes more than 10 mA/cm$^2$. The value of 5 μm (efficiency 5.61%) was chosen as the optimal thickness of the photoactive $Cu_2O$ layer, since its further increase by each 1 μm leads to an increase in efficiency by less than 0.1 %. Figure 1 (a) also shows that an increase in the concentration of defects (copper vacancies) in the $Cu_2O$ layer from $10^{13}$ cm$^{-3}$ to $10^{15}$ cm$^{-3}$ leads to an increase in efficiency from 4.14 % to 5.98 %, and a further increase in the concentration of defects to $10^{18}$ cm$^{-3}$ leads to a decrease in efficiency to 0.88 %.

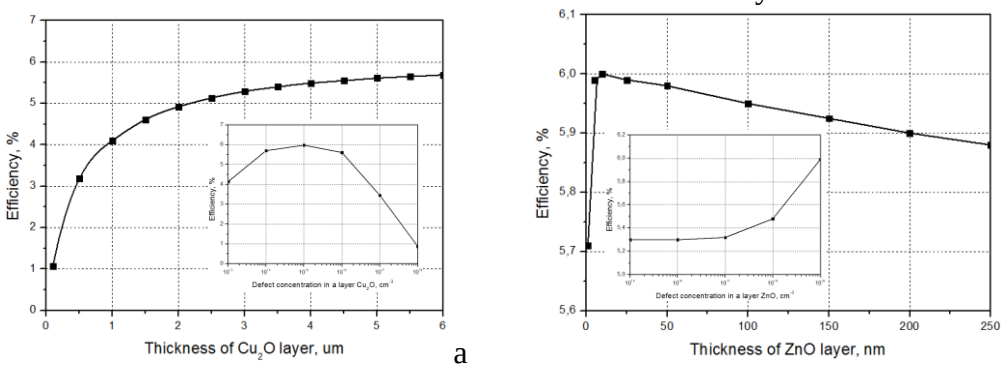


Fig. 1. Dependence of the solar cell efficiency on the thickness and the concentration of defects in the $Cu_2O$ layer (a) and in the ZnO layer (b)

In addition to the thickness and concentration of defects in the $Cu_2O$ layer, an important factor is the thickness of the ZnO window layer, which contributes to the separation of the generated electron-hole pairs in the solar cell. Figure 1 (b) shows that an increase in the thickness of the ZnO layer first leads to an increase in the efficiency of the solar cell to about 6 % at a thickness of 5-35 nm due to the best separation of the generated electron-hole pairs, and then to a decrease to 5.88 % (at 250 nm). Figure 1 (b) also shows that an increase in the concentration of defects in the ZnO layer from $10^{15}$ cm$^{-3}$ to $10^{19}$ cm$^{-3}$ leads to an increase in the efficiency from 5.3 % to 6 % and is associated with an increase in the open-circuit voltage from 0.6 V to 0.68 V and small recombination losses in the ZnO layer due to its small thickness (20 nm).

## Conclusion

This study shows the effect of the thickness and concentration of defects in $Cu_2O$ and ZnO layers on the efficiency of a solar cell. The optimal thicknesses of the $Cu_2O$ and ZnO layers were determined, which were 5 μm and 20 nm, respectively. In addition, the optimal concentrations of defects in $Cu_2O$ and ZnO layers (copper vacancies and oxygen vacancies) were determined, which amounted to $10^{15}$ cm$^{-3}$ and $10^{19}$ cm$^{-3}$, respectively. Thus, the maximum efficiency of a solar cell based on ZnO/$Cu_2O$ equal to 6 % was obtained (short circuit current density 11.25 mA/cm$^2$, open circuit voltage 0.68 V, fill factor 74.53 %). The results can be used in the development and formation of the structures of oxide solar cells.


## Acknowledgments

The study was supported by the grant of Russian Science Foundation № 23-29-00827, https://rscf.ru/project/23-29-00827/ at the Southern Federal University.


## REFERENCES


1. **Amador Perez-Tomas**. Functional Oxides for Photoneuromorphic Engineering: Toward a Solar Brain // Advanced Materials Interfaces, 6, (2019), 1900471.

2. **Stefanovich G.B., Pergament A.L., Boriskov P.P., Kuroptev V.A., Stefanovich T.G.** Charge transfer in rectifying oxide heterostructures and oxide access elements in ReRAM // Semiconductors, 50, (2016), 639.

3. **Saenko A.V., Klimin V.S., Rozhko A.A., Malyukov S.P.** Modeling the Structure of an Oxide Solar Cell // Journal of Communications Technology and Electronics, 67, 1, (2022), S108.

# The effect of the dielectric $SiO_2$ layer on the characteristics of visible-blind ultraviolet photodetectors based on ultrathin GaN epitaxial layers grown on c-$Al_2O_3$ substrates

**O. A. Sinitskaya [1✉], K. Yu. Shubina [1], D. V. Mokhov [1], A. V. Uvarov [1], A. M. Mizerov [1], E. V. Nikitina [1,2]**

[1] Alferov University, St. Petersburg, Russia;

[2] Ioffe Institute, St. Petersburg, Russia

✉olesia-sova@mail.ru

**Abstract.** In this work ultraviolet metal-semiconductor-metal and metal-insulator-semiconductor photodetectors based on GaN epitaxial layers were fabricated and their I-V characteristics were studied. It was found that the dark current of the photodetectors decreased by 76 times after introducing a 20 nm thick $SiO_2$ dielectric layer. The photocurrent to dark current ratio increased by a maximum of 35 times with a dielectric layer of 20 nm thickness.

**Keywords:** GaN, $SiO_2$, ultraviolet photodetector, metal-semiconductor-metal, metal-insulator-semiconductor.

**Funding:** The work was supported by the Ministry of Education and Science (grant №FSRM-2023-0006).

## Introduction

Nowadays visible-blind and solar-blind ultraviolet photodetectors (UV PDs) are in demand for a wide range of military and commercial applications. One of the most promising materials for the fabrication of semiconductor UV PDs is (Al)GaN. The bandgap width of (Al)GaN can be varied between 3.4 and 6.2 eV depending on the composition, corresponding to the wavelength range of 365 to 200 nm, respectively [1]. In addition, (Al)GaN has a high carrier mobility, which ensures the fast response of detectors based on this material. Moreover, the great mechanical, thermal and chemical stability of these semiconductors gives the potential for stable operation of the devices based on them in harsh environments.

There are several basic types of UV PD structure designs, among which metal-semiconductor-metal (MSM) PDs attract great attention owing to the ease of fabrication, low intrinsic capacitance, high response speed, and low noise level [2]. At the same time, due to the high dislocation density in GaN epitaxial layers, MSM PDs based on them suffer from high dark current, as it was shown in our previous work [3]. The use of $SiO_2$ layer (i.e., the conversion of MSM PDs to metal-insulator-semiconductor (MIS) PDs) can provide semiconductor surface passivation to reduce the dark current [4]. In this work, the devices of both types were fabricated and their characteristics were studied and compared.

## Materials and Methods

150–200 nm thick GaN epitaxial layers were grown by plasma-assisted molecular beam epitaxy (PA MBE) on annealed and nitrided c-$Al_2O_3$ substrates using the Veeco GEN 200 MBE system. The surface morphology of the synthesized samples was analyzed using a scanning electron microscope (SEM) and the crystallographic polarity was determined by etching in aqueous KOH solution (1:5). In addition, it was determined by the Hall effect measurements that the GaN epitaxial layer has n-type conductivity, the concentration of charge carriers was about $n \approx 1 \cdot 10^{18}$ cm$^{-3}$ and the mobility about $\mu \approx 25$ cm$^2$/(V·s). Then, the MSM PDs as well as MIS PDs using a 10 and 20 nm thick $SiO_2$ layer were fabricated. $SiO_2$ layers were deposited by plasma enhanced chemical vapor deposition using Oxford PlasmaLab System 100. Ni/Au (15/15 nm) interdigitated electrodes were formed by e-beam evaporation, resistive thermal evaporation and standard lift-off lithography. The I-V characteristics of the formed PDs were measured using an Agilent B1500A semiconductor device parameter analyzer.

## Results and Discussion

The analysis of the I-V characteristics of the formed photosensitive elements showed that the introduction of a 10 nm and 20 nm thick dielectric layer led to decrease in the dark current ($I_d$) by almost 63 and 76 times respectively at an applied bias of 5 V (Fig.1, a). It was found that the maximum photocurrent to dark current ratio ($I_{ph}/I_d$) for MSM PDs was 2.5. At the same time, the use of a 10 and 20 nm thick $SiO_2$ layer resulted in an increase in this ratio to a maximum of 4 and 35 respectively (Fig. 1, b). The results confirm that the introduction of a $SiO_2$ layer in the PDs based on ultrathin GaN epitaxial layers can help reduce their dark current and increase sensitivity.

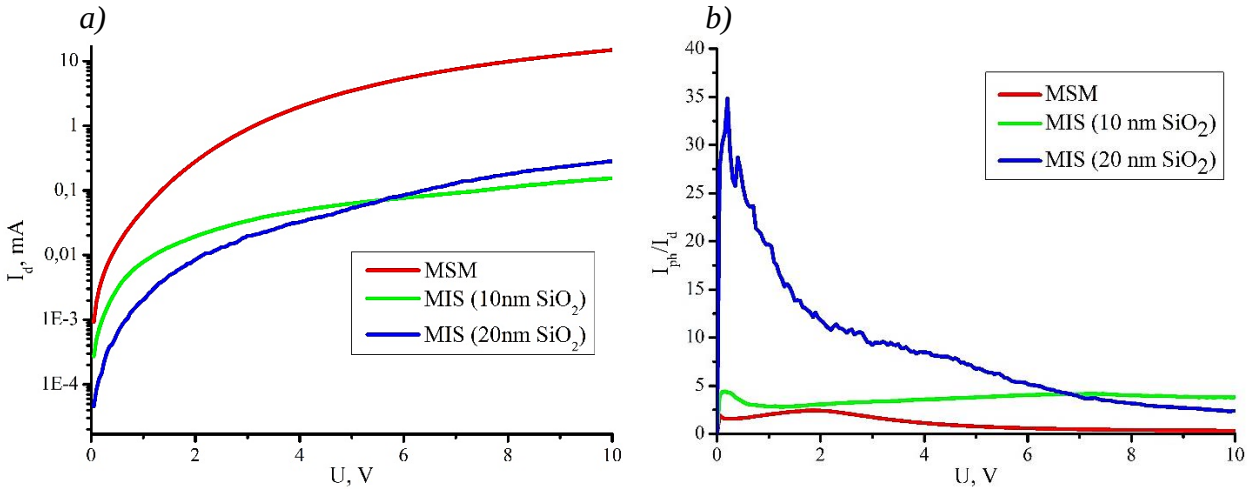


Fig. 1. Dependencies of dark current (*a*) and the photocurrent to dark current ratio (*b*) on voltage for the obtained MSM and MIS PDs

## Conclusion

In this work, it was shown that MIS PDs based on ultrathin GaN epitaxial layers have a lower dark current and a higher photocurrent to dark current ratio compared to MSM PDs based on the same epitaxial structures. Thus, the introduction of a dielectric layer can be a promising approach to increase the sensitivity of the UV PDs based on ultrathin GaN epitaxial layers.

## REFERENCES

1. **Schubert E. F.**, Light-Emitting Diodes, Cambridge: Cambridge University Press, 2006.

2. **Shi L., Chen K., Zhai A., Li G., Fan M., Hao Y., Zhu F., Zhang H., Cui Y.**, Status and Outlook of Metal–Inorganic Semiconductor–Metal Photodetectors, Laser Photonics Reviews. 15, 2000401 (2021) 1–2.

3. **Sinitskaya O. A., Shubina K. Yu., Mokhov D. V., Uvarov A. V., Filatov V. V., Mizerov A. M., Timoshnev S. N., Nikitina E. V.**, Development of visible-blind ultraviolet photodetectors based on ultrathin GaN epitaxial layers grown on c-$Al_2O_3$ substrates. St. Petersburg State Polytechnical University Journal. Physics and Mathematics, 15 (3.3) (2022) 157–162.

4. **Chen C.-H.**, AlInGaN 310 nm Ultraviolet Metal–Insulator–Semiconductor Sensors with Photo-Chemical-Vapor-Deposition $SiO_2$ Cap Layers, Optical Review. 16, 3 (2009) 371–374.

# Electrical characteristics of solar cells with silicon nanostructures

**M.A. Tkach[1]✉, D.A. Shishkina[2]**
[1]Samara National Research University, Samara, Russia
✉tcka4.rita@yandex.ru

## Abstract

Multifunctional nanoscale structures are of particular scientific and practical interest due to their unique physical properties that cannot be realized in bulk materials. Such structures include porous silicon (PC), which continues to attract attention due to its potential for creating visible radiation sources, integrating elements of opto- and microelectronics based on silicon technology.

In this work, the light and dark volt-ampere characteristics of photosensitive structures with a porous layer were studied. As a result of the experimental work carried out, the influence of etching parameters on the change in the characteristics of photosensitive structures was revealed. It turned out that with an increase in the current density during etching, both the no-load voltage and the short-circuit current decrease. At the same time, if you increase the etching time, both parameters decrease.

## Key words

Porous silicon, solar cell, VAC

## Introduction

In this paper, we considered solar cells, electronic devices that directly convert solar radiation into electricity. When creating them, it is necessary to take into account the ambiguous influence of the degree of doping of the base region on the parameters affecting their volt-ampere characteristics and causing degradation of structures. At a high doping level, the no-load voltage increases and the resistance decreases. However, strong doping leads to crystal lattice disturbances, complexation, and a decrease in the duration of the charge carriers' stay in the strongly doped region[1]. There are three different ways to increase the efficiency of silicon solar cells. The first method is to create pulling fields to increase the diffusion length of non-basic charge carriers in the region of the base layer. The second method is to create fields near the back of the element to reflect non-core carriers from it and thereby reduce the effective rate of surface recombination on this surface. The third method is to create fields near the front side of the element to accelerate the carriers photogenerated in the front layer in the direction of the p-n junction, reduce the effective rate of surface recombination on the front surface and reduce recombination in the volume of the thin front layer[2].

## Materials and methods

The initial samples were Si p-type substrates with a resistivity of ~ 1.5 ohms·cm and a surface resistance of ~ 70 ohms/cm$^2$. To create a p-n junction, diffusion was carried out, a phosphorus diffusant was used, in a diffusion furnace at 1000 degrees.

Porous silicon structures were made by electrochemical etching. To do this, $HF+C_2H_5OH$ (1:1) was used as an etchant, while the process itself was carried out for each sample at different t and the current density was increased by 2 times for some samples. One sample remained intact for further comparison of light and dark VACs.

The final stage was the application of contacts using the VUP-4 installation and obtaining dark and light volt-ampere characteristics.

## Results and Discussion

After comparing the VAC light currents of the intact sample and the etched sample at t = 10 min and the current density j = 55.1 mA, it can be seen that the no-load voltage differs by about 1.3 times, it is less for the untouched one, and the short-circuit current for the non-etched sample is 0.04 times greater.

If we compare samples that were etched for the same amount of time, but at the same time the current density of one was twice as high, we will see the following picture. The no-load voltage will be almost 6.5 thousand times greater, and the short-circuit current will be 31 times greater for the sample that was etched with a lower current density.

## Conclusion

Thus, studies have shown that the volt-ampere characteristics of solar cells largely depend on the indicators and values of current density and etching time. The difference in the coefficients of the ideality of solar cells differs several times, and later we can notice it on the graphs of the VAC.

## REFERENCES


1. **Christopher M. Proctor, Thuc-Quyen Nguyen,** Effect of leakage current and shunt resistance on the light intensity dependence of organic solar cells. – 2015. – Appl. Phys. Lett. 106. – P. 2-5.
2. **Farenbruch A., Bub R.,** Solar cells: Theory and experiment/ Trans. from English. edited by M. M. Koltun. — M.: Energoatomizdat, 1987. — P. 176-179.

# FORMATION OF ITO-BASED ANISOTROPY ORIENTING LAYERS FOR LIQUID CRYSTAL DEVICES

**A. S. Toikka** [1✉]

[1] St. Petersburg Electrotechnical University, St. Petersburg, Russia;

✉astoikka.nano@gmail.com

**Abstract.** In this paper, the influence of $CO_2$ laser ablation and surface electromagnetic waves (SEW) processing on the indium-tin oxide (ITO) was considered. The anisotropy of wetting angle for untreated, ablated and SEW-treated ITO thin films was compared. The discussed types of laser treatment are suitable to modify the ITO-based transparent contacts for molecule orienting features in the constructions of liquid crystal devices.

**Keywords:** indium-tin oxides, wetting angle, laser processing, liquid crystal devices.

## Introduction

Liquid crystal (LC) mesophase is an important material for electro-optical applications (display elements, modulation devices, laser techniques, etc.) due to the mechanical, electrical and optical properties. The basic electrically tunable LC device consists of mesophase, orienting layers, transparent contacts and substrates. In case for the application of external electric field, the LC molecules change orientation among the field. Due to the optical anisotropy of nematic liquid crystals, the effective value of LC's refractive index ($n_e$) could be described via the following equation:

$$n_e(z) = \frac{n_\perp n_\parallel}{\sqrt{\left(n_\perp \cos\theta\right)^2 + \left(n_\parallel \sin\theta\right)^2}}, \tag{0.1}$$

where $n_{/\!/}$ and $n_\perp$ are components of refractive index of LC molecule, θ is the mean value tilt angle of LC domain, $z$ – coordinate along the optical beam propagation.

It should be mentioned, that the properties of LC layers strongly depend on the distribution of molecules (θ=f(z)). This distribution could be estimated with the enough precise via the differential equation [1]:

$$K\frac{\partial^2\theta}{\partial z^2} + \frac{\Delta\varepsilon}{4\pi}E^2 \sin\theta\cos\theta = \gamma\frac{\partial\theta}{\partial t}, \tag{0.2}$$

where $K$ is the elasticity coefficient (depends on the LC material and type of deformation – twist, bend or splay), γ is the rotation viscosity coefficient, Δε is the anisotropy of dielectric permittivity, $E$ is the electric field strength.

Orienting layers control the border conditions for the distribution of LC molecules. In common case, these structures have the organic nature (for example. polyimides) and the thickness is more than 0.1 μm. They have the relatively high electrical resistance in comparison with the transparent contacts and increase the consumption power.

In the current paper, the indium-tin oxides (ITO) structures were considered for the position of orienting layer. It should be noticed that ITO is a conventional material for the transparent contacts in the visible and near-infrared ranges. Thus, the current research leads to consider the ITO as a universal material for the both functions – electrical tuning and mechanical orienting of LC molecules.

## Materials and Methods

ITO thin films were deposited on the Crown K8 substrates via the laser-oriented deposition (LOD) method. For these issues, the $CO_2$ laser (λ=10.6 μm, $P$=30 W) with the conjugated electro-mechanical modules were used [2]. The thickness of ITO films was approximately 100 nm. Then they were patterned via the $CO_2$-marker (λ=10.6 μm, $P$=21 W, $f$=1 kHz, beam diameter was 150 μm). The pattern consisted of the parallel stripes with the length 10 mm and step 5 mm.

The characterization of orienting properties was via the measurement of the wetting angle in *xz*- and *yz*-projections. The *x*-axis is parallel and *y*-axis is perpendicular to the direction of ablation. For these issues, the OCA-15 EC (Dataphysics) measurement system with the sessile drop method

were used. The parameters of drop were the following: volume 0,5-0,7 μL, material – distilled water, surface free tension – 72.8 mN/m (total), 48.1 mN/m (polar part), 24.7 mN/m (dispersive part).

## Results and Discussion

Before the laser treatment of ITO, the wetting angle for parallel component was in range $\theta_{\parallel}$=96-101˚ and for perpendicular part – in range $\theta_{\perp}$=95-99˚. The difference in two components of untreated films could be caused by the features of LOD processes. The average wetting angle anisotropy ($\Delta\theta = \theta_{\parallel} - \theta_{\perp}$) for pure ITO thin films was less than 2˚.

In case for laser treatment with $CO_2$-marker, the dramatic changes in the wetting angle distribution were observed. In directly ablated areas the wetting angle was decreased to $\theta_{\parallel}$=45-59˚ and to $\theta_{\perp}$=76-99˚ respectively.

Under the considered conditions, the OCA15-EC measured the receding wetting angle. Taking into account that the value of Young's wetting angle (it's a property of the material) was constant, it could be concluded, that the average angle deviation of the ITO surface was increased. The possible mechanism of the observed phenomena is the local heating of ITO areas under the direct laser treatment.

It should be mentioned, that for ITO thin films under $CO_2$ laser influence the additional mechanism of treatment is exists – via the surface electromagnetic waves (SEW) propagation [3]. The brief note regarding ITO/SEW structures, their relief and optical properties were demonstrated previously [4]. In terms of wetting angle, the SEW processing increased the wetting angle of ITO thin films to $\theta_{\parallel}$=98-104˚ and $\theta_{\perp}$=99-100˚ respectively.

## Conclusion

Laser treatment of ITO thin films influences on the anisotropy of wetting angle distribution. In case for direct laser ablation, the absolute value of average wetting angle anisotropy was increased to 30-32˚. Via another mechanism, SEW treatment, the precise rising of wetting angle was observed. These technological aspects could improve the orienting features of ITO-based structures in order to simplify the architecture of LC devices.

## Acknowledgments

The author would like to thank his supervisor prof. N.V. Kamanina (head of Lab for Photophysics of media with nanoobjects at Vavilov State Optical Institute) for productive discussions and seminars.

## REFERENCES

1. **Yakovlev D.A., Chigrinov V.G., Kwok H.S,** Modeling and Optimization of LCD optical performance. Chapter 4: electro-optical modes: Practical examples of LCD modeling and optimization, John Wiley & Sons, Ltd. 2015.

2. Patent RU 2405177, 2008. Authors: **Kamanina N.V., Vasil'ev P. Ya, Studeonov V.I**.

3. **Bonch-Bruevich A.M., Libenson M.N., Makin V.S., Trubaev V.V.** Surface electromagnetic waves in optics, Optical Engineering. 31(4) (1992) 718.

4. **Toikka A S.** Laser treatment of ITO thin films with Carbon Nanotubes for Liquid Crystal Devices, Journal of Physics Conference Series. 012105 (2086) (2021) 1-4. DOI: 10.1088/1742-6596/2086/1/012105.

# Measurement of threshold current in local areas of the LED chip

**I. V. Frolov** [1✉], **O. A. Radaev** [1], **V. A. Sergeev** [1,2]
[1] Ulyanovsk Branch of Kotel'nikov Institute of Radio-Engineering and Electronics of Russian Academy of Sciences, Ulyanovsk, Russia;
[2] Ulyanovsk State Technical University, Ulyanovsk, Russia
✉ufire@mv.ru

**Abstract.** A method for measuring the threshold current in local areas of an LED chip is presented. The method consists in registering of chip images at three low currents and pixel-by-pixel calculation of threshold current values by solving a system of equations compiled for three values of the approximating function. Approbation was carried out on a commercial green LEDs. It is shown that the distribution of the values of the threshold current over the chip is uneven.

**Keywords:** LED, threshold current, measurement.
**Funding:** The work was carried out within the framework of the state task.

## Introduction

Defects of light-emitting heterostructures with InGaN/GaN quantum wells create channels for the leakage of charge carriers from the active region. The threshold current is the minimum current at which emission can be detected. It characterizes the losses due to nonradiative recombination in the system of defects, the losses of charge carriers during tunneling through the potential barrier, and their leakage from the active region into the barrier layers [1]. The paper presents a method for measuring the threshold current in local areas of the LED chip, which can be used to assess the structural perfection of light-emitting heterostructures.

## Materials and Methods

To determine the threshold current $I_0$, it is necessary to measure the LED emission power at three low currents $I_1$, $I_2$, and $I_3$ ($I_1 < I_2 < I_3$), at which the quantum efficiency increases, and solve the system of equations for the *P-I* characteristic [2] of the form

$$P(I_i) = \frac{m}{2}\left(\sqrt{1+2q(I_i - I_0)} - 1\right)^2, i = 1, 2, 3 \quad (1)$$

where $m = \eta_{extr} V \frac{hc}{\lambda} \frac{A^2}{2B}$, $q = \frac{\eta_{inj}}{eV} \frac{2B}{A^2}$, $h$ is the Planck's constant; $c$ is the speed of light; $\lambda$ is the emission wavelength; $e$ is the elementary charge, $V$ is the heterostructure active region volume; $\eta_{inj}$ is the coefficient of charge carrier injection into the active region; $\eta_{extr}$ is the light emission extraction efficiency; $A$ and $B$ are the coefficients of nonradiative Shockley-Reed-Hall recombination and radiative recombination, respectively; $I_0$ is the threshold current.

The current $I_1$ is set to the lowest one that ensures the given level of accuracy. The current $I_3$ should be about 5 times less than the current $I_{max}$, at which the maximum quantum efficiency is achieved. The current $I_2$ is set from the condition $I_2 \approx 0{,}5 I_3$.

## Results and Discussion

Threshold current $I_0$ in local areas of the LED chip was measured by a hardware-software complex [3]. The images of the LED chip at currents $I_1$ = 112 nA, $I_2$ = 20 μA, and $I_3$ = 52 μA with a resolution of 5472x3648 were stored in the computer memory, then a pixel-by-pixel calculation was performed. The distribution profile of the current $I_0$ across the commercial green LED chip XRCGRN-L1-0000-00M01 shows on Figure 1. The crystal dimensions are 980×980 μm.

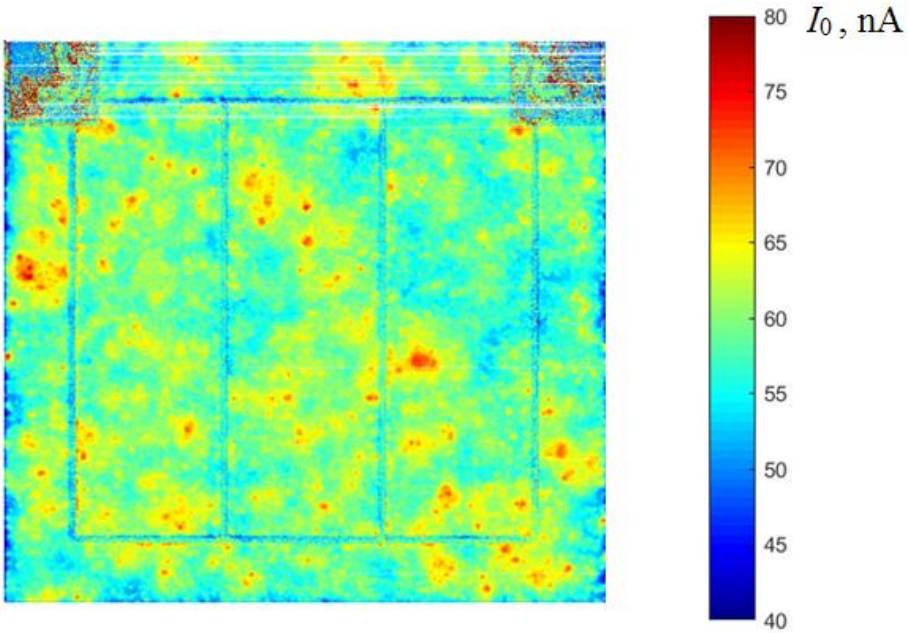


Fig. 1. The current $I_0$ distribution profile across the chip of green LED

The distribution of current $I_0$ over the chip of the investigated LED is uneven. The average value is 58 nA. There are local areas, at which values of the threshold current reaches 80 nA.

## Conclusion

The method for determining of the threshold current in the local areas of the LED chip is presented. The method has been tested on commercial green LEDs. It is shown that the distribution of the threshold current over the LED chip is uneven.

## REFERENCES

1. **Averkiev N.S., Levinshtein M.E., Petrov P.V., Chernyakov A.E., Shabunina E.I., Shmidt N.M.**, Features of the recombination processes in InGaN/GaN based LEDs at high densities of injection current, Technical Physics Letters. 35 (10) (2009) 922–924.

2. **Frolov I.V., Sergeev V.A.,** Diagnostic quality control of LEDs by local parameters of electroluminescence and photocurrent, SOLON-Press, Moscow, 2023 (In Russian).

3. **Frolov I.V., Segeev V.A., Radaev O.A.** The Method for Measuring the Distribution Profile of the 3dB Frequencies of Electroluminescence Over the Area of the LED Chip, IEEE Transactions on Instrumentation and Measurement. 72 (2023) 5000806.

# Modeling of avalanche photodiodes based on Ge/Si

**K. I. Khomyakova ✉, H. Deeb, K.A. Lozovoy, A.P. Kokhanenko**
National Research Tomsk State University, Tomsk, Russia;
✉hkris05@yandex.ru

**Abstract.** This article presents a simulation of the planar structure of an avalanche photodiode based on Ge/Si. The effect of the absorption and multiplication layers thicknesses on sensitivity, gain, bandwidth, and dark current is shown.

**Keywords:** Avalanche photodiode, single-photon detector, impact ionization, planar

**Funding:** Work with the financial support of the Russian Science Foundation grant No. 21-72-10031.

## Introduction

To date, there is a clear lack of practical single-photon detectors that operate at wavelengths > 1 μm with an ideal combination of high quantum efficiency, low noise and low afterpulse. To eliminate many disadvantages, a useful alternative to these existing detection technologies is the use of Ge as an absorber in tandem with the Si multiplication layer. The Ge band gap provides effective absorption at wavelengths in the entire visible and infrared ranges up to a limiting wavelength of approximately 1600 nm [1]. As a result, APDs with a Ge absorption layer and a Si multiplication layer can achieve very good performance with high quantum efficiency and low noise. In addition, the multiplication gain and frequency response represent very important figures of merit to determine the performance of APDs [2].

## Materials and Methods

In this work, the planar structure of an avalanche photodiode (APD) was designed and modeled. A schematic cross-section of the Ge/Si-based APD structure is shown in Figure 1. In the APD structure with reverse voltage bias, the presence of a charge layer should ensure that the electric field in the narrowband Ge absorption layer is maintained below the germanium breakdown field ($\approx 1\times10^5$ V·cm$^{-1}$) in order to avoid the tunneling effect, and in the multiplication layer Si is greater than the silicon breakdown field ($\approx 3\times10^5$ V·cm$^{-1}$) to provide impact ionization. The simulated structure has a cylindrical shape with a diameter of 25 microns and are modeled using TCAD.

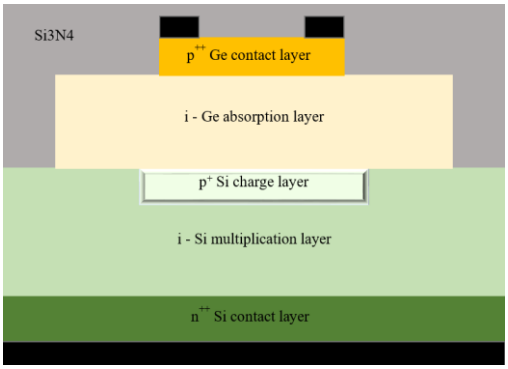


Fig. 1. Schematic cross section of Ge/Si APD

## Results and Discussion

The simulation shows the effect of the multiplication and absorption layers thicknesses on sensitivity, gain, bandwidth and dark current, which have a significant impact on the performance of the device. The responsivity of the device is directly proportional to the thickness of the absorption layer. A thicker absorption layer will absorb more photons and generate more electron-hole pairs, resulting in a higher responsivity. However, increasing the thickness of the absorption

layer may also increase the dark current and reduce the quantum efficiency. The gain of the device is proportional to the product of the multiplication layer thickness and the electric field in the layer. A thicker multiplication layer can provide a higher gain, but it can also lead to a higher breakdown voltage and a higher dark current. The bandwidth of the device is inversely proportional to the product of the absorption layer thickness and the carrier transit time. A thinner absorption layer can provide a higher bandwidth, but it may also reduce the responsivity and increase the noise.

## Conclusion

In general, optimizing the multiplication and absorption layers thicknesses in APD requires a compromise between sensitivity, gain, bandwidth, and dark current. The dimensions that provide the best performance will depend on the specific device requirements and operating conditions. The presented results of modeling APD structures will serve for the creation of experimental structures grown by the method of molecular beam epitaxy and the study of their practical parameters.

## REFERENCES

1. **Thorburn F. E., Huddleston L. L., Kirdoda J., Millar R. W., Ferre-Llin L., Yi, X., Paul D. J., Buller G. S.** High efficiency, planar geometry germanium-on-silicon single-photon avalanche diode detectors, Advanced Photon Counting Techniques. Vol. 11386 (2020) 113860N-1.

2. **Huang M., Li S., Cai P., Hou G., Su T., Chen W., Hong C., Pan D.** Germanium on Silicon Avalanche Photodiode, IEEE Journal of Selected Topics in Quantum Electronics. Vol. 24 (2018), 1-11.

# Development of a device for measuring volt-ampere and volt-watt characteristics of experimental solar cells

**V. A. Shishkin** [1✉], **I. A. Shishkin** [1], **D. A. Shestakov** [1]
[1] Samara National Research University, Samara, 443086, Russia;
✉ vladshishi@yandex.ru

**Abstract.** This paper presents an inexpensive implementation of a device for measuring volt-ampere and volt-watt characteristics in real time with an interval of less than 1 minute based on the current and voltage sensor INA219 with an accuracy of 5%. The INA219 current sensor operates on the principle of measuring low current with a built-in load resistor that is directly connected to the ground and does not damage the sensor or any other safe device in the event of a short circuit. The electronic circuit of the sensor was developed integrated with the Atmega328 microcontroller and a software interface used as a high-precision data logger for DC measurement. The SIM800L module is used to transmit data to the website. The proposed approach, together with the implementation of the prototype, is aimed at creating a sustainable and scalable solution for environmental and electrical monitoring of photovoltaic modules.

**Keywords:** photovoltaics, solar energy, arduino, volt-ampere characteristic, monitoring

## Introduction

As a rule, the parameters of solar cells are measured using measuring instruments or a solar simulator at an air mass of 1.5 solar spectrum (AM1.5) with a total radiation power of 1000 W/m2 and a temperature of 25 degrees Celsius for ground use. Solar cells used for space applications are usually characterized by the use of the solar spectrum of the air mass AM0 with a spectral brightness of 1366.1 W/m2 [1]. Compared to sunlight, solar simulators have limitations. The light produced by the solar simulator does not meet the spectrum standard, is spatially heterogeneous and unstable in time [2].

Using a voltage and current sensor at the output via a potentiometer, we can accurately obtain Vx.x. and Is.c. to evaluate the properties of a solar cell in an open area. However, practically a solar cell would act differently in a different environment. Repeated measurements are necessary to obtain the characteristics of any available solar cells before using them, as this would help other calculations to be more reliable with respect to various environmental conditions. Therefore, in this study, we propose a simple characterization method using a microcontroller, a linear potentiometer, and an INA219 sensor to make the I-V solar cell characterization process inexpensive.

## Experimental

A 90-watt lamp was used to illuminate the solar cell. This lamp illuminates the solar cell from a distance of 23 cm. Most of the solar cells manufactured on the basis of porous silicon with the use of antireflection coatings were with a power of less than 1 W and with an area of less than 0.0012 m2. Since this study focuses on low-power solar cells and low-cost operation, spatial uniformity is neglected. The lamp used creates a significant temperature. Thus, the measurement must be made quickly. A faster measurement process also improves flow stability. However, changing the resistance of the linear potentiometer too quickly will cause the measurement process to fail.

The experiment was conducted for the characteristics of experimental solar cells with an average power of 0.15 watts. The I-V curve measurements were obtained both by an experimental device and by a Keithley 2450 measuring source (Fig. 1).

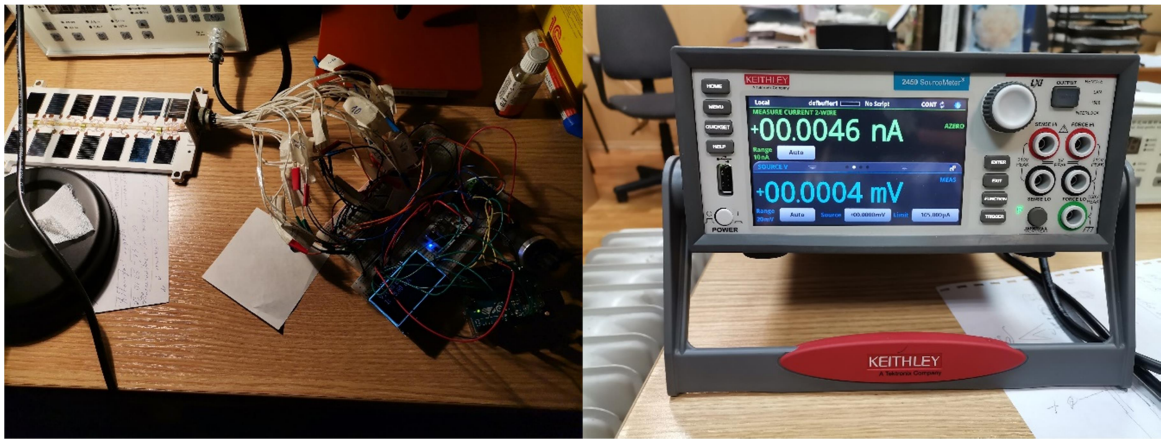


Fig. 1. Prototype of a device for measuring the volt-ampere characteristics of solar cells (left) and a Keithley 2450 source meter (right)

## Conclusion

The experiment showed that this device is able to characterize a low-power solar cell with a small difference in Vx.x. and Is.c. with an error of 5% compared to measurements of I-V curve on the Keithley 2450 meter source. This is due to the inaccuracy of the potentiometer caused by manual adjustment. Therefore, this method can be used to characterize the I-V curve of a single-crystal silicon solar cell. This method offers a cheap option for measuring the volt-ampere characteristics of any solar cell.

## Acknowledgments

This work was supported by the Foundation for Assistance to Small Innovative Enterprises, grant № 12980GU/2018.

## REFERENCES

1. **Moreno-Garcia I.M., Palacios-Garcia E.J., Pallares-Lopez V., Santiago I., Redondo M.J.G., Varo-Martinez M., Calvo R.J.R.**, Real-Time Monitoring System for a Utility-Scale Photovoltaic Power Plant. Sensors 2016, 16, 770. [CrossRef].

2. **W. Keogh, Blakers A. W.**, Natural Sunlight Calibration of Silicon Solar Cells., 17th European Photovoltaic Solar Energy Conference. Munich, Germany, (2001).

3. **Strasser T.**, **Andren F.**, **Kathan J.**, **Cecati C.**, **Buccella C.**, **Siano P.**, **Leitao P.**, **Zhabelova G.**, **Vyatkin V.**, **Vrba P.**, et al. A review of architectures and concepts for intelligence in future electric energy systems. IEEE Trans. Ind. Electron. 2014, 62, 2424–2438.

4. **Meliones A.**, **Apostolacos S.**, **Nouvaki A.** A web-based three-tier control and monitoring application for integrated facility management of photovoltaic systems. Appl. Comput. Inform. 2014, 10, 14–37.

5. **Silvestre S.**, **da Silva M.A.**, **Chouder A.**, **Guasch D.**, **Karatepe E.** New procedure for fault detection in grid connected PV systems based on the evaluation of current and voltage indicators. Energy Convers. Manag. 2014, 86, 241–249.

**A Method for Studying of color characteristics of pigments by spectrophotometry**

**Yara Jabr**
*Saint Petersburg Electrotechnical University "LETI"*
*Saint Petersburg, Russia*

**Lyudmila A. Smirnova**
*Academy if Fine Arts, St.Petersburg, Russia*

**Vadim A. Parfenov**
*Saint Petersburg Electrotechnical University "LETI"*
*Saint Petersburg, Russia*

Nowadays, in restoring and examining paintings, the search for effective analytical methods for studying pigments and paints is handy in identifying pigments and is essential in studying the characteristic of pigments and determining the time of the creation of paintings and their authorship. Many studies are used to solve such problems, including Raman and IR Fourier spectroscopy and X-ray fluorescence spectrometry. Studying the painting's pigments are an essential subject in many research areas, especially in the art and cultural fields, identifying pigments is essential in determining the characteristics of their colors and identifying the materials and glue used in them, but all the mentioned methods require the use of complex and expensive equipment, sampling, and preparation of samples. For this reason, it is of interest to use simpler (from a technical point of view) non-destructive testing methods. One of the possible approaches to solving such a problem may be the use of the spectrophotometry method. This work aimed to test the possibility of identifying paint pigments using a portable Spectro-guide 45/0 gloss spectrophotometer (manufacturer – BYK – Gardner Gmbh, Germany). During several experiments, the color characteristics of model samples were studied.

The model samples are pigment stains on sheets of paper about 2x2 cm in size, ground with various binders. In the experiments, both natural (yellow and red ochres, green earth) and synthetic (various whitewash) pigments were used, as well as their mixtures, which were rubbed with binders: traditional for painting (for example, linseed oil) and modern restoration materials (such as Loropal – carbamide-formaldehyde resin resistant to yellowing, used when tinting the loss of the colorful layer of easel painting).It was shown that the color characteristics of pigments and paints, including, for example, whitewash (lead, zinc, and titanium), have characteristic individual values of the color coordinates L*, a*, b*, which allows their Identification. the future work of our study will be placing them in the colorful layer of works of art, antique paintings, and icons, and determination of the substances involved in the formation of each used pigment.

# Investigation on the effects of the multiplication area shape on the dark count rate in InGaAs/InAlAs single-photon avalanche photodiodes

**V.V. Zavodilenko**[1,2,3✉], **A.A. Filyaev** [1,2,3], **A.V. Losev** [1,2,4], **I. D. Pavlov** [1,2,3]
[1] National University of Science and Technology MISIS, Moscow, Russia;
[2] "QRate" LLC, Skolkovo, Russia;
[3] HSE University, Moscow, Russia;
[4] National Research University of Electronic Technology MIET, Zelenograd, Russia
✉ v.zavodilenko@goqrate.com

**Abstract.** In this paper the influence of the multiplication area shape on the dark count rate (DCR) of InGaAs/InAlAs single-photon avalanche photodiodes (SPADs) is discussed. This study is carried out within the framework of SPAD design parameter optimization. The diode structure has been simulated in the T-CAD calculation environment.

**Keywords:** multiplication area, dark count rate, single-photon avalanche photodiodes, single-photon detector.

**Funding:** The study was commissioned by JSCo «RZD».

## Introduction

Single-photon avalanche diode (SPAD) for detecting radiation with wavelength $\lambda$ = 1550 nm can be made of various materials. The development of SPADs based on materials such as Si/Ge, InGaAs/InP and InGaAs/InAlAs continues in the scientific community [1–2]. So, a promising structure such as InGaAs/InAlAs will be investigated in this work.

The advantage of the InAlAs material as a multiplication area is its high electron mobility, which allows the excited avalanche to be quenched much faster and the structure to be transferred to an equilibrium state. Thus, this device can have a higher limiting frequency and better afterpulse characteristics compared to a device with a multiplication area made of InP material.

In the present work we investigated the influence of the shape of the multiplication area on the dark count rate of InGaAs/InAlAs SPADs in order to optimize its design parameters.

## Materials and Methods

The modelling was carried out with the T-CAD system. In the T-CAD simulation, specific values of the carrier lifetime were set as a parameter to calculate the recombination rate according to the Schockley-Reed-Hall mechanism. Also, radiative and Auger recombination were taken into account in the calculation. In finite element modelling, a system of equations consisting of continuity equations for electrons and holes and Poisson's equation was solved.

Three SPAD structures with different multiplication area shapes were proposed. The first structure with two levels of the multiplication area and a sharp transition, the second structure with three levels of the multiplication area and a sharp transition, and the third structure with three levels of the multiplication area and a smooth transition. The width of the multiplication area in the active region was the same in all structures, and was 0.8 μm.

## Results and Discussion

The simulation and analysis of electric field strength profiles and impact ionization in different structures have shown that creation of smooth transitions at the level boundaries of the multiplication area is an extremely effective method of DCR reduction in SPAD. If it was possible to achieve sufficiently smooth transitions (see Fig. 1) in the design of the device so that the dark count rate in the local boosts was not more than 20 dB greater than in the active region of the device, a three-level multiplication area can be used.

The main advantage of three-level multiplication area structure with a smooth transition is the low local increase in electric field strength (see Fig. 1). Such effect leads to higher value of quantum efficiency of SPAD during its operation.

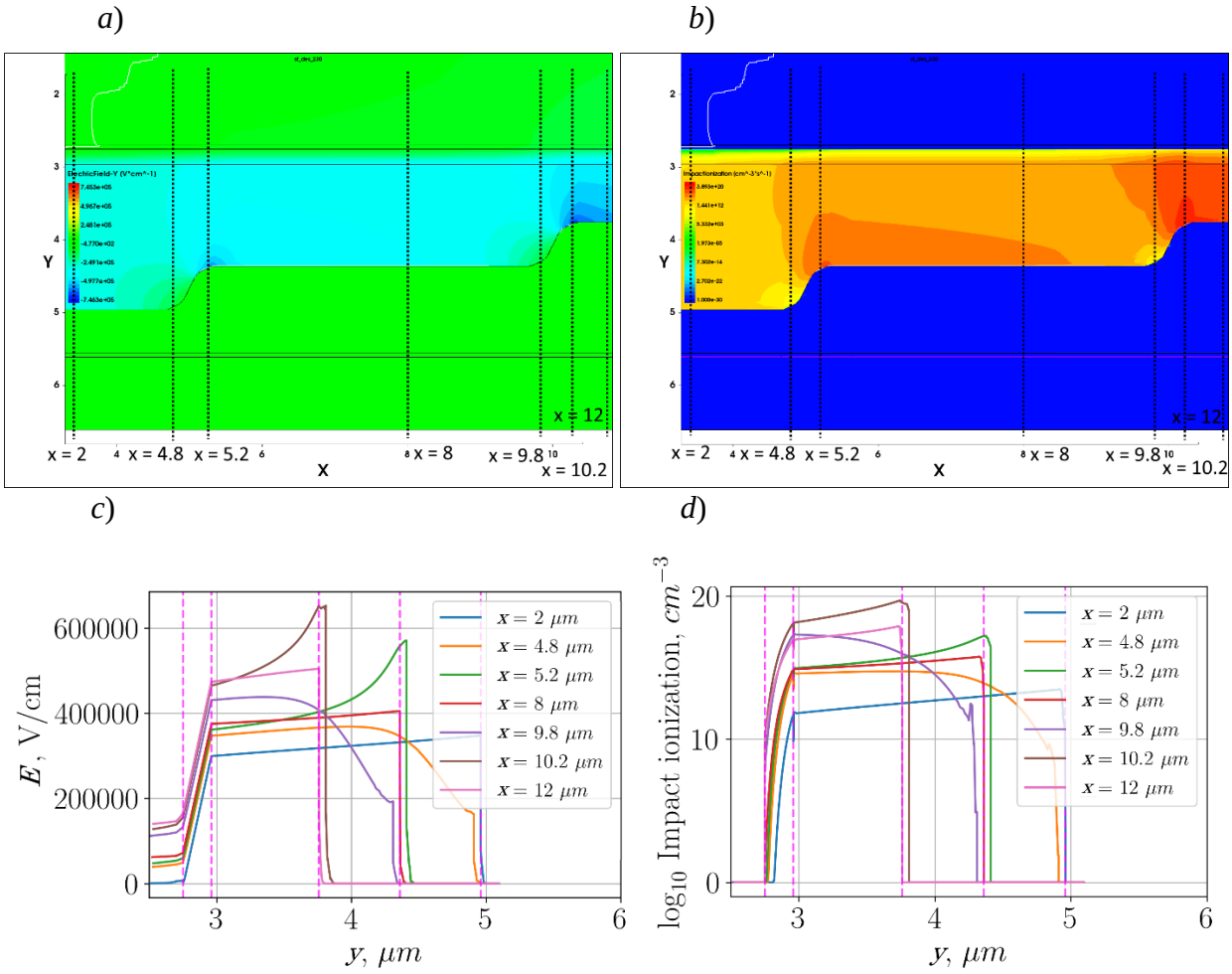


Fig. 1. A structure with three levels of the multiplication area with a smooth transition: (*a*) thermal map of the electric field strength *E* distribution; (*b*) thermal map of the impact ionization (*c*) graph of the electric field strength distribution over the cross sections shown in figure (*a*); (*d*) graph of the impact ionization distribution over the cross sections shown in figure (*b*)

## Conclusion

Therefore, a structure with three levels of multiplication area with a smooth transition is the most optimal. The developed SPAD structure with three levels of multiplication area and smooth transitions can also be used for avalanche photodiode devices operating in linear mode. This device has the following property: when the intensity increases by an order of magnitude, the current will similarly change by an order of magnitude, which is convenient in terms of the linearity of the characteristic. Moreover, the device has a small dark current, and therefore a low signal to noise ratio.

## Acknowledgments

The study was commissioned by JSCo «RZD».

## REFERENCES

1. **Baek S. H., Yang S. C., Park C. Y., Park C. W., Cho S. B., Ryu S. W.,** Room temperature quantum key distribution characteristics of low-noise InGaAs/InP single-photon avalanche diode, Journal of the Korean Physical Society. 78 (7) (2021) 634-641.

2. **Lee Y. S., Wu P. L., Chen Y. J., Shi J. W.,** Neat temporal performance of InGaAs/InAlAs single photon avalanche diode with stepwise electric field in multiplication layers, IEEE Access. 9 (2021) 32979-32985.

# Modernization of quantum frequency standard with optical pumping

**K G Arinushkina[2]✉, A P Valov[2], D A Boldarev[1], R A Dmitriev[2] and V V Davydov[1,2]**
[1]Peter the Great Saint-Petersburg Polytechnic University, Saint Petersburg, Russia;
[2]The Bonch-Bruevich Saint Petersburg State University of Telecommunications, Saint Petersburg, Russia;
✉k-arinushkina@mail.ru

**Abstract.** The development of information transmission systems, satellite navigation systems, metrological service systems leads to the need for constant modernization of the currently used quantum frequency standards. The paper presents a method for upgrading the quantum frequency standard in order to improve short-term stability. Experimental studies of the metrological characteristics of a quantum frequency standard with laser optical pumping have shown the effectiveness of the new development.

**Keywords:** time scale, stabilization, automatic frequency control, frequency stabilizer, cesium frequency standard, operational amplifier, remote sensing spacecraft, atomic beam tube.

## Introduction

Various scientific developments in recent decades have made it possible to make quantum standard frequencies (QFS) a source of highly stable, high-precision, spectrally pure electrical signals. The achieved frequency accuracy and stability made it possible to effectively use QFS as synchronizing generators in communication equipment and information transmission devices, as well as to use them as signal sources in radio measuring equipment.

Currently, the world continues to develop the use of satellite navigation systems in various fields of human activity. In the last decade, the GLONASS SNS has been actively developed in the Russian Federation, which, as experience shows, has a high accuracy in determining coordinates and is highly competitive compared to American, European and Chinese systems [1,2]. Improving the accuracy characteristics of the navigation system in determining coordinates in real time, in time, with an error of less than 1 m, largely depends on the improvement of the metrological characteristics of the QFS.

This paper considers the modernization of the block of the automatic frequency control system using the input of a thermal compensation device.

## Materials and Methods

The frequency standard with laser pumping on cesium-133 atoms works on the principle of adjusting the frequency of a quartz oscillator to the frequency of the cesium-133 atomic transition. To implement the noted frequency adjustment of the quartz oscillator, a microwave signal is applied to an atomic beam tube (ABT) filled with cesium-133 atoms. The ABT output signal contains a constant component and a variable that characterizes the deviation of the signal from the average value of the components of the error signal. On fig. 1. A QFS device with laser pumping is presented.

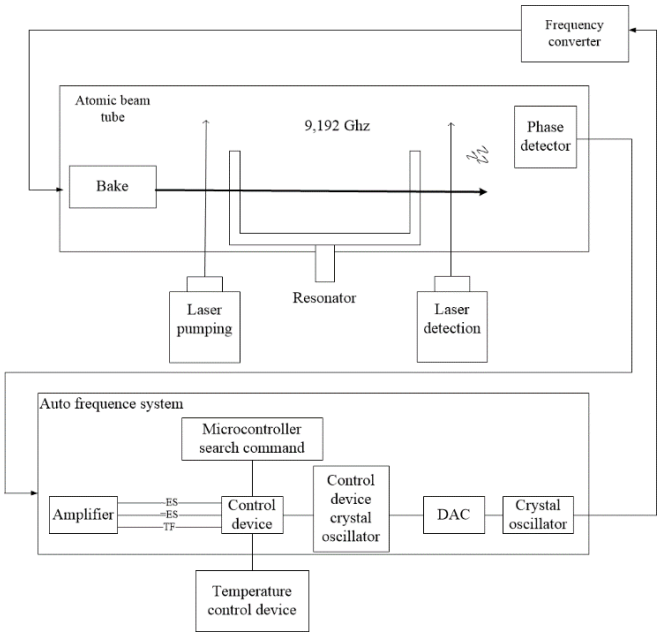


Fig. 1. QFS with laser pumping.

Fig. 2. Plot of Allan variance σy versus time t.

## Results and Discussion

The modernization of this device allows improving the metrological characteristics of the entire QFS system, since the signal from this block is used in other functional devices, including frequency converters and frequency synthesizers that form microwave signals for the quantum discriminator. The properties of these signals directly affect the metrological properties of the QFS system. On fig. 2 also shows the dependence of the change in the value of the Allan variance $\sigma_y(\tau)$ on time t for the updated and early QFS designs.

## Conclusion

The results obtained indicate an enhancement in the Allan variance $\sigma_y(t)$ by 5%. The conducted experiments have shown the efficiency of using automatic frequency control systems with the thermal compensation device developed by us.

## REFERENCES

1. **F. Riehle**, Frequency standard. Basic and applications. WILEY-VCH Verlag CmbH Co. KGaA: New-York, 2008.

2. **N. A. Lukashev, A.A. Petrov, V. V. Davydov, N.M. Grebenikova, and A.P. Valov**, “Improving performance of quantum frequency standard with laser pumping,” Proceedings of 18th International conference of Laser Optics ICLO-2018, vol. 8435889, pp. 271, Saint-Petersburg, July 2018.

# A cantilever type MEMS switch with enhanced contact force: the first results

**I. A. Belozerov**[1,2✉], **I. V. Uvarov**[1]

[1] Valiev Institute of Physics and Technology of Russian Academy of Sciences, Yaroslavl Branch, Yaroslavl, Russia;

[2] P.G. Demidov Yaroslavl State University, Yaroslavl, Russia

✉igas2580@yandex.ru

**Abstract.** MEMS switches are of particular interest for advanced radio electronic systems, but their application is limited by low reliability. The switches develop low contact force, which leads to high and unstable contact resistance. The force is usually increased by using complex shaped and large area electrodes, but a simple and compact design is more preferable. This work presents a switch based on a tiny cantilever. A technique for increasing the contact force by selecting the vertical dimensions of the device is described. The trial samples are fabricated and tested. Their performance is compared with theoretical predictions.

**Keywords:** MEMS switch, cantilever, contact force, contact resistance, pull-in voltage

**Funding:** This work is supported by the program № FFNN-2022-0017 of the Ministry of Science and Higher Education of Russia for Valiev Institute of Physics and Technology of RAS.

## Introduction

Microelectromechanical systems (MEMS) switches are actively considered as promising electronic components for RF and microwave systems [1]. Small size, low insertion loss, high isolation, and low power consumption make them attractive for use in 5G networks, adaptive antennas, aviation and space industry. A conventional MEMS switch is a cantilever located above driving and signal electrodes. Small size of the cantilever ensures mechanical stress robustness and short switching time. However, such devices usually provide a small contact force, which increases the contact resistance and makes it unstable. This work is devoted to the MEMS switch based on a compact cantilever, the vertical dimensions of which are chosen to increase the contact and restoring forces.

## Materials and Methods

The movable electrode is an aluminum beam with a length of 50 µm, a width of the fixed end of 10 µm and a width of the free end of 20 µm. The driving electrode surrounds the signal one in order to increase the area of the electric field. The lateral size and shape of the electrodes were optimized previously [2]. In the present work, the contact force $F_C$ is increased by optimizing the vertical dimensions of the switch. The proposed technique also takes into account restoring force $F_R$, pull-in voltage $V_{pull\text{-}in}$ and collapse voltage. These characteristics are calculated analytically and by the finite element method. The switch is fabricated on a thermally oxidized silicon wafer using a previously developed procedure [3]. Ruthenium is used as the contact material.

## Results and Discussion

The first step is to select the height of the contact bump. An optimal value is of 0.2 µm, at which $F_C$ = 32 µN, and the collapse occurs at a rather high voltage of 220 V. Next, the dependence of the contact and restoring forces on the cantilever thickness $t$ and the air gap $g_0$ is plotted, see Figure 1. The switch should produce $F_C$ higher than 100 µN, and the ratio $F_C/F_R$ must be lower than 3 in order to overcome stiction. These conditions are fulfilled at $t$ = 4 µm and $g_0$ = 0.6 µm. However, the fabrication of a switch with such size requires the development of technical processes. For a trial run the values $t$ = 3 µm and $g_0$ = 1 µm are chosen. These dimensions provide the contact and restoring forces of 50 µN each and the pull-in voltage of 64 V.

The fabricated switch is shown in Figure 2. The devices with a single and double cantilever have $V_{pull\text{-}in}$ of 28 and 37 V, respectively, which is significantly lower than the calculated value. The probable reason for the discrepancy is a decrease of $g_0$ due to the tilt of the cantilever under

the internal mechanical stress. After 25 thousand switching cycles, $V_{pull\text{-}in}$ of single and double switches falls to 24 and 34 V. This drop is explained by aluminum creep or relaxation of internal stress.

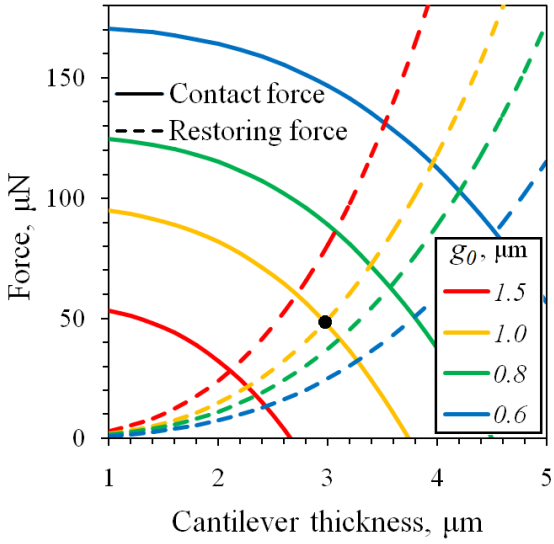


Fig. 1. Contact and restoring forces as a function of the cantilever thickness for various values of the gap.

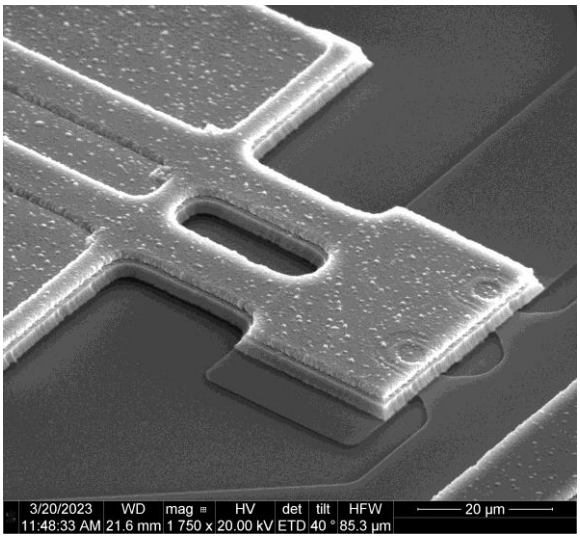


Fig. 2. SEM image of a MEMS switch based on a double cantilever.


## Acknowledgments

The study is performed using the equipment of Facilities Sharing Centre “Diagnostics of Micro- and Nanostructures”.


## REFERENCES


1. **Rebeiz, G. M.; Patel, C. D.; Han, S. K.; Ko, C.-H.; Ho, K. M. J.**, The search for a reliable MEMS switch. IEEE Microw. Mag. 2013, 14, 57-67.

2. **Belozerov, I. A., Uvarov, I. V.**, Performance optimization of the cantilever-based MEMS switch. St. Petersburg State Polytechnical University Journal. Physics and Mathematics, vol. 15, no. 3.2, pp. 140–144, 2022.

3. **Uvarov, I.V., Marukhin, N.V., Naumov, V.V.**, Contact resistance and lifecycle of a single- and multiple-contact MEMS switch. Microsyst Technol 25, 4135–4141, 2019.

# Application of the transmit birdcage coil for wireless power transfer in magnetic resonance imaging

**Oleg I. Burmistrov[1], Nikita V. Mikhailov[1], Dmitrii S. Dashkevich[1], Nikita A. Olekhno[1], Pavel S. Seregin[1]**

[1]ITMO University, 197101 Saint Petersburg, Russia

E-mail: oleg.burmistrov@metalab.ifmo.ru

**Abstract**. In this work, we develop an application of a transmit birdcage coil for wireless power transfer at higher-order birdcage modes in magnetic resonance imaging. The study includes numerical simulations and an experimental verification of a numerical model with a clinical birdcage coil. For each studied mode, we obtained numerically electric and magnetic fields inside the magnetic resonance imaging scanner with a phantom, specific absorption rate with a voxel model of human, and the resulting voltage on receiving antennas. We estimate the optimal mode for realizing wireless power transfer in magnetic resonance imaging.

**1. Introduction.** Nowadays, magnetic resonance imaging (MRI) is a key noninvasive method of medical diagnostic. MRI scanners often require additional near field antennas (local coils) placed inside an MRI scanner near the patient. Such coils require an additional power supply typically implemented with bulky cables which are uncomfortable for a patient and restrict patient positioning. Moreover, the cables and connectors require regular replacement accompanied by corresponding maintenance costs. Wireless power transfer (WPT) to local coils and devices in MRI-bore is considered as a potential solution. Currently, WPT can be implemented at a scanning frequency with power limitation about 500 mW [1] or at a different frequency with an additional transmitting antenna [2 – 3]. We propose a solution that allows using a widely spread birdcage coil which is a part of most MRI scanners instead of additional transmitting antennas. As we demonstrate, such an approach relying on the use of higher-order modes of the birdcage coil does not introduce additional artefacts in MR images since such modes are orthogonal to the scanning mode and their frequencies also considerably differ from the scanning frequency.

**2. Methods.** For numerical simulations, we apply CST Microwave Studio 2022 software package. The numerical model (fig.1a) includes the birdcage coil with a screen, a receiving system, a matching circuit, and a voxel model of a human or a phantom load for the birdcage coil. The receive system includes two orthogonal loop antennas. In the experiment, the screen consists of a copper mesh on a dielectric case with low permittivity, while in numerical simulations it is implemented as a solid copper surface. The birdcage coil corresponds to Siemens Avanto 1.5T scanner and the phantom is from General Electric MRI scanner. The matching circuit includes high quality surface mounted device (SMD) capacitors and variable capacitors. Their capacitance and equivalent serial resistance were measured with Keysight E4991B Impedance Analyser. The numerical model was verified through a comparison of S-parameters from the simulations the experiment with Planar S5048 vector

network analyser. The receive system is located at the distance of 60 mm from the edge of the birdcage.

**3. Results.** To obtain the frequencies of the birdcage coil modes, we evaluate Z-parameters in a model without a receive system. Then, we calculate a specific absorption rate and magnetic and electric fields for five modes of the birdcage coil, two of which are linearly polarized and three (including the fundamental mode at which scanning is performed) have circular polarization. Maximum efficiency is obtained for linear vertical polarization at the frequency of 31.21 MHz since the vertical antenna is closer to the edge of the birdcage coil then a horizontal one (fig. 1a). The efficiency of WPT depends on the distance between the receive system and the edge of the birdcage coil, and larger distances correspond to lower efficiency. As demonstrated by the simulations of specific absorption rate (fig.1b), the safety of WPT at a higher-order mode of the birdcage coil is better than for WPT at the fundamental mode with equal input power as electric and magnetic fields at the higher order mode do not penetrate deep into a scanned object.

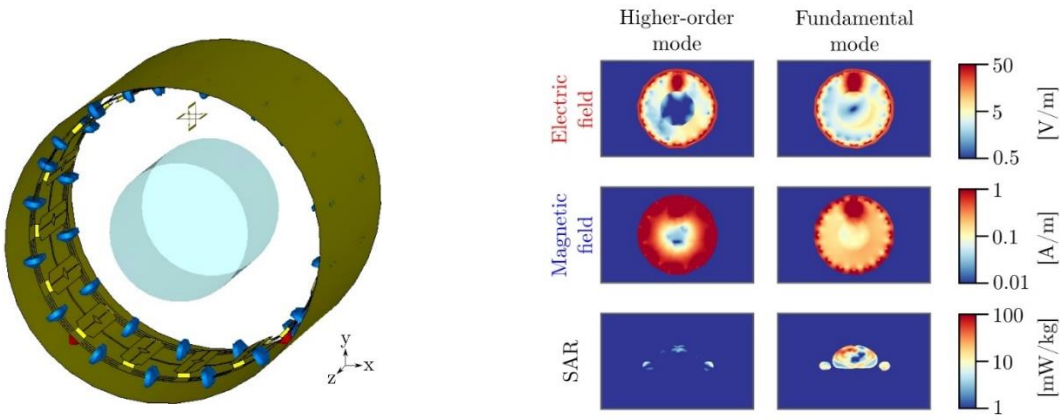


(a) (b)

Figure 1. Numerical simulations of the wireless power transfer system in MRI: (a) 3D model with a birdcage coil, screen, phantom, and receive system; (b) maps of specific absorption rate (SAR), magnetic and electric fields in axial (xy) plane for fundamental (61.67 MHz) and higher order (31.21 MHz) modes.

**4. Conclusion.** The optimal mode for WPT at the higher order modes of the birdcage coil has the frequency of 31.21 MHz and is linearly polarized. The efficiency and safety for WPT at this mode are better than for WPT at the fundamental mode. The transmitted power is sufficient to supply the main types of receive local coils and medical sensors in MRI bore. Efficiency of WPT at the higher order mode depends on the distance between the edge of the birdcage coil and the receive system, which should be considered during the placement of the receive system and local coils.

**Acknowledgments**
This work was supported by the Russian Science Foundation project No. 21-79-30038.

**References**

[1] P. Seregin, O. Burmistrov, G. Solomakha, E. Kretov, N. Olekhno, and A. Slobozhanyuk, *Phys. Rev. Applied* **17**, 044014 (2022)
[2] M. Venkateswaran, M. Kurpad, J. Brown, S. Fain and D. van der Weide, *42nd Annual International Conference of the IEEE EMBC*, 1469-1472 (2020)
[3] A. Ganti, J. Lin, T. Wynn, and T. Ortiz, *Wireless Power Transfer*, **6**, 138–153 (2019)

# Investigation of a method for improving phase noise in the frequency standard generator block

**A. P. Valov [1]✉, R. A. Dmitriev [1], D.A. Boldarev [2], V.V. Davydov[2]**
[1] The Bonch-Bruevich Saint Petersburg State University of Telecommunications, Saint Petersburg, Russia
[2] Peter the Great Saint-Petersburg Polytechnic University, Saint Petersburg, Russia;
✉tony.valov2015@yandex.ru

**Abstract.** In the modern world, information transmission systems, telecommunication and satellite navigation systems, as well as metrological services play an important role in our lives. However, the development of these systems leads to the constant need to upgrade the currently used quantum frequency standards. To improve the short-term stability of the frequency standard, a new method has been developed to upgrade the oscillator unit and the frequency standard output amplifiers. In the course of experimental studies of the metrological characteristics of the quantum frequency standard based on rubidium-87 atoms, the effectiveness of the new development was shown.

**Keywords:** Atomic clock, frequency standard, phase noise, metrology, stabilization.

## Introduction

Modern science requires accurate measurements of time and frequency to conduct experiments in various fields, including atomic physics, geodesy, radio astronomy, and satellite navigation. Quantum frequency standards (QFS) are especially important devices for ensuring the high stability of systems [1, 2].

An important functional device of the QFS is the block of the generator and output signal amplifiers (generator block), which is also the source of the QFS reference signal. Modernization of the generator block allows improving the metrological characteristics of the entire QFS, including the frequency and accuracy of time synchronization for satellite navigation. Since different QFS devices use the same signal, upgrading only individual nodes or blocks can lead to a significant improvement in the performance of the entire device.

## Materials and Methods

Generator block is used to form, multiply and maintain the amplitude of a signal with a frequency of 5 MHz in the rubidium frequency standard. The signal passes through several amplifiers and filters, and then goes to the frequency converter and synthesizer for further amplification up to the frequency of the quantum transition of rubidium-87 atoms in the quantum discriminator. The new design of the oscillator unit and frequency output amplifiers uses bipolar type transistors with low phase noise characteristics and provides high output frequency accuracy, sideband suppression and low temperature dependence. This design is unified for use in various QSC models and developed on the basis of domestic electronic components.

## Results and Discussion

According to the research results, it has been established that the new design is capable of reducing the spectral density of phase noise to a level comparable to that of a quartz generator with the best characteristics. Such a reduction in the spectral density of phase noise also allows for a reduction in their influence on subsequent devices in the frequency standard, which in turn improves short-term frequency stability.

Measurements of the old generator block design and the modified design are shown in Fig.1 and Fig.2.

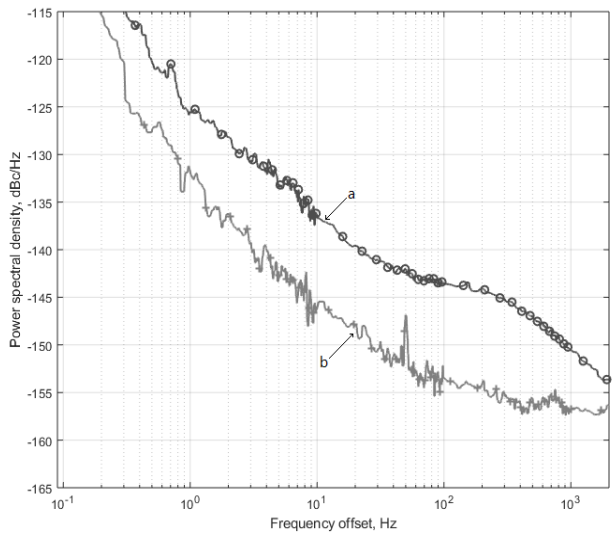


Fig. 1. Power spectral density of phase noises: a – signal of old generator block design; b − low-noise quartz oscillator

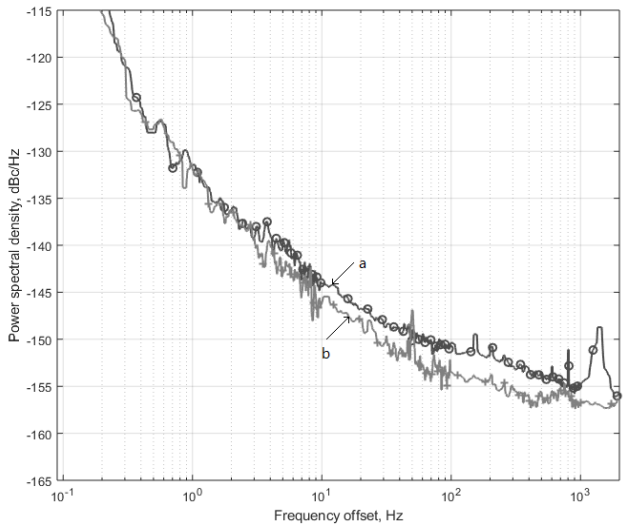


Fig. 2. Power spectral density of phase noises: a – signal of modified generator block design; b − low-noise quartz oscillator

Measurement of the root mean square deviation with a measurement time of 1 second using a sliding window over a 20-hour observation period of the output signal of the RNG with a modernized generator block and output amplifiers showed a decrease in this value compared to the old design.

## Conclusion

The results of the research on the new design of the generator block and output signal amplifiers showed the feasibility of using this solution as part of a quantum frequency standard. As a result of the tests conducted on the generator block and output signal amplifiers in the QFS, a 6% reduction in the level of spectral phase noise was recorded at tuning frequencies of 10-100 Hz, and allowed to improve the short-term frequency stability by 7%.

## REFERENCES

1. **Riehle F.,** Frequency standard. Basic and applications, WILEY-VCH Verlag CmbH Co. KGaA: New-York, 2008.

2. **Arinushkina, K., Grevsteva, A., Valov, A., Lukashev, N.** Development of the Controllable C-field Current Stabilizer for the Atomic Beam Tube of the Cesium Atom Clock. Springer Proceedings in Physics. 268 (2022) 589–596.

# Construction features of quantum frequency standard on mercury-199 ions for Global Navigation Satellite Systems

**Wang Ding**[1]✉ **and V. V. Davydov**[1, 2]
[1] Peter the Great Saint-Petersburg Polytechnic University, Saint Petersburg, Russia;
[2] The Bonch-Bruevich Saint Petersburg State University of Telecommunications, Saint Petersburg, Russia.
✉ jssdwang06@mail.ru

**Abstract.** The situation to ensure the long-term operation of atomic clocks in orbit or during a long flight in outer space (between planets) is considered. The problems that arise during the operation of various models of atomic clocks under these conditions are noted. It is established that the most promising for solving these problems is the use of atomic clocks on mercury-199 ions. One of the variants of such clock on the USA satellite has been in space for more than 3 years. Experimental data showed that without adjusting the atomic clock during communication sessions with the Earth, the frequency did not deteriorate below $10^{-13}$. This figure is much higher than the stability values for all other types of atomic clocks. Analysis of various studies has shown that the value of frequency stability in atomic clocks on mercury-199 ions is determined by the parameters of the trap and the stability of the pumping source. In this work, we propose options for determining the optimal parameters of the trap under conditions of limiting the volume and mass of atomic clocks.

**Keywords:** Global navigation satellite systems, atomic clocks on mercury-199 ions, ion trap, Mathieu equation, optimal parameters

## Introduction

With the development of science, technology and the exploration of deep space, there is a need for more accurate and stable atomic clocks under long-term operating conditions. Especially in cases where long-term contact with the ground station and the base space station is excluded. Attention gradually shifts to the atomic clocks on mercury-199 ions. Atomic clocks on mercury-199 ions are the first microwave atomic clock to be sent into space after cesium, rubidium, and passive hydrogen maser, compared to them the new atomic clocks have better advantages, such as using ion traps to trap ions, which effectively reduces the collision of ions with walls, and using spectral lamps 202 rather than lases to generate transition wavelengths (194 nm). The degradation of optical emission sources is much less. This made it possible to consider atomic clocks on mercury-199 ions the best choice for the next generation of satellite and spacecraft [1-3].

## Principle of atomic clocks on mercury-199 ions

The principle of the atomic clocks on mercury-199 ions is as follows. Mercury-199 ions are trapped in an ion trap (usually a linear ion trap that consists of four parallel rods with opposite voltages on two adjacent rods) and interact with the wavelength 194 nm generated by the mercury ion lamp 202 to complete the inversion of particle number, and at this point the fluorescence recorded by the photodetector is weakened. Then, under the action of the applied microwave field (40.5GHz), it occurs stimulated absorption, while the intensity of fluorescence increases and is locked on the local oscillator.

## Comparison of quantum frequency standard on mercury-199 ions constructions for the USA, Russia, and China

Figure 1 shows constructions of atomic clocks on mercury-199 ions for the USA, Russia, and China.

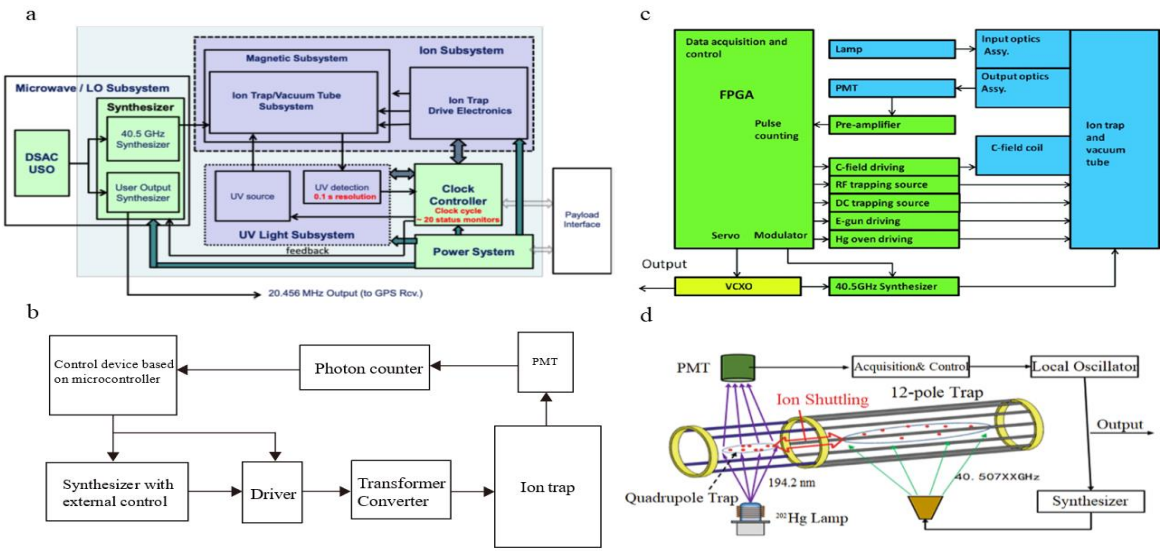


Fig. 1. Schematic diagram of the atomic clocks on mercury-199 ions of the USA, Russian and Chinese. Here a is the diagram of the USA [1], b is the diagram of Russia, c is the diagram of China [2], and d is the diagram of China for ground application [3].

The main difference in their constructions is in the ion traps: the USA uses a combination of linear (4 rods) and multipole ion traps (16 rods) with short-term stability of 7·10-14 [1], Russia and China use linear ion traps with short-term stability of 8·10-14 and 4.5·10-14 [2]. It should be noted that China also uses multipole ion traps (12 rods) for ground-based applications. There is such trap rod application in the USA and the Russian Federation.

## Conclusion

Analysis of the obtained results shows that optimizing the parameters of the rod and the choosing their configuration for a specific trap construction is a key task for developers. Limitations on the size and weight of the trap creates problems in the calculation of its parameters and the use of materials. It has been established that the most interesting solutions can be obtained using the Mathieu equation by introducing coefficients that take into account the material of the trap rods.

## Acknowledgments

This thesis was supported by the China Scholarship Council.

## REFERENCES

1. **Burt E.A., Prestage J.D., Tjoelker R.L., Enzer D.G., Kuang D., Murphy D.W., Robison D.E., Seubert J.M., Wang R.T., Ely T.A.,** Demonstration of a trapped-ion atomic clock in space, Nature. 595 (7865) (2021) 43–47.

2. **Liu, H., Chen, Y., Yan, B., Liu, G., She, L.,** Progress Towards a Miniaturized Mercury Ion Clock for Space Application, China Satellite Navigation Conference (CSNC) 2020 Proceedings. II (651) (2020) 557-561.

3. **Yan, B., Liu, H., Chen, Y., Liu, G., Wang, J., She, L.,** Research Progress on Mercury Ion Microwave Clock for Time Keeping, China Satellite Navigation Conference (CSNC 2022) Proceedings. 910 345-352.

# Investigation of a method for improving phase noise in the frequency standard generator block

**A. P. Valov** [1✉], **R. A. Dmitriev** [1], **D.A. Boldarev** [2]

[1] The Bonch-Bruevich Saint Petersburg State University of Telecommunications, Saint Petersburg, Russia

[2] Peter the Great Saint-Petersburg Polytechnic University, Saint Petersburg, Russia;

✉tony.valov2015@yandex.ru

**Abstract.** In the modern world, information transmission systems, telecommunication and satellite navigation systems, as well as metrological services play an important role in our lives. However, the development of these systems leads to the constant need to upgrade the currently used quantum frequency standards. To improve the short-term stability of the frequency standard, a new method has been developed to upgrade the oscillator unit and the frequency standard output amplifiers. In the course of experimental studies of the metrological characteristics of the quantum frequency standard based on rubidium-87 atoms, the effectiveness of the new development was shown.

**Keywords:** Atomic clock, frequency standard, phase noise, metrology, stabilization.

## Introduction

Modern science requires accurate measurements of time and frequency to conduct experiments in various fields, including atomic physics, geodesy, radio astronomy, and satellite navigation. Quantum frequency standards (QFS) are especially important devices for ensuring the high stability of systems [1, 2].

An important functional device of the QFS is the block of the generator and output signal amplifiers (generator block), which is also the source of the QFS reference signal. Modernization of the generator block allows improving the metrological characteristics of the entire QFS, including the frequency and accuracy of time synchronization for satellite navigation. Since different QFS devices use the same signal, upgrading only individual nodes or blocks can lead to a significant improvement in the performance of the entire device.

## Materials and Methods

Generator block is used to form, multiply and maintain the amplitude of a signal with a frequency of 5 MHz in the rubidium frequency standard. The signal passes through several amplifiers and filters, and then goes to the frequency converter and synthesizer for further amplification up to the frequency of the quantum transition of rubidium-87 atoms in the quantum discriminator. The new design of the oscillator unit and frequency output amplifiers uses bipolar type transistors with low phase noise characteristics and provides high output frequency accuracy, sideband suppression and low temperature dependence. This design is unified for use in various QSC models and developed on the basis of domestic electronic components.

## Results and Discussion

According to the research results, it has been established that the new design is capable of reducing the spectral density of phase noise to a level comparable to that of a quartz generator with the best characteristics. Such a reduction in the spectral density of phase noise also allows for a reduction in their influence on subsequent devices in the frequency standard, which in turn improves short-term frequency stability.

Measurements of the old generator block design and the modified design are shown in Fig.1 and Fig.2.

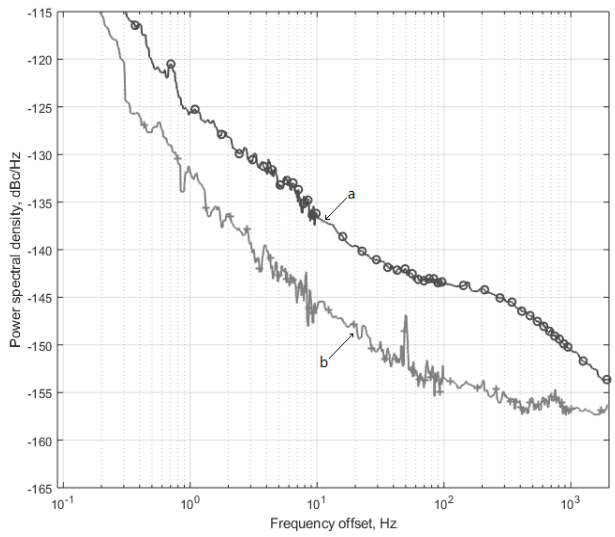


Fig. 1. Power spectral density of phase noises: a – signal of old generator block design; b − low-noise quartz oscillator

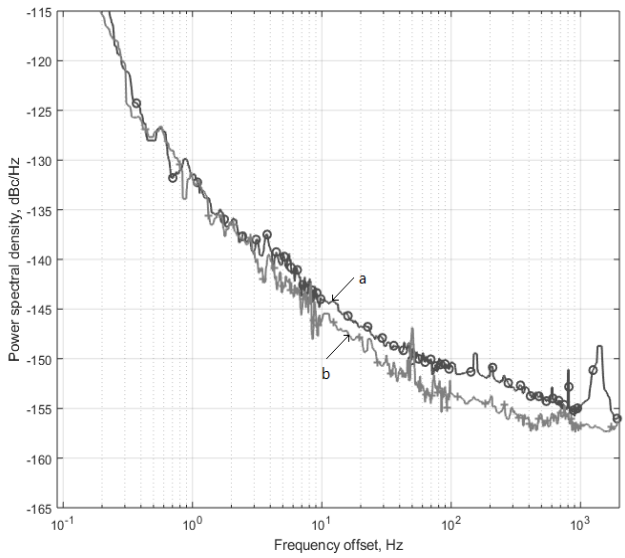


Fig. 2. Power spectral density of phase noises: a – signal of modified generator block design; b − low-noise quartz oscillator

Measurement of the root mean square deviation with a measurement time of 1 second using a sliding window over a 20-hour observation period of the output signal of the RNG with a modernized generator block and output amplifiers showed a decrease in this value compared to the old design.

## Conclusion

The results of the research on the new design of the generator block and output signal amplifiers showed the feasibility of using this solution as part of a quantum frequency standard. As a result of the tests conducted on the generator block and output signal amplifiers in the QFS, a 6% reduction in the level of spectral phase noise was recorded at tuning frequencies of 10-100 Hz, and allowed to improve the short-term frequency stability by 7%.

## REFERENCES

1. **Riehle F.,** Frequency standard. Basic and applications, WILEY-VCH Verlag CmbH Co. KGaA: New-York, 2008.

2. **Arinushkina, K., Grevsteva, A., Valov, A., Lukashev, N.,** Development of the Controllable C-field Current Stabilizer for the Atomic Beam Tube of the Cesium Atom Clock Springer Proceedings in Physics, 2022, 268, pp. 589–596.

# Long-term stability of GaAs-based pseudomorphic transistor heterostructures with InGaAs channel

**E. V. Nikitina** ✉, **T. N. Berezovskaya**, **E. I. Vasilkova,** **E. V. Pirogov**, **M. S. Sobolev**
Alferov University, Khlopina 8/3, 194021 St. Petersburg
✉ mail.nikitina@mail.ru

**Abstract.** Variation of the electrophysical and structural parameters of GaAs-based pseudomorphic transistor heterostructures with an InGaAs channel during more than eleven-year storage in natural conditions have been investigated. It was found that the values of the electrophysical parameters remained within specified limits (taking into account measurement errors) after 11 years of storage. The structural properties (thickness and composition of the InGaAs channel) of pseudomorphic heterostructures have undergone significant changes associated with the InGaAs channel layer broadening due to atomic diffusion.

**Keywords:** pseudomorphic transistor heterostructures, long-term parameter stability

**Funding:** The study was funded by the Ministry of Science and Higher Education of the Russian Federation (No. FSRM-2022-0002 (0791-2022-0002)).

## Introduction

Manufactured electronic semiconductor devices such as transistors and diodes are typically examined with a reliability testing. One of the issues leading to the device's inoperability is an ageing failure – that is a failure the probability of which increases due to accumulated deterioration over a calendar time [1]. Ageing failure may arise from the material degradation due to internal processes and (or) environmental impact.

In the present work, changes in the inner characteristics of the pseudomorphic high electron mobility transistor (pHEMT) heterostructures on GaAs substrates were investigated. Studies of the parameter stability during long-term storage of transistor structures are necessary to establish the failure mechanism, especially those resulting from a smooth change in the values of one or more parameters of the heterostructure. Defining the failure mechanism and ensuring the stability of semiconductor devices during long-term storage and operation remains relevant to this day [2, 3].

The functional purpose of the HEMT transistor heterostructures is to provide the high carrier mobility in a given range of carrier concentration values. Therefore, the observed characteristics of the structures included electrophysical parameters: concentration and mobility of the main charge carriers and the sheet resistance in the InGaAs transistor channel. Structural parameters (InGaAs channel composition and thickness) were also investigated.

## Materials and Methods

The pHEMT structures selected for testing were pseudomorphic heterostructures with high electron mobility in a system of Ga-In-Al-As materials. The conventional pHEMT heterostructure design consists of GaAs buffer layer, undoped $In_xGa_{1-x}As$ channel with a thickness of (12-15) nm and In molar fraction x = (0.16-0.18), Si-doped AlGaAs barrier layer and GaAs top contact layer. The studied transistor structures were grown on semi-insulating gallium arsenide substrates by molecular beam epitaxy (MBE) using a semi-industrial Riber49 setup.

Transistor parameter studies were carried out according to the developed testing program using certified measuring instruments to ensure the uniformity of measurements during prolonged research. Test samples put in individual plastic containers were stored indoors under normal climatic conditions. The tests were conducted regularly, and the overall duration of the studies exceeded 11 years. The concentration and mobility of the main charge carriers were determined by the Hall-based method, while the sheet resistance was examined by the eddy-current method using the non-contact resistance measurements. The photoluminescence (PL) peak wavelength was determined by measuring the PL spectrum in the center of the heterostructure. The crystalline parameters of the channel layer were also analyzed using X-ray diffraction method.

## Results and Discussion

During the design of pHEMT heterostructures, limiting values for the concentration and mobility of carriers in the InGaAs channel were established. The concentration of the main charge carriers should be at least $1.80 \cdot 10^{12}$ $cm^{-2}$ while the carrier mobility should be no less than $6.0 \cdot 10^{3}$ $cm^{2}V^{-1}sec^{-1}$. The minimum indium molar fraction in the InGaAs channel required to achieve the specified values of the electrophysical parameters was determined as 0.160 rel. units. Immediately after the MBE growth all these heterostructure parameters were equal to $1.91 \cdot 10^{12}$ $cm^{-2}$, $5.9 \cdot 10^{3}$ $cm^{2}V^{-1}sec^{-1}$, and 0.165 rel. units for electron concentration, mobility and In molar fraction in the channel respectively with a measurement error estimated to 8 %.

As was shown by the studies, the main carrier concentration value gradually decreased over time and approached the established lower boundary, while the mobility of charge carriers gradually increased. However, the values of the electrophysical parameters remained within the specified limits (taking into account the measurement error) and met the established requirements throughout the course of studies.

A simultaneous decrease in the electron concentration and increase in the electron mobility with longer storage life of the heterostructures may be associated with a variation of structural parameters (composition and thickness) in the InGaAs channel. With the indium interdiffusion, once abrupt channel-to-barrier heterointerfaces become smoothed over time and the thickness of the InGaAs channel increases, and thus the effective InAs composition decreases. Increased thickness of the InGaAs channel also leads to a decrease in the electron concentration, since the same number of carriers become distributed over the area of larger thickness.

This assumption was confirmed by the PL studies of the samples. The PL maximum monotonically shifted to shorter wavelengths with storage time and after 4 years was at the lower limit of established allowed values. The PL measurement data indicated the broadening of the InGaAs channel, since the total amount of indium in the channel remained unchanged after the end of epitaxial growth. Furthermore, the X-ray diffraction measurements showed that after 10 years of storage the indium molar fraction was $(0.140 \pm 0.005)$ rel. units, which is significantly less than the minimum allowable value.

## Conclusion

During long-term storage of pHEMT transistor heterostructures for more than eleven years, the values of their electrophysical parameters have slightly changed, although remained within the specified limits (taking into account the measurement error) still after eleven years of storage. A decrease in the carrier concentration with a simultaneous increase in the carrier mobility is associated with an alteration of the InGaAs channel structural parameters (composition and thickness). Due to atomic diffusion, the thickness of the InGaAs channel increased, and the InAs molar fraction decreased from 0.165 to 0.140 rel. units (as obtained by X-ray diffraction measurements). This effect was also evident from a decrease in the PL peak wavelength, the value of which reached its lower limit after three years of storage in natural conditions.

## REFERENCES

1. GOST 27.002-2009. Dependability in technics. Terms and definitions. Moscow: Standartinform; 2011. (in Russian).

2. **Sidnyaev N.I., Savchenko V.P., Klochkova D.V.**, Analysis of failure physics to estimate reliability indices of the radio-electronic devices in modern radar systems, Engineering Journal: Science and Innovation. 12 (2013) 35. (in Russian).

3. **Nikitina, E.V., Lazarenko, A.A., Pirogov, E.V., Sobolev M.S., Berezovskaya T.N.**, The influence of metamorphic-buffer layer design on the retention of characteristics of InGaAs/GaAs metamorphic HEMT, Technical Physics Letters. 43 (2017) 863–865.

# Construction features of quantum frequency standard on mercury-199 ions for Global Navigation Satellite Systems

**Wang Ding[1] and V V Davydov[1, 2]**
[1]Peter the Great St. Petersburg Polytechnic University, St. Petersburg, Russia
[2]Bonch-Bruevich Saint-Petersburg State University of Telecommunications, St. Petersburg, Russia

jssdwang06@mail.ru

**Abstract.** The situation to ensure the long-term operation of atomic clocks in orbit or during a long flight in outer space (between planets) is considered. The problems that arise during the operation of various models of atomic clocks under these conditions are noted. It is established that the most promising for solving these problems is the use of atomic clocks on mercury-199 ions. One of the variants of such clock on the USA satellite has been in space for more than 3 years. Experimental data showed that without adjusting the atomic clock during communication sessions with the Earth, the frequency did not deteriorate below $10^{-13}$. This figure is much higher than the stability values for all other types of atomic clocks. Analysis of various studies has shown that the value of frequency stability in atomic clocks on mercury-199 ions is determined by the parameters of the trap and the stability of the pumping source. In this work, we propose options for determining the optimal parameters of the trap under conditions of limiting the volume and mass of atomic clocks.

## 1. Introduction

With the development of science, technology and the exploration of deep space, there is a need for more accurate and stable atomic clocks under long-term operating conditions. Especially in cases where long-term contact with the ground station and the base space station is excluded. Attention gradually shifts to the atomic clocks on mercury-199 ions. Atomic clocks on mercury-199 ions are the first microwave atomic clock to be sent into space after cesium, rubidium, and passive hydrogen maser, compared to them the new atomic clocks have better advantages, such as using ion traps to trap ions, which effectively reduces the collision of ions with walls, and using spectral lamps 202 rather than lases to generate transition wavelengths (194 nm). The degradation of optical emission sources is much less. This made it possible to consider atomic clocks on mercury-199 ions the best choice for the next generation of satellite and spacecraft [1-3].

## 2. Principle of atomic clocks on mercury-199 ions

The principle of the atomic clocks on mercury-199 ions is as follows. Mercury-199 ions are trapped in an ion trap (usually a linear ion trap that consists of four parallel rods with opposite voltages on two adjacent rods) and interact with the wavelength 194 nm generated by the mercury ion lamp 202 to complete the inversion of particle number, and at this point the fluorescence recorded by the photodetector is weakened. Then, under the action of the applied microwave field (40.5GHz), it occurs stimulated absorption, while the intensity of fluorescence increases and is locked on the local oscillator.

## 3. Comparison of quantum frequency standard on mercury-199 ions constructions for the USA, Russia, and China

Figure 1 shows constructions of atomic clocks on mercury-199 ions for the USA, Russia, and China.

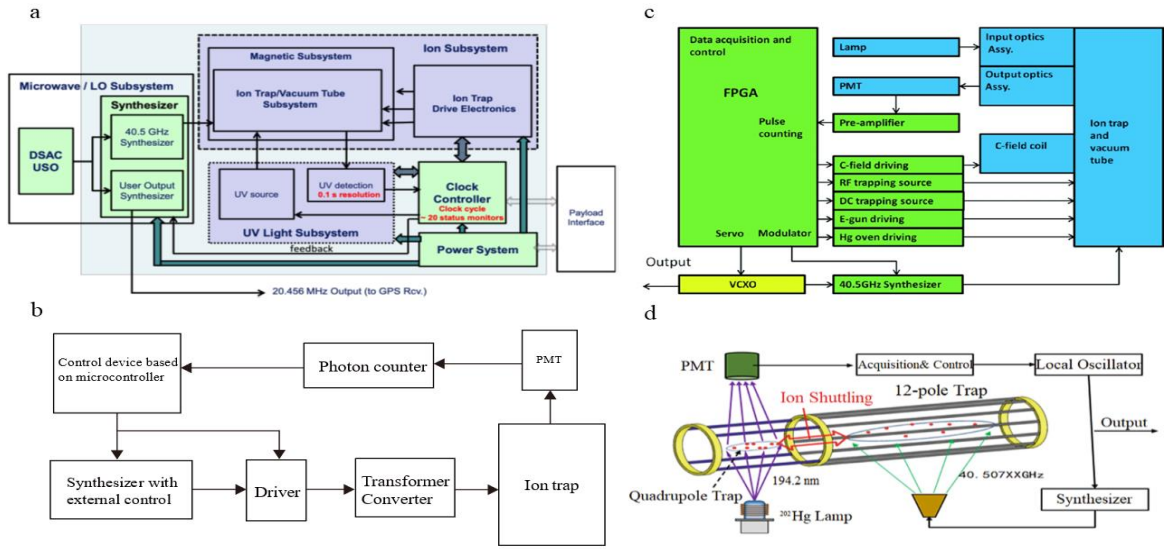


**Fig. 1.** Schematic diagram of the atomic clocks on mercury-199 ions of the USA, Russian and Chinese. Here a is the diagram of the USA [1], b is the diagram of Russia, c is the diagram of China [2], and d is the diagram of China for ground application [3].

The main difference in their constructions is in the ion traps: the USA uses a combination of linear (4 rods) and multipole ion traps (16 rods) with short-term stability of $7 \cdot 10^{-14}$ [1], Russia and China use linear ion traps with short-term stability of $8 \cdot 10^{-14}$ and $4.5 \cdot 10^{-14}$ [2]. It should be noted that China also uses multipole ion traps (12 rods) for ground-based applications. There is such trap rod application in the USA and the Russian Federation.

## 4. Conclusion

Analysis of the obtained results shows that optimizing the parameters of the rod and the choosing their configuration for a specific trap construction is a key task for developers. Limitations on the size and weight of the trap creates problems in the calculation of its parameters and the use of materials. It has been established that the most interesting solutions can be obtained using the Mathieu equation by introducing coefficients that take into account the material of the trap rods.


## Acknowledgmens

This thesis was supported by the China Scholarship Council.


## References


[1] Burt E A, Prestage J D, Tjoelker R L, Enzer D G, Kuang D, Murphy D W, Robison D E, Seubert J M, Wang R T and Ely T A 2021 *Nature* **595 (7865)** 43-47

[2] Liu H, Chen Y, Yan B, Liu G and She L 2020 *China Satellite Navigation Conference (CSNC) 2020 Proceedings: Volume II. CSNC 2020. Lecture Notes in Electrical Engineering* **651** 557-561

[3] Yan B, Liu H, Chen Y, Liu G, Liu W, Wang J and She L 2022 *China Satellite Navigation Conference (CSNC 2022) Proceedings. Lecture Notes in Electrical Engineering* **910** 345-352

# Magnetic field detector based on a magnetically controlled spin LED

**M. V. Ved✉, M. V. Dorokhin, A. V. Zdoroveyshchev, P. B. Demina, D. A. Zdoroveyshchev**
Research Institute for Physics and Technology of the Lobachevsky State University, Gagarina Ave., 23, Nizhny Novgorod, 603022.
✉mikhail28ved@gmail.com

**Abstract.** The paper describes the principle of operation of a new magnetic field detector based on a magnetically controlled spin light-emitting diode, in which the intensity and degree of circular polarization of radiation can be independently controlled by longitudinal and transverse magnetic fields respectively. The device is a combination of a spin light-emitting diode with a CoPd ferromagnetic injector and a spin valve consisting of $Cr/Co_{90}Fe_{10}/Cu/Co_{90}Fe_{10}$ layers. It is shown that in such a device it is possible to obtain a 100% change in the intensity of electroluminescence, while the degree of circular polarization is 0.4%.

**Keywords:** semiconductor spintronics, spin light-emitting diode, spin valve, GaAs.

**Funding:** This study was supported by the Russian Science Foundation (project no. 21-79-20186).

## Introduction

The development of a small-sized high-speed autonomous wireless detector (visualizer) of a magnetic field is an urgent task, since it can be widely used in various branches of science and technology. In this paper, we report on the creation of a laboratory model of a device, which operation is carried out by combining two basic elements of spintronics (a magneto-resistive element and a spin light-emitting diode), due to which it is possible to independently detect the longitudinal and transverse components of the magnetic field.

## Materials and Methods

The detector described in this paper is a magnetoresistive spin LED, which is a combination of an emitting heterostructure with an InGaAs/GaAs quantum well (QW) with a CoPd spin injector and a spin valve, which is a sequence of thin layers of $Cr/Co_{90}Fe_{10}/Cu/Co_{90}Fe_{10}$. The semiconductor light-emitting part of the studied structure was formed on an n-GaAs substrate by MOCVD in a hydrogen flow. The ferromagnetic CoPd injector and all layers of the magnetoresistive element were formed by electron beam evaporation in vacuum. At the final stage, using photolithography and chemical etching, contacts of a special shape were formed on the surface of the structures. For electrical isolation of the semiconductor structure around the mesa contacts, the parts of the structure not covered by the contacts were irradiated with $He^{++}$ ions before the deposition of the spin valve layers [1].

## Results and Discussion

Figure 1(a) shows the magnetic field dependence of the static resistance (the magnetic field was applied in the plane of the structure). The calculation of the magnitude of the magnetoresistance was carried out according to the following formula:

$$MR(B) = (R(B) - R(B_{max}))/(R(B_{max}))\cdot 100\%,$$

where R(B) is the resistance in the current magnetic field B, $R(B_{max})$ is the resistance in the maximum used magnetic field (0.2 T). It should be noted that the magnetoresistance curves for the magnetic field detector are similar to those for a separate magnetoresistive element.

Figure 1(b) shows the dependence of the relative intensity of electroluminescence (EL) of the device on the magnetic field. The observed change in the EL intensity is associated with a change in the resistance of the magnetoresistive contact layer.

It should be noted that at a current of 36 mA, the structure operates in the key mode: in a magnetic field of ±50 mT, the relative intensity takes on maximum values; in a zero magnetic field, as well as in a field above 100 mT, it is equal to zero. The most probable mechanism for

increasing the EL intensity of such a combined device in a longitudinal magnetic field is presented in [2].

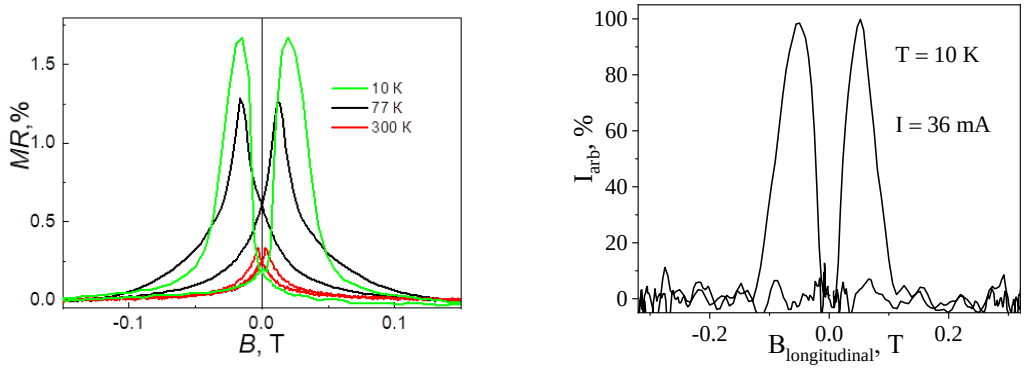


Fig. 1. (a) Magnetic field dependences of resistance for a magnetic field detector; (b) Magnetic field dependence of relative radiation intensity for a magnetic field detector.

When the developed detector is introduced into a transverse magnetic field, the EL becomes partially circularly polarized. The degree of circular polarization of EL is calculated by the formula:

$$P_{EL} = ((I_1) - (I_2)) / ((I_1) + (I_2)) \cdot 100\%,$$

where $I_1$ ($I_2$) are the relative EL intensities for left- (right-) polarized radiation.

Figure 2 shows the dependence of the degree of circular polarization of the EL on the magnetic field.

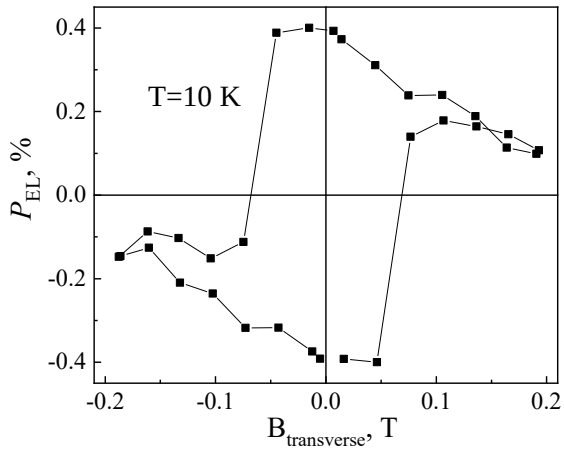


Fig. 2. Magnetic field dependence of the circular polarization degree for a magnetic field detector.

The maximum value of $P_{EL}$ was 0.4%. The linear slope in magnetic fields of more than 0.1 T (in absolute value) is presumably associated with the Zeeman splitting of the energy levels in the QW.

## Conclusion

Thus, a laboratory sample of a magnetic field detector was made, which has four independently variable states (high/low intensity radiation with right/left circular polarization), which correspond to the presence of longitudinal and transverse magnetic field components.

## REFERENCES


1. **J. P. de Souza, I. Danilov, and H. Boudinov**, Electrical isolation in GaAs by light ion irradiation: The role of antisite defects, Applied Physics Letters. 68(4) (1996) 535.

2. **Ved M., Danilov Y., Demina P., Dorokhin M., Dudin Y., Kotomina V., Kudrin A., Kuznetsov Y., Zdoroveyshchev A., Zdoroveyshchev D.**, Switching of magnetoresistive light-emitting diode by external magnetic field, Applied Physics Letters. 118(9) (2021) 092402.

# Modernization of a quantum frequency standard temperature controller with a rubidium gas cell

**E. V. Isupova[1]✉, S. Y. Shvetsov[2] and V. V. Davydov[1, 3]**
[1] Peter the Great Saint-Petersburg Polytechnic University, Saint Petersburg, Russia;
[2] Russian Institute of Radionavigation and Time, Saint Petersburg, Russia;
[3] The Bonch-Bruevich Saint Petersburg State University of Telecommunications, Saint Petersburg, Russia.
✉ isupova.e24@mail.ru

**Abstract.** An improved circuit of a quantum frequency standard temperature controller with a rubidium gas cell is presented. This frequency standard is an important part in satellite navigation systems, as it provides accuracy and stability and determines the position and speed of the satellite. To combat the main destabilizing factor – temperature – thermostating and thermoregulation are used in frequency measures. The block diagram of the thermostat is considered, and the simulation of the circuit diagram in the Micro-Cap environment is carried out. Transient processes in the circuit are analyzed and the necessary nominal values of capacitances and resistances are selected.

**Keywords:** Thermoregulation, thermostating, quantum frequency standard with rubidium gas cell, feedback, power amplifier, stability, differential amplifier, PID controller

## Introduction

One of the main factors impairing the frequency stability of the rubidium quantum frequency standard (QFS) is temperature. A change in temperature leads to a change in the values of the parameters of all elements, especially optical ones, and affects the characteristics of laser radiation. To compensate for the influence of temperature, the QFS parts are made of heat-resistant materials with possibly small temperature coefficients [1, 2]. In a wide range of temperature changes determined by operating conditions, this measure is not enough, so there is a need for the use of thermostating and thermoregulation.

Thermoregulators are a necessary and important part of the rubidium frequency standard. The rubidium lamp and the cell must be sufficiently heated to obtain the required vapor pressure [3]. Their temperature must be controlled to maintain stability. Thermoregulators also affect the heating characteristics and power of the device.

## Method of constructing and modeling the operation of the thermostat

Most rubidium QFS thermoregulators use thermistor temperature sensors, as they are sensitive, small and have good stability. To ensure good performance, they must have good thermal contact with the thermostat, as well as avoid any mechanical influences.

The classical design of the thermoregulator used in the rubidium QS is shown in Fig. 1.

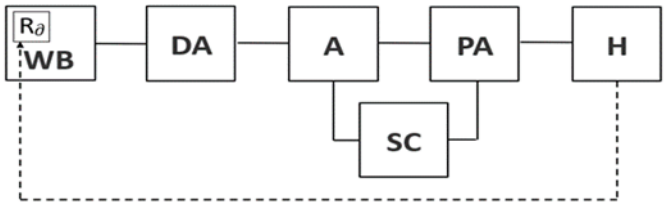


Fig. 1. Block diagram of the thermostat: $R_{\partial}$ - temperature sensor, WB – Wheatstone Bridge, DA – differential amplifier, A – amplifier, PA – power amplifier, H – heater, SC – stabilizing circuit.

The temperature sensor generates a signal proportional to the temperature value. This sensor is the arm of the Wheatstone measuring bridge. Then the signal goes to the amplifiers, which are

necessary to increase the sensitivity of the temperature control system and provide the power required for the operation of the executive bodies. In this case, the signal passes through the feedback – the stabilizing circuit. The output of the power amplifier controls the power supplied to the heater. It, in turn, is connected by temperature feedback to the sensor.

We have developed a new design of the thermostat. In this scheme, instead of an amplifier block, a proportional-integral-differentiating (PID) regulator block will be used, which will allow for a higher level of regulation. In this device, a control signal is generated to obtain the necessary accuracy and quality of the transient process. The scheme of the developed PID controller is shown in Fig. 2.

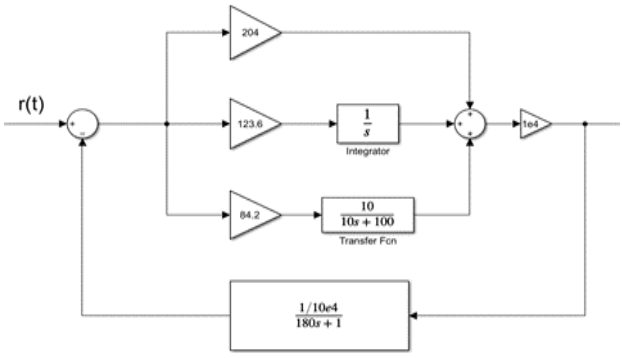


Fig. 2. The scheme of the developed PID controller.

The schematic diagram of the thermostat is assembled in the Micro-Cap environment. Modeling of transients is carried out.

Capacitances and resistances are selected in such a way that the output voltage located in the power amplifier unit instantly reacts to a single voltage surge at the input of the circuit, and the oscillatory processes after this surge are minimal.

## Results and Discussion

The use of a PID controller in the design of the thermostat allows you to increase the speed in the thermal stabilization system by 65% compared to the previously used design.

The threshold for changing the resistance of the thermistor in the Wheatstone bridge ≈ 1 Ohm allows to improve the signal-to-noise ratio of the recorded optical signal at least twice. This improves the short–term stability of the CSF frequency by 7-10%.

## Conclusion

Analysis of data on the operation of temperature control systems in various models of QSF on rubidium – 87 atoms with an optical gas cell and the results of modeling the thermostat circuit showed that the new implementation scheme works correctly, the introduction of a PID controller instead of the previously used transistor power amplifier stage improves the operation of the thermostat.

## REFERENCES

1. **Petrov A., Davydov V. and Grebenikova N.,** Journal of Communications Technology and Electronics 63(11) (2018) 1159–1164.

2. **Lukashev N.A., Davydov R.V., Glinushkin A.P., Rud' V.Y.,** Improving characteristics of microwave frequency standard on Hg-199 ions for telecommunication systems Journal of Physics: Conference Series.1326(1) (2019) 012046.

3. **Riehle F.,** Frequency standard. Basic and applications, WILEY-VCH Verlag CmbH Co. KGaA: New-York, 2008.

# Simulation and analysis of heterostructures for normally-off p-channel GaN transistor

**E.A. Kozloskaya** [1✉], **D.M. Kurbanbayeva** [1], **K.A. Tsarik** [1]

[1] National Research University of Electronic Technology, 124498 Moscow, Russia;

✉ k89296190714@gmail.com

**Abstract.** This article presents the results of simulation the heterostructure of normally-off p-channel transistor. The design of the upper layers of the heterostructure was determined for the appearance of a 2DHG at the p-GaN/AlGaN heterojunction. For the p-channel device the dependence of the transistor behavior on the thickness of the p-GaN and the impurity concentration in it is demonstrated through the study of band diagrams. Thanks to current-voltage characteristics of transistor, the dependence of the formation of a normally-on or normally-off transistor on the thickness of the p-GaN and the concentration of impurities in it was found.

**Keywords:** heterostructure, power transistor, p-channel, p-GaN, AlGaN.

**Funding:** This work was carried out with the financial assistance of the Ministry of Education and Science in the framework of state task FSMR-2022-0004

## Introduction

P-channel power transistors based on GaN have some advantages over n-channel GaN transistors, which make them useful in a variety of applications. For example, they can be used together with n-channel transistors on the same chip to create a complementary pair. This allows for the creation of devices that can operate at higher voltages and have higher gain coefficients than devices based only on n-channel GaN transistors. Some examples of the use of p-channel GaN power transistors include their use in inverters, DC-DC converters, AC-DC converters, and power supplies. However, like all new technologies, p-channel GaN power transistors have some limitations and problems. For example, they have a higher production cost than traditional silicon-based power transistors. In addition, currently, they have limited reliability. Nevertheless, with the development of production technologies and research in this area, p-channel GaN power transistors promise to become increasingly common and competitive devices in power electronics [1]. One way to create normally-off p-channel power transistors is to use metal-oxide-semiconductor field-effect transistors (MOSFETs), for example, using a dielectric based on aluminum oxide and magnesium doping of GaN. However, to achieve high performance and reliability in real-world applications, it is necessary to take into account the features of modeling GaN transistors in TCAD simulators (Technology Computer-Aided Design). Overall, modeling GaN-based power transistors in TCAD is an active area of research, and the emergence of new technologies and materials allows for improving the accuracy of results and expanding the possibilities for using GaN transistors in various fields.

## Materials and Methods

The design of the heterostructure layers is shown in Fig.1. It consisted of a 3.5 um $Al_{0.05}Ga_{0.95}N$ buffer layer, a 15 nm $Al_{0.2}Ga_{0.8}N$ barrier layer, and a 100 nm Mg-doped p-type GaN layer. Thick buffer layer should provide high breakdown voltage[2]. The 2DHG is formed at the heterointerface p-GaN with AlGaN. A layer of aluminum oxide covers the surface of the heterostructure. Modeling has been done with Sentaurus Technology Computer Aided Design (TCAD). Sentaurus TCAD contains several physical models that describe the physics of the device most closely to reality (spontaneous and piezoelectric polarization, dreff-diffusion model, thermodynamic model). Initially, at a p-GaN layer thickness of 100 nm, the impurity concentration was varied in the range from 1 to 50 $10^{18}$ $cm^{-3}$. According to the data obtained as a result of the simulation, the state of the future transistor was found: normally-on or normally-off. To do this, the I–V characteristics of the transistor were simulated at various values of the gate voltage. Then these simulations were carried out for all thicknesses in the range from 10 to 80 nm.

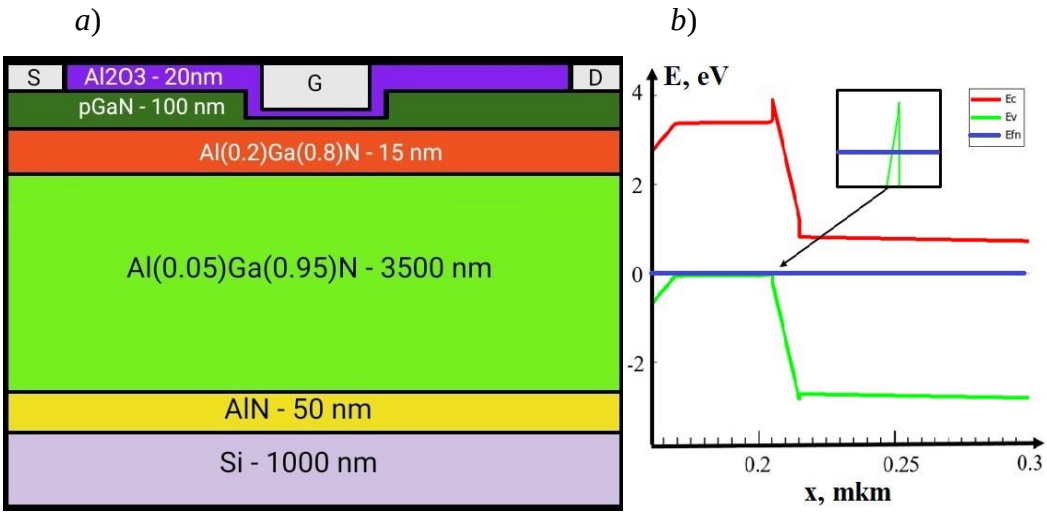


Fig. 1. Schematic cross-section (a) and band diagram (b) of a p-channel GaN transistor

## Results and Discussion

The main goal in solving the problem of choosing the design of a normally closed transistor is to study the dependence of the concentration of charge carriers in the channel on the structure parameters. These values should be such that as $h_{p+}$ decreases, it is necessary to increase the $N_{p+}$ doping values for the p-GaN layer (Fig.2).

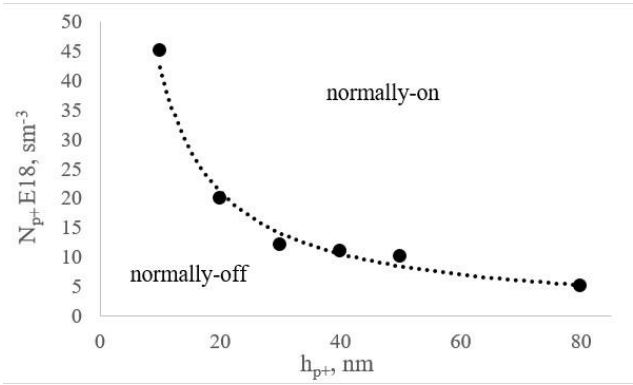


Fig. 2. Dependence of type p-channel device on p-GaN thickness and its activated impurity concentration

## Conclusion

Simulation of normally-off p-channel p-GaN/$Al_{0.2}Ga_{0.8}N$/$Al_{0.05}Ga_{0.95}N$/AlN/Si HFET (heterostructure field-effect transistor) based on a p-GaN was demonstrated. The conditions for the formation of two-dimensional hole gas were found. Using Sentaurus TCAD, the effect of heterostructure parameters on the device behaviour was investigated. On the basis of these studies the optimal composition of the heterostructure for obtaining a normally-off transistor: p+-GaN with a thickness of 50 nm the gate and impurity concentration $1\times10^{19}$cm$^{-3}$, $Al_{0.2}Ga_{0.8}N$ with a thickness of 15 nm, $Al_{0.05}Ga_{0.95}N$ with a thickness of about 3500 nm.

## REFERENCES

1. **Kachi, T.** Recent progress of GaN power devices for automotive applications. Japanese Journal of Applied Physics. 53(10) (2014) 100210.

2. **Zhang, W., Liu, X., Fu, L., Huang, R., Zhao, S., Zhang, J., ... & Hao, Y.** (2021). Investigation of normally-off GaN-based p-channel and n-channel heterojunction field-effect transistors for monolithic integration, Results in Physics. 24 (2021) 104209.

# Reconfigurable Reflectarrays for 5/6G Wireless Systems with Linear Polarization

**A. V. Lvov** [1✉], **A. N. Prikhodko** [1,2], **A. S. Shurakov** [1,2], **G. N. Goltsman** [1,2]
[1] Moscow Pedagogical State University, Moscow, Russia;
[2] National Research University Higher School of Economics, Moscow, Russia
✉av.lvov@mpgu.su

**Abstract.** Numerous studies on wireless technologies for the fifth and sixth generation networks are widely conducted at the moment. They are driven by potential opportunities of digitalization in the information society era. Further enlargement of data transfer rates is required to enhance virtual interactions in various public areas via appearance of new services and applications. In this work, we report on the development of a reconfigurable reflectarray for 5/6G wireless communication systems with linear polarization. The proposed reflectarray utilizes current controlling diodes in a metallic screen inserted in between of front and rear metallizations of a planar patch antenna array. This makes it capable of a digital beam steering on a microsecond scale. Performance of the reflectarray designed for operation at 15 GHz is described in terms of numerical simulations and prototyping. We also discuss prospects and technological challenges of fabricating a scaled-down version of the reflectarray for 150 GHz operation.

**Keywords:** reconfigurable reflectarray, 5/6G network, wireless channel, sub-terahertz communication.

**Funding:** This study was funded by the Russian Science Foundation grant number 22-79-10279, https://rscf.ru/project/22-79-10279/.

## Introduction

The studies on wireless technologies for the fifth and sixth generation (5/6G) networks are of current interest. They are driven not only by a potential enlargement of data transfer rates, but by the prospects of appearance of new services and applications as well [1]. Ultra-directional transceivers are proposed to improve connection quality in sub-terahertz (sub-THz) communication channels. This makes them less vulnerable to propagation losses and fading, but more vulnerable to blockages [2]. The issue can be resolved if reconfigurable reflectarrays are used for beam routing in sub-THz data links. The reflectarrays together with a transmitter and receiver in a wireless channel should utilize optics capable of fast beam steering [3]. In this work, we report on the development of a reconfigurable reflectarray for 5/6G networks. It makes use of a diode-based design of each cell ensuring a sub-THz beam steering on a microsecond scale or faster.

## Results and Discussion

Figure 1 illustrates schematic of a 15 GHz reconfigurable reflectarray (RRA). RRA utilizes current controlling diode switches (DSs) in a metallic screen (MS) inserted in between of front and rear metallizations of a planar patch antenna array. The latter is based on a low-loss dielectric substrate with relative permittivity $\varepsilon_r$ = 3.5 [4]. This makes the design compatible with the use of a fused quartz if operation at sub-THz frequencies is considered.

Referring to Figure 1, Gaussian beam (GB) of a linearly polarized light incident along normal to the RRA surface is reflected at angle, $\theta$, determined by the configuration of up to 3 DSs. Quantities $\mathbf{k}$ and $\mathbf{E_0}$ denote wavevector and electric field strength of incident GB. The design ensures a multidirectional beam steering by rearranging currents in MS. For turned on DSs 2–3 all over RRA and tuned on/off DS 1 in even/odd rows (or vice versa) oriented along $\mathbf{E_0}$, in-reflection phase shift between neighboring rows is approximately 180°. Thus, bidirectional beam steering is implemented. Calculated $\theta$ swings from -15° to +15° if DSs act as ideal switches. These findings are further experimentally justified.

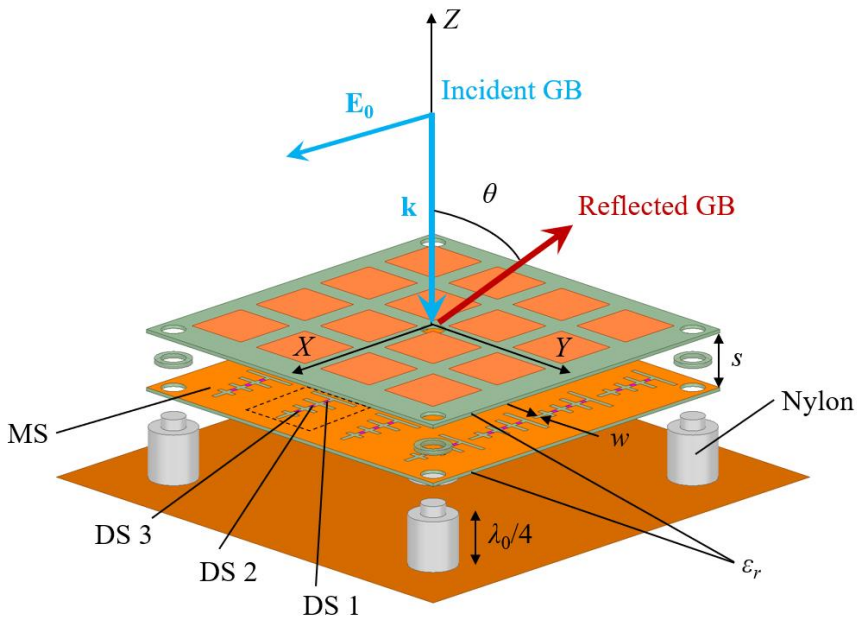


Fig. 1. Schematic of a 15 GHz RRA in action

When prototyping RRA, all DSs 2–3 are replaced by bridges and DS 1 is replaced by a bridge/gap in even/odd rows oriented along $\mathbf{E_0}$ in the dendriform slots of MS. Fabrication tolerances for the slot width, $w$, and the spacing between the top substrate of RRA and MS, $s$, are found to be the most crucial. We measure relative fabrication errors $\delta w$ = 7.2% and $\delta s$ = 9.5%, and use these values to predict margins for parameters of reflected GB. We numerically observe relative errors $\delta\theta$ = 5.9% and $\delta I$ = 7.6% for the angle of reflection and the intensity of the reflected beam, respectively. In the numerical simulations, the spacing between the substrate with MS and the ground plane is fixed to $\lambda_0/4$, where $\lambda_0$ is the free space wavelength. This is consistent with our experimental findings. Moreover, we expect reduction of $\delta w$ and $\delta s$ down to 1–2% leading to significant decrease in $\delta\theta$ and $\delta I$, when fabricating a 150 GHz RRA with the chosen form factor. This is to be achieved upon use of photo-, e-beam lithographies for deposition and patterning of thin-film metallic surfaces and precise computer-aided machining for packaging. Additionally, our simulations of RRA with different impedances of DSs in on/off states confirm usability of Schottky diodes with feasible parasitic parameters. We believe that all together proves technological robustness and suitability of the developed RRA for 5/6G wireless communication systems.

## REFERENCES

1. **Yeh C., Do Jo G., Ko Y. J., Chung H. K.**, Perspectives on 6G wireless communications, ICT Express. 9 (1) (2023) 82–91.

2. **Shurakov A., Moltchanov D., Prikhodko A., Khakimov A., Mokrov E., Begishev V., Belikov I., Koucheryavy Y., Gol'tsmanG.**, Empirical blockage characterization and detection in indoor sub-THz communications, Computer Communications. 201 (2023) 48–58.

3. **Chen Z., Ning B., Han C., Tian Z., Li S.**, Intelligent reflecting surface assisted terahertz communications toward 6G, IEEE Wireless Communications. 6 (28) (2021) 110–117.

4. FSD888T PCB laminate. URL: http://www.eltm.ru/svch-materialy-fsd.html/nid/2087. Accessed Mar. 31, 2023.

# Using Mobile Phone as a Ripeness Sensor

**I.I. Mikheev [1✉], V.D. Burtsev [1], T.S. Vosheva [1], I.M. Yusupov [2], D.S. Filonov [1]**
[1]Center for Photonics and 2D Materials, MIPT, Dolgoprudny 141701, Russia
[2]School of Physics and Engineering, ITMO University, Saint Petersburg, 197101, Russia
✉mikheev.ii@phystech.edu

**Abstract.** According to statistics, about 7 billion people currently regularly use smartphones. This paper considers the possibility of using an ordinary smartphone to determine the level of ripeness of fruits and their suitability for food. To fulfil this goal, a mobile application has been developed that can respond to changes in the signal to the telephone antenna from an external base station, depending on the immediate environment. It is shown that, depending on the dielectric constant of the product next to the antenna, its signal level changes markedly.

**Keywords:** Product Ripeness, Smartphone Sensor, Agriculture, Smartphone Application

**Funding:** The research was supported in part by the Federal Academic Leadership Program Priority 2030 (manufacturing and measuring) and by the Russian Science Foundation Project 19-79-10232 (numerical part).

Mobile phones have become firmly embedded in everyday life, and more and more applications are being developed for them to improve the quality of life, starting with geotrackers and ending with pulse and blood sugar sensors. Therefore, in this paper we decided to consider their applicability on the basis of agricultural technology. It is known that mobile antennas, most often of the IFA type [1], are high-quality resonators capable of influencing environmental changes. Thus, by placing various products in the near field of such an antenna, we expected to see different levels of the signal coming from it. The measurements obtained by this method were not directly related to classical near-field measurements [2,3], since the antenna collects the entire complex signal from the near field, and we were not aiming at obtainingan electromagnetic field map. However, it is quite important that all measurements were carried out in real time, which enables getting the result almost immediately after changing the environment.

To determine the sensitivity of the telephone antenna to external dielectrics, two telephones were involved in the experiment: one serves as a base station and distributes a fixed-power Wi-Fi signal, the second serves as a receiver, the signal from which we analyzed. Both, a numerical experiment in CST Studio Suite Software Package and measurements were carried out. In a numerical experiment, two models of phones with IFA antennas were located opposite each other at a fixed distance, and a volumetric model of the object under test was placed between them (Fig. 1(a)). The finite element method was used for calculations. To conduct a real experiment (Fig.1 (b)), a mobile application was written in the Kotlin language, capable of showing the signal strength from a WiFi antenna in real time (Fig. 1 (c)).

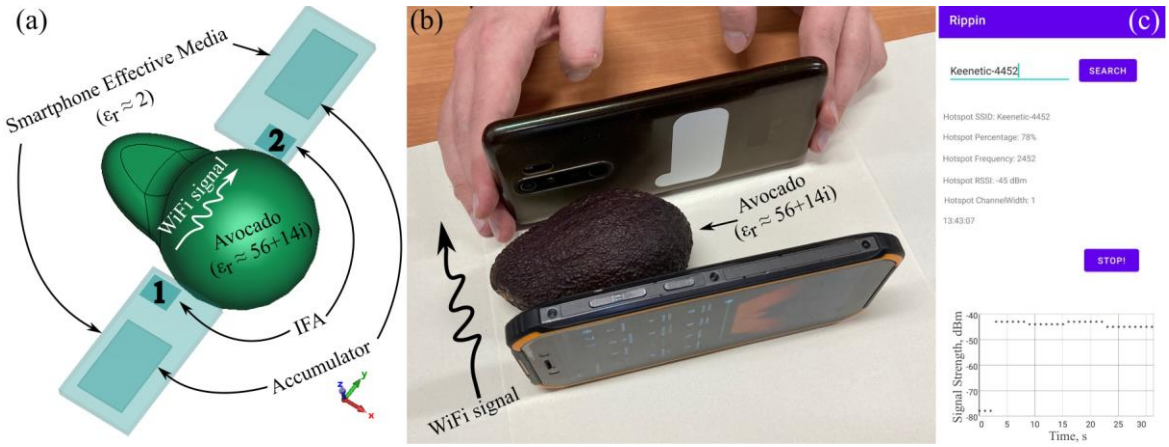


Fig. 1. Experimental setups in (a) simulation and (b) measurements; and (c) application user interface.

The results of the measurements can be seen in Figure 2. To estimate the signal strength in a numerical experiment, we launched a signal from antenna 1 (Fig. 1(a)) and received it with antenna 2. Therefore, we are interested in the transmission coefficient of such a system, S21, shown in Fig. 2(a). It is noticeable that in the free space, the signal is maximal, and with the appearance of a lossy medium in the path of an electromagnetic wave, its level drops significantly. The WifiManager Android service [4] was used to measure the signal strength in a real experiment. The data from the application (RSSI signal strength) were analyzed under the same conditions as in the simulation: in free space, for cucumber and for avocado. We conducted an experiment where two phones were placed in close proximity with an object between them, and we aimed to determine the type of the object. It turned out that avocado, having the highest loss tangent [5], from the presented cases, strongly drowns out the signal level, which is why it falls below -30 dBm at a value of about -17 dBm in free space. Cucumber occupies less volume in space and has a lower loss tangent than avocado [5], which leads to less signal damping to approximately -27 dBm. The trend predicted in the numerical experiment has been confirmed. The telephone antenna evidently has sufficient sensitivity to determine the type of product. So that it can be used to detect food freshness, opening up new possibilities for precision agriculture and quality control. In the future, it is planned to conduct long-term experiments to check changes in the dielectric characteristics of products from their aging and create an electronic library of samples.

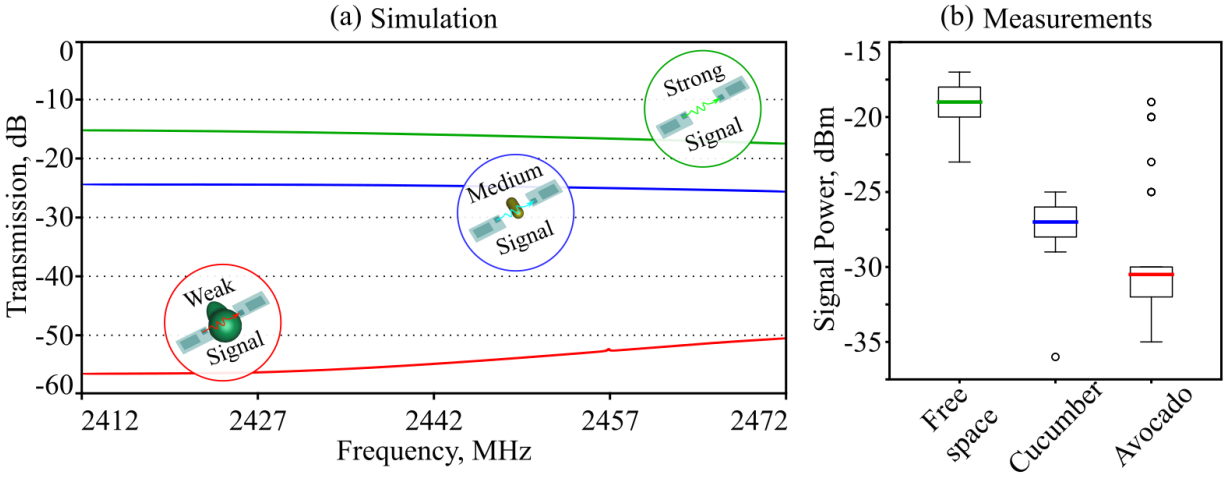


Fig. 2. Results of (a) numerical experiment and (b) measurements for different types of filler between antennas.

## References:


[1] Zhan Li, Y. Rahmat-Samii Optimization of PIFA-IFA Combination in Handset Antenna Designs // IEEE Transactions on antennas and propagation, Vol. 53, No. 5, May 2005 https://doi.org/200510.1109/8.633849 pp. 1770-1775.

[2] Baudry, D., Arcambal, C., Louis, A., Mazari, Bé., & Eudeline, P. (2007). Applications of the Near-Field Techniques in EMC Investigations. IEEE Transactions on Electromagnetic Compatibility, 49(3), pp. 485–493. doi:10.1109/TEMC.2007.902194.

[3] Nelson, S. O. (n.d.). Dielectric Spectroscopy of Fresh Fruits and Vegetables. 2005 // IEEE Instrumentation and Measurement Technology Conference Proceedings p. 362. doi:10.1109/IMTC.2005.1604135.

[4] WifiManager reference in Android documentation https://developer.android.com/reference/android/net/wifi/WifiManager, Data Access: March 2023.

[5] Rahmat-Samii, Y., & Lemanczyk, J. (1988). Application of spherical near-field measurements to microwave holographic diagnosis of antenna // IEEE Transactions on Antennas and Propagation, 36(6), pp. 869–878. doi:10.1109/8.1190

# Modeling of a capacitive MEMS-switch with «floating» electrode

**M. O. Morozov**[1,2]✉ **and I. V. Uvarov**[1]

[1]Valiev Institute of Physics and Technology of Russian Academy of Sciences, Yaroslavl Branch, Universitetskaya 21, 150007 Yaroslavl, Russia

[2] P.G. Demidov Yaroslavl State University, Sovetskaya 14, 150003 Yaroslavl, Russia

✉matvey19991@mail.ru

**Abstract.** The main characteristic of a capacitive MEMS switch is the ratio of capacitances in the open and closed states. Conventional switches have this ratio from several units to several tens. However, it can be significantly increased by mounting a «floating» electrode onto the transmission line. The analytical approach provides the capacitance ratio of the modified switch as high as 500. Finite element simulation takes parasitic capacitance into account and gives somewhat lower value. The dependence of working characteristics on the substrate resistivity and signal frequency is investigated.

**Keywords:** MEMS switch, capacitance ratio, floating potential, finite element method.

**Funding:** This work is supported by the program no. FFNN-2022-0017 of the Ministry of Science and Higher Education of Russia for Valiev Institute of Physics and Technology of RAS.

**Citation:** Morozov M. O., Uvarov I.V., Modeling of a capacitive MEMS-switch with «floating» electrode, St. Petersburg State Polytechnical University Journal. Physics and Mathematics. 16 ( ) (2023) …–…. DOI: https://doi.org/10.18721/JPM.

© Morozov M. O., Uvarov I. V., 2023. Published by Peter the Great St.Petersburg Polytechnic University.

## Introduction

MEMS switch is an electromechanical relay of micron size fabricated by microelectronic techniques [1]. It provides low insertion loss and high isolation in combination with small dimensions and low power consumption, which allows it to be used in advanced communication systems, radar equipment and other areas of radio electronics [2]. Many applications require MEMS switches with capacitive contact. A distinctive feature of this device is the ratio of capacitances in the open and closed states $C_{on}/C_{off}$ [3]. In conventional switches, this ratio varies from several units to several tens in the best case [4]. Implementation of novel design solutions significantly improves $C_{on}/C_{off}$. This work is devoted to the MEMS switch equipped by a «floating» electrode.

## Materials and Methods

The proposed MEMS switch is schematically shown in Fig. 1. The movable electrode is an aluminum beam with a length of 100 µm, which is fixed on torsion suspensions. A transmission line runs under the beam at a distance of 1 µm. A thin metal electrode is formed on top of the dielectric layer. In the open state, the potential of the electrode is floating. The capacity of the beam-line system is small, so the signal passes from the input to the output with minimal losses. In the closed state, the beam touches the electrode, and their potentials are equalized. The capacity between the beam and the line increases significantly, so the switch shunts the signal. The concept of the «floating» electrode is thoroughly described in our previous work [5].

The switch is simulated by the finite element method (FEM). The model includes a chip with a coplanar transmission line and contact pads. The switch is built into one of the grounded conductors. A test signal with the amplitude of 1 V and frequency from 1 kHz to 1 MHz is applied to the central conductor. The capacitance is calculated using the total energy of the electric field.

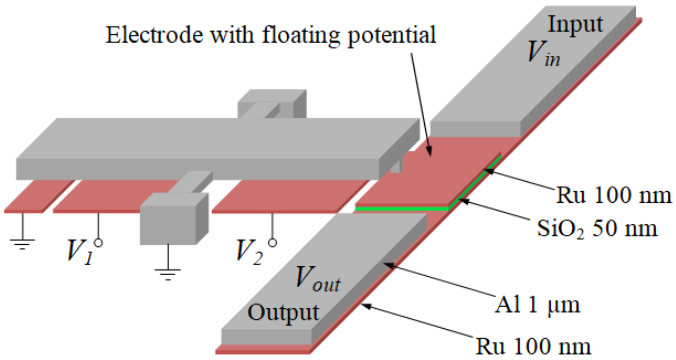


Fig. 1. Schematic illustration of the switch.

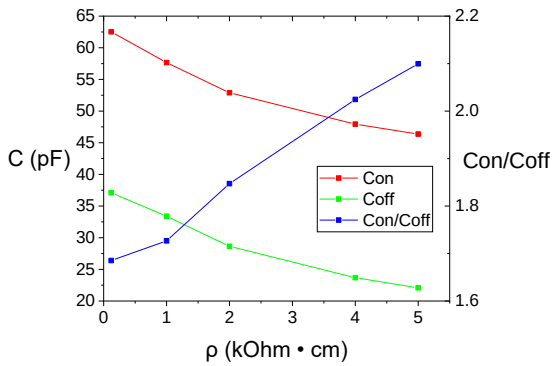


Fig. 2. Working characteristics as a function of the substrate resistivity.

## Results and Discussion

In the open state, the switch is equivalent to two series-connected capacitors. The first one is formed by the transmission line and the «floating» electrode, while the second one consists of the electrode and the beam. The second capacitance is significantly lower than the first one. Therefore, it determines total capacitance in the open state $C_{off}$ = 0.08 pF. In the closed state, the second capacitor is converted to a contact resistance, so the total capacitance is $C_{on}$ = 39.75 pF. Thus, the ideal switch has $C_{on}/C_{off}$ of about 500, which is an order of magnitude higher than the capacitance ratio for most conventional devices.

FEM simulation is used to obtain the dependence of the switch characteristics on the signal frequency $f$ and substrate resistivity $\rho$. Both $C_{on}$ and $C_{off}$ decrease with $f$. For the resistivity of 12 Ohm·cm the change is less than 1%, but for high-resistivity silicon the dependence is more pronounced. The capacitance drops with $\rho$ as shown in Fig. 2. The use of a high-resistivity substrate significantly reduces the parasitic capacitance. However, this component remains high due to large area of the contact pads and length of the transmission line. The increase of resistivity from 12 Ohm·cm to 5 kOhm·cm makes the capacitance ratio 1.3 times higher, but the simulated value is significantly lower than the analytical result. One has to improve the switch design in order to reduce the parasitic capacitance and to bring $C_{on}/C_{off}$ close to the ideal value.

## REFERENCES

1. **Hindle P.,** The state of RF and microwave switches, Microw. J. 53(11) (2010) 20–36.

2. **Haupt R.L., Lanagan M.,** Reconfigurable antennas, IEEE Antennas Propag. Mag. 55 (2013) 49–61.

3. **Kurmendra, Kumar, R.,** A review on RF micro-electro-mechanical-systems (MEMS) switch for radio frequency applications, Microsyst. Technol. 27 (2021) 2525–2542.

4. **Papaioannou G., Giacomozzi F., Papandreou E., Margesin B.,** Floating electrode microelectromechanical system capacitive switches: A different actuation mechanism, Appl. Phys. Lett. 99(7) (2011) 073501.

5. **Uvarov I.V., Marukhin N.V., Shlepakov P.S., Lukichev V.F.,** Calculation of performance of MEMS-switch with increased capacitance ratio, Russ. Microelectron. 49 (2020) 253–262.

# Development of an optical spark breakdown sensor for power distribution boards

**M G Nigamatdianov✉, V A Spiridonov.**

ITMO University, Saint-Petersburg, Russia

✉243666@niuitmo.ru

**Abstract.** The developed optical spark breakdown sensor for power distribution boards is designed to detect spark breakdowns inside switchboards of complex switchgear (GIS) up to 35 kV. The sensor detects an optical signal that is transmitted instantly to a transceiver module and activates an emergency shutdown in the required area.

**Keywords.** Spark sensor, high voltage, power grid protectors, lithium boron phosphate matrix.

**Funding.** The technical project is based on requirements specification №421244 from 21 April 2021 for a practical-oriented research and development project “Development of an optical spark breakdown sensor for power distribution boards”.

## Introduction

The developed optical spark breakdown sensor is based on the increased sensitivity of arc discharge, the radiation of which is concentrated in the UV spectrum, compared to analogs, by increasing the sensitivity of the active element to the UV radiation range. Sensing head of sensor, which contains active luminescent material based on lithium boron phosphate glass, perceives UV radiation of arc discharge, and converts it into IR spectrum, which is received by silicon photodiode through optical fiber. When the radiation is detected, the photodiode will transmit a signal to the switchgear panel emergency shutdown. The variety of existing optical spark breakdown sensors on the market is limited, but due to the current need for high-speed spark breakdown monitoring systems, the prospects for the development of this field are quite high.

## Materials and Construction of the Device

It is known that rare-earth metal ions, silver, copper, and copper chloride crystals have pronounced luminescent properties [1, 2]. Eu, Sm and Yb are among those materials which have the range of maximum sensitivity of the silicon photodetector (600–1000 nm). Europium was chosen because it has maximum of luminescence excitation in the region of spark breakdown peak and the greatest quantum yield ($\Phi_{EU}$ = 0.6, $\Phi_{Yb}$ = 0.5, $\Phi_{SM}$ = 0.3) [3].

A glass matrix was chosen to hold europium ions because it is easier and cheaper to manufacture than a crystalline matrix, more chemically resistant and more UV-resistant than a polymer matrix [4]. A lithium boron phosphate matrix with transparency in the wavelength range of 400–1000 nm was chosen as the active element. Europium ions act as activator ions of the glass, providing its luminescence property. The luminescence peak of europium ions is at a wavelength of 655 nm.

The optical spark breakdown sensor consists of a sensing head and a transmitting and receiving module (Figure 1). The sensing head detects UV radiation and transmits the light visible to the silicon photodetector to the microcontroller. It processes the signal, and the actuator disconnects the power supply.

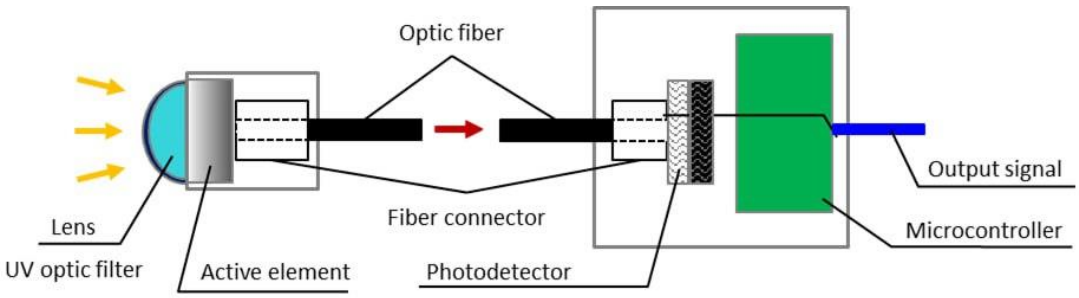


Figure 1 - Schematic representation of the main elements of an optical sensor.

## Results and Discussion

The sensor has an operating optical range of 300–400 nm, a response time of less than 30 ms, a nominal supply voltage of 200–240 V and a minimum signal to which the sensor will react of 25 W/m$^2$. The optical spark gauge is stable when used in integrated switchgears, the signal is transmitted instantly to a transceiver module and activates an emergency shutdown of the section. Due to the intense luminescence of the active element at 655 nm wavelength, the sensor is highly sensitive and has minimal false positives.

## REFERENCES

1. **Blasse G.** Luminescence of rare earth ions at the end of the century // Journal of Alloys and Compounds. — 1993. — Vol. 192, № 1. — P. 17–21.
2. **Babkina A. et al.** Temperature effect on the luminescence spectra of calcium-aluminum-borate and silicate glasses with copper (I) and silver ions // Optics and Spectroscopy. — 2014. — Vol. 116, № 1, — P. 93–93.
3. **Mutuzova M.** Synthesis and luminescent properties of complex compounds of lanthanides with ethyloxybenzoic acids. — 2015.
4. **Boboev T. et al.** Investigation of UV-irradiation effect on polymer fracture rate // Applied Physics. — 2020. — Vol. 5. — P. 93–96.

# Development and research of charger operation modes type "needle - plate" for nanoparticle charging

**A. N. Patarashvili** [1✉], **D. V. Kornyushin**[1], **M. S. Ivanov**[1], **M. Y. Aleshina**[1], **A. A. Efimov**[1], **V. V. Ivanov**[1]

[1] Moscow Institute of Physics and Technology, Dolgoprudny, Russia

✉patarashvili@phystech.edu

**Abstract.** A simple needle-plate charger with a gap of 16 mm for unipolar charging of silver nanoparticles in an air stream has been developed and manufactured. The charging efficiency and particle electrostatic losses of the designed charger were evaluated at various applied voltages and aerosol flow rates. With an increase in the applied voltage (corona discharge current) and the aerosol flow rate at a constant applied voltage, a decrease in the charging efficiency and an increase in the total losses of aerosol particles are observed. A charging efficiency of 43% with 38% electrostatic loss was achieved at a voltage of 8.1 kV (5.5 μA) and a flow of 10 L/min.

**Keywords:** charging efficiency, aerosol nanoparticle, unipolar charging, corona charger.

**Funding:** This research was funded by the Russian Science Foundation grant No. 22-79-10127.

## Introduction

The process of charging nanoparticles is of great importance in the fields of science and technology related to aerosols. The need to charge nanoparticles is seen, for example, in differential mobility analysis of submicron aerosol particles to measure distribution; deposition of nanoparticles at selected locations to form nanostructures; reduction of coagulation to obtain higher concentrations of nanoparticles. In this work, diffusion charging of nanoparticles by a unipolar ion cloud of a DC corona discharge using a "needle-plate" device is studied as the only suitable charging mechanism, as a result of which ions diffuse to the particle surface and charge transfer.

## Materials and Methods

Using a multi-spark discharge generator (m-SDG), silver nanoparticles with a size distribution in the range from 16 to 500 nm were synthesized and transported in an air stream to a needle-plate charger (NPC), in which the distance between the electrodes was 16 mm. The charged aerosol was passed through an electrostatic precipitator (ESP), at the outlet of which the concentration of particles was measured using aerosol NP analyzer SMPS 3936. To determine the internal $\eta_{intr}$ and external $\eta_{extr}$ particle charging efficiencies, electrostatic losses $L_E$ and the proportion of uncharged particles $h$, particle concentrations were measured when the NPC and ESP were turned on and off [1]. A schematic representation of the experimental setup is shown in Figure 1.

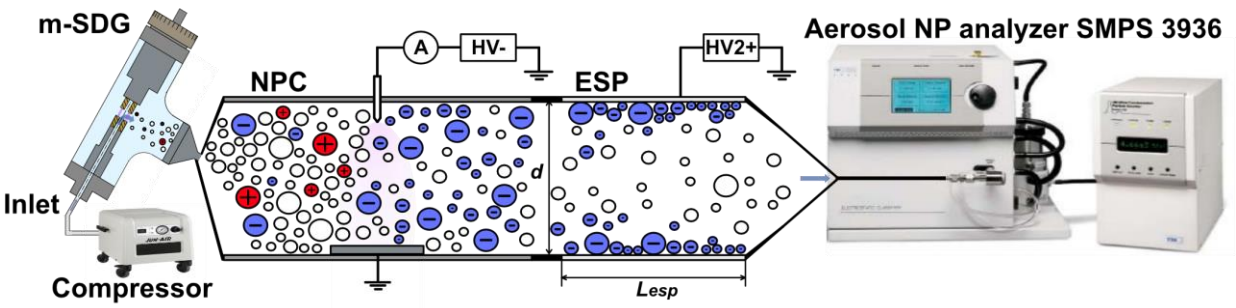


Fig. 1. The scheme of the experiment, which includes a multi-spark discharge generator (m-SDG), charger (NPC), an electrostatic precipitator (ESP) and an aerosol analyzer NP SMPS 3936

## Results and Discussion

An increase in the voltage $U$ in the NPC from 8.1 kV to 16 kV leads to an increase in the corona discharge current $I$ from 5.5 μA to 59 μA and the concentration of $N_i$ ions in the charging area, which reduces the external efficiency of $\eta_{extr}$ charging particles from 43 to 6% due to an increase in the electrostatic losses of charged particles in the increasing electric field on the NPC plate. Chart of the fractions of uncharged and charged particles at the exit from the ESP and the losses of particles at different corona discharge currents in the NPC are shown in Figure 2.

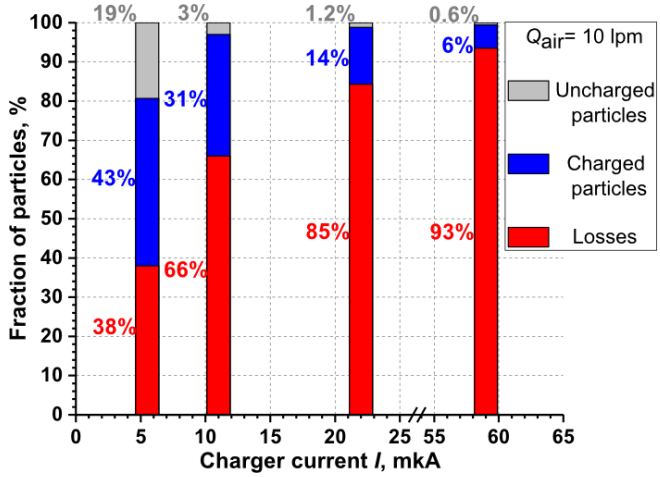


Fig. 2. Chart of the fractions of uncharged (gray) and charged (blue) aerosol particles and losses (red) of particles of the initial concentration at different corona discharge current $I$

## Conclusion

Using the example of a developed and manufactured needle-plate charger, the high efficiency of charging particles with sizes ranging from 16 to 500 nm with a small fraction of uncharged particles at the output is demonstrated. It has been found that an increase in the voltage (corona discharge current) at a constant aerosol flow rate leads to a decrease in the external charging efficiency from 43% to 6% and an increase in the loss of charged particles from 38% to 93%.


## Acknowledgments

This research was funded by the Russian Science Foundation grant No. 22-79-10127.


## REFERENCES


1. **Alonso M., Huang C. H.,** High-efficiency electrical charger for nanoparticles, Journal of Nanoparticle. 17 (2015) 1-8.

Conference materials
UDC
DOI: https://doi.org/10.18721/JPM.

# Development and research of charger operation modes type "needle - plate" for nanoparticle charging

**A. N. Patarashvili** [1✉], **D. V. Kornyushin**[1], **M. S. Ivanov**[1], **M. Y. Aleshina**[1], **A. A. Efimov**[1], **V. V. Ivanov**[1]

[1] Moscow Institute of Physics and Technology, Dolgoprudny, Russia

✉patarashvili@phystech.edu

**Abstract.** A simple needle-plate charger with a gap of 16 mm for unipolar charging of silver nanoparticles in an air stream has been developed and manufactured. The charging efficiency and particle electrostatic losses of the designed charger were evaluated at various applied voltages and aerosol flow rates. With an increase in the applied voltage (corona discharge current) and the aerosol flow rate at a constant applied voltage, a decrease in the charging efficiency and an increase in the total losses of aerosol particles are observed. A charging efficiency of 43% with 38% electrostatic loss was achieved at a voltage of 8.1 kV (5.5 μA) and a flow of 10 L/min.

**Keywords:** charging efficiency, aerosol nanoparticle, unipolar charging, corona charger.

**Funding:** This research was funded by the Russian Science Foundation grant No. 22-79-10127.

**Citation:** Patarashvili A.N., Kornyushin D.V., Ivanov M.S., Aleshina M.Y., Efimov A.A., Ivanov V.V., Development and research of charger operation modes type "needle - plate" for nanoparticle charging, St. Petersburg State Polytechnical University Journal. Physics and Mathematics. 16 ( ) (2023) …–…. DOI: https://doi.org/10.18721/JPM.

This is an open access article under the CC BY-NC 4.0 license (https://creativecommons.org/licenses/by-nc/4.0/)

© Patarashvili A. N., Kornyushin D. V., Ivanov M.S., Aleshina M.Y., Efimov A. A., Ivanov V. V., 2023. Published by Peter the Great St. Petersburg Polytechnic University.

Материалы конференции
УДК
DOI: https://doi.org/10.18721/JPM.

## Introduction

The process of charging nanoparticles is of great importance in the fields of science and technology related to aerosols. The need to charge nanoparticles is seen, for example, in differential mobility analysis of submicron aerosol particles to measure distribution; deposition of nanoparticles at selected locations to form nanostructures; reduction of coagulation to obtain higher concentrations of nanoparticles. In this work, diffusion charging of nanoparticles by a unipolar ion cloud of a DC corona discharge using a "needle-plate" device is studied as the only suitable charging mechanism, as a result of which ions diffuse to the particle surface and charge transfer.

## Materials and Methods

Using a multi-spark discharge generator (m-SDG), silver nanoparticles with a size distribution in the range from 16 to 500 nm were synthesized and transported in an air stream to a needle-plate charger (NPC), in which the distance between the electrodes was 16 mm. The charged aerosol was passed through an electrostatic precipitator (ESP), at the outlet of which the concentration of particles was measured using aerosol NP analyzer SMPS 3936. To determine the

internal $\eta_{intr}$ and external $\eta_{extr}$ particle charging efficiencies, electrostatic losses $L_E$ and the proportion of uncharged particles $h$, particle concentrations were measured when the NPC and ESP were turned on and off [1]. A schematic representation of the experimental setup is shown in Figure 1.

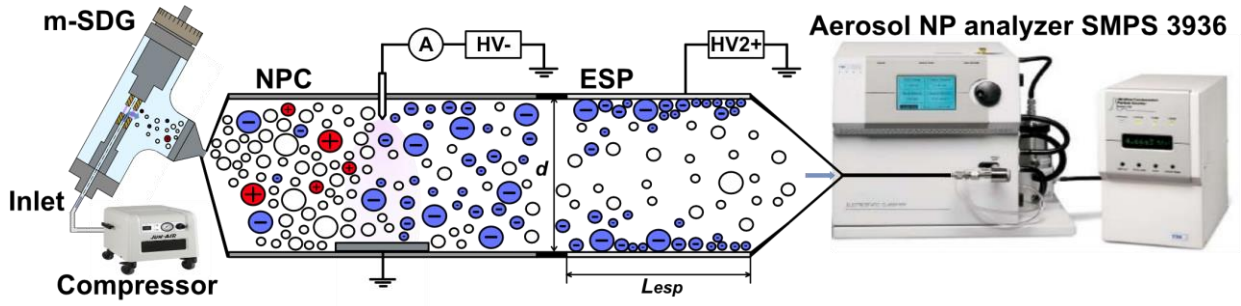


Fig. 1. The scheme of the experiment, which includes a multi-spark discharge generator (m-SDG), charger (NPC), an electrostatic precipitator (ESP) and an aerosol analyzer NP SMPS 3936

## Results and Discussion

An increase in the voltage $U$ in the NPC from 8.1 kV to 16 kV leads to an increase in the corona discharge current $I$ from 5.5 μA to 59 μA and the concentration of $N_i$ ions in the charging area, which reduces the external efficiency of $\eta_{extr}$ charging particles from 43 to 6% due to an increase in the electrostatic losses of charged particles in the increasing electric field on the NPC plate. Chart of the fractions of uncharged and charged particles at the exit from the ESP and the losses of particles at different corona discharge currents in the NPC are shown in Figure 2.

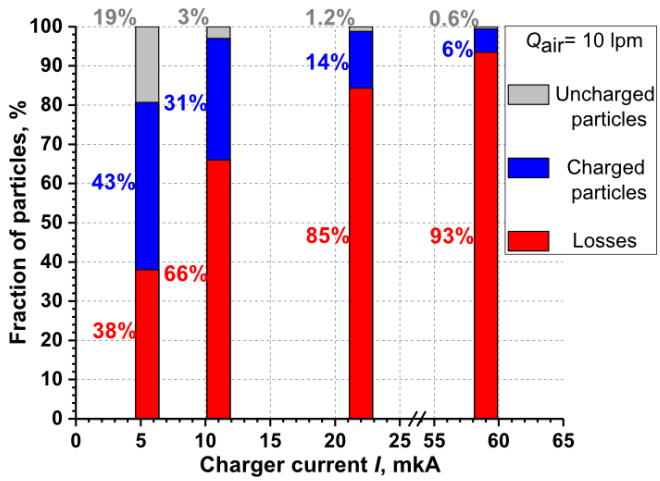


Fig. 2. Chart of the fractions of uncharged (gray) and charged (blue) aerosol particles and losses (red) of particles of the initial concentration at different corona discharge current $I$

## Conclusion

Using the example of a developed and manufactured needle-plate charger, the high efficiency of charging particles with sizes ranging from 16 to 500 nm with a small fraction of uncharged particles at the output is demonstrated. It has been found that an increase in the voltage (corona discharge current) at a constant aerosol flow rate leads to a decrease in the external charging efficiency from 43% to 6% and an increase in the loss of charged particles from 38% to 93%.


## Acknowledgments

This research was funded by the Russian Science Foundation grant No. 22-79-10127.

## REFERENCES

1. **Alonso M., Huang C. H.,** High-efficiency electrical charger for nanoparticles, Journal of Nanoparticle. 17 (2015) 1-8.

## THE AUTHORS

**PATARASHVILI Anton N.**
patarashvili@phystech.edu

**KORNYUSHIN Denis V.**
kornyushin.d@phystech.edu
ORCID: 0000-0003-4164-178X

**IVANOV Matthew S.**
ms.ivanov@phystech.edu

**ALESHINA Marina Y.**
aleshina.miu@phystech.edu

**EFIMOV Alexey A.**
efimov.aa@mipt.ru
ORCID: 0000-0003-3276-0277

**IVANOV Victor V.**
ivanov.vv@mipt.ru
ORCID: 0000-0002-9149-0468

# Initialization of synthesis in quadrupole magnetic traps using controlled plasma instabilities and spherical cumulation of shock magnetic waves

**A. I. Somov** [1]✉

[1]Samara National Research University named after Academician S.P. Koroleva, Samara, Russia

✉artem.somov.2002@mail.ru

**Abstract.** In this paper, the author considers the problem of initialization of thermonuclear fusion in a fully ionized plasma in quadrupole magnetic traps. Using the example of a magnetic field generator consisting of a system of magneto-optical quadrupole lenses, the effect of spherical cumulation of shock magnetic waves on the conditions for the occurrence of thermonuclear fusion reactions for $^{7}$Li, $^{9}$Be and $^{11}$B ions is studied. The issue of maintaining thermonuclear reactions is also raised, within which an assumption is put forward on the use of controlled plasma instability of the turbulent type to balance the instabilities formed during the synthesis and scattering of magnetic shock waves after cumulation.

The departure from some classical principles in the construction of plasma configuration models is due to the physical need to create the most optimal conditions for the occurrence of thermonuclear fusion, as well as an attempt to create nuclear fuel regeneration during reactions. A three-component plasma provides a variety of reactions that are important for the stability of the configuration, occurring in 3 stages, each of which not only releases useful energy, but also forms the necessary material for the reactions of the following cycles.

**Keywords:** quadrupole lenses, shock magnetic waves, turbulent instability, spherical cumulation.

## Introduction.

In this scheme of plasma distribution configurations inside the synthesis chamber, which consists of 4 magneto-optical quadrupole lenses (2 doubles) and 5 solenoids located between the lenses and designed to accumulate plasma after passing through the quadrupole [1]. The reactions do not proceed immediately, but are realized in 3 cycles, corresponding to the position of the plasma relative to the lenses.

During the first cycle, the "building material" for future reactions is prepared, and the plasma is heated along with its compression caused by the drift shift of ions in the magnetic field of the quadrupole lens. Plasma is heated along with its compression caused by the drift displacement of ions in the magnetic field of the quadrupole lens. The α-particles, $^{6}$Li and deuterium ions obtained during the reactions of the first cycle, as a result of being smaller relative to other ions, shift them to the center of the system, passing through the entire layer of the mixture of $^{11}$B and $^{9}$Be, which initiates a cascade of reactions of the 2nd cycle.

The pre-heated and compressed plasma of 3 kinds first enters into convection mixing: $^{7}$Li ions mix with a mixture of $^{11}$B-$^{9}$Be ions, after which shock magnetic waves are generated. The shock wave causes rapid heating of the convection mixing region, starting the process of constant energy exchange between the heated $^{11}$B-$^{9}$Be mixture, the core and the lithium shell.

The shock wave, passing through the $^{11}$B-$^{9}$Be layer, reaches the geometric center of the magnetic lens, where a small spherical bubble will be maintained, which is necessary for unlimited spherical cumulation on the cavity [2]. This leads to a rapid increase in temperature and pressure in the region of bubble collapse, and makes it possible to increase the temperature to $10^{8}$ K, which is sufficient to start thermonuclear fusion reactions.

## Materials and Methods

**Equations**, which describes spherical cumulation of shock magnetic waves could be described in the first approximation as the focusing of a wave in a heat-conducting gas [2-3]. In terms of T, we obtain:

$$\frac{d\tau}{dx}=\frac{1}{B\tau^3}\left(\frac{\frac{2\tau}{(\gamma+1)}-1}{1+\sqrt{\frac{1-8\tau(\gamma-1)}{(\gamma+1)^2}}}+\frac{1}{2}\right),\tau=\frac{T_0}{T};B=\frac{256}{3}\frac{(\gamma-1)^4}{(\gamma+1)^8}\frac{L\sigma D^5}{\rho_0 R^4} \quad (1)$$

where R is universal gas constant, $T_0$, T − initial temperature and the temperature at the front of shock wave.

To describe turbulent layer pressure, we use Turbulent Equal Distribution model (TED)[2-3]:

$$\begin{cases}\frac{d}{dt}\frac{B(x)}{n(x,t)}=0\\ \frac{dP(x)}{dx}=-\rho w\end{cases},B(x)\square kx;mw=-qBv\cos\varphi\rightarrow P(x)=\frac{\mu W v n_0\cos\varphi}{2R^2x_0}\int x^3dx; \quad (2)$$

Here $w$ − acceleration of particle in magnetic field; B(x) − magnetic field induction; x − distance from the center of the magnetic trap.

## Results and Discussion

As a result of integrating the equations (1), (2) and substitution of parameters corresponding to setting [1] we are getting graphs of these dependencies (Fig. 1):

*a*) *b*)

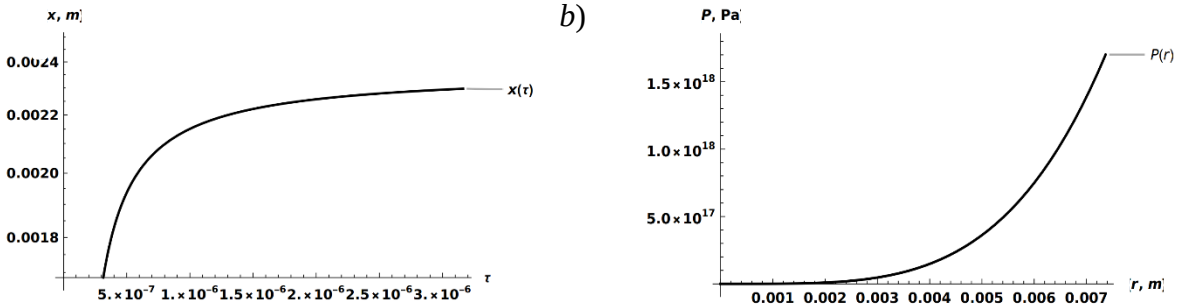


Fig. 1. Graphs of the dependence of distance of cumulation center on the relative temperature $x(\tau)$ and dependence the pressure [MPa] to the distance of from the edge of the turbulent layer P($r$) (*b*), $x$, $r$ [m]

## Conclusion

After analyse of the graphs of the obtained dependences of pressure and relative temperature on the coordinates, we can conclude that spherical cumulation does indeed take place in this configuration and makes it possible to achieve the required temperature ($10^8$ K) and pressure ($10^{18}$ Pa) for the initiation and maintenance of thermonuclear synthesis.

## REFERENCES


1. **Patent** RU 2 757 666 C1 IPC H05H 1/54 (2006.01) CPC H05H 1/54 (2021.08) Application: 2021105186, 01.03.2021.

2. **K. V. Chukbar.** Lectures on transport phenomena in plasma - Dolgoprudny: Intellect Publishing House, 2008, ISBN 978-5-91559-015-0.

3. **V. V. Yankov,** Attractors and freezing-in invariants in a turbulent plasma, UFN, 167:5 (1997), 499–516; Phys. Usp. 40:5 (1997), 477–493.

# Fiber-optic system development for the output frequency setting of a voltage-controlled oscillator at the radar station antenna complex

**V. B. Fadeenko[1]✉ and D. A. Ryzhova[1]**
[1] Peter the Great Saint-Petersburg Polytechnic University, Saint Petersburg, Russia.
✉ v21.07.96@mail.ru

**Abstract.** The necessity of introducing fiber-optic communication lines for the frequency tuning codes transmission and frequency regulation is substantiated. A new scheme is presented for constructing the radar station radiation path in the range from 1 to 18 GHz. A functional expansion of the radar station capabilities is presented through the introduction of a modernized radiation path and the study of radiation formations. Fiber-optic lines investigations have been carried out in terms of launching frequency codes and a control channel. The corresponding characteristics have been given.

**Keywords:** Fiber optic communication line, microwave signal, radar station, radiation monitoring, voltage-controlled oscillator

## Introduction

The active industry and scientific development of technological progress pose a large number of tasks to scientists. One of them is monitoring the state of air and water spaces [1]. The main reason is the harmful substances emissions increase of both into the atmosphere and into the water space. These pollutants include emissions of radioactive particles, which have a significant impact on human health. When conducting radiation monitoring, special difficulties arise in determining radioactive contamination, composition and size. Radioactive particles form a plasmoid – an ionization formation that, is able to carry pollution over long distances in the form of a cloud [2]. The main plasmoid propagation problem is the further deposition of radioactive elements on the earth's surface in the form of precipitation. Use the radar method to detect radiation formations in the atmosphere at long distances, in hard–to-reach places and control their movements is one of the ways to solve this problem. In the conditions of open sea space, this method is prevailing. An urgent task of our time is the development and modernization of multifunctional sea-based radar stations for solving various tasks: object detection; identification of targets and determination of their parameters; environmental monitoring of near-Earth space [3].

The radar method consists in detecting a weak reflected signal from the studied objects with further localization. A plasmoid is formed from particles of various kinds, reflections from which occur at different frequencies. The maximum reflected signal from the plasmoid is formed at frequencies corresponding to the resonant states of radionuclide isotopes, for example, $^{16}N$, $^{133}Xe$, $^{88}Kr$. It is necessary to conduct a frequency scan in the range from 1 to 18 GHz to determine the composition of the plasmoid, as well as to ensure the stability of the frequency tuning to study the characteristics of the detected plasmoid [2]. This paper proposes the voltage-controlled oscillator (VCO) use with digital frequency setting to adjust the frequency in a wide range. For stable operation and the possibility of monitoring the generator output frequency, it is proposed to introduce a generator control circuit and a frequency control channel based on a fiber-optic line.

## Features of a frequency voltage-controlled generator setting system construction

A voltage-controlled generator is used to generate a signal in the transmitting path of the radar. This fact makes it possible to adjust the wavelength of radiation in order to study air masses and detect ionization formations. It is necessary to control the frequency at the output of the generator, which is controlled by voltage in conditions of increased electromagnetic environment and precise frequency adjustment. Fig. 1 shows the frequency setting system by a voltage-controlled generator.

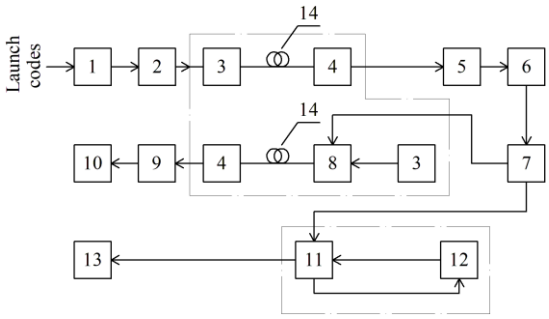


Fig. 1. Block diagram of a two-channel FOCL for VCO frequency monitoring and control: 1 - ROM, 2 - DAC, 3 – laser module with direct modulation, 4 - photodetector module, 5 - LNA based on an operational amplifier, 6 – voltage controlled analog oscillator, 7 – power divider 1:4, 8 – electro-optical modulator, 9 – ADC, 10 – indication and control device, 11 – amplifier, 12 – bandpass filter in the feedback circuit of the amplifier, 13 – short emitter-dipole of a parabolic antenna, 14 – single-mode optical fiber.

## Results and Discussion

Studies were carried out in the laboratory of the amplitude-frequency characteristics of the developed FOCL two channels, the change in frequency response from temperature T and tangential sensitivity. Fig. 2 shows the frequency response of the channel for controlling the radiation frequency of the antenna complex, which is formed by VCO.

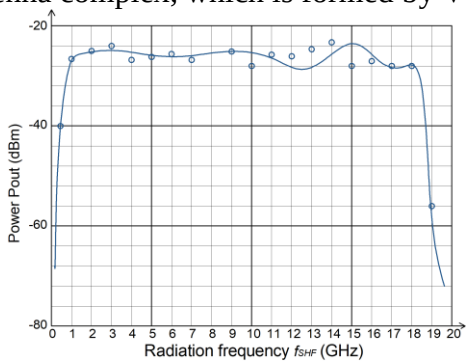


Fig. 2. FOCL Frequency response of the radiation frequency $f_{SHF}$ control channel.

The characteristic unevenness is 3 – 6 dB at a radiation frequency $f_{SHF}$ up to 18 GHz.

Temperature shift is about 0.5 dB. Therefore, the temperature factor has practically no effect on signal transmission over FOCL.

## Conclusion

The obtained results show the reliability of the developed two-channel FOCL to provide the necessary operating mode of the radiating antenna in each frequency range and to conduct research on radioactive formations. It becomes possible to localize weak reflected signals from supposed ionization radiations formed as a result of the ingress of radioactive elements into the atmosphere, and to establish a possible type of particles, since the microwave signal reflected at different frequencies $f_{SHF}$.

The FOCL developed design allows to control the operation of the antenna complex radiator at distances of the order of 100 km.

## REFERENCES

1. **Mazing M. S., Zaitceva A. Y. and Kislyakov Y. Y.,** Monitoring of oxygen supply of human tissues using a noninvasive optical system based on a multi-channel integrated spectrum analyzer, International Journal of Pharmaceutical Research. Vol. 12 (2020) 1974.

2. **Elokhin A. P**., Unconventional Methods of Radiological Environmental Monitoring and Earthquake Prediction, Atomic Energy. Vol. 117(3) (2015) 206–215.

3. **Fadeenko V. B., Fadeenko I. V., Vasiliev D. A., Davydov V. V., Rud V. Yu.,** Multifunctional radar system for remote control of environment and the Earth's surface, Journal of Physics: Conference Series. Vol. 1745 (2021) 012023.

# NUMERICAL SIMULATION OF THE PARAMETERS OF A LOW-NOISE TRANSISTOR WITH LOW POWER CONSUMPTION FOR USE AS PART OF MONOLITHIC INTEGRATED CIRCUITS OF AN ENERGY-EFFICIENT LOW-NOISE AMPLIFIER FOR USE IN THE AMPLIFICATION PATH OF A MINIATURE RADIOTHERMOGRAPH

**V. G. Tikhomirov**[1], **S. V. Chizhikov**[2✉], **A. G. Gudkov**[2], **R. S. Ignatovich** [1],
[1] Saint Petersburg Electrotechnical University "LETI", Saint Petersburg, Russia;
[2] Bauman Moscow State Technical University, Moscow, Russia
✉chigikov95@mail.ru

**Abstract.** The high current consumption of amplifying cascades in a miniature radiothermograph housing with these microcircuits existing today leads to a significant increase in temperature inside the housing with a reference noise source located there and subsequent heating of the surrounding tissues with distortion of the picture of the real field of internal temperatures of the bio-object. The existing problem can be solved by creating new active elements of specialized monolithic microwave chips - low-noise transistors, for which the requirements of high energy efficiency, primarily low heat dissipation into the surrounding space, low noise level and sufficient gain will be taken into account when designing heterostructures. The paper presents the results of numerical simulation of a low-noise transistor with low power consumption for use as part of monolithic integrated circuits of an energy-efficient low-noise amplifier for use in the amplifying path of a miniature radiothermograph.

**Keywords:** medical radiothermograph, MIC microwave, energy consumption, energy efficiency.

**Funding:** This study was funded by the Russian Science Foundation grant number 19-19-00349-П.

## Introduction

The amplifying path of a medical radiothermograph has extremely high requirements for miniaturization, an error in determining body temperature not exceeding tenths of a degree, a record low level of intrinsic noise in the microwave range, etc.

The low level of the received signals of the human body's own radiation leads to the need to provide a gain of the receiving path of about 80 dB with minimal levels of its own noise. The construction of such a path requires several chips with a total current consumption in the operating mode of the order of hundreds of milliamps. Such current consumption of amplifying cascades in a miniature radiothermograph housing, with the efficiency of these microcircuits existing today, leads to a significant increase in temperature inside the housing with a reference noise source located there and subsequent heating of the surrounding tissues with distortion of the picture of the real field of internal temperatures of the bio-object. The existing problem can be solved by creating new active elements of specialized monolithic microwave chips - low-noise transistors, for which the requirements of high energy efficiency, primarily low heat dissipation into the surrounding space, low noise level and sufficient gain will be taken into account when designing heterostructures [1].

## Materials and Methods

Heterostructures of A3-B5 group semiconductors can reasonably be considered a promising system of materials for solving the above problem. The experience gained by the authors of successful mathematical modeling and practical implementation of heterostructural microwave transistors with high electron mobility [2], suggests a reasonable probability of a successful solution to the above problem of creating a special low-noise microwave transistor with reduced heat dissipation.

## Results and Discussion

Since the element component base implemented on AlGaAs/GaAs pHEMT heterostructures has the lowest noise coefficients, it is these heterostructures that are used in the manufacture of hybrid and monolithic LNA. In this work, the parameters of a heterostructural transistor for the MIC amplification path of a medical radiothermometer were optimized. As a result of optimizing the transistor design based on the previously specified requirements, a calculated steepness characteristic was obtained, clearly showing the increased amplifying properties of the proposed transistor in the low current region, which directly leads to the possibility of a significant reduction in current consumption of the entire chip. The noise characteristics of the transistor were also simulated before and after optimization, the results of which showed that the optimized transistor design has a lower noise coefficient compared to the original one, which is shown in Figure 1. Noise at low current values remained within acceptable values.

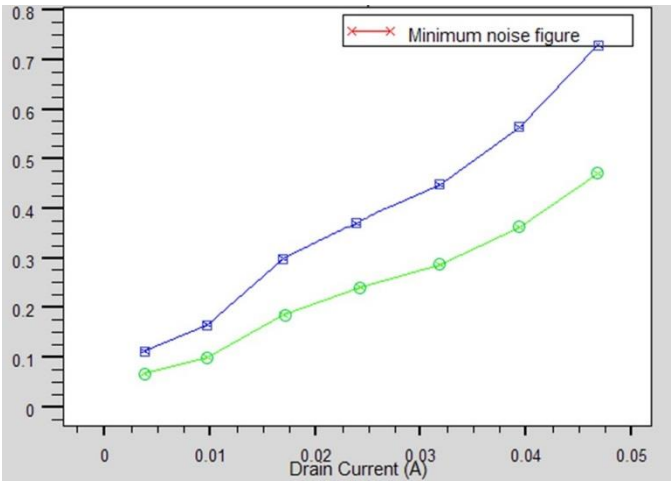


Fig. 1. Calculated characteristics of the noise characteristic of the transistor. Squares are a common design, circles are an optimized design.

## Conclusion

The presented numerical simulation results allow us to judge the possibility of significantly reducing the current consumption of the entire amplifier chip and improving its noise characteristics.

## Acknowledgments

The research was carried out with the financial support of the Russian Science Foundation as part of the scientific project No. 19-19-00349-П dated 19.05.2022.

## REFERENCES

1. **Gawande R., Bradley R.**, Low-Noise Amplifier at 2.45 GHz, IEEE Microwave Magazine. 11 (1) (2010) 122-126.

2. **Tikhomirov V.G., Gudkov A.G., Agasieva S.V., Dynaiev D.D., Popov M.K., Chizhikov S.V.**, Increasing efficiency of GaN HEMT transistors in equipment for radiometry using numerical simulation, Journal of Physics Conference Series 1410 (2019):012191.

# Galvanomagnetic properties in "size" topological insulators $Bi_2Se_3$

**V. V. Chistyakov** [1,2✉], **A. N. Perevalova** [1], **B. M. Fominykh** [1,2], **V. V. Marchenkov** [1,2]
[1] M.N. Mikheev Institute of Metal Physics UB RAS, Ekaterinburg, Russia;
[2] Ural Federal University, Ekaterinburg, Russia
✉wchist@imp.uran.ru

**Abstract.** The magnetoresistivity and Hall resistivity of thin films of a topological insulator of $Bi_2Se_3$ with a thickness of 10 nm to 75 nm in the temperature range from 4.2 to 80 K, and in magnetic fields of up to 10 T were measured. A size effect in the magnetoresistance and the Hall resistance of $Bi_2Se_3$ films was observed, i.e. linear dependence of the magnetoresistance and the Hall resistance of the film on its inverse thickness. It is suggested that a similar effect can be observed in other TIs and systems with an inhomogeneous current distribution over the cross section of the sample.

**Keywords:** topological insulators, size effect, thin films.

**Funding:** This work was carried out within the state assignment of the Ministry of Education and Science of the Russian Federation ("Spin", No. AAAA-A18-118020290104-2).

## Introduction

In recent years, topological materials have attracted great interest both from the point of view of fundamental science and due to promising prospects for practical application for the development of new devices for ultrafast nanoelectronics and spintronics. There are topological insulators [1-3] and topological semimetals [4]. In topological insulators, their bulk is a dielectric or semiconductor, and the surface behaves like a topologically protected metal with a linear dispersion law. Current carriers in the "surface" layer of topological insulators are spin-polarized and practically do not scatter on defects, which can be used in spintronics and quantum computing.

Due to the large difference in the conductivity of the bulk and surface, the electron transport of topological insulators may experience a "size" effect, i.e., the dependence of the transport properties on the thickness of the sample. Thus, the dependence of the number of transport channels in thin $Bi_2Se_3$ films on their thickness was found in [5]. The authors of [6] found the dependence of the carrier relaxation time on the thickness of the $Bi_2Se_3$ film. The paper [7] describes the size effect in the parameters of quantum oscillations of films of the $Bi_2Te_3$ topological insulator. In [8], the size effect in the conductivity of $Bi_2Se_3$ thin films was discovered; linear dependence of conductivity on their inverse thickness. Apparently, the size effect will also be observed in other electronic properties, in particular, in the magnetoresistance and the Hall Effect. The purpose of this work is to search for and study the size effect in the galvanomagnetic properties of $Bi_2Se_3$ films.

## Materials and Methods

Thin films of $Bi_2Se_3$ were grown by the molecular beam epitaxy method on $Al_2O_3$ substrates with thickness from 10 to 75 nm. The measurements of the magnetoresistivity and Hall resistivity were carried out by the conventional 4-points method at dc-current in the temperature range from 4.2 to 80 K and in magnetic fields of up to 10 T in the Collaborative Access Center "Testing Center of Nanotechnology and Advanced Materials" of M.N. Mikheev Institute of Metal Physics of the Ural Branch of the Russian Academy of Sciences.

## Results and Discussion

The performed studies have shown that the size effect, i.e. the dependence of the physical properties on the transverse dimensions of the sample is observed in the galvanomagnetic

properties of $Bi_2Se_3$ films. The magnitudes of the magnetoresistance and the Hall resistance strongly depend on the film thickness. From measurements of the field and temperature dependences of the magnetoresistance and Hall resistance of $Bi_2Se_3$ films of various thicknesses, one can estimate the values of the "surface" and "bulk" contributions to their galvanomagnetic characteristics, i.e. in the magnetoresistance and the Hall Effect, as well as to follow the changes in these contributions with the magnetic field and temperature.

In addition, to analyze the data on the Hall Effect, along with the single band model, the two band model [9] was also used, which made it possible to determine the concentrations and mobilities of both electron and hole charge carriers. The paper presents the results and comparison of data obtained in the framework of two band and single band models.

## Conclusion

As a result of the studies performed, a size effect was found in the galvanomagnetic properties of $Bi_2Se_3$ films; dependence of the magnetoresistance and the Hall Effect on the film thickness. The concentrations and mobility of charge carriers are estimated both by the one band model and by the two band model, and a comparative analysis of the results is carried out. The obtained data were analyzed within the framework of existing ideas about topological insulators.

## Acknowledgments

This work was carried out within the state assignment of the Ministry of Education and Science of the Russian Federation ("Spin", No. AAAA-A18-118020290104-2). V.V. Chistyakov, A.N. Perevalova and B.M. Fominykh are grateful to IMP UB RAS for supporting their work on the state task "Spin", which was carried out within the framework of the youth grant No. m26-22. V.V. Chistyakov and V.V. Marchenkov appreciate the support of the Ural Federal University (Priority-2030 Program).

## REFERENCES

1. **Qi X.-L., Zhang S.-C.**, Topological insulators and superconductors, Reviews of Modern Physics. 83 (2011) 1057.

2. **Mazumder K., Shirage P.M.**, A brief review of $Bi_2Se_3$ based topological insulator: From fundamentals to applications, Journal of Alloys and Compounds. 888 (2021) 161492.

3. **Liu Y., Chong C., Chen W., Huang J.A., Cheng C., Tsuei K., Li Z., Qiu H., Marchenkov V.V.**, Growth and characterization of MBE-grown $(Bi_{1-x}Sb_x)_2Se_3$ topological insulator, Japanese Journal of Applied Physics. 56 (2017) 070311.

4. **Armitage N.P., Mele E.J., Vishwanath A.**, Weyl and Dirac semimetals in three-dimensional solids, Rev. Mod. Phys. 90 (2018) 015001.

5. **Wang W.J., Gao K.H., Li Z.Q.**, Thickness-dependent transport channels in topological insulator $Bi_2Se_3$ thin films grown by magnetron sputtering, Scientific Reports. 6 (2015) 25291.

6. **Glinka Y.D., Babakiray S., Johnson T.A., Bristow A.D., Holcomb M.B., Lederman D.**, Ultrafast carrier dynamics in thin-films of the topological insulator $Bi_2Se_3$, Appl. Phys. Lett. 103 (2013) 151903.

7. **Rogacheva E.I., Budnik A.V., Nashchekina O.N., Meriuts A.V., Dresselhaus M.S.**, Quantum Size Effects in Transport Properties of $Bi_2Te_3$ Topological Insulator Thin Films, Journal of Electronic Materials. 46 (7) (2017) 3949.

8. **Chistyakov V.V., Domozhirova A.N., Huang J.C.A., Marchenkov V.V.**, Size Effect in the Electrical Conductivity of Thin Films of Topological Insulator $Bi_2Se_3$, Bulletin of the Russian Academy of Sciences: Physics. 83 (2019) 838.

9. **Luo Y., Li H., Dai Y.M., Miao H., Shi Y.G., Ding H., Taylor A.J., Yarotski D.A., Prasankumar R.P.**, Thompson J.D., Hall effect in the extremely large magnetoresistance semimetal $WTe_2$, Appl. Phys. Lett. 107 (2015) 182411.

# Improving microwave output in rubidium-87 atomic frequency standard with new automatic gain control

**A V Shavshin[1] and V V Davydov[1, 2]**
[1] Peter the Great Saint-Petersburg Polytechnic University, Saint Petersburg, Russia, 195251
[2] All-Russian Research Institute of Phytopathology, Moscow Region 143050, Russia.
✉ shavshin2107@gmail.com

**Abstract.** The need of modernize the existing scheme of automatic control of the optical signal. The presented design was created to maintain the escape power of an atomic frequency standard (AFS) based on rubidium-87 atoms at a given level, correcting changes in its operation introduced by external conditions. An improved circuit for automatic gain control with an additional link in the form of a PID controller and an improved circuit for extracting the «error» signal are presented. A separate contribution of the subtractor and PID controller to the final gain control is considered, and mathematical modeling of microwave devices included in the microwave path is carried out. The foundation of the presented automatic gain control scheme for the atomic frequency standard was confirmed by rubidium-87.

**Keywords:** Atomic frequency standard, automatic gain control, optical signal, photodetector, stimulated emission, error signal, PID controller

## Introduction

In the modern world, quantum frequency standards are indispensable sources of highly stable, spectrally pure electrical signals to consider more in-depth topics in the scientific and technical field. There are areas in which they cannot be dispensed with/ Special requirements are imposed on atomic frequency standards (AFS), which are used in navigation systems and common time systems. One of such AFSs are standards based on rubidium-87 atoms. Considering more stringent conditions for accuracy and stability of the output optical signal formation, it becomes necessary to modernize the AFS or develop new types of AFS based on other physical principles of operation. To carry out work to improve the accuracy characteristics of the AFS, in some cases it is sufficient to upgrade the functional units that directly affect total output values of the AFS. Thus, this paper presents the modernization of the path for the formation of the microwave signal of the excitation of rubidium-87 atoms [1], aimed at the formation of both the microwave signal itself and the parameters of the AFS output signal. Similar situations arise for other types of standards.

## Updated system of automatic gain control with additional adjustment elements

As can be seen from the presented description of the operation of the AFS, the AGC system is one of the most important functional units of the microwave generation path and the entire structure of the AFS. On Fig. 1 shows a modernized circuit diagram of the AGC system.

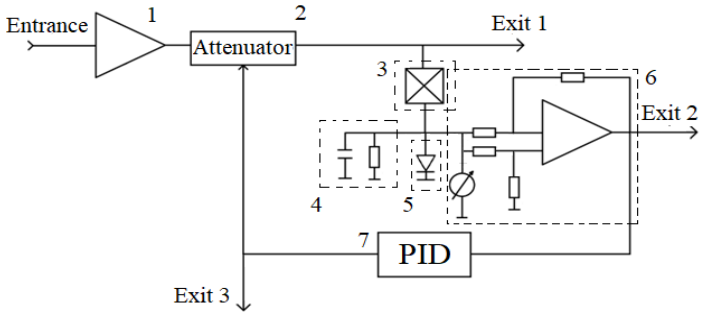


Fig. 1. Upgraded automatic gain control circuit, with the addition of a PID controller section; 2 – attenuator; 3 – directional coupler; 4 – low-pass filter 5 – detector diode, 6 – «error» signal amplifier, connected as a subtractor; 7 – PID controller.

Since the input of the system receives a signal of insufficient power, The initial task is to strengthen it so that its power is captured for the work of combating discrimination. To fulfill this condition, an amplifier was integrated (1). Then attenuator (2) will be used as a controlled element, due to the adjustment of which the output power of the signal will be adjusted. To create an "error" control signal, a portion of the original signal is applied to the AGC circuit using a directional coupler set to -3dB. (3) and the rest of the signal passes at the output of the system. Next, the «error» control signal must be straightened for the AGC system to work. Therefore, the signal passed through the directional coupler will then pass through the detector diode. (4). After detection, the signal, depending on the external operating conditions of the AFS, can have a different amplitude, based on which there is a need to be able to set the level yourself. For this, an «error» signal enhancer is used on the operational amplifier (5), connected according to the subtractor circuit. Further, the generated «error» signal is fed to the input of the PID controller (7). Depending on the values coming to the PID controller, the necessary corrective gain is analyzed, which will be applied to the attenuator.

## Results and Discussion

Thanks to dispersion, it is possible to estimate the level of stability of the frequency of atomic clocks and generators. Analyzing the obtained results, we can make sure that the addition of the AGC system in the first case improved the Allan variance values σ2(τ) by 12%, and with an additional link in the form of a PID controller, it showed an improvement by 16%. Fig. 2.

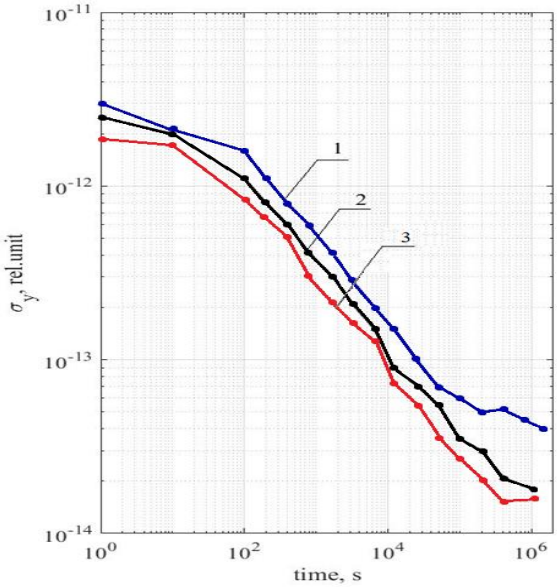


Fig. 1. Diiagram of Allan variance versus time with an upgraded AGC system (plot 3), previously used (plot 2) and without the AGC system (plot 1) in AFS.

## Conclusion

Through a series of improvements, a new AGC system was implemented for the microwave path of the ASC based on rubidium-87 atoms using a PID controller.

The results of the analysis of the operation of a prototype AFS with the developed AGC system showed that the selected schematic solution works correctly and its use improves the escape parameters of the AFS. Thanks to the new AGC system, it was possible to achieve a decrease in the values of the Allan variance by 16%.

## REFERENCES

1. **Shavshin A.V.** Development of automatic control of optical signal gain in a atomic frequency standard based on rubidium-87 atoms. IEEE 2022 VIII International Conference on Information Technology and Nanotechnology (ITNT) DOI: 10.1109/ITNT55410.2022.9848676 pp. 21991987.

UDC 53.06

# Testing the fast electrochemical micropump with PDMS membrane

**P. S. Shlepakov** [1✉], **I. V. Uvarov** [1], **A. M. Abramychev**[1], **V. B. Svetovoy**[2]
[1] Valiev Institute of Physics and Technology RAS, Yaroslavl Branch, Yaroslavl, Russia;
[2] A.N. Frumkin Institute of Physical Chemistry and Electrochemistry RAS, Moscow, Russia
✉p.shlepakov@bk.ru

**Abstract.** Microfluidic systems are widely used in various applications, including precise delivery of drugs into organs or tissues. The drug delivery system should have a compact pump with a high flow rate and precise dosage accuracy. In this work, we propose a novel micropump based on the electrochemical actuator that meets these requirements. It contains three fast membrane actuators operating peristaltically. The device has an order of magnitude smaller working part in comparison with conventional micropumps and demonstrates ultra-precise dosage, which is important for drug delivery systems. Design and testing procedure are described in detail, and working characteristics are provided.

**Keywords:** MEMS, microfluidics, micropump, alternating polarity electrolysis, electrochemical actuator.

**Funding:** This work is supported by the Russian Science Foundation, Grant No. 18-79-10038.

## Introduction

A microfluidic system is a chip with micron-sized channels and chambers for liquid. Microfluidic devices are used for many tasks in biology, chemistry, and medicine, including delivery of drugs directly to organs and tissues. This method significantly increases the effect of therapy. The lack of compact and energy-efficient pumps limits a widespread use of implantable drug delivery systems. The liquid is pumped by a reciprocating membrane driven by an actuator. The performance of the pump is defined by the driving mechanism. Several actuation principles are known to date, but an electrochemical method is the most suitable for drug delivery systems. Electrochemical actuator is a chamber with two electrodes inside, which is filled with electrolyte and closed by a flexible membrane. Electrolysis of water generates gas bubbles in the electrolyte, which create an extra pressure and push the membrane. The main disadvantage of this actuator is the slow dissolution of gases, which usually takes several minutes. A novel actuator has the dissolution time of about 1 ms due to alternating polarity electrolysis [1]. The pump based on this actuator has the working part of 3 $mm^3$ in size, which is about ten times smaller in comparison with conventional devices. Estimated flow rate and dosage accuracy are of 1.5 μL/min and 0.25 nL, respectively. This work describes the micropump design, testing procedure and performance.

## Materials and methods

The micropump contains two channels separated by a 60 μm thick polydimethylsiloxane (PDMS) membrane, see Fig. 1. Three fast electrochemical actuators are fabricated on a glass substrate. The chamber of each actuator has a diameter of 500 μm and a height of 16 μm. The chambers are formed in a photoresist SU-8 layer and contain two concentric electrodes inside. The channel for the working liquid is also formed in SU-8 and is covered by a silicon substrate. The height and width of the channel are 10 μm and 120 μm, respectively. The silicon substrate has separate filling ports for the electrolyte and working fluid. The micropump works by peristaltic deflection of actuators in a cycle of six steps shown in Fig. 2. At every step, the working channel is blocked at least by one membrane.

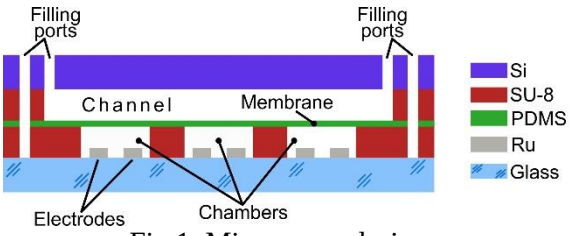

Fig 1. Micropump design

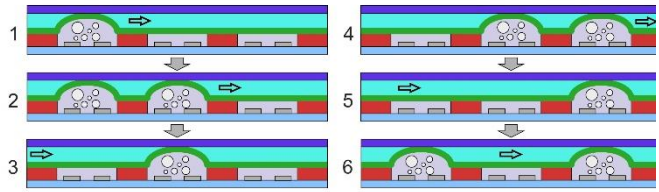

Fig 2. Working cycle of the pump

The chip has a size of 20x30x1 $mm^3$ with the working part of 3 $mm^3$. A 3D-printed sample holder is used for filling the actuators with water solution of $Na_2SO_4$, while the working channel is filled with distilled water. Six tungsten probes are installed on the contact pads and provide driving signals to the electrodes. The signal is a series of alternating polarity voltage pulses with a frequency of 500 kHz and an amplitude of 5 V. For each actuator, 40 ms long series are separated by a passive time of the same duration. The holder has a window to observe the membranes and meniscus through the glass substrate. The dosage is investigated by applying one period of driving signals. The displaced volume of liquid is found by tracking the meniscus in the working channel. In order to measure the flow rate, several tens of periods are applied to the electrodes. A path of the meniscus multiplied by the height and width of the channel gives the pumped volume, which is divided by the time of pumping.

## Results and discussion

The micropump provides the dosage of 0.14 nl, which is 40% lower than the estimated value. The reason is a reduced membrane deflection due to the presence of the working liquid in the channel. The expected stroke of 5 µm is reached at the pulse amplitude of 11 V and atmospheric air above the membrane. The working liquid in the channel loads the membrane and reduces the stroke. The measured dosage corresponds to the deflection of 2.9 µm. At the flow rate testing the meniscus moves for 1460 µm during 1.7 s. The pumping speed is of 0.06 µl/min, which is about 6 times lower than was predicted. Such a large discrepancy cannot be explained only by reduced membrane deflection. Another probable reason is a backpressure of the working liquid that increases during pumping. The deflection of the membrane is not enough to block the channel, so a backflow of the working liquid takes place. Adjusting the stroke to the channel height will eliminate the backflow and improve the performance. It may be achieved by using the explosive regime that ensures much higher stroke [1]. Nevertheless, the ratio of the flow rate to the volume of the working part is comparable to this ratio for other devices [2]. Thus, the micropump meets the requirements of drug delivery systems. Further investigation will solve existing problems.

## REFERENCES

1. **Uvarov, I. V., Lokhanin, M. V., Postnikov, A. V., Melenev, A. E., Svetovoy, V. B.**, Electrochemical membrane microactuator with a millisecond response time, Sensors and Actuators B: Chemical. 260 (2018) 12-20.

2. **Forouzandeh, F., Arevalo, A., Alfadhel, A., Borkholder, D. A.**, A review of peristaltic micropumps, Sensors and Actuators A: Physical. 326 (2021) 112602.

# Extremely high frequency Schottky diodes based on single GaN nanowires

**K. Yu. Shugurov [1✉], A. M. Mozharov [1,2], V. V. Fedorov[1], V. V. Neplokh[1], I. S. Mukhin[1,2]**

[1] Alferov University (former St. Petersburg Academic university), St. Petersburg, Russia;
[2] Peter the Great St. Petersburg Polytechnic University, St. Petersburg, Russia

✉shugurov@spbau.ru

**Abstract.** We report on the fabrication and study of a series of Schottky diodes in the ground-signal-ground topology based on individual GaN nanowires. The electrical characterization of I-V curves demonstrated relatively high ideality factor value (about 6-9) in comparison to the planar Au/GaN diodes that can be attributed to the nanowire geometry. The effective barrier height in the studied structures was defined in the range of 0.25 – 0.4 eV. The small-signal frequency analysis was employed to study the dependency of the scattering parameters in the broad range from 0.1 to 40 GHz. The approximation fitting of the experimental data indicated the record high cutoff frequency of about 165.8 GHz.

**Keywords:** gallium nitride, Schottky diode, nanowires, EHF band.

**Funding:** This study was funded by the Russian Scientific Foundation (grant №22-22-20070) and the St Petersburg Scientific Foundation (grant №08/2022).

## Introduction

Gallium nitride (GaN) is one of the most promising semiconductor materials due to the selection of important properties: wide bandgap, electrical, thermal, chemical and radiation stability. Despite the significant progress in GaN implementation and commercially available component stock, the rapid expansion of GaN in the civil microwave device industry is restrained by economical and technological factors. Among them it should be mentioned the dependency on expensive growth substrates (SiC, sapphire), and, more importantly, the necessity of buffer layer formation compensating the lattice mismatch between GaN and the substrate material. Moreover, even the synthesis on silicon provides only partial solution due to the technological complications leaving the final costs still too high, while the native GaN substrates are dramatically expensive and unavailable for massive implementations. These reasons explain why the problems of low-defective layer formation (dislocations, point defects etc.) in GaN heteroepitaxy are still requiring solution [1].

The existing limitations can be overcome with transition from classic planar structures to nanowires (NWs) having specific properties due to their geometry, i.e. high surface-to-volume ratio and developed sidewall surface. The main advantage of NWs is their high crystal quality that significantly surpasses the one of thin films, which directly influences the transport processes and allows NW-based device functionality at high current density conditions [2]. Mechanical stress associated with lattice mismatch taking place at NW growth effectively relaxes at the NW sidewalls, therefore NWs have almost no dislocation defects. Moreover, NWs do not need buffer layer even at synthesis on significantly mismatched substrate materials both in terms of lattice parameter and thermal expansion coefficient (e.g. Si). Besides the high crystal quality, NWs are also characterized with a low cross section (typically less than 200 nm cross section diameter) and elevated doping atoms solubility. This provides a low electrical capacity in the final devices while maintaining high conductivity leading to the increase of the operating speed. Such nanoobjects can be used to significantly improve the performance of high sensitive zero-bias RF/microwave/THz detectors [3]. Additionally, the NW-based structures also benefit from the advantage of the effective heat evacuation due to the high sidewall area to the NW volume ratio. To sum up, GaN NWs maintain economically motivated integration with silicon while providing an efficient solution to the synthesized material quality and suitable for HF devices.

One of the most important elements of microwave electronics is the Schottky diode as well as other device structures featuring metal-semiconductor contacts including field-effect transistors (FETs) and high-electron-mobility transistors (HEMTs). This diode type has several significant

advantages over p-n junction diodes, i.e. the relatively simple design, lower energy consumption, and absence of diffusing capacity. Therefore, Schottky diodes are extensively used in electronics, particularly in microwave receivers and mixers. In turn, Schottky-contacted NWs are in the focus of intensive research aimed at developing high sensitive and fast responsible bio/gas/chemical/photo/strain sensors for Internet-of-Things [4].

In the presented work we report on the results of the study of the Schottky diodes based on individual doped GaN NWs. We demonstrated that the operation frequencies of the proposed diodes lie in the extremely high frequency (EHF) band that is in particular demanded for the development of modern telecommunication and data transmission systems.

## Experiment

GaN nanowires were synthesized via molecular beam epitaxy (MBE) on silicon substrates. The NWs were transferred from the growth substrate into the isopropyl alcohol (IPA) via the standard ultrasonication procedure. Then the NWs were dispersed from the prepared IPA solution onto arbitrary quartz glass substrates by drop-casting method. Laser lithography and vacuum metal deposition were used to form the contact pads in the ground-signal-ground (GSG) configuration required for the frequency studies.

The frequency signal tests were performed using the experimental setup consisting of a vector network analyzer (VNA) Keysight Technologies N5234B, microwave GSG-probes, and Keithley 2401 source-meter for the bias application to the tested diodes. In this work we measured the multipolar scattering parameters (S-parameters) of the diodes in the small-signal regime in the frequency range of 0.1..40 GHz. Just prior to the frequency measurements we performed the de-embedding procedure to subtract the transmission line influence on the signal response from the studied structures. The electrophysical parameters of the studied diodes were defined using the experimental results fitting by corresponding analytic expressions of the equivalent diode circuit.

## Conclusion

In the presented work we fabricated a series of Schottky diodes based on individual n-GaN NWs. Grown NWs were transferred to the arbitrary holder for individual processing. The collected I-V test and frequency measurements data were used to define the effective barrier height value, ideality factor, as well as the parameters of the equivalent electrical circuit governing the diode performance. It was found out that the diodes are characterized by the cutoff frequencies lying in the EHF band, and withstand high current densities of hundreds of kA/cm$^2$.

## Acknowledgments

K. Yu. Shugurov and A. M. Mozharov thank the Russian Scientific Foundation (grant №22-22-20070) and the St Petersburg Scientific Foundation (grant №08/2022) for the financial support of work.

## REFERENCES

1. Zhong Y., Zhang J., Wu S., Jia L., Yang X., Liu Y., Zhang Y., Sun Q., A review on the GaN-on-Si power electronic devices, *Fundamental Research.* 2 (3) (2022) 462–75.

2. Shugurov K., Mozharov A., Sapunov G., Fedorov V., Tchernycheva M., Mukhin I., Single GaN Nanowires for Extremely High Current Commutation, *physica status solidi (RRL) – Rapid Research Letters.* 15 (4) (2021) 2000590.

3. Santoruvo G., *AlGaN/GaN Nanowires: from Electron Transport to RF Applications,* (Lausanne: École Polytechnique Fédérale de Lausanne).

4. Meng J., Li Z., Schottky-Contacted Nanowire Sensors, *Advanced Materials.* 32 (28) (2020) 2000130.

# Hardware- and User-Induced Micromobility Effects in In-Door Radio Access at 140 GHz

**T. A. Yaropolov** [1✉], **A. N. Prikhodko** [1,2], **P. V. Rozhkova** [1], **A. S. Shurakov** [1,2], **G. N. Goltsman** [1,2]

[1] Moscow Pedagogical State University, Moscow, 119991, Russia;

[2] National Research University Higher School of Economics, Moscow, 101000, Russia

✉ta.yaropolov@mpgu.su

**Abstract.** Sub-terahertz frequency band is beneficial for radio access networks of the sixth generation. Due to rather limited power capacity, there appears a necessity to equip transmitters and receivers in sub-terahertz wireless channels with high directivity antennas. This, however, leads to a potential connection failure in response to even a minor linear or angular displacement of a user equipment. This article is focused on a hardware- and user-induced micromobility effects for different scenarios of in-door radio access at carrier frequency of 140 GHz. The developed measurement setup enables fast simultaneous logging of linear and angular displacements of a user equipment with respect to radio access point and the corresponding received signal strength. Experimental data is processed by Allan variance analysis, statistics is acquired for a large number of samples. We believe that our findings should be of use in the development of beam steering solutions for reliable sub-terahertz wireless communications.

**Keywords:** user micromobility, 6G wireless system, sub-terahertz communication.

**Funding:** This study was funded by the Russian Science Foundation grant number 22-79-10279, https://rscf.ru/project/22-79-10279/.

## Introduction

Sub-terahertz frequency (sub-THz) band is beneficial for wireless radio access networks of the sixth generation (6G). It is conventionally proposed to use highly directive antennas in transmitters (Tx) of access points and receivers (Rx) of user equipment (UE) in 6G networks. In this case, reliability of wireless channel can be notably compromised if UE is mobile. User micromobility is one of the main issues in the implementation of 6G wireless communication systems [1]. In this work, we study hardware- and user-induced micromobility effects for different scenarios of in-door radio access at carrier frequency of 140 GHz. The considered scenarios are related to web searching and online gaming characterized by low-deterministic misalignment between sub-THz beams of Tx and Rx. We develop measurement setup for fast simultaneous logging of time-dependent position of UE with respect to Tx and the corresponding signal strength at Rx. Time related metrics are statistically acquired by Allan variance analysis. In addition, our measurements enable profiling of the Rx signal strength in different Tx beam planes. This should find use in the development of beamforming solutions for 6G wireless communication systems.

## Results and Discussion

We fabricate UE with linear dimensions similar to a typical large-screen smartphone to insure its realistic mechanics in user hands. UE is equipped with a motion sensor and Rx and is placed far behind a Fraunhofer distance in front of Tx. The sensor makes use of microelectromechanical systems (MEMS) accelerometers and gyroscopes and measures linear accelerations and angular velocities with respect to 3-dimensional intrinsic reference frame (IRF). Antennas of Tx and Rx have a far-field beamwidth of a few degrees. Referring to Figure 1a, the angles φ and θ are restored in the spherical coordinate system fixed to UE. They are defined as the angles between the corresponding axes of IRF at the initial moment of time $t$ = 0 ($x$(0) and $z$(0)) and during current measurement ($x$(t) and $z$(t)). The measurements are carried out with Tx providing a constant waveform signal at carrier frequency of 140 GHz and an amplitude modulation at 25 kHz. Rx is based on a waveguide Schottky diode envelope detector [2]. The readout is maintained by a selective nanovoltmeter. The detector response voltage, i.e.,

signal strength at Rx, is recorded simultaneously with the readings of accelerometers and gyroscopes by a data acquisition system. This ensures an exact correspondence of the changes in the received signal strength with the UE coordinates.

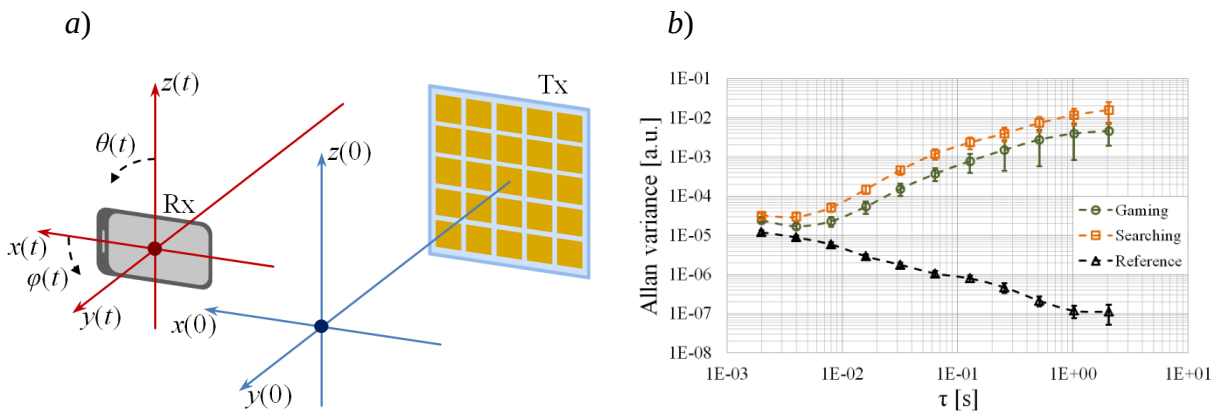


Fig. 1. (*a*) Wireless channel with static sub-THz access point and mobile UE and (*b*) experimental Allan variance curves for signal strength at UE in various application scenarios

We employ the developed measurement setup to study stability of the received signal upon a short distance transmission for online gaming and web searching scenarios. A series of independent measurements with a duration of 60 s each is conducted. The experimental data is statistically processed by Allan variance analysis. Figure 1b summarizes results of the processing, stability of the received signal for a static position of UE at the initial moment of time $t = 0$ is provided as a reference. The latter obeys a radiometer equation for integration times, τ, from 2 ms to 2 s. This ensures reliable extraction of the micromobility-induced instabilities in the received signal. For online gaming scenario, we observe white noise and drift signatures for τ of below and above 4 ms, respectively. No 1/F-noise signature is recognized. Furthermore, confidence intervals for the Allan variance values widen with increase in τ. And they are notably wider as compared to the web searching curve at any given τ. For web searching scenario, we observe 1/F-noise and drift signatures for τ of below and above 4 ms, respectively. No pronounced white noise signature is recognized. The acquired Allan variance curves also reveal high repeatability in numerous independent measurements. For both gaming and searching scenarios, we perform stability profiling for a number of planes with respect to the Tx beam. This aids to analyze contribution of UE optics design and user activity to the received signal stability. We believe that our findings should find use in the development of efficient beam steering solutions for reliable sub-terahertz wireless communication systems.

## REFERENCES

1. **Petrov V., Moltchanov D., Koucheryavy Y., Jornet J. M.**, Capacity and outage of terahertz communications with user micro-mobility and beam misalignment, IEEE Transactions on Vehicular Technology. 69 (4) (2020) 6822–6827.

2. **Shurakov A., Belikov I., Prikhodko A., Mikhailov D., Gol'tsman G.**, Membrane-integrated planar Schottky diodes for waveguide mm-Wave detectors, Microwave & Telecommunication Technology. 3 (2021) 34.

# Magneto-Electric Dipole Antenna as an Transceive Element in a Phased Array

V. D. Burtsev [1✉], N. O. Bulatov [1], A. V. Nikulin [1], P. V. Semkin [2], S. A. Kuznetsov[2], D. S. Filonov[1]

[1]Center for Photonics and 2D Materials, MIPT, Dolgoprudny 141701, Russia;
[2]Joint-Stock Company "Information Satellite Systems Reshetnev", 52 Lenina str., Zheleznogorsk, 662972, Russia
✉burtsev.vd@phystech.edu

**Abstract.** In this paper, we propose a transceive element of a phased array antenna for $K_u$ frequency band. The proposed element based on a magneto-electric dipole antenna. A substrate-integrated waveguide and a cruciform slit of a special shape are used as a feeding element. In this work, two sub-bands were selected, on each of which circular polarization was obtained by selecting the direction of driving. Both the characteristics of a single element and the radiation patterns of an antenna array made of such elements were obtained. The developed geometry meets the requirements of manufacturing on printed circuit boards. The problem of electric beam steering in such an array is considered. The results obtained indicate the prospects of using such broadband transceive elements in phased arrays.

**Keywords:** Magneto-electric dipole, Antenna, Phased Array, Sequential Feeding, SIW waveguide

**Funding:** The research was supported by the Ministry of Science and Higher Education of the Russian Federation under the project No 075-11-2022-011.

The magneto-electric dipole (MED) has been known for some time and has managed to gain popularity due to its wide operating band (up to 60% [1]), high directivity [2] and relatively simple geometry [3]. Its performance is based on constructive interference of near electromagnetic fields of a magnetic dipole (effective current frame) and an electric dipole (two poles with different potentials) [4]. Geometry of the proposed element is shown in Figure 1 (a). We have allocated the $R_x$ (RCP: 10.95-11.7 GHz) and $T_x$ (LCP: 14-14.25 GHz) ranges and built MED geometry in order for both of these bands to be covered. Since the original Γ-shaped feeding element is extremely difficult to implement for modern mass production, such a phased array would greatly lose in performance. This is why we decided to use sequential SIW feeding. Although sequential feeding causes frequency beam steering, it is quite stable when operating at the single frequency. The results obtained can be seen in Figure 1 (b), where $S_{11}$ is reflection coefficient, $S_{21}$ and $S_{41}$ are for the cross-polarizing decoupling, and $S_{31}$ is the SIW waveguide [5] characteristics.

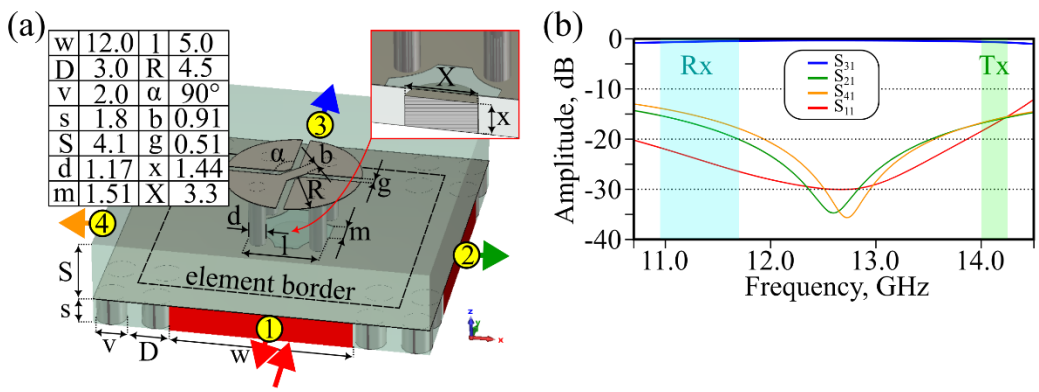


Fig. 1. The suggested MED: (a) general view with geometrical properties, (b) S-parameters regarding port 1 in the range from 10.7 GHz to 14.5 GHz.

To obtain the radiation pattern of a single MED element (Fig. 2(a)), the finite element method and the far field approximation were used. The array factor was employed to obtain the far field lattice sum (Fig.

2 (b, c)). The array period was 17 mm. It is noticeable that such an element, with the proper manufacture of feeding SIW waveguides and cruciform slits, provides circular polarizations depending on the direction of the supply, and the suggested array is capable of electrical beam steering in the presence of phase shifters. However, ellipticity, cross-polarization and level of side lobes have to be further optimized.

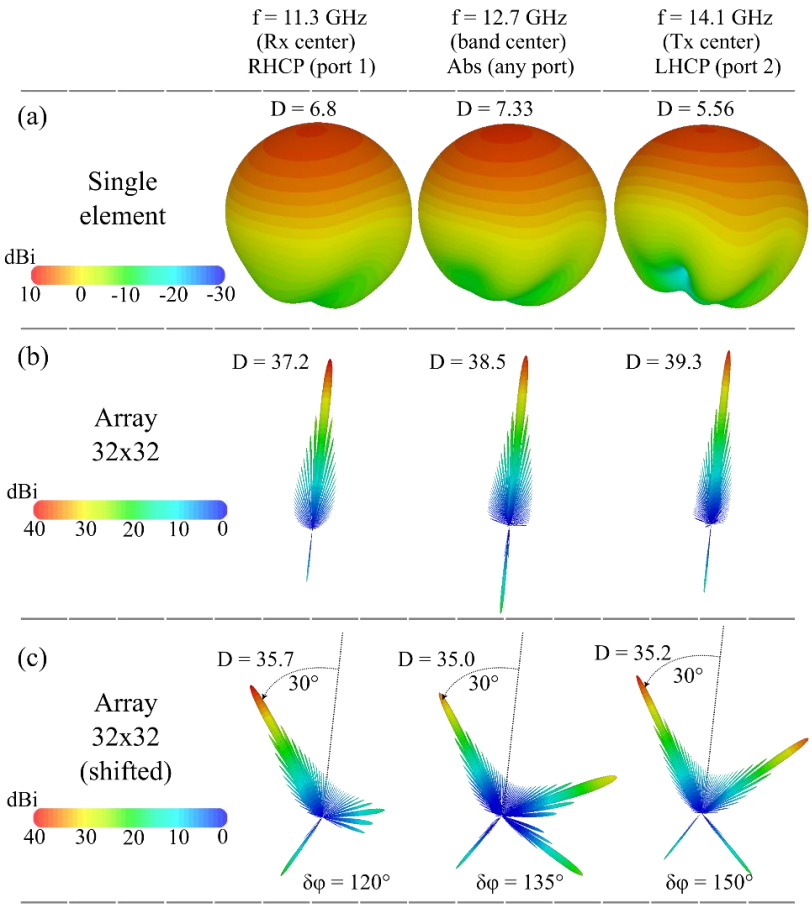


Fig. 2. Directivity patterns of the suggested MED at frequencies of 11.3 GHz, 12.7 GHz and 14.1 GHz: (a) single element, (b) in-phase fed array 32x32, and (c) phased array 32x32 radiating at 30 degrees to the normal.

**References:**


[1] Causse, A.; Rodriguez, K.; Bernard, L.; Sharaiha, A.; Collardey, S. Compact Bandwidth Enhanced Cavity-Backed Magneto-Electric Dipole Antenna with Outer Γ-Shaped Probe for GNSS Bands. Sensors 2021, 21, 3599. https://doi.org/10.3390/s21113599.

[2] Borhani Kakhki, Mehri & Dadgarpour, Abdolmehdi & Antoniades, Marco & Sebak, A. & Denidni, Tayeb. (2020). Dual Complementary Source Magneto-Electric Dipole Antenna Loaded With Split Ring Resonators. IEEE Access. PP. 1-1. 10.1109/ACCESS.2020.2982937.

[3] Limpiti, Thunyawat & Chantaveerod, Ajalawit & Petchakit, Wijittra. (2017). Design of a magneto-electric dipole antenna for FM radio broadcasting base station antenna implementation. Progress In Electromagnetics Research M. 60. 75-84. 10.2528/PIERM17061906.

[4] Li, M., Luk, KM. (2015). Wideband Magneto-electric Dipole Antennas. In: Chen, Z. (eds) Handbook of Antenna Technologies. Springer, Singapore. https://doi.org/10.1007/978-981-4560-75-7_49-1.

[5] H. Uchimura, T. Takenoshita and M. Fujii, "Development of a "laminated waveguide", in IEEE Transactions on Microwave Theory and Techniques, vol. 46, no. 12, pp. 2438-2443, Dec. 1998, doi: 10.1109/22.739232.

# Improving microwave output in rubidium-87 atomic frequency standard with new automatic gain control

**A V Shavshin**[1] **and V V Davydov**[1, 2]
[1]Peter the Great Saint-Petersburg Polytechnic University, Saint Petersburg, Russia, 195251
[2]All-Russian Research Institute of Phytopathology, Moscow Region 143050, Russia

e-mail: shavshin2107@gmail.com

**Abstract.** The need of modernize the existing scheme of automatic control of the optical signal. The presented design was created to maintain the escape power of an atomic frequency standard (AFS) based on rubidium-87 atoms at a given level, correcting changes in its operation introduced by external conditions. An improved circuit for automatic gain control with an additional link in the form of a PID controller and an improved circuit for extracting the «error» signal are presented. A separate contribution of the subtractor and PID controller to the final gain control is considered, and mathematical modeling of microwave devices included in the microwave path is carried out. The foundation of the presented automatic gain control scheme for the atomic frequency standard was confirmed by rubidium-87.

## 1. Introduction

In the modern world, quantum frequency standards are indispensable sources of highly stable, spectrally pure electrical signals to consider more in-depth topics in the scientific and technical field. There are areas in which they cannot be dispensed with/ Special requirements are imposed on atomic frequency standards (AFS), which are used in navigation systems and common time systems. One of such AFSs are standards based on rubidium-87 atoms. Considering more stringent conditions for accuracy and stability of the output optical signal formation, it becomes necessary to modernize the AFS or develop new types of AFS based on other physical principles of operation. To carry out work to improve the accuracy characteristics of the AFS, in some cases it is sufficient to upgrade the functional units that directly affect total output values of the AFS. Thus, this paper presents the modernization of the path for the formation of the microwave signal of the excitation of rubidium-87 atoms [1], aimed at the formation of both the microwave signal itself and the parameters of the AFS output signal. Similar situations arise for other types of standards.

## 2. Updated system of automatic gain control with additional adjustment elements

As can be seen from the presented description of the operation of the AFS, the AGC system is one of the most important functional units of the microwave generation path and the entire structure of the AFS. On Figure 1 shows a modernized circuit diagram of the AGC system.

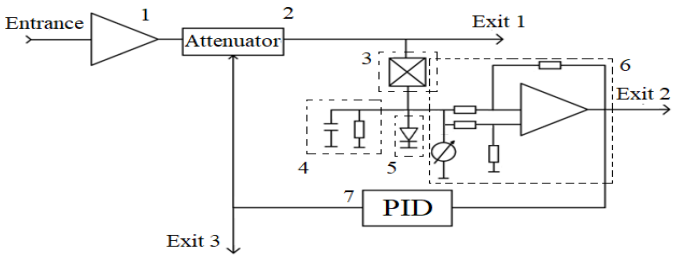


**Figure 1.** Upgraded automatic gain control circuit, with the addition of a PID controller section; 2 – attenuator; 3 – directional coupler; 4 – low-pass filter 5 – detector diode, 6 – «error» signal amplifier, connected as a subtractor; 7 – PID controller/

Since the input of the system receives a signal of insufficient power, The initial task is to strengthen it so that its power is captured for the work of combating discrimination. To fulfill this condition, an amplifier was integrated (1). Then attenuator (2) will be used as a controlled element, due to the adjustment of which the output power of the signal will be adjusted. To create an "error" control signal, a portion of the original signal is applied to the AGC circuit using a directional coupler set to -3dB. (3) and the rest of the signal passes at the output of the system. Next, the «error» control signal must be straightened for the AGC system to work. Therefore, the signal passed through the directional coupler will then pass through the detector diode. (4). After detection, the signal, depending on the external operating conditions of the AFS, can have a different amplitude, based on which there is a need to be able to set the level yourself. For this, an «error» signal enhancer is used on the operational amplifier (5), connected according to the subtractor circuit. Further, the generated «error» signal is fed to the input of the PID controller (7). Depending on the values coming to the PID controller, the necessary corrective gain is analyzed, which will be applied to the attenuator.

## 3. Results of experimental studies of the characteristics of the atomic frequency standard

Thanks to dispersion, it is possible to estimate the level of stability of the frequency of atomic clocks and generators. Analyzing the obtained results, we can make sure that the addition of the AGC system in the first case improved the Allan variance values $\sigma^2(\tau)$ by 12%, and with an additional link in the form of a PID controller, it showed an improvement by 16%. Fig. 2.

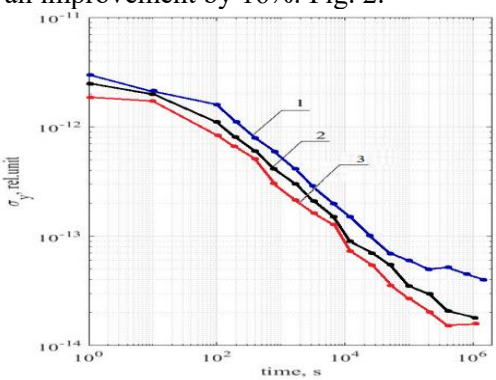


**Figure 2.** Diiagram of Allan variance versus time with an upgraded AGC system (plot 3), previously used (plot 2) and without the AGC system (plot 1) in AFS.

## 4. Conclusion

Through a series of improvements, a new AGC system was implemented for the microwave path of the ASC based on rubidium-87 atoms using a PID controller.

The results of the analysis of the operation of a prototype AFS with the developed AGC system showed that the selected schematic solution works correctly and its use improves the escape parameters of the AFS. Thanks to the new AGC system, it was possible to achieve a decrease in the values of the Allan variance by 16%.

**References**

[1] Shavshin A.V. Development of automatic control of optical signal gain in a atomic frequency standard based on rubidium-87 atoms. IEEE 2022 VIII International Conference on Information Technology and Nanotechnology (ITNT) DOI: 10.1109/ITNT55410.2022.9848676 pp. 21991987.

# ON the possibility of developing a measurement system in the millimeter wave V-band

**A. Shansho** [1✉], **I. O. Dorofeev** [1], **G. E. Dunaevskii** [1]
[1] National Research Tomsk State University 1, Tomsk, Russia;
✉ ahmadsho1@gmail.com

**Abstract.** In this paper, an approach for designing a measurement system in the V-band (60-75GHz) based on a low-frequency E4405B microwave spectrum analyzer (9 KHz-13 GHz), a phase locked backward wave Oscillator (BWO), and a 15th order harmonic mixer was presented. The characteristics of the backward wave oscillator, which serves as high frequency source in the system were improved in terms of phase noise, stability and frequency resolution. By adding a 15th order harmonic mixer, it was possible to eliminate the need for two high-frequency synthesizers, that are used in fundamental mixer-based downconverter. The proposed system can measure phase noise, frequency, reflection coefficient and transmission coefficient.

**Keywords:** backward wave Oscillator, spectrum analyzer, phase noise, frequency resolution.

## Introduction

In recent years, due to the wide development of systems and applications in the millimeter wave range, the need for measuring instruments at frequencies of this wavelength range has grown [1]. The spectrum analyzer and frequency synthesizer are the two most important devices in millimeter wave measurement systems that a research laboratory should be equipped with [2]. However, a commercially available instrument with high sensitivity and precision for measurements at frequencies above 60 GHz has not yet been developed [3]. radio spectrum analyzers for frequencies above 25 GHz are one of these instruments that are very expensive and inaccessible to the majority of researchers. Spectrum analyzers are widely utilized for measuring phase noise at low frequencies, but neither reflection nor transmission coefficients are measured with them. By connecting an external mixer [4], it is possible to extend the range of spectrum analyzer to the region of such high frequencies. In this case, the development of two tunable high-precision high-frequency synthesizers with high output power, capable of operating in the frequency range of interest for measurements, is required. One of these synthesizers is used as the input to the device under test, and the other is used to down convert the frequency to the frequency range of the spectrum analyzer. But. this solution is also very expensive, and not quite logical for the upper millimeter range.

## Method and description of the measurement system

The proposed system consists of a low-frequency, high-precision reference oscillator, two main blocks (an upconverter and a downconverter), and a directional coupler for transmit and reflection measurements, as shown in Fig. 1. The reference oscillator's output is split and fed to both an upconverter and a downconverter. The upconverter consists of a phase-frequency detector (PFD), a low-pass filter, a BWO, a 15th order harmonic mixer, a local oscillator (LO), and an amplifier. The upconverter is intended to synchronize the frequency of the BWO with the high-precision, highly stable reference oscillator and apply the BWO's output signal to the device under test. The harmonic mixer in the upconverter eliminates the need for two high-frequency oscillators because it uses the 15th harmonic of the 4-5 GHz LO to down convert the BWO's output to frequencies within the PFD range.

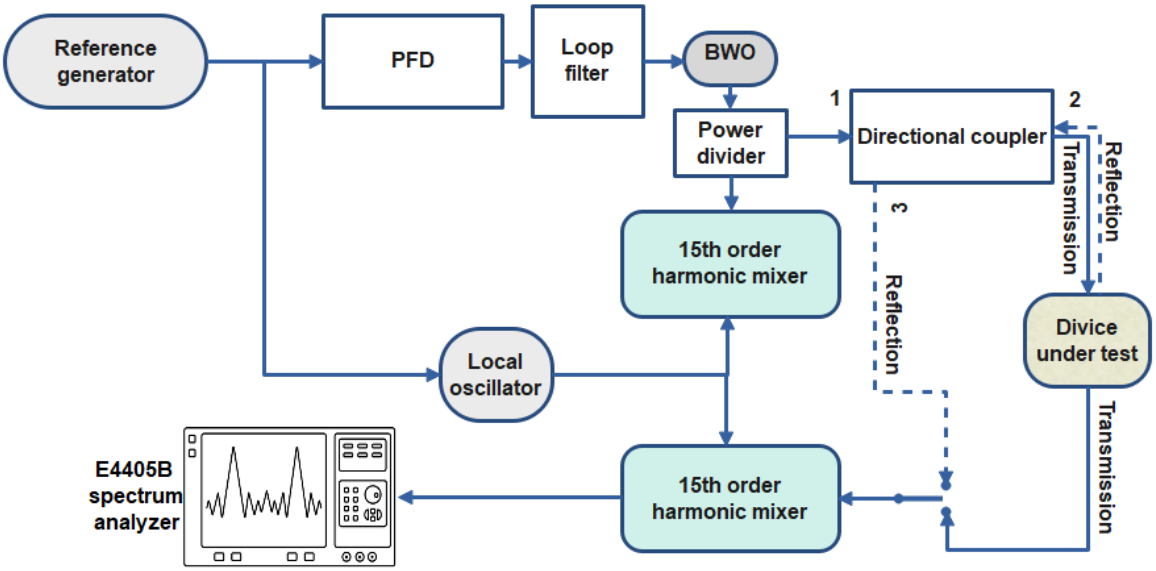


Fig. 1. Block diagram of the measurement system.

A second harmonic mixer, a low-pass filter, and an amplifier constitute the downconverter block. It is used to bring the signal from the device being tested (RF signal) within the range of the spectrum analyzer. The RF signal is mixed with the 15th harmonic of the same LO mentioned above to produce an IF signal. The IF signal is separated by a low-pass filter, amplified and fed to the input of the spectrum analyzer. The output frequency range in the V band (60-75 GHz) is fulfilled, since the local oscillator frequency in the range 4-5 GHz.

Referring to Fig. 1, the system benefit from directional coupler to measure the transmission coefficient and reflection coefficient.

## Results and Conclusion

A low frequency spectrum analyzer-based measurement system capable of measuring the phase noise of any signal between 60 and 75 GHz has been presented. The measurement system can precisely determine the transmission and reflection coefficients. The enhanced phase-locked BWO enables the system to sweep frequency with a 1 Hz resolution, and its -84 dBc/Hz@10 kHz phase noise enables the phase noise of signals less than -84 dBc/Hz@10KHz.

## REFERENCES

1. **Ferrero A., Petri D., Carbone P., Catelani M.**, Modern measurements: fundamentals and applications (1st ed.), Wiley-IEEE Press, 2015.

2. **De Andrade G. F., Barbosa E. V., Rondineau S. R.**, RF Front-End Receiver for Vehicular Satellite Communications and LNA GaAs FET Design in Ku-Band, In: Proceedings of the Workshop on Communication Networks and Power Systems (WCNPS), Brasilia, Brazil, 2020.

3. **Fuse M., Kimura Y., Otani A.**, Over 100 GHz millimeter-wave spectrum measurement system with pre-selector, In: Proceedings of the IEEE MTT-S International Microwave Symposium (IMS2014), Tampa, FL, USA, 2014.

4. **Peterson B.**, Spectrum Analysis Basics. Application Note 150. Agilent Technologies. 2013.

# Model of current-voltage characteristics of resonant-tunneling structures in the problems of studying the objective functions of optimization techniques for resonant-tunneling structures

**N. A. Vetrova**[1], **E. V. Kuimov**[1✉], **V. D. Shashurin**[1]
[1] BMSTU, Moscow, Russia;
✉ekjmo@mail.ru

**Abstract.** In the process of design and technological optimization, the problem arises of determining the gradients of current-voltage characteristics (CVC) in the space of device design parameters. However, the existing models are not suitable for solving the problem of optimizing resonant tunneling diodes (RTDs) due to the implicit relationships between the CVC parameters and the RTD design. Hence, the problem of studying objective functions arises, which makes the choice of the optimization method unreasonable. To solve this problem, a compact analytical model of current transfer has been developed, the distinguishing features of which are the allowance for interelectronic interaction and the absence of undetermined empirical correction factors. Estimates of the electron density in the quantum well of the RTD heterostructural channel and the self-consistent correction to resonant levels are obtained. The developed model makes it possible to obtain estimates comparable in accuracy with estimates of distributed models over the entire area of the positive differential resistance of the CVC with a relative error for AlGaAs structures not exceeding 1%, which meets the requirements of the design problems of modern radio electronic devices, in particular, devices for converting the frequency of radio signals for receiving-transmitting systems for various purposes. Thus, the presented compact model is promising for integration into RTD-based device design systems.

**Keywords:** mathematical modeling, resonant tunneling structures, self-consistent potential, electron density, oscillators

**Funding:** The study was supported by a grant from the Russian Science Foundation No. 22-19-00455, https://rscf.ru/project/22-19-00455/.

## Introduction

The problem of design and technological optimization of resonant tunneling diodes (RTD) for nonlinear signal converters is not completely solved today, due to the lack of analysis of the order of convergence and limitations of optimization methods (for example, gradient methods) [1,2]. The problem of such an analysis lies in the impossibility of studying the form and unimodal objective functions, which calls into question the choice of the objective function and the optimization method. The indicated problem is due to the specifics of the current-voltage characteristics (CVC) models used in the process of optimizing the RTD design [3-5], which do not allow establishing “transparent” relationships between the CVC parameters and the RTD parameters, which does not allow for the study of objective functions. Thus, the problem of constructing a qualitative and quantitative model of current transfer is relevant, the structure of which allows one to analytically study the local properties of objective functions.

## Materials and methods

For design and technological optimization of the RTD, the criterion for the compliance of the CVC of the RTD with the required one, as a rule, is formulated in the form

$$K = \int_{V_1}^{V_2} K_V\left(J_T(V), J(V)\right) dV \tag{1}$$

here $J(V)$ – RTD CVC, $J_T(V)$ – required CVC, $K_V\left(J_T(V), J(V)\right)$ – kernel, $V_1$, $V_2$ – limits of the section of the optimized CVC.

In the process of optimization, the problem arises of calculating the derivatives of $K$ with respect to the parameters of the CVC model, from which, obviously, the calculation of the

derivative of the CVC follows, which is an unsolvable task for the currently used models. Therefore, a compact current transfer model was constructed based on the following assumptions:

1. The current density and electron concentration in a quantum well are due to electrons with energy in the vicinity of resonant levels (RL);
2. The width of the switchgear is negligible compared to the thermal energy.
3. The coefficient of tunnel transparency and the local density of states in the vicinity of the RU is approximated by the Lorentz distribution.

Within the framework of the formulated assumptions, the following equations were obtained to describe the initial section of the CVC of the RTD

$$\begin{gathered} J(V) = \frac{q_e}{2\hbar}\Gamma\left( f_{2D}(\varepsilon) - f_{2D}(\varepsilon + q_e V)\right) \\ \varepsilon = \varepsilon_0 - q_e \frac{V}{2} - E_0\left(C_L f_{2D}(\varepsilon) + C_R f_{2D}(\varepsilon + q_e V)\right) \end{gathered} \tag{2}$$

руку $\varepsilon(V)$ – RL energy, $V$ – voltage, $\Gamma$ – RL width, $f_{2D}(\varepsilon)$ – 2D electron gas distribution, $\varepsilon_0, E_0, C_L, C_R$ – internal parameters of the model, $q_e$ – elementary charge, $\hbar$ - Dirac constant.

Model (2) makes it possible to analytically calculate the derivatives of CVC with respect to the model parameters, which makes it possible to analytically study the objective functions

## Results and discussion

With the help of a compact model, the CVC of the test RTDs were calculated; it was possible to obtain good agreement (the error does not exceed 1%) in the shape of the initial section.

## Conclusion

A compact model of current transfer in an RTD is presented, taking into account the self-consistent field. The developed model, due to the reduction in the time complexity of the algorithm by several orders of magnitude and the preservation of the accuracy of distributed models of current transfer, makes it possible to solve the problems of synthesizing CVC of RTDs and investigate the objective functions of design and technological optimization methods in order to increase their efficiency.

## REFERENCES


1. **Cherkasov K. V., Meshkov S.A., Makeev M. O., Shashurin V. D.**, Design and Technological Optimization of Electrical Parameters of the Wideband Balanced Microwave Frequency Mixer Based on Resonant-Tunneling Diodes, Journal of Communications Technology and Electronics. 67 (2022) 670–674.

2. **Sanyal I., Das Sarkar M.**, Parameter optimization of a single well nanoscale resonant tunneling diode for memory applications, IEEE International Conference on Electron Devices and Solid-State Circuits (EDSSC), Singapore, 01-04 June 2015, 439-442.

3. **Abramov I. I., Goncharenko I. A., Kolomejceva N. V.**, Two-band combined model of a resonant tunneling diode, Semiconductors/Physics of the Solid State. 41(11) (2007) 1395-1400

4. **Kuimov E. V., Vetrova N. A.**, Forming a Portion of Negative Differential Conductivity in the I–V Characteristic of Resonant-Tunneling Structures, Journal of Surface Investigation: X-ray, Synchrotron and Neutron Techniques. 16(1) (2022) 176-180.

5. **Liu Y., Gao B., Gong M., Shi R.**, Modeling and optimization of a double-well double-barrier GaN/AlGaN/GaN/AlGaN resonant tunneling diode, Journal of Applied Physics. (2017) 121(21) 215701.

Conference materials
UDC 538.9

# Simulation of elastic characteristics of pseudo-graphenes

**N. D. Abramenko [1]✉, M. A. Rozhkov [1,2], A.L. Kolesnikova [1,3], A.E. Romanov [1,2]**
[1] ITMO University, Kronverksky av. 49 197101 St. Petersburg, Russia
[2] Ioffe Physical-Technical Institute, RAS, Polytechnicheskaya 26, 194021, St. Petersburg, Russia
[3] Institute for Problems in Mechanical Engineering RAS, St. Petersburg, 199178, Russia
✉ndabramenko@itmo.ru

**Abstract.** This report presents the results of simulated mechanical tests of pseudo-graphenes, i.e., graphenes that include dense networks of wedge disclinations of different signs, which manifest themselves in a hexagonal carbon crystal lattice in the form of rings with broken hexagonal symmetry. On the basis of the density functional theory and the method of molecular dynamics, the elastic constants of low-energy pseudo-graphenes, consisting of 5- and 7-membered carbon rings, marked as G5-7v1 and G5-6-7v2, are found. The results obtained with the help of various potentials of interatomic interaction are compared and conclusions are drawn about their applicability.

**Keywords:** pseudo-graphene, molecular dynamics, interatomic potential, density functional theory.

## Introduction

Carbon is able to form many allotropes - solids from the same element, different in structure. For example, diamond is the hardest natural material; graphite, which is widely used (for example, as a dry lubricant and conductor), etc. Depending on their internal structure, these allotropes can exhibit different behavior of electrons on the outer electron shell responsible for the interaction between carbon atoms.

If we take one isolated atomic layer of graphite, then we get graphene - a two-dimensional carbon crystal with a hexagonal lattice. Graphene has promising applied properties: unusual electronic properties, high thermal conductivity and a unique set of mechanical characteristics. Its successful synthesis attracted much attention and marked an active growth of interest in the study of two-dimensional crystals.

The physical and mechanical properties of such materials can be controlled by external influences: mechanical, electrical, and magnetic and / or by changing the local crystalline perfection of the crystal lattice. Crystal lattice defects, in turn, change the mechanical properties (which is similar to the effects observed in ordinary three-dimensional crystals), while at the same time contributing to a change in the electrical and thermal conductivity of these crystals.

The purpose of this research is to calculate the elastic constants for G5-7v1 and G-5-6-7v2 pseudo-graphenes using the molecular dynamics method. In this paper, we will compare various interatomic interaction potentials that currently exist, and then the results will be analyzed for compliance with the results obtained using the density functional theory.

## Materials and Methods

For prediction of these materials characteristics, we used molecular dynamics method with given interatomic potential: AIREBO, Tersoff, lcbop, and others. MD calculations were done via LAMMPS software package. To validate the results, we use values, calculated with DFT as a reference. DFT calculations were performed with the use of Quantum Espresso software package with Perdew-Burke-Ernzerhof functional (PBE). Overall compared materials are pristine graphene and PGCs G5-7v1, G5-6-7v2.

## Results and Discussion

As a result of the calculations, the following were obtained:

- Elastic constants for the desired pseudo-graphenes using the density functional theory.

- Elastic constants for the desired pseudo-graphenes using the AIREBO, Tersoff, lcbop, etc. potentials.

The results of calculations obtained using the molecular dynamics method were compared with calculations based on the density functional theory. It was found that none of the interatomic interaction potentials used in our work is suitable for solving the problem of finding elastic constants for pseudo-graphenes, since no correspondence was found in the behavior between these methods. This can be explained by the fact that the potentials were developed for previously well-studied carbon materials: diamond, graphite, and graphene. Pseudo-graphenes, in turn, could be called a new class of materials for which it is necessary to refine the existing potentials of the interatomic interaction potential, or to develop a new one.

In the future, we propose to conduct the following studies:

- we propose to pay attention to a new direction in numerical modeling - creating the potential of interatomic interaction using machine learning, and try to solve the problem using this tool;

- try out other potentials not covered by our research.

## Conclusion

The elastic constants for G5-7v1 and G5-6-7v2 pseudo-graphenes were calculated using the molecular dynamics method using various interatomic interaction potentials, as well as using the density functional theory. The results obtained indicate the inapplicability of the potentials used to calculate the characteristics of pseudo-graphenes.

## Acknowledgements

The work was supported by the Russian Science Foundation (grant No 19-19-00617).

## REFERENCES

1. **K.S. Novoselov, A.K. Geim, S.V. Morozov, D. Jiang, Y. Zhang, S.V. Dubonos, I.V. Grigorieva and A.A. Firsov**, Electric Field Effect in Atomically Thin Carbon Films, Science 306(5696) (2004) 666–669; DOI: https://doi.org/10.1126/science.1102896.
2. **Y. Wei, J. Wu, H. Yin, X. Shi, R. Yang and M. Dresselhaus**, The Nature of Strength Enhancement and Weakening by Pentagon–heptagon Defects in Graphene, Nat. Mater. 11(9) (2012) 759–763; DOI: https://doi.org/10.1038/nmat3370.
3. **J.P. Perdew, K. Burke and M. Ernzerhof**, Generalized Gradient Approximation Made Simple. Phys. Rev. Lett. 77(18) (1996) 3865–3868; DOI: https://doi.org/10.1103/PhysRevLett.77.3865.

## THE AUTHORS

**ABRAMENKO NIKITA D.**
ndabramenko@itmo.ru
ORCID: 0009-0003-8538-5113

**ROZHKOV MIKHAIL A.**
MARozhkov@itmo.ru
ORCID: 0000-0001-7350-0717

**KOLESNIKOVA ANNA L.**
anna.kolesnikova.physics@gmail.com
ORCID: 0000-0003-4116-4821

**ROMANOV ALEXEY E.**
alexey.romanov@niuitmo.ru
ORCID: 0000-0003-3738-408X

Conference materials
UDC
DOI: https://doi.org/10.18721/JPM.

# Epitaxial growth of highly stressed InGaAs/InAlAs layers on InP substrates by molecular-beam epitaxy

**V. V. Andryushkin** [1✉], **I. I. Novikov** [1], **A. G. Gladyshev** [1], **A. V. Babichev** [1], **L. Ya. Karachinsky** [1], **V. V. Dudelev** [2], **G. S. Sokolovskii** [2], **A. Yu. Egorov** [3]
[1] ITMO University, St. Petersburg 197101, Russia;
[2] Ioffe Institute, St. Petersburg 194021, Russia;
[3] Alferov University, St. Petersburg 194021, Russia
✉vvandriushkin@itmo.ru

**Abstract.** In this paper we present the study of the features of epitaxial growth strain compensated superlattices based on highly stressed thin InGaAs/InAlAs layers on InP substrates by the molecular beam epitaxy. It was shown that the growth rates of the InGaAs and InAlAs bulk layers lattice-matched to InP substrates do not allow us to precisely determine the growth rates of thin highly stressed InAlAs/InGaAs strain compensated superlattices and the error is about 10 percent. The effect is related to the difference in the growth temperatures of InGaAs and InAlAs bulk layers, which affects the intensity of indium evaporation from the growth surface.

**Keywords:** molecular-beam epitaxy, superlattice, quantum-cascade lasers.

**Funding:** The authors from ITMO University acknowledge support in part by Priority 2030 program for the photoluminescence spectra and X-ray diffraction analysis. The work was carried out with financial support of the Russian Science Foundation grant no. 21-72-30020 in part of epitaxial growth of heterostructure.

**Citation:** Andryushkin V. V., Novikov I. I., Gladyshev A. G., Babichev A. V., Karachinsky L. Ya., Dudelev V. V., Sokolovskii G. S., Egorov A. Yu., Epitaxial growth of highly stressed InGaAs/InAlAs layers on InP substrates by molecular-beam epitaxy, St. Petersburg State Polytechnical University Journal. Physics and Mathematics. 16 ( ) (2023) …–…. DOI: https://doi.org/10.18721/JPM.

This is an open access article under the CC BY-NC 4.0 license (https://creativecommons.org/licenses/by-nc/4.0/)

© Andryushkin V. V., Novikov I. I., Gladyshev A. G., Babichev A. V., Karachinsky L. Ya., Dudelev V. V., Sokolovskii G. S., Egorov A. Yu., 2023. Published by Peter the Great St. Petersburg Polytechnic University.

Материалы конференции
УДК
DOI: https://doi.org/10.18721/JPM.

## Introduction

Semiconductor thin InGaAs and InAlAs layers (less than 10 nm) grown by molecular beam epitaxy (MBE) are widely used in epitaxial heterostructures for optoelectronic devices, especially mid-infrared (IR) spectral range quantum cascade lasers (QCL) [1]. $In_{0.53}Ga_{0.47}As$/ $In_{0.52}Al_{0.48}As$ heteropairs lattice-matched with the InP substrate are used for such QCL heterostructures. However, in some cases thin highly stressed InGaAs /InAlAs layers should be used [2] to increase the efficiency of QCL. The main difficulty in the growth of highly stressed InGaAs/ InAlAs layers by the MBE is the need to simultaneously meet the conditions for the exact correspondence of the molar fraction of indium in the triple solution and the layer thickness to the set values. There is a discrepancy between the molar fraction and thickness when the growth parameters are fully calibrated using the heterostructures of the InGaAs and InAlAs bulk layers during the epitaxial growth of thin highly stressed layers. This paper presents the results on Epitaxial growth of thin highly stressed InGaAs/InAlAs layers on InP substrates by molecular-beam epitaxy.

## Materials and Methods

Heterostructures for experiments were grown by MBE on InP (100) "epi-ready" quality substrates using the Riber 49 MBE machine. The vapor pressure was measured by an ion sensor. The results of measurements of the fluxes of group III elements made it possible to estimate the growth rates of the corresponding binary compounds InAs, AlAs, GaAs according to the available calibration dependencies. The temperatures of the sources were set to obtain the required growth rates of binary compounds. The measurements were carried out using a PANalytical X'pertPro with proprietary software in the geometry of Ω-2Θ. The composition and thickness of the layers were determined by modeling an experimental X-ray diffraction curve.

## Results and Discussion

Heterostructures S1 and S2 were grown on InP substrates and consisted of 400 nm thick $In_{0.53}Ga_{0.47}As$ and $In_{0.52}Al_{0.48}As$ layers respectively. X-ray analyze has shown that the deviation in the thickness/composition of the InGaAs and InAlAs test layers is 2/3% and 2.5/0.6% respectively in comparison with target values. For binary compounds growth rates were defined as 0.98 Å/s for InAs, 0.93 Å/s for GaAs, 0.90 Å/s for AlAs. The S3 heterostructure consisting of 20 superlattice (SL) periods of stressed 5 nm thickness layers $In_{0.36}Al_{0.64}As/In_{0.67}Ga_{0.33}As$ (applied for 4.8 μm range QCL) was grown after determining the growth rates of all binary compounds. The composition of InGaAs / InAlAs layers turned out to be 2.9/6.2% less than required. The thickness deviation also increased by 3.3% and 8.7% for the InGaAs and InAlAs layers, respectively. The difference in growth rates was 10%. We have observed such an effect in less stressed and consistent layers $In_{0.44}Al_{0.56}As/In_{0.60}Ga_{0.40}As$ for 5.8 μm spectral range QCL as well where the growth rates were differed by 8%. It was assumed that the effect was related to the difference in the growth temperature of InGaAs and InAlAs layers which affects the intensity of indium evaporation from the growth surface. Additional heating of the growth surface can occur from Ga and Al sources due to thermal emission of the molten material when the cell shatters are opened. Reducing the growth rate of AlAs by 10% relative to the real value made it possible to compensate the difference. Under adjusted conditions, the heterostructure consisting of 20 superlattice (S4 sample) demonstrated a much more accurate correspondence of compositions and thicknesses to the required values. To adjust the composition of the layers in the S4 structure, the temperatures of the Ga and Al sources were additionally adjusted relative to the values used during the growth of the S3 structure. As a result, a slight excess of layer thicknesses relative to the nominal value of up to 1.5% was obtained. The compositions of the layers differed by 1% and 0.9% for the InAlAs and InGaAs layers both towards a higher indium content.

## Conclusion

The error of growth rates of the InGaAs and InAlAs bulk layers is related to the difference in the growth temperature of these layers, which affects the intensity of indium evaporation from the growth surface. Additional heating of the growth surface can occur from Ga and Al sources when the cell shatter is opened due to thermal emission from the molten materials. The difference in the temperatures of the Ga and Al sources in our experiments was 80-120°C and determined the different effect of thermal emission on the growth of different layers. We believe that observed effect is universal and should be considered during the mid-IR range QCL growth in various MBE systems.

## Acknowledgments

The authors from ITMO University acknowledge support in part by Priority 2030 program for the photoluminescence spectra and X-ray diffraction analysis. The work was carried out with financial support of the Russian Science Foundation grant no. 21-72-30020 in part of epitaxial growth of heterostructure.

## REFERENCES

1. **Silvestri C., Qi X., Taimre T., Bertling K., Rakić A. D.**, Frequency combs in quantum cascade lasers: An overview of modeling and experiments, APL Photonics. 8 (2) (2023) 020902.

2. **Egorov A. Yu., et. al.**, Lasing of multiperiod quantum-cascade lasers in the spectral range of (5.6–5.8)-μm under current pumping, Semiconductors. 49 (2015) 1527.

## THE AUTHORS

**ANDRYUSHKIN Vladislav V.**
vvandriushkin@itmo.ru
ORCID: 0000-0002-7471-8627

**NOVIKOV Innokenty I.**
innokenty.novikov@itmo.ru
ORCID: 0000-0003-1983-0242

**GLADYSHEV Andrey G.**
andrey.gladyshev@connector-optics.com
ORCID: 0000-0002-9448-2471

**BABICHEV Andrey V.**
a.babichev@itmo.ru
ORCID: 0000-0002-3463-4744

**KARACHINSKY Leonid Ya.**
lkarachinsky@itmo.ru
ORCID: 0000-0002-5634-8183

**DUDELEV Vladislav V.**
Vlad@kuch.ioffe.ru
ORCID: 0000-0003-0001-7171

**SOKOLOVSKII Grigorii S.**
Gregory@kuch.ioffe.ru
ORCID: 0000-0002-8117-5018

**EGOROV Anton Yu.**
egorov@spbau.ru
ORCID: 0000-0002-0789-4241

Conference materials
UDC 535.37
DOI: https://doi.org/10.18721/JPM.

# Matrix composition effect on InGaP(As) quantum dots photoluminescence

**V. V. Andryushkin** [1✉], **I. I. Novikov** [1], **A. G. Gladyshev** [1], **A. V. Babichev** [1], **L. Ya. Karachinsky** [1], **A. Yu. Egorov** [2]
[1] ITMO University, St. Petersburg 197101, Russia;
[2] Alferov University, St. Petersburg 194021, Russia
✉vvandriushkin@itmo.ru

**Abstract.** In this paper we present the study of the features of the matrix composition effect on InGaP(As) quantum dots photoluminescence. The PL maximum of the formed QDs arrays lies in 987-1087 nm range at room temperature depending on the design of the heterostructure It was shown that using of $In_{0.17}Ga_{0.83}As$ as a covering QDs layer leads to a red-shift of the PL maximum up to 54 nm, while using of this layer as the formation surface of initial InGaP layer does not significantly effect on the InGaP(As) QDs emission wavelength.

**Keywords:** molecular-beam epitaxy, quantum dots, single-photon sources.

**Funding:** This work was supported by the Ministry of Science and Higher Education of the Russian Federation, research project no. 2019-1442 (project reference number FSER-2020-0013).

**Citation:** Andryushkin V. V., Novikov I. I., Gladyshev A. G., Babichev A. V., Karachinsky L. Ya., Egorov A. Yu., Matrix composition effect on InGaP(As) quantum dots photoluminescence, St. Petersburg State Polytechnical University Journal. Physics and Mathematics. 16 ( ) (2023) …–…. DOI: https://doi.org/10.18721/JPM.

This is an open access article under the CC BY-NC 4.0 license (https://creativecommons.org/licenses/by-nc/4.0/)

© Andryushkin V. V., Novikov I. I., Gladyshev A. G., Babichev A. V., Karachinsky L. Ya., Egorov A. Yu., 2023. Published by Peter the Great St. Petersburg Polytechnic University.

Материалы конференции
УДК 535.37
DOI: https://doi.org/10.18721/JPM.

## Introduction

Currently, the development of quantum optical information technologies leads to increase in interest of low−density quantum dots (QD) (QD density below $1 \cdot 10^{10}$ $cm^{-2}$), which can be used to create single photon sources. The quantum dots creating technology is based on the fundamental effects of self-organization of semiconductor nanostructures that occurs during the epitaxy. Earlier, we have proposed and implemented [2] an original approach to the formation of low-density InGaP(As) QDs in the spectral range of 1 μm by replacing elements of the fifth group directly during epitaxial growth by molecular beam epitaxy (MBE). This paper presents the results of the influence on optical properties of the InGaP(As) QDs overgrowth material and the formation surface.

## Materials and Methods

Heterostructures QD1–4 for experiments were grown by MBE on GaAs (100) "epi-ready" quality substrates. The QD1 heterostructure (analogue of C2 [2]) consisted of a 100-nm GaAs buffer and a 200 nm GaAs layer which was bounded by 100-nm AlGaAs barriers. The upper AlGaAs barrier layer was covered by a 5-nm GaAs layer to prevent oxidation. In the center of the 200 nm GaAs layer, a 5 nm $In_{0.49}Ga_{0.51}P$ layer was deposited. The growth temperature of the InGaP layer and the exposure in the arsenic flow for the QD1 heterostructure was reduced by 10 °C compared to the growth of C2 [2] to reduce the effect of possible over-evaporation of indium

from the growth surface. The heterostructures QD2 and QD3 differed of an $In_{0,17}Ga_{0,83}As$ 5 nm thick layer in front of the InGaP formation layer and on top of the formed QDs, respectively, while QD4 was a combination of QD2 and QD3 (see Fig.1a).

## Results and Discussion

Photoluminescence (PL) spectroscopy was used to study the optical properties of fabricated heterostructures with InGaP(As) QDs. The PL lines (Fig.1b) of the formed QDs lie in 987-1087 nm range at room temperature. A red-shift of the QDs PL maximum in the QD1 heterostructure relative to C2 by 42 nm was observed, as well as an increase in the emission intensity by 15 times, which may be due to a decrease in the growth temperature and, as a consequence, less influence of the In evaporation process from the sampls surface during epitaxial growth. According to the PL spectra of the QD1 and QD2 heterostructures, the use of $In_{0.17}Ga_{0.83}As$ as a covering layer leads to a red-shift of the PL maximum by 54 nm, while the use of this layer as a formation surface of initial InGaP (QD3) layer does not significantly effect on the InGaP(As) QDs emission wavelength. These results are confirmed by the PL spectrum of the QD4 heterostructure, which is comparable to the results obtained for QD2 heterostructure. The QD4 PL peak was 1087 nm and the intensity of the QDs emission from all the heterostructures under consideration was maximal.

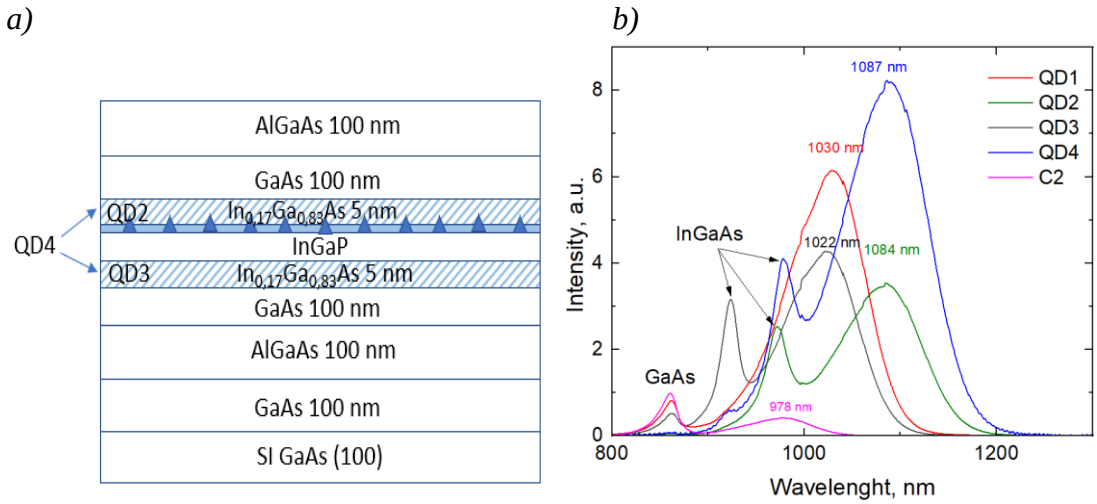


Fig. 1 Schematic representation of QD1–4 heterostructures (*a*) and PL spectra of C2[2], QD1–4 heterostructures at room temperature (*b*)

## Conclusion

The influence of $In_{0,17}Ga_{0,83}As$ layers as an overgrowth material and the formation surface of InGaP(As) QDs on their optical properties was analyzed. The use of $In_{0.17}Ga_{0.83}As$ as a covering QDs layer leads to a red-shift of the PL maximum by 54 nm, while the use of this layer as the formation surface of initial InGaP (QD3) layer does not significantly effect on the InGaP(As) QDs emission wavelength.


## Acknowledgments

This work was supported by the Ministry of Science and Higher Education of the Russian Federation, research project no. 2019-1442 (project reference number FSER-2020-0013).


## REFERENCES


1. **Schlottmann E., Schicke D., Kruger F., Lingnau B., Schneider C., Hofling S., Ludge K., Porte X., Reitzenstein S.**, Stochastic polarization switching induced by optical injection in bimodal quantum-dot micropillar lasers, Optics Express. 27 (20) (2019) 28816.

2. **Gladyshev A. G., Babichev A., Andryushkin V. V. et al.**, Studying the Optical and Structural Properties of Three-Dimensional InGaP(As) Islands Formed by Substitution of Elements of the Fifth Group, Technical Physics. 65 (2020) 2047.

## THE AUTHORS

**ANDRYUSHKIN Vladislav V.**
vvandriushkin@itmo.ru
ORCID: 0000-0002-7471-8627

**NOVIKOV Innokenty I.**
innokenty.novikov@itmo.ru
ORCID: 0000-0003-1983-0242

**GLADYSHEV Andrey G.**
andrey.gladyshev@connector-optics.com
ORCID: 0000-0002-9448-2471

**BABICHEV Andrey V.**
a.babichev@itmo.ru
ORCID: 0000-0002-3463-4744

**KARACHINSKY Leonid Ya.**
lkarachinsky@itmo.ru
ORCID: 0000-0002-5634-8183

**EGOROV Anton Yu.**
egorov@spbau.ru
ORCID: 0000-0002-0789-4241

# Droplet epitaxy of site-controlled In/GaAs(001) nanostructures with a variable distance: experiments and simulations

**S. V. Balakirev** ✉, **D. V. Kirichenko, N. E. Chernenko, N. A. Shandyba, M. S. Solodovnik**
Laboratory of Epitaxial Technologies, Institute of Nanotechnologies, Electronics and Equipment Engineering, Southern Federal University, Taganrog 347922, Russia
✉sbalakirev@sfedu.ru

**Abstract.** This paper presents a comprehensive experimental and theoretical study of the droplet epitaxial growth of In/GaAs(001) nanostructures on patterned surfaces. We observe that holes formed after overgrowth of FIB-treated surfaces by a GaAs layer are the preferred centers for the nucleation of In droplets at any temperature in the range from 250°C to 350°C. However, lower temperatures are required to provide filling of more holes and formation of an ordered array of droplet pairs. Using kinetic Monte Carlo simulations, we demonstrate growth conditions which allow filling of all holes located at variable distances in a range from 20 to 340 nm and avoiding unnecessary nucleation beyond the holes.

**Keywords:** droplet epitaxy, focused ion beams, patterned surfaces, Monte Carlo method.

**Funding:** This study was supported by the Russian Science Foundation Grant No. 21-79-00310, https://rscf.ru/project/21-79-00310/, and by the Ministry of Science and Higher Education of the Russian Federation; the state task in the field of scientific activity No. FENW-2022-0034, at the Southern Federal University.

## Introduction

Formation of ordered arrays of pre-defined nanoholes on a substrate allows prediction of nucleation sites and geometrical parameters of QDs epitaxially grown on this substrate. This approach simplifies further post-processing of heterostructures and provides a better production yield of QD-based devices. Although much attention is paid to regular arrays of nanostructures, site-controlled growth of QDs with a variable distance is also important for specific applications, such as lasers on whispering gallery modes, nanoelectronic cellular automata or quantum computation schemes based on QD molecules.

In this paper, we carry out a complex experimental and theoretical study of droplet epitaxial (DE) growth of In/GaAs(001) nanostructures on surfaces modified by focused ion beams (FIB).

## Materials and Methods

Epi-ready GaAs(001) substrates were patterned in Nova Nanolab 600 scanning electron microscope (SEM) equipped with a $Ga^+$ FIB column. Two types of arrays with an area of 5×5 μm$^2$ and a distance of 0.5 and 1 μm between treatment points were fabricated. Then, the patterned substrates were transferred to molecular beam epitaxy equipment where an oxide layer was removed and a GaAs buffer layer was grown. Next, arsenic flux was cut off to provide a background pressure in the chamber of ~$1\cdot10^7$ Pa. Then, In atoms were deposited on the surface in the amount of 3 equivalent monolayers (ML) at different substrate temperatures from 250°C to 350°C and growth rates 0.05 and 0.25 ML/s. After the droplet formation, the samples were quenched and transferred to SEM for characterization of nanostructures.

## Experimental Results

Experimental study of the DE growth on patterned surfaces demonstrated that droplets tend to occupy hole positions, except for the case of 250°C when one droplet was formed beyond holes. However, droplets are not evenly distributed over all holes, which is due to intensive decay of subcritical islands. When droplets were formed at 300°C on the surface with holes located 0.5 μm apart, site-controlled droplet formation was found in almost every hole along the array perimeter with no nucleation in the inner region (Fig. 1a), which allows to conclude that it is possible to localize nanostructures in an array with a variable distance between nucleation centers in the range from 0.5 to 3 μm. It was also found that it is possible to create arrays of In droplet pairs with close-to-unity filling of holes located at a distance of 1 μm (Fig. 1b).

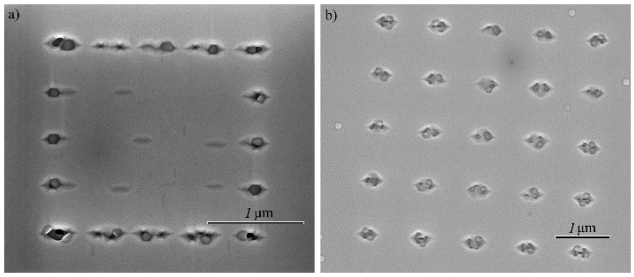


Fig. 1. SEM images of droplet arrays obtained on FIB-patterned surfaces with a distance between treatment points of 0.5 (*a*) and 1.0 μm (*b*) at different growth rates: 0.05 ML/s (*a*) and 0.25 ML/s (*b*).

## Simulations

Simulations based on a kinetic Monte Carlo model [1] demonstrated that a temperature of 300°C is too high to provide formation of site-controlled droplet pairs located 500 nm apart (Fig. 2a-b). A decrease in the temperature to 200°C leads to 100% filling of holes with absence of droplets beyond (Fig. 2c).

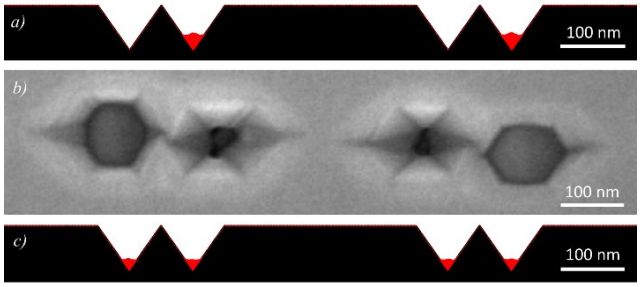


Fig. 2. Morphology of droplet arrays obtained on patterned surfaces at 300°C: *a*) simulation, *b*) SEM image – and 200°C: *c*) simulation.

The same temperature was found to be optimal for the site-controlled growth of droplets on patterned surfaces with a distance changing from 20 to 340 nm (Fig. 3). A large diffusion length of adatoms at 250°C does not allow to fill closely located holes with droplet material (Fig. 3a).

Fig. 3. Simulated morphology of droplet arrays obtained on patterned surfaces at different temperatures: *a*) 250°C, *b*) 200°C, *c*) 150°C.

A reduction in the deposition temperature to 200°C makes it possible to provide 100% selectivity, expressed as the ratio of the number of droplets located in holes to the total number of droplets and holes divided by two (Fig. 4b). A further decrease in the temperature to 150°C leads to undesirable nucleation outside the holes, which is due to a decrease in the intensity of surface diffusion and an increase in the probability of nucleation (Fig. 4c).

## Conclusion

Thus, we established technological conditions at which site-controlled formation of In droplets on patterned GaAs surfaces with variable distances between nanoholes is implemented.

## REFERENCES

1. **Balakirev S. V., Solodovnik M. S., Ageev O. A.** Hybrid Analytical-Monte Carlo Model of In/GaAs(001) Droplet Epitaxy: Theory and Experiment, Physica Status Solidi B. 255 (4) (2018) 1700360.

# Terahertz difference frequency generation in photonic crystals

**D.S. Bykov** ✉, **V.V. Davydov**
Peter the Great Saint-Petersburg Polytechnic University, Saint Petersburg, Russia

**Abstract.** The paper investigates the possibility of obtaining terahertz radiation by generating a difference frequency for near-infrared waves. As a nonlinear medium, it is proposed to use a photonic crystal based on polar semiconductors, the dispersion law of which ensures the fulfillment of the phase matching conditions. To calculate the band structure of a photonic crystal, the equation for the magnetic field of the wave, obtained from Maxwell's equations, is used. Using the Fourier method, the problem is reduced to calculating the eigenvalues of a Hermitian-symmetric matrix.

**Keywords:** difference frequency, terahertz frequency, photonic crystals.

## Introduction

At present, sources of the terahertz range, which are widely used in certain types of economic activity and everyday life, are of great interest. Security systems use THz (mm) radiation to scan luggage and people [1]. Unlike X-rays, THz radiation does not harm the body. There is also a method for imaging microscopic objects using THz radiation, thanks to which record values of sensitivity and resolution have been obtained [2, 3]. THz tomographs are beginning to be introduced into medical practice, with the help of which it is possible to examine the upper layers of the body - skin, blood vessels, muscles - to a depth of several cm. This is necessary, for example, to obtain an image of tumors. In production, THz radiation can be used for product quality control and equipment monitoring. For example, it is possible to inspect products in plastic, paper containers that are transparent in the THz spectrum, but opaque in the visible. There is an opportunity to develop high-speed THz communication systems and THz location for high altitudes and space.

## Materials and methods

In this paper, we study the possibility of obtaining terahertz radiation by generating a difference frequency for near-infrared waves. As a nonlinear medium, it is proposed to use a photonic crystal based on polar semiconductors, the dispersion law of which ensures the fulfillment of the phase matching conditions [4].

To calculate the band structure of a photonic crystal, the equation for the magnetic field of the wave, obtained from Maxwell's equations, is used.

$$-\hat{R}^{\alpha}_{\beta}\frac{1}{\mu\varepsilon(\vec{r})}\hat{R}^{\beta}_{\gamma}H^{\gamma}(\vec{r}) = k_0^2 H^{\alpha}(\vec{r}) \qquad (1)$$

Using the Fourier method, the problem is reduced to calculating the eigenvalues of a Hermitian-symmetric matrix, which can be solved using a computer.

$$S^{\alpha\lambda}_{\gamma\sigma}\varphi_{\lambda}(\vec{r})h^{\sigma\gamma} = -k_0^2\varphi_{\tau}(\vec{r})h^{\alpha\tau} \qquad (2)$$

The results obtained can also be applied to the description of the electrical component, which indicates the possibility of a complete description of all components of the generated electromagnetic wave in the THz range due to the generation of a difference frequency in photonic crystals.

## Results and discussion

It was decided to use GaAs and AlAs as materials for the photonic crystal. These materials, which are among the promising semiconductor substances, due to their properties have found wide

application in devices operating at frequencies up to 250 GHz. Such sources have low noise and higher output power. However, it must be taken into account that they, like other semiconductor substances, have resonant absorption. Gallium arsenide has 8.85 THz, while aluminum arsenide has 12.05 THz.

We will use a laser with a frequency of 282 THz as a reference signal, and an optical parametric oscillator with a generation frequency of 277 THz as a modulating signal. The difference frequency in this case will be equal to 5 THz.

As a result of solving the eigenvalue problem, a program was written, with the help of which the following dispersion characteristics were calculated in the region of frequencies used.

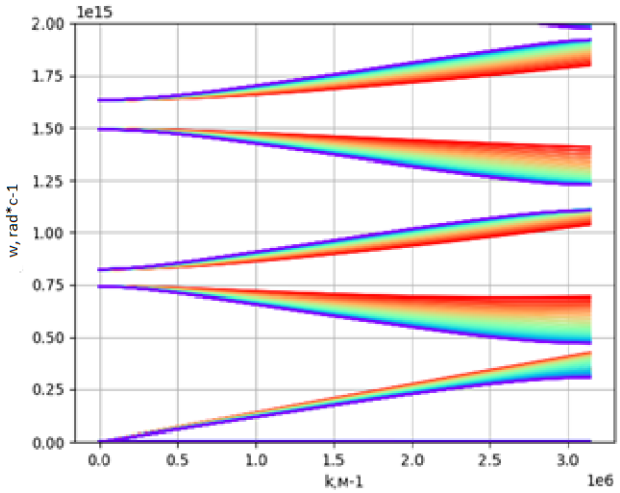


Fig. 1. Dispersion characteristic of a photonic crystal for modes propagating in different directions

## Conclusion

According to the dispersion characteristics, additional calculations were made. Sections of the surfaces of the dispersion characteristic are constructed in the form of functions kz=f(kx). The first surface has a cross section corresponding to 5 THz, and the second surface has a cross section of the difference surface corresponding to 282 and 277 THz.

Thanks to these constructions, a direction was found in the photonic crystal, in which the energy conservation law and the phase matching condition for reemission at a difference frequency corresponding to 5 THz will be fulfilled.

## REFERENCES

1. **Rumyantsev, V. V., Marem'yanin, K. V., Fokin, A. P., Dubinov, A. A., Razova, A. A., Mikhailov, N. N., Dvoretskii, S. A., Glyavin, M. Yu., Gavrilenko, V. I., Morozov, S. V.** Generation of terahertz radiation in InP: Fe crystals due to second-order lattice nonlinearity. Semiconductors 55:10 (2021) 785–789.

2. **Aleshkin, V. Ya., Dubinov, A. A.** Intracavity terahertz difference frequency generation in a two-frequency InGaAsP/InP laser with InGaAs quantum wells Quantum Electronics 39(8) (2009) 727–7303.

3. **Dubinov, A. A., Aleshkin, V. Ya., Gavrilenko, V. I., Rumyantsev, V. V., Mikhailov, N. N. Dvoretskii, S. A., Utochkin, V. V., Morozov, S. V.** THz laser generation on a hybrid surface plasmon in a HgCdTe-based structure. Quantum Electron. 51:2 (2021) 158–163.

3. **Zvonkov, B. N. Biryukov, A. A. Ershov, A.V. Nekorkin, S.M., Aleshkin, V.Ya., Gavrilenko, V.I., Dubinov, A.A., Maremyanin, K.V., Morozov, S.V., Belyanin, A.A., V.V. Kocharovsky, V.V., Kocharovsky. Vl.V.** Simultaneous TE1 and TE2 mode lasing yielding dual-wavelength oscillation in a semiconductor laser with a tunnel junction Appl. Phys. Lett. 92(021) (2008) 122.

# First-principle study of phosphorus incorporation into silicon by $PBr_3$ adsorption on Si(100)

**V. M. Shevlyuga** [1], **Y. A. Vorontsova** [1,2✉], **T. V. Pavlova** [1,2]
[1]Prokhorov General Physics Institute of the Russian Academy of Sciences, Moscow, Russia;
[2]HSE University, Moscow, Russia
✉ yuavorontsova_2@edu.hse.ru

**Abstract.** The synthesis of semiconductor nanostructures for quantum technologies requires the incorporation of phosphorus atoms into silicon with atomic precision. Here, we studied the phosphorus incorporation into the Si(100) surface by $PBr_3$ adsorption using scanning tunneling microscopy (STM) and density functional theory (DFT). The $PBr_3$ molecule is compatible with a halogen mask, which can be used to place P atoms on Si(100) with high accuracy. Based on DFT calculations, we identified the objects observed in STM on the silicon surface after $PBr_3$ adsorption. At room temperature, $PBr_3$ fully dissociate on Si(100). Heating of a $PBr_3$-dosed sample leads to the phosphorus incorporation in silicon. Thus, we have proved that the $PBr_3$ molecule can be used to incorporate P into Si(100) through a halogen mask.

**Keywords:** adsorption, phosphorus incorporation, silicon.

**Funding:** This work was supported by the Russian Science Foundation under the grant No. 21-12-00299.

## Introduction

The key problem in the synthesis of semiconductor nanostructures for quantum technologies is the incorporation of single impurities into silicon with atomic precision. Phosphine is currently used as a main source of phosphorus to create all elements of a silicon quantum chip based on single impurities [1, 2]. Phosphine ($PH_3$) is compatible with a hydrogen monolayer resist, from which a mask is created by removing individual hydrogen atoms in a scanning tunneling microscope (STM). An alternative to a hydrogen resist can be a halogen monolayer [3]. In particular, the halogen monolayer better protects the silicon surface from unwanted incorporation of phosphorus from a halogen-containing molecule than the hydrogen monolayer [4]. As a source of phosphorus compatible with the halogen resist, a halogen-containing molecule such as $PBr_3$ can be used. In this work, we study the incorporation of phosphorus into silicon by $PBr_3$ adsorption on Si(100). Studying the interaction of a molecule with a clean surface is a necessary step before studying the adsorption of a molecule through windows in a halogen mask.

## Methods

The experiments were carried out in an ultra-high vacuum (UHV) system with a base pressure of $5\times10^{-11}$ Torr. The STM measurements were performed with GPI CRYO (SigmaScan Ltd.) operated at 77K. The identification of objects after $PBr_3$ adsorption and the calculation of activation barriers of $PBr_3$ incorporation were carried out on the basis of the density functional theory (DFT).

## Results and Discussion

After $PBr_3$ adsorption on the Si(100) surface, various objects were observed in the STM. We have identified these objects using DFT calculations. The most frequently observed object is a completely dissociated molecule. We calculated one of the possible pathways for the complete dissociation of the $PBr_3$ molecule and found that $PBr_3$ dissociate at room temperature with a time scale of about 10 seconds.

Before insertion into the Si(100) surface, the P atom can diffuse. We have calculated the diffusion pathways of the phosphorus atom on Si(100) both for a clean surface and in the presence of Br atoms after $PBr_3$ dissociation. The presence of bromine atoms does not change the diffusion pathway, but the activation energy of this process on a clean surface (1.01 eV) is slightly less than with Br atoms after $PBr_3$ dissociation (1.20 eV). We found that the diffusion of

phosphorus on silicon in the presence of Br atoms should occur with a time scale of about 1 second at a temperature of about 460 K.

To incorporate phosphorus into silicon, the sample must be heated [5]. After heating the sample with adsorbed $PBr_3$ to 670 K for 5 minutes, small islands appeared on the surface. We have concluded that the islands are formed from silicon, since the height of the islands is equal to the height of the Si(100) atomic step, and Si buckling is visible on them. Silicon atoms ejected to the surface indicate the incorporation of phosphorus into silicon [5].

## Conclusion

Our results demonstrate that the $PBr_3$ molecule can be used to insert phosphorus atoms into silicon. We found out that the presence of Br atoms after $PBr_3$ dissociation does not significantly affect the phosphorus diffusion on the Si(100) surface.

## Acknowledgments

This work was supported by the Russian Science Foundation under the grant No. 21-12-00299. We thank the Joint Supercomputer Center of RAS for providing the computing power.

## REFERENCES

1. **He Y., Gorman S.K., Keith S.K., Kranz L., Keizer J.G., Simmons M.Y.,** A two-qubit gate between phosphorus donor electrons in silicon, Nature. 571(7765) (2019) 371-375.

2. **Fuechsle M., Miwa J. A., Mahapatra S., Ryu H., Lee S., Warschkow O., Hollenberg L., Klimeck G., Simmons M. Y.,** A single-atom transistor, Nature Nanotechnology. 7(4) (2012) 242-246.

3. **Pavlova T., Shevlyuga V., Andryushechkin B., Eltsov K.,** Dangling bonds on the Cl- and Br-terminated Si(100) surfaces, Applied Surface Science. 591 (2022) 153080.

4. **Pavlova T. V., Eltsov K. N.,** Reactivity of the Si(100)-2×1-Cl surface with respect to PH3, PCl3, and BCl3: comparison with PH3 on Si(100)-2×1-H, Journal of Physics: Condensed Matter. 33(38) (2021) 384001.

5. **Schofield S.R., Curson N.J., Simmons M.Y., Rue F.J., Hallam T., Oberbeck L., Clark R.G.,** Atomically Precise Placement of Single Dopants in Si, Physical Review Letters. 91(13) (2003) 136104.

# Interdigital gold electrodes for a conductometric gas sensor on the glass surface

**R.R. Gainullin** [1✉], **G.R. Nizameeva**[1,2], **E.M. Lebedeva**[1], **I.R. Nizameev**[1,3]
[1] Arbuzov Institute of Organic and Physical Chemistry, FRC Kazan Scientific Center of RAS, Kazan, Russia;
[2] Kazan National Research Technological University, Kazan, Russia;
[3] Kazan National Research Technical University Named after A.N. Tupolev-KAI, Kazan, Russia
✉e-mail: radis.g@mail.ru

**Abstract.** As a result of industrial activities, a huge amount of harmful substances is released into the environment. Timely detection of such substances is an important task for minimizing environmental problems. In this work, interdigital gold electrodes for a conductometric gas sensor were obtained by photolithography on the surface of a glass substrate. To increase the adhesion of the photoresistive film, the glass surface was subjected to etching. The roughness of the glass substrate was studied by the AFM method.

**Keywords:** Gas sensor, electrodes, adhesion, roughness.

**Funding:** The reported study was funded by the government assignment for FRC Kazan Scientific Center of RAS.

## Introduction

The constant increase in the concentration of chemicals harmful to human and animal health in the atmosphere increases the risks of various diseases. Air quality monitoring plays an important role in combating air pollution [1]. One of the most common method for detecting toxic gases is conductometric gas sensors [2].

Conductometric gas sensors are devices that measure the electrical conductivity of active material to determine the presence or concentration of certain gases. This type of sensor is particularly useful in the field of indoor air quality monitoring, as well as for the detection of hazardous gases in industrial processes. Conductometric gas sensors have high accuracy and fast response to changes in the concentration of gases in the air [3]. They can be used to detect various gases such as carbon dioxide, carbon monoxide, nitrogen oxides, ammonia, methane, and others [4-6]. The principle of operation of such sensors is based on the change in the conductivity of the gas-sensitive element in the presence of the target gas. Typically, the gas sensing element is a substrate, on the surface of which a sensitive material and conductive electrodes are deposited.

## Materials and Methods

In this work, silicate glass was chosen as the target substrate, on the surface of which interdigital gold electrodes were formed by photolithography. The surface morphology of the glass substrate, as well as the roughness, was studied by atomic force microscopy (AFM). The observation was carried out in intermittent-contact mode. Microscopic images were obtained with a resolution of 512x512 pixels per frame at a scanning speed of 1 Hz.

## Results and Discussion

During the experiments, it was found that the adhesion of the photoresist to the glass substrate is not satisfactory for creating conductive electrodes.

As is known, roughness is the main factor affecting the adhesion of films to various surfaces. In the framework of this work, the glass substrate roughness $R_a$ (arithmetic mean deviation from the absolute values of the profile deviations within the baseline) was studied by atomic force microscopy (AFM). To do this, various sections of the glass substrate were scanned. The roughness Ra was calculated by constructing topographic histograms. Ra was equal to 0.55 nm.

To increase photoresist adhesion to the glass substrate surface, it was decided to increase the glass roughness by etching. The state of the glass surface after etching was also studied using

AFM. The data obtained show an increase in roughness up to 165 nm, which is suitable for creating conductive electrodes on a glass substrate.

## Conclusion

As a result of the work, current-collecting electrodes were deposited on the surface of the glass substrate, which will be used to measure the surface resistance of the conductometric sensor's sensitive material in the toxic gases presence. The electrodes were deposited by photolithography using a film photoresist. The glass surface was etched to improve the adhesion of the photoresist film. The roughness of the glass substrate before and after etching was studied by AFM. It was found the roughness increased from 0.55 to 165 nm after etching.

## REFERENCES


1. **Dhall S., Mehta B. R., Tyagi A. K., Sood K.,** A review on environmental gas sensors: Materials and technologies, Sensors International. 2 (2021) 100116.
2. **Korotcenkov G., Cho B. K.,** Metal oxide composites in conductometric gas sensors: Achievements and challenges, Sensors and Actuators B: Chemical. 244 (2017) 182-210.
3. **Vazquez-Lopez A. Bartolome, J., Cremades, A., Maestre, D.,** High-performance room-temperature conductometric Gas sensors: materials and strategies, Chemosensors. 10 (6) (2022) 227.
4. **Mirzaei A., Lee J. H., Majhi S. M., Weber M., Bechelany M., Kim H. W., Kim S. S.,** Resistive gas sensors based on metal-oxide nanowires, Journal of Applied Physics. 126 (24) (2019) 241102.
5. **Fine G. F., Cavanagh L. M., Afonja A., Binions R.,** Metal oxide semi-conductor gas sensors in environmental monitoring, Sensors. 10 (6) (2010) 5469-5502.
6. **Dey A.,** Semiconductor metal oxide gas sensors: A review, Materials science and Engineering: B. 229 (2018) 206-217.

УДК 539.5

А.С. Гращенко (к.ф.-м.н., с. н. с., ИПМаш РАН),
С.А. Кукушкин (д.ф.-м.н., зав. лаб., ИПМаш РАН),
Ш.Ш. Шарофидинов (к.т.н., с. н. с., ФТИ им. А. Ф. Иоффе РАН)

# СТРУКТУРНЫЕ ХАРАКТЕРИСТИКИ ПОВЕРХНОСТИ ПЛЕНОК НИТРИДА АЛЮМИНИЯ-ГАЛЛИЯ НА НАНОСЛОЯХ КАРБИДА КРЕМНИЯ НА КРЕМНИИ

В настоящей работе проведены измерения структурных характеристик поверхности абсолютно новых полупроводниковых гетероструктур AlGaN/SiC/Si и AlGaN/AlN/SiC/Si. Основная особенность исследуемых гетероструктур в том, что они были выращены на гибридных кристаллах нано-SiC/Si, синтезированных методом замещения атомов. Эта уникальная методика позволяет синтезировать слой SiC внутри матрицы Si толщиной несколько нанометров за счет замены половины атомов Si на атомы C [1,2]. Для данного исследования были изготовлены кристаллические структуры нано-SiC/Si с толщиной слоя SiC 3 нм и шероховатостью поверхности менее 0.5 нм. Такие структуры были синтезированы на кристаллах Si с ориентациями (001), (011) и (111). Толщину слоев нано-SiC определяли с помощью анализа спектров, полученных методом оптической эллипсометрии, а шероховатость поверхности рассчитывали по данным оптической профилометрии. Пленки AlGaN и буферные слои AlN выращивали методом хлорид–гидридной эпитаксии [3]. Толщина пленок AlGaN, выращенных непосредственно на гибридных подложках нано-SiC/Si равна 6-9 мкм. Пленки AlGaN и буферные слои AlN в гетероструктурах AlGaN/AlN/SiC/Si имеют толщину равную 3-5 мкм и 2-3 мкм соответственно. Структуру поверхности исследуемых пленок AlGaN измеряли и визуализировали с помощью метода атомно-силовой микроскопии. Этот метод позволил определить шероховатость поверхности пленок AlGaN и измерить геометрические характеристики структуры поверхности. Показано, что структура поверхности слоев AlGaN выращенных на подложках Si с ориентациями (001), (011) и (111) кардинально отличается. Методом наноиндентирования измерены параметры приведенного модуля упругости пленок AlGaN вблизи поверхности. Экспериментально обнаружено, что буферный слой AlN существенно влияет на данные наноиндентирования пленок AlGaN в начальный момент вдавливания. Настоящая работа дает новое представление о структуре поверхности и механических свойствах пленок AlGaN, выращенных на кристаллах нано-SiC/Si, синтезированных методом замещения атомов.

Работа выполнена при финансовой поддержке министерства науки и высшего образования РФ в рамках государственного задания ФГПУ ИПМаш РАН по контракту № FFNF-2021-0001. Исследования проводились с использованием оборудования УНУ “Физика, химия и механика кристаллов тонких пленок” ИПМаш РАН, Санкт-Петербург.

1. S.A. Kukushkin, A.V. Osipov. J. Phys. D: Appl. Phys. In press. 44 (2014).
2. С.А. Кукушкин, А.В. Осипов. ФТТ 50, 1188 (2008).
3. Ш.Ш. Шарофидинов, С.А. Кукушкин, А.В. Редьков, А.С. Гращенко, А.В. Осипов. ПЖТФ 45, 711 (2019).

# Selective Area Growth of GaN/InGaN Nanowires on Si Substrates

**V. O. Gridchin [1,2✉], L. N. Dvoretckaia[1], K. P. Kotlyar[1,2], R. R. Reznik[2], A. V. Parfeneva[3], A. S. Dragunova[1,4], I. A. Melnichenko[1,4], V. G. Dubrovskii[2], G. E. Cirlin [1-3]**

[1] Alferov University, Saint Petersburg, Russia;
[2] St Petersburg University, Saint Petersburg, Russia;
[3] Ioffe Institute, Saint Petersburg, Russia;
[4] HSE University, Saint Petersburg, Russia
✉gridchinvo@gmail.com

**Abstract.** The direct integration of epitaxial III-N heterostructures on Si substrates is a promising platform for the development of optoelectronic devices. Here, we investigate peculiarities of selective area growth and physical properties of GaN nanowires on crystalline lattice-mismatched Si substrates. For the first time, the temperature–Ga/N2 flux ratio map was established for GaN nanowires grown on patterned Si/$SiO_x$ substrate. A model was developed that explains the selective growth range, which appeared to be highly sensitive to the growth temperature and Ga flux, as well as to the radius and pitch of the patterned pinholes. A light-emitting diode based on selectively grown GaN/InGaN nanowires on a Si/$SiO_x$ substrate is proposed.

**Keywords:** Nanowires, molecular beam epitaxy, light-emitting diode, growth map, selective area growth

**Funding:** The samples were grown under support of Ministry of Science and Higher Education of the Russian Federation (state task № 0791-2023-0004). The physical properties of samples were studied under financial support of St. Petersburg State University under research grant № 94031047.

## Introduction

The direct integration of epitaxial III-N heterostructures on Si substrates is a promising platform for the development of optoelectronic devices. Nanowires, due to their unique geometry, allow for the direct synthesis of semiconductor light-emitting diodes (LED) on crystalline lattice-mismatched Si wafers. The statistical nature of the III-N NW nucleation and growth process leads to inhomogeneous size distributions, in terms of both diameters and lengths, and inhibits the reproducibility of NW growth [1]. To fabricate NW-based light emitting structures, it is crucial to maintain the necessary control over the NW spacing, diameter and length and improve the size uniformity across large surface areas. All these factors directly affect the electrical transport [2] and light emission properties of the GaN NW ensembles [3].

One way to grow uniform arrays of GaN NWs is selective area growth (SAG) on patterned substrates. Here, we investigate peculiarities of selective area growth and physical properties of GaN nanowires on crystalline lattice-mismatched Si substrates.

## Materials and Methods

Microsphere lithography was employed to form the pinholes in the $SiO_x$ mask layer. This patterning method provides sub-micrometer lateral resolution in a versatile, scalable and cost-effective way [4]. The GaN NWs were grown using PA-MBE on pre-patterned one-quarter 2 inch $SiO_x$/Si(111) substrates in a Riber Compact 12 MBE equipped with Ga, In, Si, Mg effusion cells and $N_2$ plasma source. Prior to growth, the substrates were heated up to a temperature of 915 °C and annealed for 20 min to remove the native oxide. It should be noted that heating to this temperature enables native oxide desorption without the destruction of the growth oxide mask. The $N_2$ flow was fixed at 0.4 sccm, and the nitrogen plasma source power was fixed at 450 W. We then carried out the series of experiments with different beam equivalent pressures (BEPs) for the Ga flux at a constant substrate temperature. Next, we increased the substrate temperature in steps of 5 °C and carried out MBE growth at the same Ga BEPs as before. Overall, the growth

experiments were conducted within a rectangular range in the temperature–Ga BEP plane from 820 to 850 °C, for the temperature, and from $1 \times 10^{-7}$ Torr to $5 \times 10^{-7}$ Torr, for the Ga BEP.

The morphology of the samples was studied with scanning electron microscopy (SEM) using a Supra 25 Zeiss SEM. The photoluminescence (PL) measurements were recorded at room temperature and 6 K using a He–Cd metal-vapor laser with a wavelength of 325 nm at 6.5 mW. The laser spot diameter was 100 µm. The PL signal was detected using a DK480 Spectral Products monochromator and a single-channel Si detector in synchronous detection mode (SRS 510, Stanford Research Systems, Sunnyvale, USA).

## Results and Discussion

In this work, we studied the effect of temperature and the III/V flux ratio with different Ga fluxes and a fixed N2 flux on the SAG of GaN NWs on patterned $SiO_x$/Si(111) substrates using plasma-assisted molecular beam epitaxy (PA-MBE). A growth diagram separating three domains - SAG in the absence of any parasitic NWs on the mask surface, parasitic growth and no growth - was obtained as a function of the temperature and III/V flux ratio. A dedicated model was developed that explained the SAG growth map and showed that the growth selectivity was influenced not only by the temperature and Ga flux but also by the geometrical parameters of the template. As a result, the possibility of SAG growth of GaN NWs on patterned $SiO_x$/Si(111) substrates critically depends on the correct choice of temperature and III/V flux ratio for pinholes of a given size and pitch. We synthesized n-GaN NWs and LED n-GaN/InGaN/p-GaN NWs using selective-area MBE growth on Si substrates with prepatterned $SiO_x$ layers. The PL measurements revealed that the synthesized NWs have a relatively broad optical response. The measured EL spectra for the fabricated LED devices demonstrated a peak located around 500–520 nm and wide IR tail. The results of the EL measurements are consistent with the PL study.

## Conclusion

This study should be useful for obtaining regular arrays of GaN NWs without any parasitic growth on a mask surface and can be extended to other material systems and growth techniques. A possibility of LED fabrication based on the regular arrays of GaN/InGaN NWs was shown. The obtained results open up new prospects for the creation of LEDs on Si substrates.

## REFERENCES

1. **Consonni V.,** Self-induced growth of GaN nanowires by molecular beam epitaxy: A critical review of the formation mechanisms. Phys Status Solidi Rapid Res Lett. 7(10) (2012) 699-712.

2. **Motayed A., Vaudin M., Davydov A.V., Melngailis J., He M., Mohammad S.,** Diameter Dependent Transport Properties of Gallium Nitride Nanowire Field Effect Transistors. Appl. Phys. Lett. 90(4) (2007), 043104.

3. **Sekiguchi H., Kishino K., Kikuchi A.,** Emission Color Control from Blue to Red with Nanocolumn Diameter of InGaN/GaN Nanocolumn Arrays Grown on Same Substrate. Appl. Phys. Lett. 96(23) (2010), 231104.

4. **Zhang Z., Geng C., Hao Z., Wei T., Yan Q.,** Recent Advancement on Micro-/Nano-Spherical Lens Photolithography Based on Monolayer Colloidal Crystals. Adv. Colloid Interface Sci. 228 (2016), 105–122.

# Carboxymethylcellulose as effective agent to regulate properties of silver nanoparticle-based conductive inks

**E. V. Darkhanov** [1,2✉], **E. A. Danilov**[2]
[1] HSE Tikhonov Moscow Institute of Electronics and Mathematics (MIEM HSE), Moscow, Russian Federation;
[2] JSC Research Institute «NIIgraphite», Moscow, Russian Federation.
✉makaroch817@gmail.com

**Abstract.** In the present work, the properties of suspensions of silver micro- and nanoparticles (silver inks) developed for subsequent application in printed electronics technology are investigated. It is proposed to maintain the resistance to deposition and to particle agglomeration by using carboxymethylcellulose as a stabilizer. The main attention is paid to the influence of the carboxymethylcellulose concentration on the main properties of suspensions: specific conductivity, viscosity, average particle size, surface tension. In the course of our studies, we were able to determine the concentration of carboxymethylcellulose that provided suitable properties and stability of the suspensions for above 4 weeks. We were also able to overcome the undesirable coffee ring effect after deposition.

**Keywords:** silver ink, silver suspensions, printed electronics, carboxymethylcellulose.

## Introduction

Printed electronics is one of the headline trends of modern electronic technologies. This is mainly due to the fact that thin films can be printed much more technologically and effectively as compared to classic technologies. Electron lithography and photolithography are generally used to deposit thin film structures. These techniques require many expensive and time-consuming steps. Therefore, much interest is attracted currently to spray coating [1] or inkjet printing [2]. Inkjet printing involves liquid or colloid inks containing the necessary component (i.e. metal nanoparticles) being deposited onto the substrate through a printing nozzle. The substrate is then dried to retain a pattern of metal thin film. Inkjet printing was successfully used to manufacture flexible displays [3], photovoltaic cells [4], sensors [5], antennae [6], transistors [7].

Although inkjet printing principles are quite simple, there is a number of limitations to wide-scale use of the technology. Most of these limitations are linked with the inks' properties and manufacturing. Required technology should satisfy several requirements:

- Ink synthesis should be straightforward and scalable;
- Inks should have low viscosity;
- Particle size should be low to prevent precipitation and clogging of the nozzle;
- Inks should provide high resolution after drying;
- Films and contact tracks should have low resistance.

In the current work, we aimed to manufacture electrically conductive inks based on silver micro- and nanoparticles as per abovementioned requirements. We used carboxymethylcellulose (CMC) as stabilizer and assessed its influence on suspensions properties.

## Materials and Methods

CMC solutions with concentrations of 0.1–1.0 mg/ml were manufactured by dissolving (40ºC) at moderate stirring (100 rpm) of CMC powder in a mixture of distilled water and ethanol (50 vol.%). Suspensions of silver nanoparticles (obtained via electrical wire explosion technique) were obtained by ultrasonic dispersion of silver nanopowder (1 mg/ml, mean size ca. 60 nm) in carboxymethylcellulose solutions for 7 hours (Melfiz MEF391 horn-type device, 200 W). After drop-casting the films they on glass surface they were dried at 170 deg.C and evaluated via scanning electron microscopy (Hitachi TM3000).

Particle size distributions were studied by dynamic light scattering using the Malvern Zetasizer Nano S.

Electrical conductivity was measured by conductivity meter S230 (Mettler Toledo). Viscosity was measured by vibrational viscometry, SV-10 (A&D), frequency 30 Hz). The surface tension of the suspensions was evaluated by droplet counting method.

## Results and Discussion

All of the obtained suspensions were homogeneous with no signs of precipitation over at least 1 week. Dynamic viscosity (figure 1a) was in the range 1.82-2.18 mPa·s suitable for inkjet applications (the authors of [8] suggest 1-25 mPa·s as the optimal range). It is noteworthy that viscosity did not significantly depend on CMC concentration, although polymers tend to increase viscosity even at low concentrations. Surface tension dropped above 0.6 mg/ml CMC concentration, but all of the obtained values (28.92-36.72 mN/m) fell within the applicable range 25-50 mN/m [10], so CMC has a pronounced surfactant effect in the system.

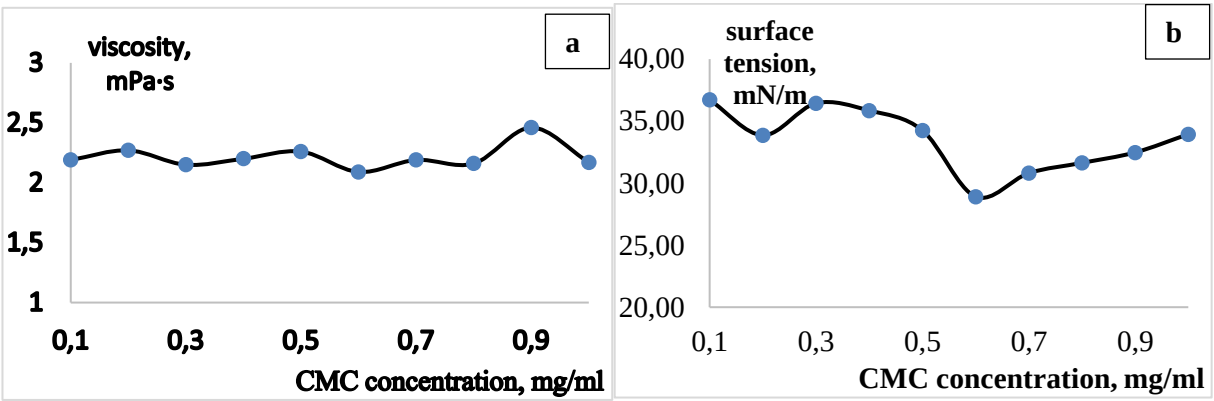


Fig. 1. Dependence of viscosity (a) and surface tension of silver nanoparticles-based inks on CMC concentration

The main purpose of using CMC is to provide control over particle size and suspension stability. Mean particle size (figure 2a) shows complex dependence on CMC concentration, but minimal particle size was observed at 0.8 mg/ml, the distribution itself being lognormal with minimal shoulder due to agglomerates.

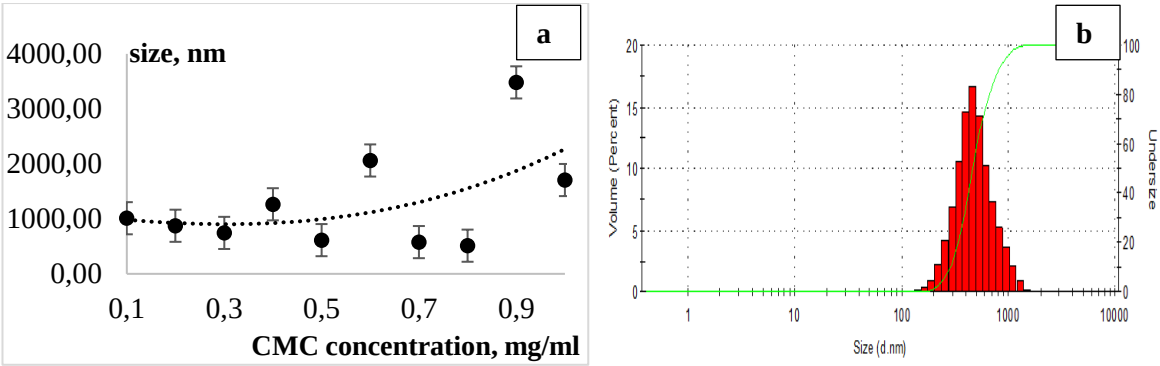


Fig. 2. Dependence of mean particle size of silver nanoparticles-based inks on CMC concentration (a) and typical particle size distribution (b)

A series of scanning electron microscopy studies on droplets suggest that increasing CMC concentration above 0.6 mg/ml suppresses the so-called “coffee ring” effect due to limited liquid media-air and particle-air surface tension (figure 3). This is very important for printed contact for contact tracks formation as non-uniform drying tends to decrease film resistance and decreases printing accuracy.

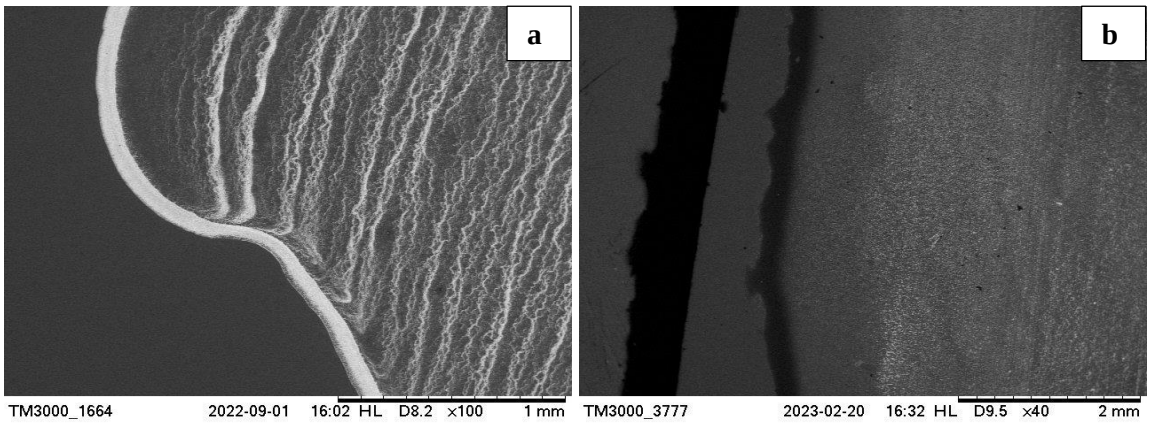


Fig. 3. SEM images of dried droplets of inks at 0.1 (a) and 0.8 mg/ml (b) CMC concentration

A series of additional studies suggest that CMC concentration of 0.8 mg/ml is about optimal for the studied ink formulation as it provides:

- Minimal particle size;
- Very high suspension stability (particle size distribution remains stable and lognormal for at least 4 weeks);
- Minimal surface tension suppresses “coffee ring” effect.

## Conclusion

As the study shows, CMC concentration has strong effect on silver nanoparticles-based inks, especially on surface tension and particle size distributions after ultrasonic treatment. It was shown that CMC concentration of 0.8 mg/ml provides manufacturing of highly stable inks with uniform particle size distribution, low viscosity and surface tension while conductive films based on this ink formulation are very promising for printed electronics applications as they are uniform and show no “coffee ring” effect.

## REFERENCES

1. **Siegel A. C., Phillips S. T., Dickey M. D., Lu N., Suo Z., Whitesides G. M.**, Foldable printed circuit boards on paper substrates, Advanced Functional Materials. – 2010. – T. 20 – №. 1. – 28–35.

2. **Žitňan M., Müller L., Zub K., Schubert U. S., Galusek D., Wondraczek L.**, Low-cost inkjet printing of thin-film mullite structures, International Journal of Applied Glass Science. – 2022. – T. 13 – №. 1. – 135–142.

3. **Chen Y., Au J., Kazlas P., Ritenour A., Gates H., McCreary M.**, Flexible active-matrix electronic ink display, Nature. – 2003. – T. 423 – №. 6936. – 136–136.

4. **Hoth C. N., Choulis S. A., Schilinsky P., Brabec C. J.**, High photovoltaic performance of inkjet printed polymer: fullerene blends, Advanced Materials. – 2007. – T. 19 – №. 22. – 3973–3978.

5. **Wang C. T., Huang K. Y., Lin D. T., Liao W. C., Lin H. W., Hu Y. C.**, A flexible proximity sensor fully fabricated by inkjet printing, Sensors. – 2007. – T. 10 – №. 5. – 5054–5062.

6. **Mäntysalo M., Mansikkamäki P.**, An inkjet-deposited antenna for 2.4 GHz applications, AEU-International Journal of Electronics and Communications. – 2009. – T. 63 – №. 1. – 31–35.

7. **Okimoto H., Takenobu T., Yanagi K., Miyata Y., Shimotani H., Kataura H., Iwasa, Y.**, Tunable carbon nanotube thin-film transistors produced exclusively via inkjet printing, Advanced materials. – 2010 – T. 22 – №.36. – 3981–3986.

8. **Fernandes I. J., Aroche A. F., Schuck A., Lamberty P., Peter C. R., Hasenkamp W., Rocha T. L.**, Silver nanoparticle conductive inks: Synthesis, characterization, and fabrication of inkjet-printed flexible electrodes, Scientific reports. – 2020 – T. 10 – №. 1. – 1–11.

# Ab initio modelling of In wetting layer formation on As-stabilized GaAs during first stages of droplet epitaxy.

**D. D. Dukhan✉, S. V. Balakirev, M. S. Solodovnik**
Laboratory of Epitaxial Technologies, Institute of Nanotechnologies, Electronics and Equipment Engineering, Southern Federal University, Taganrog 347922, Russia
✉duhan@sfedu.ru

**Abstract.** In this work we conduct theoretical study of In wetting layer formation on surface of As-stabilized GaAs(001) during droplet epitaxy using density functional theory to calculate dependence of adsorption energies on In coverage. Results show that with increase in coverage wetting layer lowers its adsorption to surface leading subsequent adatoms to have better mobility affecting size and surface density of metal nanodroplets and quantum dots based on them.

**Keywords:** density functional theory, GaAs, indium, adsorption energy, critical thickness, droplet epitaxy, molecular beam epitaxy

**Funding:** This work was supported by the Russian Science Foundation Grant No. 22-79-10251 and by the Ministry of Science and Higher Education of the Russian Federation Grant No. FENW-2022-0034 at the Southern Federal University.

## Introduction

Epitaxial growth of nanostructures on surface of A3B5 compounds is one of the most promising directions in nanoelectronics and nanophotonic today. At the same time, the question of how to control the kinetics of growth processes still remains relevant due to the diversity of the studied systems and growth mechanisms. Droplet epitaxy is flexible method for growth of quantum dots (QD) allowing to independently control shape, size and density of resulting self-assembled nanostructures. It relies on formation of metal droplets from single wetting layer (Volmer-Weber growth mode) that then are crystallized by annealing in group-V element atmosphere. Initial droplet formation is crucial in this process as it defines size and distribution of resulting crystalline QDs. In this work, we study the adsorption energy of In wetting layer forming on the As-stabilized GaAs surface depending on substrate coverage in order to understand the kinetics of formation of the first wetting layer that is required for subsequent adatoms to follow Volmer-Weber growth mode, forming 3D nanostructures.

## Methods

Ab initio calculations of 2x2x4 GaAs(001) slab model (Fig. 1) were conducted using Density functional theory (DFT). It was applied by using the Vienna ab initio simulation package (VASP) [1] with the projector augmented wave potential construction. For approximating the exchange-correlation functional we used Perdew's generalized-gradient-approximation (PBE). DFT+U method based on Dudarev's approach [2] was used to properly describe interactions of d-band electrons. Considering size and periodic boundary conditions of simulation cell, calculated coverages were 0.125, 0.25, 0.375, 0.5, 1 and 1.125 ML. Adsorption energy per adsorbate atom was obtained by formula (1)

$$Eads / adsorbant = -(E_{GaAs+In} - E_{GaAsclean} - E_{In} \cdot N) / N \qquad (1)$$

where $E_{GaAsclean}$ is total free energy of pristine GaAs surface, $E_{In}$ – Indium energy in gaseous form, $N$ – number of adatoms in simulation cell and $E_{GaAs+In}$ is energy of reconstructed surface with adatoms. Minus sign is needed to turn negative values of $E_{ads}$ into positive allowing for better readability of results.

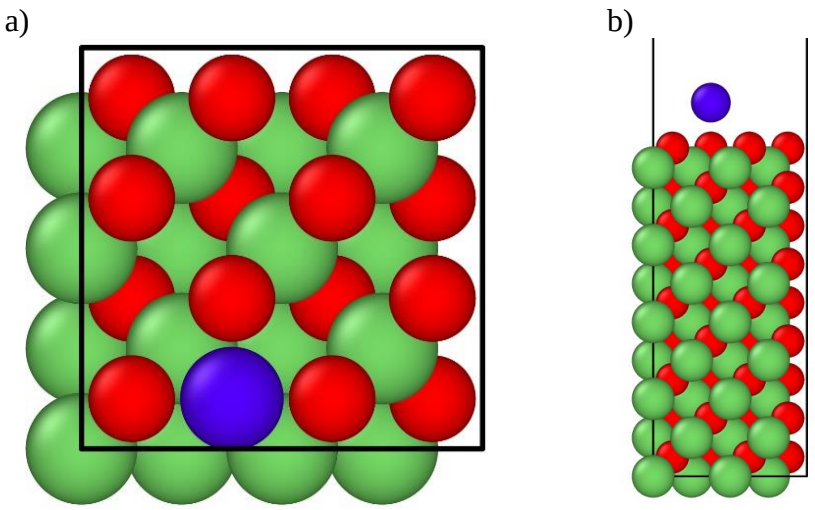


Fig. 1. Top view (a) and front view (b) of simulation cell

## Results and Discussion

Calculations showed that $E_{ads/adatom}$ highly varies depending on coverage. Highest $E_{ads}$ of 8.48 eV was shown for coverage of 0.125 ML which results from adding 1 adatom in 2x2 simulation cell. Being very high for a single adatom this value can be explained by induced reconstruction of pristine GaAs surface. Row $Eads_{full}$ in Table 1 shows other Eads values, where $E_{GaAs+In}$ is compared to pristine $E_{GaAsclean}$. There is significant decrease in Eads which nonlinearly goes down to 3.755 eV, meaning that something in growth process of wetting layer significantly weakens its interaction with substrate. If we calculate energy of reconstructed surface without adatoms and use it in place of $E_{GaAsclean}$ we can somewhat limit reconstructions influence on Eads. Doing this we decreased $Eads_{(0.125\ ML)}$ down to 3.466 eV showing that reconstruction have significant impact on Eads. Row $Eads_{lim}$ shows approximation of adsorption energy without reconstruction contribution $E_{rec}$. It is obtained by replacing $E_{GaAsclean}$ with $E_{GaAs+In}$ of previous coverage step. This also gives us approximation of adsorption energy per individual adatom. Values change from 3.466 to 2.751 eV showing that even exclusion of $E_{rec}$ from full Eads does not change the trend of it going lower. This can lead to higher rates of surface diffusion of following adatoms forming QDs increasing their size and decreasing density.

Table 1

**Adsorption energy depending on coverage**

| Coverage | 0.125 ML | 0.25 ML | 0.375 ML | 0.5 ML | 1 ML | 1.125 ML |
|---|---|---|---|---|---|---|
| $Eads_{full}$ (eV/ads) | 8.483 | 6.022 | 5.161 | 4.710 | 3.881 | 3.755 |
| $Eads_{lim}$ (eV/ads) | 3.466 | 3.561 | 3.438 | 3.360 | 3.052 | 2.751 |

## References

1. Kresse G., Furthmüller J. Efficient iterative schemes for ab initio total-energy calculations using a plane-wave basis set //Physical review B. – 1996. – T. 54. – №. 16. – C. 11169.

2. S. L. Dudarev, G. A. Botton, S. Y. Savrasov, C. J. Humphreys, and A. P. Sutton, Phys. Rev. B **57**, 1505 (1998).

# Effect of plasma-chemical treatment of Si(001) substrates on the subsequent epitaxial growth of GaAs

**M M Eremenko [1]✉, L S Nikitina [2], J Y Jityaeva [3], E A Lakhina [1], V.S. Klimin [2], O A Ageev [2]**

[1] Laboratory of Epitaxial Technologies, Southern Federal University, Taganrog 347922, Russia

[2] Institute of Nanotechnologies, Electronics and Equipment Engineering, Southern Federal University, Taganrog 347922, Russia

[3] Research Laboratory of Functional Nanomaterials Technology, Southern Federal University, Taganrog 347922, Russia

✉eryomenko@sfedu.ru

**Abstract.** In this work, we investigated the effect of plasma-chemical treatment of silicon substrates on the subsequent epitaxial growth of GaAs. It is shown that a change in processing modes did not lead to a strong change in the root-mean-square roughness of the initial silicon surface. It was found that under the same growth conditions GaAs is formed on substrates differently depending on the silicon treatment mode: from individual crystallites with nanowires to a structure intergrown from individual crystallites.

**Keywords:** molecular beam epitaxy, silicon, GaAs, monolithic integration, plasma-chemical treatment, scanning electron microscopy.

**Funding:** This work was funded by the Ministry of Science and Higher Education of the Russian Federation; the state task in the field of scientific activity No. FENW-2022-0001.

## Introduction

High-quality formation of III-V semiconductors, in particular GaAs, on silicon is one of the main tasks of modern nanophotonics [1]. However, the growth of a polar semiconductor on a nonpolar substrate leads to the formation of antiphase domains. Also, the growth of GaAs on silicon leads to a large number of threading dislocations, which are obtained due to the difference in the lattice constants of both materials. Therefore, to date, many methods have been explored for the formation of III-V semiconductors on silicon in order to reduce the resulting dislocation density and eliminate antiphase domains in the final structures [1]. In this work, we used plasma-chemical treatment of silicon substrates to obtain a developed morphology on the surface of silicon wafers, which, as expected, will allow the subsequent nucleation of monolithically integrated GaAs nanostructures.

## Materials and Methods

The epitaxial growth of GaAs on samples with plasma-chemical treatment was studied using a SemiTEq STE35 MBE setup with solid-state sources. Plasma-chemical processing was carried out in combined fluoride plasma in the modes of chemical polishing (CP) and reactive ion etching (RIE). After processing, the samples were scanned by atomic force microscopy (AFM) to determine the root-mean-square (RMS) surface roughness. According to the scan results, it was revealed that the RMS roughness of the untreated original surface was 0.171 nm, while after processing in fluoride plasma in CP and RIE modes, the RMS roughness was 0.295 and 0.312 nm, respectively. After treatment, the samples were placed in a growth chamber, where they were preliminarily annealed at 600°C for 60 minutes. After annealing, without changing the temperature, GaAs was deposited with a thickness of 200 nm and with a growth rate of 0.25 ML/s.

## Results and Discussion

The results of experimental studies (Fig. 1) demonstrate differences in the final morphology of the grown nanostructures. It is shown that GaAs nanocrystallites with periodically occurring GaAs nanowires grow on a sample with RIE treatment (Fig. 1a, b). It should be noted that the nanowires grow in the <111> direction at an angle of 54.7º to the substrate surface. These results allow us to state that the nanowires obtained during the growth process inherit the structure of the silicon substrate.

Studies of epitaxial growth on samples treated in fluoride plasma in the CP mode showed that a change in the processing mode led to an increase in density and the formation of a GaAs structure spliced from individual crystallites (Fig. 1c, d). It is important to note that there is no growth of GaAs nanowires on the surface. It is likely that such a change in the morphology and mode of epitaxial growth is associated with an increase in the intensity of GaAs nucleation processes on the Si surface with a shift towards two-dimensional growth, which leads to suppression of the growth of GaAs nanowires.

Next, the samples were examined by AFM. Based on the obtained results, the degree of filling of the Si surface with the GaAs epitaxial material was estimated, which was 67% for samples obtained during growth on substrates treated with plasma chemically in the RIE mode and 94.8% when processing silicon substrates in the CP mode. The results obtained also confirm that, under the same growth conditions, changing the mode of plasma-chemical treatment of the silicon surface from RIE to CP leads to a gradual change in the GaAs growth mechanism from island to two-dimensional.

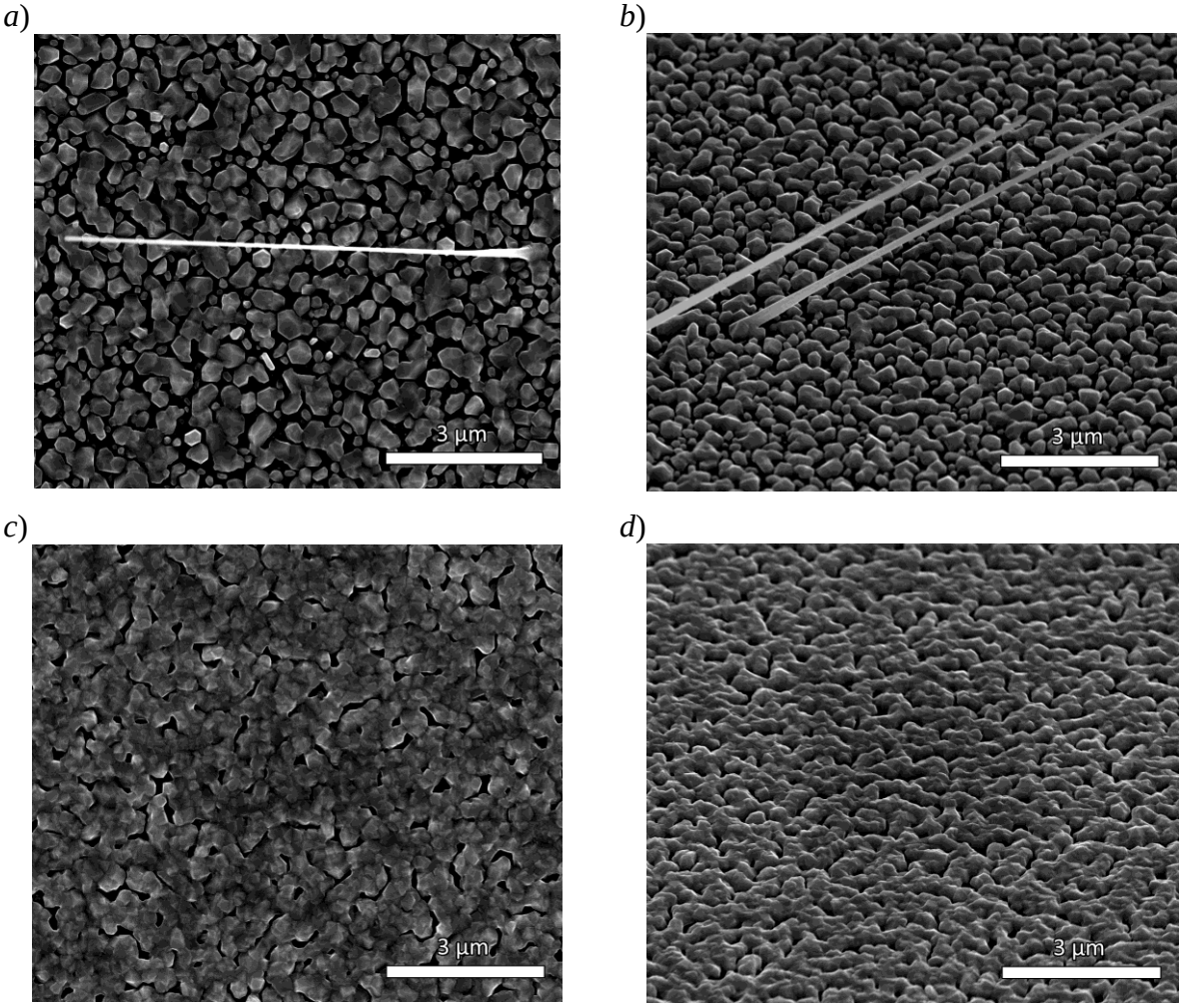


Fig. 1. SEM images of GaAs structures grown at $T$ = 600ºC, $H$ = 200 nm, $V$ = 0.25 ML/s on silicon substrates with different processing modes: (a, b) RIE, (c, d) CP.

## Conclusion

In conclusion, it can be said that a change in the regime of plasma-chemical treatment of Si affects the subsequent epitaxial growth of GaAs, despite the fact that the RMS roughness of the sample surfaces after treatment does not differ much from each other.

## REFERENCES

1. **Du Y., Xu B., Wang G., Miao Y., Li B., Kong Z., Dong Y., Wang W, Radamson H. H.**, Review of Highly Mismatched III-V Heteroepitaxy Growth on (001) Silicon, Nanomaterials. 12 (5) (2022) 741.

# Hard-template synthesis of microporous $SiO_2$ particles

**D. A. Eurov** [1✉], **D. A. Kirilenko** [1], **E. Yu. Stovpiaga** [1], **D. A. Kurdyukov** [1]
[1] Ioffe Institute, 194021 St. Petersburg, Russia
✉edan@mail.ru
(post@mail.ioffe.ru)

**Abstract.** A simple and facile method for the synthesis of monodisperse microporous spherical silica particles is proposed. The method is based on a traditional Stöber technique with the use of ammonium metavanadate acting as hard template for the micropore formation. The thus obtained silica particles possess an interconnected system of micropores that determines high values of their specific surface area and pore volume.

**Keywords:** Hard template, microporous silica, ammonium metavanadate, spherical particles.
**Funding:** This work was funded by the Russian Science Foundation, project no. 23-79-00018.

## Introduction

In today's world high-capacity inflammable and ecologically safe microporous materials are in high demand across various industries [1]. Materials of this kind are used, for example, in selective adsorption [2], catalysis [3], and as molecular sieves [4]. Zeolites and $AlPO_4$ are widely used microporous materials possessing a specific surface area (SSA) of up to 600 $m^2g^{-1}$ and pore volume ($V_p$) of up to 0.4 $cm^3g^{-1}$ [5]. Amorphous silica (a-$SiO_2$) has a number of advantages such as fast and facile synthesis, high thermal and chemical stability [6], low toxicity [7], which makes it promising as an alternative for creating microporous materials. The main way to synthesize silica particles (SP) is the Stöber method [8], which is based on a hydrolysis of tetraethyl orthosilicate (TEOS) in an $NH_3$-$H_2O$-$C_2H_5OH$ medium and allows obtaining highly monodisperse (with standard size deviation less than 3%) spherical particles of a-$SiO_2$. However, the thus obtained particles are nonporous. There are two approaches to forming micropores within the silica particles: post-synthetic treatment of nonporous SPs or modification of the Stöber process by changing the composition of the reaction mixture. Micropores within the particles obtained are frequently isolated from each other, which makes it difficult to obtain large values of SSA and $V_p$. Molecules of adsorbate (e.g., $N_2$) cannot penetrate inside the pores and they are not included into the useful volume of the particles. Thus, the development of a method for obtaining microporous SP with interconnected pore structure is an urgent technological problem. In the present study, an approach is implemented to synthesizing monodisperse spherical microporous SP by Stöber process with the use of ammonium metavanadate as a porogen.

## Results and Discussion

The silica particles were synthesized by hydrolysis of TEOS in a concentrated solution of ammonium metavanadate in a $H_2O$-$C_2H_5OH$-$NH_3$ mixture traditionally used in Stöber process [8]. To obtain a solution of $NH_4VO_3$ a weighed portion of commercially available $V_2O_5$ powder was dissolved in a $H_2O$-$C_2H_5OH$-$NH_3$ mixture heated to 60°C under ultrasonic agitation, which leaded to the formation of saturated aqueous-alcoholic solution of ammonium metavanadate. After that TEOS was added to the obtained solution, as a result of hydrolysis of which spherical particles of amorphous silica were formed.

Fig. 1 shows $N_2$ adsorption-desorption isotherm for the particles obtained. It can be seen that the isotherm has a shape characteristic of microporous materials. The SSA of the particles calculated by BET was found to be 320 $m^2$ $g^{-1}$. The pore volume was 0.25 $cm^3$ $g^{-1}$. The NLDFT pore size distribution (Fig. 1, inset) demonstrates a well pronounced peak with a maximum at ~1 nm. Apparently, $NH_4VO_3$ present in the solution acts as a template for the formation of micropores. Silica produced as a result of TEOS hydrolysis adsorbs ions from a saturated $NH_4VO_3$ solution with the formation of associates of hydrated amorphous $SiO_2$ with $VO_3^-$ and $NH_4^+$. Due to the high concentration of $NH_4VO_3$ in the reaction mixture the silica contains, apparently, not individual ions but associated complexes of several ions. After the synthesis the obtained particles are washed with water, as a result of which the dissolution of the complexes occurs with the

formation of voids in their place – micropores. Moreover, the obtained SSA and $V_p$ values allow to conclude that the particles contain not isolated micropores, but their interconnected system.

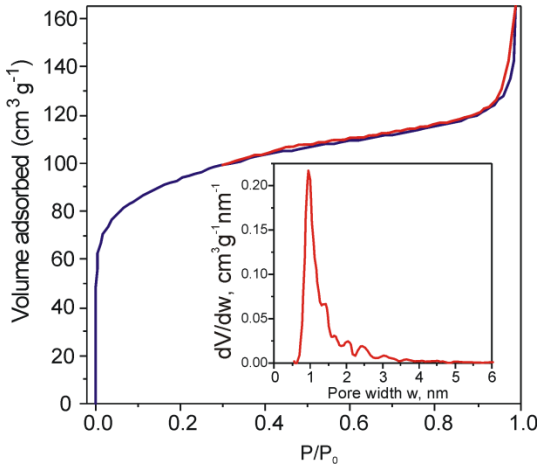


Fig.1 $N_2$ adsorption-desorption isotherm (77 K) of the particles. Inset: NLDFT pore size distribution.

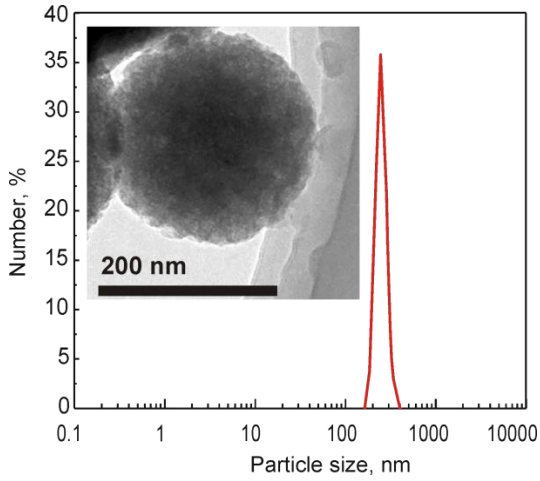


Fig.2 DLS size distribution of the particles. Inset: TEM image of a particle

The synthesis conditions similar to those in the Stöber process (namely reaction mixture composition, temperature and time) allowed obtaining highly monodisperse spherical silica particles. According to DLS measurements (Fig. 2) an average diameter of the particles was found to be 265±10 nm. The typical TEM image (Fig. 2, inset) demonstrates that the particles have spherical shape and clearly seen pores. Note, that the value of the particle diameter measured from TEM data correlates with that obtained from the DLS measurements.

## Conclusion

An approach for the synthesis of $SiO_2$ particles by Stöber method with the use of ammonium metavanadate as hard template made it possible to obtain highly monodisperse spherical silica particles possessing microporous structure. Micropores within the particles form an interconnected system resulting in high values of SSA (~320 m$^2$ g$^{-1}$) and Vp (~0.25 cm$^3$ g$^{-1}$) of the particles. The obtained particles may find use, for example, in adsorption or catalytic applications.

## REFERENCES


1. **Doustkhah E., Ide Y.,** Microporous layered silicates: old but new microporous materials, New Journal of Chemistry. 44 (2020) 9957–9968.

2. **Uguina M.A., Serrano D.P., Van Grieken R., Vènes S.**, Adsorption, acid and catalytic changes induced in ZSM-5 by coking with different hydrocarbons, Applied Catalysis A: General. 99 (1993) 97–113.

3. **Khan W., Jia X., Wu Z., Choi J., Yip A.C.K.**, Incorporating Hierarchy into Conventional Zeolites for Catalytic Biomass Conversions: A Review, Catalysts. 9 (2019) 127.

4. **Marcilly C.R**., Where and how shape selectivity of molecular sieves operates in refining and petrochemistry catalytic processes, Topics in Catalysis. 13 (2000) 357–366.

5. **Shüth F., Sing K.S.W., Weitkamp J.**, Handbook of Porous Solids, Wiley, Weinheim, 2002.

6. **Schwanke A.J., Balzer R., Pergher S.**, Handbook of Ecomaterials, Springer, Cham, 2017.

7. **Dong X., Wu Z., Li X., Xiao L., Yang M., Li Y., Duan J., Sun Z.**, The Size-dependent Cytotoxicity of Amorphous Silica Nanoparticles: A Systematic Review of in vitro Studies, International Journal of Nanomedicine. 15 (2020) 9089–9113.

8. **Stöber W., Fink A., Bohn E**., Controlled growth of monodisperse silica spheres in the micron size range, Journal of Colloid and Interface Science. 26 (1968) 62–69.

# Study of morphology and composition of nanoscale GaN and AlGaN heterostructures obtained by PA MBE technique on the silicon substrates with the use of porous silicon as buffer layer

**D.S. Zolotukhin[1], A.S. Lenshin[1], P.V. Seredin[1] and A.M. Mizerov[2]**

[1] Voronezh State University, Voronezh, Russian Federation;
[2] SPbAU RAS, Academician University, Saint-Petersburg, Russia Federation;
✉ zolotukhinspb@gmail.com

**Abstract.** In this work, we study the optical and structural properties of AlGaN epilayers grown by plasma-assisted molecular beam epitaxy on the AlN buffer layer which was performed on regular Si substrate and compliant Si substrate with a preformed porous silicon layer. The AlGaN layers formed on the por-Si buffer revealed a 10% higher intensity of photoluminescence spectra corresponding to the better crystalline quality in comparison with ones formed on regular Si substrate.

**Keywords:** AlGaN, epitaxy, buffer layer, porous silicon

**Funding:** The study was carried out with the financial support of the Russian Foundation for Basic Research within the framework of scientific project No. 19-72-10007.

## Introduction

Heterostructures on the basis of (Al, Ga)N system attract great interest since they are currently used as for the fabrication of radiation-hardened high temperature high mobility transistors (HEMT), as for the application of optoelectronic devices operating in UV range. Combination of AIIIN materials with silicon devices or signal processing opens new ways for appearance of the new functional units that could merge high-quality optoelectronic characteristics of AIIIN and the developed more profit-proved technologies on the basis of Si substrates.

However, the formation of III-N/Si heterostructures is yet impeded due to the differences in the thermal expansion coefficient and latticed parameters which results in the generation of the high density of threading dislocations and some other defects thus impairing the instrument characteristics of the terminal devices. One of the perspective technological processes providing possibility of obtaining high functional properties in the fabricated hybrid heterostructures can be based on the usage of the compliant structured silicon substrate composed of porous silicon

## Materials and Methods

The layers of porous silicon (~100 nm) were obtained by electrochemical etching of single-crystalline silicon wafers of KDB type with (111) orientation in fluorine acid solution, similar to that one described in [1,2]. GaN and AlGaN epitaxial layers on the substrates of two types were grown in a common growth process by molecular beam epitaxy with the addition of plasma-activated nitrogen (PA MBE) in the Veeco Gen 200 facility. Surface morphology was studied with the use of atomic force microscopy (AFM) and scanning electron microscopy (SEM).

## Results and Discussion

Applying the X-ray diffractometry technique, photoelectron, and photoluminescence spectroscopy it was shown that thin AlGaN/AlN heterostructures formed on the hybrid substrate were characterized by the minimum residual stresses and up to 10% more intensive photoluminescence in comparison with ones formed on regular Si substrate.

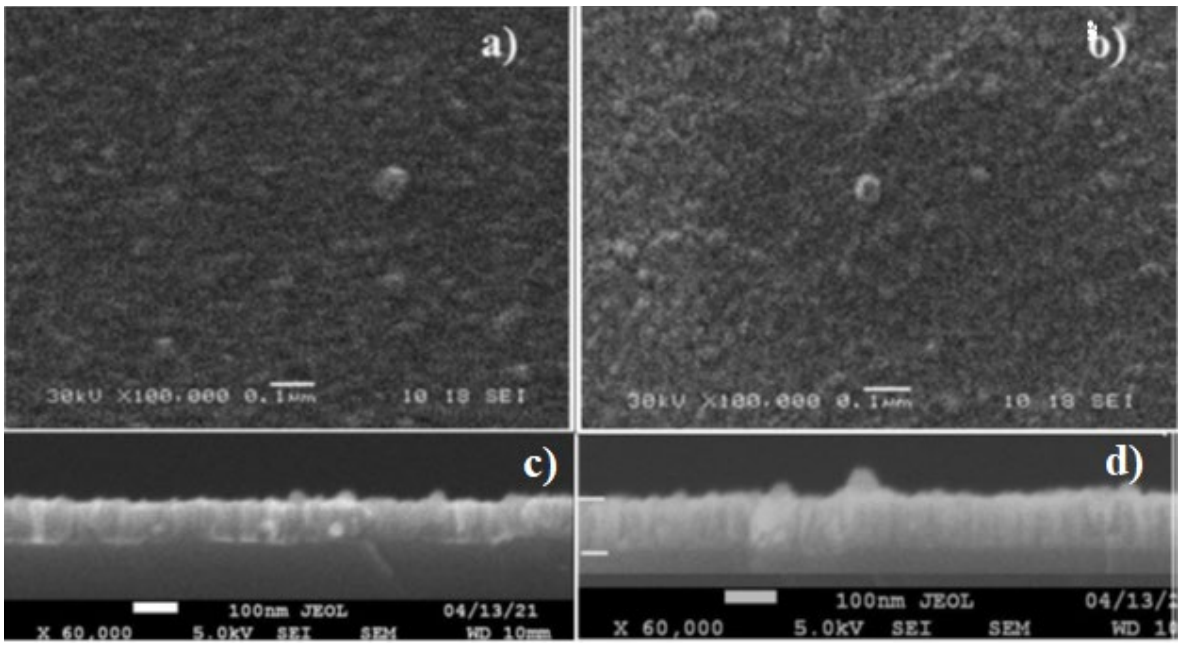


Fig. 1. The SEM images of the $Al_xGa_{1-x}N/AlN/Si$ and $Al_xGa_{1-x}N/AlN/$*por-Si*/Si heterostructures surfaces (**a**,**b**) and cross-sections (**c**,**d**) respectively.

**Acknowledgments**

The research results were partially obtained with the scientific equipment of the Collective Use Center of Voronezh State University.

**REFERENCES**

1. **Seredin P .V., Lenshin A.S., et al**. Ultrathin nano-sized Al2O3 strips on the surface of por-Si//Mat. Sci. in Sem. Proc. (39) (2015) 551-558.
2. **Seredin P.V., Goloshchapov D.L., Lenshin A.S. et al.** Influence of por-Si sublayer on the features of heteroepitaxial growth and physical properties of InxGa1-xN/Si(111) heterostructures with nanocolumn morphology of thin film // Physica E (104) (2018) 101-110.

# Study of the temperature dependence of the conductivity of ZnO/Au nanorod arrays exposed to ultraviolet irradiation

**A. P. Ivanisheva** [1✉], **V. V. Petrov** [1]

[1] Institute of Nanotechnologies, Electronics, and Equipment Engineering, Southern Federal University, Taganrog, Russia;

✉a.starnikova@mail.ru

**Abstract.** Arrays of ZnO nanorods of vertical orientation were synthesized by the hydrothermal method on quartz substrates. The nanorods had a length of 500–800 nm and an average cross section of 40–80 nm. Gold nanoclusters with average sizes of 9 ± 1 nm and 4 ± 0.5 nm were formed over the ZnO nanorods by vacuum thermal evaporation. To fabricate resistive sensor elements, the films were provided with V/Ni contact metallization over nanorods. The study of the electrophysical characteristics of arrays of ZnO/Au nanorods showed that the simultaneous action of temperature and UV-irradiation leads to the temperature independence of the conductivity of the sensor structure.

**Keywords:** ZnO, nanorods, electrophysical properties, ultraviolet irradiation.

**Funding:** This study was supported by the Russian Science Foundation under grant No. 23-29-00742, [https://rscf.ru/en/project/23-29-00742/] at the Southern Federal University.

## Introduction

It is known that unmodified ZnO films and nanostructures (nanofibers, nanorods, nanosheets, etc.) show high sensitivity to $NO_2$ and other gases (no worse than 1 ppm) at operating temperatures of 200 ºC and higher. Modification of ZnO nanofilms and nanostructures with gold (Au) clusters can lead to a significant increase in sensitivity and selectivity, but the operating temperature decreases insignificantly. During photoactivation of unmodified ZnO films and nanostructures by UV-irradiation, the sensitivity limit of the sensors becomes 1-10 ppm already at room temperature or close to it [1]. However, studies of the electrophysical characteristics of ZnO/Au nanorod arrays under the simultaneous effect of temperature and UV-irradiation have not been conducted so far. These studies are the purpose of this work.

## Materials and Methods

Arrays of ZnO nanorods of vertical orientation were synthesized by the hydrothermal method on quartz substrates. The nanorods had a length of 500–800 nm and an average cross section of 40–80 nm. On top of ZnO nanorods, gold nanoclusters with average sizes of 9 ± 1 nm (ZnO/Au(1) sample) and 4 ± 0.5 nm (ZnO/Au(2) sample) were formed by vacuum thermal evaporation. For the final formation and stabilization of the electrophysical characteristics of the ZnO/Au nanostructures, annealing was performed at a temperature of 300°C for 2 hours. Further, to fabricate sensor elements, V/Ni contact metallization with a metal layer thickness of 0.2 μm was formed over the nanorods by thermal vacuum evaporation.

## Results and Discussion

Studies of electrophysical properties of the obtained samples were carried out on a hardware-software measuring complex, which allows to carry out measurements of electrophysical characteristics of sensor structures, including under the influence of UV-irradiation [2]. Earlier we investigated the dependences of resistance (R) of the obtained samples on the working temperature (T) [3]. Temperature dependences of the logarithm of conductivity of samples of ZnO/Au nanorod arrays are approximated by a linear function Research has shown a significant dependence of the resistance of the sensor structure on the heating temperature. The activation energy of conduction (Ea) was calculated based on the Arrhenius equation (1).

$$G = G_0 \cdot exp^{-Ea/k \cdot T}, \quad (1)$$

where $k$ is the Boltzmann constant, $G_0$ is the coefficient that considers the conductivity of the material.

It was calculated that Ea is 0.23 and 0.28 eV for the ZnO/Au(1) and ZnO/Au(2) samples, respectively, in the temperature range of 35-300°C.

In the present work, additional studies were carried out, in which the sample was heated and simultaneously irradiated with UV-irradiation from a LED with a wavelength of 400 nm with an emission intensity of 133 μW/cm$^2$. Figure 1 shows the dependence of the conductivity (G) of the samples under study on the operating temperature with simultaneous exposure to UV-irradiation.

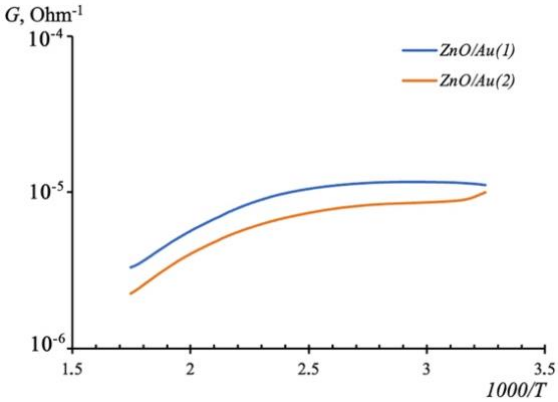


Fig. 1. Dependence of the conductivity of ZnO/Au(1) (blue line) and ZnO/Au(2) (orange line) samples on the operating temperature (T) under simultaneous exposure to UV-irradiation

Studies have shown that the conductivity of arrays of ZnO/Au nanorod samples in the temperature range of 35–200°C under simultaneous exposure to temperature and UV-irradiation is practically independent of temperature. This effect is a consequence of the fact that the generation of charge carriers in arrays of ZnO/Au nanorods under the action of UV-irradiation is much higher than the temperature generation of charge carriers. At temperatures above 200°C, the resistance begins to increase, which may be due to the processes of thermal recombination of charge carriers.

## Conclusion

These studies show that the simultaneous effect of temperature and UV-irradiation leads to an insignificant temperature dependence of the conductivity of sensor structures based on arrays of ZnO/Au nanorods. This property is positive for the manufacture of industrial gas sensors, since with simultaneous exposure to temperature and UV-irradiation, special devices for stabilizing their temperature are not required.


## Acknowledgments

Electrophysics measurements were conducted using equipment from the Centre for Collective Use, Microsystem Technics and Integral Sensors, Southern Federal University (SFedU).


## REFERENCES


1. **Chizhov A.S., Rumyantseva M.N., Gaskov A.M.** Light Activation of Nanocrystalline Metal Oxides for Gas Sensing: Principles, Achievements, Challenges. Nanomaterials 11 (4) (2021) 892.

2. **Gulyaeva I.A., Ivanisheva A.P., Volkova M.G., Storozhenko, V.Yu., Khubezhov S.A., Bayan E.M., Petrov V.V.**, Investigation of electrophysical, photo- and gas-sensitive properties of ZnO–$SnO_2$ sol–gel films J. Adv. Dielect. 13 (2023) 2245002.

3**. Ivanisheva A.P., Sysoev V.V., Abdullin Kh.A., Nesterenko A.V., Khubezhov S.A., Petrov V.V.**, The Application of Combined Visible and Ultraviolet Irradiation to Improve the Functional Characteristics of Gas Sensors Based on ZnO/$SnO_2$ and ZnO/Au Nanorods. Chemosensors 11(3) (2023) 200.

# FORMATION OF GE-BASED NANOSTRUCRUTRES ON WURTZITE A3B5 NANOWIRES

**I. Ilkiv[1,2] ✉, K.P. Kotlyar[1], D.A. Kirilenko[3], A.V. Osipov[4], G. Cirlin[1,2,5]**

[1] St. Petersburg State University, St. Petersburg, Russia

[2] Alferov University, St. Petersburg, Russia

[3] Ioffe Institute, St Petersburg, Russia

[4] 4Institute of Problems of Mechanical Engineering, St. Petersburg, Russia

[5] Institute for Analytical Instrumentation of the RAS, St. Petersburg, Russia

✉fiskerr@ymail.com

**Abstract.** Experimental results of studying the germanium deposition on the surface of wurtzite $Al_xGa_{1-x}As$, GaN and InAs nanowires are presented. The formation of germanium based nanostructures, such as radial conformal shell, stripes having one-dimension structure, as well as quantum dots on the lateral nanowire surfaces is discussed. The inheritance of the crystal structure during the growth of germanium on the lattices-matched surfaces is shown.

**Keywords:** nanowires, semiconductors, molecular-beam epitaxy, wurtzite germanium.

**Funding:** The samples were grown under the support of grant 0791-2023-0004. Structural studies were done under financial support of St. Petersburg State University grant no. 94031047.

## Introduction

Ge is one of the most successful materials for fabrication of near-infrared detectors, but the use of Ge in active photonic devices remains challenging due to its indirect bandgap. Various strategies have been proposed to facilitate the emissivity of Ge thin films, including tensile straining, alloying with Sn, P diffusion doping, and defect engendering. Much attention has also been paid to fabrication of Ge nanostructures, such as nano-dots and wires, exhibiting size-dependent effects. It is well established that group IV semiconductors may form in the metastable hexagonal-diamond phase. Conversely to the stable cubic phase, hexagonal Ge has been predicted to have a direct bandgap structure. As a result, efficient light emission from hexagonal Ge and SiGe alloys has recently been achieved[1].

In this work we looked into the feasibility of using $Al_xGa_{1-x}As$, GaN and InAs nanowires (NWs) as a substrates for the growth of Ge based nanostructures.

## Materials and Methods

The nanostructures were synthesized using a Riber Compact 21 EB200 MBE setup equipped with effusion sources for growing III–V semiconductors and with e-beam source for the evaporation of germanium. Thus, this equipment allowed us to form heterostructured A3B5-Ge NWs in a single technological cycle. At first, we synthesized arrays of NWs on Si(111) substrates. Then we lowered the substrate temperature to 300°C and conducted the deposition of germanium with a rate of ~0.2 Å s–1 for 20 min. After the completion of growth, the samples with NW arrays were cooled to room temperature and unloaded to study the morphological properties by scanning electron microscopy. The structural properties were studied by Raman spectroscopy and transmission electron microscopy.

## Results and Discussion

We have demonstrated hexagonal Ge stripes grown by MBE on the side facets of wurtzite AlGaAs NWs. The effect is attributed to the non-wetting growth mode in this material combination, conversely to the case of conformal Si, Ge and SiGe shells on GaP and GaAs NW sidewalls. This conclusion is supported by the fact that Ge forms continuum shells if grown under the same conditions on the side facets of pure GaAs NWs. DFT calculations of the volumetric energies suggest Ge-16R or Ge-6H hexagonal polytype. In any case, hexagonal crystal phase of Ge stripes is attested by HR TEM and the additional Raman peak at 200 $cm^{-1}$.

It its turn, we demonstrated the growth of 3D epitaxial Ge nanoislands around GaN nanowires. Cross-sectional TEM verified the surface faceting of the GaN core nanowires as well

as the Ge quantum dots. Raman spectroscopy revealed the asymmetric line shape of Ge QDs, which could be caused by the inhomogeneous sizes of the QDs as well as the phonon confinement. The Raman results also indicate strain relaxation in uncapped Ge QDs, as well as strain shifting in Ge QDs additionally capped with GaN.

## Conclusion

In summary, non-uniform growth of germanium on wurtzite A3B5 NW side facets was demonstrated. Non-uniform growth can be used for the fine tuning of morphology, crystal structure, electronic and optical properties of Ge and NW-Ge heterointerfaces.

## References

[1] **Fadaly E. M., Dijkstra A., Suckert J. R., Ziss D., van Tilburg M. A., Mao C., Ren Y., Lange V. T., Korzun K., Kölling S., Verheijen M., Busse D., Rödl C., Furthmüller J., Bechstedt, F., Stangl J., Finley J. J., Botti S., Haverkort J., Bakkers E. P. A. M.**, Direct-bandgap emission from hexagonal Ge and SiGe alloys, Nature580(7802) (2020) 205-209.

## Acknowledgments

The samples were grown under the support of grant 0791-2023-0004. Structural studies were done under financial support of St. Petersburg State University grant no. 94031047.

# Deep-level emission tailoring in ZnO nanostructures grown via hydrothermal synthesis

**S. A. Kadinskaya[1,2]✉, V. M. Kondratev[1,2], A. Kusnetsov[1,2], A. I. Lihachev[3], A. V. Nashchekin[3], I. Kh. Akopyan[4], A. Yu. Serov[4], M. E. Labzovskaya[4], S. V. Mikushev[4], B. V. Novikov[4], I. V. Shtrom[4,5], A. D. Bolshakov[1,2]**

[1] Alferov University, St. Petersburg, Russia

[2] Moscow Institute of Physics and Technology, Dolgoprudny, Russia

[3] Ioffe Institute, St. Petersburg, Russia

[4] Saint Petersburg State University, St. Petersburg, Russia

[5] IAI RAS, St. Petersburg, Russia

✉kadinskaja@spbau.ru

**Abstract.** Development of the new approaches for synthesis of luminescent semiconductor nanomaterials is of high demand. In this work, nano- and microstructures of zinc oxide were synthesized by the hydrothermal method to provide new insight onto the optimization of this material optical properties. The possibility of controlling the synthesized ZnO geometry and morphology using various surfactants during the synthesis was demonstrated. Further study of the structures obtained by PL spectroscopy made it possible to observe a correlation between the hydrothermal growth conditions and the obtained ZnO nanostructures optical properties. This property, together with the ability to control the structures geometry, opens up new possibilities for their application in nanophotonics, UV-VIS and white light sources.

**Keywords:** zinc oxide, hydrothermal, nanowire, photoluminescence, deep level emission, PEI, sodium citrate

**Funding:** Ministry of Science and Higher Education of the Russian Federation: Grants FSMG-2021-0005, FSRM-2023-0009.

## Introduction

Zinc oxide (ZnO) is one of the promising materials for development of UV emitters due to the band gap (3.37 eV at room temperature) and high exciton binding energy (60 meV) [1]. In addition, ZnO is inexpensive, relatively abundant, chemically stable, easily synthesized, and non-toxic. Although a wide variety of ZnO-based light-emitting devices (LEDs) have been developed so far, their performance, light-emitting ability, and production technology are still below expectations.

## Materials and Methods

Hydrothermal synthesis [2] is a common method for obtaining ZnO nanocrystals, characterized by low cost and high scalability, as well as wide possibilities for controlling the morphology of the resulting nanostructures through the use of surfactants. In the course of this work, 3 samples were synthesized on Si (111) substrates using $Zn(NO_3)_2$ and HMTA: without the use of surfactants, using sodium citrate, and using polyethyleneimine. As a result, nanostructures of the following morphologies were obtained (figure 1): rods with a length to thickness ratio of approximately 10:1, hexagonal ZnO microcrystals, and ZnO nanowires (NWs).

## Results and Discussion

During the work, PL spectra were obtained for all samples (figure 2). PL spectroscopy study demonstrates strong NBE emission in the UV region in all of the synthesized samples associated with an exciton on a neutral donor ($D_0X$). The obtained spectra demonstrate the different response in the visible range governed by the deep levels. The sample synthesized without the surfactants has an efficient response in the visible, centered near 620 nm. This band is often associated with excess zinc including Zn interstitial ($Zn_{in}$) and lack of oxygen such as vacancies ($V_O$) [3,4]. Use of sodium citrate leads to the DLE in the green region centered near 500 nm. This behavior is associated with the excess oxygen and zinc vacancies [3,4]. Use of PEI makes it possible to suppress the DLE. These effects are associated with a variation in the balance between zinc and

oxygen ions in the growth solution provided by the change in the chemical composition of the growth medium.

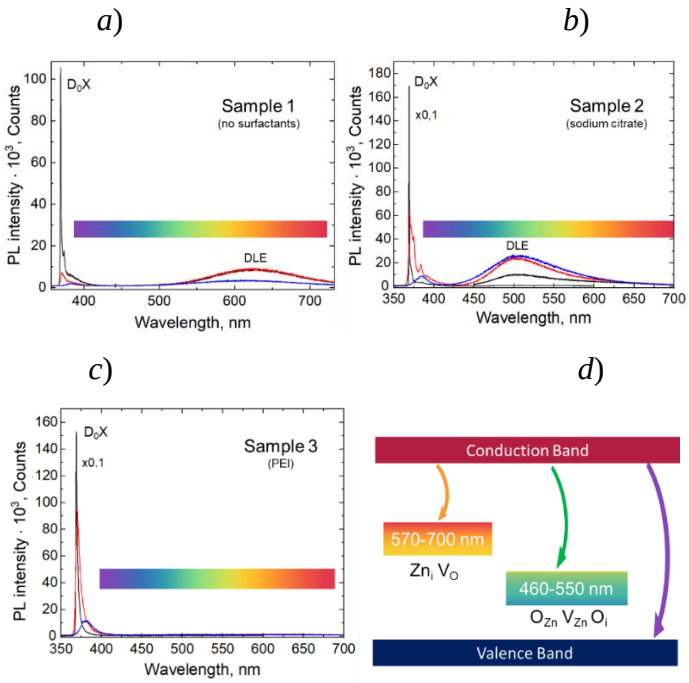


Fig. 2. PL spectra taken in a wide spectral range at different temperatures: a) Sample 1 (without surfactant), b) Sample 2 (with sodium citrate), NBE region of the spectrum is multiplied by 0.1, c) Sample 3 (with PEI) NBE region of the spectrum multiplied by 0.1, d) Schematic representation of the deep levels and corresponding radiative transitions.

## Conclusion

The obtained results demonstrate the prospects for use of the technologically feasible hydrothermal method to develop light-emitting structures based on zinc oxide. The spectral characteristics of such structures can be tailored in a wide range by changing the growth medium composition opening the way for fabrication of UV-VIS and white light sources for biology, disinfection and lighting.

## Acknowledgments

A.D.B. and A.K. acknowledge financial support of the microscopic studies by the Ministry of Science and Higher Education of the Russian Federation (Grant FSMG-2021-0005). S.A.K. and V.M.K acknowledge financial support of the synthesis from the Ministry of Science and Higher Education of the Russian Federation (FSRM-2023-0009).

## REFERENCES

1. **Özgür Ü., Alivov Ya. I., Liu C., Teke A., Reshchikov M. A., Doğan S., Avrutin V., Cho S-J and Morkoç H.**, A comprehensive review of ZnO materials and devices, Journal of Applied Physics 98 (2005) 041301.

2. **Gerbreders V., Krasovska M., Sledevskis E., Gerbreders A., Mihailova I., Tamanisa E., Ogurcovs A.,** Hydrothermal synthesis of ZnO nanostructures with controllable morphology change, CrystEngComm 22 (2020) 1346-58

3. **Galdámez-Martinez, A., Santana, G., Güell, F., Martínez-Alanis, P.R., Dutt, A.**, Photoluminescence of ZnO Nanowires: A Review. Nanomaterials 2020, 10, 857, doi:10.3390/nano10050857.

4. **Lima, S.A., Sigoli, F., Jafelicci Jr, M., Davolos, M.**, Luminescent Properties and Lattice Defects Correlation on Zinc Ox-ide. Int. J. Inorg. Mater. 3 (2001) 749–754.

# Investigation of the optical properties of carbon films in the sp2, sp3- hybridized state during thermal annealing

**V. A. Kazakov[1✉], A. V. Kokshina[1], A. G. Razina[1], O. V. Vasilyeva[1], S. I. Ksenofontov[2], A. N. Lepaev[3]**

[1]Chuvash State University named after I.N. Ulyanov, Cheboksary, Russia;
[2]Chuvash State Pedagogical University named after I.Y. Yakovlev, Cheboksary, Russia;
[3]Cheboksary Institute (branch) of the Moscow Polytechnic University, Cheboksary, Russia
✉cossac@mail.ru

**Abstract.** The optical properties of carbon films in the sp2 (amorphous carbon) and sp3 (diamond-like carbon)- hybridized state synthesized by the ion-plasma method with subsequent heat treatment at various temperatures in air using spectrophotometry and raman scattering methods were investigated.

**Keywords:** amorphous carbon, diamond-like carbon, sp2-hybridization, sp3-hybridization, thermal annealing

## Introduction

Thin carbon films are of interest as functional layers for third-generation organic and hybrid photoelectric converters, transparent conductive electrodes in electronics, and protective and antireflection layers in optics [1–4]. Due to differences in chemical bonds in the sp (linear-chain carbon, carbine), sp2 (amorphous carbon), sp3 (diamond-like carbon) - hybridized state, the thermal oxidation of films of different allotropic forms of carbon should occur differently. Annealing is significantly affected by impurities in carbon films, in particular, when they are doped with metal atoms during synthesis.

## Materials and Methods

DLC films were deposited on a modernized vacuum ion-plasma setup URM.3.279.070 Almaz at a vacuum of ~$10^{-1}$ Pa according to the procedure described in [4]. Amorphous carbon films were deposited on a UVR-3M setup in Ar+ glow discharge plasma at a voltage of 2 kV.

Methods of Raman spectroscopy and thermogravimetry are used to analyze the phase composition and the presence of impurities in carbon materials. However, thermogravimetry requires a significant mass of samples, and Raman spectroscopy in the visible range shows the presence of only the sp2 phase [5] (its share in the DLC is up to 30-50%), analysis of the sp3 phase requires UV-Raman spectroscopy.

## Results and Discussion

The optical transmission spectra of carbon films on a glass substrate before and after annealing at a temperature of 400 $^0$C are shown in fig. 1. The transmission spectra of sp2, sp3-hybridized carbon materials before annealing have the same character, for example, as films of amorphous and diamond-like carbon before annealing, where the transmission coefficient characterizes the thickness, presence, and imperfection of the sp2 phase.

The enlightenment effect of carbon films associated with the oxidation and delocalization of free π-electrons of the sp2 phase responsible for light absorption appears after heating up to 400 $^0$C. Moreover, after annealing, spectra 1 and 2 have significant differences in the region of 350-700 nm, which allows not only to determine the temperature of thermal decomposition of samples, but also to analyze the sp3 phase content in diamond-like carbon samples by optical methods.

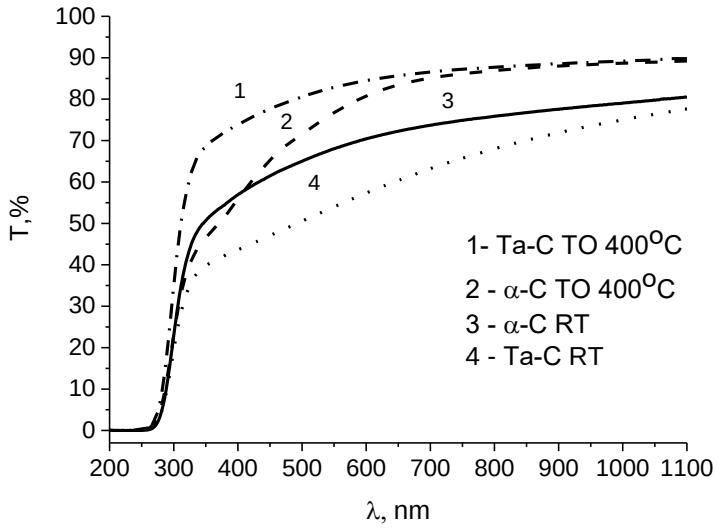


Fig. 1. Optical transmission spectra of a film of amorphous carbon (α-C) and diamond-like carbon (DLC) on a glass substrate during heat treatment (HT) 400 $^{0}$C and room temperature (RT).

## Conclusion

Thus, it is shown that Raman spectroscopy in the visible excitation region does not allow to fully identify different phases (sp2-sp3) of carbon. Spectrophotometry is not used to analyze the sp3 phase content in DLC, which is due to the similarity of transmission spectra in the optical range. However, annealing in air up to 400 $^{0}$C leads to a significant difference in the transmission spectra. The obtained results can be used to determine the temperature of the beginning of thermal oxidation of carbon samples and to determine the phase composition (mass content of the sp3 phase in diamond–like carbon films).

## REFERENCES

1. **Коншина Е. А.** Amorfnyj gidrogenizirovannyj uglerod i primenenie ego v opticheskih ustrojstvah, Saint Petersburg, ITMO Research Institute, 2010.

2. **Robertson J.** Diamond-like amorphous carbon: Mater. Sci. Eng. R Reports. 37 (2002) 129–281.

3. **Panosyan Z. R., Khachatrian A. Z., Hayrapetyan D. B., Voskanyan S. S., Yengibaryan Y. V.** Three-layer antireflection diamond-like carbon films on glass: J. Contemp. Phys. 50 (2015) 72–8.

4. **Flood P., Babaev V., Khvostov V., Novikov N., Guseva M.** Carbon Material with a Highly Ordered Linear-Chain Structure: Material with a Highly Ordered Linear-Chain Structure. Polyynes. Synthesis, Properties, and Applications ed E by F Cataldo (FL: CRC, Boca Raton, FL) (2005) 219–52.

5. **Vysotina E. A., Kazakov V. A., Polyansky M. N., Savushkina S. V., Sivtsov K. I., Sigalaev S. K., Lyakhovetsky M. A., Mironova S. A., Zilova O. S.** Investigation of the Structure and Functional Properties of Diamond-Like Coatings Obtained by Physical Vapor Deposition: J. Surf. Investig. 11 (2017) 1177–84.

# Creation of a GaMnAs ferromagnetic semiconductor by a combined laser method

**I. L. Kalentyeva [1]✉, O. V. Vikhrova[1], Yu. A. Danilov[1], D. A. Zdoroveyshchev[1], A. V. Kudrin[1], V. P. Lesnikov[1], A. E. Parafin[2]**

[1] Research Institute for Physics and Technology of UNN, Nizhny Novgorod, Russia;
[2] O Institute for Physics of Microstructures, RAS, Nizhny Novgorod, Russia
✉ kalenteva@nifti.unn.ru

**Abstract.** GaMnAs layers fabricated by pulsed laser deposition in vacuum followed by annealing with KrF excimer laser pulses have been studied. As a result of annealing, there is a significant increase in the hole conductivity of the layers and a significant change in the form of the magnetic field dependence of the magnetization at room temperature. The study of galvanomagnetic properties shows the existence of ferromagnetism in GaMnAs layers with a Curie temperature reaching 90 K. The observed effects allow us to conclude that the applied pulsed laser action leads to the dissolution of MnAs inclusions, electrical activation of Mn, and, as a result, to the formation of a single-phase ferromagnetic GaMnAs semiconductor.

**Keywords:** ferromagnetic semiconductor, GaMnAs layers, Curie temperature, pulsed laser deposition

**Funding:** This work was supported by the Russian Science Foundation (project no. 23-29-00312).

## Introduction

The Ferromagnetic semiconductors have great prospects, since they make it possible, in particular, to implement the control of magnetic properties by an electric field, to create spin field-effect transistors of a vertical design, resonant tunnel diodes, and devices with magnetization switching due to spin-orbit interaction (spin-orbit torque) [1]. This paper presents the results of studying the features of a GaMnAs ferromagnetic semiconductor fabricated by a new method that uses a combination of low-temperature pulsed laser deposition in vacuum (PLD-V) and pulsed laser annealing (PLA).

## Materials and Methods

GaMnAs layers were deposited on *i*-GaAs (100) wafers by evaporation of solid targets (undoped GaAs and high-purity Mn) with a focused YAG:Nd laser beam ($\lambda$ = 532 nm). The process temperature ($T_g$) varied from 200 to 350°C. The manganese content was 0.17, and the layer thickness reached ~50 nm. Then the samples were subjected to pulsed laser annealing using an LPX-200 excimer laser (working mixture KrF, wavelength 248 nm, pulse duration 30 ns, laser radiation energy density $P$ = 400 mJ/cm$^2$).

The magnetization of the structures was measured at room temperature using a magnetometer with a variable field gradient. Studies of galvanomagnetic properties were carried out using a Janis CCS-300S/202 closed-cycle helium cryostat at temperatures of 10–300 K in the range of magnetic fields ± 3600 Oe.

## Results and Discussion

All GaMnAs layers fabricated by the PLD-V method show high values of sheet resistance ($R_s$) at room temperature: the value of $R_s$ increases from ~ $10^7$ до ~ $10^9$ Ohm with an increase of $T_g$ from 200 to 350°C. After applying pulsed laser annealing, the conductivity of GaMnAs films increases significantly ($R_s$ ~ 880–2970 Ohm). The hole concentration $p$ calculated from measurements of the Hall effect reaches ~ $2.8\cdot10^{20}$ cm$^{-3}$, and the effective mobility $\mu_{eff}$ ~ 4–5 cm$^2$/V·s. This fact testifies to the activation processes that occur under the action of PLA, leading to the incorporation of manganese atoms into the sites of the gallium sublattice and, thereby, contributing to the appearance of hole conductivity. At lower temperatures of layer formation (200 and 250°C), the degree of electrical activation of the impurity is much higher.

The initial GaMnAs structures exhibited nonlinear (with a hysteresis loop) magnetic-field dependences of the magnetization $M(H)$ at room temperature, associated with the presence of a ferromagnetic semi-metallic compound MnAs in the inclusion layers [2]. After laser annealing, the dependences $M(H)$ become linear (fig.1a). The existence of ferromagnetism in GaMnAs layers with a Curie temperature reaching 90 K is shown (fig.1b). The spontaneous Hall resistance ($R^S_H$) is proportional to the spontaneous magnetization $M_S$ and characterizes the ferromagnetic ordering in the structures.

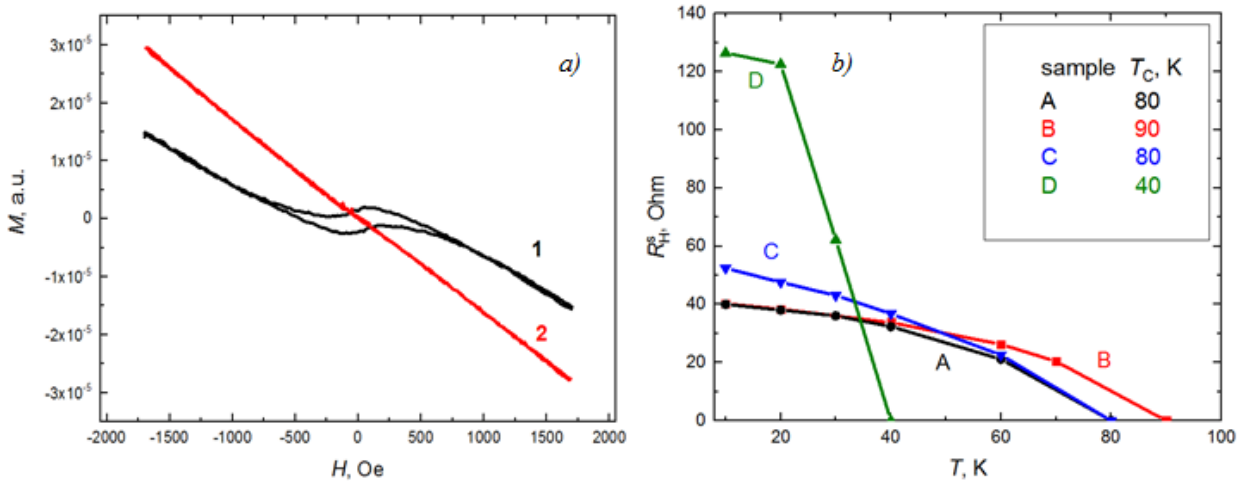


Fig. 1. *a*) Magnetic field dependences of the magnetization at a room temperature for the initial (curve 1) and annealed (curve 2) structure samples with a GaMnAs layer fabricated at 300°C. An external magnetic field was applied in the plane of the layer. *b*) Temperature dependences of the Hall spontaneous resistance determined using the Arrott procedure for samples with different $T_g$,°C: A – 200, B – 250, C – 300, D – 350.

## REFERENCES


1. **C. Song, B. Cui, Fangsen Li, Xiangjun Zhou, F. Pan**, Recent progress in voltage control of magnetism: Materials, mechanisms, and performance, Progress Mater. Sci. 87, (2017) 33-42.

2. I**.L. Kalentyeva, O.V. Vikhrova, Yu.A. Danilov, M.V. Dorokhin, B.N. Zvonkov, Yu.M. Kuznetsov, A.V, Kudrin, D.V. Khomitsky, A.E. Parafin, P.A. Yunin, D.V. Danilov,** Effect of pulsed laser annealing on the properties of (Ga,Mn)As layers, Journal of Magnetism and Magnetic Materials. 556 (2022) P.169360.

# Determination of graphene concentration in dispersions using integral methods

**T. S. Kalyakin** [1,2✉], **E. A. Danilov**[2]
[1] JSC Research Institute «Graphite», Moscow, Russian Federation;
[2] Mendeleev University of Chemical Technology of Russia, Moscow, Russian Federation.
✉t.s.kalyakin@gmail.com

**Abstract.** This article explores a method for determining the concentration of graphene suspension using the integral method based on the Beer-Lambert-Bouguer law for direct ultrasonic exfoliation method. The results showed nonlinear dependence of conductivity on concentration, indicating fundamental differences in the mechanism of exfoliation at different solid phase concentrations. Graphene suspensions in ethylene glycol also exhibited low transmittance in visible spectrum, which requires the use of other research methods for higher concentrations. Extinction coefficients were determined to calculate the concentration of graphene in the suspension, which allows for the calculation of light absorption in the solution at a certain concentration and path length of light. The obtained results can be useful for further use of graphene in optoelectronic devices.

**Keywords:** graphene, Beer-Lambert-Bouguer law, concentration, exfoliation.

## Introduction

Graphene is a unique material that attracts wide attention of scientists all over the world due to its properties, including high electrical conductivity, mechanical strength, as well as thermal and chemical stability [1,2]. It can be used in various fields of science and technology. One such area is optoelectronics, where graphene can be used as a transparent electrode or light-absorbing material. The most suitable method for obtaining graphene is liquid-phase exfoliation, as it goes through a single technological stage, preserves the integrity of the graphene layer structure, and allows the production of a convenient suspended graphene for further use [3,4]. However, it is important to know the concentration of the solid phase in these suspensions, as it can significantly affect the properties of the resulting material. Thus, we attempted to study a method for determining the concentration of graphene in ethylene glycol using an integral method based on the Beer-Lambert-Bouguer law (also known as the BLB method) [5].

## Materials and Methods

We used natural graphite (GE brand) and ethylene glycol (extra pure, ECOS-1 JSC) as starting materials. In order to remove mineral impurities and defects, graphite powder with an ash content of up to 10% by weight underwent thermal treatment in an industrial graphite furnace at 2800°C and heat treatment in freon-12 atmosphere at 2200°C (technology of VNIIEI JSC). After treatment, the content of mineral impurities did not exceed 0.01% by weight, and the maximum particle size was 200 μm.

The concentration of the dispersed phase varied in the range of 20 to 0.01 mg/ml. Graphene was obtained using liquid-phase exfoliation with an ultrasonic disperser Melfiz MEF-391 with a horn-type probe. The dispersions were processed for 7 hours.

Electrical conductivity was measured using the Seven Compact Conductivity meter S230 (Mettler Toledo, Switzerland) with an InLab 710 sensor.

Optical spectra were obtained using the Cary 60 UV-Vis spectrophotometer (Agilent Technologies) in a quartz cuvette with an optical path length of 1 cm.

## Results and Discussion

Based on the provided data (figure 1a), it can be concluded that there is a non-linear relationship between the electrical conductivity and concentration in graphene suspensions in EG. This suggests that the mechanism of graphene suspension preparation (exfoliation) and the appearance of electrical conductivity likely have fundamental differences at different

concentrations of the solid phase. Further research is required to analyze and understand these results in more detail.

According to the results of the study, graphene suspensions in ethylene glycol showed low transmittance for visible light in most of the investigated concentration range. Because of this, only low concentrations of graphene in the range up to 0.1 mg/mL were studied for the use of the integral method. Other research methods will be required for higher concentrations. Spectra for concentrations of 0.1, 0.05, 0.025, and 0.01 mg/mL are presented below, on which the calculation was performed (figure 1b).

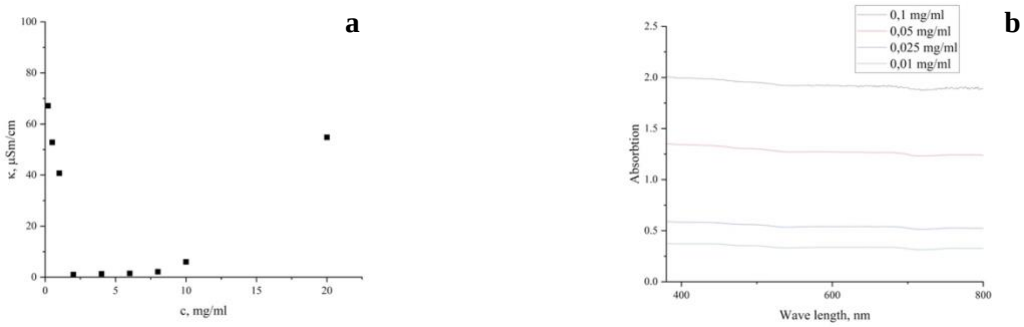


Fig. 1. Dependence of electrical conductivity on the concentration of solid phase after 7 hours of ultrasound treatment (a) and spectra of absorption for the investigated concentrations (b)

Applying the Beer-Lambert-Bouguer law, which is one of the fundamental laws of optics used to measure the concentration of solutions, it is possible to establish a relationship between light absorption and the concentration of the solution.

We have first evaluated extinction coefficients, which are a measure of a substance's ability to absorb light of a certain wavelength. The extinction coefficient allows the calculation of light absorption in the solution at a given concentration and path length of light.

$$A = \varepsilon l c, \quad (1)$$

where $A$ – absorbtion, $\varepsilon$ – extinction coefficient, $l$ – light path length (1 cm), $c$ – concentration

Collected data is shown in table 1.

Table 1

**Extinction coefficient calculation**

| Wave length, nm | Concentration, mol/l | Absorption | Extinction coefficient, $l \cdot mol^{-1} \cdot cm^{-1}$ |
|---|---|---|---|
| 850 | 0,000833 | 0,3250 | 241,66 |
| | 0,002083 | 0,5205 | |
| | 0,004167 | 1,2422 | |
| | 0,008333 | 1,8795 | |
| 750 | 0,000833 | 0,3260 | 244,04 |
| | 0,002083 | 0,5249 | |
| | 0,004167 | 1,2420 | |
| | 0,008333 | 1,9047 | |
| 650 | 0,000833 | 0,3389 | 246,44 |
| | 0,002083 | 0,5411 | |
| | 0,004167 | 1,2643 | |
| | 0,008333 | 1,9146 | |
| 550 | 0,000833 | 0,3329 | 247,32 |
| | 0,002083 | 0,5371 | |
| | 0,004167 | 1,2724 | |
| | 0,008333 | 1,9219 | |
| 450 | 0,000833 | 0,3680 | 256,39 |

| | | | |
|---|---|---|---|
| | 0,002083 | 0,5759 | |
| | 0,004167 | 1,3293 | |
| | 0,008333 | 1,9802 | |

In order to confirm the accuracy of the calculations, a separate sample was selected for which experimental measurements of light absorption at a known concentration of graphene were carried out (~ 0,025 mg/ml). The calculated and experimental values of light absorption closely matched (see table 2).

Table 2

**Calculation of the concentration of a separately prepared dispersion**

| Wave length, nm | Absorbtion | Extinction coefficient, $l \cdot mol^{-1} \cdot cm^{-1}$ | Concentration, mg/ml |
|---|---|---|---|
| 1050 | 0,25314 | 277,46 | 0,0258 |
| 950 | 0,28367 | 245,41 | 0,0268 |
| 850 | 0,29503 | 241,66 | 0,0263 |
| 750 | 0,29322 | 244,04 | 0,0262 |
| 650 | 0,28272 | 246,44 | 0,0267 |
| 550 | 0,28464 | 247,32 | 0,0265 |
| 450 | 0,25911 | 256,39 | 0,0275 |

Therefore, optical absorption technique indeed allows one to estimate the concentration of graphene suspensions in the technologically used range, results not being very dependent on the wavelength used.

## Conclusion

As a result of the conducted research, a nonlinear relationship between the electrical conductivity and the concentration of graphene suspension in ethylene glycol was established suggesting that establishing accurate concentration estimate for graphene suspension is a very important issue for developing conductive inks. An integral method for determining the concentration of graphene in the suspension was proposed based on the Beer-Lambert-Bouguer law, and corresponding calculations were performed. It was shown that low concentrations of graphene (up to 0.1 mg/ml) have sufficiently low transmittance in the visible region for the BLB analysis to be performed. Some convergence of results was observed for the calculated concentrations at different wavelengths, indicating that this method of determining the concentration of the suspension is acceptable and reasonably accurate. Therefore, simple and express optical absorption technique is applicable to retain graphene suspension concentration where gravimetric or other routine types of analysis lead to incorrect estimations.

## REFERENCES


1. **Geim A. K., Novoselov K. S.**, The rise of graphene, Nature Materials. 6(3) (2007) 183-191.
2. **Choi W., Lahiri I., Seelaboyina R., Kang Y.** Synthesis of Graphene and Its Application, Critical Reviews in Solid State and Materials Science. 35(1) (2010) 52-71.
3. **Xu Y., Cao H., Xue Y., Li B., Cai W.**, Liquid-phase exfoliation of graphene: an overview on exfoliation media, techniques, and challenges, Nanomaterials. 8(11) (2018) 942.
4. **Samoilov V. M., Danilov E. A., Nikolaeva A. V., Yerpuleva G. A., Trofimova N. N., Abramchuk S. S., Ponkratov K. V.** Formation of aqueous suspensions using fluorinated surfactant-assisted ultrasonication of pristine graphite, Carbon. 84 (2015) 28-46.
5. **Landsberg G. S.**, Optics, M.: PhysMathLit. (2006).

Conference materials
UDC 546.3-126:544.2
DOI: https://doi.org/10.18721/JPM.

# The features of formation of oxide porous structures based on $SiO_2$ – $SnO_2$

**K.B. Kim[1✉], S.I. Niftaliev[1], A.S. Lenshin[1,2]**
[1] Voronezh State University of Engineering Technologies, Voronezh, Russian Federation;
[2] Voronezh State University, Voronezh, Russian Federation;
✉kmkseniya@yandex.ru

**Abstract.** Porous silicon was obtained by electrochemical anodizing of single-crystalline silicon KEF (111). The films of tin-oxide were deposited over porous silicon using sol-gel method. Deposition of tin oxide on the porous silicon was shown to increase the charge accumulation in the presence of reducing gases. It means that sensors based on tin oxide and porous silicon results in the increase of their sensitivity to reducing gases.

**Funding:** The study was carried out with the financial support of the Russian Foundation for Basic Research within the framework of scientific project No. 22-73-00154.

## Introduction

At present porous silicon is actively applied in multi-sensor systems since it is characterized by a great specific surface providing its high sensitivity to gases. In order to increase stability of the system porous silicon was covered by the film of tin oxide. The choice of $SnO_2$ is specified by a great specific surface, wide band gap, low cost, high availability of chemical reactions the gases, high sensitivity and non-toxicity of the material . One of the most convenient ways to obtain composite materials with a high porosity is sol-gel technique.

## Materials and Methods

Substrates with porous silicon were obtained by electrochemical anodizing of single-crystalline silicon KEF (111). In order to prepare sols highly hydrolyzed compound was used – ethyl ether of orthosilisic acid (TEOS, $Si(OC_2H_5)_4$). Reaction of TEOS hydrolysis and polycondensation were conducted in the presence of tin chloride ($SnCl_2{\cdot}2H_2O$). The properties of obtained composite materials were evaluated by the following methods: atomic-force microscopy (AFM), scanning electron microscopy (SEM), X-ray energy-dispersion spectroscopy (EDX) and impedance spectroscopy.

## Results and Discussion

Analysis of the results obtained by AFM and SEM techniques shows that under metal-oxide deposition onto porous silicon its structure becomes more textured and formation of a great number of nanoscale granules (less than 100 nm) is observed along with the large pores. Thickness of the cross section is of about 9,7 μm, size of the large pores is of about 1 μm. EDX analysis also supports the presence of phases involving tin on the surface of the samples. When analyzing experimental results we used equivalent scheme approximation meaning that the obtained frequency dependences of Z' and Z" can be approximated by the known impedance components of the simulated electrical circuit. Analysis of the obtained hodograph curves makes it possible to conclude that the relaxation peak is shifted to the higher frequency region in the presence of reducing gases; the frequency in this case is increased by 2 times. When comparing the least values of characteristic time of the charge accumulation for the samples with tin dioxide ($SnO_2$) nanoparticles deposited on silicon and porous silicon it was found that these values were observed for the samples deposited on porous silicon.

## Conclusion

Sol-gel method can be successfully used for the formation of tin oxide films on porous silicon. Deposition of tin oxide films on porous silicon results in an increase of circular frequency for the maximum value of reactive component in the impedance. An increase of the charge accumulation in the presence of reducing gases is observed for oxide porous $SiO_2$ – $SnO_2$ structures. And it means that the sensors fabricated on the basis of this nanostructured material will demonstrate considerably higher sensitivity to the reacting gases.

# Study of arsenic flux effect on thermal desorption of GaAs native oxide and surface morphology

**D. V. Kirichenko✉, N. E. Chernenko, N. A. Shandyba, S. V. Balakirev, M. S. Solodovnik**
Laboratory of Epitaxial Technologies, Institute of Nanotechnologies, Electronics and Equipment Engineering, Southern Federal University, Taganrog 347922, Russia
✉dankir@sfedu.ru

**Abstract.** In this work, we study of arsenic flux effect on the native oxide thermal desorption processes of and surface morphology of GaAs(001) substrates. We have shown that GaAs exposure in the As flux during stage of oxide thermal desorption significantly modulates the processes of native oxide decomposition and its chemical interaction with substrate materials, leading to a decrease in the density and an increase in average size of pits formed as a result of etching. A decrease in the oxide thickness leads to a decrease in the pits' density, but practically does not affect their average size.

**Keywords:** native oxide desorption, gallium arsenide, native oxide, molecular beam epitaxy, A3B5.

**Funding:** This work was funded by the Ministry of Science and Higher Education of the Russian Federation; the state task in the field of scientific activity No. FENW-2022-0034.

## Introduction

One of the actively developing approaches to controlling the characteristics of A3B5 quantum dots is the use of substrate surfaces pre-structured in various ways. Since not all modification methods provide for high-vacuum substrates transport between technological chambers for subsequent epitaxial growth, issues related to the inevitable oxidation of the surface and precise removal of the oxide to preserve the morphology formed at the previous stages become increasingly important. At the same time, despite the rather deeply studied processes of A3B5 semiconductors native oxide formation, its composition and methods for its removal, the question related to molecular arsenic effect on the oxide desorption processes and surface morphology remains open.

## Materials and Methods

To study of molecular arsenic flux effect on the native GaAs oxide thermal desorption of, we used epi-ready GaAs(001) wafers with a nominal oxide thickness of ~3 nm and epitaxial GaAs structures with oxide thickness of about 1 nm. Native oxide was removed in the MBE growth chamber in the two ways: according to the standard procedure and by annealing in the arsenic (As) flux.

## Results and Discussion

We studied the morphology of the samples by SEM and AFM (Fig. 1). The results of AFM imaging studies are summarized in Table 1.

Table 1

**GaAs surface parameters after native oxide removal**

| № sample | Oxide thickness, nm | Arsenic flux | Density, $\mu m^{-2}$ | Average (maximum) depth, nm | Average (maximum) diameter, nm | RMS roughness |
|---|---|---|---|---|---|---|
| #a | 3 | | 77 | 6.3 (12) | 17 (48) | 0.832 |
| #b | 3 | + | 30 | 11 (26.5) | 41 (105) | 2.236 |
| #c | 1 | | 30 | 3 (4) | 30 (56) | 0.404 |
| #d | 1 | + | 14 | 4.8 (5) | 36 (75) | 0.566 |

As can be seen from the presented data, the removal of native oxide of epi-ready GaAs(001) wafers (thick oxide layer) in As flux leads to a noticeable (twofold) decrease in the density of pits formed as a result of the interaction of the oxide with the substrate material, which worsens the surface morphology, as well as to an increase in their geometric dimensions (depth and diameter).

A decrease in the oxide thickness leads to a sharp (by several times) decrease in the density of pits and their sizes. At the same time the As flux influence has the same character – pits' density and size are reduced in comparison with standard procedure.

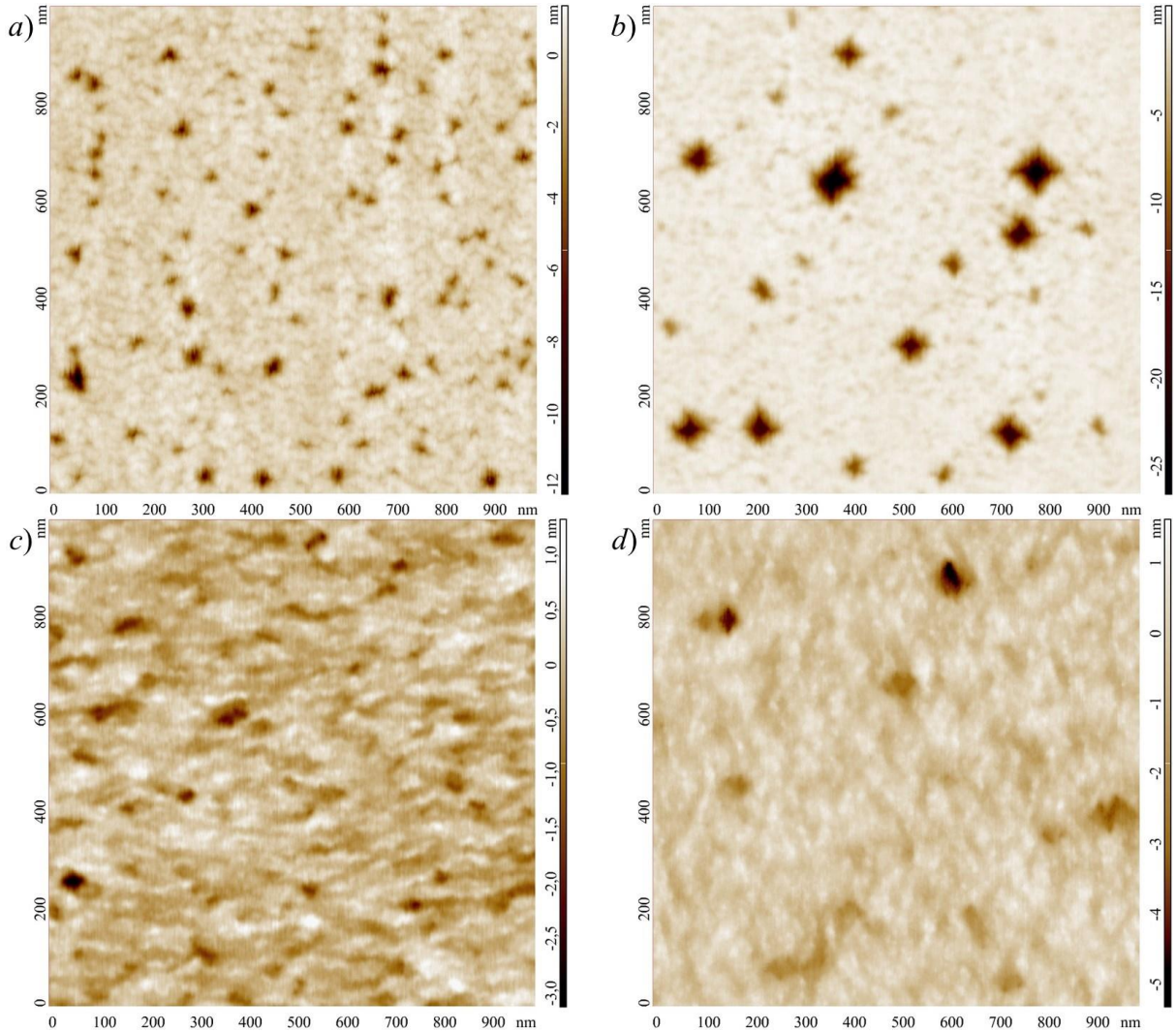


Fig. 1. AFM images of the GaAs surface after removing oxide of various thickness: 3 nm (a-b) and 1 nm (c-d) without (a, c) and with (b, d) As flux

We attribute this behavior of the system to the fact that the addition of As at the stage of oxide removal leads to the binding of Ga atoms released as a result of the thermal decomposition of GaAs (with an activation temperature of about 530°C) in already open areas of the substrate surface, which prevents their migration to areas with oxide. This leads to suppression of the main mechanism of thermal desorption of the oxide at high temperatures – decomposition of $Ga_2O_3$ which is the main component of GaAs native oxide. Thus, at the surface areas masked by oxide, the removal of $Ga_2O_3$ becomes possible only due to the enhanced decomposition of the substrate material directly under the oxide, which leads to the accumulation of excess Ga, followed by the formation of nanosized droplets and activation of the droplet etching of the substrate material. The proposed mechanism explains well the formation of pits with much larger geometric dimensions and lower density. A decrease in the total density of pits with a decrease in the thickness of the oxide layer can be associated with the suppression of the interaction reactions between the oxide components ($Ga_xO_y$ and $As_xO_y$) at earlier stages, leading, in turn, to a decrease in the content of the thermally stable $Ga_2O_3$ phase in the oxide film.

## Conclusion

The results obtained can be considered when developing methods for the pre-growth treatment of surfaces modified in various ways for the purpose of subsequent epitaxial synthesis.

# Creation of a GaMnAs ferromagnetic semiconductor by a combined laser method

**I.L. Kalentyeva[1], O.V. Vikhrova[1], Yu.A. Danilov[1], D.A. Zdoroveyshchev[1], A.V. Kudrin[1], V.P. Lesnikov[1], A.E. Parafin[2]**

[1]Research Institute for Physics and Technology of UNN, Gagarina Avenue, 23/3, Nizhny Novgorod, 603022
[2]Institute for Physics of Microstructures, RAS, GSP-105, Nizhny Novgorod, 603950

istery@rambler.ru

**Abstract**. GaMnAs layers fabricated by pulsed laser deposition in vacuum followed by annealing with KrF excimer laser pulses have been studied. As a result of annealing, there is a significant increase in the hole conductivity of the layers and a significant change in the form of the magnetic field dependence of the magnetization at room temperature. The study of galvanomagnetic properties shows the existence of ferromagnetism in GaMnAs layers with a Curie temperature reaching 90 K. The observed effects allow us to conclude that the applied pulsed laser action leads to the dissolution of MnAs inclusions, electrical activation of Mn, and, as a result, to the formation of a single-phase ferromagnetic GaMnAs semiconductor.

## 1. Introduction

Ferromagnetic semiconductors have great prospects, since they make it possible, in particular, to implement the control of magnetic properties by an electric field, to create spin field-effect transistors of a vertical design, resonant tunnel diodes, and devices with magnetization switching due to spin-orbit interaction (spin-orbit torque) [1]. This paper presents the results of studying the features of a GaMnAs ferromagnetic semiconductor fabricated by a new method that uses a combination of low-temperature pulsed laser deposition in vacuum (PLD-V) and pulsed laser annealing (PLA).

## 2. Experimental technique

GaMnAs layers were deposited on *i*-GaAs (100) wafers by evaporation of solid targets (undoped GaAs and high-purity Mn) with a focused YAG:Nd laser beam ($\lambda$ = 532 nm). The process temperature ($T_g$) varied from 200 to 350°C. The manganese content was 0.17, and the layer thickness reached ~50 nm. Then the samples were subjected to pulsed laser annealing using an LPX-200 excimer laser (working mixture KrF, wavelength 248 nm, pulse duration 30 ns, laser radiation energy density $P$ = 400 mJ/cm$^2$).

The magnetization of the structures was measured at room temperature using a magnetometer with a variable field gradient. Studies of galvanomagnetic properties were carried out using a Janis CCS-300S/202 closed-cycle helium cryostat at temperatures of 10–300 K in the range of magnetic fields ± 3600 Oe.

## 3. Results and discussion

All GaMnAs layers fabricated by the PLD-V method show high values of sheet resistance ($R_s$) at room temperature: the value of $R_s$ increases from ~ $10^7$ до ~ $10^9$ Ohm with an increase of $T_g$ from 200 to 350°C. After applying pulsed laser annealing, the conductivity of GaMnAs films increases significantly ($R_s$ ~ 880–2970 Ohm). The hole concentration $p$ calculated from measurements of the Hall effect reaches ~ $2.8 \cdot 10^{20}$ cm$^{-3}$, and the effective mobility $\mu_{eff}$ ~ 4–5 cm$^2$/V·s. This fact testifies to the activation processes that occur under the action of PLA, leading to the incorporation of manganese atoms into the sites of the gallium sublattice and, thereby, contributing to the appearance of hole conductivity. At lower temperatures of layer formation (200 and 250°C), the degree of electrical activation of the impurity is much higher.

The initial GaMnAs structures exhibited nonlinear (with a hysteresis loop) magnetic-field dependences of the magnetization $M(H)$ at room temperature, associated with the presence of a ferromagnetic semi-metallic compound MnAs in the inclusion layers [2]. After laser annealing, the dependences M(H) become linear (fig.1a). The existence of ferromagnetism in GaMnAs layers with a Curie temperature reaching 90 K is shown (fig.1b). The spontaneous Hall resistance ($R^S_H$) is proportional to the spontaneous magnetization $M_S$ and characterizes the ferromagnetic ordering in the structures.

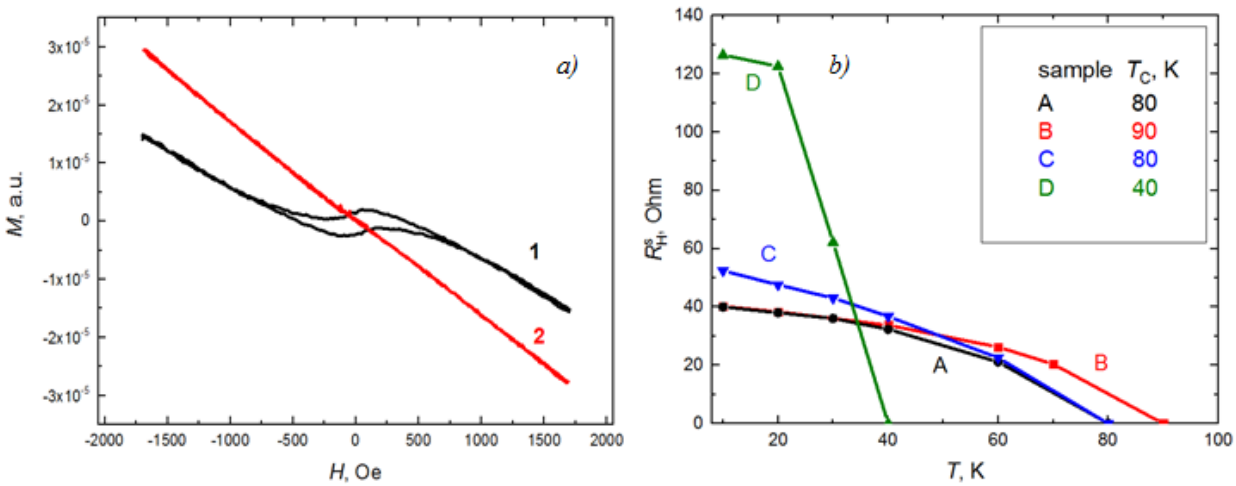


**Figure 2.** *a*) Magnetic field dependences of the magnetization at a room temperature for the initial (curve 1) and annealed (curve 2) structure samples with a GaMnAs layer fabricated at 300°C. An external magnetic field was applied in the plane of the layer. *b*) Temperature dependences of the Hall spontaneous resistance determined using the Arrott procedure for samples with different $T_g$,°C: A – 200, B – 250, C – 300, D – 350.


**Acknowledgments**

This work was supported by the Russian Science Foundation (project no. 23-29-00312).


**References**


[1] C. Song et al. Progress Mater. Sci. **87**, 33 (2017).

[2] I.L. Kalentyeva et al. J. Magn. Magn. Mater. **556**, 169360 (2022).

# Novel methods for synthesizing high-quality thin films through short and ultrashort high-power pulsed magnetron sputtering

**Vasily Kozhevnikov, Vladimir Oskirko, Andrey Solovyev, Andrey Kozyrev, Sergey Rabotkin, Vyacheslav Semenov, Artem Pavlov**

Institute of High Current Electronics SB RAS, 2/3 Akademichesky ave., 634055 Tomsk, Russian Federation

Vasily.Y.Kozhevnikov@ieee.org

**Abstract**. The article focuses on researching the high-power impulse magnetron sputtering process (HiPIMS) in two pulse duration regimes: short (~10 µs) and ultrashort (~1 µs), through both experimental and theoretical studies. These HiPIMS forms are particularly interesting because of the advanced ion vapor deposition (IPVD) capabilities they offer. By utilizing these discharge regimes in magnetron sputtering systems, it is possible to significantly increase the ion current average density of the target material metal fraction, while maintaining the same average pulse power. This results in thin films with high adhesion and density, and optimal deposition rates that surpass those achievable through traditional HiPIMS forms.

The present study investigates the factors responsible for the increase in average ion current density on the substrate in short and ultra-short pulsed magnetron sputtering systems, commonly known as s-HiPIMS and us-HiPIMS, respectively. In the experimental section, we employ short HiPIMS pulses to a copper target while maintaining a constant average discharge power of 1 kW and a peak current of 150 A. To conduct this experiment, we collaborated with "Applied Electronics" company (Tomsk, Russia) to design a specialized pulsed-power voltage supply with low output inductance. Our results indicate that reducing the duration of voltage pulses from 50 µs to 4 µs leads to a significant increase in the average ion current density on the substrate, from 2 to 7 mA/cm². Additionally, optical emission spectroscopy revealed an increase in the number densities of $Ar^+$, $Cu^+$, and $Cu^{2+}$ ions. The charge composition measurements of total ion flux to the substrate show that charged particles, particularly $Cu^+$, are delivered to the substrate over a considerably longer time than the voltage/current pulse duration. These findings suggest that the discharge afterglow effects play a crucial role in the coating IPVD process.

In the second part of this paper, we provide a theoretical explanation for the role of afterglow effects in s-HiPIMS and us-HiPIMS discharges. To this end, we formulated an original spatially-averaged model of the discharge ionization region (IRM). This model enabled us to calculate the non-stationary average plasma number densities in the ionization region, as well as the averaged values of the charged and neutral particles fluxes directed towards the substrate. Our theoretical calculations within the proposed IRM framework demonstrated that plasma dissipation during the afterglow phase had a length of approximately 150 µs, regardless of whether the voltage pulse lasted for 5 µs or 50 µs. The decay of the ionization region plasma resulted from the appearance of outward ion fluxes when the discharge voltage

switched off, and the electric field drawing IR ions to the target disappeared. Our ongoing theoretical simulations of s-HiPIMS and us-HiPIMS discharges showed excellent agreement with the experimental data on the average values of ion current density pulses on the substrate obtained above. This convincingly indicates the correctness of our interpretation of the studied physical phenomenon. The obtained experimental and theoretical results reveal new prospects for the use of s-HiPIMS and us-HiPIMS operation modes in single- and dual-magnetron sputtering systems.

The work was carried out within the framework of the state assignment of the Ministry of Science and Higher Education of the Russian Federation on the topics FWRM-2021-0006, FWRM-2021-0007, FWRM-2021-0014.

UDC 620.3

# On the wetting of PET substrates with Multicomponent Graphene Oxide Dispersions

**I. A. Komarov** [1✉], **E. A. Danilov**[1]
[1] JSC Research Institute «NIIgraphite», Moscow, Russian Federation.
✉master_kom@mail.com

**Abstract.** In this work, we investigate wetting properties of polymer PET substrates with graphene oxide multicomponent dispersions. Overcoming poor wettability polymer substrates like PET, promising for flexible electronics applications, with commercially available water graphene oxide suspensions is proposed to solve by adding organic components. We used dimethylacetamide and Tamiya Laquer Thinner to successfully show the decrease of wetting angle. Moreover, we showed stability of dispersion with DMA within more than 6 months and LT within more than several weeks and also found out that drying time of droplets of mixed dispersions with different additives may vary more than 15 times that is important for choice of the preferred deposition method.

**Keywords:** Graphene Oxide, mixed dispersions, organic solutions, DMA, PET substrate.

## Introduction

Carbon nanomaterials, especially graphene derivatives that include graphene oxide (GO) and reduced graphene oxide (rGO) are very promising materials for different applications in flexible electronics [1], chemical and biological sensors [2], energy storage systems [3], drug delivery platforms [4] etc. One of the main requirements for flexible devices is large-area uniform conductive and dielectric nanomaterials-based layers. Highly uniform films can be formed on polymer substrates via different methods such as Langmuir-Blodgett technique [5], dip-coating [6], spin-coating [7], spray coating [8] or roll-to-roll technology [9] and many others, but only the latter three are compatible with at least small batch production. On the other hand, most of commercially available GO forms are water suspension with poor wettability of polymer substrates. This limitation can be overcome by mechanical or plasma pre-treatment, but in case of need of nanometer thick films those cannot be applied. On the other hand, wettability can be improved by the dispersion's properties themselves.

In the current study, we tried to introduce additional organic components to the water-based GO suspension. Additional components in the dispersion media should at least provide good dispersibility of GO. According to the data obtained from [10], GO can form long-time stable dispersions in such organic solvents (besides water) as dimethylformamide (DMF), N-methylpyrrolidone (NMP) and tetrahydrofuran (THF), and less stable in ethylene glycol, acetone and toluene. On the other hand, it is known that dimethylacetamide (DMA) is a good dispersion media for carboxylized carbon nanotubes [11].

Thus, we tried to form a multicomponent mixed dispersion media that contains water-based GO suspension, DMA and Tamiya lacquer thinner (ethyleneglycol, butylglycol, methylisobutylketone) (LT) at different GO concentrations. We investigated wettability of these multicomponent GO dispersions with respect to PET substrates, their morphology and Raman spectra.

## Materials and Methods

Dispersions were prepared from commercially available GO water suspension (4,7 mg/ml) produced by improved Hummer's method (LLC "MIP Graphene", Russian Federation). Additional components: ultrapure DMA (EKOS-1, Russian Federation), Laquer Thinner (Tamiya Ink., Japan) were mixed with initial suspension with 50 :50 ratio.

As a substrate for film deposition, we used high opacity PET film without additional surface treatment. Substrates with 5 x 10 mm dimensions were cleaned with 2-propanol and water and dried in the 2 bar airflow.

For wetting angle investigations, we used home-made device with 3,5x lens, digital camera for optical photos of dispersion droplets with further image processing using ImageJ software.

Optical images of morphology and Raman spectra were obtained by InVia Raman spectrometer (Renishaw, UK).

## Results and Discussion

Dependence of wetting angle on the additional organic component of the dispersion, GO concentration and drying time is shown in the figure 1a. Submitted data for each point was averaged over eight samples. From these data, one can see that dispersion with LT as additional component has two shoulders with approximate linear dependence of wetting angle (under and above 0,05 mg/ml concentration). Drying time on the concentration dependence can be approximated with linear function. This result, on the one hand, means that we reached basic goal to reduce wetting angle. Initial GO water suspension wetting angle is 41,6 °. On the other hand, pronounced dependence of wetting angle may be used to efficiently control wetting properties. High volatility (low drying time) of LT-based dispersion is due to the basic purpose of the LT as a dilutant for enamel paint for airbrush applications. We can see that the use of the LT as a second component makes this dispersion perspective for spray coating of thin GO films.

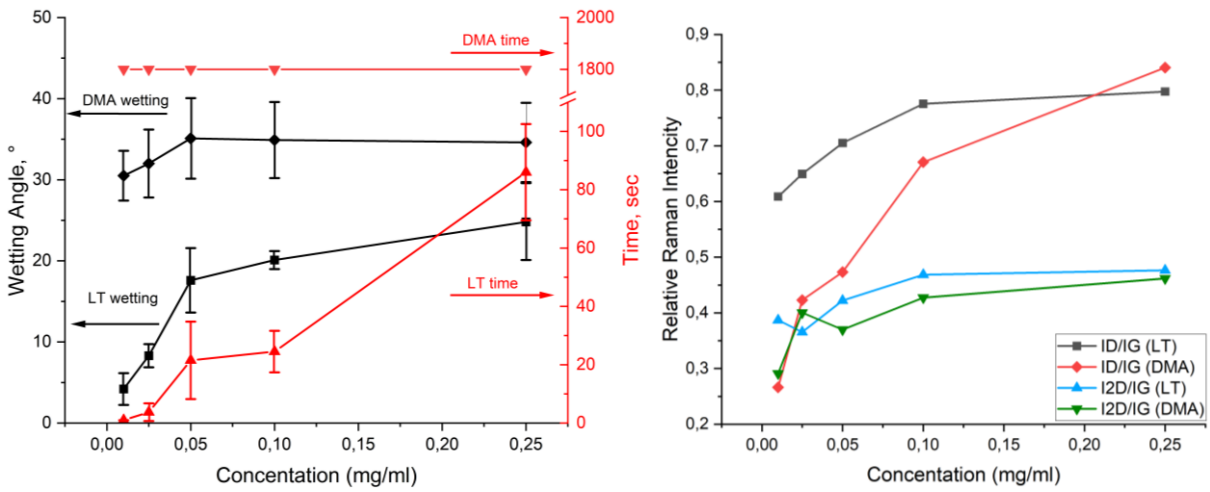


*a*) *b*)

Fig. 1. Dependence of wetting angle and drying time on the type of the additional component and GO concentration (*a*); dependence of main Raman bands ratios of deposited films on the GO concentration.

Dispersion with DMA on the contrary did not show strong dependence of the wetting angle or time on the GO concentration. This mixture also showed decrease in wetting angle, but the decrease is much lower than in case of LT. We suppose that in case of DMA addition the dispersion properties are primarily affected by water. Low reduction of wetting angle and drying time in range of tenth minutes confirm the abovementioned fact.

Drying time in range of tenth of minutes means that DMA-containing dispersion will be better for spin-coating deposition due to the characteristic time of spin-coating process (few minutes). Drying time in the case of DMA addition is at least 15 times more than in case of LT.

Analysis of morphology images and $I_D/I_G$ and $I_{2D}/I_G$ Raman band ratios shows that concentration of GO under the 0,05 mg/ml leads to the island-type film formation. Difference is that in case of LT we observe islands as mixture of many small flakes, whereas in case of DMA islands are relatively large individual multilayered GO flakes. Over the 0,05 mg/ml concentration films are uniform. Raman spectra and band ratio are classic for thin GO films [12].

## Conclusion

In this work, we showed the possibility to decrease and control wetting angle on GO suspension/PET interface by adding organic components to the commercially available GO water-based suspension. We found out that addition of the dilutant for enamel paints leads to the formation of highly volatile dispersion that will be perspective for spray coating. Addition of DMA leads to the formation of much lower volatile dispersion that may be efficiently used for spin-coating deposition due to the at least 15 times larger drying time.

## REFERENCES


1. **Gilshteyn E. P et al**. Mechanically Tunable Single-Walled Carbon Nanotube Films as a Universal Material for Transparent and Stretchable Electronics. ACS Appl. Mater. Interfaces. 2019, 11, 27327–27334.
2. **Freddi S et al**. Development of a Sensing Array for Human Breath Analysis Based on SWCNT Layers Functionalized with Semiconductor Organic Molecules. Advanced Healthcare Materials. 2020, 9, 2000377.
3. **Liu Y. et al.** Challenges and Opportunities Towards Fast- Charging Battery Materials. Nat. Energy 2019, Vol4, pp. 540–550.
4. **Oliveira A.M.L. et al.** Graphene Oxide Thin Films with Drug Delivery Function. Nanomaterials. 2022, 12, 1149.
5. **Holm A et al**. Langmuir-Blodgett Deposition of Graphene Oxide — Identifying Marangoni Flow as a Process that Fundamentally Limits Deposition Control. Langmuir. 2018, 34, 33, 9683–9691.
6. **Luis Gustavo Baptista Machuno et al**. Multilayer Graphene Films Obtained by Dip Coating Technique. Materials Research. 2015; 18(4), 775-780.
7. **Nguyen A.N. et al**. Spin Coating and Micro-Patterning Optimization of Composite Thin Films Based on PVDF. Materials. 2020, 13, 1342.
8. **Struchkov N.S. et al**. Uniform graphene oxide films fabrication via spray-coating for sensing application. Fullerenes Nanotubes and Carbon Nanostructures. 2020, 28, 214-220.
9. **Wells R.A. et al**. Roll-to-Roll Deposition of Semiconducting 2D Nanoflake Films of Transition Metal Dichalcogenides for Optoelectronic Applications. ACS Appl. Nano Mater. 2019, 2 pp 7705-7712.
10. **Konios D et al**. Dispersion behaviour of graphene oxide and reduced graphene oxide. Journal of Colloid and Interface Science. 2014, 430, 108-112.
11. **Komarov I. A. et al**. Chemiresistive Sensors for Thrombin Assay Based on Nanosize Carbon Nanotube Films on Flexible Supports. Biomedical Engineering. 2018, 51, 377-380.
12. **Jiang-Bin Wu et al**. Raman spectroscopy of graphene-based materials and its applications in related devices. Chem. Soc. Rev. 2018, 47, 1822.


## THE AUTHORS


**KOMAROV Ivan A.**
master_kom@mail.ru
ORCID: 0000-0002-6397-6671

**DANILOV Egor A.**
danilovegor1@gmail.com
ORCID: 0000-0002-1986-3936

# Local elastic heterogeneity significantly affects the stiffness of composite systems

**D. A. Conyuh**[1✉], **A. A. Semenov**[1], **Ya. M. Beltukov**[1]
[1] Ioffe Institute, Saint-Petersburg, Russia;
✉Conyuh.Dmitry@mail.ioffe.ru

**Abstract.** The local elastic properties of strongly disordered host material are investigated using the theory of correlated random matrices. A significant increase in stiffness is shown in the interfacial region, which thickness depends on the strength of disorder. It is obtained that this effect plays a crucial role in nanocomposites, in which interfacial regions are formed around each nanoparticle.

**Keywords:** Amorphous materials, random matrix theory, nanocomposites.

**Funding:** This study was funded by the Russian Science Foundation (grant No 22-72-10083).

## Introduction

Revealing the microscopic nature of the inhomogeneous elastic properties of strongly disordered systems is the main goal of past and current research. Examples of such systems are amorphous materials. Due to their disordered structure, amorphous glasses and polymers demonstrate the non-affine deformations under uniform stress. These deformations are the result of the local elastic heterogeneity and are manifested on the typical heterogeneity length scale, which is estimated as tens of interatomic distances [1, 2]. If the size of an amorphous medium is much larger than its heterogeneity length scale, one can use the macroscopic elastic moduli to describe the mechanical properties of this system. However, in composite systems containing amorphous materials, some regions may have small typical sizes. An important example is nanocomposites, in which the size of nanoinclusions may be comparable to the heterogeneity length scale of the host amorphous medium [3]. Therefore, it is essential to study the local elastic properties of amorphous solids, especially near the interface with other materials.

## Materials and Methods

In this work, the theory of the correlated random matrices was applied to find the local elastic properties of disordered systems. In the framework of this theory, one can present the force-constant matrix $\Phi$, which determines the linear elastic properties of particular amorphous solid, in the next universal form

$$\Phi = AA^T, \tag{1}$$

where A is some rectangular $N \times K$ matrix. The ith row of the matrix A corresponds to the ith degree of freedom, and the kth column corresponds to the kth bond. Each bond may involve several degrees of freedom, which affects the number of non-zero elements in kth column of the matrix A. The dimensionless parameter $\varkappa = K/N - 1$ varies in a wide range of values $0 \le \varkappa < \infty$ and controls the relationship between stiffness and disorder in the system [4].

For an amorphous solid, the matrix A has a random nature. One can assume that the matrix elements $A_{ij}$ are random numbers. However, due to the fact that the strongly disordered system is near the stable equilibrium on the verge of stability loss, there is a correlation between the elements of the matrix A. In the general case, this correlation is described by the pair correlations $\langle A_{ik}A_{jl}\rangle = C_{ij,kl}$, where the angle brackets denote the averaging over different realizations of A. Recently, using the theory of correlated random matrices, the analytical form of the vibrational density of states and the dynamical structure factor was obtained, and the boson peak length scale $\xi_{bp} \sim \kappa^{-1/2}$ was attributed to the heterogeneity length scale [4].

To study the inhomogeneous elastic properties, one can find the effective force constant matrix $\Phi_{eff}$ as a non-random substitution of the random force constant matrix, which gives the same average response to external forces. Using the diagram technique and assuming that the elements of the matrix A are Gaussian random numbers, the relation between the effective force constant matrix $\Phi_{eff}$ and the correlation matrix C can be found, which allows us to study the local elastic heterogeneity of strong disordered systems.

## Results and Discussion

Using the random matrix model of amorphous solids with homogeneous and isotropic statistical properties, a continuous equation for effective local elastic contrast $\alpha(\mathbf{r})$ was obtained:

$$\alpha(\mathbf{r}) = 1 + \xi^2 \Delta \ln(\alpha(\mathbf{r})), \tag{2}$$

where $\xi$ is the dimensional parameter of the system, and $\Delta$ denotes the Laplacian. It reveals the increase of the stiffness of amorphous solid near the boundary with a more rigid and ordered body. The typical thickness of the boundary layer with increased stiffness is $\xi \sim \varkappa^{-1/2}$. Far away from the boundaries $\alpha(r)$ has an exponential decay to 1 with a typical length $\xi$. For the strongly disordered amorphous solids $\varkappa << 1$, the heterogeneity length scale $\xi$ is much larger than the typical interatomic size in the system. The scaling of $\xi$ with the strength of disorder emphasizes the role of disorder in the formation of the boundary layer with increased stiffness.

The effect under study is important for macroscopic elastic moduli of nanocomposites with the amorphous host material. The numerical model of an amorphous solid with rigid spherical inclusions was studied to demonstrate this effect (see Fig. 1). It was shown that the shell with enhanced elastic properties is formed around each nanoparticle. The thickness of this shell is of the order of $\xi$, which results in the increased effective radius of nanoparticles, which significantly increases the macroscopic elastic moduli of the nanocomposite. The obtained results are in agreement with the calculation results of the molecular dynamic model of polystyrene with $SiO_2$ nanoinclusions [3].

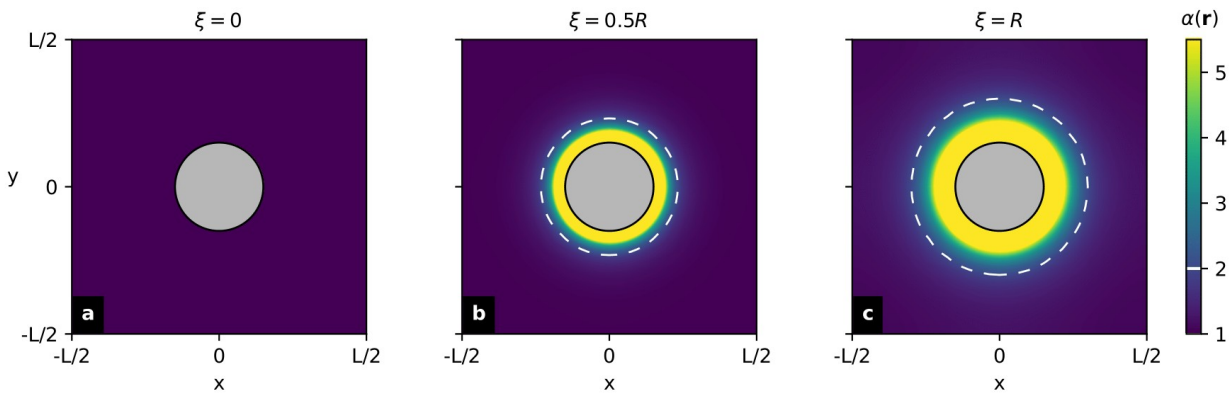


Fig. 1. The distribution of the effective local elastic contrast $\alpha(\mathbf{r})$ around a spherical rigid inclusion (indicated by a gray circle) into a sample with different values of the heterogeneity length scale $\xi$. The white dotted line shows the shell on which the effective contrast $\alpha(\mathbf{r}) = 2$.

## REFERENCES


1. **Leonforte F., Boissiere R., Tanguy A., Wittmer J. P., Barrat J. L.**, Continuum limit of amorphous elastic bodies. III. Three-dimensional systems, Physical Review B. 72 (22) (2005) 224206.

2. **Maloney C. E.**, Correlations in the elastic response of dense random packings, Physical Review Letters. 97 (3) (2006) 035503.

3. **Beltukov Y. M., Conyuh D. A., Solov'yov I. A.**, Local elastic properties of polystyrene nanocomposites increase significantly due to nonaffine deformations, Physical Review E. 105 (1) (2022) L012501.

4. **Beltukov Y. M., Kozub V. I., Parshin D. A.**, Ioffe-Regel criterion and diffusion of vibrations in random lattices, Physical Review B. 87 (13) (2013) 134203.

# SPECTROSCOPY OF DIAMOND PLATES ALLOYED WITH BORON AND NICKEL

[1] **A.A. Kostin 1** ✉, [1] **A.S. Volkov2**
[1]Northern (Arctic) Federal University named after M.V. Lomonosov 1, Arkhangelsk, Russia
✉a.kostin@narfu.ru

**Abstract.** Diamond plates with boron and nickel inclusions were studied by infrared and impedance spectroscopy.

The spectra obtained by the infrared method were plotted in the frequency range of 1000 – 1500 $cm^{-1}$. Dependencies of the specific electrical conductivity of diamond plates are given in the range $10^{-2}$ – $10^{-7}$ Hz. Correlation of the data obtained by these methods allows us to characterize the diamond plate.

**Keywords:** diamond plates, spectrometry, electrical conductivity.

## Introduction

Various impurities introduced into the crystal structure of diamond lead to a change in its physical properties. Diamond wafers are a promising material; in the long term, studies of technical diamonds can contribute to the development of optical quantum magnetometers [3]. Diamond wafers, depending on various types and concentrations of impurities, can be used as sensors, in particular, magnetic field sensors [2]. It is known that diamond with boron impurities can be used in electronics as semiconductor elements [4]. In this paper, the electrophysical properties of diamond plates with boron and nickel impurities are compared, and the correlation between impedance spectra and IR spectra parameters is presented.

## Materials and Methods

The plates of technical diamonds doped with nickel and boron are used in this work. IR spectra were obtained with the FT-801 spectrometer at room temperature in the range of wave numbers from 1000 to 1500 $cm^{-1}$. Spectra of specific electrical conductivity of diamond plates were obtained with the Novocontrol Concept 80 impedance spectrometer in the frequency range from $10^{-2}$ – $10^{-7}$ Hz and in the temperature range from -100°C to 230°.

## Results and Discussion

In an earlier experiment [1], the temperature dependences of the static σs and high-frequency σ∞ parameters of the specific electrical conductivity (Fig. 1) of diamond plates with boron and nickel admixtures were obtained, corresponding to the low-frequency and high-frequency regions of the frequency range under study:

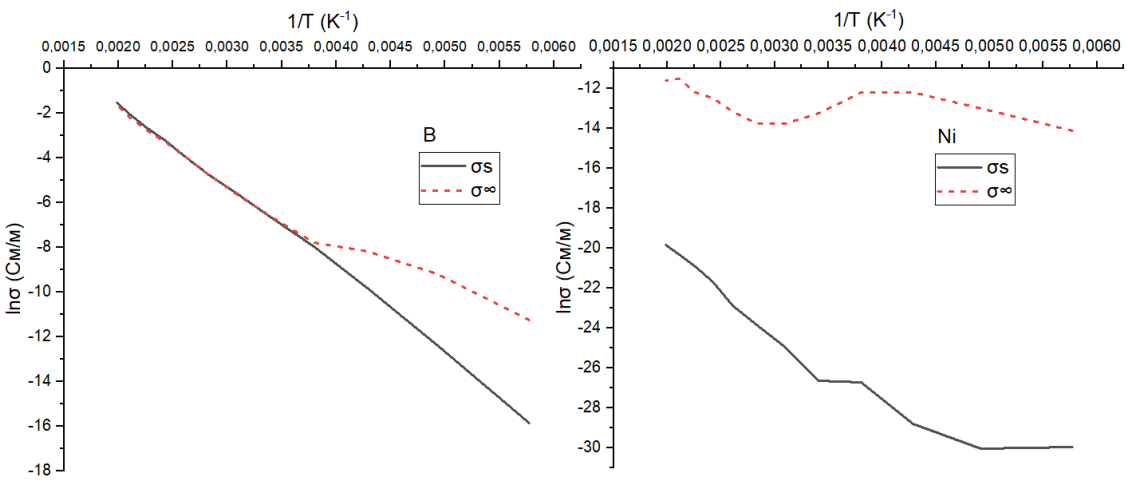

Fig. 1 Dependence of static and high-frequency parameters of specific electrical conductivity for the sample with boron (left) and nickel (right) admixture

As can be seen from the above dependences, below the temperature of -10°C there is a change in the conduction mechanism for the sample with boron admixture. The presence of several temperature ranges with different values of the activation energy is related to the behavior of boron impurities in the diamond plate structure. It is difficult to analyze which particles affected the conductivity of the diamond plate with nickel admixtures from the curves of dependence of conductivity on temperature.

In the future, it is planned to conduct a study of local areas of these plates. Using infrared spectroscopy to identify the concentration of impurities in local areas. Using scanning tunneling microscopy to analyze the volt-ampere characteristics in these local areas and correlate these data.

**Acknowledgments**

The research was supported by the state task of the Russian Federation No. FSRU-2022-0008

## REFERENCES

1. Костин А.А., Капустин С.Н. ЛОМОНОСОВСКИЕ НАУЧНЫЕ ЧТЕНИЯ СТУДЕНТОВ, АСПИРАНТОВ И МОЛОДЫХ УЧЕНЫХ – 2022. Сборник материалов конференции в 2-х томах. Том 2. Министерство науки и высшего образования Российской Федерации, Северный (Арктический) федеральный университет имени М.В. Ломоносова. 2022, Издательство: Северный (Арктический) федеральный университет имени М.В. Ломоносова (Архангельск)

2. Yinan Hu , Geoffrey Z. Iwata, Lykourgos Bougas , John W. Blanchard. Rapid Online Solid-State Battery Diagnostics with Optically Pumped Magnetometers Applied Sciences. — October 2020; Accepted: 3 November 2020; Published: 6 November 2020.

3. А.Н. Анисимов, Р.А. Бабунц, И.Д. Бреев, А.П. Бундакова, И.В. Ильин, М.В. Музафарова, П.Г. Баранов Сканирующий оптический квантовый магнитометр, основанный на явлении выжигания провалов. — Письма в ЖТФ, 2016, том 42, вып. 12.

4. V. S. Bormashova , S. A. Tarelkina, b, S. G. Bugaa, b, *, A. P. Volkova , A. V. Golovanova, b , M. S. Kuznetsova, N. V. Kornilova, D. V. Teteruka, N. V. Lupareva, S. A. Terent'eva, and V. D. Blank Electrical Properties of High-Quality Synthetic Boron-Doped Diamond Single Crystals and Schottky Barrier Diodes on Their Basis. THE STUDY OF STRUCTURE AND PROPERTIES PHYSICAL METHODS FOR STUDY AND CONTROL.

## THE AUTHORS

**KOSTIN Alexey A.**
*Northern (Arctic) Federal University named after M.V. Lomonosov*
17 Severnaya Dvina, 163002 Arkhangelsk, Russia
a.kostin@narfu.ru
ORCID: -

**VOLKOV Aleksandr S.**
*Northern (Arctic) Federal University named after M.V. Lomonosov*
17 Severnaya Dvina, 163002 Arkhangelsk, Russia
a.s.volkov@narfu.ru
ORCID: -0000-0002-3816-3441
Посмотреть профиль этого автора в ORCID

# Doping and thermoelectric characteristics of $Ge_{0.3}Si_{0.7}$:$P_{\delta}$ synthesized by powder sintering

**Yu. M. Kuznetsov** [1✉], **M. V. Dorokhin** [1], **P. B. Demina** [1], **I. V. Erofeeva** [1], **A. V. Zdoroveyshchev** [1]

[1] Lobachevsky state university, Nizhny Novgorod, Russia;

✉y.m.kuznetsov@unn.ru

**Abstract.** The paper describes the technological parameters of the formation of the $Ge_{0.3}Si_{0.7}$ solid solution in a spark plasma sintering unit. A new method for alloying a solid solution during synthesis from a source of silicon phosphide is proposed. A comparative analysis of the transport and thermoelectric properties of the obtained samples depending on the dopant concentration is given.

**Keywords:** thermoelectric, figure of merit, Seebeck coefficient, germanium silicon, silicon phosphide.

**Funding:** The work was supported by the Ministry of education and science of Russian Federation in the frames of federal task (project № FSWR-2023-0037).

## Introduction

Thermoelectrics are materials that convert thermal energy into electrical one. The thermoelectric figure of merit (*ZT*) is a dimensionless coefficient that characterizes the conversion efficiency which is determined by the expression [1]: $ZT = \alpha^2 T/\rho \cdot \lambda$, where $\alpha$ – Seebeck coefficient, $\rho$ – resistivity, $\lambda$ – thermal conductivity.

For instrumental implementation, the material must possess $ZT > 1$. The recent trends are directed towards studying the *ZT* of $Ge_xSi_{1-x}$ semiconductor ceramics formed by nanopowder sintering. Such materials have a record low λ while maintaining high α and low $\rho$ [2].

## Experimental technique

A feature of this work is the use of non-toxic SiP as a source of a donor dopant of a GeSi solid solution. Such an approach makes it possible to avoid the use of toxic P, thereby significantly facilitating work with the initial powders. The powders were obtained by preliminary and fine grinding in a Fritsch Analysette 3 Pro ball mill and a Fritsch Pulverisette 6 planetary mill (250 rpm, 6 hours), respectively. The average particle size of the powder mixture was estimated on a Jeol JSM-IT300LV scanning electron microscope to be ~ 1 μm. The powders were sintered in a DR-SINTER SPS-625 Spark Plasma Sintering System (SPS) at a pressure of 70 MPa and a temperature of 1040 $^{o}$C. The sintering rate was 50 $^{o}$C/min. A series of four samples was formed, in which the concentration of P was varied.

The registration of the temperature dependence of $\alpha$ was carried out during the creation of a controlled temperature gradient with subsequent measurement of the thermo-EMF signal. The value of $\rho$ was measured using a standard four-contact circuit. The temperature dependence of $\lambda$ was obtained by the method of stationary heat flow. The concentration of free charge carriers was calculated from the magnetic field dependence of the Hall resistance. Measurement techniques are described in [3–4].

## Results and Discussion

The experimentally obtained temperature dependences of the thermoelectric parameters of the samples are shown in Figures 1–4. In addition, the results are compared with the record-breaking characteristics of $Ge_{0.2}Si_{0.8}$:$P_{0.02}$ from [2], a distinguishing feature of which was an extremely small powder particle size of ~30 nm.

The largest *ZT* in the entire measured temperature range is possessed by a sample containing 1.5 at. %. (*ZT* = 1.16), which is only 9% less than stated in [2]. At the same time, a significantly simplified technology was used in our work.

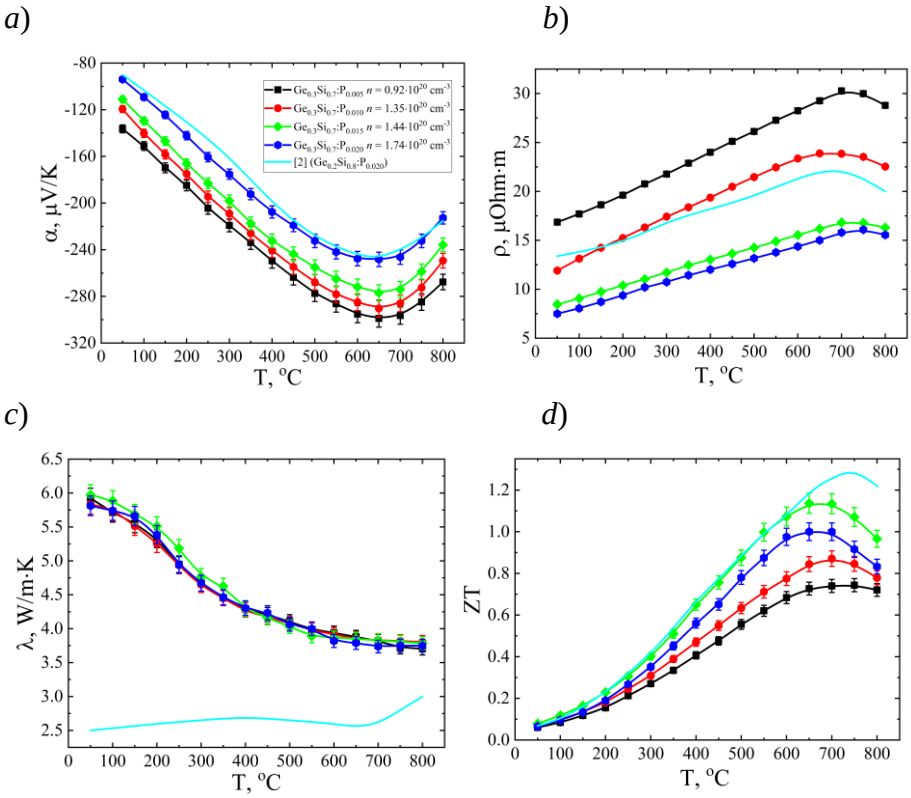


Fig. 1. Temperature dependence of Seebeck coefficient (*a*), resistivity (*b*), coefficient of thermal conductivity (*c*), thermoelectric figure of merit (*d*)

## Conclusion

The paper shows a new method of doping with phosphorus nanostructured thermoelectric materials based on a solid solution of germanium-silicon in the process of synthesis by spark plasma sintering. The optimum level of doping is established, at which high values of *ZT* are achieved.


## Acknowledgments

This work was supported by the state task of the Ministry of Education and Science of the Russian Federation (project no. FSWR-2023-0037). The authors are grateful to Dr. A. Yu. Zavrazhnov and I. N. Nekrylov for the synthesis of SiP, as well as to the engineer of the NIFTI UNN A. V. Voronin for experiments on sample sintering.


## REFERENCES


1. **Hicks D, Dresselhaus M. S.**, Thermoelectric figure of merit of a one-dimensional conductor, Physical Review B. Vol. 47 (1993) 16631.

2. **Wang X. W., Lee H., Lan Y. C., Zhu G. H., Joshi G., Wang D. Z., Yang Z., Mut A. J., Tang M. Y., Klatsky J., Son S., Dresselhaus M. S., Chen G., Ren Z. F.,** Applied Physics Letters. Vol. 93 (2008) 193121.

3. **Mochalov L. A., Kuznetsov Yu. M., Dorokhin M. V., Fukina D. G., Knyazev A. V., Kudryashov M. A., Kudryashova Yu. P., Logunov A. A., Mukhina O. V., Zdoroveyshchev A. V., Zdoroveyshchev D. A.,** Thermoelectrical properties of ternary lead chalcogenide plumbum-selenium-tellurium thin films with excess of tellurium prepared by plasma-chemical vapor deposition. Thin Solid Films. Vol. 752 (2022) 139244.

4. **Dorokhin M. V., Boldin M. S., Uskova E. A., Boryakov A. V., Demina P. B., Erofeeva I. V., Zdoroveyshchev A. V., Kotomina V. E., Kuznetsov Yu. M., Lantsev E. A., Popov A. A., Trushin V. N.,** Formation of a fine-grained $Si_{1-x}Ge_x$ thermoelectric by spark plasma sintering. Technical Physics. Vol. 67 (15) (2022) 2402–2409.

# Analysis of homoepitaxial growth of Si on Si(100) in a wide temperature range by reflection high-energy electron diffraction

**O. I. Kukenov** ✉, **A. S. Sokolov, V.V. Dirko, K.A Lozovoy., A.P. Kokhanenko**
National Research Tomsk State University, Tomsk, Russia
✉okukenov@mail.ru

**Abstract.** To create idealized nanostructures, it is important to understand the surface morphology for given growth parameters. The paper shows the effect of temperature on the ratio of intensities and periods corresponding to the growth of Si steps with different types of superstructure. The analysis was carried out in directions [100] and [110].

**Keywords:** molecular beam epitaxy, reflection high-energy electron diffraction, step-flow growth of silicon, homoepitaxy.

**Funding:** Work with the financial support of the Russian Science Foundation grant No. 21-72-10031.

## Introduction

Progress in the field of semiconductor nanoelectronics is inevitably accompanied by stricter requirements for the quality and accuracy of grown nanostructures. The purest epitaxial structures with a minimum number of defects are obtained by molecular beam epitaxy (MBE). The creation of high quality nanostructures is impossible without a precise surface control method. The method of reflection high-energy electron diffraction (RHEED), implemented in the MBE method, has proven to be a universal means of control of the surface morphology in the in situ growth of semiconductor nanostructures [1–2].

## Materials and Methods

Homoepitaxial step-flow growth of Si on Si(100) occurs with the formation of alternating steps of two types: steps with a 1x2 superstructure and steps with a 2x1 superstructure [3]. After chemical cleaning and subsequent high-vacuum annealing of the Si(100) substrate at a temperature of 1000°C, Si/Si(100) was synthesized at a growth rate of 0.09 ML/s in the substrate temperature range from 200 to 800°C. In the analysis of the surface during growth by the RHEED method in the [110] direction, a bimodal nature of the intensity oscillations was observed. It lies in the fact that two alternating maxima of different intensity are observed, each of which corresponds to its own period of oscillations. The larger intensity maximum corresponds to the growth of steps with the 1x2 superstructure, in which the atoms in the dimer are located along the direction of the incident electron beam. The smaller maximum corresponds to the formation of steps with a 2x1 superstructure, in which the dimers are located across the electron beam. When analyzing the surface during growth by the RHEED method in the [100] direction, changes in the intensities of reflections from the 1x2 and 2x1 superstructures were observed with a change in the growth temperature.

## Results and Discussion

In the course of studying the homoepitaxial growth of Si/Si(100) in the [110] direction by the RHEED method, the temperature dependences of the ratio of the intensities of local maxima near the 00 reflection in the range of 200–550 another. The applicability of the described technique for determining the ratio of the areas of steps of two superstructures in the [110] direction is confirmed by the consistency of the results obtained with the results obtained by the method of other authors in the [100] direction in terms of reflections from 1x2 and 2x1 superstructures [4]. When analyzing the reflections from the 1x2 and 2x1 superstructures lying in the Laue zone ~ 1/2, in the diffraction patterns in the [100] direction with respect to the electron beam, the intensity ratios of these reflections were obtained in a wide temperature range. It is shown that the curves obtained by both methods have a maximum at a temperature of 550°C, which indicates the predominance of one type of superstructure on the surface. Far from this temperature, the areas of

steps of both types are approximately equal. The temperature dependence of the ratio of the growth periods of steps with different superstructures in the range of 200–550°C qualitatively coincides with the previously described curves.

## Conclusion

The temperature dependence of the intensity ratio in the [100] direction relative to the electron beam at low and medium temperatures repeats the curve obtained in the [110] direction and complements it in the high temperature region. In addition, the ratios of the oscillation periods have a temperature dependence similar to that of the intensity ratios.

## REFERENCES


1. **Hafez M. A., Zayed M. K., Elsayed-Ali H. E.**, Review: Geometric interpretation of reflection and transmission RHEED patterns, Micron, Rep. 159 (2022) 103286.
2. **Dirko V. V., Lozovoy K. A., Kokhanenko A. P., Voitsekhovskii A. V.**, High-resolution RHEED analysis of dynamics of low-temperature superstructure transitions in Ge/Si(001) epitaxial system, Nanotechnology, 33(11) (2022) 1–8.
3. **Voigtlander B.**, Fundamental processes in Si/Si and Ge/Si epitaxy studied by scanning tunneling microscopy during growth, Surf. Sci. Rep. 43 (2001) 127-254.
4. **Esin M. Yu., Nikiforov A. I., Timofeev V. A., Tuktamyshev A. R., Mashanov V. I., Loshkarev I. D.,. Deryabin A. S, Pchelyakov O. P.**, Formation of a stepped Si(100) surface and its effect on the growth of Ge islands, Physics and technology of semiconductors. 52(3) (2018) 409-413.

# Chirality induction in atomically thin colloidal CdSe nanostructures

**D. A. Kurtina** ✉, **R. B. Vasiliev**
Moscow State University, Moscow, Russia
✉kurtinadaria@gmail.com

**Abstract.** Chiral nanostructures exhibiting different absorption of right- and left-handed circularly polarized light are of rapidly growing interest due to their potential applications in various fields. Here, we have studied the induction of chirality in atomically thin (0.6 and 0.9 nm thick) CdSe nanoplatelets grown by a colloidal method and coated with L-cysteine and N-acetyl-L-cysteine ligands. We conducted an analysis of the optical and chiroptical properties of atomically thin CdSe nanoplatelets, which was supplemented by a detailed analysis of the composition and coordination of ligands. Different signs of circular dichroism were shown for L-cysteine and N- acetyl-L-cysteine ligands, confirmed by different coordination of these ligands on the basal planes of nanoplatelets. A maximum value of the dissymmetry factor of $(2–3) \times 10^{-3}$ was found for N-acetyl-L-cysteine ligand in the case of the thinnest nanoplatelets.

**Keywords:** 2D semiconductors, CdSe nanoplatelets, excitons, chirality, circular dichroism, ligand exchange.

**Funding:** This study was funded by the RSF, grant number 22-13-00101.

## Introduction

Chirality is a fundamental phenomenon of nature in which the structure cannot be combined with its mirror image. Recently, chiral colloidal nanoparticles and nanostructures [1] have been of great interest, demonstrating different absorption of light with right and left circular polarization (circular dichroism, CD) or rotation of the plane of polarization of light (optical activity), as well as the emission of photons of a given circular polarization (luminescence with circular polarization). Chiral nanostructures have promising applications in biochemical, photonic and optoelectronic technologies, such as enantioselective separation and asymmetric catalysis, optical technologies and spintronics [1,2]. To obtain chiral nanoparticles from achiral semiconductors, chirality induction is used, i.e., the creation of optical activity of nanoparticles induced by chiral ligands [3]. However, understanding how the interaction of anisotropy, crystal structure, and ligand coordination in 2D nanostructures leads to strong optical activity and high CD signal remains an unsolved problem.

## Materials and Methods

In this paper, chirality induction was investigated in atomically thin colloidal nanostructures based on CdSe during the exchange of native long-chain ligands for chiral ligands of L-cysteine (L-Cys) and N-acetyl-L-cysteine (L-AcCys). Two-dimensional nanostructures of the composition $[Cd_{(n+1)}Se_{(n)}L_{(2)}]$ were synthesized, L is an X-type organic ligand (oleic acid anion), n is the number of monolayers, with extremely thin thicknesses of 0.6 and 0.9 nm (2.5 and 3.5 monolayers), specified with atomic accuracy, and lateral dimensions of 100-200 nm to achieve a pure 2D mode of quantum confinement for excitons and enhance their interaction with chiral ligands on the basal planes of nanoparticles. L-cysteine was compared with the more sterically volumetric cysteine derivative N-acetyl-L-cysteine. The developed protocols for the exchange of ligands in organic solvents of different polarities made it possible to completely cover the basal planes. The composition and coordination of ligands on the basal planes of nanoparticles were analyzed in detail using Fourier transform IR spectroscopy (FTIR). Optical and chiroptic properties of chiral atomically thin CdSe nanoplates were studied using absorption spectroscopy, luminescence and circular dichroism (CD).

## Results and Discussion

The TEM images of ligand-exchanged NPLs showed the preservation of the 2D morphology and crystal structure. Rolled nanosheets with lateral sizes of about 100 nm were found for CdSe NPLs coated with the L-AcCys ligand, similarly to OA-coated NPLs. Electron diffraction confirmed the preservation of the crystal structure of zinc blende. EDX mapping confirmed homogeneity of L-AcCys ligand covering of the basal planes of CdSe NPLs. Different signs of circular dichroism have been established for L-cysteine and N-acetyl-L-cysteine ligands, which is confirmed by the different coordination of these ligands. The maximum value of the dissymmetry factor (2-3) × $10^{-3}$ was found for N-acetyl-L-cysteine for extremely thin nanostructures.

## Conclusion

This work demonstrates that the exchange with cysteine-based ligands on the basal planes of atomically thin CdSe NPLs leads to an effective induction of chirality with distinct bands of CD exciton transitions. We successfully grew atomically thin 2.5 and 3.5 ML (0.6–0.9 nm thick) CdSe with zinc blende modification nanoplatelets covered by long-chain ligand by the colloidal method in ODE–OA–cadmium acetate system. Exchange with chiral ligands induces a shift of excitonic bands due to the thiolate group hybridization, together with the appearance of strong CD bands in CD spectra. The values of the dissymmetry factor for ultimate atomically thin nanoplatelets exceed those for thicker samples. At the same time, the dissymmetry factor for the N-acetyl- L-cysteine ligand exceeds the value for L-cysteine, confirming that the N-acetyl-L-cysteine is of interest for inducing chirality, along with the commonly used L-cysteine. Exchange of the N-acetyl-L-cysteine ligand to L-cysteine leads to an inversion of the CD spectra, which emphasizes the reorientation of the molecular dipoles of the chromophore of the ligand and the exciton transition in the core of the nanoplatelet. Our work gives new strategies for the synthesis of chiral 2D nanostructures.

## Acknowledgments

FTIR experiments were carried out using the equipment purchased by funds from the Lomonosov Moscow State University Program of the Development. TEM experiments were carried out using equipment of the “Nanochemistry and Nanomaterials” center, supported by the Program of Development of Lomonosov Moscow State University. The CD measurements were carried out on the equipment of the Shared-Access Equipment Centre “Industrial Biotechnology” of Federal Research Center “Fundamentals of Biotechnology” Russian Academy of Sciences.

## REFERENCES

1. Ma W., Xu L., de Moura A.F., Wu X., Kuang H., Xu C., Kotov N.A. Chiral Inorganic Nanostructures // Chem. Rev. 2017. Vol. 117.

2. Naaman R., Paltiel Y., Waldeck D.H. Chiral Molecules and the Electron Spin // Nat. Rev. Chem. 2019. Vol. 3.

3. Kurtina D.A., Grafova V.P., Vasil’eva I.S., Maksimov S.V., Zaytsev V.B., Vasiliev R.B. // Materials. 2023. Vol. 16.

# Formation of symmetrical nanoholes by local droplet etching for site-controlled growth of single quantum dots

**E. A. Lakhina✉, N. E. Chernenko, N. A. Shandyba, D. V. Kirichenko, S. V. Balakirev, M. S. Solodovnik**

Laboratory of Epitaxial Technologies, Institute of Nanotechnologies, Electronics and Equipment Engineering, Southern Federal University, Taganrog 347922, Russia

✉lakhina@sfedu.ru

**Abstract.** In this paper, we study local etching of the GaAs(001) surface by Ga droplets at various technological conditions. Effects of the deposition temperature and thickness, interruption time, annealing temperature and arsenic background pressure are discussed. A minimum deposition thickness of 1.5 ML Ga is found to be sufficient to etch the GaAs surface. We demonstrate that an increase in the annealing temperature leads to a decrease in the hole depth and an increase in their diameter. For the first time, we obtain symmetrical nanoholes of pyramidal shape with a low surface density (~$1\cdot10^8$ cm$^{-2}$) allowing subsequent formation of single quantum dots for high-efficiency quantum photonic devices.

**Keywords:** epitaxy, local droplet etching, gallium arsenide, A3B5.

**Funding:** This work was supported by the Russian Science Foundation Grant No. 22-79-10251, https://rscf.ru/project/22-79-10251/, and by the Ministry of Science and Higher Education of the Russian Federation Grant No. FENW-2022-0034 at the Southern Federal University.

## Introduction

InAs quantum dots (QDs) obtained by molecular beam epitaxy (MBE) on GaAs substrates have broad prospects for application in quantum photonic devices due to their unique optical properties. However, for the full implementation of these devices, QDs must have a low surface density to be considered as single objects as well as high lateral symmetry, which can be achieved using the preliminary formation of nanoholes by a method of local droplet etching.

The purpose of this work is an experimental study of technological conditions of Ga/GaAs(001) droplet etching which make it possible to obtain symmetrical pyramidal-shaped nanoholes with a density of about $1\cdot10^8$ cm$^{-2}$.

## Materials and Methods

After MBE growth of 250-nm-thick GaAs buffer layer on the (001) surface, the arsenic source was closed to provide a low background pressure in the chamber (from $1.5\cdot10^{-7}$ Pa to $3.5\cdot10^{-7}$ Pa). Then, Ga atoms were deposited on the surface in the amount of 1.1 to 5 equivalent monolayers (ML) at different substrate temperatures in the range from 400 to 500°C. At the next stage, the substrate was annealed to 550°C, 580°C, and 610°C for 15 and 30 minutes. After the annealing, the samples were cooled down and unloaded from the chamber for characterization in atomic force (AFM) and scanning electron microscopes (SEM).

## Results and Discussion

AFM images of hole arrays obtained after etching by droplets formed at various deposition amounts of Ga at a temperature of 500°C are shown in Fig. 1. An analysis of the results obtained indicates that 1.1 ML Ga is not enough to obtain droplets capable of etching deep nanoscale regions of the surface. At the same time, in other cases, there are arrays of holes with different average diameters which increase as the amount of deposited material increases. The depth of the formed holes increases from 1.6 nm for 2 ML to 5.3 nm for 5 ML Ga, which is associated with an increase in the droplet volume.

An increase in the annealing temperature from 580°C to 610°C leads to a decrease in the hole depth from 4.3 to 1.0 nm and an increase in their average diameter from 103 to 159 nm. Despite the removal of the characteristic rim formed as a result of droplet crystallization in the arsenic flux at the boundary of the triple point, a decrease in the depth and an increase in the hole diameter reduce the attractiveness of using the holes formed at $T$ = 610°C due to a decrease in the

probability of island nucleation in them or the potential initiation of polycentric nucleation observed in holes with a large diameter.

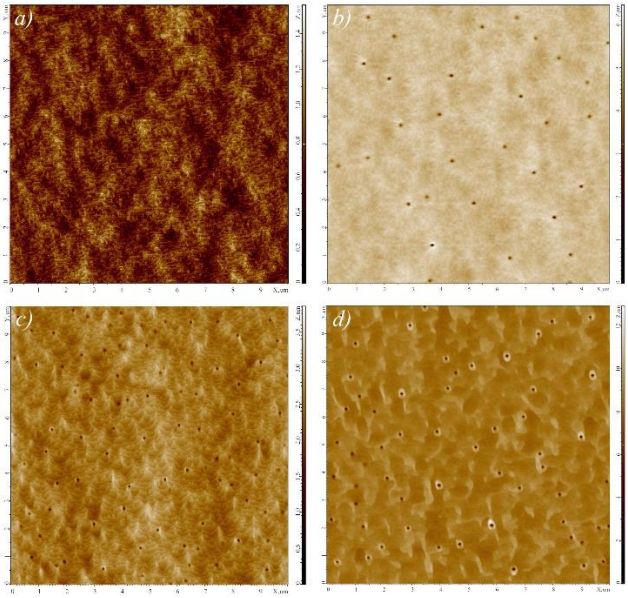


Fig. 1. AFM images of the GaAs surface after etching by droplets formed at various amounts of deposited Ga: 1.1 ML (a), 1.5 ML (b), 2.0 ML (c) and 5 ML (d).

Symmetric pyramidal holes with the required surface density were obtained by reducing the background arsenic pressure to values below $1.5 \cdot 10^{-7}$ Pa with the annealing at 550°C during various time periods from 15 to 30 min. Fig. 3 shows AFM and SEM images of the obtained samples, as well as a cross-section of a typical nanohole for two mutually perpendicular directions.

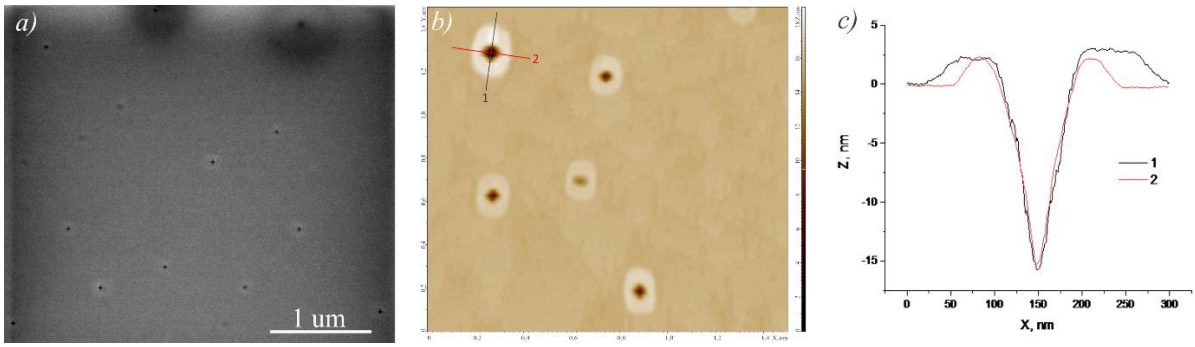


Fig. 2. GaAs surface after etching by Ga droplets at an arsenic pressure of 1.5 $10^{-7}$ Pa and different annealing time: a) 30 min (SEM image), b) 15 min (AFM image), c) AFM cross sections of the hole shown in Fig. 3b.

According to AFM cross sections in Fig. 3c, a typical hole for the obtained samples has sidewalls in the form of flat faces and the same shape and size in different lateral directions. The hole is characterized by the presence of an extended 2-nm-high rim, which has an anisotropic shape due to the difference in the surface diffusion coefficients depending on the direction. However, the hole depth in this case reaches 15 nm, which has a positive effect on the further localization of epitaxial nanostructure within it.

## Conclusion

Thus, pyramidal nanoholes for the subsequent localization of highly symmetrical QDs in them can be obtained on the GaAs(001) surface by local etching with Ga droplets at a low background arsenic pressure (below 1.5 $10^{-7}$ Pa) and annealing temperature of 550°C.

# Optical and electrochemical properties of a composite material based on PEDOT-PSS and oriented nickel fibers

**E. M. Lebedeva [1✉], G. R. Nizameeva [1,2], R. R. Gainullin [1], V.V. Kuznetsova [1,3], S. V. Spiridonov [3], I. R. Nizameev [1, 3]**

[1] Arbuzov Institute of Organic and Physical Chemistry, FRC Kazan Scientific Center of RAS, Kazan, Russia;

[2] Kazan National Research Technological University, Kazan, Russia;

[3] Kazan National Research Technical University Named after A.N. Tupolev-KAI, Kazan, Russia

✉e-mail: elgina.lebed@mail.ru

**Abstract.** In this paper, to improve the efficiency of dangerous gas detection, it is proposed to use composite materials by introducing oriented nickel fibers into the PEDOT-PSS polymer chain. The electrochemical behavior of the PEDOT-PSS film and the PEDOT-PSS/oriented nickel fibers composite material in a 0.1 M C16H36BF4N solution in acetonitrile was studied. The possibility of using the obtained material to create optical sensors for greenhouse gases was shown.

**Keywords:** gas sensor, PEDOT-PSS, glass three-electrode electrochemical cell, bandgap

**Funding:** The reported study was funded by the government assignment for FRC Kazan Scientific Center of RAS.

## Introduction

Studies of composite materials based on a polymer matrix and various functional materials dispersed in this matrix [1], such as metal oxide nanoparticles, graphene, carbon nanotubes, etc., have been widely developed in recent years. The increased interest in such materials is associated with the possibility of their application in supercapacitors [2], in catalysis, and also as an active element in greenhouse gas sensors (such as carbon dioxide and nitrogen dioxide) [3]. The creation of composite materials for sensors is of particular interest, given the relevance of the problem of monitoring the environment. Among the conductive polymers used to create composite materials, PEDOT-PSS occupies a special place [4] due to such properties as stability, high and controllable conductivity, and commercial availability [5]. However, pure PEDOT-PSS film has low greenhouse gas sensitivity. Therefore, to increase the efficiency in the detection of toxic gases, it is advisable to develop composite materials by introducing various materials into the PEDOT-PSS polymer matrix. In this work, oriented nickel fibers are introduced into PEDOT-PSS, which are evenly distributed in a porous polymer matrix.

## Materials and Methods

The performance of sensors is determined by chemical and physical properties that must remain stable over a long period of time. In the course of this work, the electrochemical properties of a pure PEDOT-PSS polymer film and a composite PEDOT-PSS/oriented nickel fibers were studied. Electrochemical studies were carried out in a glass three-electrode cell. A fluoroplastic cylindrical tube was used as the working electrode, into the end of which glassy carbon 3 mm in diameter was pressed. A platinum electrode was used as a counter electrode, and a silver chloride electrode (Ag/AgCl) in a saturated NaCl solution was used as a reference electrode. A solution of 0.1 M $C_{16}H_{36}BF_4N$ (tetrabutylammonium tetrafluoroborate) in acetonitrile was used as the electrolyte. All potential values of the electrode under study are given relative to the Ag/AgCl silver chloride electrode.

## Results and Discussion

Electrochemical studies showed the stability of PEDOT-PSS and PEDOT-PSS/oriented nickel fibers in the cycling range from -1.2 V to 1.2 V (Figure 1). With a further increase in the

cycling range, the electrical properties of the films begin to deteriorate, and at potentials above 1.2 V, a sharp increase in the anode current is observed, associated with the irreversible oxidation of the PEDOT-PSS film. It is known that PEDOT-PSS is a transparent conductive polymer with a wide bandgap. The bandgap of the PEDOT-PSS film was calculated from the CV curves. It turned out to be equal to 1.56 eV, which is in good agreement with the literature data. For the composite film PEDOT-PSS/oriented nickel fibers, the bandgap remained unchanged. This suggests that this material can still be used as an optical sensor for the express analysis of greenhouse gases.

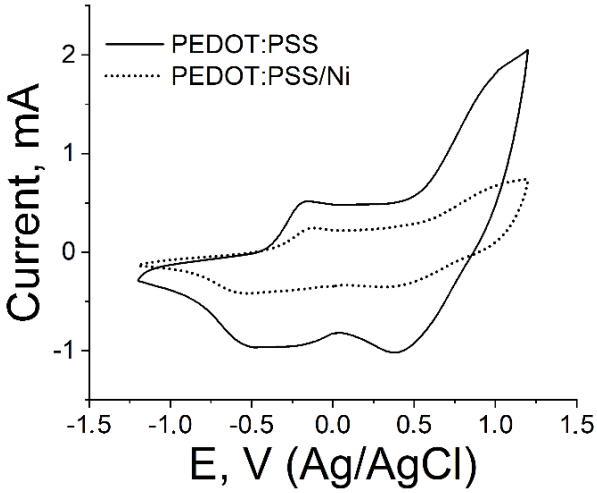


Fig. 1. Cyclic voltammograms of PEDOT-PSS and PEDOT-PSS/ oriented nickel fibers.

## Conclusion

The composite material was obtained by introducing oriented nickel fibers into the PEDOT-PSS polymer matrix. Electrochemical studies of the PEDOT-PSS film showed that, at potentials above 1.2 V, the polymer is overoxidized. From the results of the CV curves, the bandgap for PEDOT-PSS and PEDOT-PSS/oriented nickel fibers was calculated, the value of which for both materials is 1.56 eV.

## REFERENCES

1. **Yao X., Cui Y.**, A PEDOT: PSS functionalized capacitive sensor for humidity, Measurement. 160 (2020) 107782.

2. **Ouyang, J. Y.**, Recent advances of intrinsically conductive polymers, Acta Phys.-Chim. Sin. 34 (11) (2018) 1211-1220.

3. **Kaur G., Kaur A., Kaur H.**, Review on nanomaterials/conducting polymer based nanocomposites for the development of biosensors and electrochemical sensors, Polymer-Plastics Technology and Materials. 60 (5) (2021) 504-521.

4. **Mantione D., Del Agua I., Sanchez-Sanchez A., Mecerreyes D.**, Poly (3, 4-ethylenedioxythiophene)(PEDOT) derivatives: Innovative conductive polymers for bioelectronics, Polymers. 9 (8) (2017) 354.

5. **Gao N., Yu J., Tian Q., Shi J., Zhang M., Chen S., Zang L.**, Application of PEDOT: PSS and its composites in electrochemical and electronic chemosensors, Chemosensors. 9 (4) (2021) 79.

Conference materials
UDC 535.372
DOI: https://doi.org/10.18721/JPM.

# Effect of femtosecond irradiation on the luminescence of $CsPbI_3$ perovskite crystals in borogermanate glass

**A. L. Losin** ✉, **A. N. Babkina**, **R. D. Kharisova, E. V. Kulpina, K. S. Zyryanova, M. M. Sergeev**
[1] ITMO University, St. Petersburg, Russia;
✉arthurlosin1@gmail.com

**Abstract.** The article demonstrates femtosecond-laser-induced crystallization of $CsPbI_3$ perovskite nanocrystals in borogermanate glass with no additional heat treatment. With an increase in the laser radiation energy, the mean size of the precipitated crystals increases, which leads to the luminescence redshift towards 700 nm.

**Keywords:** Cesium lead iodide perovskite, borogermanate glass, femtosecond irradiation, laser-induced crystallization.

**Funding:** This work was funded by Russian Science Foundation (No. 19-72-10036).

**Citation:** Losin A. L., Babkina A. N., Effect of femtosecond irradiation on the luminescence of $CsPbI_3$ perovskite crystals in borogermanate glass, St. Petersburg State Polytechnical University Journal. Physics and Mathematics. 16 ( ) (2023) …–…. DOI: https://doi.org/10.18721/JPM.

This is an open access article under the CC BY-NC 4.0 license (https://creativecommons.org/licenses/by-nc/4.0/)

© Author A. A., Author B. B., 2023. Published by Peter the Great St. Petersburg Polytechnic University.

Материалы конференции
УДК 535.372
DOI: https://doi.org/10.18721/JPM.

## Introduction

Cesium lead halide ($CsPbX_3$) quantum dots (QDs) have attracted big attention because of their remarkable optical properties, such as size-dependent emission wavelengths, narrow emission spectra and high photoluminescence quantum yields [1]. They possess great potential applications in light-emitting diodes, lasers, solar cells and photodetectors. Traditionally, heat-treatment is a favorable way to realize controllable nucleation and crystal growth, and the optical properties of QDs can be guaranteed for a long-term period. On the other hand, femtosecond laser [2], due to its short pulse width and high peak power, can induce high transient temperature field, which is enough for the nuclei formation of QDs. Nonlinear absorption process happens while the fs laser interacts with the glass matrix, leading to the destruction of the glass network and the redistribution of atoms at the laser focal area, which is beneficial for ion migration to form nanocrystals and for the reduction in crystallization temperature.

Here, the luminescent properties of $CsPbI_3$ nanocrystals, obtained by laser-induced crystallization in borogermanate glass are demonstrated.

## Materials and Methods

The initial glass matrix had the following composition: 6.67 ZnO-5.81 $Na_2O$-31.3 $B_2O_3$-50.53 $GeO_2$ mol. %. The synthesis was carried out in air atmosphere at a temperature of 950°C using closed quartz crucibles. For the subsequent nucleation of $CsPbI_3$ perovskite nanocrystals, $CsCO_3$, PbO and KI were added to the batch composition. The luminescence spectra were

studied with a Renishaw inVia Raman Microscope of 100 - 3200 $cm^{-1}$ working range at room temperature with the excitation wavelength of 633 nm and 50x build-in lens. Laser-driven crystallization was obtained by ANTAUS femtosecond laser (AVESTA, pulse duration 224 fs, pulse frequency 50 kHz). The pulses number at the laser exposure in the bulk material ranged from 500 to 500 000. The laser radiation energy varied from 0.01 to 3.23 μJ.

## Results and Discussion

Figure 1a shows photographs of the patterns obtained by varying the power and duration of laser exposure. Figure 1b shows the luminescence spectra obtained after different laser energy. The luminescence maximum lies in the region of 680–700 nm and the FWHM is about 30-40 nm, which is typical for $CsPbI_3$ perovskite nanocrystals in glass. As the laser radiation energy decreased, the luminescence spectrum of the nanocrystals shifted from 700 nm to 680 nm, while FWHM increased from 35 to 45 nm. Such transformations of the luminescence of semiconductor crystals indicate the presence of a size effect: with an increase in the mean size of QDs, the luminescence spectrum shifts into long wavelengths and narrows. This means that with an increase in the laser exposure energy, the mean size of the crystals increases. It has been shown [3] that perovskite crystals precipitate only during the subsequent heat treatment of glass; in our case, this is observed immediately after laser exposure.

*a*) *b*)

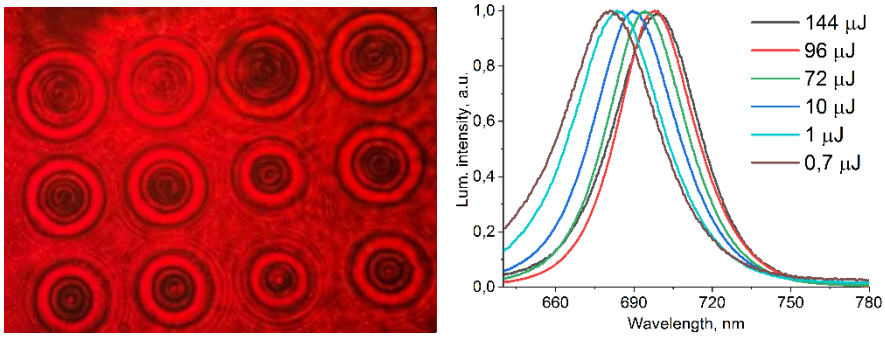


Fig. 1. Photo of patterns in glass after femtosecond irradiation (*a*) and luminescence spectra of $CsPbI_3$ QDs obtained after different laser energy exposure (*b*)

## Conclusion

Femtosecond-laser-induced crystallization of $CsPbI_3$ perovskite nanocrystals in borogermanate glass with no additional heat treatment was demonstrated. With an increase in the laser radiation energy, the mean size of the precipitated crystals increased, which led to the luminescence redshift from 680 up to 700 nm and FWHM decrease from 45 down to 35 nm.

## REFERENCES

1. **Protesescu L., Yakunin S., Bodnarchuk M. I., Krieg F., Caputo R., Hendon C. H., Yang R. X., Walsh A., Kovalenko M. V.**, Nanocrystals of Cesium Lead Halide Perovskites (CsPbX3, X = Cl, Br, and I): Novel Optoelectronic Materials Showing Bright Emission with Wide Color Gamut, Nano Lett. 15 (6) (2015) 3692–3696.

2. **Sun K., Tan D., Fang X., Xia X., Lin D., Song J., Lin Y., Liu Z., Gu M., Yue Y., Qiu J.**, Three-dimensional direct lithography of stable perovskite nanocrystals in glass, Science. 375 (6578) (2022) 307–310.

3. **Huang X., Guo Q., Kang S., Ouyang T., Chen Q., Liu X., Xia Z., Yang Z., Zhang Q., Qiu J., Dong G.**, Three-Dimensional Laser-Assisted Patterning of Blue-Emissive Metal Halide Perovskite Nanocrystals inside a Glass with Switchable Photoluminescence, ACS Nano 14 (3) (2020) 3150–3158.

## THE AUTHORS

**LOSIN Arthur L.**
arthurlosin1@gmail.com
ORCID: 0009-0009-6544-3674

**BABKINA Anastasiia N.**
babkina.anastasya@bk.ru
ORCID: 0000-0003-0784-1585

**KHARISOVA Rufina D.**
harisovarufina@gmail.com
ORCID: 0000-0000-0000-0000

**KULPINA Ekaterina V.**
katrinakulpina@yandex.ru
ORCID: 0000-0003-2896-2896

**ZYRYANOVA Ksenia S.**
ms.z.k.s@mail.ru
ORCID: 0000-0001-6733-1443

**SERGEEV MAKSIM M.**
e-mail: mmsergeev@itmo.ru
ORCID: 0000-0003-2854-9954

# Doping and thermoelectric characteristics of $Ge_{0.3}Si_{0.7}:P_{\delta}$ synthesized by powder sintering

**Yu M Kuznetsov[1], M V Dorokhin[1], P B Demina[1], I V Erofeeva[1] и A V Zdoroveyshchev[1]**

[1]Lobachevsky state university, 603022, Russia, Nizhny Novgorod, Gagarin Avenue 23 b.3

E-mail: y.m.kuznetsov@unn.ru

**Annotation**. The paper describes the technological parameters of the formation of the $Ge_{0.3}Si_{0.7}$ solid solution in a spark plasma sintering unit. A new method for alloying a solid solution during synthesis from a source of silicon phosphide is proposed. A comparative analysis of the transport and thermoelectric properties of the obtained samples depending on the dopant concentration is given.

## 1. Introduction

Thermoelectrics are materials that convert thermal energy into electrical one. The thermoelectric figure of merit (*ZT*) is a dimensionless coefficient that characterizes the conversion efficiency which is determined by the expression [1]:

$$ZT = \alpha^2 T/\rho\lambda, \quad (1)$$

where $\alpha$ – Seebeck coefficient, $\rho$ – resistivity, $\lambda$ – thermal conductivity.

For instrumental implementation, the material must possess $ZT > 1$. The recent trends are directed towards studying the *ZT* of $Ge_xSi_{1-x}$ semiconductor ceramics formed by nanopowder sintering. Such materials have a record low $\lambda$ while maintaining high $\alpha$ and low $\rho$ [2].

## 2. Experimental technique

A feature of this work is the use of non-toxic SiP as a source of a donor dopant of a GeSi solid solution. Such an approach makes it possible to avoid the use of toxic P, thereby significantly facilitating work with the initial powders. The powders were obtained by preliminary and fine grinding in a Fritsch Analysette 3 Pro ball mill and a Fritsch Pulverisette 6 planetary mill (250 rpm, 6 hours), respectively. The average particle size of the powder mixture was estimated on a Jeol JSM-IT300LV scanning electron microscope to be ~ 1 μm. The powders were sintered in a DR-SINTER SPS-625 Spark Plasma Sintering System (SPS) at a pressure of 70 MPa and a temperature of 1040 °C. The sintering rate was 50 °C/min. A series of four samples was formed, in which the concentration of P was varied.

The registration of the temperature dependence of α was carried out during the creation of a controlled temperature gradient with subsequent measurement of the thermo-EMF signal. The value of $\rho$ was measured using a standard four-contact circuit. The temperature dependence of $\lambda$ was obtained by the method of stationary heat flow. *ZT* was calculated using formula (1). The concentration of free charge carriers was calculated from the magnetic field dependence of the Hall resistance. Measurement techniques are described in [3].

## 3. Results

The experimentally obtained temperature dependences of the thermoelectric parameters of the samples are shown in Figures 1-4. In addition, the results are compared with the record-breaking characteristics of $Ge_{0.2}Si_{0.8}:P_{0.02}$ from [2], a distinguishing feature of which was an extremely small powder particle size of ~30 nm.

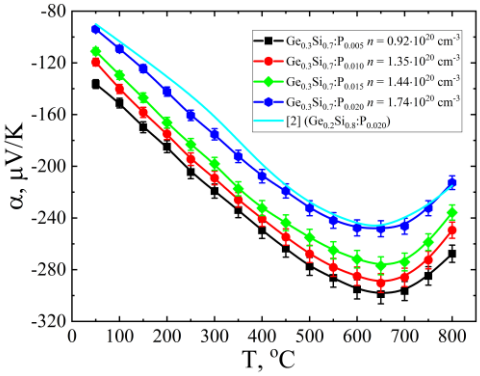


**Figure 1.** Temperature dependence of $\alpha$

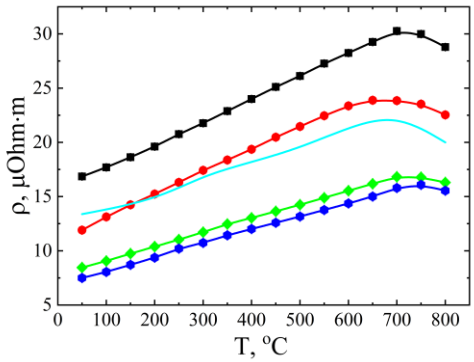


**Figure 2.** Temperature dependence of $\rho$

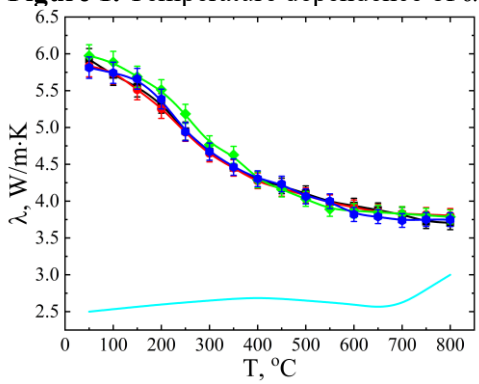


**Figure 3.** Temperature dependence of $\lambda$

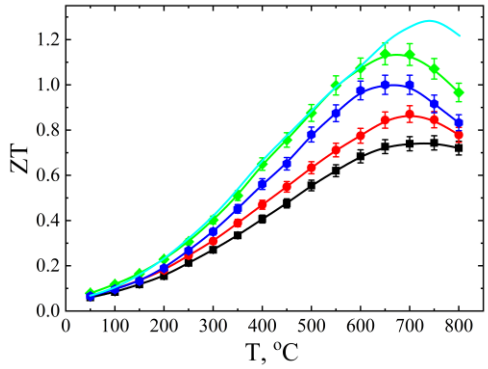


**Figure 4.** Temperature dependence of $ZT$

The largest ZT in the entire measured temperature range is possessed by a sample containing 1.5 at. %. ($ZT = 1.16$), which is only 9% less than stated in [2]. At the same time, a significantly simplified technology was used in our work.

## 4. Conclusions

The paper shows a new method of doping with phosphorus nanostructured thermoelectric materials based on a solid solution of germanium-silicon in the process of synthesis by spark plasma sintering. The optimum level of doping is established, at which high values of $ZT$ are achieved.


## Acknowledgement

The work was supported by the Ministry of education and science of Russian Federation in the frames of federal task (project № FSWR-2023-0037). The authors are grateful to Dr. A.Yu. Zavrazhnov and I.N. Nekrylov for the synthesis of SiP, as well as to the engineer of the NIFTI UNN A.V. Voronin for experiments on sample sintering.


## References


[1] Hicks D and Dresselhaus M S 1993 *Phys. Rev. B* **47** 16631

[2] Wang X W, Lee H, Lan Y C, Zhu G H, Joshi G, Wang D Z, Yang Z,Mut A J, Tang M Y, Klatsky J, Son S, Dresselhaus M S, Chen G, and Ren Z F 2008 *Appl. Phys. Lett.* **93** 193121

[3] Erofeeva I V, Dorokhin M V, Lesnikov V P, Kuznetsov Yu M, Zdoroveyshchev A V, Pitirimova E S 2017 *Sem.* **51** 1403

# Flexible Green Perovskite $CsPbBr_3$ LED Integrated with SiNW Array

**V. A. Mastalieva [1✉], V. V. Neplokh [1,2], A.A. Yakubova [1,2], E.A. Vyacheslavova [1], A.S. Gudovskikh [1], D.M. Mitin [1,2], S.V. Makarov [3], I.S. Mukhin [1,2]**

[1] Alferov University, Saint Petersburg, Russia;

[2] Peter the Great St. Petersburg Polytechnic University, Saint Petersburg, Russia;

[3] ITMO University, Saint Petersburg, Russia

✉strindberg76@mail.ru

**Abstract.** Flexible optoelectronic devices have attracted significant attention due to their potential applications in wearable technology, biomedical devices, and flexible displays. In this article, we report on the fabrication and characterization of a flexible green light-emitting diode (LED) based on silicon nanowires and CsPbBr3 perovskite nanocrystals. The device exhibits a peak emission wavelength of 530 nm with a full width at half maximum of 27 nm. The flexibility of the LED was demonstrated by its ability to be bent to a radius of curvature as small as 5 mm without significant changes in its optical properties. The results suggest that the proposed flexible LED has potential applications in flexible optoelectronics.

**Keywords:** silicon nanowires, perovskite, $CsPbBr_3$ thin film, silicon, LED.

**Funding:** This study was funded by grant from the Russian Science Foundation № 22-79-10286

## Introduction

Flexible light-emitting diodes (LEDs) have emerged as a promising technology for various applications due to their flexibility, lightweight, and ease of integration with various substrates. Among various materials, silicon and perovskite nanocrystals have attracted significant attention as promising candidates for flexible LEDs. In this thesis, we present the design, fabrication, and characterization of a flexible green LED based on silicon nanowires and CsPbBr3 perovskite nanocrystals. The device exhibits excellent optical properties and mechanical flexibility, which make it suitable for various applications in flexible optoelectronics.

## Materials and Methods

1. Sample Fabrication

1.1. Fabrication of LED-on-Silicon

Fabrication of an LED on a silicon substrate took place in several stages. The first stage was the deposition of ytterbium metal onto NWs on a substrate in order to protect the silicon material during the subsequent etching in a mixture of $O_2$ and $CF_4$ plasma.

In order to encapsulate 5.6 μm long Si NWs into PDMS we utilized the G-coating method which is ideal for creating thin PDMS membranes [1]. We mixed a commercial PDMS (Dow Corning Sylgard 184) in a standard base to curing agent ratio of 10 to 1 to form the silicone membrane. To achieve electrical contact formation, we used $O_2/CF_4$ plasma etching to open the tips of NWs and ensure a consistent thickness of the PDMS membrane at approximately 4.5 μm, revealing the NW top parts above the PDMS membrane surface. After revealing the Si NW top parts, the substrate was treated with a hydrochloric acid (HCl) to remove the metal from the exposed SiNW tips. [2] The surface of the sample was then treated in oxygen plasma with $O_2$ flow parameters of 60 sccm and the RF power of 400 watt. After treating the NW top parts, perovskite in a volume of 20 μl was spun on the surface of the sample at 600 rpm, spin acceleration 600 rpm/sec for 1 minute, then dried on a hotplate at 60 degrees for perovskite crystallization. Transparent, flexible SWCNT films were used to form square contact pads of

about 1 $mm^2$. After applying SWCNT pads to the surface of the sample, electroluminescence measurements were made for the as-processed LED-on-Si samples.

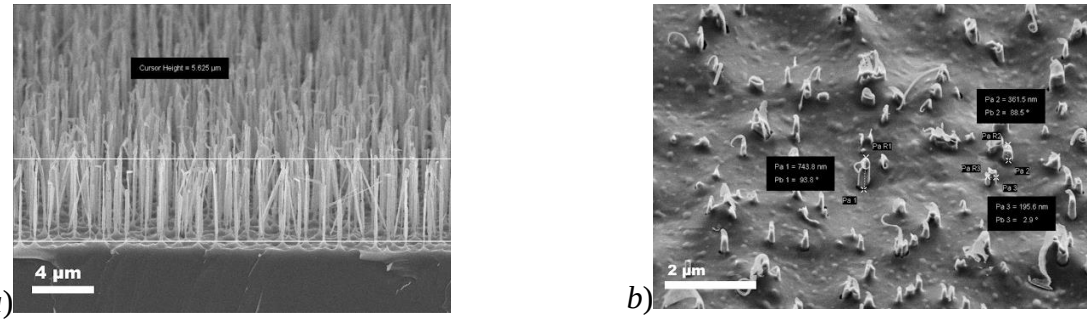


*a*) *b*)

Fig. 1. SEM image of Si NWs on a substrate produced by metal-stimulated chemical etching of silicon without polymer (*a*) SEM image of revealed top parts of Si NWs in the PDMS membrane after etching of the PDMS in $O_2/CF_4$ plasma mixture (*b*)

1.2. Fabrication of Flexible Green Membrane

After the measurements have been taken the PDMS/NW membranes were mechanically peeled from the Si substrate using a microtome blade. The membranes were then flipped to apply the bottom contact, and 1mm2 SWCNT contact pads were again applied directly opposite the top contact pads, resulting in several areas on both sides of the membrane that were in contact with SWCNT.

## Results and Discussion

2. Electroluminescence Characterization

To test the fabricated samples of LEDs-on-Si and flexible LEDs, we used a Keithley 2400 sourcemeter and a probe station. For the LEDs-on-Si, the front contact was made directly on the SWCNT contact pad, while the rear contact was made to the metallized Si substrate using the conductive table of the probe station. The flexible LED samples were contacted in a similar manner. The EL spectrum of a representative LED-on-Si (Figure 2) was obtained at a different current of 115mA. The EL line position is 530 nm, and the full width of the half-maximum is 27 nm.

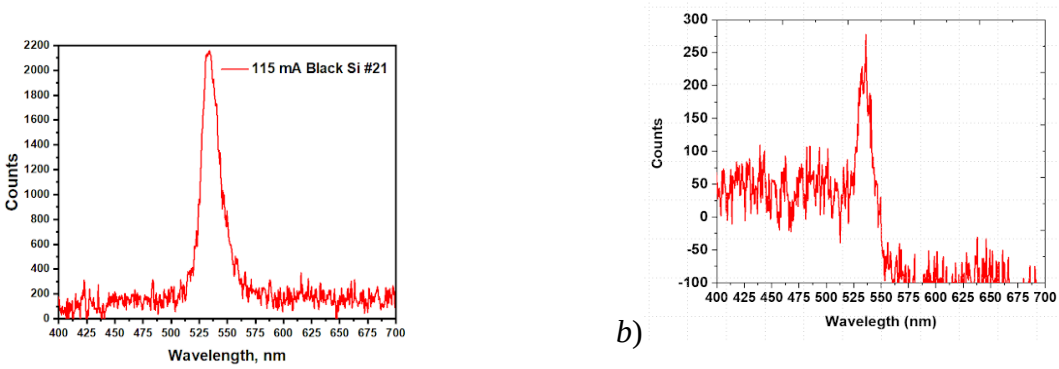


*a*) *b*)

Fig. 2. Luminescence graph from the LEDs-on-Si excited by an electric field with a current of 115 mA (*a*) Luminescence graph from the flexible LEDs (*b*)

## Conclusion

In conclusion, we have successfully demonstrated the novel design, fabrication, and characterization of flexible green LEDs based on silicon nanowires and $CsPbBr_3$ perovskite nanocrystals. The device exhibits excellent optical properties and mechanical flexibility, which make it a promising candidate for various applications in flexible optoelectronics.


## Acknowledgments

The research was supported by grant from the Russian Science Foundation № 22-79-10286


## REFERENCES


1. **Kochetkov, F.M.; Neplokh, V.V.; Deriabin, K.V.; Fedorov, V.V.; Bolshakov, A.D.; Eliseev, I.E.; Mikhailovskii, V.Y.; Ilatovskii, D.A.; Krasnikov, D.V.; Tchernycheva, M.** Fabrication and electrical study of large area free-standing membrane with embedded GaP NWs for flexible devices. Nanotechnology 2020, 31, 46LT01.
2. **Morozov I** 2020 Physico-technological foundations of microstructuring processes for the creation of vertically oriented photoconversion structures based on silicon: Dis. Cand. Tech. Sciences 161.

# Two-photon lithography of composite nanostructures for bioelectronic applications

**D. T. Murashko [1✉], E. P. Otsupko [1], P.N. Vasilevsky [1,2], D.I. Ryabkin[1,3]**

[1] National Research University of Electronic Technology (MIET), Moscow, Russian Federation;

[2] Institute of Nanotechnology of Microelectronics of the Russian Academy of Sciences, Moscow, Russian Federation;

[3] Sechenov First Moscow State Medical University, Moscow, Russian Federation;

✉skorden@outlook.com

**Abstract.** Two-photon lithography is an addictive technology that enables the creation of precise and complex three-dimensional composite nanostructures with subdiffraction resolution. Materials formed by this method are capable of responding to external influences, which in the future will allow the creation of materials for tissue engineering, microsensors or devices for bioelectronic applications.

The described composite nanostructure was formed from a dispersion consisting of the following components: bovine serum albumin, rose Bengal as a photoinitiator, and multi-walled carbon nanotubes. These components were dissolved in phosphorus buffer solution. The Ti:saphire fs laser was used to form the composite nanostructure with the size of 100x100 μm. Laser exposure characteristics were: pulse duration 140 fs, wavelength 800 nm, pulse frequency 80 MHz, laser power up to 30 mW. The formation of the structure was confirmed by atomic force microscopy images. The investigation of the mechanical properties showed that the Young's modulus of the formed composite nanostructure was ~200 GPa, and its hardness was ~1.6 higher compared to the bovine serum albumin without filaments. The investigation of the conductive properties showed that the formed composite nanostructure has the conductive properties when the applied voltage is in the range of -3 to 3 V.

**Keywords:** composite nanostructures, carbon nanotubes, two-photon polymerization, laser

**Funding:** The study was supported by the Russian Science Foundation grant No. 22-75-00089, https://rscf.ru/project/22-75-00089/.

## Introduction

Two-photon lithography, also known as two- or multiphoton laser lithography, is a technique for creating three-dimensional structures with a resolution of less than 100 nm using laser light. When exposed to a near infrared (NIR) laser, the source material photopolymerises in the focal volume region to form complex micro- and nanostructures.

Two-photon lithography is based on the phenomenon of multiphoton absorption, a non-linear process in which an atom or molecule transitions to an excited state by absorbing two or more photons simultaneously [1].

A special feature of multiphoton laser lithography is direct printing in volume. The non-linear nature of the two-photon absorption and the relatively small absorption cross section of the materials allow the spatial confinement of the excitation near the beam trap, so that direct laser printing in volume can be achieved without layer-by-layer material deposition [1].

## Materials and Methods

Synthetic photoresists are not used for biological applications due to the cytotoxicity of the resins they contain. To create a biocompatible structure, polysaccharides and proteins, which are the main elements of the extracellular matrix, are usually used [2, 3]. We chose bovine serum albumin (BSA) as the biopolymer because of its wide availability and well-studied properties. The organic dye rose Bengal with an absorption peak at 540 nm was used as the photoinitiator.

Despite their excellent biocompatibility and wide availability, natural polymers have inferior physical and chemical properties compared to synthetic photoresists. Therefore, multi-walled carbon nanotubes (MWNTs) "Taunit-M" were added to the material to improve the mechanical properties and provide electrical conductivity. The outer diameter of the tubes is 10-

30 nm, the inner diameter is 5-15 nm and the length is greater than 2 μm [4]. Carbon nanotubes were dissolved in 5 g/l distilled water. BSA, rose Bengal and MWNT were dissolved in phosphate buffer solution.

The structure was formed using a femtosecond pulsed Ti:sapphire laser. The irradiation wavelength was 800 nm, the pulse duration was 140 fs and the repetition frequency was 80 MHz. An OAGP-10-S optical attenuator with a Glan prism was used to control the irradiation power (up to 30 mW). Focusing of the laser radiation onto the sample was performed using an optical microscope with 60x magnification (NA = 0.65). The samples were moved under the radiation using an XY 8MTF motorised scanning stage.

## Results and Discussion

The mechanical properties of the nanostructure were investigated using the Nanoscan-4D Compact nanohardness tester. The study of mechanical properties showed that the Young's modulus for the formed nanostructure is ~200 GPa and its hardness is 1.6 times higher compared to albumin without filler. In a study of the electrical conductivity properties, it was found that the formed composite nanostructure exhibits conductive properties when a voltage in the range of -3 to 3 V is applied. The slide shows images of the formed nanostructure obtained with an atomic force microscope and the main characteristics of the structure.

## Conclusion

We have studied the possibilities of using two-photon lithography for the production of composite nanostructures. The process of forming composite nanostructures using two-photon lithography is presented. Mechanical and conductive properties of composite nanostructures studied.

## REFERENCES

1. **Ovsianikov A.** Investigation of two-photon polymerization technique for applications in photonics and biomedicine. – Cuvillier Verlag, 2009.

2. **Skliutas E. et al.** Photopolymerization mechanisms at a spatio-temporally ultra-confined light //Preprints. – 2020.

3. **Wang X. et al.** Biomaterial-based microstructures fabricated by two-photon polymerization microfabrication technology //RSC advances. – 2019. – Vol. 9. – N 59. – P. 34472-34480.

4. Сайт ООО "НаноТехЦентр" [Электронный ресурс]. URL: http://www.nanotc.ru/producrions/87-cnm-taunit (дата обращения: 02.03.2023)

# Microwave synthesis and modification of carbon dots for application as labels in immunoassay

**P. D. Nasirov✉, S. A. Novikova, E. D. Gribova, V. V. Kriger, G. A. Bondarenko, P. P. Gladyshev**

Dubna State University, Dubna, Russia

✉npd.19@uni-dubna.ru

**Abstract.** Since their discovery, carbon dots (CDs) have been of great scientific interest due to their unique properties, including strong fluorescence and biocompatibility, which determine their potential application in biosensorics, bioimaging, drug delivery, and many other fields. This paper presents new approaches for the synthesis of highly luminescent and easily surface-modifiable CDs developed in the process of searching for solutions to the problem of CD's application in immunochromatographic analysis.

**Keywords**: carbon dots, nanoparticles, immunoassay.

## Introduction

In immunochemical methods of analysis as labels stand for forming an analytical signal depending on the analyte concentration colloidal gold nanoparticles are typically used. Such systems are expensive, have high detection limits and low efficiency. Quantum dots are much more advanced labels allowing to achieve a high level of sensitivity in immunochemical analysis. However, they are still very expensive and have several disadvantages, such as high cost, biotoxicity, and the need for surface modification preceding their conjugation with biomolecules. CDs can serve as an alternative to quantum dots. CD-based systems can have sensitivity comparable to system based on the latter, while the CDs themselves are biocompatible, easy to synthesise and cheap to produce. The implementation of CDs as analytical labels in immunoassay is complicated by three main disadvantages of ones compared to quantum dots: low stability, polydispersity, and lower quantum yield of luminescence. In this work two new approaches for the synthesis of CDs designed to fix some of the common problems are shown.

## Results and Discussion

Two samples of CDs were obtained by microwave synthesis: by polycondensation of Tris with CA and by aldol-croton condensation of acetone. Tris is a polar compound that has a relatively high dielectric loss tangent and can react with CA through the formation of amide and ester bonds. Thus, under the action of microwave study these substances are able to condense vigorously, forming a branched structure. This property made it possible to obtain CDs with good optical characteristics. The obtained CDs have excellent solubility in polar solvents such as water, alcohols, DMF, DMSO, THF, have a narrow and symmetrical fluorescence peak with a maximum at 405 nm and high for this class of objects quantum yield of luminescence equal to 34.22%, which may be due to the effect of cross-linked enhanced emission (CEE). Polyacetylene glycolide (PAG)-based CDs obtained by aldol-croton condensation of acetone are initially characterised by low solubility in water and good solubility in alcohols and aprotonic polar solvents such as DMSO and DMF, have a broad fluorescence peak with a maximum around 460 nm and a quantum yield of 24.45%. The fluorescence properties of these CDs may be due to the semiconducting nature of the nanosized polymer globules formed by aldol-croton condensation in the reaction medium, and directly depend on the number of conjugated C=C bonds and the continuity of the conjugated chains. Such a system is a convenient platform for further modification since chemical bonding of functional fragments to C=C bonds can be easily accomplished by many different methods. In this work the method of hydrophilisation of the CDs by radical addition of mercaptoethylamine (MEA) in the presence of acetic acid and 4,4'-azobis-(4-cyanovaleric acid) as initiator was used. As a result, MEA-modified PAG-based CDs showed excellent solubility in all polar solvents, including water. However, functional agents integrated in the structure of polymer fragments with the

breaking of multiple bonds cause the breakage of the resonant chain, which may be the reason for the decrease in the quantum yield of luminescence to 19.03% after hydrophilisation.

## Conclusion

At this research point CA- and Tris-based CDs have the best optical properties, which include intense absorption in the UV region, narrow and symmetric fluorescence peak, and high fluorescence quantum yield (34.22%). It makes them protentially good for use as labels in immunoassay. As compared to the former, PAG-based CDs have worse optical characteristics. However, these are an excellent platform for obtaining more complex structures due to easy surface modification.

## REFERENCES

1. **Hou H. et al.,** Carbon quantum dots and their derivative 3D porous carbon frameworks for sodium-ion batteries with ultralong cycle life //Advanced materials, 2015, Vol. 27, №. 47, P. 7861-7866.

2. **Zhu S. et al.,** Non-conjugated polymer dots with crosslink-enhanced emission in the absence of fluorophore units //Cellular Polymers, 2016, Vol. 35, № 2, P. 88-90.

3. **Zhu S. et al.,** The photoluminescence mechanism in carbon dots (graphene quantum dots, carbon nanodots, and polymer dots): current state and future perspective //Nano research, 2015, Vol. 8, P. 355-381.

4. **de Medeiros T. V. et al.,** Microwave-assisted synthesis of carbon dots and their applications //Journal of Materials Chemistry C, 2019, Vol. 7, № 24, P. 7175-7195.

# Investigation of gallium phosphide nanowires conductivity with a doped shell

**K. N. Novikova [1,2]✉, A. A. Vorobyev [1], A.S. Goltaev[1], S.V. Fedina[1,2], V.V. Fedorov[1,2], D.M. Mitin[1,2], A.M. Mozharov[1,2]**

[1] Alferov University, Saint Petersburg, Russia;

[2] St. Petersburg State Polytechnic University, Saint Petersburg, Russia

✉novikova_k@spbau.ru

**Abstract.** In this paper, we present a method of growth of gallium phosphide nanowires with a doped shell. A doping level of $10^{17}$ $cm^{-3}$ was obtained. A technique for creating an ohmic contact to a gallium phosphide single whisker was proposed and implemented.

**Keywords:** Molecular beam epitaxy, GaP, «core-shell», single nanowires, ohmic contact

**Funding:** The research was supported by the Russian Science Foundation grant № 22-79-10286

## Introduction

Gallium phosphide is widely used in nanophotonics as LEDs [1] and photodetectors of UV radiation [2]. This semiconductor material has a wide bandgap of 2.27 eV with indirect zone structure and a relatively high refractive index beside other visible transparent material. Relaxing elastic stresses on the NW side make possible to synthetize high crystalline quality NW arrays even on mismatched substrates, such as Si [3], which can reduce the cost of production. The addition of nitrogen and arsenic to GaP makes it direct-gap material, which allow to fabricate light-emitting diodes and photodiodes based on NWs. To operate it is necessary to add doped emitter layers to the diode structure in addition to the active region but the electron doping of GaPAs NWs is the sticking point of the technology [4].

## Materials and Methods

In this work, we explored the conductivity of core-shell nanostructures based on self-catalyzed GaP:Si NWs grown on an Si(111) substrate using molecular-beam epitaxy. The core and shell were synthesized by vapor-liquid-crystal and vapor-crystal process respectively. To study NW electronic properties the substrate was treated by ultrasonic method to make suspended NW in the liquid. The suspend was applied to quartz substrate to achieve forming a NW layer. Laser lithography was used to form the necessary pattern to the tips of single NWs lying on the substrate. The creation of ohmic contacts to gallium phosphide is difficult due to the high density of surface states. To prevent NW destroying we used non-alloyed low temperature contacts based on Pd/Si materials [5] completed the Ni adhesion and Al conductive layers. During annealing, Si penetrated through Pd and Ni and doped the near-surface region of NWs, which locally increase the electron doping density and penetration of the metal-semiconductor interface. Current-voltage characteristics (I-V) were obtained for NWs with contacts after its annealing at different temperatures (from 175 to 350 $^{0}$C).

## Results and Discussion

Changes in the I-V depending on the annealing temperature of the contacts showed on Figure 1. The transition to a linear I-V is achieved at T=350 $^{0}$C. According to the current-voltage characteristics, the conductivity and the doping level of n-GaP NWs was estimated at 3 S/cm and at $10^{17}$ $cm^{-3}$, respectively.

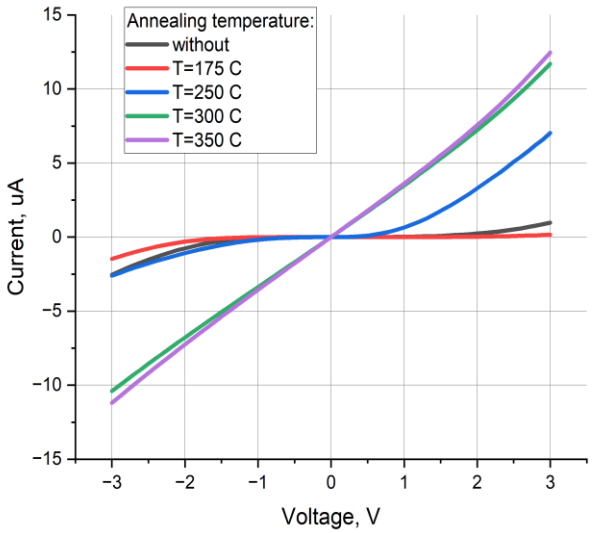


Fig. 1. Current-voltage characteristic depending on the contact annealing temperature

## Conclusions

We have shown a technique to grow NWs with a doped shell. The I-V dependence on the annealing temperature was studied and the optimal parameters to achieve the linear I-V were determined.

## Acknowledgments

The research was supported by grant from the Russian Science Foundation № 22-79-10286

## REFERENCES

1. **HAI N. G. C.** Liquid phase epitaxial growth and fabrication of gallium phosphide green light emitting diodes. – 2004.

2. **Blank T. V., Goldberg Y. A., Konstantinov O. V.** Temperature dependence of the performance of ultraviolet detectors //Nuclear Instruments and Methods in Physics Research Section A: Accelerators, Spectrometers, Detectors and Associated Equipment. – 2003. – Т. 509. – №. 1-3. – С. 109-117.

3. **Fedina S. V.** et al. Processes of formation of epitaxial arrays of self-catalytic GaP nanowires on Si (111) //Journal of Physics: Conference Series. – IOP Publishing, 2021. – Т. 2103. – №. 1. – С. 012127.

4. **Fritze S.** et al. High Si and Ge n-type doping of GaN doping-Limits and impact on stress //Applied Physics Letters. – 2012. – Т. 100. – №. 12. – С. 122104.

5. **Park M. H.** et al. The Si/Pd ohmic contact to n-GaP based on the solid phase regrowth principle //Journal of applied physics. – 1997. – Т. 81. – №. 7. – С. 3138-3142.

# Investigations of the mobility and concentration of charge carriers in nanostructured thermoelectric materials PbTe and GeTe obtained by spark plasma sintering

D.V. Pepelyaev[1]✉, A.A. Sherchenkov[1], Yu.I. Shtern[1], M.Yu. Shtern[1], M.S. Rogachev[1]
[1]National Research University of Electronic Technology, Zelenograd, Russia
✉pepelyaev-dima@mail.ru

**Abstract.** Nanostructured thermoelectric materials PbTe (n-type) and GeTe (p-type) were obtained by spark plasma sintering. Temperature dependences of electrical conductivities for nanostructured PbTe and GeTe were measured and compared with those for TE materials prepared by hot pressing. Measuring the mobility and concentration of charge carriers at a temperature of 300 K showed following results: for PbTe (n-type) the mobility was 128.8 $cm^2 V^{-1}s^{-1}$ and the concentration was $6.25\times10^{19}$ $cm^{-3}$; for GeTe (p-type) the mobility was 68.7 $cm^2 V^{-1}s^{-1}$, and the concentration was $1.09\times10^{20}$ $cm^{-3}$.

**Keywords:** nanostructured, thermoelectric materials, SPS, mobility, concentration

**Funding:** This study was funded by the Russian Science Foundation grant number 21–19-00312.

## Introduction

Thermoelectric generators (TEG) are one of the alternative and promising technologies for converting thermal energy into electrical energy. However, TEGs have not yet been widely used in practice. First, this is due to the low efficiency of thermoelectric materials from which TEGs are fabricated. The highest efficiency among middle-temperature thermoelectric (TE) materials, which are most suitable for using waste heat for generation of electricity, are PbTe (n-type) and GeTe (p-type). Currently, new nanostructured materials are being developed to increase the efficiency of TE materials [1]. However, the electrophysical properties of nanostructured materials, which are determined by the mobility and concentration of charge carriers, are inferior to the properties of TE materials obtained by the traditional method. In this regard, the purpose of this work was to develop a technology of obtaining nanostructured middle-temperature TE materials PbTe (n-type) and GeTe (p-type) and to study the conductivity, mobility and concentration of charge carriers in them.

## Materials and Methods

The developed technology of obtaining nanostructured PbTe (n-type) and GeTe (p-type) by spark plasma sintering (SPS) includes the following steps: 1) direct fusion of initial components of stoichiometric composition in a quartz ampoule; the process of PbTe synthesis was carried out at a temperature of 1050 °C for 180 minutes; GeTe was synthesized at a temperature of 950 °C for 120 minutes; 2) the resulting synthesized materials were crushed in a tungsten mortar to a particle size of 1-3 mm; 3) grinding in knife-type mill to a particle size of 0.25-0.5 mm; 4) grinding in a planetary ball mill for 60 minutes; 5) spark plasma sintering in the following modes: for PbTe a pressure of 80 MPa, a sintering temperature of 450 ° C and a sintering time of 5 minutes were used; for GeTe a pressure 50 MPa, a sintering temperature of 500 °C, and a sintering time of 5 minutes were used.

The studies of the temperature dependence of the electrical conductivity were carried out on the hardware and software complex developed by the scientific team. For measurements TE material samples were prepared in the form of a cylinder 10-20 mm high, and 25-100 $mm^2$ in area. The formation of the Ni contacts was carried out by the method of chemical deposition.

To measure the mobility and concentration of TE materials charge carriers, the Hall method was used on the HMS-5000 facility (Ecopia). Hall coefficient ($R_H$) measurements were carried out on samples $7\times7\times4$ $mm^3$at room temperature, magnetic field of 0.55 T, current of 10 mA.

## Results and Discussion

Figure 1 show the temperature dependences of electrical conductivities for nanostructured PbTe and GeTe (PbTe-SPS, GeTe-SPS) and for comparison for TE materials prepared by hot pressing (PbTe-HP, GeTe-HP).

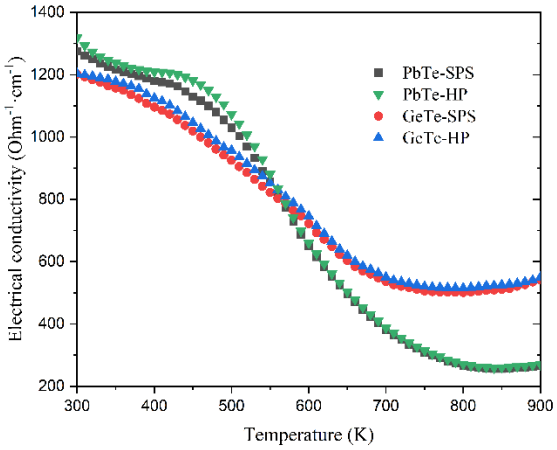


Fig. 1. Temperature dependences of electrical conductivities for PbTe and GeTe

As can be seen from the figure, the electrical conductivities for nanostructured PbTe and GeTe materials are close to those of TE materials prepared by hot pressing.

The results of measuring the mobility and concentration of charge carriers in TE materials are presented in Table 1.

Table 1

**Mobilities and concentrations of charge carriers in PbTe and GeTe**

| Materials | $R_H$, cm$^3$ C$^{-1}$ | Mobility, cm$^2$ V$^{-1}$s$^{-1}$ | Concentration, cm$^{-3}$ |
|---|---|---|---|
| SPS | | | |
| PbTe (n-type) | 0.1 | 128.8 | $6.25\times10^{19}$ |
| GeTe(p -type) | 0.057 | 68.7 | $1.09\times10^{20}$ |
| HP | | | |
| PbTe (n-type) | 0.15 | 195 | $4.17\times10^{19}$ |
| GeTe(p -type) | 0.06 | 70 | $1.04\times10^{20}$ |

The results obtained for the concentration and mobility of charge carriers for nanostructured TE materials have similar values for thermoelectric materials obtained by hot pressing.

## Conclusion

Thus, the development of the fabrication technology of nanostructured thermoelectric materials PbTe (n-type) and GeTe (p-type) by the SPS method was carried out. It has been established that the electrical conductivities, concentration and mobility of charge carriers for nanostructured TE materials are close to those of thermoelectric materials obtained by hot pressing. Thus, the developed fabrication technology of nanostructured PbTe (n-type) and GeTe (p-type) by the SPS method allows to obtain TE materials with high electrical properties.


## Acknowledgments

This work was supported by the Russian Science Foundation (project number 21–19-00312).


## References


1. **Shtern M.Yu., Sherchenkov A.A., Shtern Yu.I., Rogachev M.S., Babich A.V.**, Thermoelectric properties and thermal stability of nanostructured thermoelectric materials on the basis of PbTe, GeTe, and SiGe, Nanotechnol. Russ. 16 (2021) 363–372.

Conference materials
UDC 538.9
DOI: https://doi.org/10.18721/JPM.

# A change in the morphology of multilayer porous silicon with a stepwise decrease in the etching current density

**A. S. Lenshin [1,2], Ya. A. Peshkov [1✉], D. S. Zolotukhin [1], O. V. Chernousova [2], S. V. Kannykin [1], M. V. Grechkina [1], B. L. Agapov [1]**
[1] Voronezh State University, 394018 Voronezh, Russia;
[2] Voronezh State University of Engineering Technologies, 394036 Voronezh, Russia
✉tangar77@mail.ru

**Abstract.** In this paper we produced multilayer porous silicon under different electrochemical etching parameters. The stepwise reduction of the etch current density resulted in a two-layer structure with different porosity layers. The porosity of the multilayers was evaluated by X-ray reflectometry. In addition, a step change in the etching technique resulted in an increase in layer thicknesses, silicon nanoparticle size and pore diameter.

**Keywords:** porous silicon, X-ray reflectivity, multilayers.

**Funding:** This work was supported by the Russian Science Foundation (Grant No. 19-72-10007). Part of the work was supported by a grant from the Ministry of Science and Higher Education of the Russian Federation (No. FZGU- 2020-0036) as part of the State Task for Universities.

## Introduction

The use of porous silicon (PSi) has been well established in photonics devices, biosensors and nanomedicine [1]. Recently, however, the use of PSi as a buffer layer for thin film growth of various materials ranging from metals to $A^{III}B^{V}$ semiconductors has attracted particular attention. The main advantage of PSi is the ability to control its surface morphology. Fine tuning of porosity (P), roughness, pore size, etc. allows PSi to be used as a substrate to reduce mechanical stress and improve adhesion. Moreover, the PSi buffer layer makes it possible to grow epitaxial thin films of materials with a high lattice mismatch on silicon. One type of controlled porous substrate design is a multilayer nanostructure having several alternating porous layers with different P in each layer. In this paper the effect of the process regimes on the surface morphology of the multilayer PSi is presented.

## Materials and Methods

The PSi samples were obtained by electrochemical etching (ECE) of single crystal silicon wafers. Multilayer PSi with different *P* values was obtained by varying the current density (*j*) of electrochemical anodisation. The etching time (*t*) for all samples was the same (Table 1). The etching mode was chosen so that the average current density of the ECE was 35 mA/cm$^2$. X-ray reflectivity (XRR) was used to estimate the surface *P* value. XRR is based on the dependence of the position of the critical angle of the total outer reflection on the electron density of the medium [2]. Knowledge of the critical angle PSi ($\theta_{c\text{-}PS}$) and the crystalline silicon substrate ($\theta_{c\text{-}Si}$) allows us to calculate the porosity from the ratio: $P(\%)=[1-(\theta_{c\text{-}PS}/\theta_{c\text{-}Si})^2]\cdot 100$. X-ray reflectivity of PSi samples for porosity measurements was carried out using an ARL X'TRA X-ray diffractometer in the Bragg-Brentano geometry (Cu$K_\alpha$). The surface morphology was studied by atomic force microscopy (AFM) and scanning electron microscopy (SEM). Image processing and data analysis were carried out with Gwyddion and ImageJ software.

## Results and Discussion

Analysis of the PSi XRR profiles showed that the porosity of single-layer sample No. 1 was 25%. Changing the etching regime to a two-stage one with a current density drop from 50 to 20 mA/cm$^2$ in sample no. 2 led to the formation of an additional subsurface porous layer ($P_t$)

with a porosity of about 69%. At the same time, $P_b$ of the deep layer is close to the porosity of a single layer sample and is equal to 33%. A further increase in the number of etching stages to four for sample No. 3 with a smooth change in current density (Table 1) also led to the formation of a two-layer structure. The near-surface layer has a porosity of 52%, which is significantly less than that of the two-stage sample, and the porosity of the deep layer turned out to be about 35% and almost does not differ from the porosity of the deep layers of the previous samples.

AFM images of the PSi surface show that silicon particles with an average size of about ($z$) 12 nm are formed in a single-layer sample. At the same time, the change to a multi-stage etching mode leads to a significant increase in the particle size on the PSi surface to 15-16 nm. However, the root mean square roughness ($\sigma$) almost does not change. The average pore diameter ($D$) on the PSi surface was estimated from the analysis of SEM image data. Single-layer and two-stage samples have the same average pore diameter of about 210 nm. An increase in the number of etching stages in sample No. 3 leads to an increase in the average pore size to 242 nm. The thickness ($L$)of the porous layer of single-layer sample No.1 is about 8.2 μm. A change in the etching technique resulted in a significant increase in the overall film thickness. Moreover, the transition from a two-step to a four-step mode resulted in an increase in both the top layer thickness ($l_t$) and the bottom layer thickness ($l_b$). The results of our work show how, by changing the etching modes, it is possible to fine-tune the morphology of the surface layer of the multilayer PSi, while preserving the parameters of the deep porous layer.

Table 1

**PSi sample production conditions and morphology obtained from XRR measurements, SEM and AFM observations**

| Sample | $J$, (mA/cm$^2$) | $t$, min | $P_t/P_b$, % | $z$, nm | $\sigma$, nm | $D$, nm | $L$, μm | $l_t/l_b$, μm |
|---|---|---|---|---|---|---|---|---|
| 1 | 35 | 4 | 25/- | 12 | 2.6 | 210 | 8.2 | - |
| 2 | 50/20 | 2/2 | 69/33 | 15 | 3.4 | 209 | 13.9 | 8.0/5.9 |
| 3 | 50/40/30/20 | 1/1/1/1 | 52/35 | 16 | 3.0 | 242 | 14.9 | 8.3/6.6 |

## Conclusion

We have fabricated a series of porous silicon multilayers with different layer thicknesses using electrochemical etching. An increase in the number of steps of changing the etching current density led to the formation of a two-layer structure with different porosity values. The four-step etching mode with a sequential decrease in the etching current led to a significant increase in the average pore diameter. Nevertheless, the average size of silicon nanoparticles and the surface roughness of all samples almost does not change. The total thickness of the porous silicon film increases with an increase in the number of steps of changing the current density. It is worth noting that changing the parameters of sample manufacturing affects the porosity of only the top layer, while the porosity of the bottom layer remains almost unchanged.

## Acknowledgments

The research results were partially obtained with the scientific equipment of the Collective Use Center of Voronezh State University.

## REFERENCES

1. **Moretta R., De Stefano L., Terracciano M., Rea I.,** Porous Silicon Optical Devices: Recent Advances in Biosensing Applications, Sensors**.** 21 (2021) 1336.

2. **Buttard D., Dolino G., Bellet D., Baumbach T., Rieutord F.,** X-ray reflectivity investigation of thin p-type porous silicon, Solid State Commun. 1 (10) (1998) 1–5.

# Metamorphic epitaxial structures for low-barrier mixing microwave diodes

**I.V. Samartsev ✉, B.N. Zvonkov**

Research Institute of Physics and Technology, Nizhny Novgorod State University, Nizhniy Novgorod 603022, Russia

✉woterbox@mail.ru

**Abstract.** The results of studies of InP/GaAs heterostructures based on metamorphic layers with stepwise and digital changes in composition are presented. The electrophysical characteristics of diodes fabricated on the basis of these structures are compared with diodes grown on matched substrates with GaAs active layers. It is shown that the use of InP/GaAs diodes in a triple balanced mixer made it possible to reduce the local oscillator signal power by a factor of 20.

**Keywords:** Metalorganic chemical vapor deposition, semiconducting III-V materials, semiconducting indium compounds, microwave devices.

## Introduction

Growing InP films on GaAs substrates is a promising direction for combining the advantages of both types of semiconductors, and also has great potential for creating highly efficient electronic circuits. In this regard, considerable efforts of researchers have been directed to the development of artificial InP/GaAs substrates and devices based on them.

The main problem hindering the widespread use of artificial InP/GaAs substrates is the presence of a large number of defects in the upper epitaxial layer of InP due to mismatch of crystal lattices [1]. One of the most promising ways to solve the problem is the use of metamorphic buffers with variable composition [2, 3], which allow you to smoothly move to the desired crystal lattice constant and band gap.

In this work, mixing microwave diodes based on heteroepitaxial InP/GaAs structures were fabricated. The electrophysical characteristics of the diodes were studied. The possibility of using heterostructures in the development of broadband diode mixers based on a monolithic integrated circuit made on a new element base – monolithic integrated diode microassemblies on eight mixing diodes was also investigated.

## Experimental samples

In this paper, two types of transient buffer layers were investigated. The first type of buffer structure of type "A" was an $In_xGa_{1-x}P$: Si buffer with a stepwise change in the composition of x from 0.49 (first layer) to 0.98 (8th layer). The total thickness of the layers of the stepped buffer was 864 nm. After the buffer layer, an n-InP contact layer with a thickness of 1800 nm was grown. The doping level of the buffer and contact layers was maintained at about $10^{18}$ $cm^{-3}$. The last to grow was a 140 nm thick active layer of n-InP doped with silicon to a concentration of $10^{17}$ $cm^{-3}$.

The second type of buffer, the "B" type structure, was a digital buffer in which layers were alternated, matched by the lattice parameter with the substrate and with the final active layer. In our case, a pair of layers $In_{0.49}Ga_{0.51}P$ and InP were used. The essence of a digital buffer is a sequential step-by-step change in the thickness of the layers in a pair in opposite directions. The first pair consisted of a 3 nm thick InP layer and a 57 nm thick $In_{0.49}Ga_{0.51}P$ layer. In subsequent pairs of layers, the thickness of InP increased discretely by 3 nm at each step, and the thickness of $In_{0.49}Ga_{0.51}P$ decreased by the same amount, respectively. Thus, the last pair were InP layers with a thickness of 57 nm and $In_{0.49}Ga_{0.51}P$ layers with a thickness of 3 nm. A total of 19 pairs of layers with a total thickness of 1140 nm were grown.

After the buffer layer, a contact layer of n-InP with a thickness of 1440 nm was grown. The doping level of all buffer and contact layers was maintained at about $10^{18}$ $cm^{-3}$. The last was

grown an active layer of n-InP with a thickness of 150 nm, doped with silicon to a concentration of $10^{17}$ $cm^{-3}$. Layer thicknesses for both types of structures were calculated based on an average growth rate of 0.6 nm/sec.

Diodes with an active GaAs layer grown on matched substrates (A91147-3) were used as reference ones. On the basis of structures of type "A", "B" control single Schottky diodes with beam contact were made.

## Results and discussion

According to the CVC of single diodes, it can be seen that single diodes made on the basis of the "A" type structure showed more stable characteristics in comparison with diodes based on the "B" type structures, therefore a triple balanced mixer (TBM) was fabricated on their basis.

Figure 1 shows the dependence of the conversion factor of mixers in the frequency range of the 2-40 GHz heterodyne signal for mixers made on the basis of diodes with an InP active layer of tapa "A" structures and diodes with a GaAs (A91147-3) active layer. Where the conversion factor is the conversion loss determined by the difference in the power of the intermediate frequency signal and the power of the input microwave signal.

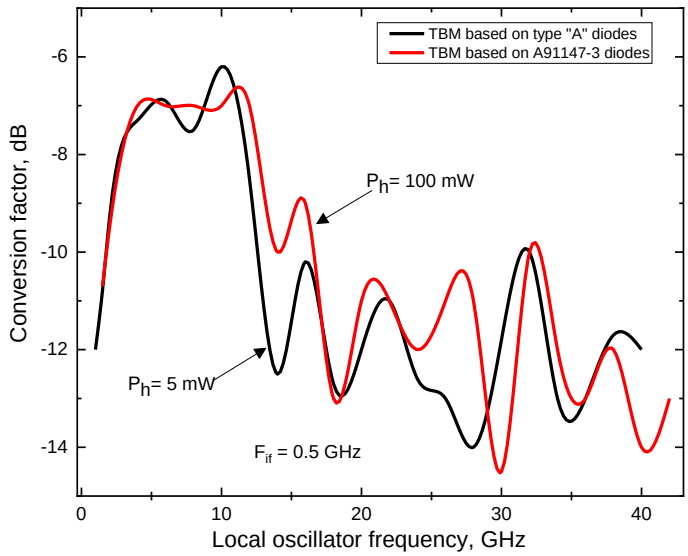


Figure 1. Results of the measurement of the frequency characteristics of TBM made on the basis of diodes with an active layer of GaAs (A91147-3), and on the basis of diodes of type "A".

## Conclusions

The signal power of the heterodyne when using TBM based on GaAs diodes was 100 mW, whereas in the case of using diodes of type "A" - 5 mW. Thus, the use of low-barrier InP diodes on a GaAs substrate made it possible to reduce the signal power of the heterodyne by 20 times. At the same time, as can be seen from Figure 1, there is no deterioration in conversion losses in the entire frequency range of the mixer. This result has a high practical value in the design of triple and double balanced mixers with a large number of diodes.

## References

[1] Y. Okuno, T. Kawano, J. Cryst. Growth. 145, 338 (1994).
[2] Y. Sun, J. Dong, S. Yu, Y. Zhao, Y. He. Sci. Mater. Electron. 28, 745 (2017).
[3] Y. He, W. Yan, P. Dai, J. Yu, J. Dong. J. of Mat. Sci.: Materials in Electronics. 30, 7203 (2019).

# Development of the surface morphology of germanium upon irradiation with gallium ions

**M. A. Smirnova [1]✉, V. I. Bachurin [1], D. E. Pukhov [1], L. A. Mazaletsky [1], M. E. Lebedev[1], A. B. Churilov [1]**

[1] P.G. Demidov Yaroslavl State University

✉ masha_19957@mail.ru

**Abstract.** Experimental studies of the germanium surface morphology development under irradiation with a focused gallium ion beam at different angles of incidence and fluences are presented. It is shown that a nanoporous structure formes in the near-surface layer starting with a dose of $5{\cdot}10^{15}$ cm$^{-2}$.This leads to the formation of a sponge-like morphology with a wall thickness of about 20 nm and a depth up to 150 nm with an increasing dose. Changing the ion beam incidence angle with respect to the surface normal leads to a tilt of the pores walls in the collinear direction.

**Keywords:** semiconductor, Ge, ion irradiation, surface morphology, pores, sponge-like relief, angle dependence, dose dependence.

**Funding:** This study was performed with financial support from the Ministry of Education and Science of the Russian Federation within the framework of the state assignment of the P.G. Demidov Yaroslavl State University of topic no. 0856-2020-0006.

## Introduction

Germanium is characterized by a rather high mobility of charge carriers and is widely used as a solar cell and optoelectronics elements. In recent years, this material has been considered as an electrode in lithium batteries [1]. In the last case, to increase the electrode-electrolyte system electrical capacity, it is advisable to expand the electrode area without changing its dimensions. The surface area can be enlarged due to the formation of a surface porous structure, applying electrochemical treatment of Ge [2], the method of spark discharge [3], etc. Interest in the method of nanopores formation in thin Ge layers under ion irradiation of the surface with different sorts of ions arose as early since 1977 [4]. A detailed review concerning the application of ion irradiation for the formation of porous Ge is available in the monograph [5]. The results of an experimental study of the morphology development of the Ge surface irradiated with a $Ga^+$ focused ion beam depending on the fluence and the ion beam incidence angle are presented in this paper.

## Materials and Methods

The irradiation experiments of a monocrystalline Ge with a 30 keV $Ga^+$ ion beam were carried out in a Quanta 3D 200i facility. Four experimental series of rasters were produced for a comprehensive study of possible morphological features of germanium surface.

The first series was devoted to explore the effect of scanning type (serpentine, raster and circle) on the resulting surface topography. For this purpose, four rectangular and two circular rasters were produced. The fluence of $10^{18}$ cm$^{-2}$ and the incidence angle of the ion beam $\theta = 30°$ remained the same in this series. The rasters for the second series were produced at fixed values of the incidence angle of the ion beam $\theta = 30°$, fluence $10^{18}$ cm$^{-2}$ and beam current 3 nA. An ion beam diameter was varied: 66 nm (focused), 300 nm, 2 μm, 4 μm and a overlap was varied from 30 to 95%, respectively. Increasing the overlap value simultaneously with decreasing the focus degree is necessary to ensure continuity of scanning. The main irradiation parameters of the third series: fluence was varied from $10^{15}$ cm$^{-2}$ to $5{\cdot}10^{18}$ cm$^{-2}$, $\theta = 0°$, beam current 3 nA and 66 nm beam diameter. The fourth series was produced at a fixed fluence of $10^{18}$ cm$^{-2}$, $\theta = 0 - 85°$. The other irradiation parameters were the same as in the third series. The surface topography of all samples was explored ex situ by Supra 40 electron microscop in detail.

## Results and Discussion

In the following study, it was found that the scan type and the focusing degree of the ion beam (diameter value) have no fundamental influence on the surface topography formation, all other conditions remaining equal.

With a step-by-step increasing of the fluence, there is a noticeable modification of the surface relief. The transition from an initially smooth surface to a rough one is observed at a fluence of $10^{15}$ cm$^{-2}$. The thickness of the modified layer amounts to 10 nm. Starting with a fluence of $5{\cdot}10^{15}$ cm$^{-2}$ and up to $10^{16}$ cm$^{-2}$ active formation of a porous surface structure occurs. The thickness of the modified layer increases up to 90 nm, the pore diameter grows from 20 to 50 nm, respectively. Steady-state sponge-like surface morphology has been obtained in the fluence range from $5{\cdot}10^{16}$ cm$^{-2}$ to $5{\cdot}10^{18}$ cm$^{-2}$. The thickness of the sponge layer in this case rises up to 150 nm. It is notable that the wall thickness between pores in the fluence range from $10^{16}$ cm$^{-2}$ to $5{\cdot}10^{18}$ cm$^{-2}$ remains constant (20 nm). In other words, the relief develops deeper into the sample bulk.

It was established that changing the incidence angle of the ion beam $\theta$ causes to a change the tilt of the pores walls $\alpha$. Both angles were measured with respect to the surface normal. The tilt direction of this walls is collinear to the direction of incidence ion beam. The dependence $\alpha$ on $\theta$ has a direct proportionality character in the whole range of angles under examination.

## Conclusion

Qualitative and quantitative analyses of the Ge surface morphology irradiated with a 30 keV $Ga^+$ ion beam were carried out. No morphological features of the germanium surface were observed due to changes in scan type and focus degree of the ion beam.

It was found that an increase of the fluence entails structural modifications of the surface topography. At a fluence of $10^{15}$ cm$^{-2}$, the surface of the sample becomes rough. In the fluence range from $5{\cdot}10^{15}$ cm$^{-2}$ to $10^{16}$ cm$^{-2}$ the development of a porous surface structure occurs. When a fluence increase up to $5{\cdot}10^{18}$ cm$^{-2}$, a steady-state surface morphology (sponge-like) is observed. The mechanism of pore formation at low fluences and the formation of a sponge-like Ge surface structure at higher doses can be explained in terms of the kinetics of ion beam induced defects in the amorphous Ge layer [6].

The deviation of the relief development direction (into the sample bulk) from the normal is due to a corresponding change of $\theta$. It is assumed that the mechanism of pore nucleation in the near-surface layer is similar to the previous case. The difference is that in the process of dose accumulation (up to $5{\cdot}10^{17}$ cm$^{-2}$) the pores are extending in the collinear direction to the ion beam, and they form tunnels. In other words, anisotropic etching of Ge with 30 keV $Ga^+$ ions at angles of incidence different from normal is observed.

## Acknowledgments

This study was performed with financial support from the Ministry of Education and Science of the Russian Federation within the framework of the state assignment of the P.G. Demidov Yaroslavl State University of topic no. 0856-2020-0006 and using equipment of the Facilities Sharing Center of scientific equipment “Diagnostics of micro- and nanostructures”.

## REFERENCES

1. **Graetz J., Ahn C. C., Yazami R., Fultz D.**, Nanocrystalline and thin film germanium electrodes with high lithium capacity and high rate capabilities, Journal of The Electrochemical Society,151 (5) (2004) A698-A702.

2. **Flamand G., Poortmans J., Dessein K.**, Formation of porous Ge using HF-based electrolytes, Physica status solidi (c), 2 (9) (2005) 3243-3247.

3. **Jing C., Zhang C., Zhang X., Zhou W., Bai. W., Lin T., Chu J.**, Fabrication and characteristics of porousgermanium films, Science and Technology of Advanced Materials, 10 (2009) 065001(1-6).

4. **Foti G., Vitli G., Davies J. A.**, Molecular and atomic damage in germanium, Radiation Effects, 32 (1977) 187-191.

5. **Stepanov A. L., Nuzhdin V. I., Rogov A. M., Vorobyov V. V.**, Formation of layers of porous silicon and germanium with metal nanoparticles, Fitzpress, Kazan, 2019.

6. **Böttger R., Heinig K-H., Bischoff L., Liedke B., Facsko S.**, From holes to sponge at irradiated Ge surfaces with increasing ion energy—an effect of defect kinetics?, Applied Physics A, 113 (2013) 53-59.

# Quality Control Methods of Silicon Wafer Diode Array for TV Tubes

**A. A. Sokolova[1]✉, S. D. Proskuryakova[1] and V. V. Davydov[1, 2]**
[1] Peter the Great Saint-Petersburg Polytechnic University, Saint Petersburg, Russia;
[2] The Bonch-Bruevich Saint Petersburg State University of Telecommunications, Saint Petersburg, Russia.
✉ nanasokol@list.ru

**Abstract.** The need to continue developments to improve the technical characteristics of night vision devices with silicon-based photodetectors with a shifted red border to the near IR is substantiated. A technique for testing silicon wafers with a diode grid and an experimental stand for its implementation have been developed. The research results are presented.

**Keywords:** Laser radiation, infrared range, diode grid, target, control, surface quality, photosensitivity.

## Introduction

At present, devices using silicon targets are still in demand both for military equipment and for detecting infrared radiation [1, 2].

Improving the characteristics of devices can be achieved by introducing new technologies and materials into the process of their production [2]. One of the most important tasks that is being solved to improve the characteristics of these devices is to obtain a high photosensitivity of the array in the near-IR range at a low noise level. This condition can be implemented in various ways, such as increasing the number of diodes in the grid, as well as improving the quality of processing processes. Effective quality control techniques are essential to avoid scrap and deterioration of inserts. The development of this technique and experimental setup for its implementation is the goal of this work.

## Control method, experimental stand, and results

The process of manufacturing a silicon wafer is very complex and long. It can be broken down into four main cycles: oxidation, photolithography, chemical rounding, and control. Our job is to control. On Fig. 1a shows the appearance of a silicon wafer ready for installation in the device.

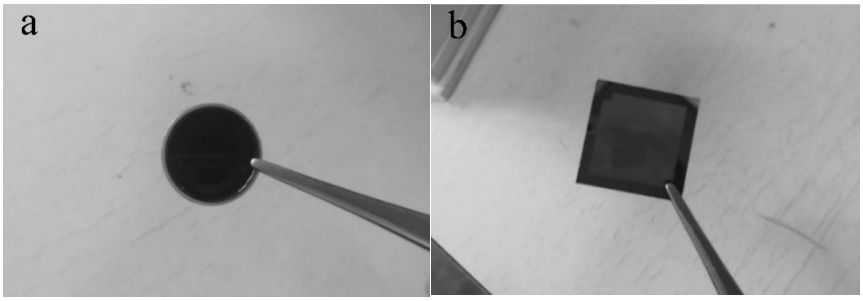


Fig. 1. a - Appearance of the finished silicon wafer, b - Appearance of the wafer for control before chemical rounding.

It was found that the probability of defects (only mechanical) that can occur when varnishing the plate is about 0.01%, with a chemical rounding of about 0.05%. This is unimportant in terms of production. On Fig. 1b shows the plate before the control as an example.

Let us establish that when testing plates, it is necessary to distinguish between the central and edge zones. The edge zone is no more than 3 mm from the edge. The main defects must be installed in the central zone. The main types of defects are divided into the absence of diodes or diode network, etching defects, polysilicon deposition defects and mechanical defects. In addition, it is necessary to provide control over the values of the spectral sensitivity and quantum yield. On

Fig. 2 shows a block diagram of the experimental stand developed by us for the implementation of the proposed methodology.

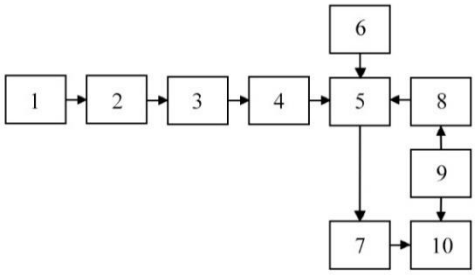


Fig. 2. Structural diagram of the stand for measuring photosensitive parameters: 1 - Power supply and measurement of the mode of the radiation source, 2 - Radiation source, 3 - Radiation attenuator, 4 - Reflective glass, 5 - Camera for a photosensitive device with leads, 6 - System for supplying voltage to the elements of the device, 7 - Digital multimeter, 8 - microscope, 9 - camera, 10 - personal computer.

For an example in Fig. 3 shows the spectral sensitivity (in mA/W) of the photodiode array of the manufactured prototype plates No. 1 and No. 2. For plate No. 2, the characteristics are given for various values of the accelerating voltage $U_{bv}$.

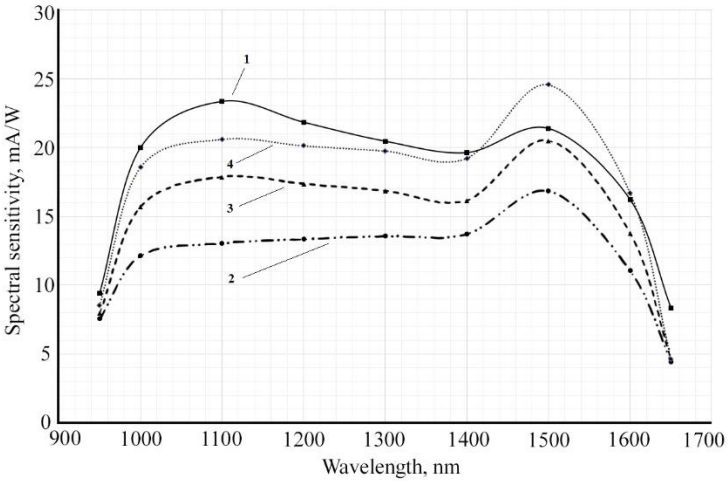


Fig. 3. Spectral dependences of the sensitivity of photodiodes for different values of the bias voltage. Graphs 1, 2, 3 and 4 correspond to the following plates and bias voltages: 1 - No. 1 ($U_{bv}$ = 3.6V); 2 - No. 2 ($U_{bv}$ = 2.4V); 3 - No. 2 ($U_{bv}$ = 2.6V); 4 - No. 2 ($U_{bv}$ = 2.8V).

In the results obtained in Fig. 3 confirm the characteristics that are defined by the requirements for the parameters of silicon wafers with an array of photodiodes.

## Conclusion

The studies carried out and the data obtained have shown the validity of using the technique developed by us to control the quality of the diode grid of silicon wafers. The developed experimental stand allows to study the parameters of the manufactured plates manufactured under various modes of the technological cycle. This will allow solving various problems, both to improve the photosensitive parameters of the plate, and to reduce rejects in their production.

## REFERENCES

1. **Ainbund, M.R., Mironov, D.E., Pashuk, A.V. Mironov, A.V., Solomonov, V.V., Zabrodsky, A.V., Nikolaev V.I.** Silicon electronically sensitive pin-line irradiated from the reverse side. Izvestiya vuzov Rossii. Radioelectronics. 22(5) (2019) 80 - 92.

2. **Konstantinov, P.B., Kostyukov, E.V., Chernokozhin, V.V.** Electronic image signal generator for 5th generation image intensifier tubes. Electronic technology, series 2, Semiconductor devices. 223(2) (2009) 62 - 68.

# Electrochemical synthesis of CdTe nanostructures

**K. B. Stinskaya** [1✉], **S. A. Bedin** [1,2], **I. S. Volchkov** [2]
[1] Moscow Pedagogical State University, Moscow, Russia;
[2] Federal State Institution "Federal Research Center "Crystallography and Photonics" of the Russian Academy of Sciences, Moscow, Russia
✉gallifrei2002@gmail.com

**Abstract.** Cadmium telluride is a semiconductor with a band gap of ~1.45 eV at room temperature, therefore CdTe nanostructures are applied in photoelectronics. In this work, we demonstrate synthesis of cadmium telluride nanostructures. The effect of electrochemical cell potential and the nature of the surface on sample composition is demonstrated.

**Keywords:** electrochemical synthesis, nanowires, cadmium telluride, track membrane.

**Funding:** This work was carried out within the framework of the State Assignment of the Moscow Pedagogical State University with the support of the Ministry of Education of the Russian Federation AAAA-A20-120061890084-9 and the Scientific School of the Russian Federation НШ-776.2022.1.2.

## Introduction

CdTe nanostructures in the form of thin films are widely used in photoelectronics: in solar cells and X-ray detectors [1–5]. For solar cells, an absorbing layer in the form of a thin CdTe film is obtained by electrochemical deposition of a layer on FTO glass with a two-electrode scheme using cadmium nitrate and sulfate precursors [1, 2]. CdTe layer for an X-ray detector is galvanically deposited on a CdS/FTO glass substrate using a two- or three-electrode scheme [3]. The development of CdTe nanostructures in the form of nanowires will increase the effective surface area of the active layer. There are several more methods for creating CdTe nanowire structures: chemical vapor deposition, thermal evaporation, and solvothermal synthesis [1–5]. These methods usually require higher temperatures, pressures and more expensive equipment than electrochemical synthesis. Electrochemical synthesis has advantages in simplicity and allows control over the size, shape, and composition of nanowires. In this method, one can use a template, while the material is synthesized in the pores of the selected template and it becomes possible to change the geometry of the resulting structure.

## Materials and Methods

Firstly, the CdTe was deposited on gold layer without dielectric matrix. The deposition process was carried out in a two-electrode electrochemical cell at room temperature from an electrolyte with an insoluble carbon anode. The composition of an electrolyte, that was used for deposition: CdSO4 - 1 M/l, TeO2 - 0.1 μM/l. The synthesis was provided in a potentiostatic mode, the potential on the cell varied from 2.3 to 2.6 V (Fig. 1*a*).

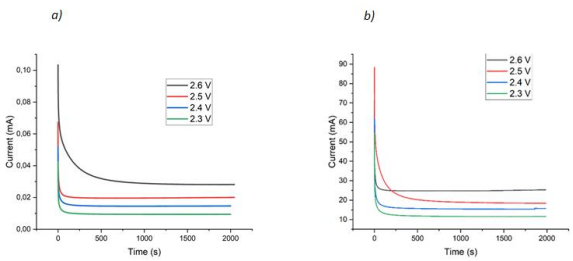


Fig. 1. The deposition curve for CdTe crystal layers (*a*) and for CdTe nanowires (*b*)

Secondly, template method for the electrochemical synthesis of CdTe nanowires is used. Polymer track membrane (TM) was chosen as the template. The synthesis was carried out in several stages. At the first stage, a gold layer was deposited on one of the sides of template by vacuum coating. Next, using a gold layer as a cathode, CdTe was electrochemically deposited in the TM pores. The deposition process was carried out under the same conditions (Fig. 1*b*).

## Results and Discussion

In the first series of experiments, layers with crystals were obtained, which were analyzed using microscopy and X-ray diffraction methods. On the micro photos (Fig. 2) one can see the change of crystal colour with the increasing of potential, it can be assumed that the composition is changing, and this is confirmed using an X-ray diffraction pattern (Fig. 3*a*).

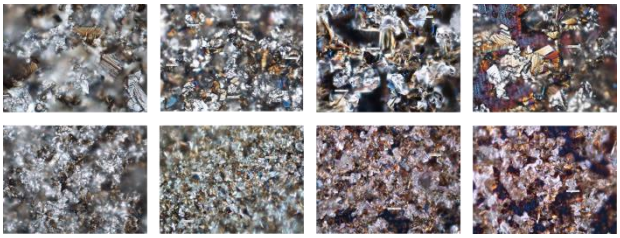

Fig. 2. Microscopy of synthesized CdTe crystal layers

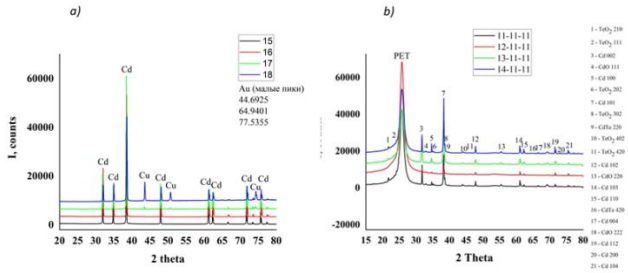


Fig. 3. The X-ray pattern of samples with CdTe crystal layers (*a*) and with CdTe nanowires (*b*)

In the second series, vertically orientated nanowires were synthesized. Using the same potential regimes as for the first series, X-ray pattern shows that we have different composition.

## Conclusion

A series of samples with layers of crystals and with partially filled pores and “overgrowths”, the exit of the material above the surface of the template, were made.

The composition of the deposited material depends on the potential and on the nature of the surface. It was found out that, when deposited on a flat surface and inside the pores of a track membrane, the compositions of the material are different, which, apparently, is due to the features of the diffusion of components inside the pores.

## REFERENCES

1. **Echendu O. K., Okeoma K. B., Oriaku C. I., Dharmadasa I. M.** Electrochemical Deposition of CdTe Semiconductor Thin Films for Solar Cell Application Using Two-Electrode and Three-Electrode Configurations: A Comparative Study. Advances in Materials Science and Engineering. 2016. V. 2016. P. 1–8.

2. **Salim H. I., Patel V., Abbas A., Walls J. M., Dharmadasa I. M**. Electrodeposition of CdTe thin films using nitrate precursor for applications in solar cells. Journal of Materials Science: Materials in Electronics. 2015. V. 26, № 5. P. 3119–3128.

3. **Shams H., Gabal H. A., Soliman M., Ebrahim S., Agamy S.** Electrochemical Deposition of CdTe Thin Film for CdS/CdTe X-Ray Sensor. International journal of enviromental science. 2020. V. 5. P. 85–103.

4. **Bagal V. S., Patil G. P., Suryawanshi S. R., More M. A., Chavan P. G.** Vapour–liquid–solid-assisted growth of cadmium telluride nanowires and their field emission properties. Micro & Nano Letters. 2016. V. 11, № 3. P. 160-163.

5. **Williams B. L., Mendis B., Bowen L., Halliday D. P., Durose K.** Vapor-Liquid-Solid Growth of Cadmium Telluride Nanowires by Close-Space-Sublimation for Photovoltaic Applications. MRS Proceedings. 2011. P. 1350.

# Photocatalytic properties of NiO – gold plasmonic nanocomposite

**V. M. Studzinsky[1,2]✉, A. S. Kondrateva[1,2], I. M. Komarevtsev[1,2], Y. B. Enns[1,2], A. V. Kazakin[1,2], E. A. Pitirimova[3], P. A. Karaseov[2], M. V. Mishin[1]**

[1]Alferov University, St. Petersburg, Russia

[2]Peter the Great Saint-Petersburg Polytechnic University, St. Petersburg, Russia

[3]Lobachevsky University, Nizhny Novgorod, Russia

✉ studzinskij.v@edu.spbstu.ru

**Abstract.** Promising ways to increase the efficiency of photo-degradation of organic substances on coatings based on transition metal oxides is studied. Nickel oxide films were deposited by magnetron sputtering onto a silicon surface. The effect of a deposited NiO annealing on its internal structure has been investigated. The properties of nickel oxide structures with embedded gold nanoparticles were also studied. Glycerol was chosen as a model pollutant. The possibility of decomposition of the pollutant on gold nanoparticle activated nickel oxide under visible radiation is shown.

**Keywords:** Transition metal oxides, photodegradation, gold nanoparticles, plasmonics, nanocomposites.

## Introduction

In modern society, environmental pollution with organic substances is an issue, so the possibility to decompose organic compounds to simple components is an important problem that has to be addressed. Transition metal oxides (TMOs) have the electro-optical properties permitting relatively high photodegradation efficiency [1]. Methods of such coating deposition have been developed [2]. At the same time, TMO has a large band gap, which shifts the light absorption band to the ultraviolet region [3]. To improve efficiency, it would be profitable to shift the absorption to the visible range. Plasmonic nanoparticle incorporation into a TMO matrix significantly affects the properties of the resulting composite, and makes it possible to tune the photodegradative ability of such coatings.

## Results and Discussion

A (100) crystalline silicon (KeF 4.5) was used as a substrate. Nickel oxide was grown by magnetron deposition [2]. Structure of nickel oxide with embedded gold nanoparticles [2] was also prepared for studies. Thermal annealing was used to recrystallize some samples. A drop of a low-concentration glycerol solution in isopropyl alcohol was applied to silicon, nickel oxide, and the nanocomposite structure and kept until the alcohol evaporated. The residual spot was irradiated with a 380 nm or 532 nm laser beam with a power of 10 mW in a continuous mode. The degree of decomposition of organic compounds was determined by the changes fuond in the Fourier IR spectra. The thickness of the polluting layer was calculated according to the Beer–Lambert–Bouguer law. Decomposition under the violet light was found on all types of substrates. A significant increase in the decomposition of organic compounds under the action of a 380nm laser on the structure was also shown in comparison with silicon and nickel oxide. Photodegradation under the green light is found on the nickel oxide with embedded particles..

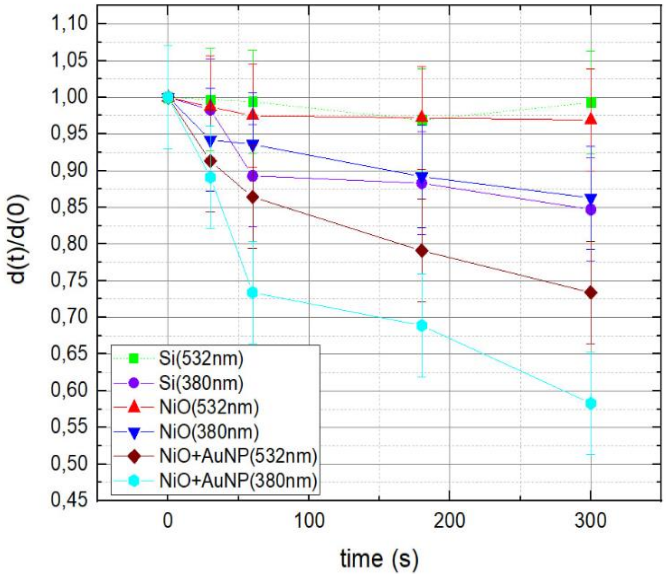


Figure 1. Degree of the organic layer degradation vs time of irradiation with different wavelength.

## Conclusion

Degradation of an organic glycerol film on a nickel oxide surface under 380 nm and 532 nm light irradiation is studied. Gold nanoparticle embedding into metal oxide matrix significantly increases the efficiency of glycerol degradation under UV irradiation. Moreover, nanocomposite system is found to be able to degrade organics under green light irradiation, which is not observed on silicon and pure nickel oxide surface.

## Acknowledgments

Authors wishing to acknowledge the Ministry of Science and Higher Education for financial support assistance (project № FSRM-2023-0009).

## REFERENCES

1. **Kondrateva A. et al.** 2020 *Semiconductors* 54, 1885
2. **Konev D. et al.** 2021 *J. Phys.: Conf. Ser.* 2086, 012018
3. **Zhang E.** *at al*. 2015. *Nanoscale*. **45**, 19293.

# Optimization triple-cation perovskite thin films by PEAI additive

**D. A. Tatarinov [1], A. P. Pushkarev [1], S.V. Makarov [1,2]**

[1] ITMO University, School of Physics and Engineering, St. Petersburg, 197101, Russia;

[2] Qingdao Innovation and Development Center, Harbin Engineering University, Qingdao 266000, China.

dmitry.tatarinov@metalab.ifmo.ru

**Abstract.** This work presents an additive engineering approach to prepare structurally stable highly crystalline triple-cation and mixed-anion perovskite thin film by using 5 mol% doping of perovskite with phenethylammonium iodide (PEAI). Such an additive provides increase in grain size up to 20 % and preserves surface morphology of non-encapsulated films for at least 6 months at ambient conditions.

## 1. Introduction.

Metal-organic perovskites have shown rapid progress in the field of high-performance optoelectronics. The most notable progress has been made in the field of perovskite photovoltaics [1-3]. For example, today the efficiency of energy conversion in single-junction perovskite solar cells is 25.7 % [4], which in turn makes these devices competitive with existing technologies based on polycrystalline silicon and CIGS. The remarkable performance of lead halide perovskites in solar cells can be attributed to their long carrier lifetimes and high carrier mobility. However, there are still problems such as J-V curves hysteresis, ion migration, low resistance to oxygen and moisture that prevent perovskites from large-scale production of the devices showing long-term operation. The efforts of the scientific community have been aimed at solving these problems, for example, by introducing additional passivating layers and searching for new perovskite compositions [5]. From this point of view, multi-cation perovskite films passivated with large-molecule ammonium salts seems a promising solution.

## 2. Results and discussion

In this work, to create perovskite thin films we used two types of solutions – CsFAMAPbBrI as a reference solution and same solution with 5 mol% additive of phenethylammonium iodide. These films were obtained by single-step spin-coating technique with anti-solvent dripping to do smooth morphology of resultant films. It was established for 500 nm thin films that the additive reduces roughness by 2 times and increases the average grain size up to 20 % as compared to that of the reference sample, respectively.

To study the influence of the additive on stability of the films morphology and structure of perovskite the obtained samples were stored at ambient conditions (19–22 °C and relative humidity of 20–30 %). Notably, the studied films were not encapsulated or protected from oxygen and moisture. The quality of the films morphology has been monitored for 6 months. The pure mixed-cation perovskite composition film completely converted to the non-conducting yellow phase for 3 months. Unlike the reference film, the perovskite film with 5 mol% PEAI did not show any visible changes on surface quality after 3 months of observation. Moreover, after 6 months study of the obtained films stability, the perovskite film with 5 % additive of PEAI did not completely pass into the non-conductive phase, however, discontinuity of the film was revealed due to the appearance of a large number of pinholes. In the meanwhile, the color of the did not change that implies no structural transformation of the material. These observations are confirmed by data derived from powder XRD measurements of the initial and aged samples.

## 3. Conclusion

We demonstrate the newest method of improving quality and stability of triple-cation and mixed anion thin films perovskite. Additive into perovskite solution increase grain's sizes of resulting films up to 20 %, showed incredible stability at ambient conditions for 6 months without any

encapsulations. This kind of films can be use in optoelectronic devices as a photoactive layer to improve quality and stability for whole devices. The additive strategies have great potential to improve the PCEs and the long-term stability of the PSCs suitable for commercialization.

**Acknowledgments**
The work was supported by the Ministry of Science and Higher Education of the Russian Federation (Project 075-15-2021-1349).

**References**

[1] H. J. Snaith, Perovskites: The emergence of a new era for low-cost, high-efficiency solar cells. J. Phys. Chem. Lett.4, 3623–3630 (2013).
[2] S. D. Stranks, H. J. Snaith, Metal-halide perovskites for photovoltaic and light-emitting devices. Nat. Nanotechnol.10, 391–402 (2015).
[3] V. D'Innocenzo, G. Grancini, M. J. P. Alcocer, A. R. S. Kandada, S. D. Stranks, M. M. Lee, G. Lanzani, H. J. Snaith, A. Petrozza, Excitons versus free charges in organo-lead tri-halide perovskites. Nat. Commun.5, 3586 (2014).
[4] National Renewable Energy Laboratory, https://www.nrel.gov/pv/assets/pdfs/best-research-cell-efficiencies-rev211214.pdf.
[5] Tang, G.; You, P.; Tai, Q.; Wu, R.; Yan, F. Performance Enhancement of Perovskite Solar Cells Induced by Lead Acetate as an Additive. Sol. RRL 2018, 2, 1800066

# $Mg_2Si$ film on Si: Pulsed RDE Growth, Structure, Electrophysical, Thermoelectrical and Photoelectrical Properties

**I. M. Chernev [1✉], E. Y. Subbotin [1], A. G. Kozlov [2], A. V. Gerasimenko [3], A. Yu. Ustinov [3], N. G. Galkin [1], M. V. Poliakov [4,5], L. S. Volkova [4], A. A. Dudin [4], A. S. Gouralnik [1]**

[1] Institute of Automation and Control Processes FEB RAS, Vladivostok, Russia;
[2] Institute of High Technologies and Advanced Materials, FEFU, Vladivostok, Russia;
[3] Institute of Chemistry FEB RAS, Vladivostok, Russia;
[4] Institute of Nanotechnology of Microelectronics of the RAS, Moscow, Russia;
[5] Merzhanov Institute of Structural Macrokinetics and Materials Science, RAS (ISMAN), Chernogolovka, Moscow Region, Russia
✉ chernev@iacp.dvo.ru, igor_chernev7@mail.ru

**Abstract.** $Mg_2Si$ film (~ 800 nm thick) was grown by pulsed reactive deposition Mg on Si(111) at 340 °C in UHV. Structural investigations by XRD and cross-sectional x-HRTEM demonstrate high crystal quality and almost 100% texture of the film. The EDX depth profiling investigations demonstrate the presence of the oxygen in the film volume. The Hall measurements show the intrinsic p-type conductivity with carrier concentration of $6\times10^{18}$ $cm^{-3}$, carrier mobility ~134 $cm^2/V\cdot s$ and resistivity 7.7 mΩ·cm at room temperature. For the p-type $Mg_2Si$ films, so high values have not been observed before, they are very similar to those for the high quality bulk n-$Mg_2Si$. The p-type conductivity can be associated with either unintentional doping with oxygen or/and Mg vacancies because non-equilibrium and very fast growth process. The photoresponse extending up to 1400 nm was observed at room temperature. The power factor is 0.6 $\mu W/m\times K^2$ and 26.5 $\mu W/m\times K^2$ at room temperature and 410 K, respectively.

**Keywords:** magnesium silicide, silicon, films, epitaxy, reactive epitaxy, pulsed deposition, crystal structure, microscopy, transport properties.

**Funding:** This study was funded by the state budget "Physics of low-dimensional structures and semiconductor nanomaterials" № [0202-2021-0002]. A.G. K. acknowledges the state support under the Russian Federation Government grant for scientific researches conducted under supervision of leading scientists in Russian institutions of higher education, scientific foundations, and state research centers of the Russian Federation [Project Proposal no. 075-15-2021-607].

## Introduction

$Mg_2Si$ is a narrow band semiconductor ($E_g$~ 0.6-0.8 eV), it is a promising material for Si based devices for infrared range applications (SWIR detectors and solar cells) [1] and thermoelectric energy conversion [2]. Usually, $Mg_2Si$ is a n-type semiconductor almost irrespective to a synthesis method. The best monocrystalline $Mg_2Si$ samples were obtained by Bridgman method and demonstrated the carrier density $10^{15}$-$10^{16}$ $cm^{-3}$, mobility 450-480 $cm^2/V\cdot s$ and resistivity 1.4-2.0 Ω·cm at RT [3]. The p-type $Mg_2Si$ is highly required for preparing p-$Mg_2Si$/n-Si heterojunction SWIR sensors and p-type legs for high effective thermoelectric double leg generators based on n- and p-$Mg_2Si$. $Mg_2Si$ of the p-type has been obtained by overcompensation with Ag but this resulted in a significant decrease in carrier mobility down to 40-70 $cm^2/V\cdot s$. Recently it was shown that there is another way to obtain the p-type $Mg_2Si$. In this case the p-type conductivity was caused by Mg vacancies that represented acceptors [4]. But these samples were prepared by magnetron spattering on $Al_2O_3$ substrates, had pretty poor crystal quality and modest transport characteristics [4].

In this work we demonstrate a ~ 800 nm thick $Mg_2Si$ film prepared on Si (111) by ultra-fast Mg deposition (≈$10^4$ nm/s) at the substrate temperature 340 $^0$C. Its structure, electrophysical, thermoelectrical and photoelectrical properties are presented.

## Results and Discussion

$Mg_2Si$ film was prepared on Si(111)-1000 Ω·cm substrate by ultra-fast deposition of high purity Mg at $T_{sub}$ ≈ 340°C. Fig. 1(a) demonstrates the XRD data and it could be clearly seen that

only the peaks of the $Mg_2Si$ planes (111), (222) and (333), as well as Si peaks (111) and (222) are present. The SEM image (see inset) shows the film of the thickness ~800-900 nm. The obtained $Mg_2Si$ film exhibits the intrinsic p-type conductivity with carrier density $6\times10^{18}$ $cm^{-3}$, mobility 134 $cm^2/V\cdot s$ and resistivity 7.7 mΩ·cm. The film showed the spectral photoresponse extending up to 1400 nm at room temperature. It was demonstrated the power factor 0.6 $\mu W/m\times K^2$ and 26.5 $\mu W/m\times K^2$ at room temperature and 410 K, respectively.

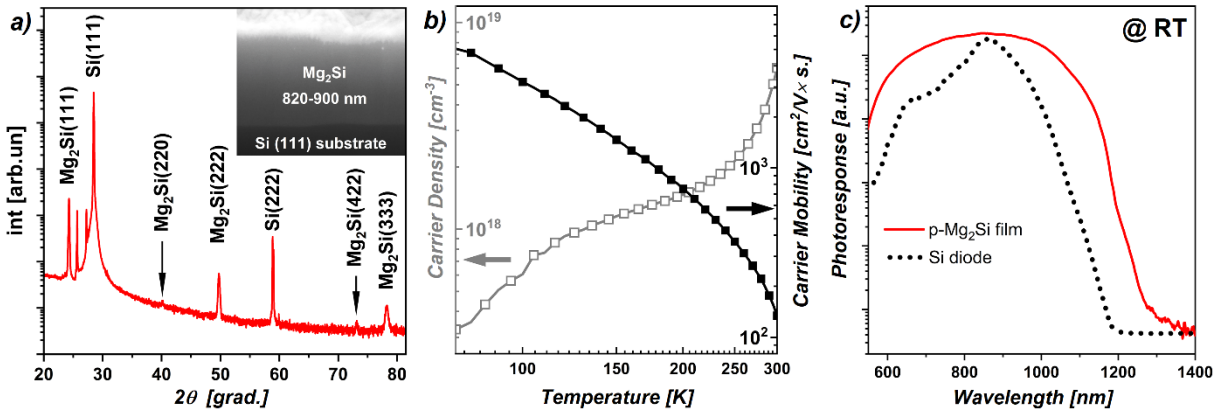


Fig. 1. (a) - XRD patterns of $Mg_2Si$ film and SEM image (see the insertion), (b) - Temperature dependence of the carrier mobility and concentration for grown $Mg_2Si$ film, (c) photo EMF spectra for the p-$Mg_2Si$ film and reference Si diode.

We speculate that p-type of majority carriers can be related with oxygen interstitials and/or vacancies ($V_{Mg}$, $V_{Mg2Si}$) which occur owing to the specific synthesis method used. High carrier mobility can be explained by high crystal quality. It should be mentioned that the carrier density can be further increased by doping; this is in our plans.

## Conclusion

High crystal quality ~800 nm thick $Mg_2Si$ film was formed by pulsed Mg deposition onto Si at 340 $^0$C. Hall measurements showed the intrinsic p-type conductivity with carrier mobility 134 $cm^2/V\cdot s$, density $6\times10^{18}$ $cm^{-3}$ and resistivity 7.7 mΩ·cm. These parameters are very similar to those for high quality bulk n-$Mg_2Si$. The spectral photoresponse of the film extends up to 1400 nm. The power factor is 0.6 $\mu W/m\times K^2$ and 26.5 $\mu W/m\times K^2$ at room temperature and 410 K, respectively.

## REFERENCES


1. **El-Amir A.A.M., Ohsawa T., Nabatame T., Ohi A., Wada Y., Nakamura M., Fu X., Shimamura K., Ohashi N.,** Ecofriendly $Mg_2Si$-based photodiode for short-wavelength IR sensing, Mater. Sci. Semicond. Process. 91 (2019) 222–229.

2. **Zaitsev V. K., Fedorov M. I., Gurieva E. A., Eremin I. S., Konstantinov P. P., Samunin A. Yu., Vedernikov M. V.,** Highly effective $Mg_2Si_{1-x}Sn_x$ thermoelectrics, Phys. Rev. B 74 (2006) 045207.

3. **Udono H., Tajima H., Uchikoshi M., Itakura M.,** Crystal growth and characterization of $Mg_2Si$ for IR-detectors and thermoelectric applications, Jpn. J. Appl. Phys. 54 (2015) 07JB06.

4. **Katagiri A., Ogawa S., Uehara M., Sankara Rama Krishnan P.S., Kurokawa M., Matsushima M., Shimizu T., Akiyama K., Funakubo H.,** Growth of (111)-oriented epitaxial magnesium silicide ($Mg_2Si$) films on (001) $Al_2O_3$ substrates by RF magnetron sputtering and their properties, J. Mater. Sci. 53 (2018) 5151-5158.

# Study of InAs/GaAs quantum dots formation in subcritical growth modes on patterned substrates

**N. E. Chernenko [1]✉, I. S. Makhov [2], S. V. Balakirev [1], D. V. Kirichenko [1], N. A. Shandyba [1], N. V. Kryzhanovskaya [2], M. S. Solodovnik [1]**

[1] Laboratory of Epitaxial Technologies, Institute of Nanotechnologies, Electronics and Equipment Engineering, Southern Federal University, Taganrog, Russia

[2] International Laboratory of Quantum Optoelectronics, HSE University, St. Petersburg, Russia

✉nchernenko@sfedu.ru

**Abstract.** In this work we present the results of experimental studies of the InAs/GaAs quantum dot (QD) formation in subcritical growth modes on substrates patterned in various ways: by local droplet etching and by modified oxide desorption technique. We have shown that the using of growth surface nanopatterning allows to localize the formation of self-assembled nanostructures (including QD) in nanoholes at subcritical deposition thicknesses and to suppress a wetting layer formation. Our results have also shown that the nanohole shape which largely depends on the formation method has a critical influence on the nucleation and growth of self-organized nanostructures and their optical properties.

**Keywords:** quantum dot, A3B5, wetting layer, nanopatterning, molecular beam epitaxy, nanostructure, self-organization

**Funding:** This work was supported by the Russian Science Foundation Grant No. 22-79-10251 and by the Ministry of Science and Higher Education of the Russian Federation Grant No. FENW-2022-0034 at the Southern Federal University.

## Introduction

The unique properties of semiconductor QDs make them promising objects for creating micro- and nanoscale light sources on their basis, including non-classical light, which act as active elements of integrated nanophononics and systems of quantum communications and quantum computing. In this regard, there is a need to develop methods for precise control of QD parameters, such as size, shape, chemical composition, etc. From this point of view, the most promising approach seems to be based on the pre-growth structuring of the substrate surface, i.e. controlled formation of nanoholes on the surface, which later act as nucleation centers for self-organizing nanostructures. The aim of our work is to study the influence of the method of forming nanoholes, as well as their sizes and shapes, on the processes of formation of nanostructures in them, as well as the possibility of obtaining QDs at subcritical thicknesses and without a wetting layer.

## Materials and Methods

For experimental study we used two ways to nanopattern GaAs substrates: local droplet etching (LDE) and modified oxide desorption technique. Both methods allow in situ formation of nanosized pit (or nanoholes) on the surface, but their shape is quite different. During LDE processing, bowl-shaped nanoholes with a diameter of about 100 nm, a depth of several nanometers and a density of about $10^8$ μm$^{-2}$ are typically formed on the surface. In the case of oxide desorption patterning, an array of faceted nanoholes with 35 nm in diameter, at least 5 nm in depth (according to AFM data) and $10^9$ μm$^{-2}$ in density is formed on the surface. After surface nanopatterning stage we grew of InAs layer with thickness varied from 0.1 to 1.5 monolayers (ML). Also we grew the same heterostructure with InAs layer (1.5 ML) without nanopatterning surface which we used as a reference sample. For PL study we repeated the same structures placed them in the central part of AlGaAs/GaAs/AlGaAs heterostructure.

## Results and Discussion

The results of experimental studies have shown that the shape and size of the nanoholes, depending on the method and mode of their preparation, has a key effect not only on the selectivity

of nucleation processes, but also on the nature of growing nanostructures, as well as their optical properties.

As it can be seen from Fig.1(a), in the case of LDE, oval nanostructures of small height (1–2 nm) are formed on the surface, the lateral size of which is much larger than the size of the initial nanoholes, 150–200 nm. In the case of oxide desorption patterning, pronounced QDs are formed on the surface, rising up to 3 nm above the surface level, the size of which is non-linearly correlated with the size of the original nanoholes (Fig.1(b)). At the same time, a large number of small QDs are also present on the surface, the formation of which is due to the initially high surface roughness.

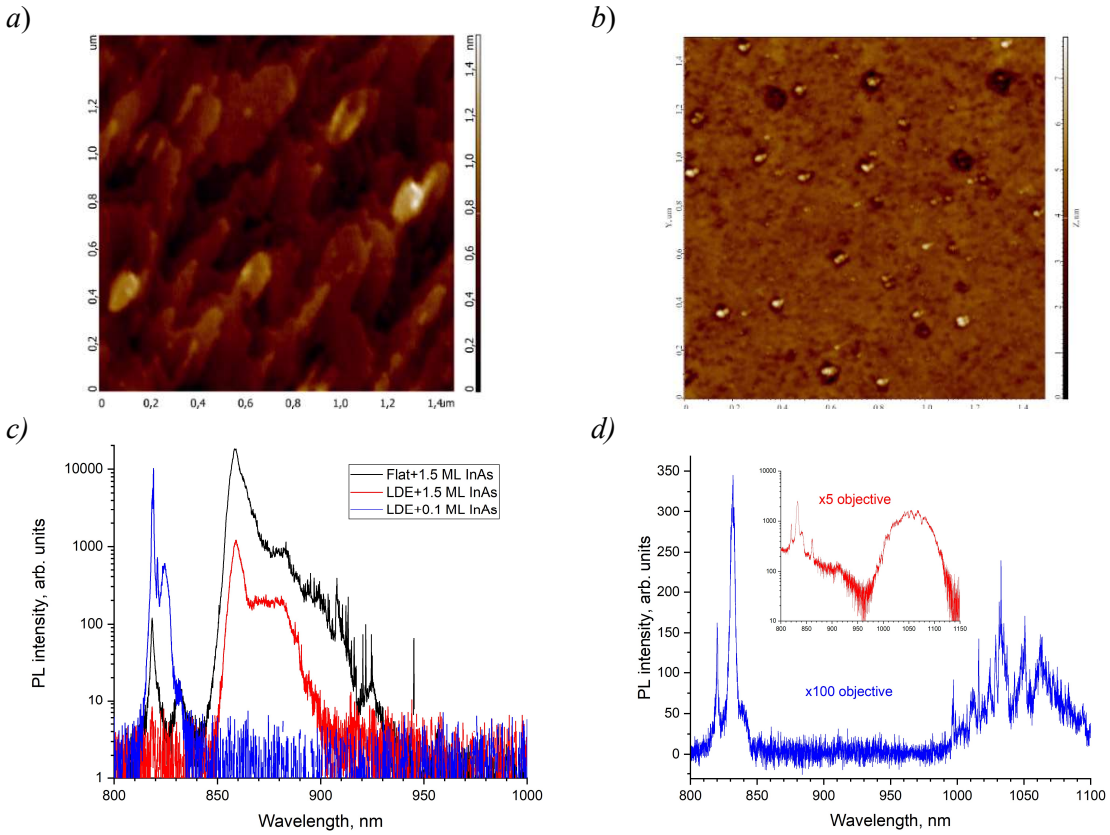


Fig. 1. AFM and PL characterization of InAs nanostructures on substrates patterned: (a) and (c) by LDE and (b) and (d) by modified oxide desorption technique respectively

An analysis of the PL spectra shows that the InAs nanostructures on the LDE-structured are optically inactive, which may indicate their defectiveness due to their too large sizes (Fig.1(c)). It is clearly seen that, at large deposition thicknesses, the spectra of such samples are similar to the spectrum of the reference sample, with the only exception that there are no single QD lines (above 900 nm). A decrease in InAs deposition thickness leads to the disappearance of the 860–900 nm shoulder, and then to a decrease in the WL intensity (840–860 nm). We attribute this to the fact that most of the deposited material accumulates in the nanostructures formed in the nanoholes, as we said earlier, even at 0.1 ML.

In the case of oxide desorption patterning, the PL spectra contain a set of individual QD lines in the range of 1000 – 1150 nm, while the WL line is absent, which indicates a full redistribution of deposited material between QDs.

## Conclusion

Thus, we have experimentally shown that the using of growth surface nanopatterning allows to localize the formation of self-assembled nanostructures (including QD) in nanoholes at subcritical deposition thicknesses and to suppress a wetting layer formation. We have also shown that the nanohole shape which largely depends on the formation method has a critical influence on the nucleation and growth of self-organized nanostructures and their optical properties.

# Effect of ion dose and accelerating voltage during Si(111) surface FIB treatment on GaAs nanowires growth

**N. A. Shandyba** [1✉], **D. V. Kirichenko** [1], **N. E. Chernenko** [1], **V. A. Sharov** [2,3], **S. V. Balakirev** [1], **M. S. Solodovnik** [1]

[1] Laboratory of Epitaxial Technologies, Institute of Nanotechnologies, Electronics and Equipment Engineering, Southern Federal University, Taganrog 347922, Russia

[2] Alferov University, Saint Petersburg 194021, Russia

[3] Ioffe Institute, Saint Petersburg 194021, Russia

✉shandyba@sfedu.ru

**Abstract.** Experimental studies of the dose and accelerating voltage effect during Si(111) surface ion-beam treatment on the substrate structure and GaAs nanowire growth processes have been carried out. We have shown that only dose of embedded Ga ions influences the nanowire characteristics while the accelerating voltage of ion beam and ions distribution in the near-surface layer are of secondary importance in the used range of modes.

**Keywords:** nanowires, gallium arsenide, focused ion beam, molecular beam epitaxy, A3B5.

**Funding:** This work was funded by the Ministry of Science and Higher Education of the Russian Federation; the state task in the field of scientific activity No. FENW-2022-0034.

## Introduction

Semiconductor nanowires (NWs) have unique properties which makes them promise for the creation of opto- and nanoelectronics devices. However, this requires the development of effective approaches to the NW characteristics management: geometric, structural, optical, etc. One of such approaches is based on the pre-growth modification of the surface by the method of Ga focused ion beams (FIB) [1]. At the same time, the influence of FIB and its modes on NW growth processes remains practically unexplored. In this work, we study the dose and accelerating voltage effect during ion-beam treatment of the Si(111) surface on the substrate structure and the GaAs nanowire growth processes.

## Materials and Methods

Experimental studies were carried out on epi-ready Si(111) p-type substrates. Groups of arrays with dimensions of 5×5 μm at accelerating voltage of 10, 20 and 30 kV and implantation dose of 0.01 – 10.4 pC/μm$^2$ were formed on the substrate surface by FIB with Ga ion source. Epitaxial GaAs NW growth was carried out after preliminary annealing in vacuum on modified substrates at a temperature of 600°C with a nominal deposition rate of 0.25 ML/s for 48 min by the MBE method. The samples were analyzed by SEM and Raman spectroscopy.

## Results and Discussion

Quantitative analysis of GaAs NW arrays geometric parameters based on SEM images and subsequent statistical processing of the obtained data made it possible to plot dependences of the main NW arrays parameters for 10, 20 and 30 kV (Fig. 1). It is clearly seen that the dependencies for various accelerating voltage correlate well with each other. At the same time, the nonlinear dependence of the main NW parameters on the treatment dose is visible. We associate this with the interaction of embedded Ga ions with the $SiO_x$ surface layer during the annealing process. At low doses, this leads to the formation of an additional masking oxide layer as a more thermally resistant compound $Ga_xO_y$ which suppresses the NW growth and significantly reducing their density (Fig. 1a). At the same time, the NW length and diameter reach maximum values (above the reference values) (Fig. 1b, c). An increase in the ion dose leads to etching of the oxide layer due to a raise of ion flow from the substrate, forming an array of nanopores which stimulates the NW formation and leads to a sharp increase in their density. Also, the NW length decreases and becomes smaller than outside the modification area which is associated with an increase in the NW density under conditions of a limited material source. However, the NW diameter is almost equal to the reference values (61 ± 5 nm) which may indicate an approximately identical (in size)

ensemble of initial catalyst droplets (Ga). A further increase in the dose leads to the complete removal of the native $SiO_x$ layer and to nanoscale droplets formation at the annealing stage. This causes to the large number formation of parasitic phase GaAs crystallites and to a change in the NW growth mechanisms which, accordingly, leads to a change (decrease) in the values of all key parameters. At the same time, the NW length and diameter are sharply reduced.

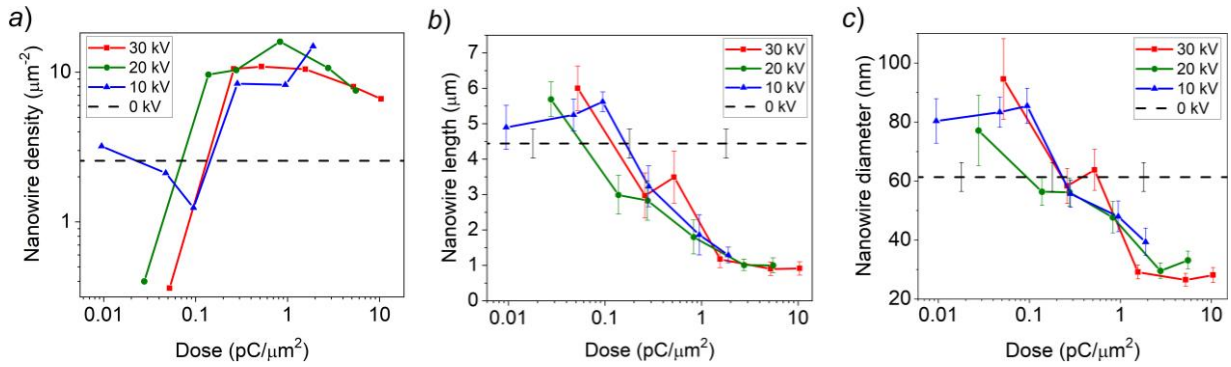


Fig. 1. Dependences of the density (a), length (b) and diameter (c) on Ga ion dose. Dash lines correspond to values for unmodified areas.

The influence of accelerating voltage plays a secondary role in this case. So, for a dose of ~ 0.3 pC/μm$^2$ (Fig. 2) the NW density values at accelerating voltages of 10, 20 and 30 kV are approximately equal and amount to 8.4, 10 and 10.5 μm$^{-2}$, respectively (Fig. 1a). The average length and diameter values of the obtained NWs are also approximately equal: $3.23 \pm 0.58$, $2.83 \pm 0.56$ and $2.97 \pm 0.64$ μm and $56 \pm 5$, $56 \pm 5$ and $58 \pm 6$ nm for 10, 20 and 30 kV, respectively (Fig. 1b, c). We assume that this is due to the complete restoration of the modified substrate areas crystal structure at the selected annealing parameters which is confirmed by the results of Raman spectroscopy.

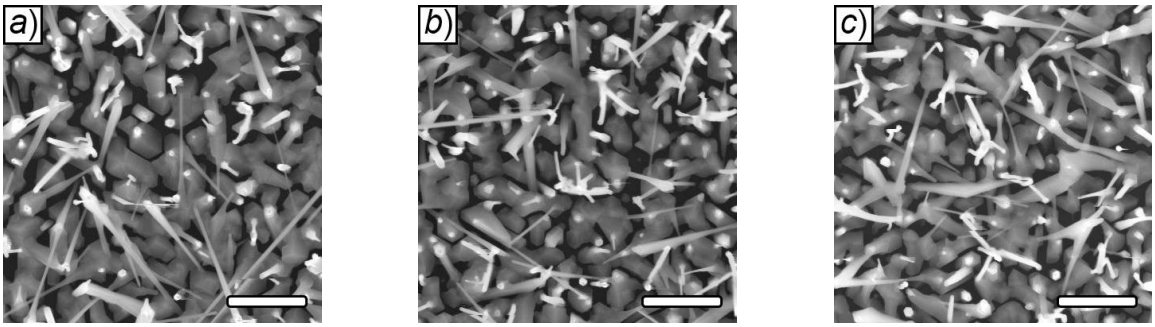


Fig. 2. SEM images of modified areas after GaAs nanowire growth for the same Ga ion dose (~ 0.3 pC/μm$^2$) and accelerating voltage of 10 kV (a), 20 kV (b) and 30 kV (c). Scalebar is 1 μm.

## Conclusion

Thus, it can be concluded that the magnitude of the accelerating voltage and, consequently, the ions distribution in the near-surface layer, when using an all-over processing pattern, have practically no effect on the NW ensemble parameters. The NW characteristics are completely determined only by the amount of the implantation dose. At the same time, the effect of the dose on the NW parameters cannot be explained by the formation of catalytic centers due to the segregation of embedded Ga atoms during annealing. Apparently, this is due to the feature of the ion's interaction during ion-beam treatment with the near-surface layer of the substrate and requires further study.

## REFERENCES

1. **Shandyba N., Balakirev S., Sharov V., Chernenko N., Kirichenko D., Solodovnik M.**, Effect of Si(111) Surface Modification by Ga Focused Ion Beam at 30 kV on GaAs Nanowire Growth, International Journal of Molecular Science. 24 (1) (2023) 224.

# Quality Control Methods of Silicon Wafer Diode Array for TV Tubes

**A. A. Sokolova[1]✉, S. D. Proskuryakova[1] and V. V. Davydov[1, 2]**
[1] Peter the Great Saint-Petersburg Polytechnic University, Saint Petersburg, Russia;
[2] The Bonch-Bruevich Saint Petersburg State University of Telecommunications, Saint Petersburg, Russia.
✉ nanasokol@list.ru

**Abstract.** The need to continue developments to improve the technical characteristics of night vision devices with silicon-based photodetectors with a shifted red border to the near IR is substantiated. A technique for testing silicon wafers with a diode grid and an experimental stand for its implementation have been developed. The research results are presented.

**Keywords:** Laser radiation, infrared range, diode grid, target, control, surface quality, photosensitivity.

## Introduction

At present, devices using silicon targets are still in demand both for military equipment and for detecting infrared radiation [1, 2].

Improving the characteristics of devices can be achieved by introducing new technologies and materials into the process of their production [2]. One of the most important tasks that is being solved to improve the characteristics of these devices is to obtain a high photosensitivity of the array in the near-IR range at a low noise level. This condition can be implemented in various ways, such as increasing the number of diodes in the grid, as well as improving the quality of processing processes. Effective quality control techniques are essential to avoid scrap and deterioration of inserts. The development of this technique and experimental setup for its implementation is the goal of this work.

## Control method, experimental stand, and results

The process of manufacturing a silicon wafer is very complex and long. It can be broken down into four main cycles: oxidation, photolithography, chemical rounding, and control. Our job is to control. On Fig. 1a shows the appearance of a silicon wafer ready for installation in the device.

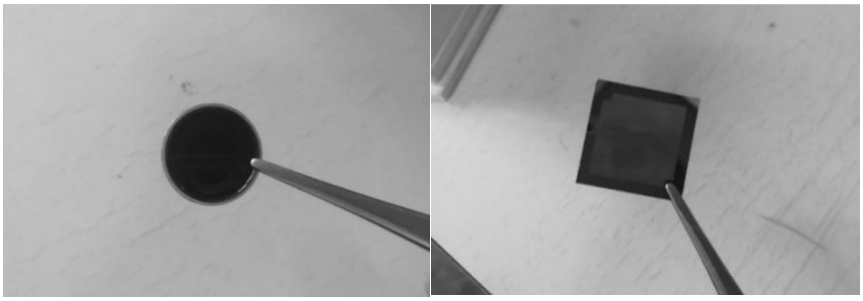

Fig. 1. a - Appearance of the finished silicon wafer, b - Appearance of the wafer for control before chemical rounding.

It was found that the probability of defects (only mechanical) that can occur when varnishing the plate is about 0.01%, with a chemical rounding of about 0.05%. This is unimportant in terms of production. On Fig. 1b shows the plate before the control as an example.

Let us establish that when testing plates, it is necessary to distinguish between the central and edge zones. The edge zone is no more than 3 mm from the edge. The main defects must be installed in the central zone. The main types of defects are divided into the absence of diodes or diode network, etching defects, polysilicon deposition defects and mechanical defects. In addition, it is necessary to provide control over the values of the spectral sensitivity and quantum yield. On

Fig. 2 shows a block diagram of the experimental stand developed by us for the implementation of the proposed methodology.

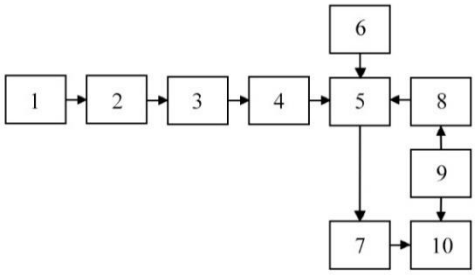


Fig. 2. Structural diagram of the stand for measuring photosensitive parameters: 1 - Power supply and measurement of the mode of the radiation source, 2 - Radiation source, 3 - Radiation attenuator, 4 - Reflective glass, 5 - Camera for a photosensitive device with leads, 6 - System for supplying voltage to the elements of the device, 7 - Digital multimeter, 8 - microscope, 9 - camera, 10 - personal computer.

For an example in Fig. 3 shows the spectral sensitivity (in mA/W) of the photodiode array of the manufactured prototype plates No. 1 and No. 2. For plate No. 2, the characteristics are given for various values of the accelerating voltage $U_{bv}$.

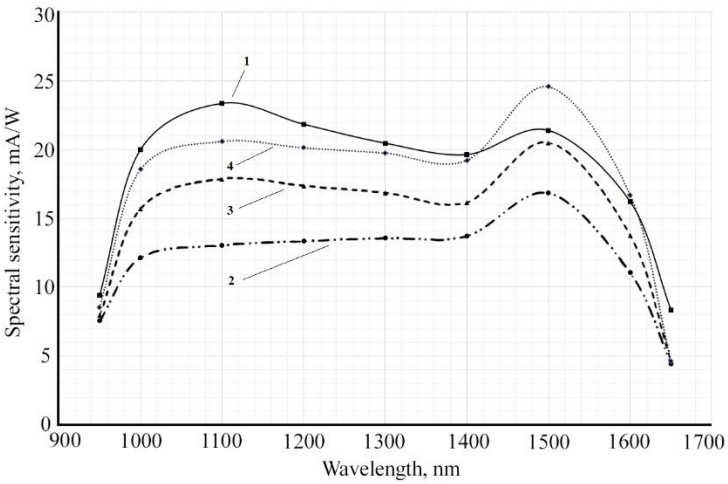


Fig. 3. Spectral dependences of the sensitivity of photodiodes for different values of the bias voltage. Graphs 1, 2, 3 and 4 correspond to the following plates and bias voltages: 1 - No. 1 ($U_{bv}$ = 3.6V); 2 - No. 2 ($U_{bv}$ = 2.4V); 3 - No. 2 ($U_{bv}$ = 2.6V); 4 - No. 2 ($U_{bv}$ = 2.8V).

In the results obtained in Fig. 3 confirm the characteristics that are defined by the requirements for the parameters of silicon wafers with an array of photodiodes.

## Conclusion

The studies carried out and the data obtained have shown the validity of using the technique developed by us to control the quality of the diode grid of silicon wafers. The developed experimental stand allows to study the parameters of the manufactured plates manufactured under various modes of the technological cycle. This will allow solving various problems, both to improve the photosensitive parameters of the plate, and to reduce rejects in their production.

## REFERENCES

1. **Ainbund, M.R.** Silicon electronically sensitive pin-line irradiated from the reverse side / M.R. Ainbund, D.E. Mironov, A.V. Pashuk, V.I. Zubkov, A.V. Solomonov, V.V. Zabrodsky, A.V. Nikolaev // Izvestiya vuzov Rossii. Radioelectronics. - 2019. - T. 22. - No. 5. - P. 80 - 92.

2. **Konstantinov, P.B.** Electronic image signal generator for 5th generation image intensifier tubes / P.B. Konstantinov, E.V. Kostyukov, V.V. Chernokozhin // Electronic technology, series 2, Semiconductor devices. - 2009. - T. 223. - No. 2. - C. 62 - 68.

# Gas sensors based on zinc oxide nanorods with colloid quantum dots

**A. E. Shepeleva [1], S. A. Gurin [1], M. D. Novichkov [1], A.A. Bobkov [2], A.A. Ryzhov [1]**

[1] Joint-stock company "Scientific Research Institute of Electronic-Mechanical Devices", Penza, Russia;

[2] Department of Microelectronics St. Petersburg State Electrotechnical University, St. Petersburg, 197022, Russia

✉ anastasiya.shepeleva.01@mail.ru

**Abstract.** A design and technological solution for increasing the temporal stability of gas sensors based on the nanorods-colloidal quantum dots structure is presented. For this purpose, zinc oxide nanorods oriented predominantly to the surface normal were grown by the hydrothermal method. Silicon nitride, followed by etching to the level of zinc oxide colloidal dots in an inductively coupled plasma using a gas mixture based on sulfur hexafluoride, was deposited onto the resulting structure by RF magnetron sputtering. Silver nanoparticles with a plasmon effect were deposited onto the resulting structure by centrifugation.

**Keywords:** Gas-sensitive material, nanorods, optical radiation, silver nanoparticles.

## Introduction

The functionalized light-sensitive material is able to enter the excitation stage by means of radiation, which allows it to transfer electrons to the gas-sensitive material [1]. This role is played by colloidal quantum dots and silver nanoparticles, which have a plasmon effect. The mechanism of detected gases sensitivity by metal oxide materials is the conversion of optical radiation into charge carriers through the use of colloidal quantum dots. This solution makes it possible to circumvent the problem of replacing the thermal pump. Optical pumping of the system in the visible radiation range reduces the recovery time of the sensor layer.

However, low temporal stability due to oxidation and the formation of new compounds on the surface of the sensing element remains a common problem, for which a passivating layer of silicon carbide was applied in the presented work.

## Materials and Methods

Zinc oxide, with specified dimensions, structure, porosity and morphology, has become widely used as the main material for a gas sensitive element [2, 3].

Zinc oxide nanorods grown by the hydrothermal method were coated with a passivating film of silicon carbide, which has a high chemical resistance to acids and alkalis [4], after which it was etched to the level of zinc oxide colloidal dots in an inductively coupled plasma of sulfur hexafluoride and oxygen, which provides the best results from defect-free morphology point of view [5].

To convert optical radiation into charge carriers, at the final stage of the technological cycle, silver nanoparticles with a diameter of about 50 nm were deposited by centrifugation. The nanoparticles themselves were obtained by the boron hydride method.

## Results and Discussion

The gas-sensitive characteristics of the resulting sensor with a passivating layer of silicon carbide and deposited silver nanoparticles were tested under the influence of isopropanol vapor (Figure 1).

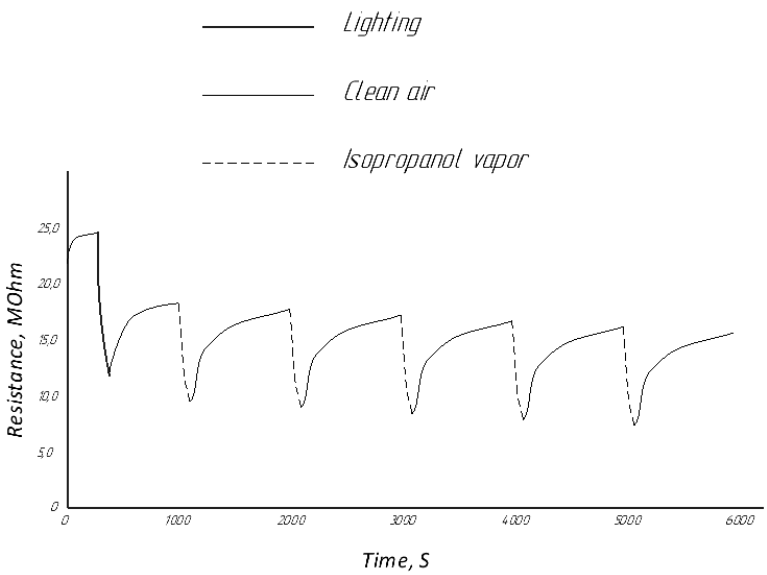


Figure 1. Gas- sensitive characteristics.

Analysis of the obtained results showed that the structure with silver nanoparticles made it possible to increase the layer sensitivity, but the recovery time increased, which is due to the accelerated decomposition of the detected gas due to the participation of silver nanoparticles as a high-efficiency oxidation catalyst. It is also worth noting that the introduction of a passivating layer of silicon carbide increased the electrical parameters stability due to a decrease in oxygen vacancies and surface poisoning.

## Conclusion

The low resistance to poisoning of gas sensitive elements based on semiconductor metal oxides leads to a decrease in temporal stability. To solve this problem, silicon carbide, followed by etching to the level of colloidal dots, on which quantum nanorods dots of silver nanoparticles were deposited was deposited on the surface of a gas sensor based on zinc oxide. Measurements showed that the presented structure has a high stability of electrical parameters, as well as high sensitivity due to silver nanoparticles adsorbed on the surface.

## REFERENCES

1. **Islam, Md. Ashraful & Khan, I..** (2012). ZnO/Ag Composite Nanoparticles for Surface Plasmon Resonance Based Sensor Application in UV-Vis Region. International Journal of Advancements in Research & Technology (IJOART), ISSN: 2278-7763.

2. **Theerthagiri, J.; Salla, S.; Senthil, R.A.; Nithyadharseni, P.; Madankumar, A.; Arunachalam, P.; Maiyalagan, T.; Kim, H.S.** A review on ZnO nanostructured materials: Energy, environmental and biological applications. Nanotechnology 2019, 30, 392001.

3. **Meng F. et al.** Detection of four alcohol homologue gases by ZnO gas sensor in dynamic interval temperature modulation mode //Sensors and Actuators B: Chemical. – 2022. – T. 350. – C. 130867

4. **Volokhov, I. V.** Study of the Properties of High-Sensitivity Thermally-Stable Thin-Film Resistance Strain Gauges for Integral Pressure Sensors / **I. V. Volokhov, S. A. Gurin, I. R. Vergazov** // Measurement Techniques. – 2016. – Vol. 59. – No 1. – P. 80-86. – DOI 10.1007/s11018-016-0921-5.

5. **Okamoto N., Ohki T., Masuda S., Kanamura M., Inoue Y., Makiyama K., Imanishi K., Shigematsu H., Kikkawa T., Joshin K., Hara N.** SiC backside via-hole process for GaN HEMT MMICs using high etch rate ICP etching//Proc. Int. CS MANTECH Conference. May 18th-21st. 2009. Tampa, Florida, USA.

# PHOSPHINE-FREE SYNTHESIS OF SELENIDE COLLOIDAL QUANTUM DOTS

**I. A. Shuklov** [1✉]

[1] Moscow Institute of Physics and Technology (Ntl. Res. Univ.), Institutsky per. 9, 141700, Dolgoprudny, Moscow reg., Russia.

✉shuklov.ia@mipt.ru

**Abstract.**

Metal selenide colloidal quantum dots have promising properties for applications in many fields such as gas sensing, food quality control, car accessories for orientation under low-visibility conditions, Infrared detectors for spectrometers. The wide application of selenide nanoparticles is limited due to a number of reasons. High requirements to the equipment for preparation of these materials in an inert atmosphere as well as poor reproducibility of modern synthetic procedures are some of the major reasons for very limited application of the selenide quantum dots today.

Preparation of mercury and lead selenide colloidal nanoparticles by standard phosphine based procedures are especially affected by these problems. In this paper we report the application of selenium precursor prepared by dissolution of elemental selenium by action of sodium borohydride in oleylamine in the synthesis of lead selenide and mercury selenide quantum dots. The optical properties of the obtained quantum dots are investigated. This reagent is more easily prepared and less affected by conditions as a common phosphine based precursors. The impact of the reaction conditions and isolation procedures on the size distribution is reported. The work-up procedures are developed. The possible constitution of the selenium precursor is discussed.

**Keywords:** quantum dots, nanoparticles, selenides, hot-injection synthesis

**Funding:** This study was funded by Russian Science Foundation (Project No 23-23-00300).).

## Introduction

Metal chalcogenide colloidal quantum dots (CQDs) is promising materials for applications in many fields based on their physical properties. Cadmium selenide CQDs is already found application in QLED TVs. Very recently SWIR-video cameras based on PbS CQDs were commercialized by several firms. Many other applications like solar cells, bioimaging markers, lasers, gas sensors, food quality control, Infrared detectors for spectrometers are under development.

Selenide nanoparticles are interested for application in near-IR. PbSe has band gap 0.28 eV and Exciton bohr radius about 46 nm. These properties allow to obtain PbSe CQDs with a first absorption peak from 800 to 3200 nm.[1] Band gap of lead selenide CQDs and therefor optical properties could be estimated by following formula reported by Moreels et al.[2]

$$E_0 = 0.278 + \frac{1}{0.016d^2 + 0.209d + 0.45}$$

HgSe is a semimetal in bulk with bang gap 0 eV, HgSe has spectral tunability from 800 up to 12000 nm based on intra- or interband adsorption.

The wide application of selenide nanoparticles is limited due to a number of reasons. They are more air-sensitive and less developed than PbS CQDs. [3-5] High requirements to the equipment for preparation of these materials in an inert atmosphere as well as poor reproducibility of modern synthetic procedures are some of the major reasons for very limited application of the selenide quantum dots today.

Preparation of mercury and lead selenide colloidal nanoparticles with commonly used trioctylphosphine suffer from these problems. Herein we report the application of selenium

precursor prepared by dissolution of elemental selenium by action of sodium borohydride in oleylamine in the synthesis of PbSe and HgSe quantum dots.

**Results and Discussion**

Two selenium precursors could be prepared by dissolution of selenium in oleylamine (OLA). One by heating to the temperatures about 200 °C and the second one by addition of sodium borohydride [6-7]

We successfully applied OLA/$NaBH_4$/Se reagent for the preparation of both HgSe and PbSe CQDs. Mercury selenide CQDs prepared at 100 °C possess absorption peak about 5200 nm (Figure 1). From the absorption spectra could be assumed intraband transition nature of this signal. The interband peak is not present in the absorption spectra. TEM analysis revealed spherical nanoparticles with a mean size of 25 nm.

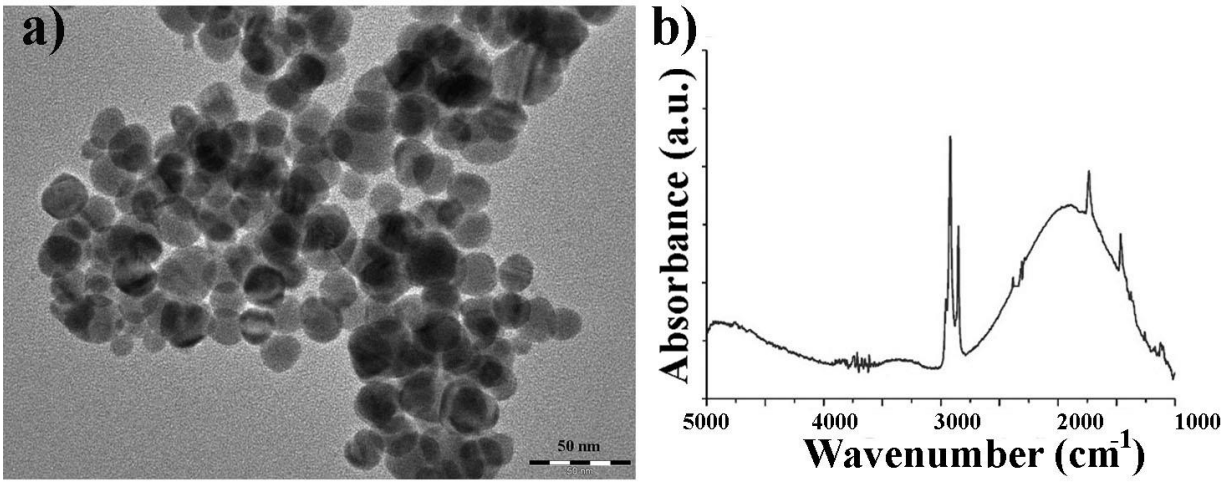


Fig. 1.HgSe CQDs a) TEM Image and b) absorption spectrum in 5000 -1000 cm-1 range on the HATR Ge-plate.

Lead selenide CQDs require higher temperatures for synthesis.

**Synthesis of mercury selenide**. Mercury precursor is prepared by dissolution of 20 mg mercury chloride in 6 ml of dry oleylamine in two-necked flask at 120°C within 1 h in Ar-flow. Selenium-precursor is prepared in a Schlenk-tube from selenium powder (58 mg) and sodium borhydride (27 mg) in 6.5 ml of dry oleylamine. 1 ml of selenium-precursor is added swiftly to the solution of cooled mercury-precursor at 100°C. Reaction time by vigorous stirring is 5 minutes. Reaction is quenched by adding 1 ml 1-dodecanethiol and immediate cooling with ice bath. Nanoparticles are purified by 2 x redispersing in tetrachloroethylene and precipitation with methanol. Sample of HgSe are dispersed in tetrachloroethylene for storage and characterization.

**Conclusion**

Selenium precursor prepared by dissolution of elemental selenium by action of sodium borohydride in oleylamine could be interesting alternative for the preparation of lead selenide and mercury selenide quantum dots. The obtained PbSe CQDs possess first absorption peak at 2200 nm. The obtained HgSe CQDs possess intraband absorption peak at 5000 nm.

**REFERENCES**

1. **Shuklov, I.A.; Razumov, V.F.** Lead chalcogenide quantum dots for photoelectric devices, Russ. Chem. Rev. (89) (2020) 379-391.

2. **Moreels, I.; Lambert, K.; De Muynck, D.; Vanhaecke, F.; Poelman, D.; Martins, J.C.; Allan, G.; Hens, Z.** Composition and Size-Dependent Extinction Coefficient of Colloidal PbSe Quantum Dots, Chem. Mater. (19) (2007) 6101-6106.
3. **Ganeev, R.A.; Shuklov, I.A.; Zvyagin, A.I.; Dyomkin, D.V.; Smirnov, M.S.; Ovchinnikov, O.V.; Lizunova, A.A.; Perepukhov, A.M.; Popov, V.S.; Razumov, V.F.** Synthesis and low-order optical nonlinearities of colloidal HgSe quantum dots in the visible and near infrared ranges, Optics Express (29) (2021) 16710-16726.
4. **Ganeev, R.A.; Kim, V.V.; Shuklov, I.A.; Popov, V.S.; Lavrentyev, N.A.; Ponomarenko, V.P.; Mardini, A.A.; Dyomkin, D.V.; Milenkovič, T.; Bundulis, A.; et al**. Third harmonic generation in the thin films containing quantum dots and exfoliated nanoparticles. Applied Physics B (128) (2022) 202.
5. **Shuklov, I.A.; Toknova, V.F.; Lizunova, A.A.; Razumov, V.F.** Controlled aging of PbS colloidal quantum dots under mild conditions. Materials Today Chemistry (18) (2020) 100357.
6. **Goubet, N.; Jagtap, A.; Livache, C.; Martinez, B.; Portalès, H.; Xu, X.Z.; Lobo, R.P.S.M.; Dubertret, B.; Lhuillier, E.** Terahertz HgTe Nanocrystals: Beyond Confinement. Journal of the American Chemical Society (140) (2018) 5033-5036.
7. **Hou, B.; Benito-Alifonso, D.; Webster, R.; Cherns, D.; Galan, M.C.; Fermín, D.J.** Rapid phosphine-free synthesis of CdSe quantum dots: promoting the generation of Se precursors using a radical initiator. Journal of Materials Chemistry A (2) (2014) 6879-6886.

**Application of linear chain carbon films for sensitive elements of humidity sensors**

**A. V. Smirnov[1]✉, P.S. Platonov, A. V. Kokshina[1], V. A. Kazakov[1], D.V. Petrov[1], O. V. Vasilyeva[3], S. I. Ksenofontov[2], A. N. Lepaev[3]**

[1]Chuvash State University named after I.N. Ulyanov, Cheboksary, Russia

[2]Chuvash State Pedagogical University named after I.Y. Yakovlev, Cheboksary, Russia;

[3]Cheboksary Institute (branch) of the Moscow Polytechnic University, Cheboksary, Russia;

✉fizteh21@yandex.ru

**Abstract.** The paper considers the technology of synthesis and study of film metal electrodes with a film of linear-chain carbon. Relative Humidity Sensor Created, Recovery Time and Sensitivity Measured.

**Keywords:** film electrodes, silver films, tin films, linear chain carbon, relative humidity, sensor.

## Introduction

Humidity is an important parameter in various fields of science and technology. Relative humidity sensors are widely used in various fields (agriculture, medicine, industry) and are designed to control optimal conditions (storage of agricultural products 85-95%, living quarters 40-45%, etc.).

For example, a higher humidity value around electronic devices increases the conductivity of insulators; in turn, this can change the operating properties of semiconductor devices and lead to dangerous situations. That is why proper timing of its detection, measurement and control is essential. There are several applications of humidity sensors in many sectors of our modern life and these sectors include pharmaceuticals and healthcare, automotive, household appliances, food and beverages, and agriculture.

Currently, several technologies are used to measure relative humidity, using the property of various structures to change their physical parameters (capacitance, resistance, conductivity, etc.) depending on the degree of saturation with water vapor. For existing humidity sensors, there are such disadvantages as a long surface recovery time after several cycles of adsorption-desorption of water molecules, relatively low sensitivity. Therefore, it is important to search for new materials that expand the capabilities of humidity sensors.

## Materials and Methods

The moisture sensor structure was prepared as follows. On a ceramic substrate with Ag and Me (Sn, Ti, Al) deposited on two film electrodes with different electrochemical potentials, spaced on the substrate relative to each other at a distance of 0.1-2.0 mm, made by thermoresistive vacuum deposition. The second layer covered the surface with a film of linear chain carbon (LCC) with a thickness of 2000 Å. After that, the substrate with the electrodes deposited on it and the LCC film is annealed in a muffle furnace at a temperature of 400°C for 10 min. The sputtering structure is shown in Figure 1.

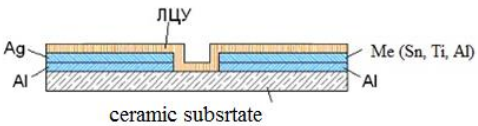

Figure 1. Humidity sensor coating structure

LCC films were obtained by plasma deposition of graphite evaporated by a pulsed arc discharge in a vacuum, moreover, the plasma is created outside the region of the arc discharge discharge gap in the form of compensated currentless carbon plasma bunches with a density of $5\cdot10^{12}$ -$1\cdot10^{13}$см$^{-3}$, a duration of 200-600 μs, repetition rate of 1-5 Hz, while in the process of carbon material deposition, carbon plasma is stimulated with an inert gas in the form of an ion flow with an energy of 150-2000 eV, which is directed perpendicular to the carbon plasma flow.

The structure of LCC films consists of many layers, each of which consists of chains of carbon atoms in sp1 hybridization, oriented normal to the layer surface. The chains are united by van der Waals forces into a hexagonal structure with a distance of about 5 Å between them. The presence of delocalized electrons belonging to the entire LCC molecule ensures metallic conductivity along the chain. The absence of a connection between the chains makes the film a dielectric in the perpendicular direction.

## Results and Discussion

For the measurement, a stand was assembled (Fig. 2) to saturate the samples with water vapor. A Keithley digital programmable multimeter is connected to the electrodes of the sensing element.

Figure 2 . Stand for measuring the output signal of the humidity sensor

At the first stage of adsorption, the $H_2O$ molecule is chemically adsorbed on the active layer of the sensor with the formation of an adsorption complex, then an OH- group is formed on the surface. Then another water molecule reaches the surface and binds to neighboring hydroxyl groups through a hydrogen bond.

The results of measurements of the electric potential difference depending on the relative humidity were investigated and presented in Figure 3. LCC films increase the generated EMF by an order of magnitude. The sensor generated a voltage of 715 mV at RH = 80% of the sensor with Ag, Sn electrodes with LCC and NaCl films.

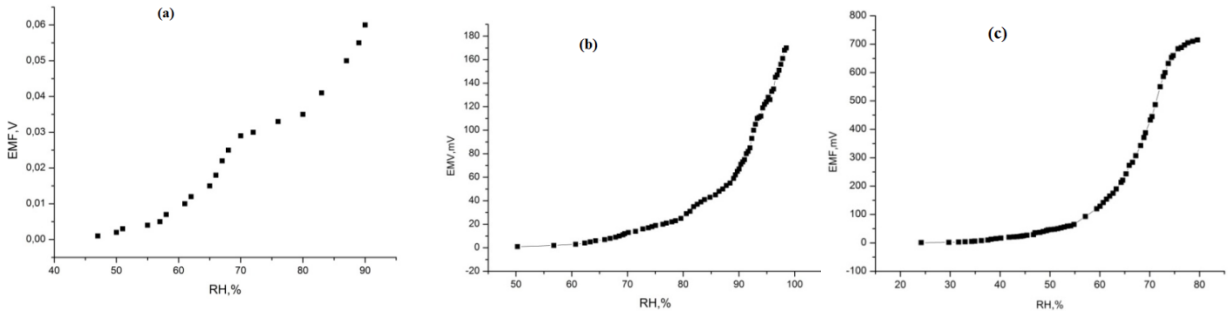


Figure 2. The dependence of generated EMF on related humidity for elements: (a) - (Al(k)-Ag)/(Sn-Al(k)) on substrate ; (b) - Al(k)-(Ag-ЛЦУ)/(Sn-ЛЦУ)-Al(k) on substrate ; (c)- Al(k)-(Ag-ЛЦУ)/(Sn-ЛЦУ)-Al(k) on substrate with NaCl films

To measure the surface recovery time after the adsorption of water molecules on a metal carbon sensor, the sample is placed under a vessel preliminarily saturated with moisture to RH = 95% and then exposed to RH = 25% humidity under ambient conditions. For all humidity sensors, the estimated recovery time was 50-60 seconds. The sensitivity of our sensor with NaCl exceeds the results obtained in [2, 3]. Below is a table that presents the results of measuring the sensitivity of film structures with a combination of electrodes Ag and Me (Sn, Ti, Al).

| Structure of humidity sensors | Sensitivity, mV/RH% |
|---|---|
| Al(k)-(Ag-ЛЦУ)/(Ti-ЛЦУ)-Al(k) on substrate | 4.80 |
| (Al(k)-Ag)/(Sn-Al(k)) on substrate | 1.13 |
| Al(k)-(Ag-ЛЦУ)/(Al-ЛЦУ)-Al(k) on substrate | 5.28 |
| Al(k)-(Ag-ЛЦУ)/(Sn-ЛЦУ)-Al(k) on substrate | 1.74 |
| Al(k)-(Ag-ЛЦУ)/(Sn-ЛЦУ)-Al(k) on substrate with NaCl films | 12.91 |

## Conclusion

Thus, a sensitive element of a potentiometric type humidity sensor with an output signal - EMF between film electrodes was synthesized. The sensor showed good sensitivity and fast response. Due to the developed surface and structural features (bends of carbon chains with carbon atoms), the LCC film increases the sensitivity of the created structure.

## Acknowledgments

The work was supported by a grant from scientific schools of the Chuvash State University named after I. N. Ulyanov (project «Experimental and theoretical studies of technologies for creating new hybrid metal-carbon nanostructures and development of sensors for a wide range of functional purposes»).

## REFERENCES

1. Kochakov V.D., Novikov N.D. Interkalirovanie v plenku lineino-cepochechnogo ugleroda // Vestrnik Chuvashskogo Universiteta.2007.№3.S.20-25

2. Dennis JO, Ahmed AY, Khir MH. Fabrication and Characterization of a CMOS-MEMS Humidity Sensor.

3.Humidity response properties of a potentiometric sensor using LaF3 thin film as the solid electrolyte Guoliang Sun, Hairong Wang, Zhuangde Jiang. Rev. Sci. Instrum. 82, 083901 (2011); http://dx.doi.org/10.1063/1.3617471

# Investigation of Photoconverter in IR Range Based on an Array of InAs Nanowires Synthesized by the MBE Method

**A.S. Goltaev[1✉], A.M. Mozharov[1,2], K.N. Novikova[1,2], A.A. Maksimova[1], V.V. Fedorov[1,2], I.S. Mukhin[1,2]**

[1] Alferov University, St. Petersburg, Russia

[2] Peter the Great St. Petersburg Polytechnic University, St. Petersburg, Russia

✉goltaev@goltaev.ru

**Abstract.** The active development of fiber-optic communication systems has stimulated the scientific and industrial communities to create efficiency optoelectronic devices that operate in the near and mid-infrared (IR) ranges. Of particular interest is indium arsenide (InAs) material, specifically, nanowire nanocrystals. Due to their unique characteristics, nanowires provide a wide range of possibilities for controlling the bandgap profile, optical and electronic confinement, as well as exhibiting a high absorption coefficient and a high quantum efficiency of the diode. In this study, InAs NWs were synthesized on a p-Si substrate and a technological process for creating a photodiode was developed. In addition, the primary electrical and spectral characteristics of the sample were measured.

**Keywords:** IR photodiode, indium arsenide, InAs, nanowires, NWs, MBE, postprocessing.

**Funding:** This study was funded by the Russian Scientific Foundation (RSF project 22-19-00494) and the Ministry of Science and Higher Education of the Russian Federation (FSRM-2023-0007).

## Introduction

In recent years have seen a particular interest in the study of quasi-one-dimensional InAs NWs for IR optoelectronics [1]. Due to the narrow bandgap, these structures exhibit a high carrier mobility of 10 000 $cm^2/V\cdot s$ and high absorption from the visible to the mid-infrared range (1.2¬ – 3.5 μm). An important feature of NWs is the possibility of capturing light by a region of space around the NW with a total region diameter of the order of half a wavelength, thereby breaking the rigid relationship between the volume of the active region and the absorptivity. This cannot be said about structures based on bulk semiconductor materials. Thus, the use of InAs NWs opens up prospects for creating highly efficient infrared photodetectors, which positively affects the signal-to-noise ratio. This cannot be said about structures based on bulk semiconductor materials. Thus, the use of InAs NWs opens up prospects for creating highly efficient infrared photodetectors.

## Materials and Methods

Arrays of InAs nanoheterostructures substrate were synthesized on a p-Si (111) using the molecular beam epitaxy (MBE) method. A all over Al contact was formed on the bottom of the sample using vacuum thermal deposition, with prior treatment in hydrofluoric acid. Then the sample was annealed for 10 minutes at 300°C to form an ohmic contact. A transparent infrared photoresist SU-8 dielectric layer was deposited using a spin-coating method to provide electrical isolation NW tips and Si substrate. The thickness SU-8 was controlled by scanning electron microscopy and adjusted by oxygen plasma etching. The NW tips was processed in a 1:10 HCl solution, after which a transparent ITO contact layer was formed through a mask using high-frequency magnetron sputtering. Finally, the electrical and spectral characteristics of the completed structure were evaluated at temperatures of 100-300K.

## Results and Discussion

Figure 1(a) shows a general view of the finished structure. The current-voltage curve shows diode characteristics and low leakage currents (Fig. 1(b)). The measurement of the external quantum efficiency showed a value of 0.3-0.4% for a range of 1.3-1.65μm (at a temperature of 100K). We assume that the obtained data turned out to be low due to the short lifetime of charge carriers, since there is a frequent change of wurtzite and zincblende phases [2]. Numerical simulation assumes near to 100% internal quantum efficiency with structure homogeneity and ideal conditions [3].

*a*) *b*)

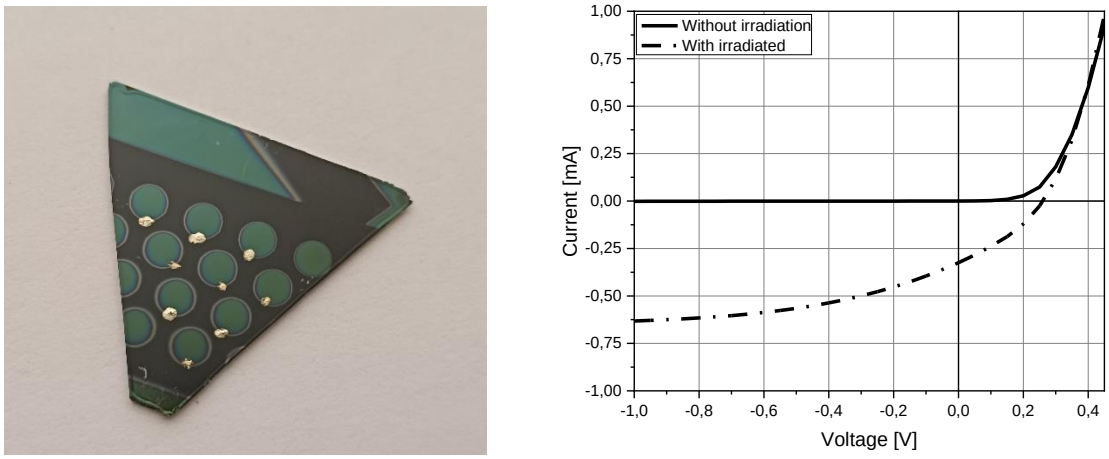


Fig. 1. (*a*) Optical image of the finished structure, (*b*) Current-Voltage Curve

## Conclusion

In this work, InAs nanowires was synthesized by molecular beam epitaxy on p-Si substrate. Post-processing methods were used to form the sample for the electrophysical and spectral measurements. This structure shows diode characteristic and spectral sensitivity in mid IR range.

## Acknowledgments

This work was financially supported by the Russian Scientific Foundation (RSF project 22-19-00494) for NWs epitaxial growth. Electrical measurements were financially supported by the Ministry of Science and Higher Education of the Russian Federation (FSRM-2023-0007).

## REFERENCES

1. **Xu, T., Wang, H., Chen, X., Luo, M., Zhang, L., Wang, Y., ... & Yu**, **C**. Recent progress on infrared photodetectors based on InAs and InAsSb nanowires. Nanotechnology, 31(29) (2020) 294004.

2. **Fedorov, V., Vinnichenko, M., Ustimenko, R., Kirilenko, D., Pirogov, E., Pavlov, A., ... & Mukhin, I.**. Non-Uniformly Strained Core–Shell InAs/InP Nanowires for Mid-Infrared Photonic Applications. ACS Applied Nano Materials 2023

3. **Dvoretckaia, L., Mozharov, A., Pavlov, A., Polozkov, R., & Mukhin, I.** Numerical study of detectivity for near-IR photodetectors based on InAsP NWs. Scripta Materialia, 226, (2023) 115246.

# Synthesis of Perovskite Nanoparticles in Suspension using Microfluidic Approach

**Qinghao Song,[1,2] Irina G. Koryakina,[2,*] Sergey V. Makarov, [1,2] and Mikhail V. Zyuzin[2]**

[1] *Qingdao Innovation and Development Center, Harbin Engineering University, Qingdao 266500, P. R. China*
[2] *Department of Physics and Engineering, ITMO University, 191002 St. Petersburg, Russian*

[*] *irina.koryakina@metalab.ifmo.ru*

**Abstract:** In this study, stable perovskite nanoparticles in suspension were successfully synthesized with microfluidic technology. By controlling flow rate of the reagents supply into the co-flow of microfluidic chip the synthesis of various sizes of perovskite nanoparticles in the range of 0.5-1.8 $\mu m$ was achieved with high reproducibility. Additionally, to achieve stability of perovskite suspension the amount of oleylamine and oleic acid was varied. Overall, this study provides the methodology of an up-to-date approach for controlled synthesis of perovskite particles with controlled size distribution. © 2023 The Author(s)

## 1. Introduction

Perovskite nanocrystals are a promising alternative to traditional inorganic semiconductor nanocrystals in various application fields such as photonics, optoelectronics, and bioimaging. [1] Perovskite nanocrystals possess high absorption coefficients, variable shape [2], long carrier diffusion lengths, and high charge carrier mobilities, which make them ideal candidates for further application as light emitting diodes and lasers. However, the controlled synthesis of the perovskite nanocrystals is still limited by the challenge of reproducible synthesis with a narrow size distribution.

One of the alternative synthesis technologies of perovskite particles is microfluidics. Microfluidic technology enables rapid manipulation and precise control of liquids on the microscale [3]. This technology has the advantages of simple operation, high precision and reproducibility. Thus, the synthesis of stable and controllable perovskite nanocrystals through microfluidic technology offers a promising solution to the challenge in repeatability of similar size. The development of more efficient and reliable methods for synthesizing perovskite nanocrystals will help accelerate their practical applications in aforementioned fields.

## 2. Experimental Method

### *2.1. Microfluidic chip fabrication*

Firstly, the curing agent and PDMS base in a ratio of one to ten were mixed and degassed; secondly, the prepared PDMS mixture was poured into the master mold and degassed multiple times to eliminate air bubbles; furthermore, to cure the liquid PDMS the master molds were placed in the oven at 80 °C for two hours; finally, the prepared replicas and glass were treated in the oxygen plasma and sealed together. To strengthen the formed connection, the chips were placed on a hot plate at 100 °C for 1 hour.

### *2.2. Chemical synthesis*

To obtain $CsPbBr_3$ perovskite precursor, 64 g of CsBr was mixed with 110 g of $PbBr_2$ and 3 mL of DMSO in a N2-filled glovebox and shaken for 10 min to obtain a clear solution. The prepared perovskite precursor was further used for the synthesis.

### *2.3. Microfluidic synthesis*

First, the prepared reagents (isopropyl alcohol and perovskite precursor) need to be placed in two different syringes. The two syringes are then fixed to the syringe pump and the same flow rate is set according to the size of the nanoparticles required. The synthesis reaction can be clearly observed using ancal microscope. To obtain different size of perovskite particles the flow rate of the reagents supply is varied in the range of 10 to 200 uL/min, as presented in the table 1.

### 2.4. *Stable suspension*

Synthesized perovskite particles are collected at the output of the microfluidic chip in a centrifuge tube containing a mixture of 1 $mL$ of toluene, 100 $\mu L$ of oleylamine and 100 $\mu L$ of oleic acid. At the end of the entire microfluidic synthesis reaction, the output sample is shaken well for 2 minutes and waited for 30s to allow all perovskite particles to be stably suspended in the solution.

## 3. Results

Scanning electron microscopy (SEM, Quanta 200, FEI, Netherlands) with an acceleration voltage of 20 kV was used to structurally characterize the samples. The samples were drop-cast on silica substrate for further SEM analysis. The SEM images were then analyzed to estimate the average size of the perovskite particles in the samples (Table 1), which were obtained by varying the flow rate of the reagents in the microfluidic chip.
Figure 1 shows the dependency of the perovskite particles average size on the flow rate of the reagents supply into the co-flow microfluidic chip. The observed trend suggests that nanoparticles size is decreasing with increasing flow rate.

| Sample | Flow Rate($\mu L/min$) | Reaction Time(t) | Average Size($\mu m$) |
|---|---|---|---|
| #1 | 10 | 314 | 1.137±0.565 |
| #2 | 20 | 155 | 1.213±0.531 |
| #3 | 50 | 74 | 0.882±0.394 |
| #4 | 100 | 62 | 1.041±0.341 |
| #5 | 150 | 26 | 0.415±0.231 |
| #6 | 200 | 12 | 0.711±0.316 |

Table 1. Size variation of the obtained perovskite particles size on the flow rate of the reagents supply.

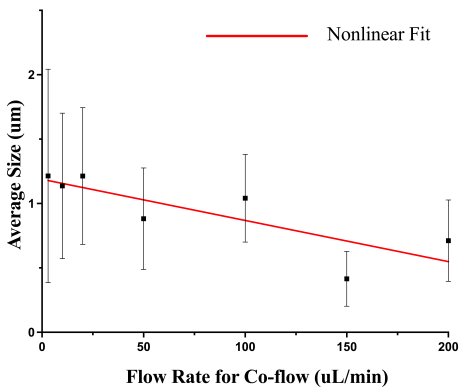


Fig. 1. The dependency of the perovskite particles average size on the flow rate of the reagents supply into the co-flow microfluidic chip.

## 4. Acknowledgements

This work was supported by the Russian Science Foundation (Project 21-73-20189).

## References

1. Sutherland B R, Sargent E H. Perovskite photonic sources[J]. Nature Photonics, 2016, 10(5): 295-302.
2. Tang, B.; Hu, Y.; Dong, H.; Sun, L.; Zhao, B.; Jiang, X.; Zhang, L. An All-Inorganic Perovskite-Phase Rubidium Lead Bromide Nanolaser. Angew. Chem. 2019, 131, 1628016286.
3. Koryakina I G, Naumochkin M, Markina D I, et al. Single-Step Microfluidic Synthesis of Halide Perovskite Nanolasers in Suspension[J]. Chemistry of Materials, 2021, 33(8): 2777-2784.

# Study of n-diamond and carbon nanowalls structure synthsized by the RF-PECVD

**A.M. Mumlyakov, E.A. Pershina, A.A. Shibalova, M.V. Shibalov, Yu.V. Anufriev, I.A. Filippov, V.V Sen', M.A. Tarkhov**

Institute of Nanotechnology of Microelectronics of Russian Academy of Science, Leninsky Prospekt 32A, Moscow 119991, Russia

email: mumlyakov.a@inme-ras.ru

**Abstract.** In this work, a hybrid n-diamond-carbon nanowalls structure was synthesized on a 100 mm diameter silicon wafer using RF-PECVD (CCP type). This structure was analyzed by transmission microscopy and X-ray diffraction. It was found that the addition of carbon monoxide (CO) to a gas mixture of methane ($CH_4$), argon (Ar), and hydrogen ($H_2$) leads to the formation of n-diamond nanocrystals in the basal layer. Using plasma surface treatment techniques, the carbon nanowalls were fully removed and the lower layer consisting of n-diamond was studied separately, for which X-ray diffraction results of a separate n-diamond phase were obtained for the first time.

## 1. Introduction

Carbon nanowalls (CNWs) - structures consist of graphite-like two-dimensional sheets oriented almost perpendicular to the substrate surface. Vertical orientation, open and ultra-thin edges of graphite sheets, large specific surface area, and open areas between graphite sheets forms the unique morphological and structural properties of CNWs. The most important step in the CNWs synthesis process is the formation of the interface layer between the substrate and the carbon walls, called the basal layer. It ensures uniform distribution of heat and electric current in the substrate plane and plays an important role in the contact resistance and nucleation of CNWs. In our studies, we found that addition of extra carbon source to the gas mixture ($Ar/CH_4/H_2$) in the form of carbon monoxide (CO), produce unique interface layer consisting of new-diamond (n-diamond, FCC-carbon).

## 2. Experimental technique

Silicon p-type wafers with a diameter of 100 mm were used as initial substrates. The synthesis of carbon nanowalls was performed in a reactor with a high-frequency capacitively coupled plasma. A gas mixture of Ar, $CH_4$, CO, and $H_2$ was used as gas precursors, with a 200 sccm:10 sccm:7.5 sccm: 2.5 sccm ratio, respectively.

The structural analysis was carried out using the Empyrean diffractometer by Malvern Panalytical with Cu Kα1-radiation. The structure of n-diamond-carbon nanowalls was investigated by HRTEM using the JEOL JEM-2100 Plus microscope at an accelerating voltage of 200 kV.

## 3. Results

The diffraction pattern of the sample synthesized without CO (Fig.1a, blue graph) shows peaks at angles 2θ equal to 25.4°, 43.0°, 45-46°, 78.5° related to carbon nanowalls. For the sample synthesized with CO addition (Fig.1a, red graph), additional peaks at 2θ angles equal to 44.6°, 52.1°, 76.7°, 93.2°, 98.8°. In accordance with the literature data the detected peaks belong to the n-diamond phase [1].

Fig.1b shows a general view of the CNWs-Si interface of the sample synthesized with CO. As can be seen on the TEM image, individual n-diamond nanocrystals have formed at the CNWs-Si interface. The average size of the observed particles, is 10 nm.

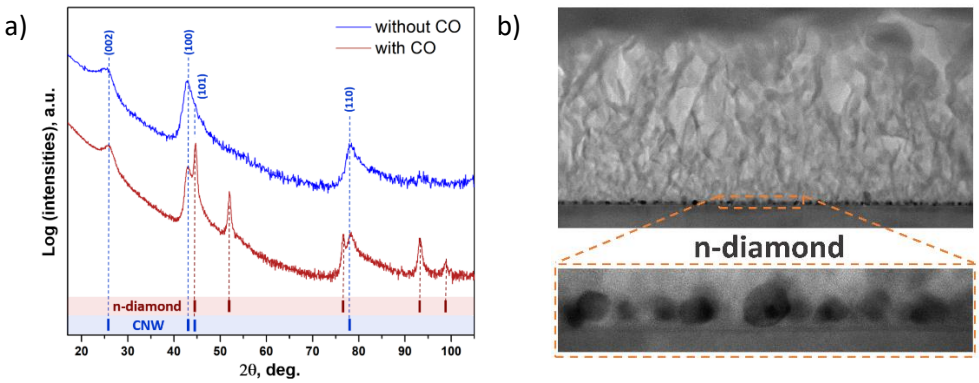


**Fig. 1.** a) X-ray diffraction pattern obtained at sliding incidence of radiation for the sample without CO (blue graph), sample with CO (red graph). (b) Cross-sectional TEM images of CNWs grown on Si substrate with CO.

Since the literature does not present experimentally obtained X-ray diffraction patterns for the n-diamond phase without overlapping peaks from accompanying phases, we remove CNWs from the hybrid structure. The resulting diffraction pattern (Fig.2) clearly shows peaks at 2θ angles equal to 44.6°, 51.8°, 76.4°, 93.0°, and 98.5° for the Kα1 position for a range of 2θ angles from 25° to 105°. The ratio of intensities is presented in Fig.2. The number of reflexes, their relative position and ratio of intensities allow us to confirm that the n-diamond structure is described by the crystallographic group $Fm\bar{3}m$, as it was suggested in several works [2].

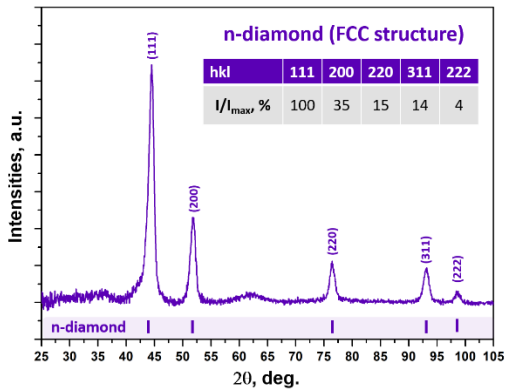


**Fig. 2.** Experimentally obtained X-ray diffraction pattern for the n-diamond nanocrystalline phase with an indication of the relative intensity of each peak.

## 4. Conclusion

The hybrid structure of n-diamond- carbon nanowalls was successfully synthesized in a capacitive coupled plasma discharge using a mixture of carbon monoxide, methane, hydrogen, and argon. It was shown that CO added to the gas mixture was the key to the formation of n-diamond nanocrystalls. Due to the selective removal of CNWs from the hybrid structure, X-ray diffraction pattern were experimentally obtained for the n-diamond phase without overlapping peaks from accompanying phases.


## Acknowledgments

The authors are grateful to Grant № FFFG-2022-0003 in support of the Ministry of Science and Higher Education of the Russian Federation. Fabrication and characterization of the samples were carried out at large scale facility complex for heterogeneous integration technologies and silicon + carbon nanotechnologies.


## References


[1] Peng, J. L., et al. "Nano-crystals of c-diamond, n-diamond and i-carbon grown in carbon-ion implanted fused quartz." *International Journal of Modern Physics B* 15.23 (2001): 3107-3123.

[2] Palatnik, L. S., et al. "y carbon Sov. Phys." *JETP* 60 (1984): 520-522.

# Ultrathin Cr and Fe monosilicides on Si(111) substrate: formation, optical and thermoelectrical properties

**K. N. Galkin [1✉], I. M. Chernev [1], E. Yu. Subbotin [1], A. M. Maslov [1], O. V. Kropachev [1], D. L. Goroshko [1], E. V. Argunov [2], A. K. Gutakovskii [3], N. G. Galkin [1]**

[1] Institute of Automation and Control Processes, FEB RAS, Vladivostok, Russia;
[2] National University of Science and Technology (MISIS), Moscow, Russia;
[3] Rzhanov Institute of Semiconductor Physics, SB RAS, Novosibirsk, Russia
✉galkinkn@iacp.dvo.ru

**Abstract.** In this study, the formation, crystal structure, optical and thermoelectric properties of ultrathin films of iron and chromium monosilicides are considered, which exhibit optical and thermoelectric properties characteristic of semimetals with a low density of states near the Fermi level and the main contribution of holes to the Seebeck coefficient in the temperature range 120 – 400 K and the transition to its negative values at T> 400 K.

**Keywords:** chromium monosilicide, iron monosilicide, films, epitaxy, solid-phase epitaxy, films growth, optical properties, thermoelectrical properties.

Funding: The study of the formation, structure and properties of Fe and Cr monosilicides was financially supported by the Russian Science Foundation grant number [22-12-00036].

## Introduction

In recent years, there has been renewed interest in the study of monosilicides of transition metals such as Cr, Mn, Fe, and Co with the cubic structure B20 of space group $P2_13$ [1], which exhibit interesting electrical [2], thermoelectric [3] and magnetic [4] properties. Most of the experimental studies were carried out for single crystals and bulk polycrystals. The epitaxial growth of ultrathin films on silicon may be of interest from the point of view of changes in their structure due to stresses. But the growth of films with a thickness of a few nanometers has not been previously carried out and their properties have not been studied.

## Materials and methods

Growth experiments were carried out in an ultrahigh vacuum setup with a base vacuum of $2x10^{-10}$ Torr, equipped with a slow electron diffraction analyzer, chromium (Cr) and iron (Fe) sublimation sources, a quartz thickness gauge, a three-coordinate manipulator, and a holder for four samples. The growth of films of Cr and Fe monosilicides (CrSi and FeSi) on n-Si(111) substrates with high resistivity ρ=1000 Ohm×cm (FZ1000) was carried out by solid-phase epitaxy (T=350 °C) after high-temperature annealing of silicon substrates at T = 1250 ºC. The calculated thickness of the deposited metal layers was 3 nm for chromium and 2 nm for iron. After unloading from the growth chamber, the morphology of the grown films was studied on a Solver P47 scanning probe microscope. The reflection and transmission spectra were recorded on spectrophotometers: U-3010 (Hitachi) and VERTEX v80 (BRUKER). The structure of the films was studied by high-resolution transmission electron microscopy (HRTEM) on cross sections using a JEOL-4000EX microscope (ISP SB RAS). The thermoelectrical measurements were carried out in a $He_2$ atmosphere in a temperature range from 80 to 473 K in a Cryotel laboratory setup (MISIS).

## Results and discussion

AFM studies of the morphology of CrSi and FeSi films showed that they are continuous and smooth with an RMS roughness of 0.3 to 1.2 nm. The HRTEM images of the cross sections of two samples confirmed the continuity of the ultrathin films and their small thickness (CrSi: 3.2 nm and FeSi: 2.85 nm), which proves good agreement with the calibration data of the metal deposition rate. Some inhomogeneity of their HRTEM images is caused by the oxidation of its upper layer after unloading from the growth chamber and storage for a month before sample

preparation for HRTEM. The film/Si interface is not atomically smooth, which indicates the use of Si atoms from the substrate during film formation. The FFT image of the films showed reflections from CrSi and FeSi silicides. For individual CrSi (FeSi) nanograins, there are epitaxial relations: CrSi(210)||Si(111) и CrSi[001]||Si[$1\bar{1}0$] (FeSi(111)||Si(111), FeSi[$\bar{1}\bar{1}2$]||Si[$1\bar{1}0$] и FeSi[$1\bar{1}0$]||Si[$11\bar{2}$]).

According to the transmission and reflection spectra for ultrathin CrSi and FeSi films in the transparency region of the silicon substrate, their refractive index and extinction spectra were calculated using the RT procedure [5]. It has been established that the spectra of the absorption coefficients of both films depend almost linearly on the photon energy, which is associated with the semimetallic or bad-metal nature of absorption with a small overlap of bands at the Fermi level and somewhat above it.

Thermoelectric measurements for samples with CrSi and FeSi ultrathin films in the temperature range of 120–450 K showed that the Seebeck coefficient remains positive (50–200 μV/K) up to 400 K and then (at 400–470 K) changes sign to negative, which is due to both with a decrease in the concentration of holes in the films and with an increase in the contribution of the substrate electrons in competition with holes in the film. However, the extremely high negative Seebeck coefficient of the substrate (from -300 μV/K at T=470 K to -1500 μV/K at T=280 K) [6] was not detected at lower temperatures, which proves the predominant contribution of the films to the thermo-EMF signal over the entire temperature range up to 400 K. The temperature dependences of the power factor are calculated and it is shown that its maximum value of 5 mW/(cm × $K^2$) at a temperature of 250 K is observed for an ultrathin FeSi film with a thickness of 2.85 nm, while for a CrSi film it sharply increases to 4.5 mW/(cm ×$K^2$) with decreasing temperature.

## Conclusion

Ultrathin CrSi and FeSi films with thicknesses of 2.85 - 3.2 nm on silicon with (111) orientation were grown by solid-phase epitaxy at a temperature of 350 °C. The epitaxial orientations for both films were established from the HRTEM data and their deformations were established. It is shown that the films have a semimetallic nature of absorption at photon energies up to 1.1 eV. During thermal generation of carriers in films, along with a significant Seebeck coefficient ((50–200 μV/K) at temperatures from 100 to 400 K, record values of the power factor of 4–5 mW/(cm × $K^2$) were observed, which is promising for thin film thermal converters.

## REFERENCES


1. **Dutta P., Pandey S. K.**, Investigating the electronic structure of MSi (M = Cr, Mn, Fe & Co) and calculating $U_{eff}$ & $J$ by using cDFT, Computational Condensed Matter. 16 (2018) e0035(1-7).

2. **Pshenay-Severin D. A., Ivanov Yu. V., Burkov A. T., Novikov S. V., Zaitsev V. K., Reith H.**, Electronic structure and thermoelectric properties of transition metal monosilicides, Journal of Electronic Materials. 47 (2018) 3277–3281.

3. **Grigoriev S. V., Maleyev S. V., Okorokov A. I., Chetverikov Y. O., Böni P., Georgii R., Lamago D., Eckerlebe H., Pranzas K.**, Magnetic structure of MnSi under an applied field probed by polarized small-angle neutron scattering, Phys. Rev. B. 74 (2006) 214414(1-10).

4. **Antonov A. S., Novikov S. V., Pshenay-Severin D. A., Burkov A. T.**, Thermoelectric properties of cobalt monosilicide and its alloys, Semiconductors. 53 (2019) 667–672.

5. **Galkin N. G., Maslov A. M., Konchenko A. V.**, Optical and photospectral properties of $CrSi_2$ A-type epitaxial films on Si(111), Thin Solid Films. 311 (1997) 230–238.

6. **Galkin N. G., Galkin K. N., Dotsenko S. A., Serhiienko S. A., Khovaylo V. V., Gutakovskii A. K.**, Effect of embedding of $CrSi_2$ and β-$FeSi_2$ nanocrystals into n-type conductivity silicon on the transport and thermal generation of carriers, Appl. Surf. Sci. 566 (2021) 150620(1-13).

# HOM interference of coupled photons in a waveguide beam splitter

**Yu. V. Tsykareva** [1✉]

[1] Northern Arctic Federal University named after M.V. Lomonosov, Arkhangelsk, Russia;

✉yu.cykareva@narfu.ru

**Abstract.** Currently the theory of linear beam splitters has already been created and well developed, the main difference of which is simple mathematical expressions and the consideration of two key cases - with monochromatic and non-monochromatic photons. The main difference between these types of photons is that non-monochromatic photons are frequency dependent. In this paper, we consider the influence of the HOM effect in a linear beam splitter, taking into account the type of photons, each of the cases is considered separately, and a comparative analysis is carried out. The development of the theory of the HOM effect can be useful for quantum technologies, in particular for the creation of a linear optical quantum computing.

**Keywords:** quantum entanglement, HOM interference, HOM effect, photons.

**Funding:** The work was supported by Russian Science Foundation grant № 20-72-10151.

The Hong-Ou-Mendel effect (HOM effect) was discovered and experimentally demonstrated by Hong et al. in 1987 [1] and theoretically described in [2]. In this paper, we will consider its implementation on a linear beam splitter consisting of a substrate and two waveguides on it, closely converging in the center, with two input and output ports, and with detectors at each output port. The essence of the effect under consideration is that two identical single-photon waves fall on the beam splitter in a ratio of 1:1 (with reflection coefficients R and transmittance T close to 1/2), one for each input port. When photons are identical, they cancel each other out. The HOM effect often takes place both in fundamental works on quantum mechanics and in practical implementations of quantum technologies [3]. A simple theoretical explanation of the HOM effect has been found based on the constant coefficients R and T and the statistical distribution of bosonic photons [4, 5]. In this interpretation, we are not interested in what happens to the incident photons in the beam splitter. To do this, we consider lossless with constant coefficients R and T (i.e., "ordinary" beam splitters), and the beam splitter is the source of two other photons, subject to bosonic statistics. Choosing the values of the coefficients R = T = 1/2 and substituting them into the expression for the wave function of photons at the output ports of the beam splitter from [4], it turns out that in this case the photons come out in pairs, i.e. the probability will be P = 1/2 for each of the detectors, which contradicts the classical idea of the separation of two beams of light with coefficients R = T = 1/2. In the classical representation, at R = T = 1/2, there can be 4 options: 1. the first and second photons hit detectors 1 and 2, respectively; 2. the first and second photons hit detectors 2 and 1, respectively; 3. the first and second photons hit detector 1; 4. The first and second photons hit detector 2.

As a result, there are 4 equally probable events, which obviously gives the probability P = 1/4 for each of them. This phenomenon is called the HOM effect and is a good way to test the quantum properties of not only photons but other particles as well. In other words, in the HOM effect, the probability of photons hitting the first detector, and for the second detector P1,2 = (R − T )2, with equal R and T will be equal to zero. If we consider non-monochromatic photons, but identical (frequency-dependent beam splitters), then choosing R = T = 1/2, we take into account frequency-dependent fluctuations of the beam splitter coefficients, which were not previously taken into account. These issues will be discussed in detail in this work.

## REFERENCES

1. **Hong, C. K. , Ou, Z. Y., Mandel, L.,** Measurement of subpicosecond time intervals between two photons by interference, Physical Review Letters. 59 (1987) 2044–2046.

2. **Salvat, F., Martinez, J. D., Mayol, R., Parellada J**., Analytical Dirac-Hartree-Fock-Slater screening function for atoms (Z=1–92), Physical Review A. 36 (2) (1987) 467-474.

3. **Ou, Z.-Y.**, Multi-Photon Quantum Interference, Springer, New York, 2007.

4. **Makarov, D.N**, Theory of HOM interference on coupled waveguides, Optics Letters. 45 (2020) 6322–6325.

5. **Makarov, D.N.**, Fluctuations in the detection of the HOM effect, Scientific Reports 10 (2020) 20124.

# Localization microscopy of single photon emitters in locally strained monolayer semiconductor

**Artem Abramov** [1✉], **Igor Chestnov** [1], **Ivan Iorsh** [1], **Vasily Kravtsov** [1]
[1] ITMO University, Saint-Petersburg, Russia
✉artem.abramov@metalab.ifmo.ru

**Abstract.** Integration of single photon emitters with nanophotonic structures on a chip is key for the development of future quantum optoelectronic devices. Here we study the formation of single photon emitters in a $WSe_2$ monolayer by local nanoindentation with an atomic force microscope probe. Using the bichromatic photoluminescence-imaging approach, we define the spatial locations of single photon emitters with deep sub-wavelength accuracy. From atomic force microscopy profiles, we calculate strain field maps in the nanoindented regions of the $WSe_2$ monolayer and extract local strain parameters at the experimentally determined emitter locations.

**Keywords:** Single photon emitter, two-dimensional materials, nanophotonics, quantum optics.

**Funding:** This research was supported by Priority 2030 Federal Academic Leadership Program.

## Introduction

Single photon emitters (SPEs) are important elements for applications in quantum communication and computing devices [1]. One of the promising platforms for creating single photon emitters is provided by two-dimensional transition metal dichalcogenides (TMDs) [2]. Deformation of a two-dimensional material, for example, by the probe of an atomic force microscope (AFM), can lead to the formation of SPEs in TMD monolayers [3, 4]. The practical advantage of this approach is the possibility of forming arrays of emitters in specified locations on the chip due to the precise positioning of the AFM probe and the integration of emitters with nanophotonic structures on the chip. However, the integration accuracy is limited by the size of the nanoindent.

## Results and discussion

In this work, we investigate the formation process of SPEs in a WSe2 monolayer by local deformation with an AFM probe. To this end, we detect photoluminescence (PL) signal and determine the position of each emitter within the nanoindented region on a deep sub-wavelength scale using the bichromatic photoluminescence-imaging (PL-imaging) approach [5, 6]. Our experimental sample is $SiO_2$(1 μm)/Si substrate with silver alignment marks on the surface, covered with a thin layer of PMMA polymer. $WSe_2$ monolayer is transferred to the polymer. The array of single photon emitters is fabricated in the $WSe_2$ monolayer by the method of local deformation by the AFM probe (Fig. 1a). SPEs with wavelength greater than 750 nm are selected spectrally and by polarization (Fig. 1b). We verify the single-photon character of the fabricated emitters via second order correlation function measurements, and we have the best achieved value $g(2)(0) = 0.02$.

The bichromatic PL-imaging approach consists in simultaneous illumination of the sample with 632.8 nm HeNe laser to excite the photoluminescence of the SPE and with light with a longer wavelength to illuminate the alignment marks. Reflected light and PL of SPE are imaged on the CMOS camera (Fig. 1c). The alignment marks are also visible on the AFM map due to the swelling of the PMMA above them (Fig. 1d). The coordinates of the centers of the alignment marks and the emitters were obtained from orthogonal linear scans of the AFM map and the optical image using Gaussian function fitting (Fig. 1e). The exact position of the SPE is defined by converting the coordinates of the alignment marks and the SPE from the optical image to the AFM map of the structure. On average, the uncertainty of the SPE position obtained from a series of images was less than 60 nm. We then superimpose the SPE positions with the map of strain fields, which was calculated from the AFM profiles (Fig. 1f). The parameters of local deformation obtained via this

procedure will help better understand the process of formation of single photon sources in a two-dimensional semiconductor at the microscopic level.

The results of our research work are important for the practical application of the local deformation method in the creation of single photon generators for quantum communication and computing devices.

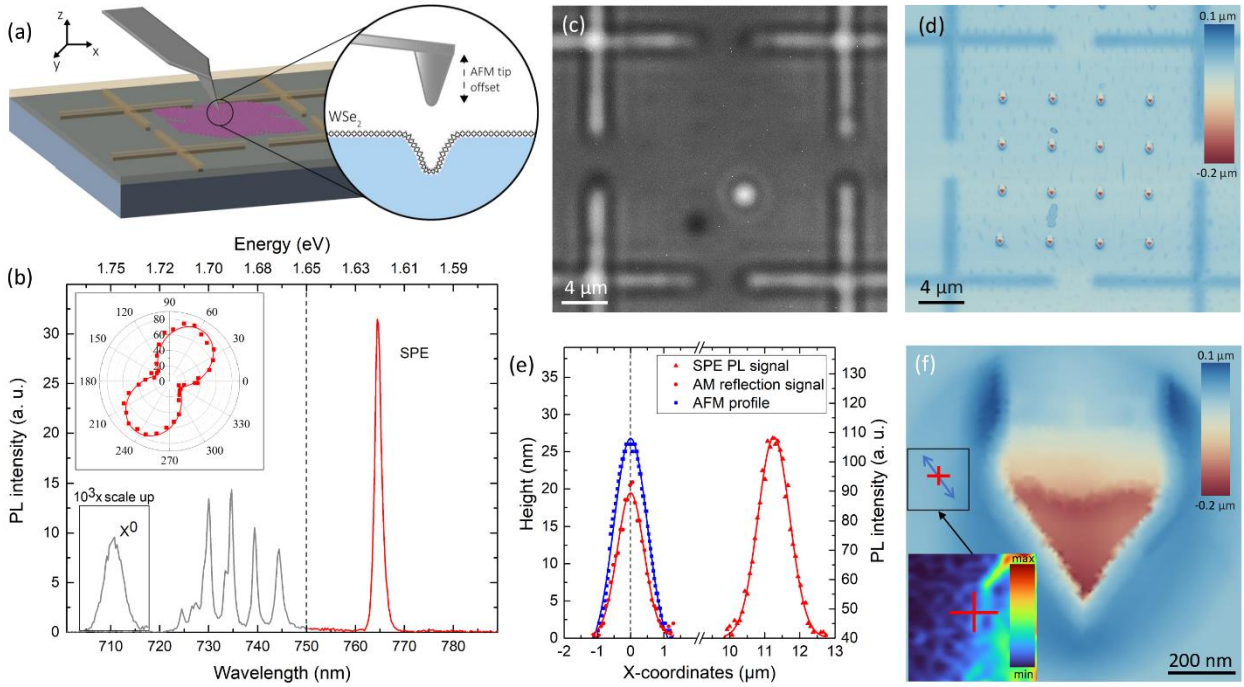


Figure 1: (a) Schematic of SPE fabrication process in $WSe_2$ monolayer by the AFM probe on the sample with alignment marks. (b) The photoluminescence spectrum one of the SPE in $WSe_2$ monolayer formed on a nanoindet (the wavelength of the emitter radiation is 764 nm). The filtration of 750 nm LPF is schematically shown. The spectrum of neutral exciton $X^0$ of $WSe_2$ monolayer is shown in the down inset. The polarization dependence is shown in the upper inset. (c) Optical image of the photoluminescence from a single SPE and reflected light by the alignment marks. (d) AFM scan of a sample with an array of nanoindents in $WSe_2$ monolayer and alignment marks (coincides with Fig. 1c). (e) Orthogonal line cuts (x-axis) of the photoluminescence image, showing the profile of the SPE emission (red triangle symbols) and of the image of the alignment mark (red square symbols) and their Gaussian fits (red lines). Orthogonal line cut of the AFM scan, showing the profile of the alignment mark (blue square symbols) and its Gaussian fit (blue line). (f) The exact position of the SPE near the indent (the size of the cross shows uncertainty). The blue arrow shows the polarization of the SPE. The inset shows the position of the SPE on the strain map.

## REFERENCES


1. Aharonovich, I., Englund, D. & Toth, M. Solid-state single-photon emitters. Nature Photonics 10, 631–641 (2016).
2. Koperski, M. et al. Single photon emitters in exfoliated WSe2 structures. Nature nanotechnology 10, 503–506 (2015).
3. Rosenberger, M. R. et al. Quantum calligraphy: writing single-photon emitters in a two-dimensional materials platform. ACS nano 13, 904–912 (2019).
4. Li, X. et al. Proximity induced chiral quantum light generation in strain-engineered WSe2/NiPS3 heterostructures. arXiv preprint arXiv:2203.00797 (2022).
5. Thompson, R. E., Larson, D. R. & Webb, W. W. Precise nanometer localization analysis for individual fluorescent probes. Biophysical journal 82, 2775–2783 (2002).
6. Sapienza, L., Davan ̧co, M., Badolato, A. & Srinivasan, K. Nanoscale optical positioning of single quantum dots for bright and pure single-photon emission. Nature communications 6, 1–8 (2015).

Conference materials
UDC 537.876.4
DOI: https://doi.org/10.18721/JPM.

# Photoluminescence anisotropy in hybrid nanostructures based on gallium phosphide nanowire and 2D transition metal dichalcogenides

**M. A. Anikina[1,2]✉, A. Kuznetsov[1,2], A. N. Toksumakov[1,3], V. V. Dremov[1], D. A. Ghazaryan[1], V. V. Fedorov[2,4], A. V. Arsenin[1], V. S. Volkov[1], A. D. Bolshakov[1,2]**
[1] Moscow Institute of Physics and Technology, Dolgoprudny, Russia
[2] Alferov University, Saint Petersburg, Russia
[3]Emanuel Institute of Biochemical Physics RAS, Moscow, Russia
[4]Peter the Great St. Petersburg Polytechnic University, Saint Petersburg, Russia
✉ anikina_mar@spbau.ru

**Abstract.** Integration of nanophotonic structures having different geometry is a well-established way to promote desired optical effects. This work is aimed at study of the optical properties of a hybrid structure based on a transition metal dichalcogenides (TMDC) thin layer and III-V nanowires. Complementary employment of these nanostructures promotes efficient guiding of the TMDC photoluminescence along the substrate plane. The structures were studied by μ-Raman μ- photoluminescence spectroscopy at room temperature. We demonstrate experimentally guiding of the TMDC photoluminescence through the individual nanowires and analyze this phenomenon. The results of the work shed a light on new ways for fabrication of integrated optical circuitry components.

**Keywords:** photonics, photoluminescence, 2D TMDC, III–V semiconductors, nanowires, Raman spectroscopy

**Funding:** Ministry of Science and Higher Education of the Russian Federation (Agreement 075-03-2023-106, project FSMG-2021-0005; Grant FSRM-2023-0009). Russian Science Foundation (grant No. 22-19-00738).

© Anikina M.A., Kuznetsov A., Toksumakov A.N., Dremov V.V., Ghazaryan D.A., Fedorov V.V., Arsenin A.V., Volkov V.S., Bolshakov A.D., 2023. Published by Peter the Great St. Petersburg Polytechnic University.

Материалы конференции
УДК 537.876.4
DOI: https://doi.org/10.18721/JPM.

## Introduction

Thin layers of transition metal dichalcogenides (TMDCs) are a large family of two-dimensional materials with a number of unique physical properties. It is especially interesting that some of these materials exhibit an efficient photoluminescence response in the visible and near-infrared ranges [1]. One of the problems limiting the usage of these materials for the creation of devices is the low absorption capacity due to their small thickness. It is possible to optimize absorption by using resonant optical structures. Such structures include nanowires (NWs) of semiconductor compounds. It should be noted that these structures are able to support both resonant modes and waveguide modes, that makes them suitable for making elements for anisotropic signal output. So, it becomes possible to fabricate nanoscale radiation sources for optical data processing on-chip systems.

## Materials and Methods

The aim of this work is to make and study the optical properties of a hybrid structure based on a thin layer of molybdenum disulfide ($MoS_2$) and NWs of gallium phosphide (GaP). Thin layers

of $MoS_2$ were synthesized by mechanical exfoliation of bulk crystals. GaP NWs were grown on a Si (111) substrate by molecular beam epitaxy using the vapor–liquid–solid mechanism [2].

The transfer of GaP NWs to TMDC layers was carried out by a drop-cast technique: a small piece of the Si substrate with a vertical array of NWs was placed into isopropanol and treated in an ultrasonic bath. A small volume of the suspension was dropped onto the $Si/SiO_x$ substrate with thin TMDC layers. NWs were additionally positioned with an AFM probe to achieve a suitable geometry of the fabricated structure.

The structures were studied by μ-Raman and μ-photoluminescence (μ-PL) techniques at room temperature. The measurements were carried out on a Horiba LabRAM HR 800 spectrometer equipped with a confocal microscope with a 100x magnification objective (N.A. = 0.9). A table with piezoelectric controllers facilitated precise positioning of the laser beam, making it possible to measure PL maps with a high spatial resolution and in steps of less than 100 nm. The excitation source was a 532-nm solid-state laser with diode pump.

## Results and Discussion

The optical image (Fig. 1a) shows the obtained sample based on the GaP NW and the thin TMDC layer. The difference between $MoS_2$ vibrational modes $E^1_{2g}$ and $A_{2g}$ on the Raman spectrum can be used to estimate the number of material layers [3]. This difference is 21.2 $cm^{-1}$ in our case, corresponding to the $MoS_2$ bilayer. The PL intensity map of the hybrid structure (Fig. 1f) demonstrates the PL emission from the $MoS_2$ layer. The corresponding PL spectra (Fig. 1g) show two features: emission occurs as a result of direct A and B exciton transitions at the K point of the Brillouin zone according to the electronic band structure [4]. It should be noted, that a decrease in the PL signal is observed along the NWs lying on the $MoS_2$ layer (Fig. 1f). This can be related to the field localization inside the NWs, which will be discussed in detail below.

One of the NW was moved with an AFM probe (Fig. 1b) for a detailed study of the light propagation along a single NW. The Raman spectrum of the NW tip in area 2 (Fig. 1e) shows only GaP vibrational modes, which indicates that there are no TMDC layers under it. However bright spots can be seen on the PL integral intensity map of area 2 (Fig. 1c) obtained in the $MoS_2$ emission range (600–715 nm). The waveguiding of GaP NWs were earlier reported for various wavelengths [5]. Thus, the NW promotes waveguiding for both the initial excitation radiation and secondary PL signal, which is the response of the $MoS_2$ layer under the laser excitation. The PL spectrum corresponding to the bright spot (Fig. 1h) correlates with the result shown in Fig. 1g, which confirms the earlier suggestion about the waveguiding of the NW. The tip of the neighboring NW was moved only in area 1 (Fig. 1b) as a result of manipulating by the AFM probe. Therefore, the presence of the second spot on the PL integral intensity map of area 2 can be explained by the NWs optical coupling [6].

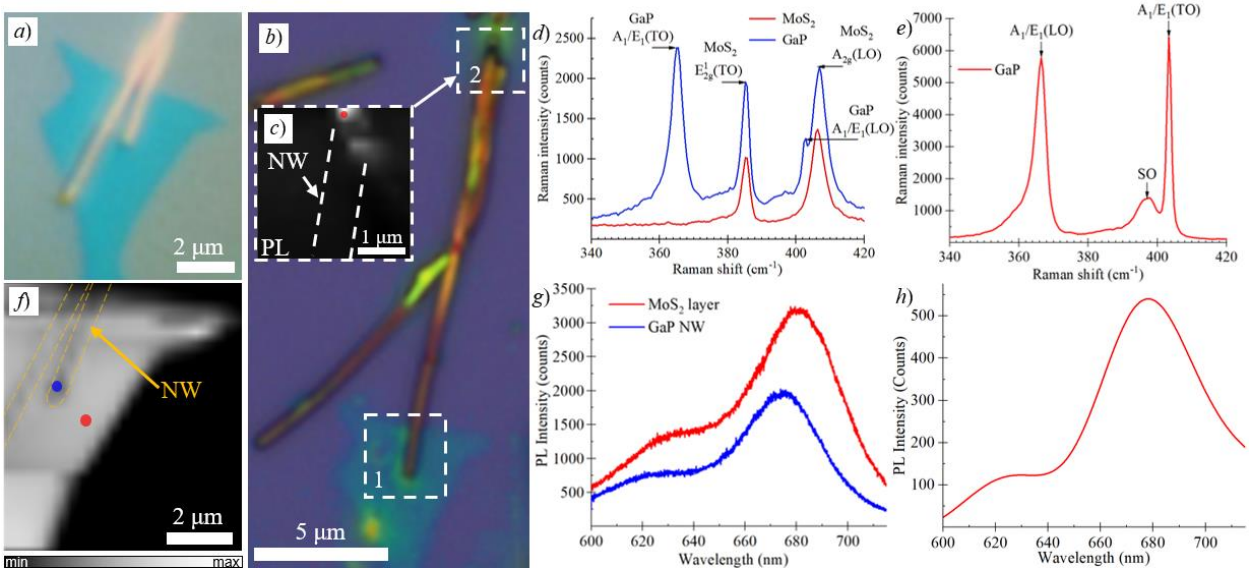

Fig. 1. Characterization of hybrid structures based on $MoS_2$ and GaP NWs: Optical image of the hybrid structure before (a) and after manipulation with the AFM probe (b); RT PL integral intensity map of area 2 (c); Raman spectra of $MoS_2$ layer and GaP NW in area 1 (d); Raman spectrum of the NW tip in area 2 (e); RT PL integral intensity map of area 1 before manipulation with the AFM probe (f); PL spectra of the $MoS_2$ layer and GaP NW in area 1 (g); PL spectrum of the transmitted signal: with excitation at area 1, and signal collection in area 2 (h)

## Conclusion

We demonstrate that a hybrid structure based on thin layers of $MoS_2$ and GaP NWs exhibits anisotropic photoluminescence due to the combination of the TMDC layers radiative properties and the semiconductor NWs waveguiding. This result proves the possibility of directional transmission of optical signals at the nanoscale, which makes such structures promising for applications in integrated photonics.


## Acknowledgments

M.A.A. thanks the Ministry of Science and Higher Education of the Russian Federation (agreement 075-03-2023-106, project FSMG-2021-0005) for support of the structures fabrication. V.S.V. acknowledges support of the spectroscopy by the Russian Science Foundation (grant No. 22-19-00738). A.K. thanks the Ministry of Science and Higher Education of the Russian Federation (Grant FSRM-2023-0009) for support of the data analysis.


## REFERENCES


1. **Tonndorf P., Schmidt R., Böttger P., Zhang X., Börner J., Liebig A., Albrecht M., Kloc C., Gordan O., Zahn D. R., de Vasconcellos S. M.**, Photoluminescence emission and Raman response of monolayer $MoS_2$, $MoSe_2$, and $WSe_2$, Optics express. 21 (4) (2013) 4908–4916.
2. **Fedorov V. V., Bolshakov A. D., Dvoretckaia L. N., Sapunov G. A., Kirilenko D. A., Mozharov A. M., Shugurov K. Y., Shkoldin V. A., Cirlin G. E., Mukhin I. S.**, Self-catalyzed mbe-grown gap nanowires on Si(111): V/III ratio effects on the morphology and crystal phase switching, Semiconductors. 52 (2018) 2092–2095.
3. **Ye M., Winslow D., Zhang D., Pandey R., Yap Y. K.**, Recent advancement on the optical properties of two-dimensional molybdenum disulfide ($MoS_2$) thin films, Photonics. 2 (1) (2015) 288–307.
4. **Splendiani A., Sun L., Zhang Y., Li T., Kim J., Chim C. Y., Galli G., Wang F.**, Emerging photoluminescence in monolayer $MoS_2$, Nano letters. 10 (4) (2010) 1271–1275.
5. **Kuznetsov A., Fominykh N., Kondratev V., Fedina S. V.**, GaP Nanowire Waveguides, 2022 Conference of Russian Young Researchers in Electrical and Electronic Engineering (ElConRus), IEEE. (2022) 1126–1129.
6. **Anikina M. A., Roy P., Kadinskaya S. A., Kuznetsov A., Kondratev V. M., Bolshakov A.D.**, Numerical Study of GaP Nanowires: Individual and Coupled Optical Waveguides and Resonant Phenomena, Nanomaterials. 13 (1) (2023) 56.


## THE AUTHORS


**ANIKINA Maria A.**
anikina_mar@spbau.ru
ORCID: 0000-0002-5522-5026

**KUZNETSOV Alexey**
alkuznetsov1998@gmail.com
ORCID: 0000-0001-7143-6686

**TOKSUMAKOV Adilet N.**
adilet.toksumakov@phystech.edu
ORCID: 0000-0001-5016-1054

**DREMOV Viacheslav V.**
dremovs54@gmail.com
ORCID: 0000-0000-0000-0000

**GHAZARYAN Davit A.**
dav280892@gmail.com
ORCID: 0000-0002-8620-8560

**FEDOROV Vladimir V.**
burunduk.uk@gmail.com
ORCID: 0000-0001-5547-9387

**ARSENIN Aleksey V.**
arsenin.mipt@gmail.com
ORCID: 0000-0002-7506-4389

**VOLKOV Valentyn S.**
vsv.mipt@gmail.com
ORCID: 0000-0003-2637-1371

**BOLSHAKOV Alexey D.**
bolshakov@live.com
ORCID: 0000-0001-7223-7232

# The growth dynamic of Au/Ag alloy nanoparticles in glass

**E. S. Babich** [1✉], **S. A. Scherbak** [1], **V. P. Kaasik** [1]
[1] Alferov University, St. Petersburg, Russia
✉ babicz_e@spbau.ru

**Abstract.** The work is devoted to growth of Au/Ag alloy nanoparticles on a glass substrate by heat treatment of glass containing silver ions and gold nanoparticles. Results of optical and morphological characterizations of the formed nanoparticles, and numerical modeling results of optical properties of Au/Ag nanoparticles are presented and analyzed. The impact of regime of the heat treatment on the proportion of Ag in the alloy nanoparticles is revealed.

**Keywords:** alloy nanoparticles, silver, gold, glass.

**Funding:** This research was funded by the Russian Science Foundation (agreement No. 22-22-20005 dated 23 March 2022) and St. Petersburg Science Foundation (agreement No. 04/2022 dated 13 April 2022), project No. 22-22-20005.

## Introduction

Glass substrates with metal nanoparticles (NPs) are widely used in nanophotonic devices because of unique optical properties of NPs and good chemical and thermal stability of glasses. The NPs increase the efficiency of all types of scattering at the wavelength of surface plasmon resonance (SPR) of NPs and demonstrate ultrafast optical nonlinearities of the second and third orders [1]. Thus, to provide the best performance, the spectral position of SPR of NPs should be adjusted so that it corresponds to the excitation/scattering wavelength. It is proposed to fabricate alloy NPs consisting of two metals, and adjust spectral position of SPR of alloy NPs by changing their composition (ratio of the metals content in NPs) [2]. In this work, we demonstrate the method to form Au/Ag alloy NPs on the glass substrate and reveal the impact of regime of NPs grow on the proportion of Ag in the alloy NPs.

## Materials and Methods

The method that allows the formation of Au/Ag NPs directly on a glass substrate consisted of heat treatment of the soda-lime glass containing both $Ag^+$ ions and Au NPs [3]. In this study, we varied the temperature of the heat treatment from 250°C to 600°C with the same time of the treatment, 15 min. The Au NPs were formed in the glass prior the heat treatment by annealing Au film, which was deposited on the glass in thickness of ~5 nm, at 650°C for 30 min. The $Ag^+$ ions were introduced in the glass by silver-to-sodium ion exchange described elsewhere [4].

The absorbance spectra of the formed Au/Ag NPs were obtained using an UV-VIS spectrophotometer. The lateral sizes and height of the NPs were obtained using both a scanning electron and an atomic-force microscopes. Numerical modeling of the optical characteristics of Au/Ag NPs was performed in COMSOL Multiphysics®.

## Results and Discussion

The numerical modeling of Au/Ag NPs demonstrated that the alloy NPs are characterized by the only optical resonance, which shifts to the lower wavelengths with an increase in the proportion of Ag in Au/Ag NPs. The comparison of the numerical modeling results with the results of optical characterization of the formed NPs and analysis of their morphology revealed that the proportion of Ag in the obtained Au/Ag NPs depends on the temperature of the heat treatment. The increase of the temperature from 250°C to 600°C resulted in increasing Ag proportion in Au/Ag NPs from ~15% to ~48%. The change of the composition of Au/Ag NPs allowed adjusting spectral position of SPR in the range of 500-570 nm, as demonstrated in Fig. 1.

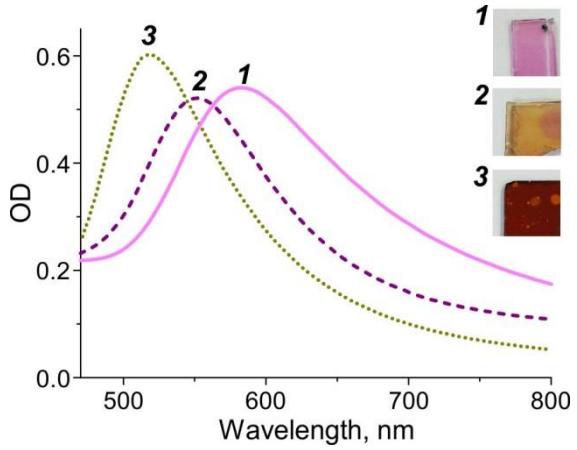


Fig. 1. Absorbance spectra of the glasses containing Au NPs (*1*), and both $Ag^+$ ions and Au NPs after heat treatment at 250°C (*2*) and 600°C (*3*). Insets: photos of the corresponding samples.

## Conclusion

The growth dynamic of Au/Ag alloy NPs in glass was revealed. It is demonstrated, spectral position of SPR of alloy NPs can be positioned by selecting the regime of the glass heat treatment, which determines the Ag proportion in alloy NPs.

## REFERENCES

1. **Gonçalves M. R., Minassian H., Melikyan A.**, Plasmonic resonators: fundamental properties and applications, Journal of Physics D: Applied Physics. 53 (44) (2020) 443002.

2. **Pawar S., Teja B. R., Nagarjuna R., Ganesan R., Nag A.**, Probing the surface composition effect of silver-gold alloy in SERS efficiency, Colloids and Surfaces A: Physicochemical and Engineering Aspects. 578 (2019) 123638.

3. **Babich E., Reduto I., Lipovskii A.,** Diffusive formation of Au/Ag alloy nanoparticles of governed composition in glass, Nanomaterials. 12 (23) (2022) 4202.

4. **Skvortsov A., Babich E., Lipovskii A., Redkov A., Yang G., Zhurikhina V.,** Raman scattering study of amino acids adsorbed on a silver nanoisland film, Sensors. 22 (14) (2022) 5455.

Conference materials
UDC
DOI: https://doi.org/10.18721/JPM.

# Photoluminescence study of InGaAs/GaAs quantum dots with bimodal inhomogeneous broadening

**A. V. Babichev** [1✉], **D. S. Papylev** [2], **A. M. Nadtochiy** [3,4], **Yu. S. Tkach** [1], **N. V. Kryzhanovskaya** [3,4], **S. A. Blokhin** [1], **V. N. Nevedomsky** [1], **A. G. Gladyshev** [3], **N. A. Maleev** [1], **L. Ya. Karachinsky** [3], **I.I. Novikov** [3]

[1] Ioffe Institute, Saint Petersburg, Russia;
[2] ITMO University, Saint Petersburg, Russia;
[3] Alferov University, Saint Petersburg, Russia;
[4] National Research University Higher School of Economics, Saint Petersburg, Russia

✉ a.babichev@mail.ioffe.ru

**Abstract.** The results of the photoluminescence spectra studying of InGaAs/GaAs quantum dots grown by Stransky-Krastanov growth mode are presented. Molecular-beam epitaxy and metal-organic chemical vapor deposition were used to grow InGaAs/GaAs QDs for comparative analysis. An analysis of the photoluminescence spectra at ultralow pump levels resulted that the ensemble of quantum dots grown by means of metal-organic chemical vapor deposition exhibits photoluminescence corresponding to QDs ground states at the same time ensemble of QDs grown by molecular-beam epitaxy demonstrate the bimodal behavior – presence of two characteristic ensembles of InGaAs/GaAs QDs with different sizes and different peaks of photoluminescence.

**Keywords:** molecular-beam epitaxy, metal-organic chemical vapor deposition, gallium arsenide, InGaAs, Stransky-Krastanov growth mode.

**Acknowledgment:** Optical properties were partly studied on the equipment of the large-scale research facilities «Complex optoelectronic setup», HSE University.

**Funding:** The authors from Ioffe Institute acknowledge support in part by the grant of the Russian Science Foundation No. 22-19-00221, https://rscf.ru/project/22-19-00221/ for the structure design, MBE epitaxy, and the study of photoluminescence spectra of MBE-grown structures. A.M. Nadtochiy and N.V. Kryzhanovskaya thanks project FSRM-2023-0010 Ministry of Science and Higher Education of the Russian Federation for support of the study of photoluminescence spectra of MOCVD-grown structures.

## Introduction

The usage of optically pumped quantum dots (QDs) micropillar lasers with vertical microcavities is preferable to realize the optical reservoir computing (RC) scheme [1–4] due to low power consumption of photonic RC, high spectral homogeneity, small pitch and diameters of microlasers in relation with VCSELs case [5]. Due to possibility of the precise control of microlasers diameter, it is possible to realize a dense array of spectrally homogeneous microlasers emitting in a frequency-range of about 50 GHz (~200 μeV) required for RC [3].

This paper presents the results on study of the optical properties of 980 nm range InGaAs QDs grown by molecular-beam epitaxy (MBE) according to the Stransky-Krastanov growth mode and a comparison with the results for InGaAs QDs grown by metal-organic vapor phase epitaxy (MOCVD).

## Materials and Methods

For the first structure InGaAs QDs were formed by deposition of $In_{0.63}Ga_{0.37}As$ layer with thickness of 2.6 monolayers (ML) using the Stransky-Krastanov mode and MBE. The deposition rate was 0.55 Å/s. In case of MOCVD (structure no. 2) QDs were formed by deposition of $In_{0.63}Ga_{0.37}As$ layer with thickness of 2.5 ML and the deposition rate was 0.68 Å/s.

The photoluminescence (PL) spectra were studied at 13 K in a wide range of excitation power densities. Optical pumping was carried out by a Yag:Nd laser at a wavelength of 532 nm with a 150 mW CW output power, which corresponds to the excitation power density ~ 5 kW/cm$^2$.

The range of laser power attenuation using neutral filters was ($1 – 3\times10^{-6}$). Temperature studies of the PL spectra were also carried out in the temperature range of 13–325 K at a moderate excitation power of 4.5 mW.

## Results and Discussion

For the first structure grown by the MBE technique, the presence of additional lines in the short-wavelength spectral region was observed, which were remained unchanged starting from a certain pump level even at ultra-low excitation pump densities (cf. figure 1). This behavior was discussed earlier [6] and can be associated with the presence of two ensembles of QDs with different sizes. For the structure no. 2 grown by the MOCVD, a decrease in the half-width of the PL spectrum was observed at low excitation pump densities, and the shape of the spectra was more symmetrical in comparison with the results for structure no. 1 under identical pumping conditions.

Temperature studies of the PL spectra (the behavior of the FWHM value, as well as the integral intensity/amplitude of the PL peak versus temperature) also confirmed the previously mentioned assumption about the presence of two characteristic ensembles of QDs with different sizes in the structure no. 1 grown by the MBE.

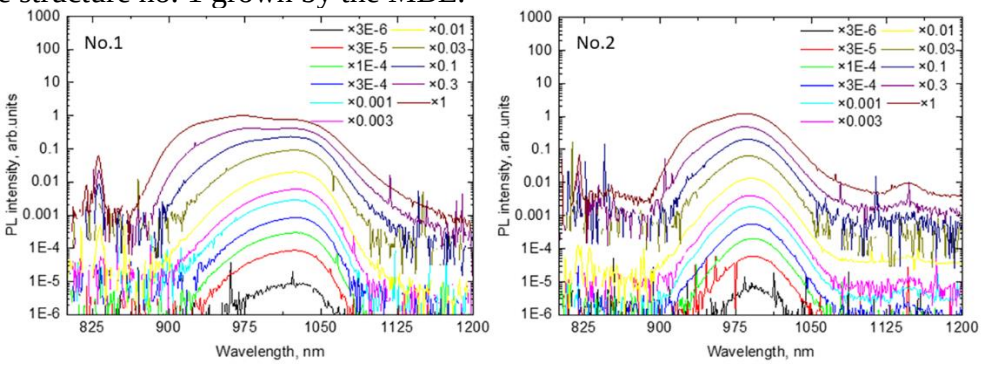


Fig. 1. PL spectra of structure no. 1 (left panel) and structure no. 2 (right panel), measured at 13 K.

## Conclusion

Low-temperature studies of the PL spectra in a wide range of excitation power densities have been carried out. It was shown that the structure with QDs grown by the MOCVD demonstrates PL through the ground states in the ensemble of QDs. It is shown that the structure with QDs grown by the MOCVD contains one ensemble of QDs. In turn, for the structure with QDs grown by the MBE, the presence of additional lines in the short-wavelength spectral region at a low temperature and pumping was observed, which can be associated with the presence of two ensembles of QDs.

## REFERENCES

1. **Heuser T., Grose J., Holzinger S., Sommer M. M., Reitzenstein S.** Development of Highly Homogenous Quantum Dot Micropillar Arrays for Optical Reservoir Computing, IEEE J. Sel. Top. Quantum Electron. 26 (1) (2020) 1–9.

2. **Andreoli L., Porte X., Heuser T., Große J., Moeglen-Paget B., Furfaro L., Reitzenstein S., Brunner D.** Optical pumping of quantum dot micropillar lasers, Opt. Express. 29 (6) (2021) 9084–9097.

3. **Heuser T., Große J., Kaganskiy A., Brunner D., Reitzenstein S.** Fabrication of dense diameter-tuned quantum dot micropillar arrays for applications in photonic information processing, APL Photonics. 3 (11) (2018) 116103.

4. **Shih C.-W., Limame I., Krüger S., Palekar C. C., Koulas-Simos A., Brunner D., Reitzenstein S.** Low-threshold lasing of optically pumped micropillar lasers with $Al_{0.2}Ga_{0.8}As/Al_{0.9}Ga_{0.1}As$ distributed Bragg reflectors, arXiv preprint arXiv:2301.08026 (2023).

5. **Heuser T., Pflüger M., Fischer I., Lott J. A., Brunner D., Reitzenstein S.** Developing a photonic hardware platform for brain-inspired computing based on 5 × 5 VCSEL arrays, JPhys Photonics. 2 (4) (2020) 044002.

6. **Wang H. L., Ning, D., Feng, S. L.** Temperature dependence of the optical properties of InAs/GaAs self-organized quantum dots with bimodal size distribution, J. Cryst. Growth. 209 (4) (2000) 630–636.

## THE AUTHORS

**BABICHEV Andrey V.**
a.babichev@mail.ioffe.ru
ORCID: 0000-0002-3463-4744
**PAPYLEV Denis S.**
papilew.denis@yandex.ru
ORCID: n/a
**NADTOCHIY Alexey M.**
al.nadtochy@mail.ioffe.ru
ORCID: 0000-0003-0982-907X
**TKACH Julia S.**
polubavkina@mail.ru
ORCID: 0000-0003-2740-9810
**KRYZHANOVSKAYA Natalia V.**
nataliakryzh@gmail.com
ORCID: 0000-0002-4945-9803
**BLOKHIN Sergei A.**
blokh@mail.ioffe.ru
ORCID: 0000-0002-5962-5529
**NEVEDOMSKY Vladimir A.**
nevedom@mail.ioffe.ru
ORCID: 0000-0002-7661-9155
**GLADYSHEV Andrey G.**
glad@mail.ioffe.ru
ORCID: 0000-0002-9448-2471
**MALEEV Nikolay A.**
maleev.beam@mail.ioffe.ru
ORCID: 0000-0003-2500-1715
**KARACHINSKY Leonid Ya.**
karach@switch.ioffe.ru
ORCID: 0000-0002-5634-8183
**NOVIKOV Innokenty I.**
novikov@switch.ioffe.ru
ORCID: 0000-0003-1983-0242

# Enhancing the Analytical Arrayed Waveguide Multiplexer Model with Spectrum Analysis and Taper Optimization Techniques

**I.V. Babichek**[1,2✉], **A.A. Sapegin**[2], **E.S. Shamin**[1,2,3], **V.V. Svetikov**[3,4]
[1] MIPT (NRU), Moscow, Russia;
[2] JSC «MERI», Zelenograd, Russia;
[3] JCS «ZNTC», Zelenograd, Russia;
[4] Prokhorov General Physics Institute of the Russian Academy of Sciences
✉babichek.iv@phystech.edu

**Abstract.** An analytical arrayed waveguide multiplexer model is presented and expanded using techniques described in this paper. At first it is demonstrated how the s-parameters of the model could be evaluated. Then it is explained how to determine a taper's geometry from its spectrum. It involves obtaining an amplitude-phase distribution at the input of an arrayed waveguide grating multiplexer from the spectrum of the central output channel and determining a taper's geometry parameters from its input and output fields. Additional analysis was performed to describe the relationship between the shape of the AWG spectrum and the AWG input channel field distribution.

**Keywords:** AWG, arrayed waveguide grating, mux, demux, taper, flat-top, optimization, design, s-parameters.

## Introduction

The Fourth Industrial Revolution is ongoing [1]. The moment when there are more devices connected to the Internet than there are people on the planet has already passed. The development of neural networks and the so-called Internet of Things both call for unprecedented increases in communication channel bandwidth. Further increase in performance of electric devices leads to an increase in power consumption [2]. Therefore, currently new methods of processing and transmitting data are being researched, especially using information carriers other than electrons, in order to maintain the Moore's law-predicted rate of development [3]. This is the reason for the emergence of integrated photonics — a branch of science that uses light as a data carrier to build microcircuits.

An optical (de)multiplexer, one of the key components of integrated photonics, divides the signal along the wavelength or combines signals with different wavelengths into one. This feature determines the network bandwidth because each wavelength serves as a separate channel for the transmission of information. Using these devices, a transmission speed of 3.2 Tbit/s over a distance of more than 40 km was achieved in 1999 [4]. Since lasers are currently used to produce light and their instability within the spectral width of one channel starts to be noticeable, further channel densification is problematic [5]. In order to compensate for this, the so-called flat-top form of the transmission characteristic of the multiplexer is used. This technology makes it possible to increase the transmission speed by almost two times [5].

The "Arrayed Waveguide Grating" (hereinafter AWG) multiplexer's design accomplishes the aforementioned tasks. The choice of the focal spot's shape and the waveguide tapers at the input/output is all that is required to obtain the required shape of the spectrum. There are several mathematical models that address the issue of modeling the shape of a spot from the geometric parameters of AWG, and this topic is frequently covered in scientific articles [6]. The task of finding tapers with the most effective conversion of spot energy can only be accomplished numerically. The main issue is that the device's size is orders of magnitude larger than the wavelength. Standard photonics calculation programs must therefore set a fine sampling, which results in long numerical calculations. There is a need for a solution that will speed up calculations of the AWG spectrum using the existing approximations and the developed theory.

## Model description

A specialized program has been created to address this issue. Its main benefit in terms of calculation speed is the use of the Huygens-Fresnel integral, which binds the field at the boundaries of Free Propagation Region (FPR) of AWG and enables the use of the Fast Fourier Transform algorithm, as opposed to numerically calculating the field at each point. To determine which portion of the energy of one mode of a specific input waveguide is transmitted as one mode of a specific array waveguide, the overlap integral of the resulting field of each waveguide mode is taken with each of the array modes. As a result, AWG can be represented as an s-parameter matrix, which is a matrix of transfer coefficients. Using the array mode renormalization method, crosstalk computation errors are reduced [7].

A spectrum can be produced by convolution using a given spot shape and taper field shape. The task of figuring out the input and output taper's shape is made easier because this enables the process to be reversed and determines the spot shape that must be used to implement a particular spectrum shape. The convolution theorem can be used to derive:

$$S(\chi) = \int_{-\infty}^{+\infty} F(\chi - x) M(x) dx$$

$$\hat{S}(\omega) = \hat{F}(\omega) \cdot \hat{M}(\omega)$$

$$\chi \sim d\lambda$$

where $F$ is focal spot intensity profile and $M$ is mode field intensity profile. Hats denote Fourier transformation.

For the study of impact of taper shape in its output field several polynomial edge functions (such as straight, linear, and parabolic) were used as the taper wall shapes.

These findings allow one to calculate the desired waveguide geometry and then, using the aforementioned program and variation principle, to optimize the mean square error.

## Results and Discussion

In this study, the simulation results of two AWG modelling methods — s-parameter matrix computation and taper geometry determination from output spectrum — were presented. In addition, the amplitude-phase distribution of the input waveguide field's influence on the final spectrum was assessed.

## REFERENCES


1. **Schwab K.,** The fourth industrial revolution. Currency, 2017.
2. **Krasnikov G.Ya., Zaitcev N.A.,** Nanoelectronics: status, challenges and prospects. Nano- and microsystem technology. – 2009. – № 1(102). – С. 2-5. – EDN JXZUBV.
3. **Wang Z.,** Integrated nanophotonics for "More than Moore". Diss. 2017.
4. **Scheerer C., Glingener C., Färbert A., Elbers J. P., Schöpflin A., Gottwald E., Fischer G.,** 3.2 Tbit/s (80× 40 Gbit/s) bidirectional WDM/ETDM transmission over 40 km standard singlemode fibre. Electronics Letters 35.20 (1999): 1752-1753.
5. **Wildermuth E.,** Performance optimization of flat-top passband arrayed waveguide grating demultiplexers. Diss. ETH Zurich, 2000.
6. **Klekamp, A., Münzner R.,** Calculation of imaging errors of AWG. Journal of lightwave technology 21.9 (2003): 1978.
7. **Kleijn E., Smit M.K., Leijtens X.J.M.,** New analytical arrayed waveguide grating model. Journal of lightwave technology 31.20 (2013): 3309-3314.

# EXCESS LEAKAGE OF INFORMATION IN QKD WITH PASSIVE SIDE CHANNELS

**D. V. Babukhin** [1,2]✉, **D. V. Sych** [2]
[1] Qrate LLC, Novaya av. 100, Moscow 121353, Russia;
[2] P.N.Lebedev Physical Institute, Russian Academy of Sciences, , Moscow, 119991, Russia
✉dv.babukhin@gmail.com

**Abstract.** Passive side channels of the photon source make quantum key distribution (QKD) protocols insecure. To restore security, we need to incorporate the leakage through the side channel into the secret key estimate, but there is no definitive way to do that. In this work, we compare several practical methods of secret key rate estimating in QKD protocols with photon distinguishability side channel. We calculate upper bounds on secret key generation rates, using two reinterpretations of eavesdropper excess information – the effective error method and the a-priori loss method. We demonstrate that the effective error method provides tighter upper bound on the secret key rate than a-priori loss. Our results refine the toolbox of estimating security of QKD protocols with passive source side channels.

**Keywords:** Quantum key distribution, source side channels, BB84 with decoy states.

## Introduction

Theoretical QKD protocols, which promise unconditional security, are based on idealistic model of optical hardware. These models often differ from real devices performance. The gap between practice and theory leads to excess leakage of information about secret key towards an eavesdropper through side channels. There are many reasons why such leakage can occur, and the problem of estimating and/or eliminating unwanted leakages of information is an active research topic [1].

Photon distinguishability side channel is one of such side channels, which provide the eavesdropper with additional information. This kind of such channel does not require any active interaction between the eavesdropper and hardware of legitimate users, so this side channel is passive. In recent paper [2], there was introduced a practical method to estimate excess leakage of information through the photon distinguishability side channel in a BB84 decoy state protocol. This method uses reinterpretation of additional information of the eavesdropper to calculate a so-called *effective error* – a cumulative parameter, which incorporates both eavesdropping on the protocol and on the passive side channel. This method is aimed to be a convenient practical tool to estimate security of QKD. Here we further refine the idea of this method.

## Materials and Methods

We reinterpret excess information of the eavesdropper such that this amount of information influences legitimate sides instead of the adversary. The main idea is moving the excess information in the secret key equation (first equality sign in formula (1)) to the a-priori term (second equality sign in formula (1)) or to the a-posteriori term (third equality sign in formula (1)):

$$R^{\Delta}=1-h(Q)-(h(Q)+\Delta h)=1-h(Q^{\Delta})-h(Q)=1-\Delta h-2h(Q) \tag{1}$$

Moving excess information to the a-priori term corresponds to Bob knowledge about Alice before measurement or, alternatively, to the randomness of Alice source; this interpretation constitutes the *a-priori loss method* of estimating QKD security. Contrary, moving excess information to the a-posteriori term corresponds to information gain about Alice photon state after Bob's measurement; this interpretation constitutes *the effective error method.*

Using these methods, we can calculate secret key rates in the BB84 protocols with decoy states in two ways: using the effective error method

$$R_1^{\Delta}=Q_1\left(1-h\left(e_1^{\Delta}\right)\right)-fQ_{\mu}h\left(E_{\mu}^{\Delta}\right) \tag{2}$$

and using the a-priori loss method

$$R_2^{\Delta} = Q_1\left(1 - \Delta h - h\left(e_1\right)\right) - fQ_\mu h\left(E_\mu\right). \tag{3}$$

The main purpose of the current work is to compare these two methods and to define which one provides a tighter upper bound on the secret key rate for the BB84 decoy state protocol with a passive source side channel.

## Results and Discussion

In Fig. 1 we provide secret key rates for two estimation approaches described above. We use standard parameters of QKD setups – optical fiber attenuation $\alpha = 0.2$, average photon number per pulse $\mu = 0.5$, optical error rate 1%, dark count probability $Y_0 = 10^{-5}$, and error correction efficiency $f = 1.1$.

We conclude that the effective error method provides tighter upper bound on the secret key generation rate than the a-priori loss method. This result illustrates imbalance in interpreting excess eavesdropper information as an information change of legitimate sides.

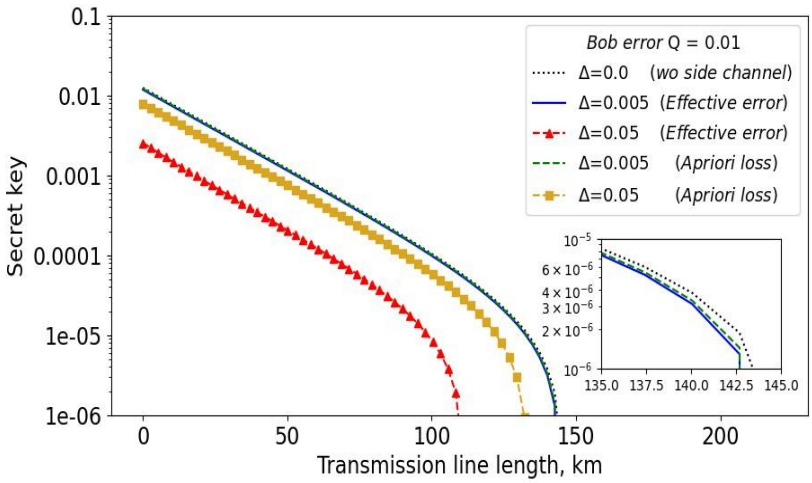


Fig. 1. Secret key rates , calculated with two method – the effective error method and a-priori loss method – for different values of side channel leakage parameter $\Delta$.

## Conclusion

Here we provided an extended analysis of the method to estimate QKD security with passive source side channels, proposed in [2]. We show that assigning the loss of excessive error to a-posteriori outcome of legitimate receiver provides tighter estimate of the secret key upper bound than in the case of a-priori information loss. This finding allows us to definitely use the effective error method as a practical way to estimate security of QKD with passive side channels, compared to a-priori information loss interpretation.

## REFERENCES

1. **V. Scarani, C. Kurtsiefer**, The black paper of quantum cryptography: real implementation problems, Rev. Mod. Phys. 1 (560) (2014) 27–32.

2. **D. V. Babukhin, D. V. Sych**, Joint eavesdropping on the BB84 decoy state protocol with an arbitrary passive light-source side channel, arXiv2211.13669

# Features of monitoring the state of viscous media by refraction

**V. A. Bazhanova**[1]✉ **and V. V. Davydov**[1, 2]
[1] Peter the Great Saint-Petersburg Polytechnic University, Saint Petersburg, Russia;
[2] The Bonch-Bruevich Saint Petersburg State University of Telecommunications, Saint Petersburg, Russia.
✉ vieronika.bazhanova.2003@mail.ru

**Abstract.** The article grounds a necessity of liquid media control using refractometer. A method for monitoring liquid media, including mixtures, using refractometric measurements is proposed. A system of equations has been developed to determine the composition of the medium, which consists of components that have not reacted chemically. The results of experimental studies are presented.

**Keywords:** Liquid, refraction, refractive index, concentration, light-shadow boundary, state media control.

## Introduction

Reliable control of viscous media in laboratories during experiments and production during control of technical processes is necessary [1, 2]. It is very important to study any substance without disturbing its structure and physical properties. It is necessary for further research of the substance on higher resolution instruments to confirm the detected deviation and to establish the reason of the deviation.

## Abbe type refractometer design

To determine the composition of the substance, the optical phenomenon of full internal reflection of light in the prism in contact with the medium under study is used. The Abbe type refractometer is designed with an additional light prism that allows measurements to be made in daylight or artificial light. Also, the advantage of the device is the lack of power from line, which allows to explore a large number of viscous media. In Fig. 1 present an improved optical construction of the refractometer, allowing for the refractive index measurement of the viscous medium using the upper and lower prism.

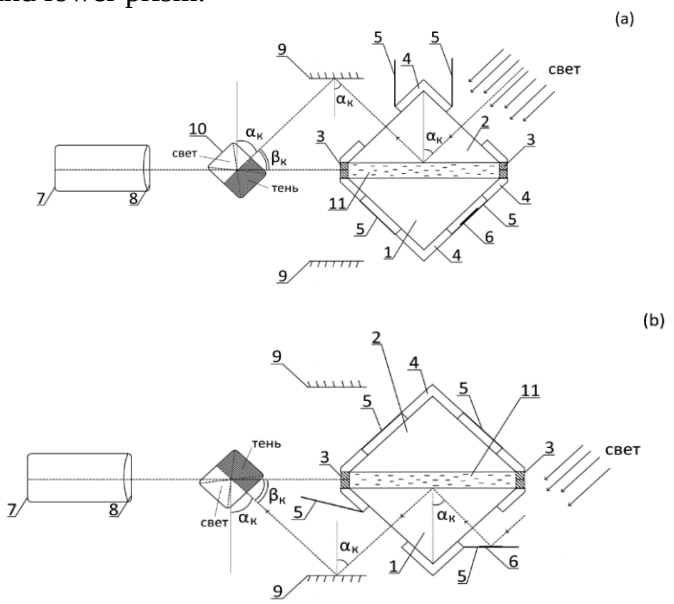


Fig 1. Measurement of refractive index when light falls on upper (a) and lower (b) prism.

## Results of Abbe type refractometer performance and its discussion

The results of measuring the refractive index of oil «Sloboda» ($n_1$ = 1.472) and oil mixture («Sloboda» and «Oleyna») are shown in Fig. 2 (*a*, *b*). The refractive index of mixture is different from «Sloboda» ($n_{12}$ = 1.4713). Consequently, «Oleyna's» index of refraction is varies from «Sloboda's» index of refraction.

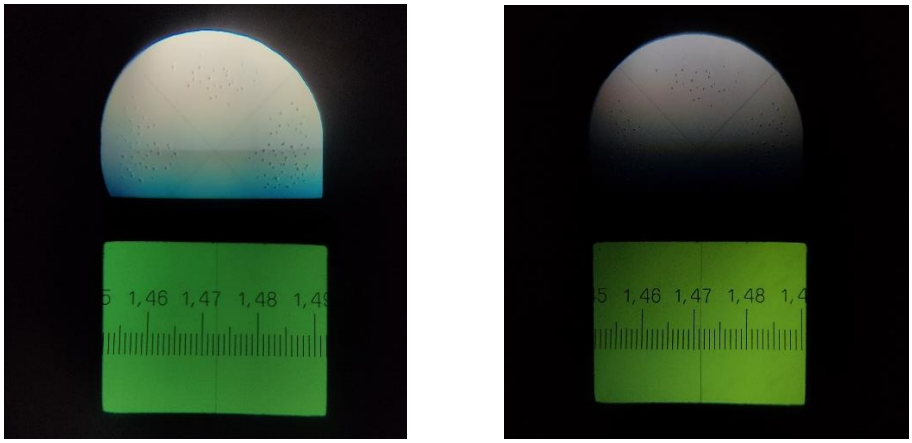


*a*) *b*)

Fig 2. Refractive indexes of oil «Sloboda» (*a*) and oil mixture «Sloboda» and «Oleyna» (*b*)

To determine the ratio of oils in this mixture, a system of equations (1): refraction equation and mass equation can be constructed.

$$\begin{cases} k_1 n_1 + k_2 n_2 = n_{12} \\ V(k_1 \rho_1 + k_2 \rho_2) = m_{12} \end{cases} \quad (1)$$

where $k_1$ – oil concentration of «Sloboda», $k_2$ – oil concentration of «Oleyna», $n_1$ – refractive index of oil «Sloboda», $n_2$ - refractive index of oil «Oleyna», $n_{12}$ - refractive index of the oil mixture, $\rho_1$ - oil density of «Sloboda», $\rho_2$ - oil density of «Oleyna», $m_{12}$ – mass of the oil mixture.

## Conclusion

The result shows a deviation from the standard sunflower oil condition. It was obtained using less than 1 ml of the studied oil. This is one of the advantages of refractometers. The combination of refractometric measurements with the determination of other physical properties of the studied substance allows to analyze complex mixtures and determinate the composition of many industrial products and biological objects at the sampling site in less than a minute.

## REFERENCE

1. **Karabegov M.A.**, Ways of improving the accuracy of analytical instruments, Measurement Techniques, 52(1) (2009) 97–104.

2. **Chen J., Guo W., Xia M., Li W., and Yang K.**, In situ measurement of seawater salinity with an optical refractometer based on total internal reflection method, Optics Express, 26(20) (2018) 25510–25523.

# Effect of a bifurcation meter on microwave transmission through a one-dimensional chain of qubits

**D. S. Pashin** [1], **M. V. Bastrakova** [1,2]✉
✉bastrakova@phys.unn.ru
[1] Lobachevsky State University of Nizhni Novgorod, Nizhny Novgorod, Russia;
[2] Russian Quantum Center, Moscow, Russia

**Abstract.** In this work, we study the initialization method of qubits during interaction with single-photon fields in a microwave waveguide. Using the method of the effective non-Hermitian Hamiltonian, the influence of the state of the measuring Josephson oscillator on the microwave transmission in such a system was theoretically found.

**Keywords:** qubit, bifurcation, microwave photon, resonator.

**Funding:** The work was supported by UNN within the framework of the strategic academic leadership program "Priority 2030" of the Ministry of Science and Higher Education of the Russian Federation.

## Introduction

At present, experiments on nondemolition measurement of arrays of noninteracting qubits placed in a one-dimensional open waveguide [1] have been implemented, as well as metamaterials have been created that allow controlling the band gap of such a waveguide by tuning the qubits frequencies [2]. This work is devoted to the generalization of the technique fornondemolition measurement of superconducting qubit state by a Josephson bifurcation amplifier when interacting with single-photon fields in one-dimensional a microwave waveguide. Particular attention is paid to the influence of the meter on the transmission and reflection factors of the microwave signal in such a system. It is assumed that the control of the states of qubits occurs due to their capacitive coupling with the resonator.

## Results and Discussion

To describe and study microwave transport processes, we find it convenient to use the projection operator formalism and the method of the effective non-Hermitian Hamiltonian to solve the generalized scattering problem. In the one-photon approximation there is the probability of photon absorption by a qubit in addition to the probabilities of transmission and reflection. Note that one of the first applications of this method for investigating microwave transmission through a one-dimensional qubit chain was presented in the paper [3].

When the measuring oscillator is in the ground state it introduces a minimal perturbation into the behavior of the photon. Fig.1 shows the dependences of the coefficients of transmission,

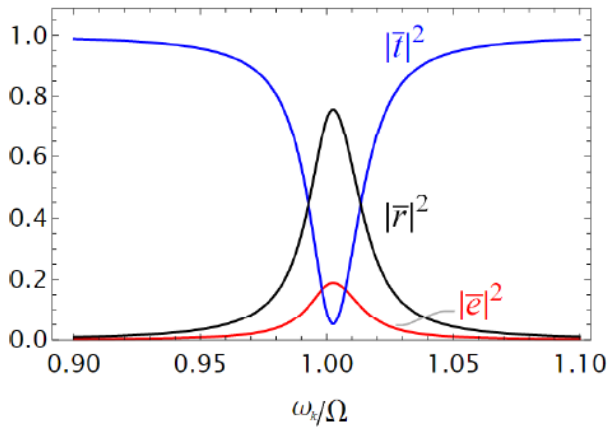


Fig. 1. Dependences of the probabilities of transmission, reflection of a photon, and probability of qubit excitation on the frequency of a incident photon $\omega_k$. At the initial moment of time, the measuring oscillator and the qubit were in their ground states.

reflection of a photon and excitation of a qubit depending on the ratio of the frequency of the incident photon $\omega_k$ and the natural frequency of the qubit $\Omega$. The resulting dependences are in good agreement with the known results [3], when the probabilities of photon reflection and qubit excitation rapidly decrease with distance from the resonant frequency.

Fig.2a-b shows that the effect on microwave transmission increases with an increase in the average occupation number of the measuring oscillator initial state. In contrast to the simplest Jaynes-Cummings model, when the coupling of a qubit to a resonator shifts the effective frequency of the qubit without changing the resonance curve, in this case there is a non-trivial change in the dependence of the qubit excitation probability on the photon frequency with a change in the initial level number of the measuring oscillator. Such a change in the resonance curves is due to the the Fock basis is not eigen for the measuring oscillator.

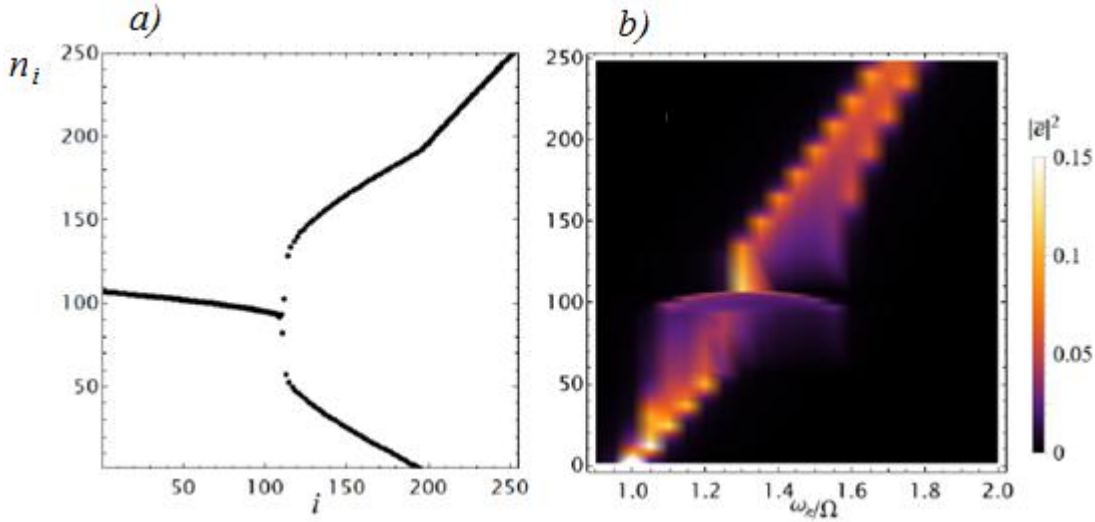


Fig. 2. (*a*) Dependence of the average occupation number of the measuring oscillator level number. The separation of the spectrum into two branchs occurs near the separatrix energy [4]. (*b*) Dependence of the qubit excitation probability on the average occupation number of the measuring oscillator initial state and the incident photon frequency.

## Conclusions

When considering two qubits with measuring oscillators, the dependences of the amplitude of the excitation probability of an individual qubit on various system parameters were found. In array of two identical qubits, the resonance curve could become asymmetric. This effect is associated with the interference of the incident and reflected photons.

## REFERENCES


[1] **Schmitt V., Zhou X., Juliusson K., Royer B., Blais A., Bertet P., Vion D., Esteve D.**, Multiplexed readout of transmon qubits with Josephson bifurcation amplifiers. Phys. Rev. A 90 (2014) 062333.

[2] **Brehm J.D., Poddubny A.N., Stehli A., Wolz T., Rotzinger H., Ustinov A.V.**, Waveguide bandgap engineering with an array of superconducting qubits. npj Quantum Mater. 6 (2021) 10.

[3] **Greenberg Ya.S., Shtygashev A.A.**, Non-Hermitian Hamiltonian approach to the microwave transmission through a one-dimensional qubit chain. Phys. Rev. A 92 (2015) 063835.

[4] **Pashin D.S., Bastrakova M.V., Satanin A.M., Klenov N.V.**, Bifurcation Oscillator as an Advanced Sensor for Quantum State Control. Sensors 22 (2022) 6580.

# Optical spectroscopy of GaAs/AlGaAs quantum dots

**E. A. Basheguroва[1], E. I. Deribina[1], Yu. V. Kapitonov[1]**
[1]St Petersburg University, Saint-Petersburg, Russia
st096206@student.spbu.ru

**Abstract:** In this work GaAs/AlGaAs semiconductor with quantum dots was studied using its photoluminescence (PL) spectroscopy. Such pair of materials was used due to the close values of lattice constant of barrier and dot materials, which leads to low level of strain inside the sample. Growth of the heterostructure is carried out by the droplet epitaxy – this method gives possibility to control various parameters of sample: density of quantum dots (QD), volume of the dot. A structure with small sparse QDs were studied. For achieving most full information about samples, several experiments have been carried out single QD PL measurements, PL depending on coordinates on sample and PL depending on temperature of samples. Analysis of spatial dependency of PL spectra was used to distinguish signals origin from different quantum-sized structures.

**Keywords:** quantum dots, photoluminescence, semiconductors, GaAs/AlGaAs, quantum heterostructures.

**Funding:** this work was supported by the RFBR project 19-52-12046 and by the Ministry of Science and Higher Education of the Russian Federation (Megagrant no. 075-15-2022-1112).

## Introduction

Studying structures based on GaAs/AlGaAs is of interest because the lattice constant values of the material of the dot and its barrier are similar, leading to low internal stress in the sample. Low-temperature PL spectra contains several resonances related to different quantum-sized structures. However, attribution of all peaks to corresponding structures is not present in the literature. In [1] two spectrally-resolved ensembles of QDs were studied (dots A and dots B). However, the origin of these two ensembles was not understood. In this work we were able to find the spatial corelation between these two ensembles. So, dots A are quantum dots and B are quantum size structures associated with the objects being studied. The main aim of our work was to determine which part of the sample structure corresponds to certain parts of the spectrum, as well as how these objects are interacting in the semiconductor.

## Materials and methods

A sample T874 containing sparsely located dots was grown according to recipe described in [1]. The sample was grown using the droplet epitaxy method in our laboratory, which allows for control of the growth process, resulting in samples with precisely defined parameters. To obtain microphotoluminescence spectra, a green laser at 532 nm was focused on the sample by the 50x microlens. The temperature was maintained at 4 K using a closed-cycle helium cryostat Montana. A spectrometer equipped with a CCD-camera was used to obtain spectra.

The micrometre stage moved by the stepper motor was used to record the spatial dependency of the PL spectra with micrometre resolution.

## Results and Discussion

After conducting all the experiments, it can be said which peaks belong to which structure on the photoluminescence graph of sample T874 (Fig. 1, a).

In Fig. 1, a, the following resonances were distinguished (starting from the low-energy): carbon contamination of the sample, three-dimensional crystalline structure of gallium arsenide, studied QDs, related them quantum size structures, quantum well, and AlGaAs barrier with 38% aluminium content.

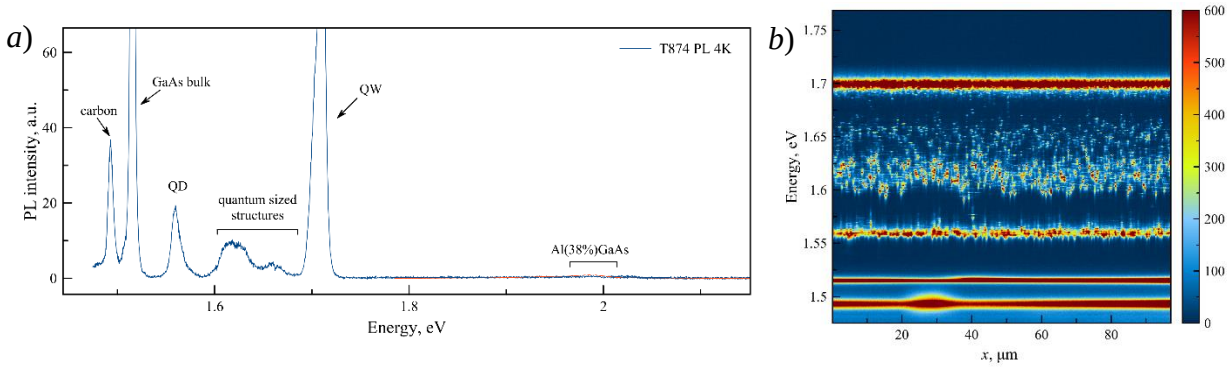


Fig. 1. Graph of the photoluminescence intensity and energy of PL of heterostructures in T874 sample semiconductor under 532nm light with 4K temperature (*a*); colormap of PL energy and coordinate of T874 sample under 532nm light with 4K temperature.

After processing the spectra of the dependence of photoluminescence energy on coordinate (Fig. 1, b), it can be concluded that quantum dots and related structures are located close to each other. Additionally, it is possible to identify dependencies in the appearance and disappearance of peaks when moving the laser beam across the sample.

## Conclusion

The result of the conducted research was the description of the photoluminescence spectra from a GaAs/AlGaAs semiconductor sample with quantum dots. The spectrum description in [1] was supplemented, and quantum dots of two different types turned out to be quantum dots and other quantum-sized structures.

## Acknowledgments

This work was carried out on the equipment of the SPbU Resource Center "Nanophotonics".

## REFERENCES

1. **Ulhaq A., Duan Q., Zallo E., Ding F., Schmidt O. G., Tartakovskii A. I., Skolnick M. S., and Chekhovich E. A.,** Vanishing electron g factor and long-lived nuclear spin polarization in weakly strained nanohole-filled GaAs/AlGaAs quantum dots, Phys. Rev. B 93, 165306.

# Terahertz radiation detection using graphene noise thermometry method

**P. I. Bondareva [1]✉, K. V. Shein [1,2], A. N. Lubchak [1,2], R. I. Izmaylov [1,3], M. G. Rybin [4], I. A. Gayduchenko [2] and G. N. Goltsman [1,2]**

[1]Moscow Pedagogical State University, Moscow, 119435, Russia;
[2] National Research University Higher School of Economics, Moscow, 101000, Russia;
[3] National Research Nuclear University MEPhI (Moscow Engineering Physics Institute), Moscow, 115409, Russia;
[4] Prokhorov General Physics Institute, Moscow, 119991, Russia
✉p.bondareva2016@yandex.ru

**Abstract.** In this paper we investigate a novel approach to inventing graphene-based terahertz bolometers using noise thermometry. Graphene is a unique material for detecting radiation in the terahertz range due to its record low electron heat capacity and weak electron-phonon coupling. This results in sufficient heating of graphene electron system under terahertz radiation. The main challenge in the realization of graphene terahertz detectors arises due to weak graphene resistance dependence on temperature. Here, we solve this problem by measuring noise spectral density in graphene devices using lock in amplifier technique. The measured thermal noise is directly depend on electron temperature and can be used as detector signal as well as probe of electron temperature under terahertz radiation. The obtained experimental data can be used to optimize modern graphene terahertz detectors and develop new ones.

**Keywords:** graphene, THz detectors, bolometers, noise thermometry.

**Funding:** The research was supported by RSF (project No. 23-72-00014).

## Introduction

Recently terahertz range (THz) of EM spectrum has been of great interest due to a wide spectrum of potential applications: medical diagnostics, nondestructive testing, security systems, and data transmission [1]. These and many other applications require fast, sensitive THz detectors that can be easily combined into arrays.

Graphene is a unique material for detecting radiation in the terahertz range [2]. Firstly, it has a gapless structure and absorbs electromagnetic radiation in a wide range of frequencies. Secondly, graphene has a record low electron heat capacity and weak electron-phonon coupling. This in turn leads to a strong heating of its electronic subsystem under the influence of incident electromagnetic radiation [3] presenting a unique platform for the development of sensitive bolometers based on graphene [4]. The main challenge in the realization of graphene terahertz detectors arises due to weak graphene resistance dependence on temperature [5]. To achieve strong response one can artificially increase weak temperature dependence of the graphene resistance by embedding defects, nanostructuring, or opening a band gap in bilayer graphene [5]. This, in turn, leads to a decrease in the operation speed of the detector.

Here we explore a novel approach to inventing graphene-based THz bolometers using noise thermometry [6]. The heating of electrons caused by the absorption of THz radiation is detected by measuring noise spectral density in graphene devices using lock in amplifier technique. The potential advantages of this approach include high sensitivity, as well as the ability to easily multiplex detector signals, which allows the creation of detector arrays.

## Device fabrication

Our detectors are three-electrode devices in which the graphene acts as a conduction channel and also has a gate electrode to control the concentration of charge carriers in the device. Our detectors are manufactured as follows. At the first stage, metallic marks were formed by standard methods of photolithography and electron-beam sputtering. Then the graphene was synthesized by the CVD method and transferred to a silicon substrate [7]. This method of graphene

synthesis by chemical vapor deposition is one of the most efficient and economical ways of graphene production. It allows to increase the area of the substrate, covered by the graphene, and make several experimental samples at once.

Next, contact electrodes were formed using positive electron lithography in a bilayer electron resist and V/Au electron-beam evaporation. In a subsequent step we formed the graphene channel using lithography and plasma etching in $O_2$. Also, by means of electron lithography we formed the covers from dielectric $Al_2O_3$, and the gate electrode was made by means of vanadium-gold layer sputtering.

## Experiment and discussion

After device fabrication the transport characteristics of graphene were measured. According to the obtained data we can say that the devices are based on high quality graphene. Next noise spectral density of graphene was measured at room temperature in the region of white noise under two conditions: without radiation and under sub-THz radiation. We used a backward-wave oscillator with frequency of 129 GHz as THz source. The measurements were performed using the standard built-in noise measurement functions of the Lock-in sr830 synchronous amplifier. To prove the thermal origin of measured noise we calibrated lock-in amplifier, using resistors of known rating. The experiment revealed that the noise spectral density of graphene device increases markedly in the presence of THz radiation. This behavior is associated with changes in electron temperature of graphene. The noticeable dependence of the spectral noise density under sub-THz radiation suggests that this method is suitable for estimating the electron temperature of graphene devices.

## Conclusion

In conclusion, we demonstrate the detection of sub-THz radiation using graphene noise thermometry. The measured noise is depend on electron temperature and can be used as detector signal as well as probe of electron temperature under terahertz radiation. The obtained data can be used to optimize existing THz detectors based on the electron heating effect, for example, photo-thermoelectric detectors [8], as well as develop new ones.

## Acknowledgments

The research was supported by RSF (project No. 23-72-00014).

## REFERENCES

1. **Dhillon, S. S**. et al, The 2017 terahertz science and technology roadmap. J. Phys. D Appl. Phys. 50, 043001 (2017).

2. **A. Rogalski, M. Kopytko, P. Martyniuk.**, Two-dimensional infrared and terahertz detectors: Outlook and status; Applied Physics Reviews. - 2019.

3. **Gabor, Nathaniel M.**, et al, Hot carrier–assisted intrinsic photoresponse in graphene, Science 334.6056 (2011): 648-652.

4. **Du, Xu**, et al, Graphene-based bolometers, arXiv preprint arXiv:1308.4065 (2013).

5. **Chen, Jian-Hao**, et al, Intrinsic and extrinsic performance limits of graphene devices on SiO2, Nature nanotechnology 3.4 (2008): 206-209.

6. **Spietz, L**., Primary electronic thermometry using the shot noise of a tunnel junction, Science 300, 1929–1932 (2003).

7. **Gayduchenko, I. A.**, et al, Manifestation of plasmonic response in the detection of sub-terahertz radiation by graphene-based devices, Nanotechnology 29.24 (2018): 245204.

8. **Bandurin, D. A.**, et al, Dual origin of room temperature sub-terahertz photoresponse in graphene field effect transistors, Applied Physics Letters 112.14 (2018): 141101.

# Luminescent nanoparticles' double-diffusion observed by fluorescence recovery technique using laser scanning microscopy

**L. N. Borodina** [1✉], **A. V. Veniaminov** [1]
[1] ITMO University, St.Petersburg, Russia
✉ lnborodina@itmo.ru

**Abstract.** We show that when studying diffusion by the fluorescence recovery after photobleaching technique modified by the authors (Stripe-FRAP), the changes not only in the photoluminescence quantum yield, but also in the diffusion coefficient of nanoparticles under laser irradiation should be considered. The paper presents the results of simulation and experiments with colloidal solutions of semiconductor quantum dots and carbon dots. A new approach to studying the diffusion of nanoparticles makes it possible to observe the system in its intact and phototransformed forms.

**Keywords:** luminescent nanoparticles, diffusion, luminescent laser scanning microscopy, hydrodynamic size.

**Funding:** This research was funded by the Ministry of Science and Higher Education of the Russian Federation, Goszadanie No. 2019-1080, and by the RPMA grant of School of Physics and Engineering of ITMO University. The authors express their gratitude to the ITMO University Core Facility Center “Nanotechnologies”

## Introduction

Luminescent nanoparticles such as quantum dots and carbon dots have found various applications in photonics, bioimaging, and targeted drug delivery. Various optical methods are used to study the motion and size of nanoparticles. In this work, to study the diffusion of luminescent nanoparticles and determine their hydrodynamic sizes, we develop a modified method for the fluorescence recovery after photobleaching, Stripe FRAP, which will allow not only for determining the diffusion coefficient of nanoparticles, but also for studying its photoinduced change under the action of laser radiation.

## Materials and Methods

The technique developed and used for studying the diffusion of luminescent nanoparticles is based on the fluorescence recovery after photobleaching technique (FRAP) [1], but in our case, we study not the integral change in the luminescence intensity resulting from photobleaching, but the spatial distribution of the luminescent signal intensity.

The essence of the Stripe-FRAP is the creation of a photoinduced spatial luminescence inhomogeneity in the form of a stripe and subsequent analysis of post-exposure changes in the luminescence pattern. The intensity distribution along the coordinate perpendicular to the strip is approximated using a Gaussian function or a combination of at least two Gaussian functions. The diffusion coefficient can then be determined from the slope of the profile width squared vs. time.

Using this technique, it is possible to study solutions of luminescent molecules and colloidal particles ranging in size from several angstroms to tens of microns, i.e., it is possible to study any systems in which luminescence changes under the action of light, including nanostructured materials in living and fixed cells.

## Results and Discussion

The object of study were colloidal solutions of semiconductor quantum dots of the CdSe/ZnS core/shell type with an average diameter of about 6 nm. It is known that the intensity of their PL QDs can either increase or decrease under laser irradiation. While FRAP experiments with QDs in hexane demonstrated just broadening of photoinduced stripe (Fig. 1a), in the experiments with their carboxyethyl acrylate solutions we observed quite unusual appearance (Fig. 1b) of luminescent images and the corresponding luminescence intensity profiles (Fig. 2). More complex profiles than the conventional Gaussian-shaped ones were found. The data can be explained under

the assumption that not only the photoluminescence (PL) quantum yield, but also the diffusion coefficient of nanocrystals change under the action of light. In this case, to describe the luminescence profile, it was found necessary to consider the distribution of nanoparticles in both the initial and phototransformed forms and use the difference of two Gaussian functions with one center for fitting the data (Fig. 1*b*), by some analogy with the effect of additional gratings in holographic relaxometry [2].

*a*)

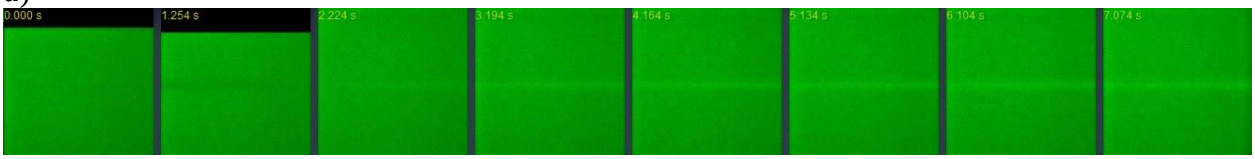


*b*)

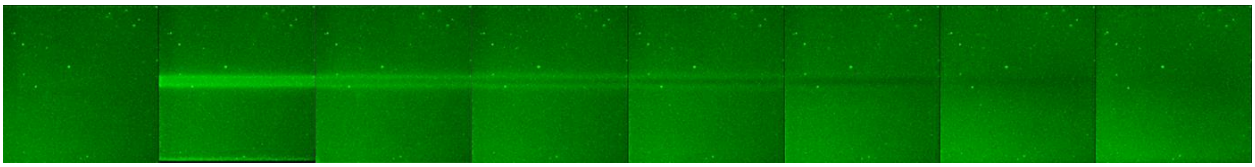

Fig. 1. Two exemplary series of sequential images of scanned areas of photoactivated quantum dots solutions in hexane (*a*) and carboxyethyl acrylate (*b*), without and with photoinduced diffusivity change, respectively

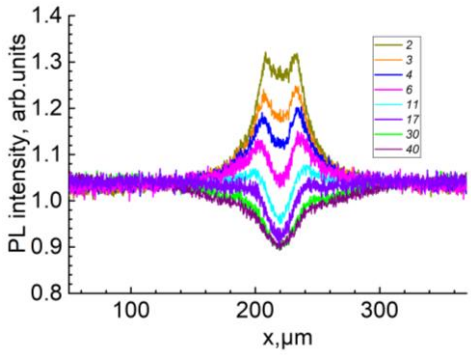


Fig. 2. Transversal profiles of photoluminescence intensity across the exposed stripe demonstrating photoactivation accompanied with the increase in diffusivity, corresponding to the case (*b*) in Fig. 1

## Conclusion

It was found that in a number of experimental cases, the existing model does not describe the stripe FRAP signal shape. A description of such experimental data can be obtained under the assumption that illumination changes not only the luminescence quantum yield, but also the particle diffusion coefficient. The simulation has shown that a change in the diffusion coefficient can indeed affect the PL distribution and makes it possible to describe the detected unusual distributions. In addition, simulations show that the desaturation on which the method was originally based is not necessary to implement the FRAP technique.

## Acknowledgments

The authors are grateful to Irina Arefina and Ilia Vovk of ITMO University for sharing her experience and knowledge in luminescence of carbon dots and the theory of physics of nanostructures.

## REFERENCES

1. **Lorén N., Hagman J., Jonasson J.K., Deschout H., Bernin D., Cella-Zanacchi F., Diaspro A., McNally J.G., Ameloot M., Smisdom N, Nydén M., Hermansson A.-M., Rudemo M., Braeckmans K.,** Fluorescence recovery after photobleaching in material and life sciences: putting theory into practice, Quarterly reviews of biophysics. 3 (2015) 323–387.

2. **Veniaminov A.V., Bartsch E.,** The Shape of the Relaxation Curve in Diffusion Measurements with the Aid of Photoinduced Gratings. Optics and Spectroscopy. 101 (2) (2006) 290–298.

# Spatial self-phase modulation of light in liquid dispersions based on conjugates of phthalocyanines and carbon nanotubes

**P. N. Vasilevsky** [1,2✉], **M. S. Savelyev** [1,3], **A. Yu. Tolbin** [4],
**D. I. Ryabkin** [1,3], **A. Yu. Gerasimenko** [1,3]

[1] Institute of Biomedical Systems, National Research University of Electronic Technology, 124498 Zelenograd, Moscow, Russian Federation;

[2] Institute of Nanotechnology of Microelectronics of the Russian Academy of Sciences, 119991 Moscow, Russian Federation

[3] Institute for Bionic Technologies and Engineering, I. M. Sechenov First Moscow State Medical University, 119991 Moscow, Russian Federation

[4] Institute of Physiologically Active Compounds at Federal Research Center of Problems of Chemical Physics and Medicinal Chemistry, Russian Academy of Sciences, 142432 Chernogolovka, Moscow Region, Russian Federation

✉pavelvasilevs@yandex.ru

**Abstract.** The growth in the power of laser systems makes the problem of protecting photosensitive elements of optical systems and visual organs from high-intensity radiation an urgent issue. This work explores the possibility of optical limitation of quasi-continuous laser radiation using liquid dispersions of conjugates of phthalocyanines and carbon nanotubes. It has been found that the laser beam passes through the studied materials unchanged at low power (<100 mW), and then begins to expand with the appearance of an interference pattern. The use of a limiting diaphragm makes it possible to block part of the laser radiation, which leads to the attenuation of the laser radiation passed through the "sample-diaphragm" system. This phenomenon can be used to protect light-sensitive elements in optical systems.

**Keywords:** laser radiation, carbon nanotubes, phthalocyanines, spatial self-phase modulation, optical limiting.

**Funding:** The study was supported by the Russian Science Foundation grant No. 22-75-00089, https://rscf.ru/project/22-75-00089/.

## Introduction

At present, sources of high-intensity laser radiation are widely used in optical systems for industrial, medical, and scientific purposes. However, the problem of protecting the organs of vision and photosensitive sensors from exposure to high-intensity laser radiation arises [1]. A promising method of protection is the use of passive optical limiters, which are transparent at low intensity and begin to reduce their transmission only when the threshold value is reached.

In this regard, an important task is the search for new nonlinear optical materials, the transmission of which depends on the intensity of the incident laser radiation. In this work, liquid dispersions of conjugates of metal-free phthalocyanines and single-walled carbon nanotubes (SWCNT+PcHH) were studied under the influence of quasicontinuous femtosecond laser radiation. Carbon nanotubes and phthalocyanines have unique properties that make them promising for optical limiting [2].

## Materials and Methods

Irradiation was carried out in a quasi-continuous mode. To generate laser radiation, a Coherent Chameleon Ultra titanium-sapphire pulsed femtosecond laser was used. The pulse repetition frequency was 80 MHz, the pulse duration was 140 fs, and the wavelength was 800 nm. The optical path length in the nanodispersed medium was 2 mm. During irradiation, the cuvette was positioned horizontally. To limit the laser radiation, a diaphragm with a diameter of 0.15 cm was installed. The size of the diaphragm was chosen so that the radiation completely passed through it in the absence of a sample.

SWCNT+PcHH were mixed in distilled water and dimethylformamide (DMF). The concentration of nanoparticles in the dispersion was 0.025 mg/mL. To create a homogeneous liquid dispersion, processing was carried out in an ultrasonic homogenizer for 1 hour.

## Results and Discussion

To study the limiting power and calculate the nonlinear refractive index using the Fresnel-Kirchhoff diffraction integral, the dependences of the power transmitted through the "sample-diaphragm" system on the incident power as well as spatial profiles were obtained (Fig. 1). It is found that the transmitted power increase linearly at low incident power. However, a sharp decrease in transmission is observed when the incident power reaches ~130 mW and ~100 mW for dispersion in water and DMF, respectively. This is due to the fact that at these powers the laser beam begins to expand significantly. A further increase in power leads to a further expansion of the beam with the formation of an annular structure. The appearance of such an interference pattern is a consequence of spatial self-phase modulation. In this case, due to the Gaussian shape of the incident beam, the change in the refractive index will be different at different points of the medium, forming a refractive index gradient, which leads to the self-defocusing effect.

*a*) *b*) *c*)

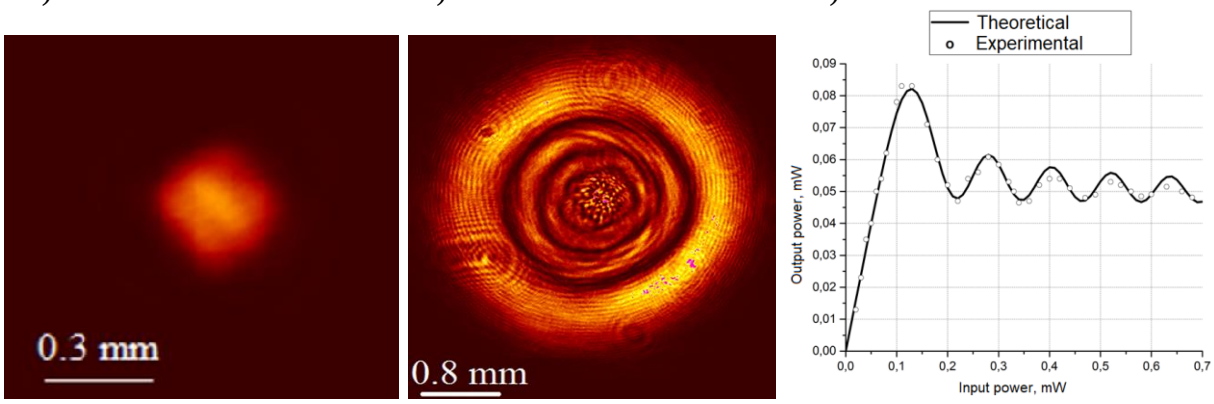


Fig. 1. Shape of the beam passed through the SWCNT+PcHH dispersion in DMF at an incident radiation power of 10 mW (*a*) and 300 mW (*b*) and dependence of the transmitted power on the incident power (*c*)

At the same time, the phase of the laser radiation changes in the medium, which leads to the appearance of an interference pattern on the screen. The dark areas correspond to radiation that is in antiphase, and the light areas correspond to interference maxima. Based on the results of calculations, the values of the nonlinear refractive index of 0.19 and 0.29 $cm^2/MW$ were obtained for SWCNT+PcHH in water and DMF, respectively.

## Conclusion

It was shown that the laser beam changes spatial beam profile when a threshold value of the incident power is reached. The appearance of an interference pattern is a consequence of spatial self-phase modulation. The beam expansion can be used to limit the intensity of laser radiation. Thus, SWCNT+PcHH dispersions can be used as an optical limiters for the protection of optical systems sensors and visual organs.

## REFERENCES

1. **Geis M. W., Bos P. J., Liberman V., Rothschild M.**, Broadband optical switch based on liquid crystal dynamic scattering, Optics express. 24 (13) (2016) 13812-13823.

2. **Ramya E., Momen N., Rao D. N.**, Preparation of multiwall carbon nanotubes with zinc phthalocyanine hybrid materials and their nonlinear optical (NLO) properties, Journal of nanoscience and Nanotechnology. 18 (7) (2018) 4764-4770.

# The effect of laser radiation on properties of platinum nanoparticles produced in a gas discharge

**O. V. Vershinina✉, E. M. Filalova, A. A. Lizunova, E. S. Khramov, V. V. Ivanov**
Moscow Institute of Physics and Technology, Dolgoprudny, Russia
✉ seraia.ov@phystech.edu

**Abstract.** This study was devoted to effect of (или influence) the laser radiation of different wavelengths (355, 527 and 1053 nm) on the properties of platinum nanoparticles synthesized by a gas discharge method. The results confirmed that all three types of lasers can be used to change the morphology and size of platinum nanoparticles. It was shown that the obtained nanoparticles have a maximum of plasmon resonance in the ultraviolet region in the wavelength range from 200 to 300 nm regardless of the type of the radiation. Simulated extinction spectra for monodisperse platinum particles calculated according to the Mie theory were in good agreement with the experimental ones.

**Keywords:** Platinum nanoparticles (Pt NPs), spark discharge, laser radiation, plasmon resonance, ultraviolet (UV).

**Funding:** This work was financially supported by the Russian Science Foundation (project № 22-19-00311, https://rscf.ru/en/project/22-19-00311/).

## Introduction

The catalytic and optical properties of Pt NPs make them applicable to a wide range of scientific and applied industries, such as optics, electronics, medicine and fuel cells [1]. Pure platinum nanoparticles with various sizes can be obtained by gas discharge [2] with a plasmon resonance in the UV region with a peak at a wavelength of (200-500 nm) depending on the particle size [3]. It is known that it is possible to influence the dimensional and optical parameters of nanoparticles by laser radiation [4]. This study presented the results of the effect of laser radiation on the morphology, structural and optical properties of aerosol nanoparticles of metallic platinum by exposing the aerosol flow of nanoparticles to laser radiation of wavelengths 355, 527 and 1053 nm, as well as theoretical extinction spectra of Pt NPs of various diameters.

## Materials and Methods

Primary Pt NPs were synthesized in the spark discharge in an atmosphere of high purity argon (99.9999%) during the electrical erosion of Pt electrodes with purity 99.9999% which have hollow cylinders shape with an outer diameter 8 mm and cylinder wall thickness 1 mm. Excess gas pressure was 0.6 atm while the aerosol flow varied from 50 to 600 ml/min.

The interaction of radiation with aerosol nanoparticles was carried out in a laser modification cell developed by us, which combines an aerosol flow with a laser beam along its length. In such a system, nanoparticles absorb a fraction of the radiation energy, which is converted into heat and spent on partial or complete modification, practically without heating the environment. In the experiments, we used pulsed lasers with the wavelength of 355, 527 and 1053 nm (TECH-1053, “Laser-export” Co. Ltd., Moscow, Russia) with a pulse duration of about 40 ns and controlled pulse repetition rates in the range of 10 Hz–10 kHz.

The obtained samples of the synthesized NPs were studied by the transmission electron microscope (TEM) JEM-2100. Extinction spectra of Pt NPs in chromatographic isopropanol were measured on a JASCO V-770 spectrophotometer. Data on agglomerate size distributions were obtained from a TSI SMPS 3936 aerosol spectrometer.

## Results and Discussion

According to the TEM images (fig.1), an average size of aggregated primary platinum nanoparticles is 5.9±2.4 nm. Interaction with laser radiation with a wavelength of 355 nm gives the primary nanoparticles partial enlargement and appearance of spherical particles with sizes up

to 190 nm. Laser radiation at wavelengths of 527 and 1054 nm makes it possible to obtain spherical individual platinum nanoparticles with sizes from 50 to 250 nm.

Within the Mi formalism, a physicomathematical model has been implemented to calculate the extinction cross sections for monodispersed spherical Pt NPs, simulated extinction spectra are shown in Fig. 2. The experimental extinction spectra for Pt NPs have an absorption peak at a wavelength of 273 nm, after modification by any type of laser, the extinction spectra are characterized by several peaks in the UV and visible regions.

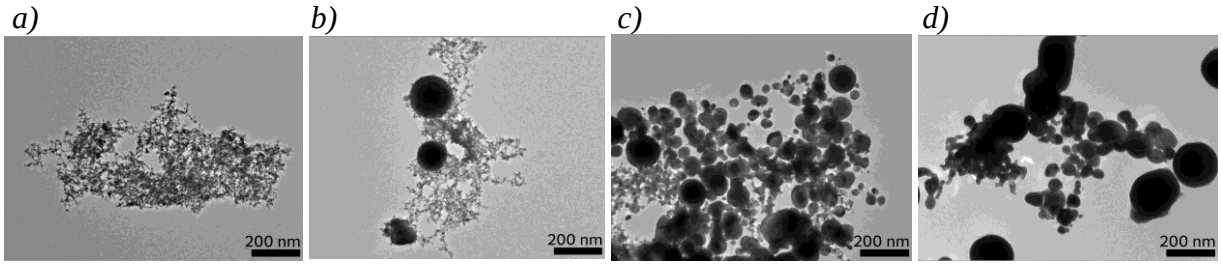


Fig. 1. TEM images of primary Pt NPs (no laser) *(a)*; UV laser (*b*); green laser (*c*); red laser (*d*)

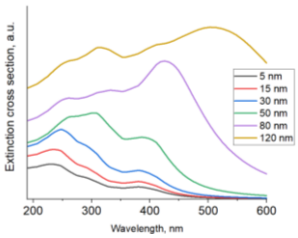


Fig. 2. Simulatedextinction spectra for platinum nanoparticles with the diameter from 5 to 120 nm

## Conclusion

Platinum nanoparticles with different morphologies and sizes varying from 5 to 250 nm were obtained in a gas discharge using additional laser modification at different wavelengths in a gas flow. The obtained Pt NPs have a wide particle size distribution and an extinction peak in the UV region. The best modification (shape transformation from aggregates to individual nanoparticles) is achieved by using green and infrared lasers. The calculations carried out according to the Mie theory showed that the extinction spectra of monodisperse platinum particles with sizes from 5 to 120 nm consist of several peaks, one of which is located in the UV region in the range from 230 to 315 nm.

## Acknowledgments

This work was financially supported by the Russian Science Foundation (project № 22-19-00311, https://rscf.ru/en/project/22-19-00311/).

## REFERENCES

1. **Kruis F.E., Fissan H., Peled A.,** Synthesis of Nanoparticles in the Gas Phase for Electronic, Optical and Magnetic Applications - a review. Journal of Aerosol Science. 29 (5-6) (1998) 511–535.

2. **Efimov, A. A., Arsenov, P. V., Borisov, V. I., Buchnev, A. I., Lizunova, A. A., Kornyushin, D. V., Tikhonov S. S., Musaev A. G., Urazov M. N., Shcherbakov M. I., Spirin D. V., Ivanov, V. V.,** Synthesis of nanoparticles by spark discharge as a facile and versatile technique of preparing highly conductive Pt nano-ink for printed electronics. Nanomaterials. 11 (1) (2021) 234.

3. **Gharibshahi, E., Saion, E., Johnston, R. L., Ashraf, A.,** Theory and experiment of optical absorption of platinum nanoparticles synthesized by gamma radiation. Applied Radiation and Isotopes.147 (2019) 204-210.

4. **Khabarov, K. M., Filalova, E. M., Nouraldeen, M., Kameneva, E. I., Musaev, A. G., Tikhonov, S. S., Ivanov, V. V.,** Effect of Au Nanoparticle Agglomeration on SERS Signal Amplification. Nanomaterials 13(5) (2023) 812.

# Modelling the influence of planar waveguide cladding thickness on the absorption efficiency of a superconducting NbN strip.

**Vovk N. A[1,2], Shibalov M. V[1], Mumlyakov A. M[1], Korneeva Yu.P[1]. Asharchuk I. M[1], Smirnov K. V[2] and Tarkhov M. A[1]**

[1] Institute of Nanotechnology of Microelectronics of the Russian Academy of Sciences, Moscow 119991,Russia
[2] Higher School of Economics - National Research University, 101000, Russia

e-mail: nvovk@hse.ru

**Abstract**: This paper reports simulation results for 1550 nm wavelength absorption efficiency of a superconducting NbN nanowire matching with a single-mode Si3N4 waveguide depending on $SiO_2$ cladding thickness. Simulation results for straight, U- and W-shaped strips shows that with perfect planarization (no top cladding) the absorption coefficient per unit length is 0.7, 1.6 and 2.5 dB/µm, respectively.

## 1. Introduction

Planarization technology of multilayer CMOS structures is one of the key steps in nano- and microelectronics manufacturing. Without planarization, each successive layer applied follows the topology of the previous layers, creating undesirable steps and steep slopes on the surface of the new layer, which degrades its performance. Photonic integrated circuits (PIC), used for converting optical signals into electrical signals, are multilayer structures comprising such basic elements as waveguides, electro-optical modulators, photon detectors and quantum emitters [1]. The main element for planarization of such circuits is the waveguide cladding layer, on which the control and detection elements of radiation are placed.

In this paper, we calculate the effect of $SiO_2$ cladding layer [2] on the efficiency of pulling an evanescent wave from a $Si_3N_4$ waveguide by a superconducting NbN nanostrip.

## 2. Materials and Methods

The first step in PIC design is to determine the compatibility of the operating wavelength with the waveguide material. At the telecommunication wavelength of 1550 nm, $Si_3N_4$-based platforms (refraction index n=2.01) exhibit record low optical absorption [3]. To localise the optical mode of radiation in the $Si_3N_4$ waveguide, a cladding layer with a lower refractive index, $SiO_2$ (n=1.44), is used in the planar implementation [2].

In this paper we consider a single-mode radiation propagation with a wavelength of 1550 nm, which is defined by the geometry of the waveguide cross section of 1 x 1 µm$^2$. As a superconducting material NbN, which is widely used for single-photon detectors [4], is chosen. NbN refractive index at 1550 nm is 5.23-5.82i, where the multiplier of the imaginary part is responsible for light absorption by the material.

The transmittance characteristic of a planar waveguide is defined as $\ln\left(\frac{P_{out}}{P_{in}}\right)$, where $P_{out}$ is the output signal power, $P_{in}$ is the input signal power. And according to the Boeger-Lambert-Bera law considering the superconducting strip as an absorbing medium, the transmittance is defined as $-\alpha \cdot L_{NbN} = \ln\left(\frac{P_{out}}{P_{in}}\right)$, where $L_{NbN}$ is the strip length, α is the absorption coefficient. Simulations are performed for different strip configurations: a single strip, a strip with one turn (U-shape) and a strip with two turns (W-shape). The width of the strip is 100 nm, the gap is 50 nm and the thickness is 5 nm.

## 3. Results

The simulations were performed in COMSOL Multiphysics software in the Electromagnetic Waves, Beam Envelopes (ewbe) physics section using the finite element method. Figure 1 shows the simulation results which presents the effect of the top cladding thickness, which varied from 0 to 50 nm on the trapping of the NbN evanescent wave with a length of 36 µm for straight strip, a length of 25 µm for U-shape strip and a length of 18 µm for W-shape strip. For the strip under consideration and its

geometrical dimensions with perfect planarization ($d_{clad}$=0 nm) the maximum absorption coefficient is 28% for straight strip, 44% for U-shape and 49% for W-shape strips, which gives the absorption coefficient per unit length 0.7, 1.6 and 2.5 dB/µm for listed topologies, respectively.

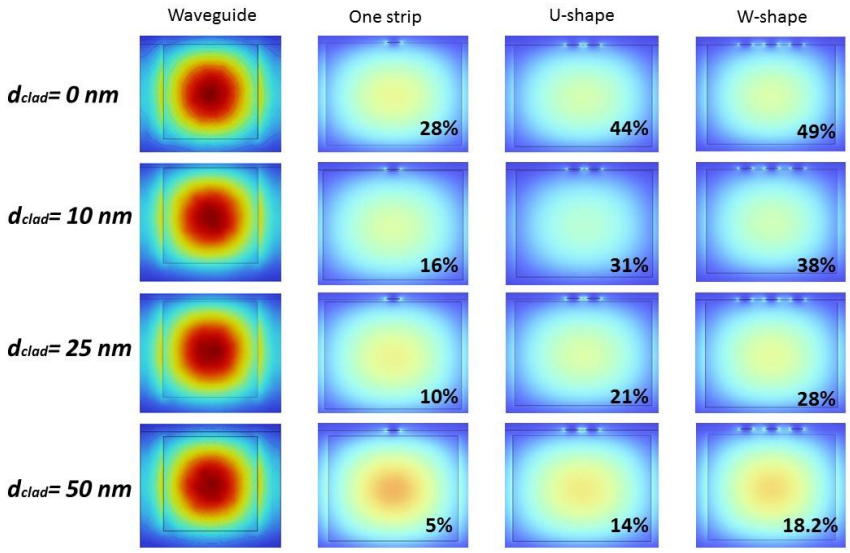


**Figure. 1.** Simulation results of optical power distribution in a planar waveguide with different shapes of NbN s trip at different thicknesses ($d_{clad}$) of the cladding layer.

## 4. Conclusion

In this paper, the dependence of waveguide mode absorption by a superconducting NbN strip of different topology on the thickness of the waveguide cladding after the planarization operation has been calculated. Simulation results allows determining absorption efficiency per unit length of superconducting NbN strip with different configuration. The proposed calculation can be used to design a NbN single photon detector coupled to a single-mode waveguide-and determine the length of NbN strip to achieve 100% absorption efficiency, with a fixed thickness of the waveguide cladding layer. Such detector is used in quantum computing and cryptography applications.

## Acknowledgments

The work was supported by project 1021061509690-0-1.2.1. Ministry of Education and Science of the Russian Federation.

## References

[1] Ali Elshaar et. *al.* 2020 *Nature Photonics*; **14(5)** 285-298
[2] Martin Pfeiffer *et. al*. 2018 *IEEE Journal of Selected Topics in Quantum Electronics*. **24(11)**
[3] Jared Bauters *et. al*. 2011. *37th European Conference and Exposition on Optical*
[4] Oliver Kahl et. al. 2015. *Scientific Reports*. **5(1)**, 1-11

# Linear transmission of waveguides based on perovskite $MAPbBr_3$

**N. V. Glebov [1✉], Masharin[1], A.Mikhin[1], S. Makarov[1,2], and A. Samusev[1,3]**
[1] ITMO University, School of Physics and Engineering, St. Petersburg, 197101, Russia;
[2] Qingdao Innovation and Development Center, Harbin Engineering University, Qingdao 266000, Shandong, China;
[3] Experimentelle Physik 2, Technische Universität Dortmund, 44227 Dortmund, Germany
✉nikita.glebov@metalab.ifmo.ru

**Abstract.** The strong coupling of exciton resonance in perovskite materials with high-Q optical cavities resulted in the appearance of half-light half-matter quasiparticles known as exciton-polaritons. Thanks to their hybrid properties, these quasiparticles provide a prospective platform for highly nonlinear and energy-efficient devices such as all-optical switches and transistors. In this work, we demonstrate the fabrication of perovskite-based 2D waveguide, supporting the strong light-matter coupling regime with integrated coupler and decoupler elements, represented as grating structures, and observe linear transmission of this system. The realization of such a system allows us to study the nonlinear dependence of the propagation high-intensity pulse in the polariton guided mode. These findings offer novel opportunities for managing exciton-polariton nonlinearities at room temperature and pave the way for the observing and study self-modulated pulsed up to solitons in a highly nonlinear system. Our results provide an important step for the development of nonlinear on-chip polaritonic devices based on halide perovskite in planar on-chip geometry.

## Introduction

Photonics encompasses both theoretical and practical aspects of utilizing optical signals, with a focus on developing energy-efficient optical computing devices. To achieve this goal, it is essential to create systems with robust and strong optical nonlinear properties, where light can be manipulated by light. One promising direction is the study of systems that support strong light-matter coupling and exciton-polariton modes, but in modern nanophotonics there is still a problem with materials that support strong light-matter coupling, are easily fabricated and are compatible with planar geometry.

Perovskite materials have emerged as one of the most promising candidates for next-generation optoelectronic devices due to their unique properties such as high absorption coefficient, long carrier diffusion length, and tunable bandgap [1]. Recently, half-light half-matter quasiparticles which are called exciton polaritons, in strong light-matter coupling have been observed in perovskite materials in easily fabricated planar resonators. [2]. The presence of exciton-polaritons within perovskite presents a fresh avenue for managing the interplay between light and matter, potentially resulting in the creation of innovative photonic apparatuses that boast superior efficiency and performance. Hybrid perovskites, such as MAPbBr3, have demonstrated significant potential for practical applications in planar geometry in nonlinear photonics due to the crucial role of polaron effects that mediate interparticle interactions [3].

The resulting polaron-mediated exciton-polaritons remain stable and strongly interacting at room temperature, as demonstrated by large nonlinear blueshifts of lower polariton branch energy under resonant femtosecond laser pulse excitation. As was shown earlier, in the waveguide polariton mode can exhibit exotic effects due to strong nonlinearities such as solitons [4]. To investigate the nonlinear dependence of the polariton resonance on laser pumping power in this work, we create for the first time a waveguide with a coupler – decoupler based on halide perovskite and demonstrate the linear transmission through this system.

## Results and Discussion

We fabricated thin films based on halide perovskite MAPbBr3 by spin-coating method in a glove box with a dry nitrogen atmosphere. The fabricated samples were characterized by atomic force microscopy, which revealed that the thickness of the fabricated samples was 130 nm and the roughness did not exceed 10 nm. We then fabricated photonic crystal waveguides with a coupler and a decoupler which are 1D grating structures. These structures are 1d periodic gratings of 50x50

μm2 spaced more than 50 μm apart, and their geometry was selected on the basis of numerical calculations. We characterized these structures with an atomic force microscope and found that the period was 300 nm, and the modulation was 50 nm.

To verify the presence of a strong light-matter interaction in our fabricated samples, we measured the angle-resolved reflectance spectra with both TE and TM polarizations using a setup for the Fourier plane imaging allowing them to perform the angle-resolved spectroscopy measurements at room temperature. We used a two coupled oscillator model to fit the polariton mode and confirm the strong light-matter coupling. This suggests that our samples exhibit a significant degree of light-matter coupling and hold promise for use in experiments with nonlinear transmission.

Following this, we examined the linear transmission of the system with integrated coupler and decoupler elements we had created. To achieve this, we utilized a halogen lamp to introduce an optical wave which was coupled through the input grating and propagated along the waveguide for a distance of 50-100 μm before decoupling through the decoupler. We analyzed the angular dependence of the optical transmission spectra using both TE and TM polarizations, using the same setup with angular resolution and filtering out the slit signal originating solely from the decoupler.

## Conclusion

In this study, we successfully fabricated high-precision waveguides supporting the strong coupling regime with input and output elements of radiation using perovskite MAPbBr3, which enabled us to observe linear transmission. By utilizing a halogen lamp and analyzing the angular dependence of the optical reflectance spectra with both TE and TM polarizations, we were able to fit the polariton mode and confirm the strong light-matter regime using a two coupled oscillator model. Moving forward, we anticipate that these samples will allow us to investigate the nonlinear dependence of polariton resonance on laser pulse pumping, leading to the suppression of power-dependent losses at high pulse energies and the crossing of the blue-red shift of the central frequency of the pulse.

## REFERENCES


1. **Makarov S. et al.** Halide-Perovskite Resonant Nanophotonics, Advanced optical materials. – 2019. – T. 7. – No. 1. – C. 1800784.
2. **Glebov N. et al.** Mechanical scanning probe lithography of perovskites for fabrication of high-Q planar polaritonic cavities, arXiv preprint arXiv:2301.01016. – 2023.
3. **Masharin M. A. et al.** Room-Temperature Polaron-Mediated Polariton Nonlinearity in MAPbBr3 Perovskites, ACS Photonics 2023 10 (3), 691-698
4. **Li P. et al.** Two-dimensional CH3NH3PbI3 perovskite nanosheets for ultrafast pulsed fiber lasers, ACS applied materials & interfaces. – 2017. – T. 9. – №. 14. – C. 12759-12765.

# Features of measuring the time of longitudinal relaxation $T_1$ in condensed media by nuclear magnetic resonance using the modulation method in weak magnetic fields

**A. A. Goldberg[1]✉, I. D. Kochetov[1], V. V. Davydov[1, 2, 3]**
[1] Peter the Great Saint-Petersburg Polytechnic University, Saint Petersburg, Russia;
[2] The Bonch-Bruevich Saint Petersburg State University of Telecommunications, Saint Petersburg, Russia;
[3]All-Russian Research Institute of Phytopathology, Moscow Region, Russia.
✉ artemiy.goldberg@mail.ru

**Abstract.** The features of determining the times of longitudinal $T_1$ and transverse $T_2$ relaxation using small-sized NMR relaxometers are considered. The applicability of the modulation method in small-sized NMR relaxometers for signal registration is substantiated. The advantages of using the modulation method for recording the NMR signal in comparison with the others are noted. A formula is obtained for determining $T_1$ from two measurements of the amplitude of the NMR signal at different modulation frequencies $\tau$ from the Bloch equations. The obtained formula is considered, and the results are given for those cases when the solution of the Bloch equation is applicable.

**Keywords:** small-sized NMR relaxometer, Bloch equation, Giulotto method.

## Introduction

One of the tasks of nuclear magnetic resonance (NMR) in studying condensed matter is determining the times of longitudinal $T_1$ and transverse $T_2$ relaxation [1]. It is most important when using small-sized NMR relaxometers for express control of the state of condensed media [2]. In the case of express control, the registration of the NMR signal is carried out in a weak magnetic field with $B < 100\ mT$ (restrictions on the weight of the device design) using an independent power source. It creates problems using pulsed methods (Hann and Carr-Purcell spin echo) in small portable NMR relaxometers to measure $T_1$ and $T_2$ [1]. A gap between the magnet poles of at least 80 mm is required to implement these methods to accommodate the coil system, which increases the weight of the device and the impulse voltage of several hundred volts (restrictions on battery charge) [2]. Therefore, measurements of $T_1$ and $T_2$ in small-sized NMR relaxometers record the signal using a modulation technique.

## The NMR signal using the modulation method

When using the modulation method, the NMR signal is formed in the form of a decaying non-periodic oscillation. Fig. 1 shows the recorded NMR signal from tap water at $T = 290.2\ K$.

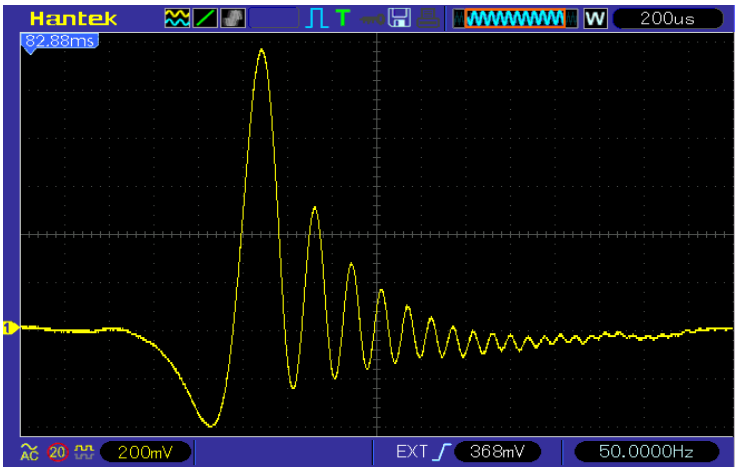


Fig. 1. The recorded NMR signal is a signal from tap water using a modulation technique.

The time $T_2$ is determined from the envelope's decay constructed from the tops of the peaks. The inhomogeneity of the magnetic field is considered in the area where the registration coil is located [1]. Difficulties arise with the measurement of $T_1$. Experimental studies have shown that it is extremely difficult to use the frequency measurements of the Giulotto method [3] to determine $T_1$ in the design of a small-sized NMR relaxometer.

In a weak magnetic field B, the resonant frequencies, when the modulation frequency of the magnetic field B changes, differ from each other by fractions of a hertz. Recording these frequencies requires high resonance tuning accuracy, which can only be achieved under laboratory measurement conditions. In the case of using the device in the field, such a measurement mode is challenging to implement. In addition, the formula for determining $T_1$ in the Giulotto method [3] was obtained from the Bloch equations without considering the features of recording the NMR signal in a weak magnetic field using the modulation technique [2]. Also, Bloch's equations did not consider the effect of magnetic field modulation on the magnetization of the condensed medium. Therefore, considering all the factors in the Bloch equations, we obtained a formula for determining $T_1$ from two measurements of the NMR signal amplitude at different modulation frequencies $\tau$.

$$M = M_0 [1 - (1 - \exp(-\tau / T_1)) / (1 + \exp(-\tau / T_1))] \quad (1)$$

## Results and Discussion

Let's consider an NMR signal recorded at a frequency of 100 *Hz* and an NMR signal recorded at a frequency of 120 *Hz*. Two NMR signals actually exist, the time $T_1$ of the medium under study exists, and the equation has no solutions that fit the constraints. And in the case of recording signals at frequencies of 10 and 100 *Hz*, the equation has solutions. Therefore, it is necessary to consider various cases and determine the boundary conditions for which solutions of the Bloch equation are applicable. Let's look at some of these cases in more detail.

1) $\tau_1 = 300\ \mu s$, $\tau_2 = 200\ \mu s$
   a) $A_1 = 1.14\ V$, $A_2 = 0.89\ V$: the equation has no solutions;
   b) $A_1 = 0.89\ V$, $A_2 = 1.14\ V$: the equation has one solution, but it does not satisfy the constraint $T_1 \in [0.001; 21]$ (s);
2) $\tau_1 = 0.01\ s$, $\tau_2 = 0.005\ s$, $A_1 = 1.04\ V$, $A_2 = 0.87\ V$: the equation has two solutions, but they do not satisfy the constraint;
3) $\tau_1 = 0.0025\ s$, $\tau_2 = 0.0014\ s$, $A_1 = 1.04\ V$, $A_2 = 0.87\ V$: the equation has one solution, but it does not satisfy the constraint;
4) $\tau_1 = 0.1\ s$, $\tau_2 = 0.01\ s$, $A_1 = 1.68\ V$, $A_2 = 0.87\ V$: the equation has no solutions.

## Conclusion

The use of equation (1) to determine the $T_1$ time for various media has shown that there are a number of features when performing calculations. These features are related to the relationship between the modulation frequencies that are used to register the NMR signal. Thus, it is necessary to conduct further research to determine the limits of applicability of the obtained formula.

## REFERENCES


1. **Leshe A.** Nuclear induction. Veb Deustscher Verlag Der Wissenschaften Berlin, 1963.
2. **Davydov V.V., Dudkin V.I., Vysoczky M.G., Myazin N.S.** Small-size NMR Spectrometer for Express Control of Liquid Media State: Applied Magnetic Resonance. 51(7) (2020) 653–666.
3. **Chiarotti G., Cristiani G., Giulotto L., Lanzi G.** A Nuclear Inductor for Measurements of Thermal Relaxation Times in Liquids: II Nuovo Cimento. 12(4) (1954) 519-525.

# Features of the research of liquid media by the optical differential method during express control

**D. S. Provodin[1], A. A. Goldberg[1✉], I. D. Kochetov[1], V. V. Davydov[1, 2, 3]**
[1] Peter the Great Saint-Petersburg Polytechnic University, Saint Petersburg, Russia;
[2] The Bonch-Bruevich Saint Petersburg State University of Telecommunications, Saint Petersburg, Russia;
[3]All-Russian Research Institute of Phytopathology, Moscow Region, Russia.
✉ artemiy.goldberg@mail.ru

**Abstract.** The features of the research of liquid media in express control using the refraction phenomenon are considered. The advantages of using the differential method for the analysis of liquid media in comparison with others are noted. A new method for studying liquid media in a large range of variations of the refractive index n is proposed. An Anderson cuvette has been developed for conducting research with the necessary accuracy, due to a change in the discreteness of the measurement scale *n*. The results of experimental research of different media are given.

**Keywords:** refraction, liquid media, express control, Anderson differential cuvette, refractive index.

## Introduction

At the present time express control of a large number of liquid media using refraction requires measurements of the refractive index in the range from 1.32 to 2.34 (with a measurement error of at least 0.001) [1, 2]. Such a complex problem can be solved only using the differential method [3]. The main problem that arises when solving this problem is related to taking into account the specifics of changing the trajectory of the laser radiation axis in the Anderson differential cuvette. The mathematical models used to determine the refractive index *n* in the differential method do not take into account the specifics associated with the thickness of the partition and the material of the cuvette. This leads to errors in the measurement of *n*. Therefore, solutions to eliminate these shortcomings are proposed in our work.

## Anderson differential cuvette

To study the features of the formation of the axis of the trajectory of laser radiation in the differential Anderson cuvette, its model was made (Fig. 1).

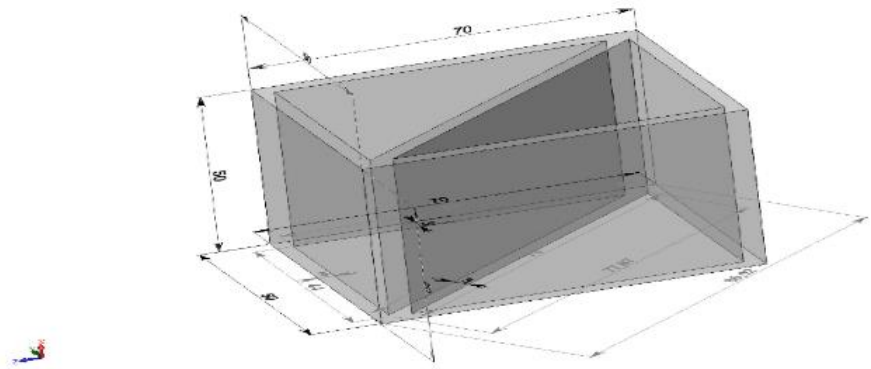


Fig. 1. The 3D model of differential cuvette of Anderson. All size presented in *mm*.

In this design of the cuvette, the partition is made of the same material as the walls of the cuvette. For such a design of the cuvette, it was found that the optimal value of the partition thickness is 3 *mm* for the cuvette faces with sizes of 50 and 60 *mm*. This allows you to get the maximum resolution when registering a laser radiation signal on a photodiode ruler along the width

of the laser beam. This makes it possible to obtain a minimum error when measuring the displacement of the axis of laser radiation, by which the value of *n* is determined.

## Results and Discussion

The results of the research of tap water are presented in Fig. 2 as an example.

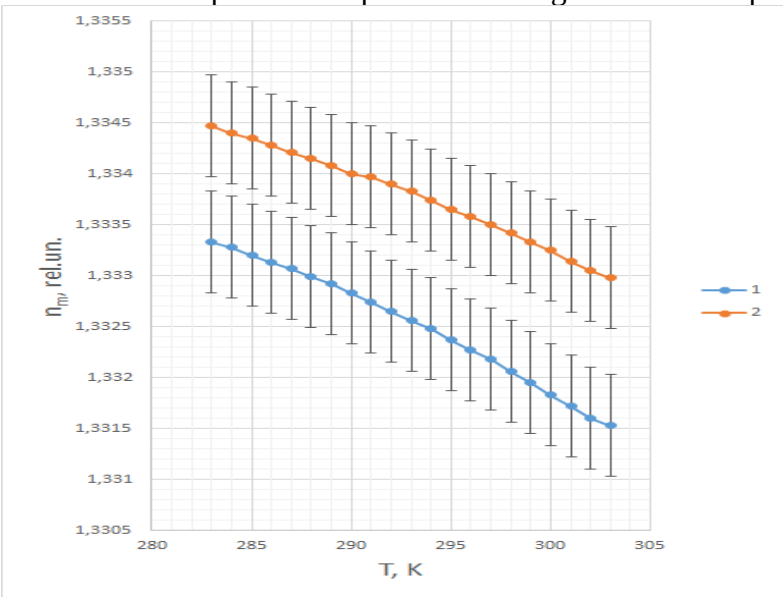


Fig. 2. The dependence of the change in the refractive index n and tap water on temperature *T*. Graphs correspond to the state of tap water: 1 - there are no oxides in the water, 2 - there are oxides in the water.

The analysis of the obtained results on the research of the temperature dependence of the refractive index on the temperature *T* showed that they correspond with the data of other scientists [3]. Comparisons of these results with the data obtained on another refractometer (NAR 2T) confirmed their correspondence to reality.

## Conclusion

The obtained research results confirm the validity of taking into account the features in the Anderson differential cuvette of the propagation of the laser radiation axis to obtain *n* values with an error of at least 0.0001.

In addition, taking into account the features in the mathematical model to determine the n features of the formation of the trajectory of the laser radiation axis in the Anderson differential cuvette allows you to change the discreteness of the refractometer scale from 0.001 to 0.0001 (without changing the location of the main elements of the device). This allows us to examine the state of media in which the range of *n* varies from 1.2 to 2.2 or from 1.3 to 2.3, or 1.4 to 2.4 with an error of 0.001 (changing the design of the cuvette and the reference liquid in it). With the use of one device, the entire range of *n* changes in liquid media is overlapped, which was previously unavailable. Further, after determining the value of *n*, we can switch to a narrow range of 0.1 with a scale discreteness of 0.0001 and determine the value of *n* up to the fourth digit with an error of 0.0001. Higher measurement accuracy is not required for express control.

## REFERENCES

1. **Bhardwaj V. K., Maini S.** Compact and self-aligned fluid refractometer based on the Doppler-induced self-mixing effect Applied Optics. 59(10) (2020) 3064–3072.

2**. Guo W., Li R., Yu L., Chen J., Xia M., Li W., Yang K.** Self-referenced technology for refractive index measurement under mechanical vibration and temperature fluctuation Applied Optics. 58(7) (2019) 1862–1867.

3. **Chen J., Guo W., Xia M., Li W., Yang K.** In situ measurement of seawater salinity with an optical refractometer based on total internal reflection method Optics Express. 26(20) (2018) 25510–25523.

# Numerical simulation of endocytosis of metallic nanoparticles with various geometry

**D. R. Dadadzhanov** [1✉], **N.S. Petrov**[1], **T. A. Vartanyan** [1]

[1] International Research and Education Centre for Physics of Nanostructures, ITMO University, Saint-Petersburg 197101, Russia.

✉daler.dadadzhanov@gmail.com

**Abstract.** Extinction, absorption and scattering cross-section of silver and gold nanoparticles with spherical, elongated and cuboid shape have been studied. We demonstrated a red-wavelength shift of localized surface plasmon resonance band of plasmonic nanoparticles as a result of their uptake modelling by a cell during phagocytosis process.

**Keywords:**LSPR, plasmon, silver, gold, nanoparticle, endocytosis.

**Funding:** This work was supported by the Russian Science Foundation, Project 22-72-10057

## Introduction

Basic research in the field of nanomaterials has contributed to the rapid development of targeted drug delivery technology. In turn, noble metal nanoparticles have proven themselves as biomarkers or targets in photothermal therapy [1, 2]. First of all, this is achieved due to their plasmonic properties, namely due to localized surface plasmon resonance (LSPR), which arises due to the resonant vibration of free charge carriers in the metal [3]. Plasmon properties depend not only on the characteristics of the nanoparticles themselves (size or material), but also on the dielectric constant of the environment [4]. It is known that the size, shape, charge, and presence of active substances on the surface of metal nanoparticles play a decisive role in their endocytosis into cellular media. However, at the moment, there is no comprehensive understanding of the mechanisms and kinetics of nanoparticle endocytosis. Meanwhile, the contrast in the dielectric permittivity difference for the extracellular medium (n = 1.33) and the bilipid layer of the cell (n = 1.4) makes it possible to measure the position of metal nanoparticles relative to the interface between two biological media by measuring the LSPR spectral shift using far-field absorption spectroscopy methods [4 ]. Thus, the study of the kinetics of endocytosis during the absorption of metal nanoparticles is of great scientific interest not only from the physical point of view, but also from the point of view of biomedicine. The purpose of this work is to establish the physical patterns of endocytosis of silver and gold nanoparticles depending on their size and shape.

## Materials and Methods

The spectral properties of nanospheres and nanorods based on silver and gold were studied by numerical finite element methods using the COMSOL Multiphysics® software. The permittivity of silver and gold were taken from the experimental work of P. B. Johnson and R. W. Christy [5]. To study the endocytosis of NPs, a sphere with a radius of 250 nm and a refractive index of n=1.4 was modeled, imitating the bilipid layer of the cell membrane.

## Results and Discussion

The spectra of the absorption, scattering and extinction cross sections of nanospheres and nanorods were studied during the transition from the cellular nutrient medium (n=1.33) to the intracellular medium (n=1.37) through the membrane layer. The radius of the nanospheres varied from 5 nm to 50 nm. The length of the nanorod varied from 20 nm to 100 nm with a fixed radius of 5 nm. Dependences of the LSPR maxima on the position of silver and gold nanoparticles were obtained in the course of modeling endocytosis. It was shown that when gold and silver nanoparticles pass through the cell membrane, a spectral shift of the LPR to the long wavelength region of about 8 nm is observed. It was also found that when a metal nanosphere approaches, LPPR splitting is observed, which is subsequently removed when the nanoparticle is in the intracellular environment.

## Conclusion

In our work we suggested using plasmon resonance phenomenon to monitor the endocytosis – the process in which a cell capture solid particles – in the far field spectroscopy. The numerical

results of the realistic endocytosis model for single nanoparticle penetrated through a thin cell membrane has been numerically developed in COMSOL Multiphysics.

## REFERENCES


1. **Kim M., Lee J. H., Nam J. M.** Plasmonic photothermal nanoparticles for biomedical applications //Advanced Science. – 2019. – T. 6. – №. 17. – C. 1900471.
2. **Manrique-Bedoya S. et al.** Computational Modeling of Nanoparticle Heating for Treatment Planning of Plasmonic Photothermal Therapy in Pancreatic Cancer. – 2019.
3. **Stepanov A. L. et al.** Optical properties of metal nanoparticles //ICONO 2010: International Conference on Coherent and Nonlinear Optics. – SPIE, 2011. – T. 7993. – C. 543-552.
4. **Baryshnikova K. V., Petrov M. I., Vartanyan T. A.** Plasmon nanoruler for monitoring of transient interactions //physica status solidi (RRL)–Rapid Research Letters. – 2015. – T. 9. – №. 12. – C. 711-715.
5. **Johnson P. B., Christy R. W.** Optical constants of the noble metals //Physical review B. – 1972. – T. 6. – №. 12. – C. 4370

Conference materials
UDC 535.14
DOI: https://doi.org/10.18721/JPM.

# Pockels cell performance in N-photon demultiplexer

**M. A. Dryazgov**[1,2✉], **S. S. Straupe**[2], **S. P. Kulik**[2], **A. A. Korneev**[1,2]
[1] Higher School of Economics - National Research University, Moscow, Russia;
[2] Lomonosov Moscow State University, Moscow, Russia
✉mdryazgov@hse.ru

**Abstract.** We demonstrate a new circuit for spatial demultiplexing of N successive photons using only one Pockels cell. We demonstrate the principle of operation of the loop circuit and the time characteristics of the Pockels cell used. We determine the minimum performance of the Pockels cell used from its maximum switching frequency.

**Keywords:** photons demultiplexing, single-photon source, Pockels cell.

**Funding:** This study was funded by Russian Science Foundation (RSF) Grant No. 22-12-00353.

**Citation:** Dryazgov M. A., Kulik S. P., Straupe S. S., Korneev A. A., Pockels cell performance in N-photon demultiplexer, St. Petersburg State Polytechnical University Journal. Physics and Mathematics. 16 ( ) (2023) …–…. DOI: https://doi.org/10.18721/JPM.

This is an open access article under the CC BY-NC 4.0 license (https://creativecommons.org/licenses/by-nc/4.0/)

© Dryazgov M. A., Kulik S. P., Straupe S. S., Korneev A. A., 2023. Published by Peter the Great St. Petersburg Polytechnic University.

Материалы конференции
УДК 535.14
DOI: https://doi.org/10.18721/JPM.

## Introduction

Applied tasks of quantum optics, such as, for example, boson sampling, require operations on several photons [1]. However, the most common sources of single indistinguishable photons generate one photon per pump pulse [2]. This leads to the need to use demultiplexing, that is, the separation of photon sequence into channels for operations on them [3]. The most effective way of demultiplexing is the use of a Pockels cells (PC) [4-5]. PC changes the polarization of photons to orthogonal, which makes it possible to separate them using polarization beam splitters (PBS). The downside of this scheme is the need to use N-1 PC for demultiplexing N photons.

We propose a scheme where elements of linear optics are used for the spatial separation of photons, and only one PC is needed to demultiplex N photons. We determine the minimum performance of the Pockels cell used from its maximum switching frequency

## Principal scheme

The principal scheme of the proposed demultiplexer is shown in Fig. 1 (a). Photons are reflected from the triangle prism and mirrors, entering a closed loop with length $L_{loop}$. With the accumulation of N photons in the loop, the PC rotates the polarization of photons by 90 degrees, which leads to the exit of spatially separated photons from the loop.

The voltage on the PC keys is shown in Fig. 1(b). By changing the periods of the keys, it is possible to accumulate photons in the loop and release them, as shown in Fig. 1(c). The minimum PC switching period is 72 ns due to technical limitations. For $\Delta t = 12$ ns, this makes it possible to obtain the minimum number of demultiplexed photons N = 5.

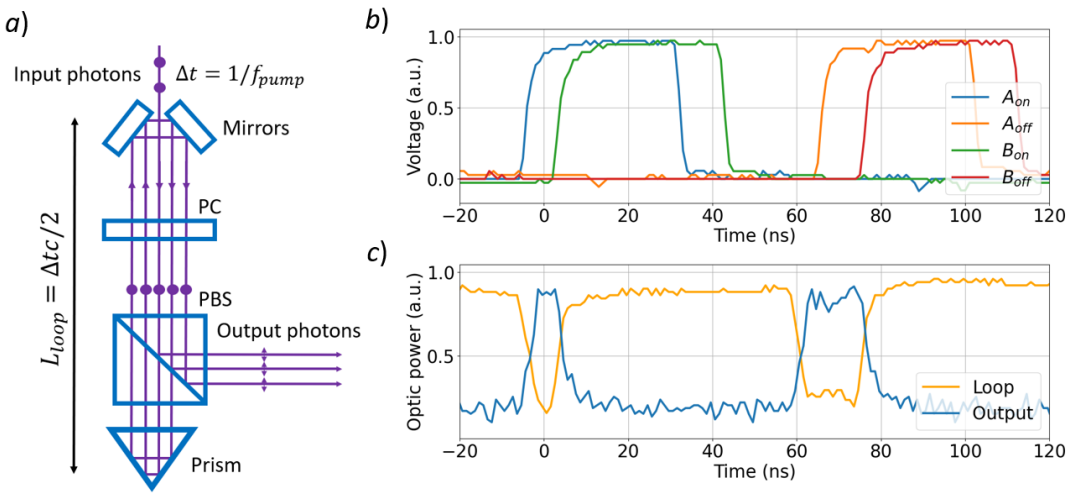


Fig. 1. (*a*) Principal scheme of the spatial demultiplexer for 3 photons. (b) Voltage per time in PC keys. (c) Optical power per time in loop and output respectively.

## Conclusion

Proposed scheme for spatial demultiplexing of photons, requiring only elements of linear optics and one PC. The scheme is easily scalable and the maximum number of demultiplexed photons depends only on geometric constraints. For the described Pockels cell, the possible number of demultiplexed photons is $N \geq 5$.

## REFERENCES

1. **Wang, H., et. al.**, High-efficiency multiphoton boson sampling. Nature Photonics, 11(6) (2017) 361–365.

2. **Schöll, E. et. al.**, Resonance Fluorescence of GaAs Quantum Dots with Near-Unity Photon Indistinguishability. Nano Letters, 19(4) (2019) 2404–2410.

3. **Münzberg, J. et. al.**, Fast and efficient demultiplexing of single photons from a quantum dot with resonantly enhanced electro-optic modulators. APL Photonics, 7(7) (2022) 070802.

4. **Rakhlin, M. V. et. al.**, Demultiplexed single-photon source with a quantum dot coupled to microresonator. Journal of Luminescence, 253 (2023) 119496.

5. **Hummel, T. et. al.**, Efficient demultiplexed single-photon source with a quantum dot coupled to a nanophotonic waveguide. Applied Physics Letters, 115(2) (2019) 021102.

## THE AUTHORS

**DRYAZGOV MIKHAIL**
mdryazgov@hse.ru
ORCID: 0000-0003-1576-265X

**KYLIK SERGEY**
sergei.kulik@physics.msu.ru
ORCID: 0000-0001-7681-7162

**STRAUPE STANISLAV**
straups@yandex.ru
ORCID: 0000-0001-9810-1958

**KORNEEV ALEXANDER**
alex.korneev78@gmail.com
ORCID: 0000-0002-0116-9591

Conference materials
UDC
DOI: https://doi.org/10.18721/JPM.

# Numerical simulation of the optical properties of a hybrid system based on gallium phosphide nanowires and 2D transition metal dichalcogenides

**R.P. Eresko[1]✉, E.S. Zavyalova[1], A. Kuznetsov[1,2], A.D. Bolshakov[1,2]**
[1]Alferov University, Saint Petersburg, Russia;
[2]Moscow Institute of Physics and Technology, Dolgoprudny, Russia
✉rodioneresko@gmail.com

**Abstract.** Transition metal dichalcogenides is a promising platform for nanophotonics owing to their peculiar optical properties including efficient luminescence in 2D geometry. For the practical implementation, it is necessary to develop ways for directed output of the luminescence from the 2D material. For this purpose, nanoscale waveguides can be employed. Here we numerically investigate a system based on gallium phosphide (GaP) nanowire (NW) and thin layers of molybdenum diselenide/ molybdenum disulfide ($MoS_2$/$MoSe_2$). We demonstrate the possibility of using such a system as a source of highly directed optical output. The use GaP NWs as submicron waveguides promotes significant increase of the photoluminescence output directivity from $MoSe_2$ and $MoS_2$ thin layers, making it possible to integrate this hybrid system into optical chips.

**Keywords:** gallium phosphide, nanowires, transition metal dichalcogenides, photoluminescence, molybdenum diselenide, molybdenum disulfide.

**Funding:** Authors acknowledge support of the research work by Ministry of Science and Higher Education of the Russian Federation (Agreement 075-03-2023-106, project FSMG-2021-0005; Grant FSRM-2023-0009).

© Eresko R.P., Zavyalova E.S., Kuznetsov A., Bolshakov A.D., 2023. Published by Peter the Great St. Petersburg Polytechnic University.

Материалы конференции
УДК
DOI: https://doi.org/10.18721/JPM.

## Introduction

Hybrid systems based on TMDC and nanoscale waveguides are of particular interest because of the possibility to combine several features different structures possess. GaP NWs are promising candidates for the development of key components (both passive and active) in the field of integrated photonics. Due to the unique optical properties of GaP NWs (low losses in the entire visible and IR range, high refractive index [1]), they allow to increase the TMDC radiation output directivity, which opens up the possibility of introducing these hybrid systems into integrated optical circuits.

## Material and methods

In this work, we study propagation of the photoluminescence of TMDC through an individual GaP NW to demonstrate theoretically effects of the NWs dimensions on the optical phenomena. System with the following geometry and parameters was studied: 0.7 nm thick $MoS_2$ ($MoSe_2$) monolayer with a 6 µm long part of GaP NW placed on it on a Si substrate with a 300 nm thick $SiO_2$ layer. We utilized numerical simulation methods (FDTD, FDFD) in Ansys Lumerical software, the calculations were carried out for NW diameters of 300, 250, 200, and 150 nm. A model Gaussian beam with a wavelength of 532 nm was used to analyze the interaction of the laser excitation with GaP NW/TMDC system. Photoluminescence (PL) from TMDC

monolayers was simulated using dipole sources, which spectral emission range was 625-725 nm and 740-860 nm for $MoS_2$ and $MoSe_2$, respectively [2].

## Results and Discussion

Numerical simulation performed few phenomena: 1) delocalization of the electromagnetic field occurred due to the NW diameter decreasing inside the GaP NW yield the enhancement at the NW/TMDC interface; 2) the localization of the TMDC PL field inside the NW is higher in the case of the transverse polarization than for the parallel orientation in relation to the NW axis; 3) the NW quality factor (Q-factor) decreasing indicates electromagnetic field stronger delocalization due to the resonant modes energy leakage. Eventually, observed effects can yield, firstly, local PL enhancement near the NW in the case of small diameter and, secondly, highly anisotropic optical output through the NW.

## Conclusion

We demonstrated that the electromagnetic field localization decreases with a GaP NW diameter reduction. Strong field displacement from the NW causes its localization enhancement on the GaP NW/TMDC interface. To sum up, choosing the NW diameter high enough for waveguiding allows to output TMDC radiation with a very high directivity. The results open new pathways for the system based on GaP NWs and 2D TMDC utilizing in integrated photonic circuits as a radiation source with high output directivity.

## REFERENCES

1. **Aspnes D.E., Studna A.A.,** Dielectric functions and optical parameters of si, ge, gap, gaas, gasb, inp, inas, and insb from 1.5 to 6.0 ev, Physical Review B. 27 (985) (1983) 2.

2. **Kioseoglou G., Hanbicki A.T., Currie M., Friedman A. L., Jonker B.T.,** Optical polarization and intervalley scattering in single layers of MoS2 and MoSe2, Scientific reports. 1(6) (2016) 25041.

## THE AUTHORS

**ERESKO Rodion P.**
rodioneresko@gmail.com
ORCID: 0009-0006-3863-7076

**ZAVYALOVA Eseniya S.**
ladieseniya@gmail.com
ORCID: 0009-0003-5049-538X

**KUZNETSOV Alexey**
alkuznetsov1998@gmail.com
ORCID: 0000-0001-7143-6686

**BOLSHAKOV Alexey D.**
bolshakov@live.com
ORCID: 0000-0001-7223-7232

# Luminescence kinetic of nanosized $CsPbBr_3$ QDs

**A. A. Zharkova** [1✉], **D. S. Saranin** [1], **A. R. Ishteev** [1], **D. O. Melikhova** [1], **S. I. Didenko** [1]
[1] NUST MISIS, Moscow, Russia;
✉m146137@edu.misis.ru

**Abstract.** $CsPbBr_3$ quantum dots have been studied as a luminophore for scintillators that could be used in the technology of ionizing radiation detectors. The main optical process that characterizes luminophore parameters is the kinetic of luminescence. In order to study optical parameters one phase of $CsPbBr_3$ quantum dots was isolated from the solution by using 400 nm filter and placed in toluene. Time resolved photoluminescence was measured for received sample by using ultraviolet laser diode (λ = 372 nm) as a source. Empirical expression from decay time plot was obtained. The expression described model of luminescence kinetic for 400 nm sized $CsPbBr_3$ quantum dots. According to the magnitude of empirical parameter received from the expression it was concluded that the recombination mechanism of luminescence on traps predominated for the studied samples of $CsPbBr_3$ quantum dots. The expression could be used for modeling optical proprieties for nanosized $CsPbBr_3$.

**Keywords:** $CsPbBr_3$, quantum dots, luminophore, scintillator, kinetic of luminescence.
**Funding:** This study was funded by FASIE contract number 17535ГУ/2022

## Introduction

Perovskites materials are manufactured using low-temperature technologies and have properties suitable for optoelectronic devices. One of the perovskites applications can be the creation of a scintillator based on them. The most promising materials for this application are quantum dots (QDs) like $CsPbBr_3$ QDs, since there is no self-absorption problem for structures smaller than the luminescence wavelength [1-3]. Despite technology results the mechanism of luminescence process is unknown and highly depends on perovskite composition [4]. The luminescence kinetic is characterized by the dependence of the light output intensity (I) on the decay time (t). Measuring the time resolved luminescence and approximation results on model of luminescence kinetic will help to understand mechanism of luminescence process for $CsPbBr_3$.

## Materials and Methods

During the process of QDs production the phases, that are too large to have quantum proprieties, could appear. These phases have self-absorption issue that could misrepresent the result of time resolved luminescence measurement. Due to this reason $CsPbBr_3$ QDs were filtered by 400 nm filter and then were placed in toluene which is anti-solvent for $CsPbBr_3$ QDs.

Time resolved photoluminescence was measured for received sample by using ultraviolet laser diode (λ = 372 nm) as a source and a streak camera. The resulting plot was normalized. The model from resulting plot was made by using Becquerel theory [5]. There are monomolecular and recombination types of luminescence kinetics. The equitation for monomolecular model is written below:

$$I = I_0 \exp(-kt), \tag{1}$$

where $I_0$ is initial intensity of luminescence,
$k$ is the process rate coefficient.

The equitation for recombination model is written below:

$$I = \frac{I_0}{(1+Mt)^p}, \tag{2}$$

where $M$ is the recombination parameter,

$p$ is an empirical parameter that determines the function hyperbolicity.

Magnitude of p parameter could be between 1 and 2. If magnitude of p parameter is close to 1 mechanism of recombination with ionized center will be dominating, if it is close to 2 trapping mechanism will be dominating.

## Results and Discussion

In order to determine the type of luminescence, resulting plot was converted into linearizing coordinates of exponential function (Figure 1a) and also it was approximated by a hyperbolic function of time f(t) using the least squares method (Figure 1b).

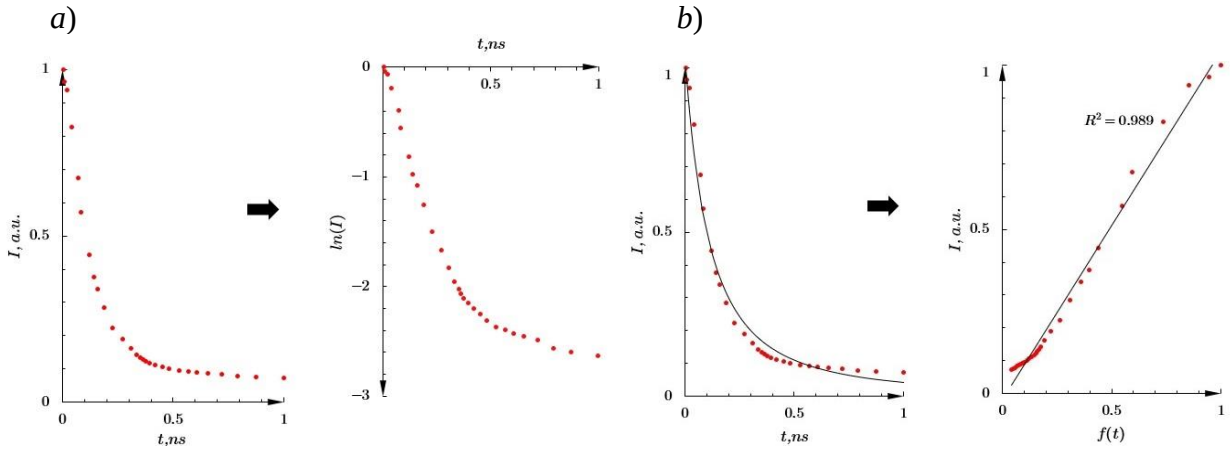


Fig. 1. Linearizing coordinates by an exponential function(a) and approximation by a hyperbolic(b)

Since the graph is not linearized in exponential coordinates, the recombination model should be used for approximation. By selecting the constants, the function can be approximated by the expression:

$$I = \frac{1}{(1+5.12t)^{1.78}}, \tag{3}$$

The hyperbolic nature of the dependence of intensity on time describes the recombination type of luminescence kinetic.

## Conclusion

It could be postulated that recombination mechanism of luminescence on traps is predominated for $CsPbBr_3$ QDs according to the value of the empirical parameter (p = 1.78) .

## REFERENCES


1. **Zhang Y. et al.** Metal Halide Perovskite Nanosheet for X-ray High-Resolution Scintillation Imaging Screens // ACS Nano. 2019.

2. **Chen W. et al.** X-ray radioluminescence effect of all-inorganic halide perovskite $CsPbBr_3$ quantum dots // J. Radioanal. Nucl. Chem. 2017. Vol. 314, № 3.

3. **Heo J.H. et al.** High-Performance Next-Generation Perovskite Nanocrystal Scintillator for Nondestructive X-Ray Imaging // Adv. Mater. 2018. Vol. 30, № 40.

4. **Zhou F. et al.** Halide Perovskite, a Potential Scintillator for X-Ray Detection // Small Methods. John Wiley & Sons, Ltd, 2020. Vol. 4, № 10.

5. **Berberan-Santos M. N., et al.** Mathematical functions for the analysis of luminescence decays with underlying distributions: 2. Becquerel (compressed hyperbola) and related decay functions //Chemical Physics. – 2005. – Vol. 317. – №. 1. – P. 57-62.

Conference materials
UDC
DOI: https://doi.org/10.18721/JPM.

# Towards versatile photonics based on GaP nanowires decorated with carbon dots

**E. S. Zavyalova[1]✉, A. Kuznetsov[1,2], M.A. Rider[3], M.S. Kovova[3], A.D. Bolshakov[1,2]**
[1]Alferov University, Saint Petersburg, Russia;
[2]Moscow Institute of Physics and Technology, Dolgoprudny, Russia
[3]ITMO University, Saint Petersburg, Russia
✉ladieseniya@gmail.com

**Abstract.** Carbon dots (CDs) are promising nanostructures in the field of photonics owing to the ease of fabrication, tunable and efficient emission. Here we synthesize carbon dots with the use of hydrothermal synthesis and decorate dense gallium phosphide (GaP) nanowires array with the dots. Feasible drop-casting deposition technique is found promising as the fabricated hybrid structures demonstrate efficient luminescence mapped along the nanowires surface with confocal microscopy. This experimental data together with the numerical calculations demonstrate enhancement of the dots luminescence by the resonant optical property of the nanowire acting as an efficient waveguide. The obtained results unveil the path for fabrication of novel photonic devices via decoration of optically dense nanowires with carbon dots for enhanced and directed emission.

**Keywords:** carbon dots, gallium phosphide, nanowires, confocal microscopy, photoluminescence

**Funding:** Authors acknowledge the Russian Science Foundation (grant № 20-72-10192).

© Zavyalova E.S., Kuznetsov A., Rider M.A., Kovova M.S., Bolshakov A.D., 2023. Published by Peter the Great St. Petersburg Polytechnic University.

Материалы конференции
УДК
DOI: https://doi.org/10.18721/JPM.

## Introduction

Development of new photonic nanomaterials is aimed at fabrication of efficient, bio-compatible and feasible structures. One of the shining stars in this field is carbon dots (CDs). These peculiar nanostructures having dimensions in the sub - 10 nm range attract a lot of attention during the last decade due to cheap and green production, low toxicity and chemical inertness making it perfectly bio-compatible, and promising optoelectronic properties including efficient absorption, tunable emission [1] and nonlinear optical phenomena [2].

On the way to successful implementation of the CDs in the photonics and lighting there is a problem of the aggregation of these nanostructures impairing the emission efficiency. Suppression of the CDs aggregation can be employed via dispersion over the proper nanostructures or smart molecular assembly. Semiconductor nanowires (NWs) represent several advantages for integration with CDs.

GaP NWs is the perfect platform for nanophotonics. Pristine GaP exhibits low optical losses for the wavelengths exceeding 500 nm while dilution of this material with arsenic provides an easy way for bandgap engineering. In this study we demonstrate a simple protocol of the GaP NWs/CDs hybrid structures fabrication and study their optical properties. These nanostructures demonstrate good chemical stability and efficient luminescence. Due to resonant optical properties of GaP NWs, the CDs luminescence is enhanced owing to the Purcell effect.

## Materials and Methods

Carbon dots were synthesized by a hydrothermal method with the following procedure [3]. The following precursors were added to the autoclave with a Teflon beaker: 1.05 g of citric acid (Sigma Aldrich), 340 µl of ethylenediamine (Sigma Aldrich), and 10 ml of distilled water, then stirred it all until the citric acid was completely dissolved. After that, the autoclave was placed in an oven for 5 hours at a temperature of 200 °C. After cooling, the reaction products were passed through a syringe filter with a pore diameter of 0.22 µm to remove a large fraction. The filtered solution was placed in a dialysis tube (MWCO 3.5 kDa) for 24 hours to remove low-molecular-weight compounds and residual unreacted components. As-grown dense array of vertical NWs are approximately 30 um long and about 200 nm thick without sufficient tapering. To fabricate the CDs/ GaP NW hybrid structures CDs water solution was drop-casted over the sample with vertical NWs. The prepared sample was then imaged with SEM and confocal luminescent microscopy. For numerical simulation of a single nanowire the finite-difference-time-domain (FDTD) method was used (Ansys Lumerical Software). A NW with a height of 5 um was vertically oriented on the Si substrate. The simulation was performed for three diameters: 200, 150, and 80 nm. Photoluminescence from carbon dots was simulated using dipole sources in a spectral range of 500-650 nm.

## Results and Discussion

SEM images demonstrate peculiar phenomena of the NWs bundling with time with the formation of huts shaped by several NWs. This bundling is even prominent in a 3D confocal false color luminescent image depicted. All of the samples exhibit luminescence. Hybrid CDs/NW structures exhibit peak emission at 487 nm. The sample exhibits the most intense luminescence observed at the tips of the hut formed by the bundled NWs. This is a clear manifestation of the NW waveguiding properties provided by the GaP NWs having sufficient cross-section diameter (~200 nm in our case). PL excited in CDs gets coupled with the guided mode of the wire. This radiation is then scattered the most efficiently at the defects and end facet of the structure leading to the most intense signal collection at these particular sites. This phenomenon was confirmed by numerical simulations of the separate NWs.

## Conclusion

We demonstrated that hybrid structures fabricated by the drop-cast deposition technique exhibit effective luminescence. Due to waveguiding nature of NWs, the highest photoluminescence intensity is observed at the edge of the structure, that was verified both experimentally and using numerical simulations. The results indicate that such a hybrid system can be used to amplify and direct radiation in photonic devices.

## REFERENCES


1. **Rani, U. A., Ng, L. Y., Ng, C. Y., & Mahmoudi, E.**, A review of carbon quantum dots and their applications in wastewater treatment. Advances in Colloid and Interface Science, (2020) 102124.
2. **Zhang, X., Zhang, Y., Wang, Y., Kalytchuk, S., Kershaw, S. V., Wang, Y., … Rogach, A. L. (2013)**. Color-Switchable Electroluminescence of Carbon Dot Light-Emitting Diodes. ACS Nano, 7 (12) (2013) 11234–11241.
3. **Kozhushner, M. A., Bodneva, V. L., Oleynik, I. I., Belysheva, T. V., Ikim, M. I., & Trakhtenberg, L. I. (2017).** Sensor Effect in Oxide Films with a Large Concentration of Conduction Electrons. The Journal of Physical Chemistry C, 121 (12) (2017) 6940–6945.

## THE AUTHORS

**ZAVYALOVA Eseniya S.**
ladieseniya@gmail.com
ORCID: 0009-0003-5049-538X

**KUZNETSOV Alexey**
alkuznetsov1998@gmail.com
ORCID: 0000-0001-7143-6686

**RIDER Maxim A.**
riderm24@mail.ru
ORCID: 0009-0003-4890-683X

**KOVOVA Mariia S.**
mariakovova@mail.ru
ORCID: 0009-0003-7988-7520

**BOLSHAKOV Alexey D.**
bolshakov@live.com
ORCID: 0000-0001-7223-7232

# Application of optical methods for quality control of dairy products using data mining

**Zanevskaya M.Y[1] ✉, Mazing M.S.[2], Gubina E.V.[3], Zaitceva A.Y.[2], Romanova V.V.[2,4]**

[1] St. Petersburg State University of Aerospace Instrumentation, St. Petersburg, Russia

[2] Institute of Analytical Instrumentation, Russian Academy of Sciences, St. Petersburg, Russia

[3] Peter the Great St. Petersburg Polytechnic University, St. Petersburg, Russia

[4] St. Petersburg State Institute of Technology, St. Petersburg, Russia

✉mazmari@mail.ru

**Abstract.** A portable wireless optical system has been investigated, which allows to carry out an express quality assessment of the dairy products composition. The data obtained as a result of the experiment showed the prospects of using spectrophotometric methods of analysis and machine learning methods to control the quality of dairy products in various branches of the dairy industry.

**Keywords:** spectrophotometric methods, dairy products, principal component method

## Introduction

In recent years, there has been a growing trend toward more accurate determination of the quality of dairy products around the world. This is due to the fact that one of the most common forms of adulteration is the addition of any substances, including synthetic ones, in dairy products to increase their volume and weight.

Quality control of dairy products is one of the most important stages in the production process at enterprises, since the quality of finished products as a whole depends on the objective assessment of various parameters, properties and safety of raw materials.

The existing modern methods of comprehensive assessment of the quality of raw materials used for dairy products production are quite labor-intensive and require qualified and trained personnel [1].

In light of this problem, the number of studies devoted to the problems of assessing the quality of dairy products is growing [2]. All this points to the need to develop new methods of assessment, which will allow to quickly determine the quality of dairy products and identify the presence of adulteration. Thus, due to the large volume of processed products, optical methods of monitoring are gaining popularity. The aim of the work is to create new approaches to the analysis of dairy products for production processes using spectrophotometric methods and modern machine learning algorithms.

## Materials and Methods

In the course of the work, 18 milk samples were studied, 10 of which were industrially produced and 8 were from individual farms. The study was performed using a developed portable wireless optical system, the measuring unit of which consists of an array of 18 fast-acting photosensitive elements operating at wavelengths from 410 to 940 nm, and 3 emission sources [3]. There are operating modes of both pulse illumination of the sample and continuous illumination. The data obtained from the measuring module are transmitted to a PC via Bluetooth wireless technology.

## Results and Discussion

As a result of the subsequent multivariate statistical analysis of the data, individual reproducible "digital images" of each sample in the form of a combination of optical sensor indices were obtained.

To visualize the qualitative analysis of the composition of the studied samples, diagrams representing a set of numerical values of sensor responses by wavelength for each sample of dairy products were constructed. Figure 1 shows a diagram with the averaged values of the sensor responses of the samples of both groups of dairy products.

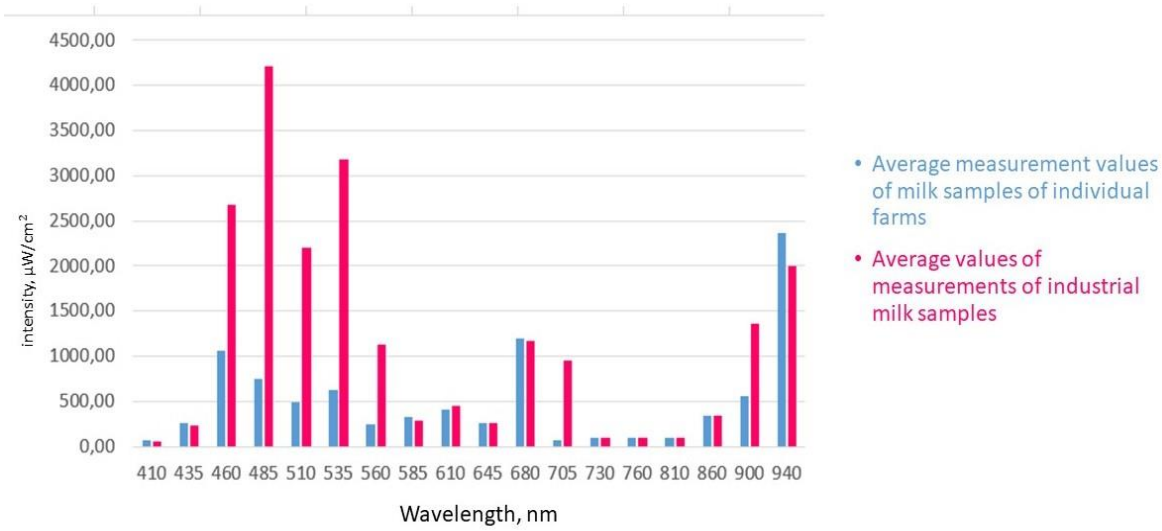


Fig. 1. Obtained averaged spectra of two groups of dairy products.

The following trends can be traced on the graph: the peaks of intensity of radiation of samples of dairy products of industrial production are noticeable at the beginning of the spectrum at wavelengths of 460-535 nm, while the peaks of intensity of samples of dairy products from individual farms, in contrast, are located at the end of the spectrum at the wavelength of 940 nm. The data obtained were also analyzed by methods of data mining, in particular, by the principal component method, which revealed a tendency to group dairy product samples depending on the type of production (industrial or farming method of production).

## Conclusion

Thus, the obtained results indicate the promising use of spectrophotometric methods of dairy products analysis using data mining. This express method can be recommended for qualitative assessment of the composition of dairy products and detection of adulteration in the composition.


## Acknowledgments

The work was supported by the Ministry of Science and Higher Education of the Russian Federation (project 075-15-2021-1057).


## REFERENCES


1. **Burmistrov D. E. et al.** Application of optical quality control technologies in the dairy industry: an overview //Photonics. – Multidisciplinary Digital Publishing Institute, 2021. – Т. 8. – №. 12. – С. 551.
2. **Holroyd S. E.** The use of near infrared spectroscopy on milk and milk products //Journal of Near Infrared Spectroscopy. – 2013.
3. **Mazing M. S. et al.** Monitoring of oxygen supply of human tissues using a noninvasive optical system based on a multi-channel integrated spectrum analyzer //International Journal of Pharmaceutical Research. – 2020. – Т. 12. – №. Suppl. ry 2. – С. 1974-1978.

# Features of spectroscopy of hydrocarbon media by optical method using X-ray radiation

**V. A. Kalashnikov**[1]✉ **and V. V. Davydov**[1,2]
[1] Peter the Great Saint-Petersburg Polytechnic University, Saint Petersburg, Russia.
[2]All-Russian Research Institute of Phytopathology, Moscow Region, Russia;
✉ vitea18092001@gmail.com

**Abstract.** Spectroscopy of hydrocarbon media by optical method using X-ray radiation is an important tool for studying the structure of molecules and atoms in hydrocarbon media. This method allows obtaining information about the chemical composition and structure of hydrocarbon compounds, as well as about the physical properties of the medium, such as density and temperature.

**Keywords:** Spectroscopy, X-ray radiation, hydrocarbon media, analyzer, crystal analyzer, characteristic line, detection unit.

## Introduction

In the context of deteriorating fuel quality and consumption volumes, an important task is to develop reliable control systems. One of these systems is spectral analyzers. The main function of spectral analysis is the registration and accumulation of the light spectrum, the digitization of the received signal depending on the wavelength and subsequent analysis using a personal computer. A spectrometer is an imaging system that distributes many monochromatic images in the detector plane (through the input slit). The parameters of the gap affect the performance of the spectrometer - optical resolution, bandwidth. The diffraction grating forms the spectrum of light wavelengths and partially affects the optical resolution of the spectrometer. The number of strokes affects the amount of variance. The wavelength range of the spectrometer is inversely proportional to the dispersion of the lattice due to the fixed geometry. The wider the dispersion, the higher the resolution of the spectrometer.

## Features of working with hydrocarbon media

When working with hydrocarbon media, with gasoline and diesel fuel, the sample under study is irradiated with an X-ray tube. As a result of the interaction of X-ray radiation with matter in the sample under study, secondary fluorescent radiation occurs, in the spectrum of which there are characteristic lines of those elements that are part of the sample. The presence of lines of this element in the spectrum indicates its presence in the sample, and the intensity of these lines allows us to judge the concentration of the elements. The principle of operation of the analyzer is based on the sequential isolation by the crystal-analyzer of the characteristic line of fluorescent sulfur radiation and background radiation of the sample under study, excited by the radiation of the X-ray tube, registration of the intensity of the lines and background. This is realized by rotating the angle of the analyzer crystal relative to the angle. A feature of this study is to obtain the maximum value of the intensity of the radiation reflected from the analyzer crystal by fine-tuning the angle of total internal reflection.

## Modernization of the X-ray optical analyzer circuit

The tested fuel may be a mixture of several hydrocarbon media in different proportions. In this case, in the studied mixture, the lines of the spectrum are located close enough to each other, and it is possible with a "rough" adjustment of the angle not to obtain the necessary resolution. To solve this problem, the scheme of the X-ray optical analyzer was modernized on the basis of my studies of various hydrocarbon mixtures (for example, mixtures of two gasolines AI-92 and AI-95 in various concentrations, a mixture of diesel fuel with gasoline AI-92 and others). The formation of such a mixture is possible during the transportation of fuel, when all the fuel has not been drained from the tank and then another one has been added. When the "tanker" moves, the media are mixed and a mixture is formed. Such fuel in some cases is not recommended to use.

In Fig. 1 shows the structural diagram of the X-ray optical analyzer and the course of X-rays.

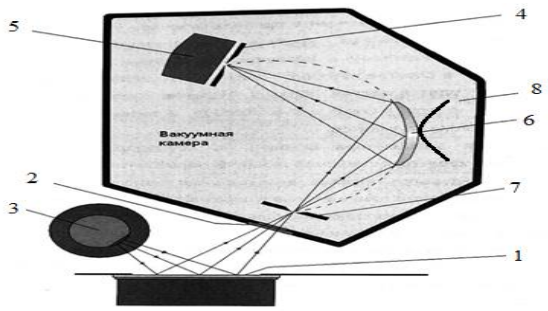


Fig. 1. Structural diagram of the analyzer: 1 – sample under study, 2 – entrance window, 3 – X-ray tube, 4 – receiving (output) slit, 5 – detection unit, 6 – crystal-analyzer, 7 – entrance slit, 8 – adjustment pad.

The primary radiation (3) excites fluorescent radiation in the sample under study (1), which through the window (2) of the measuring chamber and through the input slit (7) enters the focusing crystal-analyzer (6), which isolates from the spectrum of the sample a characteristic line corresponding to the reflection conditions according to the Wolfe-Bragg law:

$$n\lambda = 2\,\mathrm{d}\,sin\,\alpha$$

Where $n$ – reflection order ($n = 1, 2, ...$), $\lambda$ – wavelength of incident radiation, d – crystal analyzer interplane distance, $\alpha$ – the angle of incidence of radiation on the crystal.

The isolated radiation of the crystal-analyzer (6) focuses into the receiving slot (4) of the detection unit (5), the signal from which is received by the input of the amplifier-discriminator, detection (5), the signal from which is received to the input of the amplifier-discriminator, then to the input of the counting device. To refine this analyzer, an adjustment pad was added, which can mechanically change the angle at which light enters the samples. In Fig. 2 presents the registered spectrum from gasoline AI-92

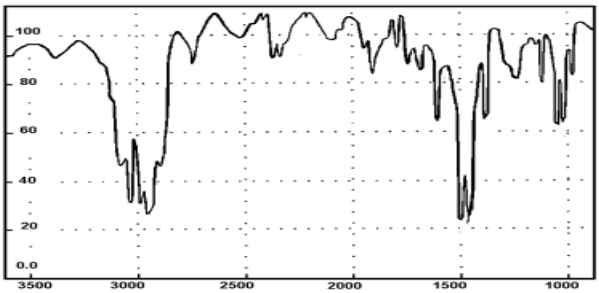


Fig. 2. Spectrum of gasoline AI-92

## Conclusion

Such refinement of the spectrometer allows to increase the accuracy of measurements, which is critically important in the analysis of hydrocarbons. This makes it possible to determine the concentration of hydrocarbons in the sample with greater accuracy by increasing the range of recorded values, which, in turn, improves the quality of their analysis.

## REFERENCES

**1. Kashaev R.S., Kien N.C., Tung T.V., Kozelkov O.V.** Fast Proton Magnetic Resonance Relaxometry Methods for Determining Viscosity and Concentration of Asphaltenes in Crude Oils. Journal of Applied Spectroscopy. 86(5) (2019) 890–895.

**2. Bocian, P., Biernat, K. Matuszewska, A., Bukrejewski, P., Noworyta, K.R.** Electrochemical impedance spectroscopy studies of gasoline oxidative stability – Attempt to devise new gasolines chemical stability index. Fuel 288 (2021) 119620.

# CHARGE RELAXATION AFTER EXPOSURE TO BARRIER AND CORONA DISCHARGE OF POLYLACTIDE FILMS

**A. M. Kamalov** [1✉]

[1] Peter the Great St.Petersburg Polytechnic University, St.Peterburg, Russia;

✉kamalov_am@spbstu.ru

**Abstract.** In this work, it is shown that the effect of a corona discharge and a dielectric barrier discharge differs in depth of charge penetration and relaxation time. The relaxation time and the mechanism of charge relaxation in polylactide films were determined using TSD currents. Experimental data are analyzed on the basis of modern ideas about the mechanism of charge relaxation. The activation energies are calculated based on a model that takes into account the intrinsic conductivity of the dielectric. By the method of computer modeling, the complex spectra of TSD currents are decomposed into separate elementary maxima, which are described by 1st-order kinetics, and the activation energies corresponding to them are determined.

**Keywords:** polylactide, relaxation, charge, current

**Funding:** Grant for young scientists the Ministry of Education and Science Russia МК-4346.2022.4

## Introduction

One of the most technologically advanced ways to modify the surface of dielectrics is corona discharge charging and dielectric barrier discharge at atmospheric pressure. Corona discharge, as well as DBD, is formed in a non-uniformly strong electric field between electrodes. This non-uniform electric field is influenced by the geometry configuration of the electrode which will then affect the resulting ionization.

The aim of the work is to compare the relaxation of the charge accumulated after exposure to corona and barrier discharge.

## Materials and Methods

The objects of this study are samples of polylactide films, which thickness was 25±5 μm.

A dielectric barrier discharge (DBD) was created in an ionization cell, which consists of ceramic plates with electrodes divided by an air gap (1 mm thick). The method of DBD film surface treatment was shown in the previous work [1]. The PLA film was charged in DBD for 2 minutes at a voltage of 3.2 kV with a frequency of 25 kHz.

Corona discharge method allows to produce electrets with homocharge. The sample is placed on a ground electrode, the other electrode is a needle with a negative potential. A metal grid is placed between the needle and the sample. Biased by a negative potential supply, the grid limits the maximum voltage on the sample. The charging process ends with the potentials of the grid and the surface of the sample becoming equal [2]. The PLA film was charged in a corona discharge for 1 minute, there was a voltage of 6 kV on the corona electrode, and 400V on the grid.

Charge relaxation processes were studied by the method of thermally stimulated depolarization current (TSDC) under heating of samples at a constant rate of 2 K/min. The TSD current was measured in an open circuit, as provided by an insulating layer of PTFE film 40 μm thick arranged between the charged film and the electrode.

## Results and Discussion

Relaxation processes in polylactide films after exposure to corona and barrier discharge were determined using the TSD current method. Since the samples were charged at room temperature 22oC, which is lower than the glass transition temperature of the PLA. Then, after processing in the corona and barrier discharge, a homocharge will accumulate in the PLA film.

As can be seen from Fig.1. There are 2 maxima for each mode on the TSD current curves.

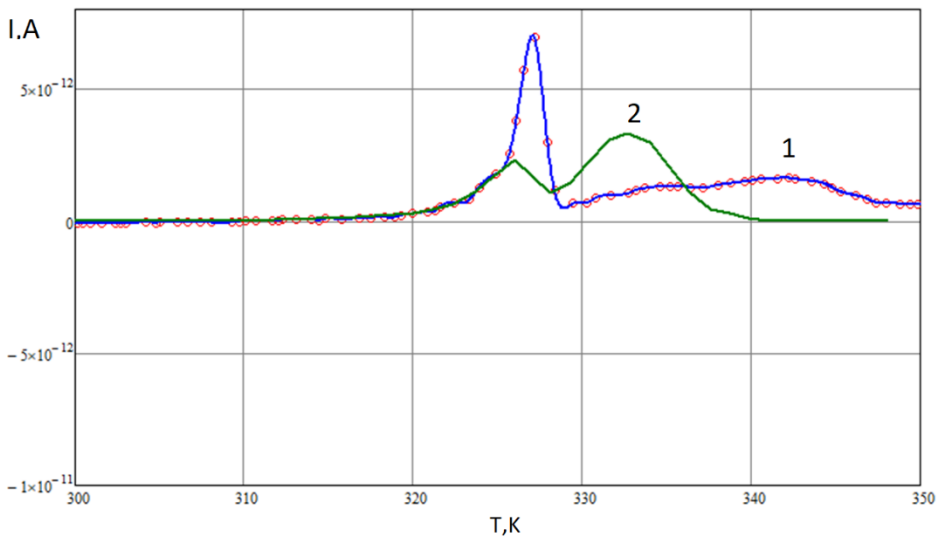


Fig. 1. TSD current for PLA film after: 1-corona, 2-barrier discharge

## Conclusion

Relaxation processes in the PLA film after exposure to corona discharge and dielectric barrier discharge were determined using the TSD current method. The activation energies of relaxation maxima were determined using the computer simulation method.


## Acknowledgments

Grant for young scientists the Ministry of Education and Science Russia MK-4346.2022.4


## REFERENCES


1. **Kamalov, A., Smirnova, N., Kolbe, K., Borisova, M., Bystrov, S., Didenko, A., Vlasova, E., Yudin**, Activation of R-BAPB polyimide with cold plasma dielectric barrier discharge for improvement of cell-material interaction V., J. Appl. Polym. Sci. 2022, 139( 42), e53024. https://doi.org/10.1002/app.53024

2. **M. Borisova, A. Kamalov, N. Jayasinghe and A. Chiriateva**, "Charge Relaxation and Kinetic Accumulation of Non-woven Polypropylene and Polyimide Films," 2022 Conference of Russian Young Researchers in Electrical and Electronic Engineering (ElConRus), Saint Petersburg, Russian Federation, 2022, pp. 1332-1334, doi: 10.1109/ElConRus54750.2022.9755471.

# Glass poling: surface environment effect

**G. Kan [1✉], I.V. Reshetov [1,2], S.A. Scherbak [1], A.A. Lipovskii [1]**
[1] Alferov University, Khlopina 8/3, St. Petersburg, Russia
[2] Peter the Great St. Petersburg Polytechnic University, Polytechnicheskaya 29, St. Petersburg, Russia
✉kan@spbau.ru

**Abstract.** For the first time we demonstrate essential effect of liquid environment on the second harmonic generation (SHG) by thermally poled soda lime glasses. It is shown that non-polar environment of anode surface of a poled glass does not influence the SHG, while ionic and polar environment result in the SHG decay. The decay time decreases with the increase of ionic concentration in the environment. These findings change existing views on the origin of SHG in poled soda lime glasses and show that their poling-induced second order optical nonlinearity strongly correlates with the state of poled glass surface.

**Keywords:** glass poling, surface charge, second harmonic generation.

**Funding:** The study was funded by the Ministry of Science and Higher Education of Russian Federation, project FSRM-2023-009.

## Introduction

Soda-lime-silicate glass is capable of losing isotropy under DC electric field treatment of the heated glass followed by cooling the glass under the field applied. Such processing is known as thermal poling [1]. In thermal poling, hydronium ions formed in the vicinity of anodic electrode enter the glass and replace sodium ions drifting in the glass towards the cathodic electrode. The thickness of the glass region containing hydronium ions instead of sodium ones falls in the range of several microns. An essential feature of this subanodic region is the appearance of the second-order optical nonlinearity (SON) and, respectively, optical second harmonic (SH) generation initially forbidden in glasses because of their isotropy. According to common views, the SON originates from about three orders of magnitude difference of hydronium and sodium mobility in the glass. This difference results in the formation of a “frozen” spatial electric charge at the interface of regions containing hydronium and sodium, which, in its turn, in combination with the third order optical nonlinearity allowed for centrosymmetric materials, generates SON – so called EFISH effect [2]. An alternative explanation of the SON supposes that it originates from orientation of dipoles formed in the glass in the course of the penetration of hydronium ions, the orientation being stimulated by the electric field of the “frozen” charge [3]. However, till now the presence of dipoles was not directly confirmed, and, moreover, the influence of additional electric charges, possibly captured by the glass surface in poling, cannot be excluded. Recently found ten-fold increase in the SH signal from the poled glass subjected to DC voltage at room temperature [3] allows supposing essential influence of these charges on dipolar orientation, if any, and gives a rise to a question about positioning of the dipoles. This study is aimed to clarify the role of the surface of the glasses on SON and presents the behavior of SH in poled glasses, which surface is immersed in liquid environments differing in polarity and ionic dissociation.

## Materials and Methods

In the experiments we used one mm thick soda-lime microscope slides “Menzel”. After washing in petroleum ether the samples were poled during 20 min at 250 °C under 1300 V DC in open-anode configuration, the details of the poling procedure are presented elsewhere [4]. To vary the environment of anodic/cathodic surface of the slides a drop of different liquids - deionized (DI) water, kerosene, sodium chloride, acid and alkali was placed on the poled slides and pressed with 0.2 mm thick coverslip glass. SH signal from the initially poled glass slides and these slides with liquids/coverslips was characterized using online measurements of the second harmonic signal excited by IR laser beam falling at 63 degrees angle on the glass surface, other details of the measuring scheme being described in our paper [5].

## Results and Discussion

Firstly, the effect of DI water on the cathodic and anodic side of the poled glass was investigated (Fig. 1*a*). This showed that water-immersing of cathode side of the glass almost does not affect the SH signal, while subjecting the anode side to DI water caused gradual relaxation of the SH signal. Probing of other liquids has shown that the rate of the SH signal relaxation is essentially determined by the type of environment (Fig. 1*b*). For example, when immersed in kerosene, the SH signal from anode side of the glass did not relax, and in a NaCl solution relaxed quickly. In the latter case, the stronger the solution, the faster relaxation. The relaxation observed can be interpreted as the compensation of a surface charge absorbed at the surface of the poled glasses by ions presenting in the solution. This finding changes the existing idea about the predominant role of the EFISH effect as an origin of the SHG in poled soda-lime glasses and shows that their SON strongly correlates with the state of poled glass surface.

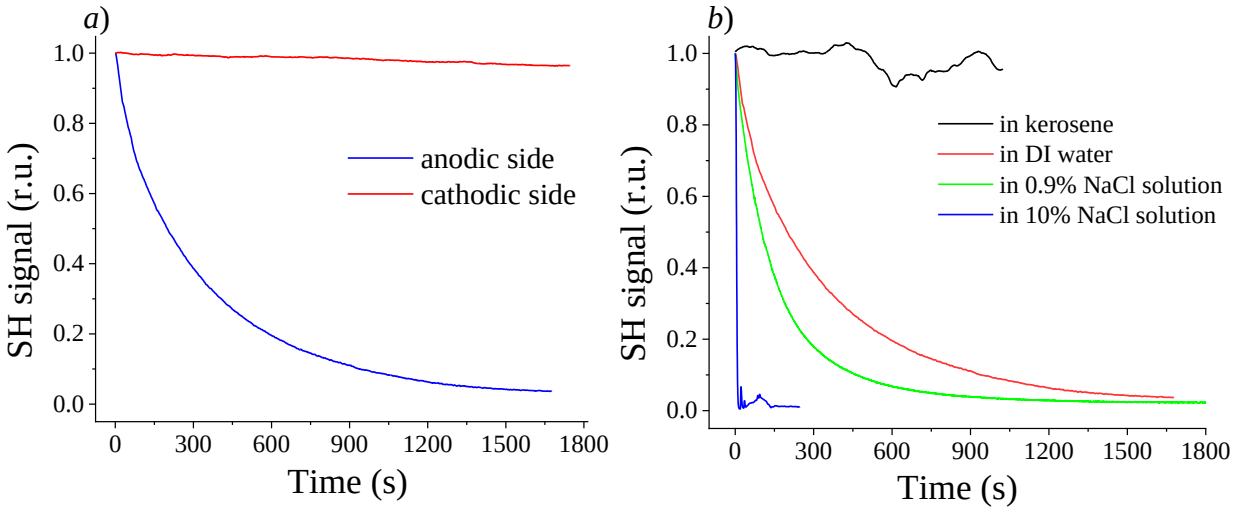


Fig. 1. Relaxation of second harmonic signal from the glass with anodic and cathodic sides placed in deionized water (*a*) and with anodic placed in different environments (*b*)

## Conclusion

Finally, for the first time we show that the second harmonic generation in a poled soda lime glass can be essentially influenced by a liquid environment of the glass. This evidences that existing views of the poling-induced second order optical nonlinearity of such glasses should be modified.


## Acknowledgments

The authors thank V.P. Kaasik for the assistance in the second harmonic measurements.


## REFERENCES


1. **Myers, R.A.; Mukherjee, N.; Brueck, S.R.J.**, Large second-order nonlinearity in poled fused silica, Optics letters 16 (22) (1991): 1732–1734.

2. **Guillet de Chatellus, H.; Freysz, E.**, Measurement of the third-order susceptibility of glasses by EFISH of femtosecond pulses, Optics express 9 (11) (2001): 586–591.

3. **Reshetov, I.; Scherbak, S.; Tagantsev, D.; Zhurikhina, V.; Lipovskii**. **A.**, Giant Enhancement of Optical Second Harmonic in Poled Glasses by Cold Repoling, The Journal of Physical Chemistry Letters, 13(25) (2022) 5932–5937.

4. **Scherbak, S.A.; Kaasik, V.P.; Zhurikhina, V. V; Lipovskii, A.A.**, Poling of Glasses Using Resistive Barrier Discharge Plasma, Materials (Basel). 15 (23) (2022) 8620.

5. **Scherbak S. A.; Reshetov I. V.; Zhurikhina V. V.; Lipovskii A. A.**, Second harmonic generation by surface of poled glasses: modeling and measurement of maker fringes, St. Petersburg Polytechnic University Journal - Physics and Mathematics. 14 (3) (2021) 95–113.

# INVESTIGATION OF TWO STATE LASING IN MICRODISKS WITH InAs/GaAs QUATUM DOTS AT DIFFERENT TEMPERATURES

**A. A. Karaborchev** [1✉], **I. S. Makhov** [1], **K. A. Ivanov** [1], **M. V. Maximov**[1,2], **M. M. Kulagina**[3], **Yu. A. Guseva**[3], **A. E. Zhukov** [1], **N. V. Kryzhanovskaya**[1]

[1] HSE University, Saint-Petersburg, Russia

[2] Alferov University, Saint-Petersburg, Russia

[3] Ioffe Institute, St. Petersburg, Russia

✉alekskaraborchev@gmail.com

**Abstract.** The evolution of two-state lasing in microdisk lasers with InAs/GaAs quantum dots with temperature is investigated. Threshold currents were measured for microdisks with cavity diameters of 9, 20, 24 and 28 μm at various temperatures. For microdisks of 20, 24 and 28 μm in diameter modeling of temperature evolution of threshold currents was performed by solving the rate equations. A good agreement between experimental and theoretical data was obtained.

**Keywords:** Two-state lasing, microdisks, photoluminescence, quantum dots

**Funding:** The study was supported by Russian Science Foundation grant № 22-72-00028 (https://rscf.ru/project/22-72-00028/).

## Introduction

Over the past few decades, the requirements for devices in the field of data transmission have been continuously growing. An increase in the data transfer rate can be solved through the use of photonic integrated circuits [1]. The application of microlasers with disk and ring cavities supporting the propagation of whispering gallery modes (WGM) with high Q-factors as radiation sources for photonic integrated circuits is relevant.

The use of quantum dots (QD) as an active region opens up the possibility of implementation of two-state lasing [2]. In microlasers with QD active region and low optical losses, lasing is possible at different optical transitions: at relatively low currents lasing occurs via the ground state (GS) optical transitions. Further increase of the injection current can results in lasing via the first excited (ES1) optical transitions. Thus, by means of current variation it is possible to control the appropriate lasing wavelengths in the QD laser. Threshold currents for the GS and ES1 lasing strongly depend on optical loss in the structure, which also depends on the temperature. To date, the influence of temperature on two-state lasing in microdisk structures has been studied rather poorly, so this work will be devoted to this problem.

## Materials and Methods

The heterostructure was grown by molecular beam epitaxy on an $n^+$-type GaAs substrate. A GaAs buffer layer is located on the substrate, followed by an $Al_{0.25}Ga_{0.75}As$ *n*-type cladding layer, their thicknesses were 0.5 and 2.5 μm, respectively. The active region comprises 10 layers of self-organizing InAs QDs with a thickness of 2.5 monolayers followed by deposition of 5 nm $In_{0.15}Ga_{0.85}As$. QD layers are separated by 35 nm thick GaAs layers. A cladding layer of *p*-$Al_{0.25}Ga_{0.75}As$ with a thickness of 2.2 μm is located above the active region, followed by a 200 nm $p^+$-GaAs contact layer. The microdisk cavities were obtained by photolithography and plasma chemical etching. The microlasers are about 28, 24, 20 or 9 μm in diameter and about 6 μm height. To measure temperature dependencies of microlasers characteristics, the structures were mounted on a copper radiator with a built-in resistive heater, a temperature sensor and a PID controller. To reduce the effect of self-heating of the lasers, the electroluminescence spectra were measured at a pulsed current with a frequency of 4 kHz and a pulse duration of 300 ns. The inductive probe was used to measure the amplitude of the pulsed current. Radiation through the lens and optical fiber was fed into the Andor Shamrock 500i monochromator, detection in which was carried out with a cooled InGaAs array.

## Results and Discussion

Spontaneous electroluminescence spectra were measured for the initial analysis of the structures. Four emission bands attributed to the ground; first, second (ES2) and third (ES3) excited optical transitions were observed. The positions of the maxima of these bands were 1265, 1170, 1100 and 1040 nm, respectively. Also, a weak peak from InGaAs quantum well was observed near 970 nm.

Next, the threshold current values for microdisk lasers were measured at different temperatures. The threshold current for the GS lasing increases with increasing temperature which is associated with an increase in losses. The increase in loss with temperature is associated with increase of free charge carrier absorption as well as with blur of Fermi distribution of charge carriers over QD states. Herewith the appropriate decrease in the threshold current density is observed for the ES1 lasing with temperature increase. The characteristic temperature for microdisks of 28, 24 and 20 μm in diameter is the same and is about 150 K. This means that the processes occurring with increasing temperature are the same for these microdisks. However, for a microdisk of 9 μm, in which two-state lasing is observed via ES1 and ES2 transitions, the characteristic temperature is lower and is only 35K. Also, for each microdisk, a certain critical temperature at which the two-level laser generation disappears was revealed.

A numerical modelling of the temperature evolution of threshold currents in microlasers with cavity diameters of 28, 24 and 20 μm was carried out by solving the rate equations for all QD states. The model used is described in detail in [3]. The obtained times, used in model as parameters, were as follows: spontaneous recombination time is 0.4 ns, transition time between QD levels is 0.55 ps, time of the electron capture to QDs is 27 ps.

## Conclusion

Thus, the temperature evolution of two-level laser generation in microdisks with QDs was investigated. The obtained characteristic temperatures were 150 K for 28, 24 and 20 μm microdisks and 35 K for 9 μm one. The highest temperature stability was shown by a microdisk with a diameter of 28 μm for which laser generation was observed up to 110°C. Theoretical curves describing the dependences of threshold currents on the temperature were calculated. The simulation coincided with the experimental data.

## Acknowledgments

The work was carried out on the equipment of the large-scale research facilities «Complex optoelectronic stand».

## REFERENCES

1. **Elshaari A.W., Pernice W., Srinivasan K., Benson O., Zwiller V.**, Hybrid integrated quantum photonic circuits, Nature Photonics. 14 (2020) 285-298.

2. **Markus A., Chen J. X., Paranthoën C., Fioreet A.**, Simultaneous two-state lasing in quantum-dot lasers, Applied Physics Letters. 82(12) (2003) 1818-1820.

3. **Markus A., Fiore A.**, Modelling carrier dynamics in quantum-dot lasers, Phys. Stat. Sol. (a). 201 (2004) 338-344.

# Generation of spatiotemporal optical vortices using Kretschmann setup for transverse magnetic and transverse electric polarizations

**A. I. Kashapov** [1,2✉], **E. A. Bezus** [1,2], **D. A. Bykov** [1,2], **L. L. Doskolovich** [1,2]

[1] Image Processing Systems Institute of RAS — Branch of the FSRC "Crystallography and Photonics" RAS, 151 Molodogvardeyskaya St., Samara 443001, Russia;

[2] Samara National Research University, 34 Moskovskoe shosse, Samara 443086, Russia

✉ar.kashapov@outlook.com

**Abstract.** We show that the Kretschmann setup consisting of a prism, a metal layer, and an optional dielectric layer can be used for generating spatiotemporal optical vortices (STOVs) in reflection. The numerical simulation results demonstrate that the STOV generation is performed with high quality for both transverse magnetic (TM) and transverse electric (TE) polarizations of the incident wave. The obtained results may find application in novel analog optical computing and optical information processing systems.

**Keywords:** Kretschmann setup, optical computing, optical vortices.

**Funding:** This work was funded by the Russian Science Foundation (project No 19-19-00514).

## Introduction

An optical vortex (OV) beam is a beam possessing a zero in the field amplitude and, hence, a phase singularity. OV beams find various applications in optics, including optical trapping, communication, and microscopy. The formation of spatiotemporal optical vortices (STOVs) using various techniques has been a subject of intensive research in recent years [1]. Here, we demonstrate that the Kretschmann setup, which consists of a dielectric prism with a metal layer, provides a simple and efficient platform for generating STOVs for the cases of both TM- and TE-polarized incident radiation.

## Results and Discussion

We study the structure in the Kretschmann configuration (Fig. 1*a*) consisting of a SF11 glass prism, a gold (Au) metal layer (thickness $h_{met}$), and an optional silicon dioxide ($SiO_2$) coating (thickness $h_c$). As examples, two cases are considered, namely, TM- and TE-polarized spatiotemporal incident optical pulses with Gaussian envelope ($\sim \exp[-(x/\sigma_x)^2 - (t/\sigma_t)^2]$, where $\sigma_x$ and $\sigma_t$ define the size of the incident pulse) at central wavelength 407.5 nm. In the first case (TM-polarization), $h_c = 0$ (conventional Kretschmann setup), $h_{met} = 22.5$ nm, $\theta_0 = 44°$, $\sigma_x = 50$ µm, and $\sigma_t = 125$ fs. In the second case (TE-polarization), $h_c = 54.6$ nm ("generalized" Kretschmann setup), $h_{met} = 15.9$ nm, $\theta_0 = 34°$, $\sigma_x = 120$ µm, and $\sigma_t = 72$ fs. The normalized RMSD values of the envelopes of the reflected pulses numerically calculated using method [2] from the "model" one (Fig. 1*b*) are 3.31% and 3.35% for TM- and TE-polarizations, respectively.

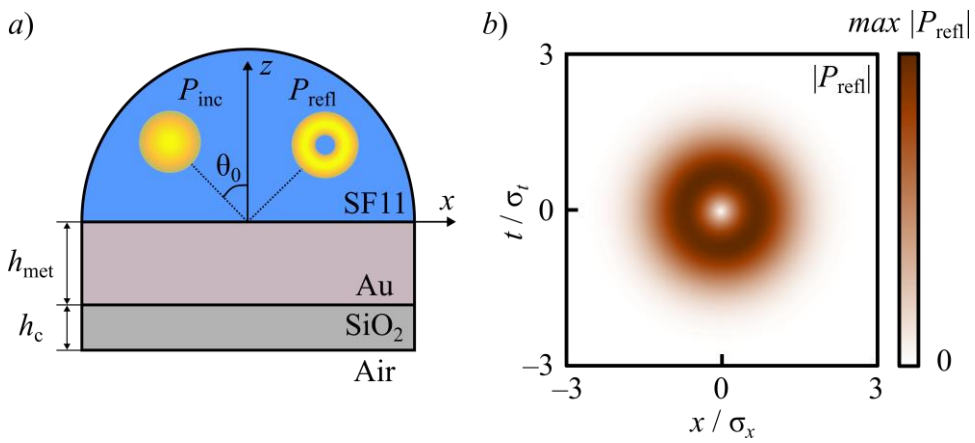


Fig. 1. (*a*) Generalized Kretschmann setup; (*b*) amplitude of the spatiotemporal envelope of the pulse generated upon reflection from the investigated structure

## Conclusion

It was shown that the conventional Kretschmann setup enables generating an STOV in case of TM-polarization. The introduction of an additional dielectric layer enables the STOV generation also in the case of TE-polarization. In both cases, STOVs are generated with high quality, NRMSD values not exceeding 4%. The presented results are promising for application in analog optical computing and optical information processing systems.

## REFERENCES

1. **Bliokh K.Y.,** Spatiotemporal vortex pulses: Angular momenta and spin-orbit interaction, Phys. Rev. Lett. 126 (24) (2021) 243601.

2. **Moharam M. G., Pommet D. A.**, **Grann E. B., Gaylord T. K.,** Stable implementation of the rigorous coupled-wave analysis for surface-relief gratings: enhanced transmittance matrix approach, J. Opt. Soc. Am. A. 12 (5) (1995) 1077–1086.

# Surface modification influence on silica based pillars properties

**A Kondrateva[1], I Komarevtsev[1,2], Y Enns[1,2], A Kazakin[1,2], V Studzinsky[2], A Uvarov[1], E Vyacheslavova[1], P Karaseov[2], M Mishin[1]**

[1]Alferov University, St. Petersburg, Russia
[2]Peter the Great Saint-Petersburg Polytechnic University, St. Petersburg, Russia

**Abstract.** Two-dimensional (2D) semiconducting materials, such as transition metal oxides (TMO), are promising in nanomechanics, optoelectronics, and sensors of various type. In each of these fields, tuning its properties including aspect ratio, strain, doping level, especially on the nanoscale, provides . Photo-induced current transfer through nanocomposite structures consisting of $TiO_2$ and NiO layers activated with gold nanoparticles (AuNP). AuNPs are situated on top of $SiO_2$ nano-pillars embedded into TMO layers. Nano-pillar array with AuNPs is prepared by previously described two-step technique using cryogenic plasma etching. $TiO_2$ and NiO are formed by magnetron sputtering. Optical and electric characteristics of these structure are investigated. Possibility to adjust photo-response of the nanocomposite by heterostructure topology tuning is demonstrated.

## 1. Introduction

Transition metal oxides (TMO) are actively studied due to their properties promising for a number of applications. Their internal properties are strongly influenced by the environment at the nanoscale, especially in the case the size is constrained to thin layer. Such two-dimensional structures are promising for nanomechanics, optoelectronics and sensors of various types [1, 2]. In addition to the breadth of application, it is important that TMOs are suitable for use in MEMS technology without any significant changes in the technological chain. The control over internal stresses, doping, and temperature in two-dimensional materials is important for both nanomechanical performance and localized optical radiation [3].

## 2. Results

A (100) single-crystal silicon wafer was covered by 80 nm thick $SiO_2$ layer using plasma-chemical deposition. Thin gold films were deposited onto the oxide by thermal evaporation. The Au film thickness was 10, 6, 4, and 2.5 nm. Subsequent high-temperature annealing of the deposited film convert it to a quasi-ordered gold nanoparticle (AuNP) array. The size and shape of nanoparticles depend on the initial film thickness, annealing temperature and time, ambient used. In this study, films were annealed in the air for 60 min at 550°C.

$SiO_2$ pillar-like array structure was formed by cryogenic plasma-chemical etching. Silicon oxide layer was etched in $CHF_3$ plasma using a modernized Plasmalab System100 ICP 380 unit. AuNP array served as a mask. Etching was performed in cyclic etching-cooling mode, i.e. by alternating etching-cooling steps. Optimal $SiO_2$ plasma etching parameters are: temperature 250 K, ICP power 700 W, CCP power 40 W, pressure 3 mTorr, $CHF_3$ flow rate 30 sccm, etching time 60 seconds.

Transition metal oxide coating was deposited over the formed AuNP-$SiO_2$ pillar structures using the technology described in detail in [4, 5]. Analysis of the SEM images of the obtained samples showed that in the case of etching under the mask of AuNP with an average diameter of about 300 nm, vertical nanostructures are formed. A decrease in the average size of the masking AuNP resulted in the formation of cone-shaped particles, probably due to partial removal of the mask material. An analysis of the reflection spectra of the formed structures showed that, as a result of the modification of the samples, optical activity appears in the visible part of the spectrum. The optical characteristics of the formed structures suggest their wide potential suitability for applications in optoelectronics and sensors.

## 3. Acknowledgments

Authors wishing to acknowledge the Ministry of Education foundation for financial support assistance (№ FSRM-2023-0009).

## References

[1] Zhu C R 2013 *Phys. Rev. B* **88** 121301
[2] Steinhoff A; Kim J-H, Jahnke F, Rösner M, Kim D-S, Lee C, Han G H, Jeong M S, Wehling T O, Gies C 2015 *Nano Lett.* **15** 6841–6847
[3] Nieminen T, Tiwary N, Ross G, Paulasto-Kröckel M 2023 *Micromachines* **14** 698
[4] Enns Y, Kondrateva A, Mishin M 2020 *J. Phys. Conf. Series* **1695**(1) 012115
[5] Vorobyev A, Enns Y, Kondrateva A, Bespalova P, Komarevtsev I, Mishin M 2022 Int. *Youth Conf. El.Telecom. IT* **268** 349

# Effect of the thickness of plasmonic gold nanostructures on the Surface Enhanced Raman Scattering enhancement factor

**D. V. Kornyushin [1]✉, A. G. Musaev[1], O. V. Vershinina[1], M. S. Ivanov[1], E. I. Kameneva[1], I. A. Volkov[1], A. A. Efimov[1], V. V. Ivanov[1]**

[1]Moscow Institute of Physics and Technology, Dolgoprudny, Russia

✉kornyushin.d@phystech.edu

**Abstract.** In this work, we study the influence of the thickness of plasmonic nanostructures on the surface-enhanced of Raman spectroscopy (SERS). Plasmonic nanostructures were formed in the form of square areas 3 mm × 3 mm in size and 0.3 to 0.5 μm thick using dry aerosol printing by focusing deposition of gold nanoparticles with an average size of 9.5 ± 0.5 nm. The highest surface enhancement of Raman scattering (RS) for methylene blue (MB) and bispyridylethylene (BPE) organic substances was obtained on plasmonic nanostructures with a thickness of 0.4 μm. The results obtained made it possible to estimate the enhancement factor, in comparison with conventional Raman scattering: for MB $k_y \approx 5.5 \times 10^6$, for BPE $k_y \approx 8.0 \times 10^6$.

**Keywords**: nanoparticles, gold, focusing deposition, plasmonic nanostructures, SERS.

**Funding**: This research was funded by the Ministry of Science and Higher Education of the Russian Federation (state contract № 075-03-2023-106, project identifier FSMG-2022-0036 and state contract no. 075-03-2023-106, project identifier 0714-2020-0007).

## Introduction

Surface Enhanced Raman Scattering (SERS) is a spectroscopy technique that can greatly enhance the sensitivity of traditional Raman spectroscopy. SERS can be used in areas such as biochemistry and biosensors, catalysts, materials science, food additives, and pesticides [1, 2]. In this work, we evaluated the effect of the thickness of plasmonic nanostructures (PN) formed by gold nanoparticles using «dry» aerosol printing on the surface enhancement of Raman scattering and the SERS signal enhancement factor using organic substances: methylene blue (MB) and 1,2-bis(4-pyridyl)ethylene (BPE).

## Materials and Methods

Gold nanoparticles are synthesized in a pulsed gas-discharge generator (Figure 1a) in nitrogen $N_2$ flow and transported to a coaxial nozzle (Figure 1b) with a $Q_a$ flow of 1 L/min for deposition on a substrate. The focusing gas $Q_{sh}$ is also supplied to the coaxial nozzle at a flow rate of 0.1 L/min. Using an optical 3D-profilometer Sensofar S-neox, the thickness of the formed PN is studied, which is controlled by the formation time. Raman spectra are obtained using a Thermo Scientific™ DXR instrument with a laser wavelength of 780 nm. MB and BPE with concentrations ranging from $10^{-6}$ to $10^{-3}$ mol/l were chosen to assess signal enhancement.

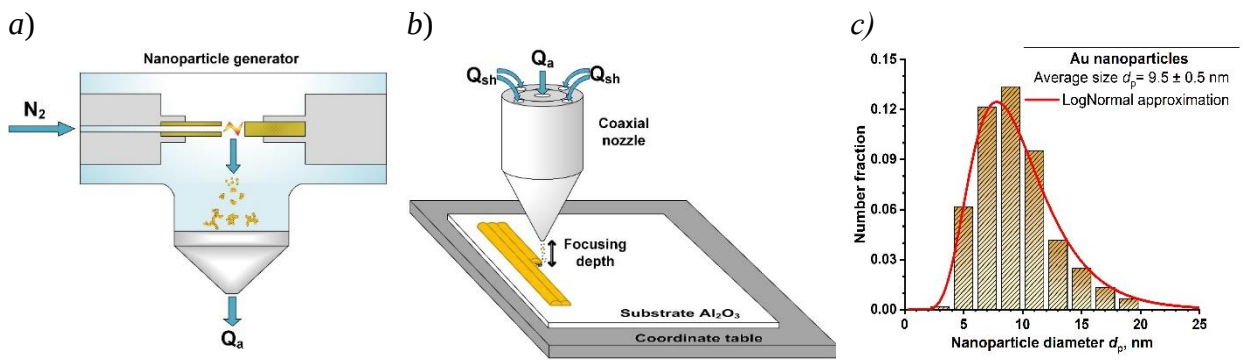


Fig. 1. The scheme of the experimental setup: nanoparticles generator (*a*) and focused deposition of nanoparticles through a coaxial nozzle on a moving substrate attached to a coordinate (*b*); Au particle size distribution (*c*)

## Results and Discussion

In a pulsed gas-discharge generator, gold nanoparticles with an average size $d_p = 9.5 \pm 0.5$ nm were synthesized (Figure 1c). PN in the form of square pads 3 mm × 3 mm in size were formed by «dry» aerosol printing. The thickness of PN in the range from 0.3 μm to 0.5 μm was controlled by changing the time of their formation. Figure 2 shows Raman scattering spectra of MB with substance concentrations in the range from $10^{-6}$ to $10^{-3}$ mol/l, obtained on gold PN of various thicknesses. According to the research results, it was found that PN with a thickness of 0.4 μm showed the best amplification of the Raman spectra. Also, the obtained results made it possible to estimate the enhancement factor of the Raman signal $k_y$ [3]. The calculated values for PN with a thickness of 0.4 μm: for MB $k_y \approx 5.5 \times 10^6$, for BPE $k_y \approx 8.0 \times 10^6$.

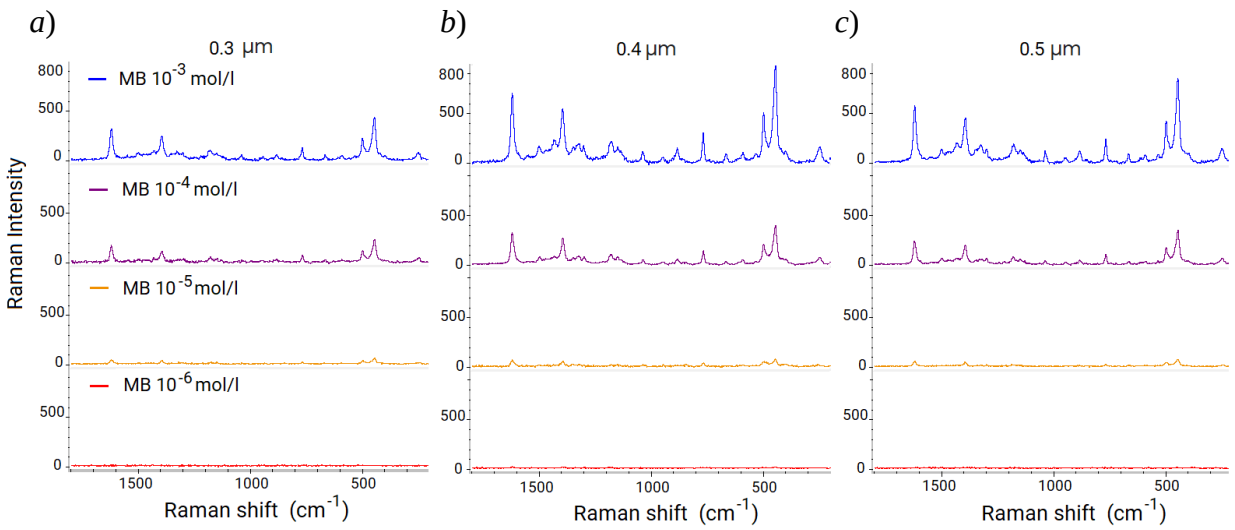


Fig 2. Raman spectra for methylene blue (MB) obtained on gold PN 0.3 μm (a), 0.4 μm (b) and 0.5 μm thick (c), after deposition of MB solutions with concentrations from $10^{-6}$ to $10^{-3}$ mol/l

## Conclusion

Using «dry» aerosol printing, the possibility of forming gold PN with the SERS-effect and amplifying the signal of such organic substances as MB and BPE with an amplification factor $k_y$ of the order of $10^6 – 10^7$ is demonstrated. According to the results of measurements, it was shown that PN with a thickness of 0.4 μm turned out to be optimal compared to structures with a thickness of 0.3 μm and 0.5 μm, since they have a higher detection limit and Raman enhancement factor $k_y \approx 5.5 \times 10^6$ for MB и $k_y \approx 8.0 \times 10^6$ for BPE.

## Acknowledgments

This research was funded by the Ministry of Science and Higher Education of the Russian Federation (state contract № 075-03-2023-106, project identifier FSMG-2022-0036), as part of studying the synthesis of nanoparticles in gas-discharge chamber and their focused deposition on an alumina-ceramic substrate for the formation of plasmonic nanostructures and the Ministry of Science and Higher Education of the Russian Federation (state contract no. 075-03-2023-106, project identifier 0714-2020-0007) for support of surface-enhanced Raman spectroscopy studies.

## REFERENCES

1. **Zhang W., Jiang L., Piper J. A., Wang Y.,** SERS nanotags and their applications in biosensing and bioimaging, Journal of Analysis and Testing. 2 (2018) 26–44.

2. **Pang S., Yang T., He L.,** Review of surface enhanced Raman spectroscopic (SERS) detection of synthetic chemical pesticides. TrAC Trends in Analytical Chemistry, 85 (2016) 73–82.

3. **Le Ru E. C., Blackie E., Meyer M., Etchegoin P. G.,** Surface Enhanced Raman Scattering Enhancement Factors: A Comprehensive Study, The Journal of Physical Chemistry C. 37 (111) (2007) 13794–13803.

# Doping and thermoelectric characteristics of $Ge_{0.3}Si_{0.7}$:$P_{\delta}$ synthesized by powder sintering

**Yu. M. Kuznetsov** [1✉], **M. V. Dorokhin** [1], **P. B. Demina** [1], **I. V. Erofeeva** [1], **A. V. Zdoroveyshchev** [1]

[1] Lobachevsky state university, Nizhny Novgorod, Russia;

✉y.m.kuznetsov@unn.ru

**Abstract.** The paper describes the technological parameters of the formation of the $Ge_{0.3}Si_{0.7}$ solid solution in a spark plasma sintering unit. A new method for alloying a solid solution during synthesis from a source of silicon phosphide is proposed. A comparative analysis of the transport and thermoelectric properties of the obtained samples depending on the dopant concentration is given.

**Keywords:** thermoelectric, figure of merit, Seebeck coefficient, germanium silicon, silicon phosphide.

**Funding:** The work was supported by the Ministry of education and science of Russian Federation in the frames of federal task (project № FSWR-2023-0037).

## Introduction

Thermoelectrics are materials that convert thermal energy into electrical one. The thermoelectric figure of merit (*ZT*) is a dimensionless coefficient that characterizes the conversion efficiency which is determined by the expression [1]: $ZT = \alpha^2 T/\rho \cdot \lambda$, where $\alpha$ – Seebeck coefficient, $\rho$ – resistivity, $\lambda$ – thermal conductivity.

For instrumental implementation, the material must possess $ZT > 1$. The recent trends are directed towards studying the *ZT* of $Ge_xSi_{1-x}$ semiconductor ceramics formed by nanopowder sintering. Such materials have a record low λ while maintaining high α and low $\rho$ [2].

## Experimental technique

A feature of this work is the use of non-toxic SiP as a source of a donor dopant of a GeSi solid solution. Such an approach makes it possible to avoid the use of toxic P, thereby significantly facilitating work with the initial powders. The powders were obtained by preliminary and fine grinding in a Fritsch Analysette 3 Pro ball mill and a Fritsch Pulverisette 6 planetary mill (250 rpm, 6 hours), respectively. The average particle size of the powder mixture was estimated on a Jeol JSM-IT300LV scanning electron microscope to be ~ 1 μm. The powders were sintered in a DR-SINTER SPS-625 Spark Plasma Sintering System (SPS) at a pressure of 70 MPa and a temperature of 1040 $^{o}$C. The sintering rate was 50 $^{o}$C/min. A series of four samples was formed, in which the concentration of P was varied.

The registration of the temperature dependence of $\alpha$ was carried out during the creation of a controlled temperature gradient with subsequent measurement of the thermo-EMF signal. The value of $\rho$ was measured using a standard four-contact circuit. The temperature dependence of $\lambda$ was obtained by the method of stationary heat flow. The concentration of free charge carriers was calculated from the magnetic field dependence of the Hall resistance. Measurement techniques are described in [3–4].

## Results and Discussion

The experimentally obtained temperature dependences of the thermoelectric parameters of the samples are shown in Figures 1–4. In addition, the results are compared with the record-breaking characteristics of $Ge_{0.2}Si_{0.8}$:$P_{0.02}$ from [2], a distinguishing feature of which was an extremely small powder particle size of ~30 nm.

The largest *ZT* in the entire measured temperature range is possessed by a sample containing 1.5 at. %. (*ZT* = 1.16), which is only 9% less than stated in [2]. At the same time, a significantly simplified technology was used in our work.

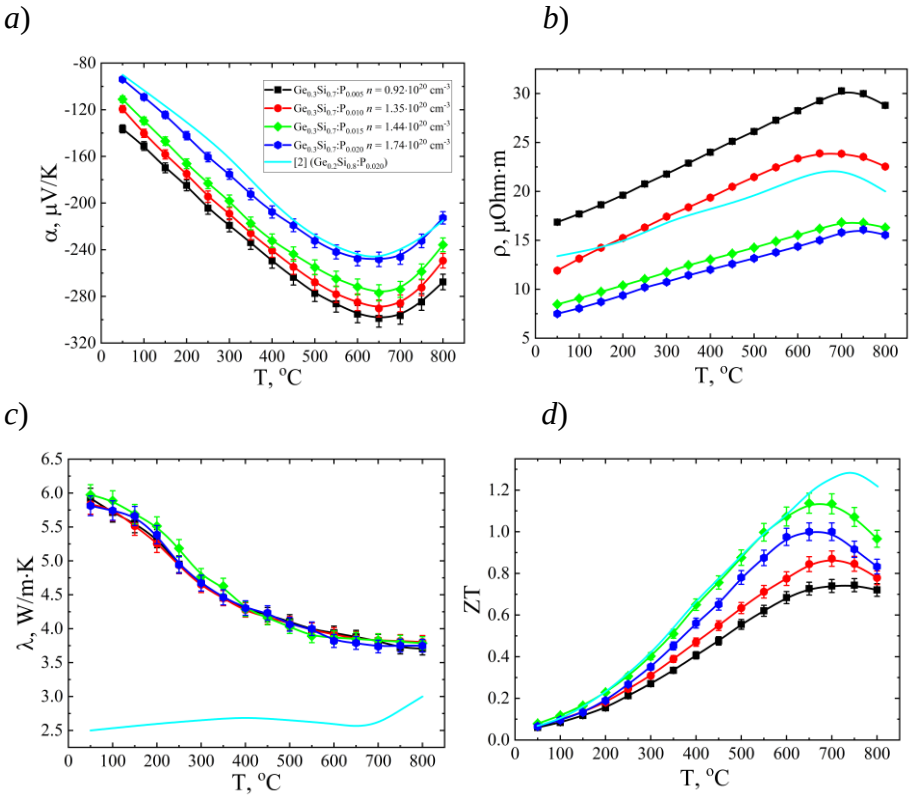


Fig. 1. Temperature dependence of Seebeck coefficient (*a*), resistivity (*b*), coefficient of thermal conductivity (*c*), thermoelectric figure of merit (*d*)

## Conclusion

The paper shows a new method of doping with phosphorus nanostructured thermoelectric materials based on a solid solution of germanium-silicon in the process of synthesis by spark plasma sintering. The optimum level of doping is established, at which high values of *ZT* are achieved.


## Acknowledgments

This work was supported by the state task of the Ministry of Education and Science of the Russian Federation (project no. FSWR-2023-0037). The authors are grateful to Dr. A. Yu. Zavrazhnov and I. N. Nekrylov for the synthesis of SiP, as well as to the engineer of the NIFTI UNN A. V. Voronin for experiments on sample sintering.


## REFERENCES


1. **Hicks D, Dresselhaus M. S.**, Thermoelectric figure of merit of a one-dimensional conductor, Physical Review B. Vol. 47 (1993) 16631.

2. **Wang X. W., Lee H., Lan Y. C., Zhu G. H., Joshi G., Wang D. Z., Yang Z., Mut A. J., Tang M. Y., Klatsky J., Son S., Dresselhaus M. S., Chen G., Ren Z. F.,** Applied Physics Letters. Vol. 93 (2008) 193121.

3. **Mochalov L. A., Kuznetsov Yu. M., Dorokhin M. V., Fukina D. G., Knyazev A. V., Kudryashov M. A., Kudryashova Yu. P., Logunov A. A., Mukhina O. V., Zdoroveyshchev A. V., Zdoroveyshchev D. A.,** Thermoelectrical properties of ternary lead chalcogenide plumbum-selenium-tellurium thin films with excess of tellurium prepared by plasma-chemical vapor deposition. Thin Solid Films. Vol. 752 (2022) 139244.

4. **Dorokhin M. V., Boldin M. S., Uskova E. A., Boryakov A. V., Demina P. B., Erofeeva I. V., Zdoroveyshchev A. V., Kotomina V. E., Kuznetsov Yu. M., Lantsev E. A., Popov A. A., Trushin V. N.,** Formation of a fine-grained $Si_{1-x}Ge_x$ thermoelectric by spark plasma sintering. Technical Physics. Vol. 67 (15) (2022) 2402–2409.

# Analysis of optical properties of quantum dots doped microspheres

**K. Kurassova** [1✉], **D. R. Dadadzhanov** [1], **N. A. Toropov** [1]
[1] ITMO University, St. Petersburg, Russia;
✉camillka713@gmail.com

**Abstract.** AgInS quantum dots doped polyacrylamide microspheres were prepared via microfluidics dripping method. The luminescent properties of polymer particles at various excitation power values were studied. Luminescence intensity of AgInS quantum dots solution and AgInS quantum dots doped polyacrylamide microspheres was increasing until 3.65 mW and 4.25 mW of excitation power, respectively. Further increase of the excitation power had no effect on luminescence intensity of both samples.

**Keywords:** microresonators, whispering gallery mode, quantum dots, luminescence, excitation power.

**Funding:** This work was supported by the Russian Science Foundation, Project 22-72-10057.

## Introduction

In recent years, microlasers that combine whispering gallery resonators and fluorescent materials have been rapidly emerging. Such lasers significantly broaden the opportunities for advancement of in vivo and in vitro biosensors, since narrow resonance linewidth can be used for analysis of biological tissues by a set of characteristics [1]. For example, Shubert with colleagues have investigated and successfully monitored contractility in cardiac tissue using biointegrated microresonators [2].

Many reports of dye doped microlasers fabrication have been published [3, 4]. However, since organic dyes are highly susceptible to photobleaching, we suggest utilizing quantum dots as a more photostable dopant. To ensure biocompatibility, polymers and quantum dots with lower toxicity are proposed for whispering gallery mode (WGM) microlasers generation. In this contribution, we reveal luminescent properties of microspheres doped with quantum dots.

## Materials and Methods

High-temperature solution-phase approach was used for the synthesis of hydrophilic AgInS quantum dots (AIS QD) with ZnS shell. A series of semiconductor QDs selected by size was obtained by their selective deposition from the initial polydisperse colloid solution. AIS QD doped polyacrylamide (PAM) microspheres were prepared via microfluidics dripping method. Concentrated AIS QD solution were mixed with acrylamide, TEMED was added to promote the acrylamide polymerization process.

The luminescent properties of AIS QD and polymer microspheres doped with AIS QD were studied with a laser scanning confocal microscope Zeiss LSM 710. A semiconductor 405 nm laser was used to excite luminescence of quantum dots.

## Results and Discussion

A 10 μL drop of AIS QD solution and a 15 μL drop of AIS QD doped PAM microspheres in oil were deposited on a glass slide. 10x/0.75 objective was selected for the samples study. Excitation power varied from 0.05 mW to 6.05 mW with a 0.6 mW step for both samples. Additional 10 mW excitation power measurement of PAM microspheres sample was taken. Luminescence spectra of AIS QD solution and PAM microspheres with AIS QDs are shown in Fig. 1a and 1b, respectively.

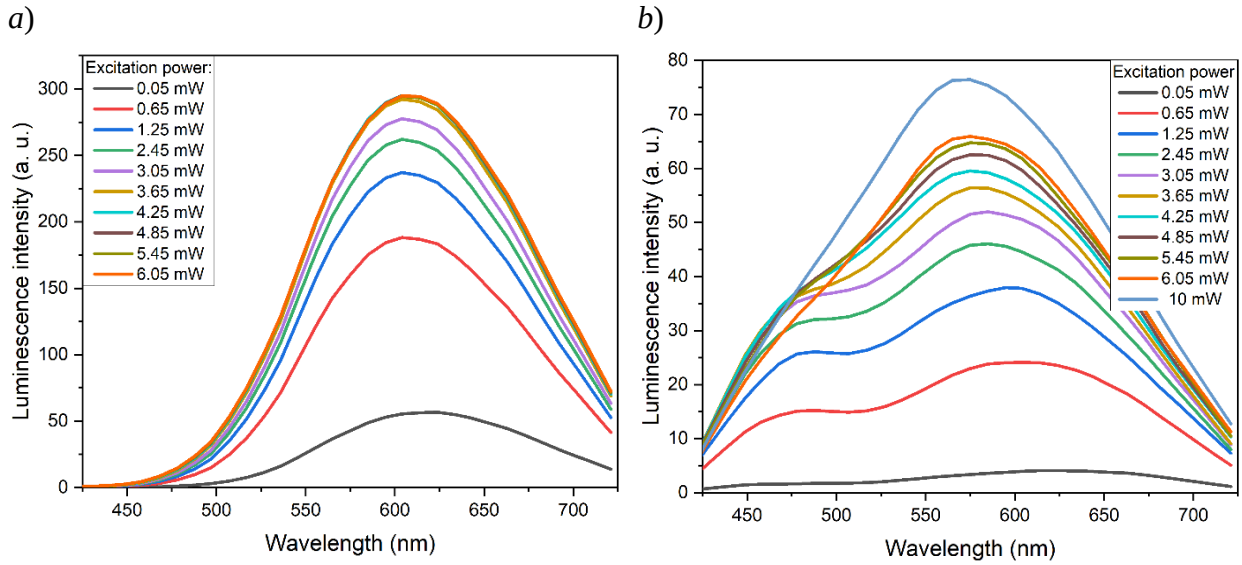


Fig. 1. Luminescence spectra of AIS QD (*a*) and PAM microspheres with AIS QD (*b*)

A rapid increase of the luminescence intensity of the AIS QD solution is observed as we vary excitation power up to 3.65 mW. A further increase of excitation power does not affect the luminescence intensity. No photobleaching of QDs is detected with the increase of excitation power due to the high diffusion rate of undamaged QDs into the region of "bleached" QDs caused by the high concentration of the solution.

The luminescence intensity of PAM microspheres with AIS QDs noticeably rises as a result of excitation power increase as well. Excitation power ceases to affect the luminescence intensity when it reaches 4.25 mW. Increasing the excitation power up to 10 mW did not destroy the polymer particle, since no decrease in the luminescence intensity was observed.

## Conclusion

The influence of the excitation power on the luminescent properties of polymer microresonators doped with quantum dots were studied. Luminescence intensity of AIS QD solution and AIS QD doped PAM microspheres was increasing until 3.65 mW and 4.25 mW of excitation power respectively.

## Acknowledgments

We greatly acknowledge Dr. Nikita Filatov from St. Petersburg Academic University for providing the PAM microspheres.

## REFERENCES

1. **Toropov N., Cabello G., Serrano M. P. [et al.]**, Review of biosensing with whispering-gallery mode lasers, Light: Science & Applications. 10 (1) (2021).

2. **Shubert M., Woolfson L., Barnard I. R. [et al.]**, Monitoring contractility in cardiac tissue with cellular resolution using biointegrated microlasers, Nature Photonics. 14 (7) (2020) 452–458.

3. **Kuwata-Gonokami M., Takeda K.**, Polymer whispering gallery mode lasers, Optical materials. 9 (1–4) (1998) 12–17.

4. **François A., Rowland K. J., Shahraam Afshar V., Henderson M. R., Monro T. M.**, Enhancing the radiation efficiency of dye doped whispering gallery mode microresonators, Optics express. 21 (19) (2013) 22566–22577.

# Effect of the thickness of plasmonic gold nanostructures on the Surface Enhanced Raman Scattering enhancement factor

**D. V. Kornyushin [1]✉, A. G. Musaev[1], O. V. Vershinina[1], M. S. Ivanov[1], E. I. Kameneva[1], I. A. Volkov[1], A. A. Efimov[1], V. V. Ivanov[1]**

[1]Moscow Institute of Physics and Technology, Dolgoprudny, Russia

✉kornyushin.d@phystech.edu

**Abstract.** In this work, we study the influence of the thickness of plasmonic nanostructures on the surface-enhanced of Raman spectroscopy (SERS). Plasmonic nanostructures were formed in the form of square areas 3 mm × 3 mm in size and 0.3 to 0.5 μm thick using dry aerosol printing by focusing deposition of gold nanoparticles with an average size of 9.5 ± 0.5 nm. The highest surface enhancement of Raman scattering (RS) for methylene blue (MB) and bispyridylethylene (BPE) organic substances was obtained on plasmonic nanostructures with a thickness of 0.4 μm. The results obtained made it possible to estimate the enhancement factor, in comparison with conventional Raman scattering: for MB $k_y \approx 5.5 \times 10^6$, for BPE $k_y \approx 8.0 \times 10^6$.

**Keywords**: nanoparticles, gold, focusing deposition, plasmonic nanostructures, SERS.

## Introduction

Surface Enhanced Raman Scattering (SERS) is a spectroscopy technique that can greatly enhance the sensitivity of traditional Raman spectroscopy. SERS can be used in areas such as biochemistry and biosensors, catalysts, materials science, food additives, and pesticides [1, 2]. In this work, we evaluated the effect of the thickness of plasmonic nanostructures (PN) formed by gold nanoparticles using «dry» aerosol printing on the surface enhancement of Raman scattering and the SERS signal enhancement factor using organic substances: methylene blue (MB) and 1,2-bis(4-pyridyl)ethylene (BPE).

## Materials and Methods

Gold nanoparticles are synthesized in a pulsed gas-discharge generator (figure 1a) in nitrogen $N_2$ flow and transported to a coaxial nozzle (figure 1b) with a $Q_a$ flow of 1 L/min for deposition on a substrate. The focusing gas $Q_{sh}$ is also supplied to the coaxial nozzle at a flow rate of 0.1 L/min. Using an optical 3D-profilometer Sensofar S-neox, the thickness of the formed PN is studied, which is controlled by the formation time. Raman spectra are obtained using a Thermo Scientific™ DXR instrument with a laser wavelength of 780 nm. MB and BPE with concentrations ranging from $10^{-6}$ to $10^{-3}$ mol/l were chosen to assess signal enhancement.

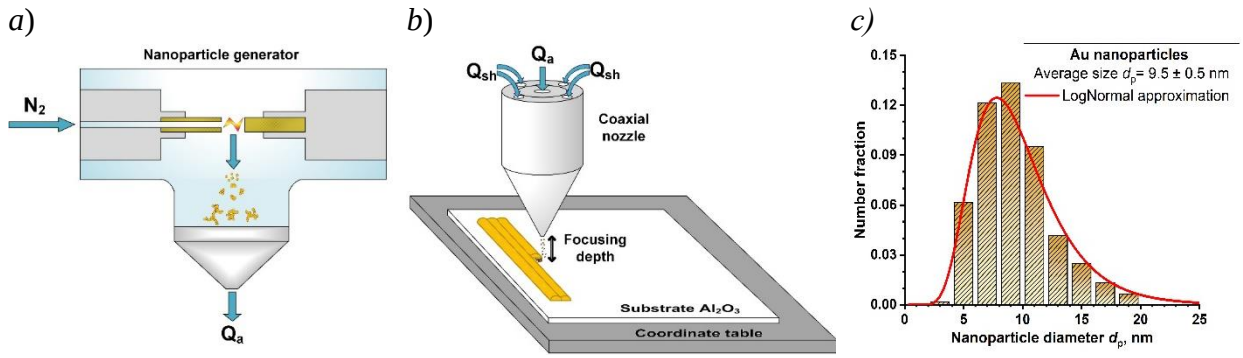


Fig. 1. The scheme of the experimental setup: nanoparticles generator (*a*) and focused deposition of nanoparticles through a coaxial nozzle on a moving substrate attached to a coordinate (*b*); Au particle size distribution (*c*)

## Results and Discussion

In a pulsed gas-discharge generator, gold nanoparticles with an average size $d_p$ = 9.5 ± 0.5 nm were synthesized (figure 1c). PN in the form of square pads 3 mm × 3 mm in size were formed by «dry» aerosol printing. The thickness of PN in the range from 0.3 μm to 0.5

μm was controlled by changing the time of their formation. Figure 2 shows Raman scattering spectra of MB with substance concentrations in the range from $10^{-6}$ to $10^{-3}$ mol/l, obtained on gold PN of various thicknesses. According to the research results, it was found that PN with a thickness of 0.4 μm showed the best amplification of the Raman spectra. Also, the obtained results made it possible to estimate the enhancement factor of the Raman signal $k_y$ [3]. The calculated values for PN with a thickness of 0.4 μm: for MB $k_y \approx 5.5 \times 10^6$, for BPE $k_y \approx 8.0 \times 10^6$.

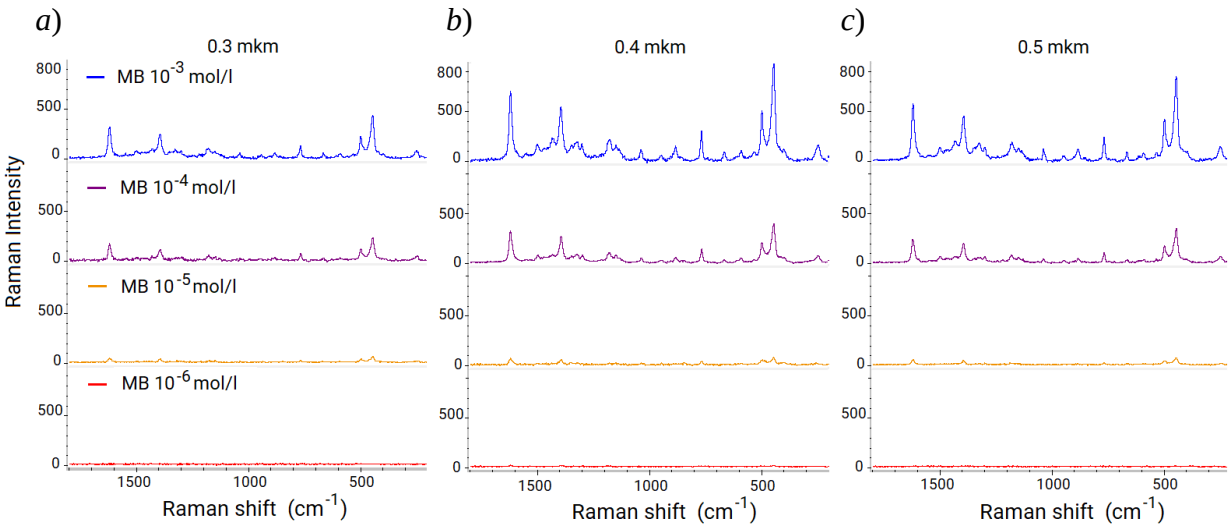


Fig 2. Raman spectra for methylene blue (MB) obtained on gold PN 0.3 μm (a), 0.4 μm (b) and 0.5 μm thick (c), after deposition of MB solutions with concentrations from $10^{-6}$ to $10^{-3}$ mol/l

## Conclusion

Using «dry» aerosol printing, the possibility of forming gold PN with the SERS-effect and amplifying the signal of such organic substances as MB and BPE with an amplification factor $k_y$ of the order of $10^6 – 10^7$ is demonstrated. According to the results of measurements, it was shown that PN with a thickness of 0.4 μm turned out to be optimal compared to structures with a thickness of 0.3 μm and 0.5 μm, since they have a higher detection limit and Raman enhancement factor $k_y \approx 5.5 \times 10^6$ for MB и $k_y \approx 8.0 \times 10^6$ for BPE.


## Acknowledgments

This research was funded by the Ministry of Science and Higher Education of the Russian Federation (state contract № 075-03-2023-106, project identifier FSMG-2022-0036), as part of studying the synthesis of nanoparticles in gas-discharge chamber and their focused deposition on an alumina-ceramic substrate for the formation of plasmonic nanostructures and the Ministry of Science and Higher Education of the Russian Federation (state contract no. 075-03-2023-106, project identifier 0714-2020-0007) for support of surface-enhanced Raman spectroscopy studies.


## REFERENCES


1. **Zhang W., Jiang L., Piper J. A., Wang Y.,** SERS nanotags and their applications in biosensing and bioimaging, Journal of Analysis and Testing. 2 (2018) 26–44.

2. **Pang S., Yang T., He L.,** Review of surface enhanced Raman spectroscopic (SERS) detection of synthetic chemical pesticides. TrAC Trends in Analytical Chemistry, 85 (2016) 73–82.

3. **Le Ru E. C., Blackie E., Meyer M., Etchegoin P. G.,** Surface Enhanced Raman Scattering Enhancement Factors: A Comprehensive Study, The Journal of Physical Chemistry C. 37 (111) (2007) 13794–13803.

# Reflection spectroscopy of excitons in wide quantum well of InGaAs/GaAs

**M. A. Maksimov** [1], **R. S. Nazarov** [1]
[1] St Petersburg University, Saint-Petersburg, Russia
st095854@student.spbu.ru, roma-384@yandex.ru

**Abstract.** In this work we explore the optical reflection from excitons in wide (95 nm) quantum wells of InGaAs/GaAs heterostructures at Brewster's angle geometry. By adding only small (1.5-2) percentages of InGaAs we've managed to create a wide quantum well where quantization of kinetic energy of excitons happens. As different energy levels appear, corresponding transitions between them occur and features on the reflection spectrum become visible. This research is of current scientific interest as via reflection spectroscopy it is possible to study quantum beats – an effect which plays a key role in development of modern optical appliances: ultrafast terahertz emitters and optical relays.

**Keywords:** quantum wells, InGaAs/GaAs, reflection, excitons, quantum beats, semiconductors, heterostructures.

**Funding:** this research has been funded by the Ministry of Science and Higher Education of the Russian Federation (Megagrant no. 075-15-2022-1112).

## Introduction

В настоящее время работы по исследованию отражения в широких квантовых ямах представляют значительный научный интерес для обнаружения квантовых биений – явления, важного для понимания квантовой запутанности и лазерной генерации без инверсии заселенностей, а также для создания ультрабыстрых оптических приборов [1].

## Materials and Methods

Для исследования отражения в нашей лаборатории была выращена методом молекулярно-пучковой эпитаксии гетероструктура InGaAs/GaAs с процентным содержанием индия в 1.5-2%. Это позволило сформировать широкую (95 нм) квантовую яму в которой происходит квантование поступательной энергии экситонов и, как следствие, возникает множество наблюдаемых на спектрах отражения переходов меж существующими в яме энергетическими уровнями.

Для получения спектров отражения образец с исследуемой квантовой ямой был помещен в криостат Janis (by Lake Shore Cryotronics**)** и в течение всего эксперимента поддерживался при постоянной температуре в 11К и также проводилась оптическая накачка непрерывным спектром галогеновой лампы. Чтобы минимизировать нежелательное в данной работе отражение от поверхности образца все измерения проводились в геометрии угла Брюстера, при котором в заданной поляризации наблюдается лишь отражение от квантовой ямы в глубине образца (980 нм от поверхности). С помощью монохроматора МДР-41 с CCD матрицей был получен спектр отражения в диапазоне длин волн от 820 до 830 нм.

## Results and Discussion

Полученные экспериментальные данные позволяют говорить об отражении от экситонов в широкой квантовой яме. Наблюдаемые на спектре (рис. 1) резонансы от близко расположенных энергетических уровней говорят о возможности изучения в данной гетероструктуре квантовых биений посредством, например, фотонного эха [2].

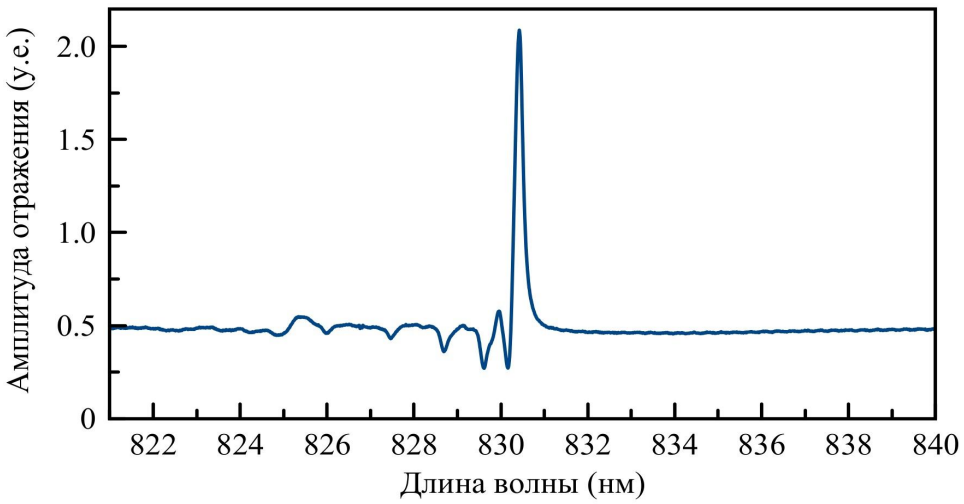


Fig. 1. Reflection spectrum of excitons in a wide quantum well of InGaAs/GaAs.

**Acknowledgments**

The work has been carried out on the equipment of the St. Petersburg University's Resource Center "Nanophotonics"

**REFERENCES**

1. **Sim, S., Lee, D., Trifonov, A.V. et al.** Ultrafast quantum beats of anisotropic excitons in atomically thin ReS2. Nat Commun 9, 351 (2018).

2. **Raiber, S., Faria Junior, P.E., Falter, D. et al.** Ultrafast pseudospin quantum beats in multilayer WSe2 and MoSe2. Nat Commun 13, 4997 (2022).

# Ultraviolet photoluminescence enhancement of zinc oxide nanocrystals in colloidal mixtures with spark discharge aluminum nanoparticles

**D. Malo [1,2]✉, A. A. Lizunova [1], O. V. Vershinina [1], E. M. Filalova [1], V. V. Ivanov [1]**
[1] Moscow Institute of Physics and Technology, Dolgoprudny, Moscow region, Russia
[2] Damascus University, Damascus, Syria
✉ malo.d@mipt.ru

**Abstract.** This work investigated ultraviolet photoluminescence enhancement in mixture colloids of zinc oxide with aluminum nanoparticles. Aluminum nanoparticles, synthesized by spark discharge method, were with an average size 22.3 ± 7.7 nm and five aluminum colloids with various concentrations from 0.001 g/L to 0.015 g/L were obtained in isopropyl alcohol solution. While zinc oxide colloid was with a concertation 0.22 g/L and an average size of the particles 26.6 ±7.4 nm. In our research, we have achieved photoluminescence enhancement up to 2.4-fold of zinc oxide emission at wavelength 377 nm in mixture colloids of zinc oxide with aluminum nanoparticles at an excitation wavelength 325 nm.

**Keywords:** Photoluminescence (PL), ultraviolet (UV), colloidal mixture, spark discharge method, aluminum nanoparticles (Al NPs), zinc oxide nanoparticles (ZnO NPs).

**Funding:** This work was financially supported by the Russian Science Foundation (project № 22-19-00311, https://rscf.ru/en/project/22-19-00311/).

## Introduction

Nowadays, interest in the synthesis of Al NPs and structures has especially increased after the theoretical substantiation of the use of aluminum as a cheap and promising material with surface plasmon resonance in UV region which makes it possible to enhance the photoluminescence of organic dyes and semiconductor structures by several times and actively can used in various fields of science and technology [1-2]. In this research, we obtained colloids of plasmonic Al NPs, synthesized by spark discharge method, and their mixtures with an ultraviolet phosphor, namely, ZnO NPs and we studied the effect of plasmonic Al NPs to enhance the photoluminescence in liquid dispersions in the UV region of the spectrum.

## Materials and Methods

ZnO NPs colloid (0.22 g/L) was prepared by the method which is described in [2] by dilution using chromatographically pure isopropyl alcohol (Scharlau). Al NPs were synthesized using the aerosol spark discharge generator [1], that used in atmosphere of argon of purity 6.0 at pressure 1.2 atm with Al electrodes (solid cathode 8 mm in diameter, anode with the hole 3.5 mm), discharge voltage 1.5 kV, discharge period 2 ms, gas flow 600 mL/min and one hour for passivation with argon 4.8. For Al NPs colloids, citric acid in chromatographically isopropyl alcohol (0.01 g/L) (buffer solution) was used as surface active agents to form stable Al dispersions with the desired dimensional parameters. Then, ultrasonic treatment of dispersion (0.4 g/L) of Al NPs was carried out for 30 minutes to crush agglomerated particles. Five suspensions of Al NPs were prepared with different concentrations 0.001, 0.003, 0.005, 0.010 and 0.015 g/L by dilution with buffer solution.

At room temperature, to study PL enhancement at an excitation wavelengths of 325 nm, mixtures of ZnO NPs with Al NPs (v:v) (1:1) were prepared and compared with mixture of ZnO NPs with pure isopropanol (1:1).

The size and crystal structure of primary NPs were received by transmission electron microscope (TEM) Jeol JEM 2100 (200 kV). The UV-vis-NIR spectra and luminescence emission were obtained using JASCO V–770 and JASCO FP–8300 spectrometers, correspondingly.

## Results and Discussion

According to TEM and electron diffraction images, spherical shape and core-shell structure with metal crystal core and oxide shell for Al nanoparticles were observed. The average primary

particle size of Al NPs, which formed large agglomerates, was 22.3 ± 7.7 nm, while 26.6 ± 7.4 nm for ZnO NPs.

The photoluminescence spectra of ZnO NPs colloid 0.22 g/L and its mixtures with Al NPs colloids of different concentrations were obtained at an excitation wavelength 325 nm (Fig. 1, a).

*a)* *b)*

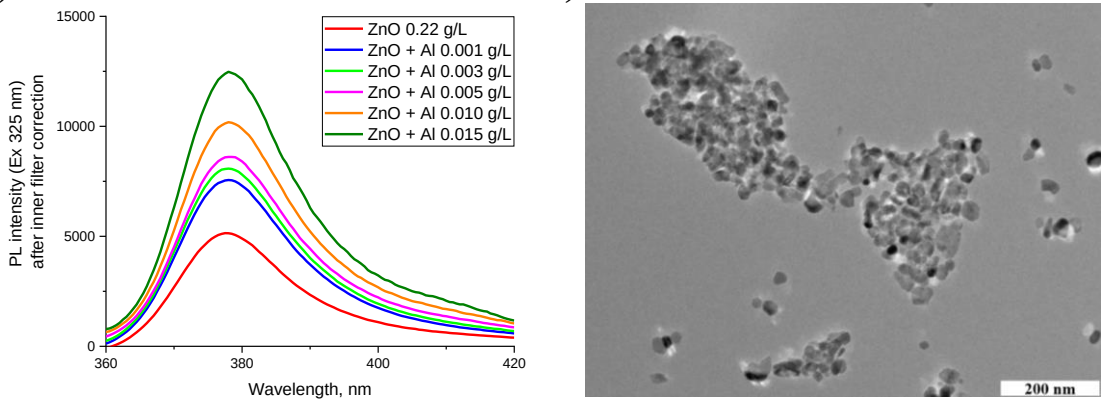


Fig. 1. Photoluminescence emission spectra at an excitation wavelength 325 nm of pure ZnO NPs colloid (0.22 g/L) and its mixtures with Al NPs colloids of various concentrations (from 0.001 to 0.015 g/L) (*a*); TEM image of an Al-ZnO complex found in the colloidal mixture of Al 0.003 g/L with ZnO 0.22 g/L (*b*)

It was found that an increase in photoluminescence intensity of ZnO nanoparticles 0.22 g/L up to 240% at an emission wavelength 377 nm was observed with an increase in the concentration of Al nanoparticles from 0.001 to 0.015 g/L.

## Conclusion

We demonstrated that photoluminescence enhancement of ZnO NPs in presence of plasmonic Al NPs, synthesized by spark discharge method, at an excitation wavelength 325 nm was achieved up to 2.4-fold in UV region at an emission wavelength 377 nm in colloid solutions.

So, these promising colloids can be used as nano-ink to fabricate biomedical and optoelectronic sensors in ultraviolet region of the spectrum based on Al nanostructures.

## Acknowledgments

This work was financially supported by the Russian Science Foundation (project № 22-19-00311, https://rscf.ru/en/project/22-19-00311/).

## REFERENCES

1. **Borisov V. I., Lizunova A. A., Mazharenko A. K., Malo D., Ramanenka A. A., Shuklov I. A., Ivanov V. V.,** Aluminum nanoparticles synthesis in spark discharge for ultraviolet plasmonics, Journal of Physics: Conference Series, IOP Publishing. 1695 (2020) 012021.

2. **Lizunova A. A., Malo D., Guzatov D. V., Vlasov I. S., Kameneva E. I., Shuklov I. A., Urazov M. N., Ramanenka A. A., Ivanov V. V.,** Plasmon-enhanced ultraviolet luminescence in colloid solutions and nanostructures based on aluminum and ZnO nanoparticles, Nanomaterials. 12 (22) (2022) 4051.

# Optical studies of InGaAs/GaAs quantum well mesa structures treated with hydrogen $H_2$ plasma and passivated via $AlO_x$ layer

**I. A. Melnichenko**[1,2✉], **N. V. Kryzhanovskaya**[1], **A. M. Nadtochiy**[1], **M. G. Kozodayev**[3], **R. R. Hakimov**[3], **A. A. Vorobiev**[2], **Yu. A. Guseva**[4], **A. M. Mozharov**[2], **A. E. Zhukov**[1]

[1] HSE University, St. Petersburg, Russia

[2] Alferov University, St. Petersburg, Russia

[3] Moscow Institute of Physics and Technology, Moscow, Russia

[4] Ioffe Institute, St. Petersburg, Russia

✉imelnichenko@hse.ru

**Abstract.** A significant increase in photoluminescence intensity and a decrease in the surface recombination rate for passivated mesa-structures with InGaAs/GaAs quantum well were demonstrated.

**Keywords:** InGaAs/GaAs QW, passivation, ALD, photoluminescence, lifetime

**Funding:** This study was supported by by the Russian Science Foundation (grant # 22-72-10002, https://rscf.ru/en/project/22-72-10002/). Support of optical measurements from the Basic Research Program of the National Research University Higher School of Economics is gratefully acknowledged.

## Introduction

The active region in modern semiconductor optoelectronic devices, like WGM microlasers, is primarily comprised of quantum wells (QWs) or quantum dots (QDs). Microlasers with active region based on QDs have such advantages as low generation threshold and high temperature stability [1]. Nevertheless, as the diameter of such a QD-based microlaser decreases, the problem of gain saturation at the QD ground state and switching to generation at the excited state becomes relevant. A solution in such a case could be the usage of QWs instead. However, the problem of diameter reduction is also relevant for the QWs. Due to the free lateral transport of the charge carriers in the QWs, the effect of nonradiative recombination on the sidewall surfaces of the microlaser becomes important. To solve this problem, a technique of mesas surface passivation can be proposed. This technique includes different approaches: it can be chemical passivation, such as a sulfide or nitride surface layer creation. Another passivation method is the deposition of oxides or wide energy gap materials such as GaP, GaN, $Al_2O_3$ [3-5].

In this work, the effect of surface treatment with $H_2$ plasma and following deposition of an $AlO_x$ layer by atomic layer deposition (ALD) method on the photoluminescence of microdisk mesa structures was investigated. For this purpose epitaxial structures on a GaAs substrate with a single $In_{0.2}Ga_{0.8}As$/GaAs quantum well and a superlattice of 10 alternating GaAs/AlAs layers in diameter range of 3-20 μm were studied.

## Materials and Methods

Epitaxial structures with a single $In_{0.2}Ga_{0.8}As$/ GaAs quantum well, and with a GaAs/AlAs superlattice structure were created on a GaAs (100) substrate via molecular beam epitaxy. The single InGaAs/GaAs QW was 10 nm thick and was separated from the GaAs superlattice by a 100 nm thick buffer. After, the interchange of 10 nm thick GaAs and AlAs layers each ten times, which called the supperlatice, was grown. The 200 nm thick $Al_{0.39}Ga_{0.61}As$ layer was grown to prevent carrier leakage from quantum-confined active region to the substrate. Microdisc mesa structures of various diameters from 3 to 20 μm were created using photolithography and plasma chemical etching. Obtained mesa structures were treated in hydrogen $H_2$ plasma during 10 minutes and then further passivated using the ALD method with 10 nm thick aluminium oxide ($AlO_x$).

Photoluminescence (PL) spectra were measured using an Integra Spectra NT-MDT confocal microscope at room temperature. The excitation laser radiation (YAG:Nd 527 nm) was focused using a 20x micro-lens (Mitutoyo, M Plan APO NIR) with numerical aperture NA = 0.4 into a spot up to ~5 μm in diameter. Detection was performed using a Sol Instruments MS5204i

monochromator and a cooled CCD Si camera (Andor iVac). Time-resolved photoluminescence (TRPL) spectra of the mesa-structures were investigated at room temperature with picosecond time resolution using the up-conversion method. The femtosecond mode-locked Ti:Sapphire "Coherent Mira 900" laser on 780 nm wavelength and FOG-100 module (CDP Systems) were used. The time-resolved signal was registered using a monochromator and a photomultiplier tube.

## Results and Discussion

The PL spectra of mesa structures of different diameters were studied at room temperature before and after hydrogen $H_2$ plasma treatment and further 10 nm $AlO_x$ ALD passivation (Fig. 1(a)). The PL peak at 1.47 eV corresponds to the GaAs/AlAs superlattice, and the PL maximum at 1.24 eV characterizes the transition in a single $In_{0.2}Ga_{0.8}As$/GaAs QW. The maximum of PL intensity for the ground transition of $In_{0.2}Ga_{0.8}As$/GaAs QW was ~ 8.3 times, for the GaAs/AlAs superlattice ~ 3.7 times for a mesa structure with a diameter of 8.4 μm. For the mesas of other diameters PL intensity also increased, but by a smaller number of times.

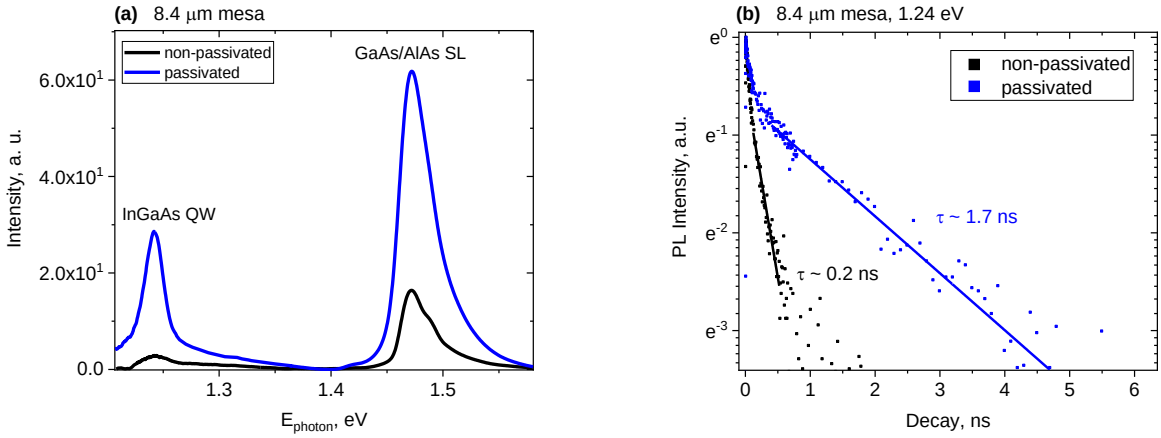


Figure 1. (a) PL spectrum and (b) PL kinetics for unpassivated and treated with hydrogen $H_2$ plasma and passivated with 10 nm $AlO_x$ layer 8.4 μm diameter mesa-structures.

To study the differences in the carrier dynamics of passivated and non-passivated structures, time-resolved photoluminescence measurements were performed using the ap-conversion method (Fig. 1(b)). The charge carrier lifetime $\tau_{decay}$ in the $In_{0.2}Ga_{0.8}As$/GaAs QW was obtained using the function $I_{PL}(t) = Ae^{-t/\tau_{decay}}$, which fits the experimental data well. The lifetime for passivated mesa structures was 1.7 ns versus 0.2 ns obtained for mesa structures without passivation. The increase in lifetime in passivated structures is associated with a decrease in the surface recombination rate.

## Conclusion

It is shown that the hydrogen $H_2$ plasma treatment and subsequent 10 nm thick $AlO_x$ passivation layer formed by atomic layer deposition on the sidewall surface of mesa structures with $In_{0.2}Ga_{0.8}As$/GaAs QW and GaAs/AlAs superlattice can be effectively used to suppress nonradiative recombination.


## Acknowledgments

This study was supported by by the Russian Science Foundation (grant # 22-72-10002, https://rscf.ru/en/project/22-72-10002/). Support of optical measurements from the Basic Research Program of the National Research University Higher School of Economics is gratefully acknowledged.


## REFERENCES


1. **Arakawa Y., Sakaki H.**, Multidimensional quantum well laser and temperature dependence of its threshold current, Applied physics letters. 40 (11) (1982) 939-941.

2. **Boroditsky M. et al.,** Surface recombination measurements on III–V candidate materials for nanostructure light-emitting diodes, Journal of Applied Physics. 87 (7) (2000) 3497-3504.

3. **Arab S. et al.**, Effects of surface passivation on twin-free GaAs nanosheets, ACS nano. 9 (2) (2015) 1336-1340.

4. **Lunt S. R. et al.,** Chemical studies of the passivation of GaAs surface recombination using sulfides and thiols, Journal of Applied Physics. 70 (12) (1991) 7449-7467.

5. **Ashby C. I. H. et al**., Ultraviolet photosulfidation of III-V compound semiconductors: A new approach to surface passivation, Applied physics letters. 64 (18) (1994) 2388-2390.

# Investigation of phase shift in waveguides with chalcogenide glasses

**A. E. Mitrofanova**[1, 2, 4] ✉, **I. D. Skuratov** [1,2], **V. V. Svetikov** [3,4]
[1] JSC « Molecular Electronics Research Institute», Moscow, Russia
[2] Moscow Institute of Physics and Technology, Dolgoprudny, Russia
[3] Prokhorov General Physics Institute, Russian Academy of Sciences, Moscow, Russia;
[4] JSC « Zelenograd Nanotechnology Center, Moscow », Moscow, Russia
✉mitrofanova.ae@phystech.edu

**Abstract.** The paper presents a numerical study of the propagation of the waveguide mode in a waveguide with films of chalcogenide glasses, a numerical analysis of the phase change of the waveguide mode depending on the phase state of chalcogenide glass and geometric parameters of the structure.

**Keywords:** integrated optics, chalcogenide glasses, phase shift.

## Introduction

Currently, chalcogenide materials are widely used to create memory cells. Such devices are based on the principle of changing optical and electrical properties when the phase state of the glass film changes from amorphous to crystalline. Laser or electric pulses are used to switch the phase state.

Special attention is paid to the study of Ge–Sb–Te (GST) glasses, which have high optical contrast [1] and short phase-state switching time (<50ns) [2].

This makes it possible to consider the possibility of using GST-225 (Ge2Sb2Te5) thin films in optical switching devices. GST-225 has a high refractive index in both amorphous (n=4.69) and crystalline (n=8.03) phase states [4]. Applying sections of a thin GST film to a waveguide allows to change the phase velocity of the mode in this section of the waveguide by capturing part of the propagating mode (Fig. 1). This effect can be used to create a controlled phase change.

*a)* *b)*

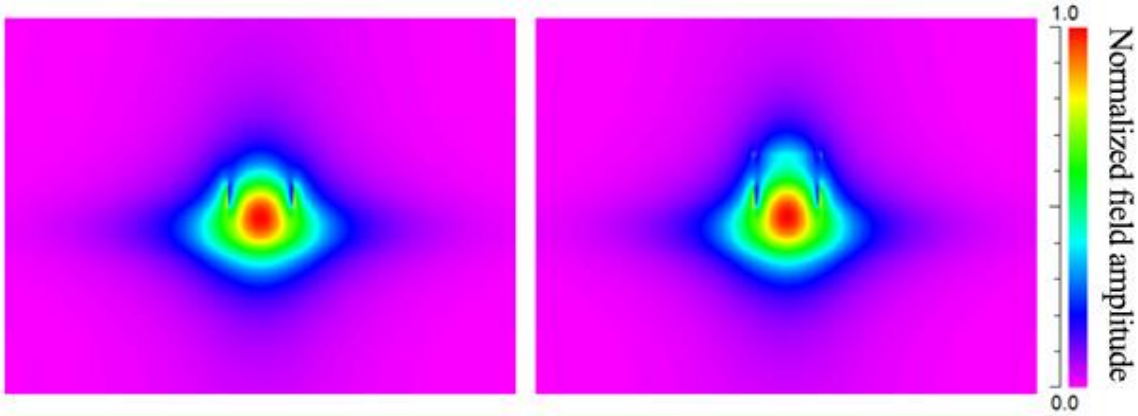


Fig. 1. Distribution of the optical field in a waveguide without a GST layer (a) and in a waveguide with a thin GST film (b)

## Results and Discussion

In the course of the work, the possibility of creating a discrete phase shift using elements based on GST-225 thin films was investigated. Calculations were carried out for waveguide structures based on SOI. A numerical analysis of the phase shift depending on the geometric parameters of the structure and the phase state of the GST-225 film was performed using the BPM numerical calculation. The results obtained made it possible to determine the optimal thickness of the film and the buffer layer separating it from the waveguide. A numerical model of the Mach-Zehnder interferometer with a discrete phase adjustment was constructed based on the performed analysis. The results of the model usage are presented and discussed.

## REFERENCES


1. **Guo P., Sarangan A. M., Agha I.,** A review of germanium-antimony-telluride phase change materials for non-volatile memories and optical modulators, Applied sciences. – 2019. – T. 9. – №. 3. – C. 530.

2. **Kozyukhin S. A.** et al., Phase change memory materials and their applications //RUSSIAN CHEMICAL REVIEWS. – 2022. – T. 91. – №. 9.

3. **Bokarev V. P., Krasnikov G. Y.,** Estimation of the change in the physicochemical properties of Nanosized crystalline materials //Doklady Physical Chemistry. – SP MAIK Nauka/Interperiodica, 2008. – T. 420. – C. 96-99.

4. **Kim H. J.** et al., PCM-net: a refractive index database of chalcogenide phase change materials for tunable nanophotonic device modelling //Journal of Physics: Photonics. – 2021. – T. 3. – №. 2. – C. 024008.

5. **Singh V.** et al., Chalcogenide glass materials for integrated infrared photonics : дис. – Massachusetts Institute of Technology, 2015.

# High-$Q$ band-edge resonances in one-dimensional arrays of dipolar scatterers

**M. S. Mikhailovskii** [1✉], **M. A. Poleva** [1], **M. S. Sidorenko** [1], **Z. F. Sadrieva** [1], **M. I. Petrov** [1], **A. A. Bogdanov** [1,2], **R. S. Savelev** [1]

[1] School of Physics and Engineering, ITMO University, Saint Petersburg 197101, Russia

[2] International Joint Research Center for Nanophotonics and Metamaterials, Harbin Engineering University, Sansha road 1777, Qingdao 266404, China

✉m.mikhailovskii@metalab.ifmo.ru

**Abstract.** In this work, we study dipolar oscillations in the infinite and finite one-dimensional arrays of scatterers supporting dipole resonances. We show that the presence of two responses of different types for a single scatterer in an infinite chain can lead to a change in the behavior of dispersion curve from monotonic to nonmonotonic by fine tuning the resonant frequencies of each type of resonance. In turn, the nonmonotonic dispersion curve allows the collective modes of a finite chain to interact at close frequencies through the radiation continuum, resulting in a mode with strongly suppressed radiative losses for some optimal distance between the scatterers. We demonstrate that the interaction of the two types of resonances allows the optimal distance between the scatterers to be varied to realistic values. Numerical simulations and experimental verification in the microwave spectral range confirmed the main theoretical findings.

**Keywords:** interaction of resonances, dielectric resonators, nanophotonics, band-edge modes, microwave prototyping.

**Funding:** This work was supported by the Russian Science Foundation, Grant No. 22-72-10047.

## Introduction

The model of coupled dipolar scatterers is relevant for description of the arrays of cold atoms as well as for the arrays of particles with purely dipole response. Due to the interference of radiation from individual dipoles, arrays of dipoles support collective resonant oscillations, characterized by suppressed radiative losses and consequently high $Q$-factors, scaling as $Q \propto N^3$, where $N$ is the number of the dipoles in the array [1, 2]. Such collective modes are interesting for their ability to store quantum information in the context of quantum optics [2], as well as for the possibility of significant increase of light-matter interaction strength in arrays of optical nanoresonators [3, 4].

Recently, it was shown theoretically that coupling between two or more collective modes via radiation continuum that occurs under variation of the parameters of such structures can significantly boost the quality factor of one of the modes [5]. The underlying physics is based on interference between the band-edge collective mode and a standing mode in the array, which occurs for a certain critical value of the period $a_{cr} \approx 0.2\lambda_r$ (where $\lambda_r$ is the resonant wavelength of a single dipole), when the dispersion of an infinite array becomes nonmonotonic. Such qualitative modification of the dispersion substantially affects the properties of the eigenmodes of the finite array, leading to the formation of spatially localized states with dramatically suppressed radiative losses with quality factors scaling as $Q \propto N^{\alpha}$, where $\alpha \approx 7$.

When considering an array of optical dielectric nanoresonators, the approximation of a single-dipole response usually fails, and one has to take into account at least two types of response of an individual scatterer simultaneously, which are electric dipole (ED) and magnetic dipole (MD) responses in the most simple and relevant case. At the same time, such a small critical period $a_{cr} \approx 0.2\lambda_r$ obtained for a chain of EDs is practically impossible to achieve due to technological restrictions on the precise fabrication of the chain of the nanoparticles. Hence, it is important to study the effect of interference between different modes in a single scatterer and in a chain on the characteristics of the band-edge resonances.

## Results and Discussion

We have constructed a coupled-dipole model with both ED and MD responses in each scatterer. The MD polarizability was determined only by the resonant term, while the ED one also

included quasistatic response. Using the dipole model, we calculated the dispersion diagrams for the chain of coupled resonators with ED and MD types of resonant modes (Fig.1, a). We have revealed that the presence of both electric and magnetic dipole responses in a particle leads to the increase of the critical period, i.e., when the dispersion changes its behaviour from monotonic to nonmonotonic, to the realistic values $a_{cr} \gtrsim 0.3\lambda_r$ (Fig.1, b). This can be achieved by proper adjustment of the spectral separation between ED and MD resonant frequencies $\omega_e$ and $\omega_m$ respectively.

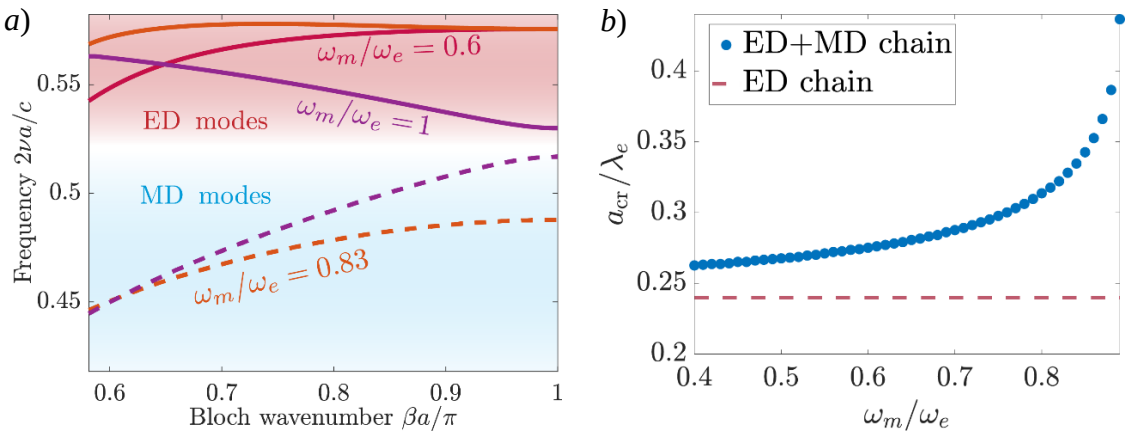


Fig. 1. Dispersion diagram of an infinite one-dimensional array of particles for a different ratios of resonant frequencies $\omega_e$ and $\omega_m$ (*a*). The critical period $a_{cr}$, at which the ED mode dispersion curve becomes nonmonotonic, vs the different ratios of resonant frequencies $\omega_e$ and $\omega_m$ (*b*).

For realistic dielectric particles this can be done by changing the size and/or the shape of the particles [6]. Calculations for the finite chains showed that they possess eigenmodes with the quality factors also scaling as $Q \propto N^7$, as in the model with a single-dipole type response, which indicates that the responsible mechanism for such increase of the *Q*-factor is the interaction between two collective modes via radiation continuum. Finally, we have calculated and experimentally measured the properties of the ceramic resonators in the microwave frequency range, which confirmed the main theoretical findings.

We believe that our findings will enrich the existing approaches for design of the compact optical nanostructures supporting high-*Q* states.


## Acknowledgments

This work was supported by the Russian Science Foundation, Grant No. 22-72-10047.


## REFERENCES


1. **Blaustein, G. S., Gozman, M. I., Samoylova, O., Polishchuk, I. Y., Burin, A. L.**, Guiding optical modes in chains of dielectric particles, Optics Express, 15 (25) (2007), 17380-17391.

2. **Zhang, Y. X., Mølmer, K.**, Theory of subradiant states of a one-dimensional two-level atom chain, Physical review letters, 122 (20) (2019), 203605.

3. **Rutckaia, V., Heyroth, F., Schmidt, G., Novikov, A., Shaleev, M., Savelev, R. S., Schilling, J., Petrov, M.**, Coupling of germanium quantum dots with collective sub-radiant modes of silicon nanopillar arrays, ACS Photonics, 8 (1) (2020), 209-217.

4. **Hoang, T. X., Ha, S. T., Pan, Z., Phua, W. K., Paniagua-Domínguez, R., Png, C. E., Chu, H.-S., Kuznetsov, A. I.**, Collective Mie resonances for directional on-chip nanolasers, Nano Letters, 20 (8) (2020), 5655-5661.

5. **Kornovan, D. F., Savelev, R. S., Kivshar, Y., Petrov, M. I.**, High-Q localized states in finite arrays of subwavelength resonators. ACS Photonics, 8 (12) (2021), 3627-3632.

6. **Evlyukhin, A. B., Reinhardt, C., Chichkov, B. N.**, Multipole light scattering by nonspherical nanoparticles in the discrete dipole approximation, Physical Review B, 84 (23) (2011), 235429.

# The research of nonlinear optical phenomena in silicon slot waveguide structures

**S. M. Murzagalina** [1,2,3✉], **I. D. Skuratov** [1,2]
[1] JSC « Molecular Electronics Research Institute», Moscow, Russia
[2] Moscow Institute of Physics and Technology, Dolgoprudny, Russia
[3] JSC « Zelenograd Nanotechnology Center, Moscow », Moscow, Russia
✉murzagalina.sm@phystech.edu

**Abstract.** This work is devoted to the study of nonlinear phenomena in silicon waveguides, as well as in silicon-organic hybrids, which help to obtain improved characteristics of the initial device by compensating for the limitations imposed by second- and third-order nonlinearities in Si. The slot waveguide model is analyzed using computational methods such as the finite element method, the finite difference method in the time domain, and the singular perturbation method.

**Keywords:** nonlinearity, doped polymers, slot waveguides

## Introduction

The silicon technological foundation has the great potential in conjunction with electronics, photonics and quantum technologies. It has opportunities in performing as solution for growing demands in such applications as data processing and telecommunications industry. Using the linear optical phenomena significant quantity of devices have been implemented on the SOI platform, for example optical buffers, interconnections [1] and sensors.

The second and third-order nonlinearities provide optical power losses, but in same time nonlinear optical effects may lead to new applications such as multiplexing and modulating signals. Therefore, researchers come across with the new challenge – to create the device with minimal losses and best functional characteristics.

## Materials and Methods

The second-order nonlinearity in silicon is lower due to the centrosymmetric crystal structure, while the third-order nonlinearity is high and caused by such effects as two-photon absorption, forced scattering, four-wave displacement and the Kerr effect. To solve that problem was carried out an analysis of various materials, among them silicon-organics hybrids (SOH), which also has strong second and third-order nonlinearities [2]. The propagation of optical radiation in waveguide structures is influenced by both the properties of silicon and SOH materials [3]. Currently, the model of slot waveguide with nonlinear properties is under development. It consists of silicon strips with a high refractive index and a nanoscale gap with a low refractive index, which formed between them. This configuration is capable of providing new applications, such as optical capture, optical switching and sensors technology. In order to adapt the model to new applications, waveguides are coated with dopped polymer or other organic substances, such as the Ormocore polymer, in which both second- and third-order nonlinearities are demonstrated. Such waveguides are good candidates for electro-optical modulators with high data transfer rates

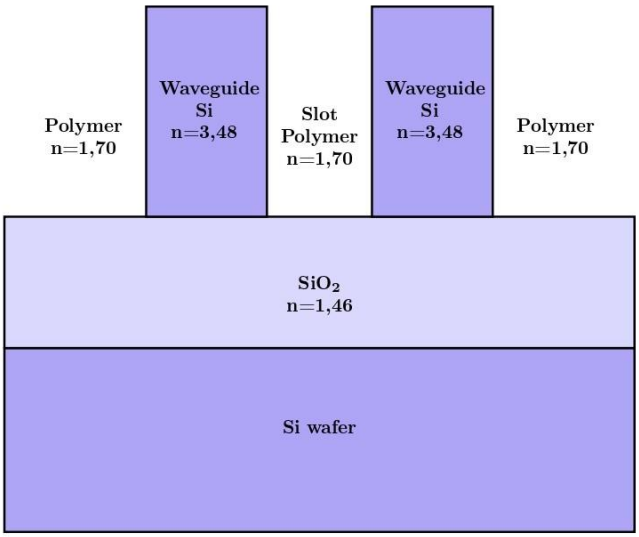


Fig. 1. Planar overview of waveguide parameters

and optical signal processing devices [4]. These devices have advantages such as high efficiency and integration with new materials conformant with CMOS.

The analysis of this structure is carried out using software for modeling based on the finite element method (FEM) and the finite difference method in the time domain (FDTD). In order to minimize optical losses, it was decided to optimize the geometric parameters of the model using machine learning methods. An analytical approach to obtain the parameters of a slot waveguide with nonlinear characteristics using the singular perturbation technique (SPT) is also considered. SPT is used to study the behavior of waveguides with spatial perturbation [5] and weak second- and third-order nonlinearities, leading to solutions with sufficiently high accuracy [6].

## Results and Discussion

In this paper, an analysis of silicon-organic compounds with second- and third-order nonlinearities was carried out, the polymer Ormocore was selected as a coating for waveguides. Modeling and optimization of geometric parameters of devices based on slot waveguides are under development.

## REFERENCES


1. **Valeev A.S., Krasnikov G.Y**. Manufacturing technology of intracrystal and intercrystal interconnections of modern ASIC// Microelectronics. 2015. vol. 44. No. 3. pp. 180-201

2. **Leuthold J. [et al.]**, "Silicon Organic Hybrid Technology—A Platform for Practical Nonlinear Optics," in Proceedings of the IEEE, vol. 97, no. 7, pp. 1304-1316, July 2009, doi: 10.1109/JPROC.2009.2016849.

3. **Lipson M. [et al.]**, "Guiding, modulating, and emitting light on Silicon-challenges and opportunities," in Journal of Lightwave Technology, vol. 23, no. 12, pp. 4222-4238, Dec. 2005, doi: 10.1109/JLT.2005.858225.

4. **Palmer R. [et al]**, Low power Mach–Zehnder modulator in silicon-organic hybrid technology //IEEE Photonics Technology Letters. – 2013. – Т. 25. – №. 13. – С. 1226-1229.

5. **Nayfeh A.H., Asfar O.R.** Parallel-plate waveguide with sinusoidally perturbed boundaries //Journal of Applied Physics. – 1974. – Т. 45. – №. 11. – С. 4797-4800.

6. **Yokota M. [et al.]**, Guided transverse-magnetic waves supported by a weakly nonlinear slab waveguide //JOSA B. – 1993. – Т. 10. – №. 6. – С. 1096-1101.

# Nanooscillators based on carbon whiskers for detectors of optomechanical effects

**I. V. Nadoyan[1,2]✉, N. A. Solomonov[1], K. N. Novikova[1], V. A. Sharov[1], L. S. Logunov[2], D. A. Kislov[2], M. I. Petrov[2], I. S. Mukhin[1,3]✉**

[1] St. Petersburg Academic University, St. Petersburg 194021, Russia

[2] ITMO University, St. Petersburg 197101, Russia

[3]Peter the Great St. Petersburg polytechnic university, St. Petersburg, 195251, Russia

✉ nadoyan@spbau.ru, ✉imukhin@spbau.ru

**Abstract.** A new mechanical resonance method for determining the effect of photoinduced heating and optical forces from laser radiation on nanoresonance systems based on carbon whiskers was developed. We demonstrate a fast and universal method for manufacturing the resonant nanodetectors with detecting the effect of optical radiation on the properties of nanoobjects. The nanomechanical whisker-based resonator was grown on a tungsten needle using an electron beam induced deposition approach implemented in a scanning electron microscope. Silicon particle supporting optical Mie resonance was localized at the end of a carbon whisker . The influence of laser radiation on the mechanical properties of nanoresonators was experimentally revealed, and the trajectory of their movement at the first mechanical mode was visualized. The demonstrated approach to detecting the influence of optical radiation on the vibrational characteristics of nanooscillators paves the way for new photothermal and optomechanical sensors.

**Keywords:** Nanowhiskers oscillations, silicon nanoparticle, optical heating, optical powers sensing

## Introduction

The study of the effect of optical radiation on micro- and nanoobjects is of particular interest for the development of optomechanical, chemical, and biological applications [1]. In particular, the study of the effect of laser radiation on the mechanical properties of nanooscillators based on single carbon whiskers (CNWs) can be used to develop various types sensors [2,3]. The mechanical oscillations of CNWs with a localized spherical silicon particle can be visualized in a scanning electron or optical microscope, which distinguishes them from the existing sensors, which require rather complex optical, mechanical or electronic systems.

CNWs were grown from the residual atmosphere in a scanning electron microscope (SEM) chamber by focusing an electron beam on a tungsten tip and had a small mass and eigen frequencies in the MHz range, which provides high sensitivity in detecting forces of the order of piconewtons. In this case, a nanoparticle (fig. 1 a) and a lensed fiber for inputting laser radiation can also be located inside the vacuum chamber. This approach allows to operate without deterioration of vacuum, which is of great importance for detecting small forces. This method does not require any additional specific equipment other than nanomanipulation tools inside the microscope [4]. To detect the influence of optical radiation on nanomechanical oscillations, the laser beam was focused on Si particle located at the end of whisker and the change of amplitude-frequency characteristic (AFC) was registered. . Such approach enables the study of new optomechanical and photoinduced effects under intense optical radiation.

## Materials and Methods

The resonant detector consists of carbon nanowhiskers grown at the end of a tungsten needle. A tubular piezoelectric transducer with a signal generator of a special form "AKIP - 3413/3" was used as an oscillation generator. A sharp tungsten needle was fabricated by electrochemical etching in a 5% KOH solution. Carbon whiskers were grown using the electron beam induced deposition method using hydrocarbon groups from the residual atmosphere in the SEM chamber. In this case, the trajectory of the electron beam determines the shape of the deposited carbon nanoobject, which makes it possible to control the geometry of the whisker. The sensor consists of a tungsten needle

placed in a piezotube vibration transducer with a carbon nanowhisker, at the end of which a silicon nanoparticle is localized. To obtain the AFC of the whisker, we used the simple method, based on the SEM visualization of oscillations (fig. 1 b). When the oscillator frequency coincides with the resonant frequency of the nanoresonator, the SEM image of the whiskers is blurred and takes the form of a fan. The localization of the nanoobject at the free end of the whisker was performed using "pick-and-place" method, which consists in capturing the nanoparticle with the tip of the nanomanipulator located in the SEM chamber and transferring it to the specified positionn. The particle can be reliably fixed by carbon welding. We use optically resonant silicon nanoparticles obtained by laser ablation. For optical illumination, we employ a laser diode with a wavelength of 658 nm, equipped with a voltage regulator to select the values of the radiation power. To input laser radiation into the SEM chamber, we used a lens fiber with a maximum output power of 3 mW, deposited with an ITO film with a focal length of ~6 μm, spot diameter of ~3 μm, and aperture of 0.385.

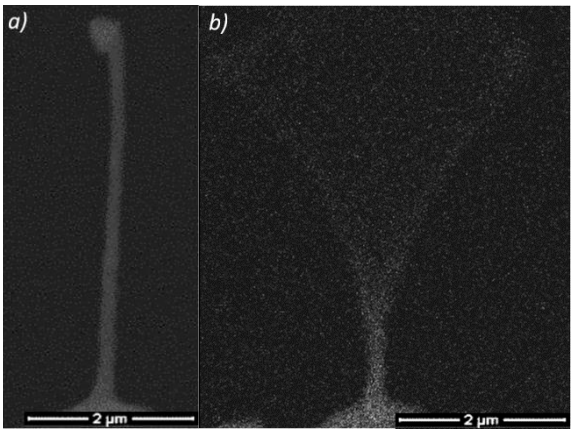


Fig. 1. CNWs with a localized silicon particle *(a)* and visualization of whisker oscillations with a particle *(b)*

## Results and Discussion

To study the effect of laser radiation on nanoobjects, the AFC of a whisker with a localized particle were acquired before and after switching on the laser. At a radiation power of 75 μW, a decrease in the resonant frequency of the whisker by 16 kHz and an increase in the oscillation amplitude by 161 nm were recorded (see fig.2).

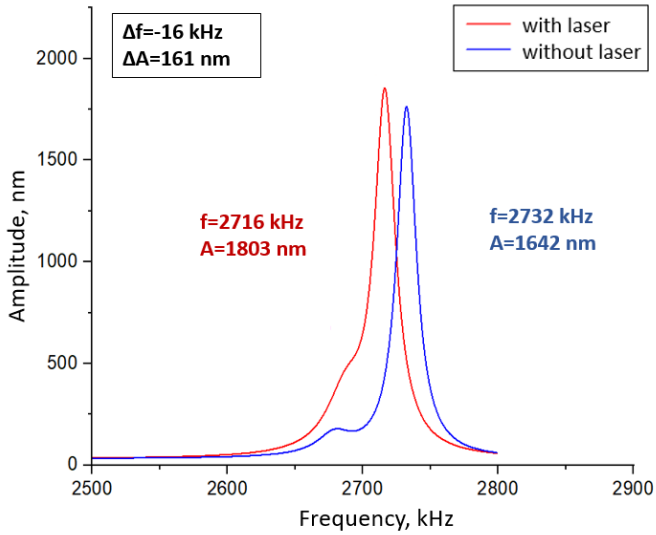


Fig. 2. AFC of a nanowhisker with a silicon particle before and after switching on the laser

## Conclusion

The obtained effect of optical radiation on the vibrational properties of nanooscillators in the form of a shift of the resonant frequency and amplitude change can be caused by thermo-induced parametric resonance or the optical forces.

D.K., and M.P. acknowledge the support of experimental studies of NW vibrational resonances by Russian Science Foundation under the grant 20-72-10141. I.M. acknowledges the Russian Federation President Council support under the grant MK-2428.2020.2.

## REFERENCES

1. **Zemánek P., Volpe G., Jonás A., Brzobohaty O.** Perspective on Light-Induced Transport of Particles: From Optical Forces to Phoretic Motion. Adv. Opt. Photonics (2019) 11.

2. **Mukhin I. S., Fadeev I. V., Zhukov M. V., Dubrovskii V. G., Golubok A. O.** Ultramicroscopy (148) (2015) 151–157.

3. **Lukashenko S. Y., Mukhin I. S., Komissarenko F. E., Gorbenko O. M., Sapozhnikov I. D., Felshtyn M. L., Uskov A. V., and Golubok A. O.** Phys. Status Solid A (2018) 215 1800046.

4. **Denisyuk A. I., Komissarenko F. E., Mukhin I. S.** Electrostatic Pick-and-Place Micro/Nanomanipulation under the Electron Beam. Microelectron. Eng. 121 (2014) 15−18.

# OPTICAL PROPERTIES A HYBRID STRUCTURE OF NANOPOROUS ALUMINA MATRIX ON SILVER NANOPRTICLE ARRAY SUBSTRATE

**I. Yu. Nikitin** [1✉], **L. N. Borodina** [1], **A. A. Starovoytov** [1], **I. A. Gladskikh** [1]
[1] ITMO University, Saint-Petersburg, Russian Federation;
✉nikitin0igor512@gmail.com

**Abstract.** New type of plasmonic hybrid structure has been fabricated and studied. The silver nanoparticle substrates were obtained via physical vapor deposition and annealing in the normal atmosphere. After that, the thick aluminium film was deposited and anodized, so that a porous matrix was formed. It was found that the structure reflection strongly depends on the anodization process installation and regime, that the pulsed current profile makes the structure scatter light near the absorption maxima. Plasmon resonance from the nanoparticles is observed otherwise, though the mirror reflection is decreased. The luminescent properties of the structures have also been studied with and without rhodamine 6G dye in alumina pores.

**Keywords:** Plasmonics, Nanoporous alumina, Sensors, Anodization, Luminescence enhancement

**Funding:** The sample fabrication and spectroscopy measurements was funded by the RPMA grant of School of Physics and Engineering of ITMO University and by the Russian Science Foundation grant no. 21-72-10098, luminescence measurements and optical microscopy were funded by the Ministry of Science and Higher Education of the Russian Federation, Goszadanie No. 2019-1080

## Introduction

In some applications, such as light emitting diodes and sensor construction it is important to use fluorophores with a distinct luminescence spectrum. Sometimes these systems have got a low quantum yield. Plasmonic structures have proven to be effective in enhancing luminescence intensity because of the Purcell effect [1,2]. If the luminescent agent takes place near the nanoparticle but has no straight contact with it the luminescence increases, but the luminescence quenching is observed after the contact with the nanoparticles due to the plasmon coupling [3]. Anodic alumina-based structures are a new class of materials that absorb luminescent agents in their nanopores, increasing the material concentration and thus luminescence intensity. In other works plasmonic structures have been deposited on the surface of anodic alumina, or grown inside via electroplating, but reproducibility and luminescence intensity enhancement of these materials are quite low . In this work a new type of hybrid alumina-silver plasmonic structure has been fabricated, where anodic alumina is used not only as a spacer, but also as a source of excitation, where Forster resonant energy transfer occurs. Different optical and morphological properties have been analyzed and different parameter influence has been determined.

## Materials and Methods

First, the glass substrates were cleaned with ethanol and deionized water. Then the substrates were held in Piranha solution (1:3 $H_2O_2$:$H_2SO_4$) for 1 h. After that the substrates have been washed with deionized water and dried with the flow of nitrogen. The cleaned substrates were then placed in a vacuum chamber (Kurt J. Lesker, USA) at the pressure of remnant gases of about $10^{-6}$Torr. The thickness was registered via resonance-frequency method with the Sigma 242 (Sigma Instruments, USA) block. 10 nm of silver has been deposited. After deposition all the samples have been annealed at 250ºC in the air atmosphere. An Al film with equivalent thickness of 160 nm has been deposited on nanoparticle array substrates as well as on the clean substrates. Then all the samples have been anodized in 0,3M oxalic acid at 40V for 40s, 50s and 60s respectively.

## Results and Discussion

On Fig 1, the absorption and reflection spectra of the hybrid structure are depicted.

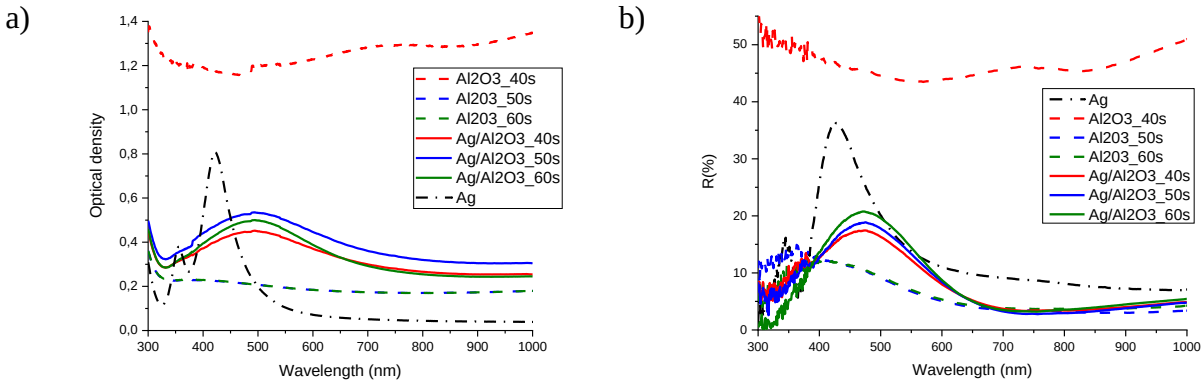


Fig 1. Optical density (a) and reflectance spectra (b) of the silver nanoparticles (Ag), anodic aluminium oxide (Al2O3) and a hybrid structure (Ag/Al2O3)

The maximums in the spectrums correspond to plasmon resonances in silver nanoparticles. A red shift is present in absorption for the hybrid structures, because the anodic alumina that covers silver nanoparticles influences localized plasmon resonance. The reflectance of the structure also has plasmon resonance, but the reflectance coefficient is generally smaller, than for the silver nanoparticles, because of the scattering in the pores of anodic alumina. The increased absorption and reflection of the anodic alumina at 40 seconds can be explained with the thick aluminium film, that hasn`t been anodized. A change in anodization regime strongly influences the hybrid structure optical properties.

The luminescent properties of the structure prove to be quite interesting. Anodic alumina has its own luminescence maxima on about 500 nm, because of the luminescent F-centers, that are formed, during the anodization process [4,5]. When a rhodamine 6G dye is placed in the structure, the excitation is transferred from the pores to the dye molecules in the vicinity of the F-centers. The Purcell effect also occurs in the hybrid alumina-silver structures, and the luminescence intensity increases.

## Conclusion

A new type of the hybrid structures has been fabricated. Both Forster resonance energy transfer and Purcell effect help to increase the dye luminescence intensity there. However, it is difficult to evaluate the energy transfer effectiveness, because the molecules in the pores are oriented chaotically and are located on the different distances from the F-centers. Nevertheless, the increase in luminescence intensity can be clearly observed, making this structure an ideal candidate for luminescent sensors and light emitting diodes.

## Acknowledgments

Mr. Nikitin is grateful to Nashyokin A.V. for valuable comments and help with obtaining the images from the scanning electron microscope.

## REFERENCES

1. Nikitin I.Y. et al. Optical properties of a hybrid films of J-aggregates and aluminum oxide formed on an island Ag film // 2022 Int. Conf. Laser Opt. ICLO 2022 - Proceedingss. Institute of Electrical and Electronics Engineers Inc., 2022.
2. Amendola V. et al. Surface plasmon resonance in gold nanoparticles: A review // J. Phys. Condens. Matter. 2017. Vol. 29, № 20.
3. Maoz B.M. et al. Amplification of chiroptical activity of chiral biomolecules by surface plasmons // Nano Lett. 2013. Vol. 13, № 3. P. 1203–1209.
4. Gao T., Meng G.W., Zhang L. De. Origin of the blue luminescence in porous anodic alumina films formed in oxalic acid solutions // Chinese Phys. Lett. 2003. Vol. 20, № 5. P. 713–716.
5. Valeev R.G., Petukhov D.I., Kriventsov V. V. Structure and Optical Properties of thin Porous Anodic Alumina Films Synthesized on a Glass Surface // Phys. Procedia. 2016. Vol. 84, № July. P. 415–420.

# Manganese-doped red-emissive carbon dots as dual-modal nanoprobe for bioimaging

**S. O. Ondar [1,2], A. A. Vedernikova [1], Z.F. Badrieva [1], E.A. Brui [1], E. A. Stepanidenko [1✉]**
[1] ITMO University, Saint-Petersburg, Russia;
[2] Saint-Petersburg State Institute of Technology, Saint-Petersburg, Russia;
✉eastepanidenko@itmo.ru, stepanidenko.e@mail.ru

**Abstract.** Luminescent carbon nanodots (CDs) are low-toxic nanomaterial with a tunable emission in a wide spectral range and various functional groups on the surface. Therefore, CDs are perspective for biomedicine application as luminescent nanoprobe, for drug-delivery, sensing etc. Doping of CDs with paramagnetic metals allows expanding the range of applications of CDs and fabricating a multimodal nanoprobe for bioimaging. In this study, we present CDs based on widely available and inexpensive precursors – citric acid and manganese, which possess excitation-dependent photoluminescence (PL) in spectral range from 450-620 nm and good $r_1$ and $r_2$ relaxivity. The synthesized CDs are an excellent candidate as a new dual-modal nanoscale probe for bioimaging.

**Keywords:** carbon dots, photoluminescence, MRI, multimodal bioimaging, Mn-based contrast agents

**Funding:** The study was supported by the Russian Science Foundation (RSF) grant No. 22-73-00090, https://rscf.ru/project/22-73-00090/. Part of the work devoted to MR experiments was supported by a grant for scientific school НШ-2359.2022.4.

## Introduction

Due to biocompatibility, low-toxicity, high photostability as well as exceptional optical properties in the long-wavelength spectral range, CDs can be used as luminescent nanoprobe for bioimaging [1]. By the doping of CDs by various heteroatoms it is possible to control morphology and optoelectronic transitions of CDs. Doping of CDs with paramagnetic metals, such as manganese allows formation of new contrast agent (CA) for MRI with a better performance than well-known commercial CAs [2]. Such CDs are perspective as dual-modal nanoprobes for both MR- and PL-bioimaging for noninvasive diagnosis. In this work, CDs with long-wavelength PL up to 620 nm and good $r_1$ and $r_2$ relaxivity were synthesized from citric acid, formamide and different source of manganese $Mn^{2+}$.

## Materials and Methods

The CDs were synthesized by the solvothermal synthesis method at 180°C during 12 h from 0.5 g citric acid in 5 ml of formamide and 0.127 g $Mn(CH_3COOH)_2x4H_2O$ (MnAc, **CD-1**) or 0.065 g $MnCl_2x4H_2O$ (**CD-2***)*. To purify CDs from unreacted precursors, stock solutions were dissolved in 30 ml of ethanol and precipitated by centrifugation during 15 min at 6k rpm. This procedure was performed 3 times, then the precipitants were dissolved in deionized (DI) water and transferred to dialysis tubes (3.5 kDa) for dialysis against DI water for 1 day.

The absorption spectra of the solutions were obtained using a UV-3600 spectrophotometer (Shimadzu); PL excitation-emission (PLE-PL) maps were recorded on a Cary Eclipse fluorescence spectrometer (Agilent). The metal content in CDs was determined by inductively coupled plasma-emission spectrometer (ICPE-9000 Shimadzu). Relaxivity was measured using a 1.5 T clinical MRI scanner (Magnetom Espree, Siemens Helthineers). For this, T1 and T2 maps of the samples were acquired based on inversion-recovery (TR=6000 ms, TE = 92 ms, TI = 35/100/200/400/800/1600/3200/4000/5000 ms) and multi-echo turbo spin-echo (TR = 6000 ms, TE = 8.6/325/642 ms) pulse sequences, correspondingly.

## Results and Discussion

Analysis of optical properties of CDs (Figure 1) showed that both CD-1 and CD-2 had optical transitions in UV-Vis spectral range and demonstrated excitation dependent PL band. The

PL band at 420-550 nm excited at 350-450 nm are correspond to the optical transitions inside the citric acid-based CDs core. The long-wavelength PL centered at 620 nm upon excitation at 550 nm are due to surface states associated with $sp^2$-hybridized carbon domains and can also be caused by transitions associated with manganese in the CD's structure. These results are in good agreement with previous studies [3].

CD-1 and CD-2 were investigated as CAs for MRI. Analysis showed changes in the time of spin-lattice (T1) and spin-spin (T2) relaxation of protons with increasing of $Mn^{2+}$ concentration. The resulting relaxivity values ($r_1$ and $r_2$), calculated from the slope of the linear trend (relaxation rate vs. concentration) were $r_1$ = 4.34 L $mmol^{-1}s^{-1}$ and $r_2$ = 42.24 L $mmol^{-1}s^{-1}$ for CD-1 and $r_1$ = 6.71 L $mmol^{-1}s^{-1}$ and $r_2$ = 67.06 L $mmol^{-1}s^{-1}$ for CD-2. Thus, both relaxivities for sample CD-2 were slightly higher than for CD-1, which indicates a higher contrast activity.

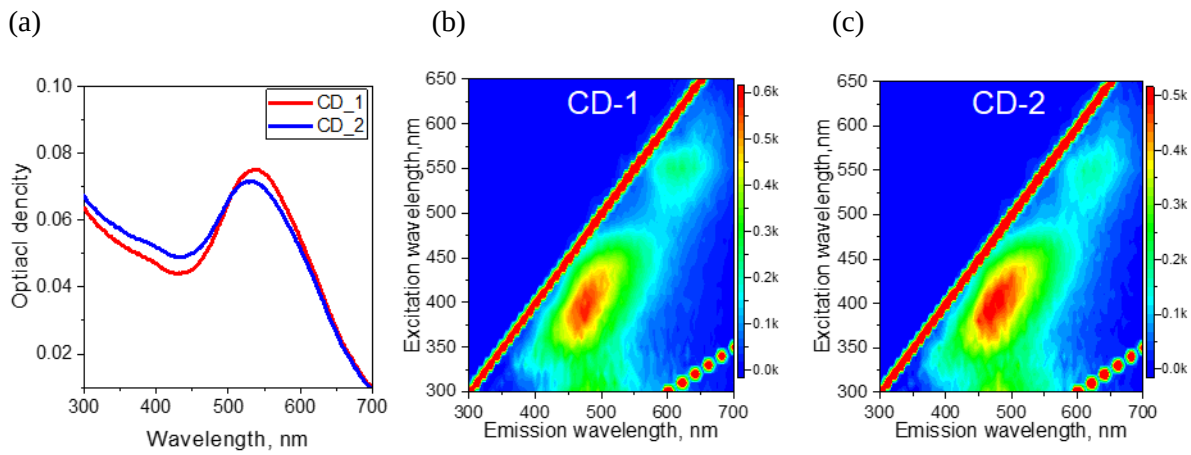


Fig. 1. Absorption spectra (*a*) and PL-PLE maps (*b*,*c*) of aqueous solutions of samples CD-1, CD-2

## Conclusion

In summary, we have suggested manganese-doped CDs with long-wavelength emission, which are capable of influencing relaxation time during MRI, that makes these CDs desirable as nanoscale dual-modal probe for bioimaging during non-invasive visualization. Application of red-emissive CDs will help to decrease autofluorescence during PL bioimaging, and combination of PL and CAs properties in one nanoprobe will allow achieving higher efficiency and accuracy during diagnostics.

## Acknowledgments

The authors express their gratitude to the ITMO University Core Facility Center "Nanotechnologies". Determination of metal concentration in samples were performed on equipment of the Chemical Analysis and Materials Research Centre of the St. Petersburg State University Research Park. MRI analysis was performed on equipment of the St. Petersburg State University and the Almazov National Medical Research Center.

## REFERENCES

1. **Dan Q., Xiayan W., Yuping B., Zaicheng S.,** Recent advance of carbon dots in bio-related applications, JPhys Materials, Vol 3 (2) (2020) 022003.

2. **Zhe J., Penghui A., Chen S., Tingjian W., Changxiang Y., Ling Y., Wei G.,** Manganese-Doped Carbon Dots for Magnetic Resonance/Optical Dual-Modal Imaging of Tiny Brain Glioma, ACS Biomaterials Science & Engineering, Vol. 4 (6) (2018) 2089–2094.

3. **Zhang, B., Wang, B., Ushakova, E. V., He, B., Xing, G., Tang, Z., Rogach, A. L., Qu, S.,** Assignment of Core and Surface States in Multicolor-Emissive Carbon Dots. Small 2022, 2204158.

# Measurement of the focal length of a lensed fiber made by chemical etching and reflow

**A. S. Pankov[1✉], L. O. Zhukov [1], A.I. Shmyrova[1], A.R. Kornilicyn[1], R.S. Ponomarev[1]**
[1] Perm State University, integrated photonics laboratory, Perm 614990, Russia;
✉lab.photon.psu@gmail.com

**Abstract.** The paper presents the results of measuring the focal length by using a Fabry-Perot interferometer and the diameter of the mode field by using an infrared camera of lensed fibers made by chemical etching and reflow.

**Keywords:** lensed fibers, mode diameter field, focal length.

**Funding:** The work was carried out within the framework of the state assignment of the Ministry of Science and Higher Education of the Russian Federation (topic No.121101300016-2).

## Introduction

Optical fibers with microlenses at the end, also called lensed fibers, are widely used in integrated and fiber optics to increase the efficiency of input/output radiation [1]. They are designed to optimize the connection of fiber light guides with various optical components. The light at the output of such fibers is focused at a finite distance and gathered into a beam with a certain diameter of the mode field up to 2 microns [2]. At the same time, the shape of the lens plays an important role in the efficiency of radiation accommodation. The paper presents focal length and diameter measurement methods for the lensed fibers mode field (MFD) created by chemical etching and by stretching-melting.

## Focal length measurement of the lensed fiber

The lensed fibers focal length was measured by using a Fabry-Perot interferometer [3].

The light beam generated by a laser with a wavelength of 1550 nm passed through a circulator. One part of this beam directed to the optical power meter without disturbance. The second part directed into a fiber lens. The interferometer object beam directed at the mirror surface. After being reflected, the beam returned to the fiber, passing through which it also entered optical power meter. The mutual position of the fiber lens relative to the mirror surface was varied by using a micropositioner. Visual control was carried out by using a technical vision camera.

With the help of a power meter, the signal depending on the position of the fiber relative to the mirror surface was recorded. The result of the measurement is the distribution of optical power from the distance between the lens and the mirror. The distribution is an interference signal with an average parabolic profile, the vertex of which corresponds to the focal length of the lens.

## Measuring the diameter of the mode field

To determine the values of the diameter lensed fibers mode field, an infrared camera [4] with near-field shooting was used.

The lens fixed in the snap-in and connected to a radiation source with a wavelength of 1550 nm was located at a focal length relative to the lens of the infrared camera. The diameter of the lensed fiber mode field was determined as a result of processing the image obtained from the infrared camera matrix with fixed shooting parameters. The calibration of the camera was carried out relative to a single-mode fiber with a flat end. Numerical results of the parameters of some lensed fibers created by various methods are given in the table below.

Table 1

**Numerical results of the parameters of lensed fibers**

| Sample number | focal length, µm | MFD, µm | Production method |
|---|---|---|---|
| 12.58.7.02.23 | 4.5 ± 0.5 | 4.5 ± 0.5 | chemical etching |
| 15.31.7.02.23 | 27.0 ± 2.0 | 2.0 ± 0.5 | stretching-melting |

## Results and Discussion

A obtained data comparative analysis shows that the characteristics of the final product vary depending on the method lensed fiber was produced. Lenses made by etching have the smallest focal length. Lenses made by stretching with subsequent melting have the minimum mode field. It is demonstrated, that the use of a Fabry-Perot interferometer to measure the focal length, and an infrared camera to determine the mode field, is sufficient to conduct a comparative analysis of the manufactured lensed fibers quality and make recommendations for improving their production methods.

## REFERENCES


1. **Ounnas B, Sauviac B, Takakura Y et al.,** Transactions on Antennas and Propagation, IEEE. 63 (12) (2015) 5612.

2. Datasheet. Tapered and lensed fibers, OZ Optics. URL: https://www.ozoptics.com/ALLNEW_PDF/DTS0080.pdf. Accessed March 15, 2023.

3. **Li E**., Characterization of a fiber lens, Optics Letters. 31 (2) (2006) 169.

4. **Malki A, Bachelo R and Van Lauwe F.,** Pure and Applied Optics Two-step process for micro-lens-fiber fabrication using a continuous CO2 laser source, Journal of Optics A. (3) (2001) 291.

# Tuning the luminescence response of a photonic crestal with Ge(Si) nanoislands by changing the etching depth of holes

**A. V. Peretokin**[1,2✉], **M. V. Stepikhova**[1], **D. V. Yurasov**[1], **A. V. Novikov**[1,2], **M. V. Shaleev**[1], **D. V. Shengurov**[1], **A. N. Yablonskiy**[1], **E. E. Rodyakina**[3], **S. A. Dyakov**[4]

[1] Institute of Physics of Microstructures RAS, st. Akademicheskaya, 7, 1 Afonino, Kstovsky district, Nizhny Novgorod region, Russia;

[2] UNN them N.I. Lobachevsky, Gagarin Ave., 27, Nizhny Novgorod, Russia;

[3] Institute of Semiconductor Physics A.V. Rzhanov SB RAS, 13 Lavrentiev Ave., Novosibirsk, Russia;

[4] Skolkovo Institute of Science and Technology, st. Nobelya, 3, Moscow, Russia

✉aperetokin@ipmras.ru

**Abstract.** The dependences of the luminescence response and the band structure of two-dimensional photonic crystals (PhC) with Ge(Si) nanoislands on the depth of hole etching are studied in this work. The features that arise in the band structure of PhCs are revealed, and the optimal etching parameters providing the greatest increase in the intensity of the photoluminescence signal of nanoislands are determined. The emergence of a BIC-mode with a near-zero group velocity is experimentally studied.

**Keywords:** photonic crystals, silicon photonics, photonic bound states in the continuum

**Funding:** The work was funded by Russian Science Foundation grant number #19-72-10011. Facilities of "Physics and technology of micro- and nanostructures" Center at IPM RAS were used.

## Introduction

Today, the problem of creating near-IR radiation sources on silicon remains is actual and unresolved. One of solutions to the one is SiGe structures with Ge(Si) nanoislands. In such structures, luminescence is observed in the wavelength range of 1.2–1.6 μm at room temperature [1]. The formation of two-dimensional PhCs makes it possible to achieve a higher enhancement of the photoluminescence (PL) signal [2]. The greatest enhancement of the PL signal is achieved when the spectral coincidence of the photoluminescence maximum of nanoislands with the selected PhC mode. The main method for controlling the spectral position of modes is to change the PhC parameters, namely, the period (a) and the ratio r/a, where r is the hole radius. However, this requires high precision in the manufacture of PhCs, which is not always possible. Another possibility for modifying the band structure of a PhC is to change the hole etching depth. Varying the etching depth can lead to the appearance of new features in the band structure of the PhC, which is also interesting from the fundamental point of view. The use of etching depths smaller than the depth of the active layer (Ge(Si) nanoislands) should have a positive effect on the radiating properties of PhCs. From the point of view of practical applications, a shallow etching depth is preferable for the creation of light-emitting diode structures with a PhC.

In this study, we demonstrate the dependence of the luminescence response of a PhC on the hole etching depth and show the features of the band structure of a PhC that appear. We will also experimentally study the band structure of PhC and show a flat dispersion for the BIC-mode with near-zero group velocity.

## Materials and Methods

We studied a series of PhC samples with a hexagonal lattice of holes, with the following parameters: lattice constant $a$=500–700 nm, filling factor $r/a$ = 0.25 ($r$ - the hole radius). Initially, we grew a sample with a total thickness of the waveguide layer of 335 nm and the depth of the nanoislands was 130–200 nm (5 layers of nanoislands separated by ~17 nm thick Si layers), and then split sample into 5 parts. For each part of the sample, we formed PhC holes with different depths: 80, 130, 190, 250, and 335 nm by reactive ion etching. We studied the luminescent properties of PhC using the standard micro-photoluminescence spectroscopy setup. The objective Mitutoyo M Plan APO NIR 10x (NA = 0.26) was used to focusing the laser beam. The PL signal

is pumping by a solid-state laser at a wavelength of 532 nm and detected by a cooled Ge detector. The spectral resolution of the setup was provided by the Fourier-spectrometer Bruker IFS 125 HR. We studied the band structure of PhCs using original diagram direction micro-PL spectroscopy setup [3].

## Results and Discussion

On fig. Figure 1a shows the micro-PL spectra of the obtained PhCs with a lattice period *a*=650 nm. As can be seen from the figure, the nature of the spectra and the intensity of the PL signal of the PhC depend to a large extent on the etching depth of the holes. At a small hole etching depth, a “weak” PhC grating is formed, in which the mode's dispersion intersect each other and, as a result, a wide spectrum is observed, which is seen at an etching depth of 80 nm. As the etching depth increases, the modes shift, their dispersion characteristics intersect less with each other, as a result of which the spectrum becomes narrower and narrow intense lines appear in it. Due to this, the intensity of the signal should also increase, but another dependence is visible from the figure. The most intense spectrum is observed at an etching depth of 130 nm, when the PhC grating is "strong" and the layer of nanoislands is not yet affected. At a shallower etching depth, the PL intensity is lower, since the PhC is “weak.” With a further increase in the etching depth, the signal intensity begins to decrease due to the increasing contribution of the non-radiative recombination of hole's sidewalls. These two factors are multidirectional, so there is an optimal etching depth at which a sufficient increase in signal intensity is observed due to the resonant interaction of nanoislands with PhC modes and a small contribution from non-radiative recombination.

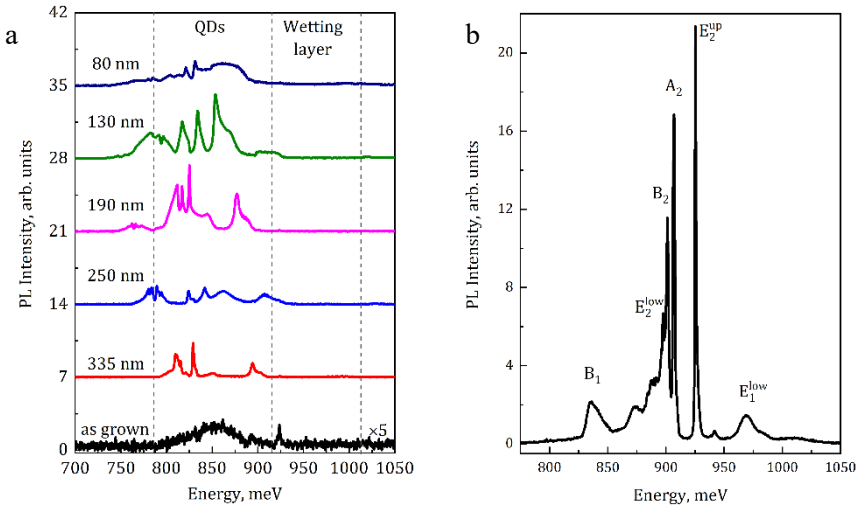


Fig. 1. a – PL spectra for the as-grown sample and PhCs with a=650 nm and filling factor 0.25. Etching depths are indicated near each spectrum. Vertical dashed lines denote the emission range related to the Ge QDs and to the wetting layer; b – PL spectrum of a PhC with *a*=550 nm, *r/a*=0.25, etching depth 250 nm.

Of all the PhCs we studied, we are most interested in the PhC with the parameters xxc, the spectrum of which is shown in Figure 1b. Extremely narrow lines are observed in it (Q-factor ~1950). The most intense line is formed by the $E_2^{up}$ mode, which is the BIC-mode. According to preliminary results of numerical simulation, this mode has a near-zero group velocity, which should also increase its Q-factor. To confirm this, we will carry out an experimental study of the band structure of the PhC.

## REFERENCES


1. **V. Ya. Aleshkin, N. A. Bekin, N. G. Kalugin,** *et al.* / JETP Letters. V. 67, № 1, 48,1998.
2. **S. A. Dyakov, M. V. Stepikhova, A. A. Bogdanov** *et al.* / Laser & Photonics Review. V. 15, 2000242, 2021.
3. **A. V. Peretokin, M.V. Stepikhova, A.V. Novikov** *et al.* / Photonics and Nanostructures - Fundamentals and Applications, V. 53, 101093, 2022.

# Optical properties of photo-thermo-refractive glasses doped with terbium

**V. V. Pesnyakov** [1✉], **A. I. Ignatiev** [1], **N. V. Nikonorov** [1]
[1] ITMO University, Saint-Petersburg, Russia;
✉v.pesnyackoff@yandex.ru

**Abstract.** The optical properties of cerium-free photo-thermo-refractive glass doped with terbium has been investigated in present paper. It is shown that after UV exposure and subsequent heat treatment silver nanoparticles are to be appear in the glass with the plasmon resonance absorption peak at about 430 nm.

**Keywords:** PTR glass, plasmon resonance, silver nanoparticles, terbium.

## Introduction

Photo-thermo-refractive (PTR) glasses are photosensitive glasses that are widely used in various optical schemes due to the possibility of recording volume Bragg gratings [1]. The photosensitivity of PTR glass is determined by the presence of an absorption band of cerium, which is in the UV region of the spectrum (310 nm). But for now, there is one significant drawback - the inability to record a hologram using visible light. Overcoming this obstacle will allow using cheaper and more affordable light sources operating in visible spectral range for holograms recording [2]. Also, there will be possible to create complex holographic optical elements such as holographic lenses.

In this work PTR glasses with replaced $CeO_2$ by $Tb_4O_7$ were studied. The choice of Tb is explained by its energy levels which allow to obtain photo-electron in two stages. On the first stage UV exposure under 370 nm excite electron to $^5D_3$ level. From this energy level it relaxes to the lower metastable $^5D_4$ level and then, on the second stage, absorbs photon and excites to the $5d4f^7$ level which provides photoelectron to start a classical PTR photochemical process [3].

## Materials and Methods

In this research PTR glasses with $Na_2O$-$ZnO$-$Al_2O_3$-$SiO_2$ matrix doped with photosensitizers such as $Tb_4O_7$ (1 mol.%), $Sb_2O_3$ (0,04 mol.%), $Ag_2O$ (0,06 mol.%) were studied. To find the value of glass transition temperature ($T_g$) the scanning calorimeter STA 449 F1 Jupiter (Netzsch) was used. The obtained $T_g$ for the glasses under the study was around 490 °C. Absorption spectra in UV-vis regions were measured with Perkin Elmer Lambda 650 spectrophotometer.

The glass was melted in an electrical furnace in a quarts crucible at the temperature of 1480°C. Optical homogeneity was provided by platinum stirrer. After annealing in muffle furnace glass was cut form of small plates 2 mm width which then were polished. Samples were UV irradiated with mercury lamp and then thermally treated in muffle furnace under 500 °C for 10 hours.

## Results and Discussion

Absorption spectra were measured before (initial), after UV irradiation to mercury lamp for 10 minutes and after heat treatment for 10 hours. Results are presented in figure 1. To verify the contribution of exactly UV radiation in the silver nanoparticles formation, the same glass plate sample was partly UV irradiated and fully heat treated in a furnace. It can be seen that in irradiated part of a sample (Tb 1 mol.%10H 500C UV) there is a broad plasmon resonance absorption peak correlated with silver nanoparticles in glass. For previously processed sample these stages were done twice which resulted in enhanced plasmon resonance absorption peak located at around 430 nm (Tb 1 mol.% after add. treatment).

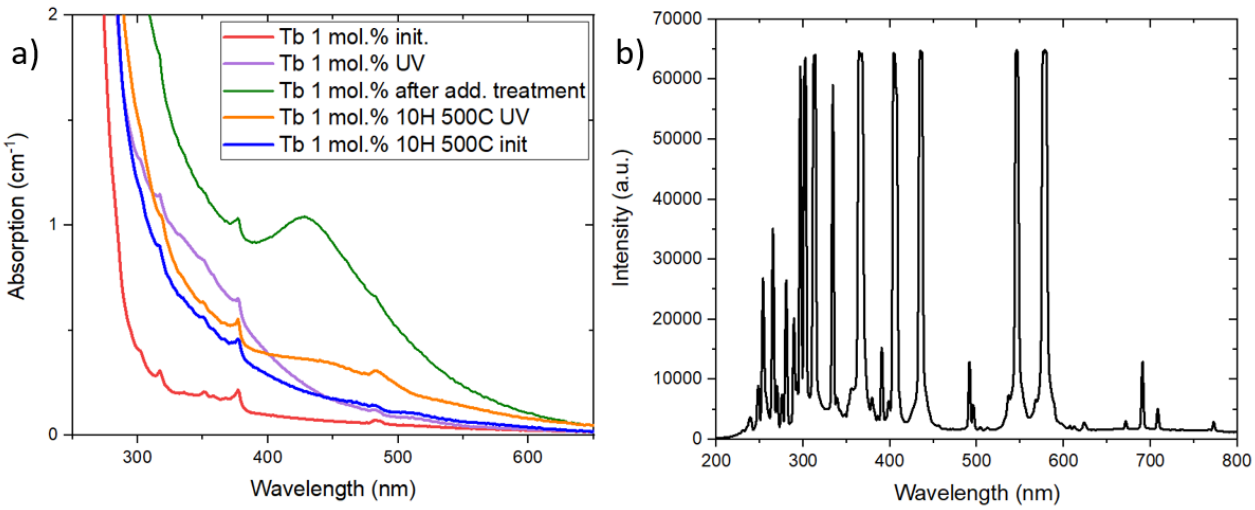


Fig. 1. Absorption spectra for Tb 1 mol.% (init), after UV irradiation (UV) and subsequent heat treatment (10H 500C UV) and after additional treatment (after add. treatment) (*a*) and spectrum of the mercury lamp (b)

From the mercury lamp spectrum (figure 1(b)) it can be concluded that it has exactly the needed wavelength at around 375 nm to excite electron firstly from the ground state to $^5D_3$ and then at around 490 nm to excite further from $^5D_4$ level to $5d4f^7$ as was described above.

## Conclusion

The absorption spectra of PTR glass doped with Tb were measured before, after UV irradiation with a mercury lamp, and after heat treatment of irradiated glasses. There is a plasmon resonance absorption peak at the absorption spectra of the studied glasses located at 430 nm which corresponds to the presence of silver nanoparticles in the studied PTR glass. This indicates that terbium-doped PTR glass exhibits a photosensitivity.

## REFERENCES

1. **Glebov, Alexei L., et al.** Volume Bragg gratings as ultra-narrow and multiband optical filters. Micro-Optics 2012. Vol. 8428. SPIE, 2012.

2. **Kompan, Fedor, et al.** Photo-thermo-refractive glass with sensitivity to visible and near IR radiation. Optical Materials Express 6.12 (2016): 3881-3891.

3. **Dubrovin, Victor, Nikolay Nikonorov, and Alexander Ignatiev**. Bromide photo-thermo-refractive glass for volume Bragg gratings and waveguide structure recording. Optical Materials Express 7.7 (2017): 2280–92

# Experimental study of data transmission in a long-haul passive span fiber-optic line with high information capacity

**A.A. Pozdnyakov** [1], **E.I. Andreeva** [1]

[1] The Bonch-Bruevich Saint-Petersburg State University of Telecommunications, St.Petersburg 193232, Russia

✉me022@mail.ru

**Abstract.** In the course of an experimental study, the possibility of building a line with an information capacity of 1 Tbit/s km using standard components for DWDM systems with nonlinear dispersion compensation was shown. The calculation of the optimal parameters of the system has been carried out. It is shown that for given values of range *L*, chromatic dispersion *D*, transmission rate *B*, it is possible to choose the optimal input power of bit pulses $P_o$, which provides the best signal-to-noise ratio at the reception.

**Keywords:** fiber optic cable, optical fiber, dispersion, optical soliton

## Introduction

The task of implementing the long-haul high-speed transport line remains relevant. Of particular interest is the system built on standardized DWDM-system components. The operation of high-speed communication lines is usually limited by the effect of group velocity dispersion [1-5]. The pulse is broadened, losing energy in the bit interval. Since solitons can maintain their shape due to the balance between nonlinear and dispersive effects in the region of anomalous dispersion of fibers, their use could improve the performance of such communication systems [1-3].

## Theoretical Description

The equation of pulse propagation in an optical fiber in the case of taking into account dispersion, nonlinearity, and losses [1, 2]:

$$i\frac{\partial q}{\partial Z}+\frac{1}{2}\beta_2\frac{\partial^2 q}{\partial T^2}q=-i\Gamma q\,,$$

nonlinear Schrödinger equation, where *q(z, t)* is the pulse amplitude, $\beta_2$ – is the group velocity dispersion vg related to the fiber dispersion parameter *D* by the relation: $\beta_2=-\lambda^2 D/(2\pi c)$, $\lambda$ – is the wavelength, *c* – is the light velocity,

$$\Gamma=\frac{\pi c\alpha T_o^2}{\lambda^2 D}=\alpha L_D,$$

where $\alpha$ – is the optical loss, $L_D$ – is the dispersion length: $L_D = T_o^2/\beta_2$.

where the value of $T_o$ is related to the pulse full width at half maximum $T_{FWHM}$ =1,76 $T_o$.:

In the case of $\Gamma > 1$, a soliton solution of the Schrödinger equation can be obtained under the condition [2-3]

$$P_o=a_0^2\frac{\beta_2}{\gamma T_o^2},$$

$P_o$ – is the initial soliton pulse power, $\gamma$ – is the non-linear parameter, and $a_o=\sqrt{\frac{2\alpha L}{1-exp(-2\alpha L)}}$.

For SSMF (standard single mode fiber) typically $\beta$ = 20 ps$^2$/km, $\gamma$ = 1.2 W$^{-1}$km$^{-1}$, $\alpha$ = 0.023 km$^{-1}$. For transmission length *L* = 100 km, $P_o$ = 20 dBm.

## Computer modeling

Computer modeling allows to identify the mechanisms that determine the performance characteristics of the system. It is shown that the greatest contribution is made by such a nonlinear effect as self- phase modulation (SPM). The use of this effect makes it possible to increase the output optical signal-to-noise ratio (OSNR), which ensures high communication quality, in the absence of the need to turn on the dispersion compensator. Results of computer modeling in

OptiSystem program is presented in fig.1, where Q ~ $OSNR^2$. The optimal initial pulse power is 18 dBm, which is in good agreement with the calculated value.

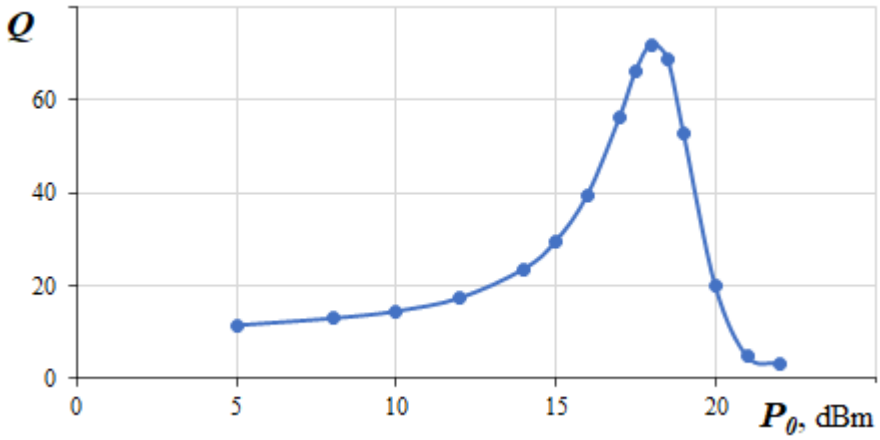


Fig. 1. Dependence of Q-parameter on the pulse input peak power $P_o$. Results of computer simulation

## Experimental Results and Discussion

The study was conducted at wavelength $\lambda$=1536 nm. SSMF was used as the transmission path. The used transponder provided bit rate $B$ = 10 Gbit/s, $L$= 100 km. Losses in the multiplexer did not exceed 6 dB and were compensated by an optical Er-amplifier. The results of OSNR measurements versus the initial power $P_o$ are shown in Fig.2. The best OSNR was obtained at $P_o$=18 dBm, which is in good agreement with computer simulations.

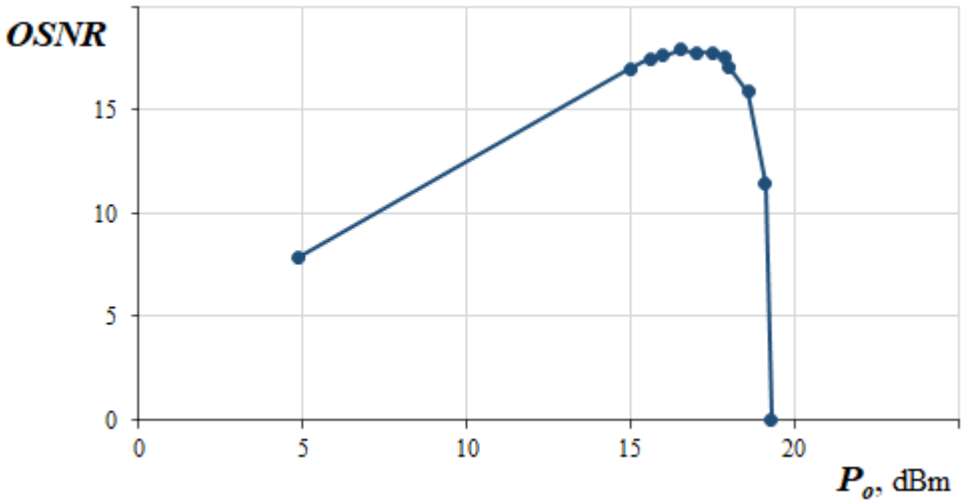


Fig. 2. Dependence of *OSNR* on the input pulse peak power $P_o$.

## Conclusion

During the experimental study, the possibility of constructing a line with an information capacity of 1 Tbit/s km using sources for DWDM systems was successfully demonstrated.

## REFERENCES

1. Agrawal G. Fiber-Optics Communication Systems. 5th Edition. New York, 2021.

2. Agrawal G. Nonlinear Fiber Optics. 6th Edition. Elsevier, 2019.

3. Shcherbakov A.S., Andreeva E.I. Performance Data of Lengthy-Span Soliton Transmission System. Optical Fiber Technology, Vol. 2 (1), P. 127-133, 1996.

4. Andreeva E. I., Bylina M.S., Glagolev S.F. Properties of Temporary Optical Solitons in Optical Fibers and the Possibility of their Use in Telecommunications. Proceedings of Telecommunication Universities. Vol. 4(1) (2018.). P. 5-12.

5. Mollenauer L.F. Solitons in Optical Fibers: Fundamentals and Applications. New York: Academic Press, 2006.

# ANALYTICAL DESCRIPTION OF SPP GENERATION WITH STRUCTURED SUBSTRATES

**Alexey Proskurin** [1✉], **Anton Dyshlyuk** [2], **Andrey Bogdanov**[1,3], **Oleg Vitrik**[2]
[1] School of Physics and Engineering, ITMO University, St Petersburg, Russia;
[2] Institute of Automation and Control Processes (IACP) FEB RAS, Far Eastern Federal University (FEFU) and Vladivostok State University of Economics and Service (VSUES), 690041 Vladivostok, Russia
[3] Engineering University, Qingdao Innovation and Development Center, Sansha road 1777, 266000, Qingdao, Shandong, China
✉alexey.proskurin@metalab.ifmo.ru

**Keywords:** SPP excitation, surface plasmon polaritons, structured substrates.

## Introduction

While surface plasmon polaritons (SPPs) were initially discovered as anomalies of the reflection spectra in the 1900s [1], plasmonics as a distinct research area had not developed until the 1960s. Since then, plasmonics has become an active and rapidly growing field with significant contributions to various scientific areas, including biosensing [2] and Raman spectroscopy [3]. The local increase in the concentration of the electromagnetic field of the SPP further expands the range of possible applications, such as the miniaturization of optical integrated circuits and squeezing optical guided modes at telecommunication frequencies down to the nanoscale [4].

One of the challenges in plasmonics is the efficient generation of SPPs. The SPP generation on flat metal surfaces is achieved using various approaches, such as coupling with prisms, gratings, nanoantennas, and near-field microscopy. However, these methods are limited in their ability to control and manipulate the properties of SPPs [5].

Structured substrates have emerged as a promising approach to overcome these limitations, as they offer additional degrees of freedom in manipulating the SPPs' properties. Structured substrates can take various forms, such as nanohole arrays, nanorod arrays, and periodic gratings, and support different types of SPP modes, including waveguide modes.

Several analytical and numerical methods have been proposed to model the excitation of SPPs on structured substrates [5]. These methods often involve solving complex equations that require significant computational resources or sophisticated analytical techniques, limiting their practical applicability. Therefore, there is a need for simpler and more efficient methods to model SPP generation on structured substrates.

In this work, we propose a new analytical technique that utilizes mode decomposition and the Lorentz reciprocity theorem to describe the generation of SPPs on structured substrates.

## Results and Discussion

The amplitude of the scattered SPP wave reads as [6]

$$a_{SPP} = -\frac{1}{4N_0}\int_{(V)}\left(\mathbf{e_{SPP}}\cdot\mathbf{J}\right)e^{-ik_{spp}z}dV\,, \tag{1}$$

where $\mathbf{e_{SPP}} = e_x^{SPP}\mathbf{n_x} + e_z^{SPP}\mathbf{n_z}$ is the SPP mode's electric field; $e_z^{SPP}(x) = e_0 e^{-\gamma(x)|x|}$; $e_x^{SPP}(x) = e_0\frac{\sqrt{\varepsilon_{Me}}}{\varepsilon_S(x)}e^{-\gamma(x)|x|}$; $e_0 = -h_0\frac{\rho_V}{\sqrt{\varepsilon_{Me}+1}}$; $\rho_V = \sqrt{\frac{\mu_0}{\varepsilon_0}}$; $\mathbf{h_{SPP}} = h_y^{SPP}\mathbf{n_y}$ is the SPP mode's magnetic field; $h_y^{SPP} = h_0 e^{-\gamma(x)|x|}$; $\varepsilon_S(x) = \begin{cases} 1 & \text{if} \quad x \ge 0 \\ \varepsilon_{Me} & \text{if} \quad x < 0 \end{cases}$; $\gamma(x) = \begin{cases} \gamma_{Vac} & \text{if} \quad x \ge 0 \\ \gamma_{Me} & \text{if} \quad x < 0 \end{cases}$; is the arbitrary amplitude; $N_0 = \frac{1}{2}\left|\int_{(S)}\vec{e_{SPP}}\times\vec{h_{SPP}}\cdot\vec{n_z}dS\right|$ is the normalization constant; $\gamma_{Vac} = k\frac{i}{\sqrt{\varepsilon_{Me}+1}}$;

$\gamma_{Me} = -k\frac{i\varepsilon_{Me}}{\sqrt{\varepsilon_{Me}+1}}$ ; $k_{spp} = kn_{spp}$ ; $n_{spp} = \frac{\sqrt{\varepsilon_{Me}}}{\sqrt{\varepsilon_{Me}+1}}$ $\mathbf{n}_x$, $\mathbf{n}_y$ are the unitary vectors; and $\mathbf{J}$ is the current density.

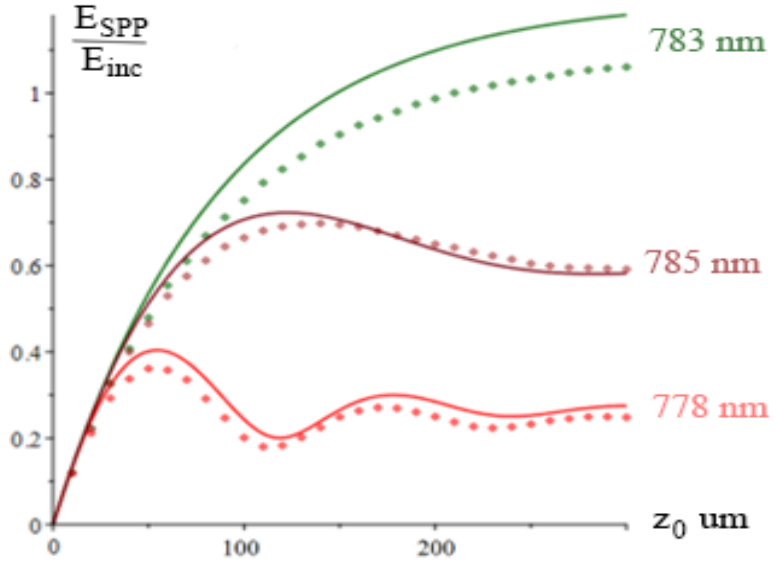


Fig. 1. The normalized value of the electric field component parallel to the plane interface at the end of the grating of length $z_0$. Different colors show calculated dependences for different grating's periods; the resonant period is 783 nm. The solid lines represent the analytical results, the dotted lines are for numerical simulation.

Eq. (1) allows calculating the SPP amplitude even for structured substrates. If the grating's height is small compared to the light free-space wavelength, the grating's period and the penetration depth to the metal, Born's approximation utilizes (1). Results of the corresponding calculations agree with the results of the full-wave numerical simulation, as shown in Fig. 1. In the resonant case, where the grating's period coincides with the SPP's wavelength, the scattering efficiency is minimal while the deviation from the resonant period both decreases the saturated SPP's amplitude and increases oscillations.

## Conclusion

Our approach offers a simple and efficient solution to calculate the SPP excitation efficiency on arbitrary structured substrates, enabling the optimization of SPP-based device performance.

## REFERENCES


1. **Wood, R. W**. "On a remarkable case of uneven distribution of light in a diffraction grating spectra." Proceedings of the Royal Society of London. Vol. 18. No. 1. 1902.
2. **Brolo, Alexandre G**. "Plasmonics for future biosensors." Nature Photonics 6.11 (2012): 709-713.
3. **Talley, Chad E., et al**. "Surface-enhanced Raman scattering from individual Au nanoparticles and nanoparticle dimer substrates." Nano letters 5.8 (2005): 1569-1574.
4. **Sorger, Volker J., et al.** "Experimental demonstration of low-loss optical waveguiding at deep sub-wavelength scales." Nature Communications 2.1 (2011): 331.
5. **Evlyukhin, A. B., and S. I. Bozhevolnyi**. "Point-dipole approximation for surface plasmon polariton scattering: Implications and limitations." Physical Review B 71.13 (2005): 134304.
6. **Snyder, Allan W., and John D. Love**. "Optical waveguide theory". Vol. 175. London: Chapman and hall, 1983.

# Optimization of the multiple quantum well HgTe/CdHgTe heterostructures parameters for the 2D plasmon-phonon generation

**A. O. Rudakov** ✉, **V. Ya. Aleshkin**
Institute for Physics of Microstructures RAS, Afonino, Nizhny Novgorod region, Kstovsky district, Russia.
✉rudackovartur@ipmras.ru

**Abstract** It is shown that in the HgTe/CdHgTe heterostructure the optimal effective band gap of a quantum well for generating plasmons is a slightly exceeding the energy of a longitudinal optical phonon in the barrier.

**Keywords:** plasmon-phonon, heterostructures, plasmon gain, effective band gap.

## Introduction

One of the topical problems of the semiconductor physics is the creation of a compact radiation source operating in the far infrared range. This problem can be solved by generating 2D plasmon-phonons in HgTe/CdHgTe heterostructures with narrow-gap quantum wells (QW). The attractive aspects of plasmon-phonon generation are high modal gains (>$10^4$ cm$^{-1}$) [1] and no need to create waveguides. The lowest value of the threshold concentration required for the generation of plasmon-phonons can be achieved if we consider the structure not with a single QW, but with a multiple quantum well structure [2]. We have studied plasmon-phonons in a structure with one QW and in a superlattice chosen as the limiting case of a multiple quantum well structure.

## Calculation model

Let us consider a plasmon-phonon propagating in the QW plane with the wave vector $\mathbf{q}$ and frequency $\omega$. The polarizability due to the motion of free carriers in a QW can be found using the random phase approximation (RPA) with allowance for a finite collision frequency [3]. The contribution associated with the QW lattice vibrations was taken into account in the QW polarizability. To calculate the QW polarizability in the RPA, the electronic spectrum in the QW is required. To find it, we used the Kane model taking into account deformation effects.

It is known that plasmon-phonons with a wave vector lying in the QW plane have the highest gain in a superlattice. In this case, the dispersion relation has the following form:

$$\tanh\left(\frac{Qd}{2}\right)+2\pi\frac{\mathrm{Re}[\chi_{tot}(\mathbf{q},\omega)]}{\mathrm{Re}[\kappa(\omega)]}Q=0, \qquad (1)$$

where $d$ is the superlattice period, $\chi_{tot}(\mathbf{q},\omega)$ is the QW polarizability associated with free carriers and vibrations of the QW lattice, $\kappa(\omega)$ is the barrier permittivity, $Q^2=q^2-\omega^2\,\mathrm{Re}[\kappa(\omega)]/c^2$. In the limit $d\to\infty$ Eq. (1) yields a dispersion relation for plasmon-phonons in a single QW structure.

Amplification of plasmons due to interband electron transitions is possible if the concentration of nonequilibrium carriers exceeds the threshold concentration.

## Results

A structure with a Cd content of 0.7 in the barrier was considered. The calculation of the band structure showed that the band gap in a 5.3 nm QW is 25 meV, and in a 5 nm QW it is 35 meV. To exclude fast recombination involving optical phonons, it is necessary that the band gap exceeds the energy of the longitudinal optical phonon. The energy of a CdTe-like optical phonon is approximately 22 meV. From the solution of Eq. (1), the spectra of plasmon-phonons in a structure with a single QW and in a superlattice are obtained. We assumed the concentration of nonequilibrium electrons and holes to be the same $n=p$. The spectrum of plasmon-phonons has the low-frequency branch and the high-frequency one. At low energies, the low-frequency branch behaves like $\omega\sim\sqrt{q}$. For the chosen QW parameters, only the high-frequency branch takes part in the amplification, since it crosses the effective band gap $E_{geff}(q)$. The effective band gap is the minimum energy of a plasmon-phonon, above which plasmon-phonon can take part in interband

transitions. The spectra of the high-frequency branches of plasmon-phonons obtained for two effective temperatures of nonequilibrium carriers are shown in Figs. 1.

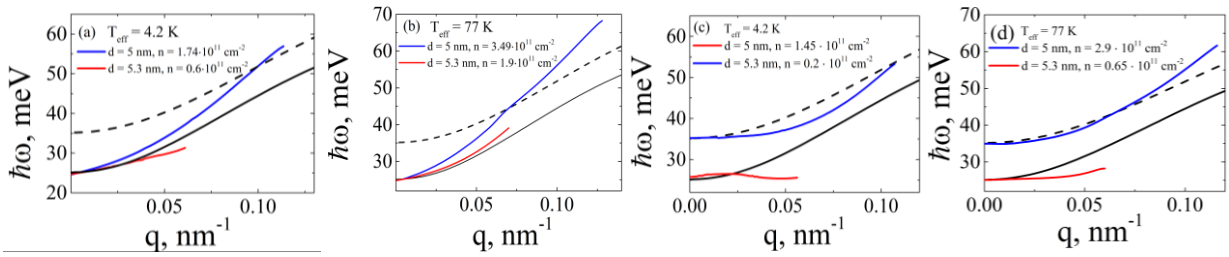


Fig. 1. High-frequency branches of the plasmon-phonon spectrum in the single QW structure (a), (b) and in the superlattice (c), (d). The black dashed and solid lines show the $E_{geff}(q)$ dependences for QW widths of 5 and 5.3 nm, respectively.

The calculated gain spectra of plasmon-phonons for the chosen concentrations of nonequilibrium carriers are shown in Figs. 2. These concentrations are close to the threshold concentrations. It can be seen from Figs. 2 (a)–(b) that in the single-well structure, a decrease in the band gap led to a decrease in the threshold concentration of nonequilibrium carriers. In a narrower gap QW, the gain begins at lower energies. This is due to the fact that, in narrower gap QWs, the intersection of the plasmon spectrum with the $E_{geff}(q)$ dependence occurs at lower energies and wave vectors.

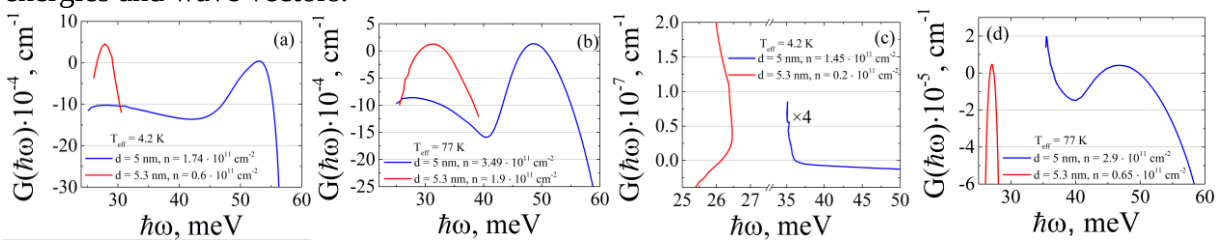


Fig. 2. The gain spectra of plasmon-phonons calculated for two $T_{eff}$ for the single QW structure (a), (b) and superlattice (c), (d).

From Figs. 2 (c)-(d) it can be seen that the transition from a single QW structure to a superlattice leads to an even greater decrease in the threshold concentration of nonequilibrium carriers. Thus, the optimal structure for generating plasmon-phonons is a superlattice with a QW band gap of 25 meV. For a given band gap, the concentration of nonequilibrium carriers close to the threshold concentration in a single QW structure is $6\cdot10^{10}$ cm$^{-2}$ at $T_{eff} = 4.2$ K and $1.9\cdot10^{11}$ cm$^{-2}$ at $T_{eff} = 77$ K. In a superlattice with a band gap of 25 meV the concentration of nonequilibrium carriers is $2\cdot10^{10}$ cm$^{-2}$ at $T_{eff} = 4.2$ K, $1.9\cdot10^{11}$ cm$^{-2}$ at $T_{eff} = 77$ K.

## REFERENCES


1. **K. Kapralov, G. Alymov, D. Svintsov, and A. Dubinov**, J. Phys.: Condens. Matter 32, 065301 (2020).
2. **Rudakov, A. O., Aleshkin, V. Y., Gavrilenko, V. I.** Journal of Optics, 24, 075001 (2022).
3. **V. Ya. Aleshkin, G. Alymov, A. Dubinov, V. Gavrilenko, and F. Teppe**, J. Phys. Commun. 4, 115012 (2020).

# The subwavelength optical elements optimization for the formation of specified diffraction patterns using high-performance computer systems

**D. A. Savelyev** [1,2]✉

[1] Samara National Research University, Samara, Russia;

[2] Image Processing Systems Institute - Branch of the Federal Scientific Research Centre "Crystallography and Photonics" of Russian Academy of Sciences, Samara, Russia

✉dmitrey.savelyev@yandex.ru

**Abstract.** The diffraction of optical vortices on annular gratings of variable height was investigated in this paper. It is shown that it is possible to optimize the relief height of the subwavelength elements in such a way that the formation of both a narrow focal segment and an optical trap is observed.

**Keywords:** subwavelength optical elements, optical vortices, FDTD, optical trap.

**Funding:** This research was funded by the Ministry of Science and Higher Education within the State assignment (project No. FSSS-2023-0006).

## Introduction

Vortex beams are laser radiation of a special structure [1], the distinctive feature of which is the presence of singular points at which the phase is not defined and the amplitude is zero. It is known that optical vortices are used to solve problems of sharp focusing [2], to form a reverse energy flow including using subwavelength axicons with different twist angles [3], for optical transmission of information [4], laser processing [5], for optical capture and manipulation [6, 7], including obtaining three-dimensional traps [7].

To form structured vortex radiation (in particular optical traps) one can use axisymmetric diffractive structures, including axicons [8], helical phase plates [9], and multiorder diffractive optical elements [10]. It should also be noted that axicons and their combinations with lenses are used to form focal spots with increased depth.

The diffraction of optical vortices of the first order on subwavelength optical microelements with a variable height of the relief to form the required distribution on the optical axis (including optical traps) was investigated in this paper. Numerical calculations of the propagation of laser radiation (3D) were performed using the finite differences in the time domain method (FDTD) using high-performance computer systems. The calculations were carried out on a computing cluster with a capacity of 850 Gflop.

## Materials and Methods

The radiation wavelength $\lambda = 1.55$ μm was considered for numerical simulation, and the Laguerre-Gauss (1,0) mode with circular polarization was considered as the input beam (the sign of the circular polarization is opposite to the sign of the introduced vortex phase singularity). In this case, a circular focal spot should form on the optical axis [7].

The size of the computational domain was 11.6λ. The computational domain is surrounded on all sides by an absorbing PML layer 1.2λ in size. The spatial sampling step was chosen to be λ/30, the time sampling step was λ/(60c), where c is the speed of light. The refractive index n of the subwavelength elements was 3.47. The height of the relief of the binary element h, corresponding to the phase π radians, in this case is equal to 0.2λ. The element lattice period is 1.05λ.

## Results and Discussion

Figure 1 shows the diffraction patterns of an optical vortex with circular polarization on the considered subwavelength optical elements. The diffractive axicons with a height $h = 0.2\lambda$ (base element) and $h = 1.7\lambda$ considered, direct ring grating (change in the height of the relief rings from the maximum in the center $h_{max} = 1.7\lambda$, to the minimum at the edge $h_{min} = 0.2\lambda$ with step 0.3λ), as well as a reverse ring grating (similar step and height, but from the minimum in the

center to the maximum at the edge). The size of the focal spot on the optical axis was estimated from the full width at half maximum (FWHM) of the intensity, depth of focus (DOF) is similar.

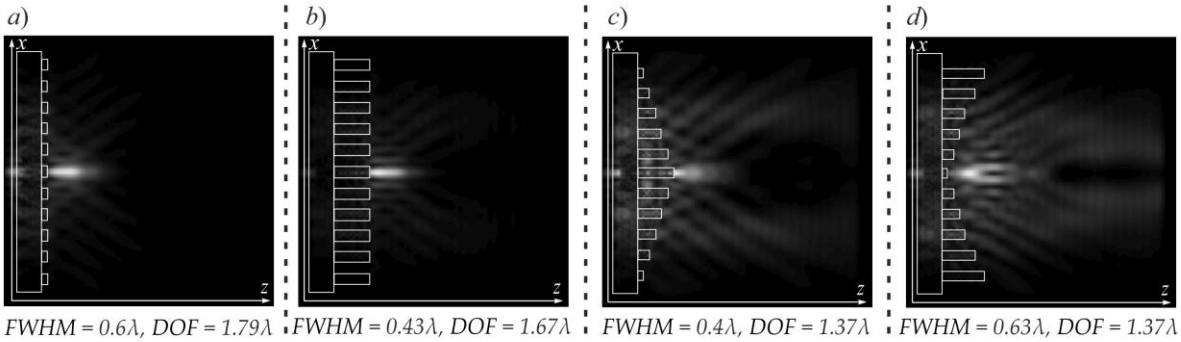


Fig. 1. The longitudinal cross section (xz) of optical vortices propagation: the diffractive axicon, h = 0.2λ (*a*) and $h_i$ = 1.7λ (*b*), the direct ring grating (*c*), reverse ring grating (*d*)

It should be noted that an increase in the relief height of the diffractive axicon led to a reduction in the focal spot size (FWHM = 0.43λ). The minimum focal spot size for the considered cases was FWHM = 0.4λ for a direct ring grating, which is 33.3% better than the case of a diffractive axicon with height h = 0.2λ. In the case of a reverse ring grating, the formation of an optical trap is observed.

## Conclusion

The finite difference time domain method was used in this paper to optimize the height of sub-wavelength ring gratings in order to form the required distributions in the near diffraction zone. It was shown that it is possible to choose the height in such a way that the formation of both a narrow focal segment and an optical trap is observed. The minimum focal spot size for the considered cases was FWHM = 0.4λ for a direct ring grating.

## REFERENCES

1. **Shen Y. et al.**, Optical vortices 30 years on: OAM manipulation from topological charge to multiple singularities, Light: Science & Applications. 8(1) (2019) 90.

2. **Rui G., Yang B., Ying X., Gu B., Cui Y., Zhan Q.**, Numerical modeling for the characteristics study of a focusing ultrashort spatiotemporal optical vortex, Optics Express 30(21) (2022) 37314–37322.

3. **Degtyarev S. A., Savelyev D. A.**, Generation and focusing of a second-order vector beam using a subwavelength optical element, Computer Optics. 46(1) (2022) 39–47.

4. **Khonina S. N., Karpeev S. V., Butt M. A.**, Spatial-light-modulator-based multichannel data transmission by vortex beams of various orders, Sensors. 21(9) (2021) 2988.

5. **Khonina S. N.**, **Ustinov A. V., Volotovskiy S. G., Ivliev N. A., Podlipnov V. V.**, Influence of optical forces induced by paraxial vortex Gaussian beams on the formation of a microrelief on carbazole-containing azopolymer films, Applied Optics. 59(29) (2020) 9185–9194.

6. **Paez-Lopez R., Ruiz U., Arrizon V., Ramos-Garcia R.**, Optical manipulation using optimal annular vortices, Optics Letters. 41(17) (2016) 4138-4141.

7. **Savelyev D. A., Karpeev S. V.**, Development of 3D Microstructures for the Formation of a Set of Optical Traps on the Optical Axis, Photonics. 10(2) (2023) 117.

8. **Khonina S. N., Kazanskiy N. L., Khorin P. A., Butt M. A.**, Modern types of axicons: New functions and applications, Sensors. 21(19) (2021) 6690.

9. **Balčytis A. et al.**, Hybrid curved nano-structured micro-optical elements, Optics Express. 24(15) (2016) 16988–16998.

10. **Kazanskiy N. L., Khonina S. N., Karpeev S. V., Porfirev A. P.**,Diffractive optical elements for multiplexing structured laser beams, Quantum Electronics. 50(7) (2020) 629.

# Optimization of a prism coupler for a THz photonic integrated metamaterial Si waveguide: simulation and experiment

**S. V. Seliverstov [1✉], S. S. Svyatodukh [1,2], A. N. Prikhodko [1,2], A. S. Shurakov [1,2], E. D. Sheveleva [1,2], and G. N. Goltsman [1,2]**

[1] Moscow State Pedagogical University, Moscow, Russian Federation;

[2] National Research University Higher School of Economics, Moscow Institute of Electronics and Mathematics, Moscow, Russian Federation

✉sv.seliverstov@mpgu.su

**Abstract.** The use of terahertz radiation to create data transmission systems with ultra-high transfer rate still remains a kind of *terra incognita* of our time. The main difficulty in using terahertz radiation for these purposes is associated with high losses in standard metal waveguides at these frequencies. One of the possible solutions is the use of all-dielectric waveguides. So, the coupling waveguides of this type with other devices is an actual and scientifically significant task. In this paper we present the results of simulating and measuring the insertion loss of a coupling prism interface for a terahertz waveguide based on metamaterial high resistive silicon platform. The obtained $S_{21}$ parameter value of -0.5 dB for a coupler apex width of 90 μm and a coupler length of 3500 μm at frequency of 150 GHz is in good agreement with the experimentally measured one. These devises will be a part of the future next-generation terahertz data communication system with a high data transfer rate.

**Keywords:** terahertz photonics, waveguide coupling, photonic integrated circuit, metamaterial waveguide.

**Funding:** The study was supported by a grant from the Russian Science Foundation No. 21-72-10119, https://rscf.ru/project/21-72-10119/.

## Introduction

Latest advances in such modern fields as internet of things or big data processing have led to the need to dramatically increase the rate of wireless data transmission. The solution to this problem is possible by transfer to higher frequencies of the carrier signal. In particular, the use of terahertz (THz) range of the electromagnetic radiation spectrum looks promising. For the effective use of radiation in this range, it is necessary to solve a number of problems related primarily to the fact that THz radiation is strongly absorbed by water vapor contained in the atmosphere. There are some transparency windows in the THz water vapor absorption spectrum, but their use makes it possible to create a THz data transfer system that operates only at short distances (about the size of a room) [1]. These systems will operate like Wi-Fi, but will have a much higher data transfer rate. For example, in [2], a such system with data transfer rate reaches of up to 1 Tbit/s is demonstrated. Another challenge is that metal waveguides used for such tasks are not acceptable in THz range, because they demonstrate a rather high insertion loss in this range. An obvious solution under such conditions is the use of all-dielectric waveguides [3]. In this regard, matching waveguides of this type with other devices is an actual and scientifically significant task.

## Materials and Methods

In this paper we present the results of simulating and measuring the insertion loss of a coupling interface based on a prism geometry for a THz waveguide formed on metamaterial high resistive silicon (HRSi) platform. The parameters of the waveguide and the effective medium around it were chosen in such a way that a single $TE_1$ radiation mode could propagate inside it. Details can be found in [4]. We used the finite element method in the simulation. The simulation frequency was 150 GHz. The process of manufacturing of the experimental samples consisted of applying a Cr mask, plasma-chemical etching of Si unprotected by the mask, and subsequent separation of the substrate into individual chips. A photograph of the fabricated sample taken from an electron microscope is shown in Fig. 1(b). In the experiment, the fabricated waveguide sample with prism couplers on both sides of the waveguide was installed in a metal holder, which made it

possible to place the coupler exactly in the center of a rectangular metal waveguide. A backward wave oscillator was used as a radiation source. A Schottky diode was used as a detector.

## Results and Discussion

At the 150 GHz frequency, the dependences of the $S_{21}$ parameter on the width of the coupler apex for various values of its length were simulated. The measurements were carried out with a sample in which the width of the coupler apex was 90 µm and the coupler length was 3500 µm. The results of the simulation and experiment is shown on Fig. 1(a).

*a*) *b*)

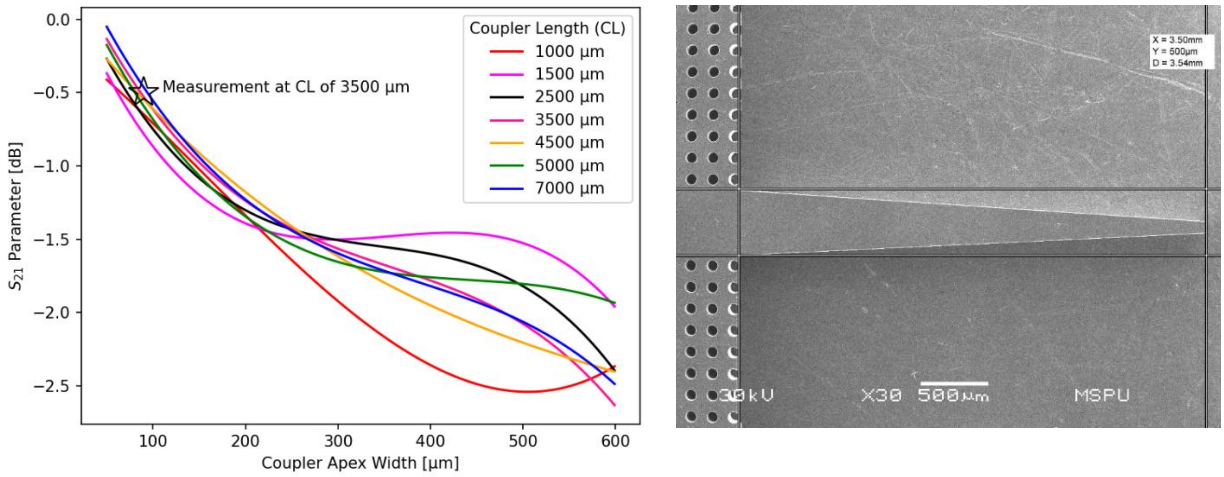


Fig. 1. Dependencies of the S21 parameter on the coupler apex width at different values of the prism length (*a*) and SEM photos of a fabricated structures (*b*)

One can see that the insertion loss decreases when the coupler apex width goes down. This can be explained by a smoother change in the average value of the permittivity in the direction along the waveguide at small values of the coupler apex width. This results in a better match between the rectangular metal and dielectric waveguides. The measured $S_{21}$ parameter value of -0.5 dB for the sample under study is in good agreement with the simulation.

+

## Conclusion

The proposed prism coupling interface have demonstrated low insertion loss at THz band. The developed structures will be the basic elements of an array of THz emitters with active adjustment of the radiation pattern. These devises will be a part of the future next-generation THz data communication system with a high data transfer rate.

## REFERENCES


1. **Boronin, P., Petrov, V., Moltchanov, D., Koucheryavy, Y., & Jornet, J. M.,** Capacity and throughput analysis of nanoscale machine communication through transparency windows in the terahertz band. Nano Communication Networks, 5(3), (2014), 72-82.

2. **Corre, Y., Gougeon, G., Doré, J. B., Bicaïs, S., Miscopein, B., Faussurier, E., ... & Bader, F.** Sub-THz spectrum as enabler for 6G wireless communications up to 1 Tbit/s. In 6G Wireless Summit (2019, March).

3. **Gao, W., Yu, X., Fujita, M., Nagatsuma, T., Fumeaux, C., & Withayachumnankul, W.,** Effective-medium-cladded dielectric waveguides for terahertz waves. Optics express, 27(26), (2019), 38721-38734.

4. **Seliverstov Sergey, V., Svyatodukh Sergey, S., Prokhodtsov Aleksey, I., & Goltsman Grigory, N.** Simulation of terahertz photonic integrated antenna. St. Petersburg Polytechnic University Journal. Physics and Mathematics, 60(3.2), (2022), 370-374.

# Classifying Topology in Waveguide Lattices using Deep Learning

**E. O. Smolina** [1,2✉], **L. A. Smirnov** [1,2], **A. S. Khorkin** [1], **N. S. Kulikov** [1], **D. A. Smirnova** [1,2]

[1] Department of Control Theory, Nizhny Novgorod State University, Gagarin Av. 23, Nizhny Novgorod, 603950 Russia;

[2] Institute of Applied Physics, Russian Academy of Science, Nizhny Novgorod 603950, Russia

✉smolina@ipfran.ru

**Abstract.** We utilize deep learning techniques to classify topological phases in leaky photonic lattices based solely on intensity measurements, eliminating the need for complex phase retrieval procedures. We developed a neural network that accurately identifies topological properties in dimerised waveguide arrays with leaky channels, under realistic experimental conditions. We investigate the use of transfer learning to train models on clean data and apply them to disordered systems, reducing the requirement for extensive training on each new system.

**Keywords:** deep learning, photonic lattice, topological phases.

**Funding:** This work was supported by the Ministry of Education and Science under the contract 0729-2021-013. E.O. Smolina acknowledges support from the BASIS Foundation (grant 22-1-5-80-1).

Topological photonics offers promising opportunities for efficient optical information processing, thanks to the resilience of topological states of light against disorder [1]. These states are characterized by integer topological invariants, making it crucial to accurately probe them for both fundamental and practical purposes. To overcome the difficulties of traditional methods like band tomography, we suggest utilizing deep learning techniques as an alternative approach.

We focus on dimerised waveguide arrays with feasible leaky channels (SSH model, see Fig.1 *a)*) and aim to classify a finite sample by determining the topology of the sample edges from the intensity distribution measured at the output of $N_c$ central waveguides (where $N_c<N$ and N is the total number of waveguides in the SSH array). The edge of the main lattice can be either trivial or non-trivial, depending on the lattice termination by strong or weak bond. The non-trivial edge supports midgap topological edge states, and there are four possible configurations: 01 (left trivial, right non-trivial), 11 (left non-trivial, right non-trivial), 10 (left non-trivial, right trivial), and 00 (left trivial, right trivial).

Previous research [2] has demonstrated the possibility of calculating the topological invariant of a band in certain systems using the output field distribution projector. However, this method requires knowledge of the complex-valued field, which can be difficult to retrieve. To address this challenge, we have developed a new approach that utilizes the deep learning techniques to determine the lattice topology solely based on the output intensity profile. Firstly, we generated a dataset by solving the tight-binding equations numerically at different values of coupling coefficients and auxiliary environment. Our input consisted of a single waveguide, which we assumed could be shifted from the center of the lattice. Further, these datasets were utilized to train the neural network, which architecture is depicted in Fig.1 *d*))

We investigated how the accuracy of the developed network varies with a propagation distance (see Fig.1 *b)*). Our results indicate that as this parameter increases, the accuracy of the algorithms also improves, consistent with theoretical predictions [2]. Deep learning methods show sufficient accuracy, since they have a large number of parameters, which provides better fine-tuning the neural network. Our approach demonstrates promising results in classifying topological phases in leaky photonic lattices, achieving an accuracy of over 90%.

To investigate the performance and generalization abilities of our models, we employed a transfer learning approach allowing for the reuse of pre-trained models, which reduces the computational cost and time required for training. This is particularly beneficial in the context of disordered systems, where obtaining large datasets for training can be challenging. We introduce disorder into the Hamiltonian coefficients of the main array, and we consider two types of disorders: the off-diagonal disorder, and the disorder in diagonal elements (diagonal) and fix the propagation distance at L = 10.6. Incorporating disorder involves introducing a random variable to the coefficients of the Hamiltonian. Further, to we train the neural network using a non-

disordered array and test it for the disordered lattice (see Fig. 3 *c*)). The accuracy curves exhibit a comparable behaviour for both disorder types, with a decline in accuracy as the disorder amplitude increases. However, there exists a range of disorders where the previously trained neural network can be utilized with a high confidence.

Overall, our neural network can accurately determine topological properties from the output intensity distribution, even in realistic experimental conditions. The use of transfer learning allows us to train the models on clean data and then apply them to disordered systems, reducing the need for extensive training on every new system. These findings highlight the potential of our approach for a wide range of applications in various fields, such as photonics, condensed matter physics, and quantum computing.

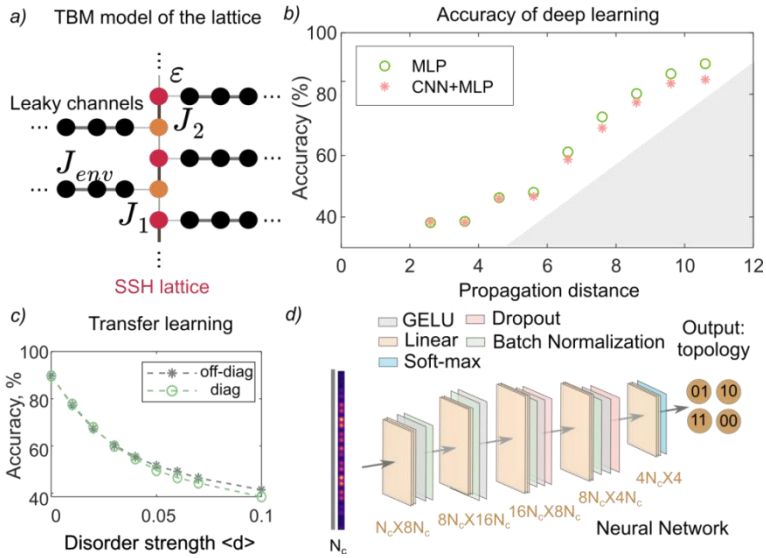


Fig. 1. *a)* Schematic of a photonic lattice with tunable radiative losses. The red and orange circles depict the main array – a one-dimensional SSH lattice. Black circles illustrate auxiliary arrays constituting leaky channels. The different dashing between the elements denote different coupling strength in the corresponding tight-binding model. (c) Accuracy of machine learning methods vs propagation distance. Transfer learning for the disordered lattice. We train neural network at the absence of disorder ⟨ d⟩ = 0 and test it at different values of disorder. Scheme of the convolutional neural network, which accepts the intensity distribution at the output facet of the lattice in the input and determines topology its edges.

**Acknowledgments**

This work was supported by the Ministry of Education and Science under the contract 0729-2021-013. E.O. Smolina acknowledges support from the BASIS Foundation (grant 22-1-5-80-1).

## REFERENCES

1. **Ozawa T., Price H.M., Amo A., Goldman N., Hafezi M., Lu L.,Rechtsman M.C., Schuster D., Simon J., Zilberberg O., and Carusotto I.,** Topological Photonics, Reviews of Modern Physics 91, (2019) 015006.

2. **Smirnova D.A., Leykam D.**, Probing Bulk Topological Invariants Using Leaky Photonic Lattices, Nature Physics 17, (2021) 632-638.

# Influence of structural disorder on the metamaterial regime

**M. A. Sogrin** [1✉], **M. V. Rybin** [1,2], **E. E. Maslova** [1]
[1] School of Physics and Engineering, ITMO University, St. Petersburg 197101, Russia;
[2] Ioffe Institute, St. Petersburg 194021, Russia
✉matvey.sogrin@metalab.ifmo.ru

**Abstract.** We present the stability of the $\varepsilon$-near-zero regime in TM polarization (the magnetic field oscillates along the rod axis). We show that the homogeneous mode in the metamaterial regime is resistant not only to a change in the shape of the structure, but also to the removal of the elements inside the structure. However, an important issue for application is the influence of structural disorder since defects in the position of structural elements are possible in real structures. We investigate the influence of the disorder degree on the stability of the homogeneous mode. The $\varepsilon$-near-zero regime is less stable in a structure with parameters close to the boundary parameters of the "photonic crystal - metamaterial" transition. Although the homogeneous mode collapses at a fixed frequency, when the frequency is changed to a lower one, we can observe a homogeneous mode in a disordered structure. Since the change in frequency is insignificant, for real structures this can mean that the $\varepsilon$-near-zero regime is resistant to the introduction of structural disorder.

**Keywords:** metamaterials, homogeneous mode, photonic crystals, epsilon-near-zero metamaterials, phase transition

**Funding:** This work was supported by the Russian Science Foundation (grant no. 21-19-00677).

## Introduction

Metamaterials are materials created artificially in such a way to achieve parameters that could not be achieved in natural materials. A few examples of such parameters include dielectric permittivity and magnetic permeability. There has been a growing interest in structures with one or more parameters having a value close to zero, mostly due to the fact that they could be used for various applications, such as new types of beam steerers, modulators, band-pass filters, lenses, microwave couplers, and antenna radomes [1]. It is important to note that real metamaterial structures are prone to defects in the position of structural elements; thus, a considerable issue of metamaterial development is structural disorder. The impact that defects have on metamaterial structures has been studied [2]; however, to the best of our knowledge, the effect that structural disorder has on the homogeneous mode in dielectric metamaterials has not yet been investigated.

In this work, we study the stability of the homogeneous mode in $\varepsilon$-near-zero metamaterial in TM polarization (the magnetic field oscillates along the rod axis). We demonstrate that the homogeneous mode in the metamaterial regime is independent on the shape of the structure or the presence of the elements inside the structure. We investigate the influence of the disorder degree on the stability of the homogeneous mode and conclude that the $\varepsilon$-near-zero regime is less stable in a structure with parameters close to the boundary parameters of the ”photonic crystal - metamaterial” transition.

## Materials and Methods

Multiple scattering theory was used to calculate the distribution of electromagnetic fields [3]. For each particle, there is a correlation between the amplitude of the incident field and the scattered field. Those values are connected by the equation, which can be solved using linear algebra methods [4]. It is important to note that a self-consistent equation considers all acts of scattering and rescattering by all particles. Further, the multiple scattering theory can be easily extended to a conditional number of particles.

In this work, we consider square-shaped structures consisting of dielectric rods with radius r and dielectric permittivity $\varepsilon$, which are located at the nods of a square lattice, lattice constant a. There are two types of square-shaped structures considered in this work: a uniformly filled structure (hereinafter referred to as a continuous structure) and a square with rods removed from the center (hereinafter referred to as a hollow structure). Continuous structures consist of

approximately 1600 rods, and hollow structures consist of approximately 1300 rods. Dielectric permittivity $\varepsilon$ in the examined structures ranges from 30 to 50, while fill factor r/a ranges from 0.07 to 0.1.

## Results and Discussion

We analyze the distribution of the electromagnetic field in TM polarization (the electric field oscillates along the axis of the rods) in the structure with $\varepsilon$ = 30 and r/a = 0.1. Due to the fact that the homogeneous mode in metamaterial structure is independent of shape [5], we are able to remove the rods from the center of the structure in order to investigate field behavior. It was discovered that in the metamaterial regime, the homogeneous mode fills the entire volume of the structure and is independent on the orientation of the crystal axes.

As was mentioned before, there is a probability of defects in real metamaterial structures. Thus, there was a need to imitate such defects during the research. A disorder was put in the structure artificially by adding a value of the shift $\Delta t$ to the coordinates of the rods, both by the x axis and by the y axis. The shift is given by $\Delta t = R \cdot \sigma$, where $\sigma$ is the disorder degree and R is a random variable from the range of [-1; 1]. Figure 1 demonstrates the difference in homogeneous mode observed in the structure with different sets of parameters. As can be seen, for the structure with $\varepsilon$ = 40 and r/a = 0.07 the homogeneous mode collapse is noticeable for $\sigma$ = 0.002, while for the structure with $\varepsilon$ = 50 and r/a = 0.1 the homogeneous mode collapse is only reached with $\sigma$ = 0.005. These results conclude that the homogeneous mode collapse rate is lower for greater $\varepsilon$ values. As shown in the work [6], a change in the fill factor by 0.001 is sufficient to initiate the transition from a metamaterial to a photonic crystal. Hence, it can be assumed that the rate of the collapse of the homogeneous mode in the metamaterial structure is correlative to the proximity of the parameters of the structure to the boundary of the phase transition.

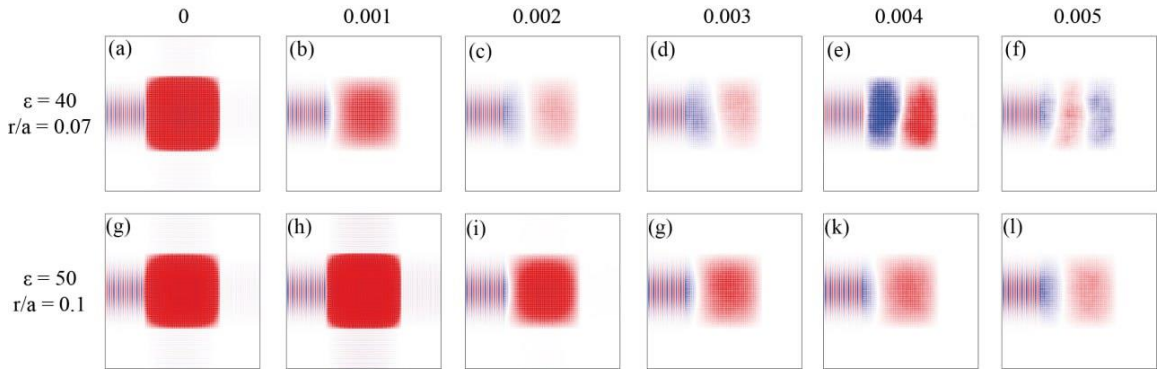


Fig. 1. Dependence of electromagnetic field intensity on the structural disorder degree $\sigma$ in metamaterial structure with various sets of parameters: (a)-(f) dielectric permittivity $\varepsilon$ = 40 and filling factor $r/a$ = 0.07; (g)-(l) dielectric permittivity $\varepsilon$ = 50 and filling factor $r/a$ = 0.1 .

## Conclusion

Thus, we have investigated the stability of the $\varepsilon$-near-zero regime in TM polarization (the magnetic field oscillates along the rod axis). We have shown that the homogeneous mode in the metamaterial regime is unaffected by a change in the shape of the structure as well as the removal of the elements inside the structure. We have investigated the influence of the disorder degree on the stability of the homogeneous mode. It was discovered that the $\varepsilon$-near-zero regime is less stable in a structure with parameters close to the boundary parameters of the "photonic crystal - metamaterial" transition. Although the homogeneous mode collapses at a fixed frequency, when the frequency is changed to a lower one, we can observe a homogeneous mode in a disordered structure. Since the change in frequency is insignificant, for real structures this can mean that the $\varepsilon$-near-zero regime is resistant to the introduction of structural disorder.

## REFERENCES


1. **Mendhe S. E., Kosta Y. P.** Metamaterial properties and applications //International Journal of Information Technology and Knowledge Management. – 2011. – Т. 4. – №. 1. – С. 85-89.

2. **Nguyen V. C., Chen L., Halterman K.** Total transmission and total reflection by zero index metamaterials with defects //Physical review letters. – 2010. – Т. 105. – №. 23. – С. 233908.

3. **Gao X. et al.** Formation mechanism of guided resonances and bound states in the continuum in photonic crystal slabs //Scientific reports. – 2016. – Т. 6. – №. 1. – С. 1-7.

4. **Dmitriev A. A., Rybin M. V.** Combining isolated scatterers into a dimer by strong optical coupling //Physical Review A. – 2019. – Т. 99. – №. 6. – С. 063837.

5. **Maslova E. E., Limonov M. F., Rybin M. V.** Dielectric metamaterials with electric response //Optics letters. – 2018. – Т. 43. – №. 22. – С. 5516-5519.

6. **Li S. V., Kivshar Y. S., Rybin M. V.** Toward silicon-based metamaterials //ACS Photonics. – 2018. – Т. 5. – №. 12. – С. 4751-4757.

# Features of express control of volatile hydrocarbon media and their mixtures in visible light

**G. V. Stepanenkov[1]✉, D. V. Vakorina[1] and V. V. Davydov[1, 2]**
[1]The Bonch-Bruevich Saint Petersburg State University of Telecommunications, Saint Petersburg, Russia.
[2] Peter the Great Saint-Petersburg Polytechnic University, Saint Petersburg, Russia
✉ 261199g@gmail.ru

**Abstract**. The necessity of developing new techniques for the express control of hydrocarbon media and their mixtures, especially volatile ones, is substantiated. The problems that arise when controlling the state of volatile hydrocarbon media using the phenomenon of refraction are noted. A new technique for determining the state of volatile hydrocarbon media and their mixtures has been developed. The use of the new method allows to determine the composition and percentage content of the components in hydrocarbon mixtures. The design of a small-size refractometer for realization of the new technique is developed. The results of experimental research are presented.

**Keywords:** hydrocarbon medium, mixture, refraction, express control, refractive index, visible light, light-shadow boundary, concentration, measurement error.

## Introduction

The reduction of energy resources in the world, as well as high prices of raw materials have led to the need for their careful use. One of the priority directions in the field of their rational use is the development of fast and reliable methods of express - control of the state of condensed media. It should be noted that express - control is now in demand in many areas of human activity. In recent years, a number of rather stringent requirements have become imposed on the instruments and methods of express control. The main of them is connected with the fact that measurements of various parameters of the medium did not introduce irreversible changes in it. Almost for all liquid media - it is necessary to obtain a confirmation of the results of express control on devices of high resolution in a special laboratory. In addition, the methods used in express control should be applicable to the study of a large number of media. The error of measurement of parameters should be no more than 1.5 %. These requirements are currently satisfied by only two methods: nuclear magnetic resonance (NMR) and refraction [1, 2]. Refractometers have an undeniable advantage over small-sized NMR spectrometers and relaxometers in size, mass, and cost [1-3].

## Measurement technique and refractometer design

For the light-shade boundary, by which we will measure the refractive index $n_m$ we will use daylight (for example, radiation from the Sun). In its spectrum there is a yellow line Na ($\lambda = 589.3$ nm), on which measurements of refractive indices of condensed media are made for comparison with standard ones made in laboratories. This requires that light enters only the face of one of the prisms. The second prism must not receive light. As a result, the light-shadow boundary is formed at the output of prism 1 (lower prism) and $n_b$ is measured. Then the light coming to prism 1 is blocked and the light goes to prism 2 (upper prism) and $n_t$ is measured. The temperature $T$ of the medium under study is constantly monitored. During our measurements of $nt$ and $n_b$ it is necessary to realize everything very quickly (in 6-8 seconds), so that significant movements between the media in the measured layers do not occur. In our proposed sealed volume evaporation of volatile hydrocarbon media will not occur in such a time. The temperature also does not change so quickly. To determine the concentrations of the media in the mixture, we use the refraction equation:

$$n_m = K_1 n_1 + K_2 n_2 + \ldots\ldots + K_n n_n \qquad (1)$$

where $n_m$ is the refractive index of the medium measured at the initial moment ($n_m = n_t = n_b$), $n_1$, $n_2$ ..... $n_n$ are the refractive indices of the media of which the mixture under study may consist,

$K_1$, $K_2$ ..... $K_n$ are the coefficients that characterize the relative content of various media in the mixture under study (in case it is necessary to determine the percentage content, these coefficients are multiplied by 100%). Experience with volatile hydrocarbon media and analysis of the results of various studies showed that in equation (1) two terms should be left initially:

$$n_m = K_1 n_1 + K_2 n_2 \tag{2}$$

Taking into account our developed measurement technique and the data obtained, equation (2) takes the following form:

$$n_m = K_1 n_b + K_2 n_t \tag{3}$$

For practical implementation of our developed method, we assembled a new optical design of the laboratory refractometer layout. In the design, the possibility of placing the liquid medium in a sealed volume, which is located between two prisms, was realized. Also, control of the visible light entering the two prisms was realized (possibility to measure the refractive index of the medium using the upper or lower prism). Fig. 1 (*a*, *b*) shows the refractometer block diagram and the course of optical beams for two cases of measurement: (*a*) – $n_t$, (*b*) – $n_b$.

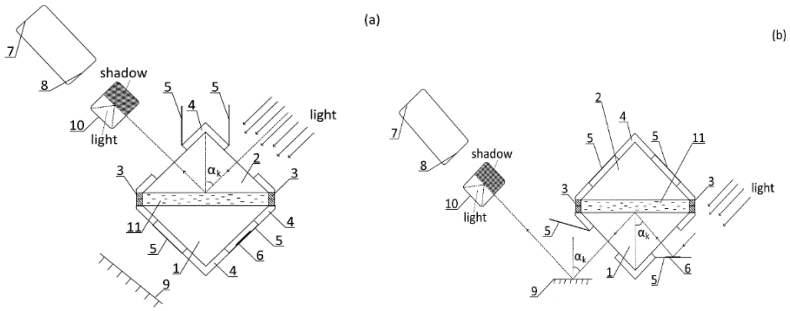


Fig. 1. Schematic diagram of the optical part of the refractometer and ray path for the upper (*a*) and lower (*b*) prisms: 1 - lower triangular prism (material leucosapphire), 2 - upper triangular prism (material leucosapphire), 3 - silicone spacers, 4 - rotating prism mount, 5 - closing flap, 6 - mirror, 7 - eyepiece, 8 - lens on movable mount, 9 - mirror, 10 - plate for registration of the light-shade border, 11 - medium under study.

## Conclusion

The analysis of the results of experimental studies showed the adequacy of our developed technique for determining the state of hydrocarbon media, as well as the composition of two-component and three-component mixtures and their respective concentrations during express control.

It should be noted that the presented solution of the problem of controlling the condition of volatile hydrocarbon media significantly expands the possibilities of express control using the refraction phenomenon. In the future, it is possible to expand the possibilities of the developed technique to determine the composition and concentrations of the components in the mixtures consisting of four or more hydrocarbon media.

## REFERENCES

1. **Karabegov M. A.,** A method of increasing the accuracy of analytical instruments by structural correction. Measurement Techniques, 2009, V. 52(10), pp. 1126–1133.
2. **Rodriguez E. V., Guzman Chavez A. D.,** Application of the generalized linear model to enable refractive index measurement with thermal sensitive interferometric sensors. Optics Communications, 2022, V. 524, pp. 128765.
3. **Calhoun W. R., Maeta H., Combs A., Bali L. M., Bali S.,** Measurement of the refractive index of highly turbid media. Opt. Lett., 2010, V. 35(8), pp. 1224–1226.

# Fabrication of amorphous ZBLAN high-Q WGM microspheres

**T.S. Tebeneva [1]✉, A.E. Shitikov [1], O.V. Benderov[2], A.V. Rodin[2], V.E. Lobanov[1], I.A. Bilenko[1,3]**

[1] Russian Quantum Center, Skolkovo, Russia;
[2] Moscow Institute of Physics and Technology, Dolgoprudny, Russia
[3] Faculty of Physics, Lomonosov Moscow State University, Moscow, Russia
✉tetasia19@gmail.com

**Abstract.** Fabrication method of the high-Q whispering gallery modes (WGM) microspheres from amorphous fluoride ZBLAN was developed. The achieved Q-factor $(5.4\pm0.4)\cdot10^8$ for the 310 μm ZBLAN microsphere at 1.55 μm is determined by material losses.

**Keywords:** ZBLAN, WGM, fabrication, microspheres.

## Introduction

The advantage of combination of the small mode volume and high-quality factor in optical microresonators with WGM allows to produce effective and compact devices for different photonic applications [1]. One of the suitable amorphous materials for WGM microresonators is ZBLAN glass (a group of glasses with the composition ZrF4-BaF2-LaF3-AlF3-NaF). It is transparent in the wide spectral range from 250 nm to ~4.5 μm, with a low refractive index (~1.5 [2]), and has low glass transition temperature (~265 °C). ZBLAN is also suitable for doping with various rare earth elements and applicable for the development of high-efficient microlasers and amplifiers [3]. In our work, we upgraded an original fabrication method based on melting commercially available ZBLAN optical fiber to obtain high-Q ZBLAN microspheres with diameters from 250 to 400 μm. The fabricated WGM microresonators have the intrinsic Q-factor determined by material losses - $(5.4 \pm 0.4)\ 10^8$ at 1.55 μm [4].

## Fabrication of microresonators

Fluoride ZBLAN microspheres were made of the commercial optical fibers by melting technique. In our work we used optical fibers with the following parameters: step-index single-mode ZBLAN fiber - 9/125 core/clad diameters, NA = 0.19 by Thorlabs. The fabrication process can be divided in the three stages: preliminary preparation of the optical fiber, melting and cooling processes, and quality control of the fabricated microresonators. Fiber preparation is usually the longest and most important step in the ZBLAN microresonator fabrication process. As a heating element we used a home-made nichrome coil (with the 3 mm length and 2 mm in diameter) that was placed on the precise XYZ translational stage. As the temperature inside the heating element rises, the fiber turns into spherical shape. The duration of the heating is 2 seconds. During this time the temperature inside the heating element (measured with the termocouple in the center of the coil without fiber) reaches 500 °C. After that, the cooling process begins - the microresonator cools down at room temperature (22 °C). The main advantage of this method of fabrication is the easiness and speed of realization. The whole fabrication process from the preparation of the optical fiber to WGM microresonator takes only about 10 minutes. We have fabricated the high-Q microspheres from 250 to 400 μm in diameter (Fig. 1).

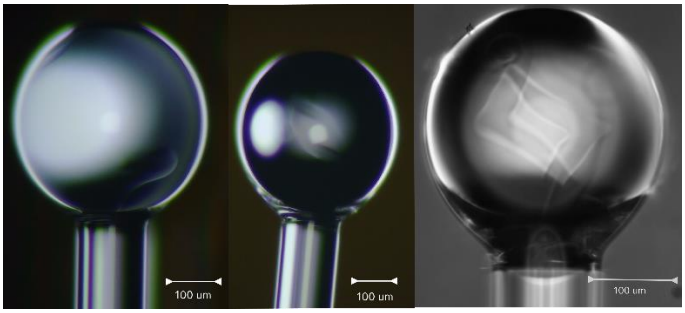


Fig. 1. Enlarged image of the manufactured ZBLAN microspheres with good surface quality with diameters of 333 μm, 381 μm and 270 μm (from left to right respectively). Patterns in the lower and central parts of the ZBLAN microspheres appear due to the thermal modification of the core of the fiber.

For WGM microresonators the quality of the surface, among other factors, is crucial for the quality factor. During fabrication we have identified three main problems that cause surface deformation of the microsphere (Fig. 2). The first one and the most difficult to avoid is caused by crystallization (Fig. 2 (a)). To avoid the crystallization during fabrication we selected experimentally step-by-step the values of the temperature and duration of the heating. The next (Fig.2 (b)) is related to the temperature contrast on the microresonator during heating (causes shape deformation and tilt of the microsphere) and the way to solve it is to use a high-symmetry heating element [5]. Damages in the Fig.2 (c) arises from the preliminary fiber preparation, when the dust particles or other inhomogeneities left on the fiber surface and after melting into the surface of the microresonator. This case depends entirely on preliminary fiber preparation.

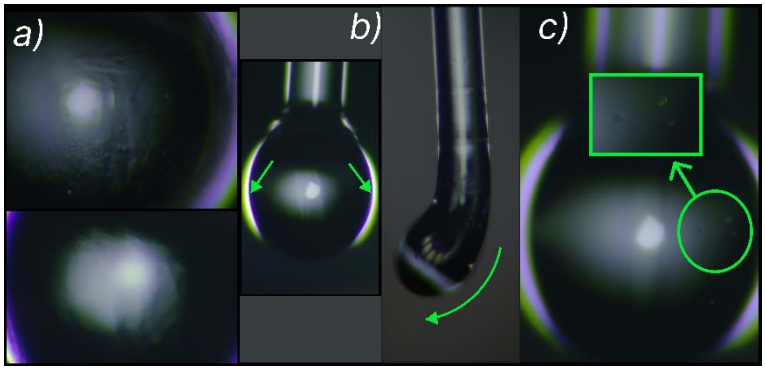


Fig. 2. Three main surface deformations that may appear during the manufacturing process. (a) shows crystallization on the surface. (b) is related to the temperature contrast. (c) shows fused inhomogeneities and dust particles on the surface.

## Near-IR characterisation

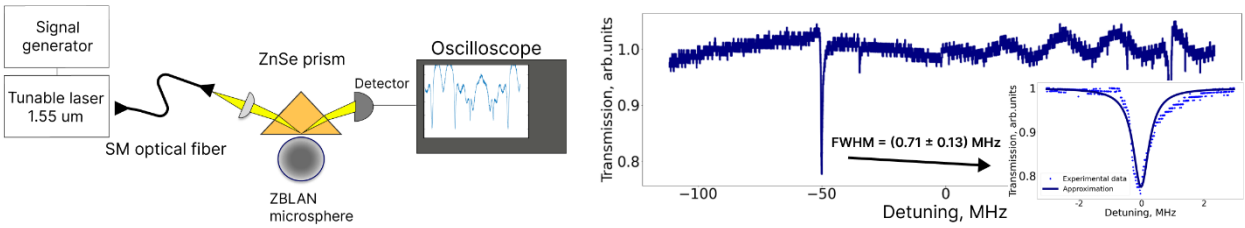


Fig. 3. Experimental setup and transmission spectrum for ZBLAN microspheres at 1.55 μm.

A tunable 1.55 μm continuous wave laser diode pig-tailed with optical fiber was used to excite WGM. The full linewidth measured at half maximum (FWHM) for the resonance curve was 1.0 MHz (measured at critically coupling regime), which corresponded to intrinsic Q-factor of (5.4 ± 0.4) $10^8$ for 310 μm microsphere. The experimental setup and transmission spectrum are presented in Fig. 3. The calculated absorption-limited Q-factor at 1.55 μm for the used fiber specifications gives ~ 5 $10^8$. Therefore, we fabricated ZBLAN microresonators with the quality factor (at 1.55 μm) that is determined by material losses in ZBLAN.

## REFERENCES


1. **Matsko A., Savchenkov A.A., Strekalov D., Ilchenko V., Maleki L.**, Review of Applications of Whispering-Gallery Mode Resonators in Photonics and Nonlinear Optics, IPN Progress Report, Vol. 42 (2005).
2. **Zhang L., Gan F., Wang P.**, Evaluation of refractive-index and material dispersion in fluoride glasses, Applied Optics, Vol. 33, 50–56 (1994).
3. **Deng Y., Jain R.K., Hossein-Zadeh M.**, Demonstration of a cw room temperature mid-IR microlaser, Optics Letters, Vol. 39, 4458-4461 (2014).
4. **Tebeneva T.S., Shitikov A.E., Benderov O.V., Lobanov V.E., Bilenko I.A., Rodin A.V.**, Ultrahigh-Q WGM microspheres from ZBLAN for the mid-IR band, Optics Letters, Vol. 47, 6325-6328 (2022)
5. **Way B., Jain R.K., Hossein-Zadeh M.**, High-Q microresonators for mid-IR light sources and molecular sensors, Optics Letters, Vol. 37, 4389-4391 (2012).

# Investigation of microdisk lasers with optically coupled waveguide

**N. A. Fominykh [1,2]✉, E. I. Moiseev [1,2], S. D. Komarov [1], Yu. A. Guseva [3], M.M. Kulagina [3], K. A. Ivanov [1], A. I. Lihachev[3], S. A. Mintairov [3], N. A. Kalyuzhnyy [3], R. A. Khabibullin [4], R. R. Galiev [4], A. Yu. Pavlov [4], K. N. Tomosh [4], N. V. Kryzhanovskaya [1], A. E. Zhukov [1]**

[1] HSE University, St. Petersburg, Russia

[2] Alferov University, St. Petersburg, Russia

[3] Ioffe Institute, St. Petersburg, Russia

[4] IUHFSE RAS, Moscow, Russia

✉fominy-nikita@yandex.ru

**Abstract.** The output emission from microdisk lasers into waveguides fabricated of the same epi-structure was studied. We investigate the electroluminescence spectra received from microlaser and from the end of the coupled waveguide. The lasing threshold at room temperature was studied for microlasers having different coupling parameters.

**Keywords:** Quantum well-dots, microdisk laser, whispering gallery modes, waveguide.

**Funding:** The study was supported by a grant from the Russian Science Foundation № 22-72-10002, https://rscf.ru/project/22-72-10002/.

## Introduction

An application of optical interconnects on a microchip compared to electronic ones leads to an increase in speed and a decrease heat generation and power consumption of devices [1, 2]. Whispering gallery modes (WGM) have high quality factor (up to $10^7$ for passive Si devices, up to $10^5$ for $A_3B_5$ microdisk (MD) lasers with a diameter of about 30 μm) and low output losses [3]. Thus, WGM semiconductor lasers with MD optical cavity can be used as compact radiation sources for optical communication on a microchip [4]. The central symmetry of MD lasers results in absence of directional emission. This fact complicates the application of MD lasers as optical interconnects on a microchip. Effective way to achieve direct emission output of MD lasers is optical coupling with a waveguide (WG) [5]. This configuration is planar and quite easily implemented on a microchip. In this work we study the output emission of semiconductor MD lasers into a coupled WG formed from the same epitaxial heterostructure in planar geometry.

## Materials and Methods

The studied structures were fabricated by MOCVD on an n+-GaAs substrate with an active region representing a 5-layer array of InGaAs/GaAs quantum well-dots. WGs and MD resonators (15, 30 and 40 μm in diameter), as well as narrow gaps between them (0–200 nm) were formed by electron lithography and plasma-chemical etching (Figure 1). We used AgMn/Ni/Au metallization to form disk contacts to the p+-GaAs layer at the tops of the mesas. The GaAs substrate was thinned to approximately 100 μm, and a solid electrical AuGe/Ni/Au n-contact was fabricated on its reverse surface.

Electroluminescence (EL) of MD lasers was excited by a stabilized DC current with a Keithley 2400 Series SourceMeter® power supply. The EL spectra were collected by Mitutoyo M Plan Apo NIR HR 50x objective and analysed with a Yokogawa AQ6370C optical spectrum analyser. In order to avoid the influence of light emitted from the MD laser on the WG spectra we moved the focus of the objective to the end of the coupled waveguide that maximally removed from the excited MD laser.

## Results and Discussion

The lasing threshold current at room temperature were studied depending on the coupling parameters. Despite laser generation of single microlasers with 15 μm diameter coupled MD lasers of this diameter didn't show any laser generation. 30 μm MD lasers had two times higher threshold current than single disks. However, for 40 μm microlasers we didn't observe any crucial differences in the threshold currents of single MDs and MDs coupled with WG. The distance between microlaser and WG didn't affect threshold current.

The lasing spectra of the studied 30 µm microlaser with 200 nm gap between the MD laser and the WG received from the microlaser itself and from the WG are shown in Figure 2. The presence of the same lasing mode on the MD and WG spectra evidences of the coupling between the microlaser and the WG. The lasing spectra received from the WG has lower intensity compare to that received from the MD laser. We assume that such intensity decrease is caused by the absorption of the WG active region (inset to Figure 2) and can be avoid by pumping the WG with electric current.

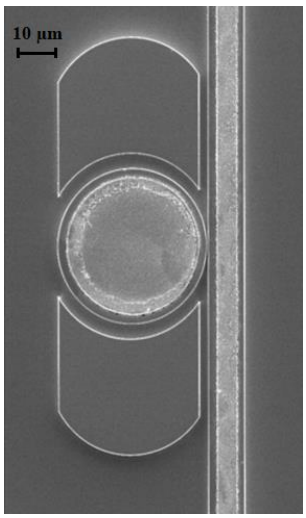


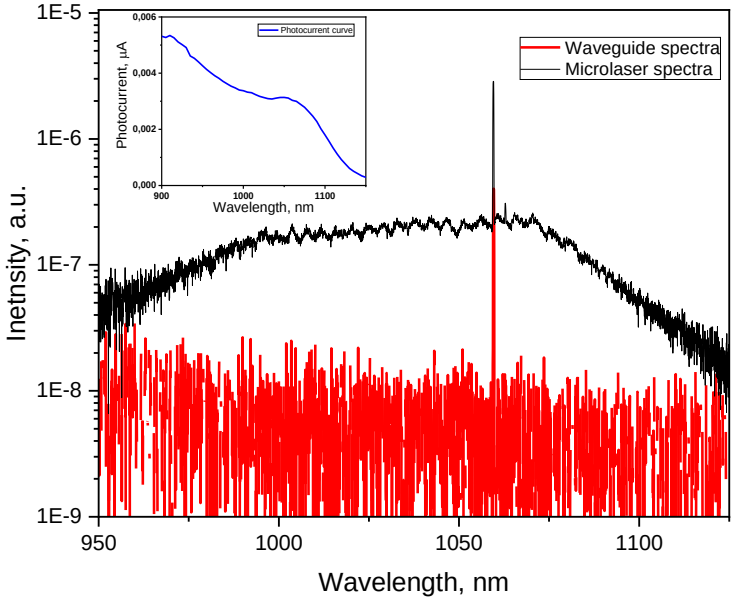


**Figure 1.** Image of 40 µm MD lasers with 200 nm gap between the microlaser and the coupled WG received by scanning electron microscopy (SEM) on JSM 7001F

**Figure 2.** The lasing spectra of the 30 µm MD laser with 200 nm gap between the MD laser and the WG received from the microlaser itself and from the WG, an inset shows the photocurrent curve for the studied WG.

## Conclusion

An optical coupling of MD lasers with waveguides fabricated of the same epi-structure was realized. The increase of the MD diameter leads to less sensitivity of microlaser to the loss caused by coupled WG so 40 µm MD lasers coupled with WG didn't have any crucial differences in threshold currents compared to single microlasers. The intensity decrease of the WG spectra caused by absorption of its active region can be avoid by pumping the WG with electric current.


## Acknowledgments

The work was carried out on the equipment of the large-scale research facilities "Complex optoelectronic stand". SEM characterization was performed using equipment owned by the Federal Joint Research Center "Material science and characterization in advanced technology".


## REFERENCES


1. **Koseki S.** et al. Appl. Phys. Lett., 94 (5), 0511102009 (2009).

2. **Arakawa Y.** et al. Appl. Phys. Lett., 40 (11), 939–941 (1982).

3. **Savchenkov A. A.** et al. Opt. Express, 15 (11), 6768 (2007).

4. **Kryzhanovskaya N. V.** et al. Journal of Physics D: Applied Physics, 54 (45), 453001 (2021).

5. **Choi S. J.** et al. IEEE Photonics technology letters, 15 (10), 1330-2 (2003).

# Investigation of the optical properties anisotropy of black phosphorus by FTIR spectroscopy

**S. A. Khakhulin** ✉, **O. E. Lakuntsova**, **D. D. Firsov**, **O. S. Komkov**
Saint Petersburg Electrotechnical University "LETI", Saint Petersburg, Russia
✉khsmn@ya.ru

**Abstract.** The reflectance anisotropy spectroscopy method, as well as the methods of polarized reflectance and transmittance measurements, were applied to study black phosphorus – a narrow-gap layered semiconductor. Against the background of a significant crystal absorption anisotropy in the range of 0.26–0.42 eV, a polarization-dependent feature in the reflectance anisotropy spectra of such crystals is obtained in the region of 0.33 eV. This feature is presumably associated with a direct interband transition $E_0$, which is allowed when linear polarization of incident radiation is along the AC crystal direction, and forbidden in the case of ZZ direction.

**Keywords:** Black phosphorous, reflectance anisotropy spectroscopy, in-plane anisotropy, FTIR spectroscopy.

**Funding:** The study was supported by the Russian Science Foundation, grant No. 22-29-20141 and the St. Petersburg Science Foundation (grant under agreement No. 18/2022 dated April 14, 2022).

## Introduction

Black phosphorus is a layered direct-gap semiconductor crystal with a direct interband transition energy of ~0.3 eV [1] corresponding to the mid-IR range. The crystal consists of atomic layers connected to each other by weak van der Waals forces, which makes it possible to obtain single layers of a semiconductor by exfoliation. With a decrease in the number of layers in the structure, the band gap of the material increases, the value of which for a monolayer reaches ~2 eV. This feature makes it possible to create photonics devices with a wide optical range from mid-IR to visible based on black phosphorus layers [2].

A black phosphorus crystal in the plane of layer has two orthogonal nonequivalent crystallographic directions "zigzag" (ZZ) and "armchair" (AC), where differences in chemical bond lengths and atomic arrangement lead to a significant anisotropy of optical properties. According to the data available in the literature, the absorption of optical radiation when the incident radiation is polarized along the AC direction is orders of magnitude more intense [1]. This feature of the crystal is of great importance for the creation of polarization-sensitive emitters, as well as receivers of optical radiation based on the material under consideration.

## Materials and Methods

To reveal the practically significant features of the band structure of a semiconductor material, in our work we present a polarization-sensitive study of a black phosphorus crystal. To characterize the optical properties of the material, we employ the novel method of modulation Fourier-transform infrared (FTIR) reflectance anisotropy spectroscopy [3]. The essence of this method consists in modulating the direction of probe radiation linear polarization in the sample plane along the AC and ZZ directions and recording the normalized difference in the reflectance coefficients $2(R_{AC} - R_{ZZ})/(R_{AC} + R_{ZZ})$. In addition, the transmittance and reflectance spectroscopy methods with the direction of incident radiation polarization along AC and ZZ are used.

## Results and Discussion

In the obtained transmittance spectrum of black phosphorus, a sharp absorption edge is observed in the range of 0.26–0.3 eV with position of linear polarization of the radiation incident on the sample along the AC direction. In the case of the ZZ direction, we obtained uniform decrease in the range of 0.32–0.52 eV. The same character of behavior is demonstrated by the curves of polarized reflectance with polarizations of the incident radiation along the corresponding

crystallographic directions. The reflectance spectrum of radiation polarized along AC contains a weak peak in the region of 0.33 eV. The state of the surface of industrially obtained black phosphorus crystals significantly complicate the registration and interpretation of ordinary reflectance spectra, as well as the specifics of the mid-IR range in which studies are carried out. The use of a reflectance anisotropy spectroscopy modulation technique significantly increases the signal-to-noise ratio, and also allows us to highlight relatively small changes in the reflectance coefficient. As a result, in the obtained spectrum a broad negative peak in the range of 0.26–0.42 eV is observed, which is associated with a significant anisotropy of the reflectance coefficients of black phosphorus. Against the background of such a signal, a relatively narrow peak stands out with a maximum at an energy of 0.33 eV. Such a feature can be associated with a direct interband transition, which is allowed when the polarization of the incident light is along the AC direction and forbidden in the case of ZZ.

## Conclusion

Thus, we have experimentally characterized the features of the black phosphorus' optical properties associated with the anisotropy of optical transitions in this material. The information obtained is in demand in the creation of polarization-sensitive photodetectors and light emitters in the mid-IR range based on black phosphorus.

## REFERENCES


1. **Wang X., Lan S.** Optical properties of black phosphorus, Advances in Optics and photonics. 8 (4) (2016) 618-655.
2. **Xia F., Wang H., Hwang J. C., Neto A. C., Yang, L.** Black phosphorus and its isoelectronic materials, Nature Reviews Physics. 1 (2019) 306-317.
3. **Firsov D. D., Khakhulin S. A., Komkov O. S.** Fourier-Transform Infrared Reflection Anisotropy Spectroscopy of Semiconductor Crystals and Structures: Development and Application in the Mid-Infrared, Applied Spectroscopy. (2023).

# Study of the Temperature Dependence of the Energy Spectrum of Metamorphic In(Ga,Al)As/GaAs Heterostructures Using the FTIR Photoreflectance Spectroscopy Method

**I. V. Chumanov** [1✉], **D. D. Firsov** [1], **O. S. Komkov** [1]

[1] St. Petersburg Electrotechnical University "LETI", Saint-Petersburg, Russia

✉i.chumanov2000@gmail.com

**Abstract.** In this work, the optical properties of In(Ga,Al)As/GaAs metamorphic heterostructures were studied in the temperature range of 79-300 K. The measurements were carried out for a series of samples containing a double quantum well and superlattices in their structure. The results obtained correlate with previous studies, and also demonstrate new features that have not been observed before. Among these features is the detection of a spin-split signal from the superlattice and its splitting in the spectrum as the sample temperature is lowered.

**Keywords:** semiconductors, optics, heterostructures, superlattices, quantum well, photoreflectance method, FTIR spectroscopy.

**Funding:** The study was supported by the Russian Science Foundation, grant No. 22-29-20141 and the St. Petersburg Science Foundation (grant under agreement No. 18/2022 dated April 14, 2022).

## Introduction

In(Ga,Al)As/GaAs heterostructures with a metamorphic buffer layer are a promising basis for optoelectronic components in the mid-infrared range (3-5 μm) [1]. Light emitting diodes and laser diodes based on them can be used for various applications, such as gas analysis, optical wireless communication systems, control of chemical processes, etc. The active region of the investigated structures consists of an InSb type II submonolayer insertion inside an InAs/InGaAs type I quantum well. This approach provides a better retention of charge carriers and an overlap of the electron and hole wave functions, as compared to type I quantum wells. The peculiarity of the structures under study is the presence of superlattice regions at the edges of the double quantum well, which form a waveguide layer and provide compensation for mechanical stresses in the structure.

## Materials and Methods

In this work, we studied the optical properties as a function of temperature for heterostructures grown by molecular beam epitaxy on a GaAs substrate with a (In,Al)As metamorphic buffer layer. The heterostructures consisted of $In_XAl_{1-X}As$ and $In_XGa_{1-X}As$ epitaxial layers, as well as superlattices based on these materials. The spectra were measured using the photoreflectance method based on the use of Fourier-transform infrared (FTIR) spectroscopy [2]. The research setup consisted of a Vertex 80 FTIR spectrometer, an InSb photodetector cooled to liquid nitrogen temperature, an SR-830 lock-in amplifier, and lasers with wavelengths of 405 nm and 809 nm, the radiation of which was mechanically modulated at a frequency of 2.5 kHz. The samples were placed in an optical cryostat cooled with liquid nitrogen. To analyze the line shape of the photoreflectance spectra, a specialized processing algorithm was used [3].

## Results and Discussion

As a result of the analysis of the experimental data, signals from direct interband transitions in the $In_{0.75}Ga_{0.25}As$ and $In_{0.75}Al_{0.25}As$ layers were found, which agrees with our previous results [4]. Signals corresponding to transitions between miniband edges in the superlattice were also found. In addition, a peak was observed in the spectra, which was assigned to the energy taking into account the spin-orbit splitting. An example of a photoreflectance spectrum obtained at room temperature is shown in Fig. 1(*a*). The spectrum shows signals from the miniband edges of the $In_{0.82}Ga_{0.18}As/In_{0.75}Al_{0.25}As$ superlattice at 0.56 eV and 0.597 eV, and a broad peak at 1.023 eV resulting from spin-orbit splitting.

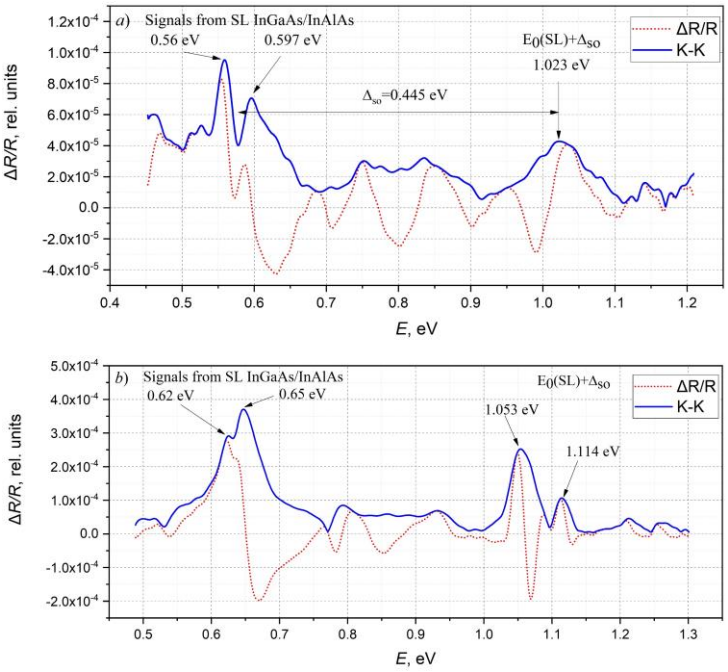


Fig. 1. Photoreflectance spectra (ΔR/R) and transformed spectrum (K-K) at temperatures of 300 K (*a*) and 79 K (*b*)

In the spectrum at 79 K (Fig. 1(b)) the observed shift of the critical points towards higher energies is associated with the temperature change in the band gap and the corresponding shift in the relative position of the energy levels in the heterostructure. The most interesting result is the confident separation of the peak corresponding to the spin-orbit split signal from the superlattice into two separate signals. Thus, it is possible to experimentally estimate the miniband width in $In_{0.82}Ga_{0.18}As/In_{0.75}Al_{0.25}As$ superlattices, which is 61 meV at 79 K, which is the first such result for this type of heterostructure.

## Conclusion

The obtained results turned out to be very interesting, since with decreasing temperature the peak corresponding to the signal from the superlattice, taking into account the spin-orbit splitting, is divided into two, as a result of which it was possible to estimate the magnitude of the splitting. This enables a more detailed analysis of the energy structure of the In(Ga,Al)As/GaAs heterostructures, which may enable a better understanding of their parameters in the future studies.

## Acknowledgments

The authors are grateful to V.A. Solov’ev and M.Yu. Chernov (Ioffe Institute) for providing the heterostructures for research.

## REFERENCES

1. **Ivanov S. V., Chernov M. Y., Solov'ev V. A., Brunkov P. N., Firsov D. D., Komkov O. S.** Metamorphic InAs (Sb)/InGaAs/InAlAs nanoheterostructures grown on GaAs for efficient mid-IR emitters. Progress in Crystal Growth and Characterization of Materials, 65 (1) (2019) 20-35.

2. **Frisov D. D., Komkov O. S.** Photomodulation Fourier transform infrared spectroscopy of semiconductor structures: features of phase correction and application of method. Technical Physics Letters, 39 (2013) 1071-1073.

3. **Hosea T. J. C.** Estimating Critical-Point Parameters of Modulated Reflectance Spectra. physica status solidi (b), 189 (2) (1995) 531-542.

4. **Firsov D. D., Chernov M. Y., Solov’ev V. A., Komkov O. S.** Characterization of In (Ga, Al) As/GaAs metamorphic heterostructures for mid-IR emitters by FTIR photoreflectance spectroscopy. Journal of Physics: Conference Series (Vol. 2086 (1) (2021) 012140). IOP Publ.

# Development of a compact high-resolution digital microscope for the research of micro- and nanostructures

**D. V. Shevchenko[1]✉, D. S. Provodin[1] and V. V. Davydov[1, 2]**
[1] Peter the Great Saint-Petersburg Polytechnic University, Saint Petersburg, Russia;
[2] The Bonch-Bruevich Saint Petersburg State University of Telecommunications, Saint Petersburg, Russia.
✉ shevchenko.dv@edu.spbstu.ru

**Abstract.** The need to develop a compact mobile high-resolution digital microscope for the research is substantiated. Disadvantages of modern mobile digital microscopes designs are considered. The design of the low-cost compact mobile digital microscope is developed and assembled. The results of studies of different objects are presented.

**Keywords:** nanostructures, digital microscope, image, resolution, different materials.

## Introduction

Microscopy has been an essential tool in scientific research for centuries, enabling scientists to observe structures and objects that are too small to be seen with the naked eye. Over the years, microscopy techniques have evolved significantly, from the first compound microscopes to the more advanced electron microscopes. In fact, digital microscopy have gained special popularity due to their opportunity to conduct more in-depth research and analyze data with computers. [1] Nowadays, microscopes are used in a wide range of scientific fields, including biology, medicine, chemistry, material science, engineering, etc. [2] However, despite immense advantages, they have some disadvantages. As a rule, microscopes are large and heavy, making them difficult to transport to different locations. Additionally, the cost of high-quality models can be high, so it causes limited affordability to many researchers.

## Materials and Methods

As a consequence, creating a simple microscope model that considers the above disadvantages is an actual problem. The design of the device which can be one of the solutions to this problem is presented in Fig.1.

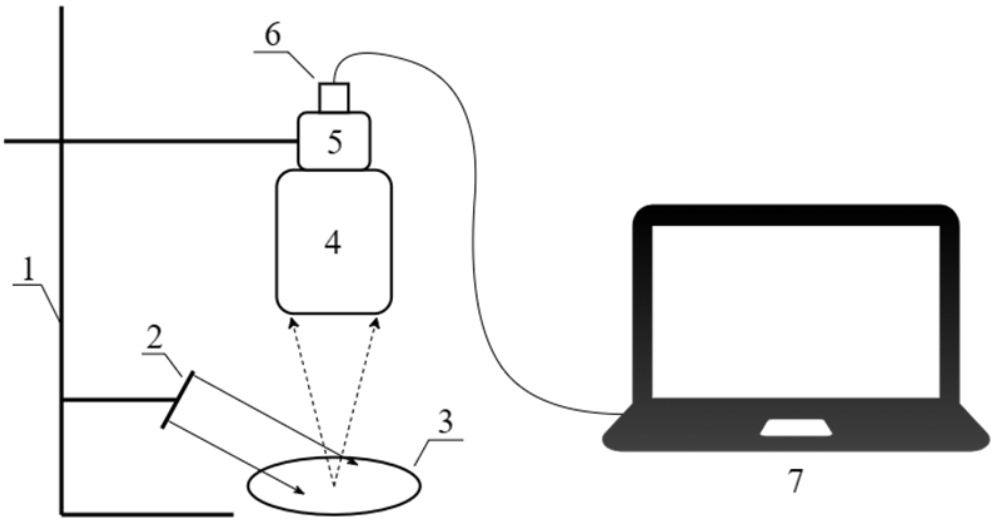


Fig.1. Diagram of the digital microscope: 1 – modular tripod, 2 – LED matrix, 3 – investigated object, 4 – lens, 5 – transitional cylinder, 6 – photosensitive matrix, 7 – image reading laptop/PC.

The developed model implies the possibility of a lens replacing, allowing to increase microscope magnification without loss of image quality. Also, the microscope can be easily taken apart, compactly packed and moved for a long distance. Another design advantage - the device

can be powered by the PC or laptop that it is connected to. Besides, user can zoom in or out the image and increase the contrast of its investigated part with software. The PC or laptop screen displays a real-time data, which can be quickly saved and transmitted over long distances.

## Results and Discussion

The results of studies using produced construction of microscope are shown in Fig.2,3.

*a)* *b)*

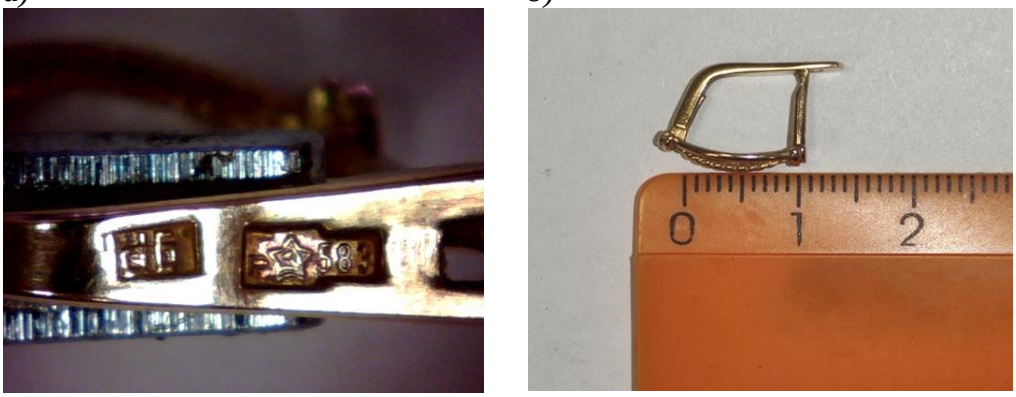


Fig.2. The image of the object obtained with the microscope (*a*) and the size of the object (*b*).

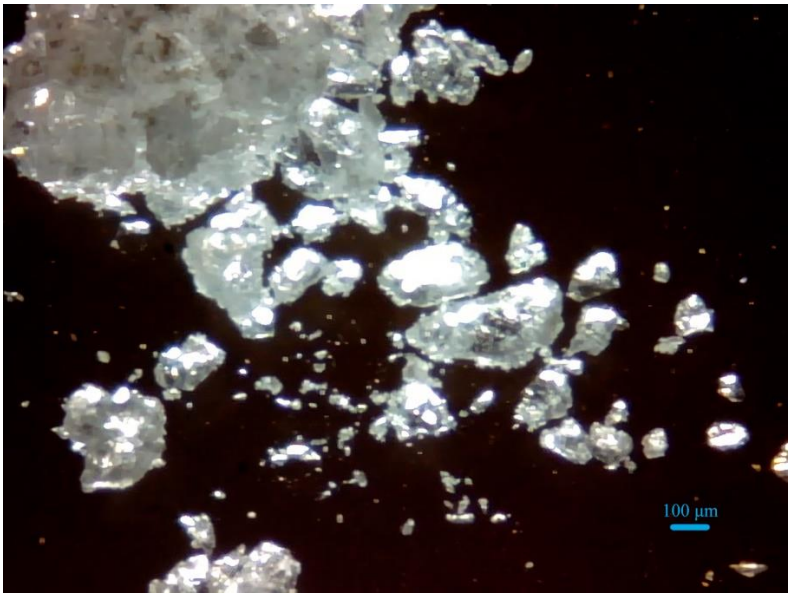


Fig.3. Sugar crystals under the microscope.

## Conclusion

Conducted research allowed to determine the possibility of using the developed model of the microscope. It can be used to obtain images of various objects, e.g. structures, defects and small details on a material surface. The range of magnification laid down in the design is confirmed by the clarity of images obtained during studies. In addition, the main directions of the design improvements are defined. Further development will be aimed at increasing of magnification, image quality and distance to object under study.

## REFERENCES

1. **Lozano M., Gamarra B., Hernando R., Ceperuelo D.**, Microscopic and virtual approaches to oral pathology: A case study from El Mirador Cave (Sierra de Atapuerca, Spain), Annals of Anatomy. 239 (2022) 151827.
2. **García-Bonillo C., Texidó R., Gilabert-Porres J., Borrós S.**, Plasma-induced nanostructured metallic silver surfaces: study of bacteriophobic effect to avoid bacterial adhesion on medical devices, Heliyon. 8(10) (2022) 1-12.

# Reversible multiple optical switching of $Ge_2Sb_2Te_5$ thin films for reflective display applications

V.B. Glukhenkaya[1✉], N.M. Tolkach[2], P.I. Lazarenko[1], A.A. Sherchenkov[1]
[1]National Research University of Electronic Technology, Zelenograd, Russia
[2]Ryazan State Radio Engineering University, Ryazan, Russia
✉kapakycek2009@yandex.ru

**Abstract.** The crystallization and amorphization processes of GST thin films under pulsed laser exposure were investigated. It was found that the optimal laser mode for GST crystallization and re-amorphization is 50 mW/10 μs and 106 mW/50 ns respectively. We demonstrated the 11-multiple write/rewrite/erase uniform-area of GST thin film on the surface of large-sized GIA site for reflective display applications.

**Keywords:** GST, reversible optical switching, reflective display, multiple switching

**Funding:** This study was supported by the Russian Science Foundation project number 20-79-10322.

## Introduction

Today in the area of nanophotonic and integrated optic Great attention is paid to the developing of non-volatile reversible high-speed optical elements with tunable optical properties based on Ge2Sb2Te5 (GST). Thin films of this material have high-rate phase transformations (< 50 ns) from amorphous to crystalline states accompanied by the appearance of the large optical contrast between states [1]. These advantages make it possible to develop color multilayer GST/ITO/Al/substrate (GIA) structures for information display systems. In these structures the primary color can be varied in a wide range and is determined by the ITO thickness, and the GST phase state effects on the tint of the GIA structure and its reflectivity. Reversibility and tunability of optical properties in the visible and IR-light in such elements is achieved by laser exposure on GST layer. However, the switching modes and operational capabilities of such structures haven't been definitely established. So, the aim of this work is investigation of the crystallization and amorphization processes of the GST thin films under pulsed laser exposure and to determine parameters of reversible multiple optical switching of GST for colorful tunable elements for reflective display applications.

## Materials and Methods

The thin films of multilayer structures GIA were deposited by the magnetron sputtering. The layer thicknesses were chosen according to the literature data and simulation results so that the color of the GIA structure corresponded to the RGB-colors. In this paper demonstrates experimental results of green GIA structure (GST-10 nm; ITO-240 nm; Al-100 nm). The simulation in Mathcad was performed with using of Fresnel's formulas and refractive index n(λ) and extinction coefficient k(λ) obtained by ellipsometry for each layer. The formed structures were irradiated by ns-laser (403 nm, Pmax=106 mW) for crystallization and amorphization modes respectively. Laser modification was carried out in the scanning mode. A focused beam diameter was 1 μm. Structural transformations in GST before and after laser exposure were measured by Raman spectroscopy (Integra Spectra, 532 nm, 10 mW).

## Results and Discussion

Figure 1 (a) shows the results of as-deposited amorphous GST film irradiation by laser pulses with power in the range from 40 to 80 mW and 0.1-100 μs pulse duration. Crystallization scanning rate was 2 Hz. It can be seen that irradiation by pulses with a power of 50 mW and 5-100 μs leads to the appearance of area-uniform optical contrast (the original yellow-green region becomes bright green). Raman scattering results showed, that such laser exposure leads to the crystallization of amorphous GST (fig. 1, (c), blue curve). To determine the laser modes of laser-crystallized regions re-amorphization, the large-sized area of the initial amorphous film

(75x130 μm$^2$) was pre-crystallized by 50 mW CW-laser. Then, this large-sized area was irradiated by laser pulses with power in a range from 75 to 106 mW and 40-110 ns pulse duration (fig. 1, (b)). This laser modification also leads to changes in the surface reflectivity of the GST film: irradiation with 96-106 mW and 50-80 ns accompanied color changes from bright green to yellow-green, characteristic color for pre-crystallized and initial amorphous films respectively, according to Raman spectra results (fig. 1, (c), red curve). Re-amorphization scanning rate was 0.5 Hz. The size of all formed irradiated areas was 10x10 μm$^2$.

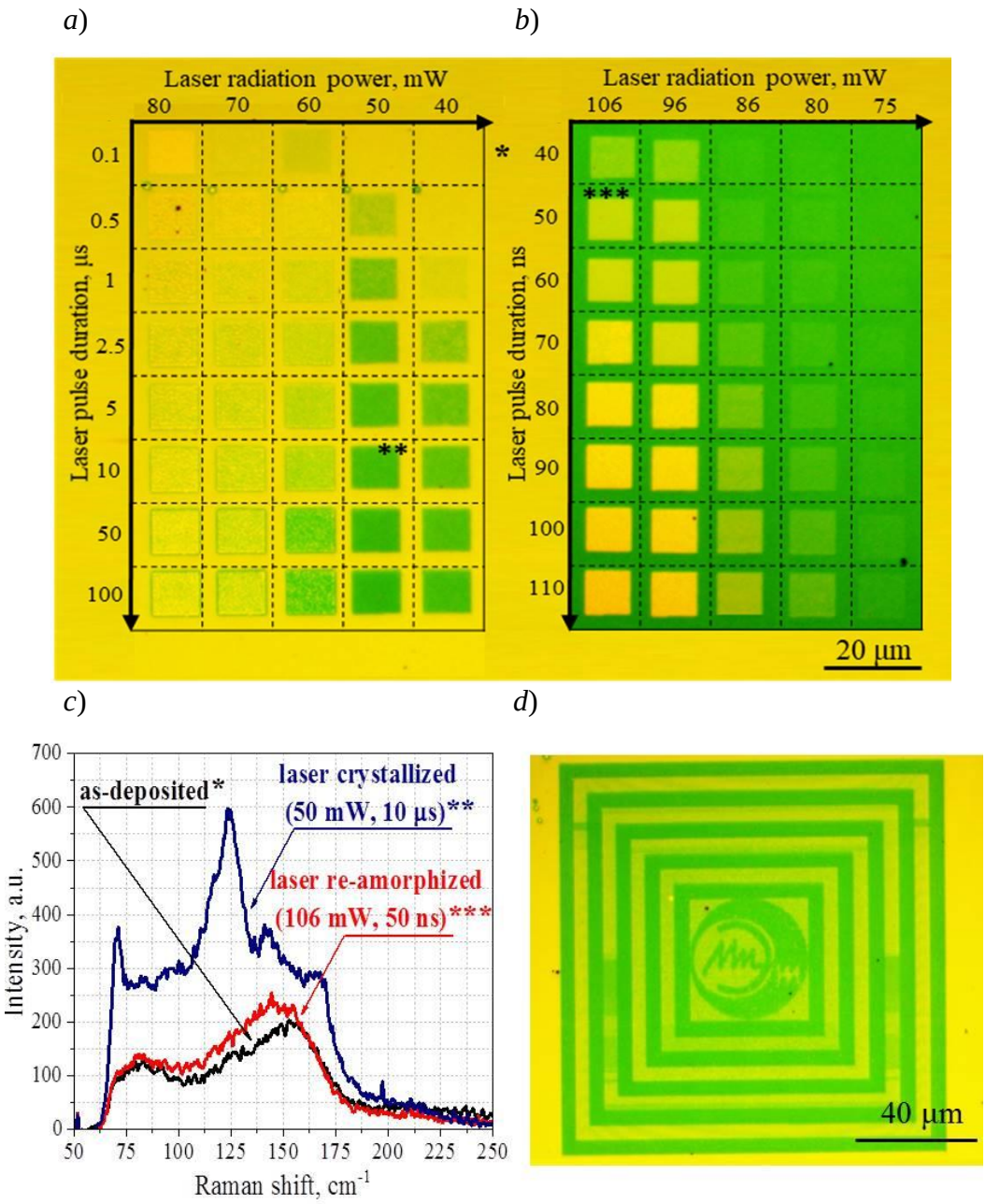


Fig. 1. Map of modes selection for laser crystallization (a); map of modes selection for laser amorphization (b); Raman spectra of as-deposited*, laser crystallized** and laser re-amorphized*** GST thin film (c) and demonstration of reversible multiple GST switching by ns-laser pulses (d). The sign «*» marks the areas where the Raman spectra were obtained.

According to obtained results, the reversible 11-multiple optical switching was demonstrated (fig. 1, (d)): the formation of bright green crystalline and yellow-green re-amorphized regions were obtained by pulsed laser exposure with 50 mW/10 μs and

106 mW/50 ns respectively. The size of the switched area monotonically decreased from 130x130 to 40x40 $\mu m^2$ at scanning rate 2 Hz.

## Conclusion

The crystallization and amorphization processes of GST thin films under pulsed laser exposure were investigated. It was found that the optimal laser mode for GST crystallization and re-amorphization is 50 mW/10 μs and 106 mW/50 ns respectively. Reversible multiple non-volatile optical switching of GST thin film has been performed. We demonstrated the possibility of 11-multiple write/rewrite/erase uniform-area on the surface of large-sized GIA site for reflective display applications.

## Acknowledgments

This work was supported by Russian Science Foundation (project No. 20-79-10322).

## References

1. **M. Wuttig, H. Bhaskaran, T. Taubner.** Phase-change materials for non-volatile photonic applications. Nature Photonics 11 (2017) 465-476.

# Investigation of photon emission via inelastic tunneling of electrons from laser-printed gold nanobumps using scanning tunneling microscopy

**N. A. Solomonov [1,2✉], D. V. Lebedev [1,3,4], V. A. Shkoldin [1], D. V. Permyakov [5], A. M. Mozharov [1,4], L. N. Dvoretskaya [1], A. V. Arhipov [2], D. Pavlov [6,7], A. A. Kuchmizhak [6,7] and I. S. Mukhin [1,2]**

[1] Alferov University, Saint Petersburg, Russia;
[2] Peter the Great St.Petersburg Polytechnic University, Saint Petersburg, Russia;
[3] Institute for Analytical Instrumentation of the Russian Academy of Sciences, Saint Petersburg, Russia;
[4] Saint Petersburg State University, Saint Petersburg, Russia;
[5] ITMO University, Saint Petersburg, Russia;
[6] Far Eastern Federal University, Vladivostok, Russia;
[7] The Institute of Automation and Control Processes, Vladivostok, Russia;
✉solomonov.nik@gmail.com

**Abstract.** We experimentally investigated the light emission resulting from inelastic electron tunneling (IET) in the transition with hemispherical gold nanoantennas – nanobumps (d=500 nm, h=300 nm) created by direct fs-laser printing. Using a scanning tunneling microscope-induced luminescence (STM-L), we recorded the spatial distribution of local density of optical states (LDOS) and obtained a series of I-V tunneling curves to spectrally characterize the IET processes under ultrahigh vacuum and ambient conditions. Our results show that the introduction of nanobump into the tunnel transition enhance the photon emission intensity by increasing the LDOS in the nanobump region and the appearance of additional optical resonance in the visible range near 520 nm, which agrees well with our numerical calculation results.

**Keywords:** Au nanoantenna, femtosecond laser printing, nanoscale on-chip light sourse, inelastic tunneling, scanning tunneling microscope.

**Funding:** The work was supported by the Russian Science Foundation (grant № 21-79-10346).

## Introduction

Recent breakthroughs in nanofabrication and plasmonic have rekindled the scientific community's interest in studying tunneling processes occurring in sub-nanometer insulator gaps within metal-insulator-metal (MIM) structures, specifically, the light emission that results from inelastic electron tunneling (IET). These has led to the development of visible and near-infrared light sources based on IET, which exhibit exceptional characteristics, including sub-nanometer dimensions, electrically-tunable radiation wavelengths determined by gap bias voltage, and ultrafast response times, on the order of several femtoseconds. However, their practical implementation is hindered by their low external quantum efficiency (EQE) with a simple sourse design and the complexity of technologies that are not compatible with CMOS in the manufacture of sources with high EQE.

To overcome these challenges, we propose the use of direct printing with focused femtosecond laser pulses (FSLP) to manufacture a simple, integrally compatible, and scalable IET source [1]. FSLP allows us to create arrays of gold nanoantennas of hemispherical shape with controlled size (d=500 nm, h=300 nm), which can potentially enhance EQE and simplify integration into optoelectronic chips. Our approach offers a promising pathway for advancing IET sources towards commercialization.

## Materials and Methods

The initial sample is a 50 nm gold film deposited on an optically smooth glass substrate by electron beam evaporation without additional adhesive layers. FSLP was carried out by single 200-fs laser pulses (532 nm) focused on the surface of the sample with a focal spot of ~0.34 microns. The sample was installed on a micropositioning platform that provides a raster layout with a

minimum step of 50 nm. The morphology of nanoantennas was studied using scanning electron microscopy (Zeiss Supra 25) (Fig. 1, a) and scanning tunneling microscopy (Omicron UHV VT AFM/STM) (Fig.1 b). The recording of STM-L (Fig.1 c) was carried out by tunnel scanning with a Pt/Ir probe (DPT10) with a synchronic recording of the optical signal using a photon counter with a spectral range of 400-900 nm in an external optical circuit [2]. To study the processes of inelastic tunneling, several series of I-V curves were obtained through a tunnel gap over a nanoantenna (Fig. 1 d) [3]. Final I-V curve is an averaging of at least 80 curves using filtering.

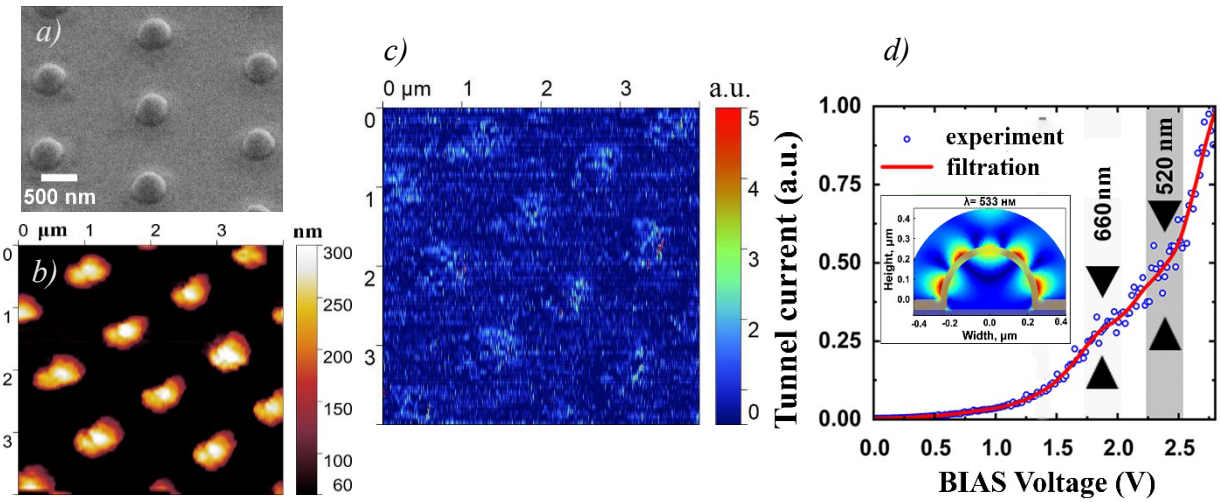


Fig.1 Nanoantenna characterization: (a) SEM image; (b) SEM morphology; (c) STM-L luminescence map normalized for tunnel current; (d) I-V tunnel transition over the nanoantenna

## Results and Discussion

Comparison of the current-normalized STM-L map (Fig.1 c) with the morphology map (Fig.1 b) clearly indicates an increase in luminescence in the area corresponding to nanoantennas, which correlates well with an increase in LDOS due to the introduction of optical nanoantennas. The I-V measurements in the tunnel junction over gold nanoantenna (Fig.1 d) show features at bias voltages of 1.87 V and 2.38 V that correspond to additional resonances at 520 and 660 nm, respectively. Such features are absent in the characteristics of a flat area in a region far from the matrix. The feature at 520 nm is in good agreement with the numerical simulation of the 4th order mode (533 nm) of the golden nanobump, presented in the inserted image (Fig.1 d).

## Conclusion

The fact of increasing the efficiency of IET sources by introducing gold nanoantennas manufactured using simple FSLP technology into the tunnel contact zone opens up a fundamental possibility of using such approach in the manufacture of commercial optoelectronic chips.

## REFERENCES

1. **Pavlov, D. V., et al.,** Laser-induced surface relief nanocrowns as a manifestation of nanoscale Rayleigh-Plateau hydrodynamic instability, Applied Surface Science. 511 (2020): 145463.

2. **Lebedev, Denis V., et al.,** Indirect Detection of the Light Emission in the Local Tunnel Junction." physica status solidi (RRL)–Rapid Research Letters 14.3 (2020): 1900607.

3. **Lebedev, Denis V., et al.,** Scanning Tunneling Microscopy-Induced Light Emission and I (V) Study of Optical Near-Field Properties of Single Plasmonic Nanoantennas, The journal of physical chemistry letters. 12.1 (2021): 501-507.

# Optical properties of hybrid structures based on InGaN nanowires and colloidal quantum dots

**T. Shugabaev [1,2✉], V. O. Gridchin [1,2,4], A. I. Khrebtov [1,2], I. A. Melnichenko [1,3], A. S. Kulagina [1,2], V. V. Lendyashova [1,4], N. V. Kryzhanovskaya[1,3], G. E. Cirlin[1,2,4]**

[1] Alferov University, St. Petersburg, Russia;
[2] St. Petersburg State University, St. Petersburg, Russia;
[3] HSE University, St. Petersburg, Russia;
[4] Ioffe Institute, St. Petersburg, Russia
✉talgashugabaev@mail.ru

**Abstract.** In this work, we propose a simple method to enhance the photoluminescence (PL) of InGaN nanowires (NWs) using CdSe/ZnS colloidal quantum dots (QDs). It is found that decoration the surface of InGaN NWs with QDs leads to an increase in the integral and peak photoluminescence intensity by more than 3 times.

**Keywords:** InGaN nanowires, CdSe/ZnS quantum dots, photoluminescence, hybrid nanostructures.

**Funding:** The InGaN NWs were grown under support of Ministry of Science and Higher Education of the Russian Federation (state task № 0791-2023-0004). The physical properties of samples were studied under financial support of St. Petersburg State University under research grant № 94031047.

## Introduction

InGaN NWs are good solid states candidates for creating new generation light emitting devices [1]. Free lateral surfaces of NWs and a small footprint between NWs and an underlying substrate provide efficient strain relaxation on the NW sidewalls without forming structural defects, as a result, InGaN NWs can be grown on Si [2]. Moreover, the thermodynamic features of the InGaN NWs growth process allow to vary the In content over a wide chemical range in order to obtain emitting nanostructures in the entire visible range [3]. However, the low quantum efficiency of InGaN compounds, even in the modification of NWs in the green and red spectral regions, remains an urgent problem for modern research.

Therefore, hybrid systems based on metal nanostructures and semiconductor NWs are being actively studied to improve the luminescence properties of the latter [4]. Another approach to enhance the luminescence of initial NWs is the nonradiative Förster mechanism of energy transfer (FIRET) by decorating the NW surface with colloidal quantum dots [5]. In this work, we study the effect of CdSe/ZnS colloidal QDs on the photoluminescence of InGaN NWs.

## Materials and Methods

The InGaN NWs were grown on 1-inch n-type Si(111) substrate using Riber Compact 12 MBE system equipped with In and Ga effusion cells and a nitrogen plasma source. Prior to the growth, the substrate was thermally treated at 920 °C to remove silicon oxide from the growth surface. The substrate temperature was then decreased to 605 °C. At this moment, an atomically clean growth surface was detected by in-situ reflection high-energy electron diffraction showing (7x7) surface reconstruction. After stabilization of the substrate temperature, the nitrogen plasma source was ignited and the Ga and In shutters were simultaneously opened. The growth lasted 20h. The nitrogen flux and power of the nitrogen plasma source were set at 0.4 sccm and 450 W, respectively. Beam equivalent pressures of In and Ga measured by the Bayard-Alpert vacuum gauge were equal to each other and amounted to $1 \cdot 10^{-7}$ Torr.

The NWs synthesized in this way have an InGaN/GaN core/shell structure [2]. Moreover, the FIRET mechanism manifests itself at a small distance between the participants in the energy transfer [5]. Therefore, to achieve FIRET between the CdSe/ZnS QDs and the InGaN core, we kept the initial NW array in an aqueous KOH solution to remove the GaN shell. 12 μl of the QDs

solution in toluene ($C \approx 10^{-6}$ M) were deposited on a substrate with InGaN NWs using a micropipette to create hybrid nanostructures.

PL spectra were obtained using an Integra Spectra (NT-MDT confocal microscope at room temperature. The Nd:YLF laser operating in continuous mode (527 nm wavelength) was used for excitation. The excitation laser beam was focused using a 100x objective (Mitutoyo, M Plan APO NIR) with a numerical aperture NA = 0.5. The same objective was used to collect the photoluminescence signal of nanostructures. The radiation was directed to the entrance slits of the monochromator (Sol Instruments MS5204i) using mirrors. Detection was performed using a cooled InGaAs CCD array (iDus).Morphological properties of the samples were examined using a SUPRA 25 C. Zeiss scanning electron microscope (SEM).

## Results and Discussion

CdSe/ZnS QDs demonstrate PL in the green region of the spectrum (maximum PL wavelength 530 nm). The diameter of QDs is about 2.5 nm.

The core/shell InGaN/GaN NW array has an average height of 2.1 μm with a diameter of about 140 nm. After processing this sample in an aqueous solution of KOH, we obtained core InGaN NWs with an average diameter of 60 nm. InGaN NWs have a noticeable PL at room temperature (RT) in the range of 600–700 nm. The PL intensity is enhanced by a factor of 3.2 after decoration the surface of the initial NW array with QDs (see fig.1).

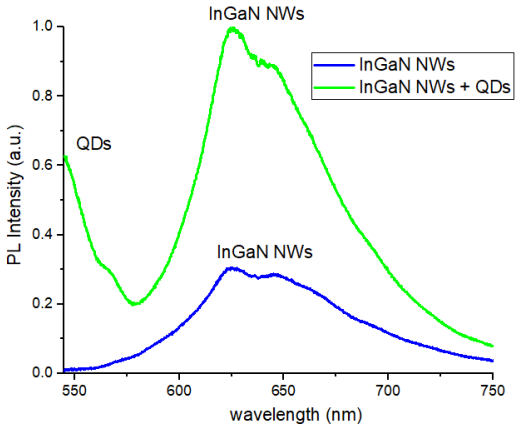


Fig. 1. RT PL spectrum of InGaN NW array before and after deposition QDs.

## Conclusion

To conclude, we have synthesized InGaN NWs on the Si substrate by plasma-assisted MBE. The obtained sample has RT PL peaks in the red region of the visible spectrum. The deposition of colloidal QDs on the surface of InGaN NWs allowed to enhance the PL of the initial nanostructures. The results obtained are of interest for the development of optically efficient devices based on NWs.

## REFERENCES

1. **Ra, Y.-H., et al.** Understanding the P-Type GaN Nanocrystals on InGaN Nanowire Heterostructures. ACS Photonics, (6) (2019) 2397–2404.

2. **Gridchin, Vladislav O., et al.** Multi-colour light emission from InGaN nanowires monolithically grown on Si substrate by MBE. Nanotechnology 32(33) (2021) 335604.

3. **Roche, Elissa, et al.** Circumventing the miscibility gap in InGaN nanowires emitting from blue to red. Nanotechnology 29(46) (2018) 465602.

4. **Pescaglini, Andrea, and Daniela Iacopino.** Metal nanoparticle–semiconductor nanowire hybrid nanostructures for plasmon-enhanced optoelectronics and sensing. Journal of Materials Chemistry C 3(45) (2015) 11785-11800.

5. **Khrebtov Artem Igorevich, et al.** "Nonradiative energy transfer in hybrid nanostructures with different dimensions." Physics and Technology of Semiconductors 53(9) (2019) 1289-1292.

# Mechanisms of Residual Polymer Removal in Solvent Mixtures after the Graphene Transfer and Effects on Channel Conductivity Gate Control

**N. P. Nekrasov** ✉, **A. V. Romashkin**, **L. A. Barsukov, K. G. Nikitin, D. D. Levin, I. I. Bobrinetskiy, V. K. Nevolin**

National Research University of Electronic Technology, Moscow, Russia

✉8141147@gmail.com

**Abstract.** After graphene transfer, solvent mixtures were used to remove residual PMMA, which efficiency was estimated by AFM, Raman spectroscopy, CVC. Post-treatment gives: stress relaxation (2D peak shift compared with trichloroethylene), 2D/G intensity ratio 1.1 changes to 2.6, graphene regions without PMMA are >50 nm; threshold point is shifted to zero but the conductivity, mobility reduce. Ethanolamine functionalizes both PMMA and graphene.

**Keywords:** graphene transfer, polymer removal, sensor, polymethylmethacrylate.

**Funding:** This work was supported by Russian Science Foundation, agreement No. 19-19-00401 (development of PMMA removing techniques); grant of the President of the Russian Federation No. MK-4010.2022.4 (AFM, Raman study).

## Introduction

The removal of polymer residuals, that left after graphene transfer used for sensor channel, is still an important problem [1].

To remove the PMMA residual layer, solvents mixtures were used: tetrahydrofuran (THF):water, diacetone alcohol (DAA):water, ethanolamine (EA):THF at 65 °C. Rinsing efficiency was estimated by AFM, Raman spectroscopy and CVC measurements.

## Results and Discussion

In comparison with trichloroethylene (TCE), for DAA:water there are: stress relaxation (2D peak shifts from 2696 to 2690 cm–1, Fig. 1a), no 2D/G ratio change (~1.1), although the layer thickness increased (from 3.7 to 4 nm, Fig. 1b) and graphene was partially removed.

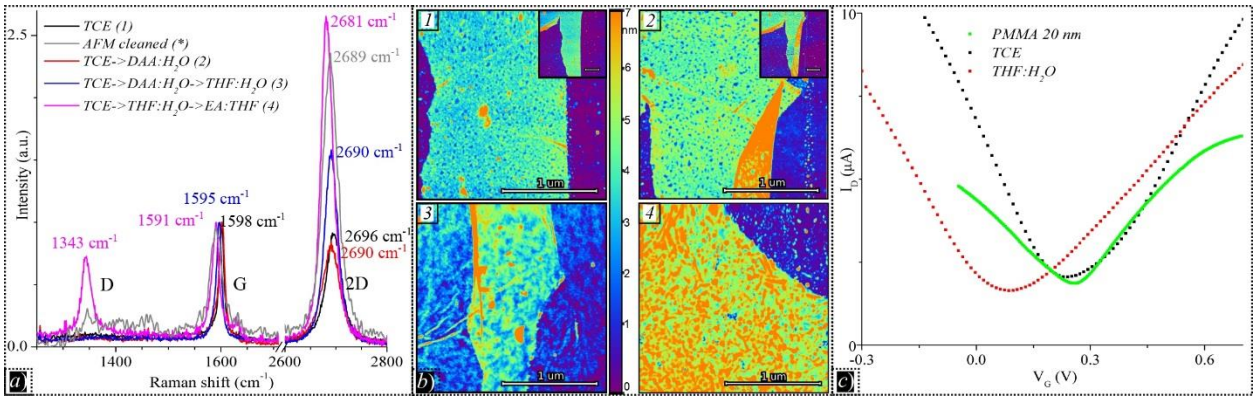


Fig. 1. Raman spectra (*a*), AFM (*b*) and CVC (*c*) of graphene after rinsing in various solvents

For THF:water, 2D/G increases to 1.6-1.9, which with AFM (thickness ~2.2 nm), indicates that graphene regions without PMMA increased to ~50 nm. But PMMA residuals are still observed on AFM. Mobility, CVC slope, sensor response remains low even with a small amount of PMMA residuals. 2D/G of AFM cleaned graphene was higher: ~2.7. For EA:THF, the 2D peak is shifted from 2690 to 2681 cm–1 and 2D/G increases to 2.6 which points to extended graphene regions without PMMA. Therefore EA functionalization of PMMA helps to remove PMMA, but graphene is functionalized too (D/G~0.7). Although the AFM thickness is ~5 nm.

Despite the PMMA partial removal with the 2D/G increasing (>1.5 is considered acceptable [2]) and the threshold point shifting to zero (Fig. 1c), the conductivity and mobility decrease. That

is explained by the graphene regions alternating with and without PMMA, which differ in properties (polar groups of PMMA form a local potential change near the channel [3]).

## REFERENCES


1. **Tyagi A., Mišeikis V., Martini L., Forti S., Mishra N., Gebeyehu Z. M., Giambra M. A., Zribi J., Frégnaux M., Aureau D., Romagnoli M., Beltram F., Coletti C.** Ultra-clean high-mobility graphene on technologically relevant substrates, Nanoscale. 14 (6) (2022) 2167-2176.

2. **Nekrasov N., Jaric S., Kireev D., Emelianov A. V., Orlov A. V., Gadjanski I., Nikitin P. I., Akinwande D., Bobrinetskiy I.,** Real-time detection of ochratoxin A in wine through insight of aptamer conformation in conjunction with graphene field-effect transistor, Biosensors and Bioelectronics. 200 (2021) 113890.

3. **Choi W., Shehzad M. A., Park S., Seo Y.,** Influence of removing PMMA residues on surface of CVD graphene using a contact-mode atomic force microscope, RSC advances. 7(12) (2017) 6943-6949.

# Development of an Automated System for Measuring Bioimpedance for the Study of Body Composition

**V. V. Antipenko**✉, **E. A. Pecherskaya, D. E. Tuzova, D. V. Yakushov, J. V. Shepeleva**
Department of Information and measuring equipment and metrology, Penza State University, Penza 440026, Russia;
✉v.antipenko7@yandex.ru

**Abstract.** Bioimpedance analyzers are non-invasive instruments that practitioners use to measure physiological parameters of body composition. The existing technology for measuring bioimpedance is constantly being improved, and more and more commercially available analyzers that do not solve the problems with measurement errors and the information content of the obtained data appear on the market. This article proposes an automated bioimpedance measurement system for studying body composition with a reduced impedance measurement error up to 1% and an increase in the information content of the human body composition due to the expansion of the impedance frequency measurement from 0.3 kHz to 2000 kHz.

**Keywords:** bioimpedance, current source, circuit, model, object.

## Introduction

The development of new approaches to both hardware and software for bioimpedance analysis in recent years has significantly increased its capabilities and expanded the list of both already implemented and promising applications [1]. Although the technology has been improved, it is currently difficult to obtain high-quality measurements of physiological parameters with most commercially available bioimpedance analyzers because they do not detect large amounts of fat under the skin [2].

The creation of an automated system is based on the idea of measuring human bioimpedance, with improved measurement accuracy (impedance measurement error up to 1%) and an increase in the information content of the human body composition, due to the expansion of the measurement of the impedance frequency range from 0.3 kHz to 2000 kHz [3].

## Structural Diagram of the Automated Bioimpedance Measurement System

The automated bioimpedance measurement system includes a measurement object, a measuring unit (highlighted by a dotted line in Figure 1) and a personal computer. The object of measurement can be either a person or a calibration device. In the case of measuring human parameters, the measuring unit is connected to the object through measuring electrodes (not shown in the diagram). The calibration device is connected to the measuring unit through a connector and it is necessary for calibrating the measuring unit before operation.

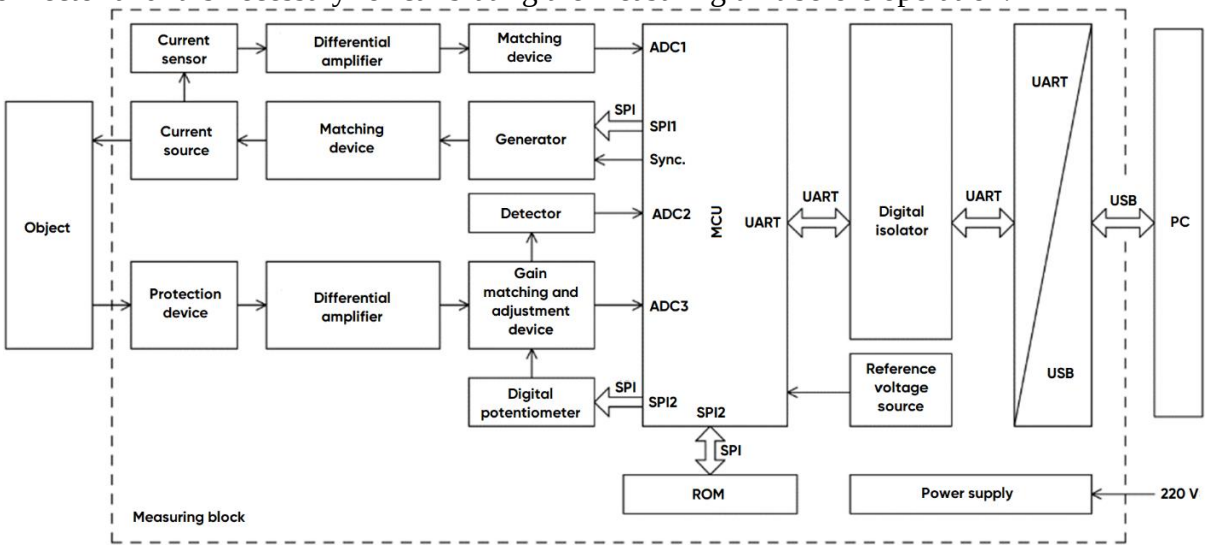


Fig. 1. Structural diagram of an automated system for measuring bioimpedance.

The calibration device imitates the parameters of the electrode-human cell transition. The personal computer is intended for processing, displaying and storing the measurement results. The measuring unit operates under the control of a microcontroller, to which a ROM is connected to store calibration coefficients, the number of the measuring unit, and other service information. The voltage reference source generates the voltage with high accuracy and temperature stability for the ADC operation. The microcontroller is connected to a personal computer through a digital isolator and an interface converter. The digital isolator prevents leakage current from flowing into the personal computer, and also additionally protects a person from electric shock (in the grounding absence of the personal computer case).

To form a sinusoidal signal, a generator, which is controlled via the SPI interface is provided. The current source generates a sinusoidal current on the measurement object. The voltage drop across the object is measured by a differential amplifier with an input ESD protection circuit. The matching and gain control device is controlled by a digital potentiometer, which makes it possible to change the gain of the entire receiving path. From the output of the matching and gain control device, the signal is fed to the input of the ADC3 of the microcontroller, as well as to the detector, which extracts the signal amplitude and feeds it to the input of the ADC2 of the microcontroller. To assess the shape of the flowing current, a current sensor is provided, the voltage from which is measured by a second differential amplifier, after which the signal is fed to the matching device and to the input of the ADC1 of the microcontroller.

## Conclusion

The development of new approaches to both hardware and software for bioimpedance analysis in recent years has significantly increased its capabilities and expanded the list of both already implemented and promising applications. Although the technology has been improved, it is currently difficult to obtain high-quality measurements of physiological parameters with most commercially available bioimpedance analyzers because they do not detect large amounts of fat under the skin.

## REFERENCES

1. **Tronstad C., Strand-Amundsen R.**, Possibilities in the application of machine learning on bioimpedance time-series, J Electr Bioimp, vol. 10, pp. 24-33, 2019.

2. **Freeborn T. J., Crircher S.**, Artifacts in Localized Multi-Frequency Bioimpedance Measurements, IFAC PapersOnLine 54-15 pp. 55-60, 2021.

3. **Antipenko V. V., Pecherskaya E. A., Zinchenko T. O., Artamonov D. V., Spitsina K. Yu., Pecherskiy A V.**, Development of an automated bioimpendance analyzer for monitoring the clinical condition and diagnosis of human body diseases, J. Phys. Conf. Ser. 1515 (5), 2020.

# Microfluidic Device for the Synthesis of Cellular Microspheroids in Double Emulsion Droplets for 3D Bioprinting

**D. A. Belousova [1✉], P. S. Pleshakov [1], N. A. Filatov [1], A. S. Bukatin [1,2]**
[1] Laboratory of Renewable Energy Sources, Alferov Saint Petersburg National Research Academic University of the Russian Academy of Sciences, 194021 Saint Petersburg, Russia;
[2] Laboratory of Bio and Chemosensor Microsystems, Institute for Analytical Instrumentation of RAS, 198095 Saint-Petersburg, Russia
✉dbelousovaaa@gmail.com

**Abstract.** For the efficient production of 3D bioinks for printing artificial tissues and organs, it is promising to synthesize cellular microspheroids in double emulsion drops. The main advantage of using this method is that microspheroids are formed much faster than when implementing the classical approach of creating cellular spheroids. In this work, we investigated the formation of microspheroids from model CT-26 EGFP cells in double emulsion droplets. To do this we developed microfluidic chips with two flow-focusing droplet generators which allow to generate double emulsions in one chip. Also the method for selective treatment of microchannels with a hydrophilic/hydrophobic coating was developed. Our results show the average time of clustering and formation of microspheroids from encapsulated into droplets cells does not exceed 2-4 hours.

**Keywords:** double emulsion, cell microspheroids, 3D bioink, 3D bioprinting, microfluidic chips, droplet microfluidics.

## Introduction

Currently, 3D bioprinting technologies for the synthesis of artificial tissues and organs are being actively developed [1]. One of the challenges in this area is the development of methods for the efficient production of high-resolution 3D bioinks (material for bioprinting). Classical approaches are based on the creation of cell spheroids (250–500 μm in diameter) on agarose matrices [2]. This approach is poorly scalable, provide highly polydisperse spheroids. Additionally there are problems of cell survival inside large spheroids. At the same time, in 3D bioprinting, the spatial resolution of printing is limited by the large sizes of spheroids.

In this direction, droplet microfluidics technologies have great potential, which provide control of liquid flows at microscales in special microfluidic chips, usually consisting of co-flow or flow-focusing droplet generators, which allow to form monodisperse water-in-oil droplets of a given size. In addition to simple two-phase emulsions, complex multiple emulsions are of great interest, in which one microdroplet contains single or multiple internal compartments (for example, a “water-oil-water” double emulsion). When working with cells, this allows you to create favorable conditions for their life (for example, better gas exchange).

In particular, it was proposed to use double emulsion drops in microfluidic chips for the synthesis of cellular microspheroids (e.g. in the range of 30 – 90 μm in diameter). Wherein, such spheroids can be released with or without microgel encapsulation for their use in tissue engineering. One of the advantages of such system is that it takes approximately 150 minutes for the aggregation of encapsulated cells into spheroids, while other technologies require approximately 1 to 4 days [3]. Also, this method has the ease of culturing cells. However, the formation of a double emulsion in microfluidic chips is a laborious task. The first problem is to form stable monodispersed emulsion generation in a single chip. It is required to select the composition of phases (selection of surfactants) to stabilize the emulsion and prevent coalescence. The second problem is the instability of the hydrophilic and hydrophobic coatings of microchannels in a single microfluidic chip. Because of this, either the monodispersity of the droplets is disturbed, or the formation of a double emulsion is completely disrupted.

## Materials and Methods

In this work, studies were carried out on the formation of a double emulsion of the type "water-oil-water" in microfluidic chips. For this, soft lithography methods [4] were used to fabricate various microfluidic chips with two droplet generators. For their production, polydimethylsiloxane (PDMS) kit with a curing agent and a liquid silicone base was used. For the manufacture of microchips, the proportion of the agent to the base was 1:10. Polymerization took place during heat treatment in an oven (SNOL 67/350) at 65°C for 4 hours. To obtain a hydrophilic coating of the inner walls of the microchannels, we developed a corona discharge treatment, followed by covering with a PVA solution (1% polyvinyl alcohol; aqueous solution). All microfluidic chips had 3 inputs for different liquids: inner phase – deionized water or RPMI medium with CT26-EGFP cells, middle phase – mineral oil (330779 light, Sigma-Aldrich) or fluorocarbon (HFE-7500), outer phase – deionized water. To study the formation of microspheroids from cells, a model cancer cell line CT26-EGFP was chosen. Standard cellular techniques were used to work with them. Cells incubation was carried out in a Sanyo MCO-18AC incubator at 37°C and 5% $CO_2$. The experiments were carried out using a Leica DM 4000B LED optical microscope with a Ximea xiC MC023MG-SY-UB camera and a microfluidic pressure controller with pressure controller with pneumatic interfaces [5].

## Results and Discussion

As a result of the research, designs of microfluidic chips were developed to generate a double emulsion in a single chip. Also the method for selective treatment of microchannels with a hydrophilic/hydrophobic coating was developed. More than 10 samples of PDMS/glass microfluidic chips were made. The study of the formation of CT26-EGFP cell microspheroids in double emulsion drops showed that the size of microspheroids can be controlled depending on the concentration of cells in the initial solution. The average time of clustering and formation of microspheroids does not exceed 2-4 hours. Additionally, studies were carried out on their release from emulsion drops and subsequent cultivation.

## REFERENCES


1. **Du X.,** 3D bio-printing review, *IOP Conference Series: Materials Science and Engineering*. Vol. 301 No. 1 (2018) p.012023.
2. **Li M., Fu T., Yang S., Pan L., Tang J., Chen M., Liang P., Gao Z., Guo L.,** Agarose-based spheroid culture enhanced stemness and promoted odontogenic differentiation potential of human dental follicle cells in vitro, *In Vitro Cellular & Developmental Biology-Animal*. 57 (2021) 620-630.
3. **Jiang W., Li M., Chen Z., Leong K. W.,** Cell-laden microfluidic microgels for tissue regeneration, *Lab on a Chip. 16* (23) (2016) 4482-4506.
4. **Filatov N. A., Denisov I. A., Evstrapov A. A., Bukatin A. S.,** Open-Source Pressure Controller Based on Compact Electro-Pneumatic Regulators for Droplet Microfluidics Applications, *IEEE Transactions on Instrumentation and Measurement*. *71* (2022) 1-10.
5. **Bukatin A. S., Mukhin I. S., Malyshev E. I., Kukhtevich I. V., Evstrapov A. A., Dubina M. V.,** Fabrication of high-aspect-ratio microstructures in polymer microfluid chips for in vitro single-cell analysis, Technical Physics. 61 (2016) 1566-1571.

# Single-molecule characterization of nucleosome stability using '603' nucleosome position sequence

**V.A. Vinnik[1], I.D. Goncharov[1], D.A. Ianchik[2], A.A. Alekseev[1✉], A.N. Arseniev[1], G.E. Pobegalov[3,4], M.A. Khodorkovskii[1]**

[1] Peter the Great St. Petersburg Polytechnic University, Saint-Petersburg, Russia
[2] Saint-Petersburg State University, Saint-Petersburg, Russia
[3] The Francis Crick Institute, London, United Kingdom
[4] University College London, London, United Kingdom
✉a.alekseev@nanobio.spbstu.ru

**Abstract.** In this thesis we describe the DNA preparation protocol for characterization of nucleosome stability at the single-molecule level. The preparation of the DNA construct involved the insertion of the '603' nucleosome positioning sequence into 11.3 kbp plasmid vector using Gibson Assembly cloning. The final DNA construct was used to reconstitute nucleosomes by gradient salt dialysis. The reconstitution of nucleosomes was confirmed by measuring force-extension behavior of individual nucleosomes using dual trap optical tweezers. The obtained results could be further used to study the interaction of nucleosomes with regulatory proteins at single-molecule level.

**Keywords:** nucleosome, chromatin remodeling, single-molecule biophysics, optical tweezers.

## Introduction

Nucleosome is the basic building component of chromatin and consists of 147 base pairs of DNA wrapped ~1.65 times around histone octamer. Nucleosomes play a significant role in the accessibility of the eukaryotic genome and are involved in the processes of DNA replication, DNA repair and transcription [1]. During these processes nucleosomes interact with a variety of regulatory proteins, which can lead to the alteration of nucleosome structure and stability providing the access to the DNA bound to the nucleosome core.

Reconstitution of nucleosomes using specific sequences exhibiting a high affinity for histone octamers is one of the ways to examine nucleosomes and their interactions with regulatory proteins *in vitro* [2]. In this work we describe the preparation of a DNA-construct containing a single '603' nucleosome position sequence (NPS). The designed DNA-construct allowed addressing the mechanical stability of individual '603' nucleosomes using single-molecule technique.

## Materials and Methods

The preparation of the desired DNA construct consisted in the insertion of '603' NPS into the plasmid vector prl574rpoC previously used for single-molecule experiments [3]. To this end DNA fragment containing '603' NPS was fused with two DNA fragments derived from prl574rpoC using Gibson Assembly (Figure 1*a*). Overlapping DNA regions were introduced with a polymerase chain reaction. For single-molecule manipulation the final plasmid vector containing '603' NPS was digested with SacI restriction enzyme and ligated with biotinylated oligonucleotides.

The linearized 11.5 kbp DNA construct containing single '603' NPS was used for nucleosome reconstitution by salt gradient dialysis. To this end, mix of histones and DNA was sequentially dialyzed against the buffer containing (2 M - 1.5 M – 1 M – 0.5 M – 0.25 M - 0.1 M - 0.02 M - 0.01 M) of NaCl. Each round of dialysis was carried out for 25 minutes at 22°C.

To address the unwrapping of reconstituted nucleosomes upon mechanical stretching, a combination of dual trap optical tweezers setup with microfluidics was used. Manipulations with single DNA molecules containing nucleosome particles were made with the use of 2.1 μm streptavidin-coated polystyrene beads. During the experiment single DNA molecules containing nucleosome were tethered between two optically trapped beads due to the biotin-streptavidin binding. Force-extension curves were measured by increasing the distance between optical traps with 0.15 μm/s velocity and simultaneously measuring the applied tension.

## Results and Discussion

The insertion of '603' NPS was identified by enzymatic restriction analysis and Sanger sequencing. After reconstitution of nucleosomes on linearized DNA with biotinylated ends, the behavior of the obtained complex was analyzed at the single-molecule level. Combination of optical tweezers with the multichannel microfluidic chamber allowed sequentially trapping of beads and attaching single DNA containing nucleosome particle. After this, the force-extension behavior of the complex was measured. The obtained force-extension curves (Figure 1*b*) were in general similar to those of naked dsDNA: about zero force region was followed by an increase in tension when bead-to-bead distance become close to the contour length of the used DNA, under tension of ~60 pN the overstretching plateau, an intrinsic mechanistic feature of duplex DNA, was observed. However, in the range of 10 - 45 pN tension force-extension curves exhibited an abrupt saw-tooth-like shift which corresponds to the unwrapping of inner turn of nucleosome as described previously [4]. The unwrapping of '603' nucleosomes, examined in this work, occurred under tension 24 ± 8 pN (Figure 1*c*) and was accompanied by 19 ± 4 nm increase in length of the tether.

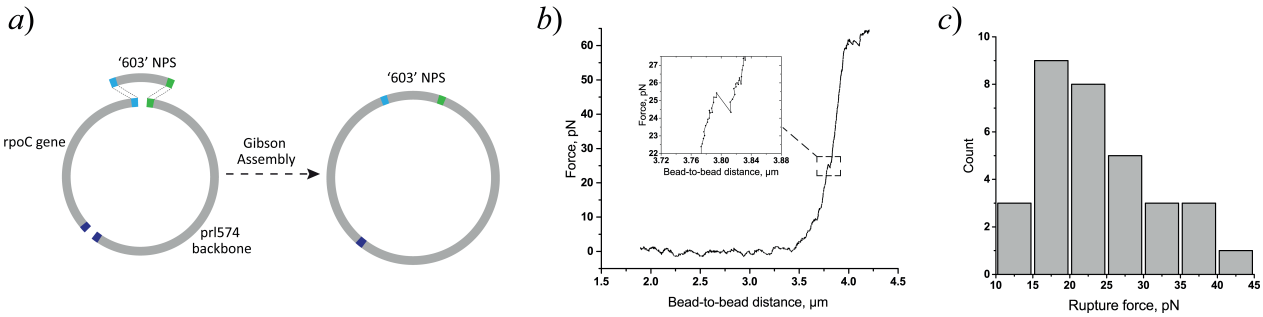


Fig 1. Single-molecule characterization of '603' nucleosomes. *a*). Design of plasmid vector containing '603' NPS. *b*). Representative force-extension curve of '603' nucleosome particle. *c*). Rupture force distribution.

## Conclusion

The DNA construct containing single '603' nucleosome was successfully designed and used in single-molecule experiment. The stability of '603' nucleosomes was characterized at single-molecule level. The approved methods could be further used to study the impact of regulatory proteins on nucleosome stability.

## Acknowledgments

The authors acknowledge the group of Olga Lavrik (Institute of Chemical Biology and Fundamental Medicine, SB RAS, Novosibirsk) for providing purified histones and '603' NPS.

## REFERENCES

1. **Lai W. K., Pugh B. F.**, Understanding nucleosome dynamics and their links to gene expression and DNA replication, Nature reviews Molecular cell biology. 18 (9) (2017) 548-562.
2. **Lowary P., Widom J.**, New DNA sequence rules for high affinity binding to histone octamer and sequence-directed nucleosome positioning, Journal of molecular biology. 276 (1) (1998) 19-42.
3. **Alekseev A., Pobegalov G., Morozova N., Vedyaykin A., Cherevatenko G., Yakimov A., Baitin D., Khodorkovskii M.**, A new insight into RecA filament regulation by RecX from the analysis of conformation-specific interactions, Elife. 11 (2022) e78409.
4. **Spakman D., King G. A., Peterman E. J., Wuite G. J.**, Constructing arrays of nucleosome positioning sequences using Gibson Assembly for single-molecule studies, Scientific Reports. 10 (1) (2020) 9903.

# Combining single-photon miniature fluorescence microscopy and electrophysiological recording to study the activity of mouse hippocampal neurons *in vivo*

**Vinokurov E.K.[1], Erofeev A.I.[1], Vlasova O.L.[1], Bezprozvanny I.B. [1,2]**

[1] Laboratory of Molecular Neurodegeneration, Institute of Biomedical Systems and Biotechnology, Peter the Great St. Petersburg Polytechnic University, St. Petersburg, Russian Federation
[2] Department of Physiology, University of Texas Southwestern Medical Center at Dallas, Dallas, TX, United States of America

E-mail: eg.vinokurov@yandex.ru , alexander.erofeew@gmail.com

**Abstract.** The investigation of the fundamental and applied foundations of brain function constitutes a priority domain of contemporary science. *In vivo* studies provide data on the activity of the neural network, which is a set of neurons and other types of cells connected to each other and performing certain physiological functions. Neural networks are responsible for the intricate and highly organized workings of the brain, and their operation influences both the mental and physical dimensions of human existence. Nevertheless, the noteworthy advancements in brain research thus far remain limited as they have been achieved *in vitro* or *ex vivo*, so brain research *in vivo* is an important task of modern neurobiology and neurodegeneration. In this project, we have developed a multi-electrode that combines miniature fluorescence microscopy *in vivo* with electrophysiological recording techniques, which can help to identify Alzheimer's disease abnormalities at the neural network level.

## Introduction

*In vivo* visualization of neuronal activity can be achieved through the use of specialized sensors that fluoresce in response to changes in ion concentration, such as calcium. The GCaMP family of genetically encoded calcium indicators is a hybrid of green fluorescent protein (GFP), calmodulin (CaM) and M13 (myosin light chain kinase peptide sequence). GCaMP sensors are widely represented in scientific practice and are often used in studies of neuronal activity. Calcium signaling, which links membrane excitability and biological cell functions, plays an important role in neuronal activity imaging [1,2]. Additionally, the technique of calcium imaging allows for the recording of large populations of neurons, providing an opportunity to understand functional relationships [3,4].

The technology of *in vivo* calcium imaging using a single-photon miniature fluorescence microscope (miniscope) is an important modern tool for studying neuronal networks in various brain regions. The use of the miniscope makes it possible to record neuronal activity on freely moving laboratory animals, in contrast to the traditionally used two-photon imaging.

However, the achievable temporal resolution is limited by the slow (millisecond) kinetics of $Ca^{2+}$ binding, because genetically encoded calmodulin-based $Ca^{2+}$ fluorescent indicators always show an extended fluorescence attenuation time. In other words, registration of high-frequency action potentials may be limited by the dynamics of the calcium sensor. Consequently, calcium imaging *in vivo* does not reflect the entire activity of neural networks and does not provide a complete understanding of what underlies memory formation, learning, sleep, social behavior, feeding and disturbances in these processes [5,6]. One possible way to solve this problem is to combine electrophysiological registration and *in vivo* calcium imaging.

## Results

In this work, we developed a multielectrode combined with a gradient lens and adapted to its dimensions. This multielectrode is a three-layer rectangular structure of polyimide film and thermoformed contact/conducting gold tracks. On one side of the film are 12 exposed conductive contacts for recording local field potentials, and on the other side are a similar number of conductive tracks for connecting a connector that transmits data to the processing board (Figure 1).

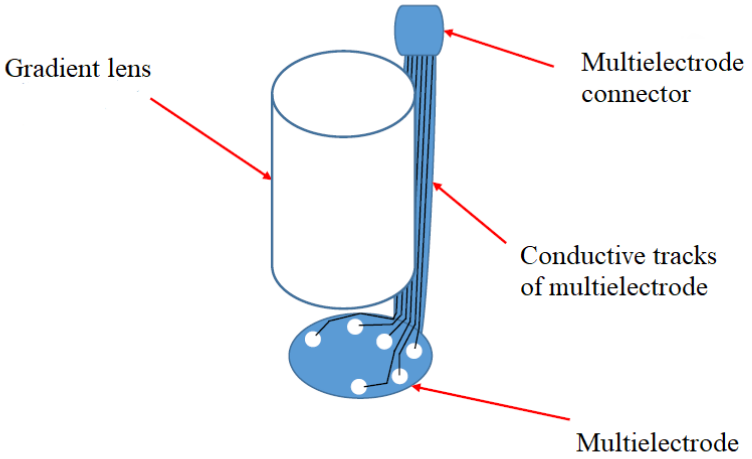


**Рис.1** Multielectrode combined with GRIN-lens.

The multielectrode that has been developed enables the integration of *in vivo* calcium imaging using a miniscope and electrophysiological registration. This approach will make it possible to study the activity of neural networks in more detail, as well as to map the brains of freely moving laboratory animals with high spatial and temporal resolution, which will expand the possibilities of research in the field of neurobiology.

The aim of our future work will be to analyze the activity of hippocampal neurons based on miniature fluorescence microscopy data and parallel recording of the local field potential using the developed multielectrode in wild-type laboratory mice and with an Alzheimer disease model in the evaluation of conditionally reflexive freezing. This research will reveal Alzheimer's disease abnormalities at the neural network level and, as a consequence, suggest potentially new treatments or mechanisms of pathology associated with progressive memory loss in Alzheimer's disease. In addition, the ability to study individual neurons *in vivo* in neural networks using a miniscope and electrophysiological recording will make it possible to evaluate the effects of potential therapeutic agents that can be used to treat various diseases, including neurodegenerative ones.

**Acknowledgments**
This research was funded by the Russian Science Foundation grant no. 22-75-00028 (A.I.E.)

## References

1. Berridge, M.J., Neuronal calcium signaling. Neuron.
2. Bezprozvanny, I.B., Mattson, M.P., Neuronal calcium mishandling and the pathogenesis of Alzheimer's disease. Trends Neurosci.
3. Timko, B.P., et al., Electrical recording from hearts with flexible nanowire device arrays. Nano Lett.
4. Khodagholy, D., et al., Highly conformable conducting polymer electrodes for *in vivo* recordings. Adv. Mater.
5. Cai, D.J., et al., A shared neural ensemble links distinct contextual memories encoded close in time. Nature.
6. de Groot, A., et al., NINscope, a versatile miniscope for multi-region circuit investigations. Elife.

# Molecular dynamics calculation of NADH rotational diffusion times in aqueous – methanol solutions

**D. A. Volkov [1,2]✉, I.A. Gorbunova [1], M.E. Sasin [1], O. S. Vasyutinskii [1]**
[1] Ioffe Institute, Saint-Petersburg, Russia
[2] Peter the Great St.Petersburg Polytechnic University, Saint-Petersburg, Russia
✉dinvol99@gmail.com

**Abstract.** Molecular dynamics of reduced nicotinamide adenine dinucleotide (NADH) in water-methanol solutions was performed. Diffusion times were acquired for each methanol concentration by two different methods and compared with previously experimentally determined values.

**Keywords:** molecular dynamics, GROMACS, NADH, rotational diffusion time.

**Funding:** This study was funded by Russian Science Foundation, grant number 23-22-00230.

## Introduction

Computer modeling is important part of modern physics, especially biophysics and molecular dynamics. Classical trajectory molecular dynamics is often used for dynamics calculations related to fluorescent molecules as quantum calculations are still impossible for large systems such as coenzymes. This study is focused on dynamic research of coenzyme nicotinamide adenine dinucleotide (NADH) that plays an important role in regulation of metabolic processes in living cells. The main aim of this work was the calculation of rotational diffusion times of NADH in water-methanol solutions at various concentrations and comparison of the results obtained with rotational diffusion times previously determined in the two-photon experiments [1].

## Materials and Methods

Computer simulations of NADH dynamics were performed by GROMACS 2020.1 software. In all simulations CHARMM36-jul2021 forcefield was used to gain molecular parameters. These parameters were defined from quantum chemistry calculations as well as determined from experiment. Structure file of NADH was taken from charm-gui small molecule library in pdb format. Simulation of NADH was performed at 300 K and normal atmospheric pressure. The energy of the system was minimized and then system was equilibrated. NVT equilibration was performed with velocity-rescale (Bussi) algorithm for temperature coupling. NPT equilibration was performed with Berendsen algorithm for pressure coupling. Equilibrated system was underwent classical trajectory molecular dynamics calculations for 300 ns with a time step of 2 fs.

## Results and Discussion

Seven molecular trajectories of NADH for different methanol concentrations were acquired from computer modeling and were analyzed with self-made codes written in Python. This analysis allowed to determine conformation distributions for each methanol concentration and allowed calculation and diagonalization of moments of inertia for each step of trajectory and each conformation. Two alternative methods were used for determination of rotational diffusion times. The first method was based on NADH conformation distributions. It was found that there were three different conformation groups: folded, intermediate, and unfolded that could be defined by distances (R) between nicotinamide and adenine centers of mass. The folded conformation ($N_f$) was characterized by R<5.5 Å, unfolded conformation ($N_{un}$) by R > 12 Å, and intermediate conformation ($N_m$) by 5.5 Å<R <12 Å. As was shown that all conformational groups could be considered as a prolate top. Under this assumption the geometrical factor f was calculated for each conformation and then used with Stokes-Einstein-Debye equation (1) for determination of the corresponding rotational diffusion times $\tau_i$.

$$\tau_i = Cf_i \frac{\eta V}{kT}, \tag{1}$$

where $i = f,m,un$.

The rotational diffusion time of the molecular ensemble ($\tau_r$) was calculated according to:

$$\frac{1}{\tau_r} = \frac{N_f}{\tau_f} + \frac{N_m}{\tau_m} + \frac{N_{un}}{\tau_{un}} \tag{2}$$

The second method used calculation of rotational diffusion times $\tau_n$ at each timestep of 2 fs. These diffusion times were then used for construction of the mean anisotropic fluorescence decay intensity according to the expression:

$$I(t) = \sum_n \frac{1}{N} e^{-\frac{t}{\tau_n}} \approx I_0 e^{-\frac{t}{\tau_r}}, \tag{3}$$

where $N$ is full number of timesteps

The time $\tau_r$ was compared with that determined experimentally [1]. The comparison between experimental and theoretical rotational diffusion time is shown in figure 1.

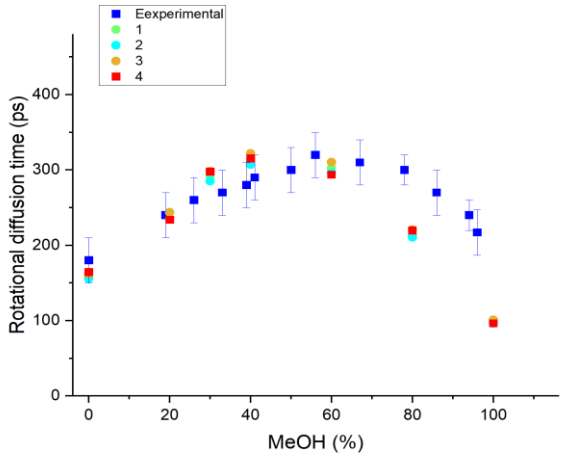


Fig. 1. Experimentally determined and calculated rotational diffusion time of NADH in water-MeOH solutions. Blue squares are experimental results [1]. The symbols 1, 2, 3 are rotational diffusion time values calculated with first method at different parameters V and C in eq 1. The symbols 4 represent the calculation results obtained with the second method.

## Conclusion

The results of MD calculation for low concentration of methanol was in a good agreement with experimental results. Difference between experiment and theoretical results for higher concentrations can be explained by difference of solvation of different concentration of methanol, which should change rotational diffusion times of molecules.

## REFERENCES


1. **Gorbunova, I. A., Sasin, M. E., Rubayo-Soneira, J., Smolin, A. G., & Vasyutinskii, O. S.** Two-photon excited fluorescence dynamics in NADH in water–methanol solutions: The role of conformation states. *The Journal of Physical Chemistry B. 124*(47) (2020) 10682-10697.

2. **Radoszkowicz, L., Huppert, D., Nachliel, E., & Gutman, M.** Sampling the Conformation Space of FAD in Water− Methanol Mixtures through Molecular Dynamics and Fluorescence Measurements. *The Journal of Physical Chemistry A*, *114*(2), (2010) 1017-1022.

3. **Anderton, Robert M., and John F. Kauffman.** "Temperature-dependent rotational relaxation of diphenylbutadiene in n-alcohols: a test of the quasihydrodynamic free space model." *The Journal of Physical Chemistry* 98.47 (1994) 12117-12124.

# New opportunities for studying the oxygen saturation of blood hemoglobin in capillaries and tissues

**S. Msokar[1,2], R. V. Davydov[2,3,4]✉, M. S. Mazing[5], D. D. Isakova[4] and M. A. Yakusheva[2]**
[1] Higher Institute for Applied Sciences and Technology, Damascus, Syria;
[2] Peter the Great Saint-Petersburg Polytechnic University, St. Petersburg, Russia;
[3] All-Russian Research Institute of Phytopathology, Moscow Region, Russia;
[4] The Bonch-Bruevich Saint Petersburg State University of Telecommunications, St. Petersburg, Russia.
[5] Institute for Analytical Instrumentation of the Russian Academy of Sciences, St. Petersburg, Russia.
✉davydovrv@spbstu.ru

**Abstract.** A new method of express diagnostics of the health state based on the results of non-invasive measurements of the pulse waveform, pulse values, blood pressure, and oxygen saturation of blood vessels and tissues is considered. The feature of these measurements is that they can be carried out both in the hospital and at home (a person can implement them independently). To measure tissue oxygen saturation, a new optical hardware-software complex has been developed, which is compact and portable. The results of experimental studies of pulse waves of various people are presented.

**Keywords:** oxygen saturation, pulse wave, blood, tissues

## Introduction

In recent years, for many reasons, the issues of express diagnostics of the functional state of human health in various situations have received increased attention [1-3]. In contrast to the many methods of express diagnostics, pulse oximetry has not exhausted its possibilities for obtaining additional information about the state of human health in various situations, the potential of which has yet to be fully explored [2, 3].

One of the new solutions for obtaining additional information about human health is using new optical systems developed by us for the simultaneous registration of pulse wave signals and tissue oximetry. We process them with the combination of diagnostic information into a database and compare them with data obtained earlier by other methods. It allows obtain additional information about health in a short time, using new equipment and techniques, both for measuring and processing the recorded signals to interpret the integral signal.

## 2. Materials and Methods

The main goal of all work in this area is to increase the reliability of data on the state of the human body, which are obtained after processing the results of measuring pulse waves and changes in tissue oxygen saturation. To successfully achieve the main target, we have developed a combined system for express diagnostics of the state of human health. Its block diagram is shown in Fig. 1.

An optical sensor developed by us for registering a pulse wave and an optical system for studying tissue oximetry and a standard device for measuring pressure are placed at three points on the hands to carry out measurements. It should be noted that, unlike previous studies, all measurements are carried out synchronously.

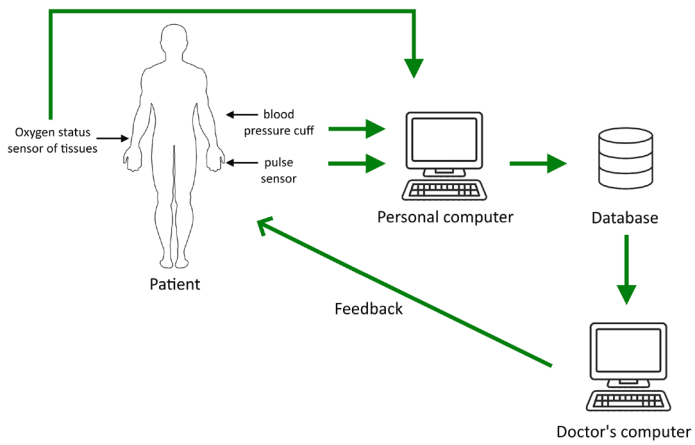


Fig. 1. The scheme for monitoring the state of human health in express mode.

## Results and Discussion

Fig. 2, as an example, presents the results of the registration of pulse waves from people of different age groups.

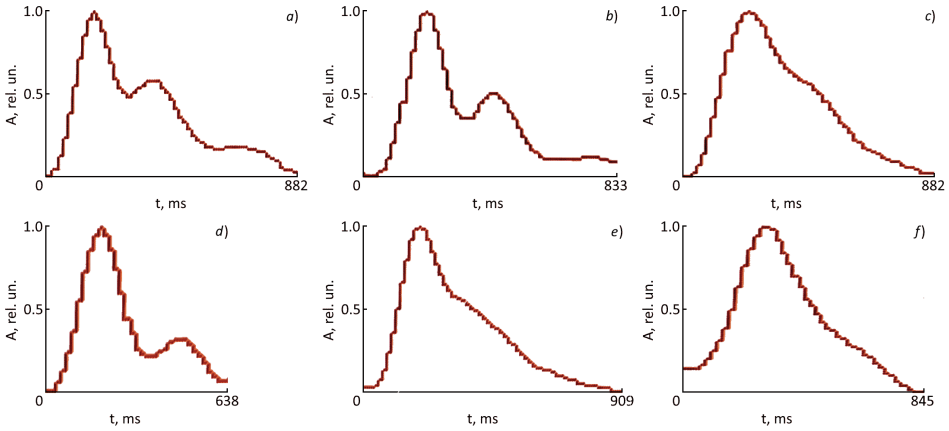


Fig. 2. One period of the pulse wave of patients. Age of male patients: (*a*) 20 years old, (*b*) 30 years old, (*c*) 56 years old. Age of female patients: (*d*) - 22 years, (*e*) - 28 years, (*f*) - 40 years.

The results show that the new system makes it possible to detect minor deviations in pulse waveforms and tissue oxygen saturation problems, which were hard to do on the previously used equipment.

## Conclusion

Comparing data on human health obtained using the new methods and devices with examination data on certified clinical equipment showed a high degree of agreement. It confirms the validity of the methods and optical devices we developed for the integrated monitoring of the work of the human cardiovascular system in a short-time period.

## REFERENCES

1. **Nascimento L. M. S.d., Bonfati L. V., Freitas M. L. B., Junior J. J. A., Siqueira H. V. and Stevan S. L.**, Sensors and Systems for Physical Rehabilitation and Health Monitoring-A Review, Sensors. 20(15) (2020) 4063.

2. **Allen J.**, Photoplethysmography and its application in clinical physiological measurement, Physiological Measurement. 28(3) (2007) R1-39.

3. **Fine J., McShane M. J., Coté G. L., and Scully C. G.**, A Computational Modeling and Simulation Workflow to Investigate the Impact of Patient-Specific and Device Factors on Hemodynamic Measurements from Non-Invasive Photoplethysmography, Biosensors. 12(8) (2022) 598.

Conference materials
UDC
DOI: https://doi.org/10.18721/JPM.

# Application of a Pre-processing Algorithm for Ultra-high resolution Electrocardiosignals

**K. V. Zaichenko** [1], **A. S. Afanasenko** [1,2], **A. A. Kordyukova**[1], **E. A. Denisova**[1✉], **D. O. Sevakov**[1,2], **E. P. Logachev**[1]
[1] Institute for analytical instrumentation Russian academy of sciences, Saint-Petersburg, Russia;
[2] Saint-Petersburg State University of Aerospace Instrumentation, Saint-Petersburg, Russia
✉tiranderel@yandex.ru

**Abstract.** Every year there are more and more people suffering from diseases of the cardiovascular system (CVS), in particular, coronary heart disease (CHD). To obtain more complete information about the stages of coronary heart disease development, was performs studies on modeling this disease in experimental animals based on the use of a new author's method of ultra-high resolution electrocardiography (UHR ECG) [1,2]. However, the recorded electrocardiosignals (ECS) are influenced by various factors. In this work is proposed an algorithm for preprocessing the ECG obtained by the UHR ECG method. The following tasks solved: development of an algorithm for filtering ECS obtained from low-frequency (LF) and high-frequency (HF) channels of their registration; selection of characteristic points of ECS from LF-channels, which are analogous to the information obtained using a standard ECG [2]. The result of the algorithm described in the work allows to obtain satisfactory values of RMSE, SNR, signal processing time, as well as to find the PQRST peaks of the cardiogram.

**Keywords:** electrocardiogram, algorithm, passband filter, ultra-high resolution electrocardiography, Fourier, root mean square error, signal-to-noise ratio

**Funding:** The work has been supported by Education and Science Ministry of Russian Federation, State task No. 075-01157-23-00, project No. FZZM-2022-0011

## Introduction

Every year there are more and more people suffering from diseases of the cardiovascular system (CVS), in particular, coronary heart disease (CHD). To obtain more complete information about the stages of its development, the staff of the laboratory "Radio and optoelectronic devices for early diagnosis of pathologies of living systems" of the Institute of analytical instrumentation of the Russian academy of sciences performs studies on modeling this disease in experimental animals based on the use of a new author's method of ultra-high resolution electrocardiography (UHR ECG) [1,2]. However, the recorded electrocardiosignals (ECS) are influenced by various factors. The purpose of this work is to develop an algorithm for preprocessing the ECG obtained by the UHR ECG method. To do this, it is necessary to solve the following tasks: development of an algorithm for filtering ECS obtained from low-frequency (LF) and high-frequency (HF) channels of their registration; selection of characteristic points of ECS from LF-channels, which are analogous to the information obtained using a standard ECG [2].

## Materials and Methods

As it is known, a useful ECS for a standard ECG method is recorded in the frequency range from 1 to 100 Hz. Therefore, the first stage of preprocessing the ECS from the LF-channel is the use of a bandpass filter with the appropriate bandwidth. In addition, the use of a notch filter allows you to reduce harmonics corresponding to network interference and a constant component.

Next, it is necessary to remove artifacts that arise from accidental exposure to the object of study. To do this, points with maximum and minimum amplitudes are identified among the signal samples. The resulting range of values is divided into 100 sections. At each section, the number of values of the signal samples is calculated, and among the sections, the one where the maximum number of points hit is allocated. If the number of points in a section is less than 0.001 of the maximum number of points that hit any section, then the signal samples whose amplitudes hit this

section are considered outliers. Further investigation of the ECS obtained by the UHR ECG method consists in isolating characteristic signal points from the LF-channel to compare the coordinates of these points with the counts in the HF-channel. This will allow us to detect previously unknown markers of cardiac pathologies that manifest due to UHR ECS.

To selecting the characteristic points of the ECG, the standard command for ECG processing is used - wfdb.processing [3]. This function identifies two groups of points: suspicious for R-peaks and suspicious for PQST-peaks. If one of the found points is higher by 3 standard deviations from the base line, then it is a P, T or R peak. A point above the base line is followed by a point below (Q or Speak).

## Results and Discussion

As the initial signal, the ECG received from the experimental rat from the LF-channel of the II-th lead was used [3]. Fig.1. shows: a) ECS before and after processing; b) ECS with highlighted characteristic points.

a) b)

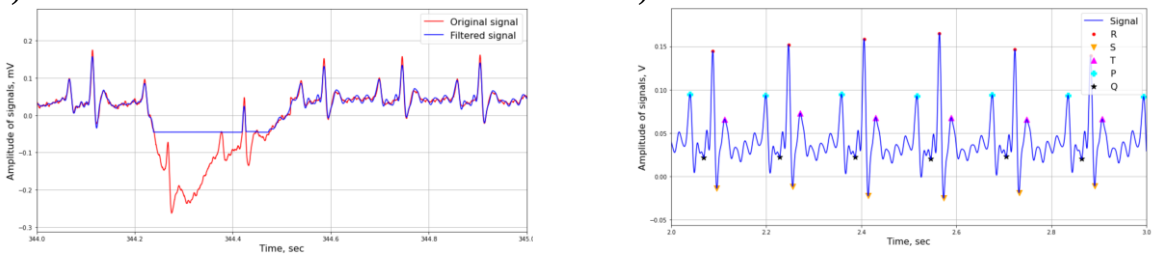


Fig. 1. - a) ECS before and after processing; b) ECS with highlighted characteristic points

To demonstrate the efficiency of the algorithm, the values of parameters such as the RMS deviation RMSE = 0.035, the signal-to-noise ratio SNR = 4.37 dB of the filtered signal, as well as the processing time of one recording of the signal with a length of 56.2 minutes TIME = 17.1 min are given.

## Conclusion

The described algorithm of filtering and primary processing of the UHR ECG allows filtering the signal with minimum distortion of useful information, as well as highlighting the characteristic points of the ECS recorded from the LF-channel. On the other hand, the studies have revealed certain limitations in the use of the developed algorithm. The main one is related to the need to adjust the parameters of the function when changing the experimental animal. In this regard, the work on further improvement of the developed application software and the development of new methods of filtering UHR ECG have to be performed.

## Acknowledgments

The work has been supported by Education and Science Ministry of Russian Federation, State task No. 075-01157-23-00, project No. FZZM-2022-0011.

## REFERENCES

1. **Zaichenko K.V., Kordyukova A.A., Logachev E.P., Luchkova M.N.,** Application of Radar Techniques of Signal Processing for Ultra-High Resolution Electrocardiography. Biomedical Engineering. 2019, no. 55(1), pp. 31–35
2. **Zaichenko K.V., Gurevich B.S., Kordyukova A.A.,** Method of Reliable Electrocardiographic Control of Ischemia Appearance in Investigations with Experimental Animals. IEEE Xplore library. 2021, no. 13-14, pp. 0078–008.
3. Processing — wfdb "4.1.0" documentation. URL: https://wfdb.readthedocs.io/en/latest/processing.html. Accessed Mar. 10, 2023

# New opportunities for studying the oxygen saturation of blood hemoglobin in capillaries and tissues

**R V Davydov[1,2,3], M S Mazing[4], D D Isakova[2], M A Yakusheva[1], S. Msokar[1]**

[1]Peter the Great St. Petersburg Polytechnic University, St. Petersburg, Russia;
[2]Bonch-Bruevich St. Petersburg State University of Telecommunications, St. Petersburg, Russia;
[3]All-Russian Research Institute of Phytopathology, Moscow Region, Russia;
[4]Institute for Analytical Instrumentation of the Russian Academy of Sciences, St. Petersburg, Russia

davydovrv@spbstu.ru

**Abstract**. A new method of express diagnostics of the health state based on the results of non-invasive measurements of the pulse waveform, pulse values, blood pressure, and oxygen saturation of blood vessels and tissues is considered. The feature of these measurements is that they can be carried out both in the hospital and at home (a person can implement them independently). To measure tissue oxygen saturation, a new optical hardware-software complex has been developed, which is compact and portable. The results of experimental studies of pulse waves of various people are presented.

## 1. Introduction

In recent years, for many reasons, the issues of express diagnostics of the functional state of human health in various situations have received increased attention [1-3]. In contrast to the many methods of express diagnostics, pulse oximetry has not exhausted its possibilities for obtaining additional information about the state of human health in various situations, the potential of which has yet to be fully explored [2, 3]. One of the new solutions for obtaining additional information about human health is using new optical systems developed by us for the simultaneous registration of pulse wave signals and tissue oximetry. We process them with the combination of diagnostic information into a database and compare them with data obtained earlier by other methods. It allows obtain additional information about health in a short time, using new equipment and techniques, both for measuring and processing the recorded signals to interpret the integral signal.

## 2. Materials and Methods

The main goal of all work in this area is to increase the reliability of data on the state of the human body, which are obtained after processing the results of measuring pulse waves and changes in tissue oxygen saturation. To successfully achieve the main target, we have developed a combined system for express diagnostics of the state of human health. Its block diagram is shown in Figure 1.

An optical sensor developed by us for registering a pulse wave and an optical system for studying tissue oximetry and a standard device for measuring pressure are placed at three points on the hands to

carry out measurements. It should be noted that, unlike previous studies, all measurements are carried out synchronously.

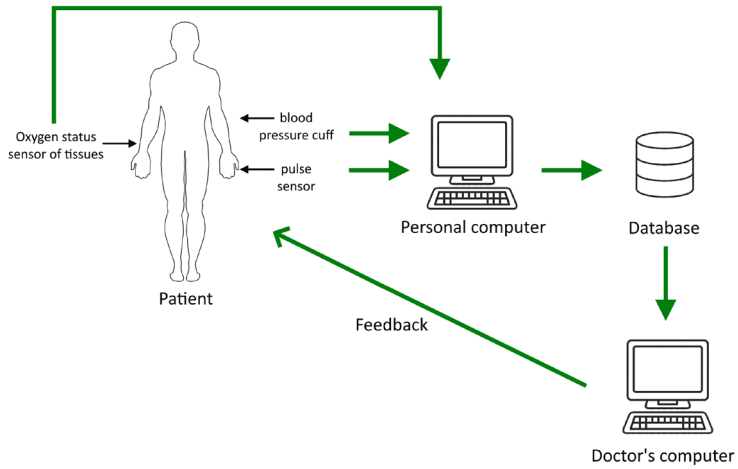


**Figure 1.** The scheme for monitoring the state of human health in express mode.

## 3. Results and Discussion

Figure 2, as an example, presents the results of the registration of pulse waves from people of different age groups.

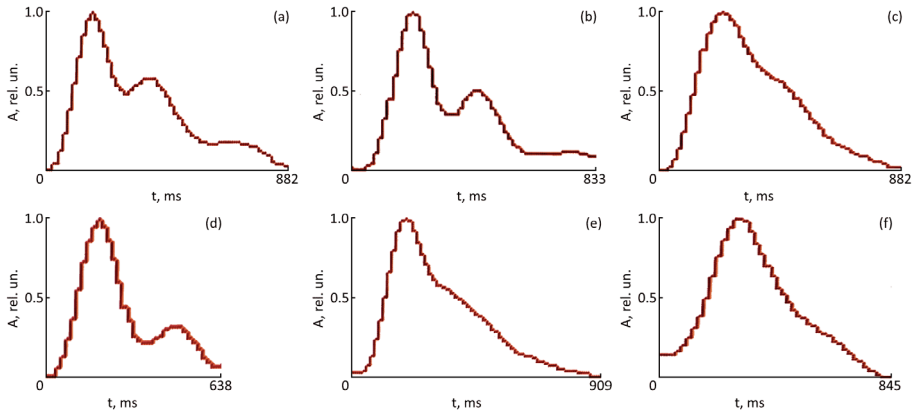


**Figure 2.** One period of the pulse wave of patients. Age of male patients: (a) 20 years old, (b) 30 years old, (c) 56 years old. Age of female patients: (c) - 22 years, (d) - 28 years, (e) - 40 years.

The results show that the new system makes it possible to detect minor deviations in pulse waveforms and tissue oxygen saturation problems, which were hard to do on the previously used equipment.

## 4. Conclusion

Comparing data on human health obtained using the new methods and devices with examination data on certified clinical equipment showed a high degree of agreement. It confirms the validity of the methods and optical devices we developed for the integrated monitoring of the work of the human cardiovascular system in a short-time period.

## References

[1] Nascimento L M S.d, Bonfati L V, Freitas M L B, Junior J J A, Siqueira H V and Stevan, S.L. 2020 *Sensors* **20** 4063

[2] Allen J 2007 *Physiological Measurement* **28** R1–R39

[3] Fine J, McShane M J, Coté G L, and Scully C G 2022 *Biosensors* **12** 598

# Converting Bio-microscope into Lithography Machine: Proof-of-Concept

**P M Dubina, A A Abelit, N A Boitsova, and D D Stupin**

[1]Alferov University, Khlopina 8/3, 194021 St. Petersburg, Russia
E-mail: filipp.dubina@gmail.com, Stu87@ya.ru

**Abstract.** Nowadays, bioelectronics are widely used for solving important problems of the healthcare, biology, and biosensing. However, the great difference between the biolectronic device fabrication industry and the laboratories, where such devices are used, remains a bottleneck for further progress in this area. For overcome this barrier, we have developed the technology for microlithography – the essential process for creating bioelectronic devices – for which required only typical equipment of the biological laboratory and market-avaliable reagents. Using our technology, we have prepared the microstructures with resolution 10-100 $\mu$m, which is enough for making bioelectrodes, in particular, for bioimpedance devices or for vision prosthetic care implants.

## 1. Introduction

The most important step in microelectronic production, and bioelectronic devices particularly, is the process of formation of structures with a certain topology on a substrate [1]. One of the most common methods for solving this problem is lithography, a technology based on changing the solubility of the photosensitive polymer material (photoresist). The lithographers, apparatus providing such operation, are typically expensive and incompatible with the conditions of the bio-laboratories. However, today almost no bio-laboratory is complete without the use of a fluorescent microscope with UV-pumping lamp and motorized stage. This apparatus, in fact has no significant technical differences with scanning lithographer. Moreover, they are equipped with additional devices for precision installation of samples and software for automating sample movements, changing lighting parameters, and therefore they can be used for providing lithography process directly in bio-applications laboratories. Using this idea, we have proposed a paradigm for converting a fluorescence microscope into a lithographer for bioelectronic device fabrication.

## 2. Materials and methods

As an apparatus for providing lithography, we have used the Zeiss Observer.Z1 confocal microscope (Zeiss, Germany) equipped with a metal halide illuminator HXP 120 (LEj JENA GmbH, Germany) and motorized XY stage. We used dry film negative photoresist AQUA MER ME720 (Zhuhai Dynamic Technology, China) for 50 $\mu$m thickness placed between layers of lavsan and polyethylene film and 1% aqueous solution of sodium carbonate (Na2CO3) for developing purposes. Thin film deposition was improved by pre-dissolving it in ethanol in a mass ratio of 1:1.5 and spin coating it for two minutes on cover glass 24x24 mm (Menzel-Gläser, Germany). The defects were never possible to fully eliminate, but this technique allowed us to significantly reduce the film thickness.

## 3. Results

The obtained results are presented in Fig. 1. As can be seen, the proposed technology allows us to create structures with resolution from 10 to 100 $\mu$m, which satisfies the requirements for electrodes in bioelectronic devices in studies of single cells and their populations [2–4]

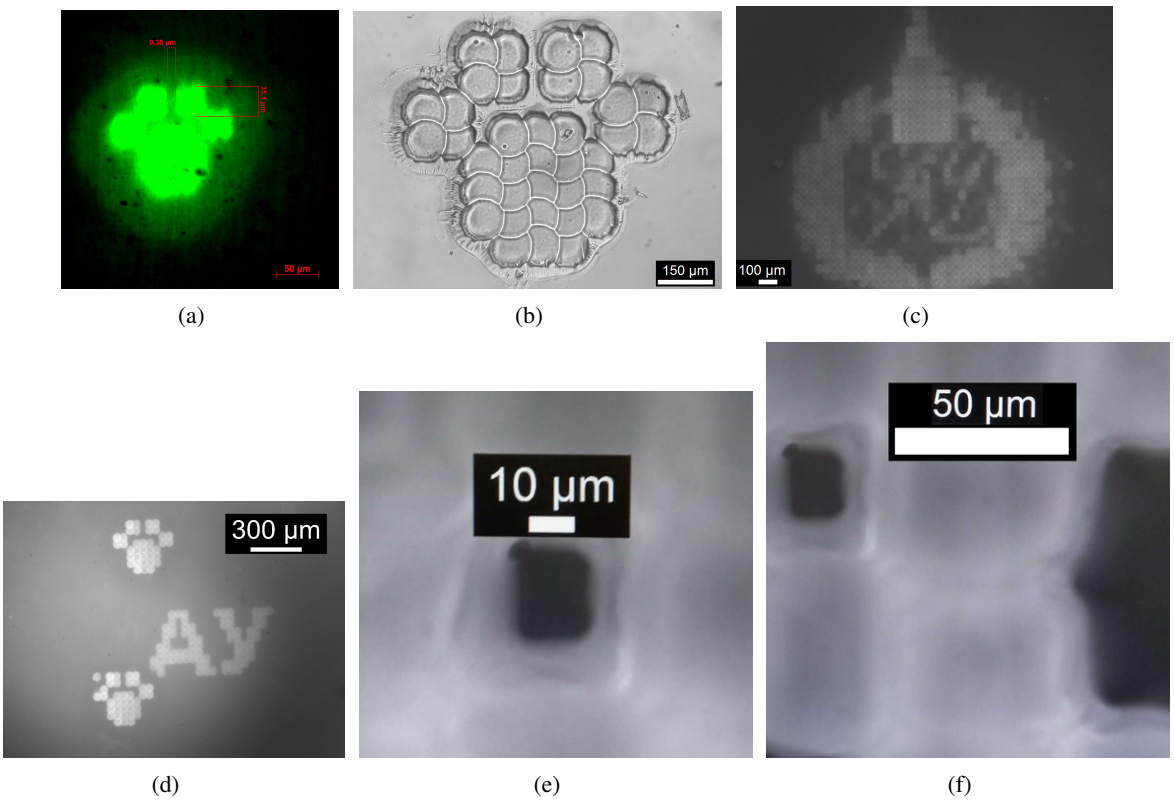


(a) (b) (c)

(d) (e) (f)

**Figure 1.** Different structures created by our technology. (a) Fluorescence structure "Catspaw", (b) Exposed photoresist structure "Catspaw", (c) Academic University monochrome fluorescence logo; (d) Acadeimic University abbreviature with "Catspaw" structures; (e) The pit in photoresist with 10 $\mu$m resolution; (f) The pixel of photoresist with 50 $\mu$m resolution.

## 4. Conclusion

In this study, we have developed the technology for providing lithography using convenient apparatus for biological laboratories. We have shown, that usage of the modern confocal microscope allows to creating microstructures with resolution up to 10 $\mu$m at a relatively low cost of consumables, which makes our approach very promising for creating bioelectronic devices and for spreading their application into our life and new science and industry areas. We hope that the results of our research bring into new level progress in bioelectronics a help to solve actual problems of healthcare, ecology, pharmacology, and cell research.

## Acknowledgements

Author express their gratitude Lihachev A.I., Kotlyar K.P., and Dubina M.V. for comprehensive assistance and support.

## References

[1] Moreau W M 1988 *Semiconductor Lithography: Principles, Practices, and Materials* 1st ed Microdevices (Springer US)
[2] Stupin D D, Kuzina E A, Abelit A A, Emelyanov A K, Nikolaev D M, Ryazantsev M N, Koniakhin S V and Dubina M V 2021 *ACS Biomaterials Science & Engineering* **7** 1962–1986
[3] Wegener J, Keese C R and Giaever I 2000 *Experimental cell research* **259** 158–166
[4] Neroev V, Astakhov Y, Lobanova M and Stupin D el al 2018 *Russian ophthalmology journal* **11** 3–27

# Obtaining a phototoxic complex based on silver nanoparticles and riboflavin generating reactive oxygen species

**I. I. Evstratova[1,3,4], P. A. Demina[1,2,4], E. D. Belitskaya[1], A. V. Zalygin[1,3], V. A. Oleynikov[1,3], E. V. Khaydukov[1,2,4], A. N. Generalova.[1,2]**

[1] Russian Academy of Sciences, Shemyakin-Ovchinnikov Institute of Bioorganic Chemistry, Moscow, Russia

[2] Russian Academy of Sciences, Institute of Photonic Technologies "Crystallography and Photonics" Moscow, Russia

[3] National Research Nuclear University "Moscow Engineering Physics Institute", Moscow, Russia

[4] Moscow State Pedagogical University, Moscow, Russia

✉irina.evs02@gmail.com

**Abstract:** As an alternative to antibiotics, it is possible to use a method that leads to the death of microorganisms and does not cause the development of resistance - antimicrobial photodynamic therapy. This work demonstrates the use of flavin mononucleotide, which acts as a photosensitizer capable of generating singlet oxygen and other reactive oxygen species which destroy biomolecules. The effectiveness of its action increases in the case of the use of silver nanoparticles with antibacterial activity. This study presents the development of approaches for the controlled increase in the effectiveness of antimicrobial photodynamic therapy using FMN-silver nanoparticle complexes.

**Keywords:** reactive oxygen species (ROS), DPPH, riboflavin, triethanolamine, AgNPs

**Funding:** The article was prepared as part of the work on the topic «Laser technologies for biomedical applications» (№ 122122600055-2) under the state order of the Ministry of Education of the Russian Federation.

## Introduction

A promising alternative to antibiotics is antimicrobial photodynamic therapy based on the generation of reactive oxygen species (ROS) upon irradiation of a photosensitizer. ROS destroy biomolecules and lead to the death of microorganisms. The literature demonstrates the successful use of flavin mononucleotide (a derivative of vitamin B2), which in the triplet state (after irradiation) is a strong oxidizing agent and can also act as a photosensitizer capable of generating singlet oxygen. It is known that the efficiency of ROS action increases significantly when used in the form of hybrid organic-inorganic nanoparticles based on metals and metal oxides [1]. Creation of nanoparticles that combine the antibacterial activity of silver nanoparticles and the phototoxicity of flavin mononucleotide, as well as the study of their mechanism of action, is an urgent task.

## Materials and Methods

**Chemicals.** Silver nitrate "Serva", Germany; Riboflavin ampoule, JSC Pharmstandard-UfaVITA, 10 mg/ml; Sodium citrate "helicon", Moscow State University, Russia; 2,2-diphenyl-1-picrylhydrazine, SigmaAldrich; Triethanolamine, SigmaAldrich. **Equipment.** "Evolution 200" spectrophotometer, Thermo scientific (Thermo, USA); Raman spectrometer, Renishaw inVia Qontor confocal Raman microscope; LED device "Polyronic"; Dynamic Light Scattering Analyzer, DynaPro NanoStar. **Methods.** To prepare a colloidal solution of silver nanoparticles by reducing silver nitrate with sodium citrate, 50 ml of a silver nitrate solution with a concentration of 0.4 mg/ml and 10 ml of sodium citrate with a concentration of 0.5 mg/ml were prepared. A solution of sodium citrate was added dropwise to a solution of silver nitrite with constant stirring on a magnetic stirrer and heating in a water bath to 70–80°C for 4–6 hours.

## Results and Discussion

The optical absorption of the initial components and their complexes did not change for 1 h. When irradiated with light at a wavelength of 365 nm, the formation of lumichrome, which is a product of FMN photodegradation, was observed already after 30 s (Fig. 1a), and the absorption of silver nanoparticles slightly increased with a slight shift of the peak to the blue region, which is

probably due to the appearance of a finer fraction of nanoparticles. In the case of the FMN-silver nanoparticle complex, the peaks of FMN photoproducts were not detected under irradiation, and an increase in absorption was observed when the peaks were smoothed (Fig. 1b), while the FMN fluorescence in the complex was almost 2 times higher and its quenching upon irradiation was 29%, in contrast to FMN, which had about 46% fluorescence loss (Figs. 1c). This may be due to the formation of a complex based on electron transfer, since FMN is an efficient acceptor, while nanoparticles can act as an electron donor. During irradiation, such ROS are generated as superoxide anion (O2• −), hydroxyl radical (•OH), and singlet oxygen (1O2). The formation of radicals was recorded by the decrease in the absorption of the stable diphenylpicrylhydrazyl radical at a wavelength of 525 nm, which is responsible for the reaction with the resulting radicals. In the case of individual components of the complex, there was practically no change in the peak value at a wavelength of 525 nm, but an increase in the shoulder in the spectrum of silver nanoparticles at a wavelength of 420 nm was noted. In the case of hybrid complexes, an extreme dependence was recorded with the maximum production of radicals during irradiation for 150 s. It is known that the efficiency of generating FMN radicals increases when using amines, for example, triethanolamine [2], which was confirmed by a decrease to 30 s in the time required for the appearance of radicals (Fig. 1d).

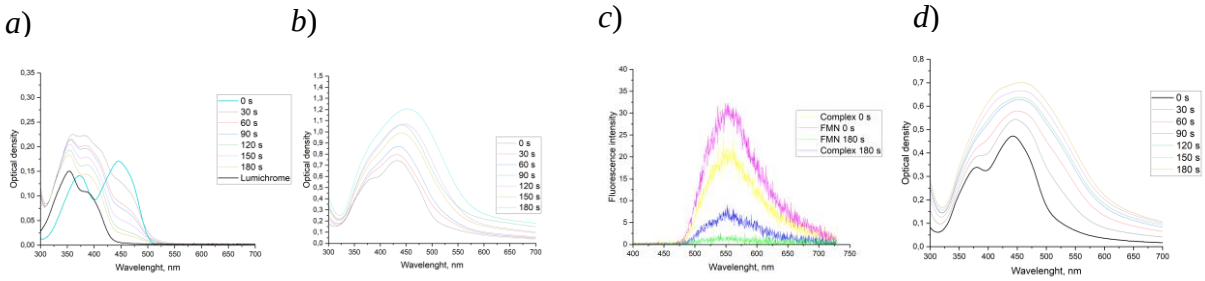


Fig. 1. (a), (b), (d) absorption spectrum of flavimononucleotide, flavimononucleotide complex with silver nanoparticles, and flavimononucleotide complex with silver nanoparticles with the addition of triethanolamine and diphenylpicrylhydrazyl, respectively; (c) fluorescence spectrum of the flavimononucleotide and the complex of the flavimononucleotide with silver nanoparticles.

## Conclusion

By creating complexes with silver nanoparticles and FMN, adding triethanolamine as an activator, one can monitor the formation of the complex and the formation of ROS by the optical properties, as well as control the optical properties and the generation of radicals.

## Acknowledgments

The authors express their gratitude to the Priority-2030 program, conducted under the guidance of young promising researchers, the laboratory "Laser Technologies for Biomedical Technologies" of the Moscow State Pedagogical University.

## REFERENCES

1. **María Belén Rivas Aiello, Fiorela Ghilini, Joaquín E Martínez Porcel, Lisandro Giovanetti, Patricia L Schilardi, Daniel O Mártire,** Riboflavin-Mediated Photooxidation of Gold Nanoparticles and Its Effect on the Inactivation of Bacteria, LANGMUIR, 2020 P. 8272-8281.
2. **Iqbal Ahmad, Kefi Iqbal, Muhammad Ali Sheraz, Sofia Ahmed, Tania Mirza, Sadia Hafeez Kazi and Mohammad Aminuddin, Photoinitiated,** Polymerization of 2-Hydroxyethyl Methacrylate by Riboflavin/Triethanolamine in Aqueous Solution: A Kinetic Study, International Scholarly Research Notices, 2013.

# Effect of increasing in ion current flowing through a nanocapillary approaching the charged surface in liquid

**M. V. Zhukov[1]✉, S. Yu. Lukashenko[1], I. D. Sapozhnikov[1], M. L. Felshtyn[1], O. M. Gorbenko[1], S. V. Pichakhchi[1] and A. O. Golubok[1]**

[1] Laboratory of scanning probe microscopy and spectroscopy, Institute for Analytical Instrumentation RAS, St. Petersburg 198095, Russia;

✉ cloudjyk@yandex.ru

**Abstract.** The ion current-distance dependence I(z) between hollow nanopipette tip and soft, polyethylene sample surface immersed in electrolyte is studied by means of direct current scanning ion-conductance microscope (DC-SICM). The borosilicate glass capillaries with an internal diameter of 100 nm and taper angle of ~ (3-5)˚ at the pointed end are fabricated and used as SICM probes. Besides the usual behavior of I(z) DC-SICM curves with monotonic ion current decline while tip approaching surface the unusual dependences with growth and decline area is observed that we called as "peak-effect". The features of "peak-effect" are studied at various aqueous NaCl buffer concentration, nanopipette aperture sizes, applied voltages, ion currents and bath temperatures.

**Keywords:** ion current, scanning ion-conductance microscope, nanopipette, tip, peak-effect

## Introduction

The nanocapillaries are widely used in biology, for instance, for visualization of soft biological objects in liquid by scanning ion-conductance microscope (SICM) due to its low invasiveness, in «patch-clamp» technique, nanoprecision manipulation of nano- and microobjects, etc [1]. The standard direct current SICM (DC-SICM) based on the simple geometric model of ion current decreasing near the sample surface was first described by Paul Hansma in 1989 [2]. In the DC-SICM the ion current through glass nanopipette (NP) probe filled with electrolyte decreases as NP approaches to the sample immersed in electrolyte because the surface of the sample blocks the flow of ions. This dependence of decreasing ion current when approaching the surface makes it possible to use a feedback loop for surface topography visualization according to the principle of scanning probe microscopy (SPM).

However, the behaviour of the ion current flowing through the NP near the sample surface is not so simple and may contain unexpected areas of current growth. Thus, in contrary, at the [3, 4] the effect of ion current growth when NP approaches to the sample was demonstrated. At the same time, the authors of [3, 4] focused on the area with a monotony current increasing, but do not study the peak area on the I(z) dependency when NP approaches the sample surface which we'll call the “peak-effect” (PE).

The aim of the work was to study the PE on the current-distance I(z) curves between the NP and the sample at various aqueous NaCl buffer concentration, nanopipette aperture sizes, applied voltages, bath temperature and saturation currents away from the sample.

## Materials and Methods

Borosilicate glasses NP have been fabricated by thermal melting and rupture at PMP-107 (MDI inc., USA). A “hand-made” SICM measuring head and a control/data acquisition unit have been used based on SPM Nanotutor (NT-SPb, Russia). The quality of the NP has been controlled using a scanning electron microscope (SEM) Quanta Inspect (FEI, USA). The inner diameter of the NP tip was ~ 100 nm or smaller with a tip taper angle of ~ 3-5˚, resistance of the NP ~ 100 MOhm. Chlorinated silver filaments AgCl were used as electrodes, and an aqueous NaCl solution (0.1; 0.9 and 10% wt.) were used as a buffer. The set up scheme is shown in Figure 1.

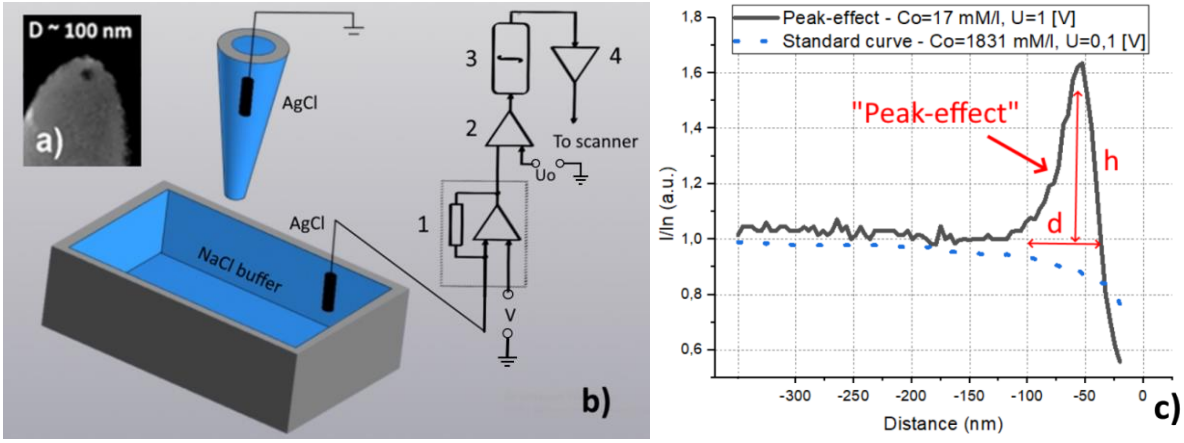


Figure 1. The typical SEM-image of the NP tip (a); scheme of the SICM set up, where 1 - current-voltage converter, 2 - differential amplifier, 3 – integrator, 4 - high voltage amplifier (b); I(z) retracting curves with and without "peak-effect" (c) with peak height (h, nA/%) and peak width (d, nm). The y-axis shows the current normalized to the saturation current (In).

## Results and Discussion

We studied the features of the current-distance I(z) curves at different interaction parameters (I - from 1 to 9 nA, U - from 0,3 to 1 V) and NaCl buffer concentration (0,1%, 0,9%, 10%). With a decrease in the buffer concentration, due to a decrease in conductivity, the capture current decreases, and the applied voltage has to be increased. It was found that under our conditions, the peak is more noticeable at the retract curves for NaCl buffer concentrations of 0.1 and 0.9% (standard saline solution). The maximum value of the peak was about 80% from the saturation current at a width of about 50 nm (at 1.4 nA and 1 V). Peak height and width for 0.9% NaCl buffer decrease when decrease U and I, specifically peak height ~15% and width ~50-120 nm at 0.5V (current 8 nA) to ~10% and ~20-40 nm at 0.3V (current 5 nA). In some cases, there is a large hysteresis in the approach and retraction curves, which, as a rule, is strongly manifested when measuring from an array of different points. A small PE in the centre and bottom of the I-Z curve was revealed at 10% NaCl buffer with h ~7% and d ~50 nm. In mixed mode (0.1% NaCl buffer in a pipette, 10% NaCl buffer in a bath), the current-voltage characteristic is unstable and changes with time, a "smoothed" peak appears ~2-5% at a width ~200 nm. In Addition, in the mixed mode, an inverse peak (to the other direction) is fined with a h ~ 18% and d ~50 nm. Distance from the beginning of the current drop to the sample: 0.1% NaCl buffer - 20-50 nm, 0.9% NaCl buffer - 50-150 nm, 10% NaCl buffer - 200-300 nm, mixed mode 0.1-10% NaCl buffer - 50-300 nm. Thus, the largest PE is seen at 0.1%, the smallest and inverted peaks in mixed mode, at 10% there is peak phenomena in the centre and bottom of the I(z) curve. It should be noted that the effect does not always appear, and when measuring from an array of points, the probability of finding PE is about 50%. It follows from the data that, with a high degree of probability, PE appears when an I(V) dependence of NP has a diode-like form [5]. Moreover, it is found that an increase in the bath temperature (up to 30-40 ºC) leads to appearance of PE on the I(z) curves.

## Conclusion

The appearance of a peak on the approach curve can be the reason for the unstable operation of the scanning probe microscope in the DC SICM mode. Indeed, the servo system in the DC SICM mode is tuned to decrease the ion current as the probe approaches the sample. If the reference value of the current in the DC SICM mode has a value that falls into the area of increasing current when the nanopipette approaches the sample surface, instabilities and noise will appear on the SICM image.

## REFERENCES


1. **Von Eysmondt, H., & Schäffer, T. E.** Scanning Ion Conductance Microscopy and Atomic Force Microscopy: A Comparison of Strengths and Limitations for Biological Investigations, Springer International Publishing: Scanning Ion Conductance Microscopy. (2022) 23-71.

2. **Hansma, P. K., Drake, B., Marti, O., Gould, S. A. C., & Prater, C. B.** The scanning ion-conductance microscope, Science. 243 (4891) (1989) 641-643.

3. **Clarke, R. W., Zhukov, A., Richards, O., Johnson, N., Ostanin, V., & Klenerman, D.** Pipette–surface interaction: current enhancement and intrinsic force, Journal of the American Chemical Society. 135 (1) (2013) 322-329.

4. **McKelvey, K., Kinnear, S. L., Perry, D., Momotenko, D., & Unwin, P. R.** Surface charge mapping with a nanopipette, Journal of the American Chemical Society. 136 (39) (2014) 13735-13744.

5. **Zhukov, M. V., Lukashenko, S. Y., Sapozhnikov, I. D., & Golubok, A. O.** Creation and study of liquid nanojunction using SPM-base technology, Journal of Physics: Conference Series. 1695 (1) (2020) 012167.

# Coating of hydrophilic chalcogenide quantum dots with carboxymethyl chitosan for lateral flow immunoassay applications

**V. V. Kriger ✉, E. A. Sidorov, N. N. Troshkina, E. D. Gribova, P. P. Gladyshev**
Dubna State University, Dubna, Russia
✉ vladlena.k576@mail.ru

**Abstract.** Quantum dots (QDs) is a class of fluorescent label widely using for biological and biomedical applications. The unique optical properties of QDs make them promising tool as fluorescent markers and analytical labels of proteins. To apply them in biological fluids it is essential to coat QDs with biocompatible polymers. In this study CdTe/CdS/ZnS QDs with mercaptopropionic acid as stabilizer was coated with carboxymethyl chitosan (CMC) by electrostatic interactions. The physicochemical properties of resulting QDs-CMC were studied by absorption and fluorescence spectroscopy, dynamic light scattering and capillary zone electrophoresis.

**Keywords:** Quantum dots, chitosan, immunoassay.

**Funding:** This study was conducted with the financial support of The Foundation for Assistance to Small Innovative Enterprises in Science and Technology (No. 17262ГУ/2022).

## Introduction

Currently, colloidal quantum dots (QDs) have drawn tremendous attention as promising tool for *in vivo* imaging and biosensoric applications. The unique optical properties make them exciting alternative for conventional analytical labels in lateral flow immunoassay (LFIA). To apply QDs in bioanalysis their surface usually coating with biocompatible polymers with different functional groups for attachment of biological molecules. The most commonly used polymeric coating is chitosan. Chitosan is a natural, glucosamine polysaccharide which display good biocompatibility. However, chitosan is insoluble in neutral and alkaline media. As a result, the coating is conduct in an acetic acid medium. Low pH values lead to protonation of anionic stabilizers of QDs (for example: thioglycolic acid, mercaptopropionic acid (MPA), 2-mercaptoethanol, etc) and decrease of quantum yield. In addition, chitosan does not have carboxyl groups required for protein conjugation by the carbodiimide-succinimide method.

## Results and Discussion

Analyzing a number of articles [1–6], usually chitosan is dissolved in acetic acid and mix with solution of negative charged nanoparticles (NPs). Since chitosan does not have carboxylic groups which required to protein conjugation by carbodiimide-succinimide method and negatively charged QDs degrade in acid solutions it is necessary to modify chitosan.

Carboxymethylation of chitosan is conducted by alkylation of chitosan with monochloroacetic acid in sodium hydroxide medium according to [7] (fig. 1).

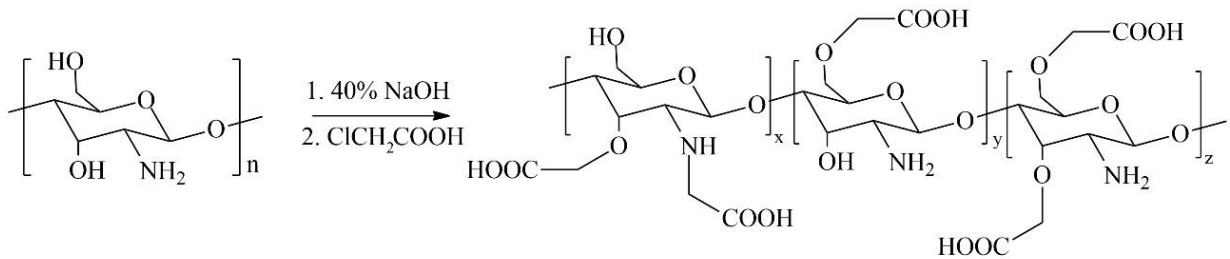


Fig. 1. Carboxymethylation of chitosan

Further, the resulting CMC was used for coat CdTe/CdS/ZnS-MPA QDs by electrostatic interaction according to fig. 2.

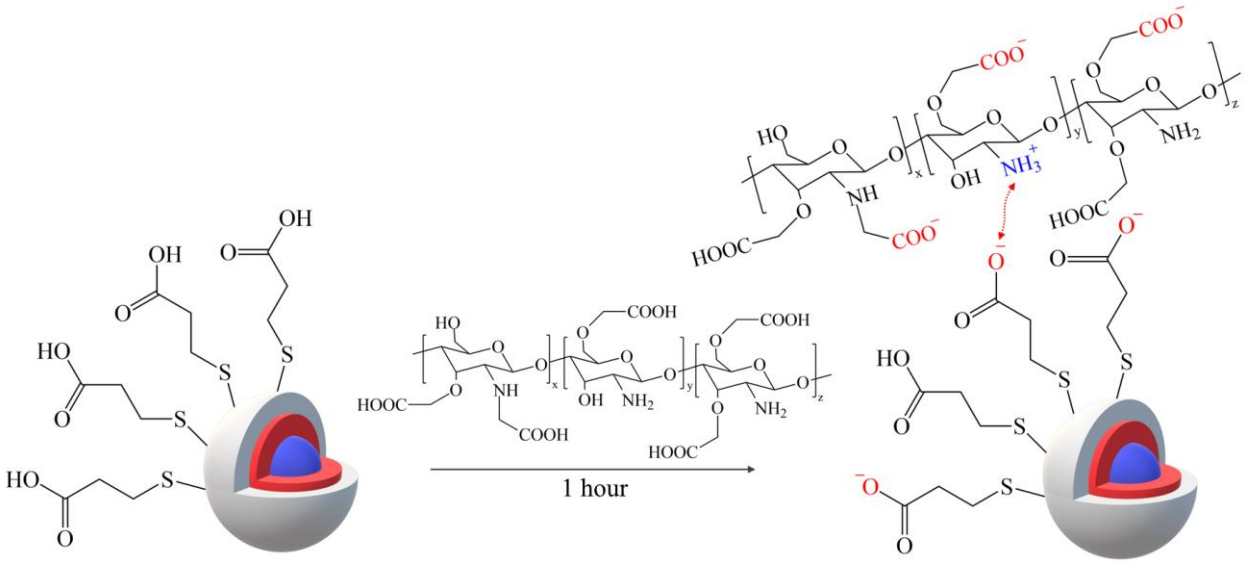


Fig. 2 – Scheme of coating of CdTe/CdS/ZnS-MPA QDs with CMC

To define the physicochemical properties and the possibility of application in bioanalysis, the obtained QDs-CMC were studied by absorption and fluorescence spectroscopy, dynamic light scattering and capillary zone electrophoresis.

## Conclusion

The carboxymethylation of chitosan makes it possible to coat hydrophilic QDs in a neutral medium, and add carboxyl groups into the structure of chitosan for conjugation by the carbodiimide-succinimide method. Based on the data obtained, the resulting QDs-CMC are suitable as analytical labels of protein for LFIA.

## REFERENCES


1. **Ghormade V., Gholap H., Kale S., Kulkarni V., Bhat S., Paknikar K.**, Fluorescent cadmium telluride quantum dots embedded chitosan nanoparticles: a stable, biocompatible preparation for bio-imaging, Journal of Biomaterials Science, Polymer Edition. 26 (1) (2015) 42–56.

2. **Qi P., Zhang T., Shao J., Yang B., Fei T., Wang R.**, A QCM humidity sensor constructed by graphene quantum dots and chitosan composites, Sensors and Actuators A: Physical. 287 (2019) 93–101.

3. **Dogan Ü., Kasap E., Cetin D., Suludere Z., Boyaci I. H., Türkyılmaz C., Ertas N., Tamer, U.**, Rapid detection of bacteria based on homogenous immunoassay using chitosan modified quantum dots, Sensors and Actuators B: Chemical. 233 (2016) 369–378.

4. **Nie Q., Tan W. B., Zhang Y.**, Synthesis and characterization of monodisperse chitosan nanoparticles with embedded quantum dots, Nanotechnology. 17 (1) (2005) 140.

5. **Korolev D. V., Shulmeyster G. A., Evreinova N. V., Syrovatkina M. S., Istomina M. S., Postnov V. N., Aleksandrov I. V., Krasichkov A. S., Galagudza, M. M.**, Theranostic Platforms Based on Silica and Magnetic Nanoparticles Containing Quinacrine, Chitosan, Fluorophores, and Quantum Dots, International Journal of Molecular Sciences. 23 (2) (2022) 932.

6. **Sarkar T., Bohidar H. B., Solanki P. R.**, Carbon dots-modified chitosan based electrochemical biosensing platform for detection of vitamin D, International journal of biological macromolecules. 109 (2018) 687–697.

7. **Siahaan P., Mentari N. C., Wiedyanto U. O., Hudiyanti D., Hildayani S. Z., Laksitorini, M. D.**, The optimum conditions of carboxymethyl chitosan synthesis on drug delivery application and its release of kinetics study, Indonesian Journal of Chemistry. 17 (2) (2017) 291–300.

# Study of Field-Effect Transistor Channel Based on Bioconjugate of Far-Red Fluorescent Proteins and Carbon Nanotube

**A. S. Kudriavtseva✉, N. P. Nekrasov, I. I. Bobrinetskiy**
National Research University of Electronic Technology, Moscow, Russia;
✉lekassy2000@gmail.com

**Abstract.** Development of bionanoelectronics hybrids are considered as perspective way for novel optoelectronic device developed. In the paper, we demonstrate the formation of conjugates based on biopolymers and carbon nanotubes due to a π-π stacking and NHS ester reaction. The controllability of a modified transistor channel under the influence of irradiation at the absorption peak of a fluorescent protein was studied. Optoelectronics properties of novel devices have been studied.

**Keywords:** bioconjugates, field-effect transistors, carbon nanotubes, far-red fluorescent protein.

**Funding:** This work was supported by Russian Science Foundation, agreement No. 19-19-00401

## Introduction

Carbon nanotubes and light sensitive far-red fluorescent proteins mKate2 are promising elements for optoelectronic devices [1]. Nanotubes are sensitive and react with the environment, and their cylindrical shape makes it possible to minimize the area of contact with the protein, i.e. preserve its structure and avoid fluorescence “quenching”. In an excited state, mKate2 affects the conductivity of CNTs, thus nanotubes convert an optical signal into an electrical one.

## Materials and Methods

In this work, we used semiconducting and quasimetallic single-walled carbon nanotubes (SWCNTs) grown by chemical vapor deposition in a bottom-gate transistor configuration. It is highly doped (p++) 100 mm Si substrate with 300 nm thermal SiO2 with source and drain 100/15 nm Au/Ti electrodes [2]. Using NHS ester reaction and π-π stacking [3], far-red fluorescent proteins mKate2 were attached to carbon nanotubes.

## Results and Discussion

We studied the photoresponse of the mKate2-modified SWCNT transistors by irradiation at different wavelengths (fig. 1).

*a*) *b*)

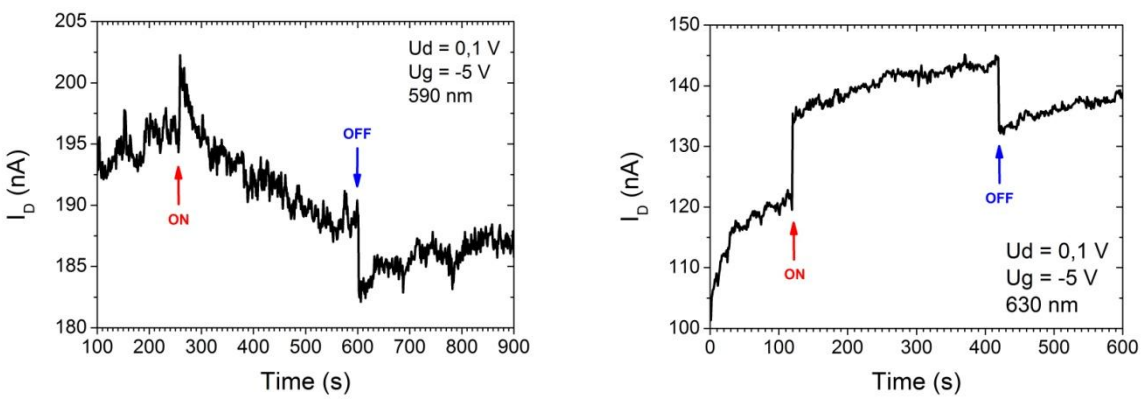


Fig. 1. Time course current evolution of the mKate2-SWCNT FET at 590 nm (a) and 630 nm (b) illumination

Irradiation of a field-effect transistor with a wavelength of 590 nm (fig. 1a) leads to a decrease in conductivity due to compensation of the main charge carriers in the nanotube by photogenerated electrons in the protein. The charge transfer process involves the proton channels within the protein body limiting the time of response [4]. In comparison, 630 nm (fig. 1b) doesn't cause the decrease of nanotube current, and response is related to modulation of Schottky barrier either between nanotube an electrodes or nanotube-nanotube intersection.

## Conclusion

In this work we have demonstrated a biohybrid SWCNT device developed using π-π stacking and NHS ester reaction with fluorescent protein. The transistor is photosensitive at wavelengths corresponding to the absorption of a far-red fluorescent protein.

## REFERENCES


1. **Ou Q., Yang B., Zhang J., Liu D., Chen T., Wang X., Hao D., Lu Y., Huang J.**, Degradable photonic synaptic transistors based on natural biomaterials and carbon nanotubes, Small. 17(10) (2021) 2007241.

2. **Emelianov A. V., Nekrasov N. P., Moskotin M. V., Fedorov G. E., Otero N., Romero P. M., Nevolin V. K., Nasibulin A. G., Bobrinetskiy I. I.**, Individual SWCNT Transistor with Photosensitive Planar Junction Induced by Two-Photon Oxidation, Advanced Electronic Materials. 7(3) (2021) 2000872.

3. **Nekrasov N., Kireev D., Emelianov A., Bobrinetskiy I.**, Graphene-based sensing platform for on-chip ochratoxin a detection, Toxins. 11(10) (2019) 550.

4. **Gwyther R. E., Nekrasov N. P., Emelianov A. V., Nasibulin A. G., Ramakrishnan K., Bobrinetskiy I., Jones D. D.**, Differential Bio-Optoelectronic Gating of Semiconducting Carbon Nanotubes by Varying the Covalent Attachment Residue of a Green Fluorescent Protein, Advanced Functional Materials. 32(22) (2022) 2112374.

# Fabrication of porous hydrogels containing hyaluronic acid by photoinduced crosslinking

***V.I. Kuzyaeva*[1], *A.V. Sochilina*[1,2,3], *A.G. Savelyev*[1], *R.A. Akasov*[1,2], *A.N. Generalova*[1,2].**

**[1] FSRC «Crystallography and Photonics» RAS, Moscow, Russia**
**[2] Shemyakin-Ovchinnikov Institute of Bioorganic Chemistry RAS, Moscow, Russia**
**[3]Moscow Pedagogical State University, Moscow, Russia**
**e-mail:** kuzyaeva.valeriya@mail.ru

**Abstract.** Biocompatible hydrogels have gained much attention in tissue engineering, preferably as scaffolds providing the cell attachment and viability in the hydrogel bulk. This requires fabrication of the hydrogels with pores, the sizes of which are in the range of 100-300 μm, most optimal for cell growth. The composition of hydrogels or method of fabrication may affect the formation of porous structure. We prepared hydrogels via photoinduced crosslinking of hyaluronic acid modified with glycidyl methacrylate under irradiation at different wavelengths using two various photoinitiators. The hydrogel structure was varied by blending hyaluronic acid with other modified polymers of natural origin (gelatin and pullulan) with grafted vinyl moieties or using filler (sucrose). The most optimal pore sizes for cell growth were obtained for hydrogels derived from modified hyaluronic acid, with the addition of sucrose or processed with the single freeze-thaw cycle. The produced hydrogels demonstrated lack of cytotoxicity with HaCaT cells incorporated inside gel bulk.

**Keywords:** pores, scaffolds, photoinduced crosslinking, biopolymers, bioink.

**Funding:** This study was supported by Russian Science Foundation under grant № N° 21-79-10384.

## 1. Introduction

Biocompatible hydrogel scaffolds have recently gained increasing interest in tissue engineering, with manufacturing suitable scaffolds for cell culture and tissue regeneration remaining an intensive area of development [1]. Cell attachment and viability are strongly correlated with pore size. The average size of animal cells is ~10-30 μm; the most optimal sizes of hydrogel pores for their growth are within 100 to 300 μm [2]. Porous matrix can be produced by various methods such as fiber bonding, salt leaching, foaming and 3D printing. Moreover, the various components of hydrogel can exert influence on the formation of pore sizes during gelation. In our study, the emphasis was made on the evaluation of the factors which can tune pore size.

## 2. Materials and methods

2.1 The photocompositions (inks)

All inks for the formation of hydrogels were made on the basis of modified polymers of natural origin – hyaluronic acid (mHA), pullulan (mPul) and gelatin (mGel) – prepared by using the method of grafting moieties with double bonds through polymer-analogous reaction with glycidyl methacrylate [3]. Sucrose was added to the composition of some inks to study the effect on the pore formation. To activate the process of crosslinking by irradiation upon wavelengths of 450 and 660 nm, two photoinitiators of the type II were used: flavin mononucleotide (FMN) and pyridine-substituted phthalocyanine (Pht) [4]. Co-initiators chosen from compounds with amino groups (for FMN) and with thiol groups (for Pht) provide the efficiency of photoinitiators.

2.2 Photo crosslinking

To form hydrogels of the equal volume, silicone molds opened on both sides (height 1 mm, diameter 6 mm) were used. The ink was placed in a mold clamped between two slides and exposed with laser radiation at wavelength of 450 nm (600 MW power) if FMN was contained [5], or 660 nm (2500 MW power) if Pht was contained.

2.3 Pore measurement

The gel pore images were acquired using a scanning electron microscope after hydrogel shock freezing in liquid nitrogen and lyophilic drying.

2.4. *In vitro* study

The human keratinocytes HaCaT were entrapped into the ink during fabrication, and their growth within the gel bulk was demonstrated using fluorescent microscopy.

## 3. Results and Discussion

The pore size of formed gels varied from 5 to 100 μm depending on the constituents. The pore sizes of hydrogels based on mHA with FMN and with Pht almost did not differ and amounted within 30-50 μm. The smallest pores (2-20 μm) were evaluated in the hydrogels based on mGel and mPul, as well as in their mixtures with mHA. Insignificant changes in pore size during the treatment of mixtures of mHA with mGel and mPul with the enzyme hyaluronidase, as well as their more prominent enzymatic degradation compared to hydrogels based on pure mHA, suggested that mGel and mPul make the main contribution to the formation of the structure. Restricted mHA crosslinking was likely due to the high level of affinity with water compared with other biopolymers.

It was found that utilization of sucrose capable of being removed after irradiation led to the formation of larger pores (50-100 microns) in hydrogels obtained in the presence of FMN. The same effect can be achieved by using the freezing-thawing technique for polymer compositions in the range of temperatures from -30 to -5 °C, when a similar increase in pore size was observed.

The *in vitro* study of HaCaT cells embedded in hydrogel bulk demonstrated fluorescence of Calcein-AM on 3$^{rd}$ day of experiment which indicates good cell viability in such environment.

## Conclusion

Hence, the most auspicious hydrogel scaffolds are based on mHA with the addition of sucrose or treated with a single freeze-thaw cycle, since they have the most optimal pore size for cell growth. Likewise, the developed compositions can be used as bioinks with incorporated cells.

## Acknowledgments

The authors thank Alexander Efimov and Lijo George from Tampere University for the synthesis of water-soluble phthalocyanine.

The work was partly prepared under the state order of the Ministry of Education of the Russian Federation № 122122600055-2.

## REFERENCES

1. Drury J. L., Mooney D. J. Hydrogels for tissue engineering: scaffold design variables and applications //Biomaterials. – 2003. – T. 24. – №. 24. – C. 4337-4351.
2. Han Y. et al. Effect of pore size on cell behavior using melt electrowritten scaffolds //Frontiers in Bioengineering and Biotechnology. – 2021. – T. 9. – C. 629270.
3. Sochilina A. V. et al. Preparing Modified Hyaluronic Acid with Tunable Content of Vinyl Groups for Use in Fabrication of Scaffolds by Photoinduced Crosslinking //Russian Journal of Bioorganic Chemistry. – 2021. – T. 47. – C. 828-836.
4. George L. et al. Photodynamic self–disinfecting surface using pyridinium phthalocyanine //Dyes and Pigments. – 2017. – T. 147. – C. 334-342.
5. Savelyev A. G. et al. Flavin mononucleotide photoinitiated cross-linking of hydrogels: Polymer concentration threshold of strengthening //Journal of Photochemistry and Photobiology A: Chemistry. – 2017. – T. 341. – C. 108-114.

# Implementation of electrical impedance tomography

**A. I. Levin ✉, E. A. Pecherskaya , Yu. A. Varenik, J. V. Shepeleva**
Department of Information and measuring equipment and metrology, Penza State University, Penza 440026, Russia
✉levin.alescha2013@ yandex.ru

**Abstract.** The method of electrical impedance tomography, which calculates images of the electrical conductivity inside the body based on surface measurements is considered. The basis of the method is an alternating electric current, which is supplied to various configurations of injecting and detecting electrodes located on the body surface and the potential field that arises in its volume is measured. It is shown that each link of the hardware that implements the electrical impedance tomography method has an impact on the final visualization. The implementation essence of the software part of the method based on the Laplace equation is stated. It is advisable to use the results of the work when monitoring the respiratory and cardiovascular systems using a chest belt with electrodes.

**Keywords:** electrical impedance tomography, analog-to-digital converter, biological object, impedance.

## Implementation of the EIT hardware

The hardware implementation of electrical impedance tomography (EIT) is as important as the image reconstruction algorithm. It plays a decisive role in the excitation of a part of the body and, accordingly, is in direct contact with the tested biological object (patient). When receiving and transmitting data, due to nonlinearity and extremely incorrect formulation of the inverse problem, the image reconstruction quality is sensitive to the error measured by an analog-to-digital converter (ADC)in this case. In the last decade, a variety of high-precision automatic measuring devices and advanced measurement methods have been proposed to reduce measurement noise, but with inherent systematic errors. Meanwhile, data transfer mode and speed, convenience, power consumption and cost are also key indicators in EIT medical imaging, where this medical imaging method is required to monitor changes in the impedance of physiological and pathological conditions in real time [1].

It is shown that each link of the hardware has an impact on the final EIT visualization. For example, electrodes located at the front end of a highly sensitive detection system. The electrodes are in direct contact with the human body, thus, any signals on them, including useful information, noise, artifacts, contact resistance, polarization voltage, etc., will be amplified and processed in the subsequent circuit and ultimately affect image reconstruction results. Therefore, the calculation of the electrode parameters, its dimensions, quantity and sensory ability is especially important. A small number of electrodes (<16) in the EIT will reduce the measurement sensitivity, and too many electrodes will reduce the measurement speed (>16). The Standard EIT configuration uses 16 electrodes.

Their location on the patient is also important. It is a competent arrangement that determines the amount of "high-quality" information contained in the measurement processes, the conditionality of the inverse EIT problem and the EIT measurements reliability. The electrodes position affects the reconstruction quality of the resulting image. Typically, electrodes are placed in the intercostal space between the 4th and 6th ribs. A number of researchers in their works claim that the most favorable angles between the injecting and detecting electrodes are in the range from 60 to 150 degrees [2].

## Implementation of the EIT software

The EIT essence is the inverse problem of determining the impedance, where the relationship between the electric field and the electric current is determined. There are two

methods for obtaining electrical impedance. The first method is to establish a stable voltage across the object's surface and then evaluate the impedance distribution over the current flowing through the object. The main EIT method is to apply a stable current to the object and evaluate the impedance distribution by measuring the boundary voltage, which is discussed in this summary. Measurement methods are usually divided into two-electrode and four-electrode approaches. Current injection and voltage measurement are performed from the same pair of electrodes in the first approach, where the strategy can be easily implemented, but the measurement values are always inaccurate due to the contact impedance.

Usually, a number of mathematical methods: Newton - Gauss, the method of finding a unique solution of the Laplace equation under the Newman boundary condition are used to construct the EIT image.

In particular, based on Maxwell's equation, Ohm's law and the law of charge conservation, Laplace's equation can be obtained as follows:

$$\nabla[\sigma(\mathrm{r})\nabla\varphi(\mathrm{r})] = 0, \mathrm{r} \in \Omega, \quad (1)$$

where φ is the electric potential, Ω is the measured area.

In this case, the boundary condition on the electrodes will be as follows:

$$\sigma(\mathrm{r})\frac{\partial\varphi(\mathrm{r})}{\partial \mathrm{n}} = \mathrm{j}, \mathrm{r} \in \Omega, \quad (2)$$

where j is the current density at the electrodes, Ω is the boundary of the body.

The relationship between excitation, system response and measurement can be easily represented as follows:

$$\bar{V} = F\big(\sigma(r)\big)|_j, \quad (3)$$

where σ(r) is the conductivity distribution, V is the theoretical boundary stress, and F is a non-linear function representing the conductivity distribution space in the measurements space [3].

## Conclusions

The EIT ability to detect conductivity changes finds application in the monitoring of the respiratory and cardiovascular systems using a chest belt with electrodes.

The conductivity changes are caused by the lung's expansion with each breath and the blood movement with each heartbeat. Continuous monitoring of vital physiological parameters of ventilated patients in the intensive care units or operating rooms will provide healthcare professionals with additional information about the patient's health status or the therapy effectiveness, which can improve patient outcomes. According to the business plan of startup company Swisstom, 3.8 million people are ventilated annually in developed countries, about 15% of them receive acute lung injury, and about 5% (190,000 patients) of ventilated patients eventually die from acute lungs injury.

## REFERENCES

1. **Aleksanyan G.K., Shcherbakov I.D., Sulyz A.V., Tetelev M.V.** Problems of implementation of algorithms for the reconstruction of multi-angle electrical impedance tomography.// Modern science-intensive technologies. - 2019. - No. 12-2. – P. 243-248.

2. **Korzhenevsky A.V.** Research electrical impedance tomograph, available for manufacturing in non-standard conditions. Journal of radio electronics [electronic journal]. 2021. No. 9. https://doi.org/10.30898/1684-1719.2021.9.5.

3. **G. Uhlmann**, "Electrical impedance tomography and Calderón's problem," Inverse Problems, vol. 25, 2009, DOI 10.1088/0266-5611/25/12/123011.

# Femtosecond laser oocyte enucleation without a fluorescent dye.

D. Yu. Martirosyan[1✉], A. D. Zalessky[1], A. A. Osychenko[1], U. A. Tochilo[1] and V. A. Nadtochenko[1]

[1] N.N. Semenov Federal Research Center of Chemical Physics, Russian Academy of Sciences, Kosygina 4, Moscow, Russia

✉e-mail: petrosyan359@gmail.com

**Abstract.** Preparation of the recipient cytoplast through the enucleation is important for assisted reproductive technologies and somatic cell nuclear transfer. Enucleation by the femtosecond laser may improve the recipient cytoplast preparation technique, but it ordinary requires the use of a fluorescent dye for metaphase plate visualization. In this work we investigate an ability to perform femtosecond laser oocyte enucleation without a fluorescent dye. We demonstrate that metaphase plate being visualized under the polarization microscopy can be successfully eliminated by the femtosecond laser.

**Keywords:** femtosecond laser, enucleation, polarization microscopy

**Funding:** This work is supported by the Russian Science Foundation under grant № 21-75-10155. The work was performed on facilities of ACBS Center of the Collective Equipment (no. 506694, FRCCP RAS) and large-scale research facilities № 1440743.

## Introduction

Removal of DNA by femtosecond laser nanosurgery methods has been shown in several research with the use of a fluorescent dye Hoechst 33342 [1-3], which also acts as a photosensitizer. The method proved to be an effective and non-invasive tool for microsurgical operations. The method has a number of advantages over traditional methods, such as the transfer of somatic cell nuclei. The efficiency and safety of using a near-infrared laser for the enucleation has been shown in our previous works [3]. Our studies have shown the absence of DNA after local treatment of the cell with a femtosecond laser pulse. However, the fluorescent dye has a detrimental effect on living cells, including for UV detection. More, for clinical applications (e.g., mitochondrial replacement therapy), the use of the dye is unacceptable.

In this work we develop a novel approach of femtosecond laser oocyte enucleation without the use of a fluorescent dye. Using the method of polarization contrast, we were able to locate the metaphase plate, then enucleate with a femtosecond laser.

## Materials and Methods

Oocytes were received by the standard scheme [3]. For the metaphase plate visualization, the oocytes were dyed with 5 µg/ml Hoechst 33342 dye (B2261, Sigma-Aldrich) for 15 minutes in M2. After that, all oocytes were dyed with BioTracker™ 488 Green Microtubule Cytoseleton Dye (Sigma-Aldrich, SCT142) and for 35 minutes to visualize spindle microtubules (concentrations in M2 medium 200 µl - 0.5 µl). The fission spindle was visualized in polarized light by Olympus IX3-SLICSI microscope.

The laser system is described here [3]. Briefly, in these experiments we used $\lambda = 790$ nm, $\upsilon = 7$ kHz, pulse energy 4 nJ; continuous laser pulse thinned out by pulse select (acousto-optical pulse picker, developed for the special demands of femtosecond laser technology). Each oocyte subjected to laser nearly 3-5 minutes.

## Results and Discussion

In mouse oocytes without staining, the spindle was localized (Fig. 1, A, B). Polarization contrast visualizes only the fission spindle, which consists of microtubules, and not the metaphase plate, which is surrounded by microtubules (Fig. 1, C). We exposed the laser to the entire area of the fission spindle, which was established using polarization contrast. It was possible to choose the

parameters of laser exposure, at which the destruction of DNA actually occurred (Fig. 1, D), but the sample did not boil. We proved the destruction of DNA during enucleation without the use of a dye by staining samples after laser exposure.

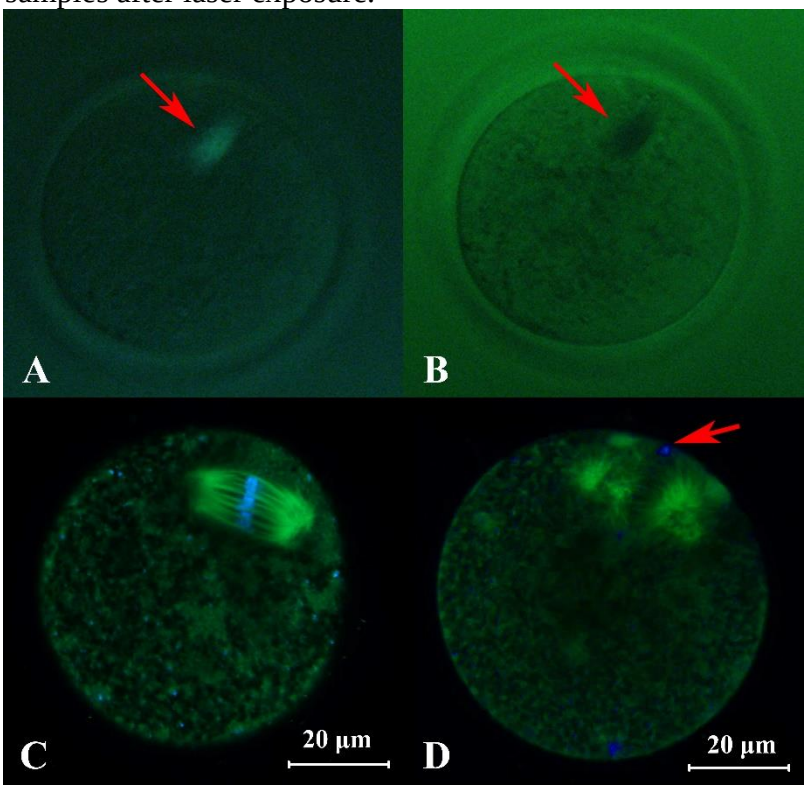


A, B - image of the oocyte in polarized light at different angles. The arrows show the spindle, which contains the metaphase plate. C - confocal image of an oocyte without laser exposure. D - confocal image of an oocyte irradiated to the fission spindle region (staining after laser irradiation). Blue color - metaphase plate, green - microtubules.

## Conclusion

Here we demonstrate a novel technique of femtosecond laser oocyte enucleation accompanied with polarization microscopy. This method allows us to eliminate DNA within the cell non-invasively and without using staining. More, the cell is not exposed to the UV phototoxic effects, and the time of sample preparation for enucleation is reduced.

## REFERENCES

1. **Shakhbazyan A.K., Sviridova-Chailakhyan T.A., Karmenyan A.K., Krivokharchenko A.S., Chiou A., Chailakhyan L.M.**, The Use of Laser for Obtaining Recipient Cytoplasts for Mammalian Nuclear Transfer, Doklady Biologycal Sciences 428 (2009) 1–4.

2. **Kuetemeyer K., Lucas-Hahn A., Petersen B., Lemme E., Hassel P., Niemann H., Heisterkamp A.**, Combined multiphoton imaging and automated functional enucleation of porcine oocytes using femtosecond laser pulses, Journal of Biomedical Optics 15 (4) (2010) 046006.

3. **Osychenko A.A., Zalessky A.D., Tochilo U.A., Martirosyan D.Yu., Silaeva Y.Yu., Nadtochenko V.A.**, Femtosecond laser oocyte enucleation as a low-invasive and effective method of recipient cytoplast preparation, Biomed. Opt. Express 13 (3) (2022) 1447–1456.

# Development of an experimental stand for studying the characteristics of ion currents

**O A Mikhailova[1], M V Zaitseva[2], I E Antifeev[2], D G Petrov[2], V V Davydov[1, 3]**
[1] Peter the Great Saint-Petersburg Polytechnic University, Saint Petersburg, Russia;
[2] Institute of Analytical Instrumentation of the Russian Academy of Sciences, Russia;
[3]All-Russian Research Institute of Phytopathology, Russia
✉ lesya101201@gmail.com

**Abstract.** The task of measuring low currents is relevant today. We proposed a solution in the form of an installation for creating and studying ionic currents. It consists of a base made of PDMS, a glass slide with conductive zones, and electrodes. As a result of the assembly, a channel was formed between two conductive zones, which was the micropore model. The created micrometer-sized pore makes it possible to study the characteristics of microcurrents along with the more time-consuming nanopores to create. Preliminary calculations show the suitability of the created stand for measuring currents in the voltage range of 1-100 mV, and the current strength of 0.1-5 μA.

**Keywords:** Ion currents, current measurement, micropore

## Introduction

Today, an important task in modern science is the need to measure small currents. There are methods for measuring ion currents based on the use of: pointer devices, Hall effect microcircuits, resistive current sensors [1]. In this case, an experimental setup is needed to create and study ionic currents, which will make it possible to investigate the dependence of currents on such parameters as electrolyte composition, pore shape, etc. An example of such a setup can be a bench based on an artificial (model) micropore. The paper proposes a layout of such an installation (experimental stand), presents its characteristics. The presented experimental stand makes it possible to study biophysical and biochemical processes in a micropore, which can significantly expand the use of such methods for DNA analysis [2].

## Materials and Methods

To create an experimental stand on a glass slide 26x76x2 mm in size, conductive zones 17x8 mm in size were formed by applying a layer of silver, for this, use the reaction of a silver mirror:

$$Ag2NO3 + NH4OH + HCOH = HCONH4 + 3NH3 + 2Ag$$

The formation of conductive zones is shown in Fig.1. After that, 10x8 mm gold pads were deposited on the silver-coated conductive zones by galvanic deposition. After that, the sections of the plate with deposited silver, untreated with gold, were electrochemically chlorinated.
The model micropore for the installation is made of polydimethylsiloxane (PDMS), for this purpose, two through holes 15x4 mm were made in a bar measuring 25x15x5 mm, connected by a channel 2 mm long with a cross section of 0.5x0.02 mm. A master mold was designed for casting the base with two chambers, where a channel was applied between the two chambers using a laser. The form filled with PDMS was thermostated at +75 C for 4 hours. At the end of polymerization, the base (bar) was removed from the mold and fixed on a glass slide so that the through holes in the bar corresponded to the conductive zones.
At the final stage of assembling the experimental stand, chlorine-silver electrodes were fixed in the resulting chambers above the conductive zones. As a result of the assembly, a channel was formed between two conductive zones, which was the micropore model.

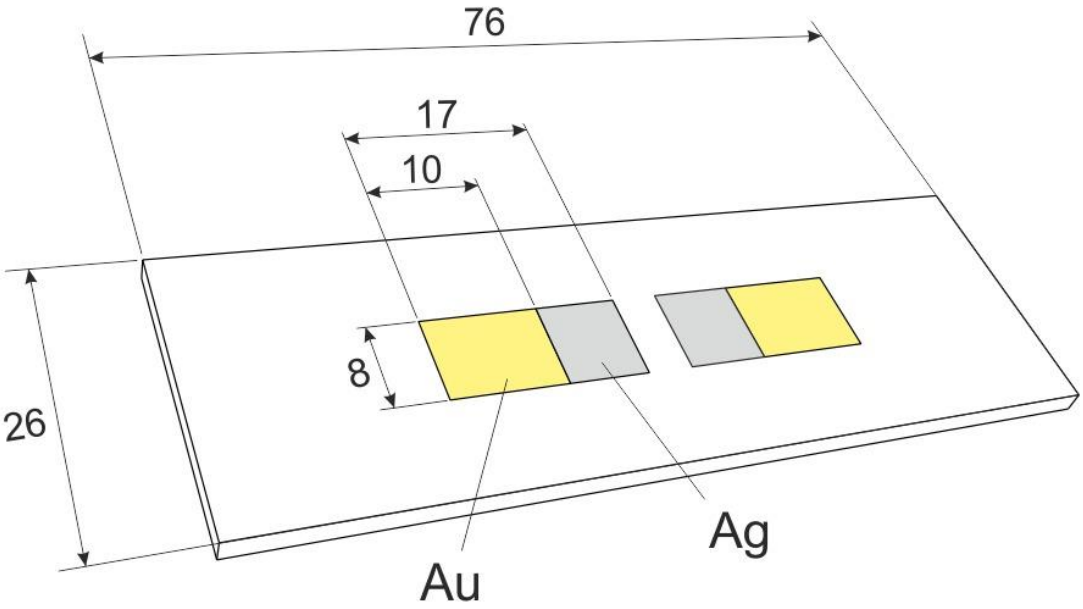


Fig. 1. Formation of conductive zones on a slide

## Results and Discussion

Based on the results of the work, an experimental stand was created to study the characteristics of ion currents. The created experimental stand on a polymer (PDMS) base 25x15x5 mm in size with two chambers 15x4x5 mm in size, each with a volume of 300 mm3. At the same time, the resulting pore had a section size of 0.5x0.02 mm with a length of 2 mm.

Preliminary calculations show the suitability of the created stand for measuring currents in the voltage range of 1-100 mV, and the current strength of 0.1-5 μA. The created experimental stand allows the measurement of microcurrent values when changing such parameters as the composition of the electrolyte and the shape of the channel. The geometric parameters of the micropore can be set at the stage of modeling the shape for a part made of PDMS. The created micrometer-sized pore makes it possible to study the characteristics of microcurrents along with the more time-consuming nanopores to create.

In the future, it is planned to use the created experimental stand to develop a device for measuring small currents through various artificial micropores.

## Conclusion

The created experimental stand allows the measurement of microcurrent values when changing such parameters as the composition of the electrolyte and the shape of the channel. The geometric parameters of the micropore can be set at the stage of modeling the shape for a part made of PDMS. The created micrometer-sized pore makes it possible to study the characteristics of microcurrents on a par with more time-consuming nanopores to create.

In the future, it is planned to use the created experimental stand to develop a device for measuring small currents through various artificial micropores.

## REFERENCES

1. **Mikhailova, O.A.,** Antifeev, I.E., Petrov, D.G., Davydov, R.V. Development of a device for picoampere currents measuring, Scientific and technical statements of SPbSPU. Physical and mathematical sciences. 15(2022) 102-106.

2. **Lebedev, D.,** Malyshev, G., Ryzhkov, I., Mozharov, A. Focused ion beam milling based formation of nanochannels in silicon-glass microfuidic chips for the study of ion transport, Microfluid Nanofluid. 51(2021) 1 -10.

# Application of Raman spectroscopy and SERS for the detection of fungi-destructors capable of biodegradation of cultural heritage at the State Tretyakov Gallery

**A. G. Musaev[1]✉, D. A. Avdanina[2], S. G. Kalinin[2], I.A. Volkov[1], A.A. Zhgun[2]**
[1]Moscow Institute of Physics and Technology, Dolgoprudny, Russia
[2] Research Center of Biotechnology RAS, Moscow, Russia
✉kuzemin@phystech.edu

**Abstract.** We explored the possibility of using Raman spectroscopy and SERS for the analysis of molds using the example of strains collected from exhibits of the State Tretyakov Gallery. The fungi contained in the samples were cultivated on the surface of aluminum oxide substrates containing plasmonic nanostructures based on silver and gold nanoparticles. The mapping of samples using Raman spectroscopy made it possible to visualize the distribution of organic substances contained in mold fungi. The purpose of the study is to develop a methodology for the identification of fungi, including those that destroy cultural heritage.

**Keywords**: nanoparticles, silver, gold, fungi, plasmonic nanostructures, Raman spectroscopy, SERS, mapping, diagnostics of biodeterioration of cultural heritage.

## Introduction

When studying cultural heritage objects, highly sensitive non-invasive methods are used to establish the necessary measures for their conservation and/or restoration. Raman spectroscopy is a promising method for high-precision molecular diagnostics, as it can identify compounds based on their structural "fingerprints" [1]. However, the main limitation of Raman spectroscopy is its low sensitivity to compounds with a small interaction cross-section, which requires the use of bulk samples or concentrated solutions for research [2]. Raman spectroscopy with surface-enhanced signal (SERS), based on the "plasmon resonance" that occurs when electromagnetic radiation acts on metal nanoparticles (such as gold or silver), can enhance Raman scattering and significantly increase the sensitivity of the method [2]. The main advantages of SERS are its non-invasiveness, *in situ* applicability, speed, and reliable spectral response.

## Materials and Methods

In the course of the study of the microbiome of the State Tretyakov Gallery (Moscow, Lavrushinsky lane, 10), more than 100 microbiological samples were collected from exhibits and surfaces within the halls of ancient Russian painting [3]. The microorganisms in the samples were cultivated, with a particular focus to fungi-destructors of tempera paintings, such as: *Aspergillus versicolor* STG-25G, *Mucor circinelloides* STG-30, *Ulocladium* sp. AAZ-2020a STG-36, *Cladosporium halotolerans* STG-52B, *Simplicillium lamellicola* STG-96, *Aspergillus protuberus* STG-106, *Penicillium chrysogenum* STG-117 and others. To explore the possibility of using Raman spectroscopy to analyze fungal strains we developed a method for cultivating fungi on the surface covered with plasmonic nanostructures (Fig. 1). The studied objects are freeze-dried mold

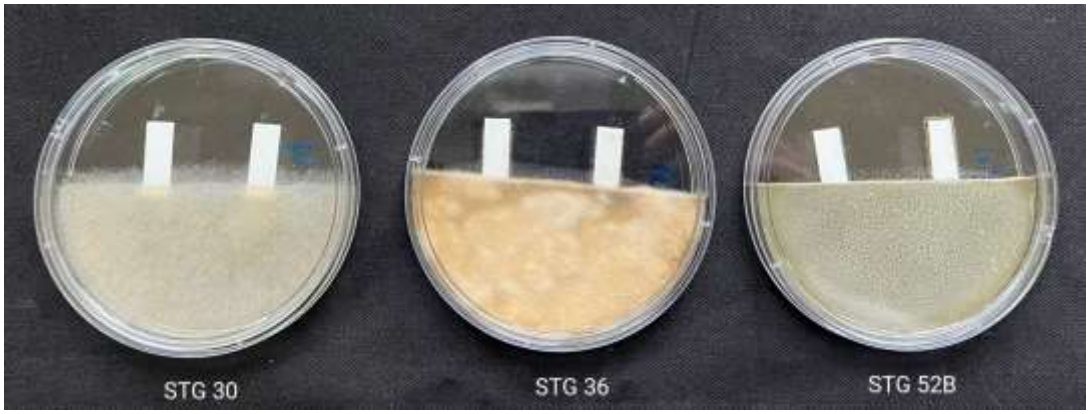


Fig. 1. Cultivation of fungi on Petri dishes, the edge of the plates is partially immersed in agar. Mycelium and spores of fungal strains STG-36, STG-30, STG-56B are visible

fungi, which are part of various morphological forms, such as mycelial hyphae, sporangia, conidiospores. The Raman spectra were recorded on a Thermo Scientific™ DXR. The measurement parameters were selected based on the results and using published studies [1-2]. In the automatic mapping mode (1 µm step), two-dimensional contrast maps of samples (up to 100 x 100 µm size) were obtained. Mapping reflects the distribution of the intensity of specific lines in the Raman spectra (Fig. 2).

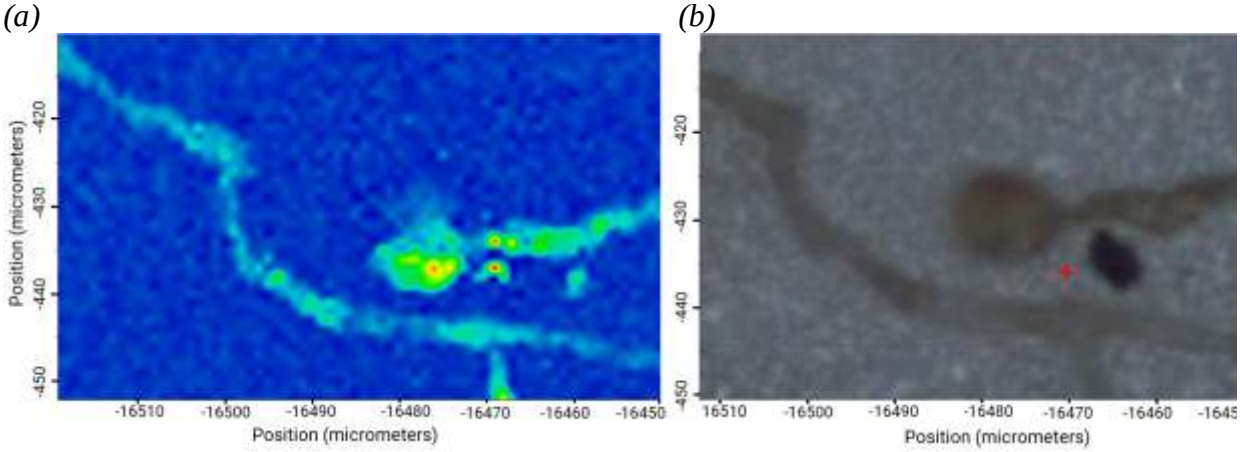


Fig. 2. Mapping of a Ulocladium sp. AAZ-2020a STG-36 grown on the surface of silver nanoparticles: *(a)* - contrast map showing the intensity distribution of the Raman signal at 1100 $cm^{-1}$; *(b)* is the corresponding optical image on an aluminum oxide plate with gold nanostructures.

## Results and Discussion

Mapping of molds using Raman spectroscopy made it possible to visualize areas with the highest content of organic compounds on the site. We did not observe a significant difference in the signal intensity between samples on plasmonic particles and those on a substrate without particles. This may be due to insufficient contact between sample and nanoparticles. The resulting spectra indicate that laser radiation caused carbonization of the organics in the compounds under study, which makes it difficult to identify these substances.

## Conclusion

Further improvement of our Raman spectroscopy technique will make it possible to analyze both individual structures of microscopic fungi and multicomponent systems. Their taxonomic identification is possible based on the chemical composition and visualization of the distribution of fungi and their spores, as well as isolated secondary metabolites, without complex preliminary preparation with strain separation.

## Acknowledgments

This research was funded by the Ministry of Science and Higher Education of the Russian Federation (state contract no. 075-03-2023-106, project identifier 0714-2020-0007) for support of surface-enhanced Raman spectroscopy studies.

## REFERENCES

1. **Siyao Liu, Yuqing Chen, Ying Wang and Guohua Zhao** Group-Targeting Detection of Total Steroid Estrogen Using Surface-Enhanced Raman Spectroscopy // Analytical Chemistry 2019, 91 (12), P. 7639–7647

2. **Dina N. E., Gherman A-M. R., Chiş V., Sârbu C., Wieser A., Bauer D, Haisch C.** Characterization of Clinically Relevant Fungi via SERS Fingerprinting Assisted by Novel Chemometric Models // Analytical Chemistry 2018, 90 (4), P. 2484–2492

3. **Zhgun A., Avdanina D., Shumikhin K., Simonenko N., Lyubavskaya E., Volkov I., Ivanov V.** Detection of potential biodeterioration risks for tempera painting in 16th century exhibits from State Tretyakov Gallery // PLOS ONE.2020. Vol 15, N 4

# Rapid manufacturing of microfluidic molds using a metal laser engraver

**E. I. Naumov** [1,2✉], **V. V. Grigorev** [1], **I. E. Antifeev** [3], **N. A. Filatov** [1], **A. S. Bukatin**[1,3]

[1] Alferov Saint Petersburg National Research Academic University of the RAS, Saint Petersburg 194021, Russia;

[2] Peter the Great St.Petersburg Polytechnic University, Saint Petersburg 195251, Russia;

[3] Institute for Analytical Instrumentation of the RAS, St. Petersburg 198095, Russia

✉naumove2000@gmail.com

**Abstract.** "Soft-lithography"-method, which includes photolithography of a master mold and subsequent polymer curing, remains the gold standard for manufacturing microfluidic chips in the laboratory. However, it still has disadvantages. For instance, it is highly complex to manufacture channels with non-rectangular cross-section. We developed a novel technique which uses a commercially available laser engraving machine for mold fabrication and simplifies the implementation of the above-mentioned task. We also developed a test mold to determine the limitations of our technique. According to measurements, the minimal lateral size for structures was 250 μm and the minimal height was 100 μm, which could be used in experiments reported in cellular biology. After the performance test we were able to design and fabricate different chips for biomedical applications (e.g., circulating tumor cells isolation) without using UV-lithography. Now we analyze the efficiency of the chips and try to expand the use of our method.

**Keywords:** microfluidic chips fabrication, master-molds, laser engraving, micropumps, inertial microfluidics, circulating tumor cells isolation.

**Funding:** Disclose all sources of funding of the study, providing project titles and/or grant numbers if available (e.g.: This study was funded by [name of funder] grant number [xxx]).

## Introduction

Microfluidic chips are intensively used for different applications like organ-on-a-chip technologies and cancer research [1,2]. "Soft-lithography" is widely used for chip fabrication. It is a multi-step procedure which includes mold fabrication (using UV-lithography) and subsequent replica molding (using polydimethylsiloxane (PDMS)). UV-lithography provides the incomparable accuracy, resolution and reproducibility [3].

However, master molds, which are produced in one cycle of UV-lithography, could be only used for chips with rectangular cross-section channels. Whereas microfluidic devices could have channels with triangular, trapezoidal (inertial devices) or semicircular (microvalves) cross-section, or depth alteration along the channel (micromixers) [4,5]. In such cases the master mold is made layer by layer (e.g., a semicircular cross-section is approximated by a stepped figure). This drastically increases the workload and requires considerable time.

## Materials and Methods

We developed a novel technique which uses a commercially available laser engraving machine for mold fabrication. High power fiber pulsed laser in the 1,55 μm band was used for brass plate ablation. To determine the limitations of our technique we developed a test mold. On the test mold the following structures were presented: channels with rectangular and semicircular cross-section, cylinders, square cuboids, isosceles triangles and "Greek crosses". The figures were rescaled (shrinked) several times, to determine the resolution of our method. All figures were repeated twice at different heights: 100 μm and 250 μm. Channels were repeated twice, all other elements were repeated 5 times to provide a greater sample size.

## Results and Discussion

According to measurements, the minimal lateral size for positive structures was 200 μm and the minimal height was 100 μm. The rectangular channels with the width smaller than 250 μm could also be fabricated, but they become deformed due to melting. The cross-section of these channels becomes parabolic. But it is still suiting several biomedical applications.

We fabricated a microfluidic valve-based liquid dispenser from [6]. It was rescaled, considering the limitations of our method. The height of the channels was 100 μm, the minimal width was 200 μm. The average valve closing pressure was measured as 100 kPa. The produced dispenser can pump liquid after each iteration. The pressure inside the pneumatic layer is controlled with external programmed electromagnetic valves. The average volume of a liquid (distilled water) pumped with each iteration is 230 nl.

## Conclusion

The developed method is competitive in relation to other rapid manufacturing technologies and is also suitable for producing devices for biomedical applications.

Now we have developed a 600 μm wide spiral channel with a trapezoidal cross-section that could be used for circulating tumor cells isolation. The dimensions of the manufactured chip were close to the design, also the roughness of the surface acceptable. Now we are working on studying its performance and a possible application for cancer research.

The test mold could be used as a benchmark for manufacturing not only of chambers and channels but also of channels bifurcation in mixers and droplet-microfluidic devices. Therefore, it could be used as a benchmark also for other rapid prototyping techniques used for microfluidic chip fabrication like micromilling, 3D-printing, maskless lithography etc.

## Acknowledgments

The work was supported by the Russian Science Foundation (Project No 20-74-10117).

## REFERENCES

1. **Leung C.M., de Haan P., Ronaldson-Bouchard K. et al.**, A guide to the organ-on-a-chip, Nat Rev Methods Primers. 2 (2022) 33.

2. **Garcia-Cordero J.L., Maerkl S.J.**, Microfluidic systems for cancer diagnostics, Curr Opin Biotechnol. 65 (2020) 37-44.

3. **Kukhtevich I.V., Belousov K.I., Bukatin A.S. et al.**, Microfluidic chips for the study of cell migration under the effect of chemicals, Tech. Phys. Lett. 42 (2016) 478–481.

4. **Razavi Bazaz S., Rouhi O., Raoufi M.A. et al.**, 3D Printing of Inertial Microfluidic Devices, Sci Rep. 10 (2020) 5929.

5. **Fabozzi A., Della Sala F., di Gennaro M. et al.**, Design of functional nanoparticles by microfluidic platforms as advanced drug delivery systems for cancer therapy, Lab Chip. 23 (5) (2023) 1389-1409.

6. **Zhang, Wenhua, et al.**, PMMA/PDMS valves and pumps for disposable microfluidics Lab on a Chip 9.21 (2009): 3088-3094.

# New amphiphilic PEG-chlorin for creating conjugates with hydrophobic upconverting nanoparticles

**M. E. Nikolaeva[1✉], R.A. Akasov[1], E. V. Khaydukov[1] , M. A. Maslov[2]**
[1]Moscow State Pedagogical University, Moscow, Russia;
[2] Lomonosov Institute of Fine Chemical Technologies, MIREA—Russian Technological University, Moscow, Russia
✉mesarycheva@mail.com

**Abstract.** Photodynamic therapy (PDT) is a promising treatment of tumors that based on the photoactivation of photosensitizer (PS) followed by reactive oxygen species (ROS) generation and tumor cells death. In the current research, we propose nanocomplex based on upconversion nanoparticles capable of converting IR light into photons in the visible range to activate theamphiphilic derivative of chlorin $p_6$ as a photosensitizer. The synthesis of this nanocomplex was described, and its optical properties, including FRET, were characterized. This nanocomplex could be proposed for PDT treatment of tumors.

**Keywords:**chlorine $p_6$, upconverting nanoparticles, polyetelenglycol, PEG, FRET.

**Funding:** The article was prepared as part of the work on the topic «Laser technologies for biomedical applications» (№122122600055-2) under the state order of the Ministry of Education of the Russian Federation.

## Introduction

Recently, photodynamic therapy (PDT) has become a promising treatment for various diseases, including oncology [1]. PDT allows selective disrupt tumors due to the cytotoxicity effect of light-activated photosensitizers (PS), and this leads to less adverse effects compared to chemotherapy and radiotherapy. The main limitation of PDT is low penetration of visible light used to activate PS. The excitation of PS by near-IR radiation in the “transparency window” of biological tissues makes it possible to increase the depth of light penetration and expand the boundaries of PDT application. One approach to solve this problem is the use of UCNPs that absorb light at 975 nm and produceintense fluorescence in the visible region. The Förster mechanism (FRET) from UCNPs to PS significantly increases the upconversion rate if the absorption band of PS coincide as much as possible with the intense fluorescence band of UCNPs. Upconverting $NaYF_4$:M (M=$Yb^{3+}$:$Er^{3+}$)/$NaYF_4$ nanoparticles have intense bands in the emission spectrum at 660 nm and 540 nm, which most closely coincides with the intense band in the absorption spectrum of chlorin $p_6$ (661 nm) [2].The derivatives of Chlorophyll a are widely used as photosensitizers due to their availability, biosafety, good spectral properties [3]. In the current research we propose UCNPs loaded with an amphiphilic derivative of chlorophyll a (chlorin $p_6$) to obtain nanocomplexes with PDT properties.

## Results and Discussion

The synthesis of UCNPs was carried out in high-boiling solvents, namely oleic acid and 1-octadecene, and the carboxyl groups of oleic acid during the synthesis formed coordination bonds with the electron-deficient metal surface that resulted in the formation of hydrophobic nanoparticles. For the synthesis of UCNP, we used the technique developed by Nechaev A.V. et al. [4], which makes it possible to obtain monodisperse $NaYF_4$:M (M=$Yb^{3+}$:$Er^{3+}$) particles with a high conversion yield. The synthesized nanoparticles with the mean size 75 ± 5 nm exhibited intense anti-Stokes photoluminescence upon excitation with light at 975 nm. The integral conversion coefficient of nanoparticles was 14% in the saturation mode at an excitation intensity of 10 W/cm$^2$.

To create UCNP complexes with PS and study the nonradiative energy transfer, we prepared a derivative of chlorophyll a with a hydrophobic octadecylamine residue and a hydrophilic $PEG_{2000}$ residue in pyrrole rings A and D of the macrocycle.

For the synthesis of chlorophyll *a* derivative with an octadecylamine residue in the pyrrole ring D **(Figure 1).**

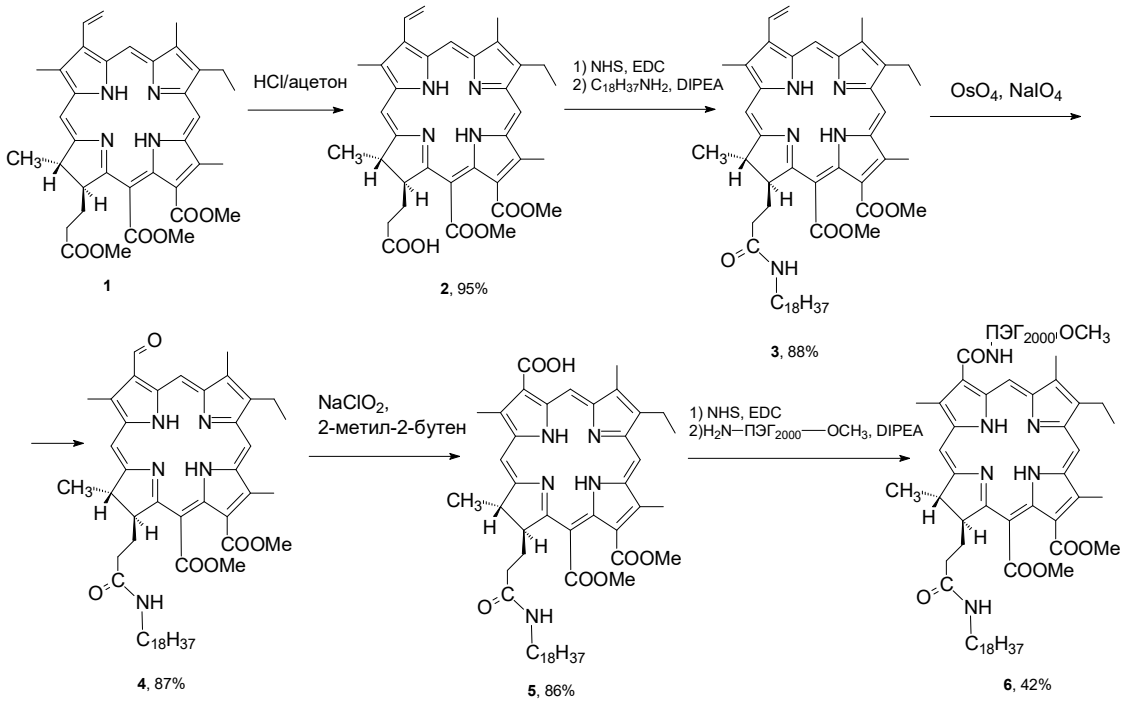


**Figure 1.** Scheme for obtaining the amphiphilic derivative of chlorin $p_6$

The amphiphilic derivative of chlorin $p_6$ **6** was used to modify the surface of UCNP due to non-covalent (with oleic acid residues) interactions. For this, UCNP was dispersed in chloroform at a concentration of 1 mg/ml. Then a solution of chlorine in chloroform was added to the particles (the ratio of nanoparticles:chlorin by weight was 1:2), and the resulting mixture was sonicated for 3 min. The suspension was diluted with isopropanol and centrifuged at 6000 rpm for 30 min. The coincidence of the absorption band of chlorins (661 nm) and the fluorescence band of the upconverting nanoparticle made it possible to observe nonradiative energy transfer from nanoparticles to chlorophyll a derivatives.The efficiency of nonradiative energy transfer for the amphiphilic derivative of chlorin **6** was 19%

## Conclusions

Upconversion nanoparticles loaded with octadecylamine-substituted derivatives of chlorin $p_6$ were obtained and characterized. The intense energy transfer from UCNPs to chlorin was observed, and the efficiency of nonradiative energy transfer was estimated as 19%. This nanocomplexcouldbe proposed for PDT treatment of tumors.


## Acknowledgments

The article was prepared as part of the work on the topic «Laser technologies for biomedical applications» (№122122600055-2) under the state order of the Ministry of Education of the Russian Federation.


## References


1. Dolmans D.E.J.G.J., Fukumura Jain, R. K. *Nat. Rev. Cancer,* **2003**, 3, 375–380.
2. A. V. Nechaev, M. E. Nikolaeva, I. M. Asharchuk, K. V. Khaydukov, E. V. Khaydukov, V. A. Semchishen, A. F. Mironov.*Macroheterocycles,* **2016**, 9 (4), 361-365.
3. Guo H.C., Qian H.S., Idris N.M., Zhang Y. *Nanomed-Nanotechnol.,* **2010,** 6, 486–495.

4. KhaydukovE.V., MironovaK.E., SemchishenV.A., GeneralovaA.N., NechaevA.V., KhochenkovD.A., StepanovaE.V., LebedevO.I., ZvyaginA.V., DeyevS.M., PanchenkoV.Y. *ScientificReports*, **2016**, 6, 35103.

# Features of using the esCCO method to determine a person's condition

**E. V. Porfirieva[1]✉ and V. V. Davydov[1, 2]**
[1] Peter the Great Saint-Petersburg Polytechnic University, Saint Petersburg, Russia;
[2] The Bonch-Bruevich Saint Petersburg State University of Telecommunications, Saint Petersburg, Russia.
✉ porfirieva.ev@edu.spbstu.ru

**Abstract.** The necessity of expanding the use of the esCCO method to determine the state of human health, especially if he is in a critical and close to it state, is justified. In this case, it is important to get the necessary information in a shorter period of time than using other methods. The features of the application of the esCCO method for determining a person's condition in various situations by changing cardiac output are established. Examples of registration of various parameters for calculating cardiac output using esCCO technology and experimental data on changes in cardiac output over time are presented.

**Keywords:** Human condition, cardiovascular system, cardiac output, vital parameters.

## Introduction

Nowadays, there are many factors that affect a person's condition. The state of human health in the course of life, basically, worsens. Therefore, in order to slow down the process of deterioration, people use various means and medications. To make sure of the effectiveness of their use, a quick and effective health monitoring is necessary. Special attention is paid to the methods of express diagnostics [3]. Among them, express diagnostics of the state of the cardiovascular system is most in demand, since diseases of such important organs are most common. In addition, diseases and damage to the cardiovascular system have a significant impact on other human organs. Among these methods, express diagnostics based on electrocardiogram (ECG) analysis, echocardiogram, daily monitoring and the esCCO method have received the greatest application [1]. The esCCO method (estimated Continuous Cardiac Output — calculated continuous measurement of cardiac output) has a number of features that distinguish it from other methods considered. Its use makes it easier and better to find out the necessary information. In addition, the advantage of the esCCO method is minimally invasive and accessible in various aspects of medicine. This method allows for a smaller number of different manipulations to obtain more detailed data. esCCO combines several different research methods. In addition, simultaneous measurements on different devices allows you to more accurately notice changes in the state of human health. The use of esCCO technology improves the quality of monitoring of hemodynamic parameters during treatment of any intensity: not only during serious surgical operations, but also during less risky procedures, which, however, can still lead to complications from the point of view of hemodynamics.

## Features of using the esCCO method

It should be especially noted that more recently the measurement of cardiac output required catheterization of the pulmonary artery. This was available only to cardiologists. The development of the esCCO method made it possible to change this situation. In fact, the esCCO method is a calculated continuous cardiac output [1, 2], calculated on the basis of vital activity parameters. To obtain this parameter, ECG electrodes, a SpO2 finger sensor and a NIAD cuff are required, which excludes direct contact with human internal organs. There are 2 types of esCCO calibration: minimally invasive and non-invasive calibration. In our case, a non-invasive type of calibration is used. The Nihon Kohden Bsm PVM-2703 bedside monitor is used for measurements (Fig. 1), in which this technique is implemented.

Fig. 1. Nihon Kohden Bsm PVM-2703 bedside monitor (with esCCO).

The pulse signal received on the photodetector must be transformed in such a way as to take into account the areas where transients occur, and then isolate the useful signal. The value of the useful signal will change in direct proportion to the amount of scattered radiation, which means the amount of hemoglobin and oxyhemoglobin in the blood, the change of which occurs under the influence of pulse waves.

## Results and Discussion

For example, Fig. 2 shows the change in the minute cardiac output, which is calculated using esCCO technology.

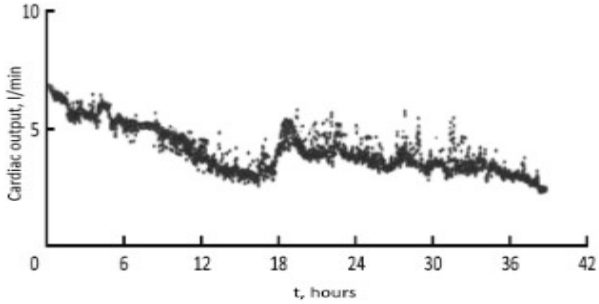


Fig. 2. The dependence of the change in the minute cardiac output on time

Analysis of the data obtained shows that the human condition is unstable. Processes occur in the body that change over time, leading to various cardiovascular disorders. This leads to an increase in minute cardiac output (CO) and a decrease in blood pressure and vascular resistance. Therefore, in various situations, it is also desirable to monitor these parameters of patients.

It should be noted that an essential feature of the esCCO methodology is that special skills and additional sensors are not required when making measurements. The method is easy to use and can be used by specialists of various profiles.

## Conclusion

The results obtained by us show that the esCCO technique is the most effective and practical for use in various cases. With its help, the diagnosis of a person's health can be carried out during treatment of any intensity (not only during serious operations), but also during less risky procedures that can lead to complications, for example, from the point of view of hemodynamics.

## REFERENCES

1. **Bataille, B., Bertuit, M., Mora, M., Mazerolles, M., Cocquet, P., Masson, B., Moussot, P., Ginot, J., Silva, S., Larché J.** Comparison of esCCO and transthoracic echocardiography for non-invasive measurement of cardiac output intensive care, British Journal of Anaesthesia. 109(6) (2012) 879-88.

2. **Biais, M., Berthezène, R., Petit, L., Cottenceau, V., Sztark, F.** Ability of esCCO to track changes in cardiac output, British Journal of Anaesthesia. 115(3) (2015) 403-410.

3. **Mazing, M.S., Zaitceva, A.Y., Kislyakov, Y.Y., Avdyushenko, S.A.** Monitoring of oxygen supply of human tissues using a noninvasive optical system based on a multi-channel integrated spectrum analyzer. International Journal of Pharmaceutical Research. 12 (2020) 1974–1978.

# Miniature potentiometric system for determination of $H^+$, $K^+$, $Na^+$, $Cl^-$, $NO_3^-$ - and $Ca^{2+}$ ions in liquid biological environment

**V.V. Romanova[1,2], V.S. Sibirtsev[1,3], A. Yu. Zaitseva[1]**

[1] Institute for Analytical Instrumentation of the Russian Academy of Sciences, St. Petersburg, Russia;

[2] St. Petersburg State Institute of Technology, St. Petersburg, Russia;

[3] St. Petersburg State Chemical and Pharmaceutical University, St. Petersburg, Russia.

✉venjo@mail.ru

**Abstract.** The device of the potentiometric system developed by us (including a set of 6 miniature measuring cells including PVC-membrane electrodes selective to presence in the analyzed solutions of $H^+$, $K^+$, $Na^+$, $Ca^{2+}$, $Cl^-$ and $NO_3^-$ ions, the most widespread in biological environments, is described, and one central "reference" cell with a chlorosilver reference electrode) and testing of the system with aqueous solutions of HCl, KCl, NaCl, $NaNO_3$ and $CaCl_2$ at concentrations from $10^{-1}$ to $10^{-5}$ M. This confirmed the usefulness of the developed potentiometric multisensor system for the analysis of the ionic composition of biological environment.

**Keywords:** potentiometry, potentiometric sensor, ionic composition, miniature system, biological environment, plasticized membranes, multisensor system.

## Introduction

Ion-selective electrodes are an attractive tool for analyzing the ionic composition of various multicomponent aqueous solutions (which include most biological environment) due to their simplicity of operation, low cost, short analysis time, and the possibility of miniaturizing the sensors and automating the analysis process [1-4].

In this connection, the aim of our work was to develop and test the potentiometric system consisting of a set of 6 miniature measuring cells (MC) including PVC-membrane electrodes selective to the presence of $H^+$, $K^+$, $Na^+$, $Ca^{2+}$, $Cl^-$ and $NO_3^-$ ions (the most common in biological environment) in the analyzed solutions and one CRC with chlorosilver reference electrode.

## Materials and Methods

Our system was based on the method of direct potentiometry, based on transformation of activity of target ions ($H^+$, $K^+$, $Na^+$, $Ca^{2+}$, $Cl^-$ or $NO_3^-$, respectively) into electromotive force (EMF), described by the Nernst equation.

Each of the 6 MC included in the developed potentiometric multisensor system and located around the central ""reference" cell (CRC) was a case made on a 3D-printer from PETG filament (see Figure 1). This housing was divided inside by a horizontal partition (HP). The lower (next to the HP) section of the case of MC has a volume of 1 ml and three side fittings. One of them (the central one filled with agar-agar with KCl) served as a "salt bridge" connecting the MC with the CRC. Whereas the other two fittings served to input and output the analyzed solution from the MC and connect the MC to each other.

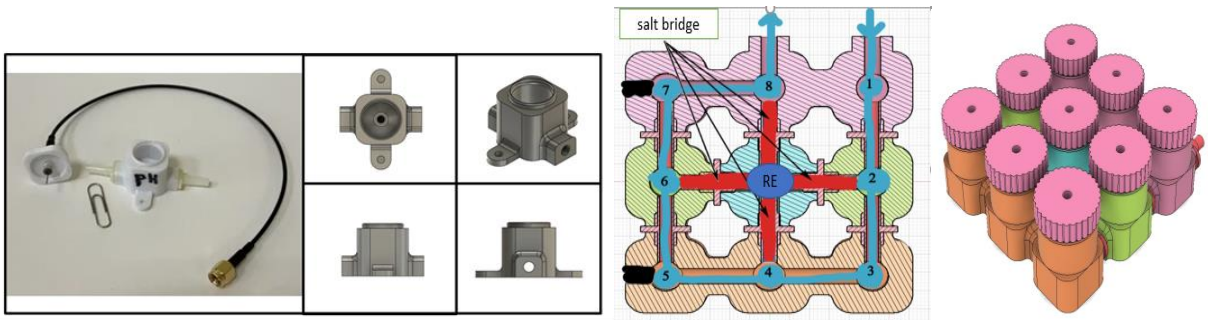


Fig. 1. Schematic diagram of our developed potentiometric multisensor system.

In the middle of the HP there was a hole, which was sealed with an ion-selective membrane made of polyvinyl chloride plasticized with di-2-ethylhexylsebacinate (DOS), o-nitrophenyloctyl ether (oNPOE), or 2-fluorophenyl-2-nitrophenyl ether (2F2N) with an organic ionophore added during the assembly of the measuring cell.

Then, the upper (with respect to the HP) part of the MC (also having a volume of 1 ml) was filled with a solution of 2 M KCl - while the lower (with respect to the HP) part of the MC was filled either with the solution to be analyzed or (between the measurements) with a solution with a given concentration of the ion measured by this MC.

After that, the top of the MC was closed with a cover in which a silver wire, galvanically coated with AgCl and slightly short of the HP, connected to the screened current collector was installed.

The CRC of the developed potentiometric multisensor system had the same case and lid as the MC considered above - only completely filled with 2 M KCl solution, without a HP.

## Results and Discussion

At approbation of our developed potentiometric multisensor system, we filled it in turn as the analyzed media with aqueous solutions of HCl, KCl, NaCl, $NaNO_3$ and $CaCl_2$ with concentrations $10^{-1}$, $10^{-2}$, $10^{-3}$, $10^{-4}$ and $10^{-5}$ mol/l. The data obtained in measurements of these solutions confirmed a high sensitivity of the developed MC to the target ions ($H^+$, $K^+$, $Na^+$, $Ca^{2+}$, $Cl^-$ or $NO_3^-$, respectively) at the absence of such sensitivity to non-target ions, as well as high reproducibility and linearity between values of potential differences between measuring cell and CRC (measured with high-resistance millivoltmeter and commutator of signals received from current leads of MC and CRC) and negative decimal logarithms of molar concentrations of target ions (calibration equations: $pH = 5 - 0{,}02 \cdot E_H$, $pK = 2{,}6 - 0{,}03 \cdot E_K$, $pNa = 2{,}3 - 0{,}02 \cdot E_{Na}$, $pCa = -4{,}6 - 0{,}04 \cdot E_{Ca}$, $pCl = -1{,}4 - 0{,}02 \cdot E_{Cl}$, $pNO_3 = 0{,}28 + 0{,}02 \cdot E_{NO3}$, – for voltages measured in mV) in the whole range of investigated concentrations of these ions (from $10^{-5}$ to $10^{-1}$ M).

## Conclusion

At approbation of our developed potentiometric multisensor system, having carried out researches of solutions with known concentrations $H^+$, $K^+$, $Na^+$, $Ca^{2+}$, $Cl^-$ and $NO_3^-$ ions, we have made sure of high enough stability, selectivity and sensitivity of our system in relation to ionic composition of researched solutions. These results confirmed the suitability of our developed potentiometric multisensor system for the analysis of the ionic composition of biological environment.

## Acknowledgments

The work was supported by the Ministry of Science and Higher Education of the Russian Federation (project 075-15-2021-1057).

## REFERENCES

1. **Mikhelson K.N.**, Electrochemical sensors based on ionophores: current state, trends, prospects. // Russian Chemical Journal. 2008. VOL. LII. №2. C. 30-36.
2. **Vlasov Yu.G., Ermolenko Yu.E., Legin A.V., Rudnitskaya A.M., Kolodnikov V.V.,** Chemical sensors and their systems. // Journal of Analytical Chemistry. 2010. T. 65. № 9. C. 900-919.
3. **Sibirtsev V.S., Olekhnovich R.O., Samuylova E.O.**, Assessment of integral toxicity of water resources by instrumental methods of analysis. // SGEM Conference Proceedings. 2017, V. 17. № 61. P. 507–514.
4. **Guzenko M.M., Zaitseva A.Yu.**, Intelligent sensor system for ranking the ionic composition of breast milk. // Scientific instrumentation. 2022. T. 32. № 4. C. 58-67.

**Determination of the isoelectric point of the antibody to Sars-Cov-2 by molecular modeling for conjugation with quantum dots**

**S. K. Rudnykh[1]✉, E. D. Gribova[1], K. T. Kholmurodov[12], P. P. Gladyshev[1], N. A. Polotnyanko[1]**

[1]Dubna State University, Moscow region, Universitetskaya 19, Dubna 141980, Russia.

[2]Joint Institute for Nuclear Research, Moscow region, 6 Joliot-Curie, Dubna, 141980, Russia

✉ rudnih@yandex.ru

**Abstract.** The fundamental property of antibodies (Abs) and other proteins is the isoelectric point (pI). PI is the pH at which a particular molecule or surface carries no net electrical charge. It is possible to predict the behavior of the Abs-substrate complex and select optimal conjugation conditions, knowing the surface charge distribution and pI. In this paper, pI of the Abs to SARS-COV-2 CA521 FALA (code PDB 7 e23) was calculated by molecular modeling and conjugation of this Abs with multilayer chalcogenide quantum dots (QDs) was performed.

**Keywords:** antibodies, isoelectric point, molecular modeling, quantum dots.

## Introduction

Various analytical labels are used to visualize biomolecule complexes. It should be mentioned that test-systems with QDs as fluorescent labels have extremely high sensitivity [1]. It has a number of unique optical properties, such as a narrow and symmetrical fluorescence peak, high fluorescence brightness, wide excitation band and photostability. Due to these properties, it is possible to reduce detection limits and increase the sensitivity of test-systems based on QDs. pI is one of the most significant characteristics of Abs, affecting its orientation during conjugation with QD's surface [2]. Currently, there is no physico-chemical method for determining the local charge on the Abs surface. The influence of various factors on the surface charge can be estimated using the molecular modeling method. It is necessary to know the surface charge of antibodies for conjugation and obtaining a complex with high analytical characteristics (Fig.1).

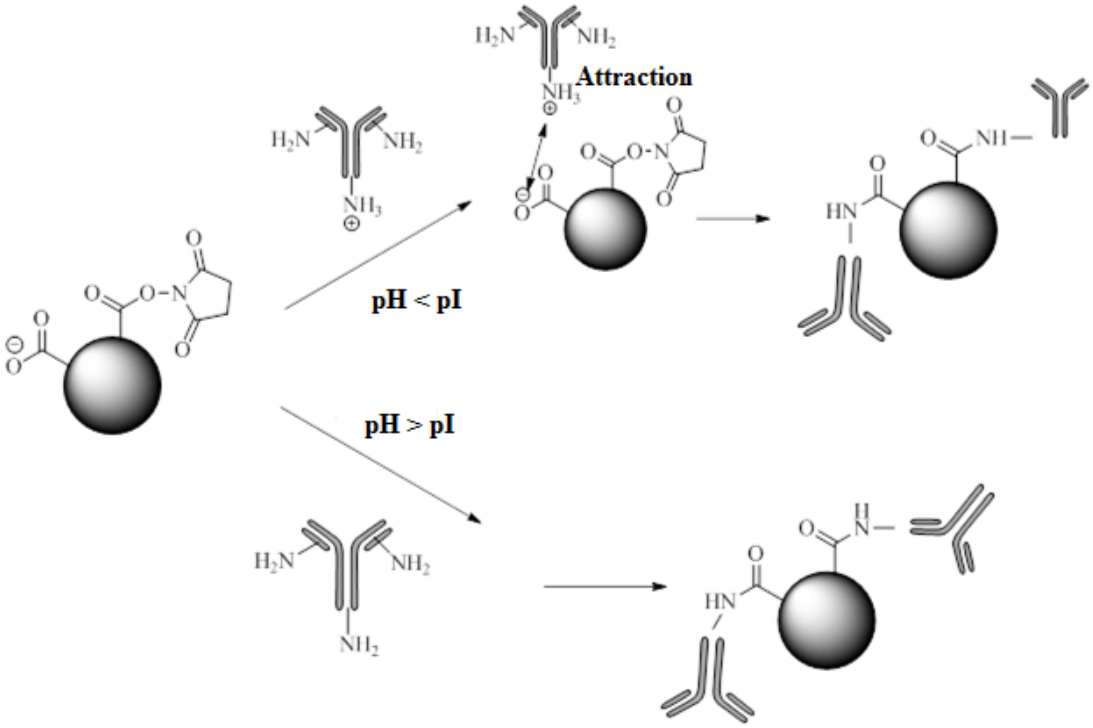


Fig. 1. Activating carbodiimide binding reagents that provide a carboxyl-functionalized QDs matrix with a distinct surface charge that can attract Abs

Figure 1 shows one of the most popular ways of attaching Abs to nanoparticles via amines. Amino groups of Abs are located on their entire surface, and are reactive without any chemical modification with various QD groups. In turn, the surface carboxyl groups of QD, before binding to Abs, must be activated using 1-ethyl-3-(3-dimethylaminopropyl)carbodiimide (EDC) and N-hydroxysuccinimide (NHS). Adsorption of Abs on the carboxyactivated surface of QD is the most acceptable strategy using the force of ion interaction. By controlling the immobilization conditions, the carboxyl-activated matrix has rapid reversible electrostatic adsorption and covalent binding, and the activating reagent has a significant effect on the orientation of bound biomolecules. As can be seen from Figure 1, for oriented conjugation, it is necessary to create a pH below the isoelectric point of the protein, since in this case the crystallizing fragment of the antibody acquires a positive charge, and due to the electrostatic interaction covalently binds to the lower part of the antibody, leaving the antigen-binding pocket open.

## Materials and Methods

The simulation method and the calculation of the energy minimization of the molecule were carried out in the Amber complex on the "Govorun" supercomputer at JINR, Dubna. The electrostatic surface potential of the antibody surface was calculated at different pH of the solution: pH 5, pH 7.4 and pH 8.5. The calculation was performed in PyMOL 3.3 (PDB code: 7e23) using the APBS Electrostatics plug-in with a range of ± 5 kbT/e.

## Result and Discussion

The CA521 antibody consists of 120 amino acid residues formed from 14 amino acids. Among them there are acidic amino acids (Arg, His and Lys), basic amino acids (Asp and Glu) and other neutral amino acids. The charge of amino acids depends on the pH value of the medium and on the structure of their radical. With a decrease in the concentration of hydrogen ions in the solution, their separation from the amino group and the carboxyl group of amino acids increases. When the pH decreases, the $H^+$ ions present in the solution are attached to the amino and carboxyl groups - the charge of the amino acid becomes positive. Variant structures of Abs at different pH were constructed and analyzed from the native protein using the Amber complex. The calculation results showed that the number of all positively charged residues (basic): 6 Lys and 8 Arg and all negatively charged residues (acidic) 10 Asp and 14 Glu compensate each other at pH 7.4. Thus, the isoelectric point of the CA521 FALA antibody is (pH=7.4). The results obtained were used in practice, when conjugating Abs with multilayer chalcogenide QD by carbodiimide binding. The experiment was performed at a pH value below pI (pH=5.5) and above pI (pH 7.5). The success of conjugation was assessed by the fluorescence intensity of the Abs-QD complex. In the case of conjugation at pH 7.5, the fluorescence intensity on the test strip was 200% higher. The final results of the study can be used in the development of test systems for the identification of pathogenic biological agents, with improved analytical characteristics.

## REFERENCES

1. Farias P. M. A., Fontes A., Galembeck A., Figueiredo R., Santos B. S. Fluorescent II-VI semiconductor quantum dots: Potential tools for biolabeling and diagnostic // Journal of the Brazilian Chemical Society. – 2008. – T. 19, № 2. – C. 352-356.

2. Matsuda Y., Mendelsohn B. A. An overview of process development for antibody-drug conjugates produced by chemical conjugation technology // Expert Opinion on Biological Therapy. – 2021. – T. 21, № 7. – C. 963-975.

3. Gao S. P., Rojas-Vega F., Rocha-Martin J., Guisan J. M. Oriented immobilization of antibodies through different surface regions containing amino groups: Selective immobilization through the bottom of the Fc region // International Journal of Biological Macromolecules. – 2021. – T. 177. – C. 19-28.

# Modelling of laser welding of biological tissues using focused radiation

**D. I. Ryabkin** [1,2✉], **V. V. Suchkova** [1,2], **A. Yu. Gerasimenko**[1,2]
[1] I.M. Sechenov First Moscow State Medical University, Moscow, Russia;
[2] National Research University of Electronic Technology MIET, Zelenograd, Moscow, Russia;
✉ ryabkin@bms.zone

**Abstract.** Laser welding is an alternative technology for biological tissue reconstruction. The laser weld is small, liquid-tight and does not cause mechanical stress. However, thermal necrosis of the joined living tissue occurs during suture formation, and the depth of suture formation may be much less than required.

This paper proposes the use of laser radiation with dynamically varying focusing parameters to reduce the area of thermal necrosis of the attached living biological tissue and increase the depth of suture formation.

The influence of laser focusing parameters was evaluated by simulation. Absorption by biological tissue and braze was calculated according to the Bouguer-Lambert-Bera law. The degree of protein conversion in biological tissue and solder was determined using chemical kinetic methods and the Arrhenius equation. Heat transfer was calculated using the thermal conductivity equation.

Simulations showed that the use of focused radiation allowed the formation of deeper sutures with a smaller area of thermal tissue necrosis. This result will be used to improve the apparatus for laser welding of biological tissues.

**Keywords:** mathematical modeling, laser soldering, tissue reconstruction

**Funding:** The study was supported by the Russian Science Foundation grant No. 22-75-00089, https://rscf.ru/project/22-75-00089/

## Introduction

Laser welding of biological tissues is an alternative method of joining biological tissues. An important advantage of laser welding over traditional joining techniques is the small size of the suture, its impermeability to fluids and the absence of mechanical stress.

During laser suture formation, the joining area and adjacent tissues are heated. The heating inevitably results in an area of thermal necrosis of the fused living tissue. The aim of this work is to optimise the process of welding biological tissues by modelling in order to minimise the area of thermal necrosis of the tissues.

## Materials and Methods

The absorbed energy of the laser radiation was determined according to the Bouguer-Lambert-Bera law:

$$I = I_0 e^{-\int_0^L \mu(\vec{r})dl}, \quad (1)$$

where $I$ is the intensity of laser radiation after the beam passes through a layer with a thickness $L$, $I_0$ is the power of the incident laser radiation, $\mu(\vec{r})$ is absorption coefficient.

The degree of suture formation and thermal necrosis of the living tissue was determined by the conversion α at time t [1]:

$$\alpha(t) = \frac{C_t}{C_0}, \quad (2)$$

where $C_\tau$ is the concentration of denatured protein at time $\tau$, $C_0$ is the initial concentration of native protein. The degree of weld formation and thermal necrosis was taken into account α=0,63.

The conversion was calculated according to the Arrhenius equation:

$$\alpha(t) = 1 - e^{-\int_0^\tau A e^{-\frac{E_a}{RT(t)}} dt}, \quad (3)$$

where $A$ is the dimensionless pre-exponential factor of the Arrhenius equation $E_a$ is the activation energy, $R$ is the universal gas constant, $T$ is the temperature, and $t$ is the time [2-4].

Heat transfer has been calculated using the heat transfer equation:

$$\frac{\partial T(x,y,z,t)}{\partial t} - \nabla\big(a(x,y,z,t)\nabla T(x,y,z,t)\big) = f(x,y,z,t), \quad (4)$$

where $T$ is the temperature, $a$ is the thermal diffusivity, $f$ is the function of heat sources, $t$ is the time.

## Results and Discussion

Simulations showed the advantage of using focused radiation compared to plane-parallel laser radiation. The advantage was the formation of a much smaller area of thermal necrosis of the fused biological tissue. The effect was most pronounced at a suture depth of up to 0,1 mm. The greatest reduction in the area of thermal necrosis of tissue and increase in the size of the formed suture was achieved with dynamically changing parameters of laser radiation focusing.

## Conclusion

This work demonstrates the advantage of using focused laser irradiation to form laser sutures. The use of focused laser radiation makes it possible to form deeper sutures and reduce the area of thermal necrosis of the biological tissues to be joined. The obtained parameters of the laser radiation will be used in the future to improve the laser welding device for biological tissues.

## REFERENCES

[1] **Pearce J.A.,** Comparative analysis of mathematical models of cell death and thermal damage processes. Int. J. Hyperthermia, 29(4) (2013) 262-280.

[2] **Kampmeier J., Radt B., Birngruber R.,** Thermal and biomechanical parameters of porcine cornea, Cornea. 19(3) (2000).

[3] **F. Rossi, R. Pini, L. Menabuoni,** Experimental and model analysis on the temperature dynamics during diode laser welding of the cornea, J. Biomed. Opt. 12(1) (2007) 14031.

[4] **Gosalia K., Weiland J., Humayun M.,** Thermal elevation in the human eye and head due to the operation of a retinal prosthesis, IEEE Trans. Biomed. Eng. 51(8) (2004) 1469–1477.

# Investigation of the reflected irradiation characteristics from skin lesions using a multispectral light source

**K. V. Zaichenko[1] , V. S. Gurevich[1] , A. A. Kordukova[1] , A. V. Belyaev[1], V. I. Svatkina[1,2]✉**

[1] Institute for Analytical Instrumentation of the Russian Academy of Sciences, Saint Petersburg, Russia;

[2] Peter the Great St. Petersburg Polytechnical University, Saint Petersburg, Russia;

✉svyatkina.vi@edu.spbstu.ru

**Abstract.** This article is devoted to the investigation of the reflected irradiation characteristics from skin lesions in short-wave optical, ultraviolet and infra-red wavelengths with skin neoplasms for the early diagnostics of skin pathologies. The paper considers problems related to limited possibilities of visual diagnostics arising from the use of existing modern approaches to detection of malignant neoplasms and substantiates the urgency of development and introduction of new methods of diagnostics of skin pathologies. A new method of multispectral processing using a polychrome radiation source developed based on biophotonics and optoelectronics methods is proposed. Experimental study of reflected radiation from a skin area with a benign neoplasm in the abdominal region in a selected wavelength range was carried out. Digital image processing for the images in short-wavelength range was performed. The intensity distribution diagrams of reflected radiation at each wavelength in the short wavelength range were analyzed. The necessity of application of this method in medicine, for early diagnostics of malignant skin neoplasms is proved.

**Keywords:** Multispectral image processing, early diagnosis, skin neoplasms.

## Introduction

Malignant skin lesions are the most prevalent of all kinds of cancer (1). The skin is exposed to numerous external influences on a daily basis, which leads to pathologies, so early diagnosis of pathologies is an extremely urgent problem. The capacity of existing methods [2-3] is limited due to the inability of human eye to distinguish pure spectral components of light from combined ones, whichleads to loss of spectral information. As one of the solutions, multispectral image processing has been proposed, which consists of illuminating the studied object by a consequence of monochrome wavelengths and detecting the image with a photodetector [4].

## Materials and Methods

Figure 1 shows the optical diagram of the light source. The experimental studies use the set of LEDs in the short visible, ultraviolet and infrared wavelength ranges.

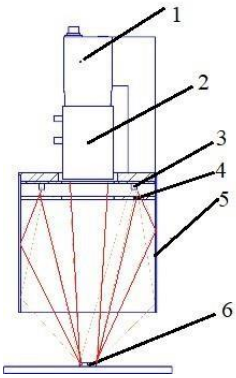


Fig. 1. Experimental setup including
1 - TV camera, 2 - lens, 3 - light source, 4 - frosted glass, 5 - frostedreflector, 6- object

## Results and Discussion

Figure 2 shows the image of a benign neoplasm in the abdomen and the intensity distribution cross section at 370 nm corresponding to the image. The image was pre-processed in MATLAB to generate the graph.

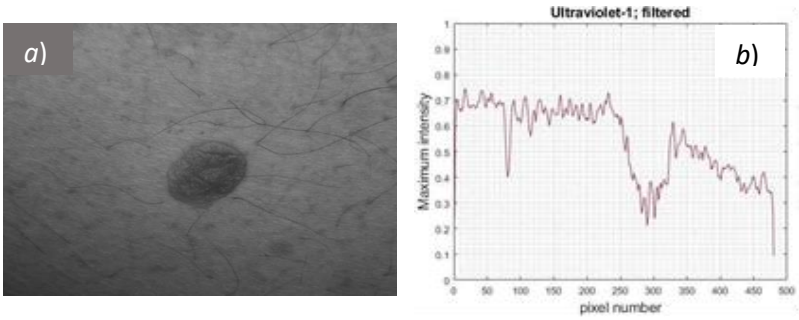


Fig. 2. Image under UV light *(a)* and intensity distribution *(b)*

## Conclusion

As a result of the work, the interaction of radiation with skin neoplasms in the selected wavelength range has been investigated. The intensity distribution graphs show an increase in radiation absorption in the area with a neoplasm and, in addition, in the area corresponding to the accompanying pigmentation. These studies are of practical interest for the further development of medicine in the field of skin neoplasm diagnosis.

## Acknowledgments

We would like to thank the state assignment of the Ministry of Education and Science no. 075-00761-22-00 "Theoretical and experimental research on the development of methods and devices for the diagnosis of early stages of the development of pathologies of human organs and systems based on ultra-high resolution instrumental electrophysiology, photonics and modern genomic technologies". State registration number FFZM-2022-0011. Due date 2022-2024.

## REFERENCES

1. **Gantsev, Sh. H., Kyzirgalin, Sh. R., Timin, K. E.**, Skin cancer. Melanoma. Guidelines for physicians, Volume 1, Oncology, GEOTAR-Media, Moscow, 2020.
2. **Solodyankina, T.N., Apanasevich, V.I., Gurina, L.N.**, Dermatoscopy as a method of diagnosis of skin melanoma, Siberian Journal of Oncology. 5 (2009) 63 - 69.
3. **Zhao, J., Lui, H., Kalia, S., Zeng, H.**, Real-time Raman spectroscopy for automatic in vivo skin cancer detection: an independent validation, Analytical and Bioanalytical Chemistry, 407 (27) (2015) 8373 - 8379.
4. **Zaichenko K.V., Gurevich B.S., Svyatkina V.I.**, A polychrome light source for the implementation of multispectral image processing method of malignant skin lesions, Scientific and Technical Journal of Information Technology, Mechanics and Optics, 22 (5) (2022) 846 - 853.

# Development of a fiber optical system for assessing the state of peripheral circulation

**D. S. Skryabin[1], M. S. Mazing[2✉], R. V. Davydov[1, 3]**

[1]Peter the Great Saint Petersburg Polytechnic University, Saint Petersburg
[2]Institute for Analytical Instrumentation of the Russian Academy of Sciences
[3]All-Russian Research Institute of Phytopathology, Russia
✉e-mail: mazmari@mail.ru

**Abstract.** A fiber-optic system for assessing the state of microhemodynamics of various biological tissues using optical oximetry methods is presented. The relevance of the development of methods for diagnosing the microvasculature by non-invasive express systems similar to the one proposed is substantiated. The advantages of the proposed non-invasive fiber-optic system for assessing the state of the microcirculation system are described.

**Keywords:** microcirculation, microhemodynamics, optical radiation, diffuse reflectance spectroscopy, hemoglobin.

## Introduction

Monitoring the state of the microvasculature provides information on the status of various diseases in the human body. Deviations in the work of the microcirculatory tissue system can indicate the presence of such pathological processes as diabetes mellitus, oncology, rheumatic diseases, and others. It is important to note that the methods for assessing microcirculation, which are currently widely used in medical practice, are stationary and require the use of expensive equipment. In this regard, the development of portable low-cost systems that will suit the principles of point-of-care testing is required.

The aim of the work is to develop a non-invasive small-sized optical system for studying microcirculatory processes and diagnosing microcirculatory disorders, the principle of which is based on optical tissue oximetry methods.

## Materials and Methods

The instrumental part of the system is presented in the form of two modules: a broadband radiation source, which is represented by a halogen lamp, and a multichannel spectrum analyzer implemented as an array of optical sensors in the visible and near infrared ranges. The input of optical radiation into the tissue under study is implemented using an optical fiber probe. The computational part of the system processes and displays the results obtained. The block diagram of the implemented fiber optic system is illustrated in Figure 1.

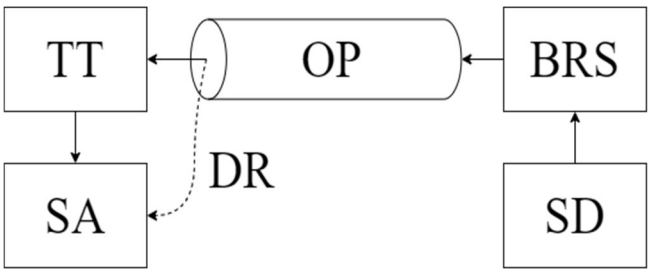


Fig. 1. Block diagram of the implemented fiber-optic system for assessing the state of peripheral circulation: SA-spectral analyzer, TT-test tissue, DR-diffuse reflection, OP-optical probe, BRS-broadband radiation source, SD-source driver.

The result of the diagnostics is the interpretation of the processed optical signals, which, in turn, are classified into groups that express the state of the microvasculature. The analysis of these data will minimize the subjective decision-making by the medical specialist. The principle of operation of the system, the structural diagram of which is shown in Figure 2, is based on the

methods of registration of backscattered radiation in the studied biological tissue and the ability of different hemoglobin fractions to absorb radiation of different wavelengths [1].

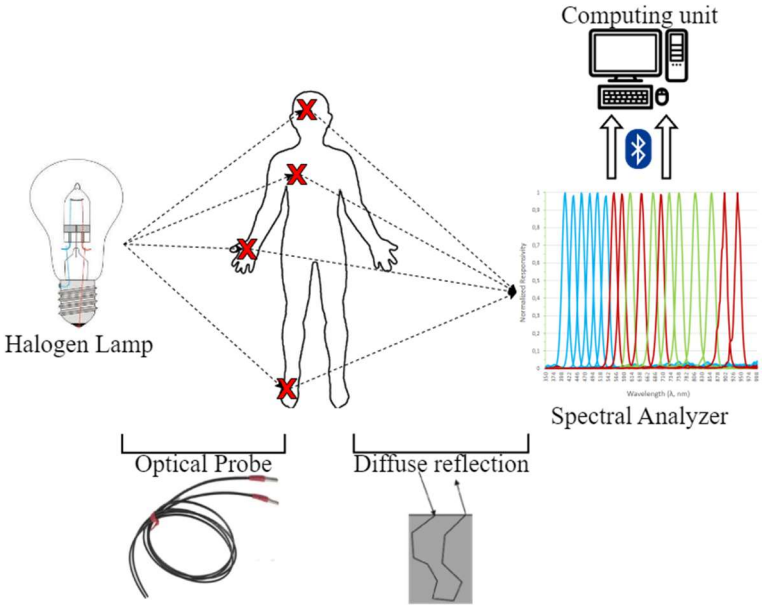


Fig. 2. Structural diagram of a laboratory model of a fiber-optic system for assessing the state of peripheral circulation.

## Results and Discussion

The use of broadband radiation in a fiber optic system makes it possible to obtain a large amount of information for the analysis and assessment of the state of microcirculatory tissue systems in the studied biological tissue. The use of a fiber probe in studies of microcirculatory systems has already shown its effectiveness in assessing blood supply parameters [2]. The fiber probe in the proposed system allows to change the distance between the radiation source and the photodetector, which in turn allows to study the microhemodynamics of tissues at different depths.

## Conclusion

The proposed fiber-optic system for assessing the state of peripheral circulation is a promising device for assessing the functional state of the microcirculatory tissue systems of the human body. The system satisfies all the principles of point-of-care testing, can be used outside the hospital and does not require the presence of qualified medical personnel.

## Acknowledgments

Improving the methods of medical and biological control of living tissues and genetic analysis, their methodological, software and instrumentation for scientific research and practical application - n.ruk. d.t.s. V.E. Kurochkin. FFZM-2022-0010. State registration number 122032300337-4.

## REFERENCES

1. **Rogatkin, D.A.** Physical foundations of optical oximetry. Meditsinskaya fizika = Medical physics. 2 (2012) 97–114. (In Russ.)

2. **Dunaev, A. V.** A Method and a Device for Evaluating the Functional State of Microcirculatory-Tissue Systems of the Human Body Based on Multiparametric Optical Diagnostics. Journal of the Russian Universities. Radioelectronics. 23(4) (2020) 77–91.

# Albumin nanoparticles for Near Infrared Bioimaging

**M. E. Stepanov** [1✉], **P. A. Demina** [1,2,3], **R.A. Akasov**[1,2,3], **G. Babayeva**[4], **A.N.Generalova**[1,2,3], **A. Parodi**[5], **E. V. Khaydukov** [1,2,3]

[1] Moscow State Pedagogical University, Moscow, Russia;
[2] FSRC «Crystallography and Photonics» RAS, Moscow, Russia
[3] Shemyakin-Ovchinnikov Institute of Bioorganic Chemistry RAS, Moscow, Russia
[4] Research Institute of Molecular and Cellular Medicine, RUDN University, Moscow, Russia
[5] Division of Biotechnology, Sirius University of Science and Technology, Sochi, Russia

✉stepanov_me@mail.ru

**Abstract.** Organic nanoparticles (NPs) based on endogenous proteins are promising platform for bioimaging since they are biocompatible, biodegradable and have no systematic toxicity. Protein nanoparticles functionalization with IR dyes is promising approach for optical bioimaging in “biotissue transparency window” (700-1700 nm). In this work we studied albumin NPs loaded with three cyanine dyes: ICG, IR-806 and IR-820 for colloidal and optical properties. Moreover, we did in vitro test on cell uptake and also showed pharmacokinetics on balb/c mice in vivo.

**Keywords:** bioimaging, albumin nanoparticles, cyanine dyes, IR-806 dye.

**Funding:** The study was prepared as part of the work on the topic «Laser technologies for biomedical applications» (№ 122122600055-2) under the state order of the Ministry of Education of the Russian Federation.

## Introduction

Biomedical imaging is a promising and rapidly developing technology combining the whole family of minimally invasive methods [1] used to get some reliable information about pathological processes *in vivo*. Each method uses some kind of penetrating radiation (X-rays, γ–rays, magnetic fields, sound waves or some other) which interact with molecular contrasting agents to create a space-resolved contrast image.

Optical bioimaging based on near infrared (NIR) light attracts great attention due to high penetration depth [2]. The approach is non-invasive and safe, it uses NIR optical window in the net extinction spectra of body tissues and water molecules (700-1700 nm) to obtain the penetration depth up to several centimeters. Most commonly, the contrasting agents are fluorescent molecules with absorption/emission spectra in this region. The main drawbacks that limit their biomedical implication are: low solubility in plasma, low quantum yields (further quenched *in vivo*) and short circulation lifetimes.

To improve the situation, dyes can be loaded into hydrophilic biocomplexes that will hide dye from environment and transport it to target area. The promising strategy is to use endogenous transporting molecules, such as albumin [3]. Being the main protein component of the blood (~40%), albumin is non-toxic, biodegradable, easy-to-functionalize, water-soluble and has long circulation lifetime [4].

In present work we have used two different types of bovine serum albumin (BSA) nanoparticles, loaded with three different cyanine dyes (ICG, IR-806, IR-820). Physico-chemical, optical properties of obtained nanocomplexes were studied. The best candidates were investigated *in vitro* for cells uptake and *in vivo* for pharmacokinetics.

## Materials and Methods

The BSA nanoparticles were obtained by precipitation in a non-solvent followed by cross-linking. The IR dye was incorporated into BSA NPs due to non-covalent interactions. The load capacity and optical properties were studied by spectrometric methods. The size distribution was measured with dynamic light scattering (DLA). *In vivo* studies were done on home-build bioimaging system [5].

## Results and Discussion

Albumin NPs were synthesized by precipitation in a non-solvent with high (H-BSA) and low (L-BSA) cross-linking degree. H-BSA and L-BSA had the same size distribution with maximum at 200 nm. As DLA study has shown, Albumin NPs loading with IR dye dramatically changes size distribution in case of L-BSA, yet it does not affect size distribution of H-BSA. Loading capacities are the same for both types of NPs. Among the entire set of the samples, the BSA@IR-806 nanocomplexes turned out to be the most stable and had the brightest fluorescence. The emission maxima position and magnitude of BSA@IR-806 and BSA@IR-820 are shown to depend on the native structure of BSA nanoparticle, namely, degree of cross-linking, as well as relative amounts of dyes and albumin, demonstrating red shifts highly desirable for the bioimaging.

*In vitro* investigation of free IR-806 demonstrated high accumulation level in epithelial cells isolated from colon tissue (caco-2) cell line in comparison with commonly used Cy-5 cyanine dye, whereas BSA nanocomplexes containing IR-806 showed no specificity. *In vivo* pharmacodynamics study of BSA-IR806 was made in comparison with free IR-806 dye. The BSA-IR806 circulation lifetime turned out to be more extended than that of free IR-806 with the same distribution in organs. The most intensive signal was observed in liver, gall-bladder and all parts of intestines.

## Conclusion

In present work the synthesis of BSA nanoparticles loaded with cyanine dyes (ICG, IR-806, IR-820) was performed for bioimaging. BSA@IR806 dye nanocomplexes were found to demonstrate high colloidal stability and unusual spectral behavior (red shifts when conjugated with BSA). *In vitro* investigation showed preferential accumulation free IR806 dye in epithelial cells isolated from colon tissue cell line, while BSA NPS loaded with IR806 showed no specificity. *In vivo* studies demonstrated pronounced time-stable accumulation of BSA@IR806 fluorescence signal in gastrointestinal tract (mainly, liver, gall-bladder and intestines). The reasons for such behavior require further investigation.

## REFERENCES


1. **Wallyn J.**, et al., Biomedical Imaging: Principles, Technologies, Clinical Aspects, Contrast Agents, Limitations and Future Trends in Nanomedicines. Pharm Res, 2019. **36**(6): p. 78.
2. **Hong G., A.L. Antaris, and H. Dai**, Near-infrared fluorophores for biomedical imaging. Nature Biomedical Engineering, 2017. **1**(1).
3. **Xu L.**, et al., Multifunctional Albumin-Based Delivery System Generated by Programmed Assembly for Tumor-Targeted Multimodal Therapy and Imaging. ACS Appl Mater Interfaces, 2019. **11**(42): p. 38385-38394.
4. **Tian R., et al.**, Albumin-chaperoned cyanine dye yields superbright NIR-II fluorophore with enhanced pharmacokinetics. Sci Adv, 2019. **5**(9): p. eaaw0672.
5. **Generalova A.N.**, et al., Submicron polyacrolein particles in situ embedded with upconversion nanoparticles for bioassay. Nanoscale, 2015. **7**(5): p. 1709-17.

# Analysis of size-dependent optical properties of lysine carbon dots produced by femtosecond laser synthesis

**A. A. Astafiev [1]✉, A. M. Shakhov [1], M. S. Syrchina [1], V. A. Nadtochenko [1]**
[1]N.N. Semenov Federal Research Center of Chemical Physics,
Russian Academy of Sciences, Kosygina 4, Moscow, Russia
✉wrongclue@gmail.com

**Abstract.** Pulsed laser synthesis of fluorescent nanoparticles from amino acids promises for fluorescent imaging. Understanding relation between nanoparticle size and absorption and fluorescence characteristics sheds light on mechanism of fluorescence and enables control of optical properties of products. To study this relation, we separated products obtained by laser synthesis from L-lysine into fractions of different size and analyzed optical properties and chemical composition of these fractions.

**Keywords:** luminescent carbon dots, femtosecond laser pulses, nanomaterials, photostability.

**Funding:** This study was funded by Russian Science Foundation, grant number № 21-72-20169. The measurements were performed in the FRCCP shared research facilities No. 506694 and large-scale research facilities No. 1440743.

## Introduction

Femtosecond laser synthesis of fluorescent carbon dots from essential amino acids, e.g. l-lysine, provides a potential route of fluorescent species formation in living cells and tissues in situ [1] and holds promise for fluorescent imaging [2-3]. Nanoparticle size is one of parameters through which optical properties of carbon dots can be controlled and manipulated.

Also, relation between size and fluorescence characteristics is indicative of the fluorescence mechanism and thus can unravel contribution of various mechanism such as quantum size effects, molecular fluorophores etc. in fluorescence. In order to reveal the relation between nanoparticle size and optical properties we employed dialysis to separate fluorescent products obtained from L-lysine aqueous solution into several factions of different sizes. Absorption and emission spectra, fluorescence quantum yields and lifetimes and other optical characteristics were then registered for each faction.

## Materials and Methods

***Synthesis and separation of products.*** Aqueous solution of L-lysine (2 mL, 0.1 g/mL) in a quartz cuvette was irradiated with trains of femtosecond laser pulses focused by a spherical lens (f=8 mm, 0.5NA). Central wavelength of laser pulses was 800 nm, repetition rate - 1 kHz, duration - 50 fs, pulse energy - 1.4 mJ. Irradiation resulted in aqueous solution of colored and fluorescent carbon dots (**Lys-CD**). This solution was dialyzed for 72 hours in a 2,000 MWCO dialysis unit and separated into dialysate with molecular weight < ca. 2 kDa (**Lys-CD-1**) and retentate (**Lys-CD-2**, molecular weight > ca. 2 kDa) (Fig.1).

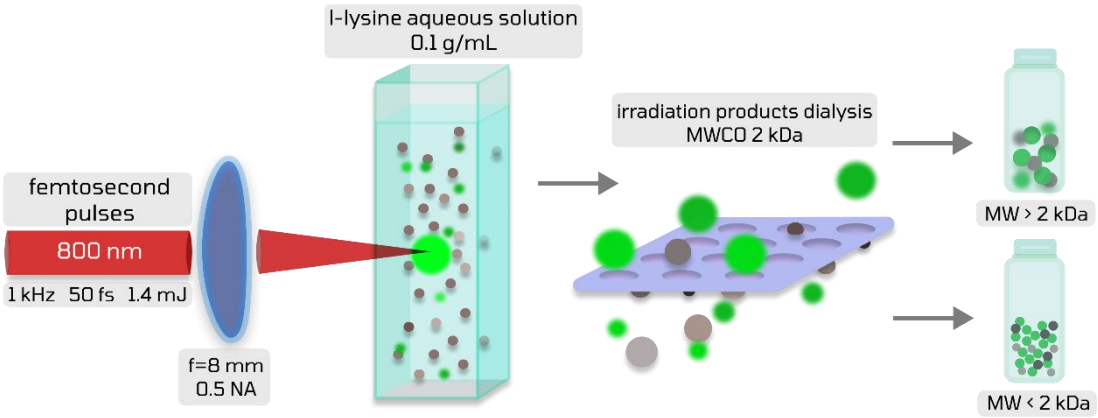


Fig. 1. Experimental setup.

***Samples characterization***. Absorption of photoluminescence spectra of samples in water were recorded with Shimadzu spectrophotometer (UV-3600) and spectrofluorometer (RF-5031 PC). Fluorescence quantum yield (356 nm excitation) was estimated with the slope method using ethanol solution of anthracene as a standard. Fluorescence decay and fluorescence anisotropy decay kinetics in aqueous solution were registered with pulsed laser excitation at 360 nm at 450 nm emission wavelength using time-correlated single-photon counting module (SPC-150N, Becker&Hickl GmbH). Fluorescence lifetime and anisotropy decay time were calculated as amplitude-weighted averages from three-exponential fit of decay kinetics. Infrared absorption spectra were collected using Bruker Lumos II FTIR microscope-spectrometer.

## Results and Discussion

Separation of carbon dots into size factions was confirmed by measurements of the anisotropy decay time which is proportional to the average hydrodynamic volume of carbon dots (**Table 1**). For Lys-CD-1 this time was still relatively large and corresponded to the hydrodynamic volume of approximately 3.1 $nm^3$. All three samples exhibited similar absorption and fluorescence spectra with emission maxima near 430 nm and excitation maxima near 350 nm. Lys-CD-2 had slightly stronger absorption in the region above 350 nm and emission in the region above 450 nm. At the same time quantum yield and fluorescence lifetime decreased considerably with increase of the carbon dots size.

Table 1

**Fluorescence characteristics of Lys-CD and its factions Lys-CD-1 and Lys-CD-2.**

| Sample | Em. minimum (nm) | Ex. maximum (nm) | Φ (%) | Lifetime (ns) | Anisotropy decay time (ns) | $I_{450}/I_{350}$ |
|---|---|---|---|---|---|---|
| Lys-CD | 429 | 351 | 6.5 | 2.29 | 1.39 | 0.109 |
| Lys-CD-1 | 428 | 348 | 7.9 | 2.72 | 0.77 | 0.091 |
| Lys-CD-2 | 433 | 352 | 4.6 | 1.85 | 2.68 | 0.149 |

Φ – fluorescence quantum yield, $I_{450}/I_{350}$ – ratio of integral fluorescence intensities under 450 and 350 nm excitation

Our results indicate that the same type of chromophores is responsible for absorption and emission of lysine carbon dots regardless of their size and quantum size effects do not contribute to their absorption and fluorescence. These chromophores are only formed within carbon dots and don't exist as separate molecules in solution. Quenching of blue fluorescence in carbon dots of large size indicates resonance energy transfer to acceptors within the same nanoparticle [4].

## REFERENCES


1. **Astafiev A. A., Shakhov A. M., Gulin A. A., Vasin A. A., Gubina M. V., Syrchina M.S., Nadtochenko V. A**. Femtosecond laser synthesis and comparative analysis of fluorescent carbon dots from L-lysine aqueous solution, Journal of Physics: Conference Series. 2086 (2021) 012121

2. **Sun Q., Qin Z., Wu W., Lin Y., Chen C., He S., Li X., Wu Z., Luo Y., Qu J.,** In vivo imaging-guided microsurgery based on femtosecond laser produced new fluorescent compounds in biological tissues, Biomedical Optics Express. 9 (2018) 581-590.

3. **Astafiev A.A., Shakhov A.M., Osychenko A.A., Syrchina M. S., Karmenyan A.V., Tochilo U.A., Nadtochenko V.A.,** Probing intracellular dynamics using fluorescent carbon dots produced by femtosecond laser in situ, *ACS Omega*. *5* (21) (2020) 12527-12538.

4. **Astafiev A.A., Shakhov A.M., Nadtochenko V.A.,** Resonance Energy Transfer Reveals the Presence of Multiple Luminescence Emission Centers within a Carbon Nanodot, *JETP Letters.* 116 (2022) 505–513.

# Miniature potentiometric system for determination of $H^+$, $K^+$, $Na^+$, $Cl^-$, $NO_3^-$ - and $Ca^{2+}$ ions in liquid biological environment

**V.V. Romanova[1,2], V.S. Sibirtsev[1,3], A. Yu. Zaitseva[1]**

[1] Institute for Analytical Instrumentation of the Russian Academy of Sciences, St. Petersburg, Russia;

[2] St. Petersburg State Institute of Technology, St. Petersburg, Russia;

[3] St. Petersburg State Chemical and Pharmaceutical University, St. Petersburg, Russia.

✉venjo@mail.ru

**Abstract.** The device of the potentiometric system developed by us (including a set of 6 miniature measuring cells including PVC-membrane electrodes selective to presence in the analyzed solutions of $H^+$, $K^+$, $Na^+$, $Ca^{2+}$, $Cl^-$ and $NO_3^-$ ions, the most widespread in biological environments, is described, and one central "reference" cell with a chlorosilver reference electrode) and testing of the system with aqueous solutions of HCl, KCl, NaCl, $NaNO_3$ and $CaCl_2$ at concentrations from $10^{-1}$ to $10^{-5}$ M. This confirmed the usefulness of the developed potentiometric multisensor system for the analysis of the ionic composition of biological environment.

**Keywords:** potentiometry, potentiometric sensor, ionic composition, miniature system, biological environment, plasticized membranes, multisensor system.

Ion-selective electrodes are an attractive tool for analyzing the ionic composition of various multicomponent aqueous solutions (which include most biological environment) due to their simplicity of operation, low cost, short analysis time, and the possibility of miniaturizing the sensors and automating the analysis process [1-5].

In this connection, the aim of our work was to develop and test the potentiometric system consisting of a set of 6 miniature measuring cells (MC) including PVC-membrane electrodes selective to the presence of $H^+$, $K^+$, $Na^+$, $Ca^{2+}$, $Cl^-$ and $NO_3^-$ ions (the most common in biological environment) in the analyzed solutions and one CRC with chlorosilver reference electrode.

## Materials and Methods

Our system was based on the method of direct potentiometry, based on transformation of activity of target ions ($H^+$, $K^+$, $Na^+$, $Ca^{2+}$, $Cl^-$ or $NO_3^-$, respectively) into electromotive force (EMF), described by the Nernst equation.

Each of the 6 MC included in the developed potentiometric multisensor system and located around the central ""reference" cell (CRC) was a case made on a 3D-printer from PETG filament (see Figure 1). This housing was divided inside by a horizontal partition (HP). The lower (next to the HP) section of the case of MC has a volume of 1 ml and three side fittings. One of them (the central one filled with agar-agar with KCl) served as a "salt bridge" connecting the MC with the CRC. Whereas the other two fittings served to input and output the analyzed solution from the MC and connect the MC to each other.

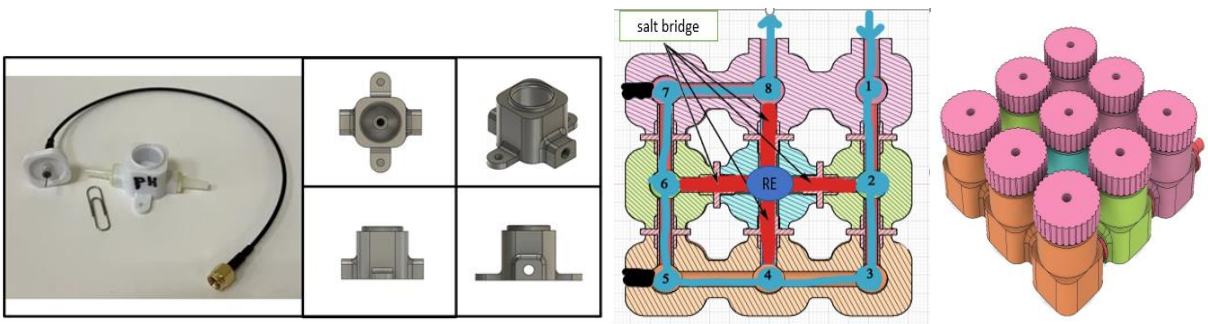


Fig. 1. Schematic diagram of our developed potentiometric multisensor system.

In the middle of the HP there was a hole, which was sealed with an ion-selective membrane made of polyvinyl chloride plasticized with di-2-ethylhexylsebacinate (DOS), o-nitrophenyloctyl ether (oNPOE), or 2-fluorophenyl-2-nitrophenyl ether (2F2N) with an organic ionophore added during the assembly of the measuring cell.

Then, the upper (with respect to the HP) part of the MC (also having a volume of 1 ml) was filled with a solution of 2 M KCl - while the lower (with respect to the HP) part of the MC was filled either with the solution to be analyzed or (between the measurements) with a solution with a given concentration of the ion measured by this MC.

After that, the top of the MC was closed with a cover in which a silver wire, galvanically coated with AgCl and slightly short of the HP, connected to the screened current collector was installed.

The CRC of the developed potentiometric multisensor system had the same case and lid as the MC considered above - only completely filled with 2 M KCl solution, without a HP and with 6 side fittings filled with agar-agar with KCl and serving as "salt bridges".

## Results and Discussion

At approbation of our developed potentiometric multisensor system, we filled it in turn as the analyzed media with aqueous solutions of HCl, KCl, NaCl, $NaNO_3$ and $CaCl_2$ with concentrations $10^{-1}$, $10^{-2}$, $10^{-3}$, $10^{-4}$ and $10^{-5}$ mol/l. The data obtained in measurements of these solutions confirmed a high sensitivity of the developed MC to the target ions ($H^+$, $K^+$, $Na^+$, $Ca^{2+}$, $Cl^-$ or $NO_3^-$, respectively) at the absence of such sensitivity to non-target ions, as well as high reproducibility and linearity between values of potential differences between measuring cell and CRC (measured with high-resistance millivoltmeter and commutator of signals received from current leads of MC and CRC) and negative decimal logarithms of molar concentrations of target ions (calibration equations: $pH = 5 - 0{,}02 \cdot E_H$, $pK = 2{,}6 - 0{,}03 \cdot E_K$, $pNa = 2{,}3 - 0{,}02 \cdot E_{Na}$, $pCa = -4{,}6 - 0{,}04 \cdot E_{Ca}$, $pCl = -1{,}4 - 0{,}02 \cdot E_{Cl}$, $pNO_3 = 0{,}28 + 0{,}02 \cdot E_{NO3}$, – for voltages measured in mV) in the whole range of investigated concentrations of these ions (from $10^{-5}$ to $10^{-1}$ M).

## Conclusion

At approbation of our developed potentiometric multisensor system, having carried out researches of solutions with known concentrations $H^+$, $K^+$, $Na^+$, $Ca^{2+}$, $Cl^-$ and $NO_3^-$ ions, we have made sure of high enough stability, selectivity and sensitivity of our system in relation to ionic composition of researched solutions. These results confirmed the suitability of our developed potentiometric multisensor system for the analysis of the ionic composition of biological environment.

## Acknowledgments

The work was supported by the Ministry of Science and Higher Education of the Russian Federation (project 075-15-2021-1057).

## REFERENCES

1. **Mikhelson K.N.**, Electrochemical sensors based on ionophores: current state, trends, prospects. // Russian Chemical Journal. 2008. VOL. LII. №2. C. 30-36.
2. **Vlasov Yu.G., Ermolenko Yu.E., Legin A.V., Rudnitskaya A.M., Kolodnikov V.V.,** Chemical sensors and their systems. // Journal of Analytical Chemistry. 2010. T. 65. № 9. C. 900-919.
3. **Sibirtsev V.S., Olekhnovich R.O., Samuylova E.O.**, Assessment of integral toxicity of water resources by instrumental methods of analysis. // SGEM Conference Proceedings. 2017, V. 17. № 61. P. 507–514.
4. **Guzenko M.M., Zaitseva A.Yu.**, Intelligent sensor system for ranking the ionic composition of breast milk. // Scientific instrumentation. 2022. T. 32. № 4. C. 58-67.

# Mathematical modeling of determination of "Premeltons" sites in DNA by ultra short laser pulses

**A. A. Kharlamova** [1✉]

[1] Department of Fundamental and Applied Physics, Northern Arctic Federal University named after M.V Lomonosov 1, Arkhangelsk 1, Russia;

✉ Kharlamova.anastasya2015@yandex.ru

**Abstract.** The article discusses a method for analyzing the structure of a molecule using ultrashort laser pulses (USP). A premelton or elongation in the structure of a molecule was chosen as a sample for theoretical modeling of the interaction of a laser pulse with a substance. A premelton is a region of a molecule in which the distance between two adjacent nitrogenous bases is increased. The study of such structures is interesting for limiting the parameters of DNA denaturation, since the process of separation of the molecule begins with the elongation region. At the moment, the study of such features of the DNA structure is difficult, electrophoresis and staining methods cannot always give an accurate result, especially on short sections of the molecule. In this paper, we theoretically model the results of the interaction of USP with a molecule in two cases, when elongation takes place and when the molecule is ideal. The results obtained show the expediency of using laser pulses as a method for determining the structure of a complex polyatomic object.

**Keywords:** ultrashort laser pulses, premelton, molecule elongation, denaturation, DNA, RNA.

**Funding:** The research was supported by the state task of the Russian Federation No. FSRU-2021-0008

## Introduction

Of great interest are the various states of DNA. The presence of elongations in the DNA structure affects the stacking interaction in the molecule, the probability of bubble birth, the rate and time of its denaturation. Elongations were first described in 1983 [1] as a discontinuity of the stacking interaction. At the same time, the H-bonds remain intact, which complicates the theoretical and experimental modeling of an object of such a conformation [2].

To determine the spatial structure of a molecule with elongations, a dye is intercalated into the molecule, which stands in the place of elongation Figure 1 b [3,4]. They also use the method of X-ray diffraction analysis Figure 1 a. Both methods do not accurately determine the location of the presence of elongation.

Today, scientists have turned to the use of ultrashort laser pulses instead of X-rays, as a tool capable of seeing the structure of a molecule at the atomic level. In this paper, we mathematically simulate the process of interaction of an ultrashort pulse with a DNA molecule having elongation in the structure and show the sensitivity of such a method to similar DNA configurations.

a) b)

Fig. 1. The result of X-ray analysis of a DNA molecule in the structure of which there are elongations between nitrogenous bases (*a*) The result of the analysis of the molecule by staining (b)

## Materials and Methods

The article proposes to consider the DNA molecule as a polyatomic system on which an ultrashort laser pulse falls. The modeling of the scattering spectrum is based on the Dirac-Hartree-Fock-Slater model [6,7].

## Results and Discussion

As a result of mathematical modeling of the interaction of USP with elongated DNA, a radiation spectrum was obtained, which we can compare with the spectrum of interaction from ideal DNA Figure 2.

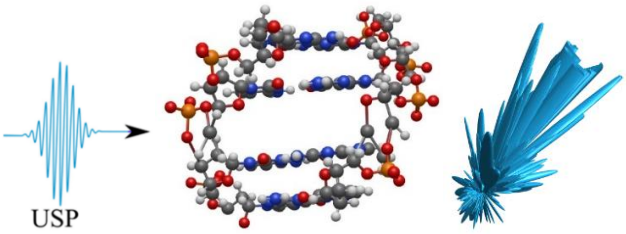


Fig. 2. The process of DNA interaction with an ultrashort pulse and obtaining a 3d spectrum

## Conclusion

After analyzing the obtained spectra, we can conclude that the ultrashort pulse method is applicable for studies of changes in the structure of DNA and RNA within several atomic distances.

## Acknowledgments

The author expresses gratitude to his supervisor Makarov Dmitry Nikolaevich for significant comments and important advice during the research and the design of this work.

## REFERENCES

1. **Shigaev A. S., Ponomarev O. A., Lakhno V. D.,** Theoretical and experimental studies of open states of DNA, Mathematical Biology and Bioinformatics: Physics and Mathematics. 8 (2) (2013) 553-664.
2. **Suryanarayana C., Norton M.**, X-Ray Diffraction: Springer Science & Business Media 2013.
3. **Sobell H.,** Stereochemistry of Actinomycin-DNA Binding: Nature New Biology. 231(24) (1971).
4. **Sobell H.,** How Actinomycin Binds to DNA: Scientific American. 231(2) (1974) 82-91.
5. **Sobell H.,** Organization of DNA in chromatin: Proc. Natl. Acad. Sci. 73(2) (1976) 3068-307.
6. **Makarov D. N., Kharlamova A. A.,** Scattering of X-ray Ultrashort Pulses by Complex Polyatomic Structures: J. Mol. Sci 23 (1) (2022) 163.
7. **Makarov D. N., Kharlamova A. A.,** Peculiarities of Scattering of Ultrashort Laser Pulses on DNA and RNA Trinucleotides: J. Mol. Sci 23(23), (2022) 15417.

## THE AUTHOR

**ANASTASIIA KHARLAMOVA**
Kharlamova.anastasya2015@yandex.ru
ORCID:-0000-0002-8192-615X

# Effect of laser pulse duration on ultrafast laser synthesis of carbon dots from toluene

**A. A. Shatov**[1✉], **A. A. Astafiev**[1], **A. M. Shakhov**[1], **V. A. Nadtochenko**[1]

[1]N.N. Semenov Federal Research Center for Chemical Physics, Russian Academy of Sciences, Kosygina 4, Moscow, Russia

✉shatovalexander98@gmail.com

**Abstract.** Pulsed laser irradiation produces luminescent carbon dots from toluene molecules in liquid medium. We examined influence of laser pulse duration on the rate of synthesis, optical properties and chemical composition of resulting carbon dots. Increase of synthesis rate with longer pulse duration demonstrates that synthesis is mediated by plasma formed at laser breakdown in medium.

**Keywords:** luminescent carbon dots, femtosecond laser pulses, laser-induced breakdown, nanomaterials.

**Funding:** This study was funded by Russian Science Foundation, grant number № 21-72-20169. The work was performed on facilities of the ACBC Center of Collective Equipment No.506694, FRCCP RAS

## Introduction

Pulsed laser irradiation is a viable method for bottom-up synthesis of carbonaceous luminescent nanoparticles (carbon dots) from aromatic compounds in liquid form. Laser pulses with duration ranging from tens of femtoseconds to nanoseconds were employed in for such a synthesis by various authors [1-4]. Pulse duration can strongly influence both nonlinear absorption and mechanisms of laser synthesis, however detailed understanding of this influence is still lacking. In order to clarify the synthesis mechanism and the role of different nonlinear absorption processes were examined how the pulse duration varied from sub-picosecond to tens picoseconds range affects the rate of synthesis of luminescent carbon dots from toluene. Also, optical and chemical characterization techniques were used to examine the effect of pulse duration on absorption and luminescence characteristics and chemical composition of carbon dots.

## Materials and Methods

### Synthesis and separation of products

500 μL of pure toluene in a closed glass flask was irradiated with trains of femtosecond laser pulses focused by a cylindrical lens (f=9.7 mm, 0.3NA) for 10 minutes. Central wavelength of laser pulses was 1033 nm, repetition rate - 1 kHz, pulse energy - 2 mJ, pulse duration in four experiments was 0.25, 1, 3 and 10 ps. After irradiation unreacted toluene was removed by drying; dried samples were then redissolved in ethanol, resulting in yellow and luminescent solutions.

### Samples characterization

Absorption of photoluminescence spectra of samples in ethanol were recorded with Shimadzu spectrophotometer (UV-3600) and spectrofluorometer (RF-5031 PC). Quantum yield of fluorescence was estimated with the slope method using anthracene in ethanol (visible fluorescence, excitation at 356) or toluene in cyclohexane (ultraviolet fluorescence, excitation at 260 nm) nm as standards. Fluorescence lifetime and anisotropy decay time were calculated as amplitude-weighted averages from three-exponential fit of decay kinetics. Infrared absorption spectra were collected using Bruker Lumos II FTIR microscope-spectrometer in a reflection mode.

## Results and Discussion

As described previously [3] pulsed laser irradiation of toluene led to formation of colored and luminescent nanoparticles (carbon dots) with nanometer-scale diameters and graphite-crystalline lattice. The rate of carbon dots synthesis measured by absorption or luminescence intensity per irradiated volume increased sharply with increase of the pulse duration above 1 ps

(Fig. **1a**). Carbon dots samples obtained at different pulse duration had similar optical properties: strong UV absorption, strong structured luminescence in the UV range and weaker visible luminescence (Fig. **1b**). While the quantum yield of UV luminescence was nearly constant at about 23%, the quantum yield of visible luminescence increased monotonically from 3.1 to 6.6 % with increase of the pulse duration from 0.25 to 10 ps. Pulse duration also affected the shape of emission spectra. FTIR spectroscopy revealed presence of similar functional groups in all carbon dots samples: isolated and fused aromatic rings, alkyl, carbonyl and hydroxyl groups. The strength of carbonyl and hydroxyl bands increased, whereas the strength of aromatic ring vibrations decreased at longer pulse durations.

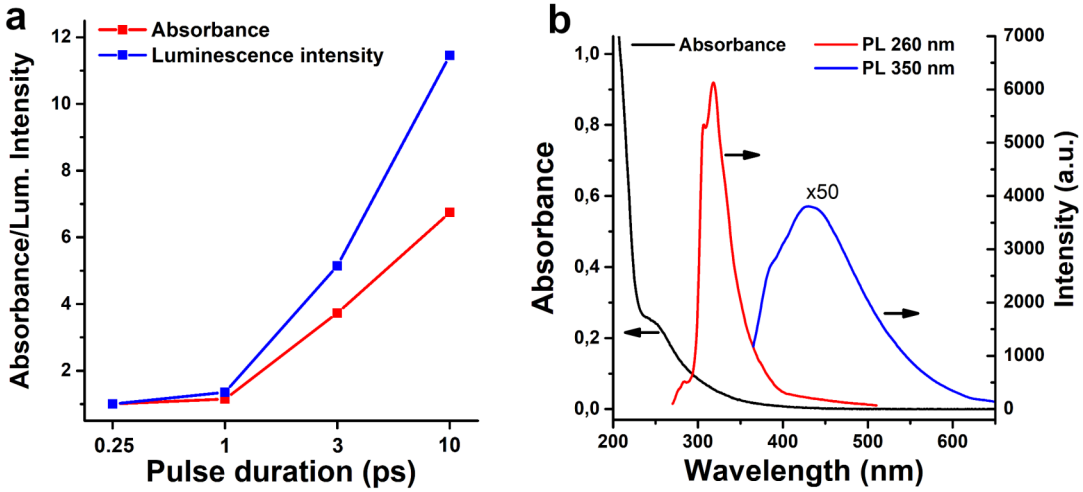


**Figure 1**. (*a*) Integral UV absorbance and luminescence intensity of carbon dots as a function of pulse duration. (*b*) UV-Vis absorbance and photoluminescence (PL, excitation at 260 and 350 nm) spectra of toluene carbon dots.

Our results indicate that carbon dots with mostly similar optical properties can be produced from toluene by laser irradiation with variable pulse duration. Despite weaker multiphoton absorption longer laser pulses produced carbon dots more effectively. This fact suggests that synthesis is mediated by electronic plasma formed by avalanche ionization in medium. Optical properties and chemical composition of carbon dots can be manipulated by pulse duration.

## REFERENCES


1. **Habiba K., Makarov V.I., Avalos J., Guinel M.J.F., Weiner B.R., Morell G.,** Luminescent graphene quantum dots fabricated by pulsed laser synthesis, *Carbon.* 64 (2013) 341-345.

2. **Yu H., Li H., Zeng X., Lu Y.,** Preparation of carbon dots by non-focusing pulsed laser irradiation in toluene, *Chem. Comm*. 52 (2016) 819-822.

3. **Astafiev A.A., Shakhov A.M., Vasin A.A., Kostina U.V., Nadtochenko V.A.,** Femtosecond laser synthesis of luminescent carbon dots from toluene, *JETP Lett.* 110 (2019) 464-471.

4. **Astafiev A.A., Shakhov A.M., Tskhvorebov A.G., Shatov A., Gulin A., Shepel D., Nadtochenko V.A.,** Nitrogen-doped carbon nanodots produced by femtosecond laser synthesis for effective fluorophores, *ACS Omega.* 7(8) (2022) 6810-6823.

Conference materials
UDC 547.458:535.56

# Optical activity anisotropy in thin films of chitosan L- and D-ascorbate

**A. B. Shipovskaya**✉, **D. A. Rudenko**, **S. L. Shmakov, N. O. Gegel**
Saratov State University, Saratov, Russian Federation;
✉Shipovskayaab@yandex.ru
(rector@sgu.ru)

**Abstract.** The specific optical rotation [$\alpha$] of thin films of chitosan L- and D-ascorbate was studied. It was found that optical activity anisotropy occurs in the analyzed systems and [$\alpha$] depends on the orientation angle θ of the film sample relative to the direction of the polarization vector of the incident light beam in the plane perpendicular to this beam. The angular dependences [$\alpha$] = $f$(θ) (indicatrices) were processed to extract the constant term $[\alpha]_0$ and four harmonics ($[\alpha]_i$, Fourier's series) determined by structure elements with the corresponding symmetry: the amorphous (isotropic) phase of chitosan ($[\alpha]_0$), irregular-shaped structures ($[\alpha]_1$), rod-shaped ones in the film plane ($[\alpha]_2$), helical ones located perpendicular to the film surface ($[\alpha]_3$), and crystalline structures ($[\alpha]_4$).

**Keywords:** chitosan, L- and D-ascorbic acid, films, optical activity, anisotropy.

**Funding:** The study was supported by a grant from the Russian Science Foundation № 22-23-00320, https://rscf.ru/project/22-23-00320/.

© Shipovskaya A. B., Rudenko D. A., Shmakov S. L., Gegel N. O., 2023. Published by Peter the Great St. Petersburg Polytechnic University.

Материалы конференции

## Introduction

Optical activity anisotropy is a vivid example of the self-organization in chiral polymer systems. This property was first discovered for lyotropic LC phases of acetic esters of cellulose [1] and subsequently found in oriented films of both acetic and basic chitosan [2]. This phenomenon consists in the manifestation of a clear functional dependence of the specific optical rotation [$\alpha$] on the samples orientation angle θ relative to the direction of the polarization vector of the incident light beam in the plane perpendicular to this beam. The decomposition of the indicatrices [$\alpha$] = $f$(θ) into individual sinusoids (harmonics) allows drawing some conclusions about the supramolecular optically active structures formed in the polymer material during its preparation.

The aim of this work was to study the chiro-optic properties of chitosan salt films obtained from solutions in L- and D-ascorbic acid in order to reveal and quantitatively describe optical activity anisotropy.

## Materials and Methods

Powdered chitosan (CS) with an average-viscosity molecular weight of 200 kDa and a deacetylation degree of 82 ± 2 mol % was used (Bioprogress LLC, RF); L-ascorbic acid (L-AscA) with 99% of the main substance (Glenvitol LLC, RF) and D-ascorbic acid (D-AscA) with 98% of the main substance (CJSC Khimreaktiv, RF). Films were cast by pouring a 2 g/dL CS solution, prepared at an equimolar CS : AscA ratio, onto a polyethylene terephthalate substrate, followed by drying in the absence of natural light at room temperature and under atmospheric pressure for 3–4 days. The film thickness was 80±2 μm.

Optical activity was recorded on a PolAAr 3001 automatic spectropolarimeter (Optical Activity Ltd, England) in the wavelength range λ = 405–589 nm at 25±0.5°C. A 20 W tungsten-halogen lamp was the light source. The experimental conditions were standard, the measurement error of rotation angles did not exceed ±0.001 deg. Spectra $[\alpha] = f(\theta)$ were recorded using a specially designed cuvette with a thermal chamber and a cell rotating around its horizontal axis and having a circular scale calibrated from 0 to 360° with a 5° step relative to an arbitrarily chosen reading direction. At least 10 film samples were used for each measurement. Three parallel experiments were carried out at each orientation angle.

The specific optical rotation $[\alpha]$ (deg mL $dm^{-1}$ $g^{-1}$) of films was calculated by the following formula:

$$[\alpha]^{20^0\,\mathrm{C}}_{\lambda,\,\mathrm{nm}} = \frac{\alpha}{\ell \cdot \rho}$$

where $\alpha$ is the measured angle of optical rotation of the film sample, deg; $\ell$ the length of the optical path, dm; and $\rho$ the density of the film material, g $cm^{-3}$.

The indicatrices $[\alpha] = f(\theta)$ were mathematically processed according to Ref. [2].

## Results and Discussion

The dispersion curves of the specific optical rotation (ORD) of thin films of CS L- and D-ascorbate were established to be of the normal type and characterized by $[\alpha]$ values close in absolute value, but opposite in sign, namely: negative for CS·L-AscA and positive for CS·D-AscA. It was found that $[\alpha]$ depended on the orientation angle θ of the film sample relative to the direction of the polarization vector of the incident light beam in the plane perpendicular to this beam.

To process the angular dependences $[\alpha] = f(\theta)$, an algorithm was used with the isolation of a constant term ($[\alpha]_0$) and four harmonics ($[\alpha]_i$, Fourier's series) determined by the structure element with the corresponding symmetry, namely: $[\alpha]_1$ corresponds to irregular shaped structures, $[\alpha]_2$ to rod-shaped ones in the plane of the film, $[\alpha]_3$ to helical ones, located perpendicular to the surface of the film, and $[\alpha]_4$ to crystalline ones. It is shown that the mean-angle specific optical rotation $[\alpha]_0$ reflects the optical activity of the amorphous phase of the sample, is characterized by simple dispersion and satisfactory agreement with the experimental ORD curves. For CS·L-AscA films, the fourth harmonic $[\alpha]_4$ had the highest amplitude, followed by $[\alpha]_2$ and $[\alpha]_3$. For CS·D-AscA film samples, $[\alpha]_4$ and $[\alpha]_2$ predominated, followed by $[\alpha]_1$ as the intensity decreases. The intensity of these harmonics for CS·L-AscA films was significantly higher compared to CS·D-AscA ones.

## Conclusion

As a result of our studies, it was found that CS L- and D-ascorbate films selectively rotated the polarization plane of polarized light passing through them, depending on the sample orientation angle relative to the direction of the polarization vector of the incident light beam in the plane perpendicular to this beam. The discovered regularities predetermine the prospects for obtaining film thermal indicators, optical filters, chiral planar waveguides and chiro-optic sensors with novel functional properties based on these systems.

## REFERENCES

1. **Shipovskaya A. B., Shmakov S. L., Kazmicheva O. F., Shchyogolev S. Yu.**, Optical activity of the anisotropic solutions of cellulose acetates in mesophasogenic solvents, Liquid Crystal. 38(3) (2011) 361–369.

2. **Shipovskaya A. B., Shmakov S. L., Gegel N. O.**, Optical activity anisotropy of chitosan-based films, Carbohydrate Polymers, 206 (2019) 476–486.

# Development of a sample preparation unit

**A. Yu. Yamanovskaya** [1, 2✉], **E. D. Serov** [1,2], **V. A. Kruglov** [1,2], **V. S. Reznik** [1,2],**D. A. Minakov** [1,2], **V. V. Davydov** [1,3]

[1]Peter the Great Saint-Petersburg Polytechnic University, St. Petersburg, Russia;
[2]Institute for Analytical Instrumentation of the Russian Academy of Sciences, St. Petersburg, Russia;
[3]All-Russian Research Institute of Phytopathology, Moscow Region 143050, Russia.
✉a.yamanovskaya@gmail.com

**Abstract.** The study performs the sample preparation unit, which can be applied for experiments with biological materials, particularly for genetic research. The main components of the system were introduced, such as positioner, sample loader and temperature control module. Test trials of the water dozing and thermal stabilization were carried out.

**Keywords:** Sample preparation, automatic dosing, temperature control, dispenser, thermostat, biological materials.

## Introduction

Temperature control and precision dosing of biological samples are important steps in biological and medical research [1, 2]. Temperature control makes it possible to maintain the temperature stability of the samples, which in turn ensures the safety of their state and properties. Automatic dosing of liquid samples improves the accuracy and speed of analysis. Manual dosing can lead to errors due to human error, is time-consuming and can cause operator fatigue [2, 3].

Automation of the sample preparation process will reduce the risk of contamination of samples and the operator during work with biological materials. This is especially important when dealing with dangerous viruses or bacteria.

Thus, the development of a sample preparation unit that performs temperature control of liquid biological samples, as well as their automatic dosing, may be necessary to improve the accuracy, speed, and safety of the process of studying biological materials, as well as to optimize the work of the laboratory.

## Sample preparation unit structure

The development of the block diagram of the sample preparation unit was carried out according to the principle of functional completeness of each individual module. The functions of the Sample preparation unit were decomposed, then the electrical modules were isolated, presented in the block diagram (Figure 1).

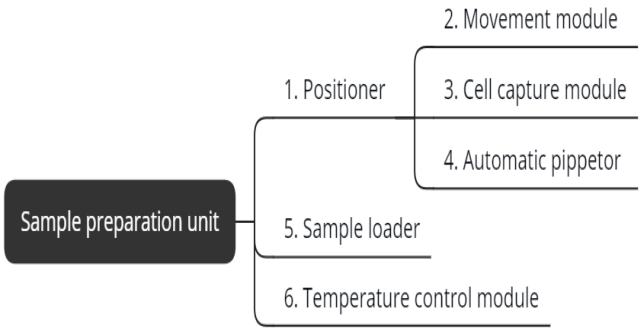


Fig. 1. Block diagram of the sample preparation unit

Due to the focus on working with biological materials, the additional functional module was performed to adopt the sample preparation unit for using in DNA sequencing. Sample loader is a module aimed to investigate the immobilization of the DNA-polymerase complex at nanoholes.

The electrical boards and software were designed for each module. The sample preparation control board is the master for all other boards: stepper boards of the positioner, the sample loader boards, and the temperature control module boards.

The RS-485 was chosen as the data interface and Modbus-RTU as communication protocol. Connecting devices of the same type to one communication line will avoid conflicts on the line and simplify further management organization.

## Results and Discussion

As a result of testing the positioner, a dosing calibration curve with deionized water was obtained.

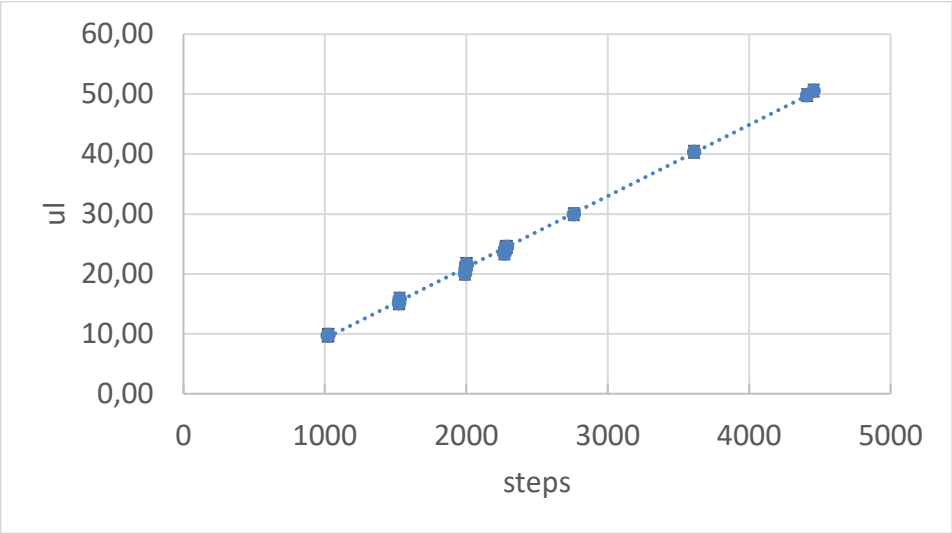


Fig. 2. Dosing calibration curve

Table 1 presents the results of testing the Temperature control module's thermostats.

Table 1

**Results of testing the thermostats**

| Measurement № | *t*, s | $T_1$, °C | $T_2$, °C | $T_3$, °C | $T_4$, °C |
|---|---|---|---|---|---|
| 1 | 714 | 8.0±0.3 | 8.1±0.2 | 8.1±0.2 | 8.0±0.2 |
| 2 | 508 | 7.9±0.2 | 8.0±0.1 | 8.0±0.2 | 7.9±0.3 |
| 3 | 809 | 8.0±0.1 | 8.0±0.2 | 7.9±0.2 | 8.0±0.1 |

*t* is stabilization time of thermostats and $T_i$ is temperature of thermostat, where i is the thermostat number

## Conclusion

The developed sample preparation unit allows automatic dosing of liquid samples with an accuracy of 1 µl and maintains the set thermostat temperature with an accuracy of 0.5 °C.

## REFERENCES

1. **Mikhailova, O.A., Antifeev, I.E., Petrov, D.G., Davydov, R.V.** Development of a device for picoampere currents measuring, Scientific and technical statements of SPbSPU. Physical and mathematical sciences. 15(2022) 102-106.

2. **Lebedev, D., Malyshev, G., Ryzhkov, I., Mozharov, A.** Focused ion beam milling based formation of nanochannels in silicon-glass microfuidic chips for the study of ion transport, Microfluid Nanofluid. 51(2021) 1 -10.

3. **Manoilov, V.V., Borodinov, A.G., Saraev, A.S., Zarutskii, I.V., Kurochkin, V.E.** Algorithms for Image Processing in a Nanofor SPS DNA Sequencer. Technical Physics. 67(4) (2022) 304–310

Conference materials
UDC 535.372
DOI: https://doi.org/10.18721/JPM.

# Investigation of fluorescent properties of FAD in solution by means of time-resolved polarized fluorescence spectroscopy.

D.V. Yashkov[1,2]✉, I.A. Gorbunova[2], M.E. Sasin[2], and O.S. Vasutinskii[2],
[1]Ioffe Institute, Russian Academy of Sciences, St. Petersburg, Russia.
[2]Peter the Great St.Petersburg Polytechnic University, St. Petersburg, Russia.
yashkov.dv@edu.spbstu.ru

**Abstract.** This paper presents the results of studies of polarized fluorescence in the intracellular coenzyme flavin adenine dinucleotide (FAD) in buffer solution. The object was one-photon and two-photon excited in the wavelength ranges from 360 to 450 nm and from 720 to 900 nm, respectively. The following molecular parameters were determined from experiment: fluorescence decay times $\tau_i$, weighting coefficients $a_i$, rotational diffusion time $\tau_{rot}$, and initial anisotropy $r$.

**Keywords:** FAD, two-photon fluorescence, TCSPC technique, quantum yield.

**Funding:** The study was funded by Russian Science Foundation under the grant # 23-22-00230.

## Introduction

Time-resolved studies of fluorescence in natural intracellular fluorophores, oxidized flavin adenine dinucleotide (FAD) in particular, are actively carried out nowadays all over the world. As was shown [1] the parameters of FAD fluorescence in solutions depend on several factors such as temperature, microenvironment conditions and coenzyme conformational states. However, more detailed studies of influence of external factors on FAD fluorescence are still needed.

## Materials and Methods

A Ti: Sapphire femtosecond oscillator tunable in the spectral range of 690-1040 nm with a pulse duration of 100 fs and a repetition frequency of 80 MHz was used as an excitation source. To generate wavelengths in the range of 360-450 nm, a second harmonic generator (Inspire Blue, Spectra Physics) was used. The average power of the laser beam focused onto the cuvette was about 600 mW. The fluorescence was collected in the direction perpendicular to the laser excitation beam, and then passed through narrow-band filters to isolate the fluorescence band at about 530 nm. The orthogonal fluorescence polarization components were separated by a Glan prism, and then simultaneously recorded by two avalanche photodiodes operating in the photon counting mode. The signals from the photodiodes were processed by a time-correlation single photon counting (TCSPC) module with a time bin of 4 ps. A global fitting algorithm was used to analyze the signals received.

## Results and Discussion

The analysis of the polarized fluorescence decay signals was performed and the following results were obtained. The dependence of the initial fluorescence anisotropy on the excitation wavelength under one- and two-photon excitation is shown in Fig. 1 (*a*).

According to Fig.1 (*a*) the ratio between fluorescence anisotropy parameters at two- and one-photon excitation was about 1.3 in average. More precisely, the anisotropy at one-photon excitation increased by about 1.5, whereas for two-photon excitation it was practically the same at all excitation wavelengths used. At the same time rotational diffusion time $\tau_{rot}$ did not depend on the excitation wavelength and was about 0.16 ns for both one- and two-photon excitations.

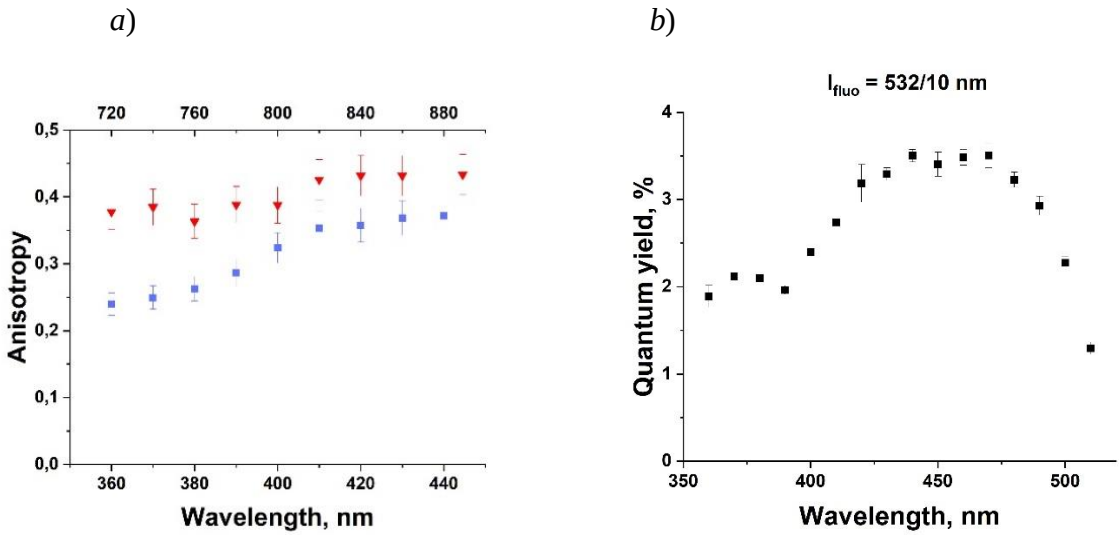


Fig. 1. *a)* Anisotropy for two-photon (red triangles) and one-photon (blue squares) excitation. *b)* Fluorescence quantum yield of FAD at the wavelength of 532/10 nm.

It was also determined that FAD fluorescence was characterized by three decay times: $\tau_1 \sim 0.03$ ns, $\tau_2 \sim 0.36$ ns and $\tau_3 \sim 2.75$ ns, that did not depend on the excitation conditions and coincided with the results reported earlier [1]. Fluorescence quantum yield of FAD as a function of excitation wavelength is shown in Fig 1 (*b*). According to Fig 1 (*b*) quantum yield of FAD changed nonlinearly with the increase of excitation wavelengths and its value under excitation at 360 nm was 1.7 times smaller than that under excitation at 450 nm. The results obtained were analyzed based on the theoretical model presented in [2].

## Conclusion

The anisotropic ($\tau_{rot}$, $r$) and isotropic ($\tau_i$, $a_i$, quantum yield) fluorescence parameters of FAD in solution were determined under one- and two- photon excitation and analyzed as a function of excitation wavelength. The dependence of anisotropy and fluorescence quantum yield of FAD on excitation wavelength was found.

## Acknowledgments

The authors are grateful to Ioffe Institute for providing the equipment used in experiments. All authors are grateful to the Russian Science Foundation for support under the grant # 23-22-00230.

## REFERENCES

1. **Van den Berg P. A. W., Feenstra K. A., Mark A. E., Berendsen H. J. C., and Visser A. J. W. G.**, Dynamic conformations of Flavin Adenine Dinucleotide: simulated molecular dynamics of the flavin cofactor related to the time-resolved fluorescence characteristics, Journal Physical Chemistry B. (106) (2002) 8858-8869

**2. Gorbunova I.A., Danilova M.K., Sasin M.E., Belik V.P., Golyshev D.P., and Vasyutinskii O. S.,** Determination of fluorescence quantum yields and decay times of NADH and FAD in water–alcohol mixtures: The analysis of radiative and nonradiative relaxation pathways, Journal of Photochemistry and Photobiology A: Chemistry. (436) (2023) 114388

Conference materials
UDC 546.05

# Development of a new synthesis pathway and pH-sensitivities' assessment of Sr-BDC Metal-Organic Frameworks (MOFs)

**Vodyashkin A.A.**[1]

*PhD Student*

[1]Peoples' Friendship University of Russia (RUDN University), Moscow, Russia

av.andrey2013@yandex.ru

**Abstract.** Sr-BDC metal–organic frameworks (MOFs), composed of strontium ions and terephthalic acid residues, were synthesized using a simple solvothermal process without the use of elevated pressure. The method is easily scalable and does not require special equipment. In addition, we assessed the optimal synthesis temperature. The structure of the MOFs was confirmed by XRD analysis, and the MOFs were analyzed by scanning electron microscopy. Moreover, we studied the stability of the obtained MOFs in different solutions to assess their pH-sensitivity.

**Keywords:** Metal-organic application, MOFs, carboxylic acids, strontium, drug delivery, pH-sensitive, cytotoxicity.

## 1. Introduction

Metal-organic framework (MOFs) are a hybrid class of materials with unique properties, different from other materials. Metal-organic compounds possess a combination of unique properties such as biocompatibility, actively developed surface area, and pH-sensitivity [1]. MOFs are one of the most studied materials, and directional synthesis methods have been created to develop materials with different properties [2]. The metal-organic compounds of strontium and carboxylic acids show high biocompatibility in relation to the human body and can be used for various biomedical tasks [3]. Therefore, the aim of this work was to study the biological properties of MOF (Sr-BDC), as well as the possibility of using this system for pH-sensitive delivery of various drugs.

## 2. Methods

*Synthesis of Sr-BDC MOFs*

Metal-organic framework Sr-BDC was prepared by a solvothermal synthesis procedure with some modifications. $SrCl_2$-$6H_2O$ (0.058 g, 0.220 mmol), 1,4- benzene-dicarboxylic acid (BDC) (0.032 g, 0.193 mmol), and 5.6 ml of DMF solvent were used as precursors, placed in a heat-resistant glass vessel, and stirred, then incubated at 120 °C for 48 h. After cooling to room temperature, the synthesized transparent crystals were repeatedly washed with 5 mL of DMF and dried at 120 °C for 24 h.

*Characterization of materials*

Scanning electron microscopy was used to determine the main parameters of strontium MOFs. The morphology of the MOFs is a fundamental factor influencing the physicochemical properties, so we carried out a study of the crystal structure by XRD analysis. The

thermogravimetric analysis was used to investigate the stability of the MOFs, and the chemical structure was confirmed by Raman spectroscopy. The biological activity of MOFs was studied by microbiological analysis and flow cytometry.

## 3. Results of the study

In the course of this work, a simple solvothermal method for the preparation of the metal-organic compound with strontium and terephthalic acid was developed. The optimal temperature parameters of the solvothermal method obtained without increased pressure were established. SEM micrographs characterizing their structure were obtained for MOFs obtained at 120 °C and 150 °C. It was also found that 90 °C was not sufficient for obtaining MOFs. The MOFs sample was studied by XRD analysis. This analysis proved the structure of the obtained Sr-BDC MOF. The high crystallinity of the resulting structure was also shown. In addition, the stability of MOFs in various solutions was studied. It was found that the obtained MOFs were stable in ethanol, DMF, and DMSO, as well as in aqueous solution. The stability of Sr-BDC was studied according to the methodology described earlier. To optimize loading conditions, buffers with different pH values (1.65; 4.5; 5.5; 6; 7; 9.18), ethanol, DMSO and DMF were used to test the sample stability times. However, if the value was higher (greater than pH=4.5), the sample dissolved. From this observation, we can conclude that sorption of the drug for the material under development should be performed either from acidic solutions (if possible) or using organic solvents such as ethanol.

This fact demonstrates the high promise and wide range of industrial applications of Sr-BDC MOFs. The study presents an alternative way to obtain Sr-BDC MOFs, allowing its use in various systems.

## 4. Acknowledgments

The publication has been prepared with the support of the «RUDN University Strategic Academic Leadership Program», Project P08 "Development of Postgraduate Research Potential"

## References

1. **Liu, C., Wang, J., Wan, J., Yu, C.** MOF-on-MOF hybrids: Synthesis and applications. Coordination Chemistry Reviews. (432) (2021) 213743.

2. **Ding, M., Cai, X., Jiang, H. L.** Improving MOF stability: approaches and applications. Chemical Science, 10(44) (2019) 10209-10230.

3. **Li, Z., Peng, Y., Xia, X., Cao, Z., Deng, Y., Tang, B.** Sr/PTA metal organic framework as a drug delivery system for osteoarthritis treatment. Scientific reports, 9(1) (2019) 17570.

**THE AUTHORS**

**Vodyashkin A.**
av.andrey2013@yandex.ru
ORCID: 0000-0003-1556-7635

Conference materials
UDC
DOI: https://doi.org/10.18721/JPM.

# Scattering antireflective nanostructured ITO coatings

**V. V. Aksenova** [1] ✉, **A. S. Pavlyuchenko** [1], **I. P. Smirnova**[1], **L. K. Markov**[1]
[1] Ioffe Institute, St.-Petersburg, Russia
✉ valeriyaakse@gmail.com

**Abstract.**
In this work, nanostructured ITO films and their optical properties were studied. It has been shown that films of nanostructured ITO grown by magnetron sputtering have scattering and antireflective properties.

**Keywords:** nanostructured coatings, antireflective coatings, ITO nanowhiskers, light scattering

**Citation:** Aksenova V.V., Pavlyuchenko A. S., Smirnova I. P., Markov L. K., Scattering antireflective nanostructured ITO coatings, St. Petersburg State Polytechnical University Journal. Physics and Mathematics. 16 ( ) (2023) …–…. DOI: https://doi.org/10.18721/JPM.

This is an open access article under the CC BY-NC 4.0 license (https://creativecommons.org/licenses/by-nc/4.0/)

© Aksenova V.V., Pavlyuchenko A. S., Smirnova I. P., Markov L. K., 2023. Published by Peter the Great St. Petersburg Polytechnic University.

Материалы конференции
УДК
DOI: https://doi.org/10.18721/JPM.

## Introduction

Transparent conductive oxides (TCO) are widely used in many applications as contact layers for various devices: solar cells, light-emitting diodes, liquid crystal displays (LCD), touch screens. Recently, the improvement of the properties of films based on indium tin oxide (ITO) has been achieved through their nanostructuring [1, 2]. This approach makes it possible to change the effective refractive index of the film due to the presence of voids in the material. When the dimensions of the formed inhomogeneities are much smaller than the wavelength of visible light, such films can be characterized by an effective refractive index that changes monotonically in the direction perpendicular to the substrate. The deposition of a film with a gradually changing effective refractive index leads to a pronounced antireflection effect within the entire range of visible spectrum and a decrease in the reflection coefficient for specular light. Another approach to the creation of antiglare coatings is the suppression of specular reflection due to diffuse light scattering at the front edge of the device. This approach makes it possible to suppress glare that occurs in multilayer devices, where reflection can occur at interlayer boundaries. In this work, we propose a combination of the two approaches, provided by creating a light-scattering gradient coating of nanostructured ITO. Nanostructured coatings of various thicknesses were formed by magnetron sputtering. For the fabricated films, their antireflective properties were studied, the transmission and reflection spectra, and the angular diagrams of the diffuse transmission of the films were measured.

## Materials and Methods

For the deposition of ITO layers, a combined film deposition system manufactured by Torr, USA was used. The nanostructured ITO films containing elongated whiskers were formed on a preheated (550 °C) glass substrate by magnetron sputtering of an ITO target with Ar ions in the constant current mode at an argon pressure of about $3 \cdot 10^{-3}$ mbar and a sputtering rate of ~3 nm/s. Under provided deposition conditions, the growth process of nanowhiskers runs according

to the vapor-liquid-solid mechanism. The structure of produced films was studied with a scanning electron microscope manufactured by JEOL Ltd., Japan. The scattering properties of the obtained films were estimated based on the angular scattering diagrams for diffuse transmission, obtained using the luminous intensity measurement system (IS-LI manufactured by Radiant Imaging Inc., USA).

## Results and Discussion

Fig. 1, *a)* shows a photo of fabricated samples of nanostructured ITO films 3.7 µm thick (0.55 µm in dense film mass equivalent) and an uncoated glass slide.

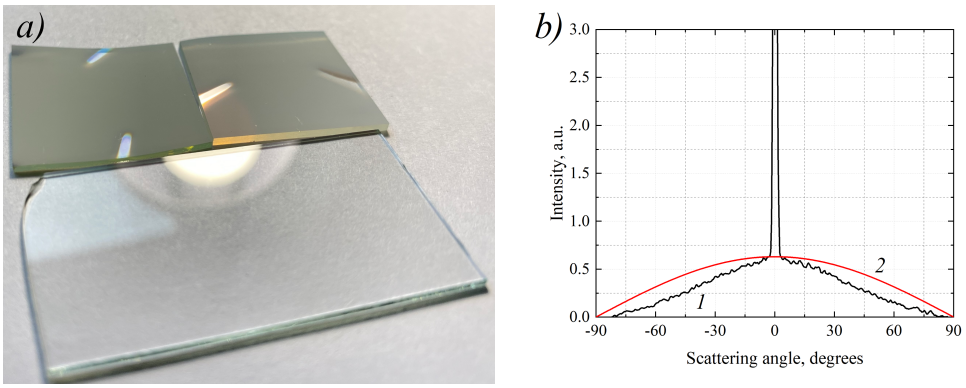


Fig. 1. *a)* Light-scattering nanostructured ITO coatings in comparison to uncoated glass *b)* Angular diagram of light scattering in the obtained samples (1) and the lambertian diffuse surface (2)

The profile of the angular diagram of transmitted light scattering in the film is shown in Fig. 1, *b)* The measurement results demonstrate that the luminous intensity of the scattered radiation is about 10% of the incident radiation. For comparison, the scattering diagram of a lambertian diffuse surface is shown, for which the luminous intensity depends on the angle as $I_0 \cos \theta$.

## Conclusion

In this work we study light-scattering nanostructured ITO films aimed for antireflective applications. Transmittance and reflectance spectra were measured, angular diagrams were obtained for the studied films. It is demonstrated that the nanostructured ITO films, obtained by magnetron sputtering, provide high antiglare ability. Thus, the possibility of producing transparent conductive anti-reflective coatings in a single technological process has been demonstrated.

## REFERENCES

1. **Yamamoto, N. Morisawa, K.** Indium Tin Oxide Conductive Nanowires Formed by Magnetron Sputtering, MRS Online Proceedings Library (OPL). 1747 (2015) 19-24.

2. **Markov L. K., Pavluchenko A. S., Smirnova I. P.** Technique of formation of the antireflection coatings based on ITO films, Semiconductors. 53(2) (2019) 181-189.

## THE AUTHORS

**AKSENOVA Valeriya V.**
valeriyaakse@gmail.com
ORCID:0000-0002-9202-6165

**SMIRNOVA Irina P.**
e-mail: irina@quantum.ioffe.ru
ORCID: 0000-0001-5313-0640

**PAVLYUCHENKO Alexey S.**
alexey.pavluchenko@gmail.com
ORCID:0000-0001-5390-276X

**MARKOV Lev K.**
e-mail: l.markov@mail.ioffe.ru
ORCID: 0000-0001-7293-1320

# Transition from indirect to direct bandgap in thin β-InSe layers

**B. R. Borodin**✉, **L. V. Kotova**, **A. I. Galimov**, **I. A. Eliseyev**, **M. V. Rakhlin**

Ioffe Institute, St. Petersburg, Russia
✉ brborodin@gmail.com

The rapid development of the field of 2D materials has led to the emergence of several classes of layered materials. The most promising semiconductors are transition metal dichalcogenides (TMDs) and group III metal monochalcogenides. Transition metal dichalcogenides are known mainly for the unique optical properties of monolayers. In contrast to TMDs, monolayers of group III metal monochalcogenides exhibit an indirect band gap, which transforms into a direct band with increasing thickness [1]. It should be noted that the transformation of the band structure is not only quantitative but also qualitative. The parabolic dispersion, characteristic of bulk monochalcogenides of group III metals, in monolayers, turns into a “Mexican hat” dispersion [2]. This type of dispersion leads to many unique electronic properties and creates conditions for observing strongly correlated electronic phenomena [3]. However, despite significant progress in the study of the properties and use of these materials in various devices, some issues remain in the shadows. For example, the exact number of InSe layers at which the band gap transitions from indirect to direct occurs has not been determined. The InSe monolayer has an indirect band gap of the “Mexican hat” type, and after a thickness of ~10 layers, the band gap becomes a direct band [4], however, the exact moment of the transition remains unknown.

In this work, thin layers of β-InSe are experimentally studied to determine the number of InSe layers at which a transition to a direct-gap structure occurs. The thickness of the investigated flakes is determined using atomic force microscopy. The use of low-temperature micro-photoluminescence (μ-PL) made it possible to detect the thickness at which photoluminescence appears, associated with a direct interband transition. The work function and visualization of changes in the electronic properties of InSe-based nanostructures were studied using Kelvin probe microscopy. It is shown that the moment of appearance of photoluminescence corresponds to a leap in the work function at a thickness of 8 layers. Thus, in this study, the moment of band gap transformation was experimentally established, which provides important information for the fabrication of devices based on InSe.

The study was supported by a grant from the Russian Science Foundation No. 22-22-20049, https://rscf.ru/project/22-22-20049/, and a grant from the St. Petersburg Science Foundation following agreement No. 21/2022 dated April 14, 2022.

1. **Guo Y., Robertson J.**, Band structure, band offsets, substitutional doping, and Schottky barriers of bulk and monolayer InSe, Physical Review Materials. 1(4) (2017) 044004.
2. **Zolyomi V., Drummond N. D., Fal'Ko V. I.**, Band structure and optical transitions in atomic layers of hexagonal gallium chalcogenides, Physical Review B. 87 (19) (2013) 195403.
3. **Lugovskoi A. V., Katsnelson M. I., Rudenko A. N.**, Strong electron-phonon coupling and its influence on the transport and optical properties of hole-doped single-layer InSe, Physical Review Letters. 123 (17) (2019) 176401.
4. **Rybkovskiy D. V., Osadchy A. V., Obraztsova E. D.**, Transition from parabolic to ring-shaped valence band maximum in few-layer GaS, GaSe, and InSe, Physical Review B. 90 (23) (2014) 235302.

# Переход от непрямой запрещенной зоны к прямой в тонких слоях β-InSe

**Б. Р. Бородин**✉, **Л. В. Котова**, **А. И. Галимов**, **И. А. Елисеев**, **М. В. Рахлин**

Физико-технический институт им. А.Ф. Иоффе РАН, Санкт-Петербург, Россия
✉ brborodin@gmail.com

Бурное развитие области 2D-материалов привело к появлению нескольких классов слоистых материалов. Наиболее перспективными полупроводниками стали дихалькогениды переходных металлов (ДПМ) и монохалькогениды металлов III группы. Дихалькогениды переходных металлов известны главным образом уникальными оптическими свойствами монослоев. В отличие от ДПМ, монослои монохалькогенидов металлов III группы демонстрируют непрямую запрещенную зону, которая с увеличением толщины трансформируется в прямую [1]. Стоит отметить, что трансформация зонной структуры носит не только количественный, но и качественный характер. Параболическая дисперсия, характерная для объемных монохалькогенидов металлов III группы, в монослоях превращается в дисперсию «мексиканской шляпы» [2]. Такой тип дисперсии приводит ко многим уникальным электронным свойствам и создаёт условия для наблюдения сильно коррелированных электронных явлений [3]. Однако, несмотря на значительный прогресс в изучении свойств и использовании этих материалов в различных устройствах, некоторые вопросы до сих пор остаются в тени. Так, например, не определено точное количество слоев InSe при которой происходит переход запрещенной зоны от непрямой к прямой. Монослой InSe имеют непрямую запрещенную зону типа «мексиканская шляпа», а после толщины ~ в 10 слоев запрещенная зона становится прямозонной [4], однако точный момент перехода остаётся неизвестным.

В данной работе экспериментально исследуются тонкие слои β-InSe, с целью определения количества слоев InSe, при котором происходит переход к прямозонной структуре. Толщина исследуемых флейков определяется с помощью атомно-силовой микроскопии. Использование низкотемпературной микро-фотолюминесценции (μ-ФЛ), позволило обнаружить толщину, при которой появляется люминесценция, связанная с прямым межзонным переходом. Работа выхода и визуализация изменений электронных свойств наноструктур на основе InSe исследовались с помощью Кельвин-зонд микроскопии. Показано, что момент появления фотолюминесценции соответствует скачку работы выхода при толщине 8 слоев. Таким образом, в данном исследовании экспериментально установлен момент трансформации запрещенной зоны, что дает важную информацию для изготовления устройств на основе InSe.

Исследование выполнено за счет гранта Российского научного фонда № 22-22-20049, https://rscf.ru/project/22-22-20049/ и гранта Санкт-Петербургского научного фонда в соответствии с соглашением № 21/2022 от 14.04.2022.

1. **Guo Y., Robertson J.**, Band structure, band offsets, substitutional doping, and Schottky barriers of bulk and monolayer InSe, Physical Review Materials. 1(4) (2017) 044004.
2. **Zolyomi V., Drummond N. D., Fal'Ko V. I.**, Band structure and optical transitions in atomic layers of hexagonal gallium chalcogenides, Physical Review B. 87 (19) (2013) 195403.
3. **Lugovskoi A. V., Katsnelson M. I., Rudenko A. N.**, Strong electron-phonon coupling and its influence on the transport and optical properties of hole-doped single-layer InSe, Physical Review Letters. 123 (17) (2019) 176401.
4. **Rybkovskiy D. V., Osadchy A. V., Obraztsova E. D.**, Transition from parabolic to ring-shaped valence band maximum in few-layer GaS, GaSe, and InSe, Physical Review B. 90 (23) (2014) 235302.

# Fractional leaky integrate-and-fire node based on single-walled carbon nanotubes networks

**Yu. O. Vasilevskaya** [1,2✉], **S. Yu. Pereverzeva** [2], **A. I. Savitskiy** [2], **R. T. Sibatov** [2]
[1] National Research University of Electronic Technology (MIET), Zelenograd, Russia;
[2] Scientific-Manufacturing Complex «Technological Centre», Zelenograd, Russia
✉fedorovauo@mail.com

**Abstract.** This work proposes a micron transistor structure based on a network of single-walled carbon nanotubes (SWCNTs) with electrolyte as an implementation of a fractional leaky integrate-and-fire node for neuromorphic computations. The structure is an artificial synapse and functions based on dynamic interactions between SWCNTs and ions in an electrochemical cell. The fractional-differential nature of the ions diffusion transport implies a long-term (exponential law) attenuation of the current between the source and drain after excitation by a gate voltage pulse. The examined cells can be integrated into a large-scale circuit to simulate the parallel signal processing and learning functions of a memristive network.

**Keywords:** carbon nanotubes, electrochemical transistor, electrolyte, synapse, dynamic logic.

**Funding:** The work was supported by the Ministry of Science and Higher Education of the Russian Federation (project FNRM-2022-0008).

## Introduction

In [1], a model of a fractional leaky integrate-and-fire node was proposed:

$$C_m \frac{d^\alpha V}{dt^\alpha} = -g_L (V - V_L) + I_{inj} \tag{1}$$

assuming that if $V(t) = V_{th}$, then a spike is generated at the moment $t$ and $V \to V_{reset}$. Herein:

$$\frac{d^\alpha V}{dt^\alpha} = \frac{1}{\Gamma(1-\alpha)} \int_0^t \frac{V'(\tau)}{(t-\tau)^\alpha} d\tau \tag{2}$$

is the Caputo fractional derivative, $V$ – the membrane potential, α – the order (exponent) of the fractional derivative ($0 < \alpha \leq 1$). In the case $\alpha = 1$, the fractional model transforms into the classical model of the threshold integrator with leakage. When the membrane potential reaches the threshold ($V_{th}$), a spike is generated and the voltage $V$ is reset to $V_{reset}$.

It is shown, in particular, that the fractional model generates reliable burst patterns in response to input noise. The voltage value before reaching the threshold correlates more strongly with the prehistory of the pulse arrival process than in the standard model. The amplification of a spike neuron in the new model follows an exponential law. The fractional model makes it possible to produce a different degree of adaptation of electrical activity by varying the fractional order of the derivative. In terms of neuromorphic computing, it is of interest to implement physical systems that exhibit properties of a fractional leaky integrate-and-fire node.

In this paper, we propose a micron transistor structure based on a SWCNTs network with electrolyte as an implementation of a fractional leaky integrate-and-fire node.

## Materials and Methods

The triode structure is a thermally oxidized highly doped KEM–0.003 silicon wafer with two gold electrodes 100–200 nm thick formed on top by the electron beam evaporation method. For contacting to the bottom side, an aluminum layer 1 μm thick was deposited by magnetron sputtering. A 2 μm interdigital gap was formed between the electrodes (Fig. 1).

*a*) *b*)

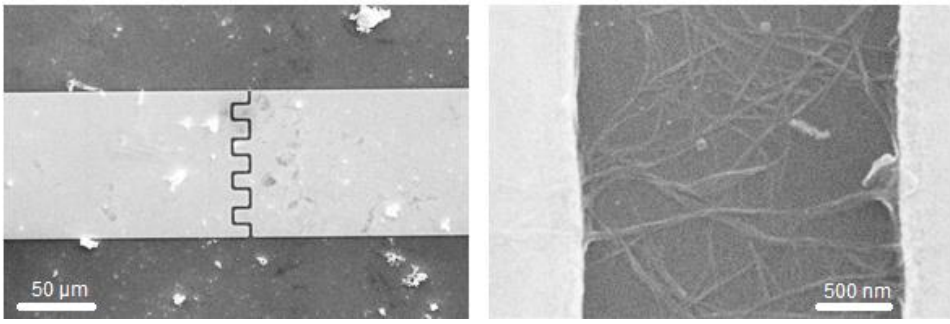


Fig. 1. SEM images of the gap between two electrodes after SWCNTs deposition (*a*) and the tangled network of carbon nanowires in the gap (*b*)

## Results and Discussion

Measurement of voltammograms of electrochemical transistors showed that the current between source and drain is controlled by the gate voltage (Fig. 2).

*a*) *b*)

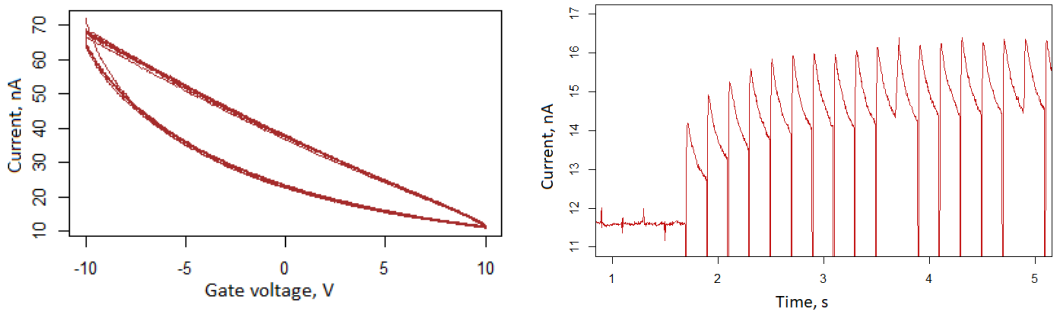


Fig. 2. Voltammogram (*a*) for SWCNTs 80 + (PVA+LiCl) with variation of the gate potential at 0.1 V between the source and drain and current responses (*b*) when a sequence of pulses is applied to the gate (duty ratio 0.2 s, pulse voltage 10 V)

When excited by a short voltage pulse on the gate, the current decay between the source and drain is described by a function with a power tail, which can be approximated by the Mittag-Leffler function that is the solution of the fractional relaxation equation (1). This fact allows considering the system as a fractional leaky integrate-and-fire node. The exponential law relaxation of the current is associated with the diffusion-controlled kinetics of the current after the excitation is removed.

## Conclusion

The micron transistor structure based on a SWCNTs network with an electrolyte can be a neuromorphic implementation of a fractional leaky integrate-and-fire node. The fractional-differential nature of the ions diffusion transport implies a long-term (exponential law) attenuation of the current between the source and drain after excitation by a voltage pulse at the gate. The examined cells can be integrated into a large-scale circuit to simulate the parallel signal processing and learning functions of a non-Markovian memristive network.

## REFERENCES

1. **Teka, W., Marinov, T. M., Santamaria, F.**, Neuronal spike timing adaptation described with a fractional leaky integrate-and-fire model, PLoS computational biology. 10 (3) (2014) e1003526.

# Filamentous crystals of potassium carbonate in a pyrotechnic flame

**S. I. Ksenofontov[1], K. Yu. Tashkova[1], A. N. Lepaev[2], O. V. Vasilyeva[3]✉, A. V. Kokshina[3], V. A. Kazakov[3], A. G. Razina[3], A. V. Smirnov[3]**

[1]Chuvash State Pedagogical University named after I. Y. Yakovlev, Cheboksary, Russia;
[2]Cheboksary Institute (branch) of the Moscow Polytechnic University, Cheboksary, Russia;
[3]Chuvash State University named after I. N. Ulyanov, Cheboksary, Russia
✉dprostokvashino@mail.ru

**Abstract.** Dispersed particles of different sizes and morphology are formed in the flame of pyrotechnic composition. Dispersed potassium carbonate particles crystallize from the liquid phase in flame zones with a sharp negative temperature gradient. The crystallization of potassium carbonate occurs from the outside of the surface, and a liquid melt is contained inside the crystal shell. It is shown that during the mechanical interaction of the crystal with the surface, the shell is destroyed and the «pouring out» melt forms filamentous crystals of potassium carbonate with new physical and chemical properties.

**Keywords:** flame, potassium carbonate, whisker, dispersed particle.

## Introduction

Aerosol-forming pyrotechnic compositions are used to extinguish the flame of flammable liquids (ethanol, acetone, gasoline). In addition to the gas component of the combustion products, condensed dispersed particles are formed in the flame. The surface of dispersed particles participates in the process of recombination of active combustion centers of the type: $H^* + H^* \rightarrow H_2$.

The rate of heat release in the flame decreases sharply with a decrease in the concentration of active centers, which leads to the process of extinction. Thus, a high concentration of dispersed particles should be preserved in the combustion products of pyrotechnic composition.

## Materials and Methods

The composition based on iditol – 11%, potassium nitrate – 70%, DCDA (dicyandiamide) – 19% was used in the work. After thorough mixing, the components were pressed into a cardboard shell with a diameter of 20 mm at a specific pressure of 1000 kG/cm$^2$. The incineration of the samples was carried out at room conditions. The combustion process was recorded using a video camera in the near infrared range of the spectrum. The temperature distribution in the flame was determined by processing the flame image by the photopyrometric method. Sampling of condensed dispersed particles on glass plates was carried out by the method of passing through a flame. In the future, the selected samples were studied by microscopy methods. The maximum temperature 1380 K is reached in the luminous flame zone. The flame temperature decreases with an increase in height above combustion surface with a gradient $dT/dh$ = 6.75 K·mm$^{-1}$. The formation of a dispersed phase is observed in this zone.

The selected samples of dispersed particles were studied using an electronic scanning microscope of the Hitachi TM–4000Plus type, since an optical microscope does not allow deciphering the morphology of particles and the elemental composition of the sample. The condensed combustion products have a complex particle structure both in shape and size. The section of the sampler in reflected electron beams is shown in figure 1. By *X*-ray spectral analysis, it is shown that among the particles there are unburned particles of organic fuel, which contain mainly carbon. There are particles of potassium carbonate in the form of particles of irregular crystal structure.

## Results and Discussion

According to the experimental conditions, the potassium carbonate formed in the flame must be in a liquid state or decompose. The melting point of potassium carbonate is 1164 K [1]. The number of such deposited particles on the sampler is quite large. Crystals of potassium

carbonate at low temperatures (T < 693 K) have a monoclinic structure, and with an increase in temperature, the crystal structure passes into a hexagonal modification. The presence of complex-shaped particles indicates that the crystallization process of the substance comes from the outer surface. The surrounding space of the particle has many nuclei. For this reason, the external shape of the particles is different.

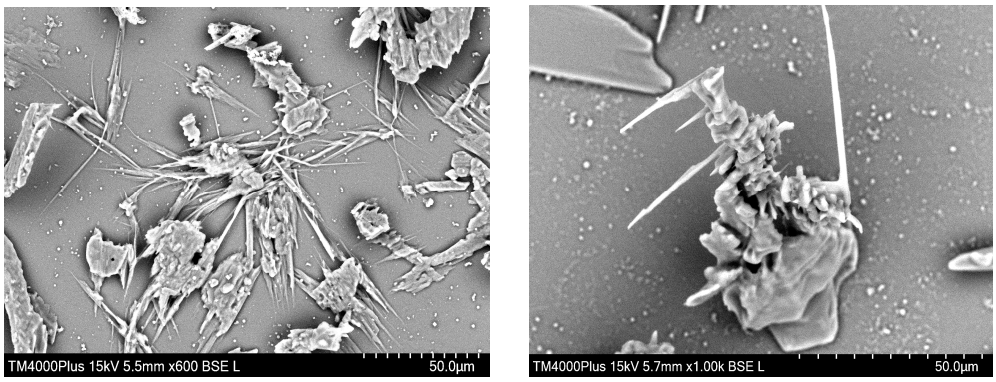


Fig. 1. Microphotograph of sampler fragments

Inside the crystal shell, it is possible to find a substance in a liquid state. When a particle collides with the surface of the sampler, the crystal shell cannot withstand the «overload» and is forced to collapse [2]. Liquid is «ejected» from the formed cracks and forms crystals in the form of threads. The spread of the length of the threads from one particle is small, since it is determined by the growth time of the threads. Filamentous crystals are located not only at the surface of the sampler, but are also observed in the form of three-dimensional structures. The time of collision and growth of filamentous crystals is small and is less than one millisecond. The interaction time is determined by the flow rate of combustion products, which does not exceed 1 m/s. The appearance of filamentous crystals from potassium carbonate in such a short time was discovered for the first time.

In the literature, filamentous crystals are called «whiskers» or whiskers (hair). On an industrial scale whiskers are obtained from refractory materials such as SiC, SiN, $Al_2O$ and MgO [3]. The time of growing whiskers up to 1 mm from the gas phase is several days, from the melt – up to several minutes. Whiskers have completely new physicochemical properties compared to single crystals, since they do not contain crystal defects.

## Conclusion

Thus, crystallization of potassium carbonate occurs from the outside of the melt. If the integrity of the capture of the crystal is violated, the melt crystallizes with the formation of whiskers.

## REFERENCES

1. **Grigorieva I. S.** Physical quantities, Moscow: Energoatomizdat, 1991.

2. **Tashkova K. Yu., Ugolkova A. S., Ksenofontov S. I., Vasilyeva O. V.** Morphology and chemical composition of pyrotechnic aerosol particles for volumetric fire extinguishing: Sat. mat. XVII International. scientific-practical conf. «Russian Science in the modern world» – Moscow : MSU (2018) 129–132.

3. **Artemyev S. R.** Properties and main methods of obtaining filamentous crystals, Eastern European Magazine Advanced technologies. 5/1 (65) (2013) 22–25.

# Gas Sensor Based on a Suspended Layer of Single Wall Carbon Nanotubes

**A. A. Vorobyev [1]✉, A.M. Mozharov [1], A.S. Goltayev [1], V.V. Sharov [1], D. M. Mitin [1]**
[1] Saint Petersburg Academic University, St. Petersburg, Russia
✉alex.spbau@mail.ru

**Abstract.** Detection and measurement of chemical compounds in the gas phase is an important task in a large number of areas of modern life such as: wearable electronics for personal monitoring of harmful gas environments and hazard prevention, process control, medical and biological sensors, gas sensors in the food industry to determine the safety of products.We have developed a gas sensor based on a layer of suspended single wall carbon nanotubes and an array of vertically oriented n-InAs nanowires. The gas sensitivity of the created sensor has been studied by the example of isopropyl alcohol vapors. The characteristic dependences of gas sensitivity in different measurement modes are revealed.

**Keywords:** single-wall carbon nanotubes, gas sensors, InAs nanowires.

**Funding:** The research was supported by grant from the Russian Science Foundation № 22-79-10286.

## Introduction

Gas sensors are widely used in various fields of science and technology [1], such as environmental monitoring, industrial production and safety, medical diagnostics, military industry and aerospace, agriculture, automotive [2]. Despite the fact that solid-state gas sensors have advantages such as small size, low power consumption, high sensitivity, low cost and low threshold for detecting a wide range of gases, their use is limited by problems such as low stable operation time and limited measurement accuracy [1].

Single-walled carbon nanotubes (SWCNTs) are distinguished by a unique combination of properties: high conductivity, transparency, chemical stability to aggressive environments, the ability to scale over large areas, ease of manufacture and low cost. Gas sensors based on SWCNTs have high sensitivity to various gases [3].

In the present work, we have developed a gas sensor based on a layer of suspended SWCNTs and an array of vertically oriented n-InAs nanowires (NWs). The gas sensitivity of the created sensor is investigated by using isopropyl alcohol (IPA) vapors atmosphere.

## Materials and Methods

Figure 1a shows a schematic representation of the created gas sensor. The array of vertically oriented n-InAs NWs was synthesized by molecular beam epitaxy on a silicon substrate (p-Si). A rear thermal burning Al-contact with a thickness ~150 nm was used as an ohmica contact to p-Si. A SWCNT layer with a thickness ~9 nm was applied to the NWs array by direct transfer method. Figure 1b shows the SEM image of the SWCNT layer on an array of vertically oriented n-InAs NWs.

A specially designed measuring stand was used to analyze the sensory properties. The design and measuring circuit are described in [4]. The signal measurements were carried out in 2 modes: *TD* – the voltage between the SWCNT layer and the Al rear contact, *TT* – the voltage between the two contacts on the surface of the SWCNT layer. IPA vapors were used as the detected gas probe.

It is important to note that the measurements were carried out at room temperature without additional heating of the gas sensor.

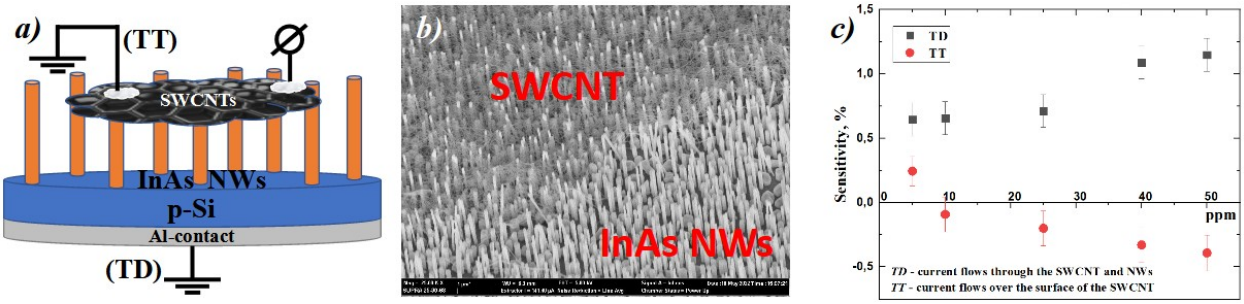


Fig. 1. (*a*) – schematic representation of the developed gas sensor based on the suspended SWCNTs layer and an array of vertically oriented n-InAs NWs, *(b)* – SEM image of the SWCNT layer and the array of vertically oriented n-InAs NWs, *(c)* – dependences of gas sensitivity in two measurement modes: *TD* – the voltage between the SWCNT layer and Al with the rear contact, *TT* – the voltage between the two contacts on the surface of the SWCNT layer.

## Results and Discussion

To analyze the sensory properties of the gas sensor the current–voltage characteristic (I–V curve) at isopropyl alcohol vapors atmosphere with different ppm concentration were obtained. Figure 1c shows the results of measuring the gas sensitivity of the created sensor. The gas sensitivity in *TD* – mode was about 1%, in *TT* – mode about 0.5%. Sensitivity was calculated as a relative change in the current flow through the structure.To calculate sensitivity in *TD* – mode, a linear region of the diode I–V curve (0.8 V) was used. *TT* – mode measurement demonstrates linear type dependence. At the same time, the sensitivity dependence type of measurement modes is different. In the case of the *TD* – mode, the current value increases with IPA vapors ppm rate, while in *TT* – mode the current value decreases with IPA vapors concentration. A more detailed explanation of this behavior will be described in the expanded version of the article.

## Conclusion

The gas sensor based on a layer of suspended SWCNTs and an array of vertically oriented n-InAs NWs was developed. The gas sensitivity of the created sensor is investigated by using different concentration of IPA vapors atmosphere in two different measuring modes.

## Acknowledgments

The research was supported by grant from the Russian Science Foundation № 22-79-10286.

## REFERENCES

1. **Varghese S. S., et al.,** Recent advances in graphene based gas sensors, Sensors and Actuators B: Chemical. 218 (2015) 160–183.
2. **Liu H., et al.,** Microhotplates for metal oxide semiconductor gas sensor applications—Towards the CMOS-MEMS monolithic approach, Micromachines. 9 (11) (2018) 557.
3. **Alrammouz R., et al.,** A review on flexible gas sensors: From materials to devices, Sensors and Actuators A: Physical. 284 (2018) 209–231.
4. **Solomatin M. A., et al.,** The UV effect on the chemiresistive response of ZnO nanostructures to isopropanol and benzene at PPM concentrations in mixture with dry and wet air, Chemosensors. 9 (7) (2021) 181.

# Influence of process parameters on the properties of microarc oxide coatings

**P. E. Golubkov [1], E. A. Pecherskaya [1✉], S. A. Gurin [1], V. S. Aleksandrov [1], D. V. Artamonov [1], A. A. Maksov [1]**

[1] Penza State University, Penza, Russia

✉pea1@list.ru

**Abstract.** In this work, an analytical description of the thickness and porosity dependences of micro-arc oxide coatings on the current density, treatment time, and concentration of electrolyte components is obtained in the form of empirical regression formulas. On the basis of the obtained equations, a technique for the formation of microarc oxide coatings with desired properties is proposed. The results of the study can be used to develop intelligent algorithms that underlie the digital twin of the micro-arc oxidation process.

**Keywords:** micro-arc oxidation, digital twin, взаимосвязь технологических параметров и свойств покрытий, empirical regression formulas, методика получения покрытий с заданными свойствами.

**Funding:** The work was supported by the grant of the Ministry of Science and Higher Education of the Russian Federation № 1022041100284-5-2.3.1. «Fundamentals of the digital twin of the technological process of forming oxide coatings with specified properties by microarc oxidation» (FSGE-2023-0005).

## Introduction

Micro-arc oxidation is a promising technological process of plasma-chemical modification of the light metals and alloys surface. Oxide coatings formed by this method have special properties and are used in many industries: automotive, oil and gas, rocket and space, aviation, electronics, medicine, etc.

Currently, there are problems associated with the technological features of the MAO process, which hinder its industrial implementation. First of all, this is the insufficient study of the mechanism of the oxide layers formation and the combined influence of many factors on the synthesized coatings properties. This causes certain difficulties in the selection of technological parameters, which leads to an increase in the energy consumption of the coating process.

A promising method for solving such problems is the development of digital twins of technological processes [1] using intelligent algorithms, which the correct operation requires a large amount of experimental data. For example, when training neural networks, in order to build training and control samples that are consistent with the results of a real MAO process, it is convenient to use regression formulas for the dependences of coating properties on process parameters and influencing factors. A review of foreign literature [2, 3] showed that not all of these dependences have a mathematical description. In addition, the analytical description of the same dependences in the works of different authors differs significantly, which is due to the peculiarities of specific technological regimes for various applications of MAO coatings. In this regard, obtaining empirical regression formulas for the dependences of coating properties on the technological process parameters is an urgent scientific task.

## Materials and Methods

MAO coatings were obtained on samples of commercial aluminum grade AD31T1 with 23x15x1.5 mm dimensions. As a current lead, pieces of aluminum wire with a diameter of 1.8 mm were used, which were insulated with a polyolefin heat shrink tube. MAO processing was carried out on a thyristor-capacitor automated MAO installation in the anode-cathode mode at a ratio of anode and cathode currents equal to 1, in four electrolytes containing 0.5 g/l NaOH and $Na_2SiO_3$ at a concentration of 80, 90, 100 and 110 g/l. The current density was 10.88; 13.99; 17.10; 20.21; 23.32 A/dm$^2$. The geometric dimensions and mass of the sample were measured

before and after MAO treatment, from which the thickness and porosity of the coatings were calculated.

## Results and Discussion

In the course of the study, a regression analysis of the experimental curves was performed, as a result of which regression equations were obtained for the thickness and porosity dependences of the coating on the current density, treatment time, and concentration of electrolyte components in the form of exponential functions. For example, Fig. 1 shows the dependence of the coating thickness on the current density for time $t$ = 60 s and various concentrations of $Na_2SiO_3$ in the electrolyte. Using the obtained regression equations, a technique for the formation of oxide coatings with desired properties has been developed and tested.

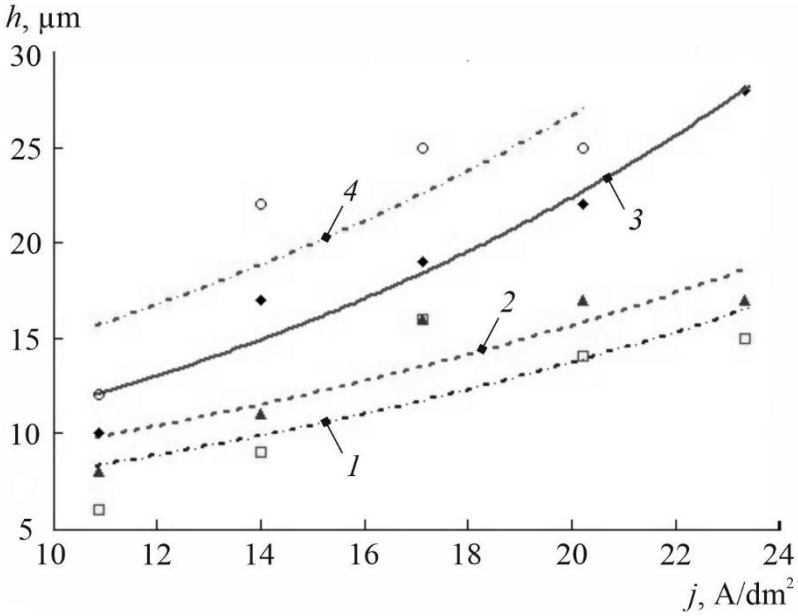


Fig. 1. Dependence of the coating thickness $h$ on the current density $j$ for time $t$ = 60 s and $Na_2SiO_3$ concentration equal to: 1 - 80 g/l; 2 - 90 g/l; 3 – 100 g/l; 4 – 110 g/l

## Conclusion

The proposed method for the oxide layers formation makes it possible, on the basis of the obtained regression equations, with the help of intelligent algorithms, to select the optimal technological regime for the synthesis of MAO coatings with desired properties. The technique can be included in the software of the digital twin of the micro-arc oxidation process.

## REFERENCES

1. **Gazenbiller E., Mansoor S., Konchakova N., Serdechnova M., Zheludkevich M., Blawert C., Hoeche D.**, Computational damage modelling of PEO coated extruded magnesium tested in slow strain rate configuration. Surface and Coatings Technology. 446 (2022) 128758.

2. **Jangde A., Kumar S., Blawert C.**, Evolution of PEO coatings on AM50 magnesium alloy using phosphate-based electrolyte with and without glycerol and its electrochemical characterization, Journal of Magnesium and Alloys. 8 (2020) 692–715.

3. **Wang X., Zhang F.**, Influence of anions in phosphate and tetraborate electrolytes on growth kinetics of microarc oxidation coatings on Ti6Al4V alloy, Transactions of Nonferrous Metals Society of China. 32 (2022) 2243-2252.

# Polishing methods for formation nanoporous anodized alumina.

**E. A. Grushevski[1], N. G. Savinski[1], O. S. Trushin[1]**

[1]Federal State Budgetary Institution of Science K. A. Valiev Institute of Physics and Technology of the Russian Academy of Sciences Yaroslavl Branch, Yaroslavl, Russia;

✉yaregor@mail.ru

**Abstract.** In the manufacture of the PAAO matrix, its quality and structural perfection primarily depend on both the grade of the aluminum alloy of the substrate and the quality of the surface. For the manufacture of PAAO, aluminum foil of high-purity aluminum with a content of 99.999% is mainly used. The technological scheme for obtaining highly organized porous aluminum oxide includes preliminary preparation of the foil surface of Al-Mn and A9 alloys with an aluminum content of 98.9% and 99.91%, respectively, by electrolytic plasma and electrochemical polishing methods in this work. Processing made it possible to obtain a surface with roughness parameters Ra = 0.012–0.016 microns. PAAO samples were obtained by double electrochemical anodizing of the prepared foil in 2 M sulfuric acid at a temperature of 30 °C and examined by scanning electron microscopy.

**Keywords:** aluminum, nanopores, electrolytic plasma, electropolishing.

**Funding:** The investigation was supported by the Program no. FFNN-2022-0018 of the Ministry of Science and Higher Education of Russia for Yaroslavl branch of Valiev Institute of Physics and Technology of RAS.

## Introduction

In the last decade, there has been a revived of interest in the fabrication of a porous alumina anode layer (PAAO). The unique properties of PAAO membranes make this material a template for various nanotechnology applications. [1-4]. In this work, we used foils with an aluminum content of 98.9% and 99.91% and a thickness of 100 and 500 µm, respectively. Due to the imperfection of the original foilsurface, it is necessary to pre-treat the surface of the foil, by electrolytic-plasma and electrochemical polishing methods.

## Materials and Methods

The roughness of the foil samples was measured using a Talystep mechanical profilometer (Taylor Hobson). To assess the surface roughness, the parameter of the height of the profile irregularities was used according to the average of the absolute values of the profile deviations.

$$R_a = \frac{1}{n}\sum_{i=1}^{n}|y_i| \qquad (1)$$

where $y_i$ are profile deviations from the baseline.

In this work, for electrolytic-plasma technology, the Al is the anode, and stainless steel is the cathode. 4% KCl+2% $C_2H_2O_4$ was used as electrolyte. The method of electrochemical polishing was also used with $H_3PO_4$ + $C_3H_8O$ + $H_2O$ as electrolyte. Aluminum is the anode, the cathode is a platinum wire.

## Results and Discussion

If a voltage of more than 200 V is applied to the cathode and anode electrodes located in an aqueous electrolyte solution, then the current density quickly reaches 30 A/cm$^2$, which causes instantaneous evaporation of water, the formation of a vapor-gas shell and the formation of a plasma discharge. High-quality polishing of aluminum and its alloys can be achieved in an electrolyte heated to 70-85 °C at a voltage >250 V [5]. The most widely used method of electrochemical methods of material processing is electro polishing, which combines high-quality polishing with obtaining a shiny surface. In this work, aluminum was polished while maintaining a current density of 25 A/dm$^2$ for 20 minutes in 40% $H_3PO_4$ + 40% $H_2SO_4$ + 6% $CrO_3$ + 14% $H_2O$.

Table 1

**Roughness data for electrolyte-plasma and electrochemical technologies.**

| N | $R_a$, µm | Sample |
|---|---|---|
| 1 | 0.67 | original foil |
| 2 | 0.016 | foil polished in $H_3PO_4 + H_2SO_4 + CrO_3 + H_2O$ |
| 3 | 0.012 | foil polished in electrolytic plasma in 4% KCl + 2% $C_2H_2O_4$ |

The method used for electrochemical anodizing of the prepared foil is a classic version of two-stage anodizing in 2 M sulfuric acid, at a voltage of 20 V and a temperature of 30 °C [6]. In order to control the effect of preprocessing on the quality of the obtained matrices, we examined PAAO chips by scanning electron microscopy. Figure 2a shows areas with different directions of net growth. The polishing process eliminates surface defects and minimizes the possibility of crossing, branching and sticking of pores.

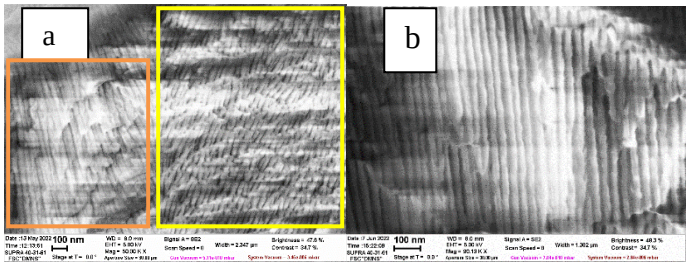


Fig. 2. SEM image of a PAAO without pre-polishing (*a*) and with pretreatment (*b*).

## Conclusion

A technological scheme for obtaining highly organized porous aluminum oxide has been developed, including preliminary preparation of the surface of aluminum foil using a method of submerged plasma glow discharge under the surface of the electrolyte, as well as an electrochemical method. PAAO samples were obtained by double electrochemical anodizing of the prepared material in 2 M sulfuric acid at a temperature of 30 °C and were investigated by scanning electron microscopy.

## Acknowledgments

The work was carried out within the framework of the State Task of the Valiev Institute of the Russian Academy of Sciences of the Ministry of Education and Science of the Russian Federation on the topic FFNN-2022-0018. Some experimental results were obtained on the equipment of the Center for Collective Using "Diagnostics of micro- and nanostructures" with the support of the Ministry of Education and Science of the Russian Federation.

## REFERENCES

1. **Safeer A., Ahmad N., Khan S., Azam L., Bashir D.**, Magnetization Behavior of Electrochemically Synthesized Co2MnSn full Heusler alloy Nanowire arrays, J. Appl. Phys. 125 (2019) Art. No. 034302.
2. **Hao Q., Huang H., Fan X.**, Assembly of gold nanoparticles into aluminum nanobowl array, Nanotechnology 28 (2017) Art. No. 105301.
3. **Masuda H., Yamada H., Satoh M.**, Highly-ordered nanochannel-array architecture in anodic alumina, Appl. Phys. Lett. 71 (1997) p. 2770.
4. **Varvaro G., Casoli F.**, Ultrahigh–density magnetic recording storage materials and media designs, Stanford: PanStanfordPublishing (2016) 509 p.
5. **Kulikov I.S., Vashchenko S.V., Kamenev A.Y.**, Electrolyte-plasma processing of materials,Belarus. Navuka, Minsk, 2010 232 p.
6. **Muratova E.N.**, Artificially and naturally ordered micro- and nanoscale capillary membranes based on anodic aluminum oxide: Cand. ... cand. tech. sciences, St. Petersburg: ETU “LETI”, 2014, 118 p.

# Synthesis of thin- film structures of vanadium oxide by spray- pyrolysis

**T. O. Zinchenko**, **E. A. Pecherskaya**✉ , **S. A. Gurin**, **P. E. Golubkov**, **V. S. Alexandrov**

Department of Information and measuring technology and metrology, Penza State University, Penza 440026, Russia;
✉pea1@list.ru

**Abstract.** Among semiconductors based on transition metal oxides, vanadium pentoxide has generated considerable interest in recent decades due to its wide range of applications. The physical properties of the films depend on certain parameters, such as the level and ratio of dopants, substrate temperature, deposition conditions, heat treatment, substrate material. As the substrate temperature increased, the films transparency increased. As the temperature increases, the film microstructure becomes thinner, which leads to an increase in the refractive index. A decrease in structural defects reduces the extinction coefficient of the films. It can also be seen that the transmission in the folds is quasi-stable with increasing temperature, indicating that the film morphology gradually improves, thus becoming more transparent..

**Keywords:** Vanadium pentoxide, spray- pyrolysis, microelectronics, thin-film.

**Funding:** This work has been supported by the grants the Russian Science Foundation, RSF 23-29-00343.

## Introduction

Among semiconductors based on transition metal oxides, vanadium pentoxide has attracted considerable interest in recent decades due to its wide range of applications [1]. Its multivalence, layered structure, wide optical band gap, good chemical and thermal stability, and excellent thermoelectric properties are characteristics that make vanadium pentoxide (V2O5) a promising material for microelectronics applications, as well as for electrochemical and optoelectronic devices. It is known to use this material as a catalyst, gas sensors, windows for a solar cell, in electrochromic devices, as well as in electronic and optical switches. Recently, there has been a growing interest in the fabrication of thin-film batteries [2]. Due to its simplicity and low cost, spray- pyrolysis is a popular chemical method for producing thin films of a large area. This method is convenient for obtaining uniform and smoother films without pinholes of the required thickness. The physical properties of films depend on certain parameters, such as the level and ratio of dopants, substrate temperature, deposition conditions, heat treatment, and substrate material [3].

## Synthesis of thin-film structures of vanadium oxide by the spray-pyrolysis method

Thin films of vanadium pentoxide were deposited on glass substrates by spray- pyrolysis using VCl3 (96%) in 40 cm3 of distilled water.

The solution particles were transferred with compressed and filtered air as a gas- carrier onto heated substrates. The nozzle-substrate distance was 32 cm. Before the substrates were placed in the reaction chamber of the installation, their surface was cleaned from possible contaminants that negatively affect the adhesion strength (adhesion). The substrate material was sodium-calcium-silicate glass (window glass) of rectangular shape.

The following substances were used: distilled water; baking soda - sodium bicarbonate (NaHCO3); ethanol (C2H5OH); chromium mixture (mixture of concentrated sulfuric acid (H2SO4) and potassium dichromate (K2Cr2O7)).

The following laboratory equipment was used: fume hood; distiller; ultrasonic bath; electric stove; chemical vessels.

The following operations were performed: treating the substrates with baking soda and washing them in tap water; ultrasonic treating the substrates in ethanol for 30 minutes (the liquid volume was determined based on the size and number of substrates); washing the substrates in distilled water; substrates treatment in a chromium mixture heated to 70 °C (the substrates were

lowered for 10 minutes into a glass with the mixture); washing the substrates in heated distilled water; (substrates were lowered into a glass with a new portion of distilled water: water spreads evenly on a carefully prepared substrate); drying the substrates on an electric stove when it is heated up to 100 °C.

As the substrate temperature increased, the films transparency increased. As the temperature increases, the film microstructure becomes thinner, which leads to an increase in the refractive index. A decrease in structural defects reduces the extinction coefficient of the films. It can also be seen that the transmission in the folds is quasi-stable with increasing temperature, indicating that the film morphology gradually improves, thus becoming more transparent. In the range 370 - 470 °C, a shift of the absorption edge from 2.4 eV to 2.6 eV was observed. As the temperature rises above 300 °C, the phase changes from amorphous to crystalline. Indeed, this increase in temperature leads to higher quality crystalline compounds, resulting in improved mobility and carrier concentration.

## Conclusion

Highly oriented nanocrystalline V2O5 films were synthesized using the spray- pyrolysis method deposited on glass substrates at various substrate temperatures. The average crystallite size is about 40 nm. It is evident from the experimental results that the crystallite size can be controlled by the deposition temperature. At high temperatures (>450°C), chemical bonds, leading to a shift in the absorption edge, were formed at the V2O5 film–substrate (glass) interface. Thus, glass substrates are not suitable for deposition at such high temperatures.

## REFERENCES

1. **Beke S.**, A review of the growth of V2O5 films from 1885 to 2010, Thin Solid Films. 519 (2011) 1761–1771.

2. **Kanan S.M., El-Kadri O.M., Abu-Yousef I.A., Kanan M.C.**, Semiconducting Metal Oxide Based Sensors for Selective Gas Pollutant Detection, J. Sens Vol. 9, (2009) 8158-8196.

3. **Mohamed H. A.,** Sintering process and annealing effect on some physical properties of V2O5 thin films, Optoelectronics and advanced materials – rapid communications, Vol. 3, (2009) 693-699.

# Study of the effect of temperature on the electrophysical parameters of ferroelectrics

**N. S. Emelyanov✉, A. E. Zhurina, E. A. Pecherskaya,**
**J. V. Shepeleva, G. V. Kozlov**
Penza State University, Penza, Russia
✉emelianoff.nikita@gmail.com

**Abstract.** Methods for studying the temperature dependences of the electrophysical parameters of ferroelectrics are systematized in order to propose a universal method that satisfies various types of ferroelectric materials. A hardware-software complex for measuring the electrical parameters of active dielectrics and products based on them has been developed. The presence of a heat chamber makes it possible to study the temperature effect on the electrophysical parameters of ferroelectrics.

**Keywords:** Ferroelectrics, temperature dependence, software and hardware complex

## Introduction

Ferroelectrics are promising materials for functional electronics due to a number of unique properties, including their non-linear response to an electric field. Based on these materials, tunable capacitors, delay lines, and phase shifters have been created [1]. At the same time, the dependence of the ferroelectrics properties on temperature in some cases limits their application [2]. In addition to temperature, the values of the electrical parameters of material samples are significantly affected by the geometric dimensions and shape of the active dielectric. Functional electronics devices use ferroelectrics, piezoelectrics and pyroelectrics of various shapes and sizes, and measuring the electrical parameters of each sample involves a large number of measurement procedures. For this reason, selective control of parameters is carried out in technological processes, which, together with the low reproducibility of parameters, causes the parameters of the created elements to deviate from the specified nominal values. At present, various methods for studying the temperature effect on the ferroelectric ceramics characteristics are known [3, 4]. In this paper, the authors propose the creation of a hardware-software complex for measuring the electrical parameters of active dielectrics and products based on them, which makes it possible to measure the electrical parameters of active dielectric samples with guaranteed accuracy, taking into account their shapes and sizes. The increase in technical and economic efficiency is achieved by increasing the measurements accuracy, reducing the time spent on research (due to automation of measurements; the introduction of new techniques that require fewer measurement experiments). The main advantage of the proposed hardware -software complex lies in the possibility of studying the temperature effect on the characteristics of specific sample of a ferroelectric material.

## Method for studying the effect of temperature on ferroelectric parameters

At present, various methods for studying the temperature effect on the ferroelectric ceramics characteristics are known [3, 4]. In this paper, the authors propose the creation of a hardware-software complex for measuring the electrical parameters of active dielectrics and products based on them, which makes it possible to measure the electrical parameters of active dielectric samples with guaranteed accuracy, taking into account their shapes and sizes. The increase in technical and economic efficiency is achieved by increasing the measurements accuracy, reducing the time spent on research (due to automation of measurements; the introduction of new techniques that require fewer measurement experiments). The main advantage of the proposed hardware-software complex lies in the possibility of studying the temperature effect on the characteristics of a specific sample of a ferroelectric material.

The sample under study is connected to the improved Sawyer-Tower measuring circuit [4]. Measuring signals proportional to the electric field strength and electric displacement in the sample after a series of transformations are transferred to the computer. To determine the

electrical parameters of various materials related to active dielectrics, modern mathematical methods of digital signal processing were used.

## Conclusion

When measuring the frequency dependences of the electrophysical materials parameters, a change in the test signal frequency is provided, when studying temperature dependences, a change in temperature in a heat chamber is provided, when measuring capacitance-voltage characteristics, a change in the bias voltage on the sample is performed. A combined measuring signal, which provides for a constant bias and an alternating voltage with the maximum possible amplitude of 500 V, is applied to the test sample it ensures the creation of the required electric field strength on the test samples.

## REFERENCES


1. **Tumarkin A., Kozyrev A., Gagarin A., Zlygostov M., Sapego E**. Ferroelectrics - Functional Materials for Various Applications. (2020) pp. 4–7.
2. **Nguyen Q. M., Anthony T. K., Zaghloul A. I.** Free-Space-Impedance-Matched Composite Dielectric Met-amaterial with High Refractive Index. IEEE Antennas and Wireless Propagation Let. 18 (12) (2019) pp. 2751–2755.
3. **Pecherskaya, E. A., Solov'ev, V. A., Metal'nikov, A. M., Varenik, Y. A., Gladkov, I. M., Ryabov, D. V.** Controlling the temporal instability of the dielectric parameters of ferroelectrics (2013) Semiconductors, 47 (13), pp. 1720–1722.
4. **Zhurina A. E., Emelyanov N. S., Pecherskaya E. A., Fimin, A. V.** The "resonance–antiresonance" method for determining the electrophysical parameters of piezoelectrics. Measuring. Monitoring. Management. Control. 3 (2022) 76 – 82.
5. **Kutnjak Zdravko.** (2008). Heat Capacity Response of Relaxor Ferroelectrics Near the Morphotropic Phase Boundary. Ferroelectrics. 369. 198.

# Determination of the electrophysical parameters of piezoelectrics using complex conductivity

**A. E Zhurina✉, E.A. Pecherskaya, N. S. Emelyanov, J.V. Shepeleva**
Penza State University, Penza, Russia
✉gelya.zhurina@mail.ru

**Abstract.** The use of piezomaterials as a substrate for a graphene structure is considered. Since the surface acoustic waves generated in piezoelectric materials, are on the surface of a solid body, piezoelectrics can act as a substrate for graphene. Methods for determining the electrical parameters of piezoelectric materials are studied and selected, the ways to improve these methods are considered. It is proposed to automate data processing in order to increase the speed and reduce the error of indirect measurement of the electrophysical parameters of piezoelectric materials.

**Keywords:** Graphene, piezoelectrics, electrophysical parameters of piezoelectrics.

## Introduction

Piezoelectric material is used in many instrument-making devices, this promising direction is associated with their use as a substrate for graphene. Graphene is a two-dimensional material; it is formed by a cellular lattice of carbon atoms [1]. Due to its unique properties, graphene is of great fundamental and applied interest. Since carbon graphene is an atomically thin material, charge carriers in graphene are very sensitive to ambient electromagnetic fields, and the ability to change the concentration of graphene carriers by applying an external gate voltage is an important feature of many graphene-based devices. The high mobility of carriers is provided by the high frequencies of optical phonons in a rigid cellular lattice, due to which the effect of electron-phonon scattering on charge transfer is insignificant compared to ordinary metals [2]. However, in most cases, graphene is deposited on a substrate, and the substrate material that creates the electric field will affect the charge carrier in the graphene wafer, making the choice of substrate material critical to device performance. Because the surface acoustic waves generated in piezoelectric materials are at the surface of a solid or at an interface between two solids, piezoelectrics can act as a substrate for graphene. They are used to control the properties of semiconductor materials and structures [3].

## Piezomaterial research

The use of a piezomaterial as a substrate for graphene puts forward certain requirements for the piezoelectrics parameters. To indirectly determine the piezoelectrics parameters, a system equations that takes into account the measured values of the frequency parameters of the product (resonance and antiresonance frequencies, quality factor), as well as the maximum voltage at the output of the measuring circuit at the resonant frequency is solved [4]. The mathematical model is the exact solution of the electromechanical problem of one-dimensional vibrations of a piezo sample, taking into account all types of energy losses. In the case of piezo-soft modes, the solution for complex conductivity is used, in the case of piezo-hard modes, for complex resistance. To implement this method, the real and imaginary parts of the complex conductivity of a piezoelectric are measured at several frequencies of the resonant region. The measurement results are used to solve the system of complex conductivity equations. The system is constructed in such a way that its equations relate the measured value of the complex conductivity to its theoretical expression in terms of the corresponding complex constants of the piezoceramics.

$$Y = j\omega[1+\frac{k^2}{1-k^2}I_D(\varphi)], \quad (1)$$

where $I_D(\varphi)$ is a function defining the dynamic side of the piezomaterial.

To remove the amplitude-frequency characteristics, a piezoelectric sample was taken in the form of a tablet based on solid solutions of lead zirconate – titanate with a piezomodule equal to $d_{33}$ = 567pKl/N (Figure 1).

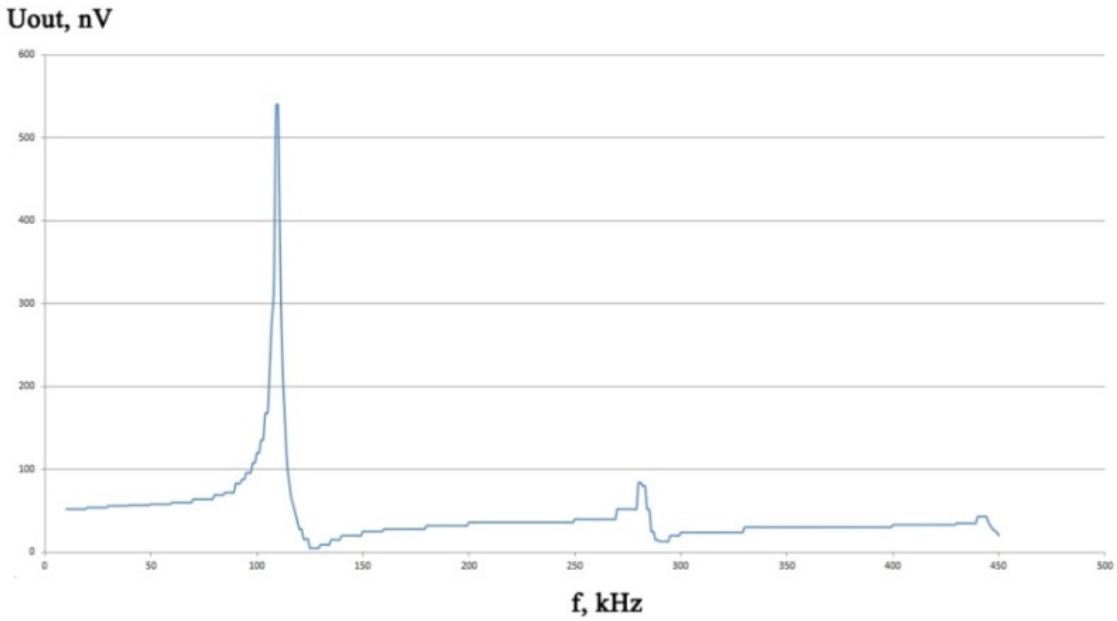


Fig. 1. Amplitude-frequency response of a piezoelectric sample in the form of a tablet based on solid solutions of lead zirconate – titanate

## Conclusion

The above method allows to determine all types of energy dissipation in a piezomaterial, complex constants are measured at one frequency. However, the method has a complex mathematical apparatus [5], so it is important to simplify the process of solving the system of equations, taking into account the formulated assumptions. An automated processing of measurement results, which contributes to an increase in its speed and a decrease in the error of indirect results of measurements of the electrophysical parameters of piezoelectric materials, is proposed.

## REFERENCES

1. **F. Junxiao.** Preparation and Application of Graphene. Academic Journal of Science and Technology 4, (2022) pp. 59 – 62.
2. **David González González, González, Francisco Guinea López, Fernando Sols Lucia**, Electronic properties of graphene on a piezoelectric substrate Propiedades electrónicas del grafeno sobre un sustrato piezoeléctrico / Madrid, (2019) p. 170.
3. **Burkov S. I., Zolotova O. P., Sorokin B. P.** The influence of uniform pressure on propagation of acoustic waves in piezoelectric layered structures. Journal of Siberian Federal University - Mathematics and Physicsthis link is disabled, 2014, 7(1), pp. 10 – 21
4. **Svetlov A. V., Nguyen N. M.** Determination of the parameters of products from piezomaterials represented by resonant four-element equivalent circuits. Measurements. Monitoring. Control. Control. No. 3 (2022) pp. 69 – 75
5. **Barkhatov V. A.,** Electromechanical model of a piezoelectric transducer. Defectoscopy, (2018) 8, pp. 3 – 15.

# Synthesis of thin-film structures of tungsten oxide by the spray-pyrolysis method

**T. O. Zinchenko**✉, **E. A. Pecherskaya**✉, **O. V. Karpanin**,
**G. V. Kozlov**, **A. A. Maksov**
[1] Department of Information and measuring technology and metrology, Penza State University, Penza 440026, Russia;
✉ pea1@list.ru

**Abstract.** Tungsten oxide ($WO_3$) is a transparent semiconductor material that has been extensively studied for applications in electrochromic windows. Polycrystalline thin films of p-type tungsten oxide ($WO_3$) were deposited by spray- pyrolysis using tungsten hexachloride ($WCl_6$) as a precursor. The technological synthesis regimes are considered and the current-voltage characteristics of the obtained coatings are constructed.

**Keywords:** Tungsten oxide, electrochromic panel, the current-voltage characteristics, spray- pyrolysis.

**Funding:** This work has been supported by the grants the Russian Science Foundation, RSF 23-29-00343.

## Introduction

Tungsten oxide ($WO_3$) is a transparent semiconductor material that has found wide application in electrochromic windows [1]. Electrochromic transmissive devices require stable conductive materials with high visible light transmittance and good electrotransport properties to switch between colored and bleached states. Regardless of which method is used for deposition, the choice of deposition parameters significantly affects the structure, morphology, and composition of the resulting film, which directly affects the optical and electrical properties of the layer. Films with high porosity or extensive grain boundaries are preferred because they support fast ion insertion-withdrawal, which effectively leads to an increase in staining efficiency and a fast switching speed between the clear and blue states of $WO_3$ [2]. Reproducibility in terms of stoichiometry, thickness, porosity, composition and crystallinity over a large area is achieved by studying the samples base and identifying the relationship between technological modes and coating properties [3].

## Synthesis of thin-film structures of tungsten oxide by the spray-pyrolysis method

Thin layers of tungsten oxide ($WO_3$) were deposited on electrically conductive antimony-doped tin oxide (ATO), also obtained by spray- pyrolysis. Precursor solutions were prepared by dissolving $WCl_6$ powder in alcohol ($C_2H_5OH$) containing acetylacetone in a 1:2 molar ratio. Cleaning of 5 x 5 cm ATO substrates was carried out by degreasing with a pH-neutral detergent, washing with deionized water, and finally ultrasonic cleaning in ethanol for 30 minutes (liquid volume was determined based on the size and number of substrates), followed by drying in compressed air. The quality control of the substrates cleaning by the degree of wettability of its surface (the substrates were lowered into a glass with a new portion of distilled water: on a carefully prepared substrate, the water spreads in an even layer). The following laboratory equipment was used to obtain the solution: fume hood; electronic balance; magnetic stirrer; chemical vessels. During the deposition, the substrate temperature and the solution molarity changed successively. Airflow pressure and spray distance (33 cm) were kept constant. The samples were annealed for 4 h at 400°C to stabilize the crystal coating structure.

Figure 1 shows the current-voltage characteristics of a sample obtained by spray-pyrolysis.

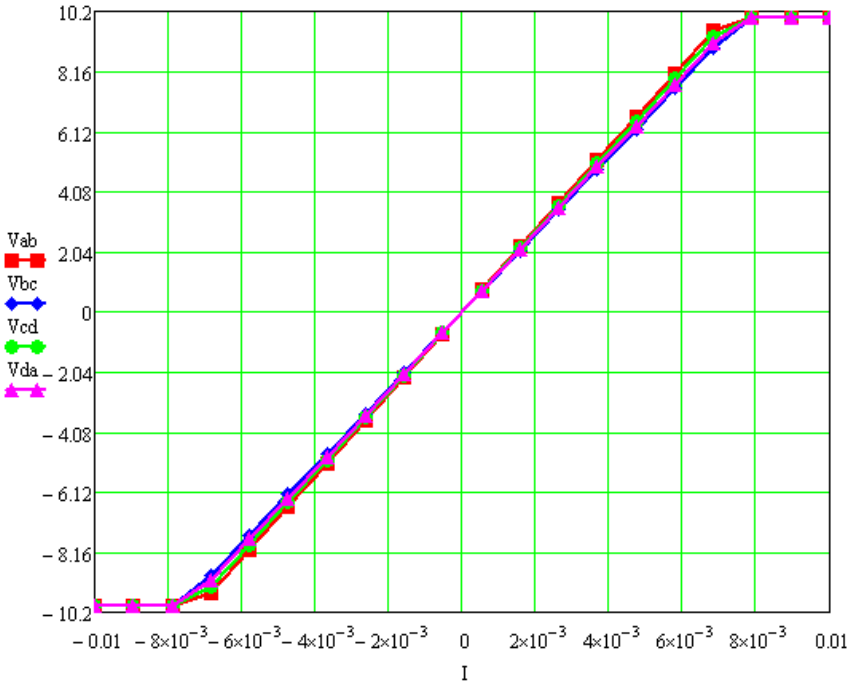


Fig. 1. Current-voltage characteristics of the sample $WO_3$

## Conclusion

Films with high porosity, high average surface roughness (67 nm) and low transparency are obtained at a deposition temperature of 280 °C. The crystalline $WO_3$ layer with peaks corresponding to the monoclinic structure was obtained after annealing at 400°C for all samples. Higher transmission values were observed as the solution molarity decreased and the precipitation temperature increased. The $WO_3$ properties have been found to be highly dependent on surface morphology.

## REFERENCES

1. **Granqvist, C.G.**, Handbook of Inorganic Electrochromic Materials, Amsterdam, Elsevier, 1995.

2. **Deepa M., Srivastava A.K., Sharma S.N., Govind, Shivaprasad S.M.,** Microstructural and electrochromic properties of tungsten oxide thin films produced by surfactant mediated electrodeposition**,** Applied Surface Science, Vol. 254 (2008) 2342-2352.

3. **Zinchenko T.O., Pecherskaya E.A., Antipenko V.V., Volik A.V., Varenik Y.A., Shepeleva A.E.,** Methodology for the Selection of Technological Modes for the Synthesis of Transparent Conducting Oxides with Desired Properties, Materials Science Forum, 1049 MSF (2022) 198-203

Conference materials
UDC 621.359.3
DOI: https://doi.org/10.18721/JPM.

# Study of composite electrode material formation features based on Super C45/$RuO_2$ and Super C45/$MnO_2$ for asymmetric planar supercapacitors

**Sh. Sh. Isokjanov** [1✉], **R. M. Ryazanov** [2], **E. P. Kitsyuk** [2], **E. A. Lebedev** [1,2]
[1] National Research University of Electronic Technology, Zelenograd, Moscow, 124498, Russia
[2] Scientific-Manufacturing Complex "Technological Centre", Zelenograd, Moscow, 124498, Russia
✉Isakjanov2997@gmail.com

**Abstract.** A method for fabricating an asymmetric planar supercapacitor with dissimilar electrodes based on Super C45/$RuO_2$ and Super C45/$MnO_2$ using the electrophoretic deposition method has been developed. The electrode topology was formed using laser engraving. The electrophoretic deposition method was chosen for sedimentation of the composite onto the surface of nickel-coated sitall plates. The features of sequential deposition of composite materials onto the substrate surface were studied, as well as the influence of electrophoresis modes on the composition and morphology of the formed electrode layers. A technology for producing compact planar supercapacitors with an asymmetric configuration for a wide range of microelectronics applications has been developed.

**Keywords:** planar supercapacitor, asymmetric supercapacitor, laser engraving, electrode material, electrophoretic deposition, suspension.

**Funding:** This work was supported by State Assignment № FSMR-2023-0003.

**Citation:** Isokjanov Sh.Sh., Ryazanov R.M., Kitsyuk E.P., Lebedev E.A., Study of the peculiarities of composite electrode material formation based on Super C45/$RuO_2$ and Super C45/$MnO_2$ for asymmetric planar supercapacitors, St. Petersburg State Polytechnical University Journal. Physics and Mathematics. 16 ( ) (2023) …–…. DOI: https://doi.org/10.18721/JPM.

This is an open access article under the CC BY-NC 4.0 license (https://creativecommons.org/licenses/by-nc/4.0/)

© Isokjanov Sh.Sh., Ryazanov R.M., Kitsyuk E.P., Lebedev E.A., 2023. Published by Peter the Great St. Petersburg Polytechnic University.

Материалы конференции
УДК 621.359.3
DOI: https://doi.org/10.18721/JPM.

## Introduction

Supercapacitors (also known as electrochemical capacitors or ultracapacitors) are particularly attractive for microelectronic devices and renewable energy production because they have excellent power and outstanding service life. The current trend in the development of miniature portable electronic devices has greatly increased the demand for ultra-thin, flexible, and durable micro-supercapacitors on a chip, which have enormous potential to complement or even replace microbatteries and capacitors. Asymmetric planar supercapacitors with dissimilar electrodes based on carbon-containing materials and transition metal oxides are promising electrochemical energy storage devices that can fully utilize the advantages of the unique properties of composite materials through combinations of different charge storage mechanisms or different redox reactions [1, 2].

In this work, the technology for manufacturing asymmetric planar supercapacitors with dissimilar composite electrodes based on Super C45/$RuO_2$ and Super C45/$MnO_2$ was investigated using the electrophoretic deposition (EPD) method.

## Materials and Methods

Sitall plates were used as a substrate, onto which a conducting nickel layer was deposited using magnetron sputtering. After that, the topological structure of the planar supercapacitor was formed using laser engraving on a CNC machine, which consisted of comb-like interdigitated electrodes nested on top of each other. To form dissimilar electrodes, suspensions were prepared based on combinations of Super C45/$RuO_2$ and Super C45/$MnO_2$, which were used as the main materials. The electrode materials were deposited sequentially in an electrophoretic cell by alternating the polarity of the power supply electrodes and the suspension. The electrophoretic deposition process was conducted in a galvanostatic mode. The main stages of creating the planar supercapacitor are schematically shown in Figure 1.

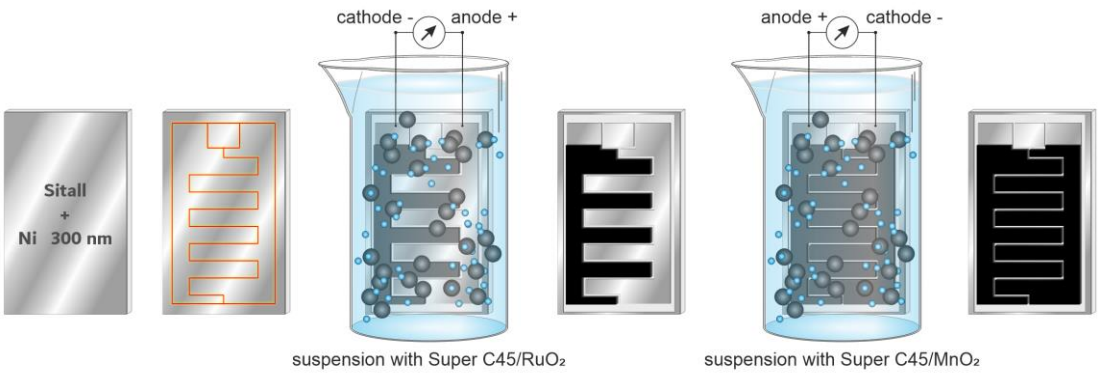


Fig. 1. Schematic representation of the way to create an asymmetric planar supercapacitor with dissimilar composite electrodes.

## Results and Discussion

The morphology and composition of the surface of the resulting coatings were studied by scanning electron microscopy. To study the electrophysical characteristics, supercapacitors were placed in a beaker with a 1 M KOH solution, and their capacitance characteristics were measured using an Elins-45X potentiostat with the supplied ES8 software for PC.

## Conclusion

In the course of the study, by varying the composition of the suspension and deposition modes, the composition of the composite electrodes was optimized. The peculiarities of the sequential local deposition of composites onto electrodes of planar supercapacitors were studied. These investigations allowed demonstrating the fundamental possibility of creating asymmetric planar supercapacitors with improved capacitance and power characteristics that are compatible with traditional integrated circuit production technology.

## Acknowledgments

This work was supported by State Assignment № FSMR-2023-0003.

## REFERENCES

1. **Wu N., Bai X., Pan D., Dong B., Wei R., Naik N., Rangrao R. P., Guo Z.,** Recent Advances of Asymmetric Supercapacitors, Advanced Materials Interfaces. Vol. 8 (1) (Jan 2021) 2001710.

2. **Kakovkina Yu. I., Isokjanov Sh. Sh., Ryazanov R. M., Lebedev E. A., Kitsyuk E. P.,** Features of the formation Super C45-$RuO_2$ based planar supercapacitor structures, St. Petersburg Polytechnic University Journal: Physics and Mathematics. 2022 Vol. 15, No. 3.2.

## THE AUTHORS

**ISOKJANOV Shakhboz Sh.**
Isakjanov2997@gmail.com
ORCID: 0000-0001-6009-9039

**RYAZANOV Roman M.**
r.m.ryazanov@gmail.com
ORCID: 0000-0002-2464-8712

**KITSYUK Evgeny P.**
Kitsyuk.e@gmail.com
ORCID: 0000-0002-4166-8408

**LEBEDEV Egor A.**
dr.beefheart@gmail.com
ORCID: 0000-0002-5085-5408

# Ice detector and chemical sensor based on superhydrophobic coating of carbon nanoparticles

**S. N. Kapustin** [1✉], **A. S. Volkov** [1], **Yu. V. Tsykareva** [1]

[1] Department of Fundamental and Applied Physics, Northern Arctic Federal University named after M. V. Lomonosov, Arkhangelsk, Russia

✉hare22@yandex.ru

**Abstract.** In previous works, a technique was proposed for obtaining a protective coating based on a xerogel of carbon nanoparticles for deposition on metal, plastic, or ceramics. The coating exhibits superhydrophobic and anti-icing properties. The dependence of the electrophysical properties of the coating on humidity, temperature, and the presence of volatile components in the air, such as hexane, alcohol, and water, has been revealed. Such a solution paves the way for the creation of a full-fledged "smart coverage".

**Keywords:** superhydrophobicity, carbon nanotubes, chemical sensors.

**Funding:** This study was funded by Russian Research Foundation grant number 22-22-20115.

## Introduction

Further development of the Arctic requires the development of methods for protecting structures, communication lines, structures and equipment from corrosion, pollution and icing. One of the methods of protection is the use of hydrophobic and superhydrophobic coatings [1].

In [2], we proposed an approach to obtain a coating from milled xerogel glued onto the surface to be protected. The xerogel was proposed to be made from carbon nanotubes (CNTs). The approach was developed in [3], where COS (carbon onion structures) obtained by a cheap and technological method were used to create a xerogel. It was proposed to move from sticking the xerogel to the deposition of nanoparticles in a solvent and the formation of a xerogel directly on the surface to be protected. In [4], the coating was presented as a two-layer coating: a heating layer of CNTs and a hydrophobic one of COS. It has been observed that the electrophysical properties of the coating depend on the concentration of impurities in the air, which may allow some segments of the coating to be used as a sensor for humidity, pollution or icing.

## Materials and Methods

The coating was applied similarly to [3]. The sputtering device consisted of a flask where nanoparticles (Taunit-M carbon nanotubes) were deagglomerated by means of a cavitation effect caused by a MEF 93.1 ultrasonic disperser with an effective power of 0.5 kW. Dispersion lasted about ten minutes, after which the resulting sol was fed into an airbrush mounted on a programmable coordinate device. Getinaks was used as a substrate. Seven or eight layers were applied one after the other as the previous one dried.

The sample was placed in a hermetically sealed chamber, which made it possible to precisely set the temperature and the concentration of impurities in the air. The conductivity of the sample was measured with a Novokontrol 80 dielectric spectrometer.

## Results and Discussion

The obtained dependences of the coating conductivity under varying conditions (temperature, humidity) are unambiguous. This suggests that the isolated fragment of the coating can be used as a chemical sensor, a humidity sensor, or to record the conditions for the onset of icing.

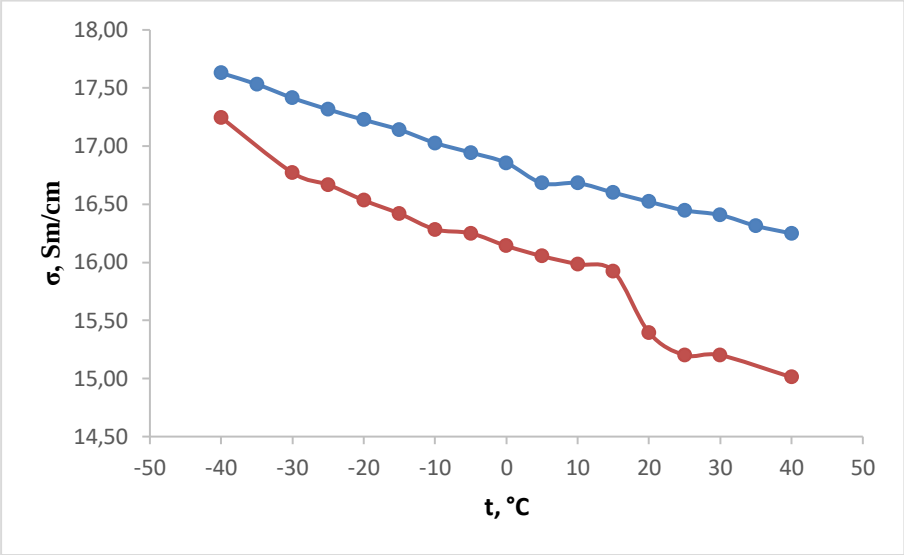


Fig. 1. Dependence of coating conductivity on temperature and humidity. The blue line is 0% humidity, and the red line is 100% humidity.

## Conclusion

The data obtained paves the way for the creation of a full-fledged "smart coverage". To accurately identify impurities in the atmosphere, one should use several areas of coating from different nanoparticles or nanoparticles with different degrees of functionalization and compare changes in their conductivity.

During the conference, data will be presented on the dependence of the conductivity of a xerogel from CNTs or COSs of various functionalizations on humidity, temperature, and concentrations of hexane, water, alcohol, and some gases, and recommendations on sensor manufacturing will be given.

## REFERENCES

1. **Nazhipkyzy M.,** Superhydrophobic materials and coatings: a review, Combustion and plasma chemistry. 4 (2020) 163-180.

2. **Eseev M.K., Goshev A.A., Kapustin S.N., Tsykareva Y.V.**, Creation of Superhydrophobic Coatings Based on MWCNTs Xerogel, Nanomaterials. 9 (2019) 1584

3. **Eseev M.K., Kapustin S.N., Lugvishchuk D. S., Mordkovich V. Z., Lyakh N. L.**, A Superhydrophobic Coating Based on Onion-Like Carbon Nanoparticles, Technical Physics Letters. 46 (2020) 1120–1123.

4. **Kapustin S., S. Zabolotny S., M. Eseev M., Tsykareva Y.**, Double-Layer Superhydrophobic Anti-Icing Coating Based on Carbon Nanoparticles, Crystals. 12(10) (2022) 1501.

# Obtaining conductive ultrathin films on based on a mixture of "carbon nanotubes - arachidic acid" by the Langmuir-Blodgett method

**M.V. Gavrikov** ✉, **G.V. Trushkov**, **V.N. Mironyuk**, **T.Y. Karatyshova**, **E.G. Glukhovskoy**
Saratov State University, Saratov, Russia
✉maks.gavrikov.96@gmail.com

**Abstract.** In this work, we investigated the possibility of forming conductive layers based on carbon nanotubes (CNTs) by using the Langmuir-Blodgett technology. It was determined that the addition of a small amount of surfactant (arachidic acid) to a solution of CNTs makes it possible to form a continuous layer on the water surface, to control its degree of compression and continuity, while maintaining its conductivity when transferred to a substrate.

**Keywords:** Carbon nanotubes, conductive layers, Langmuir-Blodgett technology.

**Funding:** This study was funded by grant from the Russian Science Foundation (project № 21-73-20057) and Saratov State University.

## Introduction

Carbon materials, in particular carbon nanotubes (CNTs), organized into a film structure have great prospects for application as electrodes for various fields, for example, for thin-film photovoltaic structures [1–2]. One of the ways to form such structures is the Langmuir-Blodgett method. It makes it possible to form monomolecular films with control over the density of molecules in a layer based on a selected substance and to transfer them to any solid substrates [3–4].

## Research and Discussion

In this work, the influence of arachidic acid (AA) as a surfactant on the formation of Langmuir monolayers of carbon nanotubes (CNT) was studied. It was determined that the addition of a small amount of AA (less than 10%) to CNT solutions allows one to expand the range in which the surface tension changes to several tens of mN/m. The change in surface tension upon compression of a CNT monolayer (without surfactant) is about 1 mN/m, since CNT is not amphiphilic substance. Thus, the addition of a surfactant opens up the fundamental possibility of controlling the degree of compression of a CNT monolayer on the water surface.

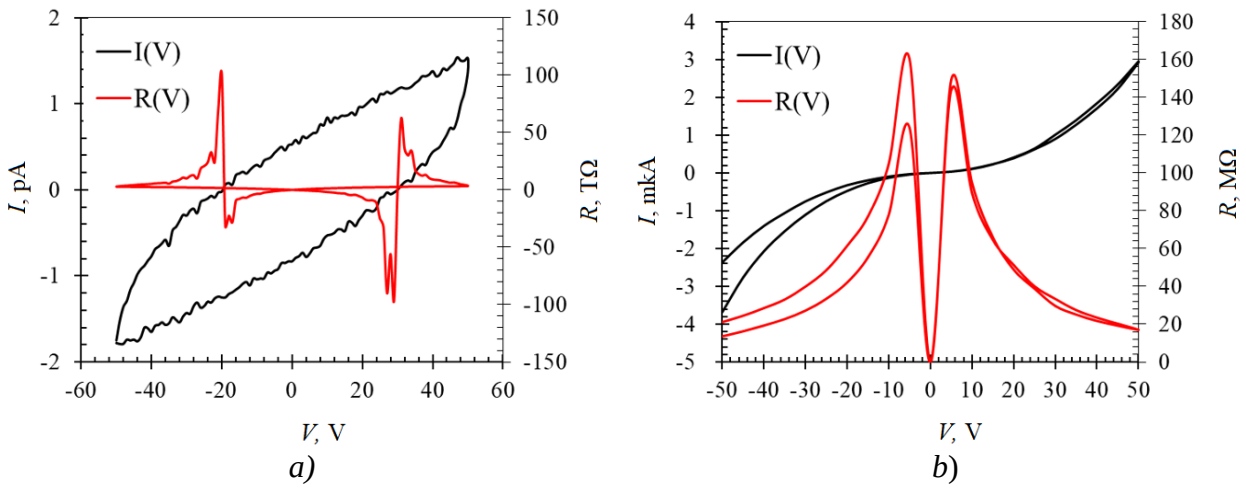


Fig. 1. Current-voltage (black line) and volt-ohmic (red line) dependencies: for a substrate without a CNT film (*a*) and with a CNT film (*b*)

The study of the relief of CNT and CNT:AA monolayers transferred to solid substrates was carried out by atomic force microscopy (AFM) and showed that the addition of surfactant to the initial solution of nanotubes also affects the microrelief of the CNT film, making it more uniform and less rough. At the same time, the quality of the monolayer transferred to the substrate increases (the coefficient of transfer of the monolayer to the solid substrate reaches values close to 1), the

density, continuity, and uniformity of its coating on the surface of the solid substrate after transfer correlates with the degree of compression of the layer on the water surface.

The conductive properties were studied by the two-probe method on substrates with a system of interdigitated electrodes with a gap between the electrodes about 300 μm. The conductivity of a structure with a single CNT-based monolayer is several MΩ. Figure 1 shows that the formed CNT-based monolayer has a structure conductivity that is 6 orders of magnitude higher than that of the substrate without a film. The addition of surfactants does not significantly affect the conductive properties of carbon films.

## Conclusion

This allows us to conclude that it is possible to use the Langmuir monolayer formation technique to create conductive ultrathin coatings based on CNT-surfactant as conductive layers in micro- and nanoelectronics devices.

## Acknowledgments

The authors are grateful to the Russian Science Foundation for the financial support of the research carried out in the project № 21-73-20057.

## REFERENCES

1. **Bindl D., Arnold M. S.**, Semiconducting carbon nanotube photovoltaic photodetectors, International Journal of High Speed Electronics and Systems. 20 (03) (2011) 687–695.

2. **Landi B. J., Raffaelle R. P., Castro S. L., Bailey S. G.**, Single-wall carbon nanotube–polymer solar cells, Progress in Space Photovoltaics. 13 (2) (2005) 165–172.

3. **Valyansky S. I.,** Nanomaterials: Langmuir films, National University of Science and Technology «MISIS», Moscow, 2014.

4. **N.O. Osvaldo, C. Luciano, A. Katsuhiko.**, The Past and the Future of Langmuir and Langmuir–Blodgett Films, Chem. Rev. 122 (6) (2022) 6459–6513.

# Investigation of the Transfer of Floating Layers of Porphin Derivatives to Solid Substrates

**V. N. Mironyuk**, **M. V. Gavrikov**, **T.Y. Karatyshova**✉, **E.G. Gluckhovskoy**
Education and Research Institute of Nanostructures and Biosystems,
Saratov State University, Saratov, Russia
✉tatochka338@gmail.com

**Abstract.** In this work, comparative studies were carried out on the transfer of floating layers of porphin derivatives onto solid substrates by the Langmuir-Schaeffer and Langmuir-Blodgett methods.
The transfer efficiency of the floating layers was estimated from the transfer coefficient and by the spectral method from the change in the height of the absorption peaks of multilayer films. It has been established that for the transfer of floating layers of symmetrically substituted porphin, the Langmuir-Schaeffer method is more efficient, and in the case of asymmetrically substituted porphins, the Langmuir-Blodgett method.

**Keywords:** Floating layers, Langmuir-Blodgett, porphyrin derivatives, solar cells, UV-Vis Spectroscopy.

**Funding:** The study supported by a grant of the Russian Science Foundation (project No. 21-73-20057) and Saratov State University.

## Introduction

Currently, directions of research on the practical application of thin-film organic dyes in photovoltaic devices are being developed. Among such materials, porphin derivatives with various substituents on the periphery of the macrocycle occupy a special place. Their macrocyclic structure with a developed π-conjugated system causes a high degree of light absorption in the ultraviolet and visible regions of the spectrum [1]. Langmuir-Blodgett (LB) technology is suitable for creating such films. loating layers are formed at the gas-air interface and then transferred to solid substrates. This technology makes it possible to form films with a given structure and create layers with a thickness of one molecule [2].

To obtain homogeneous films on solid substrates, it is necessary to take into account not only the state of the substrate surface, but also the orientation of the substrate relative to the water surface, on which a floating layer of the transported substance is formed.

In this work, a comparative study was carried out on the transfer of porphyrin derivatives: with symmetrical substitution - 5,10,15,20-tetra (4-n-methyloxyphenyl)porphine (PP1) and with asymmetric substitution - (5-(4-hydroxyphenyl) -10,15,20-tris(4-hexadecyloxyphenyl)porphine) (PP2) and 5-(4-aminophenyl)-10,15,20-tris(4-hexadecyloxyphenyl)porphin) (PP3), formulas which are shown in Fig. 1.

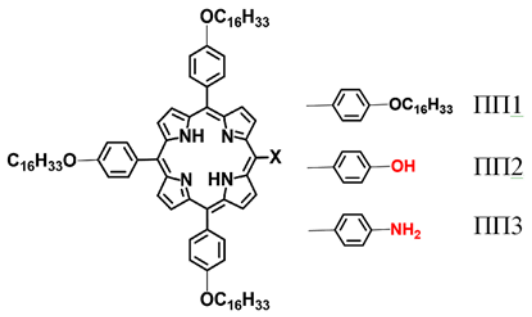


Fig.1. PP1, PP2, PP3 molecules

## Materials and Methods

Floating layers of porphin derivatives were formed at the liquid-gas interface using a KSV Nima LB Trough KN2002. The transfer of floating PP layers was carried out on glass substrates by the Langmuir-Schaeffer (LS) and Langmuir-Blodgett methods at a surface pressure of 8 mN/m, which was maintained constant by pressing the floating layer with movable barriers and

changing the area occupied by the layer. The number of transfers of each type of compounds was 6, 12, and 18. Deionized water with a resistance of 18.2 MΩ cm was used as the subphase. The transfer of layers was carried out at an aqueous subphase temperature of 22℃, which was controlled with an accuracy of 0.2℃. The transfer coefficient was calculated as the ratio of the change in the area occupied by the layer on the water surface, which occurred during the transfer, to the area of the part of the substrate on which the floating layer was deposited.

The absorption spectra of the films were recorded on a Genesys 50 spectrophotometer (Thermo FS) in the wavelength range 190–1100 nm with a step of 1 nm.

## Results and Discussion

The obtained values of the transfer coefficient indicated that the transfer of floating PP1 layers onto a solid substrate by the LB method turned out to be less efficient than for PP2 and PP3 layers. This may be due to the fact that PP1 molecules have a smaller dipole moment compared to PP2 and PP3 and, consequently, weaker interaction with the surface of the hydrophilic glass substrate.

The dependence of the transfer coefficient of floating layers PP1, PP2, and PP3 on the angle of orientation of the substrate relative to the water surface was studied. Three cases were studied: when the substrate is oriented vertically - at an angle of 90° to the water surface (the so-called LB method), when the substrate is oriented horizontally - the angle with the water surface is 0° (LSh method), and when the substrate is oriented at an angle of 45° to the surface water. For floating layers of PP1, the maximum value of the transfer coefficient was achieved when they were transferred by the LS method, which indicated a high efficiency of the process of transferring floating layers from the water surface to the surface of the glass substrate; for floating layers SP2 and SP3, the LB method turned out to be more efficient.

A similar conclusion can also be drawn from spectral studies. The absorption spectra of all studied films contain bands characteristic of tetraphenylporphyrins, consisting of an intense Cope band and a decreasing Q band. The largest increase in the intensity of the corresponding peaks with an increase in the number of transferred layers is observed for the floating layers of PP1 when they are transferred by the LS method, and for the floating layers of PP2 and PP3 when they are transferred by the LS method. LB method. In addition, for PP3, a noticeable broadening and shift of the Cope band to the short wavelength region was observed, which indicated the formation of H-type aggregates.

## Conclusion

In the course of the studies, it was found that symmetrically substituted porphins were more efficiently transferred to solid substrates by the LS method, and asymmetrically substituted porphins by the LB method. This was confirmed by the value of the transfer coefficient of the floating layer and the absorption intensity of the layered structures.

## Acknowledgments

The authors are grateful to the Russian Science Foundation for the financial support of the research carried out within the framework of project № 21-73-20057.

## REFERENCES

1. **Zeng K., Tong Z., Ma L., Zhu W., Wu W., Xie Y.**, Molecular engineering strategies for fabricating efficient porphyrin-based dye-sensitized solar cells, Energy Environ. Sci. 13 (6) (2020) 1617-1657.

2. **Mironyuk V.N., Al-Alwani A.J.K., Begletsova N.N., Gavrikov M.V., Kolesnikova A.S., Pozharov M.V., Glukhovskoy E.G.** Study of Langmuir monolayers and Langmuir-Schaefer films based on symmetrical meso-aryl-substituted porphyrin derivative, J. Phys.: Conf. Ser. 2086 (1) (2021) 012195.

# Properties of Langmuir floating layers and Langmuir-Schaeffer films based on polyaniline and arachidic acid mixture

**T. Y. Karatyshova[1]✉, V. N. Mironyuk[1], M. V. Gavrikov[1], E. G. Glukhovskoy[1]**
[1] Education and Research Institute of Nanostructures and Biosystems,
Saratov State University, Saratov, Russia
✉ tatochka338@gmail.com

**Abstract.** This paper presents the results of a study of Langmuir monolayers of polyaniline in a conducting emeraldine form. In this work, a protonated form of emeraldine polymer (dark green polyaniline, PANI) was synthesized and arachidic acid (AA) was chosen as a surfactant to obtain a "true solution" and a "true monolayer". Langmuir monolayers based on a mixture of PANI:AA were formed on the surface of water and studied by the method of compression isotherms. A certain dependence of the phase composition and mechanical properties of the monolayer on the molar ratios of PANI:AA solutions with the selected surfactant is shown. On the basis of experimental data, the dependences of the compression modulus ($C^{-1}$) on the area per molecule are plotted. Floating monolayers were transferred to the surface of glass substrates with interdigital electrodes and studied by the methods of current–voltage and capacitance–voltage characteristics. The optical and surface properties of these films on glass substrates were also studied.

**Keywords:** conductive polymers, Langmuir technology, nanostructured materials, thin films

**Funding:** The work was supported by a grant from the Russian Science Foundation (project number 21-73-20057) and Saratov State University.

## Introduction

The synthesis of conductive polymers, including polyaniline, significantly accelerated the development of flexible electronics [1-2]. When creating new devices, an important technological task is solved for the formation of highly ordered monomolecular layers. Among the various methods of producing thin films, the Langmuir-Blodgett (LB) technology stands out for the simplicity of implementation and control of the formed layers [3-6].

## Materials and Methods

Isotherms of porphyrin monolayers were formed by using KSV NIMA LB Trough 2002 KN (mediumsized bath with a compression ratio of approximately 1:9). Deionized water at a temperature of 24 °C was used as an aqueous subphase. The studies used a solution of polyaniline in chloroform with a concentration of $10^{-3}$ M. Solutions of 100 μL with a different polyaniline-arachinic acid ratio were applied to the water surface. The time of complete evaporation of the solvent was 10 minutes, after which the monolayer was compressed with two barriers at a constant speed of 13 mm/min (symmetrically compression mode). Compression isotherms showed some dependence of on the molar ratios of PANI:AA solutions deposited on the surface of the subphase. The parameters of a monolayer in a tightly packed state are determined. The maximum compression pressure was 67 mN/m. In its pure form, polyaniline poorly forms ordered monolayers on the surface of water, its maximum surface pressure during compression barely reaches 7 mN/m. The transfer of monolayer was carried out on a glass substrate with interdigital electrodes, pretreated with chloroform. Monolayers were transferred by the Langmuir-Schaeffer method (horizontal lifting) at surface pressure 20 mN/m.

## Results and Discussion

It was found that with an increase in the number of layers applied to a solid substrate, the conductive properties are improved, as well as the uniformity of the film in thickness. A positive

curvilinear dependence is observed with an increase in the proportion of arachidic acid in the mixture PANI:AK, the area occupied by the monolayer is growing at a surface pressure of 2.5 mN/m. This suggests a possible embedding of arachidic acid molecules between polyaniline molecules.

## Conclusion

The results obtained allow us to talk about the properties of PANI films formed by the Langmuir method. Relatively stable Langmuir monolayers of PANI at the air-water interface, up to high surface pressures, can be obtained using arachidic acid as a surfactant.


## Acknowledgments

The authors are grateful to the Russian Science Foundation for the financial support of the research carried out within the framework of project № 21-73-20057.


## REFERENCES


1. **Pan F., Wang S. [et al]**, An All-Solid-State Flexible Supercapacitor Based on MXene/MSA Ionogel and Polyaniline Electrode with Wide Temperature Range, High Stability, and High Energy Density, J. Molecules, 28 (4) (2023) 1-13
2. **Tran V. V. [et al]**, Recent Developments and Implementations of Conductive Polymer-Based Flexible Devices in Sensing Applications, Polymers. 14 (18) (2022) 1-29.
3. **Al-Alwani A. J. K., Mironyuk V. N., Al-Hassani A. J. [et al]**, Liq. Cryst. and their Appl. 21 (4) (2021) 74–84.
4. **Mironyuk V. N., Al-Alwani A. J. K., Begletsova N. N. [et al]**, Modeling of the interaction of porphyrin molecules in a nonpolar solvent, J. Phys.: Conf. Ser. 2086 (1) (2021) 1-5.
5. **Morales D. [et al]**, Single-Step Binary Electrostatic Directed Assembly of Active Nanogels for Smart Concentration-Dependent Encryption, Langmuir. 34 (4) (2018) 1557-1563.
6. **Kise R. [et al]**, Fluorous Property of a Short Perfluoroalkyl-Containing Compound Realized by Self-Assembled Monolayer Technique on a Silicon Substrate, BCSJ. The Chemical Society of Japan. 92 (4) (2019) 785-789.

# Photo-assisted adsorption of enzyme molecules onto a surface-modified silicon substrate

**A. V. Kozlowski** [1✉], **A. A. Serdobintsev** [1], **S. V. Stetsyura** [1]
[1] Saratov State University, Saratov, Russian Federation
✉kozlowsky@bk.ru

**Abstract.** In the frame of this work an influence of light on adsorption of enzyme molecules from an aqueous solution onto a single crystal silicon substrate with a layer of amorphous silicon (a-Si) was demonstrated by atomic force microscopy. The enzyme molecules are catalysts for specific chemical reactions in living systems and can be used as a sensitive layer in biosensors based on semiconductor, which is a transducer. The effect of illumination depends on both conductivity type of Si and the presence on the surface the layer of a-Si. Thus, the 2-beam interference pattern on the surface of the n-Si/a-Si structure before the enzyme adsorption process leads to ordered rows after enzyme deposition. This pattern not observed for p-Si/a-Si structure or bare substrate of single-crystal Si without the amorphous silicon layer. These results were explained using electron processes at the silicon/solution interface. After optimization, the developed approach can enable the production of multi-enzyme coatings for multiplex analysis.

**Keywords:** atomic force microscopy, amorphous silicon, surface charge, enzyme, layer-by-layer adsorption.

**Funding:** This study was funded by the Russian Science Foundation (project No. 22-22-00194, https://rscf.ru/en/project/22-22-00194/).

## Introduction

Structures based on silicon and a buffer polyelectrolyte layer are promising for a potentiometric bio- and chemosensors, so-called electrolyte-insulator-semiconductor (EIS) sensor [1]. As the polyelectrolyte molecules in solution have an effective charge, then layer-by-layer (LbL) technique developed by Decher [2] may be used for fabricate such structures. This technology also allows us to fabricate an enzymatic layer on the transducer surface. Multi-enzyme coatings can be fabricated by LbL adsorption [3]. However, EIS-sensors detect changes in charge only within the order of the Debye screening length from the surface.

In this work we suggest another immobilization method of enzyme molecules by means of photo-assisted adsorption. Previously, an effect of light on GOx molecules adsorption onto a silicon substrate was demonstrated [5], i.e. illumination and Si conductivity type can control over adsorption of GOx molecules. Thus, creating an interference pattern on the semiconductor surface allows fabrication of ordered structures of enzyme molecules. Also, this approach can lead to a multienzyme monolayer and to solve the problem of signal attenuation due to the Debye screening length.

## Materials and Methods

The experiments were performed with (100)-oriented single-crystalline Si wafers of n- and p-type conductivity. A layer of amorphous silicon (a-Si) was deposited by direct current magnetron sputtering method. The electron mobility of a-Si in 100 times less mobility than a single crystal. The thickness of a-Si layer was 100 nm. Then, using a system of mirrors, half wave plate and a polarizer, two linearly horizontally polarized beams were created (Figure 1a), which produce an interference pattern with a grating period of 2 μm. We used a laser with wavelength of 491 nm and an intensity value of 100 mW/cm$^2$.

After Irradiation, the samples were placed the enzyme solution. The deposition time was 10 min. The glucose oxidase (GOx, type X-S, Sigma Aldrich Co.) enzyme was used. GOx molecules were dissolved in deionized water to a concentration of 0.1 mg/mL. After GOx adsorption, the samples were rinsed in deionized water and dried in nitrogen.

The obtained samples were studied by methods of atomic force microscopy (AFM). The Kelvin probe technique was used to measure the sample work function using a device "ΔΦ" (Bespoke GmbH, Germany) with a gold grid.

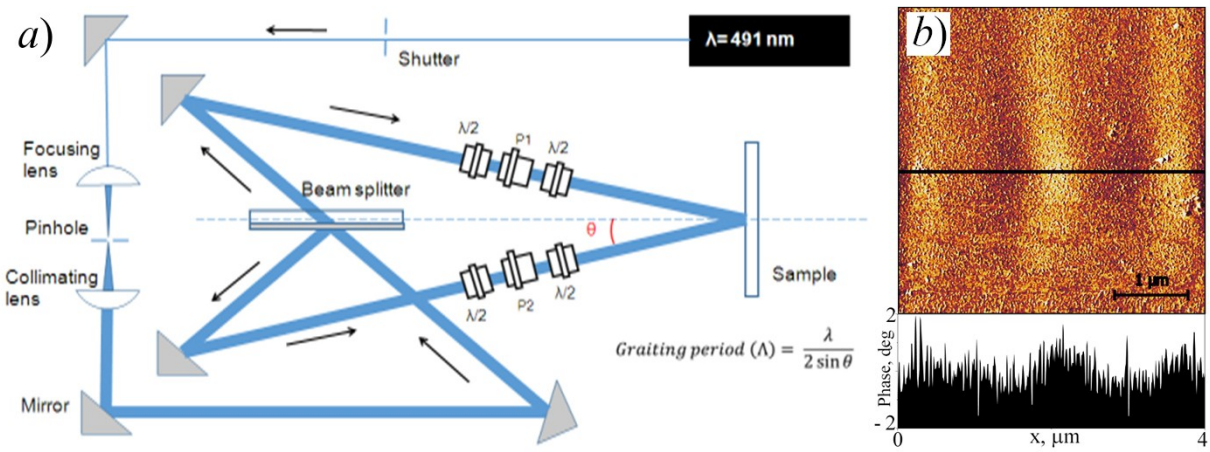


Fig. 1. Experimental setup (a) and phase contrast image (b) of GOx molecules on n-Si/a-Si structures after 1 hour of illumination at an intensity of 100 mW/cm$^2$ with an interference pattern. λ/2 - half wave plates; P1, P2 – polarizers.

## Results and Discussion

Since for the n-Si/a-Si structures the change in the work function after switching off the light is slower than in case the glass/a-Si structures, the n-Si/a-Si substrate was selected for photo-assisted adsorption of enzyme molecules.

Figure 1b illustrate AFM-image and phase contrast after 1 hour irradiation at intensity of 100 mW/cm$^2$ by interference pattern and subsequent GOx adsorption from the aqueous solution. It can be seen that on phase contrast and AFM-image there is an interference pattern handed over by the lattice period. This pattern not observed for p-Si/a-Si structure or bare substrate of single-crystal Si without the amorphous silicon layer.

## Conclusion

In the frame of this work an influence of light on adsorption of enzyme molecules from an aqueous solution onto a single-crystal silicon substrate with a layer of a-Si was demonstrated by atomic force microscopy (AFM). It was shown that the photo-memory effect observed for n-Si/a-Si and glass/a-Si structures. Thus, the 2-beam interference pattern on the surface of the n-Si/a-Si structure before the GOx adsorption process leads to ordered rows after GOx deposition. This effect is not an artifact of the AFM-image or the a-Si crystallization and it could not be detected in the case of p-Si/a-Si structures, or bare p-Si and n-Si. After optimization, the developed approach can enable the production of multi-enzyme coatings for multiplex analysis.

## Acknowledgments

This study was funded by the Russian Science Foundation (project No. 22-22-00194, https://rscf.ru/en/project/22-22-00194/).

## REFERENCES

1. **Garyfallou G.Z., de Smet L.C.P.M., Sudhölter E.J.R.,** The effect of the type of doping on the electrical characteristics of electrolyte–oxide–silicon sensors: pH sensing and polyelectrolyte adsorption, Sensors and Actuators B: Chemical. 168 (2012) 207-213.

2. **Decher G.**, Fuzzy Nanoassemblies: Toward Layered Polymeric Multicomposites, Science. 277 (1997) 1232-1237.

3. **Abouzar M.H. et al.**, Capacitive electrolyte-insulator-semiconductor structures functionalized with a polyelectrolyte/enzyme multilayer: New strategy for enhanced field-effect biosensing, Phys. Status Solidi A. 207 (4) (2010) 884–890.

4. **Stetsyura S.V., Kozlowski A.V.**, The influence of photoelectron processes in a semiconductor substrate on the adsorption of polycationic and polyanionic molecules, Technical Physics Letters. 43 (3) (2017) 285-288.

Conference materials
UDC 538.9
DOI: https://doi.org/10.18721/JPM.

# Novel impedance spectroscopy approach for nanowires based adsorption sensors

**V. M. Kondratev** [1, 2] ✉, **E. A. Vyacheslavova** [1, 3], **S. S. Nalimova** [3], **V. A. Moshnikov**[3], **A. S. Gudovskikh** [1, 3], **A. D. Bolshakov** [1, 2, 4]
[1] Alferov University, Saint Petersburg, Russia
[2] Moscow Institute of Physics and Technology, Moscow, Russia
[3] Saint Petersburg Electrotechnical University "LETI", Saint Petersburg, Russia
[4] ITMO University, Saint Petersburg, Russia
✉kvm_96@mail.ru

**Abstract.** The work is aimed at study of quasi 1-D silicon nanowires (Si NWs) adsorption properties via electrical impedance spectroscopy. This work demonstrates a novel frequency-resistive method of electrical impedance spectroscopy data analysis. The approach allows us to obtain selectivity of a resistive type nanowire based adsorption sensors.

**Keywords:** silicon, nanowires, electrical impedance spectroscopy, adsorption properties.

**Funding:** The Ministry of Science and Higher Education of the Russian Federation (Grant FSRM-2023-0009). The Ministry of Science and Higher Education of the Russian Federation (agreement 075-03-2023-106, project FSMG-2021-0005).

**Citation:** Kondratev V. M., Vyacheslavova E. A., Nalimova S. S., Moshnikov V. A., Gudovskikh A. S., Bolshakov A. D., Novel impedance spectroscopy approach for nanowires based adsorption sensors, St. Petersburg State Polytechnical University Journal. Physics and Mathematics. 16 ( ) (2023) …–…. DOI: https://doi.org/10.18721/JPM.

This is an open access article under the CC BY-NC 4.0 license (https://creativecommons.org/licenses/by-nc/4.0/)

© Kondratev V. M. et al, 2023. Published by Peter the Great St. Petersburg Polytechnic University.

Материалы конференции
УДК 538.9
DOI: https://doi.org/10.18721/JPM.

# Новый подход к анализу данных спектроскопии электрического импеданса сенсоров на основе нитевидных нанокристаллов

**В. М. Кондратьев** [1, 2] ✉, **Е. А. Вячеславова** [1, 3], **С. С. Налимова** [3], **В. А. Мошников** [3], **А. С. Гудовских** [1, 3], **А. Д. Большаков** [1, 2, 4]
[1] СПбАУ РАН им. Ж.И. Алфёрова, Санкт-Петербург, Россия
[2] Московский физико-технический институт, Москва, Россия
[3] СПбГЭТУ "ЛЭТИ", Санкт-Петербург, Россия
[4] Университет ИТМО, Санкт-Петербург, Россия
✉kvm_96@mail.ru

**Аннотация.** Работа посвящена изучению адсорбционных свойств нанонитей кремния методами спектроскопии электрического импеданса и созданию селективных сенсоров на их основе.

**Ключевые слова:** кремний, нанонити, спектроскопия электрического импеданса, адсорбционные свойства.

**Финансирование:** Министерство науки и высшего образования Российской Федерации (грант № FSRM-2023-0009). Министерство науки и высшего образования

Российской Федерации (Соглашение 075-03-2023-106 от 13.01.2023, проект FSMG-2021-0005).

**Ссылка при цитировании:** Кондратьев В. М., Вячеславова Е. А., Налимова С. С., Мошников В. А., Гудовских А. С., Большаков А. Д. Новый подход к анализу данных спектроскопии электрического импеданса сенсоров на основе нитевидных нанокристаллов // Научно-технические ведомости СПбГПУ. Физико-математические науки. 2023. Т. 16. № . С. …–… . DOI: https://doi.org/10.18721/ JPM.

Статья открытого доступа, распространяемая по лицензии CC BY-NC 4.0 (https://creativecommons.org/licenses/by-nc/4.0/)

© Кондратьев В.М. и др., 2023. Издатель: Санкт-Петербургский политехнический университет Петра Великого.

## Introduction

High surface area and peculiar electronic properties compare to bulk material and thin films are the main reason for use of nanowires in adsorption sensing. Silicon is still the most accessible material for the production of NWs, both by epitaxial and «top-down» techniques [1]. The existing works on Si NWs adsorption properties [2-3] commonly consider small amounts of target adsorbates. This paper shows the possibility of detection both water, ammonia, hydrochloric acid, isopropanol and acetone at low concentrations via electrical impedance spectroscopy and correlation between Si NWs electrical impedance and their adsorption properties [4-5].

## Materials and Methods

Si NWs were synthesized by cryogen plasmachimical etching and transferred to auxiliary substrate with concentric interdigital gold contacts. Further, nanowires were exposed to air, unsaturated vapors of water, ammonia, hydrochloric acid, isopropanol and acetone aqueous solutions followed by measurement of the nanowires impedance spectra.

## Results and Discussion

We demonstrate the possibility of unambiguous distinction of the sensory signal from water, ammonia, hydrochloric acid, isopropanol and acetone adsorption in terms of frequency-resistance impedance spectroscopy mapping.

## Conclusion

Presented sensor can be used to find diseases of the gastrointestinal tract by the qualitative and quantitative detection of ammonia and hydrochloric acid content in biological samples, and also to detect isopropanol and acetone for environmental applications.

The frequency-resistance approach of impedance spectroscopy data analysis can be directly translated to other nanomaterials to analyze their applicability in the field of biosensory.

## REFERENCES

1. **Kondratev V. M.** ***et al***, Silicon Nanowire-Based Room-Temperature Multi-environment Ammonia Detection, ACS Applied Nano Materials 5 (7), 9940-9949.

2. **Zhou X. T** ***et al***, Silicon nanowires as chemical sensors, Chemical Physics Letters. 2003, 369, 220.

3. **Park I.** ***et al***, Top-down fabricated silicon nanowire sensors for real-time chemical detection, Nanotechnology. 2010, 21, 1, 015501.

4. **Kondratev V. M.** ***et al***, Silicon nanowires based adsorption sensors for CO and NH3 detection, J. Phys.: Conf. Ser. 2021, 2103, 012229.

5. **Kondratev V. M.** ***et al***, Silicon nanowires as multi—environment sensor elements for carbon monoxide and ammonia detection, J. Phys.: Conf. Ser., 2021, 2015, 012068.

## THE AUTHORS

**KONDRATEV VALERIY M.**
*Alferov University*
Khlopina 8/3, 194021, Russia
kvm_96@mail.ru
ORCID: 0000-0002-3469-5897

**VYACHESLAVOVA EKATERINA A.**
*Alferov University*
Khlopina 8/3, 194021, Russia
cate.viacheslavova@yandex.ru
ORCID: 0000-0001-6869-1213

**NALIMOVA SVETLANA S.**
*Saint Petersburg Electrotechnical University "LETI"*
Professor Popov St. 5, 197022, Russia
sskarpova@list.ru

**MOSHNIKOV VYACHESLAV A.**
*Saint Petersburg Electrotechnical University "LETI"*
Professor Popov St. 5, 197022, Russia
vamoshnikov@mail.ru

**GUDOVSKIKH ALEXANDER S.**
*Alferov University*
Khlopina 8/3, 194021, Russia
gudovskikh@spbau.ru

**BOLSHAKOV ALEXEY D.**
*Alferov University*
Khlopina 8/3, 194021, Russia
acr1235@mail.ru
ORCID: 0000-0001-7223-7232

# Obtaining a polyimide nonwoven fabric and studying its dielectric characteristics

**V.E. Kraft, A.M. Kamalov, G.V. Vaganov, M.E. Borisova, V.E. Yudin, A.S. Nesterova**

[1]Peter the Great St.Petersburg Polytechnic University, Polytechnicheskaya, 29, St.Petersburg, Russia;
[2]Institute of Macromolecular Compounds Russian Academy of Sciences, Bolshoy Prospekt, 31, St. Petersburg, Russia

✉Sparta3006@inbox.ru

**Abstract.** This work is devoted to obtaining nonwoven fabrics from polyimides by electroforming and determining their dielectric and mechanical properties. Recently, the technology of electroforming nanofibers from polymer solutions, in particular polyimides, has been increasingly developed. Thus, composite materials with unique properties are produced. High values of the specific surface (porosity of the material) make it possible to use them in power engineering and medicine: porous electrodes, interelectrode separators, filters and sensors [1, 2].

**Keywords**: Electroforming, polyimide, nonwoven material.

## Introduction

In modern integrated circuits, materials with low dielectric constant ε are needed to reduce resistive capacitance delay and minimize crosstalk. Flexible printed circuit boards (FPCs) are widely used in complex electronic products because of their outstanding characteristics such as light weight, size and flexibility. Polyimide is most commonly used for flexible printed circuit boards: as an insulating dielectric layer between metals because of its high mechanical and heat resistance properties. However, polyimide films have a relatively high dielectric permittivity (3-3,5), which does not meet the requirements for the development of modern integrated circuits. Thus, the creation of composites based on polyimides with low dielectric permittivity has become one of the urgent tasks in the field of high-frequency and high-speed signal transmission. This paper investigates a nonwoven polyimide material obtained by electroforming from aqueous solutions of polyamidoacid salts (PAA) based on pyromellitic dianhydride (PMDA) and 4,4`-oxydiphenylenediamine (ODA) [3].

The purpose of the work is to obtain and study the mechanical and dielectric properties of polyimide nonwoven fabrics obtained by electroforming.

## Materials and Methods

It was found experimentally that the most suitable for electrospinning is 12% solution (12% PAA salt and 88% solvent), the solvent consists of 30% $H_2O$ and 70% ethyl alcohol.
Electroforming can be performed on different grounded electrodes: on a flat and on a rotating drum-collector. The electroforming process was performed in the NANON-01A unit. The average thickness of the nonwoven fabric obtained on the flat electrode was 25 μm. The obtained samples were then imidizated in an oven: 2 hours were heated to 250°C and kept at this temperature for another hour. After that, the samples were examined on different setups. Dynamic mechanical analysis (DMA) was performed on an Instron (5943) with the Bluehill software package. The dielectric properties of the material were analyzed on a NOVOCONTROL machine with the WinData software package.

Then the dielectric properties of the obtained materials will be described.

## Results and Discussion

Eventually a 25 μm thick nonwoven fabric was obtained, and it was studied for Dielectric Properties.

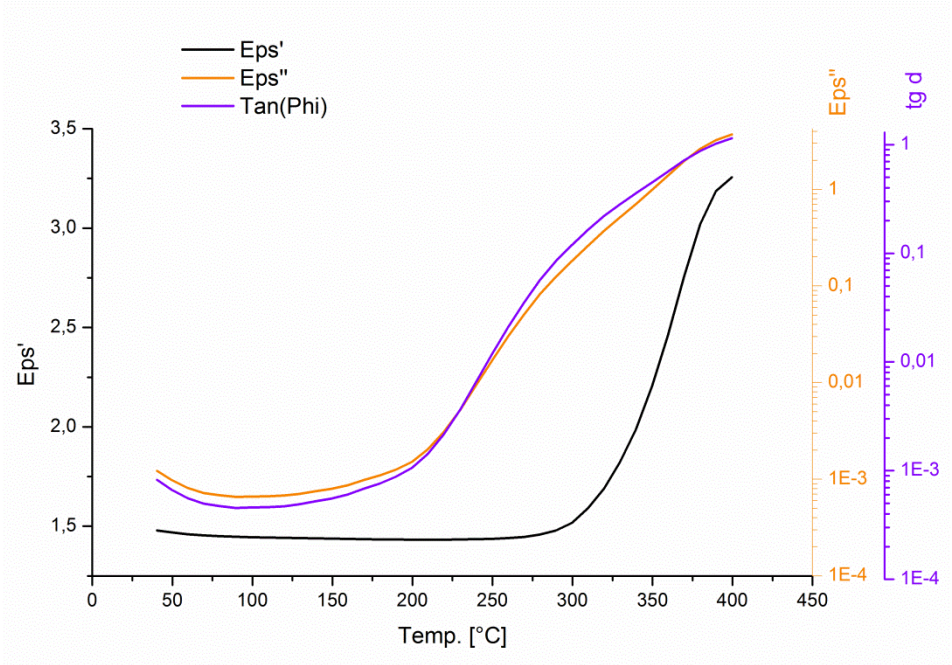


Fig. 1. Dependence of dielectric permittivity Eps′ (black line), loss factor Eps ″(orange line) and tg δ (purple line) on temperature at frequency $f$ = 15 kHz

As can be seen from Fig. 1, it turned out to achieve $\varepsilon = 1{,}5\varepsilon_0$. tg δ also turned out low. For comparison values tg δ of non-polar polymers (polyethylene, polytetrafluoroethylene) lie in range $2*10^{-4} – 5*10^{-4}$.

## Conclusion

The obtained material meets the requirements: low epsilon (due to high porosity and low dielectric permeability of polyimides), high Young's modulus, low tg δ. In the future it is planned to study the properties of nonwoven fabrics depending on the way of their production (grounded electrode), different concentration of salts, the possibility of obtaining new properties by chemical additives. It is also supposed to study the electret properties of this material: currents of TSD, etc.

## REFERENCES


**1. A.T. Matveev, I.M. Afanasov.,** Nanofibers production by electroforming. - Moscow: Lomonosov Moscow State University, 2010. - 83 p.

**2. N. Filatov.,** Electroforming of Fiber Materials. - M.: 2001. - 231 p.

**3. B. M. Svetlichny, L. A. Miagkova, T. E. Sukhanova, E. M. Ivankova.,** Synthesis of water-soluble salts of polyamide acid // High Molecular Compounds. - SPb: 2020. - pp. 83-95.

Conference materials
UDC 541.138:621.315
DOI: https://doi.org/10.18721/JPM.

# The method of formation of planar lithium-ion batteries with composite electrode materials

**N. A. Litovchenko** [1✉], **I. K. Martynova** [1], **I. M. Gavrilin** [3], **Y. O. Kudryashova** [3], **R. M. Ryazanov** [2], **E. A. Lebedev** [1,2]
[1] National Research University of Electronic Technology (MIET), Moscow, Zelenograd, Russia;
[2] Scientific Manufacturing Complex "Technological Centre", Moscow, Zelenograd, Russia;
[3] Frumkin Institute of Physical Chemistry and Electrochemistry, Moscow, Russia
✉natlitovch@gmail.com

**Abstract.** In this work, we investigated the method of formation of planar lithium-ion batteries with composite electrode materials. To form a composite cathode material based on NCA ($LiNi_xCo_yAl_zO_2$) and Super C45 the electrophoretic deposition process was used, and the anode was formed by local electrochemical deposition of germanium nanofibers. The principal possibility of formation of planar lithium-ion batteries with heterogeneous composite electrode materials located in one plane was demonstrated.

**Keywords:** planar lithium-ion battery, electrophoretic deposition, electrochemical deposition, cathode material, anode material

**Funding:** This work was supported by State Assignment № FSMR-2023-0003.

**Citation:** Litovchenko N. A., Martynova I. K., Lebedev E. A., Gavrilin I. M., Kudryashova Y. O., Ryazanov R. M., The process of forming a planar battery with composite electrode materials, St. Petersburg State Polytechnical University Journal. Physics and Mathematics. 16 ( ) (2023) …–…. DOI: https://doi.org/10.18721/JPM.

This is an open access article under the CC BY-NC 4.0 license (https://creativecommons.org/licenses/by-nc/4.0/)

© Litovchenko N. A., Martynova I. K., Lebedev E. A., Gavrilin I. M., Kudryashova Y. O., Ryazanov R. M., 2023. Published by Peter the Great St. Petersburg Polytechnic University.

Материалы конференции
УДК 541.138:621.315
DOI: https://doi.org/10.18721/JPM.

## Introduction

The key element for powering wearable electronics and microsystem devices is batteries. They must be small, lightweight, and have sufficient capacity. There are various microsized lithium-ion batteries (μLIB) with a sandwich structure, in which electrodes and electrolyte are superimposed on each other [1-3]. They are simple to fabricate, but difficulties arise when trying to integrate them with other miniature devices.

In this work, we propose a way to create a planar μLIB structure on a conductive substrate. Such a μLIB can be fabricated in a single process cycle with a power consumer. For this purpose, methods for local electrophoretic deposition (EPD) of composite cathode materials based on NCA ($LiNi_xCo_yAl_zO_2$) and Super C45 on one of the current collectors, and local electrochemical deposition (ECD) of germanium nanofibers on the second were developed.

## Materials and Methods

The substrates for the planar batteries were sitall plates with a conductive layer. Using laser engraving on a CNC machine, the structures of planar batteries were formed, representing the structures of a counter-pin converter - two combs nested into each other.

An electrophoretic cell consisting of two electrodes connected to a power supply and immersed in a beaker with a suspension was used for local formation of composite cathode materials by the EPD method. The electric field strength was varied from 30 $V/cm^2$ to 110 $V/cm^2$ and the process duration was 2 minutes. The suspension used in this work contained 1.8 mg of NCA and 0.2 mg of the carbon conductive additive Super C45 per 1 ml of isopropyl alcohol and acetone-based solvent in a 1:1 ratio. To improve the electrophoretic mobility of the active material, nickel nitrate hexahydrate at a concentration of 0.1 per 1 ml of solvent was used.

Ge nanowires were formed by electrochemical deposition from aqueous GeO2 solu-tions, using indium seeds. Electrochemical deposition of Ge nanowires was performed from electrolyte containing 0.05 M $GeO_2$, 0.5 M $K_2SO_4$ and 0.5 M of $C_4H_6O_4$.

To control the composition of the obtained samples, the method of energy dispersive X-ray spectroscopy was used. The morphology of the obtained layers was studied using a scanning electron microscope. The capacitive characteristics of the planar battery samples were studied on the basis of charge-discharge characteristics and cyclic sweeps.

## Results and Discussion

In this work the technologies of electrode formation by methods of local ECD and EPD were worked out. Optimization of the modes and compositions of the obtained layers makes it possible to control the properties of planar batteries in terms of their specific capacitance and electrical conductivity.

The topology and optimized modes of laser engraving of planar battery structures have been developed.

Features of sequential deposition of dissimilar electrode materials on different current collectors were studied, which allows to combine two processes in one technological cycle.

To measure the capacitive characteristics a special tooling made of polypropylene was created. The capacitive characteristics of planar battery mockups were studied on the basis of charge-discharge characteristics and cyclic sweeps.

## Conclusion

In this work experimental samples of planar lithium-ion batteries were obtained. The fundamental possibility of creating a planar battery with heterogeneous composite electrode materials located in one plane was demonstrated.

## Acknowledgments

This work was supported by State Assignment № FSMR-2023-0003.

## REFERENCES

1. **Li, X., Xie, P., Xiang, W., Wei, X., Huang, Y., & Shen, G.**, Micro-sized lithium-ion battery with sandwich structure, Nano Energy, 60 (2019) 772-779.

2. **Jiang, H., Zhang, Y., Lian, K., & Wang, X.**, Layer-by-Layer Assembly of 3D Microbatteries with High Energy Density, Advanced Materials, 25(31) (2019) 4494-4498

3. **Krause, T., Zhang, X., & Zeiger, D. N.**, Three-dimensional stackable microbattery arrays, Nature Communications, 2 (2011) 56.

## THE AUTHORS

**LITOVCHENKO NATALYA A**.
National Research University of Electronic Technology
1, Shokin Square, 124498, Zelenograd, Moscow, Russia
natlitovch@yandex.ru
ORCID: 0000-0001-7568-5655

**MARTYNOVA IRINA K.**
National Research University of Electronic Technology
1, Shokin Square, 124498, Zelenograd, Moscow, Russia
irisha-windsurfer@yandex.ru
ORCID: 0000-0002-6128-5244

**LEBEDEV EGOR A.**
National Research University of Electronic Technology
1, Shokin Square, 124498, Zelenograd, Moscow, Russia
dr.beefheart@gmail.com
ORCID: 0000-0002-5085-5408

**GAVRILIN ILYA M.**
Frumkin Institute of Physical Chemistry and Electrochemistry
31, Bld.4, Leninsky Prospect, 119071 Moscow, Russia
gavrilin.ilya@gmail.com
ORCID: 0000-0002-0278-1598

**KUDRYASHOVA YULIA O.**
Frumkin Institute of Physical Chemistry and Electrochemistry
31, Bld.4, Leninsky Prospect, 119071 Moscow, Russia
yulia.kudryashova@mail.ru
ORCID: 0000-0003-1359-0700

**RYAZANOV ROMAN M**.
Scientific Manufacturing Complex “Technological Centre”
1, Shokin Square, 124498, Zelenograd, Moscow, Russia
r.m.ryazanov@gmail.com
ORCID: 0000-0002-2464-8712

# REACTIVE ION ETCHING OF THIN $NBSE_2$ FILMS FOR HIGH-PERFORMANCE SUPERCONDUCTING DEVICE DEVELOPMENT

**A. N. Lyubchak [1,2]✉, N. A. Titova [1], K. V. Shein [1,2], E.V. Zharkova[3], P. I. Bondareva [1], I.A. Gayduchenko[2], and G.N. Goltsman[1,2]**

[1] Moscow Pedagogical State University, Moscow, Russia;

[2] National Research University Higher School of Economics, Moscow, Russia;

[3] Programmable functional materials lab, Brain and Consciousness Research Center, Moscow, Russia.

✉ anlyubchak@miem.hse.ru

**Abstract.** We report on the use of reactive plasma etching in sulfur hexafluoride (SF6) to etch thin superconducting films of niobium diselenide (NbSe2). The thin flakes were mechanically detached from a bulk single crystal on polydimethylsiloxane (PDMS), and wire fabrication was achieved through electron beam lithography and reactive plasma etching. By utilizing reactive plasma etching in SF6, we were able to significantly reduce the technological route by one step, as hexagonal boron nitride (hBN) was removed in SF6, allowing us to produce a wire pattern in a single etching process. Wires with different widths, ranging from 0.1 to 1μm , were obtained. Our results demonstrate the feasibility of using reactive plasma etching in SF6 for the fabrication of thin superconducting films of $NbSe_2$, offering a promising approach for the development of high-performance superconducting devices.

**Keywords:** thin films, reactive plasma etching, flake.

**Funding:** We acknowledge funding from RSF project № 21-72-10117.

## Introduction

Two-dimensional superconductors have gained significant interest in recent years due to their potential applications in a wide range of fields, from quantum circuits[1] to the development of a new generation of quantum detectors[2,3]. Among the various two-dimensional superconductors, transition metal dichalcogenides (TMDs) have received particular attention. NbSe2, a member of the TMD family, exhibits superconductivity up to one atomic layer[4]. However, when attempting to create samples with dimensions ranging from 0.1 to 0.5 μm, degradation[5] of the material has been observed. Therefore, it is crucial to explore new possibilities for structuring $NbSe_2$ thin films to enable the development of high-performance superconducting devices.

## Materials and Methods

Two-dimensional crystals were obtained by mechanical exfoliation on polydimethylsiloxane (PDMS) with adhesive tape. $NbSe_2$ crystals are transferred to the tape from which the chips will be peeled onto the polymer. To peel off the flakes, the PDMS must be pressed firmly against the selected area on the adhesive tape and torn off sharply. Next, search for suitable two-dimensional crystals on the surface of the PDMS. Figure 1 shows photos of flakes after laying on a $SiO_2$/Si substrate.

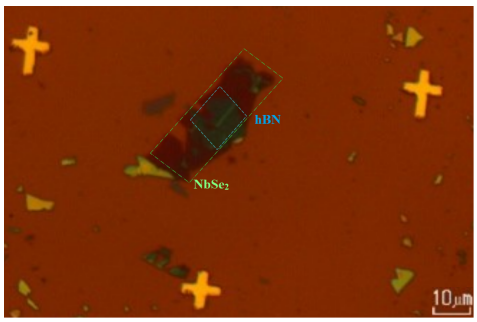


Fig. 1.Image of NbSe2 flakes on a SiO2/Si substrate with thickness of 15 nm

The first etching in SF6 is necessary to clean the surface of niobium diselenide from dirt before applying metal contacts to the flake. To do this, windows with a width of 0.5 μm and a length of 1 μm were opened at the contact points after electron beam lithography. We studied the effect of the contact material on the contact resistance. So we used several options for metallization of gold, aluminum and vanadium. The second etching in SF6 was aimed at giving the samples the necessary wire geometry. We have produced several wires with a width from 100 nm to 1 μm.

## Results and Discussion

In this study, we were able to achieve a significant reduction in the width of the samples through the use of plasma etching without loss of film quality. Specifically, we were able to reduce the width of the samples from a few units of micrometers to hundreds of nanometers. The reduction in sample width was achieved through the optimization of the plasma etching conditions. Additionally, we successfully improved the manufacturing technology of contacts to samples. Through the utilization of a cleaning process, we were able to significantly reduce the contact resistance from kOhm to 8 Ohms. Our results demonstrate that the cleaning process played a crucial role in improving the performance of the contacts. Our results suggest that the use of plasma etching is a promising approach for the reduction of sample width and the fabrication of high-performance contacts.

## Conclusion

In these theses, we propose to use reactive plasma etching of thin superconducting $NbSe_2$ films in SF6. This method of giving geometry to samples allows you to reach a wire width of several hundred nanometres. Also, the advantage of such a solution is to reduce the technological route by 1 step, since the hBN is removed in SF6, which will make it possible to produce a wire drawing in one etching process. Furthermore, we believe that our approach can be extended to the fabrication of other thin-film superconductors, which would pave the way for the development of advanced superconducting devices. Additionally, the use of reactive plasma etching in SF6 can potentially reduce the fabrication time and costs associated with the production of superconducting devices, making it a promising technique for future research and development.

## Acknowledgments

The reported study was funded by RSF, project number 21-72-10117.

## REFERENCES

1. **Wang, J. I., Yamoah, M. A., Li, Q., Karamlou, A. H., Dinh, T., Kannan, B., Braumüller, J., Kim, D., Melville, A.J., Muschinske, S.E., Niedzielski, B.M., Serniak, K., Sung, Y., Winik, R., Yoder, J.L., Schwartz, M.E., Watanabe, K., Taniguchi, T., Orlando, T.P., Gustavsson, S., Jarillo-Herrero, P., Oliver, W. D.**, Hexagonal boron nitride as a low-loss dielectric for superconducting quantum circuits and qubits, Nature materials. 21(4) (2022) 398-403.
2. **Charaev, I., Bandurin, D.A., Bollinger, A.T., Phinney, I., Drozdov, I., Colangelo, M., Butters, B., Taniguchi, T., Watanabe, K., He, X., Bozovic, I., Jarillo-Herrero, P., Berggren, K.**, Single-photon detection using high-temperature superconductors. Nat. Nanotechnol. (2023).
3. **Orchin, G. J., De Fazio, D., Di Bernardo, A., Hamer, M., Yoon, D., Cadore, A. R., Goykhman, I., Watanabe, K., Taniguchi, T., Robinson, W. A., Gorbachev, R. V., Ferrari, A. C., Hadfield, R. H.**, Niobium diselenide superconducting photodetectors, Applied Physics Letters. 114(25) (2019) 251103.
4. **El-Bana, M. S., Wolverson, D., Russo, S., Balakrishnan, G., Paul, D. M., Bending, S. J.**, Superconductor Science and Technology. 26(12) (2013) 125020.

5. **Tomori, H., Hoshi, N., Inoue, D., Kanda, A.,** Influence of microfabrication on superconducting properties of exfoliated thin films of layered superconductor NbSe2: reactive ion etching, In Journal of Physics: Conference Series. 1293(1) (2019) 012005.

# Modeling of the dynamic current-voltage characteristic of micro-arc oxidation

**O A Melnikov, P E Golubkov, E A Pecherskaya, G V Kozlov, V S Alexandrov, J V Shepeleva**

[1] Penza State University, Penza, Russia
pea1@list.ru

**Abstract**. The dynamic current-voltage characteristics of the micro-arc oxidation process were modeled by approximating the experimental curves. The dependences of the coating resistance, the ignition and quenching voltage of microdischarges on the treatment time, current density and concentration of electrolyte components are revealed. The simulation results can be used to develop a digital twin of the microarc oxidation process.

## 1. Introduction

Currently, digital twins, which include mathematical models that reflect the operation of each node in the technological chain are increasingly used for process control. For traditional industries (for example, engineering), such models are well known. For new technological processes, the task of developing digital twins is much more difficult, since there is no mathematical description of their "components". Thus, the micro-arc oxidation process (MAO) is distinguished by the interdisciplinary nature of the occurring phenomena, as a result of which the fundamental theory of this process has not yet been developed (the existing mathematical models describe only certain classes of phenomena) [1]. Therefore, modeling of the external characteristics of this process, which can be measured in practice, is of great practical importance. Thus, a large number of works are devoted to the study of the forming curve (the dependence of the maximum voltage on the processing time), which reflects the mechanism of oxide coating growth on a valve metal substrate [2]. At the same time, much less attention is undeservedly paid to the study of dynamic current-voltage characteristics (CVCs), which are also informative [3]. In particular, dynamic current-voltage characteristics make it possible to determine the electrical resistance and, consequently, the thickness of the formed coatings, as well as to study the electrical characteristics of microdischarges, which is one of the unsolved problems of the MAO process. Thus, modeling the dynamic current-voltage characteristics of the MAO process is an urgent scientific problem.

## 2. Materials and Methods

Oxide coatings samples were obtained on AD31T1 aluminum alloy substrates 23x15x1.5 mm in size. MAO processing was carried out on an automated laboratory setup in the anode-cathode mode at a sinusoidal current with a frequency of 50 Hz at current densities of 10.88; 13.99; 17.10; 20.21; 23.32 $A/dm^2$ in an electrolyte containing 0.5 g/l NaOH and 80, 90, 100 and 110 g/l $Na_2SiO_3$. The processing time was 60, 120, 240, 420 s. At each of these time moments, the current and voltage oscillograms in the galvanic cell (two periods) were measured, on the basis of which the dynamic CVCs were built.

## 3. Results and Discussion

Approximation of the anodic and cathodic ascending and falling CVC branches was performed by functions of various types (polynomial, exponential, hyperbolic tangent, etc.) in order to determine the best form of the approximating curve (its smallest deviation from the experimental dependence). As an example, Figure 1 shows the results of the approximation of the sections of microdischarges of the anode ascending branch of the CVC. A similar approach was previously used in the study of hysteresis loops of ferroelectrics [4] and was chosen because the dynamic CVC characteristics also exhibit hysteresis due to an increase in the resistance of the oxide coating with time. It has been found that the dynamic current-voltage characteristic of the MAO process is approximated by an exponential function (with the exception of microdischarge sections), which is quite reasonable due to the presence of the valve effect in the "metal-oxide-electrolyte" system. Based on the obtained approximating functions, the dependences of the coating resistance, ignition and quenching voltage of microdischarges on the treatment time, current density, and $Na_2SiO_3$ concentration in the electrolyte were revealed.

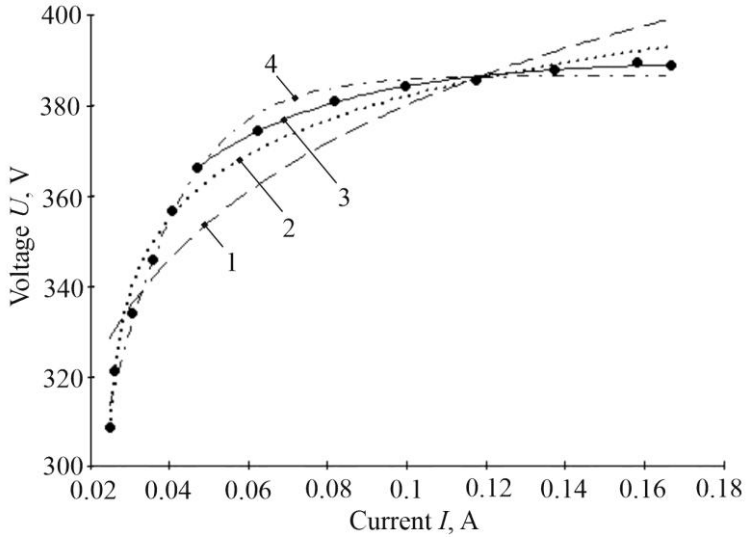


Figure.1. Approximation of the anode ascending branch of the CVC (microdischarges section): 1 – exponential function; 2 – logarithmic function; 3 – exponential function; 4 - hyperbolic tangent

## 4. Conclusion

Thus, modeling of dynamic current-voltage characteristics is an effective tool for studying and controlling the MAO process. The results of the study can be used in the development of software for the digital twin of the MAO process.


## Acknowledgments

The work was supported by the grant of the Ministry of Science and Higher Education of the Russian Federation № 1022041100284-5-2.3.1. «Fundamentals of the digital twin of the technological process of forming oxide coatings with specified properties by microarc oxidation» (FSGE-2023-0005).


## References


[1] Clyne T W and Troughton S C 2018 *Int. Mater. Reviews* **64(1)** 1-36

[2] Wang X and Zhang F 2022 *Trans. Nonferrous Met. Soc. China* **32** 2243−2252

[3] Zhu L, Ke X, Li J, Zhang Y, Zhang Zh and Sui M 2021 *Surf. and Interf.* **25** 101186

[4] Pecherskaya E A, Zinchenko T O, Golubkov P E, Pecherskiy A V, Fimin A V and Nikolaev K O 2018 *Moscow Workshop on Electronic and Networking Technologies (MWENT-2018)* 8337181

# Jamming transition and micellization in robotic swarms

**A. A. Molodtsova** [1✉], **M. K. Buzakov** [1], **A. D. Rozenblit** [1], **V. A. Smirnov** [1], **D. V. Sennikova** [1], **V. A. Porvatov** [2], **O. I. Burmistrov** [1], **E. M. Puhtina** [1], **A. A. Dmitriev** [1], **N. A. Olekhno** [1]
[1] School of Physics and Engineering, ITMO University, 197101 Saint Petersburg, Russia
[2] University of Amsterdam, 1098 XH Amsterdam, Netherlands
✉a.molodtsova@metalab.ifmo.ru

**Abstract.** In the present work, we explore experimentally two different phase transitions in active matter systems, i.e., large ensembles of particles that can independently produce motion, implementing them with the help of robotic swarms. The first is the *jamming transition* between a liquid-like state when particles can move and a solid-like state when particles form a rigid body, and the second is the formation of micelles by such active particles. For the jamming transition, we experimentally determine the critical packing density corresponding to such a transition and critical exponents characterizing power-law behavior of different physical quantities. Furthermore, we consider a micellization of teardrop-shaped robots with a broken inversion symmetry and evaluate the order parameter based on experimental data.

**Keywords:** phase transition, jamming, micellization, active matter, self-propelled particles, self-organization, swarm robotics.

## Introduction

Active matter physics is a fascinating field that explores ensembles of particles capable of converting internal or ambient energy into a directed motion. Examples of such non-equilibrium systems range from flocks of birds and schools of fish [1] to bacterial colonies [2] and colloidal micro-particles [3]. In this work, we focus on robotic swarms [4], which offer greater control over parameters of individual particles and offer more freedom in conducting experiments compared to living systems. By studying such active matter systems, we can gain insights into fundamental principles governing the behavior of complex systems and develop new technologies for applications ranging from robotics to drug delivery.

## Results and Discussion

*Jamming transition*. We start with studying the phase transition between the states of a moving “liquid” and a rigid “solid” in a system of circular-shaped robots placed in a restrictive circular barrier.

Each robot consists of a circular plastic lid and a matching base, with a circle of elastic bristles attached at the bottom. The vibration motor located at the circuit board inside the robot produces a vibration which is converted to the robot's rotation by elastic bristles. During the experiments, we study the motion of a system of 20 robots with clockwise (CW) chirality and 20 robots with counter-clockwise (CCW) chirality for different diameters of a restrictive barrier. The results are averaged over three different initial arrangements of robots in the barrier. To track the system’s motion, we capture it using a video camera and extract the positions and angular orientations of all robots using the OpenCV software package.

We demonstrate that the dependence of the average number of robots $\xi$ in connected clusters on the filling density of the system $\Phi$ follows a power law $\sim|\Phi - \Phi_c|^{\alpha}$, Fig.1(a). When the filling density reaches the critical value $\Phi_c = 0.76$ corresponding to the barrier diameter $D = 40.25$ cm, a jamming transition takes place, where the mobility of individual robots decreases sharply, and the swarm of robots turns from the active "liquid" into a solid. From our experimental data, the critical exponent $\alpha = -0.8$ with such a transition. In turn, the average angular velocity of rotation of robots follows a power law $\sim|\Phi - \Phi_c|^{\beta}$ with a critical exponent $\beta = 0.5$. We also studied different ratios of CW- and CCW-rotating robots to better understand the effects of system's composition.

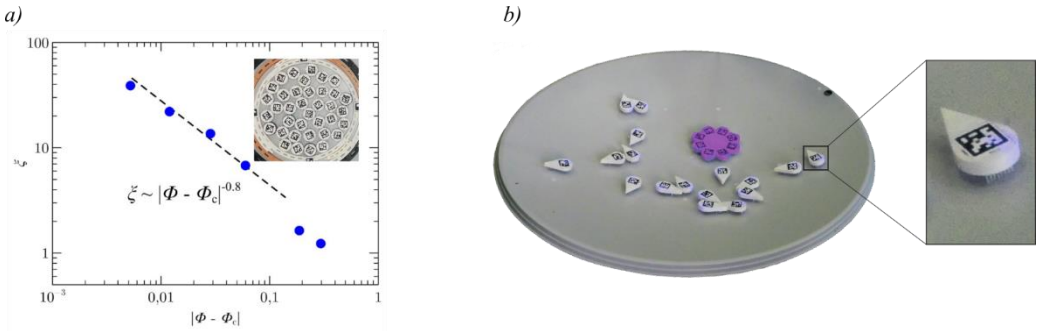


Figure 1. (*a*) Mean number of robots in a connected cluster $\xi$ for different filling ratios $|\Phi - \Phi_c|$. Inset demonstrates the experimental setup. (*b*) A swarm of robots in a parabolic dish featuring a micelle.

*Micellization.* Next, we examine swarms of teardrop-shaped robots with pointed noses and broken inversion symmetry, which were theoretically predicted to form micelles [5]. This phenomenon is associated solely with the interplay of active motion and symmetry breaking of particles, rather than with a shift in charge distribution density like in surfactants, which are also capable of forming micelles.

In this series of experiments, the robots were designed similarly to the previous scenario, but with a drop-shaped bodies, Fig.1(b). The robots' elastic bristles were arranged orthogonally to the motor axis, allowing robots to self-propel forward upon a vibration. During our experiments, we investigated the order parameter and proposed a formula for its calculation. The system had several variable parameters, including the number of robots, the position of their center of mass, the average velocity of the robots, which was adjusted by changing the pulse modulation width of the vibration motor, and the friction coefficient between side surfaces of the robots. To ensure statistical accuracy, we repeated each set of parameters five times. Our experiments reveal that micellization occurs in systems with the center of mass shifted to the nose of the robot, while there is no micellization when the center of mass is closer to the robot's center. Additionally, micelles are not formed at low filling densities of the plate with robots and at low velocities of robot's motion. Comparing the evaluated order parameters for different values of friction between robots, we found that greater friction leads to more efficient micelle formation.

## Conclusion

In this work, we perform experimental studies with swarms of moving robots that reveal the jamming phase transition occurring at the critical packing density of $\Phi_c = 0.76$, where both cluster size and angular velocities of robots experience rapid changes that follow power laws. This study is the first to experimentally determine the values of critical density and critical exponents for the onset of the jamming transition in a system of self-rotating robots. The second study examines the time dependencies of the proposed order parameter in swarms of self-propelled robots with broken inversion symmetry. By altering system characteristics such as friction, robot's velocity, and filling density, the efficiency of micelle formation can be controlled. Our study offers insights into the behavior of robot clusters and provides insights on controlling micelle formation efficiency.

## REFERENCES

1. **Filella A, Nadal F, Sire C, Kanso E, Eloy C.**, Model of Collective Fish Behavior with Hydrodynamic Interactions, Phys. Rev. Lett., 2018, Vol. 120, p. 198101.
2. **Mathijssen AJTM, Guzmán-Lastra F, Kaiser A, Löwen H.**, Nutrient Transport Driven by Microbial Active Carpets, Phys. Rev. Lett., 2018, Vol. 121, p. 248101.
3. **Villa, K., Pumera, M.**, Fuel-free light-driven micro/nanomachines: Artificial active matter mimicking nature, Chemical Society Reviews, 2019, Vol. 48, p. 4966-4978.
4. **L. Giomi, N. Hawley-Weld, and L. Mahadevan**, Swarming, swirling and stasis in sequestered bristle-bots, Proceedings of the Royal Society A: Mathematical, Physical and Engineering Sciences, 2013, Vol. 469, p. 20120637.
5. **T. Kruglov and A. Borisov**, Micellisation and aggregation of self-propelled hard circulangles, particles 2021. URL https://www.scipedia.com/public/kruglov_borisov_2022a.

# ZnO-PDMS based pressure sensors

**A. V. Nikolaeva [1✉], V. M. Kondratev [1, 2], S. A. Kadinskaya[1,2], D. E. Markina[1], F. I. Zubov[1], F. M. Kochetkov[1], A. D. Bolshakov [1, 2]**

[1] Alferov University, Saint Petersburg, Russia

[2] Moscow Institute of Physics and Technology, Moscow, Russia

✉nikalex2000@bk.ru

**Abstract.** The work is devoted to the synthesis of mechanical pressure sensors based on zinc oxide. The correlation between the mechanical load applied to the sensor and its electrophysical characteristics is shown. The results of the work are of interest for the producing of pressure sensors, in particular for miniature portable flexible health monitoring systems.

**Keywords:** ZnO, PDMS, sensor.

**Funding:** The Ministry of Science and Higher Education of the Russian Federation (Grant FSRM-2023-0009). The Ministry of Science and Higher Education of the Russian Federation (agreement 075-03-2023-106, project FSMG-2021-0005).

## Introduction

Low-dimensional structures of various compounds, in particular quasi-1-D [1] and 0-D [2] are widely used for photonic [3], sensor [4] and electronic applications [5]. Zinc oxide (ZnO) is a chemically stable, easy to synthesize and non-toxic large band gap semiconductor material (Eg=3.36 eV at room temperature) with a wurtzite crystal structure [3,4,6]. In particular, zinc oxide nanowires (NWs) have received an incredible amount of attention due to its eminient semiconducting and piezoelectric properties. The addition of zinc oxide (ZnO) fillers into a flexible polymer matrix has emerged as potential piezocomposite materials that can be used for applications such as energy harvesters and pressure sensors. Poly(dimethylsiloxane) (PDMS) as a material for polymer matrix has attracted immense interest in a wide range of fields including electronics, medical devices, adhesives, robotics and coatings due to its interesting properties such as flexibility, hydrophobicity, chemical stability, biocompatibility and high resistance to thermal and thermo-oxidative degradation in a wide temperature range [7,8]. This work is devoted to the synthesis of ZnO nanostructures via low-temperature hydrothermal method and the fabrication of mechanical pressure sensors based on them.

## Materials and Methods

The ZnO nanowires had synthesized via low-temperature hydrothermal method on the surface of the ceramic substrate with applied interdigital gold contacts. The ZnO nanowires were encapsulated in PDMS membrane by G-coating technique followed by attaching the top electrode of the same type and PDMS polymerization. The resulting structure was called a mechanical pressure sensor. The comparative sensor was fabricated using the same manufacturing protocol, only using a spin-coating technique instead of G-coating technique to apply PDMS to the ceramic substrate without ZnO NWs. Both sensors were studied by LCR meter (Keysight Technologies, USA) in terms of changes in the electrical capacitance at various weight loads.

## Results and Discussion

The fabricated sensor was subjected to different weight load ranges varied from 0 to 4512 g and its change in capacitance was measured as shown in Fig.1.

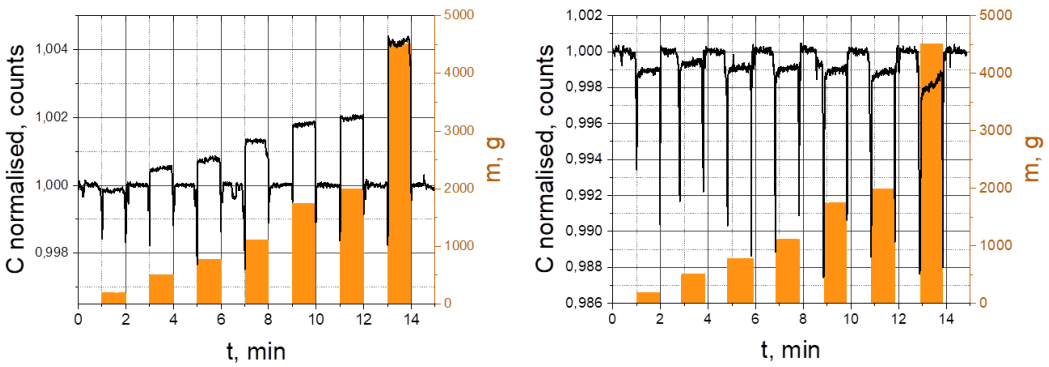


*a)* *b)*

Fig. 1. Change in capacitance of the sensor with ZnO NWs (*a*) and without ZnO NWs (*b*): step response under various weight loads varied from 0 to 4512 g

## Conclusion

In this work, we presented ZnO-based capacitive pressure sensor and investigated the effect of ZnO NWs on the output.

The results of the work are of interest for the producing of pressure sensors, in particular for miniature portable flexible health monitoring systems.

## REFERENCES


1. **Dubrovskii, V. G., Timofeeva, M. A., Tchernycheva, M., & Bolshakov, A. D.** (2013). Lateral growth and shape of semiconductor nanowires. Semiconductors, 47(1), 50–57.

2. **Sapunov, G. A., Fedorov, V. V., Koval, O. Y., Sharov, V. A., Dvoretckaia, L. N., Mukhin, I. S., & Bolshakov, A. D.** (2019). Synthesis and optical characterization of GaAs epitaxial nanoparticles on silicon. Crystal Growth & Design.

3. **Kuznetsov A, Roy P, Kondratev V M, Fedorov V V, Kotlyar K P, Reznik R R, Vorobyev A A, Mukhin I S, Cirlin G E, Bolshakov A D** / Anisotropic Radiation in Heterostructured “Emitter in a Cavity” Nanowire // Nanomaterials 2022, 12(2), 241.

4. **Kondratev, V.M.; Morozov, I.A.; Vyacheslavova, E.A.; Kirilenko, D.A.; Kuznetsov, A.; Kadinskaya, S.A.; Nalimova, S.S.; Moshnikov, V.A.; Gudovskikh, A.S.; Bolshakov, A.D.** Silicon Nanowire-Based Room-Temperature Multi-Environment Ammonia Detection. ACS Appl. Nano Mater. 2022, 5, 9940–9949.

5. **Kadinskaya S. A., Kondratev V. M., Kindyushov I. K., Kuznetsov A. and Punegova K. N.**, "Hydrothermal ZnO-based Nanostructures: Geometry Control and Narrow Band UV Emission," 2022 Conference of Russian Young Researchers in Electrical and Electronic Engineering (ElConRus), 2022, pp. 958-961.

6. **Kadinskaya S A, Kondratev V M, Kindyushov I K, Koval O Y, Yakubovsky D I, Kusnetsov A, Lihachev A I, Nashchekin A V, Akopyan I K, Serov A Y, Labzovskaya M E, Mikushev S V, Novikov B V, Shtrom I V, Bolshakov A D /** Deep-Level Emission Tailoring in ZnO Nanostructures Grown via Hydrothermal Synthesis // Nanomaterials 2023, 13, 58.

7. **Mata, A.; Fleischman, A.J.; Roy, S.** Characterization of Polydimethylsiloxane (PDMS) Properties for Biomedical Mi cro/Nanosystems. Biomed. Microdevices 2005, 7, 281–293.

8. **Jin, X.; Deng, M.; Kaps, S.; Zhu, X.; Holken, I.; Mess, K.; Adelung, R.; Mishra, Y.K.** Study of Tetrapodal Zno-Pdms Composites: A Comparison of Fillers Shapes in Stiffness and Hydrophobicity Improvements. PLoS ONE 2014, 9, e106991.

# Study of heterogeneous structures deposition on ion-exchange membranes

**M. D. Novichkov** [1✉], **S. A. Gurin** [1], **S. A. Nesterov** [2], **D. A. Shelakhaev** [2], **E. A. Pecherskaya** [2], **Yu. V. Shepeleva** [2]

[1] Joint-stock company "Scientific Research Institute of Electronic-Mechanical Devices", Penza, Russia;

[2] Federal State Budgetary Educational Institution "Penza State University", Penza, Russia

✉novichkov1998maks@gmail.com

**Abstract.** The formation process of a heterogeneous catalytic coating on the surface of ion-exchange membranes was studied in this work. It has been determined that the application of the entire catalyst volume by the thermal vacuum deposition method leads to the thermal membrane degradation and the continuous surface dusting, which leads to the proton conductivity loss. The use of the chemical deposition method results in a highly porous coating, but with low strength and durability. A combined method for obtaining a heterogeneous catalytic coating is proposed. The modes influence of obtaining the first coating layer on its properties is studied. The parameters characterizing the first coating layer, as well as the optimal values of these parameters, are determined.

**Keywords:** Heterogeneous structure, ion exchange membrane, electrolysis, hydrogen production, catalyst, precipitation.

**Funding:** The work was carried out within the framework of project No. 0748-2020-0013 "Scientific principles of the formation of heterogeneous structures by methods of physico-chemical dispersion" (state assignment to the university in the field of scientific activity. The customer is the Ministry of Science and Higher Education of the Russian Federation).

## Introduction

The use of polymer electrolytic membranes (PEM) in its original form, the process productivity is low, which requires the use of a catalyst. The intensification degree of the electrolytic process, in turn, significantly depends on its properties and structure. It was shown in [1, 2] that the implementation of the catalyst in the form of nanosized particles on the surface of a FEM is the most efficient.

## Experimental technique

The objects under study are catalytic coatings on the surface of membranes obtained by the method of thermal vacuum evaporation of platinum or palladium using a UVN-71P-3 setup. Variable parameters include: current on the evaporator ( variation range: from 200 to 600 A) and deposition time ( variation range: from 20 to 600 s)with the subsequent method of chemical deposition of platinum from a solution of H2PtCl6 or palladium from a solution of PdCl2 with constant parameters.

## Results and Discussion

The study of membranes obtained by the combined method showed that the catalytic layer has a porous structure that does not prevent the protons transport to the membrane surface. Fig. 1 and 2 show the results of energy dispersive analysis on PEM. According to the obtained total spectrum of X-ray energy dispersive analysis (Fig. 1), there are pronounced peaks of both platinum of the active catalyst layer and fluorine of the ion-exchange membrane with a minimum amount of impurities. Therefore, it can be concluded that the catalytic nanostructured coating did not completely cover the membrane structure and fully retained the characteristics and functions performed by it.

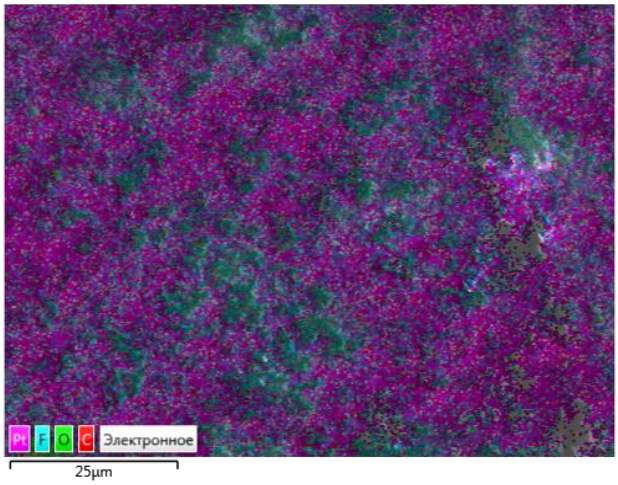


Figure 1. Multilayer spectral map

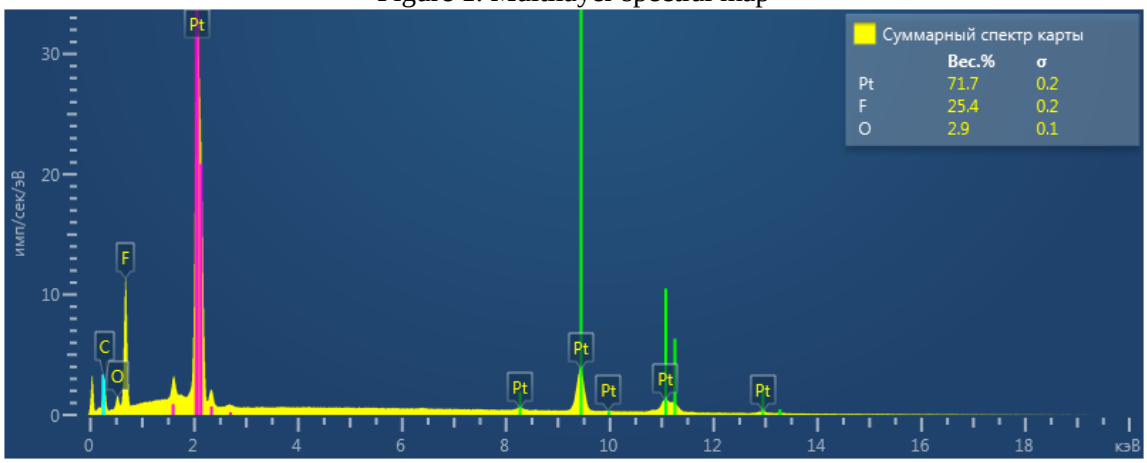


Figure 2. X-ray energy dispersive analysis of an ion-exchange membrane with a catalyst obtained by thermal evaporation in vacuum followed by chemical precipitation.

The stated assumption is confirmed by a significant increase in the hydrogen yield of about 5 times compared with the coating obtained in gentle modes by the vacuum evaporation method.

## Conclusion

The parameters of the first layer of the catalytic heterogeneous coating, at which a high efficiency of the catalyst is achieved, which is expressed in an increase in the maximum current strength in the circuit up to 5 A at a voltage of 4 V were revealed. This is a higher indicator compared to competitive technologies [3–5].

## REFERENCES

1. **A.B. Yaroslavtsev, Y.A Dobrovolsky, N.S Shaglaeva, L.A. Frolova, E.V.Gerasimova, E.A.Sanginov**., Advances in Chemistry. 2012. V. 81. No. 3. Pp. 191-220.

2. **M.Y. Zakharchenko, A.V. Kochetkov, P.M. Salov, O.V. Zakharov**., Materials Today: Proceedings. 2021 Vol. 38.Pp. 1866-1870. DOI: 10.1016/j.matpr.2020.08.488.

3. RF patent No. 2362238 IPC H01M 4/00

4. RF patent No. 2414020 IPC H01M 4/86

5. RF patent No. 2595900 IPC B01J 37/34

# Investigation of the modal composition in microstructured fibers with six cores

**V. M. Pilipova[1]✉, G. A. Pchelkin[1] and V. V. Davydov[1, 2]**
[1] The Bonch-Bruevich Saint Petersburg State University of Telecommunications, Saint Petersburg, Russia;
[2] Peter the Great Saint-Petersburg Polytechnic University, Saint Petersburg, Russia.
✉ valeriiapilipova@gmail.com

**Abstract.** In this article, research and development of microstructured quartz photonic fiber with six cores and chirality are presented. The work demonstrates the latest achievements in the field of fiber-optic technology, as well as their possible applications for improving the performance and stability of 5G and future 6G networks, contributing to the development of the Internet of Things infrastructure and ensuring reliable communication between various devices. The process of creating such a fiber, its properties, and advantages over traditional fibers are described.

**Keywords:** Microstructured optical fiber, chirality, core composition, optical vortices

## Introduction

Fiber-optic communication lines (FOCL) are a key component of modern telecommunication systems. The development of this technology is closely related to providing greater bandwidth and less signal attenuation [1]. With the improvement of the Internet and the constant increase in the volume of transmitted data, the relevance of these problems only grows. One approach to increasing the bandwidth of FOCL is dense wavelength division multiplexing (DWDM) [2]. It allows the transmission of multiple channels at different wavelengths through a single optical fiber. However, this approach has its limitations, and further reduction of the distance between carriers can lead to information loss or a sharp increase in signal attenuation. In this regard, researchers are actively working on the development of new technologies that can provide additional increases in FOCL bandwidth. A possible solution to the problem of increasing bandwidth and reducing losses in FOCL involves the use of microstructured fibers with a specific set of modes.

## Method

Research in the field of multimode fibers with 6 cores, made from high-alloy $GeO_2$ quartz glass with induced chirality, shows significant potential for improving bandwidth and reducing losses in fiber-optic communication lines. The main idea is to control and optimize the propagation of only three modes (LP01, LP11, LP21), which are necessary for stable transmission of large amounts of data with minimal losses.

To detect vortices and observe the merging of optical fields in chiral microstructured fibers with 6 cores, made from high-alloy $GeO_2$ quartz glass, a new and improved stand has been developed. This stand represents a significant improvement compared to previously used optical schemes, which had larger dimensions, losses during radiation passage, and increased temperature stabilization requirements.

## Results and Discussion

In Fig. 1, for examples of cleaved chiral microstructured fibers are presented, which were studied in the context of the distribution of optical radiation at the output. During the experiment, various parameters were investigated, including the twisting frequency $\omega_s$ and other process parameters.

The experiment demonstrated the possibility of merging the modal field in a microstructured fiber with 6 cores, made from high-alloy $GeO_2$ quartz glass with induced chirality.

*a*) *b*)

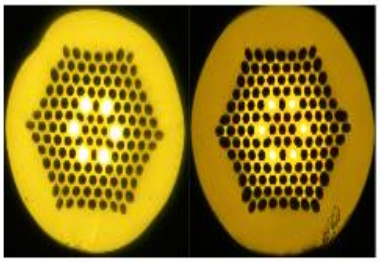

Fig. 1. Images of cross-sections of microstructured fibers with 6 cores. (a) Gradient refractive index profile, (b) step-index refractive index profile.

In Fig. 2 shows the transverse distributions at radiation of optical at output of low-mode microstructured optical fibers of the studied topology at various twisting frequencies and other technological parameters. The wavelength of radiation is 1550 nm.

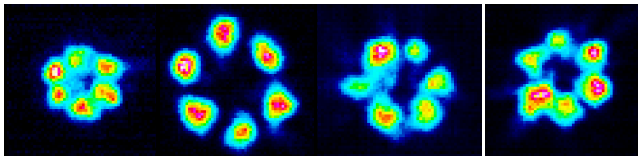

Fig. 2**.** The microstructured fibers with 6 cores: (a) laser beam profile of an optical fiber with a degree of chirality (from left to right) are determined of revolutions per minute (rp/m): 50, 100, 400, 500.

Thanks to these results, it is possible to improve the bandwidth and reduce losses in fiber-optic communication lines, which in turn contributes to the further development of telecommunication technologies and their effectiveness in various application areas. A microstructured fiber with the presented topology and a diameter of 125 micrometers was produced with various induced chirality: 50, 100, 400 and 500 rp/m.

## Conclusion

In this work, microstructured optical fibers with the presented topology are used, which are drawn with a diameter of 125 micrometers, corresponding to telecommunication standards.

The use of such microstructured fibers in fiber-optic communication lines can significantly improve their bandwidth and reduce losses, which will ultimately lead to the further development of telecommunication technologies. With the development of the Internet of Things, the increase in the number of mobile devices, and the penetration into the realm of 5G and even 6G communication, the need for more efficient and reliable communication technologies will continue to grow, making the development and implementation of microstructured fibers with a specified modal composition especially relevant.

## REFERENCES


1. **Bisyarin M. A., Kotov O. I., Hartog A. H., Liokumovich L. B. and Ushakov N. A.,** Influence of a variable Rayleigh scattering-loss coefficient on the light backscattering in multimode optical fibers. Applied Optics. 56(16) (2017) 4629–4635.
2. **Burdin V. A., Dashkov M. V., Demidov V. V., Zhukov A. E. and Bourdine A. V.,** New silica laser-optimized multimode optical fibers with extremely enlarged 100-μm core diameter for gigabit onboard and industrial networks, Fibers. 8(3) (2020) 18.

# Features of the construction photonic tensor cores for neural networks

**N. I. Popovskiy**[1] ✉, **V. V. Davydov**[1, 2], **V.Yu. Rud**[3]
[1] The Bonch-Bruevich Saint Petersburg State University of Telecommunications, Saint Petersburg, Russia;
[2] Peter the Great Saint-Petersburg Polytechnic University, Saint Petersburg, Russia;
[3] A.F. Ioffe Physicotechnical Institute, Saint Petersburg, Russia.
✉ nikitanikita24@mail.ru

**Abstract.** The demand for efficient and high-performance computing systems has led to the development of photonic-based technologies for machine learning. One of the key components of these systems is the photonic tensor core, which performs matrix operations at high speed and low power consumption. In this article, we review the features of photonic tensor cores and their construction for use in neural networks. We discuss the advantages of photonic-based technologies over traditional electronic-based systems, as well as the challenges in their implementation. We also highlight recent advancements in the development of photonic tensor cores for machine learning applications and their potential for achieving unprecedented levels of computational efficiency. This article provides insights into the development and application of photonic tensor cores for machine learning, which have the potential to revolutionize the field of artificial intelligence.

**Keywords:** photonic tensor cores, neural networks, optical computing, photonics, machine learning, deep learning, data processing.

## Introduction

Matrix operations on a general-purpose processor are performed serially and require continuous access to cache memory, which creates a bottleneck known as the "von Neumann bottleneck". Specialized architectures, such as Graphic Process Units (GPUs) and Tensor Process Units (TPUs), have been developed to reduce this bottleneck and enable advanced machine learning models. These architectures are designed with domain-specific optimizations, such as parallel processing for convolutions or Matrix-Vector Multiplications (MVM), allowing for the deployment of systolic algorithms unlike CPUs.

## Method of constructing photonic tensor cores

The advantages of using electromagnetic signals can be limited by optoelectrical and electro-optical transductions, as well as by accessing digital and nonvolatile memory repeatedly, which reduces operation speed and increases energy loss. To address these issues, an optimized photonic memory is needed for NN inference, where trained weights are rarely updated. A multi-state photonic memory device, consisting of $Ge_2Sb_2Se_5$ wires between two resonant rings, allows for entirely passive weighting functionality. Selective writing is achieved by changing the phase of the corresponding wires through local electrostatic heating, which modifies the wave-guide modal refractive index in a reversible process. This architecture offers great advantages for retaining information in a non-volatile fashion, providing a heterogeneously integrated optimized photonic memory.

The dot product engine performs the multiplication between two vectors, namely, between the ith row of the input matrix A and the jth column of the kernel B. In Fig.1, the ith row of the input matrix is given by WDM signals, which are modulated by high-speed (e.g., Mach–Zehnder) modulators. The jth column of the kernel matrix is loaded in the photonic memory by properly setting its weight states. Availing light-matter interaction with the phase- change memory, the inputs, opportunely spectrally filtered by micro-ring resonators (MRR), are weighted in a seemingly quantized electro-absorption scheme (i.e., amplitude modulation), thus performing element-wise multiplication. The element-wise multiplications are thence incoherently summed up using a photodetector, which amounts to a MAC operation (Dij).

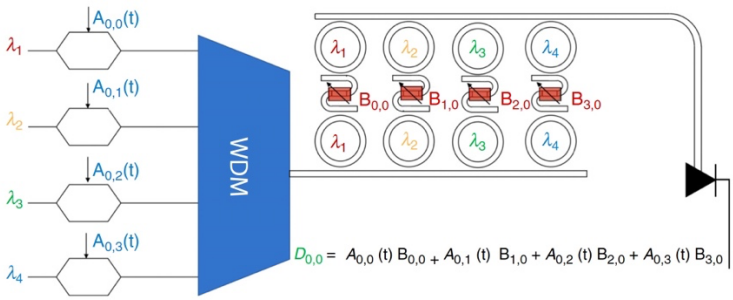


Fig. 1. Block diagram of the photonic tensor cores

## Results and Discussion

It should be noted that low-bit quantization of weights is possible during inference due to the robustness of the NN achieved through appropriate training. This results in efficient and accurate inference for low resolution quantized weights, especially for simple inference tasks at the network edge that do not require high-bit resolution. In comparison to GPUs and digital architectures, neuromorphic photonics are advantageous for specific applications that can utilize efficient light-matter interactions without domain conversion, resulting in lower overall power consumption and ns-fast inference. The proposed photonic engine is suitable for accelerating inference tasks in specific applications where obtaining a prediction in near real-time is essential, even at reduced accuracy, and where input data are already in RF or optical signal format, avoiding inefficient analog-to-digital conversion.

## Conclusion

In this research, a photonic tensor core unit is proposed for efficient and accurate inference tasks at the edge of a network. The unit relies on photonic multiplexed signals that are filtered and weighted using multi-state photonic memories based on $Ge_2Sb_2Se_5$ wires patterned on the waveguide. The photonic memories can be reprogrammed in parallel or can operate as a passive system with a preset kernel matrix. The architecture has a runtime complexity of O(1) and is limited only by the time of flight of the photon in the chip. No additional losses are introduced by the photonic memories, avoiding repeaters, and optical amplifiers. The concurrent development of new materials can enable the realization of engines based on the proposed scheme, leading to the realization of all-optical photonic tensor units that can significantly speed up intelligent tasks at the edge of the network without requiring electro-optic conversions and access to external memories.

## REFERENCES

1. **Popovskiy, N.I., Davydov, V.V., Rud, V.Y.,** Features of construction of fiber-optic communication lines with orthogonal frequency-division multiplexing, St. Petersburg Polytechnic University Journal. Physics and Mathematics. 15(3.2) (2022) 178-183

2. **Kozlova, T.I., Konovaltsev, M.I., Lebedev, R.S., Techko, O.L.,** Method for correcting the position of the laser beam, Photon - Express. 6(2021) 201-205

3. **Miscuglio, M.,** Photonic tensor cores for machine learning, Applied Physics Reviews. 7(2020) 031404-1-031404-10

4. **Danshi, W., Min, Z.,** Artificial Intelligence in Optical Communications: From Machine Learning to Deep Learning, Frontiers in Communications and Networks. 2(656786) (2021) 1-9

# A facile low-temperature approach for organics removal from $SiO_2$-CTAB mesoporous particles

**E. Y. Stovpiaga[1,✉], S. A. Grudinkin[1], D. A. Eurov[1], D. A. Kurdyukov[1]**
[1]Ioffe Institute, St Petersburg, Russian Federation
✉kattrof@gvg.ioffe.ru

**Abstract.** A simple, fast and efficient method has been developed for removing pore-forming organic substances from MCM-41 type materials without affecting their shape, structural and adsorption characteristics. The method is based on express annealing of the synthesized silica materials in vacuum at low temperatures.

**Keywords:** Mesoporous silica, template method, organics removal, CTAB, vacuum annealing.

**Funding:** This work was funded by the Russian Science Foundation, project no. 22-23-20104 and by the St. Petersburg Science Foundation, agreement no. 27/2022 (14.04.2022), https://rscf.ru/project/22-23-20104/.

## Introduction

MCM-41 type porous silica materials are actively studied owing to the wide range of their possible applications as adsorbents, in catalysis and biomedicine [1]. A template method is applied to obtain such materials with the use of micelles of alkylamines as a template. Control over the internal structure, particle and pore size is carried out by varying the synthesis conditions and the structure of surfactant template. The elimination of these organic templates from the pores is a crucial step in the synthesis of mesoporous silica materials. Thermal calcination is a common method for template removal in the laboratory due to high efficiency, easy operation, and requirement of simple equipment. The significant reduction of silanol concentrations happens during calcination (which renders the sample unsuitable for post-modification), besides, the structural shrinkage is invariably detected following template removal. In addition to the removal of organics by calcination, various post synthetic methods are also used to wash particles from surfactant in organic solvents under the action of ultrasound or microwaves [2]. As a rule, all of the above template removal methods include several successive stages, for example, washing, centrifugation, drying, etc., which significantly increases the time required to obtain the final product [2,3]. Thus, the development of a procedure for a fast, efficient, low-temperature and one-stage removal of the template from the pores of MCM-41 type particles is still a crucial task.

## Results and Discussion

In the present work, spherical mesoporous silica particles (MSP) with a diameter of 550±25 nm, synthesized by the template method using cetyltrimethylammonium bromide (CTAB) as a soft template, were selected as an object of study. The particle synthesis is described in detail in Ref. [4]. The removal of organics from the pores of MSP-CTAB particles was carried out in three different ways and then the structural characteristics of the resulting particles were compared. The first way was a traditional calcination of MSP at 550 °C in air for 6 h (MSP-a). In the second one organics were removed in two stages. The synthesized MSP particles were first washed in an alcoholic solution of HCl (0.01 M) for 10 h. Then the washed particles were annealed at 400 °C in air for 5 h (MSP-w). The third way to remove pore-forming substance was fast (within 1 h) annealing of particles at 300 °C in vacuum (MSP-vac).

The nitrogen adsorption and desorption isotherms of the MSP after removing of CTAB by different methods are shown in Fig.1a. For all the samples the adsorption isotherms have a step-like shape, which is typical of mesoporous materials. The specific surface area and pore volume values were found to be: 838 $m^2 g^{-1}$, 0.64 $cm^3g^{-1}$ for MSP-w; 822 $m^2 g^{-1}$, 0.54 $cm^3g^{-1}$ for MSP-a; 770 $m^2 g^{-1}$, 0.52 $cm^3g^{-1}$ for MSP-vac. Pore size distribution calculated by non-local density functional theory (NLDFT) for all the samples was 3.1±0.2 nm. It can be seen that the porosity characteristics of all types of particles are comparable.

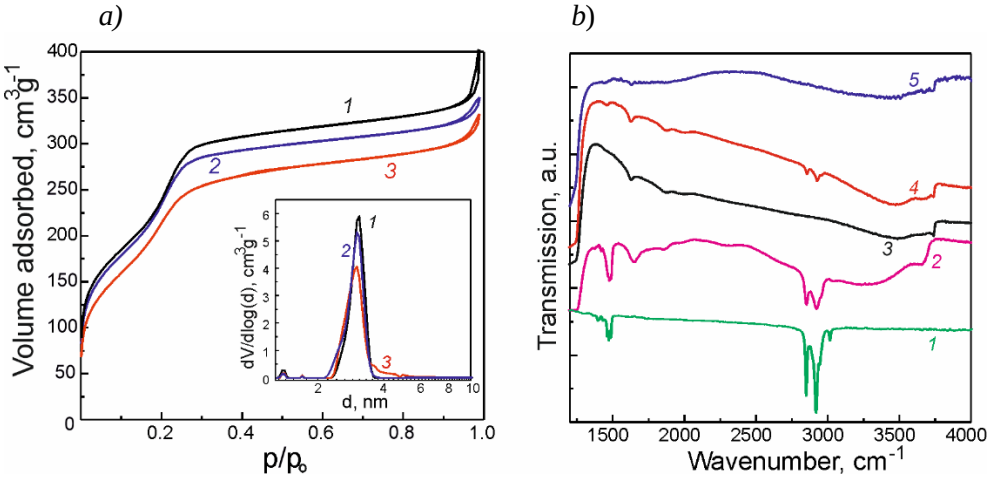


Fig. 1 (a) $N_2$ adsorption and desorption isotherms at 77 K and NLDFT pore size distribution (inset) for synthesized particles: MSP-w (*1*), MSP-a (*2*), MSP -vac (*3*). (b) FTIR spectra: (*1*) – bulk CTAB, (*2*) – as synthesized MSP-CTAB, (*3*) – MSP-w, (*4*) – MSP-vac, (*5*) – MSP-a.

Fig.1b shows the results of the FTIR study of silica particles right after the synthesis and after removal of CTAB by various methods. The band at 1630 $cm^{-1}$ present in the spectra of all MSPs corresponds to bending vibrations of H–O–H. The transmission spectra of the particles also contain a broad band at 3450 $cm^{-1}$ (Fig.1b, curves 2-5), to which OH stretching vibrations in hydrogen-bound molecules of physically adsorbed water mainly contribute. There is a weak broad band in the region 3650–3700 $cm^{-1}$ and the narrow band at 3745 $cm^{-1}$, which correspond to vibrations of terminal and single silanol groups, respectively. Thus, all types of particles contain surface hydroxyl groups, which allows for further functionalization. The absorption bands corresponding to the vibrations of carbon-containing organic groups are almost absent in the spectra of MSP-w (Fig.1b curve 3) and MSP-a (Fig.1b curve 5). At the same time, a set of weak absorption bands in the regions 1300-1500 $cm^{-1}$ and 2750-3025 $cm^{-1}$ is observed in the spectrum of MSP-vac (Fig.1b curve 4). These bands are attributed to the different vibrational modes of CH, $CH_2$, $CH_3$ and N-$CH_3$ groups characteristic of CTAB. The presence of these groups causes a slight decrease in the porosity of MSP-vac particles compared to MSP-w and MSP-a. According to the results of transmission electron microscopy and dynamic light scattering, the synthesized MSP-vac particles do not sinter during annealing in vacuum and are monodisperse and aggregatively stable.

## Conclusion

A method of low temperature vacuum annealing is developed for CTAB removal from as-synthesized mesoporous silica particles, which does not affect their size and porous structure. The proposed approach for the pore-forming template removal from MCM-41-like materials in vacuum is fast, facile and alternative to the thermal calcination and chemical treatment methods.

## Acknowledgments

The authors thank D.A. Kirilenko for TEM measurements.

## REFERENCES

1. **Tang F., Linlin L., Chen D.**, Mesoporous silica nanoparticles: synthesis, biocompatibility and drug delivery, Advanced Materials. 24 (12) (2012) 1504-1534.

2. **Ghaedi H., Zhao M.,** Review on template removal techniques for synthesis of mesoporous silica materials, Energy Fuels. 36 (2022) 2424-2446.

3. **Zanjanchi M., Jabariyan S.**, Application of ultrasound and methanol for the rapid removal of surfactant from MCM-41 molecular sieve, Journal of the Serbian Chemical Society. 79 (2014) 25-38.

4. **Trofimova E.Yu., Kurdyukov D.A., Yakovlev S.A., Kirilenko D.A., Kukushkina Yu.A., Nashchekin A.V., Sitnikova A.A., Yagovkina M.A., Golubev V.G.**, Monodisperse spherical mesoporous silica particles: fast synthesis procedure and fabrication of photonic crystal films, Nanotechnology. 24 (2013) 155601.

Conference materials
UDC
DOI: https://doi.org/10.18721/JPM.

# Effect of Al-CuO multilayer thermite structures thickness on combustion behavior

**M. E. Shiryaev[1]✉, R. M. Ryazanov[2], A. V. Sysa[2], E. A. Lebedev[1,2]**
[1] National Research University of Electronic Technology (MIET), Zelenograd, Moscow, Russia
[2] Scientific-Manufacturing Complex "Technological Centre", Zelenograd, Moscow, Russia
✉ shiryaevme@bk.ru

**Abstract.** Al-CuO multilayer thermite structures have shown potential for use in various fields such as soldering, reaction bonding, casing, and 3D assembly. The Al-CuO layers, with their high specific heat of combustion, have gained particular interest when compared to other compositions of thermite films. This study investigated the effect of the multilayer film thickness on the characteristics of the combustion reaction products. Experimental analysis revealed dependencies between the film thickness and the properties of the reaction products. The results demonstrated that changes in the thickness of the multilayer film significantly affect both the reaction and its products.

**Keywords:** multilayer structure, Al-CuO, thermite, combustion.

**Funding:** The study was supported by the Russian Science Foundation grant No. 22-29-01177, https://rscf.ru/project/22-29-01177/.

**Citation:**

Материалы конференции
УДК
DOI: https://doi.org/10.18721/JPM.

## Introduction

Thermite materials are a class of energy materials that release a large amount of energy during combustion. They consist of a metal and an oxide, which react exothermically to form a new metal and a new oxide. The reaction is highly exothermic and gives a temperature of several thousand degrees Celsius, which makes thermite materials useful for various applications, including welding, reaction bonding and the space industry [1-3].

The Al-CuO layers, with their high specific heat of combustion, have gained particular interest when compared to other compositions of thermite films. The control of the characteristics of the combustion reaction products, including the composition and morphology, is critical in many applications. Moreover, the ability to control the rate of propagation of the combustion front in wave-like thermite reactions can be crucial for certain applications.

In this study, we investigate the effect of the thickness of the multilayer Al-CuO film on the characteristics of the combustion reaction products and the rate of propagation of the combustion front.

## Materials and Methods

Multilayer thermite structures of Al-CuO were formed using the magnetron sputtering method on a substrate of sitall. The layers were prepared with different thicknesses of 2, 3, and 4 microns, which correspond to 20, 30, and 40 layers, respectively. A series of samples were prepared to investigate the effect of the thickness of the multilayer Al-CuO thermite structure on the characteristics of the combustion reaction products.

The initiation of the thermite reaction was carried out using a piezoelectric element, which delivered a mechanical impulse to the sample. The effect of the thickness of the multilayer Al-

CuO thermite structure on the character and velocity of the combustion front was investigated using high-speed video. The videos were recorded at a rate of 10000 frames per second, which allowed for accurate analysis of the combustion front. The effect of thickness on the characteristics of the reaction products was studied using a scanning electron microscope (SEM). The SEM images were analyzed to determine the morphology and composition of the reaction products.

## Results and Discussion

As a result of the study, it was determined that on samples with a thickness of 2 microns, the reaction products are evenly distributed over the surface, forming rare droplets, at 3 microns, the products are collected in large structures, and at 4 microns, the reaction products evaporate to a greater extent during combustion. It was also found that with an increase in the thickness of the film, the propagation velocity of the wave combustion front first increases and then decreases. The highest speed is achieved on a film with a thickness of 3 microns and is 10 m/s.

An increase in the overall thickness of the multilayer structure can lead to an increase in the temperature of the combustion front, and vice versa. If the reaction temperature exceeds the boiling point of one or more initial reagents or reaction products, then intense gas release occurs. On the other hand, if the reaction temperature is below the boiling point, then combustion proceeds without significant gas release and the reaction products are not separated from the substrate.

## Conclusion

In conclusion, the study investigated the effect of the thickness of multilayer thermite structures of Al-CuO on the characteristics of the combustion reaction products. The results showed that the thickness of the multilayer structure had a significant impact on both the characteristics of the reaction and its products. The high-speed video analysis revealed that the combustion front velocity increased with an increase in thickness, while the SEM analysis demonstrated a change in the morphology and composition of the reaction products. These findings provide valuable insights for the development and optimization of multilayer thermite structures for various applications.

## Acknowledgments

The study was supported by the Russian Science Foundation grant No. 22-29-01177, https://rscf.ru/project/22-29-01177/.

## REFERENCES

1. **Yang C., Hu Y., Shen R., Ye Y., Wang S., Hua T**. Fabrication and Performance Characterization of Al/Ti Multilayer Energetic Films. Advanced Materials Research, 557, (2014). 1782-1786.
2. **Zhu P., Li D., Fu S., Hu B., Shen R.** Improving reliability of SCB initiators based on Al/Ni multilayer nanofilms. The European Physical Journal Applied Physics, 63(1), (2013), 1-6.
3. **Zhu P., Shen R., Ye Y., Fu S., Li D.** Characterization of Al/CuO nanoenergetic multilayer films integrated with semiconductor bridge for initiator applications. Journal of Applied Physics, 113(18), (2013), 155-184.

# Study of the effect of solvents and surfactants on electrical properties of poly(3,4-ethylenedioxythiophene) polystyrenesulfonate films

**V. A. Pozdeev [1,2] ✉, A. V. Uvarov [1], A.S. Gudovskikh [1,2], A. A. Maksimova [1,2], E A Vyacheslavova [1]**

[1] St. Petersburg Alferov Academic University, St. Petersburg, Russia;

[2] St. Petersburg Electrotechnical University "LETI", St. Petersburg, Russia

✉pozdeev99va@gmail.com

**Abstract.** Non-ionic surfactants reduce the solution's surface tension, improving the wettability of hydrophobic substrates. Even 0.5% of Neonol can significantly affect the surface tension of the aqueous PEDOT:PSS solution on fused silica substrates. However, higher percentages of Neonol increase the electrical resistivity of the polymer layer.

**Keywords:** PEDOT:PSS, poly(3,4-ethylenedioxythiophene) polystyrene sulfonate, conductive polymer, surfactants, neonol, electrical resistance.

**Funding:** This work was supported by the Russian Science Foundation under grant number 23-22-00367

## Introduction

Poly(3,4-ethylenedioxythiophene) polystyrene sulfonate (PEDOT:PSS), is a type of conductive polymer that is utilized in various applications such as electroluminescent devices, organic field-effect transistors, organic light-emitting diodes, and various types of photovoltaic cells. Compared to other conductive polymers used in hybrid and organic solar cells, PEDOT:PSS has several advantages, including its advanced passivation effect, high conductivity, optical transparency, mechanical stability, and commercial availability [1,2]. One of the current problems is insufficient wetting of hydrophobic substrates such as silicon when using an aqueous solution of PEDOT:PSS, which leads to uneven deposition of the polymer coating. The addition of low-boiling solvents and non-ionic surfactants reduces the surface tension of the solution and increases the wettability of hydrophobic substrates with the solution [3].

## Materials and Methods

Polished fused silica wafers 400 μm thick were used as transparent dielectric substrates. A 1% aqueous solution (Sigma Aldrich, pH < 2.5) was used to form thin layers of the electrically conductive PEDOT:PSS polymer. To increase the wettability of the substrates, a non-ionic surfactant was added to the PEDOT:PSS aqueous solution in the form of a mixture of oxyethylated monoalkyl phenol derived from propylene trimers (Neonol AF 9-12 produced by Nizhnekamskneftekhim PJSC) at a volume concentration of 0.5% to 3%. Thin PEDOT:PSS films were deposited on the surface of fused silica substrates by spin-coating at 1000 rpm for 60 s. Immediately after application, the films were baked on a heating table at 130°C for 10 min. The layer thicknesses on the fused silica substrates were measured by contact profilometry on a sharp step between the surface of the layer and the substrate using an Ambios XP-1 profilometer. To measure the electrophysical properties using the Van der Pauw four-point probe method, 1 mm diameter and 500 nm thick silver contacts were thermally deposited onto the surface of the structures by vacuum evaporation. The contacts were arranged in a square shape with a side length of 1 cm. Based on the measurement results, the values of the sheet resistance and specific electrical resistance of thin PEDOT:PSS layers on the surface of fused silica with different surfactant concentrations were obtained.

## Results and Discussion

Transparent PEDOT:PSS films were evenly deposited on the surface of fused silica from an aqueous solution with Neonol concentrations from 0.5 to 3%, which made it possible to study their optical and electrophysical properties. An aqueous solution of PEDOT:PSS solution without the use of surfactants could not be applied to fused silica substrates due to poor wettability, which leads to the formation of separate droplets after the spin coating stage. With an increase in the percentage of neonol in an aqueous solution of PEDOT:PSS, the thickness of the layers at the spin coating stage increases, which is associated with a decrease in the surface tension of the solution. In this case, the optical transparency of the PEDOT:PSS layers on the fused silica surface does not

change significantly. There is also a gradual increase in the electrical resistivity of the layers with an increase in the percentage of surfactants (Fig.1), which negatively affects the conductive properties.

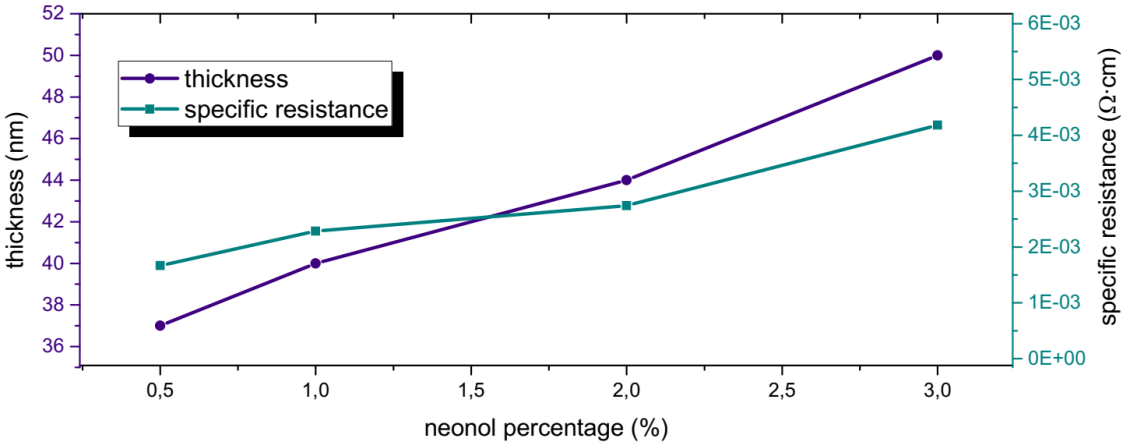


Fig. 1. Thickness and specific electrical resistance dependence on the percentage of neonol in solution

## Conclusion

Thus, the use of Neonol effectively affects the surface tension of an aqueous solution of PEDOT:PSS when applied to fused silica substrates even at a percentage of 0.5%. A further increase in the percentage of Neonol in solution increases the electrical resistivity, which worsens the conductive properties of thin layers of a transparent polymer. As a result, when applying layers of PEDOT:PSS on fused silica substrates, it is recommended to use neonol to wet the surface of hydrophobic substrates, but at concentrations of 0.5% or less.

## REFERENCES

1. **Z. Sun, Y. He, B. Xiong, S. Chen, M. Li, Y. Zhou, Y. Zheng, K. Sun,** and **C. Yang**, Angew Chem Int Ed 60, 5036 (2020). doi:10.1002/anie.201910629

2. **W. Cai, X. Gong,** and **Y. Cao**, Solar Energy Materials and Solar Cells 94, 114 (2010).doi:10.1016/j.solmat.2009.10.005

3. **K. Reuter, S. Kirchmeyer,** and **A. Elschner**, Handbook of Thiophene-Based Materials 549 (n.d.). doi:10.1002/9780470745533.ch14

# Properties of ultrathin epitaxial NbNx film on C-cut sapphire

**M.V. Shibalov, A.P. Sirotina, E.A. Pershina, A.A. Shibalova, A.M. Mumlyakov, N.V. Porokhov, M.A. Tarkhov**

Institute of Nanotechnology of Microelectronics of Russian Academy of Science, Leninsky Prospekt 32A, Moscow 119991, Russia

email: maxshibalov@gmail.com

**Abstract.** Here we report on the results of obtaining and study of epitaxial ultrathin superconductive films of niobium nitride grown on a C-plane sapphire substrate. The films were deposited from the metal-organic precursor using the plasma-enhanced atomic layer deposition. We employed X-ray diffraction, and high-resolution transmission electron microscopy techniques to study the structural properties of the films. We have also determined the quasiparticle diffusion constant, the coherence length, superconducting transition temperature and critical current density of the niobium nitride films.

**Keywords:** atomic layer deposition, niobium nitride, epitaxy, superconductivity, critical current density.

## Introduction

NbN is a type-II superconductor which superconducting transition temperature is close to 17 K. Thanks to the above, NbN is used to fabricate superconducting nanowire single-photon detectors (SNSPD) with quantum efficiency above 90% [1], photon number resolving (PNR) detectors [2], wide-range hot-electron bolometers (HEB) [3]. Extended defects, such as multiple grain boundaries of a polycrystalline film, may limit the critical current value $I_c$ [4], degrading the operational characteristics of detectors, for example, leading to temporary instability of a leading edge of an SNSPD pulse [5, 6]. That generated considerable interest of the research community in growing epitaxial NbN films on various single-crystalline substrates and epitaxial buffer layers with a lattice constant close to the lattice constant of the NbN.

## Materials and Methods

For the deposition we have chosen 2-in. wafers of sapphire substrate (0001) (C-plane). We used multistep atomic layer deposition process with TBTDEN precursor and two reactants. The reactants were $NH_3$ /Ar and $H_2$/Ar gas mixtures.

The structural analysis was carried out using the Empyrean diffractometer by Malvern Panalytical with Cu Kα1-radiation. The structure of the NbN film sample was investigated by HRTEM using the JEOL JEM-2100 Plus microscope at an accelerating voltage of 200 kV.

Magnetoresistance was measured using the four-point probe technique in the range of temperatures and magnetic field varying within the range of 0 to 7 T, applied in both parallel and perpendicular directions to the sample. The critical current was measured using Keithley 6221A precision low noise current source with two-point technique.

## Results and Discussion

Fig. 1 *a*) shows the experimental scanning curve (ω–2θ) near the sapphire symmetric reflection (0006). A (111) peak of NbNx and its satellites which only occur if the single crystalline film has a homogeneous composition in thickness and the coherent interface between film and a substrate are also shown in Fig. 1 *a*). Calculated curve is in a good agreement with the experimental one, which illustrates that the epitaxial $NbN_x$ layer grows in the plane (111) parallel to the sapphire plane (0001). The FWHM value is low and equals 0.02° indicating that most of the planes have minimum deviations from the growth direction [111]. According to the TEM investigation results, the film is also epitaxial. Planes parallel to the substrate surface with no discontinuities within the analyzed area can be seen in Fig. 1 *b*).

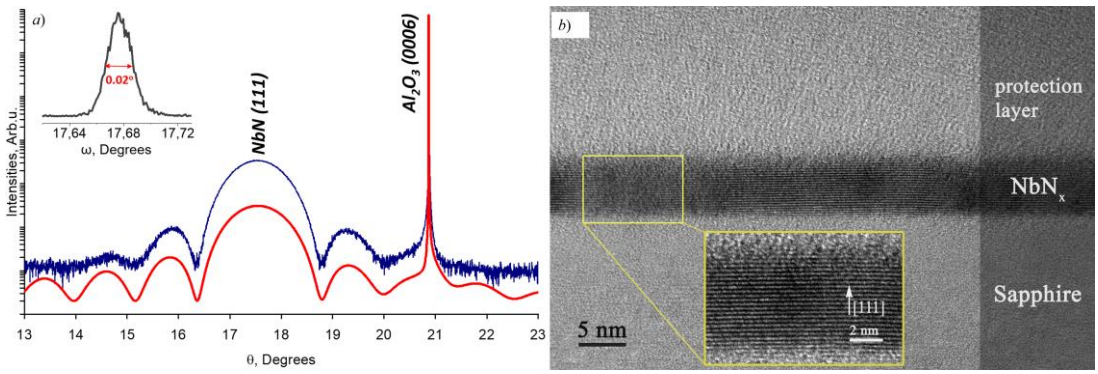


Fig. 1. Experimental scanning curve (ω–2θ) on symmetric reflections (111) $NbN_x$ and (0006) sapphire (blue) and calculated curve for the single crystalline NbN layer 3.8 nm thick (red) (*a*). HRTEM image of $NbN_x$ film (111)/$Al_2O_3$ (0001) (*b*).

The electron diffusion constant was determined with the derivative of critical field value with respect to the temperature taken at T = Tc, according to the expression in the article [7]. We obtained the value of diffusion constant to be 0.6 $cm^2/s$. The coherence length $\xi_{GL}$ at 0 K was determined by the formula from the article [8]. According to the expression, the value of the $\xi_{GL}$ equals to 4.7 nm. The R(T) of epitaxial NbN film in applied perpendicular magnet fields are given in Fig. 2 *a*). The $I_c$ value was 525 μA at a temperature of 4.2 K, which corresponds to the $J_c$ of 5.7 $MA/cm^2$. The temperature dependence of $J_c$ for this bridge is given in Fig. 2 *b*).

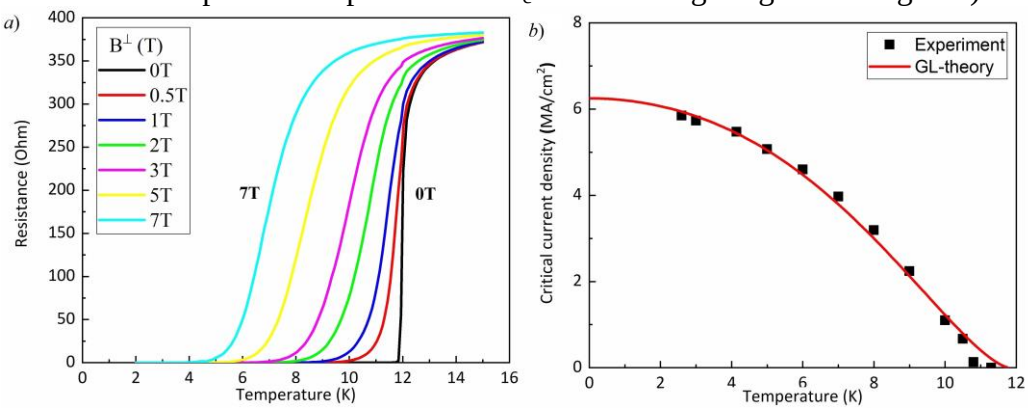


Fig. 2. R(T) of the epitaxial $NbN_x$ film in the perpendicular magnetic field (*a*). Temperature dependence of the $J_c$ in the $NbN_x$ epitaxial film microbridge (*b*).

## Conclusion

We managed to deposit an epitaxial high quality ultrathin $NbN_x$ film on the C-plane sapphire by the ALD method at 350 °C. We also have established the features of epitaxial growth of the $NbN_x$ film we deposited.


## Acknowledgments

The authors would like to acknowledge the support of the Ministry of Science, grant No. 10210610094642-1.2. Fabrication and characterization of the samples were carried out at large scale facility complex for heterogeneous integration technologies and silicon + carbon nanotechnologies.


## REFERENCES


1. **Morozov D. V. et al**. 2021 Contemporary Physics **62**, 2, 69-91.
2. **Divochiy A. et al**. 2008 Nature Photonics **2**, 5, 302-306.
3. **Lobanov** Y. et al. 2014 IEEE Transactions on Applied Superconductivity **25**, 3, 1-4.
4. **Wang G. et al**. 2017 Superconductor Science and Technology **30**, 10, 104001.
5. **You L. et al**. 2013 Aip Advances **3**, 7, 072135.
6. **Yang X. et al**. 2017 IEEE Transactions on Applied Superconductivity **28**, 1, 1-6.
7. **Skocpol W. J**. et al. 1974 Journal of Applied Physics **45**, 9, 4054-4066.
8. **Mourachkine A**. 2004 Journal of superconductivity **17**, 711-724.